2010 BEAM INSTRUMENTATION WORKSHOP PROCEEDINGS VOLUME

FOREWORD

On behalf of the Beam Instrumentation Workshop Program Committee, I am pleased to welcome you to sunny Santa Fe, New Mexico, for the 14th meeting of the Beam Instrumentation Workshop (BIW10). Sponsored by Los Alamos National Laboratory (LANL), this workshop is dedicated to exploring the physics and engineering challenges of beam diagnostic and measurement techniques for charged particle accelerators. The workshops' features include plenary and poster sessions, tutorials, vendor exhibits, multiple opportunities for informal discussions and collaborations, and the 2010 Faraday Cup Award winner presentation.

Some of the continued attributes of the workshop are its small size and continued use of the Web. Furthermore, the BIW10 continues to offer a program that has no parallel sessions so that all of its attendees may observe and interact with all fellow participants. This year, BIW10 has enhanced its relationship with the Joint Accelerator Conference Website (JACoW) by publishing its proceedings only on the JACoW site (http://accelconf.web.cern.ch). Finally, BIW10 continues the tradition established at BIW08 of providing students an opportunity to interact with workshop attendees.

Two new and important events have been added to this year's meeting:

- Expanded opportunities for vendor/attendee interaction through the presentation of Vendor Technical Orals and enhanced vendor participation.
- Technical Question and Answer period during Tuesday's working lunch.

With these new initiatives, the Program Committee hopes to boost the interest in the field of beam diagnostics instrumentation.

The organization of BIW10 has been made possible thanks to the generous support LANL's Engineering and Engineering Sciences Directorate and the Accelerator Operations and Technology Division, and the participants and vendors attending the BIW10.

A special "Thank You" must also be expressed to members of the Local Organizing Committee whose enthusiastic and outstanding efforts made BIW10 a reality.

J. Douglas Gilpatrick
BIW10 Program Committee Chairman
May 2010

Editor's Note: Full video of the tutorial orals may be found on the conference website, http://www.lanl.gov/conferences /biw10
Slides for the tutorials and most other orals are available through JACoW.

DEDICATION

Gary Smith
April 5, 1939–July 16, 2009

Gary Smith and family

The BIW Committee mourns the loss of one of its members, Gary Smith. Gary started at Brookhaven National Lab (BNL) in March 1965 and retired in June 2003.

During his tenure at BNL, he was a highly regarded engineer working on beam instrumentation. Early in his career, he worked on bubble chamber instrumentation, as well as other complex pieces of equipment, such as the horn power supply. In addition, Gary was the supervisor of the "Beamology" Group in the mid 1970s. He participated on the development of systems for AGS, Booster, RHIC, and the Spallation Neutron Source. Gary joined the BIW Committee in the early '90s and co-chaired the 2002 workshop.

Gary was a ham radio operator and enjoyed crossword puzzles and teaching his friends to ski. He liked to backpack and enjoyed taking trips to Rangeley Maine with his wife. Gary is survived by his wife, Rose; children Todd, Beth, and Jennifer; and three grandchildren. He is missed by us all...

Contents

Preface i
Foreword . . . iii
Contents . . . v
Committees . . . ix
Pictures . . . x
MOFNB01 – Femtosecond Resolution Beam Arrival Time Monitor . . . 1
MOFNB02 – Beam Arrival-Time and Position Measurements Using Electro-Optical Sampling of Pickup Signals . . . 7
MOFNB03 – A Winning Tradition: The Faraday Cup Award . . . 17
MOKNB01 – Accelerators at Los Alamos Today . . . 20
MOKNB02 – Looking Beyond LANSCE: The MaRIE Facility . . . 21
MOIMNB01 – Commissioning and First Performance of the LHC Beam Instrumentation . . . 22
MOIMNB02 – The SNS Beam Diagnostics Experience and Lessons Learned . . . 30
MOIANB01 – Operational Performance of LCLS Beam Instrumentation . . . 34
MOCNB01 – Measurement of Lattice Parameters Without Visible Disturbance to User Beam at Diamond Light Source . . . 44
MOCNB02 – Diamond Detectors as Beam Monitors . . . 49
MOCNB03 – Residual Gas X-ray Beam Position Monitor for PETRA-III . . . 53
MOCNB04 – Femtosecond Synchronization of Laser Systems for the LCLS . . . 58
MOVNB01 – Advanced Modular Oscilloscopes and Digitizers Optimized for Accelerator Applications . . . 63
TUTNB01 – Fundamentals Of Logarithmic Amplifiers And Recent Advances . . . 68
TUCNB01 – Sub-nm Beam Motion Analysis Using a Standard BPM with High Resolution Electronics . . . 69
TUCNB02 – APS Beam Stability Studies at the 100-Nanoradian Level . . . 74
TUCNB03 – Cherenkov Ring to Observe Longitudinal Phase Space of a Low Energy Electron Beam Extracted from RF Gun . . . 79
TUVNB01 – COTS Technology for High Energy Physics Instrumentation . . . 84
TUPSM001 – OTR Polarization Effects in Beam-Profile Monitors at the Fermilab A0 Photoinjector . . . 88
TUPSM003 – SNS Target Imaging System Software and Analysis . . . 93
TUPSM005 – Gas Scintillation Beam Profile Monitor at COSY Jülich . . . 98
TUPSM006 – A Non Destructive Laser Wire for H^- Ion Beams . . . 101
TUPSM007 – Multi-Channeltron Based Profile Monitor at the ISIS Proton Synchrotron . . . 106
TUPSM009 – Operational Use of Ionization Profile Monitors at Fermilab . . . 111
TUPSM010 – Residual-Gas-Ionization Beam Profile Monitors in RHIC . . . 116
TUPSM011 – Beam-Energy and Laser Beam-Profile Monitor at the BNL Linac . . . 119
TUPSM012 – Data and Analysis from a Time-Resolved Tomographic Optical Beam Diagnostic . . . 122
TUPSM013 – LANSCE Wire Scanning Diagnostics Device Mechanical Design . . . 127
TUPSM014 – LANSCE Harp Upgrade: Analysis, Design, Fabrication, and Installation . . . 132
TUPSM015 – Resolver-Based, Closed-Loop Position and Velocity Control for the LANSCE-R Wire Scanner 137
TUPSM016 – LANSCE Wire Scanner AFE: Analysis, Design, and Fabrication . . . 141
TUPSM018 – A Statistical Analysis of the Beam Position Measurement in the Los Alamos Proton Storage Ring . . . 146
TUPSM019 – Light Yield, Imaging Properties and Spectral Response of Inorganic Scintillators Under Intense Ion Irradiation . . . 151
TUPSM020 – Beam Induced Fluorescence Monitor–Spectroscopy in Nitrogen, Helium, Argon, Krypton, and Xenon Gas . . . 156
TUPSM023 – Photon Beam Position Measurements by Libera Photon Using Copper Blade Sensors at Soleil Synchrotron . . . 160
TUPSM025 – The Diagnostics' Back-End Platform Based on the In House Developed A|D|A And A|D|O Boards . . . 163
TUPSM026 – Simulation of a Cavity BPM for High Resolution Single-Pass Beam Position Measurements 168
TUPSM027 – New Beam Monitoring Instrumentation at ATF2, KEK . . . 173
TUPSM028 – LCLS Resonant Cavity Beam Position Monitors . . . 177
TUPSM029 – Design and Performance of SSRL Beam Position Electronics . . . 182
TUPSM031 – A Wire Position Monitor System for Superconducting Cryomodules at Fermilab . . . 187
TUPSM032 – High Resolution Cavity BPM for the CLIC Test Facility . . . 189

TUPSM033 – Rogue Mode Shielding in NSLS-II Multipole Vacuum Chambers . . . 194
TUPSM034 – Optimization of Small Aperture Beam Position Monitors for NSLS-II Project . . . 199
TUPSM035 – Concept of Beam Position Monitor with Frequency Multiplexing . . . 201
TUPSM037 – NSLS-II RF Beam Position Monitor . . . 205
TUPSM038 – Status of the Re-Entrant Cavity Beam Position Monitor for the European XFEL Project . . . 210
TUPSM039 – Magnetic Coupled Beam Position Monitor for the FLASH Dump Line . . . 214
TUPSM040 – Commissioning Results and Improvements of the Machine Protection System for PETRA III 218
TUPSM041 – Development of Button Electrodes for SuperKEKB Rings . . . 223
TUPSM042 – Beam Measurements of a Large Solid-Angle Beam Loss Monitor in the APS . . . 228
TUPSM043 – High-Power Hard X-ray Beam Position Monitor Development at the APS . . . 233
TUPSM044 – Bunch-by-Bunch Diagnostics at the APS Using Time-Correlated Single-Photon Counting Techniques . . . 238
TUPSM045 – Numerical Studies of Curtain Gas Jet Generation for Beam Profile Monitoring Applications in the Ultra Low Energy Storage Ring . . . 243
TUPSM046 – Influence of Dark Count on the Performance of Silicon Photomultipliers . . . 247
TUPSM047 – Beam Position Monitor Development for the USR . . . 252
TUPSM048 – Faraday Cup for Low-Energy, Low-Intensity Beam Measurements at the USR . . . 257
TUPSM049 – Measurement, Simulation, and Suppression of APS Storage Ring Vacuum Chamber TE Modes Impacting Vertical BPM Readings . . . 260
TUPSM050 – Studies of APS Storage Ring Vacuum Chamber Thermal Mechanical Effects and their Impact on Beam Stability . . . 265
TUPSM051 – The LHC Fast BCT System: A Comparison of Design Parameters with Initial Performance . 269
TUPSM053 – Analytical Method for Determining Errors in Current Measurements with a Rogowski Coil . 274
TUPSM054 – Monitoring Transverse Beam Profile with Nonuniformly-Wound Toroidal Coils . . . 278
TUPSM057 – Emittance Measurement Wizard at PITZ . . . 282
TUPSM058 – Comparison of Extraction and Beam Transport Simulations with Emittance Measurements from the ECR Ion Source VENUS . . . 287
TUPSM059 – Estimation of Profile Length in Hybrid Ion Beam Tomography . . . 292
TUPSM060 – A Low Energy Ion Beam Pepper Pot Emittance Device . . . 297
TUPSM061 – Emittance Measurements at the LBNL ECR and AECR-U Ion Sources Using a Pepper-Pot Emittance Scanner . . . 302
TUPSM062 – Bunch Length Measurements at the SCSS Test Accelerator toward XFEL/SPring-8 . . . 307
TUPSM063 – Beam Lifetime Measurements with Libera Brilliance . . . 311
TUPSM064 – An FPGA-based Bunch-by-Bunch Tune Measurement System for the APS Storage Ring . . 315
TUPSM065 – Injection Beam Dynamics in SPEAR3 . . . 318
TUPSM066 – LHC Beam Stability and Performance of the Q/Q' Diagnostic Instrumentation . . . 323
TUPSM067 – High Resolution Beam Orbit Measurement Electronics Based on Compensated Diode Detectors . . . 328
TUPSM068 – Improvements for Operational Baseband Tune and Coupling Measurements and Feedback at RHIC . . . 333
TUPSM070 – Dynamically Tuned High-Q AC-Dipole Implementation . . . 338
TUPSM071 – Digital Base-Band Tune Determination . . . 341
TUPSM072 – A Shielded Pick-Up Detector for Electron Cloud Measurements in the CESR-TA Ring . . . 345
TUPSM073 – Tune Measurement System at the ALBA Booster . . . 350
TUPSM074 – Diagnostics During the ALBA Booster Commissioning . . . 353
TUPSM075 – Beam Position Monitors Characterization for ALBA . . . 356
TUPSM076 – First Beam Measurements of the FNAL HINS RFQ . . . 359
TUPSM077 – Bunch-by-Bunch Detection of Coherent Transverse Modes from Digitized Single-BPM Signals in the Tevatron . . . 363
TUPSM080 – 11.424 GHz Stripline Transversal Filter for Sub-Picosecond Bunch Timing Measurements . 367
TUPSM081 – Stable Transmission of Radio Frequency Signals on Fiber Links Using Interferometric Delay Sensing . . . 372
TUPSM082 – Signal Processing for High Precision Phase Measurements . . . 375
TUPSM083 – The LCLS Timing Event System . . . 379
TUPSM084 – The LCLS Undulator Beam Loss Monitor Readout System . . . 384
TUPSM085 – Microwave Link Phase Compensation for Longitudinal Stochastic Cooling in RHIC . . . 389

TUPSM086 – Bunch Arrival Monitor at FERMI@Elettra . . . 394
TUPSM087 – The Copper Free FERMI Timing System: Implementation And Results . . . 398
TUPSM088 – Signal Delay Measurement Method for Timing Systems . . . 403
TUPSM089 – Reliability Tests of the LHC Beam Loss Monitoring FPGA Firmware . . . 408
TUPSM090 – Results of Background Subtraction Techniques on the Spallation Neutron Source Beam Loss Monitors . . . 412
TUPSM091 – Modeling the Optical Coupling Efficiency of the Linac Coherent Light Source Beam Loss Monitor Radiator . . . 415
TUPSM093 – New Electron Beam Diagnostics in the FLASH Dump Line . . . 420
TUPSM095 – Multi-Channel Magnet Power-Supply Ramp Controller for the IUCEEM ALPHA Synchrotron/Storage Ring with Channel Access . . . 425
TUPSM096 – Final Focus Ion Beam Intensity from Tungsten Foil Calorimeter and Scintillator in NDCX-I . . . 429
TUPSM097 – ADC Considerations and Analysis for Band Pass Sampling Systems . . . 434
TUPSM098 – NSLS-II Injector System Diagnostics . . . 437
TUPSM099 – Beam Instrumentation Requirements for the HINS Program at Fermilab . . . 442
TUPSM100 – PHIL Accelerator at LAL - Diagnostics Status . . . 446
TUPSM101 – Design Status of the Diagnostic System for the Taiwan Photon Source Project . . . 449
TUPSM102 – Diagnostics Update of the Taiwan Light Source . . . 454
TUPSM103 – Recent Upgrade of the PITZ Facility . . . 459
TUPSM104 – Beam Based Monitoring of the RF Photo Gun Stability at PITZ . . . 464
TUPSM108 – Slow Orbit Feedback at RHIC . . . 469
TUPSM109 – NSLS2 Transverse Feedback System Design . . . 473
TUPSM110 – Synchrotron Light Monitor System for NSLS-II . . . 478
TUPSM112 – Continuous Bunch-by-Bunch 16-bit Data Acquisition using DDR2 SDRAM Connected to an FPGA . . . 483
TUPSM113 – Achieving High-Speed Data Acquisition for Real-Time Beam Control and Measurement . . . 487
WETNB01 – Tuning the Beam: a Physics Perspective on Beam Diagnostic Instrumentation . . . 491
WEIMNB01 – Ion Beam Properties and their Diagnostics for ECR Ion Source Injector Systems . . . 498
WEIMNB02 – An Instrumentation Wish List for High Power/High Brightness ERLs . . . 506
WEIANB01 – LANSCE Beam Instrumentation and the LANSCE Refurbishment Project . . . 516
WEIANB02 – Development of Beam Current Monitor with High Tc SQUID at RIBF . . . 523
WECNB01 – Overview of E-XFEL Standard Electron Beam Diagnostics . . . 533
WECNB02 – Electro Optical Sampling of Coherent Synchrotron Radiation for Picosecond Electron Bunches With Few pC Charge . . . 538
WECNB03 – Beam Halo Imaging Using an Adaptive Optical Mask . . . 543
WEDNB01 – DITANET Contributing to State-of-the-Art Diagnostics Developments . . . 548
THTNB01 – Beam Loss Monitors (BLMs): Physics, Simulations and Applications in Accelerators . . . 553
THIMNB01 – Highlights from DIPAC 2009 . . . 566

Appendices **573**
List of Authors . . . 573
Institutes List . . . 579
Participants List . . . 585

COMMITTEES

2010 Beam Instrumentation Workshop Program Committee (PC)

Doug Gilpatrick, LANSCE/LANL, Chairman
Ken Jacobs, SRC/U. Wisconsin
Rhodri Jones, CERN
Kevin Jordan, TJNAF
Bob Lill, ANL
Ralph Pasquinelli, FNAL
Tom Russo, BNL
Fernando Sannibale, LBNL
Jim Sebek, SLAC/Stanford
Tom Shea, SNS/ORNL
Om Singh, BNL
Steve Smith, SLAC/Stanford
Hitoshi Tanaka, Spring-8/RIKEN
Bob Webber, FNAL
Jonah Weber, LBNL
Michelle Wilinski, BNL
Jim Zagel, FNAL

The attending PC and some LOC members at the Fall BIW10 meeting included (first row) Steve Smith, Linda Zwick, Bob Webber, Tom Shea, Kevin Jordan, and Tom Russo; (second row) Jim Sebek, Doug Gilpatrick, Om Singh, Jonah Weber, Jim Zagel, and Hitoshi Tanaka; (third row) Bob Hettel and Rod McCrady.

2010 Beam Instrumentation Workshop Local Organizing Committee (LOC)

LOC Chairman: Doug Gilpatrick
LOC Co-Chairman: Rod McCrady
DARHT Facility Coordinator: Trent McCuistian
Workshop Primary Administrator: Linda Zwick
Workshop Support Administrators: Cecilia Duenas, Jean N. Trujillo
Web Site Designer/Developer: Rich Young/Brittany Somers
Web Site Content Development & Administration: Connie Russell
Proceedings Editors: Clay Dillingham; Joe Chew (LBNL)
Technical Q&A Coordinator: John Power
Vendor Coordinator: James Sedillo
Poster Session Coordinator: Fermin Gonzales
Workshop Photographer: Derwin Martinez

Group photo taken on Monday in front of the Cathedral Basilica of St. Francis of Assisi. The original full name of the city was La Villa Real de la Santa Fé de San Francisco de Asis, or "Royally Chartered City of the Holy Faith of St. Francis of Assisi." The church is at the east end of the Plaza, near La Fonda, the conference venue.

Sunday

Registration and reception

EXIT
2010
Beam
Instrumentation
Workshop
Registration

LA TERRAZA

Monday

Faraday Cup Award

*Julien Bergoz (*far left*), representing Award sponsor Bergoz Instrumentation, and BIW10 chair Douglas Gilpatrick (*far right*), of Los Alamos National Laboratory, with co-winners Kirsten Hacker of DESY and Florian Loehl of CLASSE.*

Keynote Address

Kevin Jones, Director for Accelerator Science and Technology at Los Alamos, looks beyond LANSCE to the MARIE Facility.

Registration and reception

Exhibits and orals

Scenes from Monday's vendor reception

GMW
INSTRUMENTATION
Magnetic • Current • Fiber-Optic
CAEN
Tools for Discovery
Magnetic Metals
Our Plant Locations
Cut Cores

Tuesday

The first tutorial (Barrie-Gilbert on logarithmic amplifiers) began the day's oral program.

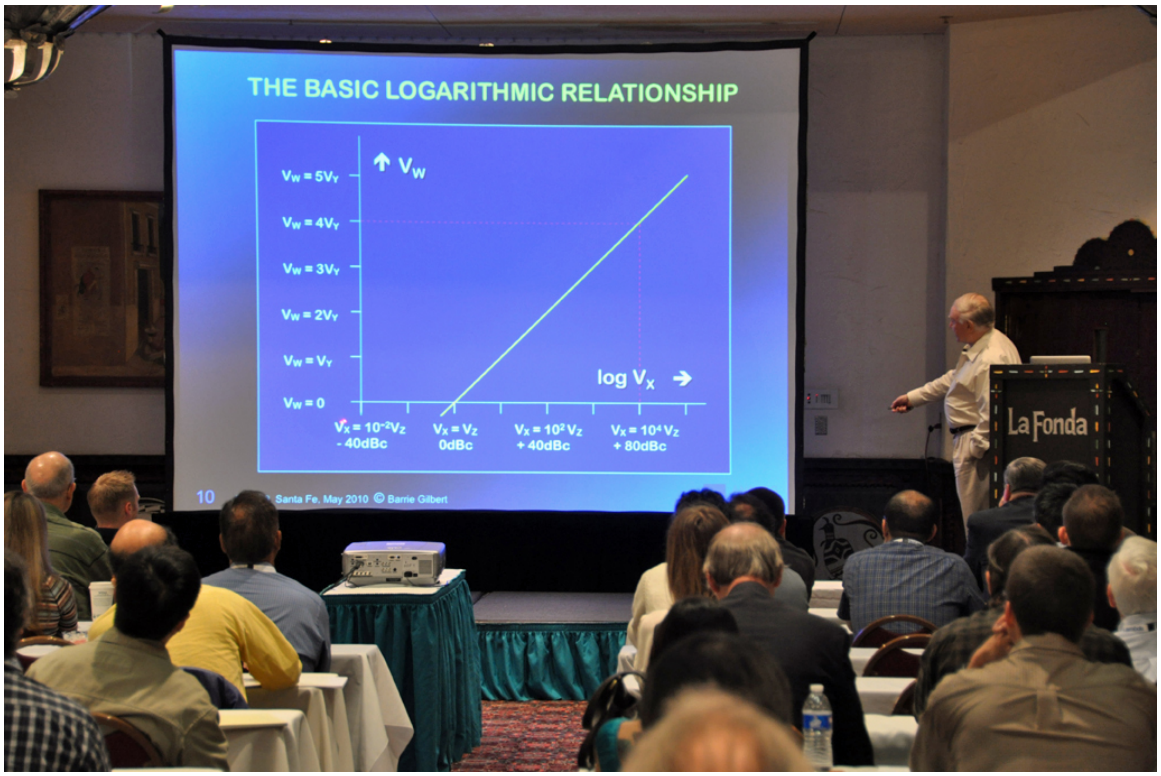

In the afternoon, a poster session in a setting of folk-art décor, plus vendor exhibits and a vendor technical oral…

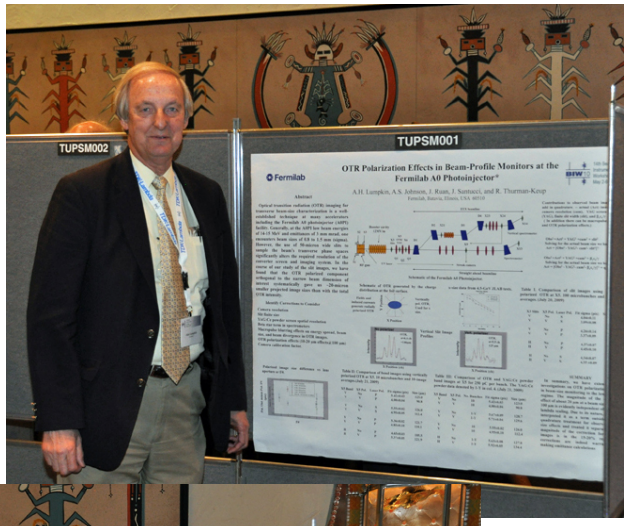

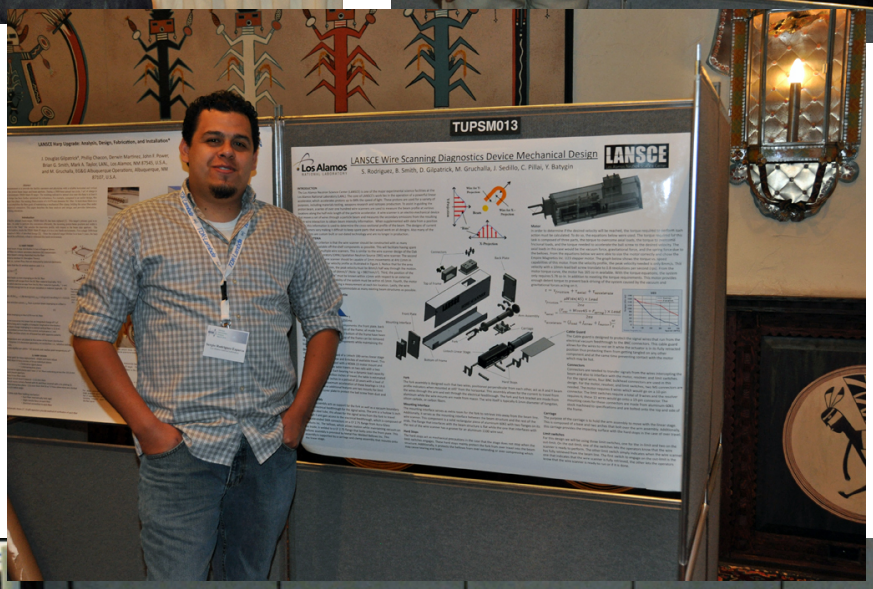

…and a technical Q&A session (chair: R.C. McCrady, LANL) over a working lunch.

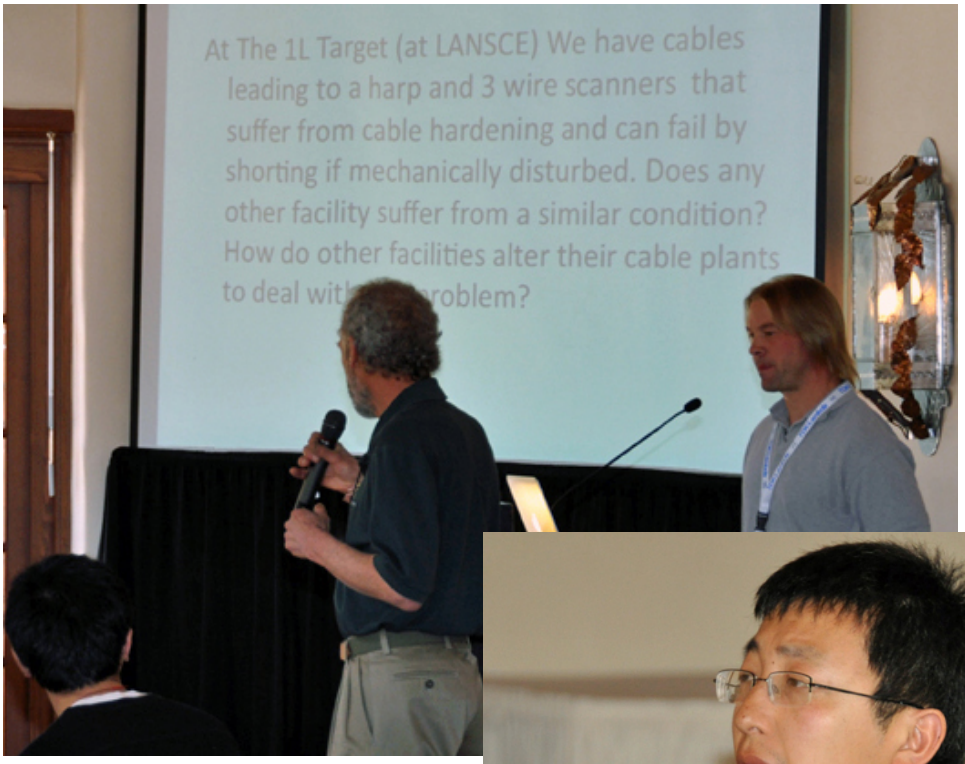

Wednesday

A tutorial oral in a handsome setting began the day's program…

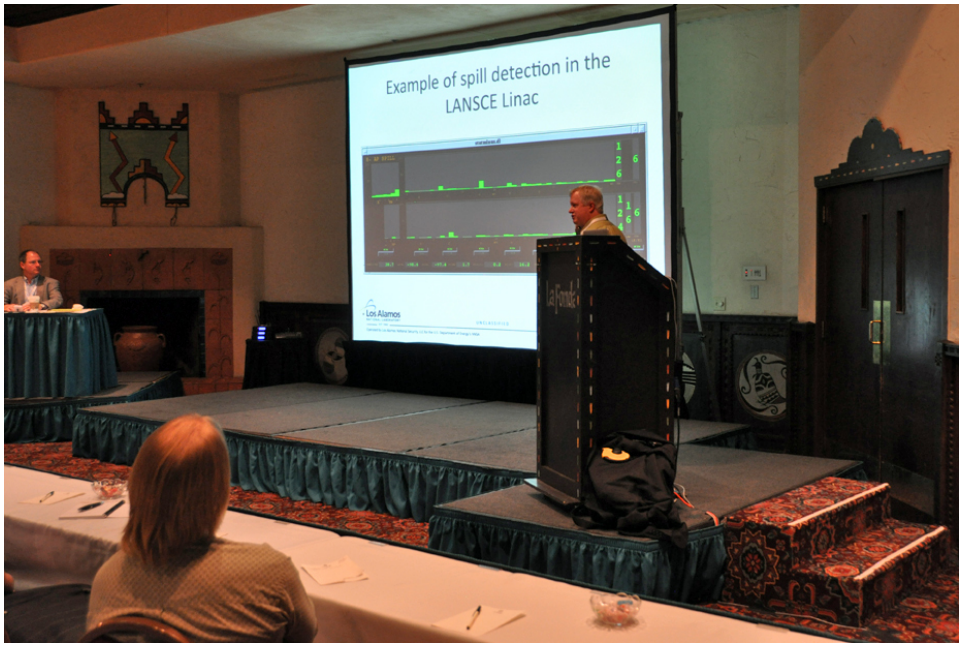

…a day that ended with a banquet at La Terraza.

The evening of the banquet featured a performance by Mariachis Sonidos del Monte.

Thursday

A tutorial oral on beam loss monitors began the day's oral program, which ended with a look forward to BIW12 (April 16-19, Marriott City Center, Newport News, VA).

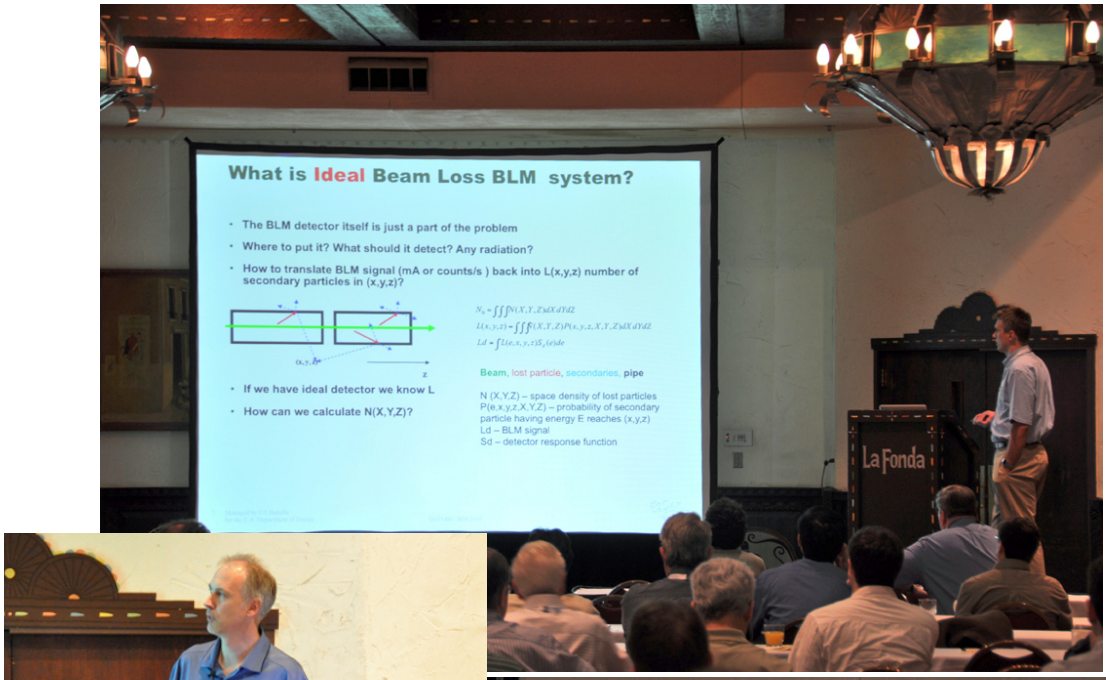

All aboard! After the last session on Thursday came a tour of the Los Alamos Neutron Science Center (LANSCE), a linac-based center that supports three user facilities.

A lecture about the facility…

…and about the experimental area

Drift-tube linac

RF gallery

Switchyard

Control room

Making It Happen

Some of the many people behind the scenes..

Cecelia Duenas of Los Alamos performed roles including editing

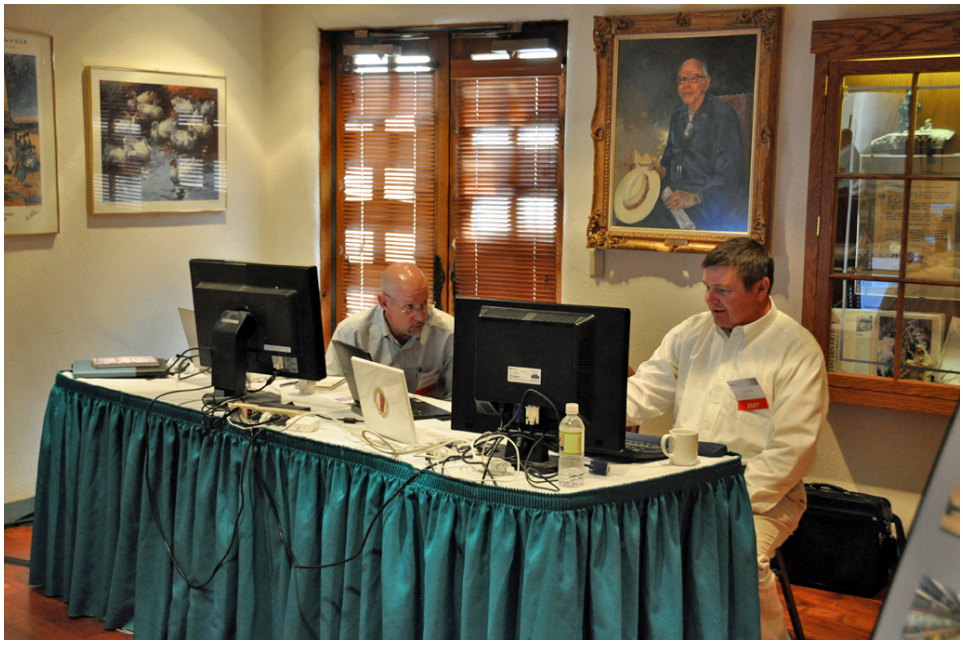

Co-editors Clay Dillingham (l.) of Los Alamos and Joe Chew of Berkeley Lab

Jean Trujillo of Los Alamos at the business desk

Peggy Vigil of Los Alamos (l.), working the registration desk, enjoys a visit from Lorie Woodmansee of La Fonda.

(l-r) Conference administrator Linda Zwick, Peggy Vigil, and Doug Gilpatrick

FEMTOSECOND RESOLUTION BUNCH ARRIVAL TIME MONITOR

F. Loehl[#*], Cornell University, Ithaca, New York, USA

Abstract

A need for femtosecond resolution beam arrival time measurements has arisen with the transition from many-picosecond-long bunches in ring-based accelerators to a few femtosecond-long bunches in high-gain free-electron lasers. Here we present an electro-optical detection scheme that uses the signal of a beam pick-up to modulate the intensity of a femtosecond laser pulse train. By detecting the energies of the laser pulses, the bunch arrival time can be deduced. We tested this scheme by distributing a laser pulse train to two locations in the FLASH linac, separated by 60 m, using length-stabilized optical fibers. By measuring the arrival times of the same electron bunches at these two locations, we determined an rms bunch arrival time resolution of 6 fs. This unprecedented monitor resolution allowed us to reduce the beam arrival time jitter from almost 200 fs down to 25 fs with an intra-bunch train feedback. In combination with a beam pick-up with a position dependent time-response, the same electro-optical detection scheme can be applied for micrometer resolution beam position measurements.

INTRODUCTION

High-gain free-electron lasers (FELs) operating in the soft and hard x-ray regimes are capable of generating light pulses with durations below 10 fs [1,2]. Even shorter light pulse durations are envisioned using schemes in which a part of the electron bunch is manipulated using a few cycle laser pulse (see, e.g., [3,4]).

In order to take full advantage of the sub-10-fs light pulses presently available (e.g., in two-color pump-probe experiments), precise measurements and eventually control of the electron bunch arrival time are required. The desired measurement resolution is on the same order as the photon pulse duration–ideally, a small fraction of it. The abovementioned manipulation schemes as well as FEL seeding schemes require a stable longitudinal overlap between the electron bunch and the laser pulse. Many of these schemes require a timing stability between the laser pulses and the electron bunches of around 30 fs or better.

In this work we present electro-optical synchronization schemes which allow for a bunch arrival-time measurement and stabilization with the before-mentioned resolution.

OPTICAL SYNCHRONIZATION SYSTEM

In collaboration with F.X. Kaertner's group at MIT, we developed an optical synchronization system to address the stringent timing requirements of FELs. Figure 1 depicts the schematic principle of the system. A mode-locked laser – the master laser oscillator (MLO) – is used as a time-reference. Its laser pulse train is distributed to the remote locations via length-stabilized optical fibers, where the respective subsystems are synchronized to the time-markers provided by the laser. These subsystems can, for example, be laser systems, which can be synchronized by optical cross-correlation techniques [5,6]; RF systems (for schemes on how to extract stable RF signals from the optical pulse train, see, e.g., [7,8]); or beam diagnostics systems such as the bunch arrival-time monitor discussed in this paper.

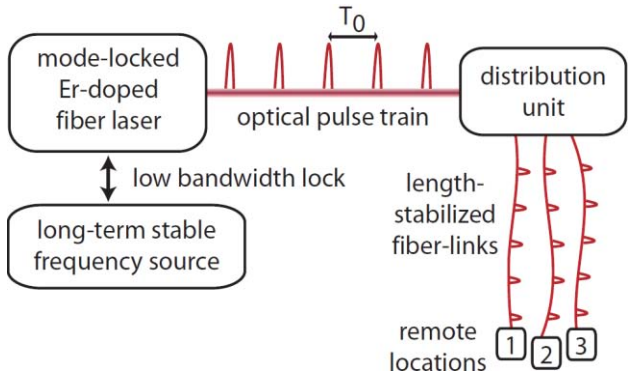

Figure 1: Schematic principle of the optical synchronization system [11].

Master Laser Oscillator

We used an erbium fiber laser operating in the soliton regime as the MLO [9,11]. It produces a train of sub-100 fs long laser pulses and operates at a repetition rate of 216.7 MHz, which is the sixth sub-harmonic of the 1.3 GHz frequency of the superconducting TESLA-type cavities used at FLASH. In order to compensate for length changes of the laser resonator due to thermal expansion or contraction, as well as due to microphonics, the laser repetition frequency is locked to a long-term stable RF oscillator. The phase lock loop (PLL) stabilizes the laser repetition rate up to frequencies of several kHz using a digital feedback loop acting on a fast piezo-mirror inside of the laser resonator. Laser timing changes occurring at frequencies larger than a few kHz are very small–significantly less than 10 fs [11]–and therefore do not need active correction. When all critical timing signals are derived from the MLO, slow timing changes below a few kHz are not critical for most applications, since most subsystems are able to follow these timing changes at a sufficiently high rate. The accuracy of the PLL is therefore not of highest importance. In our case, the timing jitter between the laser and the RF source was around 40 fs. The long-term frequency stability of the RF source is, however, of great importance when fiber links of different lengths are used. The reason is that the electron beam travel time between two locations in the

previously at DESY, Hamburg, Germany
* florian.loehl@cornell.edu

accelerator is defined by the speed of light, which is thought to be a constant, while, as we will see later, the length of the fiber links depends on the laser frequency. For a length difference of 100 m between two fiber links, a frequency change of $\Delta f / f = 10^{-8}$ causes a timing shift of around 5 fs [11]. While this can still be achieved by common quartz oscillators, large accelerators with length differences of a few kilometers between the fiber links will require an RF source with better long-term stability– for example, a clock based on a rubidium standard.

Fiber-Link Stabilization

In order to distribute the time-reference signal of the MLO without deteriorating its stability, active stabilization of the fiber link is required to in order compensate for optical length changes of the fiber blank?– for example, due to thermal effects, vibrations, or changes in the air humidity, which affect the mechanical properties of the fiber coating.

To measure the optical length of the fiber with femtosecond precision, we developed the scheme depicted in Fig. 2. Here, laser pulses from the MLO are transmitted through a dispersion compensated optical fiber. At the end of the fiber, the optical pulse train is amplified in an erbium-doped fiber amplifier, which is optimized to add a minimum amount of timing jitter to the optical pulse train [10]. While part of the laser intensity is then used for synchronization purposes, another part of the intensity is reflected by a Faraday rotating mirror and sent back to the MLO using the same optical fiber. There, the returning laser pulses are combined with pulses coming directly from the laser. In a balanced optical cross-correlator, based on a single periodically poled KTP crystal, the temporal overlap between both pulse trains is measured with sub-femtosecond resolution and length changes are compensated for with a feedback loop acting on a piezo fiber stretcher and an optical delay stage [11,12,13].

For configurations that do not require the ultimate resolution provided by the previously described scheme, we also developed an RF based scheme to detect the overlap between two optical pulse trains [14].

BUNCH ARRIVAL TIME MONITOR

A major difficulty with bunch arrival-time measurements at various locations within the accelerator against a common time reference–the transport of the reference signals–can be overcome with the system described earlier. In order to avoid deteriorating the precise timing information provided by the optical fiber links, an ideal bunch arrival-time detection scheme should directly use the laser pulses from the fiber links, and should not require any additional conversion process (e.g., from the optical signal to an RF signal) between the arrival time monitor and the fiber link.

We developed such a scheme, which uses a commercial Mach-Zehnder-type electro-optical modulator (EOM) as a key component. This is shown in Fig. 3. The modulator is driven by the transient voltage signal that the electron bunches induce in a beam pick-up. In order to be able to observe both destructive and constructive amplitude modulation, a constant phase shift is applied between both arms of the Mach-Zehnder interferometer by an additional bias voltage. The arrival-time of a reference laser pulse is adjusted such that it coincides with the zero-crossing of the pick-up signal for the nominal bunch arrival time. Variations of the electron bunch arrival time lead to variations of the modulation voltage experienced by the reference laser pulse. By detecting the amplitude of this reference laser pulse, the bunch arrival time can then be derived. This bunch arrival-time monitor (BAM) scheme was first proposed in [15].

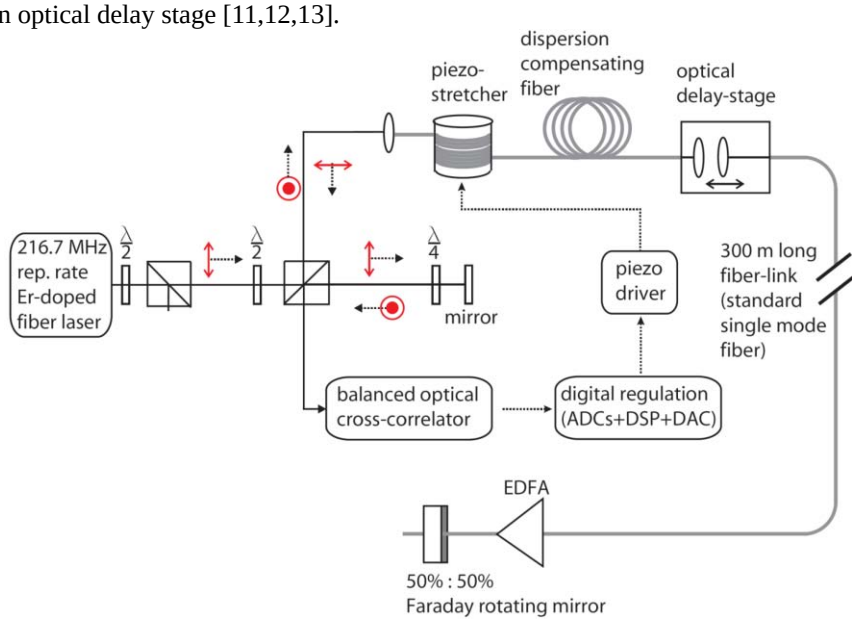

Figure 2: Principle of the fiber-link length stabilization based on an optical cross-correlator [11,12,13].

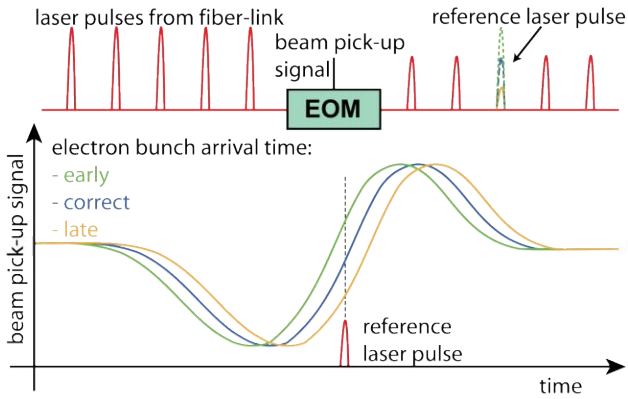

Figure 3: Principle of the bunch arrival-time monitor (BAM) [16,17].

The experimental setup of the first BAM prototypes used at FLASH is depicted in Fig. 4. The light pulses are sent through an optical delay line in which the temporal overlap between the laser pulses and the zero-crossing of the beam pick-up signal can be established. A slow feedback loop acting on the delay line ensures that the sampling time remains at the pick-up signal's zero-crossing even when the arrival-time of the electron beam changes. For that purpose and also to calibrate the BAM, the delay stage is equipped with an absolute position encoder. The beam arrival-time is then determined from the combination of the delay line position and the laser pulse amplitude after the EOM.

After the laser beam passes the first optical delay stage, a small fraction of the intensity is split and used to generate a sub-picosecond stable sampling clock for a 16 bit ADC which operates at a sampling frequency of 108 MHz (half the laser repetition rate). The remaining light is split a second time and sent to EOM1, which provides a high resolution bunch arrival-time measurement. To protect the EOM from damage, the beam pick-up signal is limited to ±5V by using a broadband limiting diode (> 26 GHz bandwidth). Since the dynamic range of this measurement is limited to around 5 ps, a second EOM is installed and driven by a strongly attenuated pick-up signal. A second optical delay stage is used to adjust the timing with respect to the first high resolution measurement.

The modulated laser pulse trains are detected with photo detectors, and in order to allow for a precise detection of the laser pulse energies, each photo detector signal is sampled by two ADCs in a particular way: one ADC samples the base line and another samples the peak of the detector signal. A large ADC analog bandwidth of around 700 MHz allows for a clean detection of single laser pulse energies.

In order to reduce the influence of laser amplitude variations as well as of noise and disturbances from electro-magnetic interferences on the beam pick-up signal, the energy of the laser pulse, which was modulated by the electron bunch, is normalized to the energy of a previous laser pulse, which arrives prior to the electron bunch. This scheme acts like a high-pass filter and strongly suppresses all disturbances from DC to frequencies of several MHz.

For bunch arrival-time measurements, a dependence of the beam pick-up signal on the position of the electron beam is undesirable and, therefore, a BPM-like button pick-up is utilized [18]. The beam position dependence is further reduced by combining the two horizontal and vertical signals, before sending them to the EOMs [11].

Figure 5 shows the normalized laser pulse energy as a function of the delay between the laser pulse arrival-time and the zero-crossing of the beam pick-up signal. The blue and the red curve show the high resolution signal of two independent bunch arrival-time monitors. The green curve depicts the response of the coarse measurement, in which the beam pick-up signal is attenuated by 26 dB.

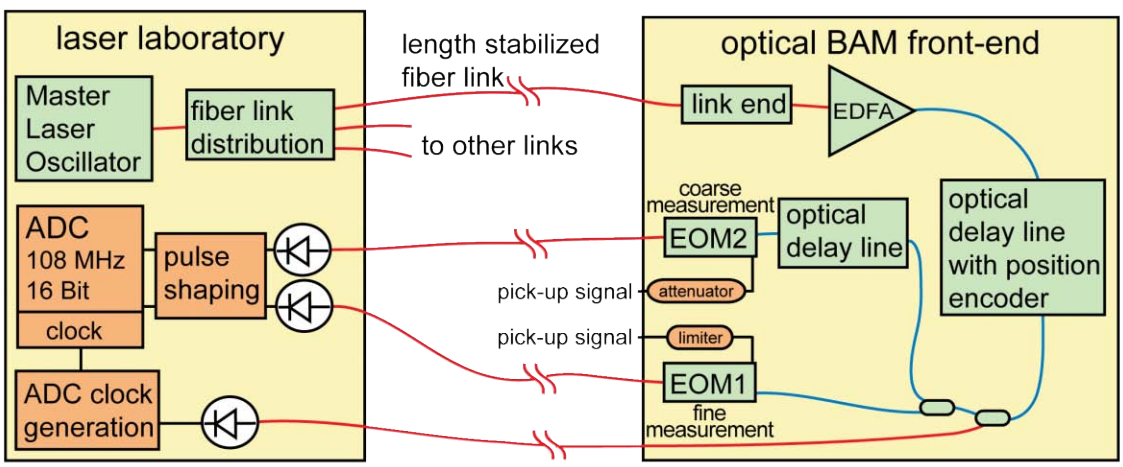

Figure 4: Simplified experimental setup as used for the first BAM prototypes at FLASH [11,17].

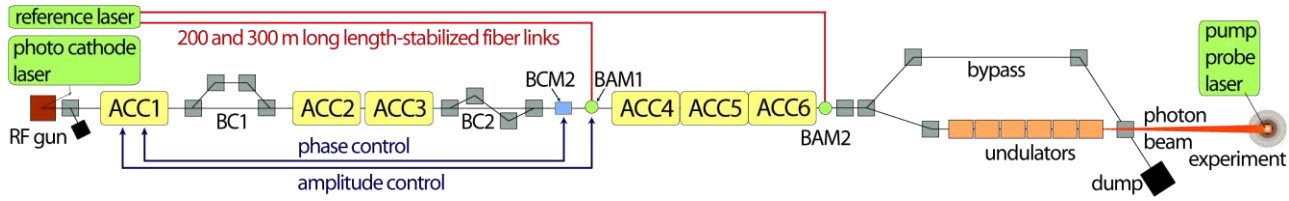

Figure 6: Installation of the BAMs in the FLASH accelerator for BAM resolution measurements. The feedback path for initial bunch arrival-time and bunch compression feedbacks is indicated as well (adapted from [16]).

While the coarse measurement nicely resembles the signal from the button pick-up, the two high resolution measurements show an over-rotation at very high and low modulation voltages which are caused by a phase shift of larger than 180° between both arms of the Mach-Zehnder interferometer in the EOM.

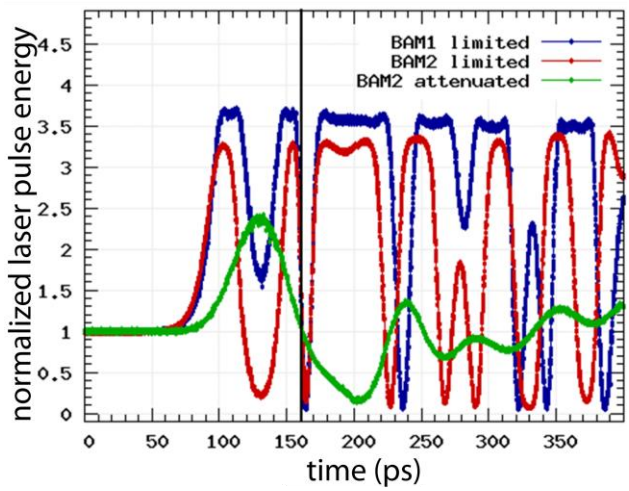

Figure 5: Normalized laser pulse energy as a function of the delay between laser pulse arrival and beam pick-up zero-crossing. The operating point is indicated as a dashed line and corresponds to an unmodulated laser pulse ([11]).

BAM Resolution

The resolution of the bunch arrival-time monitors can be evaluated from the precision with which the laser pulse energies are determined (since only a small fraction of the laser pulses is modulated by the electron beam, this value is available at all times without the need for interrupting the arrival-time measurements), and the steepness with which the normalized pulse energy changes with the delay between laser pulse and beam pick-up zero-crossing. A resolution as good as 3-5 fs could be determined for optimized settings.

In order to verify this resolution, two BAMs have been installed in a straight section of the FLASH accelerator, separated by 60 m. Each BAM was supplied by laser pulses from its own stabilized fiber link (see Fig. 6). By measuring the arrival-times of the same electron bunches with both monitors, the BAM resolution can be determined. Figure 7 shows the outcome of this measurement. The top graph presents the beam arrival-time variations measured by both monitors. The bottom graph represents the difference between both measurements. The rms noise of this difference signal is 8.4 fs, which shows that the resolution of a single BAM together with the stability of its fiber link is 6 fs or better, measured in the frequency range of around [0.00167 Hz, 15-20 GHz]. The higher cut-off frequency is determined by the bandwidth of the beam pick-up, the combiner, limiter, and the EOM.

Initial measurements on the long-term stability could be carried out yielding BAM resolutions of around 9 fs over a duration of 1.5 hours and 14 fs over a duration of 4.5 h. Since we observed steps in the difference signal between both BAMs during these long-term measurements, we believe that this is caused by changes in the electron bunch shape due to machine tuning, and slightly different response characteristics of the beam pick-ups used in both BAMs. This inherent interdependence of the BAMs on the longitudinal shape will be greatly attenuated by the linearized compression scheme (also used at LCLS) that is currently being commissioned at FLASH, which removes the picosecond-long tails in the charge distribution.

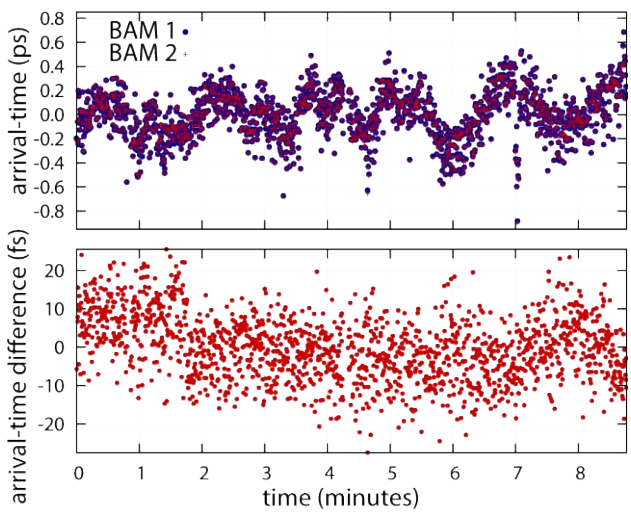

Figure 7: Electron bunch arrival time as measured with two independent BAMs. Top: readings of both BAMs. Bottom: difference signal of both BAMs (from [16]).

Bunch Arrival Time Feedback

The precise arrival-time information provided by the BAMs in combination with the ease of the required data processing makes the BAM an ideal tool for fast bunch arrival time feedbacks. The feedback scheme as depicted in Fig. 6 has been implemented at FLASH and has allowed for the stabilization of the bunch arrival-time as well as of the bunch compression process within the up to 800 µs long bunch trains. The arrival-time stability could be improved from around 180 fs to 25 fs for the later bunches in the bunch train (see [16,19,20] for more details).

Beam Position Measurements Using Electro-Optical Detection Scheme

Initial arrival time measurements have been performed with a ring-type beam pick-up, the signal of which possessed a very strong dependence on the electron beam orbit. By measuring the arrival-time of the pick-up signals at both sides of the pick-up, a measurement of the horizontal beam orbit with a 3 µm resolution was possible in addition to a precise bunch arrival-time measurement [15]. In combination with a transversely mounted strip-line pick-up, this scheme is planned to be used in the bunch compressor chicanes of FLASH to allow for measurements of the horizontal beam position with micrometer resolution over a many centimetre large dynamic range [21].

SUMMARY

A novel electro-optical detection scheme for femtosecond resolution bunch arrival time measurements was presented. In combination with an optical synchronization system, the arrival time with respect to a common time reference can be measured at distributed locations within the accelerator with a precision of better than 10 fs. This arrival time monitor provides a great tool to time-stamp events for pump-probe experiments and, due to its simplicity, can be used in fast feedback loops to stabilize the bunch arrival-time. In initial experiments we were able to improve the arrival-time stability from 180 fs to 25 fs with such a feedback.

Since the electro-optical detection scheme only requires a fast electrical transient, several other applications in addition to bunch arrival-time measurements are possible. One such application is a beam position measurement in bunch compressor chicanes with a several centimeter large dynamic range while delivering micrometer resolution [21]. Even more applications based on this scheme are imaginable, for example a laser arrival-time detection using the signal of a fast photo detector to drive the EOM, or a high resolution phase detection of RF signals.

ACKNOWLEDGEMENTS

At the first place, the author would like to thank Holger Schlarb, who initiated the concept of the bunch arrival-time monitor and the optical synchronization at FLASH. Many thanks also go to the colleagues of the optical synchronization team, who helped with endless discussions and precious ideas: Vladimir Arsov, Matthias Felber, Kirsten Hacker, Frank Ludwig, Sebastian Schulz, Axel Winter, and J. Zemella. Additional thanks go to Bernhard Schmidt and Joerg Rossbach for the great support and advice, as well as to the technicians of the FLA group without whom the realization of this project would not have been possible. Finally, Jaroslaw Szewinski's support of the FPGA firmware for the BAM ADCs was highly appreciated.

REFERENCES

[1] Y. Ding *et al.*, SLAC-PUB-13525, SLAC, 2009
[2] W. Ackermann *et al*., Nature Photonics **1**,p. 336 (2007).
[3] E.L. Saldin, E.A. Schneidmiller, and M.V. Yurkov, Optics Communications **237**, p. 153 (2004).
[4] A. A. Zholents and W. M. Fawley, Phys. Rev. Lett. **92** 224801 (2004).
[5] T. R. Schibli *et al.*, Opt. Lett. **28**, p. 947 (2003).
[6] S. Schulz *et al.*, "All-optical synchronization of distributed laser systems at FLASH", PAC 2009 Conference, Vancouver, Canada, 4-9 May, 2009.
[7] J. Kim *et al.*, Nature Photonics **2**, p. 733 (2008).
[8] M. Felber *et al.*, "Long-term femtosecond stable RF signal generation from optical pulse trains", PAC 2009 Conference, Vancouver, Canada, 4-9 May, 2009.
[9] J. Chen et al, Opt. Lett. **32**, p. 1566 (2007)
[10] F. Loehl *et al*., "Influence of Erbium-doped fiber amplifiers on the timing stability of optical pulse trains", CLEO 2008 Conference, San Jose, California, 4-9 May 2008.
[11] F. Loehl, "Optical synchronization of a free-electron laser with femtosecond precision", DESY-TESLA-FEL-2009-08 and DESY-Thesis-2009-031, 2009
[12] J. Kim *et al.*, Opt. Lett. **32**, p. 1044 (2007).
[13] F. Loehl *et al.*, "Sub-10 femtosecond stabilization of a fiber link using a balanced optical cross-correlator", PAC 2007 Conference, Albuquerque, New Mexico, USA, 25-29 June 2007.
[14] J. Zemella et al., "RF-based detector for measuring fiber length changes with sub-5 femtosecond long-term stability over 50 h", FEL 2009 Conference, Liverpool, England, 23-28 August 2009.
[15] F. Loehl *et al*., "A sub-100 fs electron bunch arrival time monitor system for FLASH", EPAC 2006 Conference, Edinburgh, Scotland, 26-30 June 2006.
[16] F. Loehl *et al*., Phys. Rev. Lett. **104** 144801 (2010)
[17] F. Loehl *et al*., "A sub-50 femtosecond bunch arrival time monitor system for FLASH", DIPAC 2007 Conference, Venice, Italy, 23-25 May 2007.
[18] K. Hacker *et al*., "Beam pick-up designs suited for an electro-optical sampling technique", FEL 2006 Conference, Berlin, Germany, 2006.

[19] F. Loehl *et al*., "Measurement and Stabilization of the Bunch Arrival Time at FLASH", EPAC 2008 Conference, Genoa, Italy, 2008.
[20] F. Loehl *et al*., "Observation of 40 fs synchronization of electron bunches for FELs", FEL 2008 Conference, Gyeongju, Korea, 2008.
[21] K. Hacker *et al*., "Demonstration of a BPM with 5 micron resolution over a 10 cm range", FEL 2009 Conference, Liverpool, England, 2009.

BEAM ARRIVAL-TIME AND POSITION MEASUREMENTS USING ELECTRO-OPTICAL SAMPLING OF PICKUP SIGNALS

K. Hacker,* DESY, Hamburg, Germany

Abstract

By using magnetic chicane bunch compressors, high-gain free-electron lasers are capable of generating femtosecond electron bunches with peak currents in the kilo-ampere range. For accurate control of the longitudinal dynamics during this compression process, high-precision beam energy and arrival-time monitors are required. Here we present an electro-optical detection scheme that uses the signal of a beam pickup to modulate the intensity of a femtosecond laser pulse train. By detecting the energies of the laser pulses, the arrival-time of the pickup signal can be deduced. Depending on the choice of the beam pickup, this technique allows for high-resolution beam position measurements inside of magnetic chicanes and/or for femtosecond-resolution bunch arrival-time measurements. In first prototypes we realized a beam position monitor with a resolution of 3 μm (rms) over a many-centimeter dynamic range and a bunch arrival-time monitor with a resolution of 6 fs (rms) relative to a pulsed optical reference signal.

INTRODUCTION

A beam arrival-time stability of ~30 fs rms (~10 μm at v=c) is desired for pump-probe experiments and is mandatory for laser-based electron beam manipulation at FLASH and the European XFEL [1]. Arrival-time jitter in these FELs is primarily created by energy-dependent path-length changes in the magnetic bunch compressor chicanes. The first bunch compressor of the FLASH linac is shown below in Fig. 1 with the orbit for an R_{16} = 350 mm and R_{56} = 620 ps plotted in green. The locations of beam pickups used for measuring the beam arrival-time and position are indicated with yellow stars.

With the accelerating RF gradient stability of 10^{-4} at FLASH, the transverse position jitter in the dispersive section of the first chicane becomes 35 μm and the longitudinal position jitter becomes 18 μm. A beam-based monitor for an RF gradient feedback system should be able to measure the beam energy by a factor of three better than the desired energy stability of $5*10^{-5}$ and this means that the resolution for a beam position measurement in the chicane must be better than 6 μm and a longitudinal time-of-flight path-length measurement should resolve 3 μm. Each measurement must have a many-centimeter range in order to accommodate different machine configurations.

Devices meeting these requirements were made possible through a technique that involves sampling the zero-crossings of electrical beam pickup signals with short laser pulses. The 20-200 fs pulses from a mode-locked erbium-doped fiber laser are sent over actively length-stabilized fiber links to distant end-stations, whereupon the amplitudes of the laser pulses are modulated by the amplitudes of the beam pickup signals with a commercially available electro-optical modulator. The modulated laser pulses then impinge upon a photodetector, and the amplitude of the photo-detector signal is recorded with an ADC, which is clocked with a signal generated from the very same laser pulse train. These sorts of measurements are vital for the pulsed optical synchronization system at FLASH and the beam-based energy and timing feedbacks upon which it relies.

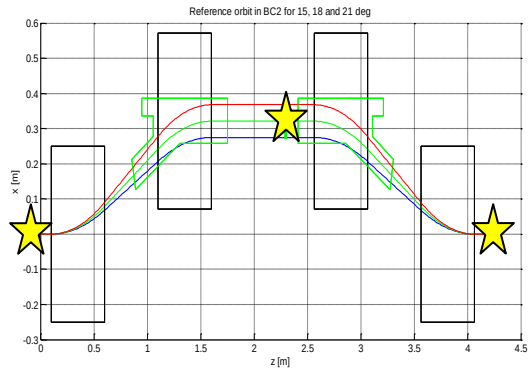

Figure 1: First magnetic bunch compressor chicane at FLASH. Dipoles are drawn in black, the vacuum chamber is drawn in green, and the locations of pickups for beam arrival-time and position measurements are indicated by yellow stars. Higher- and lower-energy particle beams travel a longer or shorter path-length through the chicane, affecting the beam arrival time after the chicane.

This technique has been verified with two types of pickups. Using two sets of broadband, button-like pickups separated by 60 m in a drift section, two independent measurements of the beam arrival-time were conducted, verifying the 6 fs (rms) resolution of the method [2,3]. In another experiment, involving a transversely mounted stripline pickup in the dispersive section of the chicane [4,5], 3 μm (rms) beam position resolution over a 10 cm range was achieved and cross-checked against a synchrotron light-based BPM [6,7]. The arrival-time measurements conducted with this stripline pickup were also cross-checked with a beam arrival-time measurement conducted upstream of the chicane with button-like pickups [7]. A description of how these measurements are locked to an RF reference follows [7].

* kirsten.hacker@desy.de

PULSED OPTICAL SYNCHRONIZATION

The pulsed optical synchronization system at FLASH relies on the delivery of short laser pulses with a stable repetition rate to remote end-stations [8]. This must be done with a high level of phase stability. This is accomplished though feedback loops, which stabilize the optical lengths of the fibers over which the pulses are sent. Such a scheme is shown below in Fig. 2. The arrival-times of the master laser oscillator pulses relative to the pulses returning to the device can be measured through optical cross-correlation or through an RF method. The optical method can get a best-case resolution of less than a femtosecond (rms) [9], but is much more expensive, unstable, and complicated than the RF method which can get a best-case resolution of 5 fs (rms) [10].

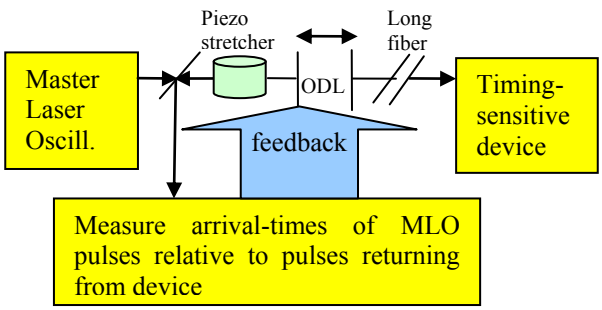

Figure 2: The optical length of a fiber link is stabilized so that the pulses from the master laser oscillator arrive at a stable time at a timing sensitive device.

The timing-sensitive device in Fig. 2 can be a laser, a beam arrival-time or position monitor (BAM or BPM), or a (yet-unproven) laser-to-RF conversion unit. Lasers are locked together using optical cross correlation and the beam arrival-time and position monitors utilize the pulsed signals from beam pickups to modulate the amplitudes of the laser pulses in a compact, commercially available device called a Mach-Zehnder Electro-Optical Modulator (EOM) shown in Fig. 3.

In Fig. 3, the laser pulses travel through LiNio3 crystal. When the crystal is under the influence of an electric field it becomes birefringent and causes a phase shift of the light that is transmitted. The electric field from the pickup signal is applied to the crystal with opposite polarities so that the phase velocity of the laser pulses increases in one arm and decreases in the other arm. When the laser pulses are recombined, they interfere constructively or destructively in proportion to the amplitude of the applied electric field.

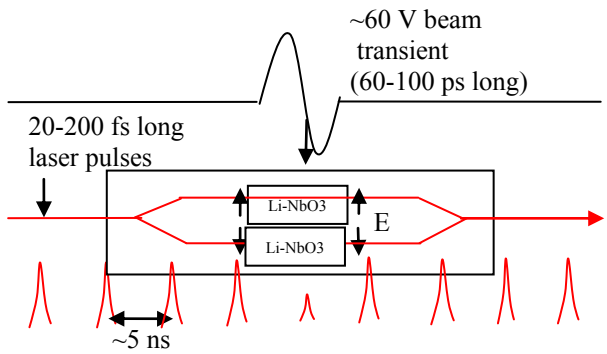

Figure 3: Mach-Zehnder Electro-Optical Modulator (EOM) used to modulate laser amplitude with zero-crossing of beam pickup signal.

The amplitudes of the modulated laser pulses are converted into electrical signals with photodetectors. The amplitudes of the electrical pulses from the photodetectors are sampled with an ADC, which is clocked with a signal generated from another photo-detector signal (Fig. 4).

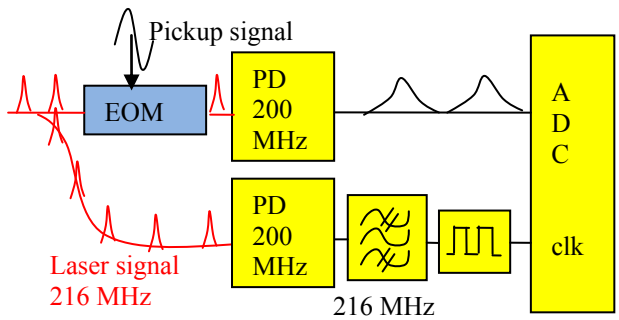

Figure 4: The arrival-time of a pickup signal is measured with by using the zero-crossing of a beam pickup signal to modulate the amplitude of a laser pulse in an electro-optical modulator (EOM). The laser pulse amplitudes are detected with a photodetector and an ADC that is clocked with a signal generated from the laser pulse train.

The measurements of the pickup signal's phase are calibrated by using an optical delay line to vary the arrival-time of the laser pulses at the EOM. With the appropriate laser timing, this enables a scan about the zero-crossing of the pickup signal and a measurement of the signal's slope in terms of the modulation of the laser pulse amplitude (Fig. 5).

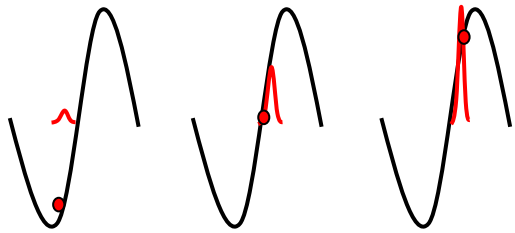

Figure 5: Scanning the arrival-time of the laser pulse (red) over the pickup pulse (black) in order to determine a calibration constant for the measurement of the arrival-time of the pickup pulse.

To give an idea of the way that the amplitude of the laser pulse changes when its arrival-time is scanned relative to the arrival-time of a pickup signal, scans for four pickup signals are plotted below in Fig. 6. The red and pink pickup signals are attenuated and an RF limiter is used with the blue and black pickup signals. When the signal is attenuated, the dynamic range increases and the resolution decreases. The signals with the larger dynamic range are used to deliver commands to an optical delay line and keep the signals with the higher resolution in range.

The black and blue signals look rather strange because of over-rotation in the EOMs. When a pickup signal amplitude exceeds the linear range of the EOM, the EOM does not just saturate and deliver a flat response; the polarization in the EOM continues to change. This is why, when the amplitude of the pickup signal is large, the black and blue signals seen in the scan shown in Fig. 6 invert.

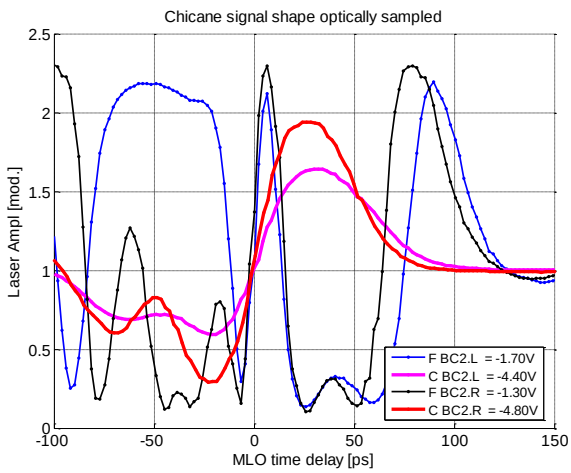

Figure 6: Laser amplitude changes as the laser arrival-time is shifted relative to four different pickup signals. The red and pink pickup signals are attenuated and an RF limiter is used with the blue and black pickup signals.

When the phase of the laser is coincident with the zero-crossing of the pickup, this optical sampling method allows for high-precision measurements of the phase of the pickup signal. The resolution of the method is determined by the accuracy with which the laser pulse amplitude can be detected and the steepness of the slope of the electrical signal. In the 6 fs resolution measurements presented in [2,3,7], the signal slope steepness was typically around 1 V/ps and the accuracy with which the laser pulses could be detected was about 0.1% of a 1V ADC input.

BEAM ARRIVAL TIME WITH BUTTONS

To generate these steep signal slopes for beam arrival-time measurements in straight sections, button-like pickups with a broadband output spectrum are used (Fig. 7). The vacuum feedthroughs used were type-N, so that the button size could be large without any steps in the coaxial line diameter. The signals from opposite buttons are combined in order to reduce the sensitivity of the phase measurement to changes in signal amplitude resulting from beam position changes. An RF limiter prevents damage to the EOM from large voltages resulting from beam spray.

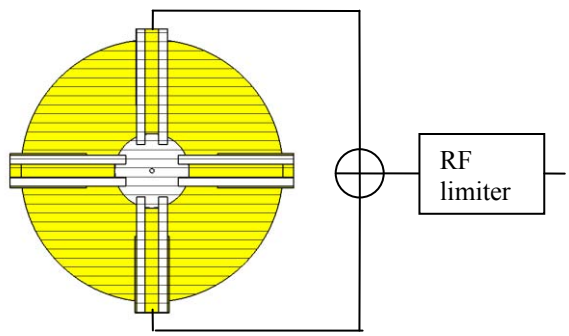

Figure 7: Cross section of broad-band button-like pickup for electro-optical sampling scheme. The signals from opposite sides are combined in order to reduce changes in amplitude that occur as a result of beam position changes. The RF limiter prevents damage to the EOM from large voltages resulting from beam spray [4,5].

Using two of these pickup assemblies, separated by 60 meters in a drift section, two cross-correlation-based, length-stabilized fiber links, and two EOM-based front-ends, the accuracy of the beam arrival-time measurement relative to the pulsed optical synchronization system reference was verified. Over short time scales, a difference of 9 fs (rms) between the two measurements was observed, implying that the measurement has a resolution of 6 fs (rms) [2,3]. Over longer time scales, the measurements differed by as much as 30 fs, with a large part of this discrepancy resulting from changes in the length of the long tail of the in-homogenously compressed bunch. With homogenous compression, the influence of longitudinal bunch shape changes is expected to be smaller [3].

Some of the 30 fs of long-term measurement drift could also be attributed to drifts of the temperatures of the fibers in the EOM front ends. Each meter of fiber will drift by 60 fs per degree C, and there are up to two meters of fiber in each EOM front-end that are not stabilized by the fiber link stabilization feedback. This is why, in subsequent versions of the EOM front-end [6,7], the chassis was actively thermally stabilized to within 0.03° C, leaving a maximum thermal drift contribution for each front-end of less than 2 fs.

BEAM ARRIVAL-TIME AND POSITION WITH PERPENDICULAR STRIPLNES

If a stripline pickup is mounted perpendicularly to the beam direction, as shown in Fig. 8, short electrical pulses will travel to the left and right sides of the pickup. If the arrival-times of these pulses are measured using the optical technique described previously, the beam position and arrival-time can be derived with

$$beam_position = \frac{c}{2} \cdot \left(arrival_left - arrival_right \right)$$

and

$$beam_arrival = \frac{1}{2} \cdot \left(arrival_left + arrival_right \right).$$

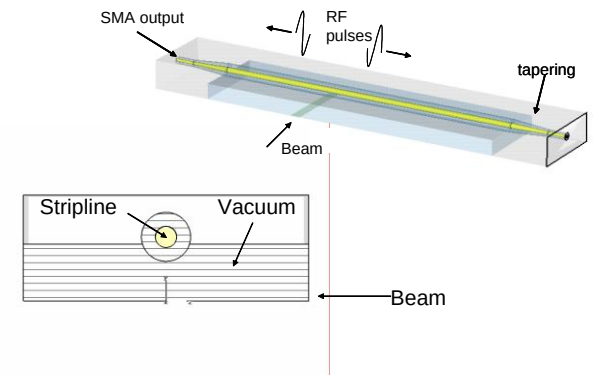

Figure 8: Top half of the perpendicularly mounted stripline BPM pickup. The pickup is suspended in a coaxially shaped channel, open to the vacuum chamber below. It is tapered to an SMA vacuum feed-through [4,5].

When the beam energy is changed, the beam position in the chicane will change in a predictable way. Measurements of the beam position, done by measuring the difference between the arrival-times of the zero-crossings of the pickup signals on an oscilloscope, are shown in Fig. 9 as a function of beam energy changes. Good agreement is observed over the full range of the pickup.

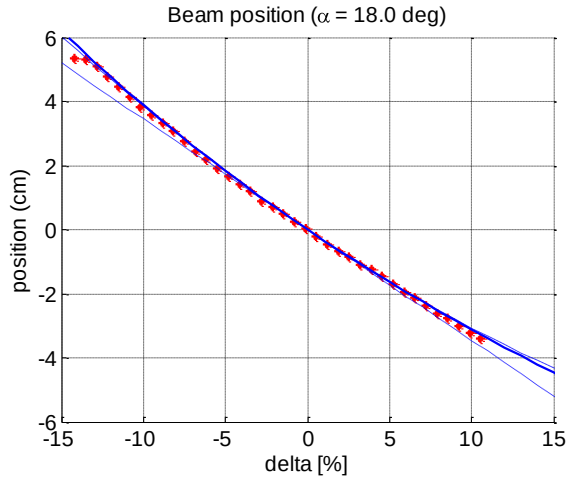

Figure 9: The beam position changes expected for a given energy change are plotted in blue for higher order dispersion terms. The measured position changes are plotted as red stars. This means that the pickup pulses from the transversely mounted stripline behave as expected when the beam position is changed over the full width of the vacuum chamber [5,7].

The signal slope remained steep when the energy spread and corresponding position spread were increased. The slope of the signal for different accelerating phases is plotted below in Fig. 10. Increasingly negative phases correspond to increasingly wider beams. This means that the pickup will function appropriately for wide beams.

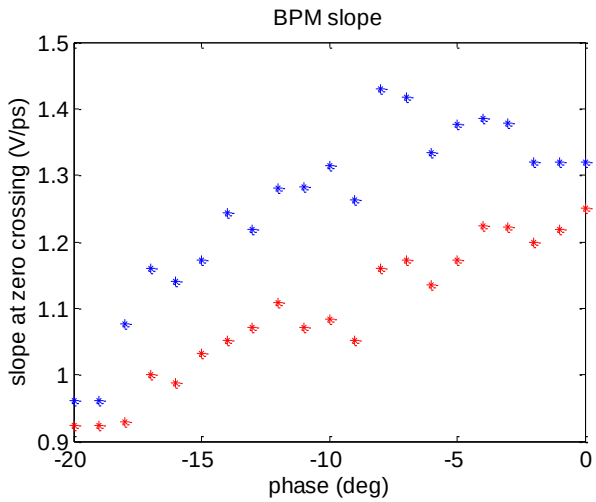

Figure 10: The slope of the pickup signal's zero crossing for different accelerating phases. Increasingly negative phases correspond to increasingly wider beams. This means that the pickup will function appropriately for centimeter wide beams [5,7].

A schematic for the optical front end for the transversely mounted stripine BPM/BAM is shown below in Fig. 11. The reference laser signal is tapped-off from a nearby length-stabilized end-point, the polarization of the signal is adjusted, the signal is amplified up to 200 mW with 4 μm gain fiber pumped from both ends, and the arrival-time at each EOM is adjusted with Optical Delay Lines (ODLs). Fiber lengths and power levels are also described in the figure.

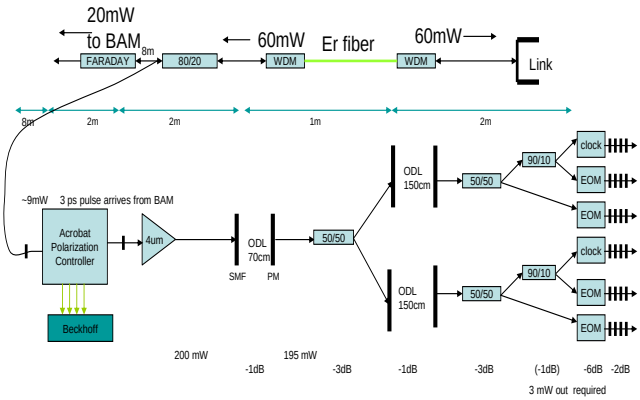

Figure 11: Schematic of optical beam arrival/position measurement front-end. An 8 m long, thermally insensitive patch-cord connects a nearby length-stabilized fiber link to the BPM chassis, whereupon the polarization is adjusted and the signal is amplified to 200 mW. The arrival-times of the laser pulses at 4 EOMs are adjusted with ODLs [5, 6].

The inside of the front-end is depicted in a top-view and a side-view in Fig. 12. In the top-view, the polarization controller is labelled with PC, the four EOMs are shown in the center, preceded by several splitters. The ODL on the left moves whenever the beam arrival-time changes, and the ODL on the right moves whenever the beam position changes. A linear encoder is mounted to the ODL on the right in order to provide an absolute position reference.

In the side-view, one of the Peltier elements used in the active thermal stabilization system is depicted in pink. Neoprene insulation is depicted in green and the surfaces of the chassis are depicted in turquoise. Heat from the plate upon which the EOMs and fibers rest is transferred to the outside of the chassis which is cooled with a fan. Stability of 0.03 degrees C has been achieved with this chassis installed in the tunnel.

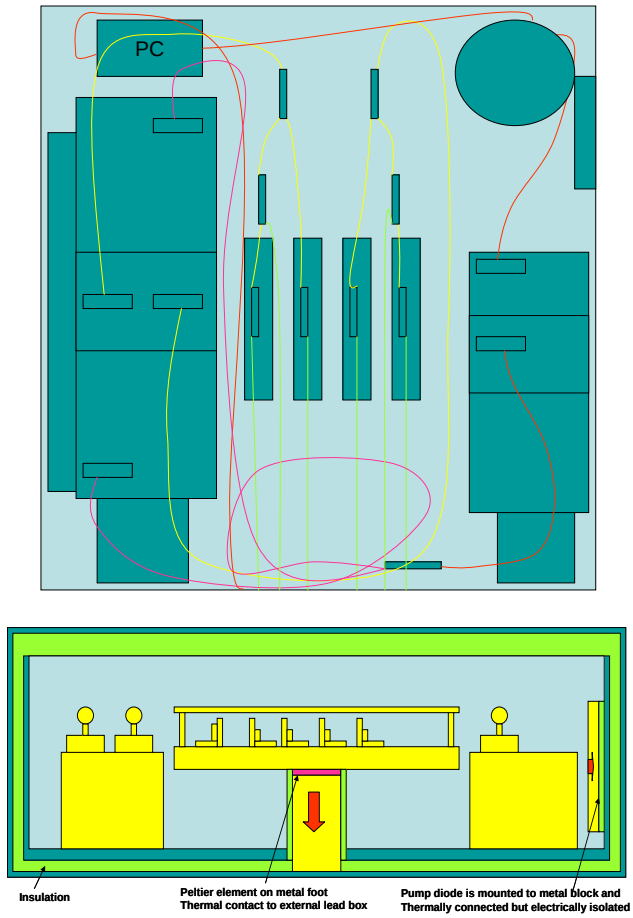

Figure 12: Physical layout of front-end chassis: (*upper*) top view with fiber routing and (*lower*) side view with thermal concept. The EOMs are depicted in the center and the optical delay lines (ODLs) are on the right and left sides of the chassis. The temperature of the plate upon which the EOMs and fibers rest is stabilized by pumping heat from the plate to the outside of the chassis, which is cooled by a fan [6, 7].

The setup described above was used in the measurements of the signals from the transversely mounted stripline pickup [7]. A similar setup with fewer EOMs is used in recent button-based beam-arrival-time measurements [12]. The older version of the optical pickup sampling front-end [3] had the disadvantages that the optical delay-stages had a low mean-time-to-failure and the chassis was not thermally stabilized.

Once the measurement set-up is commissioned, the first step is to verify the calibration of the measurement with a beam-based reference. If the calibrations of the pickup signal arrival-time measurements from both sides of the transversely mounted pickup are correct, then, when the energy of the beam is changed, the ratio of the change of the arrival-times of the signals will be equal to $(R_{56}/2+R_{16})/(R_{56}/2-R_{16})$. Fig. 13 verifies that the calibrations do satisfy this requirement, even though the beam jitter was large, requiring averaging over multiple shots.

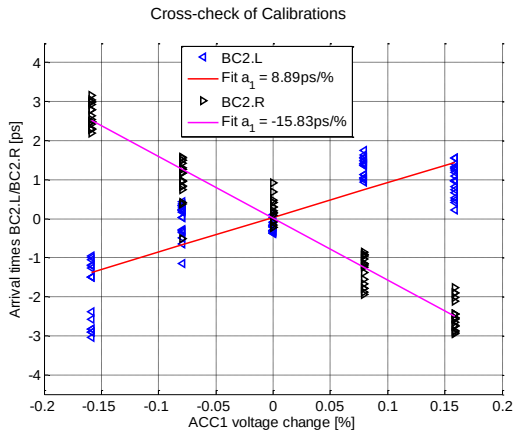

Figure 13: Verification of the calibrations of the pulse arrival-time measurements for the left and right sides of the pickup. BC2.L/BC2.R = $(R_{56}/2+R_{16})/(R_{56}/2-R_{16})$. [7].

When the transversely mounted stripline pickup is installed in a dispersive section of a chicane, it is possible to use the beam position and arrival-time information to calculate energy changes of the beam according to

$$\frac{\Delta E}{E} = R_{16} \cdot \Delta x_{chicane} \ .$$

In Fig. 14, the energy changes measured by the pickup are plotted as a function of the bunch number in the bunch train. Because the dynamic range of the measurement is small when the resolution is high, only the central portion of the bunch train is within the range of the measurement and agrees with the 0.3% amplitude change made in the set-point of the accelerator module.

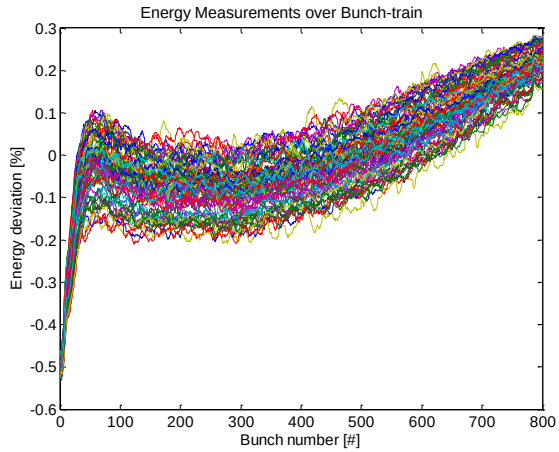

Figure 14: Changes in beam energy measured with the transversely mounted stripline monitor in the dispersive section of the bunch compressor. Because the dynamic range of the measurement is limited, only the central portion of the bunch train agrees with amplitude changes made in the set-point of the accelerator module [7].

The transversely mounted stripline pickup in a dispersive section can also measure arrival-time changes that occur prior to the dispersive section, using

$$t_{upstream} = \frac{R_{56}}{R_{16}} x - t_{chicane} \ .$$

The arrival-time upstream of the chicane is plotted in Fig. 15, as measured with the transversely-mounted stripline installed in the dispersive section of the chicane and with a button-like pickup installed upstream of the chicane. The dynamic range of the stripline measurement is exceeded near the end of the bunch train. The stripline measurement also suffered from buffer number problems, causing the measurement of the signal from the right side of the pickup to not always be from the same shot as the measurement from the left side of the pickup. Despite this problem, the 50 kHz ripple due to an RF gun oscillation is visible in both measurements, and slight adjustments to the calibration constants of each measurement can bring them into better agreement.

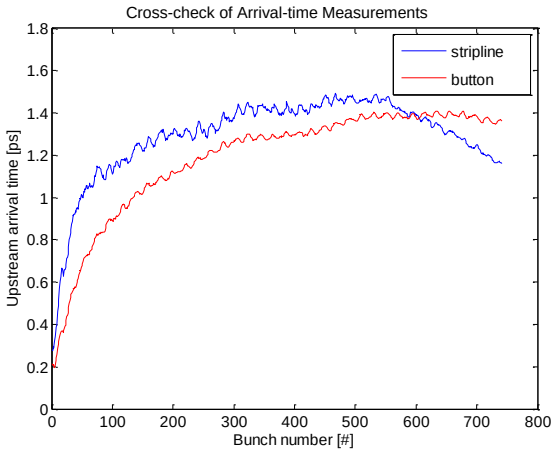

Figure 15: The beam arrival-time upstream of the chicane measured with a button pickup installed upstream of the chicane and with the stripline pickup installed in the chicane [7].

How the beam shape influences the two measurements will be actively studied in the future. In simulations, by comparing the stripline and button measurements, it should be possible to extract the beam width (energy spread) in the chicane when the beam length and height are smaller than its width (Fig. 16).

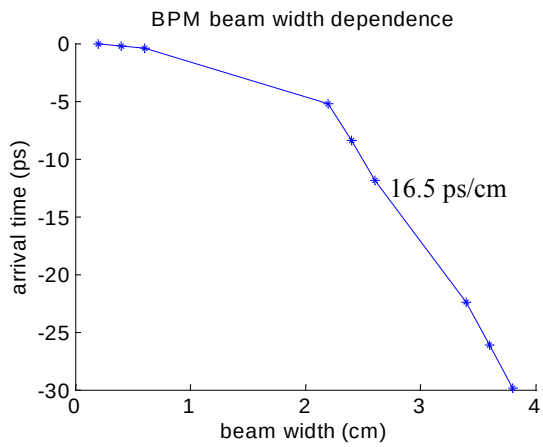

Figure 16: Simulation of the dependence of the arrival-time of a bunch at the transversely mounted stripline on the width of the bunch.

In simulations and measurements, the beam tilt also has a significant impact on the stripline measurements. By applying closed orbits bumps upstream of the chicane it is possible to control the tilt of the beam in the chicane. The tilt can be accurately measured with a synchrotron light monitor and the effect on the measurement of the beam position in the chicane with the transversely mounted stripline is plotted below in Fig. 17.

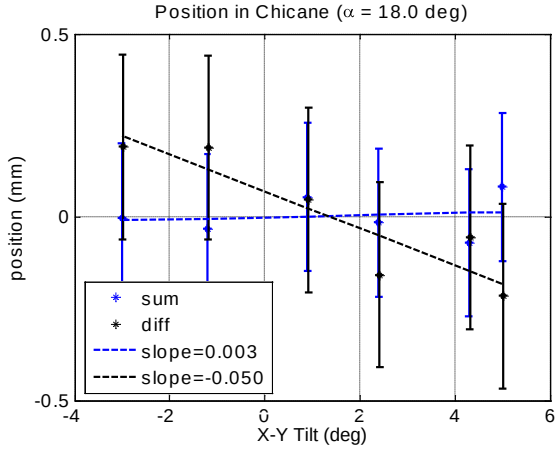

Figure 17: The position measured in the chicane as a function of the x-y tilt of the beam measured on a synchrotron light monitor. The beam width in this measurement was 50 mm (rms) [7].

While any y-z tilts can be removed by combining the signals from the top and bottom pickups, systematic errors that occur due to asymmetric distributions tilted in the x-z plane cannot be removed by any means. These errors can be as large as half a millimeter.

A final cross-check of the stripline beam position measurement can be provided by a synchrotron-light based BPM that uses two photo-multiplier tubes to determine the beam position. It is labelled PMT in Fig. 18, below.

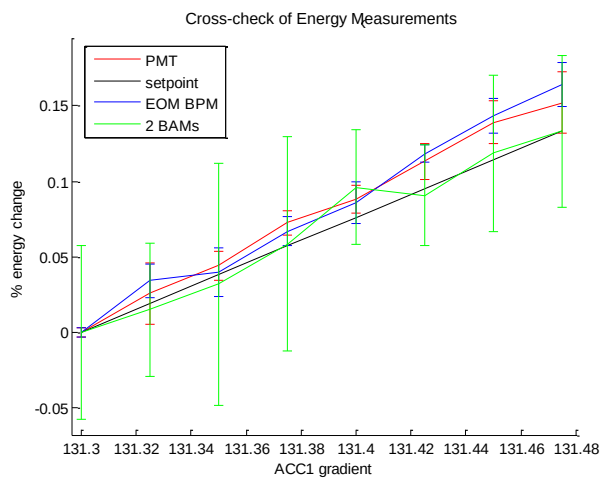

Figure 18: Changes in beam energy measured with a synchrotron light based BPM (PMT) are plotted in red, the transversely mounted stripline (EOM BPM) is plotted in blue, the setpoint of the accelerator section gradient (setpoint) is in black, and a measurement with two button pickup beam arrival-time monitors in a time-of-flight measurement (2 BAMs) is shown in green. The error bars on the 2 BAM measurement are large because a second accelerator section and bunch compressor were located between the first BAM and the second BAM [6, 7].

In Fig. 18, the gradient setpoint of the accelerator section was changed and the beam energy changes expected based on cavity regulation were plotted in black. The energy changes measured by the transversely mounted stripline are plotted in blue, the synchrotron light based measurements are in red, and the time-of-flight measurements done with two button pickup beam arrival-time monitors are shown in green. The error bars on the time-of-flight measurement are large because a second accelerator section and a bunch compressor were located between the first BAM and the second BAM [6,7]. When more BAMs are commissioned, this will not be the case and the time-of-flight measurement is expected to have an resolution that is only a factor-of-two worse than that of the transversely mounted stripline.

The main limitation of the BAM/BPM resolution is not, however, presently given by the pickup bandwidth or the ratio of the R_{56} to the R_{16}. It is determined by the stability of the beam arrival-time and position. When the beam is unstable, the ~millimeter dynamic range of the monitors must be increased by attenuating the pickup signals. This increase in dynamic range comes at the expense of resolution.

MASTER LASER OSCILLATOR RF LOCK

All of the beam arrival-time measurements quoted here have been relative to an optical reference. These would be useless measurements unless the master optical reference is locked to the master RF reference. While the master laser oscillator has excellent short-term phase stability (~4 fs (rms)), it has terrible long-term phase stability. If a source with a good short-term stability and a bad long-term stability is locked with a low-bandwidth to a source with a good long-term stability, the source with the good short-term stability will acquire the long-term stability of the device to which it is locked.

Stability is the goal when the phases of pulses produced by a Master Laser Oscillator (MLO) are measured relative to a Master RF Oscillator (MO) signal phase (Fig. 19) [11]. The measurements of this phase difference are used in a Digital Signal Processing (DSP) regulation loop to adjust the position of mirror in the MLO cavity, thereby adjusting the phase of the MLO.

In the phase measurement schematic shown in Fig. 19, the pulses from the MLO are impinged upon a 10 GHz photo-detector that resides directly within the laser housing. This is on the far left of the drawing, with laser signals drawn in red and electrical signal drawn in black. The photodetector output is sent, via a 6 meter long RF-cable, to a rack containing phase measurement RF electronics in a chassis that is temperature stabilized to within 0.001° C (rms).

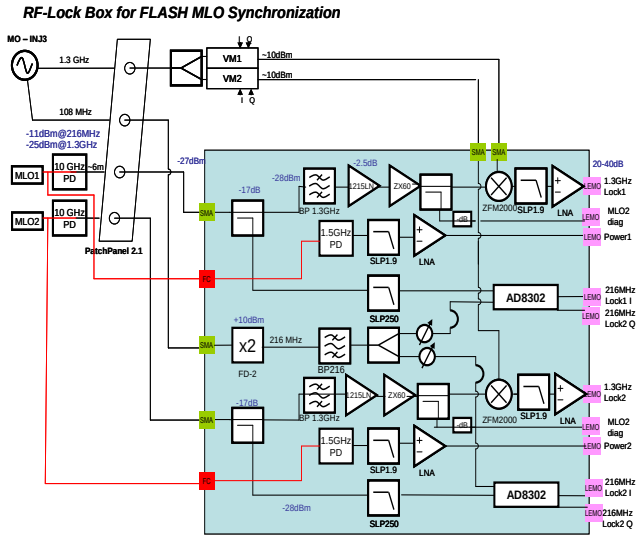

Figure 19: Schematic of MLO – MO phase measurements [11]. The pulses from the MLO (red) are impinged upon a 10 GHz photodetector that resides directly within the laser housing. The photodetector output (black) is sent, via a 6 meter long RF-cable, to a rack containing phase measurement RF electronics in a chassis (blue) that is temperature stabilized to within 0.001° C (rms) [11].

The circuit shown in Fig. 19 is designed to support two MLOs and two 1.3 GHz MLO-MO lock circuits. In the evaluation of the lock performance, one of the two identical circuits was used to lock the MLO to the MO and provide an in-loop measurement and the other was used for an out-of-loop measurement. In addition to the 1.3 GHz phase measurement circuits, a pair of AD8302 216 MHz phase and amplitude detection circuits are employed to provide a coarse reference against which bucket jumps of the PLL can be diagnosed. The MO reference is shifted with a vector modulator board that is controlled with a DAC. This functionality is used, for checks of the calibration of the circuit.

Using input signals from a signal generator instead of from the filtered photodetector signals, the noise contribution of the phase measurement circuit can be evaluated. In Fig. 20, the noise contribution of the phase measurement is less than 6.5 fs, with a majority of the noise coming from frequencies which are above the bandwidth of the PLL. These frequencies will not affect the measurement. The main noise source is the photodetector signal, which contributed ~15 fs of phase noise.

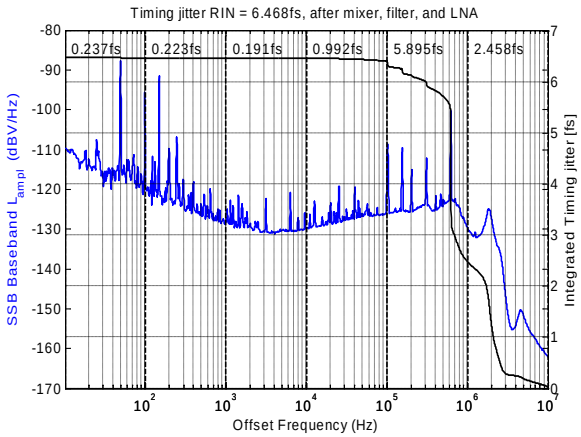

Figure 20: Noise contribution of phase measurement: baseband noise of the mixer output with amplification. Although high frequency noise is added through the amplifier, frequencies above 10 kHz are later filtered out in the regulation. The K-phi was 350 mV/deg [11].

Using input signals from a signal generator instead of from the filtered photodetector signals, the long-term drift performance of the phase measurement was below 5 fs in an undisturbed, climatized room with active temperature control within the chassis, but it jumped by 15 fs when people entered the room. Without the active temperature stabilization, the circuit drifts by 30 fs in an undisturbed, climatized room and by picoseconds when people are working in the room.

When the filtered photo-detector signals were used and the DSP regulation loop was closed, an out-of-loop drift of 77 fs was measured over an undisturbed 24-hour period (Fig. 21 (top)). The out-of-loop drift was dominated by the effects of laser amplitude drift (Fig. 21 (top)). Because the active thermal stabilization was off during this measurement, 30 fs of drift should be expected due to thermal drift. Using active stabilization of the laser amplitude and active stabilization of the phase measurement circuit temperature, the main drift sources can be overcome, leaving a MLO-MO phase lock that can be made stable on the 10 fs level [11].

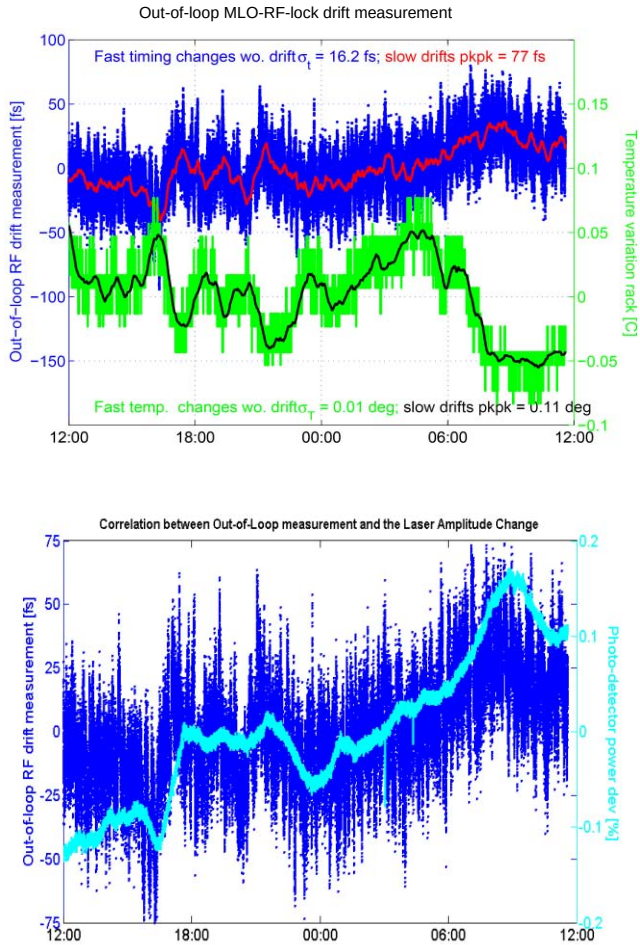

Figure 21: Laser amplitude drift (bottom) can account for 50 fs of the out-of-loop drift (top) [11].

CONCLUSIONS

- A compact electro-optical technique makes 6 fs resolution pickup signal phase measurements possible as part of a pulsed optical synchronization system.
- 6 fs resolution phase measurements enable high resolution measurements of the beam arrival-time, energy, and position.
- The optical reference against which these measurements are made is locked to a stable RF reference.

REFERENCES

[1] X-FEL Technical Design Report Sect. 4.8 2006.
[2] F. Loehl et al, "High-precision Beam Arrival Monitor", DIPAC 07, Venice, May 2007.
[3] F. Loehl, "Optical Synchronization System for FLASH", PhD Thesis, University of Hamburg, June 2008.
[4] K. Hacker *et al*., "Beam pick-up designs suited for an electro-optical sampling technique", FEL 2006 Conference, Berlin, Germany, 2006.
[5] K. Hacker et al, "Large Horizontal Aperture BPM and Precision Arrival Pickup", DIPAC 07, Venice, May 2007.
[6] K. Hacker et al, "Demonstration of a BPM with 5 μm Resolution over a 10 cm Range", DIPAC 09, Liverpool, May 2009.
[7] K. Hacker, "Measuring the Electron Beam Energy in a Magnetic Bunch Compressor", PhD Thesis, University of Hamburg, July 2010.
[8] S. Schulz *et al.*, "All-optical synchronization of distributed laser systems at FLASH", PAC 2009 Conference, Vancouver, Canada, 4-9 May, 2009.
[9] J. Kim et al., "Long-term femtosecond timing link stabilization using a single-crystal balanced cross correlator", Opt. Lett. (2007), no. 9, 1044-1046.
[10] J. Zemella et al., "RF-based detector for measuring fiber length changes with sub-5 femtosecond long-term stability over 50 h", FEL 2009 Conference, Liverpool, England, 23-28 August 2009.
[11] K. Hacker et al, "Master Laser Oscillator RF-Lock", DIPAC 09, Liverpool, May 2009.
[12] M. Bock et al, "Time-of-flight Measurement using two Beam Arrival-time Monitors", DIPAC 09, Liverpool, May 2009.

ACKNOWLEDGEMENTS

The transversely mounted stripline pickup idea came from Manfred Wendt and the electro-optical pickup signal sampling idea came from Holger Schlarb. The optical synchronization infrastructure at FLASH has been under development over the past five years by a growing group of people, without whom these measurements wouldn't exist: M. Bock, M. Felber, P. Gessler, F. Loehl, F. Ludwig, H. Schlarb, B. Schmidt, S. Schulz, J. Szewinski, A. Winter, and J. Zemella. Additional thanks go to the many technicians who contributed their time and expertise to the designs.

A WINNING TRADITION: THE FARADAY CUP AWARD

Michelle Wilinski, Brookhaven National Laboratory, Upton, NY 11973, U.S.A.

The Faraday Cup Award is given for an outstanding contribution to the development of an innovative particle beam diagnostic instrument of proven workability. "Like a 'Nobel Prize' for the beam instrumentation community," is how the 2000 winner, Kay Wittenburg of DESY, describes the Faraday Cup Award. It is presented at the Beam Instrumentation Workshop (BIW), a biennial forum for in-depth discussions of techniques for measuring particle beams produced in accelerators. The Faraday Cup winner receives a US $5,000 cash prize, $1,000 for BIW travel expenses, and a certificate of award. An acceptance speech is given at the workshop by the Awardee in the form of a talk on the design and performance of the winning instrument.

Like many other awards, the Faraday Cup Award comes with a storied tradition. The first Beam Instrumentation Workshop was organized by Richard Witkover and held at Brookhaven National Laboratory in 1989 to stimulate interaction among those in the instrumentation field. The idea for an award was conceived during round-table discussions the last day of that meeting as a way to encourage innovation among young engineers and physicists. Agreement on policies for keeping the award fair and non-commercial was reached in 1991 based on nomination and selection procedures written primarily by Bob Shafer. Naming of the award is attributed to Bob Webber. Financial sponsorship of the Faraday Cup Award is donated by Bergoz Instrumentation.

The BIW Program Committee is solely responsible for selecting the Award recipient. The Committee accepts nominations for the award approximately 12 to 18 months in advance of each BIW. Self-nomination is permitted. The award is open to candidates of any nationality for work done at any geographical location. Instrument performance must be proven using a primary charged particle beam; mere concepts or "bench-top" demonstrations are not acceptable. A description of the device, its operation and performance must be published in a journal or conference proceedings that is in the public domain. In the event of deciding between works of similar quality, preference is given to candidates in the early stages of their beam instrumentation career. The award may be shared between persons contributing to the same accomplishment. Complete rules are available at http://www.faraday-cup.com.

Since the first Faraday Cup Award in 1992, fifteen people from laboratories around the world have received the Award (see Table 1) and have gone on to continued career success. Although each prize award is a one-time event, the rewards from the prize have continued for the winners.

Table 1: Faraday Cup Award Winners

	Winner	Diagnostics
1992	Alexander V. Feschenko, INR	"Longitudinal Bunch Shape Measurement "sing Wire Probe Secondary Emission"
1993	Donald W. Rule & Ralph B. Fiorito, NSWC	"Techniques for Measuring Bunch Shapes by OTR"
1994	Edward Rossa, CERN	"Technique for Measuring the 3-D Bunch Shapes"
1996	Walter Barry, LBL and Hung-chi Lihn, SLAC	"Sub-ps e^- Bunch Shape Measurement Techniques"
1998	Andreas Peters, GSI	"Cryogenic Current Comparator"
2000	Kay Wittenburg, DESY	"Beam Loss Monitor Using PIN Diodes"
2002	Andreas Jansson, CERN	"Quadrupole Beam Pickup"
2004	Toshiyuki Mitsuhashi, KEK	"Interferometric Profile Monitor Using Synchrotron Radiation"
2006	Haixin Huang, BNL, and Kazuyoshi Kurita, Rikkyo Univ.	"Innovative Proton Beam Polarization Monitoring System"
2008	Suren Arutunian, YerPhI	"Vibrating Wire Sensor for Beam Instrumentation"
2010	Florian Loehl, CLASSE, & Kirsten E. Hacker, DESY	"Femtosecond Resolution Beam Arrival Time Monitor"

PhD students can have breakout results and winning instruments have emerged from their thesis work. In 1996, Walter Barry of Lawrence Berkeley National Laboratory and Hung-chi Lihn of the Stanford Linear Accelerator Center shared the Faraday Cup Award for development of techniques to measure the bunch shape of subpicosecond electron beams. Lihn, a PhD student at the time, sees the award as a great recognition, by experts in the field, of his years of work and ideas. Now in industry, Lihn still calls upon the skills that he developed building his winning instrument. While he did not personally continue with further development of the device, Lihn's thesis and paper

have been cited by a number of others and the ideas have been adopted in other labs.

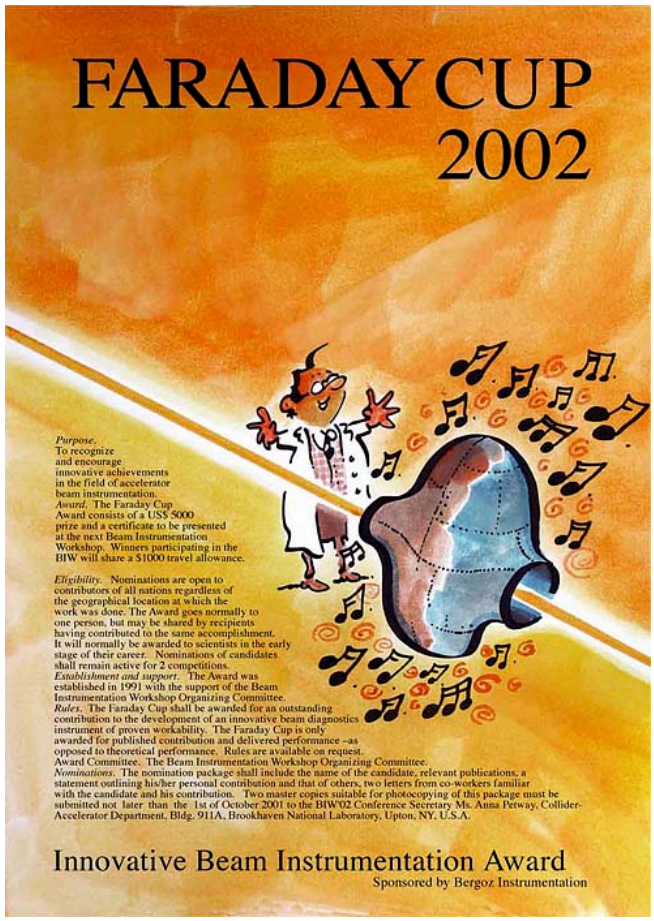

Figure 1. Example of Faraday Cup Award poster by the artist Pecub. More on the Faraday Cup Award web Site (http://www.faraday-cup.com).

Development of a magnetic quadrupole pick-up began as a simple idea that eventually became a main theme of Andreas Jansson's PhD dissertation. Working many hours at CERN with a network analyzer by his side, Jansson won the 2002 award for his pick-up which measures the quadrupole moment, or ellipticity, of a particle beam. After BIW '02, nearing the end of a CERN postdoc position and looking to widen his horizons, he visited several US laboratories and then accepted a People's Fellowship at Fermi National Accelerator Laboratory, where he continues to work. Jansson credits some of his career success to his Faraday Cup Award win and the resulting visibility.

Like Lihn, who faced different challenges when moving to an industry position, Jansson had to call on his acquired skills in his new position at FNAL. The pick-up that he had developed for the CERN PS was not optimal for the Tevatron with its dual beams and helical orbits. He started work on other instruments such as Ionization Profile Monitors and Microwave Schottky Monitors. Jansson's fondness for his PhD work is evident as he tries to keep up with the development of various quadrupole detectors by others, including quadrupole mode cavities and electro-optical devices.

In its history, the Faraday Cup Award has recognized a wide range of innovations and advancements in beam diagnostics. The very first winner of the Award, Alexander V. Feschenko of the Institute for Nuclear Research in the Academy of Sciences of Russia, won for a technique to measure the longitudinal bunch shape of a charged hadron beam with picosecond resolution using secondary emission from a fine wire probe. Bunch shape information is used to study beam dynamics and to tune an accelerator.

A device to measure three-dimensional bunch shapes of picosecond e+/e- bunches in a single shot was the winning device for Edward Rossa in 1994. He developed this using a streak camera for the CERN Large Electron Positron collider. Synchrotron radiation emitted by particles creates images of the density distribution; Rossa's optical setup provides front, top, or side views.

Applications based on radiation emitted from charged beams have resulted in several prize-winning devices. In 1993, the first joint award of the Faraday Cup was given to Donald W. Rule and Ralph B. Fiorito for their work at the Naval Surface Warfare Center – White Oak using optical transition radiation (OTR). Together they developed several techniques to measure the divergence and emittance of charged particle beams utilizing OTR produced from thin intercepting foils.

In the years since the award, Rule pursued other fields of research, but has continued contributing to beam instrumentation development in small ways. He states that the recognition of receiving the award was an encouragement to remain actively connected to the beam instrumentation community and has offered great opportunities to meet and collaborate with many interesting and exciting colleagues. Fiorito echoes these statements, indicating that the national and international awareness provided by the award directly resulted in new professional opportunities which he believes would not have otherwise been possible.

Other benefits resulted from this award. At the time of their research, studies of beam physics had just recently been established at their laboratory. The Faraday Cup Award pointed out to the Navy, as well as to the accelerator community at large, that significant new ideas could be generated outside of a traditional accelerator laboratory setting. The award also stimulated a great deal of interest in transition radiation based techniques and gradually more scientists and engineers have implemented these and related techniques at facilities around the world.

The 2000 winner, Kay Wittenburg, triumphed for the design of a beam loss monitoring detector using PIN diodes

in a coincidence configuration. His design discriminates between synchrotron radiation present in electron accelerators and radiation due to actual beam loss. The design eventually became commercialized and is now used in accelerators worldwide. DESY granted Bergoz Instrumentation a license to use the original concept of the PIN Photodiode Beam Loss Monitor, to further develop it, and to sell instruments based on this principle. Wittenburg, leader of the DESY Machine Diagnostics and Instrumentation since early 2000, believes that the development of a new idea, the overall performance, and the reliable functioning of the system was greatly important to him.

Employing synchrotron radiation for a unique beam profile monitoring system won Toshiyuki Mitsuhashi of KEK (High Energy Accelerator Research Organization, Japan) the Faraday Cup Award in 2004. Mitsuhashi labored on the development of synchrotron radiation (SR) monitors for twelve years before receiving this award, with the development of the SR interferometer being the most significant topic. He conceived the idea in 1994 while investigating the coherence of SR and determined that he would be able to use the SR interferometer for measurement of beam profile and size.

The Faraday Cup has honored 'bright' ideas based on synchrotron light, along with some 'cool' ideas as well. Andreas Peters of GSI won the 1998 award for his work on the Cryogenic Current Comparator (CCC). This device measures nanoampere DC beam current by comparing it to a known current as both are passed through a cryogenic cylinder. Since Peters' development, several groups have worked on the CCC, especially in Japan where a CCC was built at TARN-II. CCC projects are now underway at DESY and again at GSI for the FAIR project. Peters declares that the "Faraday Cup Award was a great honor and a gratification for some years of hard, but exciting, work on the CCC project at GSI". He became the beam diagnostics group leader at GSI in 2000, and believes winning the award was the "kick" to this new position. At the end of 2006, Peters became head of the accelerator operations for the Heidelberg Ion Therapy project, a heavy ion cancer treatment facility of the Heidelberg University Clinics, and he still works on special beam diagnostics topics.

A joint award was given in 2006 to Haixin Huang of BNL and Kazuyoshi Kurita of Rikkyo University for an innovative proton beam polarization monitoring system. Their design uses ultra-thin carbon filaments and an array of silicon detectors to deduce the degree of polarization from proton-carbon elastic scattering. Huang calls the award a great milestone in his career and welcomes the recognition of his and Kurita's contribution to the device. In the two years since the award, the CNI polarimeters at BNL have been upgraded, most notably with a new target drive assembly for more precise target control. Kurita is now in charge of implementing the CNI polarimeter for polarized proton projects at the new 50 GeV J-PARC accelerator currently under construction in Japan.

Suren Arutunian of the Yerevan Physics Institute received the 2008 award for developing Vibrating Wire Sensors. These sensors measure a change in frequency of a vibrating wire, have been tested on a multitude of beam types, such as electron, proton, and hard x-ray undulator beams, and can be used on other beams as well . A major advantage of using a frequency signal is that it can be transferred large distances without disturbances.

The most recent additions to the Faraday Cup Award family are Florian Loehl, presently of CLASSE (Cornell Laboratory for Accelerator-based Sciences and Education), and Kirsten Hacker of DESY. Together they worked on a femtosecond resolution beam arrival time monitor for FLASH (Free Electron Laser in Hamburg) at DESY. As PhD candidates under the direction of Holger Schlarb, they designed an electro-optical detection scheme using a beam pick-up signal to modulate the intensity of a laser pulse train, and then measure the energies of the laser pulses to determine the bunch arrival time. An expansion of the implementation of the devices is currently taking place within the optical synchronization system at FLASH. Other laboratories are also now using this system. Synchrotron Trieste implements the monitors in their Free-Electron Laser (FEL), FERMI, and the Paul Scherrer Institute (PSI) has ongoing efforts for such a system at their Swiss FEL project.

Hacker, who is about to defend her thesis at the University of Hamburg, feels that this award is quite an honor since it is not often that students are given award-worthy thesis concepts to build and test. Similarly Loehl feels that receiving the award and having his PhD work recognized by world experts in beam diagnostics is a great honor and reward for the many long days of hard, but interesting work during the last several years.

Clearly, the Faraday Cup award has been a career highlight for past winners. They all overwhelmingly acknowledge and appreciate the recognition from experts in the field and from collaborators alike. Their stories prove that innovation can come from anywhere – a student or a professional, a government accelerator facility, university, or other lab, and any geographic location.

The BIW Program Committee is eager to receive nominations for devices that are pioneering and provide new insight into particle beam measurements. If you or a colleague has developed any instrument that meets the award criteria, please nominate it for the 2012 competition by November 1, 2011.

ACCERATORS AT LOS ALAMOS TODAY

W. Scott Gibbs and J. Douglas Gilpatrick
Los Alamos National Laboratory, Los Alamos, NM, U.S.A.

Abstract

This keynote address provides a ten minute survey by LANL's Associate Director for Engineering and Engineering Science.

*

LOOKING BEYOND LANSCE: THE MARIE FACILITY

Kevin Jones and J. Douglas Gilpatrick
Los Alamos National Laboratory, Los Alamos, NM, U.S.A.

Abstract

This keynote address provides a 15-minute look at the future beyond LANSCE by the Los Alamos director of Accelerator Operations and Technology.

*

COMMISSIONING AND FIRST PERFORMANCE OF THE LHC BEAM INSTRUMENTATION

R. Jones, CERN, Geneva, Switzerland.

Abstract

This paper will outline the progress with LHC commissioning to date, detailing the performance achieved with all the main LHC beam instrumentation systems. It will include an overview of the beam loss system and its role in machine protection, along with that of the beam position system and its use for automatic orbit control. Results will be shown from the highly sensitive base band tune system as well as the bunch-by-bunch and DC beam current transformer systems, the synchrotron light monitoring systems, the wire scanner system and OTR screens.

INTRODUCTION

The first beams circulated in the LHC on 10th September 2008 in full view of the world's media. This was a resounding success, and was followed a few days later with RF captured beams circulating for several hours. Nine days on, a poor superconducting splice overheated during a hardware test at high current, creating an arc that pierced the helium containment vessel, with severe consequences. 14 months later, after a major magnet repair and consolidation programme, the LHC was once again cold and ready to take beam. Despite these efforts and the installation of a completely new Quench Protection System (QPS) its energy is currently limited to 3.5 TeV per beam. Further consolidation, requiring a long shutdown in 2012, will be necessary before it can run at its design energy of 7 TeV per beam.

A one month run at the end of 2009 saw the LHC quickly advance with optics, collimation and working point studies at its 450 GeV injection energy. Ramp commissioning to 1.18 TeV followed, ending in collisions at 1.18 TeV per beam in all of its four main experiments.

Further consolidation work was carried out on both the machine and experiments for the first two months of 2010, before the start of a 2 year run at the end of February. To date (late April 2010) the LHC is routinely ramping 2×10^{10} protons to 3.5 TeV and colliding with a β^* of 2 m in all four experiments. The emphasis now is on increasing the total intensity in the machine.

This rapid progress with beam commissioning is in a large part down to the very good beam instrumentation with which the LHC is equipped. These systems and their contributions to this commissioning effort will be the subject of the remainder of this paper.

THE LHC BTV SYSTEM

There are a total of 37 TV beam observation systems (BTV) of 7 different types installed in the LHC. Each BTV station is equipped with two screens; one a 1 mm thick alumina plate (scintillator) and the second a 12 µm thick titanium foil (to produce Optical Transition Radiation or OTR). The alumina plates are very sensitive and can observe single bunches of well below 10^9 particles, but due to their thickness significantly perturb the beam. The number of photons emitted by the OTR is much less than that of the alumina screen; on the other hand the perturbation to the beam is minimal, allowing multiple monitors to be used at the same time, as well as multi-turn observation.

First Results from the LHC BTV System

During initial commissioning the beam was steered through the transfer lines and the different sections of the machine using the alumina screens, most of the time producing very clear but completely saturated images (see Figure 1).

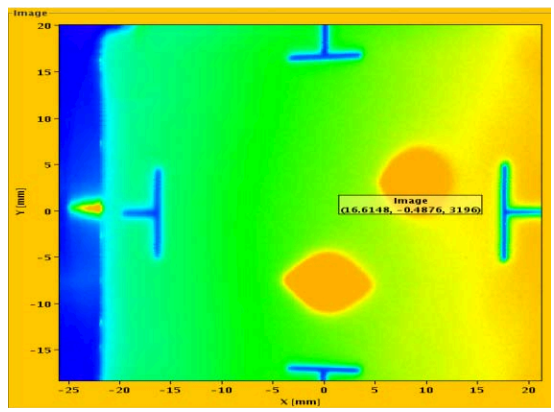

Figure 1 : The first full turn in the LHC as seen by the BTV system (10/9/2008).

After this first step the OTR screens replaced the alumina screens to reduce the blow-up of the beam, reduce the radiation due to beam losses, and produce images well suited for analysis with good linearity and no saturation. There was a possibility of observing OTR emission for even the lowest intensity pilot bunches (2×10^9 protons) due to the high sensitivity of the standard CCD cameras.

All the BTV monitors have performed very well and were extensively used during the synchronization tests and for the first beams in the LHC. The large 1 m diameter alumina screen in the dump line is still continually used to verify the correct functioning of the beam dump system (see Figure 2).

Due to the expected radiation levels in the injection regions, a gradual replacement of the standard CCD cameras with less-sensitive, radiation-hard cameras is foreseen. This will result in the loss of ability to observe pilot bunches in OTR mode.

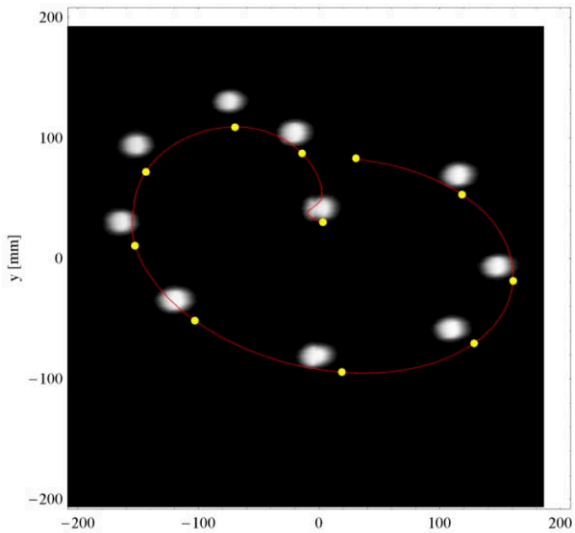

Figure 2: Checking the LHC beam dump dilution kickers with the dump line alumina screen. Predicted and measured positions of the 10 bunches used are shown.

THE LHC BLM SYSTEM

The purpose of the LHC BLM system is threefold: to protect the LHC equipment from damage; to avoid beam induced magnet quenches; and to observe losses for machine parameter tuning such as the adjustment of collimators. The protection requirements led to the placement of detectors at all likely loss locations, resulting in a total of some 4000 installed monitors. The majority of these are located around the quadrupole magnets and in the collimator regions. The signals of almost all monitors are compared with pre-defined threshold values which, if exceeded, result in a retraction of the beam permit signal and consequently a beam dump.

The LHC BLM Acquisition System

The majority of the LHC BLMs are 50 cm long, 1.5 litre, nitrogen filled ionisation chambers. These have been optimized to give an ion collection time of 85 μs, i.e., less than one LHC turn. They are located around each quadrupole magnet (six per quadrupole), in the collimator regions and at other aperture restrictions around the machine. In order to fulfil the three criteria mentioned above, the system has to cope with a total dynamic range of some 10^{13}. This is achieved by combining the ionisation chambers with secondary emission monitors (SEMs) having ~30000× smaller gain [1].

The same acquisition system is used for both the ionisation chambers and SEMs, and is based on current to frequency conversion. The signal from the detector is integrated and compared to a predefined threshold. Once this threshold is reached a one-shot is fired, which switches on a constant current source to discharge the integrating capacitor until a lower threshold is attained and the current source is switched off. In this way the frequency of the one-shot reset output is proportional to the input current from the monitor. The frequency ranges from 0.01 Hz to 1 MHz for currents of 3 pA to 300 μA respectively with linearity better than 5%. The analogue front-end counts these reset pulses using an 8-bit asynchronous counter, with each count representing a fixed amount of charge. Every 40 μs, the count from all six channels for a given quadrupole is multiplexed into a Manchester Encoded serial stream and transmitted to the surface using a Gigabit Optical Link with cyclic redundancy. The surface electronics calculates the integrated loss values for time periods of between 80 μs and 100 s and compares them to a table of threshold values that depend on the loss duration and beam energy.

The beam loss monitor acquisition is an integral part of the machine protection system, and for losses occurring on a time scale of less than 10 ms it is the only loss detection system available for the LHC. For this reason the failure rate and availability requirements are very stringent and have been evaluated using the Safety Integrity Level (SIL) approach. The system has been calculated to reach the SIL3 level, corresponding to a 10^{-3} per year probability of failing to detect a dangerous beam loss. This is achieved by duplicating the signal treatment chain for all elements after the current-to-frequency conversion, incorporating error correction and detection techniques, and constantly monitoring the availability of all monitors.

LHC BLM System Performance

There were two beam-induced triggers of the quench protection system during the injection tests of 2008, which allowed an attempt at quench reconstruction using the BLM system. The loss pattern observed in each case was almost in the centre of a bending magnet in an area with sufficient BLM coverage. Knowing the bunch intensity, impact location and loss distribution widths, it was possible to compare the measured results with GEANT4 simulations (see Figure 3). This showed a discrepancy factor of ~1.5, as a result of which the threshold values for quench prevention have been raised by ~50%.

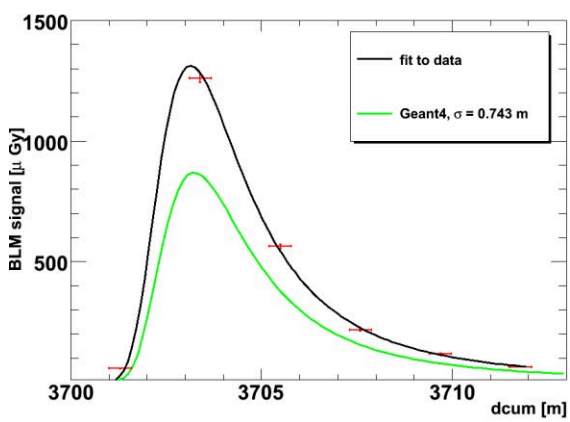

Figure 3: Comparison of measured and simulated shower evolution (data points indicate monitor locations).

The LHC BLM system is the main tool for setting-up the collimation system, which is essential for protecting the machine against damage. At the high energy and relatively low emittances of the LHC, this damage limit is quickly reached with only a few pilot bunches of 5×10^9 circulating in the machine.

Figure 4 shows the measured beam loss from all monitors for an unstable beam. The large dynamic range of the BLM system is clearly visible, with the results showing that the collimation system is performing as designed. Losses are localised to the collimator regions, giving a cleaning efficiency of better than 99.98%.

The fluctuation in the noise floor of the BLMs comes from the different cable lengths used to transport the signal from the chamber to the front-end electronics, which can be up to 700 m away in some cases. This is still below the quench level for beams at energies up to 5 TeV, but may have to be improved for nominal running at 7 TeV. One option being investigated is the use of a radiation-hard application-specific integrated circuit (ASIC) to replace the existing current-to-frequency converter, allowing electronic installation much closer to the monitor and so significantly reducing the cable lengths required.

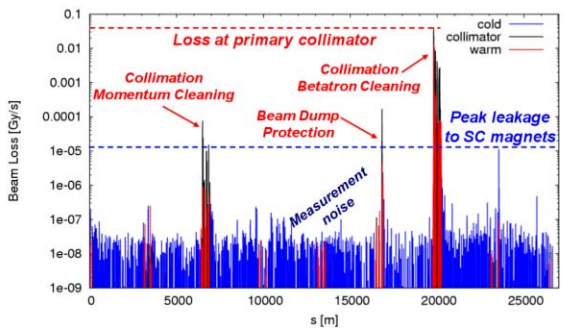

Figure 4: Beam losses throughout the LHC ring as measured during a test of the collimation system.

THE LHC BPM SYSTEM

The LHC BPM system is comprised of 1054 beam position monitors, the majority of which (912) are 24mm button electrode BPMs located in all arc quadrupole cryostats (SSS). The remaining BPMs are enlarged (34mm or 40mm) button electrode BPMs mainly for the stand-alone quadrupoles, or stripline electrode BPMs used either for their directivity in the common beam pipe regions or for their higher signal level in the large diameter vacuum chambers around the dump lines.

The beam position acquisition electronics is split into two parts, an auto-triggered, analogue, position to time normaliser, [2] which sits in the tunnel; and an integrator/digitiser/processor VME module on the surface. Each BPM measures in both the horizontal and vertical plane, resulting in a total of 2156 electronic channels [3].

First Results from the LHC BPM System

The beam threading mode, also known as FIFO mode, was used to provide the first turn position data to the operator interface. This is a totally asynchronous acquisition mode, where any triggers obtained within a specified gate are stored, processed & published. From the very first shot into the LHC, the BPM system gave excellent results while operating in this mode. Combined with powerful orbit correction software it allowed quick diagnostics of BPM polarity and machine optics errors.

Test of the Intensity Limit for the BPM System

The LHC BPM system can work in one of 2 sensitivity ranges – high or low. The threshold for the sensitivity change is conceived such that any reflections at the level of -20dB do not retrigger the system. In the high sensitivity setting the BPM system was foreseen to work correctly with bunch intensities in the range 2×10^9 to 2×10^{10} protons, with the low sensitivity setting working from 2×10^{10} protons upwards. In order to test the lower limit for auto-trigger detection the bunch intensity was varied from below 1×10^9 to around 3×10^9, while counting the number of correctly triggered BPMs in the arc of Sector 2-3. The lower limit for correct BPM functioning was found to be ~1.5×10^9 protons per bunch.

Early Performance of the LHC BPM System

The performance of the LHC BPM system has been characterised for low intensity, single bunch operation, both in trajectory and in orbit mode. From the trajectory analysis of 31 injections during the synchronisation tests in 2008 the overall rms variation in position over a timescale of some ten minutes was generally seen to be between 150-400 μm. This order of magnitude is consistent with the electronic noise estimations for bunch intensities in the range 2×10^9 to 5×10^9 protons.

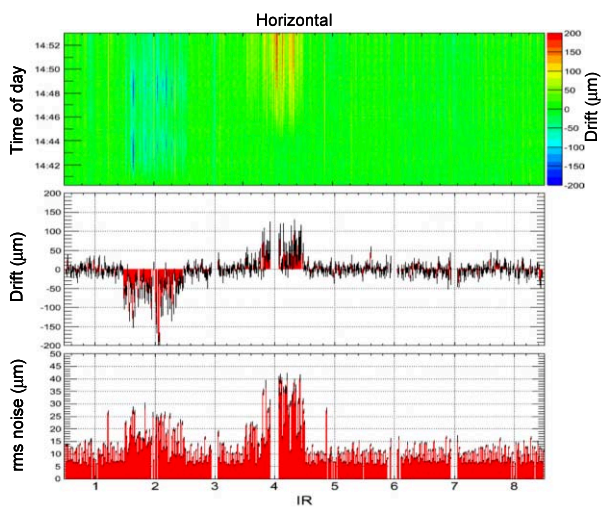

Figure 5: Orbit stability (12/9/2008).

Once the beam started to circulate, the asynchronous orbit acquisition of the BPM system (IIR mode) could be used. This provides an update of the average orbit at 25 Hz. Figure 5 shows the results of some 15 minutes worth of horizontal orbit data, with similar results obtained in the vertical plane. It can be seen that the rms noise on the measurement for the majority of the machine is between 5 and 15 µm. The alternating high/low noise peaks follow the beta function (with 45° BPM sampling), indicating that a large fraction of this noise results from the beam itself, with an additional contribution from the known COD power converter current ripple. The resolution of the BPM system in orbit mode with a single pilot bunch is therefore better than ~5 µm.

An oscillation of the position in Point 2 and a drift of the position in Point 4 are also clearly visible. These variations were traced to changes in the air temperature of the surface electronics racks in these locations and may be unacceptable for nominal LHC operation. Investigations are therefore underway to try to eliminate this problem.

Commissioning of Orbit Feedback

Full commissioning and characterisation of the LHC orbit feedback system has recently started. The system currently has a closed loop bandwidth of 0.1 Hz and is continually supplied with orbit data from all 1054 BPMs at 25 Hz. A comparison of the orbit drifts observed with and without feedback during energy ramps to 3.5 TeV is shown in Figure 6.

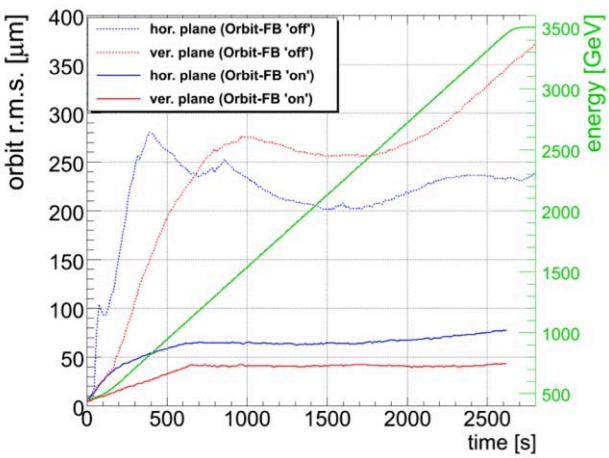

Figure 6: Comparison of orbit stability and drift with and without orbit feedback

It can be seen that although the rms orbit is significantly improved with the feedback on, there are still orbit perturbations that remain uncorrected. Analysis has shown that these are due to localised distortions that are not fully taken into account with the global correction currently being applied. Work is ongoing to address this problem and to integrate orbit feedback into day-to-day operation.

THE LHC TUNE AND CHROMATICITY MEASUREMENT SYSTEMS

The LHC base-line tune, chromaticity and coupling measurement system consists of three independent acquisition chains per beam and relies on the diode-based, base-band-tune (BBQ) technique [4] developed for the LHC and now also used in all CERN synchrotrons. The layout of these systems is described in detail in [5].

Of the three systems per beam, the first is dedicated to passive beam spectrum observation and ensures a continuous data logging for post-mortem analysis, passive beam quality monitoring and fixed displays in the control room. This passive system observes any residual beam oscillations or externally produced beam excitation.

The second system is intended for "on-demand" tune measurement, with excitation provided using dedicated tune kickers or using fast frequency sweeps ("chirp" signals) via the LHC transverse damper.

The third system is dedicated to PLL tune operation, again using the transverse damper as excitation source. While initial PLL testing has taken place, this system remains to be fully commissioned.

First Results from the LHC Tune System

Fig. 7 shows a typical tune spectrum captured at injection energy with no externally applied excitation. The calibration of the signal amplitude was performed by applying a known single frequency tone via a stripline kicker. The remarkable sensitivity of the BBQ system is clearly visible, with oscillations visible down to the tens-of-nanometres level.

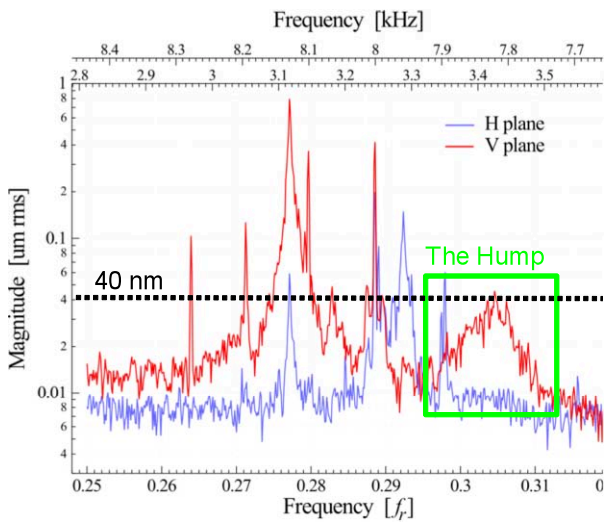

Figure 7: Typical tune spectrum resulting from residual beam oscillations. Also visible is the unknown perturbation source known as "the hump".

The figure also shows a perturbation of unknown origin in the vertical plane known as "The Hump". This wandering excitation has a quickly varying component, showing up as a wide frequency hump in the spectrum, and a slowly varying component with a ~7 minute period

which moves the whole distribution around. This causes problems whenever it crosses the tune line, resulting in emittance blow-up and beam-loss seen through a reduction in beam lifetime. Discovering the source of this is excitation is therefore becoming a priority.

Commissioning Tune Feedback

With full pre-cycling, the fill-to-fill tune stability during ramping is now typically $2\text{-}3\times10^{-3}$. However, during early commissioning the variations were up to 0.1 and are still frequently up to 0.02 due to partial magnet pre-cycles after access or sector trips for example. Tune feedback was therefore crucial early on and is still routinely used for ramping.

With the phased-locked loop (PLL) system not yet fully commissioned, the feedback relies on a peak fit of the BBQ FFT spectra to provide the tune input. The closed loop bandwidth is currently between 0.1-0.3 Hz and limited by the interaction of real-time corrections applied to the trim quadrupoles and their new QPS system. Figure 8 shows examples of ramps performed with and without tune feedback. With the feedback on a peak-to-peak tune stability of 10^{-3} has been achieved.

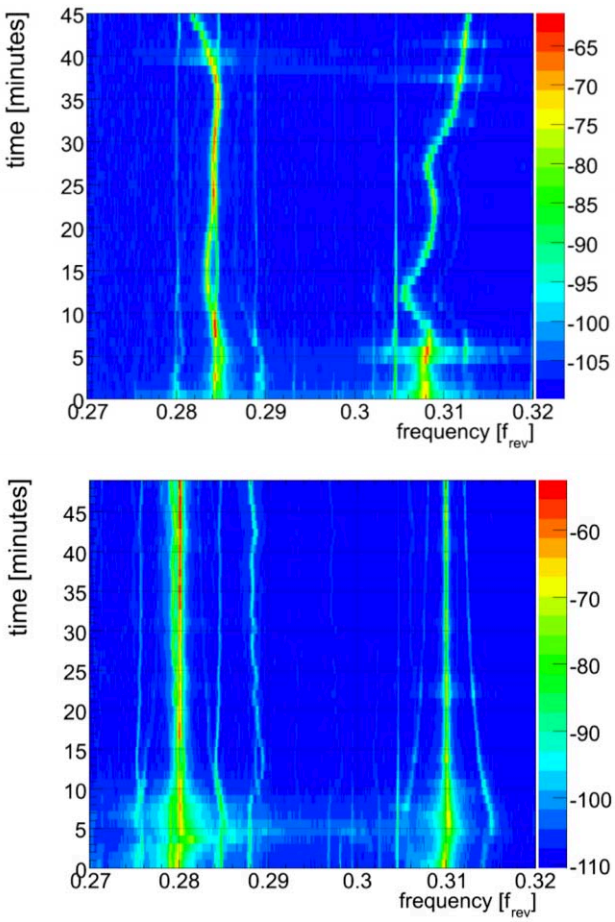

Figure 8: Tune spectra during an energy ramp without tune feedback (top) and with tune feedback (bottom).

Chromaticity Measurement

Standard chromaticity measurement performed at fixed energy by measuring the tune changes observed via the BBQ system while varying the RF frequency was operational from day 1.

The continuous measurement of chromaticity during the ramp is performed by demodulating the tune signals observed while applying sinusoidal frequency trims (see Figure 9). The modulation amplitude has had to be increased from $\Delta p/p = 10^{-5}$ at 2.5 Hz to $\Delta p/p = 10^{-4}$ at 2 Hz to overcome the tune jitter at injection, where the residual tune stability is not better than 3×10^{-4}. Using this technique the nominal chromaticity resolution of ± 2 units has been reached, with the results fed forward for the next ramps. Chromaticity feedback has not yet been attempted.

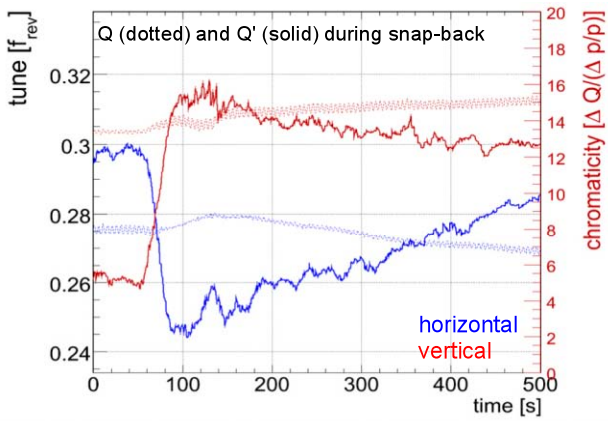

Figure 9: Continuous chromaticity measurement during the snap-back at the start of the ramp.

THE LHC WIRESCANNER SYSTEMS

Eight linear wire scanners are installed in the LHC for measuring the transverse density profile of the beam. Each beam is equipped with two wire scanners in both horizontal and vertical planes, with one available for operation and the other intended as a fully functional back-up. The scanning speed of these systems is 1 ms^{-1}. Acquisition is possible in two different modes: the standard mode, using a logarithmically amplified PMT signal, to give the average beam size over all bunches; and the bunch-by-bunch mode which relies on a fast integrator ASIC developed for the LHCb experiment working at 40 MHz to integrate the PMT signal of each bunch individually and hence give its size. To date only the standard system has been commissioned with beam.

First results from the Wire Scanner System

The wire scanners have been extensively used from an early stage to monitor the beam size and calculate its emittance. Clean signals are obtained even with single, very low intensity pilot bunches of around 5×10^{9} protons varying in size (sigma) between a few mm and ~300 µm. The resolution in the measurement of the rms beam size

under these conditions has not yet been fully evaluated, but is at the tens-of-microns level, with a reproducibility (in/out scans and repeated scans) of the same order.

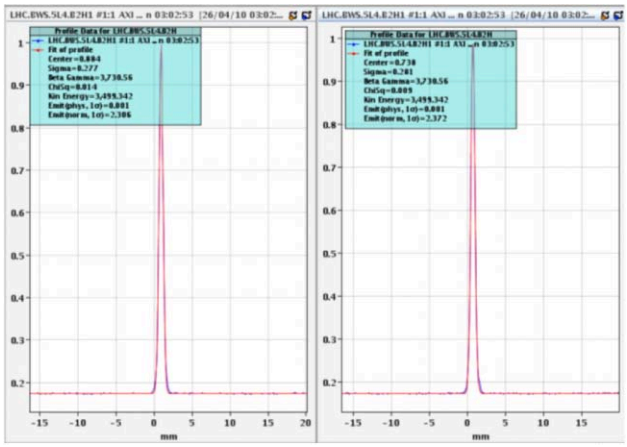

Figure 10: In and out wire scans for the horizontal plane of Beam 2 performed at 3.5 TeV (26/4/2010).

The linearity of the wirescanner system was tested by comparing the centre of the distribution with that measured with the LHC orbit system during closed bump scans. Initial results show that this linearity is better than 5% for all scanners.

The limitations of the system have also been extensively studied [6]. Simulations corroborated by SPS measurements show that a 30 µm carbon wire scanned at $1ms^{-1}$ will survive (reaching a temperature less than 4000 K) with 25% of nominal LHC beam at the 450 GeV injection energy and 7% of nominal LHC beam at 7 TeV. These limits are a function of beam size, not energy. At high energy, however, this is not the limiting factor. Simulations have shown that, between 0.4% to 2% of nominal LHC beam at 7 TeV, the first downstream magnet reaches its quench limit during a scan. The wire scanner can therefore only be used to cross calibrate the other emittance measurement devices (synchrotron light monitor for protons and rest gas ionisation monitor for ions) with limited intensity in the machine.

THE LHC SYNCHROTRON LIGHT SYSTEMS

Synchrotron light is used by two systems in the LHC:

- The abort gap monitor, which ensures that the level of protons in the 3 µs abort gap, required to accommodate the rise time of the dump line extraction kickers, remains below the magnet quench level.
- The synchrotron light monitors, which provide a continuous image of the beam.

The light detected in both of these systems comes from multiple sources. A superconducting, 5 tesla, 2 period undulator is used to produce enough photons for imaging single pilot bunches of 5×10^9 protons from the injection energy of 450 GeV to around 1.2 TeV. Above this energy the undulator radiation is shifted in wavelength into the ultraviolet and can no longer be imaged. From this stage, the dipole edge radiation from a neighbouring separation dipole takes over, and is used up to about 3 TeV. Above this energy, central dipole radiation from the same magnet is used.

The system therefore has to contend with not only the spectral and intensity variation with the increase in energy, but also the change in focus of the source.

Issues during the initial installation in 2008 led to a complete redesign of the system in 2009. This new system is built on a 4.8m long optical table located under the beam pipe and surrounded by heavy shielding to minimise future radiation problems. A motorized delay line is used to change the focus from the undulator to the dipole, while horizontal slits select the appropriate source point and optical density filter wheels control the light intensity. The table also contains a 28 m long calibration line, (the length being the distance from the beam light source to the imaging plane), used for image quality characterisation.

The LHC Abort Gap Monitoring System

The abort gap monitor is based on a gated photomultiplier (PMT), which receives ~15% of the total light collected. Its purpose is to detect the light generated by the relatively few protons which could cause a quench should they be kicked out during the beam dump kicker rise time. In order not to saturate during the passage of bunches in their nominal position, the PMT is gated off except during the 3 µs abort gap where the measurements are to be carried out.

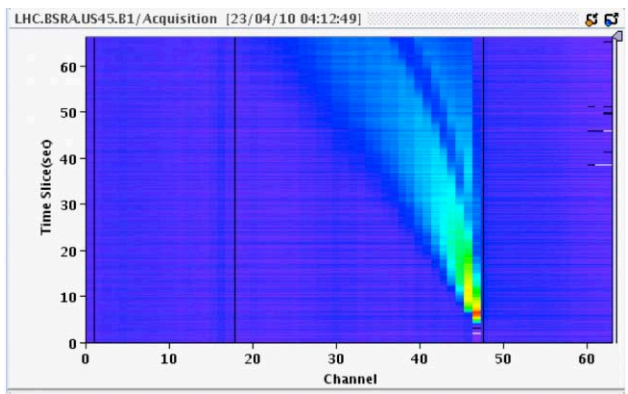

Figure 11: A single pilot bunch of 5×10^9 debunching into the abort gap when the RF is turned off.

The PMT signal is integrated over thirty 100-ns bins throughout the gap using a fast integrator ASIC developed for the LHCb experiment and also used by the fast BCT, wirescanner and collision rate monitors. The population in each of these 100ns bins is averaged over 100 ms, giving a warning to the operators once this value exceeds 10% of the quench threshold. For protons near

1.2 TeV and ions at injection energy, an averaging time of 1 second will probably be necessary to cope with the low photon flux at these energies.

Figure 11 shows the results of a test where the RF was switched off with a single pilot bunch of 5×10^9 in the machine. Debunching of the beam is clearly visible, with the abort gap quickly being populated.

The LHC Synchrotron Light Monitor

The synchrotron light monitors are continuously used to monitor the beam size in the LHC. Initially, with low intensity beams, they were also the only instruments capable of showing that there was still something in the machine if the RF tripped and debunched the beam.

Figure 12 shows a comparison of the beam size as measured continuously by the synchrotron light monitor and periodically by the wire scanner during an LHC energy ramp to 3.5 TeV. There is good agreement between the measurements during the injection plateau and the early part of the ramp, where the focus is on the undulator radiation. As the energy rises, the increase in edge radiation from the separation dipole blurs the image, leading to a measured beam size larger than that given by the wire scanners. Adjusting the focussing trombone recovers some of the image quality, which is further improved by addition of a blue filter. Further fine tuning will be necessary to reach the 3-5% error level predicted by calculations for the vertical plane.

Using the synchrotron light monitor, is has been possible to study the emittance growth observed in the vertical plane of both beams (see Figure 12 before the start of the ramp). The source of this emittance growth has not yet been determined.

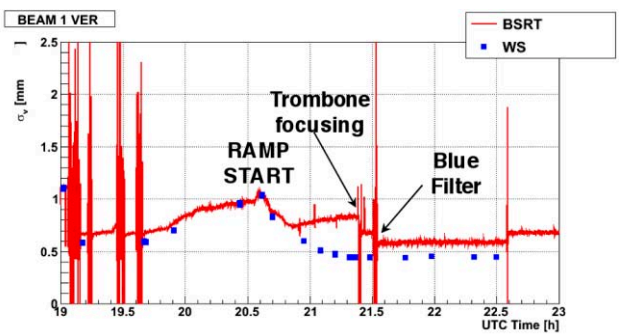

Figure 12 : A continuous measurement of the Beam 1 vertical size throughout the LHC energy ramp to 3.5 TeV. Wire scanner measurements are seen as squares.

THE LHC BCT SYSTEMS

Beam current transformers of two different kinds provide intensity measurements for the beams circulating in the LHC rings, as well as for the transfer lines from the SPS to LHC and from LHC to the dumps.

The LHC BCTDC System

The DC current transformers (BCTDC) are based on the principle of magnetic amplifiers and measure the mean current of the circulating beam [7]. Because of their operational importance, two independent systems are installed per ring. Four ranges, provided simultaneously, are used to cover the entire dynamic range of the beam from a few 10^9 to 5×10^{14} protons (~3 μA to ~900 mA).

First results from the LHC BCTDC System

The main application used to view the BCTDC acquisition is a fixed display refreshed once per second. Figure 13 shows such an acquisition for Beam 2 on September 12th 2008, with 4 successive injections of a single pilot bunch ranging in intensity from 3.5×10^9 to 6×10^9 protons and circulation times of 100 seconds to 40 minutes.

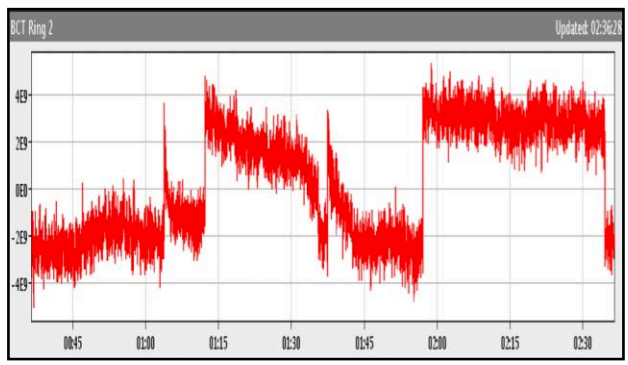

Figure 13: First circulating beam in ring 2 as seen by the BCTDC (12/9/2008).

The noise on the signal corresponds to an rms of 7×10^8 protons for a one-second integration time, which is equivalent to 1.3μA. A similar value is found for the slow fluctuations observed over several hours. This result is very good and meets expectations, although it is also a reminder that the BCTDC can only measure single pilot bunches with a limited accuracy of around 20%. A small, negative offset of ~2.5×10^9 (4.5μA) was also observed at that time and is now automatically corrected for.

The LHC Fast BCT (BCTFR/BCTFD) Systems

The LHC fast BCT systems are capable of measuring bunch to bunch intensity on a turn by turn basis. Four such systems are installed in the LHC ring (BCTFR) – one operational system and a hot spare for each beam. Each system has two parallel measurement bandwidths (providing bunch to bunch and average turn intensity) acquiring simultaneously with two different gains. Two systems per beam are also installed in the LHC dump lines (BCTFD) to measure the total dumped beam intensity.

First results from the BCTFR System

All the fast BCTs have been commissioned in each of the abovementioned measurement modes [8]. The behaviour of the system with beam is already well understood, and the calibration agrees very well with what is obtained with the DCCT over the intensity range that has so far been used in the LHC (see Fig. 14).

The main issue that still needs to be addressed is the baseline restoration, which compensates for any droop and ensures that any offset is correctly taken into account. This is very important when producing the sum of intensities over a given turn, as any slight offset is magnified by 3564, corresponding to the number of 25-ns integration periods within the 89-μs LHC revolution time. A new baseline restoration algorithm is currently being tested which should significantly improve this performance and make the system much less sensitive to the validity threshold settings that currently have to be used to ensure that only valid bunch signals are summed.

Noise levels at around 10^8 charges on the average intensity data produced every 20 ms have allowed lifetime measurements of several hundred hours to be calculated within several minutes. This has been very useful to tune-up and optimise the machine.

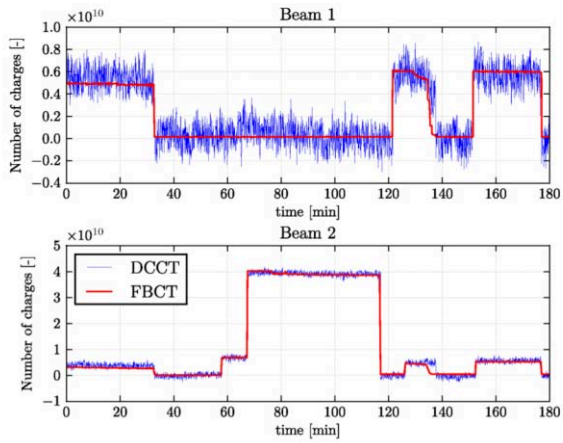

Figure 14: A comparison of fast BCT and DCCT data for various beam intensities.

SUMMARY

The commissioning **with beam** of the LHC has gone remarkably smoothly, from the first bunch injected in 2008 to the recent 30 hour physics fill at 3.5 TeV with a β* of 2 m in all experiments. The excellent quality of the LHC beam instrumentation has had a major role to play in this success, with all major systems available with near full functionality from day 1. For the machine the emphasis will now be on providing ever more intense beams while ensuring the protection of the machine. From the instrumentation side the work will switch from commissioning to optimisation.

A few remaining systems have yet to be fully commissioned, namely the LHC Schottky monitors and the LHC fast ionisation chambers for collision rate measurement in the two high-luminosity interaction regions. While first signals have been detected on both of these systems, they await higher intensities before the final commissioning can be completed.

ACKNOWLEDEMENTS

I would like to acknowledge all the members of the CERN Beam Instrumentation Group, both past and present, who have worked so hard to make these systems perform as well as they have. In the same manner I also thank all our external collaborators, who are too numerous to name, but without whom we would not have had such a successful LHC start-up with beam.

REFERENCES

[1] B. Dehning et al., "The LHC Beam Loss Measurement System", 22nd Particle Accelerator Conference, Albuquerque, NM, USA, 25 - 29 Jun 2007, p. 4192.

[2] D. Cocq, "The Wide Band Normaliser : a New Circuit to Measure Transverse Bunch Position in Accelerators and Colliders", Nucl. Instrum. Methods Phys. Res., A **416** , 1 (1998) 1.

[3] R. Jones et al., "The LHC Orbit and Trajectory System", 6th European Workshop on Beam Diagnostics and Instrumentation for Particle Accelerators, Mainz, Germany, 5-7 May 2003, p. 187.

[4] M. Gasior and R. Jones, "High Sensitivity Tune Measurement by Direct Diode Detection", 7th European Workshop on Beam Diagnostics and Instrumentation for Particle Accelerators, Lyon, France, 6-8 Jun 2005, p. 310.

[5] M. Gasior et al., "An Overview of the LHC Transverse Diagnostics Systems", CERN-LHC-PROJECT-Report-1166 (2008).

[6] M. Sapinski and T. Kroyer, C, 13th Beam Instrumentation Workshop, Tahoe City, CA, USA, 04 -08 May 2008, pp. 383-388.

[7] P. Odier et al., "The DCCT for the LHC Beam Intensity Measurement", 9th European Workshop on Beam Diagnostics and Instrumentation for Particle Accelerators, Basel, Switzerland, 25 - 27 May 2009.

[8] D. Belohrad et al., "The LHC Fast BCT System – A Comparison of Design Parameters with Initial Performance", these proceedings.

THE SNS BEAM DIAGNOSTICS EXPERIENCE AND LESSONS LEARNED

A. Aleksandrov
Oak Ridge National Laboratory, Oak Ridge, TN 37830 USA

Abstract

The Spallation Neutron Source accelerator systems are designed to deliver a 1.0 GeV, 1.4 MW proton beam to a liquid mercury target for neutron scattering research. The accelerator complex consists of an H- injector, capable of producing one-ms-long pulses at 60 Hz repetition rate with 38 mA peak current; a 1 GeV linear accelerator; an accumulator ring; and associated transport lines. The accelerator systems are equipped with a variety of beam diagnostics, which played an important role during beam commissioning. They are used for accelerator tuning and monitoring beam status during production runs. This paper gives an overview of our experience with the major SNS beam diagnostics systems.

INTRODUCTION

The SNS accelerator complex consists of an H^- injector, capable of producing one-ms-long pulses with 38 mA peak current, chopped with a 68% beam-on duty factor and a repetition rate of 60 Hz to produce 1.6 mA average current; an 87 MeV Drift Tube Linac (DTL); a 186 MeV Coupled Cavity Linac (CCL); a 1 GeV Super Conducting Linac (SCL); a 1 GeV Accumulator Ring (AR); and associated transport lines. After completion of the initial beam commissioning at a power level below nominal, the SNS accelerator complex is gradually increasing the operating power with the goal of achieving the design parameters in 2011. Results of the initial commissioning and operation experience can be found in [1]. The SNS Power Upgrade Project (PUP) [2] aims at doubling the beam power by 2016. This will be achieved by increasing the SCL and AR beam energy to 1.3 GeV and the peak current in the linac to 59 mA.

The SNS baseline design included a diverse set of beam diagnostics [3], which, for the most part, were brought on line simultaneously with other accelerator systems and which played an important role in the successful SNS commissioning and power ramp-up. As the SNS operation is shifting more and more toward neutron production for users, the roles and requirements for the beam diagnostics are changing as well. This paper describes the status and development plans for the major beam instrumentation systems.

BASELINE SET OF THE SNS BEAM DIAGNOSTICS

The original set of SNS diagnostics included beam current transformers (BCMs); beam position and phase monitors (BPMs); ionization chambers and photomultiplier tubes (BLMs); wire scanners (WS); slit-and-harp emittance scanners; phosphor view screens (VS); and Faraday cups. All of these devices were operational during the initial beam commissioning and their performance characteristics were sufficient for all of the commissioning tasks.

Beam Current Monitors

There are 23 fast beam current transformers in the SNS linac, ring, and transfer lines. They were useful during the initial commissioning until good beam transmission was established. The accuracy of the BCMs, on the order of 5%, is not sufficient for detecting a typical beam loss of .01%. Several of the BCMs are still in use for beam accounting and for protection purposes in the injector, in front of the beam dumps, and in front of the target. A typical result of the BCM measurements is shown in Figure 1.

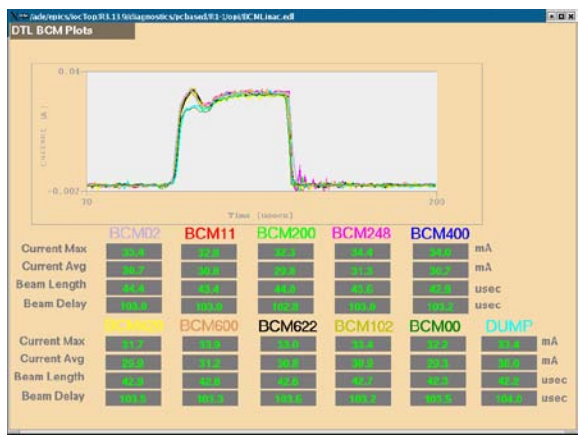

Figure 1. A beam pulse transmission from the injector to the linac beam dump measured by linac Beam Current Monitors.

Beam Loss Monitors

The SNS BLM system consists of 362 detectors measuring the secondary radiation due to beam loss. The BLMs are used as sensors in the machine protection system for shutting off the beam if the integral loss is above a certain threshold. The ionization chamber (IC) is the main detector type in the BLM system due to its simple design and immunity to radiation damage. In addition to the ICs we use several types of photo-multiplier tube based detectors (PMTs). The BLM system has worked quite reliably and typically cause less than ten hours of beam down-time per year. We encountered a few problems with the BLM system during the beam commissioning. The biggest one was significant background from the X-ray radiation produced by the RF

cavities. We were able to reduce its effect by implementing a background subtraction scheme, described in [4], but the X-ray background remains the major signal-to-noise limiting factor for the linac BLMs. The other problem was a large number of blind spots in the warm linac due to a strong dependence of the ICs signal on the location of the beam loss. We had to double the number of the ICs in the CCL in order to provide sufficient coverage. The neutron detectors, in contrast, demonstrated a poor ability for localizing the loss point, making them a good sensor for machine protection, but a less suitable device for machine tuning.

Beam Position and Phase Monitors (BPM)

The beam phase monitors are the main tools for the linac tune up which uses Time-Of-Flight algorithms. Position measurements are used for trajectory correction in the linac, ring injection set up and centering of beam on the dumps and target. Both the phase and the position are measured by the BPM system, using 160 4-lobe strip-line pick-ups installed along the beam path. A narrow-band RF front-end electronics is used in the linac and the HEBT. Base-band front-end electronics is used in the ring and the RTBT. The BPM electronics consists of a custom designed PCI board installed in a rack mounted PC running the LabView program under the Windows XPe operating system.

Figure 2. The BPM PCI card inside the PC chassis.

The BPMs demonstrated good performance during the beam commissioning. The design requirements of 0.5º for the phase resolution and 0.5 mm for the position resolution were easily met. The biggest problem with the BPM system is a relatively high frequency of unscheduled PC reboots, which are required to keep the BPMs in an operational state. A typical distribution of the reboot events for a year-long period is shown in Figure 3. We have not been able to trace this problem down to any single hardware component or software bug.

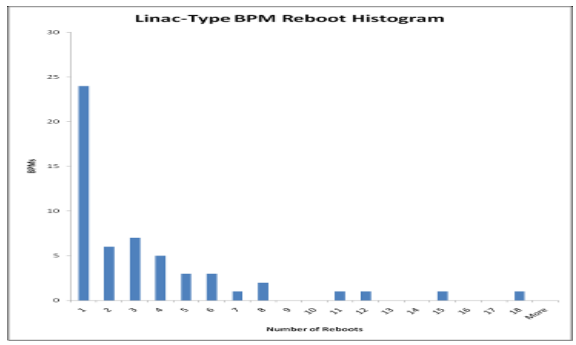

Figure 3. A typical distribution of the SNS linac BPM PC reboots for a year-long period. The number of reboots is on the x axis; the number of the BPMs is on the y axis.

Transverse Beam Profile Measurements

Conventional stepping wire scanners are used for measuring the transverse beam profiles in the normal conducting linac and the transport lines. 32 μm thick carbon wires are used in the warm linac up to 20 MeV; 100 μm thick tungsten wires are used at higher energies. The beam pulse length has to be reduced to 50 μs during the scan. The wire scanners deliver reliable profile measurements with a dynamic range of about 100. This dynamic range has been sufficient for the initial beam commissioning, and the beam core matching during operation, but it is not sufficient for beam halo and loss studies. We found that a cross-talk between the diagonal and the horizontal/vertical wires was the major factor limiting the dynamic range. The dynamic range increased significantly after we removed the diagonal wire and spread the vertical and horizontal wires farther apart. Typical profile scans before and after the modifications are shown in the Figures 4 and 5.

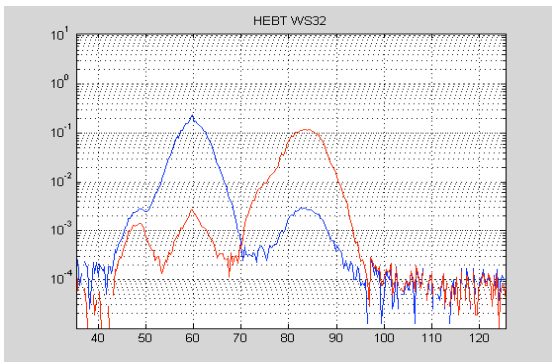

Figure 4. A typical output from the wire scanner before the modification. The vertical profile is in blue; the horizontal profile is in red. The dynamic range is limited to 100 by a cross-talk between the wires.

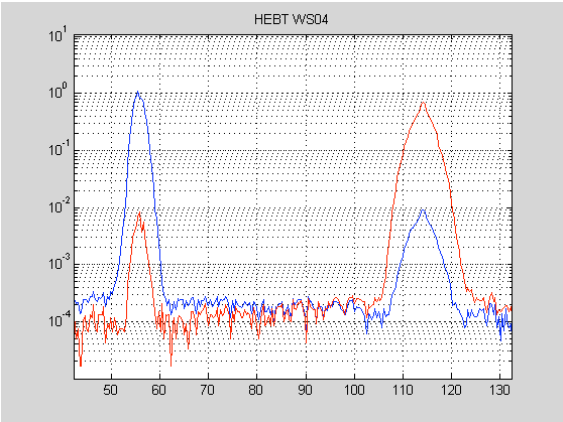

Figure 5. A typical output from the wire scanner after the modification. The vertical profile is in blue; the horizontal profile is in red. The dynamic range increased to about 10000.

A conventional slit/harp device is used for measuring the transverse emittance of the beam in the Medium Energy Beam Transport (MEBT) line. We found these measurements to be very useful for the initial beam commissioning and the acceptance tests of the RFQ and the DTL. Unfortunately, we observed a significant systematic error, up to 20-30%, in the measured emittance value. This problem has not yet been completely resolved. An example of the anomalous measurement is shown in Figure 6 in red. In this experiment the beam divergence was changed by varying the strength of an upstream focusing element. To the first order, the beam emittance should not depend, , on the beam divergence (orientation of the emittance ellipse, in other words), as illustrated by the simulation results shown in blue/green dots on the same plot. The measured emittance value showed a very strong dependence on the divergence, which can only be explained by a systematic measurement error.

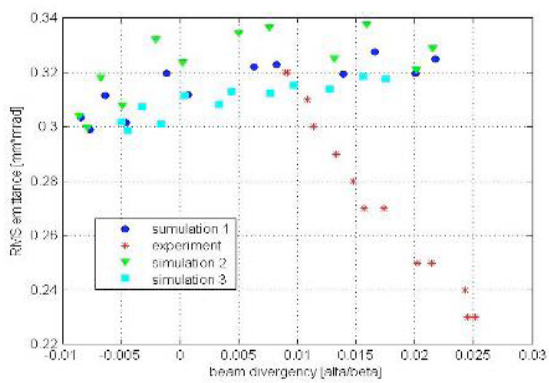

Figure 6. The measured beam emittance vs. the beam divergence (red dots) compared to the expected dependence (blue and green dots). The observed difference is attributed to a systematic error in the emittance measurements.

Longitudinal Beam Profile Measurements

There were several devices for the longitudinal bunch profile measurements available during the beam commissioning: a Laser Bunch Shape Monitor (LBSM) in the MEBT; four Bunch Shape Monitors (BSMs) in the CCL; and two BSMs in the HEBT [5]. Longitudinal bunch size measurements proved to be useful for the linac set up and troubleshooting, and the beam dynamics studies.

The BSMs have a very large dynamics range up to 10^4-10^5, as illustrated by the typical bunch profile measurement shown in Figure 7. Its time resolution of about 2 ps was sufficient for the initial beam commissioning. The resolution needs to be improved by a factor of 2 or more in order to be useful for resolving current beam dynamics issues. The plot in Figure 8 shows an example of a discrepancy between model and measurements on the order of 0.5º @805MHz (or ~1.7 ps), which requires a better resolution measurement to conclude with certainty that the model is incorrect.

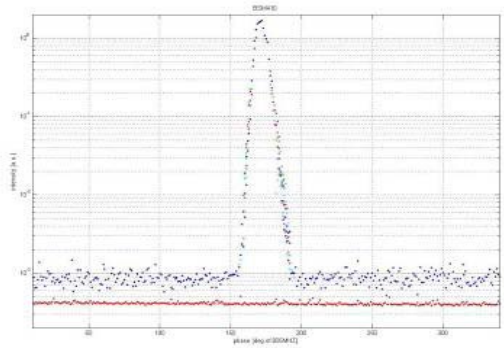

Figure 7. A typical bunch profile measured by the BSM in the SNS warm linac.

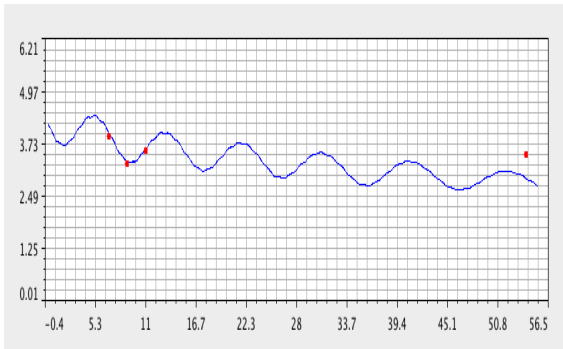

Figure 8. The bunch length along the SNS CCL. Blue line is data from the model, red dots are the BSM measurements.

The LBSM is not operational at the moment because of lack of resources to support it.

LESSONS LEARNED AND FUTURE PLANS

Our experience of a successful and timely commissioning of the SNS accelerator complex has proved, that the base-line set of diagnostics and its performance requirements were well suited for the initial

commissioning and power ramp-up. We also learned that the requirements for daily operation and post-commissioning beam study are quite different. To formulate the new requirements we need to distinguish the three main periods within the SNS operational cycle: the neutron production, the tune up for production, and the machine study time.

Neutron production period

The neutron production period currently takes about 80% of the scheduled beam time, and this fraction is steadily increasing. The most important performance metric during this period is beam availability. Therefore only systems directly involved in the beam delivery are important. Beam instrumentation systems connected to the Machine Protection System (MPS) fall in this category. These include the Beam Loss Monitors; the beam-in-gap detector; the Differential Beam Current Monitor, which protects the MEBT chopper target; the beam dump current detectors, which protects the beam dumps from excessive power; and the target power monitor. These systems have to operate at the beam rate of 60Hz. If any of the MPS significant systems fails the beam in the machine is inhibited. Increasing the redundancy is our main approach to increasing reliability of these systems. For example, we are working on the development of a single channel hot-swappable set of electronics for the BLMs to replace the existing multichannel VME based BLM electronics [6].

Machine tune up period

A machine tune up period is required after each maintenances period and currently takes about 10% of the scheduled beam time. If any single or even several diagnostics systems fail during this period, beam operation is still possible. The most important performance metrics during this period are accuracy of the data, ease of use (user friendliness), and speed of taking data. Operators should be able to perform the tune up procedures as quickly as possible, with as little support from diagnostics experts as possible. The main systems for the machine tune up are the Beam Position and Phase Monitors and the Wire Scanners. These systems have to operate at a reduced pulse rate of 1-6 Hz. The BLMs are also used for the fine tuning of the losses. Improving the user interface and increasing the speed of the mechanical devices, such as wire scanners or emittance scanner, is our main focus for these systems. For example, rewriting the software for the MEBT emittance scanner reduced the scan time from 9 min to 4 min.

Machine study period

About 10% of the scheduled beam time is dedicated to the machine study. All available diagnostics can be used during this period. If any single or several diagnostics systems fail, the beam operation is still possible. The most important performance metric during this period is accuracy of the data. Measurements are usually done by physicist, often with help from diagnostics experts. Some of the diagnostics systems for machine study can be of experimental nature or in a prototype stage of development. Beam halo measurements and transverse profile measurements in the ring are examples of such systems. These systems are required to operate at a reduced pulse rate of 1-6Hz. Our main focus in this category of diagnostics is to increase accuracy and dynamic range of beam profile measurements and provide non-interceptive measurements whenever it is possible. Examples of the non-perturbing profile measurements at SNS are the laser wire in the super-conducting linac [7] and the electron beam scanner in the proton ring [8].

ACKNOWLEDGEMENT

ORNL/SNS is managed by UT-Battelle, LLC, for the U.S. Department of Energy under contract DE-AC05-00OR22725.

REFERENCES

[1] S. Henderson, Proc. EPAC 2008, p.2892
[2] S. Henderson et. al., Proc. EPAC 2006, p.345
[3] T. Shea, Proc. DIPAC 2005, pp.6
[4] J. Pogg et al., these proceedings
[5] A. Aleksandrov et. al., Proc. PAC 2007, pp 2608
[6] A. Zhukov et al., Proc. PAC2009
[7] Y. Liu, NIM A 612 (2010), pp. 241–253
[8] W. Blokland et al., Proc. DIPAC2009

OPERATIONAL PERFORMANCE OF LCLS BEAM INSTRUMENTATION*

H. Loos†, R. Akre, A. Brachmann, R. Coffee, F.-J. Decker, Y. Ding, D. Dowell, S. Edstrom, P. Emma, A. Fisher, J. Frisch, S. Gilevich, G. Hays, Ph. Hering, Z. Huang, R. Iverson, M. Messerschmidt, A. Miahnahri, S. Moeller, H.-D. Nuhn, D. Ratner, J. Rzepiela, T. Smith, P. Stefan, H. Tompkins, J. Turner, J. Welch, W. White, J. Wu, G. Yocky, SLAC, Menlo Park, CA 94025, USA, R. Bionta, LLNL, Livermore, CA 94550, USA

Abstract

The Linac Coherent Light Source (LCLS) X-ray FEL utilizing the last km of the SLAC linac has been operational since April 2009 and finished its first successful user run last December. The various diagnostics for electron beam properties including beam position monitors, wire scanners, beam profile monitors, and bunch length diagnostics are presented as well as diagnostics for the x-ray beam. The low emittance and ultra-short electron beam required for X-ray FEL operation has implications on the transverse and longitudinal diagnostics. The coherence effects of the beam profile monitors and the challenges of measuring fs long bunches are discussed.

INTRODUCTION

The LCLS facility at the SLAC National Accelerator Laboratory [1] is the first free electron laser operating at Ångstrom wavelengths. Since 2006 the last 1 km of the SLAC linac has been upgraded to serve as the electron beam source for the FEL and new construction has been added to house the undulator and the X-ray facilities. The first x-ray operation was achieved in April 2009 [2] and a subsequent user run utilized the soft X-ray beam. After commissioning of the hard X-ray beam transport the second user run later in 2010 will take advantage of the full LCLS capabilities.

Table 1: LCLS accelerator and FEL parameters

	Design	Meas.	Unit
Repetition rate	120	30	Hz
Final energy	13.6	13.6	GeV
Charge	1	0.25	nC
Bunch length	20	8-10	μm
Peak current	3	3	kA
Emittance (injector)	1.2	0.5-1.2	μm
Slice emittance (inj.)	1.2	0.4	μm
Emittance (linac end)	1.5	0.5-1.2	μm
X-ray wavelength	1.5	1.5	Å
X-ray pulse energy	1.5	1.5-3.0	mJ
Photons per pulse	2.0	1.0-2.3	10^{12}

The ultra-high brightness electron beam necessary for the operation of an X-ray FEL requires the accurate measurement of a sub-μm emittance and sub 10 μm long electron beam in both transverse and longitudinal coordinates with state of the art diagnostics. The layout of the LCLS is depicted in Fig. 1 with the location of some of the diagnostics devices indicated. The 250 pC electron beam is generated in a laser-driven photocathode RF gun at 6 MeV and subsequently accelerated in four linac sections (L0-L3) to energies of 135 MeV, 250 MeV, 4.3 GeV, and the final energy of 13.6 GeV. After L1 and L2 the bunches are compressed in two chicanes from 750 μm to 40 μm and 10 μm. The beam is then transported through a dog-leg bend magnet system to the 100 m long undulator consisting of 33 segments and dumped in the main beam dump, whereas the generated X-ray beam enters the X-ray diagnostics, transport, and the various experimental areas (not shown). The main parameters of the electron and X-ray beam are listed in Table 1. The design parameters refer to the high charge mode at 1 nC, whereas the measured ones are given for the medium charge operating mode at 250 nC. Recently, a low charge mode with only 20 pC has been explored [3]. The beam in this mode has a slice emittance of 0.14 μm and can be compressed to an estimated final rms bunch length of about 1 μm giving the same peak current and FEL peak power, but a much shorter X-ray pulse.

Table 2: LCLS Accelerator diagnostics devices

Type	#	Nom. res.	Units
Strip Line BPM	144	5	μm
RF cavity BPM	36	1	μm
Beam current monitor	13	2	%
Phase cavity	5	100	fs
Faraday cup	2	2	%
Wire scanner	17	20	μm
YAG screen	7	15	μm
OTR screen	13	10	μm
Bunch length monitor	2	5	%
Deflecting cavity	2		

A list of all the beam diagnostics devices is given in Table 2 together with their respective highest resolution requirements for each device. In the following sections, the design and operational performance of the various diagnostics for transverse and longitudinal beam parameters, as well as some of the X-ray diagnostics will be discussed.

* Work supported by US DOE contract DE-AC02-76SF00515.
† loos@slac.stanford.edu

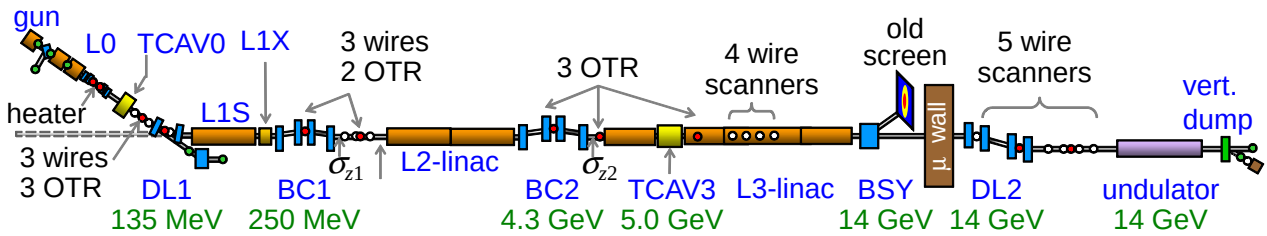

Figure 1: Layout of the LCLS accelerator.

TRANSVERSE DIAGNOSTICS

The main use of the instrumentation for transverse beam diagnostics at LCLS, beam position monitors, wire scanners, and profile monitors is for beam orbit measurement and feedback, and for transverse emittance measurement and optimization. Furthermore, these diagnostics also play an important role for measurements of longitudinal parameters with the transverse defecting cavity.

Beam Position Monitors

Most of the BPMs installed at LCLS are strip line BPMs with more than 80 of them inherited from the SLC linac and more than 60 new ones in the injector and the new transport system to the undulator. The old SLC strip line BPMs were designed to measure beams of nC charge and could not be used for LCLS operation at 20 pC. They have been upgraded over the past year with the same data acquisition electronics as for the new LCLS BPMs and have all been integrated into the EPICS control system. All strip line BPMs are continuously calibrated between beam triggers by sending 4 test pulses in each of the electrodes. Two attenuators are used to scale the signals to the charge levels at different operating modes.

A beam synchronous acquisition system enables the pulse by pulse measurement of all BPMs together with other control system parameters for up to 2800 bunches at all LCLS beam rates from single shot to 120 Hz. Besides providing shot by shot beam orbits, this acquisition system can also be used to measure the BPM resolution as shown in Fig. 2. In a model independent analysis (MIA) [4] a singular value decomposition of the matrix of measured beam orbits yields an orthogonal basis of all the different jitter and noise contributions. The strongest singular values represent correlated beam motion and the figure shows the remaining rms noise from 500 orbits after subtracting the effect of the largest 10 values. At 250 pC the average noise of the strip line BPMs is 3 μm which is well below the beam size of several 10s of μm of the LCLS electron beam. For the low charge 20 pC beam the BPM signal becomes weak and the noise rises to 25 μm rms which at many locations can be comparable to the rms beam size for this low charge.

For a stable FEL operation the beam orbit within the 100 m long undulator needs to be straight within only a few μm over a distance of several of the 33 segments. This requirement of sub-μm resolution and offset stability could be met with RF cavity BPMs [5] located at the end of each girder which supports one of the 3 m long undulator segments and a quadrupole besides the BPM. The BPMs [6] consist of two cavities, one degenerate dipole mode cavity and one reference cavity for signal normalization with both operating at 11.4 GHz. The signal is then down-converted to 40 MHz IF and analyzed in a 16 bit VME digitizer. In contrast to the strip line BPMs the calibration of the RF BPMs has to be done using signals from the electron beam itself. This can be done in two different ways. A slow method with high precision is to move the girder which supports the BPM and the respective undulator segment by known amounts and observe the change in the beam position measured by the BPM. A faster way is to use a corrector magnet to introduce an orbit oscillation upstream of the undulator whose magnitude is measured with the upstream strip line BPMs and then measuring the response of the cavity BPMs. The resolution can again be obtained

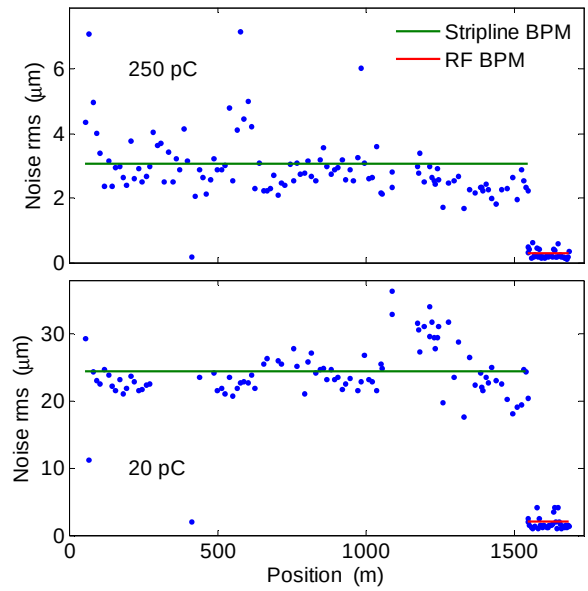

Figure 2: Measured BPM noise level along the accelerator. The top part is at 250 pC with an average noise of 3 μm for the strip line (green) and 300 nm for the RF BPMs (red), the bottom one is at 20 pC with 25 and 2 μm, respectively.

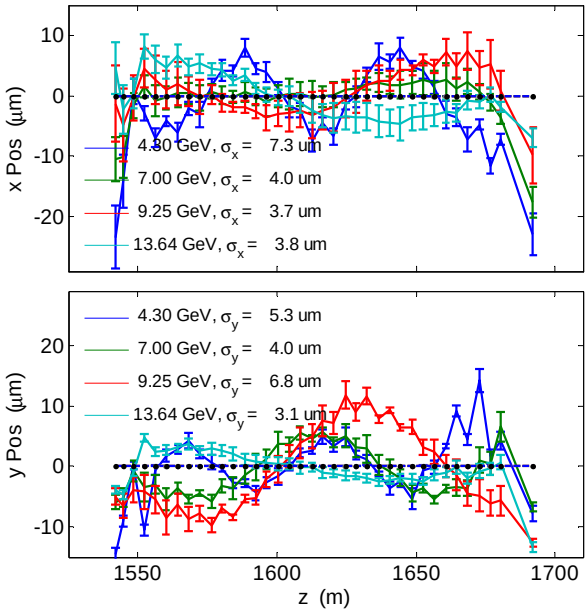

Figure 3: Beam orbit measured with RF BPMs and averaged over 50 shots in the undulator at 4 different energies after applying beam based alignment. The orbit rms deviation σ includes incoming betatron oscillation due to upstream beam jitter.

from signal correlations between BPMs and is also shown in Fig. 2. The average noise level at 250 pC of 300 nm is well below the requirement and most of the BPMs are even around 200 nm. The noise level grows to 2 μm at 20 pC.

The effect of the sub-μm RF BPM resolution can be seen in the results of the beam-based alignment (BBA) procedure for the undulator segments. The FODO lattice within the undulator is designed to be operated at the same field within the nominal energy range from 4.3 to 13.64 GeV of the LCLS electron beam. A measurement of the beam orbit at several energies spanning this range can be used to find both the deviations of the BPM positions and of the absolute beam orbit from a straight line. The position of the quadrupoles and the BPM offsets can then be corrected to generate a dispersion free beam orbit at the BPM locations [7]. Figure 3 shows beam orbits averaged over 50 beam pulses for 4 different energies after applying several iterations of the correction procedure. The remaining rms orbit deviation is only a few μm and results mostly from incoming beam position jitter.

Wire Scanners

Wire scanners are used at various locations in the accelerator to provide measurements of transverse and longitudinal beam profiles in a less interceptive way than view screens because the beam hits the wire only for a couple of pulses. A wire card holding three wires in vertical, horizontal, and one in 45 ° direction is moved through the beam at an angle of 45 ° so that each of the horizonal, vertical, and 45 ° projection can be measured. The tungsten wires have diameters of 20 - 40 μm which are matched to the respective beam size at the wire scanner location. This sets a resolution limit of 5 - 10 μm based on the finite thickness which can be subtracted from the beam size measurements in the analysis software. The wires are moved by stepper motors and transverse vibrations of the wire card of 10s of μm which were observed at the beginning of the LCLS commissioning could be significantly reduced by either the installation of gear reducers or the use of microstepping for the motors. The bremsstrahlung generated at the wires is detected with fast ion chambers, with PMTs detecting Cherenkov radiation from secondary electrons, or with PMTs looking at the light from plastic scintillator fibers strapped along the beam pipe.

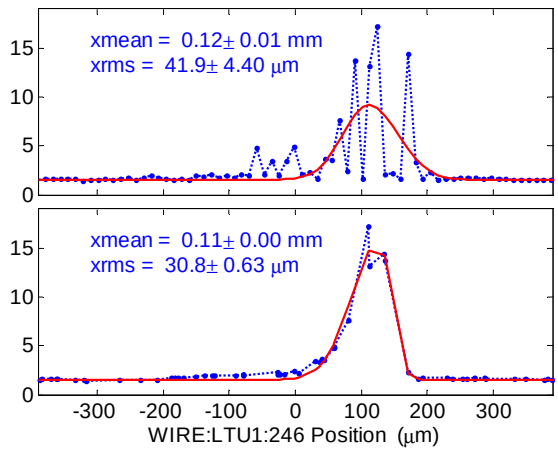

Figure 4: Beam jitter correction for wire scan data. The top part shows the PMT signal vs. the raw wire position with an rms beam size of 42 μm. In the bottom part the wire position is corrected shot by shot and the rms beam size reduces to 31 μm.

Essential for a high resolution beam size measurement is a correction of the effect of the transverse beam position jitter. This requires the synchronous measurement of the beam position at several nearby BPMs together with the PMT signal and the wire position for each bunch. A beam orbit fit then determines the distance of the beam to the wire for each bunch. This correction is particularly important in an energy spread or bunch length measurement where the transverse jitter can exceed the beam size. The effect of the jitter correction is shown in Fig. 4 for the wire scanner in a dispersive location in the DL2. The beam jitter correction also enables precise beam size measurements for emittance measurement and beta-matching of the lattice as shown in Fig. 5.

When the transverse beam jitter or a deliberate transverse motion of the beam exceeds the beam size, this can be used to measure beam profiles without scanning the wire. The profile is then sampled by the beam jitter alone. One application is to measure beam parameters in a pulse

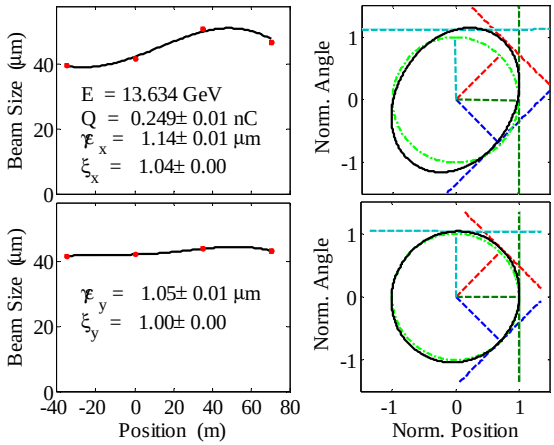

Figure 5: Emittance measurement upstream of the undulator using 4 wire scanners with 45° phase advance between them. The left panels show the measured beam sizes in the horizontal and vertical plane, and the right panels the respective normalized phase space ellipse. The dashed lines indicate the projection angle for each measurement.

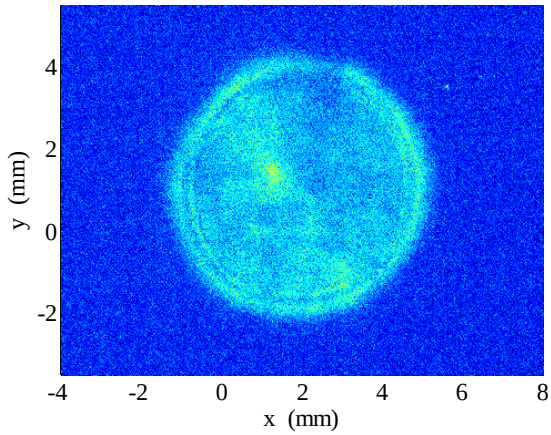

Figure 6: Electron beam distribution at 15 pC charge on a YAG screen downstream of the gun showing the electron emission pattern from the cathode.

stealing mode. The wire is parked at a location near the beam and a small fraction of the bunches at 1 Hz is transversely kicked to intercept the wire while the majority of the bunches is still delivered to the FEL user. An example of this almost non-intercepting diagnostic method is the pulse stealing bunch length measurement discussed later.

Beam Profile Monitors

The beam profile monitors enable the measurement of single shot transverse beam distributions throughout the accelerator and are mainly used for emittance, energy spread and bunch length measurements. In the low energy part of the machine at energies below 135 MeV they consist of 100 μm thin YAG:Ce crystals perpendicular to the beam and a 1 mm thick mirror behind it for viewing at 90 degrees. At 130 MeV and above, 1 μm thin aluminum foils are employed as optical transition radiation (OTR) screens at 45 degrees to the beam. Beam images from both targets are obtained with a 50 mm focus telecentric lens and a mega-pixel CCD camera with an effective pixel resolution as low as 10 μm/pixel. The depth of focus of about 1 mm provides an equally wide stripe of adequate image quality for the 45 degree OTR foils and the geometry is chosen to match the stripe direction with the dispersion direction or the streak direction of the deflecting cavity. The small resolution is sufficient to measure beam sizes as small as 25 μm whereas the large number of pixels provides a field of view necessary to measure a dispersed beam or the beam deflected with the deflecting cavity. The 12 bit ADC of the cameras equate to a S/N ratio of 1000. This gives a dynamic range of larger than 10^5 together with the two insertable neutral density filters having an attenuation of up to 1000.

The YAG screens are mainly used in the gun area at a beam energy of 6 MeV where the photon yield for OTR is too low and at higher energy in the injector where the beam size is large and saturation is not a concern. They are used in the gun area at for their high sensitivity to measure the electron beam emission pattern from the photo-cathode at a charge of only a few pC and in the injector spectrometer at 135 MeV where the beam can be streaked with a deflecting cavity to observe the longitudinal phase space. Figure 6 shows the beam spot on a YAG screen right after the gun with the gun solenoid magnet set to image the electron distribution generated on the cathode by the laser onto the downstream YAG screen. A low charge of 15 pC is necessary to avoid space charge distortions.

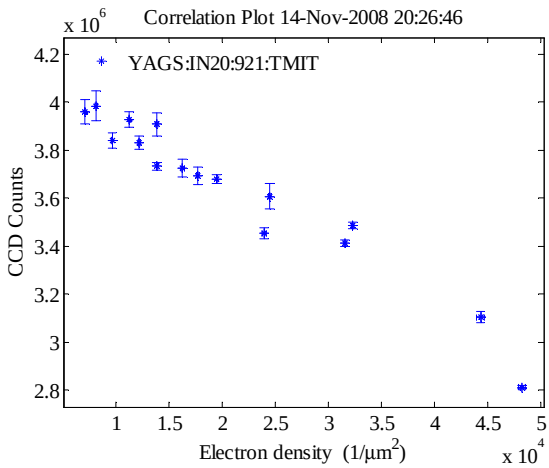

Figure 7: Image intensity of a YAG screen as a function of electron density on the crystal. The density was varied by scanning an upstream quadrupole.

For higher charges quantitative beam size measurements with a YAG screen are limited by saturation effects in the

YAG:Ce crystals. Figure 7 shows a measurement of the total CCD counts on a YAG screen in the injector spectrometer line at 135 MeV. An upstream quadrupole magnet was scanned to vary the beam size and the plot shows the integrated image intensity as a function of the calculated electron density. Saturation occurs at densities higher than $15000\,e^-/\mu m^2$ which corresponds to a rms beam size of 130 μm at 250 pC. This makes YAG screens unsuitable for most locations in the accelerator where the beam size can be significantly smaller.

The emission of optical transition radiation has about a factor 1000 lower quantum efficiency compared to scintillator screens, but it does not show saturation effects and the resolution is not limited from the finite crystal thickness. The beam going though a 1 μm foil can still be transported through the remainder of the accelerator with negligible beam loss. OTR screens were therefore installed in the injector and the BC1, BC2, and DL2 areas to measure the projected and time resolved (slice) emittance, as well as energy spread and bunch length. In the undulator for the injector laser heater two OTR foils are used to transversely overlap the electron beam with an 800 nm wavelength laser beam [8].

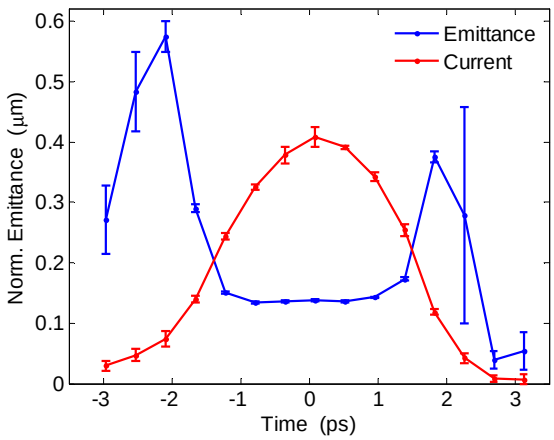

Figure 8: Measurement of the horizontal slice emittance in the injector at 20 pC. The normalized emittance in the core slices of the beam is 0.14 μm.

Originally specified to diagnose beams of a charge between 250 pC and 1 nC, the lens and camera system proved to be able to measure the time resolved beam size of a 20 pC beam in the injector with a slice charge as low as 2 pC. Figure 8 shows the result of such a measurement where the transverse deflector cavity in the injector was used to vertically deflect the electron beam and with a quadrupole scan the horizontal beam size and slice emittance could be obtained. At 20 pC the core of the beam has a normalized emittance of only 0.14 μm. Figure 9 shows the beam size a a function of the quadrupole strength for slice number 6 near the center of the beam with the beam size as small as 25 μm.

The OTR screens proved very reliable in the injector part

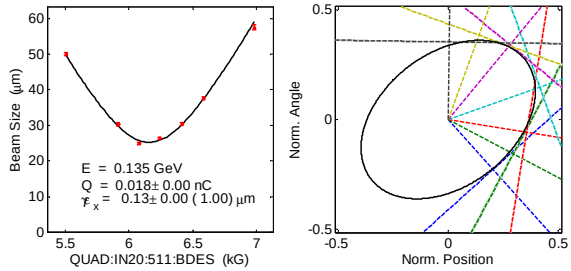

Figure 9: Beam size and normalized phase space of slice number 6 from the measurement shown in the previous figure.

of the LCLS, however, the unexpected observation of coherent effects in the optical transition radiation (COTR) in the accelerator downstream of the injector made this diagnostics much less useful. The coherent effects originate from a longitudinal structure in the beam at optical wavelengths and is manifest in a non-linear relation between charge and OTR intensity and therefore a transverse OTR distribution not proportional to the charge distribution. At long ps bunch lengths is due to longitudinal space charge forces modulating the energy distribution of the beam. After traveling through a bend magnet system with a non-zero R_{56} matrix element, the modulation appears in the time domain and the bunch emits coherent radiation. The effect on the beam size measurement can be seen in Fig. 10. The beam size is measured downstream of the 35° DL1 bend system with the strength of the dispersion correction quadrupole inside the dog-leg varied. The expected small change of a few % in beam size from the varied quadrupole strength is shown as a red line. The measured size of the OTR distribution drops by a factor of 2 around the optimum quadrupole strength of 10.8 kG where the dispersion is fully canceled. This change in apparent beam size is accompanied by a factor 3 increase in the OTR intensity (not shown).

More dramatic effects occur when the LCLS beam is compressed to bunch lengths in the range of 10s of μm to a few μm rms. Then the bunch length is only a factor 10 longer than the visible OTR wavelengths and a significant fraction of the beam can radiate coherently [9]. The light intensity can increase by up to 5 orders of magnitude and the transverse OTR distribution becomes fractured or ring-shaped.

A possible mitigation scheme is to use a YAG crystal instead of the OTR foil at locations with a large beam size. The YAG crystal surface will still emit OTR with about a factor 3 less than from a foil, but the YAG fluorescence is about 3 orders of magnitude larger than the incoherent OTR. This ratio can be further enhanced with a narrow bandpass filter at the YAG peak emission wavelength of 525 nm and a few degree tilt of the crystal to prevent the highly collimated COTR light from entering the camera optics. Such a setup was recently installed in the LCLS

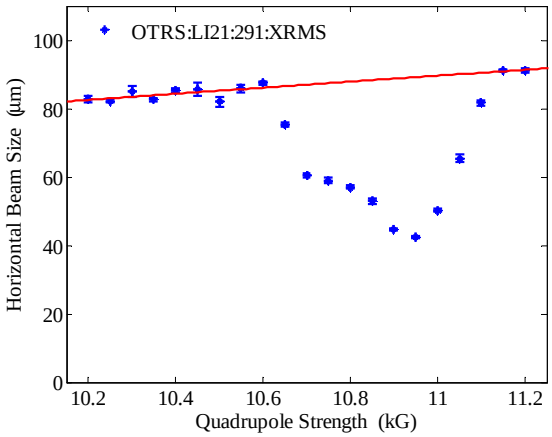

Figure 10: Measured OTR distribution rms size downstream of DL1 with the dispersion correction magnet in DL1 varied. Shown in red is a smooth line indicating the expected small change in true beam size from the varied quadrupole.

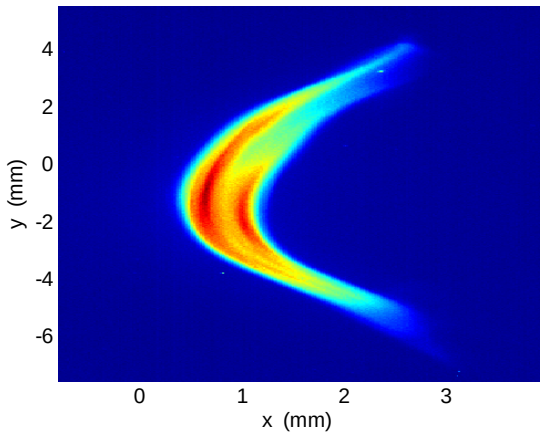

Figure 11: Longitudinal phase space on the YAG screen in the injector spectrometer. The horizontal axis is dispersed showing energy spread whereas the vertical axis is streaked by the deflecting cavity to show the temporal distribution. The image clearly shows the double peak structure in the energy distribution due to the laser heater interaction.

main dump line to replace the existing OTR screen and its performance is currently studied. The increased beam loss due to the 100 μm thick crystal is not a high concern at this location, but how to replace the OTR screens at other locations in the linac and especially upstream of the radiation sensitive undulator is an open question.

LONGITUDINAL DIAGNOSTICS

A precise measurement of both the ps long bunch length in the injector and the ultra-short bunch lengths of the compressed beam with lengths of only a few μm is essential to obtain the kA peak currents required for operation of the FEL. The absolute bunch length measurement is done with transverse deflector cavities, whereas a relative measurement needed for the longitudinal feedback uses a measurement of integrated far infrared coherent radiation from the bunches.

Transverse Deflecting Cavities

Two transverse deflecting cavities [10] are installed in the LCLS. The first one in the injector with 50 cm length is used to measure the initial bunch length and slice emittance of the beam and is operated at about 1 MV field. The phase of the cavity is set to one of the zero-crossings of the field so that the head and tail of the bunch are kicked vertically in opposite directions. This maps the longitudinal distribution onto the vertical axis and the mapping can be calibrated by changing the phase of the cavity away from the zero-crossing to observe the vertical motion of the beam centroid. The use of the deflecting cavity for time resolved emittance measurement was discussed earlier (see Fig. 8).

A measurement of the longitudinal phase space is shown in Fig. 11 with the beam observed on a YAG screen in the injector spectrometer. The horizontal axis represents the energy spread and the vertical axis the temporal distribution. The double horn structure in the energy distribution shows the effect of the laser heater to increase the uncorrelated energy spread of the beam from 3 to 10s of keV, depending on the energy of the laser heater [8].

The second, 2.44 m long transverse deflecting cavity is located in the L3 linac after the second bunch compressor and operates at 15 MV field to accommodate the much shorter bunch length there. An off-axis OTR screen located downstream of the deflecting cavity at 90 ° degree phase advance to map the vertical kick of the cavity onto vertical displacement was originally intended to measure the streaked beam profile with pulses steered onto the screen with a fast horizontal kicker magnet. The strong COTR emission from the ultrashort beam prevented reliable beam profiles and instead a lower resolution legacy phosphor screen in the beam switch yard of the SLC was used [11]. This screen is not in the LCLS beam line and requires a special beam setup, therefore more recently, a bunch length measurement was set up to use one of the 4 wire scanners in the L3 linac downstream of the deflecting cavity.

The deflecting cavity calibration factor for the wire scanner with the proper phase advance is about 2 μm/fs and the 50 fs timing jitter between the electron bunches and the cavity phase translates into 100 μm rms vertical orbit jitter at the wire scanner. This is twice the beam size and a precise jitter correction is essential. The pulse stealing mode for the wire scanners described above can be applied with the deflecting cavity triggered at 1 Hz while the pulses used for the FEL run at a higher rate of 10 to presently 60 Hz. During the 99 pulses acquired the wire is moved to 3 different off-axis positions with about 0.5 mm spacing to capture the entire beam profile. The measured PMT signals

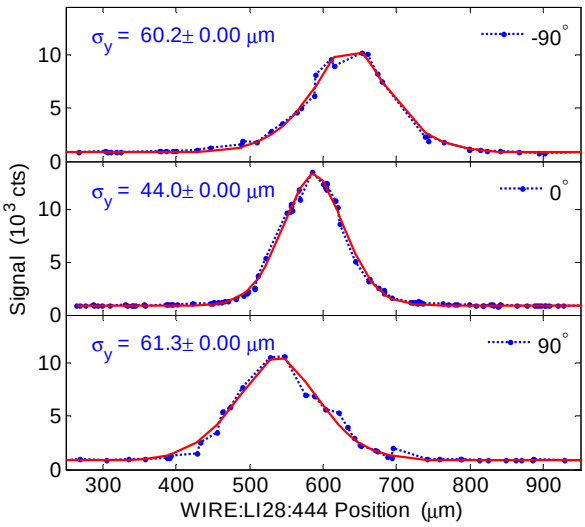

Figure 12: Beam profiles for bunch length measurement in 1 Hz pulse stealing mode. The top and bottom part show the profile with the deflecting cavity at $\pm 90^\circ$ and the wire placed at three positions. The middle part shows the intrinsic vertical beam size measured with the wire in 13 different positions. The wire locations are corrected for beam jitter.

vs. the relative position between wire and beam is shown in Fig. 12 at 250 pC for the two zero-crossing phases -90° and $+90^\circ$ and for the case with the cavity off. In this case the transverse jitter is only a small fraction of the beam size and the wire was placed at 13 different positions to obtain a full beam profile. The beam sizes are about 60 μm with and 44 μm without the cavity on.

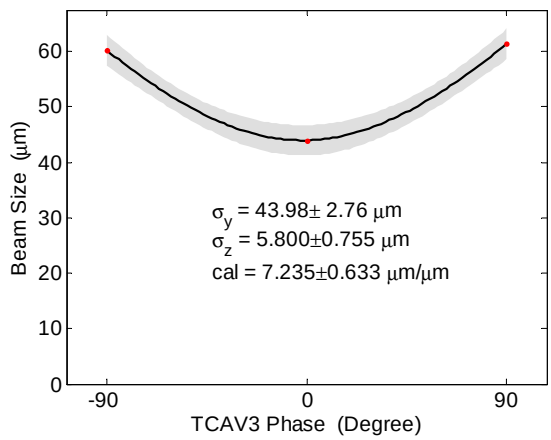

Figure 13: Bunch length measurement with wire scan in pulse stealing mode with data points from the previous figure. The data point at 0○ is with the cavity off. The bunch length is 5.8 μm.

To obtain the bunch length the intrinsic transverse beam size has to be subtracted in quadrature from the streaked beam size and then the calibration factor needs to be applied. The result is shown in Fig. 13 with a bunch length of 6 μm which was slightly more compressed than the nominal 8 μm bunch. The error on the measured length is less than 1 μm. In pulse stealing mode this measurement takes only about 5 min and can be run parasitically to the user operation to monitor the peak current with an absolute measurement.

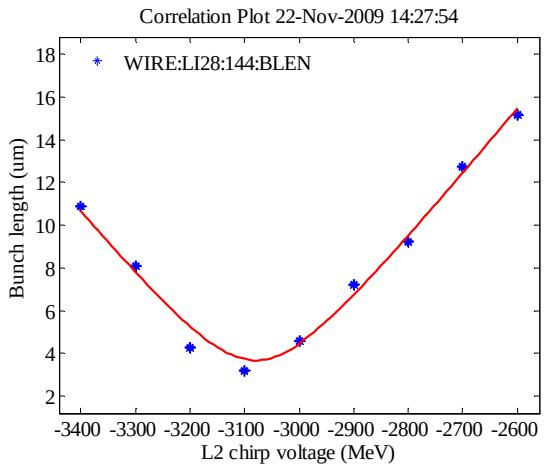

Figure 14: Scan of the bunch length vs. chirp voltage in the L2 linac. The normal operating point is around -2900 MeV with an under-compressed bunch length of 7 μm. The shortest bunch length is 3.5 μm. Shown in red is a fit to the measured bunch length assuming linear compression.

The full range of bunch lengths can be measured when the phase or equivalently the chirp voltage of the L2 linac upstream of the second bunch compressor is varied. The result of this scan using the normal scan mode of the wires at full beam rate is shown in Fig. 14 with an under-compressed beam to the right and an over-compressed beam to the left. At full compression the beam is as short as 3.5 μm.

For the 20 pC low charge operation sub-μm bunch lengths have been predicted by simulations [3]. With a smaller intrinsic beam size at low charge a measurement of much shorter bunch lengths than 3 μm should be possible. However, this has not been successful yet because the necessary jitter correction is insufficient at low charge. The BPM noise of 25 μm is of the order of the transverse beam size and the error of the size measurement is larger than the expected increase in beam size due to the streak from the deflecting cavity. A cavity operating at the X-band frequency 11.4 GHz and more than twice the voltage is in development to be placed downstream of the undulator. Such a system could have 10 times the resolution compared to the present system after BC2 and should be able to measure sub-μm bunch lengths.

Relative Bunch Length Monitors

The longitudinal feedback system for the LCLS requires a single shot non-intrusive measurement of the bunch length which does not have to be absolute. This is accomplished with relative bunch length monitors [12] using the coherent edge radiation [13] emitted from the exit edge of the last dipole magnet in each bunch compressor chicane. The radiation is emitted in a cone and reflected off the beam axis by an annular mirror with a 15 mm diameter aperture to pass the electron beam undisturbed. The radiation is imaged with off-axis paraboloidal mirrors onto pyroelectric detectors to integrate the far infrared spectral range which is strongly correlated to the bunch length. A shorter bunch emits a radiation spectrum which extends further to shorter wavelengths, thus increasing the integrated intensity. Insertable low and high pass filters can be used to optimize the wavelength range for the detector. Two bunch length monitors are installed, one after each bunch compressor. The wavelength range most sensitive to the bunch length σ_z extends from $2\pi\sigma_z$ to longer wavelengths. For the monitor after BC2 a diffusive low pass filter with 100 μm cut-off wavelength rejects the near IR radiation emitted from micro-structure within the bunch which is unrelated to the bunch length.

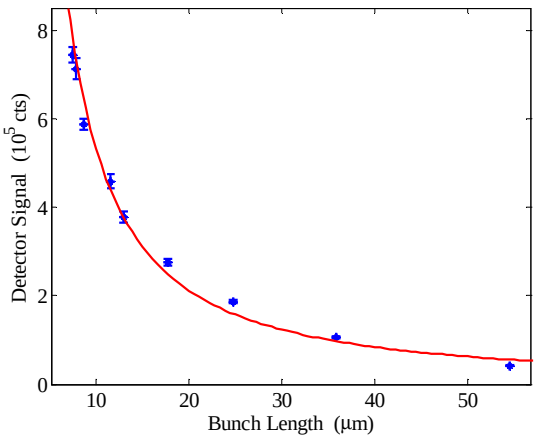

Figure 15: Calibration of the relative bunch length monitor after BC2 with an absolute measurement using the deflector cavity and a wire scanner. The red line is a fit to the data using an inverse 4/3 power law of the bunch length.

Figure 15 shows the raw signal from the pyroelectric detector after BC2 as a function of the bunch length measured with the deflecting cavity and a wire scanner in L3. The red line is a fit of the signal to the bunch length assuming a signal dependency to the inverse 4/3 power of the bunch length and a quadratic dependency to the bunch charge. The fit parameter is then used in the control system to calculate a bunch length from the shot by shot signal and convert it into a peak current value assuming a parabolic charge distribution [14]. This enables a peak current set point for the feedback system.

X-RAY DIAGNOSTICS

The diagnostics for the x-ray beam generated in the LCLS undulator is mainly located in the front end enclosure (FEE) downstream of the main dump and before the user experiments. It comprises of adjustable beam collimators, a solid and a gas attenuator system for hard and soft x-ray energies respectively, two gas detectors, a direct imager, a fixed photon energy monochromator system, and a total energy monitor. A diagnostic with a electron beam type YAG screen was installed in the main dump area in the photon beam line after the dump bend magnet system prior to the LCLS startup in early 2009 as a preliminary X-ray diagnostics before the systems in the FEE became available.

Energy Measurement

An absolute measurement of the X-ray photon energy is done by measuring the loss in energy of the electrons during the lasing interaction in the undulator. The electron beam energy is determined from the beam position in the main dump line downstream of the dump bend magnets. The determination of the energy loss has to take into account the losses due to wake fields in the narrow undulator vacuum chamber as well as losses due to spontaneous radiation emission. This is done by comparing the electron beam energy with the electron beam on the undulator beam axis with the energy when the beam is kicked on an off-axis orbit which suppresses lasing, but does not influence the other two kinds of energy loss.

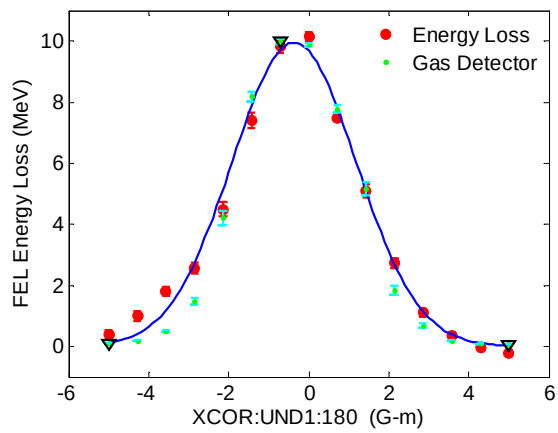

Figure 16: FEL pulse energy determination by electron beam loss and gas detector measurements.

A scan of the beam energy difference between various orbits in the undulator is shown in Fig. 16 at 4.3 GeV electron beam energy and 820 keV photon energy with the beam energy of the most disturbed orbit as zero-reference. The maximum energy loss of 10 MeV per electron at the peak corresponds to 2.5 mJ X-ray pulse energy for a bunch charge of 250 pC. This invasive measurement can then be

used to calibrate or compare the X-ray energy measurements in the FEE.

A non-intrusive single shot measurement is provided by the two gas detectors [15] in the gas attenuator system in the FEE. A section of the photon transport vacuum line can be brought to a pressure of up to 20 Torr of nitrogen gas with a differential pumping system. At the location of the gas detectors between the pumping stations the pressure is between 0.1 and 2 Torr, depending on the X-ray wavelength. The nitrogen gas being hit by the X-rays emits Auger electrons which are trapped by a magnetic field in the vacuum chamber to generate secondary electrons which in turn cause light emission in the UV from the nitrogen gas. The light is then detected by PMTs or avalanche photodiodes. The signal from the gas detectors depends strongly on the X-ray wavelength and intensity.

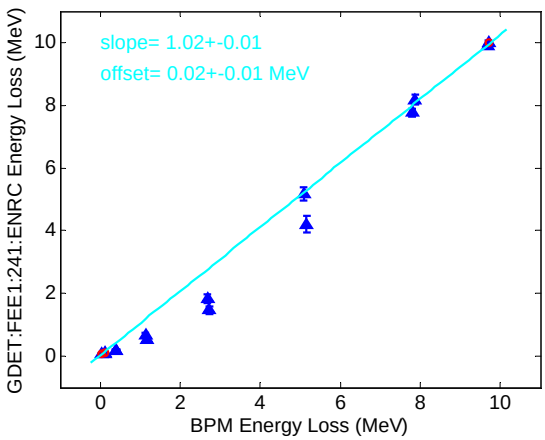

Figure 17: Gas detector calibration from energy loss scan.

Figure 17 shows the calibrated gas detector signal as a function of the energy loss as measured with the electron beam loss shown in the previous figure. This kind of calibration is done routinely whenever the photon energy is changed.

Transverse Diagnostics

The measurement of X-ray position and beam size uses the same kind of YAG:Ce crystals used for electron beam diagnostics. The two different screens mainly used are the one in the quick-change diagnostic chamber in the main dump area and the screen ona target ladder in the direct imager downstream of the X-ray attenuators. Figure 18 shows the YAG screen in the dump area with the FEL operated at 13.64 GeV. Besides the main X-ray spot in the screen center, the rectangularly shaped background of spontaneous emission shadowed by the undulator vacuum chamber and the circular ring pattern of visible light emitted from the exit edge of the first dump dipole magnet is visible. A vertical diffraction pattern from a 20 μm thick carbon wire inserted into the X-ray beam at the last undulator segment is also present in the image and can be used to estimate the transverse coherence of the X-ray beam.

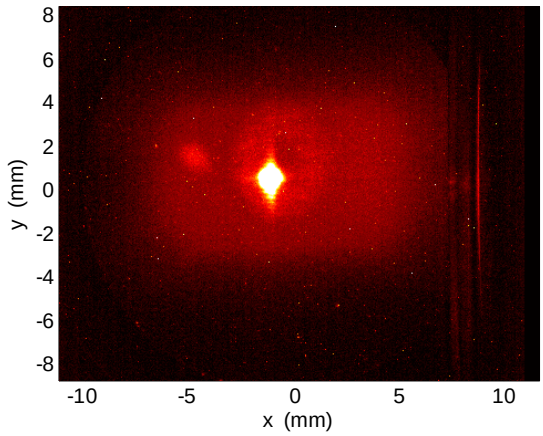

Figure 18: Image from the YAG screen in the photon beam line after the main dump at an electron beam energy of 13.6 GeV. The image shows the X-ray pulse as well as the background from spontaneous radiation and the visible ring pattern of edge radiation from the first dump bend magnet.

The X-ray beam image at 2 keV photon beam energy is shown in Fig. 19 for the narrow field of view (NFOV) direct imager with a 1 mm thick YAG crystal inserted. The camera is a high dynamic range cooled CCD with a 16 bit digitizer and a 512×512 pixel array. Besides beam size measurements, both screens are also used to measure the X-ray pulse energy as a function of undulator length to determine the gain length of the FEL. In contrast to the gas detector measurement the sensitivity of the screens can quickly be changed with light attenuators and an absolute energy measurement is not necessary.

SUMMARY

The diagnostics implemented for the LCLS electron beam has made it possible to measure and achieve all the transverse and longitudinal beam parameters required for a successful operation of the FEL. All the diagnostics are well integrated into the EPICS control system and high level Matlab applications provide automated measurement procedures and displays for all beam parameters. The unexpected appearance of COTR compromising the beam profile measurement of the compressed bunches could be offset by using existing wire scanners and installing additional ones in DL2 and the main dump. Time resolved measurements of emittance and energy spread however require the acquisition of 2-D distributions and an adequate substitute or COTR mitigation for the OTR screens has not been found yet. New diagnostics are also necessary to measure the sub-μm long bunches in the low charge operating mode and various schemes are being discussed. The commissioning of the soft X-ray user beam line will provide a single shot X-ray spectrum measurement which will complement the X-ray monochromator in the FEE operating at the fixed

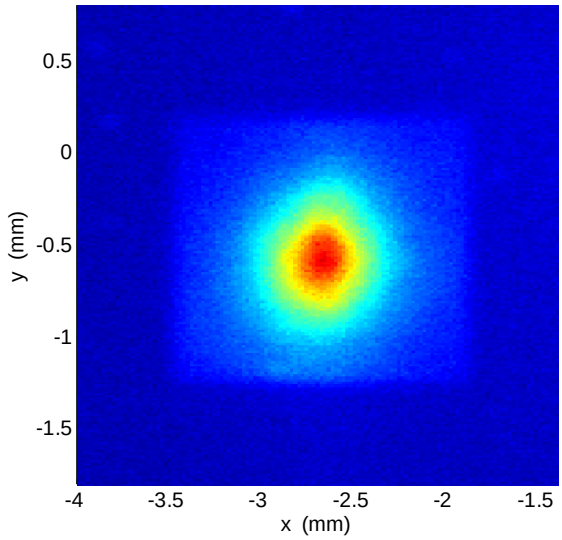

Figure 19: Image from a YAG screen in the direct imager showing the FEL pulse and the spontaneous radiation clipped by upstream collimator jaws.

photon energy of 8.3 keV. Additional instrumentation for energy measurement with a thermo-acoustic sensor will be added to the quick-change diagnostic chamber in the main dump area. One remaining issue for future diagnostics development is the absolute measurement of the X-ray pulse length.

REFERENCES

[1] J. Arthur, *et al.*, Linac Coherent Light Source (LCLS) conceptual design report, SLAC-R-593, SLAC (2002).

[2] P. Emma, Proceedings of PAC 2009, Vancouver, BC, May 2009, p. TH3PBI01 (2009).

[3] Y. Ding, *et al.*, Phys. Rev. Lett. 102 (2009) 254801.

[4] J. Irwin, *et al.*, Phys. Rev. Lett. 88 (1999) 1684.

[5] S. Smith, *et al.*, Proceedings of PAC 2009, Vancouver, BC, May 2009, p. TU3GRC05 (2009).

[6] R. M. Lill, *et al.*, Proceedings of PAC 2007, Albuquerque, NM, June 2007, p. FRPMN111 (2007).

[7] P. Emma, *et al.*, Nucl. Instr. and Meth. A 429 (1999) 407.

[8] P. Emma, *et al.*, Proceedings of PAC 2009, Vancouver, BC, May 2009, p. WE5RFP041 (2009).

[9] H. Loos, *et al.*, Proceedings of FEL 2008, Gyeongju, Korea, Aug. 2008, p. THBAU01 (2008).

[10] O. H. Altenmueller, R. R. Larsen, G. A. Loew, Rev. Sci. Instrum. 35 (1964) 438.

[11] R. Akre, *et al.*, Phys. Rev. ST Accel. Beams 11 (2008) 030703.

[12] H. Loos, *et al.*, Proceedings of PAC 2007, Albuquerque, NM, June 2007, p. FRPMS071 (2007).

[13] R.A. Bosch, Rev. Sci. Instrum. 73 (2002) 1423.

[14] J. Wu, *et al.*, Proceedings of FEL 2008, Gyeongju, Korea, Aug. 2008, p. MOPPH052 (2008).

[15] S. P. Hau-Riege, *et al.*, J. Appl. Phys. 103 (2008) 053306.

MEASUREMENT OF LATTICE PARAMETERS WITHOUT VISIBLE DISTURBANCE TO USER BEAM AT DIAMOND LIGHT SOURCE

G. Rehm, M.G. Abbott, A.F.D. Morgan, J. Rowland, I. Uzun
Diamond Light Source, Oxfordshire, United Kingdom

Abstract

With refined lattice tuning it becomes increasingly important to monitor or feedback on many parameters to keep stable optimum operating conditions. To this end we present techniques to measure betatron tune, chromaticity, betafunction magnitude/phase, and orbit response matrices all in such a way that no disturbance to the stored beam can be observed by the users of the light source. Examples of measurements for the various categories are compared to established methods, and their use in feedback schemes is discussed.

INTRODUCTION

Many measurements of lattice parameters require an excitation or change in setting that typically leads to a change in the beam position or shape. That is not acceptable during user operation in a synchrotron light source, where positional/angular stability to a fraction of a beam size/divergence is paramount (integrated motion of 10% of beam size/divergence up to 100Hz has often been quoted [1] as acceptable, but the demands are often even lower today):

- Measurement of betatron tune requires excitation of beam oscillations with a broadband signal. This is typically a kick, sweep/chirp or broadband noise delivered to the beam through a stripline or similar device. This leads to a blow up of the emittance for the duration of the excitation and following decay of the oscillations.
- Measurement of chromaticity usually requires measurement of the betatron tune at different stored beam energies. This is usually accomplished by changing the main RF frequency, which displaces the beam to a dispersive orbit in addition to the repeated blow up of the emittance from the repeated tune measurements.
- Orbit response matrix measurement requires changing of each corrector magnet one at a time and measuring the resulting differences in orbit. Again, this leads to displacements of the orbit which are many times the beam size. Furthermore, a complete response matrix measurement will take many minutes due to the large number of correctors typically present.
- Measurement of betafunction magnitude and phase is most often derived from a full orbit response matrix measurement.

On the other hand, the demand for regular measurements of all these parameters is increasing as refined tuning of machines requires continuous monitoring or feedback schemes. For example, the precise betatron tune decides the lifetime and injection efficiency, but it will vary with changes in insertion devices (IDs).

We have developed techniques which allow to perform these measurement with no visible disturbance to the user beam by either only exciting a small fraction (one bunch in a train of typically 720) for the tune measurement, or by exciting with small amplitudes (less than beam size) at high frequencies (only leads to an insignificant 'smearing' of the beam) and detecting these small signals with dedicated signal processing of longer durations. The trade off between small amplitude and longer observation time has allowed maintaining resolution at a level comparable to the standard techniques.

Common Principle of Excitation and Detection

The common principle shared by all the discussed applications is the injection of a small, sinusoidal disturbance, which is then measured by digital I/Q detectors which share the same time/frequency base as the excitation. In this way we are able to measure magnitude and phase of the response in a similar way as a lock-in amplifier does. In the following sections we will discuss the technical details of the implementations and show example measurements.

BETATRON TUNE MEASUREMENT

For the betatron tune measurement we excite the beam at a frequency near the nominal tune using a numerical oscillator (NCO) in the transverse multibunch feedback (TMBF) [2]. The beam motion is then detected in the same device by multiplying each bunch position with a

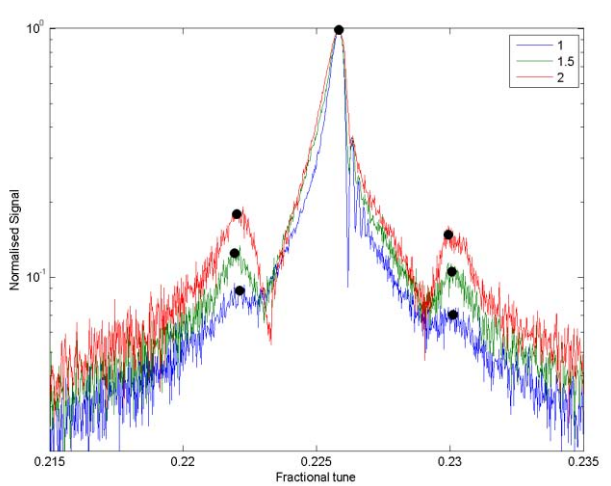

Figure 1: Horizontal betatron tune spectra for chromaticities 1, 1.5 and 2

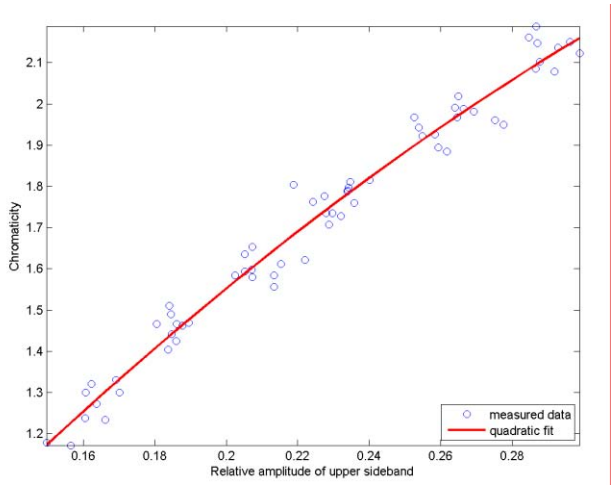

Figure 2: Measured chromaticity (by changing stored beam energy) and observed relative amplitude of a synchrotron sideband.

sine and cosine of the excitation frequency and accumulating the result for a certain period (we use 100 turns or 180μs). The frequency is then incremented by a small amount, and the process repeated for 4096 different frequencies, thus completing a sweep in less than 1 second. To operate the excitation in conjunction with the transverse multibunch feedback and to minimise the disturbance to the beam, we normally excite only one bunch, while the feedback operates undisturbed on all others.

The whole excitation and detection process is fully automated and implemented in the feedback FPGA, which delivers waveforms of I and Q per frequency point through to the EPICS driver. Inside the driver software, the sum of squares is computed and a simple peak find algorithm determines the actual betatron tune. Typical measurements of tune spectra acquired by this method can be seen in Figure 1.

CHROMATICITY MEASUREMENT

While it could be argued that the betatron tune can be more elegantly measured using a PLL that tracks the tune, the advantage of the swept excitation approach is that it also produces information about the synchrotron oscillation sidebands to the tune. From the intensity of these sidebands relative to the main line, the chromaticity can be derived. Figure 1 shows three example tune spectra for different chromaticities; the black dots indicate the peaks that have been identified by our peak search algorithm. We attempted to model the relative intensity of these peaks as described by other authors [3,4], but did not find a satisfactory fit with our observation. In the end, a measurement of the relative sideband intensities during controlled variation of the chromaticity (as measured with the standard approach of varying beam energy by changing the storage ring RF frequency) was used to create an empirical fit with a polynomial (see Figure 2). This function is now subsequently employed to give a measurement of the chromaticity from the tune spectrum available every second.

The fitting routines to identify the relative peak intensities and the empirical model to compute the chromaticity from these are current implemented in a MATLAB routine which can operate either on live tune or archived tune spectra.

BETAFUNCTION MAGNITUDE AND PHASE

Whereas the measurement of betatron tune (and the chromaticity measurement derived from the tune spectrum) required only excitation and detection in a single location in the storage ring, a measurement of betafunction requires measurement at as many locations as possible. We have used all 168 BPMs with their turn by turn (TbT) measurement capability, while exciting oscillations of the beam at betatron frequency. It is important to trigger the acquisition of TbT data synchronously on all BPMs, so that magnitude and phase of the oscillations can be computed.

With the frequency of the oscillation precisely known, the TbT data is analysed by an extension to the BPMs' EPICS driver by multiplication with a cosine/sine and accumulation over the whole stored TbT waveform with up to 2^{19} turns (equivalent to about 1 s of data with our revolution frequency of 533820 Hz). It should be noted that this upstream processing leads to massive data reduction, as we produce only one orbit reading of magnitude and phase per trigger instead of >700MB of TbT data per second from all BPMs.

The I/Q detector with accumulator over 1 s can be regarded as equivalent to a 1 Hz spectral filter on the betatron frequency, so a tight locking of time/frequency bases between the excitation (in our case the NCO in the TMBF) to the acquisition (in our case the sample clock in the BPMs) is required. We achieve this as the NCO in the

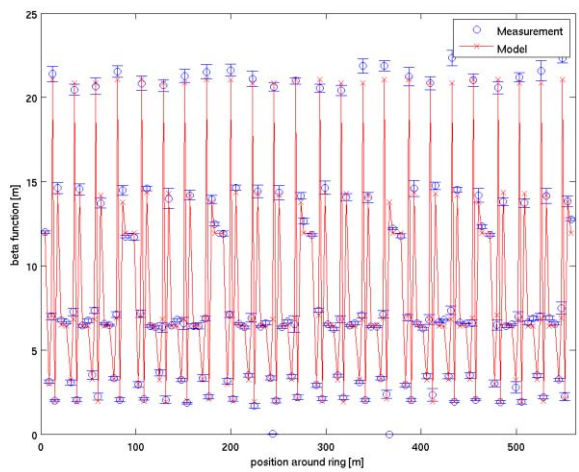

Figure 3: Measured and model beta function magnitude

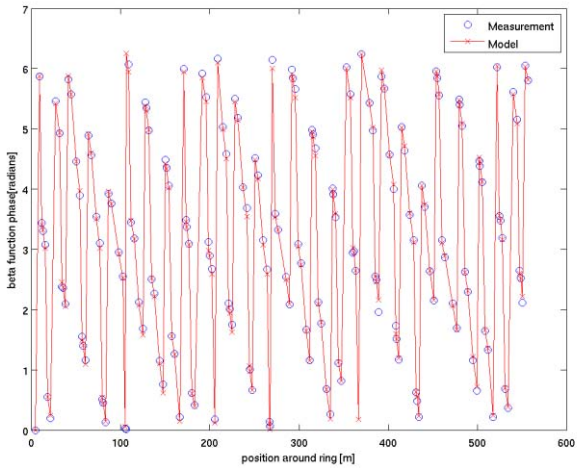

Figure 4: Measured and model beta function phase

TMBF is clocked directly by the storage ring RF frequency, while the sample clock in the BPMs is locked to the revolution clock, which is generated by division from the RF frequency.

Figure 3 shows an example measurement with an amplitude of 0.5 to 2.5 µm (depending on beta), and 9 sets of data taken from 2^{17} turns each. From the 9 sets the mean and standard deviation have been calculated and used to generate the error bars in the plot (the error is the 'predicted error' on the mean, ie 1/3 of the standard deviation of the 9 measurements). Despite the small amplitude this measurement is in excellent agreement with the model and within the expected beta beat of 10%.

Figure 4 shows the beta function phase retrieved from one of the sets of the same data. Both magnitude and phase data are of sufficient quality to allow permanent monitoring of the sanity of the optics.

CORRECTOR ORBIT RESPONSE

While all measurements presented so far used an excitation at or near the betatron frequency and using a stripline to kick the beam, we can also inject a low frequency into one corrector magnet and observe the response on all BPMs. For these lower frequencies and to the benefit of resolution, the recorded data should cover several seconds of orbit observation. On the other hand, TbT time resolution is not required, so we record the 'Fast Acquisition' data stream which is at 10072 samples/s in our case.

To ensure we are reading all BPMs synchronously we tap into the Communication Controller network which we use for the Fast Orbit Feedback (FOFB) using an additional listener node. The FOFB processing nodes are used to inject the disturbance by adding a sine wave of programmable amplitude and frequency generated from a shared time base into any of our 168 corrector magnets per plane. The excitation and measurement can take place even with the FOFB running at the same time by choosing a frequency high enough to be outside the effective bandwidth of the FOFB.

The additional listener node is capable of receiving the full stream of orbit data at 13.5 MBytes/s which it record to hard disk for later analysis. At the moment, we use 10s recordings and analyse these in MATLAB, but it is planned to move the processing into the listener node, to achieve the necessary data reduction that would simplify continuous observation.

We have tested the accuracy and repeatability of a measurement with one corrector excited at 200Hz by comparing it to the model corrector response and the response taken by the traditional method of stepping the corrector magnet and recording orbits before and after. It should be noted that the measurement results of the 200Hz excitation shown in figure 5 have been scaled to fit the model best, as currently the roll off of the magnet/vessel/power supply is not taken into consideration. Other than that the measurements are of excellent reproducibility and identify the same apparent mismatch between the actual storage ring behaviour as seen by the step change.

With respect to the resolution of the measurement, it should be taken into account that even the excitation amplitude is about 10 times less than typically used when the corrector is stepped and thus the resulting orbit changes are only in the order of 17µm RMS compared to 170µm RMS with the step change. On the other hand, the orbit is observed for 10s instead of 100ms, and consequently noise is picked up from a 100 smaller bandwidth, theoretically improving the resolution on the orbit measurement by a factor of 10, so that the reduced amplitude and extended measurement time should cancel out.

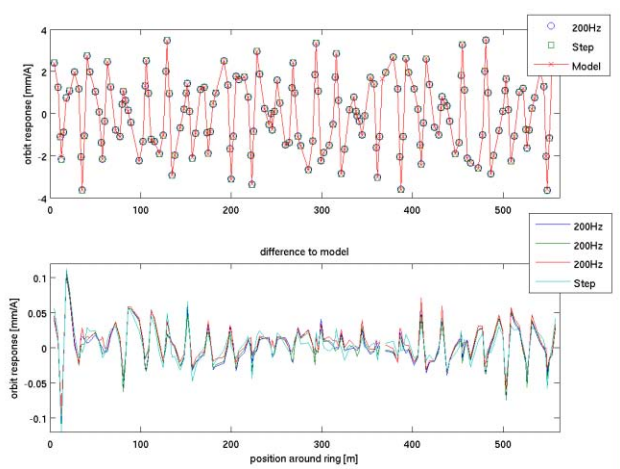

Figure 5: Corrector orbit response, measured by excitation at 200Hz and by step changing the corrector, as well as model response. The lower plot shows the difference to the model of three repeated measurements at 200Hz and one step change

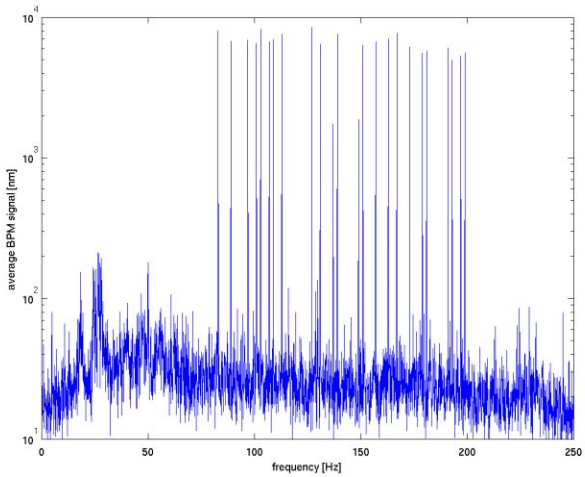

Figure 6: Beam motion spectrum averaged over all 168 BPMs during excitation with 24 frequencies on 24 corrector magnets.

Simultaneous Measurement of Excitation with Multiple Correctors

Measuring a whole corrector response matrix one by one spending 10s to observe each corrector would require about one hour of time for our 168 correctors in 2 planes. However, it is possible to excite several correctors at the same time using different frequencies, and then observe their response simultaneously by 'tuning in' on the respective frequencies. We have tried this with excitation of 24 correctors and we have chosen the 24 highest prime numbers below 200Hz as excitation frequencies to avoid any harmonic contamination of the measurements. The average beam position spectrum of all BPMs is shown in figure 6, and the 24 corrector responses compared to the model are shown in figure 7. The difference between the model and the measurement is likely to be due to a real mismatch between the machine and the model, rather than random or systematic errors in the measurement.

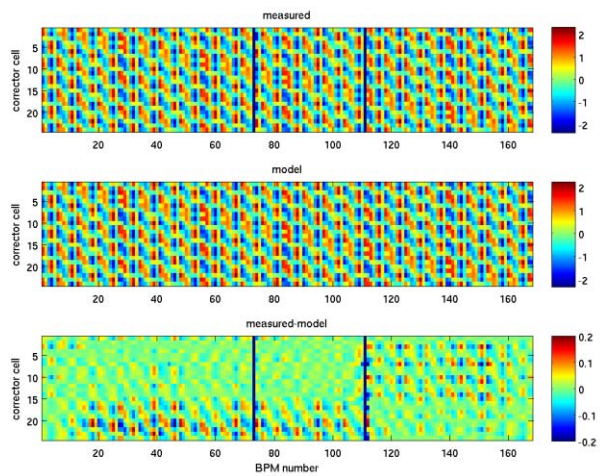

Figure 7: Partial orbit response matrix retrieved from simultaneous excitation of 24 corrector magnets, compared to the model response

For the measurement of the whole corrector response matrix there is a choice of either repeating measurements with a subset of correctors excited, or theoretically one could also excite all correctors at the same time with different frequencies. Furthermore, instead of different frequencies more complex signals which are orthogonal to each other could be chosen, for instance pseudo random codes [5]. This would have the further advantage that the disturbance is spread in spectrum and would appear just like a slight increase in the noise floor.

SUMMARY

Using the presented methods we are able to measure lattice parameters by injection and detection of a perturbation that is small compared to the beam size and thus practically invisible to light source users. The presented methods use different sources of excitation and different diagnostics systems for detection (see table 1), but they all share the common principle of injection of a single tone and phase locked detection at the same frequency.

While some of the methods are in regular use or ready to be used, further study and optimisation will be required in particular for the corrector response matrix measurement with multiple excitations in parallel. Experiments with a deliberate distortion of the storage ring optics should prove the ability to identify that.

Table 1: Systems used for excitation and detection in the four measurements and status of implementation

Measurement	Excitation	Detection	Status
Tune	Stripline TMBF	TMBF	in use
Chromaticity	Stripline TMBF	TMBF MATLAB	ready for use
β mag/phase	Stripline TMBF	EBPMs TbT data	ready for use
Corrector response	Corrector FOFB	EBPMs FA data	first tests

REFERENCES

[1] M. Boege, “Achieving Sub-Micron Stability In Light Sources”, Proceedings of EPAC 2004

[2] A.F. Morgan et al, "Performance And Features Of The Diamond Tmbf System", Proceedings of the 11th EPAC 2008, Genoa

[3] T. Nakamura, "Excitation of Betatron Oscillation under Finite Chromaticity", Proc. of the 12th Symposium on Accelerator Science and Technology 1999

[4] P.L.G. Lebrun et al., "A Betatron Tune Fitting Package for the Tevatron 21.4 MHz Schottky", Proceedings of PAC 2005, Knoxville, pp 937-939

[5] R. Gold, "Optimal binary sequences for spread spectrum multiplexing," IEEE Trans. Information Theory, vol. IT-13, pp. 619-621, 1967.

DIAMOND DETECTORS AS BEAM MONITORS

E. Griesmayer, CIVIDEC Instrumentation, Vienna, Austria
B. Dehning, E. Effinger, CERN BI, Geneva, Switzerland
D. Dobos, H. Pernegger, CERN PH, Geneva, Switzerland

Abstract

CVD diamond particle detectors are already in use in the CERN experiments ATLAS, CMS, LHCb and ALICE and at various particle accelerator laboratories in USA and Japan. This is a proven technology with high radiation tolerance and very fast signal read-out [1]. It can be used for measuring single-particles as well as for high-intensity particle cascades, for timing measurements on the nanosecond scale and for beam protection systems. The radiation tolerance is specified with 10 MGy.

INTRODUCTION

The diamond beam monitor is a solid-state ionization chamber that stands out due to its fast and efficient charge collection and its high radiation tolerance. The diamond technology gives a charge collection time of less than 1 ns and lifetime studies made at CERN showed a 50% decrease in signal ampltude at 10 MGy [2], which make this device particularly well adapted to applications in particle accelerators.

Poly-crystalline CVD diamond beam monitors have been evaluated at the CERN SPS and at LHC accelerators. The read-out was made through 250 m long coaxial cable. Tests were made on the signal-to-noise ratio, the timing resolution and the dynamic range.

A single-crystalline CVD diamond beam monitor was tested for ISOLDE at CERN for the HIE-REX upgrade. This device was used to measure the beam intensity by particle counting and for measuring the beam energy spectrum for carbon ions.

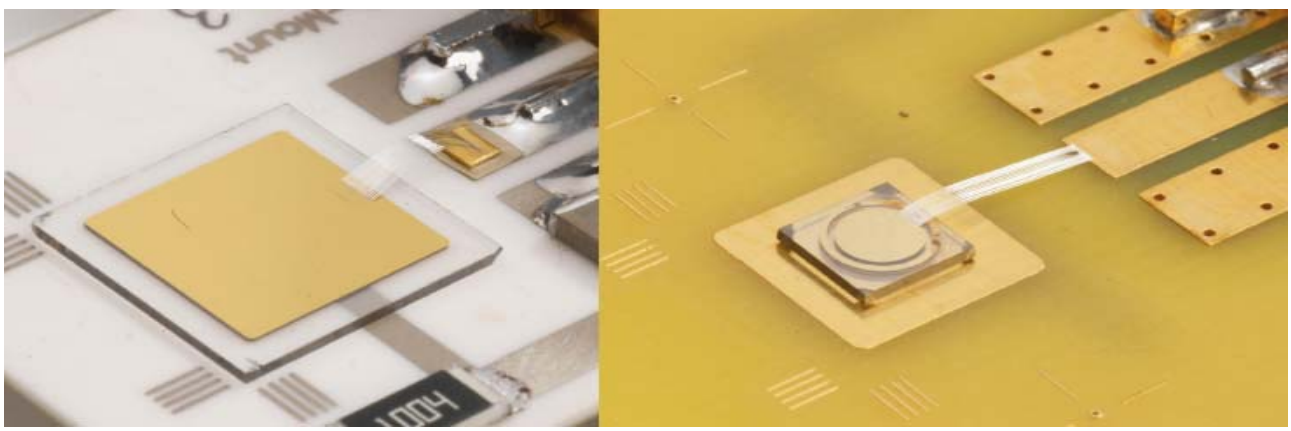

Figure 1: Single-crystalline and poly-crystalline diamond substrates, metalized with gold, are mounted on a ceramics board and a FR72 board, respectively.

TESTS AT ISOLDE

A novel beam instrumentation device for the HIE-REX (High Intensity and Energy REX) upgrade has been developed and tested at the On-Line Isotope Mass Separator ISOLDE, located at the European Laboratory for Particle Physics (CERN) in cooperation with Bergoz Instrumentation [3].

This device is based on a single-crystal CVD diamond detector (Figure 1, right picture) and is used for measuring the beam intensity, particle counting and measuring the energy spectrum of the beam. The detector is located inside the beam pipe in vacuum.

The carbon ions are completely absorbed by the diamond and the deposited energy is

converted into ionization charges, which are read out via a fast preamplifier.

In Figure 2 the time response of the detector is shown on a time scale of 10 ns/div. The persistence plot shows the detector response to single ions. The 100 MHz RF beam-bunch structure of the carbon ions is clearly resolved. The average amplitude is 100 mV and represents the ion energy of 22.8 MeV.

Test results

The energy resolution of 0.6% was measured at a carbon ion energy of 22.8 MeV, which corresponds to an energy spread of ±140 keV.

The intrinsic time resolution for a signal-to-noise ratio of 100 and an average rise time of 3 ns, is 30 ps.

TESTS AT THE SPS

In preparation for tests at the LHC accelerator, a pCVD diamond detector (Figure 1, left picture) has been evaluated as a beam loss monitor using beam halo particles. The test monitor was mounted in the SPS BA5 downstream of a LHC collimator during the LHC beam set-up [4].

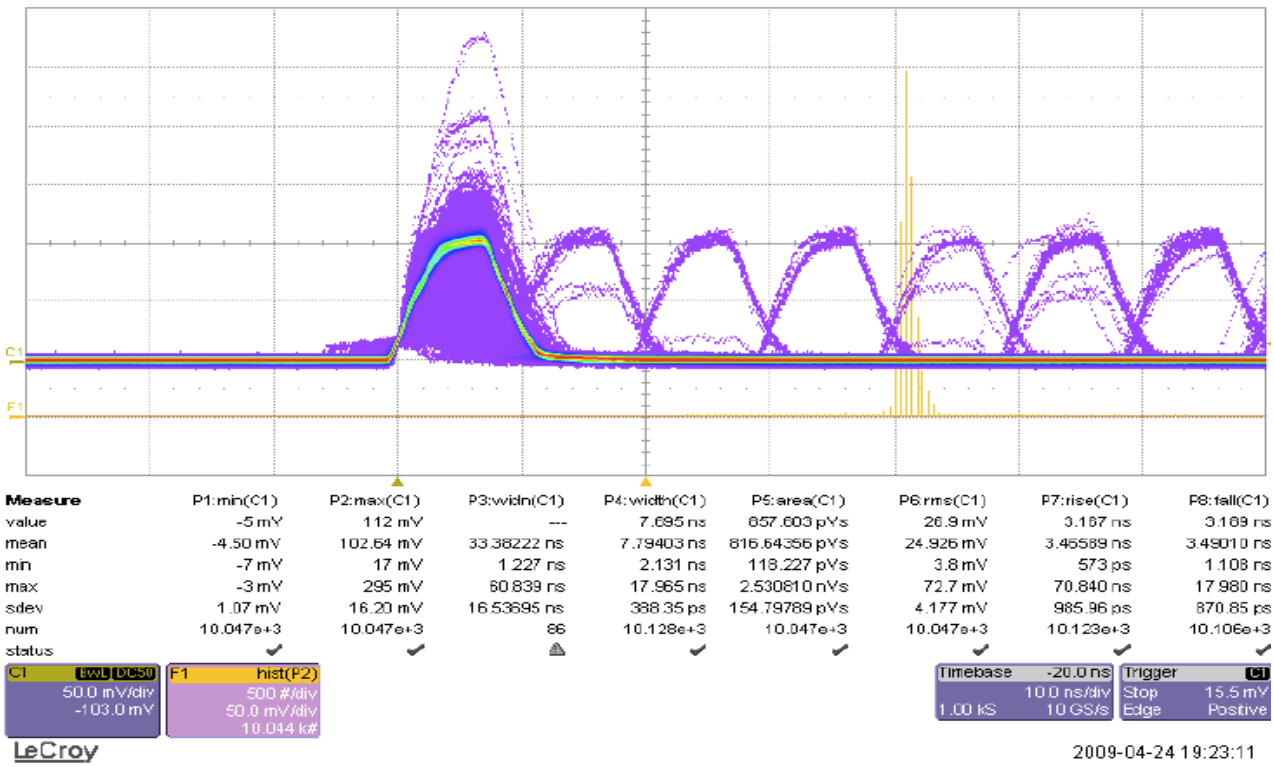

Figure 2: Time response of the diamond detector to single particles, which arrive at the RF frequency of 100 MHz.

Despite the read-out being made through 250 m of CK50 cable, the tests have shown a signal-to-noise ratio of 7, an excellent timing performance with a rise time of 2 ns, a pulse width of 5 ns and a fall time of 10 ns for single-particle detection. The dynamic range of the detector is only limited by the electronics to 1:350.

Test results

Four different types of beam loss were measured, i.e. single-particles, multi-particles, shower cascades and high-intensity beam losses as shown in Figure 3. The detector has proven its sensitivity for single particles as well as its robustness for high-intensity beam losses that saturated the electronics, which required up to 10 us for recovery.

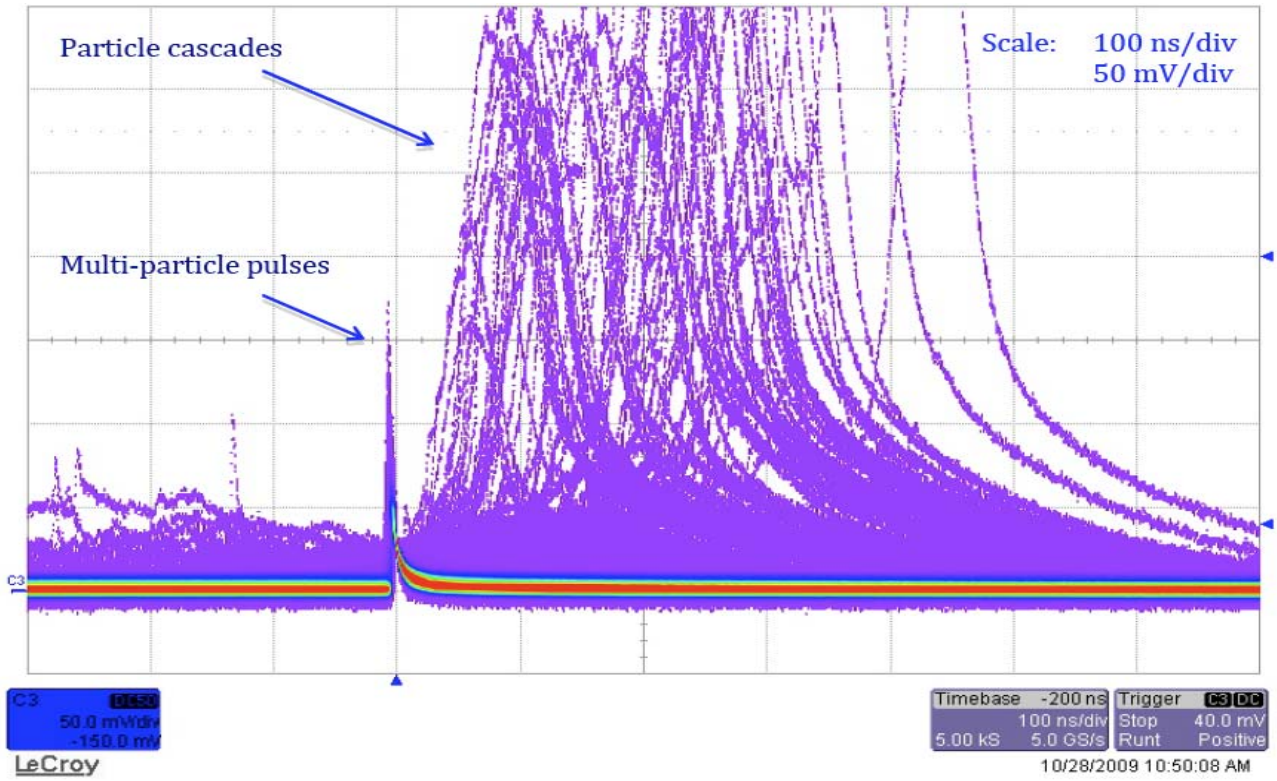

Figure 3: Time structure of beam losses in the SPS showing multi-particle pulses peaking at 200 mV (corresponding to 50 MIP particles simultaneously hitting the detector) and time extended particle cascades with amplitudes up to 1 V.

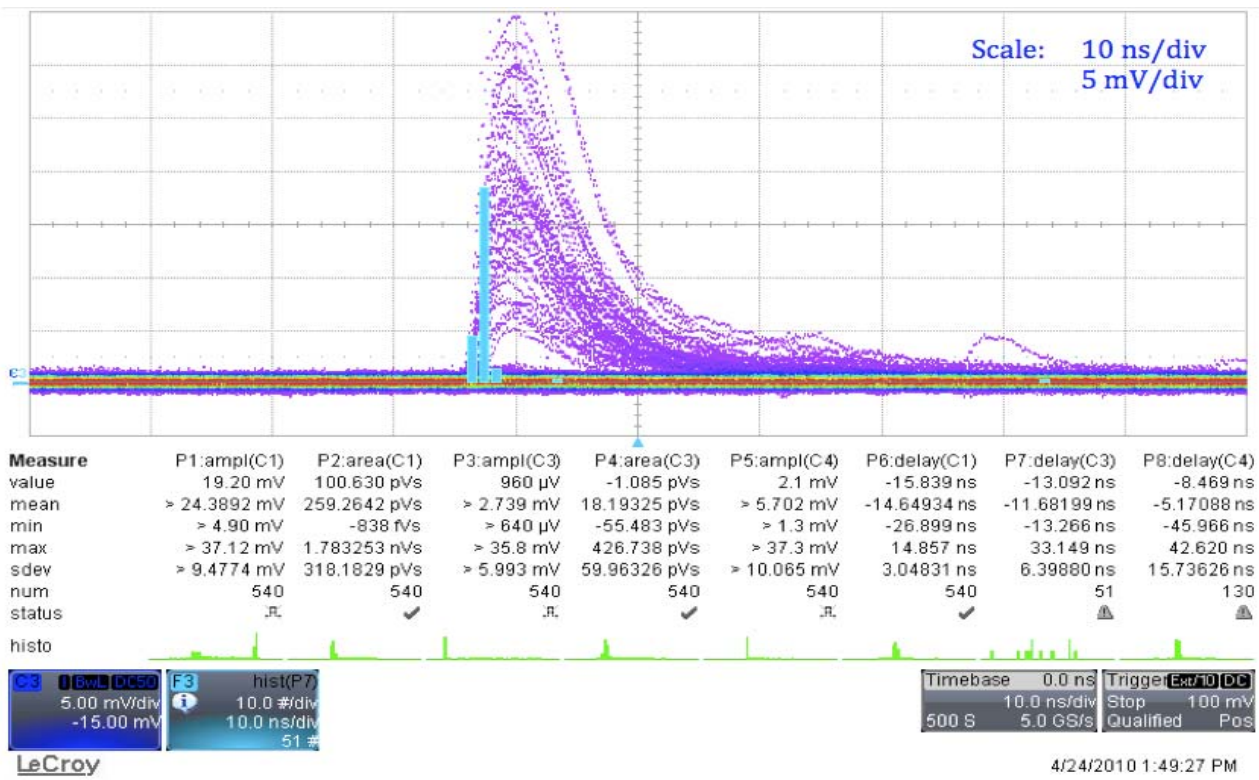

Figure 4: Time structure of beam losses (10 ns/div) and the corresponding phase histogram (1 ns per bin). Four 25 ns slots of the LHC accelerator are shown.

TEST AT THE LHC

As a result of the short single-particle resolution time, a beam-loss diagnostics instrument with 2.5 ns time resolution was built and is under test at the LHC accelerator. The diamond detector is built to resolve individual particle bunches of the 400 MHz RF buckets of LHC.

In addition, various parts of the beam can be measured, e.g. bunched beam, coasting beam, and in particular halo diagnostics with single-particle resolution can be performed. Machine protection with a reaction time < 20 ns is feasible in case of fast abnormal losses at a primary collimator.

Figure 4 shows the time structure of individual bunch losses. The rise time of 2 ns and sufficient amplitude allows a precise measurement of the arrival time. The timing histogram in Figure 4 has a bin width of 1 ns and demonstrates that the beam is well aligned with respect to the 2.5 ns long RF buckets.

Test results

Tests are still going on. Results of the tests will be published later.

SUMMARY

CDV diamond detectors where tested at three different accelerators at CERN, REX-Isolde, SPS and LHC. The tests have proven that CVD-diamond based beam instrumentation devices are feasible for a wide variety of beam instrumentation, such as particle counters, phase monitors, beam-loss monitors and spectrometers.

The high sensitivity of the detector allows single-particle detection, which is crucial for a particle counter. The dynamic range of the detector material is over many orders of magnitude [5] and mainly limited by the lifetime and by thermal parameters, which makes diamond of special interest for beam-loss and beam-intensity applications.

The rapid response of CVD diamond detectors is used for fast readout of the signals in the range of nanoseconds which is the key for single-particle counting in the range of GHz. The excellent time resolution of 30 ps can be used for time-of-flight applications. The low-noise properties of diamond can be used for energy spectrometers with energy resolutions of less than 1%.

REFERENCES

[1] H. Frais-Kölbl, E. Griesmayer, H. Pernegger, H. Kagan, ‘A Fast Low-Noise Charged Particle CVD Diamond Detector’, IEEE Trans. on Nuclear Science, Vol. 51, No. 6, p. 3833 – 3837, December 2004.

[2] By RD42 Collaboration (W. Adam et al.), ‘Radiation hard diamond sensors for future tracking applications’, NIM A, Volume 565, Issue 1, p. 278-283, September 2006.

[3] E. Griesmayer, H. Pernegger, D. Dobos, F. Wenander, J. Bergoz, H. Bayle, H. Frais-Kölbl, J. Leinweber, Thomas Aumeyr, ‘High-Resolution Energy and Intensity Measurements with CVD Diamond at REX-ISOLDE’, CERN BE-Note-2009-028.

[4] E. Griesmayer, B. Dehning, E. Effinger, H. Pernegger, D. Dobos, H. Frais-Kölbl, ‘Test of a Diamond Detector Using Unbunched Beam Halo Particles’, CERN-ATS-2010-027.

[5] J. Bol, Strahlmonitore aus Diamant für primäre Teilchenstrahlen hoher Intensität, Universität Karlsruhe, EKP IEKP-KA-2006-July 2006. 129pp.

RESIDUAL GAS X-RAY BEAM POSITION MONITOR FOR PETRA-III

P. Ilinski*, BNL, Upton, NY 11973, U.S.A.

Abstract

The development effort is driven by the need for a new type of x-ray beam position monitor, which can detect the centre of gravity of the undulator beam. A residual gas x-ray beam position monitor for the PETRA III storage ring was developed and tested.

INTRODUCTION

Blade type x-ray beam position monitors (XBMP) are currently employed at the third generation synchrotron facilities as "white" undulator beam XBPMs [1, 2]. They provide a micron accuracy resolution and are capable to withstand the high power of the undulator radiation. Nevertheless since the information of the beam position is obtained from the halo of the undulator radiation, the signal depends on the undulator gap and is affected by stray radiation from bending magnets and focusing optics. These can be overcome if XBPM will detect the centre of gravity of the undulator beam. XBPM based on the ionization of a residual gas can be considered a candidate for "centre of gravity white" beam position monitor.

RESIDUAL GAS X-RAY BEAM POSITION MONITOR

Residual gas beam profile monitors were first developed to provide beam profile measurements at charged particles accelerators [3,4]. Development of residual gas x-ray beam position monitor (RGXBPM) for PETRA III undulator x-ray beams was performed at DESY [5]. The profile monitor consists of an ion chamber operated at a residual gas pressure in which ions or electrons are drifted in a parallel electrical field towards the micro channel plate (MCP), which amplifies the signal and produces an image of the beam profile on a phosphor screen, Figure 1.

Spatial Resolution

The resolution of the residual gas beam profile monitors, which are in use at the particle accelerators is in the order of few hundreds of microns. Resolution of RGXBPM has to be substantially improved in order to comply with beam stability requirements at the third generation storage rings. Factors which define the RGXBPM resolution are: quality of the electrical field, initial kinetic energy of ions or electrons, resolution of detection system, and data processing. The electrical field has to be uniform in order to provide aberration free beam profile. Broadening of the beam profile occurs due to electrical field non-uniformity and presence of the transverse component of the electrical field. This broadening should not exceed the broadening of the beam profile, which is caused by the initial transverse kinetic energy of ions or electrons [6]. The resolution of detection system is defined by the MCP, the phosphor screen, optical coupling and signal to background ratio. A proper data processing allows sub-pixel resolution, where pixel characterizes the resolution of the detection system.

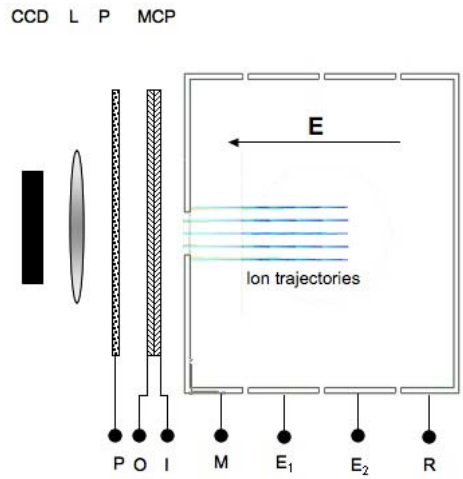

Figure 1: RGXBPM general layout: R - repeller electrode, E_1, E_2 - guide electrodes, M – mesh window electrode, I - MCP input, O - MCP output, P - phosphor screen, L - objective lens, CCD camera.

Signal Level

The signal level of the RGXBPM first of all is defined by the total x-ray cross-section of the residual gas, which depends on gas pressure and composition. Typical pressure at the beamline can be better then 10^{-9} mbar, gas composition of UHV system is mostly hydrogen and may include nitrogen, water vapor etc.

In a typical ion chamber operating at gas pressure of about 10^{3} mbar a primary photoelectron will produce an avalanche of secondary electrons, so the number of created electron ion pairs will be proportional to deposited energy divided by average energy of one electron ion pair creation (35 eV for nitrogen). The upper level of residual gas pressure for RGXBPM is limited by presence of the MCP, and should not exceed $5x10^{-6}$ mbar. At such low pressure primary photoelectrons may not produce secondary electrons before been collected. Two scenarios are presented at Figure 2 for nitrogen and hydrogen at pressure of 10^{-6} mbar, and for detector length of 1 cm. First, when only primary photoelectrons are produced: (dotes) - nitrogen, (dash-dot-dot) - hydrogen, second for high gas pressure, when all secondary electrons were produced: (dashed) - nitrogen, (dash-dot) - hydrogen.

*pilinski@bnl.gov

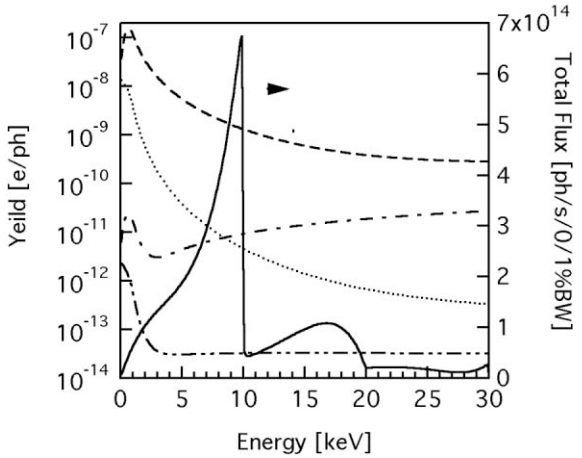

Figure 2: Electrons/ions yield at gas pressure of 10^{-6} mbar, 1-cm-collection-length; primary photoelectrons: (dotes) - nitrogen, (dash-dot-dot) - hydrogen; all secondary electrons: (dashed) - nitrogen, (dash-dot) - hydrogen.

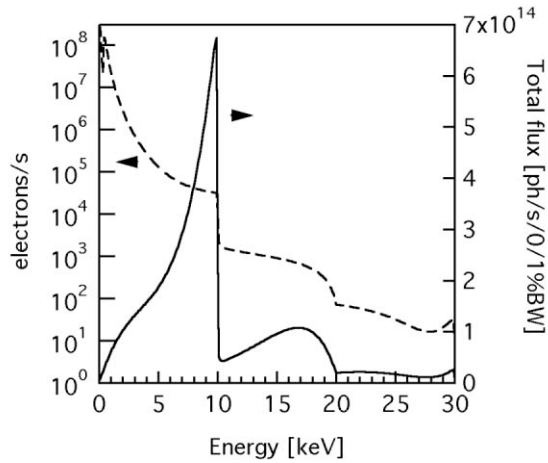

Figure 3: Current of primary photoelectrons, nitrogen gas, 10^{-6} mbar, 1-cm-collection-length; current generated by Total spectral flux of 2-m-long PETRA-III undulator, 2.9-cm-period-length, K = 0.6.

Photoelectron current, when only primary photoelectrons are produced, is presented at Figure 3 for 2-m-long PETRA-III undulator with 2.9 cm period length and for K = 0.6. As can be seen most of the photoelectrons are generated at low photon energies, even if the undulator radiation intensity at such energies is extremely low. Undulator radiation, which is "red shifted" from fundamental harmonic of undulator radiation, is radiated off-axis, which is illustrated at Figure 4 for the undulator flux distribution of 1 keV photons at 20 m for above undulator parameters. In case of low gas pressure the beam profile of integrated RGXBPM response is complicated. In case of high gas pressure, the signal is proportional to the deposited energy and observed beam profile will reflect power distribution of the undulator radiation, Figure 5.

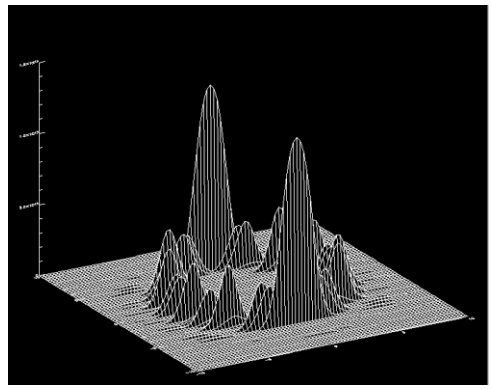

Figure 4: Flux density spatial distribution (20x20 mm^2) at 20 m of 1-keV-energy-photons, 2-m-long PETRA III undulator, 2.9-cm-period-length, K=0.6.

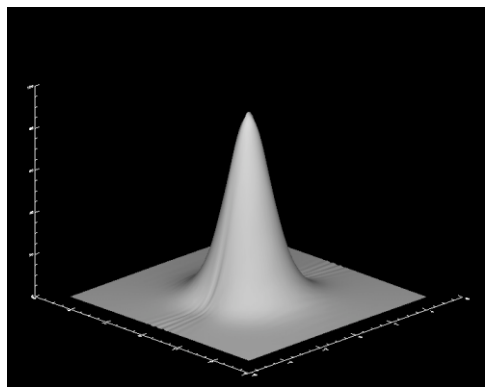

Figure 5: Undulator radiation power density distribution (10x10 mm^2) at 20 m, 2-m-long PETRA III undulator, 2.9-cm-period-length, K = 0.6.

General design

Design specifications of RGXBPM for PETRA III have limitations for dimensions due to the fact that many of PETRA-III beamlines are equipped with canted undulators and separation of beamlines at RGXBPMs locations is small. Top view of RGXBPM design for canted undulator beamlines is shown in Figure 6. One RGXBPM assembly combines two RGXBPMs to monitor vertical and horizontal beam profiles. Internal active volume and electrodes of the RGXBPM have to be protected from any scattered or fluorescent x-ray radiation. For this purpose 5-mm-thick tungsten windows (W) are positioned in front and behind of each active volume and tungsten 100-mm-logn collimators are mounted in the front and at the exit of the RGXBPM assembly, Figure 7. Inner hole diameters are 17 and 18 mm for the upstream and downstream collimators, correspondingly. All electrodes of the RGXBPM are made of 1-mm-thick stainless steel with 1.5-mm-gaps between electrodes, which provides additional shielding of the RGXBPM active volume.

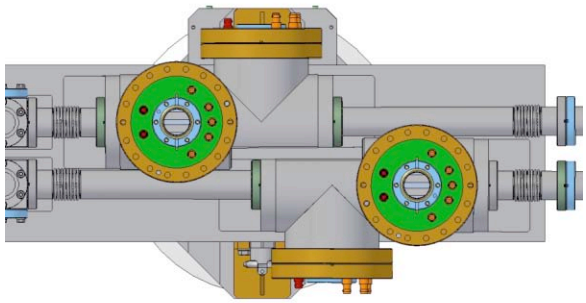

Figure 6: Top view of RGXBPM design for canted PETRA III undulator beamlines.

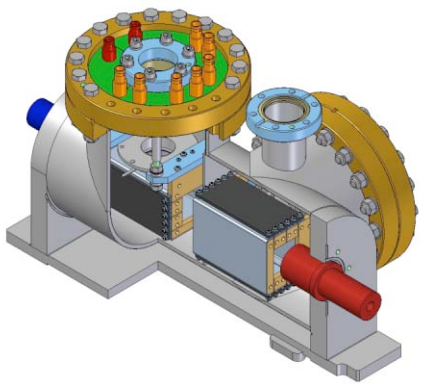

Figure 7: RGXBPM design includes vertical and horizontal monitors, upstream (red) and downstream collimators (blue).

The RGXBPM with an electrical readout equipped with Hamamatsu F3490-21S MCP with two split sow-tooth electrodes, which has effective area of 55 x 8 mm^2 and a channel diameter of 12 μm. For the RGXBPM with an optical readout a 32-mm effective diameter F2224-21P Hamamatsu MCP with a channel diameter of 10 μm and P43 phosphor screen is used. For tests a 50 mm focal length objective was used to image the beam profile from the phosphor screen onto a PCO PixelFly 12 bit CCD camera with 6.45-μm pixel size. The magnification of the optical system was chosen in order to have maximum field of view while not compromising the system special resolution, which was 15 μm/pixel.

Electrical Field Optimization

Limited space dictated a compact RGXBPM design with small active volume, which makes optimization of the electrical field within the active volume extremely difficult. The CST Particle Studio™ software program was used for electrostatic modeling and to define ion and electron particle trajectories [7].

Geometry of electrodes and size of the active volume were optimized in order to achieve best field uniformity, minimize transverse field components and to provide maximum x-ray shielding of the active volume. The length, height and width of the active volume are 80x50x60 mm, Figure 8. In order to improve quality of the electrical field, the repeller electrode (R) and the mesh electrode (M) are bent at all edges, two 12-mm-wide guide electrodes (E1, E2) are placed in between the repeller and the mesh electrodes. Tungsten windows (W) are placed in front and behind active volume, they are also electrodes, which used to improve field quality at edges of the active volume.

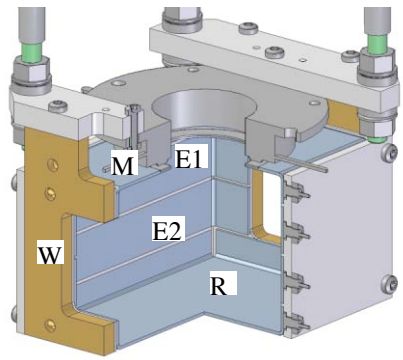

Figure 8: RGXBPM active volume.

Wiring of the RGXBPM is different for electrical and optical readouts, never the less optimal ratio of potentials was found to be the same: $(R\text{-}E_2):(E_2\text{-}W):(W\text{-}E_1):(E_1\text{-}M)$ = 22:8:8:22. Symmetrical distribution of potentials is preferable, but this will require more HV power supply channels, Figure 9.

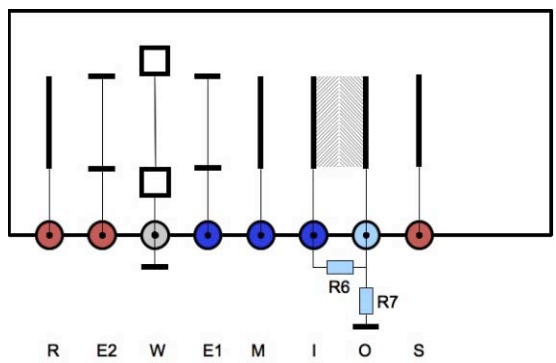

Figure 9: Symmetrical electrical wiring for optical readout, positive HV (red), negative HV (blue).

Test Results

The RGXBPM performance was tested at the ESRF ID6 beamline, where it was installed in the front-end enclosure 30 m from the center of the straight section. Straight section included planar undulators with magnetic period length of 18 mm and 34 mm. A 300-μm-thick diamond window was located at 23 m. Horizontal mask of 2 mm was located at 14 m, vertical of 4 mm at 23 m. Horizontal and vertical slits were located at 26 m. Copper, 100-mm-long collimators, were installed before and after of the RGXBPM assembly in order to eliminate forward and back scattering radiation of striking electrodes. Upstream and downstream collimators were 8 and 10 mm diameters correspondingly. Slit sizes were fully opened to 4 mm vertically by 3.5 mm horizontally, which allowed most of the undulator radiation to pass through the RGXBPM.

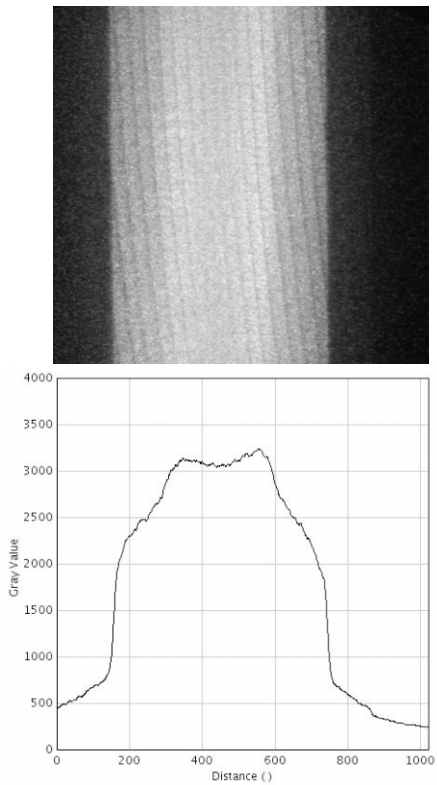

Figure 10: RGXBPM with optical readout. Image of the beam profile on the phosphor screen (top), ESRF undulator u18, 9-mm-gap, 500 ms exposure time; integrated cross-section of the beam profile (bottom).

Results of the RGXBPM test with optical readout are presented at Figure 10 for the ESRF undulator u18 at 9-mm-gap, first fundamental harmonic of undulator radiation was 16.7 keV. An image of the beam profile on the MCP phosphor screen is shown at the top picture, while the bottom is an integrated cross-section of the beam profile. Time of the CCD exposure was 500 ms. Centre of gravity was determined for each image of the beam profile, a time scan of centre of gravity is presented at Figure 11, as can be seen a 10 μm vertical translation of the RGXBPM can be clearly resolved. At the time of measurement, nitrogen gas pressure inside RGXBPM was controlled and set to be $4x10^{-6}$ mbar. For ions detection the repeller (R), guide (E2), (E1) and mesh (M) electrode potentials were set to 3800V, 1600V, 50V and -2200V, correspondingly. The MCP input (I) potential was set to -2200V, the MCP output (O) was grounded, and phosphor screen potential (S) was set to 4000V.

Integrated cross-section of the beam profile, Figure 10, has a minimum in the centre, which reflects a complex RGXBPM response of the undulator radiation, for which "red shifted" part is located off-axis, and where photoelectron yield cross-section is higher.

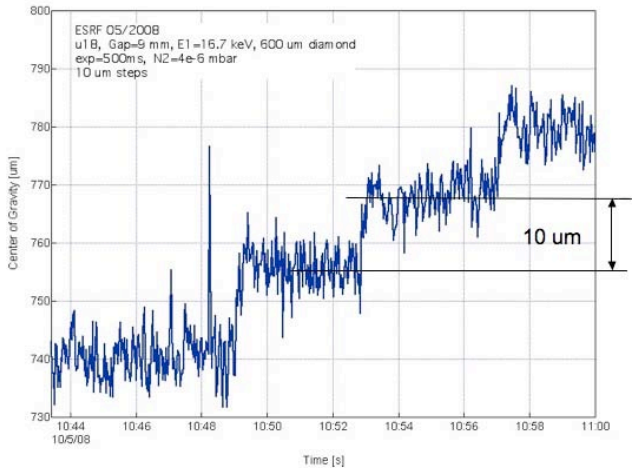

Figure 11: RGXBPM with optical readout. Time scan with 10 μm vertical translation steps of RGXBPM, u18, 9-mm-gap.

Test results of the RGXBPM with split sow-tooth electrode readout is presented at Figure 12, where time scan of signals from each electrode and normalized signal difference $(I_1-I_2)/(I_1+I_2)$ are shown for undulator u18 at gaps of 8, 10, 12 mm. For each gap entire RGXBPM assembly was scanned vertically with 20-μm-steps. At the time of measurement, the nitrogen gas pressure inside RGXBPM was $4x10^{-6}$ mbar, storage ring current 80 mA. For ions detection the repeller (R), guide (E1), (E2) and mesh (M) electrode potentials were set to 4650V, 2450V, 850V and -1500V, correspondingly. The MCP's input (I) and output (O) potentials were -1400V and -70V. Split electrodes were grounded through electrometers, signal level was 5 - 40 nA. As can be seen from Figure 13, where enlarged part of the scan from Figure 12 is shown, a 20 μm vertical translation of the RGXBPM is resolved.

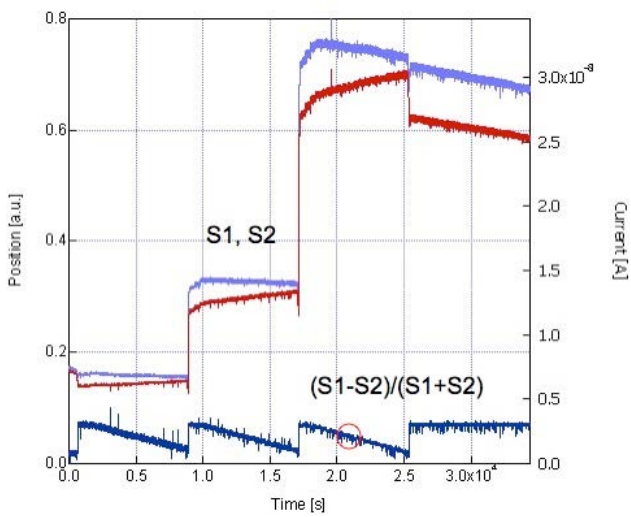

Figure 12: RGXBPM with electrical readout. Time scan with vertical translation steps of RGXBPM, u18, gaps of 8, 10, 12 mm.

Another way to test the RGXBPM was to observe controlled electron beam deflection, which occurred at the time of current injection. A time scans of normalized

signal difference $(I_1-I_2)/(I_1+I_2)$ of RGXBPM and electron beam angle deflection from e-bpms during injection are presented in Figure 14.

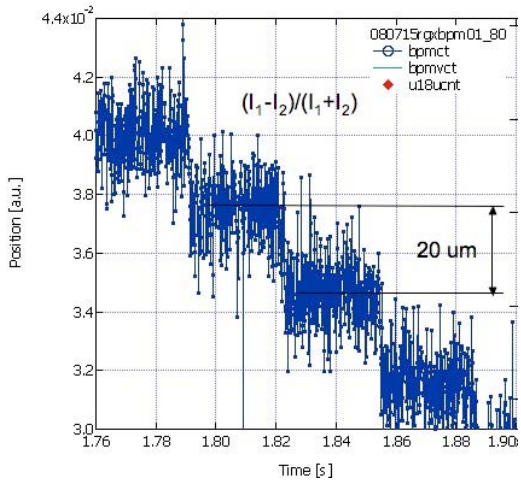

Figure 13: RGXBPM with electrical readout. Time scan with 20-μm vertical translation steps of RGXBPM, u18, 12-mm-gap.

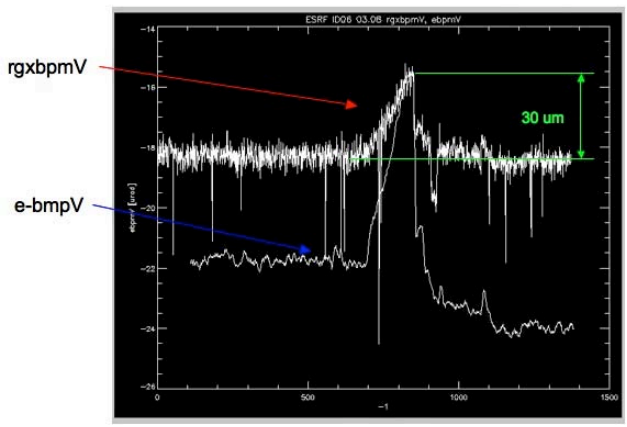

Figure 14: RGXBPM with optical readout. Time scan of beam position by RGXBPM and e-bpms during injection.

Operation of the RGXBPMs at PETRA III will be different form the results of tests at the ESRF ID06, since beamlines at PETRA III don't have fixed mask or windows. Spatial distribution of 1-keV energy photons at 20 m of PETRA III u29 with K=1.2 undulator radiation is shown in Figure 15 along with the footprint of ESRF ID06 mask. As can be seen 1-keV energy photons, which generate most of photoelectrons, will be recorded in case of PETRA III.

CONCLUSIONS

Residual gas XPBM may be sensitive to jumps of gas pressure, MCP gain non-uniformity, and instability of the HV power supplies. In case if the beam is non-symmetrical, pressure changes may be interpreted as a beam position variation. Further studies of RGXBPMs have to be performed in order to ensure its reliable operation.

RGXBPMs may be effective monitors for undulators with complex radiation distribution, such as elliptical undulators, and for soft x-ray insertion devices, for which photo ionization cross-section in residual gas is substantial.

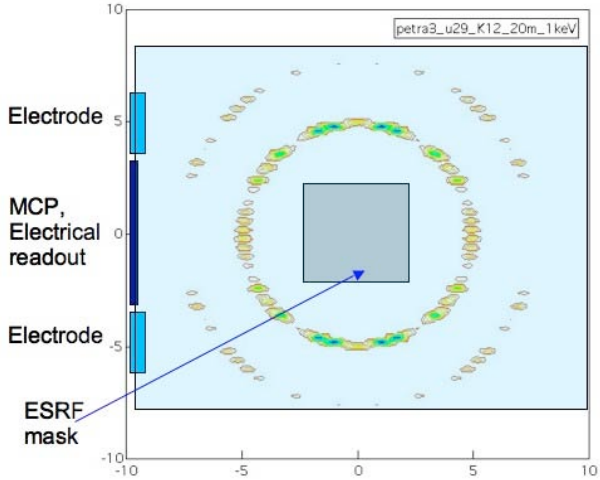

Figure 15: Spatial distribution of 1-keV energy photons at 20 m of PETRA III undulator u29, K=1.2.

AKNOWLEDGMENTS

Development of the RGXBPM was conducted at DESY with support of U. Hahn, H. Schulte-Schrepping, S. Mueller, N. von Bargen, M. Degenhardt, and T. Korsch. The authors also would like to acknowledge J.-C. Biasci, C. Detlefs, H.-C. Wille and T. Roth for their help in RGXBPM tests at the ESRF.

REFERENCES

1. O. Singh and G. Decker, "Operational Experience with X-ray Beam Position Monitors at the Advanced Photon Source", Proc. PAC 2001, Chicago, USA, 2001, IEEE 0-7803-7191-7/01, pp 539-543.
2. J. Krempasky, M. Böge, T. Schilcher, V. Schlott, T. Schmidt, "The use of Photon Monitors at the Swiss Light Source", Proc. EPAC 2004, Lucerne, Switzerland, 2004, pp 2520-2522.
3. F. Hornsta, W. H. Deluca, "Nondestructive beam profile System for the Zero Gradient Synchrotron", Proc. Six International Conference on High Energy Accelerators, M. I. I., Cambridge, MA, 1967, p. 374.
4. G. I. Budker, G. I. Dimov, V. G. Dudnikov, *Sov. At. Energy*, **22**, 441 (1967).
5. P. Ilinski, U. Hahn, H. Schulte-Schrepping, M. Degenhardt "Residual Gas X-ray Beam Position Monitor Development for PETRA III", AIP Conf. Proc. **879**, 782, (2007).
6. W. H. Deluca, "Beam Detection using Residual Gas Ionization", *IEEE NS*, **16**, 813- 822 (1969).
7. CST Particle Studio™, **CST GmbH**, Bad Nauheimer Str. 19, Darmstadt, Germany.

FEMTOSECOND SYNCHRONIZATION OF LASER SYSTEMS FOR THE LCLS*

J. M. Byrd#, L. Doolittle, G. Huang, J. W. Staples, R. Wilcox, LBNL, Berkeley, CA, USA

J. Arthur, J. Frisch, W. White , SLAC, Menlo Park, CA, USA

Abstract

The scientific potential of femtosecond x-ray pulses at linac-driven free-electron lasers such as the Linac Coherent Light Source is tremendous. Time-resolved pump-probe experiments require a measure of the relative arrival time of each x-ray pulse with respect to the experimental pump laser. To achieve this, precise synchronization is required between the arrival time diagnostic and the laser, which are often separated by hundreds of meters. An optical timing system based on stabilized fiber links that has been developed for the LCLS to provide this synchronization. Preliminary results show synchronization of the stabilized links at the sub-10-femtosecond level and overall synchronization of the x-ray and pump laser of <50 fs. We present details of the implementation at LCLS and potential for future development.

INTRODUCTION

The next generation of accelerator-driven light sources will produce sub-100-fs high brightness x-ray pulses[1]. In particular, pump-probe experiments at these facilities require synchronization of pulsed lasers and x-rays from electron beam on sub-100 fs time scales over distances of a few hundred meters to several kilometers[2,3]. Pump-probe experiments at these facilities plan to use an x-ray "probe" to produce snapshots of atomic positions within a sample some time after it is excited with a laser "pump."

Varying the time between pump and probe enables the recording of a "movie" of the dynamics in the sample, with a time resolution determined by the x-ray pulse length and the relative timing jitter and drift of pump and probe. For experiments that require minutes to hours to collect data, the relative drift of the pump and probe should be less than the x-ray pulse length.

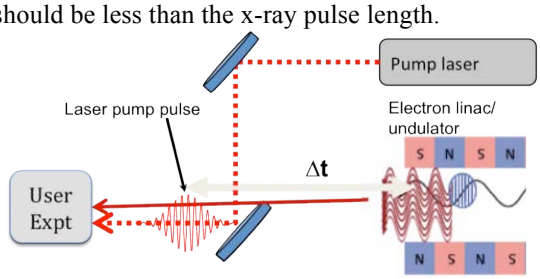

Figure 1: Layout for pump-probe timing.

One of the main challenges in reaching the level of synchronization required for pump-probe experiments is transmission of a timing signal over a relatively large facility. For example, in a facility of a kilometer in length, diurnal temperature variation results in cable length variation from several hundred ps to a nanosecond.

For the next generation of FELs, it is expected that the jitter of the electron beam with respect to the laser pump will be unacceptably large. Therefore, the goal is to measure the arrival time of each electron pulse with respect to the laser pump and allow the proper ordering of the "frames" of the movie. In this case, it is critical to synchronize the electron arrival time diagnostic with the pump laser.

STABILIZED RF SIGNAL DISTRIBUTION

One of the key features in any synchronization scheme is the ability to stably transmit a master clock signal to the remote clients with no uncontrolled relative timing drift between the clients. A schematic view of this distribution is shown in Fig. 2. The master oscillator signal is distributed over the accelerator to remote clients in a star configuration. Each link consists of a stabilized optical fiber with a second fiber carrying the error signal, a receiver for RF signal processing (RX), a synchronization head (S/H), and a remote client. The phase of the master signal is corrected at the end of each fiber link for the length variation of that link. Thus the relative timing drift

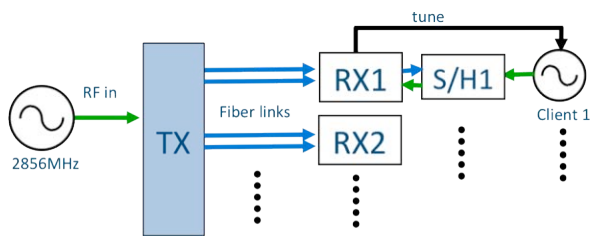

Figure 2: Schematic view of the distribution of the master clock over optical fiber. Each receiver consists of an RF signal processor (RX) and synchronization head (S/H).

of clients locked the master signal on independent fiber links does is minimized over many hours and even days.

Several approaches have been implemented to send stable signals over fiber optic links [4-8]. In our approach, each fiber link is an optical interferometer that precisely

*Work supported by by the U.S. Department of Energy under contract DE-AC02-05CH11231.
#JMByrd@lbl.gov

senses the delay variations in the link due to thermal variations of the fiber.

A schematic diagram of one of the stabilized RF transmission links is shown in Fig. 3. The fiber used for transmission is one arm of an interferometer, which tracks changes in the optical phase delay through the fiber. Variations in optical phase are observed at the receiver, along with the amplitude-modulated RF signals to be stabilized. The measured optical phase shift is used to correct the detected RF phase. To compensate for the difference between phase and group delay in the fiber, an additional correction is applied.

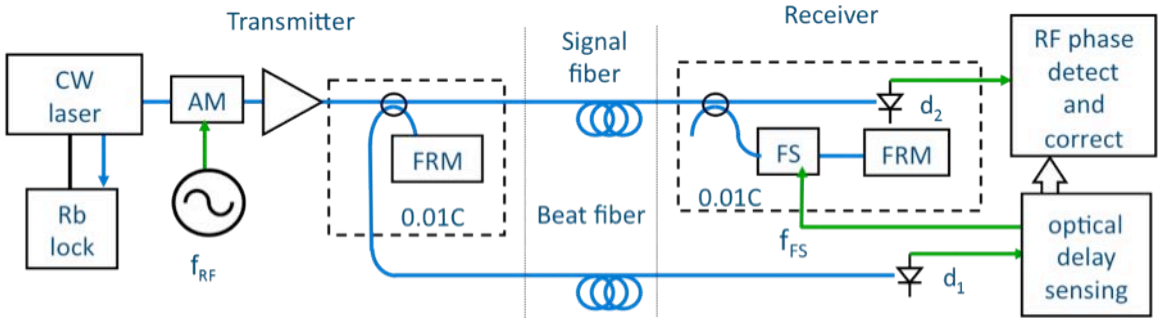

Figure 3: Schematic layout of a single channel RF transmission over an optical link. RF frequency is 2850MHz. AM: Amplitude modulator; FRM: Faraday rotator mirror; FS: optical frequency shifter. Dotted rectangles indicate components temperature controlled to ±0.01 C.

Each fiber link is one arm of a heterodyne Michelson interferometer. The reference arm is a short fiber (about 1m) with its temperature stabilized to ±0.01 C. An acousto-optic frequency shifter at the receiver end of the long arm shifts the optical frequency by 100 MHz in two passes, adding its input 50 MHz RF phase to the optical phase. The beat between the reference and reflected optical carrier is detected as a 100 MHz RF signal whose phase is compared with twice the frequency-shifting signal. The RF phase shift of this 100 MHz signal is equal to the optical phase shift in the long arm, providing an increase in temporal sensitivity of 2×10^6, the ratio of the optical to the beat frequency. Thus the 100 MHz beat signal can be sent back to the receiver over an unstabilized fiber, a novel feature of this scheme. The receiver then adjusts the frequency shifter RF phase to correct the optical phase, a function typically implemented in the transmitter[10]. This provides the ability to deliver a stable optical frequency over fiber.

The stability of our optical phase controller was verified by constructing a Mach-Zehnder interferometer out of two such heterodyne interferometers. One 2 km fiber was exposed to ambient temperature variation and and a short 2 m fiber was in a temperature controlled environment. Diurnal temperature variations caused up to 2 ns delay changes in the 2 km fiber. After correction, the overall differential phase error between two stabilized links was six optical waves peak-to-peak over ten days[11].

For stable RF transmission, the CW laser used in the interferometer must have a fractional frequency stability less than the desired fractional temporal stability of the transmission delay. For a 2 km link with 10 fs stability, this corresponds to $\Delta\lambda/\lambda=10^{-9}$. The CW laser frequency is locked to a hyperfine absorption line in Rb vapor, achieving 5 10^{-10}.

A 2850 MHz RF signal is amplitude modulated onto the optical carrier by a lithium niobate modulator. The bias point is stabilized by detecting the second harmonic of the 2850 MHz modulation in a phase-locked loop. Amplitude modulation depth is typically 70%, detected by a photodiode.

One issue with photodiode detection is amplitude modulation to phase modulation (AM-to-PM) conversion, where changes in the average optical power modulate the phase of the detected RF signal. The optical power level is set to a local maximum in the AM-to-PM photodiode response, where there is zero slope and minimal sensitivity to fluctuations in optical power. At this peak, a ±10% variation in average photocurrent causes less than 10 fs delay variation in the detected RF signal.

The receiver is a digital RF phase comparator used to compare the transmitted RF signal with a local signal to be controlled. Since the delay through coaxial cables and other RF components is temperature dependent, variations are corrected by subtracting a local calibration signal sent through both comparison paths. All processing of RF signals is done at an intermediate frequency of 50 MHz, after mixing down with a 2800 MHz local oscillator.

Due to the continuous nature of the signal, retroreflections anywhere in the fiber optic signal path can cause random fluctuations of the received RF signal phase. The measured RF signal is the vector sum of the desired signal and an interference vector whose relative angle is determined by the physical spacing of the reflections, and whose amplitude is determined by the relative optical phase of the signal and retroreflection. This relative optical phase varies rapidly with temperature, in the case of widely spaced reflections. As the amplitude of the interference vector changes, the received RF phase and amplitude vary. To suppress these effects to below 10 fs, all optical reflection losses need to be greater than 40 dB, so angle polished connectors (APCs) and high return loss components are used.

We initially characterized the performance of this system in our lab by measuring the relative time

difference between long and short stabilized links. These results are described in detail elsewhere[9]. In summary, we measured an RMS deviation of <10 fs on a 200 m fiber for over 20 hours and <20 fs on a 2.2 km fiber over 60 hours. The results of this system installed in the LCLS are described in the next section.

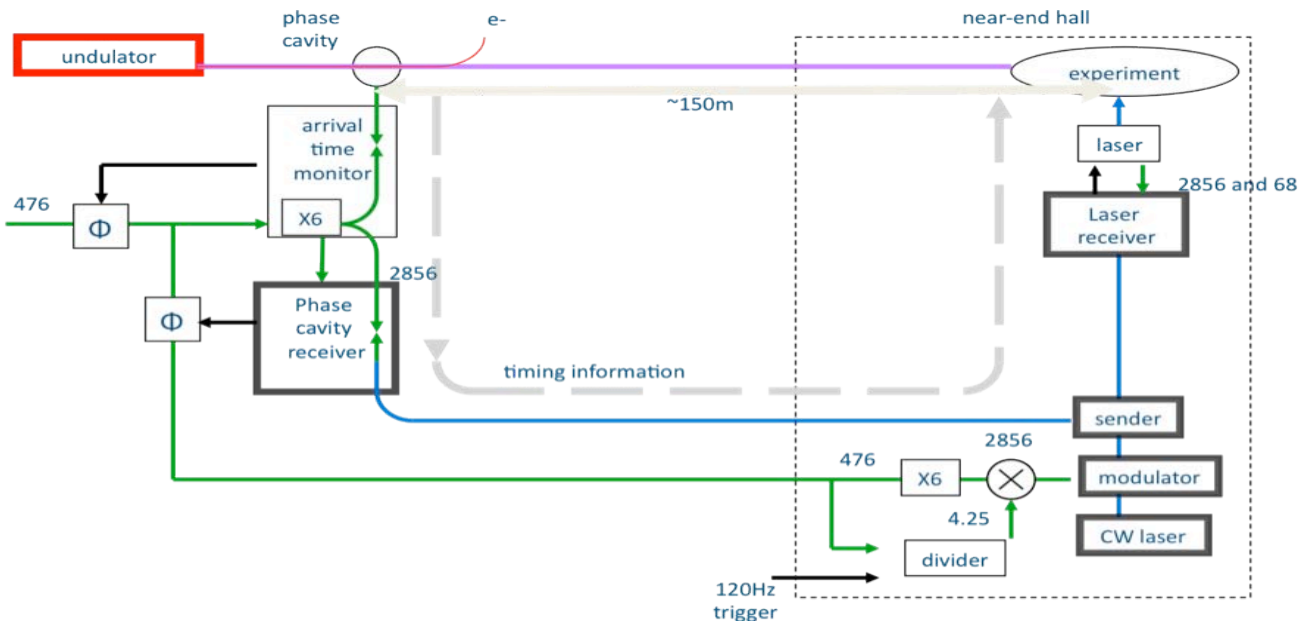

Figure 4. Detailed schematic of the signal path for synchronizing the user laser with the arrival time diagnostic (phase cavity.) The 150 m stabilized link to the phase cavity locks the optical distribution system to the average arrival time of the beam as determined by the phase cavity. Shot-to-shot variations of the beam arrival time with respect to the average are recorded and used by the experiment to sort the data in post-processing.

LCLS RESULTS

A schematic of the installation of a 2-channel synchronization system is shown in Fig. 4. The aim of this system is to synchronize the arrival time of the x-ray pulse with the user laser pulse. In the LCLS, the arrival time of each electron bunch is measured with a phase cavity. Note that the arrival time of the x-ray pulse is not necessarily the same as that of the electron bunch.

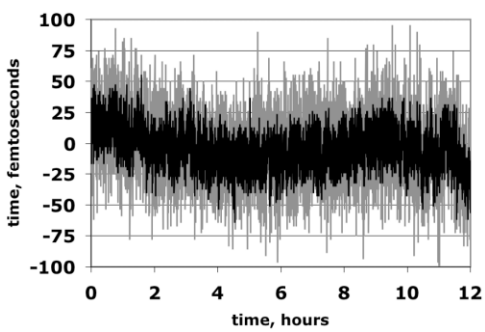

Figure 5: Relative drift of a 2856 MHz signal transmitted over the phase cavity link (2x150m) and the laser fiber (5 m) fiber. The relative time difference has an RMS deviation of 16 fs in a 1 kHz bandwidth over 12 hours. The slow drift is due to an 0.5 m unstabilized cable between the two receivers.

The phase cavity is a resonant cavity with a frequency of 2805 MHz and a Q of a few thousand. As the beam passes through the cavity, it excites a transient oscillation. The relative phase of this oscillation is compared with the phase of a 2856 MHz clock multiplied up from the 476 master oscillator signal for the LCLS. A servo loop adjusts the phase of the 2856 MHz signal such that the average beam arrival time is at the zero crossing of this clock. The relative timing of each electron bunch is measured with respect to the average arrival and reported to the user for post-processing of their data.

The fiber link transmitter is located in the first of the LCLS user areas (Near End Hall), a few meters from the user laser system. The entire transmitter and one of the receivers occupies about 2/3 of a standard 19-inch rack. One of the fiber links runs a few meters to the nearby laser. The other link runs ~150 m to the phase cavity in the linac tunnel just downstream from the undulator.

To lock the fiber links to the phase reference provided by the phase cavity, the fiber receiver adjusts the relative phase of the master clock so that the transmitted signal on the fiber links maintains a constant relative phase to the master clock.

To measure the relative stability of the two fiber links, we looped the fiber to the phase cavity back to the transmitter and compared the relative phase of the two

receivers as shown in Fig. 5. The RMS relative drift of the two links over a half day period was 16 fs. The slow drift seen in Fig. 5 is fully accounted for by the 0.5 m unstabilized cable connecting the two receivers.

The user laser is a mode-locked Ti:sapphire oscillator. A schematic of the layout for synchronizing the laser to the to the 2856 MHz reference phase is shown in Fig. 6. The phase of 7th harmonic of the laser signal observed on a photodiode in the oscillator, multiplied by 6, is compared with the reference phase. The error signal is used to correct the laser phase by driving a piezo-controlled mirror in the laser cavity. The in-loop laser control error signal over a day is shown in Fig. 7. The RMS signal over a 125 kHz bandwidth was 120 fs and over a 1 kHz bandwidth the value was 25 fs.

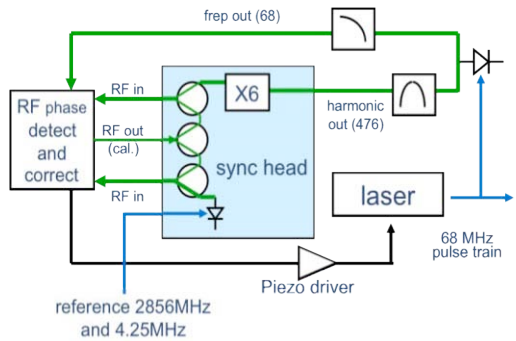

Figure 6: Schematic layout of synchronization to user laser oscillator.

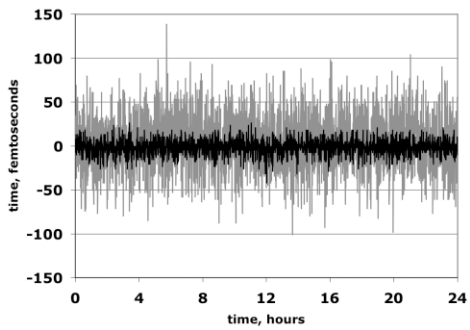

Figure 7: In-loop laser control error signal over a day. The RMS error signal was 120 fs over a 125 kHz bandwidth (gray), and 25 fs over a 1 kHz bandwidth (black).

This system was installed at the LCLS in September 2009 and ran continuously during the first LCLS user run in October 2009.

CONCLUSION

We have installed a fiber link system at the LCLS for high precision distribution of RF signals used for synchronization of a user laser with the average arrival time of the electron beam as measured with a phase cavity. We were able to regularly achieve an rms jitter and drift between two RF channels of less than 20 fs.

We locked one of the two links to the reference phase provided by the phase cavity and the other link to the mode-locked Ti:sapphire oscillator.

We achieved a 25 fs relative locking stability to the laser in a 1 kHz bandwidth. We expect to improve the stability by improving the laser pump stability and vibration isolation of the oscillator.

The fiber synchronization system operated continuously during the LCLS user run in Oct 2009 and is presently in use for the run that began in mid-April 2010. LCLS is engineering production receivers (8 channels) and upgrading the transmitter to 16-channel capability

This approach has several advantages for operation in an accelerator facility. It is easily manufacturable, expandable to many channels, and can be configured to lock to a wide variety of clients. Following the demonstration of this two-channel system, the first commercially produced subsystems are presently being tested.

We are planning several activities over the next year. These include improving the laser oscillator stability and control, transmitting higher frequencies for higher phase resolution. We also plan a full series of measurements to characterize the overall timing stability of the x-ray and laser pulses.

REFERENCES

[1] C. Pellegrini, "Overview Of Single Pass Free Electron Lasers," in Proceedings of the 10th European Particle Accelerator Conference (EPAC 06), Edinburgh, Scotland, 26-30 Jun 2006.

[2] A. M. Lindenberg, et al. "Atomic-scale visualization of inertial dynamics," Science 308, 392 (2005).

[3] A. L. Cavalieri, et al. "Clocking Femtosecond X Rays," Phys. Rev. Lett. 94, 114801 (2005).

[4] O. Lopez, A. Amy-Klein, C. Daussy, Ch. Chardonnet, F. Narbonneau, M. Lours, and G. Santarelli, "86-km optical link with a resolution of 2x10-18 for RF frequency transfer," Euro. Phys. J. D 48, 35 (2008).

[5] P. A. Williams, W. C. Swann, N. R. Newbury, "High-stability transfer of an optical frequency over long fiber-optic links," J. Opt. Soc. Am. B 25 1284 (2008).

[6] H. Kiuchi, "Highly Stable Millimeter-Wave Signal Distribution with an Optical Round-Trip Phase Stabilizer," IEEE Trans. Microwave Theory and Tech., 56, 1493 (2008).

[7] D. D. Hudson, S. M. Foreman, S. T. Cundiff and J. Ye, Opt. Lett. 31, 1951 (2006).

[8] J. Kim, J. A. Cox, J. Chen, F. X. Kartner, "Drift-free femtosecond timing synchronization of remote optical and microwave sources," Nature Photonics 2, 733 (2008).

[9] R. Wilcox, J. M. Byrd, L. Doolittle, G. Huang, and J. W. Staples, "Stable transmission of radio frequency signals on fiber links using interferometric delay sensing," Opt. Lett. 34, 3050 (2009).

[10] J. Ye, J.-L. Peng, R. Jason-Jones, K. W. Holman, J. L. Hall, D. J. Jones, S. A. Diddams, J. Kitching, S. Bize, J. C. Bergquist, L. W. Holberg, L. Robertsson, and L.-S. Ma, "Delivery of high-stability optical and microwave frequency standards over an optical fiber network," J. Opt. Soc. Am. B 20, 1459 (2003).

[11] J. W. Staples, J. M. Byrd, L. Doolittle, G. Huang, and R. Wilcox, "A Femtosecond-Level Fiber-Optics Timing Distribution System Using Frequency-Offset Interferometry," Proceedings of the 2008 Linear Accelerator Conference, M. Comyn, ed. (IEEE, 2008).

[12] A. Bruner, V. Mahal, I. Kiryuschev, A. Arie, M. A. Arbore, M. M. Fejer, "Frequency stability at the kilohertz level of a rubidium-locked diode laser at 192.114 THz," Appl. Opt. 37, 6410 (1998).

[13] S. Masuda, A. Seki, S. Niki, "Optical frequency standard by using a 1560 nm diode laser locked to saturated absorption lines of rubidium vapor," Appl. Opt. 46, 4780 (2007).

[14] F. X. Kartner, H. Byun, J. Chen, F. J. Grawert, F. O. Ilday, J. Kim, and A. Winter, "Progress in Large-Scale Femtosecond Timing Distribution and RF-Synchronization," in Proceedings of the 2005 Particle Accelerator Conference, C. Horak, ed. (IEEE, 2005).

ADVANCED MODULAR OSCILLOSCOPES AND DIGITIZERS OPTMIZED FOR ACCELERATOR APPLICATIONS

Boyd Shaw, Christopher Ziomek, ZTEC Instruments, Albuquerque, NM 87109, U.S.A.

Abstract

Modular oscilloscopes and digitizers, including those with embedded EPICS IOCs, provide powerful off-the-shelf solutions for accelerator controls and beamline data acquisition applications requiring fast sampling, high resolution and/or tight multi-channel synchronization. This presentation discusses features and capabilities of EPICS and non-EPICS LXI, VXI, PXI/cPCI and PCI oscilloscopes and digitizers as they specifically relate to accelerator and beamline applications. Modular oscilloscopes and digitizers with on-board DSP and FPGAs provide the advanced waveform acquisition and analysis capabilities of benchtop instruments with the size and channel-density advantages of modular instruments. Instruments with on-board processing, such as those from ZTEC Instruments, enable real-time waveform math and waveform parameter analysis. Advanced triggering and multiple acquisition modes are other features found on some of today's advanced modular instruments. Furthermore, instruments with embedded EPICS IOCs save users the time and money of developing their own EPICS drivers and display panels.

ACCELERATOR REQUIREMENTS FOR OSCILLOSCOPES & DIGITIZERS

Accelerator applications often challenge instrumentation manufacturers. In addition to requiring low noise and distortion during data acquisition, responsive remote instrument control and fast screen update rates are important for many machine control applications. And because large amounts of data are often captured, it becomes important to reduce the data to include only the desired information and download the information as quickly as possible so that the instrument is ready for the next acquisition.

Furthermore, it is frequently necessary to tightly synchronize many channels of data acquisition and multiple triggers across numerous instruments and across multiple chassis that may be separated by significant physical distances.

Because of the demanding technical requirements of accelerator applications, it is often necessary for engineers to develop their own custom products to meet specific requirements. However, developing custom instruments adds significant costs and time to most projects. Because of this, engineers and experimenters prefer to purchase off-the-shelf solutions whenever possible.

ATTRIBUTES OF ADVANCED MODULAR SCOPES & DIGITZERS

Advanced instrument functionality that was traditionally found only on benchtop instruments is now available on modular instruments in PXI/cPCI, PCI, LXI and VXI formats. For oscilloscopes and digitizers, this functionality includes input signal conditioning, multiple acquisition modes, advanced triggering, on-board waveform math and analysis and much more. Figure 1 illustrates some of these 'benchtop' functions as they exist in ZTEC modular instruments.

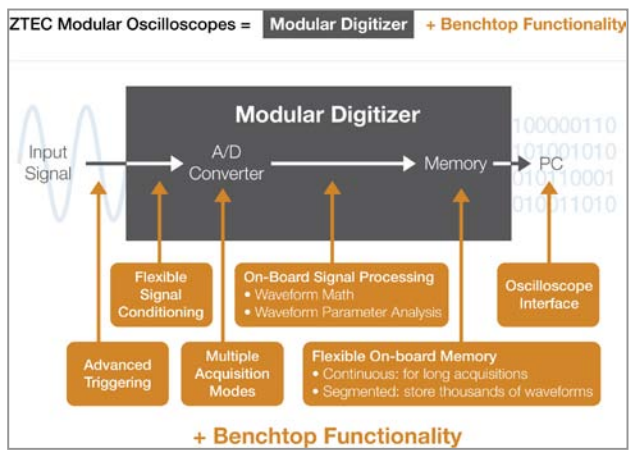

Figure 1: Benchtop functionality

Triggering

Going beyond simple rising/falling edge triggers, advanced modular oscilloscopes and digitizers add the ability to trigger on complex signal conditions, from multiple sources, just like their benchtop counterparts. For example, pulse width triggers can be configured to occur only on pulses that meet certain conditions – e.g., greater than or less than a user-defined pulse width, or inside/outside a specified range of pulse widths.

Pattern triggers are used to acquire waveforms when a user-defined pattern becomes true or false. The pattern is a combination of HIGH/LOW states on a combination of one or more input channels and/or backplane triggers like those found on PXI and VXI. For example, an instrument could be set to trigger and acquire data when Input 1 is HIGH, Input 2 is LOW and Input 3 is HIGH. See Figure 2.

Figure 2: Example of a pattern trigger

Glitch triggers look for glitches in a waveform as short as 250ps in duration and capture data when the glitch occurs. This is a valuable trigger when monitoring waveforms over long periods and is important to find out how often abnormal events occur. See Figure 3 below.

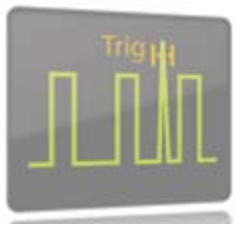

Figure 3: Example of a glitch trigger

Triggers can also be cascaded and the number of events can be counted; combining to define extremely specific trigger events. For example, the instrument could be configured to trigger on the fourth occurrence of event 'B' (e.g., a rising edge on Input 2), only after event 'A' occurs (e.g., a pattern of LOW on Input 1, HIGH on Input 3 and HIGH on Input 4).

Acquisition Modes

Similar to the discussion on triggering, some of today's advanced modular oscilloscope and digitizers have the same advanced acquisition modes that are commonly found on benchtop instruments. Beyond the default normal acquisition mode where a single waveform is captured and saved to memory, advanced acquisition modes provide options for decreasing noise, over-sampling, and other techniques that instrument operators can use to capture data in a manner more useful for a given application.

Scalar average mode takes waveform points from a user-defined number of consecutive acquisitions and averages them together (see Figure 4).

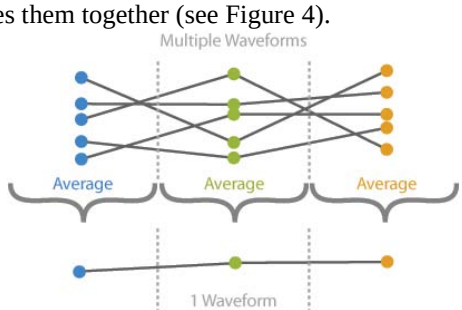

Figure 4: Scalar average mode

Averaging waveforms reduces the effects of random noise and increases measurement resolution. In contrast to scalar averaging, a high resolution acquisition mode averages a number of adjacent points in a single over-sampled acquisition, resulting in a single, higher resolution waveform (see Figure 5). With both scalar averaging and high resolution modes, the result is a single waveform with lower random noise and improved accuracy, as compared to a waveform from a normal acquisition.

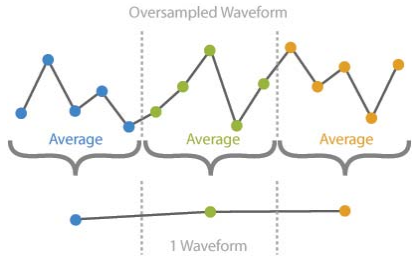

Figure 5: High resolution mode

Envelope and peak detect acquisition modes result in two waveforms that represent the maximum and minimum waveform points from either a single over-sampled acquisition (peak detect mode), or from multiple acquisitions (envelope mode). See Figures 6 and 7. Theses acquisition modes are useful for signals such as amplitude modulated signals, where it may not be necessary to capture all the data in every acquisition, but it is important to see the envelope of the waveform(s).

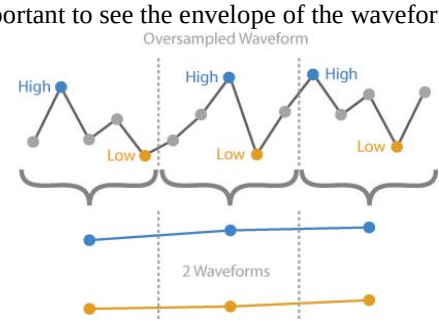

Figure 6: Peak detect mode (single acquisition)

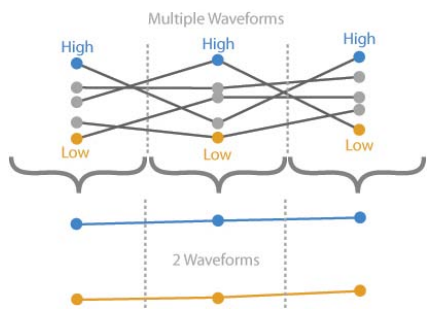

Figure 7: Envelope mode (multiple acquisitions)

Like benchtop oscilloscopes, some of today's modular oscilloscopes and digitizers have an equivalent-time acquisition mode. In equivalent-time acquisition mode, waveforms are sampled at the maximum real-time sampling rate of the instrument's analog-to-digital converters (ADCs). Each real-time acquisition fills in some points in the resultant equivalent time waveform. After many acquisitions, the equivalent time waveform fills in and appears as if it were acquired at a much faster

sampling rate. For example, on the ZTEC Instruments' ZT4610 series of oscilloscopes, the maximum real-time sampling rate is 4 GS/s; in equivalent time acquisition mode the resulting waveform has an effective sampling rate of up to 400 G/s.

High Performance Data Acquisition

Today's most advanced modular oscilloscopes and digitizers meet the demanding data acquisition requirements of accelerator beamline and control applications by offering higher ADC resolution, faster sampling, less noise and more memory than benchtop oscilloscopes.

With very few exceptions, benchtop oscilloscopes have 8-bit ADCs. 8-bit ADCs provide a maximum of 2^8, or 256 digitization levels across the full scale input range. In other words, under perfect conditions, an oscilloscope with a 10V full scale range has vertical (voltage) resolution of 10V/256, or ~39mV. Contrast that with modular oscilloscopes and digitizers that are commonly found with 12, 14 and 16-bit ADC resolution (and occasionally even more). A 16-bit ADC has 65,536 digitization levels. This represents a voltage resolution of ~153µV across a 10V full scale range, under perfect conditions.

Fast sampling is also an important aspect of waveform monitoring and data acquisition at accelerators. Often it is necessary to accurately capture very fast events. Today's 8-bit modular oscilloscopes have maximum real-time sampling rates of 4 GS/s (250ps sample spacing). High resolution instruments (those with more than 8-bit ADC resolution) typically have lower maximum real-time sampling rates as vertical resolution increases. Figure 8 shows the vertical resolution and the maximum sampling rate of ZTEC Instruments' high-resolution instruments.

Series	Resolution	Max Sampling
ZT4420	12-bit	1 GS/s (1 ns)
ZT4440	14-bit	800 MS/s (1.25 ns)
ZT410	16-bit	400 MS/s (2.5 ns)

Figure 8: Resolution and maximum sampling rate of ZTEC Instruments' high resolution oscilloscopes

High vertical resolution/accuracy, combined with low noise is a common need for waveform monitoring and data acquisition applications at accelerators. Oftentimes signals from beamline detectors and other instruments are very small and may be superimposed on top of larger signals. Clearly it is not practical to accurately characterize a signal that is a few millivolts in amplitude, riding on top of a much larger signal, if you only have 39mV of resolution (i.e., 8-bit ADC, 10V range). To capture signals such as these, it is clearly advantageous to use high-resolution instrumentation.

Noise and distortion are critical instrument attributes when measuring any signal, especially signals with small amplitudes. It is important for the instruments to have as little internal noise and as little signal distortion as possible. Noise and distortion in oscilloscopes and digitizers are typically characterized by the following measures:

- Signal-to-Noise Ration (SNR)
- Total Harmonic Distortion (THD)
- Signal-to-Noise + Distortion (SINAD)
- Effective Number of Bits (ENOB) = (SINAD – 1.76) / 6.02
- Spurious-Freed Dynamic Range (SFDR)

ZTEC Instruments' ZT4440-DP series of modular digitizers have been optimized to minimize noise and distortion, making them ideal for many accelerator applications where small signals accurately captured, sometimes superimposed on top of larger signals. Figure 9 shows the frequency response of a 10.7 MHz signal captured on the ZT4440-DP (14-bit) PXI modular digitizer. The ZT4440-DP has the following characteristics:

- SNR = 65.1 dBc
- THD = -86.7 dBc
- SINAD = 65.0 dBc
- SFDR = 81.5 dBc

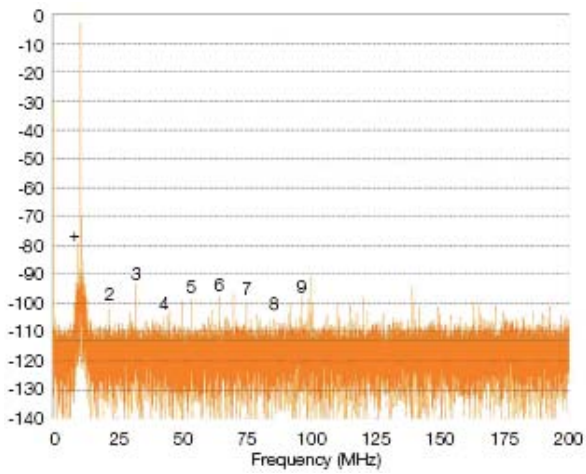

Figure 9: Frequency response of 10.7 MHz signal captured on ZTEC Instruments' 14-bit ZT4440-DP digitizer

On-Board Signal Analysis

On-board signal analysis is another key differentiator between basic modular digitizers and more advanced modular oscilloscopes. On-board signal processing and data reduction reduces data transfer time and speeds up data acquisition rates and analysis times. Instead of acquiring waveform data and then downloading it from the card to software such as MATLAB® for additional analysis, advanced modular instruments perform the math and analysis on-board the instrument, in real-time, without having to download the entire waveform.

On-board data analysis is especially important with today's long-memory instruments. With acquisition memory lengths of hundreds of millions of data points and longer, it can be very time consuming to download

every waveform from every channel, even with very fast data buses like PCI and PCI express. For most applications, it is much faster to use on-board processing to extract the desired information from the signal and reduce the data before transferring it to a PC than it is to simply download every data point that is captured.

For example, let's assume that an event is used to trigger the oscilloscope. The trigger event indicates that a pulse will occur sometime within the next 1ms, but the exact time of its occurrence within the 1ms window is unknown. The user of the oscilloscope only needs to know two bits of information: 1) when the event started relative to the trigger event and 2) the area under the pulse. If the instrument samples at 1 GS/s for 1ms, one million data points are captured. Instead of transferring all one million data points to a PC for analysis, an oscilloscope or digitizer with built-in processing can calculate the rising edge of the pulse, perform an integration of the pulse, and transfer the results of these two calculations to a PC. The amount of data transferred in this case, using on-board processing, is much less and the time required for data transfer is also less than if the entire waveform had to be transferred to a PC. These time savings are particularly significant when there are multiple instruments sharing a single bus, e.g., the PCI bus on the backplane of a PXI chassis.

ZTEC Instruments' M-Class oscilloscopes and digitizers use on-board FPGAs and DSP to perform waveform math and calculate over forty waveform parameters. On-board waveform math includes algebraic functions, integration, differentiation, Fast Fourier Transforms (FFTs), histograms, parameter trending, limit/mask testing, and others. Waveform parameters related to voltage and time are also automatically calculated. Figures 10 and 11 show some of the voltage and time parameters calculated.

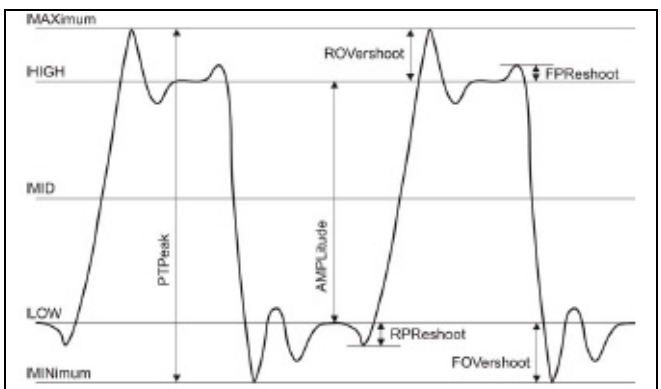

Figure 10: Some vertical-axis measurements

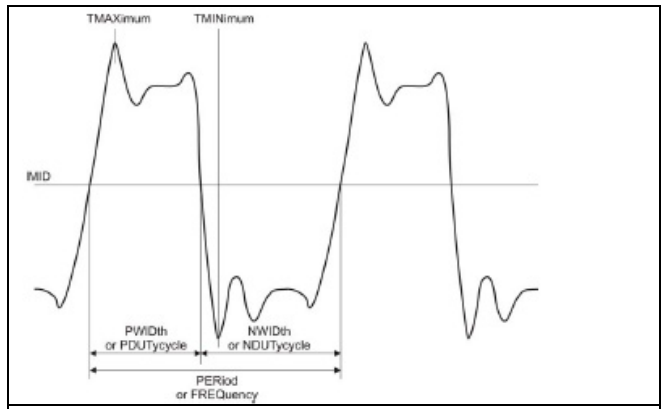

Figure 11: Some horizontal-axis measurements

EMBEDDED EPICS FOR ACCELERATOR APPLICATIONS

ZTEC Instruments became the first manufacturer to embed Experimental Physics and Industrial Control System (EPICS) in a high performance oscilloscope when it introduced its first EPICS oscilloscopes in 2008. Today, several series of ZTEC EPICS oscilloscopes are available, off-the-shelf, designed to meet the different oscilloscope/digitizer requirements of the accelerator community. This includes high speed applications and high resolution applications. High speed EPICS oscilloscopes are available with up to 1 GHz analog bandwidth, 4 GS/s, 8-bit resolution. High-resolution EPICS oscilloscopes with up to 14 bits of resolution are available as shown in Figure 12.

Series	Resolution	Max real-time sampling rate	Analog bandwidth
ZT4610	8 bit	4 GS/s	1 GHz
ZT4210	8 bit	1 GS/s	300 MHz
ZT4420	12 bit	1 GS/s	300 MHz
ZT4430	13 bit	500 MS/s	300 MHz
ZT4440	14 bit	800 MS/s	300 MHz

Figure 12: ZTEC Instruments' EPICS oscilloscopes

ZTEC's EPICS oscilloscopes have process variables (PVs) supporting all instrument functions. With roughly 900 PVs, the EPICS oscilloscopes may be controlled and monitored completely via EPICS and Channel Access (CA). Users of the EPICS oscilloscopes can modify the PV database file of each oscilloscope to better fit their application requirements. For example, the PV prefix can be modified to meet local PV naming conventions. Also, it is clearly necessary to modify the PV prefixes anytime more than one EPICS oscilloscope is on a single network so that each instrument has unique PV names. The PV database file can also be modified to include specialized forward links (FLNKs) and fanout PVs to perform special EPICS functions in a system.

By providing the free EDM and MEDM panels for the EPICS oscilloscopes, ZTEC's EPICS oscilloscopes are a complete EPICS-based solution for advanced data acquisition, data analysis and waveform monitoring.

Providing a high performance out-of-the-box solution saves users the development time and costs associated with securing their own software resources to write drivers for other off-the-shelf instruments. Figure 13 shows two EDM panels. The top panel includes basic vertical and horizontal scale control as well as real-time display of the input channel 1 waveform. The bottom panel shows waveform parameters calculated automatically on-board the instrument.

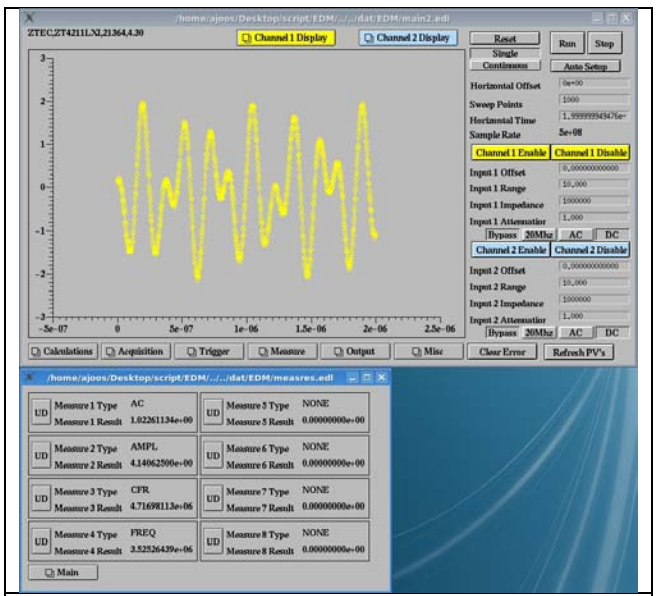

Figure 13: EDM panels for ZTEC EPICS oscilloscopes

MULTI-INSTRUMENT TIMING & SYNCHRONIZATION

Timing and synchronization of multiple instruments in a system is critically important in many accelerator applications. Depending on the measurement platform being used (e.g., PXI, cPCI, LXI) there are different ways to tightly synchronize multiple instruments over short and long distances.

PXI systems provide multiple triggers on the chassis backplane. The most accurate trigger is the PXI_STAR trigger. The PXI_STAR trigger consists of 13 propagation-matched triggers that extend from the star trigger slot (adjacent to the system slot) to the first 13 peripheral slots directly to the left of the star trigger slot. Each of the 13 trigger lines are matched to within 1 ns of propagation delay and the delay from the trigger slot to each of the peripheral slots may not exceed 5ns. In addition to tightly synchronizing multiple instruments in a single chassis, the PXI_STAR trigger may also be daisy-chained to other chassis, extending the ability to highly synchronize instruments across multiple chassis.

Accelerators around the world are now using Micro-Research Finland's event generator (EVG) and event receiver (EVR) system to provide master timing signals via fiber optic cables across large distances at accelerators. ZTEC Instruments is currently developing a solution where ZTEC's oscilloscopes are integrated with Micro-Research Finland's cPCI EVRs. The solution consists of a PXI or cPCI chassis, ZTEC EPICS IOC code loaded onto an embedded PXI or cPCI controller, multiple ZTEC PXI oscilloscopes (which are compatible with cPCI) and Micro-Research Finland's cPCI EVRs.

The LXI instrumentation standard, with which ZTEC Instruments' EPICS scopes comply, include hardware triggers for synchronizing multiple instruments. Using the eight LVDS LXI hardware trigger lines, instruments may be connected together in a daisy-chain or star configuration. Figure 14 shows the two configurations. Propagation delay between two instruments will depend on the length of the cable. While the LXI standard does not specify maximum delay times between instruments, in practice, trigger delays between instruments are very short, when trigger cables are kept to ~1m or less.

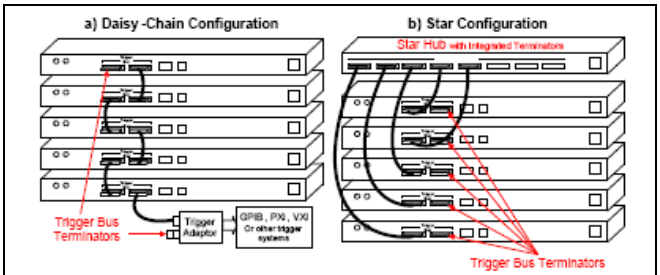

Figure 14: LXI hardware trigger configurations [5]

CONCLUSION

Today's off-the-shelf modular oscilloscopes and digitizers are becoming more and more advanced and are able to meet many of the demanding requirements of accelerator applications. In addition to the high channel density offered by modular instrumentation, today's most advanced modular instruments include advanced triggering and acquisition modes and on-board waveform math and analysis. Additionally, ZTEC Instruments EPICS oscilloscopes and digitizers offer an out-of-the-box solution for users who need a high performance waveform capture, analysis and monitoring. Modular instrumentation also provides a number of methods for tightly synchronizing multiple instruments and multiple chassis.

REFERENCES

[1] ZTEC Instruments, M-Class Digital Storage Oscilloscope, User's Manual, November 30, 2009.
[2] ZTEC Instruments, EPICS Interface User's Manual, December 7, 2009
[3] PXI Systems Alliance, "PXI Hardware Specification, Revision 2.2", September 22, 2004.
[4] Micro-Research Finland website, www.mrf.fi
[5] LXI Consortium, "LXI Standard Rev 1.2.01", section 5, November 26, 2007.

A FUNDAMENTALS OF LOGARITHMIC AMPLIFIERS AND RECENT ADVANCES

B. Gilbert
Analog Devices, Inc., Beaverton, OR, U.S.A.

Abstract

This is a tutorial address. Numerous real-world signals exhibit a large dynamic range (DR)--the ratio of the strongest amplitude to the weakest, usually expressed in decibels. These signals are often handled by high-resolution A/D converters (24 b = 144.5 dB). But these are expensive, especially when fast response is required.

Today, a large family of monolithic integrated circuits can address these needs. They compress the dynamic range of an input on a precise logarithmic scale, and provide an output representing the input expressed in dB with DR capabilities up to 200 dB, bandwidths to over 20G Hz, response times down to 1.5 ns, current-measurement capabilities from 1 pA to 10 mA in one range, and operation from supply voltages as low as 1.5 V. Many are also tiny (sometimes barely visible) and inexpensive.

This talk will present various ways by which a logarithmic response is achieved, starting with strong mathematical foundations that also provides fundamental insights as to how practical logarithmic amplifiers must be designed. The principles are then elaborated by showing several basic circuit forms to address diverse measurement requirements.

*

SUB-NM BEAM MOTION ANALYSIS USING A STANDARD BPM WITH HIGH RESOLUTION ELECTRONICS

M. Gasior, H. Schmickler, J. Pfingstner, M. Sylte, M. Guinchard, A. Kuzmin, CERN, Geneva
M. Billing, Cornell University, Ithaca, New York
M. Böge, M. Dehler, PSI, Villigen

Abstract

In the Compact Linear Collider (CLIC) project high luminosity will be achieved by generating and preserving ultra low beam emittances. It will require a mechanical stability of the quadrupole magnets down to the level of 1 nm_{rms} for frequencies above 1 Hz throughout the 24 km of linac structures. Studies are presently being undertaken to stabilize each quadrupole by means of an active feedback system based on motion sensors and piezoelectric actuators. Since it will be very difficult to prove the stability of the magnetic field down to that level of precision, an attempt was made to use a synchrotron electron beam as a sensor. The beam motion was observed with a standard button Beam Position Monitor (BPM) equipped with high resolution electronics. Beam experiments were carried out to qualify such a measurement at CesrTA (Cornell University) and at SLS (PSI, Villingen), where the residual motion of the circulating electron beams was measured in the frequency range of 5 – 700 Hz. This paper describes the results achieved along with the equipment used to measure both the residual beam motion and the mechanical vibration of machine elements.

MOTIVATION

For all new electron beam based light sources the present "race" is for always smaller beam emittance. The linear collider and FEL projects aim for even smaller beam emittances, such that mechanical vibrations of the quadrupoles start to contribute significantly to the increase of beam emittance during the passage of the beams through the linac. Extensive computer simulations [1] have been carried out for the CLIC project leading to the specifications of the required stability of the magnetic axis of the CLIC main linac quadrupoles listed in Table 1.

The required stability is at least one order of magnitude smaller than what can be achieved by passive damping and shielding of ground motion and technical noise. The present baseline for the CLIC project is an active stabilization system based on motion sensors for 5 degrees of freedom on each quadrupole and piezoelectric actuators in a closed feedback loop for stabilization [2]. It is expected that with this setup the quadrupoles can be mechanically stabilized to the required precision. One point in this approach is left open, namely whether the mechanical stabilization of a quadrupole also assures that the magnetic centre of this quadrupole is stable to the same level. Potentially coil vibrations due to coolant flow or pole tip vibrations might change the magnetic centre. Hence in the framework of the actual R&D program additional instrumentation is being developed, which would allow sensing the stability of a quadrupole down to the required level of precision. For the final experiment the stabilized quadrupole would have to be inserted into that machine, the beam steered through it with a large excursion, whilst the beam in all other quadrupoles would be steered to the minimum possible offset.

Table 1: CLIC project requirements for residual quadrupole stability above the limiting frequencies

Plane	Final focus quads	Main beam quads
Vertical	0.18 nm > 4 Hz	1 nm > 1Hz
Horizontal	5 nm > 4 Hz	5 nm > 1Hz

This paper describes pilot measurements on two synchrotron light sources exploring whether an electron beam could be used as a sensor of the quadrupole magnetic field stability. In simple experiments the residual eigen-motion of the electron beam was observed and beam spectra including the region of interest 5 –100 Hz have been recorded. In order to obtain a noise floor below the nano-meter level an optimized copy of the LHC Base Band Tune (BBQ) measurement hardware [3, 4] was used with observation periods up to many minutes.

The following chapters contain description of the front-end electronics used, results from the beam experiments at CesrTA and SLS and preliminary conclusions whether an electron beam in a synchrotron could be used as a gauge for demonstrating quadrupole stability down to the nano-meter level.

HIGH RESOLUTION BPM ELECTRONICS

Beam signals were taken from standard button BPMs "borrowed" from their native systems (orbit or transverse feed-back) for the time of experiments. The individual button signals were processed with a copy of the LHC BBQ hardware based on the direct diode detection (3D) technique [3, 4]. The principle of the technique is shown schematically in Fig. 1, with the simplified signal waveforms sketched above the characteristic nodes of the circuit.

In this scheme the pick-up electrode signals are processed by diode peak detectors, which can be considered as fast sample-and-hold circuits, with the sampling self-triggered at the bunch maxima and "held" by the parallel capacitors. The purpose of the parallel resistors is to slightly discharge the capacitors so that the next bunch with potentially smaller amplitude

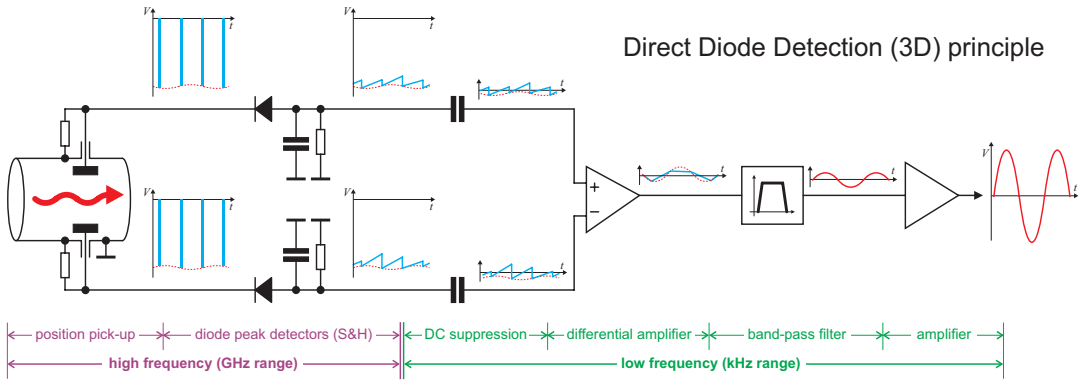

Figure 1: Direct diode detection principle with simplified signal waveforms in the key nodes of the circuit.

also contributes to the detector output signal. The series capacitors remove the DC components corresponding to the beam offset, which otherwise would take most of the dynamic range of the following acquisition or even they would have to be attenuated, together with the carried modulation, as the DC components can be as large as a few tens of volts. With the large DC part suppressed, the low frequency small beam motion signals can be amplified and filtered prior to digitalisation, which was done with 24-bit NIM digitisers [5], based on audio codecs. The digitisers were connected to an FPGA-based VME digital acquisition board (DAB) [6], performing data buffering, sample windowing and calculating spectra through the FFT analysis. Such an acquisition system, developed specifically for the LHC BBQ systems, is capable of delivering 64K-point magnitude spectra of 160 dB dynamic range [3].

The LHC BBQ system operates in the range of 0.5 – 5 kHz with proton bunches ≈1 ns long. For the experiments presented here the system components, namely diode detectors, analogue front-end and 24-bit digitisers were modified for optimal performance in the band 5 Hz – 1 kHz with much shorter electron bunches. This modified system is referred to in the paper as the low frequency BBQ (LF-BBQ).

The sensitivity of the 3D technique for beam motion observation is achieved at the expense of rejecting beam offset and intensity information, resulting in absence of amplitude scale for the beam motion. Since the experiments required absolute amplitude calibration, the high dynamic range of the system was used for a dedicated calibration procedure.

In this procedure an electromagnetic exciter, typically an orbit corrector, was driven at a given frequency with current yielding beam oscillations with amplitudes convenient for the existing BPM system for turn by turn measurements (micro-meter domain). This calibration oscillation was measured in parallel with the BPM system (calibrated in mm) and the LF-BBQ hardware yielding a measurement with a calibrated amplitude. Then the excitation level was lowered in decades and the linear response of the LF-BBQ system was verified. During all the measurements a permanent excitation tone at 20 Hz was left on at a convenient amplitude level for data cross-calibration.

VIBRATION MEASUREMENTS

Several high resolution vibration sensors were installed for the measurements for two purposes:

– contributing to a world-wide campaign of documenting ground motion effects in accelerators domains;
– verifying that the observed beam rest-motion was not caused by vibrations of the BPM itself.

The experimental setup can not be described in this paper and the reader is referred to [7] and [8]. It was verified that the BPM vibration amplitudes were too small to be important for the measurement results of the described experiments.

EXPERIMENT AT CESR-TA

Beam measurements took place in June 2009. Four diode detectors were installed directly on each port of a standard CesrTA orbit button pick-up. Two detectors of the top and bottom left buttons were connected with two ≈ 1 m long coaxial cables to the first differential input of the analogue front-end, and the two detectors of top and bottom right buttons were connected with another two cables to the second differential input of the front-end. In this way two independent measurement channels were formed. As the beam was usually close to the pick-up centre, both channels were sensitive to both, horizontal and vertical beam motion. In the presented CesrTA measurements averages of both channels are shown. The outputs of the analogue front-end were connected to the 24-bit digitiser with two ≈ 20 m long coaxial cables. The digitisers, together with the DAB in a VME crate, were located in a “data collecting room”, together with the experiment crew. Data was processed on a laptop running a LabView application, collecting data from the DAB through a VME-USB bridge.

The ADCs were clocked at 44.1 kHz and every 32 samples were replaced by their average to improve signal to noise ratio (SNR), resulting in the equivalent sampling rate of 1403 Hz. One “single” measurement consisted of taking 64 K samples during ≈ 47 s. A “full measurement”, lasting ≈ 17 minutes, consisted of taking 22 single measurements and calculating their average, in order to decrease the variance of the spectra.

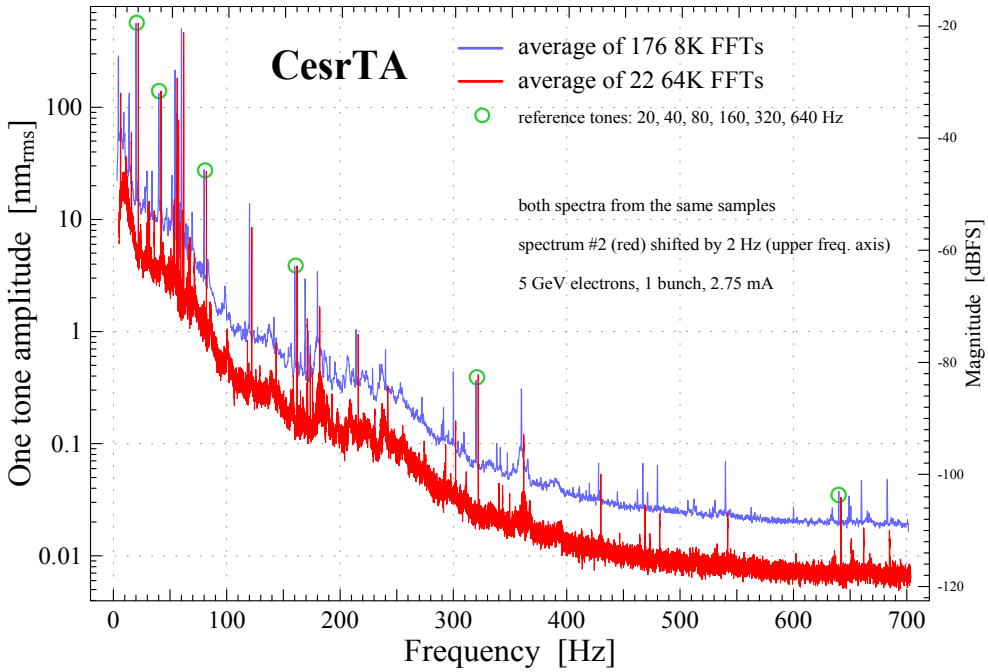

Figure 2: Typical CesrTA beam spectra.

For the amplitude calibration a vertical orbit corrector was used as an exciter. The corrector was disconnected from its native system and cabled to the "data collecting room". It was driven with a sinusoidal current of 0.5 A_{rms} at 20 Hz while the electron beam at 2 GeV was circulating in the machine. This excitation gave an oscillation amplitude of 100 μm_{rms} at the LF-BBQ pick-up location extrapolated from data of the CesrTA BPM system and scaled with the lattice functions.

Typical CesrTA beam spectra are shown in Fig. 2, taken with "as quiet beam as possible", i.e. with all feed-back systems off and at moderate beam intensity. Both shown spectra are calculated from the same beam signal samples with different processing. The spectrum with lower noise floor (red) is an average of 22 64K-point FFTs and the second spectrum is an average of 176 8K-point FFTs. The 8K spectra were calculated by dividing each of the 64K-sample records into 8 8K segments then processed separately. All samples are Hanning windowed prior to FFT processing, otherwise the spectral leakage would mask small components in the second half of the observation bandwidth. For the presented measurement 6 reference tones were used, namely at 20, 40, 80, 160, 320 and 640 Hz (green circles on the plot), with the excitation current of 7 mA_{rms} per component, resulting in the beam oscillation amplitude of 560 nm_{rms} at 20 Hz, scaling the left amplitude axis. The right amplitude axis is in dB with respect to the ADC full scale (FS). Both spectra have frequency axis shifted by 2 Hz so that the corresponding components do not overlap, but instead they are side-by-side for better amplitude comparison.

The spectra of Fig. 2 are in fact spectral amplitude densities and the time-domain amplitude measured during the calibration is their RMS integral. Nevertheless, the amplitude axis is scaled in nano-meters, which should be understood as the amplitude which would be obtained if the spectral density around a given single-tone peak was integrated. Therefore, the amplitude scale is true only for single tone components, stressed by the name of the amplitude axis. This "amplitude scale convention" was found the most representative for presenting results of the experiments. For obtaining time-domain amplitudes of any other signals than single tones a proper integration should be done, which was the case for the integrated RMS amplitudes discussed in the conclusion chapter.

By comparing the 8K and 64 K spectra of Fig. 2 it is possible to distinguish coherent and incoherent components, as amplitudes of incoherent components decrease with increasing FFT length. The other large coherent components (i.e. with similar amplitudes on both spectra) are at 60 Hz (mains harmonics) and 54 Hz. Incoherent large components are at 4.4 Hz and 13.8 Hz.

The noise floor difference between the 8 K and 64 K should be $\sqrt{8}$ i.e. ≈ 9 dB. This value is seen towards the end of the observation range, but for some, typically quite narrow, components the difference is smaller, i.e. such components are coherent only to a certain extend.

It is seen that the amplitudes of the 40, 80, and 160 Hz tones decreases with frequency (f) approximately like f^{-2}, (amplitude difference between the tones: 12, 14, 17 and 41 dB), which cannot be explained by the LF-BBQ frequency characteristic, measured in the lab to be flat within the observation bandwidth. Also it cannot be explained only by the inductance of the corrector coil (12 mH), giving with the driving source impedance the cut-off frequency of 160 Hz. However, it is certain that the attenuation of the exciter magnetic field through eddy currents in the Al vacuum chamber contributes significantly to this attenuation. A quantitative analysis of the attenuation was not carried out.

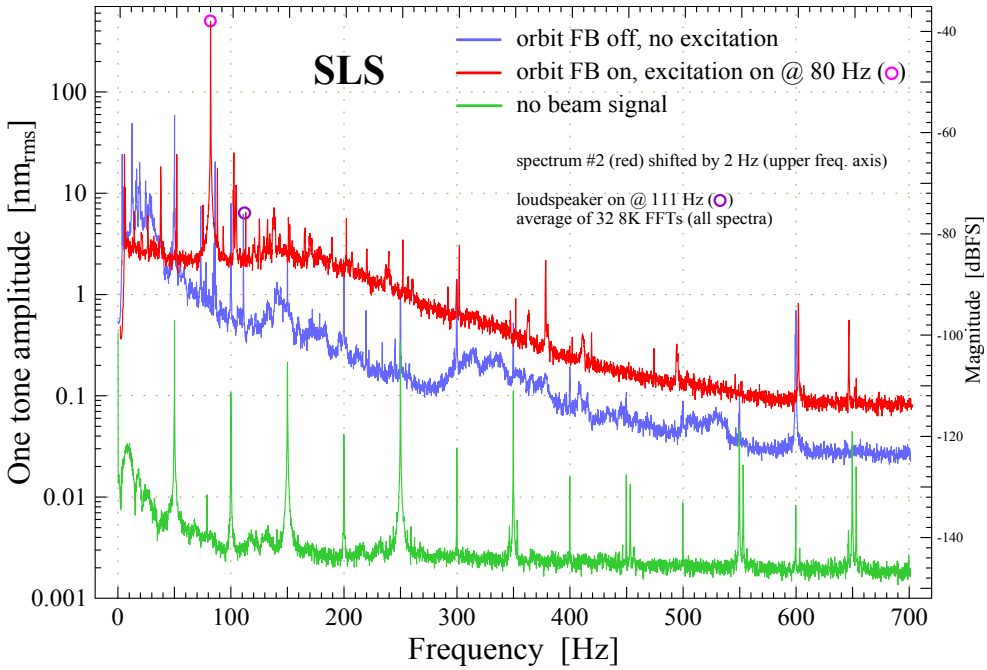

Figure 3: SLS spectra with the orbit feed-back on and off, along with a spectrum without beam.

The frequency range of interest for CLIC stabilization is 5 Hz – 100 Hz, since the excitation due to ground motion falls of rapidly with the square of the frequency. In this range the residual eigenmotion of the CesrTA beam is well above the nano-meter level, so it was concluded to repeat the experiment at an European light source, which was constructed much later and for which specific attention had been paid on stability.

EXPERIMENT AT SLS

Beam measurements took place in October 2009. As beam sensors two button pick-ups were used, one "borrowed" from the orbit system and one from the transverse feed-back system (≈ 3 m distance between the pick-ups). One top and one bottom port of each pick-up were equipped with the diode detectors, which were then connected to two differential inputs of the analogue front-end with a few m coaxial cables.

For the beam measurements at the SLS the same LF-BBQ hardware was used, with a few modifications improving further its sensitivity.

Beam excitation was done with an orbit corrector which was driven with a sine wave excitation generated by the control system. Its strength was calibrated with the BPM system at 80 Hz, high enough to be outside of the bandwidth of the orbit feed-back, which had to be on during the excitation. Due to smaller beam availability than at Cornell, the standard measurement configuration was 32 measurement of 8K samples each, taking ≈ 3 minutes.

Spectra from three such measurements with the channel of the orbit feed-back pick-up are shown in Fig. 3. One measurement was done with the excitation of 500 nm_{rms} at 80 Hz, the second is a corresponding measurement with the excitation and orbit feed-back off and the third is a reference measurement without beam. The two beam measurements were taken during the same beam store and beam conditions and the reference measurement was taken with the same settings of the analogue front-end as the beam measurements.

It is seen that the orbit feed-back attenuates the low frequency components (with a not understood exception around 4 Hz) while amplifying noise above its design bandwidth.

To excite the beam with mechanical vibrations in a controlled way, a loudspeaker was put on the machine floor near the pick-up used for the experiment. During measurements it was driven with a single tone, typically at 111 Hz, and the resulting beam oscillation is visible in the spectra of Fig. 3.

The spectrum measured without beam shows noise and interference of the electronics measured in the same conditions as the other two beam measurements. In the spectra strong interference from mains harmonics is seen, captured by the coaxial cables connecting the diode detectors with the front-end (≈ 2 m) and the front-end with the digitisers (≈ 20 m). With better cables and the digitisers much closer to the front-end this interference most likely could be significantly lowered.

Noise floor of the LF-BBQ electronics without and with beam should be similar, as the detector diodes most of the time are not conducting, turning on only with the beam pulses at amplitudes close to the beam peak voltage. For comparison the measured BBQ spectrum without beam was put on the same absolute amplitude as the other two measurements. The noise floor above 100 Hz is ≈ 3 pm_{rms}, raising to ≈ 30 pm_{rms} towards 10 Hz measured with the FFT bin width of ≈ 86 mHz, The corresponding noise densities are ≈ 10 pm/√Hz and ≈ 100 pm/√Hz, respectively.

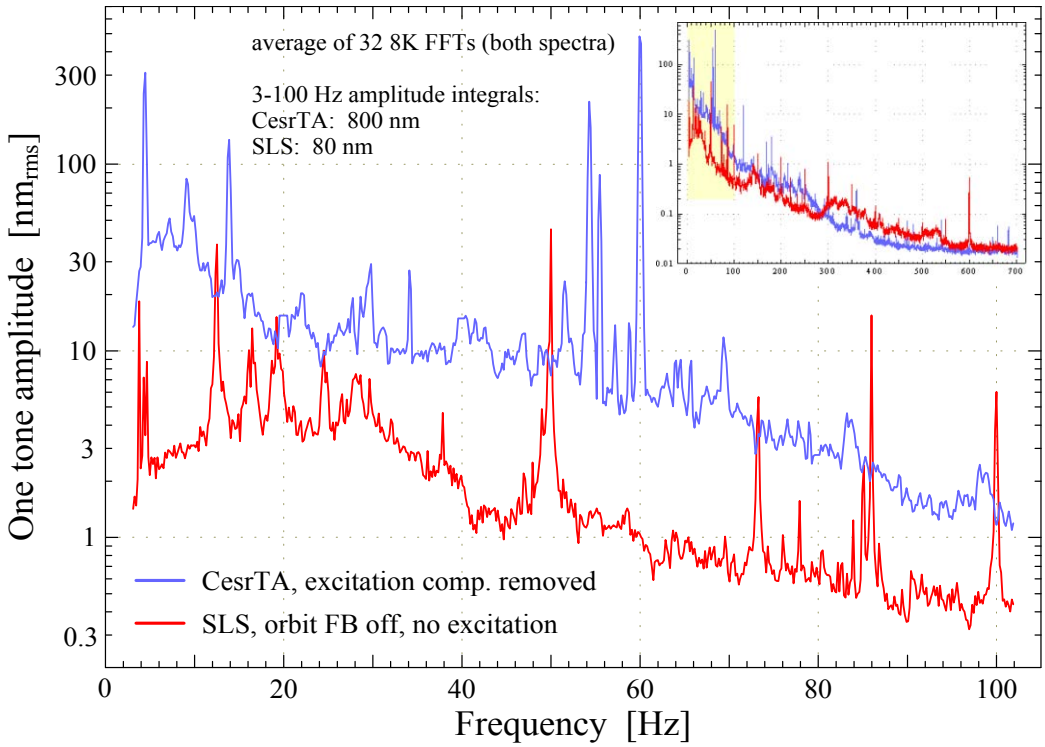

Figure 4: Comparison of CesrTA (excitation tones removed) and SLS spectra, shown in Fig. 2 and 3, respectively.

CONCLUSIONS

The spectra from both experiments at corresponding conditions are shown for comparison in Fig. 4. For this purpose the excitation tones were artificially removed from the CesrTA spectrum. The integrated beam motion for the plotted frequency range are 800 nm_{rms} and 80 nm_{rms} for CesrTA and SLS, respectively.

The defined objectives for this series of measurements had been to determine whether with the simple setup of high sensitivity BPM electronics and an electron beam of about 10 micrometer size circulating in a synchrotron the mechanical stability of one quadrupole could experimentally be verified down to the nano-meter level. Unfortunately the answer is negative, as the residual eigenmotion of the electron beam is well higher than 1 nm_{rms}, i.e. the integrated mechanical stability specification for the main beam CLIC quadrupoles for all frequencies above 1 Hz.

Since the difference to the target is quite high, the authors were discouraged to search for the origin of the beam rest-motion with the aim of compensating for the effect. A plausible candidate is electronic noise in the regulation loops of the quadrupole or bending magnet power converters and their impact on the closed orbit. Even if this hypothesis was correct, improving these regulation loops would be a considerable effort.

Future efforts will be directed to investigate the possibilities for installing the quadrupole under test in a beam extraction line with high beam duty cycle and with several BPMs before and after the quadrupole in order to be able to detect minimal changes in the beam deflection.

As a nice side product the diode-based BPM electronics, which had specially been developed for high sensitivity tune measurements, has successfully been extended to the very low frequency range and has given a noise performance which excels any other existing BPM electronics.

One can anticipate that in the near future circular light sources themselves might hit limits on their beams coming from residual mechanical vibrations of machine elements. For these cases the technique described in this paper may become a very useful diagnostics tool.

REFERENCES

[1] D. Schulte et al., “Adaptive Scheme for the CLIC Orbit Feedback”, Proceedings of IPAC2010.

[2] K. Artoos et al., “Study of the stabilization to the nanometre level of Mechanical Vibrations of the CLIC Main Beam Quadrupoles”, Proceedings of PAC’09.

[3] M. Gasior, R. Jones, “The Principle and First Results of Betatron Tune Measurement by Direct Diode Detection”, CERN LHC Project Report 853, 2005.

[4] M. Gasior, R. Jones, “High Sensitivity Tune Measurement by Direct Diode Detection”, Proceedings of DIPAC’05.

[5] A. Boccardi, M. Gasior, “High dynamic range spectral analysis in the kHz band”, Proceedings of DIPAC’09.

[6] A. Boccardi et al., “The FPGA-based Continuous FFT Tune Measurement System for the LHC (…)”, Proceedings of PAC’07.

[7] M. Sylte, “Vibration Measurements at CesrTA”, internal CERN publication, EDMS 1004462, 2009.

[8] A. Kuzmin, “PSI measurements”, internal CERN publication, EDMS 1050039, 2009.

APS BEAM STABILITY STUDIES AT THE 100-NANORADIAN LEVEL*

G. Decker, B.X. Yang, R. Lill, H. Bui, Advanced Photon Source
Argonne National Laboratory, IL 60439, USA

Abstract

Recent developments at the Advance Photon Source (APS) in the area of high-resolution beam position monitoring for both the electron and x-ray beams has provided an opportunity to study beam motion well below the measurement threshold of the standard suite of instrumentation used for orbit control. The APS diagnostics undulator beamline 35-ID has been configured to use a large variety of high-resolution beam position monitor (BPM) technologies. The source-point electron rf BPMs use commercially available Libera Brilliance electronics from Instrumentation Technologies, together with in-house-developed field-programmable gate-array-based data- acquisition digitizing broadband (10 MHz) amplitude-to-phase monopulse receivers. Photo-emission-based photon BPMs are deployed in the 35-ID front end at distances of 16 and 20 meters from the source, and a prototype x-ray fluorescence-based photon BPM is located at the end of the beamline, approximately 39 meters from the source. Detailed results describing AC noise studies will be provided.

INTRODUCTION

Shown in Figure 1 is the experimental arrangement of diagnostics associated with the APS 35-ID undulator source point.

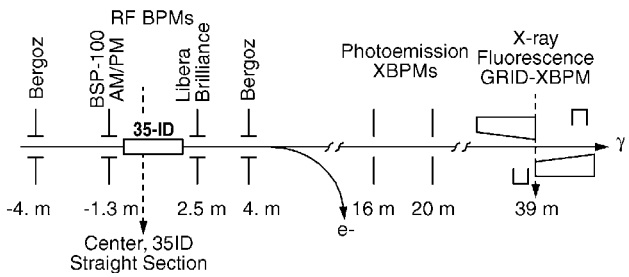

Figure 1: Array of beam position monitoring diagnostics used for beam stability studies at APS 35-ID.

This particular arrangement is unique in that 5 different BPM technologies located at 7 different locations along the beamline are all poised to provide quantitative measurements of beam position and pointing angle with unprecedented resolution. The work described in this paper is an extension of work started in 2009 in collaboration with researchers assessing BPM technologies for the NSLS-II facility now under construction [1].

*Work supported by U.S. Department of Energy, Office of Science, Office of Basic Energy Sciences, under Contract No. DE-AC02-06CH11357.

RF BEAM POSITION MONITORING

Near the source point, both narrowband and broadband rf BPM electronics are used to monitor the electron beam. Closest to the undulator, capacitive button pickup electrodes are mounted on the small-gap insertion-device vacuum chamber in sets of four, each with 4-mm diameter: two buttons above and two below the accelerator mid-plane at each station. The vacuum chamber vertical aperture is 8 mm; these pickup electrodes have very high geometric sensitivity. The upstream electrodes are connected to an in-house-designed data acquisition system: the bunch signal processor BSP-100, a field-programmable gate array (FPGA) module [2] samples a legacy broadband (10 MHz) amplitude-to-phase conversion BPM rf front end at a sample rate of 88 MS/sec, i.e., one fourth the ring's rf frequency. At the downstream station, commercial Libera Brilliance electronics from Instrumentation Technologies (Slovenia) are employed, which have recently been interfaced to the APS control system.

Due to the high sample and processing rates made possible by (FPGA) technology, and AC noise floor approaching 1 nm/√Hz are realizable. Shown in Figure 2 are data showing the performance of commercial Libera Brilliance BPM electronics in contrast to the BSP-100 data acquisition attached to the APS broadband rf BPM front end. By using a four-way splitter from a single button pickup, the noise floor was determined and compared with actual levels of (closed-loop) beam motion in the 35-ID straight section. Horizontal (X) and vertical (Y) data together with the noise floor are plotted as cumulative rms motion by integrating the power spectral density for turn-by-turn data using data sets of 0.5 and 1 second duration for the Libera and BSP-100 module, respectively. The straight lines indicate reference white noise levels.

In addition to the broadband BPMs, located +/- 4 meters from the center of the insertion device straight section, are sets of four 1-cm-diameter pickup electrodes mounted on standard large-aperture (4 cm x 8 cm elliptical) vacuum chambers. Attached to these pickup electrodes are commercial narrowband Bergoz multiplexed BPM electronics which were installed c. 2000.

PHOTOEMISSION-BASED PHOTON BPMS

In the beamline front end at 16.35 and 20 meters downstream of the undulator source point are photo-emission-based photon BPMs [3]. Due to small apertures in the front end, the detector located at 16.35 meters provides both horizontal and vertical position readbacks,

while the unit at 20 meters provides only vertical data. These type of detectors are know to be sensitive to stray sources of soft radiation emitted from nearby dipole, quadrupole and sextupole magnets. Sector 35 is unique in that the sector downstream of the source has not been realigned to reduce the stray radiation background [4].

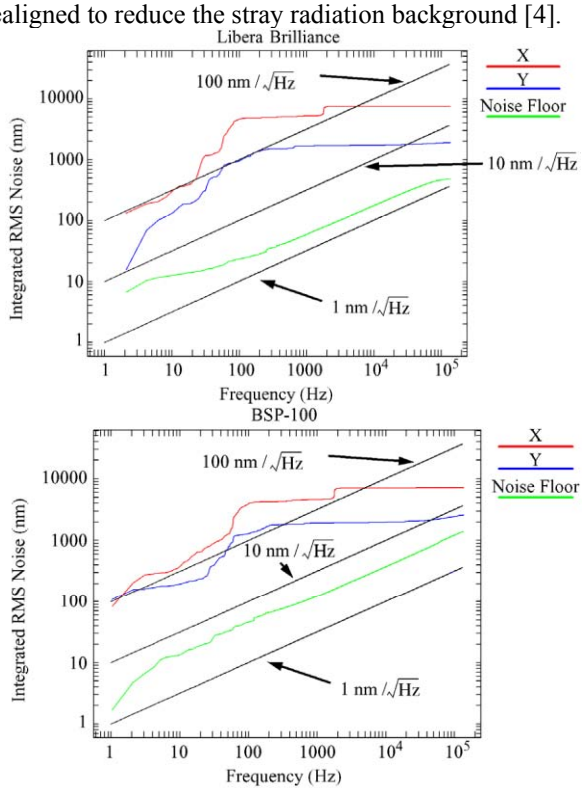

Figure 2: Integrated rms noise performance (green), with vertical (blue), and horizontal (red) beam motion for commercial Libera Brilliance BPM electronics (top) and the in-house BSP-100 module design (bottom), both attached to small-aperture pickup electrodes at the APS 35-ID source point.

HARD X-RAY FLUORESCENCE-BASED PHOTON BPM

Finally, a prototype of a new type of x-ray BPM based on hard x-ray fluorescence from copper has been installed at the end of the 35-ID beam diagnostics beamline at a distance of 38.8 meters from the center of the undulator straight section [5]. This detector is sensitive only to very hard (> 8.98 keV) x-rays and as such is immune from systematic errors associated with stray soft radiation. Shown in Figures 3 and 4 are a photo and diagram indicating the operating principle of the grazing-incidence insertion device hard x-ray fluorescence BPM (GRID-XBPM).

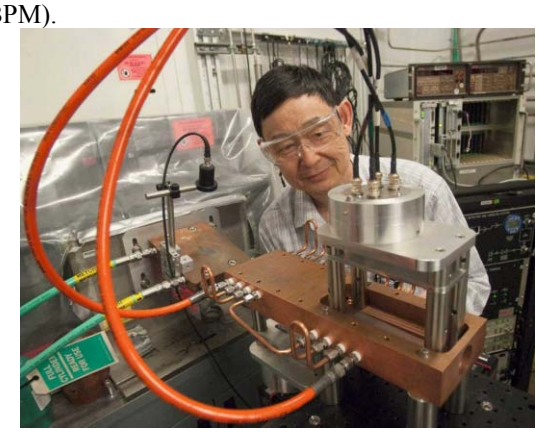

Figure 3: In-air prototype of grazing-incidence x-ray BPM.

In Figure 4, the x-ray beam, travelling left to right, first encounters a mask to protect downstream elements from misdirected beam. The XBPM proper is the center element, which resembles a mask, but sliced longitudinally with the two halves separated along the beam direction forming two ramps. X-rays striking the upstream ramp generate fluorescence x-rays that are detected with a pin-diode array below, while the

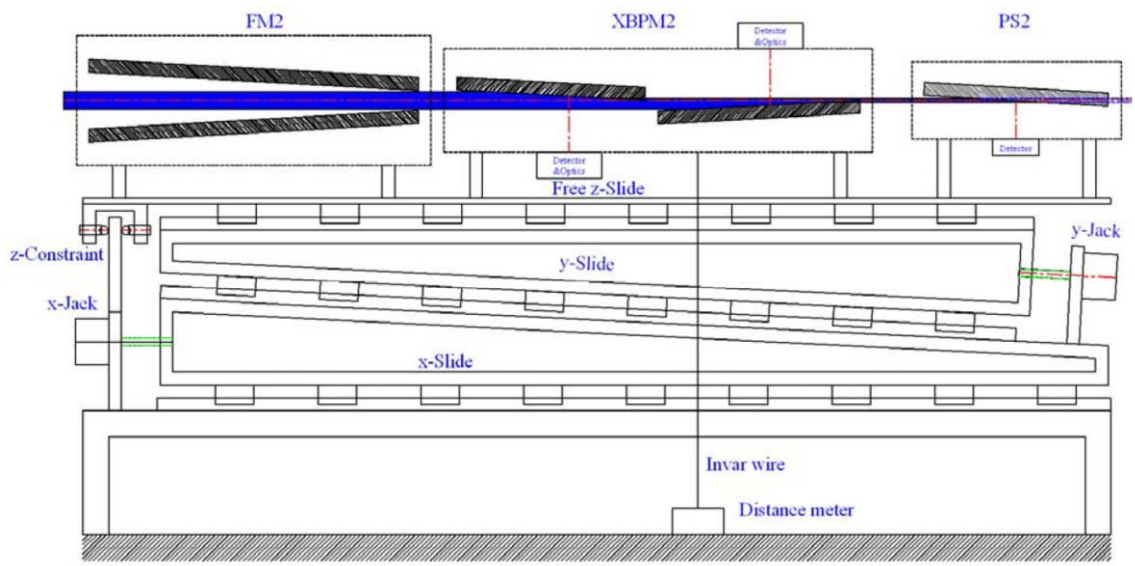

Figure 4: Diagram illustrating the operating principle of the grazing-incidence hard x-ray BPM.

downstream ramp produces x-rays that are detected with a similar array located above the midplane. In the simplest conception, the intensity difference between upstream and downstream ramps produces a signal proportional to the vertical displacement of the x-ray beam through the device. As instrumented (Figure 3), the x-ray footprint was imaged using a (large) pinhole in combination with a set of four pin diodes for each ramp.

At the downstream end of each ramp, a small rectangular trench of transverse dimensions 3 mm (horz.) by 1.5 mm (vert.) was cut along the beam direction to let the core of the x-ray beam pass. The monochromatic portion of the insertion device x-rays is located here. The far right-hand element of Figure 3 is a movable photon, shutter which has been instrumented with a single pin diode to monitor the transmitted x-ray flux. This detector is actually above the midplane in the photo, where the beam travels right to left.

Shown in Figure 5 are gap scan data comparing signals from the 35-ID photoemission-type photon BPM (top) and the hard x-ray fluorescence-based detector. Because the former is sensitive to very soft photons, the background signals present at large gap are considerable and are highly variable from one blade to the next. In contrast, the fluorescence detector is essentially immune to soft radiation, demonstrating clean exponential response across a range in signal strength of a factor of 200.

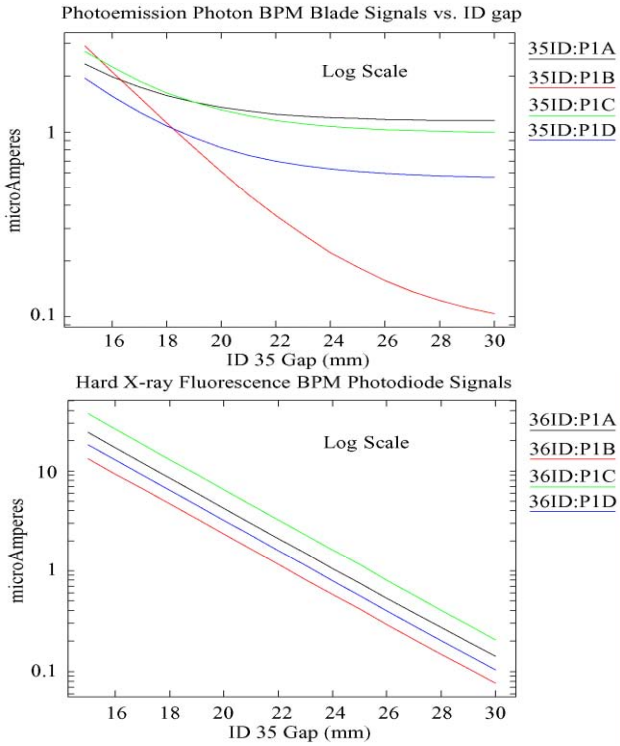

Figure 5: Comparison of gap dependence of photoemission style BPM (top) with x-ray fluorescence (bottom).

Hard X-ray BPM Calibration

Shown in Figure 6 are the photodiode currents resulting from scanning the detector across the beam (bottom) or scanning the beam across the detector using an asymmetric local closed-orbit angle bump centered on the 35-ID straight section (top). Horizontal response is on the left, and vertical on the right – note scales. For these data and that to follow, the detector was rotated by 90 degrees compared to Figure 3, for practical reasons (to allow higher heat load), effectively exchanging horizontal and vertical functionality. The abscissae for the beam scans were extrapolated from the two rf BPM channels closest to the source point, whose calibrations were carefully checked against a calibrated ring model.

With eight photodiodes to choose from, many permutations are possible to produce signals proportional to either vertical or horizontal beam position. In order to use the same electronics as for the traditional photoemission-type BPMs, two diodes from the upstream ramp were combined with two diodes from the downstream ramp to produce a single (x, y) pair of readbacks, referred to here as S36ID:P. This left a spare pair of diodes on the upstream ramp, one above and one below the midplane, and a second downstream pair. These resulted in two independent vertical readbacks, corresponding to channels S36ID:P2:Y and S36ID:P2:X (normally P2 assumes top-bottom-left-right geometry vs. a diagonal arrangement for P1).

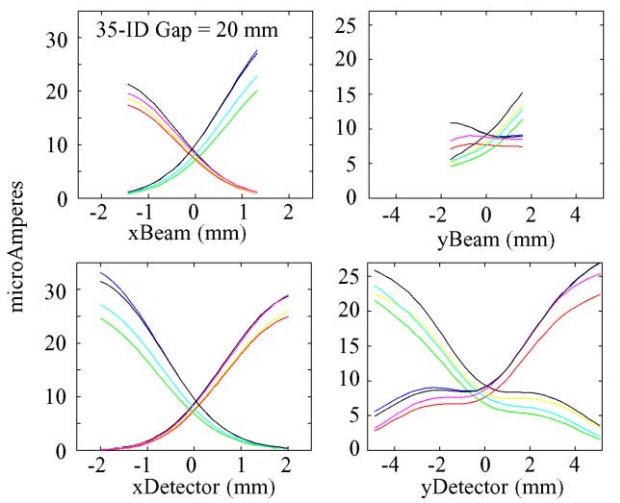

Figure 6: Beam scans (top) vs. detector scans (bottom).

Shown in Figure 7 are the resulting calibration curves, plotting difference over sum (e.g., top – bottom divided by their sum) as a function of transverse position. The beam scans were flipped left/right, and all data were shifted so as to be centered at (or at least near) the point of maximum slope. The interesting inflection point behavior for the vertical data is a consequence of the pass-through trench, which is oversized for this detector orientation.

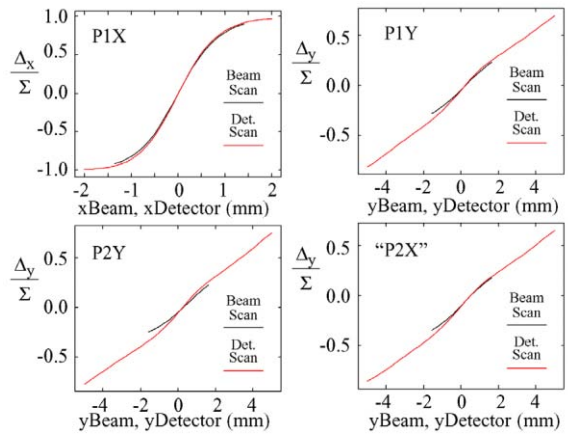

Figure 7: Calibration curves for photoemission-type hard x-ray BPM.

With the data of Figure 7 in hand, a numerical differentiation was performed, and the maximum slope provides the calibration factors desired (actually their inverse). Shown in Table 1 are the calibration factors (in mm) that are to be multiplied by the delta / sum ratio to produce position readbacks, in units of mm.

Table 1: Hard X-ray BPM Calibration Factors

Channel	Beam Cal.	Detector Cal.
S36ID:P1:X	0.8842 mm	0.8305 mm
S36ID:P1:Y	5.263 mm	4.538 mm
S36ID:P2:Y	4.987 mm	4.506 mm
"S36ID:P2:X"	5.490 mm	4.506 mm
S35ID:P1:X	3.682 mm	2.963 mm
S35ID:P1:Y	1.059 mm	0.1408 mm
S35ID:P2:Y	0.7843 mm	0.1348 mm

In this table, higher numbers imply lower sensitivity. The vertical calibration factors show a spread of + / - 5% for the calibration with beam, which is not seen for the detector calibration. This is likely due to shadowing effects of upstream apertures. Adjustments in the pinhole geometry together with reduction in the height of the pass-through slot are expected to improve vertical sensitivity in future designs. Data for the 35-ID photoemission BPM are included for completeness.

CORRELATED DATA ACQUISITION

The APS real-time feedback system operates at a sample rate of 1.534 kHz and has access to a large number of readback and control points [6]. Among its many capabilities is an oscilloscope functionality allowing synchronous acquisition of up to 40 channels. Unfortunately, the Libera and BSP-100 boxes are not yet integrated with the real-time system. Because the ring model is so well known, it is straight forward to infer the readings at these locations' pickup electrodes using a free betatron oscillation formula together with adjacent Bergoz data, which are available to the real-time system. Shown in Figure 8 are comparisons of integrated spectra for Libera and Bergoz, with the Bergoz data interpolated from the betatron formula to the Libera location as just described.

As noted in the figure, this is an unfair comparison, for two reasons: first, the Bergoz electronics are mounted on a large-aperture vacuum chamber vs. Libera, which uses a small aperture and thus has higher geometric sensitivity. Further, at least in the vertical plane, the beta functions at both the real Bergoz location and the Libera location are quite small (< 5 m); the amount of real beam motion is very small to start with. The conclusion to be drawn from Figure 8 is that the Bergoz receivers do an adequate job of characterizing horizontal motion at the undulator source point, while vertically they are limited by noise, certainly with feedback running. The fact that the lowest left-hand Bergoz curve closely follows a straight line with slope ½ supports this hypothesis. Note that the Libera data start at 2 Hz because these plots were derived from a turn-by-turn data set with duration 0.5 seconds.

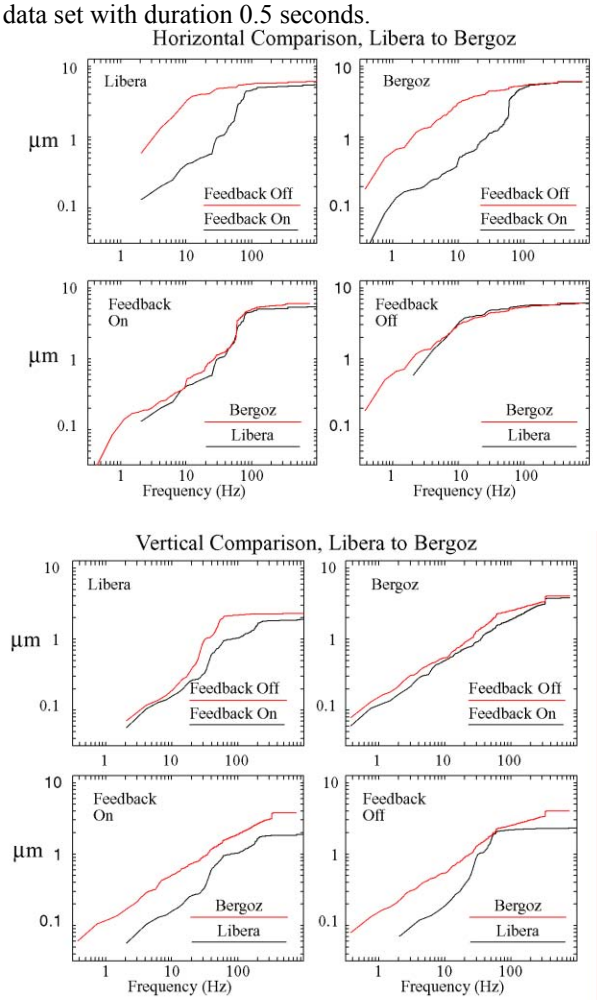

Figure 8: Unfair comparison of Libera vs. Bergoz data. Bergoz data interpolated to location of Libera pickups.

Shown in Figure 9 are integrated spectra for all BPMs along the 40-meter-long 35-ID beamline, vertically (above) and horizontally (below), with feedback on (right), and off (left). The rf BPMs at the source are in

red and black with the smallest integrated rms beam motion. Next noisiest are the front-end photoemission photon BPMs (UVBPM), and, at the end of the beamline, the hard x-ray fluorescence BPM (GRID XBPM) shows the largest amount of beam motion, as expected. With the exception of the Libera and BSP-100 vertical data, all data on each of the four panels were synchronous, from the same 1.5 kHz data set. Note the effect of the small vertical beta function at the source: there is 10 times as much beam motion at the end of the beamline compared to the source (with feedback off).

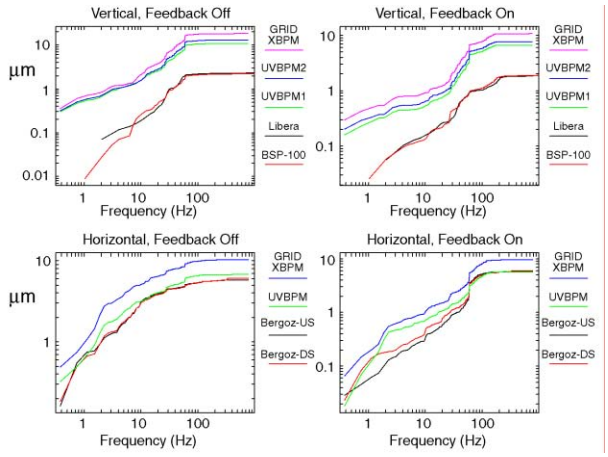

Figure 9: Integrated PSD data for BPMs along 35-ID.

As an example of the kinds of analyses that can be performed using the synchronous data provided by the real-time feedback system, shown in Figure 10 are vertical phase-space plots showing position at the various locations along the beamline on the horizontal axis, with vertical angle plotted on the vertical axis. The angle was calculated from photon BPMs UVBPM2 and the GRID-XBPM by taking their difference and dividing by their separation along the beamline (19 meters), on a sample-by-sample basis. In this particular case, angular motions cause the beam size to increase the further downstream one goes, and these small angular motions cannot be seen in this case using only (Bergoz) rf BPMs near the source.

One last example is that the two equivalent measures of vertical position at the end of the beamline, namely S36ID:P1:Y and S36ID:P2:X can be plotted against each other and fit to a straight line. The slope of this line was found to be 1.015 with feedback off and 1.028 with feedback on. More interesting is that the rms of the fit residual is a measure of instrumentation noise, equal to 2.36 or 2.48 microns, respectively. With a lever arm of 39 meters, this amounts to something like 60 nanoradians of angular resolution. Given the higher sensitivity in the horizontal plane, one can expect significantly better resolution there, with vertical improvements underway.

SUMMARY

Studies at APS beamline 35-ID have validated a new type of photon BPM with very high AC and DC resolution. This detector was successfully included in closed-loop feedback, and the beam could be steered very precisely by physically moving the mechanical translation stage upon which the detector was mounted. This mode of operation is being contemplated as part of the APS upgrade. A full in-vacuum design for a high-power version for insertion device beamline front ends is in progress.

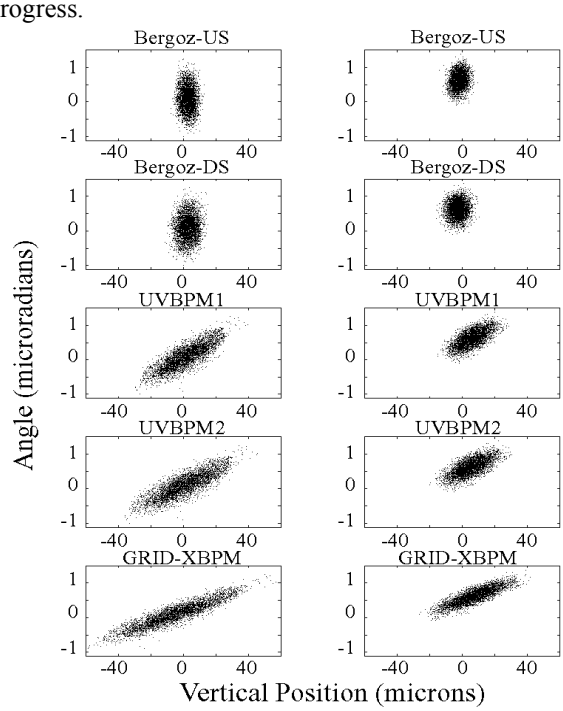

Figure 10: Vertical angle vs. position with feedback off (left) and on (right).

REFERENCES

[1] O. Singh, I. Pinayev, G. Decker, and B.X. Yang, "Comparative Studies of RF Beam Position Monitor Technologies for NSLS-II," DIPAC'09, Basel, Switzerland, July 2004, MOPD16, p. 80 (2009); http://www.JACoW.org.

[2] H. Bui, G. Decker, R. Lill, A. Pietryla, W.E. Norum, "Performance of FPGA-Based Data Acquisition for the APS Broadband Beam Position Monitor System," BIW'08, Tahoe City, CA, USA, TUPTPF001, p. 80 (2009); http://www.JACoW.org.

[3] G. Decker and O. Singh, "Orbit Feedback Using X-ray Beam Position Monitoring at the Advanced Photon Source," ICALEPCS'01, San Jose, CA, USA, WECI001, p. 249, http://www.JACoW.org.

[4] G. Decker, O. Singh, "Method for Reducing X-ray Background Signals from Insertion Device X-ray Beam Position Monitors," PRST-AB 2(11), 112801 (1999).

[5] B.X. Yang et al., "High-Power Hard X-ray Beam Position Monitor Development at the APS," these proceedings.

[6] J. A. Carwardine and F.R. Lenkszus, "Real-Time Orbit Feedback and the APS," BIW'98, AIP Conference Proceedings No. 451, p. 125 (1998).

CHERENKOV RING TO OBSERVE LONGITUDINAL PHASE SPACE OF A LOW ENERGY ELECTRON BEAM EXTRACTED FROM RF GUN *

H. Hama#, K. Nanbu, M. Kawai, S. Kashiwagi, F. Hinode, T. Muto, F. Miyahara, Y. Tanaka
Research Centre for Electron Photon Science, Tohoku University
1-2-1 Mikamine, Taihaku-ku, Sendai 982-0826, Japan

Abstract

Particle distribution of the electron beam extracted from a thermionic RF gun in longitudinal phase space is crucial for electron bunch compression. Because space charge effects in the RF gun are not fully understood, an efficient bunch compression scheme employing magnetic chicane or alpha (α-) magnet is not easily designed. In order to measure the distribution in the longitudinal phase space of relatively lower energy electrons (below 2 MeV), we have studied a novel method for direct observation of electron energy employing velocity dependence of opening angle of Cherenkov radiation. Intrinsic energy and temporal resolution are discussed by showing a numerical ray-trace simulation.

ITC-RF GUN FOR FEMTO-SECOND ELECTRON PULSE

An intense terahertz radiation source based on an electron accelerator has been developed at Tohoku University, and is called the t-ACTS project [1]. Coherent THz radiation from an isochronous ring will be provided to multiple users simultaneously as a wide-band short-pulse source. Furthermore, a free electron laser (FEL) in the THz region driven by shorter electron pulses (less than the resonant wavelength) has been studied [2], in which a theoretical simulation suggests that FEL interaction can continuously amplifies the head part of radiation pulse when the cavity length is completely tuned. Stable production of very short electron bunches is a key issue for the t-ACTS project. Photoinjectors have already successfully produced femtosecond pulses with considerable bunch charge. However, we have chosen thermionic cathode for the RF gun because of stability, multi-bunch operation, and cheaper cost. Although the bunch charge will be small (a couple of tens of pC), and then coherent enhancement of the radiation is not so strong, the space charge effect may not be a very serious concern, and the thermionic cathode should have good stability, so excellent beam quality would be expected. Moreover, high repetition operation in multi-bunch mode will open another aspect of application experiments.

The thermionic RF gun consists of two independent cavity cells to manipulate the longitudinal beam phase space (see Fig. 1), so it is named the ITC (Independently-Tunable Cells) RF gun [3]. Particle distribution in longitudinal phase space is very important for the bunch compression including the space charge effect. The ITC-RF gun has been designed so as to produce appropriate longitudinal particle distribution by changing the relative RF phase and field strengths as shown in Fig. 2.

In order to optimize the parameters for the gun, such as field strengths and phase difference between two cells, we have done some numerical simulations of the beam production for the ITC-RF gun. Because a considerable part of the charge is concentrated into the head of the extracted beam, the space charge effect acts to deviate the electron distribution from a simple smooth line. This phenomenon is difficult to understand because different

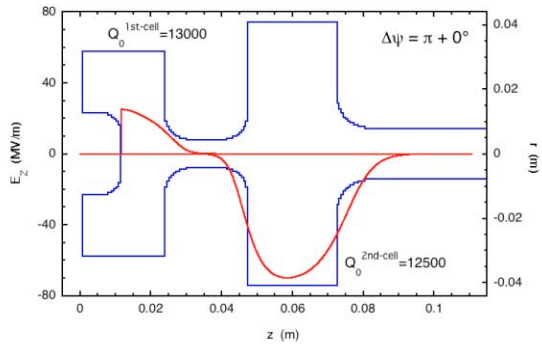

Figure 1: ITC-RF gun. A small size (ϕ = 1.85 mm) cathode of single crystal LaB_6 is employed, which can provide a beam current density of more than 50 A/cm^2.

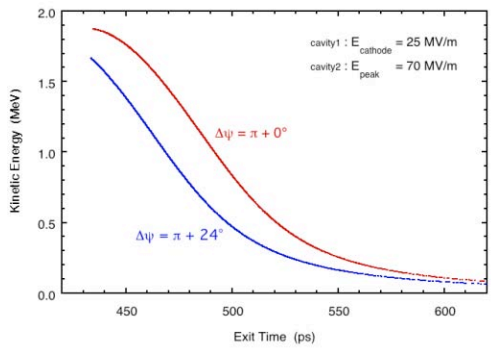

Figure 2: Particle distribution in the longitudinal phase space calculated by an FDTD code [4]. One for the phase difference of π + 0° (usual RF gun) leads higher energy. Meanwhile linear particle distribution results from phase space manipulation performed by phase tuning. Cathode current is 1.34 A for both calculations.

*Work supported by Grant-in-Aid for Scientific Research (S), the Ministry of Education, Science, Technology, Sports and Culture, Japan, Ccontact No. 20226003.
#hama@lns.tohoku.ac.jp

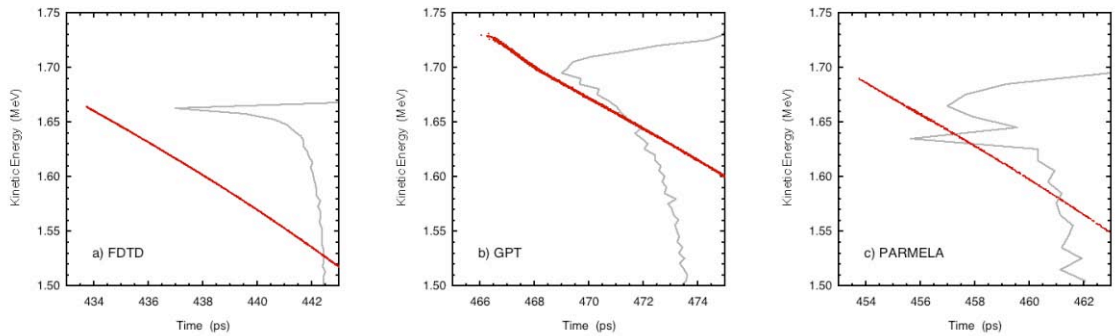

Figure 3: Longitudinal phase spaces calculated by a) the FDTD code, b) GPT, and c) PARMELA [5]. Parameters of the cavities are identical to those in Fig. 2 (the phase difference is π + 24°). Because of small differences in input geometry, the absolute energies are not the same, nor are the time origins. Although the slopes of the particle distributions are apparently in almost the same trend, the distributions around the top energy are very much different. Each code employs its own method for evaluation of the space charge effect, of course.

codes give different results as shown in Fig. 3, though almost the same results have been obtained when the particle charge is set to be zero. The phase space distribution calculated by PARMELA looks like that from the FDTD code. However, one can see a significant difference in the energy spectra, and some structure can be seen in that of PAMELA. The energy spectrum of GPT is much broader than that of FDTD, and there is a small bend in the phase space distribution.

In this study we are not going to pursue details of the simulation codes and correctness of the space charge models. We have, however, considered that direct measurement of the particle distribution in the longitudinal phase space is crucial for designing of the bunch compression scheme as well as understanding of the space charge effect.

CHERENKOV RING RADIATED FROM MeV ELECTRONS

As shown in Figs. 2 and 3, the beam energy from the ITC-RF gun is not so high (kinetic energy $T \sim 1.7$ MeV) and velocity is still slower than light, which means the particle distribution in the phase space may vary even in drift spaces due to the space charge force. Consequently a conventional analyzer magnet is not suitable for measurement of the particle energy because a considerable path length is inevitably required.

Cherenkov light is widely used for beam diagnostics and particle counters. It is well known that the Cherenkov angle θ_c is inversely proportional to the particle velocity β as

$$\cos\theta_c = 1/n(\omega)\beta, \tag{1}$$

where $n(\omega)$ is the refractive index of the Cherenkov radiator medium at a radiation frequency ω [6]. The Frank-Tamm formula gives the energy dissipation of Cherenkov radiation with a frequency region from ω_1 to ω_2 as,

$$\frac{dE}{dz} = \frac{q^2}{4\pi}\int_{\omega_1}^{\omega_2} \mu(\omega)\omega\left(1-\cos^2\theta_c\right)d\omega, \tag{2}$$

where z is the radiator length, q is the charge of the particle and $\mu(\omega)$ is the permeability of the medium. Assuming no frequency dependences of n and μ in a narrow band, the number of photons between wavelengths λ_1 and λ_2 emitted from an electron is expressed as

$$N = 2\pi\alpha z\left(\frac{1}{\lambda_1}-\frac{1}{\lambda_2}\right)\sin^2\theta_c, \tag{3}$$

where α is the fine structure constant.

As one notices from Eqs. (1) and (3), the refractive index is an important parameter for detection of the particle energy. In order to secure sufficient energy resolution in the measurement system, a derivative of Cherenkov angle $d\theta_c/d\beta$ is preferred to be large. Meanwhile the intensity of the radiation is proportional to $\sin^2\theta_c$. Figure 4 shows the Cherenkov angle and the value of $\sin^2\theta_c$ calculated for a kinetic energy region from 1.4 to 2.0 MeV. The number of photons increases with n; meanwhile the slope of the Cherenkov angle is

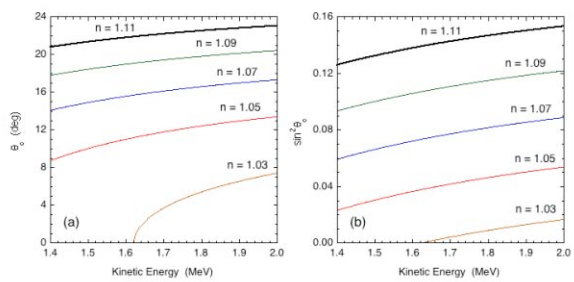

Figure 4: (a) The Cherenkov angle and (b) the value of $\sin^2\theta_c$ for various refraction indexes, plotted as a function of the kinetic energy.

gradually decreasing. Silica-aerogel has been presumed to be the radiator medium. We insist on the energy resolution and the angular resolution, so a refraction index of 1.05 has been chosen for further study. Sufficiently transparent aerogel having a higher refraction index is difficult to make.

OPTICAL ELEMENTS IN MEASUREMENT SYSTEM, LFC-CAMERA

Design Concept

Since the Cherenkov angle contains information of the particle energy, the photons having the same Cherenkov angle has to be focused on a certain position of a detector. If the focus points of different energies are aligned on a straight line, the energy distribution of the beam can be observed at once by using a semiconductor sensor. Furthermore, if information on relative arrival times into the aerogel for each particle can be preserved, we shall perform direct observation of the longitudinal phase space distribution by using a high-resolution streak camera.

The estimated photon number emitted from a single electron passing through a radiator medium of n = 1.05 with a thickness of z_R = 1 mm is approximately 0.04 for 1% bandwidth at a wavelength around 500 nm. In other words, a 1 pC bunch produces more than 200k photons. This seems to be enough to detect a single micro-pulse of the beam, because the total bunch charge of the energy range above 98% of the top energy is 20 ~ 30 pC for typical operation of the ITC-RF gun shown in Fig. 3.

Figure 5 shows a tentative optical apparatus design of the detection system we call the Linear Focal Cherenkov ring camera (LFC-camera). A turtle-back mirror gathers a part of the Cherenkov ring and confines onto the s-axis.

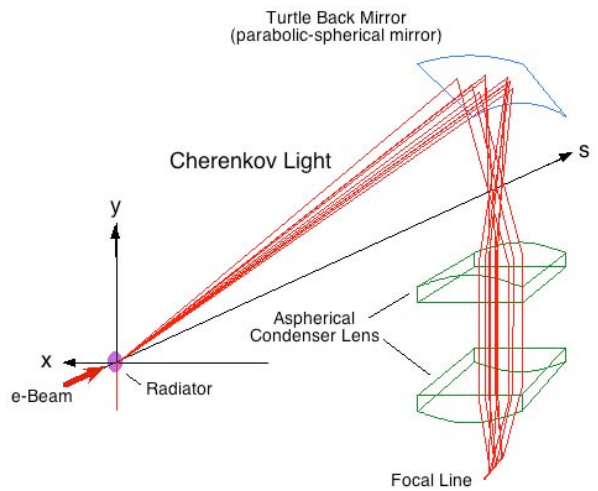

Figure 5: Schematic apparatus of the LFC-camera. The system consists of a specific (parabolic-spherical) mirror and two aspherical condenser lenses. Angular distribution of the Cherenkov radiation is imprinted onto a straight focal line.

The photons are transported and confined again by aspherical lenses. The Cherenkov angle is therefore converted into a position on a focal line.

Turtle-back Mirror

The reflecting surface of the mirror able to gather the photons of the Cherenkov ring and confine them onto a focal line is parabolic in the s-axis and spherical in the x-axis, which looks like a turtle-back carapace. As shown in Fig. 6, using a base position $(0, y_0, s_0)$ the mirror surface is expressed as

$$x^2 + y^2 - \left(-\frac{1}{2A} s^2 + \frac{A}{2} \right)^2 = 0 \quad \left(A \equiv \sqrt{{y_0}^2 + {s_0}^2} + y_0 \right). \tag{4}$$

Here, the base point has been chosen so as to make the system compact, i.e., the Cherenkov light from the electrons with a kinetic energy of 1.7 MeV hits the mirror at s_0 = 0.3 m (then θ_c = 11.8 ° and y_0 = 0.063 m).

Since the turtle-back mirror gives a focal line on the s-axis, indeed the beam axis, the photons have to be transported to outside of the beam pipe and confined again. We have intended to employ optical lenses for transport of the light and a normal incidence band-pass filter for wavelength selection because of convenience. However, spherical aberration of the lenses would be a severe issue when we like to gather the photons emitted across a large solid angle.

Aspherical Condenser Lens

Because a conventional formula of aspherical surface for the optical lenses contains many parameters, if one would like to eliminate aberration considerably, it may take a very long time to optimize the lens surface. For the moment we have designed a simple condenser lens consist of a flat surface and a one-dimensional aspherical surface, as shown in Fig. 5. The formula used to determine the surface is

$$x^2 + \left(y + gx^2 \right)^2 - \left(\frac{R}{\eta - 1} + gx^2 \right)^2 = 0, \tag{5}$$

where g is an aspherical coefficient, R is a base spherical

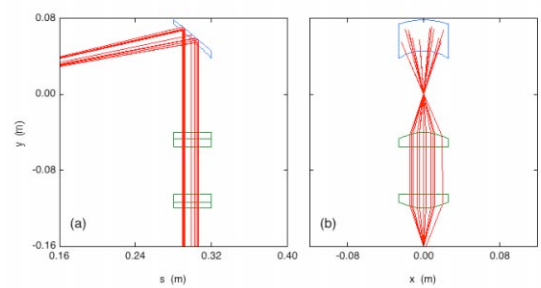

Figure 6: (a) Side view and (b) rear view of the light transport in the LFC-Camera. Red lines are light trajectories calculated by a ray-trace code assuming a point source.

curvature radius. The relative refractive index η of the lens is chosen to be 2.0, and R = 4 cm is employed in order to keep the system compact. Consequently it has turned out that the maximum acceptance can be obtained at $g \cong 23$, and approximately 10 % of the Cherenkov light emitted into the azimuthal angle of 2π is confined on the focal line 100 μm in width.

In Fig. 6, an example of calculation results from a ray-trace code we developed for ourselves is shown. As one can see in Fig. 6(b), the light passing through the far side of the lens goes out of the focal line.

CONSIDERATION FOR ENERGY AND TIME RESOLUTIONS OF LFC-CAMERA

Energy Dependence of the Focal Position

Using Eqs. (1) and (4), one can derive the focal position s_f at a particle velocity as

$$s_f(\beta) = An\beta\left(1-\sqrt{1-\left(\frac{1}{n\beta}\right)^2}\right). \quad (6)$$

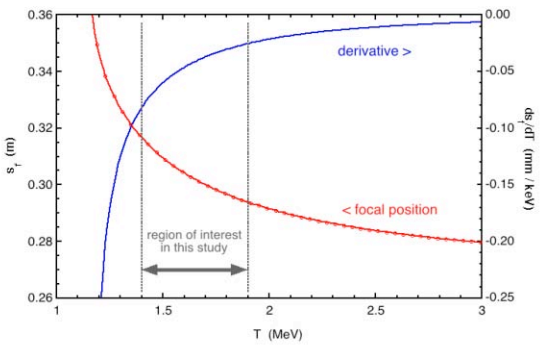

Figure 7: Red line indicates the focal position calculated using Eq. (6), and circles are results from the ray-trace code. Blue line denotes the derivative of the focal position with respect to the kinetic energy.

In Fig. 7, the focal position is plotted as a function of the kinetic energy, and its derivative ds_f/dT is also shown. Pixel size of recent CCD or CMOS is surprisingly smaller than 10 μm. That is sufficient for detection with an energy resolution of keV order, even in the 3-MeV region, if the radiation is coming from a point source.

Effect of Beam Emittance

Though transverse emittance of the beam from the RF gun is expected to be small, the finite spatial and angular spread of the beam may affect the energy resolution of the LFC-camera. We have assumed that the minimum normalized slice-emittance is equivalent to the thermal emittance of the cathode that is estimated to be about 2.5 x 10^{-7} m • rad for the ITC-RF gun. In order to evaluate the effect for the position resolution, the ray-trace calculations were performed for two different mono-

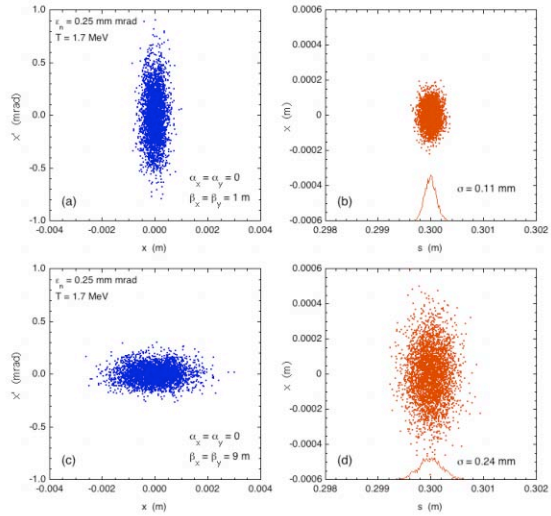

Figure 8: Particle distribution in the transverse phase space at the radiator (a) and photon distribution at the focal position (b) for a beta function of β = 1 m. Lower figures (c) and (d) are for β = 9 m.

energetic beam conditions characterized by a beta function of the Twiss parameter, such as tight focused beam on the radiator medium (β = 1 m) and loose focused one (β = 9 m).

Spreads of the focal position were 0.11 and 0.24 mm (standard deviation), respectively, as shown in Fig. 8. Since $|ds_f/dT|$ around T = 1.37 MeV is 0.037 mm/keV, those values correspond approximately to energy resolutions of 3 and 6 keV, respectively. We recognized that spatial electron distribution at the radiator mainly causes spread of the focal position, but it is less significant than we initially anticipated. We have also examined lower energies such as T = 1.4 MeV, and β = 1 m obtained energy resolutions of 2 and 4 keV, respectively. It can be concluded that the thermal emittance of the beam does not affect the energy resolution so much if we focus the beam on the radiator somewhat.

Effect of Thickness of the Radiator

Another important factor to be considered toward the energy resolution is a longitudinal position of the source point. We have supposed that the radiator thickness of z_R = 1 mm would be enough to produce sufficient number of Cherenkov photons. However, as discussed above, the spread of 1 mm on the focal line gives an energy width of ~ 30 keV at T = 1.7 keV, which is not negligibly small. If we need a thicker radiator than 1 mm, it is a matter of grave concern.

Performing the ray-trace calculation, it turned out that the turtle-back mirror gives a longitudinal focusing effect for different longitudinal source positions. Accordingly, the radiator thickness does not make considerable spread of the focal position.

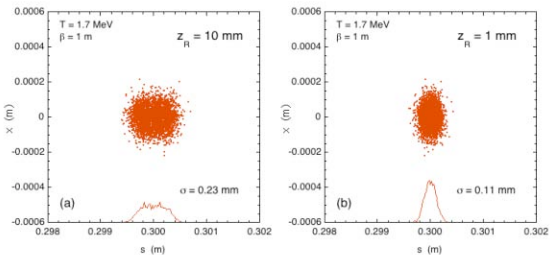

Figure 9: Focal position spread for the radiator thicknesses of (a) 10 and (b) 1 mm. The beam transverse distribution on the radiator is same as in Fig. 8(a). Refraction at the radiator surface is ignored because of the small refraction index.

As shown in Fig. 9, even the radiator of z_R = 10 mm causes a little position spread. For a case of z_R = 1 mm, we cannot see more than the beam emittance effect. This effect had not been anticipated initially but is quite acceptable because the parallel rays from the different sources are brought into a focus due to the parabolic mirror.

Time Resolution

The turtle-back mirror has been designed so as to eliminate path length difference of the rays from a single source to the 1st focal line (on the s-axis). However, deviation of the path length in the light transport and the speed of light in the aspherical condenser lenses, as well as the spatial beam distribution at the radiator, cause an intrinsic time resolution of the LFC-camera. Arrival time of the light onto the final focal line measured from the electron as it passes through the centre of the radiator medium has been derived from the ray-trace result. The arrival time was fund to have a small correlation with the longitudinal focal position, but not with the horizontal position. This fact suggests the light transport via the aspherical lenses does not affect the path length deviation so much. As shown in Fig. 10, even using a thicker radiator such as 10 mm, the intrinsic time resolution is a couple of hundred femtoseconds.

SUMMARY AND PROSPECT

We have designed a novel system for measurement of the longitudinal phase space distribution of the relatively lower energy electrons extracted from a thermionic RF gun. The system, the LFC-camera, consists of a turtle-back mirror to confine the Cherenkov ring onto a focal line and two aspherical lenses for the light transportation. Using realistic electron distributions in phase space, the numerical ray-trace was performed. Though intrinsic energy resolution and time resolution of the optical system depend on both the beam transverse size and the thickness of the radiator, those have been easily suppressed to be less than 10 keV and 0.5 ps, respectively.

We are going to continue optimization of the optical element such as aspherical lenses and to study combined use with a streak camera.

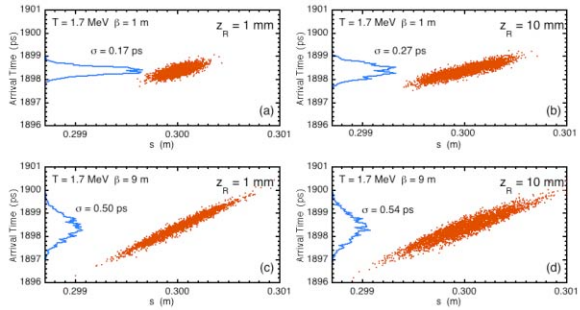

Figure 10: Two-dimensional plots of the arrival time and the longitudinal focal position. Upper figures are for β = 1 m, but for two different radiator thicknesses, (a) z_R = 1 mm and (b) z_R = 10 mm. Lower ones are for β = 9 m.

REFERENCES

[1] H. Hama et al., N. J. of Phys. 8 (2006) 292; H. Hama et al., Nucl. Instr. and Meth. A, in press.
[2] M. Yasuda, Master thesis, "Simulation study of free electron laser employing very short electron bunches", Tohoku University (2009).
[3] T. Tanaka et al., Proc. 27th Int. FEL Conf., Stanford (2005) 371.
[4] H. Hama et al., Nucl. Instr. and Meth. A 528 (2004) 371.
[5] L. M. Young and J. H. Billen, "Parmela documentation", LA-UR-96-1835, revised July 17, 2003; GPT code, http://www.pulsar.nl/gpt/index.html.
[6] J. V. Julley, "Cherenkov Radiation and Its Application", Pergamon, New York (1958) 22.

COTS TECHNOLOGY FOR HIGH ENERGY PHYSICS INSTRUMENTATION

J. Truchard, R. Marawar, A. Veeramani, M. Ravindran
National Instruments, Austin, TX 78759, U.S.A

Abstract

National Instruments (NI) uses Commercial Off-The-Shelf (COTS) semiconductor and computing technology and applies it to measurement, diagnostics and instrumentation needs. NI leverages the rapid technological advancement of the semiconductor and computer industry, while retaining the flexibility and ensuring interoperability between HW & SW. This paper elaborates how general purpose NI products and technology can be applied to specialized instrumentation, measurement and diagnostic needs in High Energy Physics (HEP). In particular we will discuss programming and processing tools, instrumentation platform with custom hardware development using FPGA.

INTRODUCTION

Until recently, most measurement, diagnostic and instrumentation applications in HEP required custom development efforts. Most COTS products did not meet the needs of the community due to high-end specifications, high availability requirements, long term serviceability aspects, closed driver stacks, limited operating system support etc. In recent years NI has led efforts to address these issues by developing state-of-the-art products that meet demanding specifications, making great progress towards reliable and redundant systems, providing long-term replacement and calibration services, support for Linux, providing register maps for open driver development and collaborating on EPICS, Tango and other middleware support. In addition, using COTS products minimizes development costs, reduces unit costs thus focusing limited resources on scientific endeavors.

Reducing Development Time

Many of the HEP applications require development of complex measurement, control and diagnostic systems. In addition, data must be processed real-time to make intelligent decisions about measurement and control parameters. For mathematical computations and simulations it would be desirable to take advantage of COTS technologies such as multicore processors and FPGAs. National Instruments LabVIEW offers scientists and engineers a unique graphical programming environment that combines control and measurement system development along with real-time high performance computing including multicore processors and FPGAs.

LABVIEW GRAPHICAL SYSTEM DESIGN

LabVIEW is a general purpose graphical programming environment used to develop measurement, test, and control systems using intuitive graphical icons and wires that resemble a flowchart. LabVIEW is supported on a variety of platforms including Microsoft Windows (2K, XP, Vista), Linux, and Macintosh. LabVIEW Real-Time, the embedded systems solution for LabVIEW, is supported on VxWorks and Pharlap targets on hardware platforms such as CompactRIO and PXI. LabVIEW offers tight integration with thousands of hardware devices and provides hundreds of built-in libraries for advanced analysis and data visualization. LabVIEW also enables parallel programming targeting Multicore CPUs and FPGAs.

As a COTS product, LabVIEW provides an extensively tested and industry validated product with multiple models of computation, leading data flow architecture and significant R&D investment that is amortized over hundreds of thousands of installations.

LabVIEW on Multicore CPU

To reduce computation time, programmers must divide applications into parallel parts using multithreading. Each of the threads can run in parallel in a multicore system. Applications that take advantage of multithreading have numerous benefits, such as more efficient CPU use, better system reliability, and improved performance. Three techniques to commonly used for reducing computation time include: task parallelism, data parallelism, and pipelining. LabVIEW is an inherently parallel programming language without having to worry about thread management or synchronization between threads. Consider two tasks shown in Fig.1. The two tasks do not have any data dependencies, so the LabVIEW compiler will automatically multi-thread the application.

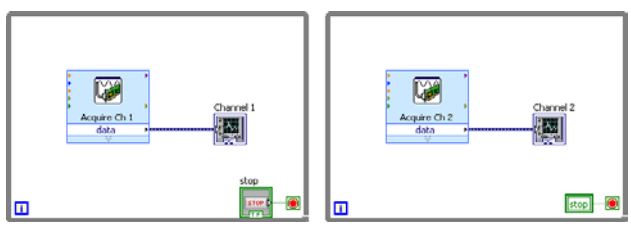

Figure 1: LabVIEW block diagram showing two tasks that will be automatically be executed in parallel.

Data parallelism can be applied to large data sets by splitting up a large array or matrix into subsets, performing the operation, and combining the result. Consider the sequential implementation, where a single core of a given CPU attempts to process the entire data set. Instead if the data set is split four parts, all the cores available will execute the data sets in parallel resulting in significant speed increase.

In real-time high-performance computing (HPC) applications such as control systems, a common and efficient strategy is the parallel execution of matrix-vector multiplications of considerable size. Typically, the matrix is fixed, and the matrix can be decomposed in advance. Measurements gathered by sensors provide the vector on a per-loop basis. For example, the result of the matrix-vector can be used to control actuators. Fig 2 shows block diagram of a matrix-vector multiplication distributed to eight cores.

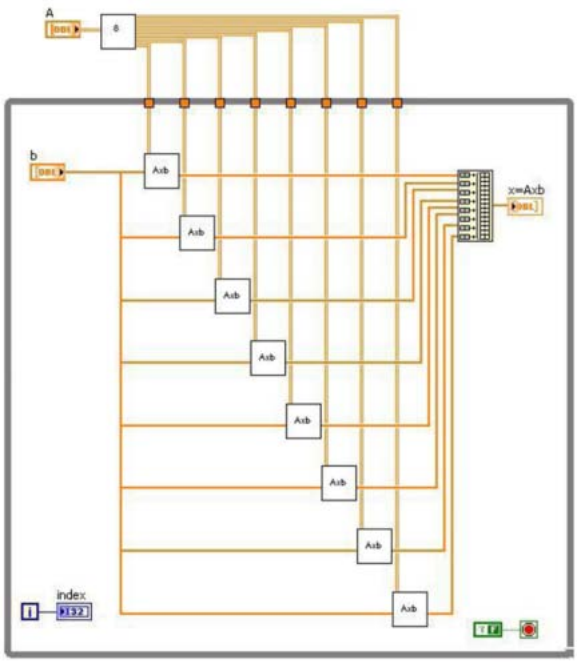

Figure 2: Matrix vector multiplication LabVIEW.

Programming FPGAs with LabVIEW

The NI LabVIEW FPGA Module uses LabVIEW embedded technology to extend LabVIEW graphical development and target field-programmable gate arrays (FPGAs) on NI reconfigurable I/O (RIO) hardware. LabVIEW is distinctly suited for FPGA programming because it clearly represents parallelism and data flow. LabVIEW programming palette is simplified to contain only the functions that are designed to work on FPGAs. The primary programming difference compared to traditional LabVIEW is that FPGA devices use integer math rather than floating-point math. Also, there is no notion of multithreading or priorities because each loop executes in independent dedicated hardware and does not have share resources — in effect, each loop executes in parallel at "time critical" priority.

With the LabVIEW FPGA, you can create custom measurement and control hardware without low-level hardware description languages or board-level design. You can use this custom hardware for unique timing and triggering routines, ultrahigh-speed control, interfacing to digital protocols, digital signal processing (DSP), RF and communications, and many other applications requiring high-speed hardware reliability and tight determinism. Thus this COTS product with hundreds of thousands of man hour R&D investment is available for HEP community to design highly customized measurement and control applications.

INTERFACING EPICS AND LABVIEW

In order to take advantage of commercial off the shelf (COTS) hardware that is available through LabVIEW, the physics community has come up with different ways to bridge LabVIEW and EPICS such as the Shared Memory Interface and Channel Access (CA) Server from Oak Ridge National Lab. National Instruments has also developed EPICS client and CA Server in addition to the EPICS IOC to LabVIEW Real-Time interface that was developed in partnership with Cosylab. Currently the main method at SNS of connecting LabVIEW with EPICS is the EPICS Shared Memory Interface [1].

LabVIEW 2009 introduced an EPICS Server which is really a configuration based CA Server. Similar to the CA Server implemented by SNS, the CA Server in LabVIEW allows LabVIEW enabled hardware to appear as an EPICS node. The processing is all done using the function blocks in LabVIEW. Using the configuration based CA Server, you choose which shared variables in LabVIEW need to be published as PVs over the CA network.

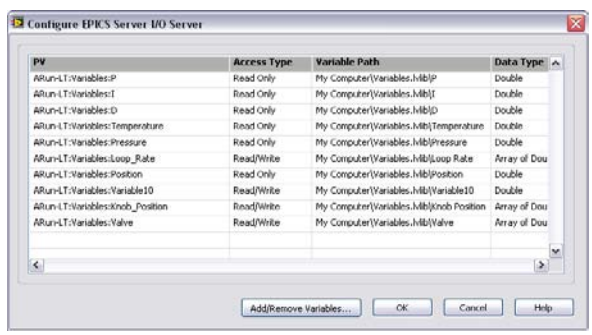

Figure3: Configuration based CA Server in LabVIEW.

The CA Server publishes value (VAL), description (DESC), timestamp (TIME) and the number of elements (NELM) in an array data type. This implementation of the configuration based CA Server can run on Windows and also in VxWorks and Pharlap RTOS. With the ability to run on Pharlap RTOS, PXI based instruments can now be integrated into an EPICS based control and data acquisition system.

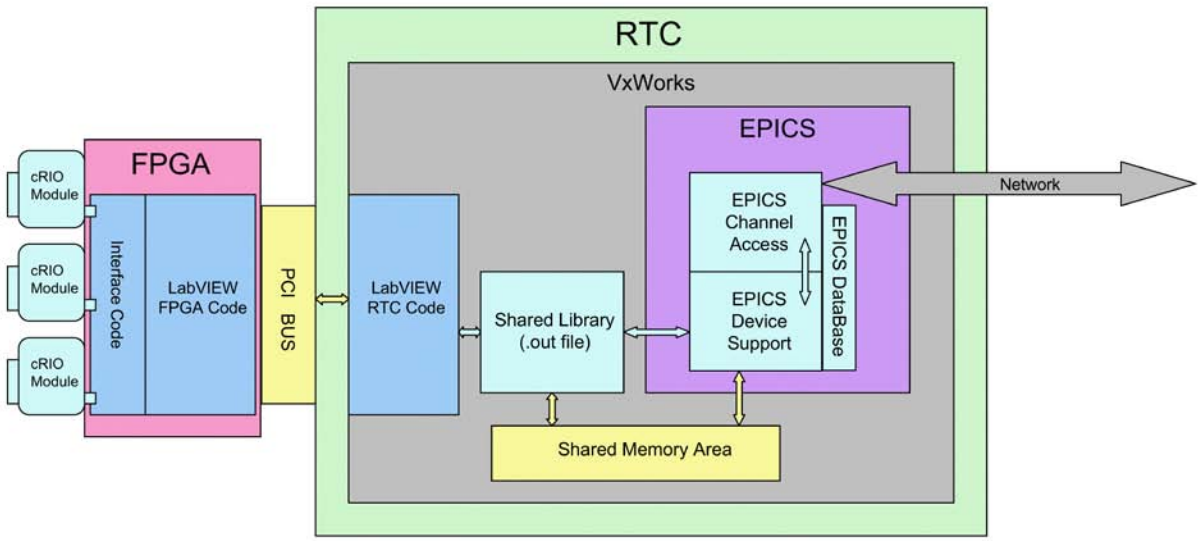

Figure 4: System architecture for running EPICS on the NI CompactRIO platform.

Another option is embed the EPICS IOC in CompactRIO, a "Programmable Automation Controller" (PAC) manufactured by National Instruments that is covered in the later section of this paper. Los Alamos National Laboratory has been working with NI to implement EPICS IOC on CompactRIO to be used in their project of upgrading the control system at the Los Alamos Neutron Science Centre (LANSCE) [2]

LEVERAGING COTS INSTRUMENTATION

PXI, or PCI eXtensions for Instrumentation, leverages COTS components while adding the necessary features such as ease of use, timing and synchronization, and rugged industrial components for enhanced reliability. In addition, PXI is an open platform enabling many industries to create custom modules for their needs.

We recommend PXI as the preferred COTS platform for the CODAC HPN due to PXI's superior offering in the following areas:

- Open, international standard
- High bandwidth PCIe/PCI COTS architecture
- Variety of I/O available, wide industry adoption
- High performance timing and synchronization
- Time network compatibility
- FPGA Custom modules on PXI
- Compatible with industry standard and custom protocols
- Scalable for large instrumentation
- Real time, Linux, Windows OS support

Because PXI is an open industry standard, today nearly 1,500 products are available from the 70+ members of the PXI Systems Alliance. Available device categories include:. analog input and output, high speed digitizers,

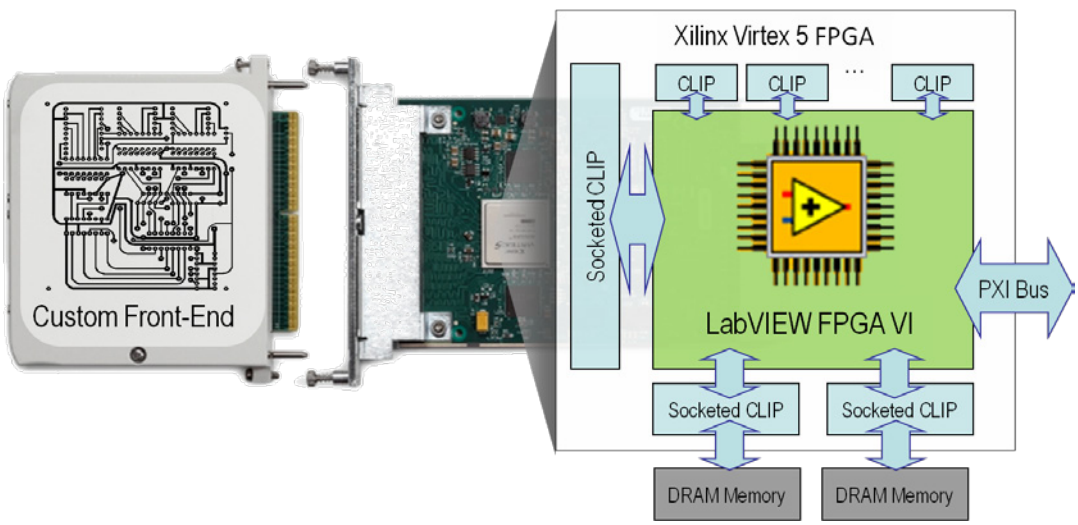

Figure 5: NI FlexRIO with custom front-end and LabVIEW FPGA programmable target.

digital input and output, timing input and output, reconfigurable I/O, power supplies and motion control, to name a few.

NI FlexRIO

The NI FlexRIO product family provides flexible, customizable I/O for NI LabVIEW FPGA. Solutions consist of NI FlexRIO FPGA Modules for PXI and PXI Express, and NI FlexRIO Adapter Modules, which add I/O to the FPGA. Together, they form a high-performance, reconfigurable instrument powered by LabVIEW FPGA. Adapter modules are available from NI and National Instruments Alliance Partners, or you can use the NI FlexRIO Module Development Kit (MDK) to build your own.

NI FlexRIO Adapter Module Development Kit You can build the exact adapter module your application needs with the NI FlexRIO MDK. This requires experience in custom printed circuit board (PCB) design and hardware description language (HDL) code development. The NI FlexRIO Adapter MDK includes electrical and mechanical specifications, example code, and design documentation.

CONTROL, DIAGNOSTICS AND AUTOMATION

National Instruments is uniquely positioned to offer COTS products that span instrumentation to measurements, diagnostics and supervisory control. National Instruments CompactRIO is a small rugged industrial control and acquisition system powered by reconfigurable I/O (RIO) FPGA technology for ultrahigh performance and customization. NI CompactRIO incorporates a real-time processor and reconfigurable FPGA for reliable stand-alone embedded or distributed applications, and hot-swappable industrial I/O modules with built-in signal conditioning for direct connection to sensors and actuators. CompactRIO represents a low-cost architecture with open access to low-level hardware resources.

Figure 6: NI CompactRIO, an FPGA hardware platform.

Each I/O module contains built-in signal conditioning and screw terminal, BNC, or D-Sub connectors. A variety of I/O types is available, including ±80 mV thermocouple inputs, ±10 V simultaneous-sampling analog inputs and outputs, 24 V industrial digital I/O with up to 1 A current drive, differential/TTL digital inputs with 5 V regulated supply output for encoders, and 250 Vrms universal digital inputs. In addition a large number of Third Party vendors develop I/O modules with wide ranging functionality and specifications. For even more flexibility, a custom module development kit is available. NI cRIO-9951 CompactRIO Module Development Kit, users can develop custom modules to meet the unique needs of particular products and applications. The kit includes CompactRIO module development software and the CompactRIO Module Development Kit user manual. Additionally, it features housing module shells and connectors from the following packages: NI cRIO-9952, cRIO-9954, and cRIO-9955

REFERENCES

[1] A.Veeramani, T. Debelle, W. Blokland, R. Dickson, A. Zhukov, “Options for Interfacing EPICS to COTS Hardware Through LabVIEW”, THD004, ICALEPCS 2009.

[2] E. Björklund, A. Veeramani, T. Debelle “Using EPICS Enabled Industrial Hardware for Upgrading Control Systems”, WEP078, ICALEPCS 2009.

OTR POLARIZATION EFFECTS IN BEAM-PROFILE MONITORS AT THE FERMILAB A0 PHOTOINJECTOR*

A. Lumpkin#, A. Johnson, J. Ruan, J. Santucci, and R.Thurman-Keup
Fermilab, Batavia, IL U.S.A. 60510

Abstract

Optical transition radiation (OTR) imaging for transverse beam-size characterization is a well-established technique at many accelerators including the Fermilab A0 photoinjector (A0PI) facility. With low beam energies of 14-15 MeV and emittances of 3 mm mrad, one observes beam sizes of 0.8 to 1.5 mm (sigma). However, the use of 50-μm wide slits to sample the beam's transverse phase spaces significantly alters the required resolution of the converter screen and imaging system. Slit-image sizes of about sigma =100 μm or less are observed, depending on drift distance and beam divergence. Moreover, the OTR polarized component perpendicular to the narrow beam dimension systematically gave us ~20-μm smaller projected image sizes than those with the total OTR intensity. This is one of the first reports of this polarization effect at such a low-gamma regime (~30).

INTRODUCTION

The opportunity for a new series of beam characterization experiments at the Fermilab A0 photoinjector (A0PI) was recognized in the last year. There is an ongoing proof-of-principle experiment to demonstrate the exchange of the transverse horizontal and longitudinal emittances [1,2]. This experiment relies on measurements of the transverse emittances and longitudinal emittance upstream and downstream of an emittance-exchange (EEX) beamline. Generally, at the low beam energies of 14-15 MeV and emittances of 3-5 mm mrad, one encounters beam sizes of 0.8 to 1.5 mm (sigma) [2]. Such beam sizes do not present a challenge to standard imaging procedures using scintillator screens or optical transition radiation (OTR) screens as described elsewhere [3]. However, the slits-emittance-measurement technique [4] which involves insertion of 50-μm wide slits to sample the beam's transverse phase spaces significantly alters the required resolution of the converter screen and imaging system. In this case, one deals with slit-image sizes of σ =100 μm or less, and depending on the drift distance one deals with images that can approach the camera resolution limit and/or the converter screen resolution limit. Beam divergence is calculated from the downstream slit image size and the relevant drift distance.

*Work supported by U.S. Department of Energy, Office of Science, Office of High Energy Physics, under Contract No. DE-AC02-07CH1135.
#lumpkin@fnal.gov

In the case of OTR imaging for transverse beam-size characterization, there is empirical evidence for gamma greater than 1000 beams that the utilization of the polarization component orthogonal to the dimension of interest results in a smaller projected image profile [5-7]. This aspect is a small fractional correction for 1-mm sized beam spots, but quite noticeable for 150-μm sized beam spots. While evaluating the slit images for emittance measurements at A0PI, we consistently found that using the OTR polarized component orthogonal to the narrow beam dimension of interest systematically gave us ~20 μm smaller projected image sizes than with the total OTR intensity. For such a low-gamma regime (~30), this is one of the first reports of this polarization effect on observed beam sizes. This correction affects the emittance values through the beam-size-divergence product.

EXPERIMENTAL BACKGROUND

The tests were performed at the Fermilab A0 photoinjector facility which includes an L-band photocathode (PC) rf gun and a 9-cell superconducting radiofrequency (SCRF) accelerating structure which combine to generate up to 16-MeV electron beams [2]. The drive laser operates at 81.25 MHz although the micropulse structure is usually counted down to 1 MHz. Due to the low, electron-beam energies and OTR signals, we typically summed over 50 micropulses with 0.25 nC per micropulse. The tests were performed in the straight-ahead line where energizing a dipole sends the beam into a final beam dump. The setup included the upstream corrector magnets, quadrupoles, the YAG:Ce and/or OTR imaging stations denoted as X3-X6, and the beam dump as schematically shown in Fig. 1. Both the YAG:Ce powder screen and the OTR screens were oriented with the surface normal at 45 degrees to the beam direction and with the viewing port at 90 degrees to the beam direction. The OTR converter was an Al-coated optics mirror that was 1.0 mm thick with a BK7 substrate and was mounted on a stepper assembly. The assembly provided vertical positioning with an option for the YAG:Ce scintillator at X5. The images were obtained with a 10-bit Firewire digital CCD camera with an optical transport consisting of a 150-mm-focal-length field lens, mirror, and a 50 mm C-mount lens on the camera. The images were captured with 8-bit resolution under the DOOCS protocol, and images were processed with MATLAB-based tools for Gaussian curve fitting to the projected profiles.

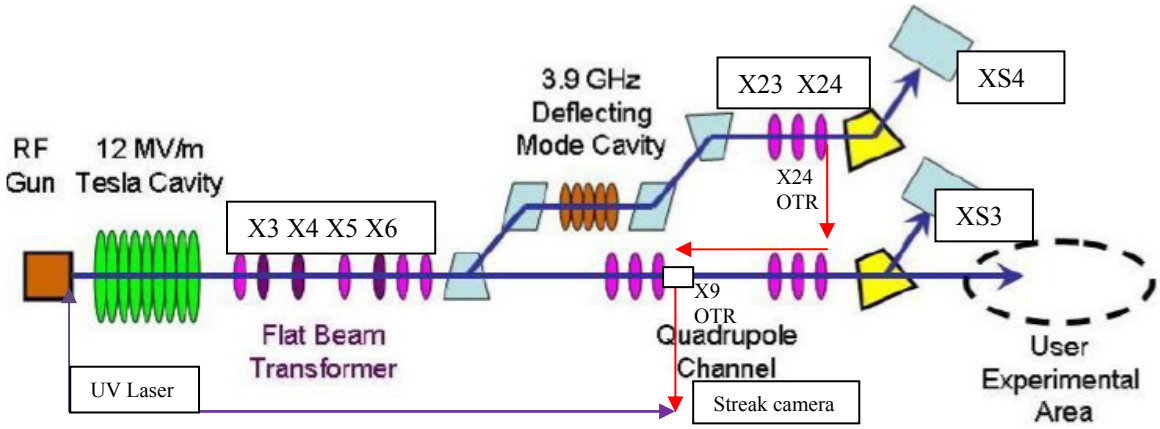

Figure 1: A schematic of the A0 photoinjector test area showing the PC RF gun, 9-cell SCRF Tesla cavity, transverse emittance stations, the OTR stations, and the exchanger beamline when the two doglegs' dipoles are powered.

After inserting the slit assemblies at X3, the initial sampling station was chosen 0.79 m downstream at X5. The slit assemblies were 3 mm thick with the 50-µm wide slits spaced 1 mm apart. The single polarizer was on a pneumatic actuator which allowed for the polarizer to be in the X5 optical path or out of it. The linear polarizer orientation of horizontal or vertical to the beam-direction-observation-direction plane was fixed, and it thus required a tunnel access to rotate manually the polarizer orientation.

OTR POLARIZATION RESULTS

It is well known that OTR is radially polarized, and this leads to a somewhat subtle effect. Some experimental teams have reported a beam-size effect when using a linear polarizer with the OTR. The experiments were performed with much higher gamma beams, such as 56000 at SLAC FFTB [5], 14000 at APS [6], and 9000 at JLAB [7]. In all cases the beam image size was reduced when using the OTR polarization component *orthogonal* to the beam dimension axis. As schematically shown in Fig. 2, the approaching beam charges induce currents in the metal plane that generate the radially polarized OTR. By selecting the vertically polarized component one suppresses the OTR that extends beyond the horizontal charge distribution and obtains a result closer to the actual x beam size.

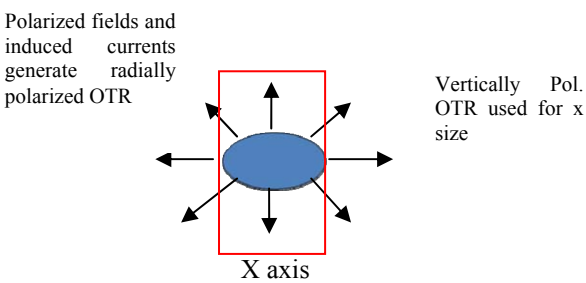

Figure 2: Schematic of the induced currents that generate radially polarized OTR when a charge distribution strikes a metal surface.

In the JLAB case at 4.5 GeV, the observed beam image size was 150 by 161 µm when using the total intensity [7]. With the linear polarizer oriented vertically in the optical path one observed an x image size of 127 µm, while with it oriented horizontally one saw a y image size of 130 µm. The studies of the effects were extended by adjusting an upstream quadrupole's focusing strength to vary the beam size. These were cross checked with results from a nearby wire scanner as shown in Fig. 3. The OTR orthogonally polarized data (black diamonds) systematically fall closer to the wire-scan data (open circles) than the total intensity data.

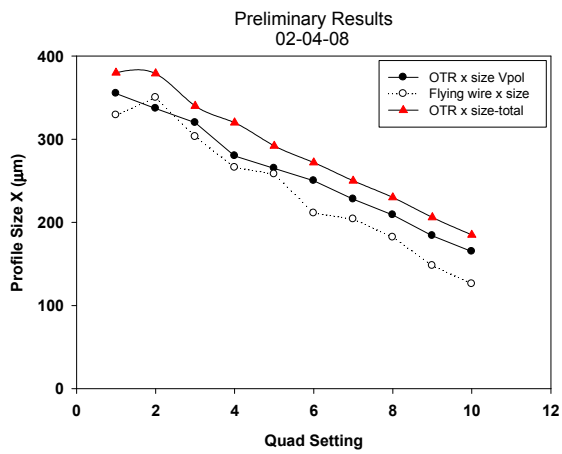

Figure 3: A comparison of the total OTR based beam size, orthogonally polarized OTR based beam size, and the flying wire based beam size for the horizontal dimension [7].

In the A0PI experiments, we systematically observe smaller beam slit images by 10-20 µm with the orthogonally polarized light than with the total OTR for slit images as seen in Fig. 4 and Table I. Since the slit images are in the range of 100 µm, this is an additional size correction. We believe these are the first reports of the effect at such low gamma, although Castellano and Verzilov evaluated a polarization effect at the single-particle-function level and at the few-micron level for a range of beam energies [8].

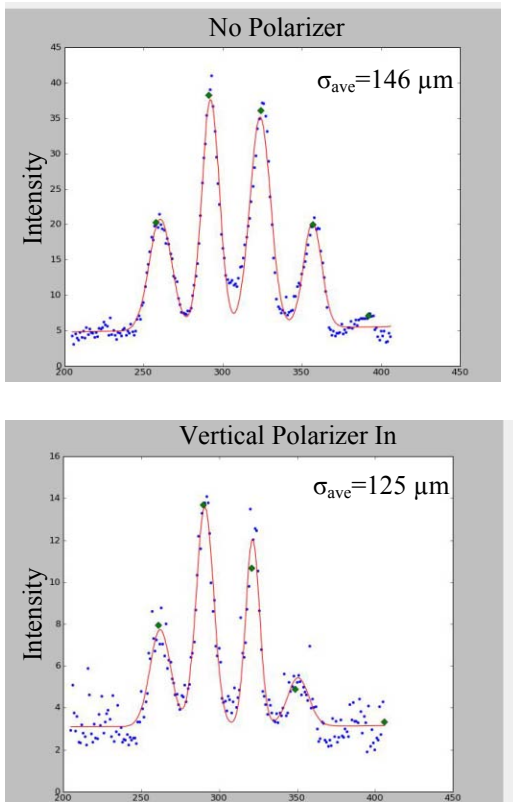

Figure 4: Comparison of X5 vertical slit images without (Upper) and with (lower) the vertical polarizer inserted. The averaged slit image profile width is 0.9 pixels or 20 μm smaller with the vertical polarizer inserted.

Table I: Comparison of OTR beam and slit images at the X5 imaging station using vertical polarization (V). The slits inserted at screen X3 are none (No), horizontal (H), and vertical (V). Five image averages were used for the slit images. (June 18, 2009)

X3 Slit	X5 Pol.	Q (pC)	Bunches	Fit sigma(pix)	Size(μm)
No	No	350	30	x, 38.5	874
No	V	350	30	x, 37.9	860
H	No	350	80	4.3	96.7
H	V	350	80	4.4	99.6
V	No	350	80	5.9	133
V	V	350	80	5.0	114
V	No	1000	80	6.8±0.1	154
V	V	1000	80	5.7 ±0.1	128

We extended these studies by another series of experiments as shown in the following tables. In these case we even checked for effects of the drive laser's S and P polarizations. Data obtained with each are indicated. As can be seen in Table II, the data are organized in columns indicating which slits were inserted at X3, which linear polarizer orientation was used in the optics before the camera at X5, the drive laser polarization, the number of bunches, the image profile fit sigma in pixels, and the size in microns. As stated earlier, the single linear polarizer was on a pneumatic actuator which allowed for the polarizer to be in the optical path or out of it. The linear polarizer orientation of horizontal or vertical to the beam-direction-observation-direction plane was fixed, and it thus required a tunnel access to rotate manually the polarizer. The data are organized in pairs, without and with the polarizer inserted. The projected image profiles in the narrow dimension were fit to a Gaussian shape and the results from ten images were averaged. The average size pixel value and the standard deviation were determined, and then the uncertainty of the mean was calculated by dividing the standard deviation by the square root of the number of samples [9]. This table clearly shows in the first four rows a systematically smaller beam vertical slit image size by 20-21 μm when the vertical polarizer is inserted versus not inserted for either laser polarization. The narrow dimension is actually the horizontal direction in this case. In addition the last four rows show that with horizontal slits inserted at X3, the vertical polarizer has little effect on the parallel vertical dimension size. This configuration should have similar intensities to that of the vertical slits so this check should preclude an intensity-dependent effect in the imaging system for the vertical polarizer data.

Table II: Comparison of slit images using vertically polarized OTR at X5. (July 20, 2009).

X3 Slit	X5 Pol.	Las. Pol.	Bunches	Sigma(pix)	Size(μm)
V	No	S	100	4.04±0.11	91.7
V	V	S	100	3.09±0.08	70.1
V	No	P	100	4.26±0.14	96.7
V	V	P	100	3.37±0.09	76.5
H	No	P	100	4.37±0.07	99.2
H	V	P	100	4.45±0.10	101.0
H	No	S	100	4.34±0.07	98.5
H	V	S	100	4.35 ±0.09	98.7

As a further test, we used an upstream quadrupole's current setting to focus in one plane and form a narrow band at the X5 location. In this case we could approach the size of the slit images, but we had more electrons contributing to the beam image than the slit sample. We actually used ten times fewer bunches for Table III results than in the OTR based slit images of Table II. The same procedure is used as for the slit images, and the vertically polarized data profiles are all smaller by 11-30 μm than the total OTR image for the vertical-band test. When we changed the quadrupole setting to produce a horizontal band with a narrow vertical size at X5, we actually saw a

larger size with the now parallel polarized vertical component.

Table III: Comparison of band images using vertically polarized OTR at X5 and 10 bunches. (July 21, 2009)

X5 Band	X5 Pol.	Las. Pol.	Sigma(pix)	Size (μm)
V	No	P	5.42±0.03	123.0
V	V	P	4.00±0.04	90.8
V	No	S	5.55±0.02	126.0
V	V	S	4.95±0.05	112.4
V	No	P	5.36±0.02	121.7
V	V	P	4.85±0.10	110.1
H	No	P	4.65±0.03	105.5
H	V	P	5.37±0.05	121.9

In the course of the tests, we also obtained data with the YAG:Ce powder screen whose surface normal is oriented at 45 degrees to the beam direction as was the OTR screen. This screen is on the same stepper motor driven actuator as the OTR screen so we could easily select it and use the same X5 optics. The results are shown in Table IV. For comparison purposes we also show the OTR data in the table. First, it is noted that there was evidence for the OTR polarization effect in rows 1,2, and secondly, no polarization effects observed (as expected) in the YAG:Ce-based beam sizes at rows 3,4. Only one bunch was used with the brighter scintillator, so we could be reducing any macropulse effects in the beam. On the average, the vertically polarized OTR band images for the vertical slits in rows 2,6 have a size of 101 μm compared to the total OTR image size of 124.5 μm and to the YAG:Ce averaged image size of 130 μm. These results are consistent with our previous hypothesis that the YAG:Ce powder screen has a limiting resolution term to be addressed [10]. If we accept the OTR polarized data as the reference, then the implied YAG:Ce X5 screen term in quadrature would be 82±9 μm. We understand these have a basic 50-μm thick YAG:Ce deposition on the 1-mm thick Al metal substrate [11].

One of the alternative explanations was that the polarized source was equivalent to a reduction in aperture in the optics, and this could lead to an improved resolution. Figure 5 shows the "polarizer out" minus "polarizer in" sigma vs. lens f/#. The red datum point was obtained with vertical slits and vertical polarizer and the blue data points were from the horizontal slits and horizontal polarizer configuration. The green datum point is calculated from slit images that weren't properly rotated so the projected size was enlarged for the polarized data. The data also reflect an asymmetry in the magnitude of the differences for the vertical and horizontal polarizer data, with the latter having statistically smaller effects by a factor of about two. However, the polarization effect persists at f/#4, albeit with low signals even with the large number of bunches in the macropulse.

Table IV: Comparison of OTR and YAG:Ce powder band images at X5 for 250 pC per bunch. The YAG:Ce powder data used only 1 bunch as denoted by 1-Y in col. 4. (July 21, 2009)

X5 Band	X5 Pol.	Bunches	Fit sigma (pix)	Size (μm)
V	No	10	5.42±0.03	123.0
V	V	10	4.00±0.04	90.8
V	No	1-Y	5.67±0.09	128.7
V	V	1-Y	5.71±0.04	129.6
V	No	10	5.55±0.02	126.0
V	V	10	4.95±0.10	112.4
H	No	1-Y	5.63±0.08	127.8
H	V	1-Y	5.92±0.05	134.4

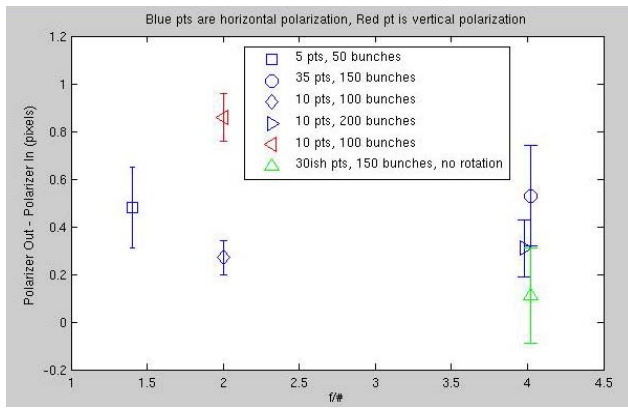

Figure 5: Plot of the "polarizer out" minus "polarizer in" observed beam size difference in pixels (with a calibration factor of 22.8 μm/pixel) versus f/#. The polarized OTR gives systematically smaller beam sizes. (July 2, 2009).

We note that the Al OTR screen is rotated around the vertical axis which fundamentally breaks the symmetry for the two radiation lobes in the horizontal axis. This is shown in Fig. 6 by a single-electron angular distribution calculation as projected for a distance of 150 mm from the source. The two horizontal lobes have different peak intensities and shapes while the vertical OTR lobes are symmetric in intensity and shape as seen in Figs. 6b and 6d. This is particularly true at low gamma (29) as indicated by these calculations. The actual beam divergence has not been convolved, but it is more than 100 times smaller than the OTR pattern's opening angle in our case. Further modeling to explore the observed beam-size polarization effect is warranted.

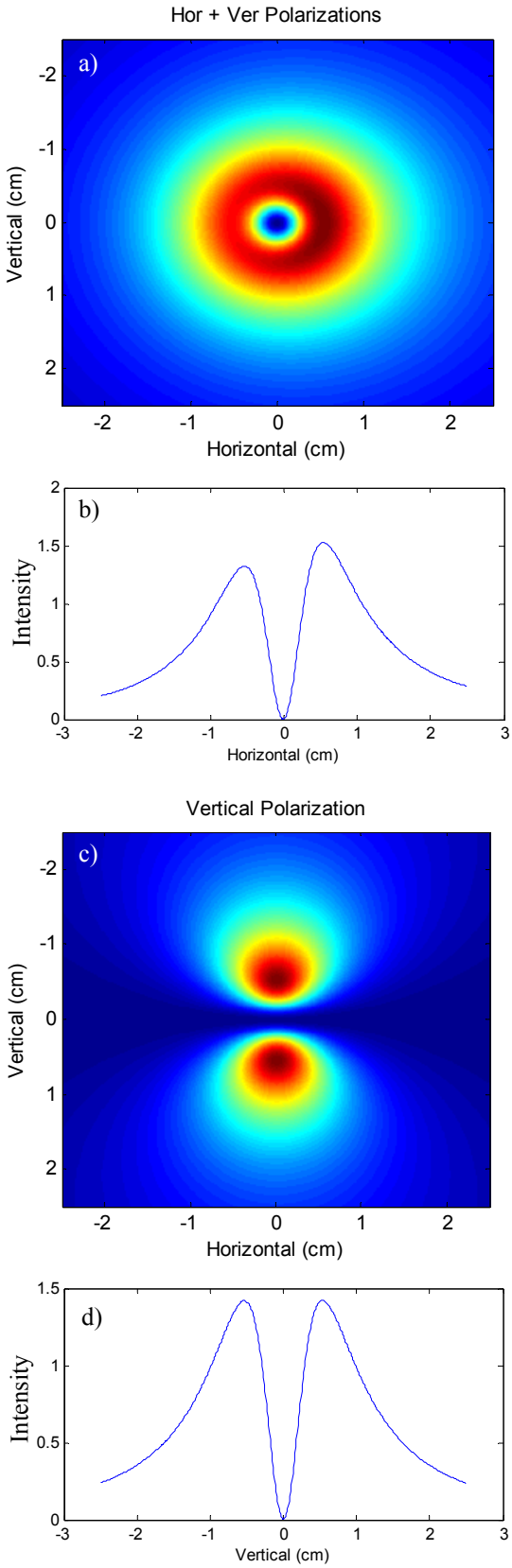

Figure 6: Calculated OTR angular distribution patterns at 150 mm from the source: a) total intensity (sum of both polarizations) b) horizontal profile c) vertically polarized component, and d) vertical profile.

SUMMARY

In summary, we have extended the investigations on OTR polarization effects in beam-size monitoring to the low-gamma regime of the A0PI. We have observed a 20-µm reduction for beam sizes around 100 µm when using the correct polarized component, and we noted this as comparable to the high-gamma results [7]. Due to its nature, we have interpreted it as a term outside of the quadrature treatment for other observed beam size effects and treated it separately. The magnitude of the correction for the slit images is in the 15-20% regime, so corrections are indeed warranted in making emittance calculations. Further modeling of the effect would enhance the understanding of the observations to date.

ACKNOWLEDGEMENTS

The authors acknowledge support from M. Wendt, H. Edwards, E. Harms, and M. Church of Fermilab.

REFERENCES

[1] T. Koeth, L. Bellantoni, D. Edwards, H. Edwards, R. P. Fliller III, "A TM110 Cavity for Longitudinal to Transverse Emittance Exchange", PAC 07, THPAS079, Albuquerque , NM , USA http://www.JACoW.org.

[2] Timothy W. Koeth et al., "Emittance Exchange at the Fermilab A0 Photo Injector", Proc. of PAC09, May 4-8, 2009, Vancouver, B.C., JACoW.

[3] E. Bravin, "Transverse Beam Profiles", Proceedings of Beam Diagnostics CERN Accelerator School, 377-406, CERN-2009-005, and references therein.

[4] C.H. Wang et al., "Slits Measurement of Emittance on TTF", International Conference on Accelerator and Large Experimental Physics Control Systems, Trieste, Italy (1999).

[5] M. Hogan, (private communication, SLAC), May 2005.

[6] A. H. Lumpkin et al., "Initial Imaging of 7-GeV Electron Beams with OTR/ODR Techniques at the APS", Proc. of PAC05, Knoxville, Tenn., p.4162. (2005), http://www.JACoW.org.

[7] Pavel Evtushenko et al., "Near-Field ODR Measurements at CEBAF" , Proc. of BIW08, Lake Tahoe, CA, p.332, (2008), http://www.JACoW.org.

[8] M. Castellano and V.A.Verzilov, Phys. Rev. ST Accel. Beams, 1:062801 (1998).

[9] L. Lyons, Statistics for Nuclear and Particle Physicists (1986).

[10] A.H. Lumpkin et al., "Spatial Resolution Limits of YAG:Ce Powder Beam-profile Monitors at the Fermilab A0 Photoinjector", Proceedings of FEL09, Liverpool, p.348, (2009), http://www.JACoW.org.

[11] K.Floettmann of DESY provided the powder screens which are described in R. Spesyvtsev's Master's Thesis,"Transverse Beam Size Measurement Systems at Photo Injector Test Facility in Zeuthen", (2007).

SNS TARGET IMAGING SYSTEM SOFTWARE AND ANALYSIS*

W. Blokland, T. McManamy, T. J. Shea, ORNL, Oak Ridge, TN 37831, U.S.A.

Abstract

A new Target Imaging System (TIS) has been installed to directly measure the size and position of the proton beam on the Spallation Neutron Source (SNS) mercury target. The proton beam, hitting a luminescent coating on the target nose, produces light that is transferred using a radiation-tolerant optical system to an image acquisition system integrated with the accelerator controls network. This paper describes the software that acquires and analyzes the image, how the system has been integrated with the SNS control system, and compares the TIS results with the indirect methods of calculating the peak densities of the proton beam.

INTRODUCTION

The Spallation Neutron Source at Oak Ridge National Laboratory now commonly operates with approximately one megawatt of beam power on the Mercury target. Each beam pulse, repeating 60 times a second, consists of about 10^{14} 1GeV protons and lasts less than 1 microsecond. The protons hit a stainless steel target filled with mercury to produce the neutrons for the experiments. The protons damage the target and this damage depends on the beam's peak power and transverse profile [1].

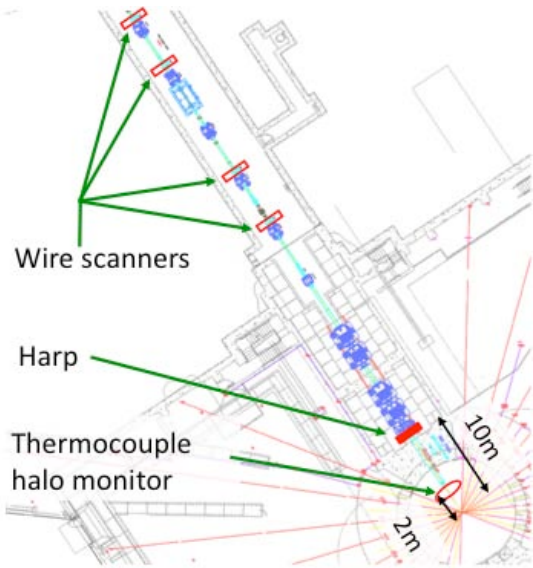

Figure 1: RTBT Instrumentation.

To assure the target lifetime, the operational procedure is to limit the beam's peak density on the target. The RTBT (Ring to Target Beam Transferline) Wizard program combines wire-scanner and harp measurements with the beam-line lattice parameters to calculate the beam size at the target. The harp is the only instrument in the RTBT that measures the transverse profile of the beam during production, see Figure 1. The RTBT Wizard produces scale factors that allow conversion of the measured beam size at the harp to an estimated beam size on the target. The harp program can then calculate the estimated peak densities on the target. If these peak intensities start to exceed the administrative limits, beam power is reduced or the transverse size is increased.

With the TIS, we can now obtain a more direct measurement of the peak intensities and use this system to safeguard the target.

SYSTEM OVERVIEW

A target imaging system was available during the commissioning of SNS and measured the first beam on target. To keep the system simple, it consisted of a fluorescent screen mounted in front of the target and a camera in the target room. It was understood that this system wouldn't last long before the radiation damage would permanently disable the system. The system showed the first beam on the first installed target and its measurements were used to estimate the spread of the beam due to scattering of the protons when passing through the proton window. This success started the drive for a permanent target imaging system. After evaluating various configurations, the choice was made to coat the actual target nose with a layer of Cr:Al2O3 and to use mirrors and a fiber bundle to bring the light out to the camera in a non-radiation environment [2,3].

System Configuration

A radiation resistant aluminum parabolic mirror collects the light from the fluorescent coating of the target. This is followed by a turning mirror and then lenses that focus the image onto a fiber bundle. Figure 2 shows the optical path through the target shielding.

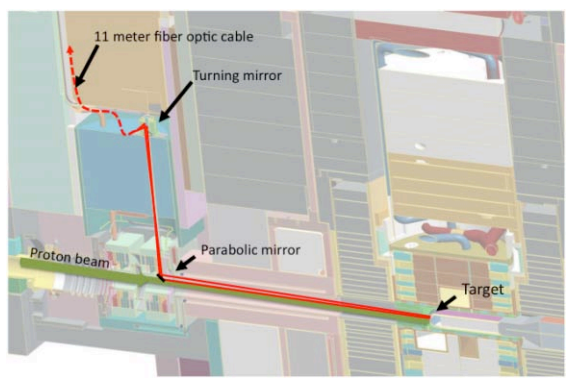

Figure 2: View of optical path with shielding.

The radiation resistant optical fiber bundle is made of 10,000 individual fibers and brings the light out to a non-

* ORNL/SNS is managed by UT-Battelle, LLC, for the U.S. Department of Energy under contract DE-AC05-00OR22725

radiation environment. This allows us to pick a camera that is not radiation resistant. The Prosilica GC750 camera was chosen for the initial installation because of previous experience with this camera and available acquisition and analysis software. Its light sensitivity was tested and found to be sufficient.

The camera is interfaced to a rackmount PC using the GigE Vision interface. The PC runs LabVIEW, which includes a driver to support the camera. A LabVIEW program acquires and analyzes the images from the camera. The results are shared with the rest of the control system over Channel Access. The camera's acquisition is triggered 4 microseconds after the beam hits the target within which time the gas scintillation has died down but the coating is still fluorescing. The overall configuration is shown in Figure 3. The TIS has been in operation for over 2000 MWHrs with the second SNS Target [4].

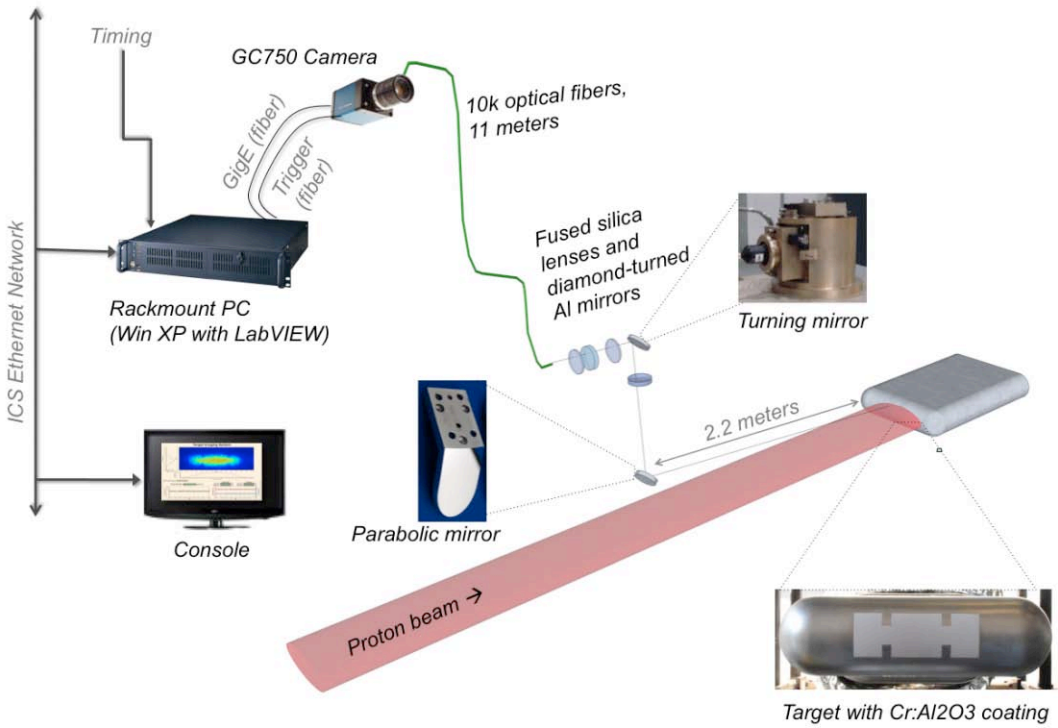

Figure 3: The configuration of the Target Imaging System.

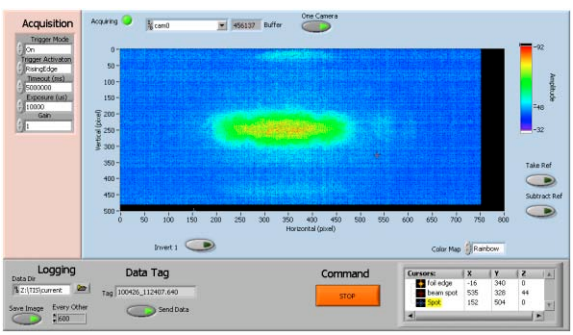

Figure 4: The image acquisition software.

IMAGE ACQUISITION

The image acquisition software, see Figure 4, allows the user to set up the camera exposure, trigger mode, and gain. The user can optionally save the images to disk. The SNS Timing card in the rackmount PC provides the trigger pulse to synchronize the camera to the proton beam.

ONLINE ANALYSIS

The goal of the online analysis is to produce RMS width, position, and peak density estimates during production. The light that is visible outside the coated area is ignored. If the beam is larger than the coated area the shape is extrapolated using the fitted function. The estimates are then calculated from the extrapolated fitted function. To calculate the peak density, we obtain the charge of the beam from the nearest beam current monitor but reduce this charge by 4% to account for estimated loss due to nuclear scattering from the proton beam window.

Preprocessing

The image analysis first optionally preprocesses the image to get rid of the fiber patters by taking the average of the top pixel values of all pixels within a square window. The goal is to reduce the variation in profile values when the image data is projected vertically and horizontally as seen in Figure 5.

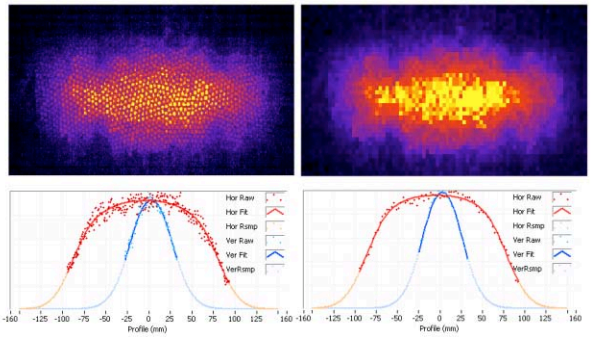

Figure 5: The fiber pattern in the image is removed by the preprocessing thus cleaning the projected profiles.

Profiles

To obtain a horizontal and vertical profile, subsections of the image are taken that are within the coating of the target but excluding the markers. The pixels in these subsections are projected to the vertical or horizontal axis to produce the profiles.

Fitting

The next step is to fit an analytical function to the profiles. Due to the injection scheme at SNS, the beam's transverse profile can significantly differ from a Gaussian function. Even a combination of two Gaussian functions cannot quite match the slope of the profiles. A super Gaussian function (with the absolute value taken of the term within the power within the exponent), however, can provide a good match for the profiles observed by the TIS and also by the upstream wirescanners and harp. The program used to evaluate different functions is shown in Figure 6. Several functions, including double Gaussians, quadratic modulated Gaussians, and super Gaussian functions were tested. The super Gaussian provided the

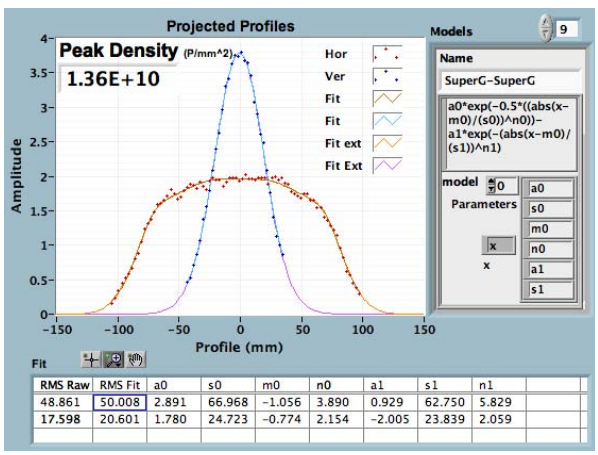

Figure 6: Program to evaluate different fitting functions for the TIS.

best results with the least amount of parameters, see also [5].

The super Gaussian function is as follows:

$$y = a \cdot \exp\left(-0.5 \cdot \left(abs\left(\frac{x-\mu}{\sigma}\right)\right)^{n}\right)$$

The background level is already zeroed using a default value or a value automatically derived from a part of the image and is not part of the fit. Varying the order of the super Gaussian allows adjustment of the flatness of the peak and the steepness of the slopes. The on-line analysis can fit a single super Gaussian or a double super Gausian with a common centroid.

An example of the super Gaussian fit is given in Figure 7. The plot shows the fits, xFit and yFit, to the profile data xProj and yProj. The super Gaussian has typically an order of about 4 for the horizontal profile and an order of about 2 for the vertical profile. With the estimated parameters of the function the profile outside of the coating area is reconstructed, xFit Rsmpl and yFit Rsmpl, and the RMS width and peak density are calculated.

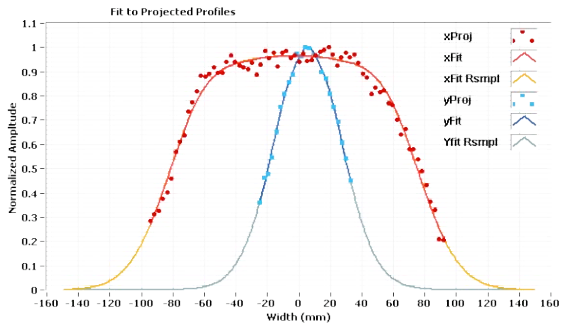

Figure 7: The reconstruction of the profile using a super Gaussian.

Under certain circumstances, such as fewer bunches in the Ring, the center of the profile can be hollow and the double super Gaussian is a good match for this situation, see Figure 8. Other more peaky profiles are possible as well but unlikely during normal operation and most studies.

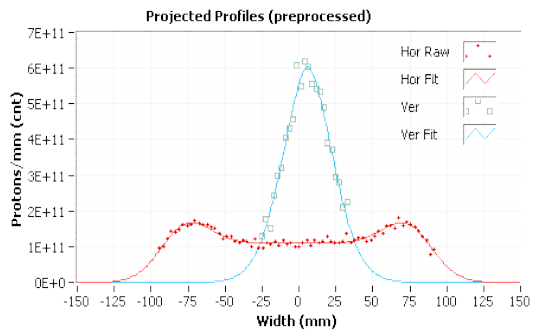

Figure 8: An example of a double super Gaussian fit for the horizontal profile.

The analysis program calculates for each image the beam parameters such as RMS width, position, peak density but also the efficiency of the image in terms of protons/count (count being the intensity of an image

pixel) to track the aging of the optical system, mostly the aging of the coating (see figure 9).

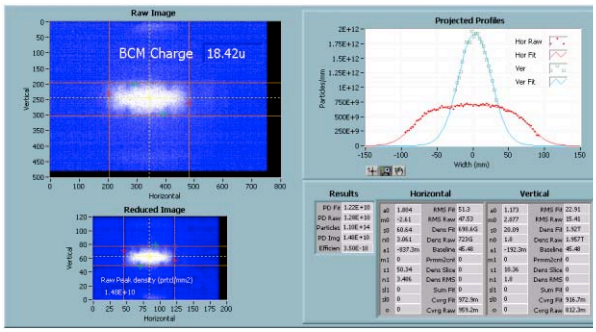

Figure 9: The main analysis program.

CONTROL SYSTEM INTEGRATION

For the TIS to be useful during operations, it must be integrated with the SNS EPICS-based control system. This is done through the Shared Memory IOC, see [6]. The LabVIEW program can now publish its results and retrieve EPICS Channel Access PVs (Process Variables) such as the beam pulse charge. The control room display of the TIS is shown in Figure 10. This is one of the first operator interfaces to be based on Control System Studio (CSS) rather than Extensible Display Manager (EDM).

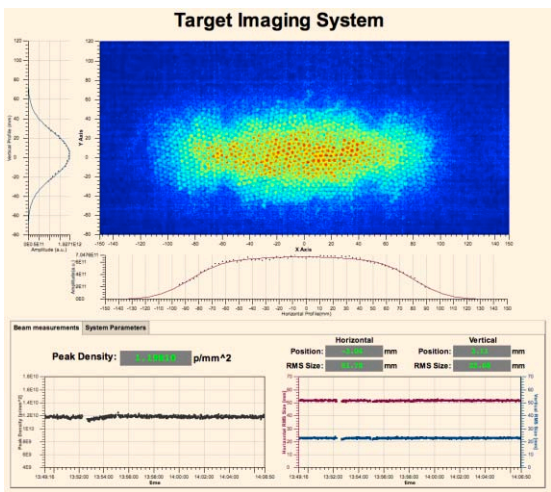

Figure 10: CSS Control Screen of the TIS.

RESULTS

Timing measurements and configuration

After passing through the proton beam window, the beam travels through 2 meters of Helium at atmospheric pressure before striking the target. When the system was first commissioned, light from scintillation of the helium gas was negligible compared to light from the coating. After the radiation damage to the coating exceeded 0.1 displacements per atom, luminescent efficiency decreased to less than 10% of its original value and the light from the gas became noticeable. A recent image is shown in figure 11. Because the target is viewed from the upper left, the light from the upstream gas appears primarily in the lower right portion of the image.

In a series of small steps, the leading edge of the camera's integration time was delayed with respect to the time of beam passage. The resulting sequence of images was analyzed to determine the exponential decay time of the light in three different regions: the center of the coating, the edge of the coating (upper left in figure 11), and the gas region (lower right in figure 11). As presented in Table 1, the decay time of the gas scintillation is significantly shorter than the decay time of the light from the coating regions. Therefore, delaying the shutter opening by a few microseconds with respect to the bunch passage rejects light from the gas.

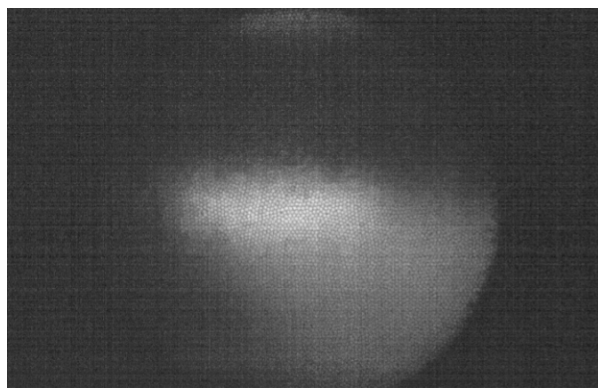

Figure 11: Image including gas scintillation.

Table 1. Decay time of luminescence.

	Coating center	Coating edge	Gas region
Low power (<1 Hz)	1.135 ms	1.133 ms	<0.01 ms*
High power (60 Hz)	0.020 ms	0.023 ms	<0.01 ms*

*measurements in gas region are limited by camera shutter risetime.

Calibration with beam

The marker features on the coating pattern are used to geometrically calibrate the system. Since there is no light source to artificially illuminate the target surface, this calibration depends on images of taken with beam on target. As seen in the example images shown in the figures, limited resolution and contrast makes it difficult to determine the location of the features. Spectroscopic measurements and optical modeling point to chromatic aberration as the culprit, and improvements in the optical system are planned.

To determine uniformity of response, a small beam is raster scanned across the coating. This technique shows that the luminescent efficiency varies by about +/- 8%.

Comparison with predicted beam properties

Data from the imaging system was analyzed with 3 independent fitting methods and then the results were compared to the RTBT Wizard predictions. Several cases of varying beam size and proton pulse intensity were analyzed. The TIS images were fit by super Gaussians functions with Mathematica and LabVIEW. Two-dimensional fits were also done over the entire coated region using Excel with either two or three Gaussian functions with different center locations. In general, good agreement was obtained between the three image fitting methods. In comparison to the RTBT Wizard predictions, the image system gave larger vertical RMS beam size by several mm and lower peak densities as shown in figure 12. The agreement with horizontal RMS sizes was closer, but still slightly larger for the TIS fits.

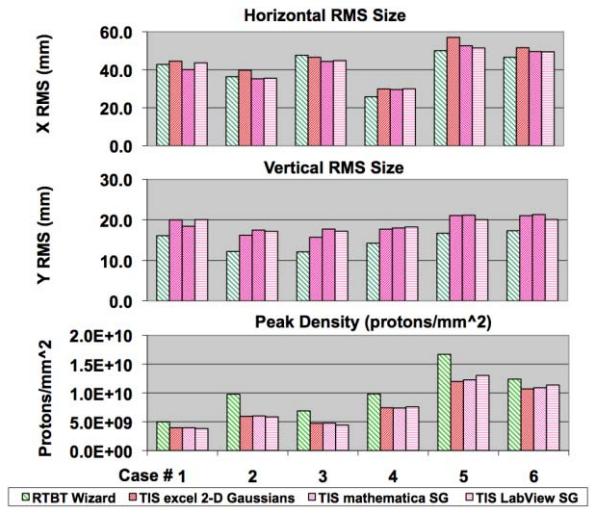

Figure 12: Comparison of size and peak density using the image system with 3 independent fitting methods and the RTBT Wizard projection.

Uncertainties

Additional studies are needed to evaluate effects that could broaden the profile measured by the TIS. Potential light sources include fluorescence caused by gamma and neutron backscattering from the target (which have a broader profile than the beam), reflections from uncoated regions and light from the helium in the beam path. Also, blurring of the image caused by chromic aberration or poor focusing could cause the apparent size to increase. There are also some uncertainties in the model used by RTBT Wizard. For example, the lattice functions have an uncertainty of about 20%. Effort to understand the discrepancy continues and lessons learned will be incorporated into future deployments of the imaging system.

CONCLUSIONS

The TIS provides a new capability to track changes and make on-line measurements of the peak density during production. The system has a demonstrated lifetime of over 2000 MW-Hrs and the current rate of degradation is minimal. We still have to do further work to improve the agreement between the RTBT Wizard predictions and the TIS results to further reduce the uncertainty in the peak density. The desire is to make this the primary tool to align beam on the target and assure the target lifetime by monitoring the peak density.

ACKNOWLEDGEMENTS

The authors wish to acknowledge the help of the SNS physics group in obtaining the RTBT wizard results in general and S. Cousineau and J. Holmes in particular. Many people have contributed to the design and construction of the target imaging system. In particular, C. Maxey led design and deployment of the current optical system, and S. Sampath led development of the target coating process.

REFERENCES

[1] R. Riemer, “Results from Cavitation Damage Experiments with Mercury Spallation Targets at the LANSCE – WNR in 2008”, ICANS 2010.

[2] T. McManamy, et. al., AccApp 2007, Pocatello, Idaho, July 29-August 2, 2007, p. 160.

[3] T. Shea, et. al., “Status of Beam Imaging Developments for the SNS Target”, DIPAC 2009.

[4] T. Shea, et. al., “Installation and Initial Operation of an On-Line Target Imaging System for SNS”, ICANS 2010.

[5] W. Blokland, “Fitting RTBT Beam Profiles: the case for the super Guassian”, Internal memo, SNS, ORNL, Nov 2009.

[6] D. Thompson and W. Blokland, “A Shared Memory Interface between LabVIEW and EPICS”, ICALEPCS 2003, pp275-277. Gyeongju, Korea, Oct 13-17 2003

GAS SCINTILLATION BEAM PROFILE MONITOR AT COSY JÜLICH *

C. Boehme#, T. Weis, Technical University of Dortmund, Germany
J. Dietrich, V. Kamerdzhiev, Forschungszentrum Jülich, Germany
J. L. Conradie, iThemba LABS, South Africa.

Abstract

The interaction of ion beams with the surrounding residual gas leads to photon emission by the excited residual gas atoms and molecules. These photons in the visible spectrum range can be used to monitor the transverse beam profile. We therefore use a multichannel photomultiplier (PMT) together with an optical imaging system. Measurements at COSY synchrotron of the Forschungszentrum Jülich are presented. The usability of the method is discussed by comparing to measurements at the iThemba LABS beamline and the beamline of the JESSICA experiment, a neutron spallation source test setup at COSY.

INTRODUCTION

The knowledge of the beam position and the transverse profile is essential for the successful operation of an accelerator facility. Due to thermal reasons high beam energy and/or high beam currents limit the use of traditional intersecting methods like wire scanners or secondary electron emission (SEM) grids. At synchrotrons non destructive methods are preferred to monitor the circulating beam, as the beam passes the interaction region many times. Even a small influence per turn would add up, leading to possible beam loss. Several kinds of diagnostic devices, using the products of the interaction between the ion beam and the residual gas, are under development or in use. Usually the devices register the ions and/or electrons produced in collisions of the beam particles with the residual gas. A few attempts have already been made to use the emitted light of the excited residual gas particles in order to monitor the beam [1]. This method has the advantage of being insensitive to electric or magnetic fields. Also the spatial and time resolution is high, allowing a single pulse measurement. The principle limitations of this method are the low cross section for light production in the visible range and the small solid angle of the optical setup. This leads to an available count rate about three orders of magnitude lower, compared to profile monitors based on residual gas ionization. Nevertheless, a wide range of applications can still be covered with this method.

MEASUREMENT TECHNIQUE

The light emitted by the residual gas is focused by a glass lens onto a multichannel photomultiplier (PMT) array, as shown in figure 1. A Hamamatsu PMT (7260-type, 32 channels, 0.8×7 mm photocathode size, 1mm pitch size) was used for these measurements. The readout was performed using a 48 multichannel current digitizer, developed at iThemba LABS [3].

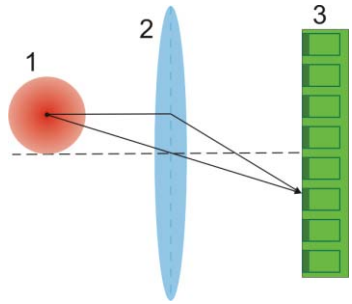

Figure 1: Measurement principle [2] (not to scale): The light from the interaction of the beam with residual gas (1) is focused by a glass lens (2) onto the multichannel photomultiplier (3).

PHOTON YIELD

While measuring the transverse beam profile using photons emitted by residual gas the only controllable parameters to influence the photon yield are the composition and pressure of the residual gas at fixed ion beam parameters. Although the increase of residual gas pressure is normally not standard practice at accelerators, this method has been successfully tested. While the residual gas mixture is given, the gas to be added can be chosen. Two gases are candidates for addition, N_2 and Xe, because both show strong light emission within the visible range and are also easily pumped out of the vacuum system.

Preliminary tests regarding the residual gas scintillation spectra were performed at a test bench [4]. A 20 keV He^+ beam passed an interaction region, where various gases could be added up to a total pressure of 10^{-3} mbar. A grid type monochromator together with a single channel PMT, that has a similar spectral response characteristics compared to the multichannel model, was used to measure the scintillation spectra. Since the ion source of the test bench uses He and H_2 is typically a dominating component of the residual gas in an accelerator, the scintillation spectra of these two gases were measured as well. The spectra are shown in figure 2

The results of the spectral measurements are in good agreement with [5]. The relative intensity at 424 nm (N_2) has been found to be less than expected. The overall results however clearly show that N_2 and Xe are

*Work supported by BMBF and NRF, Project code SUA 06/003
#c.boehme@fz-juelich.de

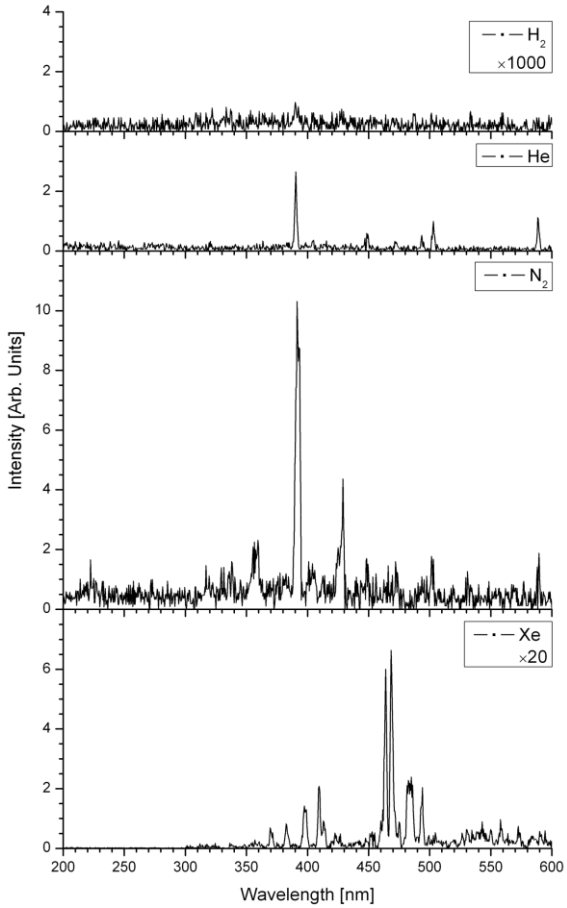

Figure 2: Scintillation spectra of H_2, He, N_2 and Xe in the visible range. The intensity scaling is common to all four measurements. For comparison the results for Xe and H_2 are multiplied by a factor of 20 and 1000 respectively.

promising candidates to boost the overall photon yield for a given total pressure. For further experiments N_2 is used, as the photon yield of Xe is slightly lower combined with a much higher price.

PROFILE MEASUREMENTS AT THE CYCLOTRON BEAMLINE

The scintillation profile monitor (SPM) was used to measure profile and position of the 3.14 MeV protons at the iTemba LABS transfer beamline. To verify the correct operation of the SPM, the beam was transversely shifted by a steering magnet. The beam position was derived from the beam profile and plotted together with the position reported by a standard beam position monitor (BPM) just downstream the SPM. Both results are in good agreement, as shown in figure 3. During the measurements, the PMT was operated at only $^2/_3$ of the maximal voltage, leaving room for about two orders of magnitude lower beam intensities or lower pressure.

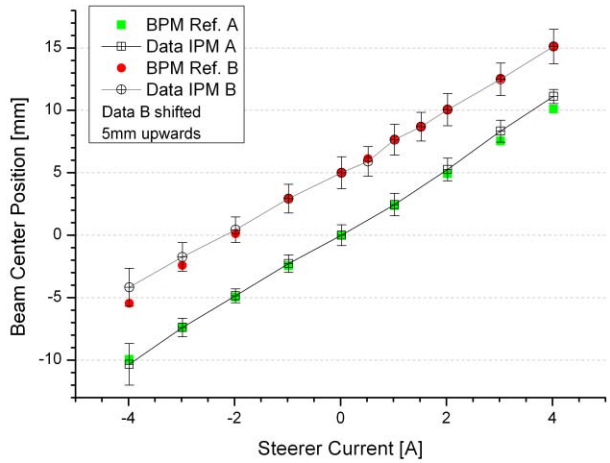

Figure 3: Beam position measured with the scintillation profile monitor (SPM A,B) and with a reference BPM at the 3.14 MeV iThemba LABS beam transfer line versus steerer current (beam current 300 μA, residual gas pressure ~ 10^{-5} mbar).

PROFILE MEASUREMENTS AT COSY

With the given residual gas pressure, residual gas mixture, the parameters of the optical system, and the PMT quantum efficiency, the calculated count rate is only 3 – 6 counts per second, depending on the proton energy within the synchrotron. Under these circumstances the signal to noise ratio is rather poor, making a reasonable measurement impossible. One possible compromise is, adding e.g. N_2 to the vacuum system near the SPM, as mentioned earlier.

Figure 4 shows the result of the profile measurement during a whole machine cycle, which in this case lasted 72 s. At injection the beam was located at its center position and was then accelerated to 1.7 GeV/c. About three seconds later the beam is displaced intentionally. The beam profile and also the center position could be successfully monitored throughout the complete cycle. During this first test the vacuum conditions were locally changed to achieve a better signal to noise ratio by manipulating the function of a vacuum pump to release deposited gas. This way the vacuum conditions could not be held stable over a long time, giving rise to variations of the overall intensity.

SCINTILLATION CROSS SECTION

Cross section calculations for the emission of photons in the visible range and a broad beam energy range are based on results from [1]. These data and the calculated cross sections obtained from our own measurements are summarized in figure 5, together with an adapted progression, derived from the Bethe formula as well as a low energy supplement based on [6].

In addition to the measurements described above, data was taken at an external beamline at COSY (JESSICA) [8]. The extracted beam passed through an enclosed chamber, where the gas composition and pressure could

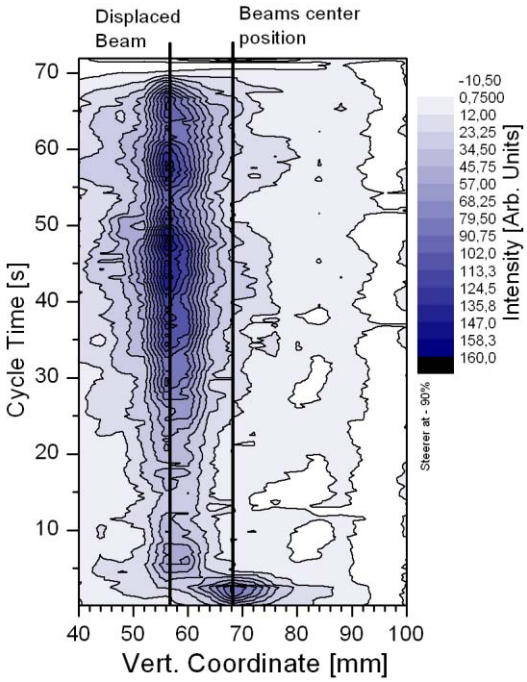

Figure 4: Beam profile versus time for a 72 s machine cycle. The beam is injected at its central orbit and then displaced. The BPM reference showed 13 mm displacement. The vacuum conditions were changing during the cycle.

be freely chosen, without affecting the vacuum system of the accelerator.

The data acquisition at the JESSICA beamline and the iThemba LABS have been performed using amplifiers equipped with automatic gain control (AGC), in order to boost the signals for transport via long cables out of the radiation area. Because of the AGC, only a mean value of the amplification factor is known, leading to an uncertainty in the cross section calculations, which can be seen in the discrepant results in figure **5**.

The measurements at COSY were performed with a different data acquisition hardware, which is described in the section 'measurement technique'. The use of this hardware results in a better knowledge of the measurement parameters. This allows a more exact calculation of the cross section, reflected in figure **5**.

CONCLUSIONS

The method of beam profile measurements based on residual gas scintillation has been evaluated. Good profile measurements results were achieved at the JESSICA beamline, despite a high radiation background. As a further development for areas like this, the light could be transported out of the radiation area with a proper optical system. Also the experiments at iThemba LABS showed a use case, when non-disturbing beam profile measurements are required. For both cases a simple, cost effective and easily maintainable system is presented. The only component which has to be assembled in vacuum is a viewport, all other components are outside the vacuum system.

For use in synchrotrons with ultra high vacuum conditions and particle energies corresponding to the minimum of the scintillation cross section, the system is beyond its limits. Here profile measurements are only possible when the conditions are changed by intention, e.g. increasing the pressure inside the vacuum system. A system based on residual gas ionization [9, 10] might be the better choice, as the event rate for ionization is about three orders of magnitude higher. Such a system usually has the disadvantage of being realized through a very complex and costly apparatus.

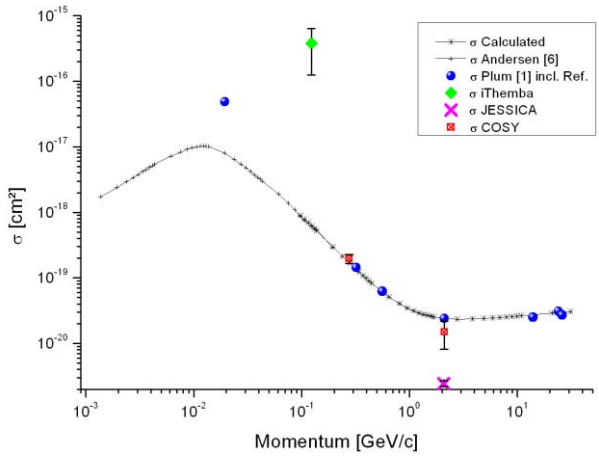

Figure 5: Cross section calculated from beam profile measurements, shown together with values from [1] and [6] as reference. Error bars represent statistical error only.

REFERENCES

[1] M.A. Plum et al., Nucl. Instr. Meth. A492 (2002), p. 74.
[2] N. I. Balalykin et al., WEHP42, Proceedings of RuPAC XIX, Dubna, 2004.
[3] iThemba LABS Annual Report 2008, p. 50.
[4] C. Boehme et al., Beam Instrumentation Test Facility, IKP Annual Report 2009, Forschungszentrum Juelich, t.b.p.
[5] Ralchenko, Yu., Kramida, A. E., Reader, J. and NIST ASD Team (2008). NIST Atomic Spectra Database (version 3.1.5). National Institute of Standards and Technology, Gaithersburg, MD. [2010, March 1] http://physics.nist.gov/asd3
[6] H. Andersen and J. Ziegler, Hydrogen: Stopping Powers and Ranges in All Elements Vol. 3, Pergamon Press 1977.
[7] J. Dietrich et al., First Beam Profile Measurements Based on Light Radiation of Atoms Excited by a Particle Beam, AIP Conf. Proc. 773, 184 (2005).
[8] N.I. Balalykin et al., WEHP42, Proceedings of RuPAC XIX, Dubna 2004.
[9] C. Boehme et al., Beam Test of the FAIR IPM Prototype in COSY, Proceedings of DIPAC2009, Basel, Switzerland.
[10] C. Boehme et al., Nondestructive Beam Instrumentation and Electron Cooling Beam Studies at COSY, Proceedings of IPAC2010, Kyoto, Japan, t.b.p.

A NON DESTRUCTIVE LASER WIRE FOR H- ION BEAMS*

C. Gabor#, STFC (RAL), ASTeC, Chilton, Didcot, U.K.
A. Bosco, G. Boorman, G. Blair, RHUL, Physics Department, London, UK
A.P. Lechtford, STFC (RAL) Isis, Chilton, Didcot, UK

Abstract

The Front End Test Stand (FETS) is an R&D project hosted at Rutherford Appleton Laboratory (RAL) with its aim to demonstrate a high power, fast chopped H- ion beam. Possible candidates of applications are Isis upgrade (RAL neutron source), future spallation sources or the Neutrino factory. The high beam power may cause problems due to its thermal power deposition on diagnostics parts introduced into the beam so non-invasive beam instruments are highly preferred to avoid those problems. Diagnostics for H- beams can benefit of laser light where photons with suitable energy are able to detach the additional electron. This method is applied to a beam profile monitor close to the ion source of the FETS beam line. The paper gives a status report of the ongoing process of experimental set-up and provides a detailed discussion of problems and recent changes.

INTRODUCTION

High Power Proton Accelerators (HPPA), capable of producing beams in the megawatt range, have many applications, including drivers for spallation neutron sources, production of radioactive beams for nuclear physics, hybrid reactors, transmutation of nuclear waste, and neutrino factories for particle physics [1,2]. These applications require high quality beams and call for significant technical development, especially at the front end of the accelerator, where beam chopping at an energy of a few MeV and high duty cycle (1…10%) are required in order to minimise beam loss and induced radioactivity at injection into downstream circular accelerators.

The Front End Test Stand (FETS) [3] project, a UK based collaboration involving RAL, ASTeC, Imperial College London, University of Warwick, Physical Department of Universidad del Pais Vasco, and Bilbao, Spain, will test a fast chopper in a high duty factor MEBT line. More recently the project is also supported by Royal Holloway, University of London. The key components of the beamline are an upgraded Isis Penning ion source with 65keV beam energy, a three solenoid Low Energy Beam Transport (LEBT) line, a high duty factor 324 MHz Radio–Frequency Quadrupole (RFQ), a MEBT section including a novel Fast–Slow beam chopper and a comprehensive set of beam diagnostics. The ion source and LEBT are currently being commissioned; the status is described in [4,5,6].

* work supported with a laser loan from Goethe-University Frankfurt, Institute of Applied Physics IAP, Germany
# corresponding author: christoph.gabor@stfc.ac.uk

Photo detachment used for beam diagnostics

For negatively charged particle beams the photo dissociation technique (also called photo detachment) offers an elegant solution to do non destructive diagnosis. Photons with an energy above the threshold for photo dissociation (H- binding energy ~0.75eV) can be used to partially neutralize the beam. For H-, and a photon with an energy of 1.5eV, the maximum cross section for photo neutralization $H^- + \gamma \rightarrow H^0 + e^-$ is about 4.0* 10^{17} cm^2. Calculations of the cross section [7,8,9] and the particle yield [10] respectively in previous experiments [11] have demonstrated that a Nd:YAG laser (2nd harmonic Nd:YAG as well diode pumped solid state (DPSS) Lasers are also possible) can be used as an effective light source.

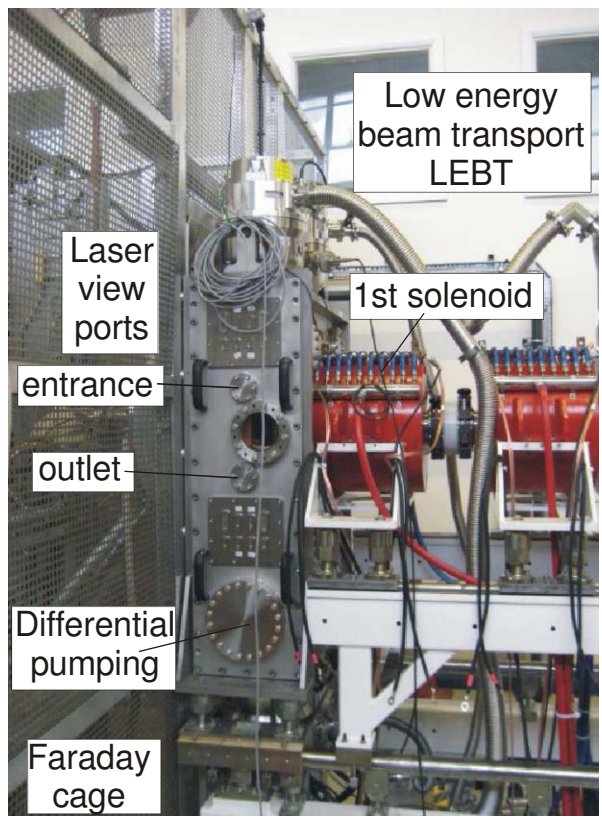

Fig 1: The differential pumping tank housing the detector with the laser mirrors. The first solenoid is as close as possible due to beam transport restrictions.

Behind the laser neutralization number and distribution of either the detached electrons or the neutrals produced in the interaction region can be analysed while the ion beam is still in use. Therefore charge separation, usually achieved using a magnetic dipole field, and a particle detector system are required. As neither the laser photons nor the recoiling photodetached electrons transfer a

significant momentum to the H^o atoms, the beam of neutralized ions has the same distribution in the six dimensional phase space as the primary beam. It is therefore appropriate to measure the H^0 beam distribution with a detector system with spatial resolution [12].

The electrons are more suitable when the total amount of neutralization, such as for the laser wire profile measurement technique, or fast detection, as for energy spread measurements using a Time of Flight (TOF) method, is required. Because of the low velocity and therefore magnetic rigidity of the electrons detached of a 65 keV H^- beam, the electrons will be (post)accelerated to 2 keV as they enter the dipole magnet to reduce any deflections by stray fields.

The final aim is to combine measurements with some computational tomographic method like the Algebraic Reconstruction Technique ART [13,14] to get the correlated transverse beam distribution of the ion beam.

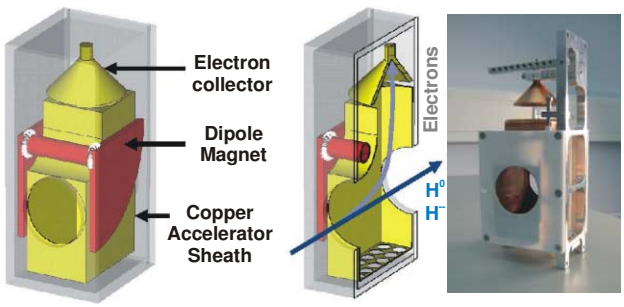

Figure 2: The detector consists of an accelerator sheath to bring the detached electrons up to speed, a magnet to separate and the Faraday cup, also biased. Not shown a suppression ring at the entrance to shield the detector of e^- produced by gas stripping in front of the detector.

EXPERIMENTAL SET-UP

The detector design for the detached electrons has been carried out by D.A. Lee [16,17]. The whole experiment is integrated in a pumping vessel, shown in Fig.1. Longitudinal space is very limited thus the first solenoid is mounted as close as possible onto the back wall of the vessel. The detector utilizes a small dipole to bend the detached electrons into the Faraday cup. Due to the low energy an acceleration sheath has been implemented to bring the particles up to +2000 V; see Figure 2. The performance of the detector is given by the voltage settings for acceleration sheath, suppression ring and bias of the Faraday cup and the magnet current of the dipole. A more detailed description of the basis of the instruments see [12,15]. The laser used for the measurements is a 500 mW, frequency doubled, diode pumped Nd:YVO_4 laser, operation at 671 nm achieving approximately 90% of the maximum photo-detachment cross section.

To compute a correlated 2D distribution (with a tomographic method, e.g., ART) two pairs of mirrors were prepared to be moved on linear and rotatable vacuum suitable piezo-driven stages to scan the laser at a variety of angles through the ion beam. Due to tight space, small mirrors were used mounted on custom-made mirror holders without adjuster screws.

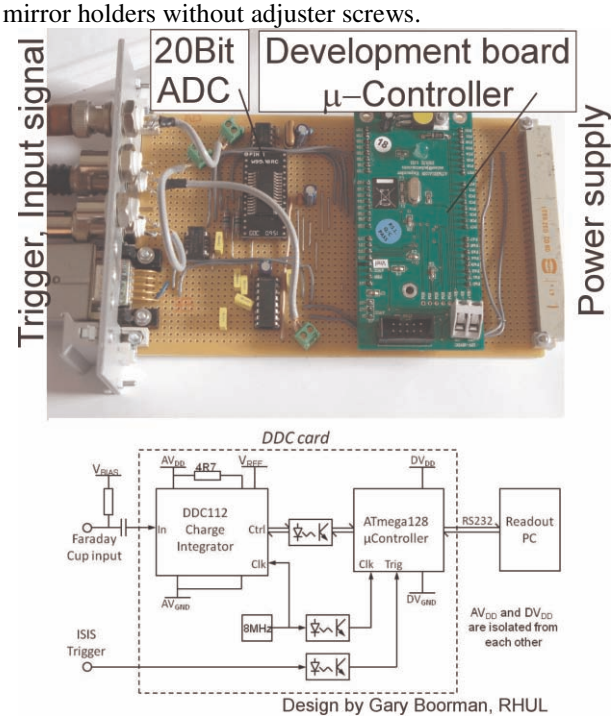

Figure 3: *Top*: The strip-board built for test purposes. The readout of the ADC is controlled by an ATMega microprocessor sitting on a development board. *Bottom*: the new circuit to avoid ground loop problems.

Initial test results

A first phase of commissioning the beam profile monitor took place in summer 2009 using the described set-up. The results are presented in detail in [17]. Here, only a brief summary should motivate further developments.

The experiments were a success insofar as functionality of the detector has been shown. But it appeared that the beam size is much bigger than assumed in simulations, so the detector hole acts as a collimator. This produces a large background signal exceeding the maximum possible charge which can be accumulated with the integrator chip DDC112. Therefore, detector settings were chosen to minimise the total average charge enabling the most sensitive measurement range of the ADC. Integrated over several thousand pulses the accumulated charge gave a mean of about 290 pC with a variance of 5 pC. This width is mainly caused by the pulse-to-pulse stability of the source and is more than you can achieve with the present DPSS laser.

CURRENT INSTALLATION STATUS

Different possibilities seem feasibly to improve the system to measure photo detached electrons. Since the closed marriage between vacuum vessel and detector it would be rather difficult to change the design fundamentally, hence a more evolutionary solution was preferred. The key to addressing the discovered problem

with the background is to go up in laser power and also to simplify the whole set-up as much as possible. Simplicity lets us prove the principle with special focus on the mirror arrangement inside the vacuum, i.e., a fixed, central position. After this basic demonstration, the aim of measuring correlated 2D beam profiles would be approached in a more empirical step by step process.

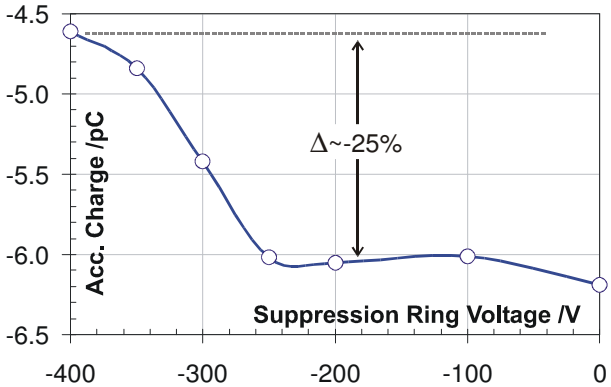

Figure 4: Variation of the suppression ring voltage. The data were taken without Faraday cup bias but an acceleration sheath potential of +1.8kV and a magnet current of 0.8A.

Laser and optics

The Institute of Applied Physics IAP, Goethe-University Frankfurt kindly loaned us a more powerful laser to carry out the photodetachment experiments. This device has a thin-disk Yb:YAG crystal emitting at 1030 nm and providing very small radius and divergence angle, and an M^2 close to theoretical possible minimum. The device has been used already for photodetachment experiments at a different set-up in Frankfurt [18].

Various other changes have been introduced as well. First of all, the optics elements (mirrors and holders; vacuum windows) have been adapted to the change in wavelength. A lot of effort was spent to improve the rigidity of all the opto-mechanical mounts inside and outside of the vacuum.

A new optical breadboard was designed and built which can be securely mounted on the outside of the drawer of the differential pumping vessel (Fig. 1), providing space for additional alignment measures. This extended breadboard is necessary due to the difference in position of the drawer unit between open and closed.

Readout electronics

The electronics mean here the current amplifier from Texas Instruments DDC112 controlled and readout by an Atmel ATMega microprocessor [15]. This concept has been migrated to a temporarily strip-board solution, Fig.3, for development purposes only. Tests with a TGA1244 pulse generator have been carried out demonstrating problems to measure charges down to sub-nano Coulomb due to a ground loop issue. This should be fixed with a new layout, also shown in Fig.3. In near future the complete electronics will be build with a PCB which will reduce problems with noise or ground loop issues further.

Another important aspect is the software to control the microprocessor and store date on a computer. So far, it was not possible to run the ADC in a so called non-continuous mode. In continuous mode the integration time is fixed given by the main trigger but in non-continuous operation it is possible to delay the integration respectively to the trigger (this is equivalent with integration across the full ion source pulse) as well as changing the integration time.

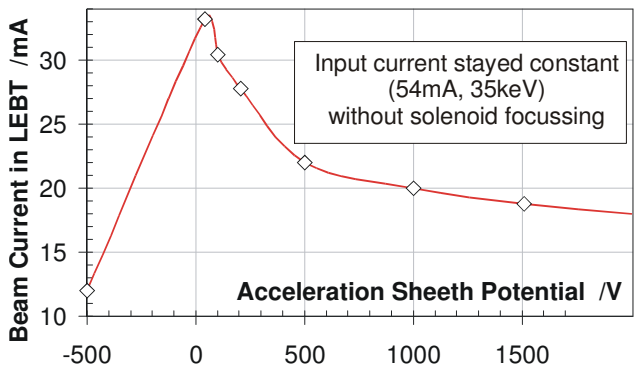

Figure 5: Variation of the jacket voltage, everything else were off. The potential of the acceleration sheath influences significantly the ion beam.

BACKGROUND MEASUREMENTS

To understand the background behaviour, several parameters of the detector were varied, and the Faraday cup signal was monitored with a scope. If not stated differently, the source produced a 54 mA beam at 35 keV beam energy. Compared with previous measurements, the behaviour is similar, but only qualitatively. The absolute numbers show a different picture, i.e., these background measurements can vary from day to day, and even if the source settings are identical the background behaviour can be quite different.

In Fig. 4 the voltage of suppression ring was varied but the sheath potential was kept constant at +1.8kV as well as the dipole (0.8A), and the Faraday cup bias was off. In the best case, a reduction of 25% could be achieved. It might be possible that the remaining signal comes from electrons produced within the detector. The suppression ring is only supposed to shield electrons due to residual gas stripping further upstream of the profile detector.

The various potentials influence not only the Faraday signal but also the beam transport through the detector. Figure 5 shows the variation of the acceleration sheath potential but everything else off. The voltage has the strongest impact on beam transportation because it has the highest potential and geometrically, the jacket shows similarities to an einzel lens. The beam current was monitored with current transformers upstream and downstream of the detector (between the second and third

solenoid of the low energy beam transport, all solenoids off).

As shown in Figure 5, the drop is significant and can be interpreted as part of the background problem since the beam widens due to the external potential by influencing the space charge compensation; a more detailed discussion is provided in [19].

Having that in mind, the variation of the beam energy should also have an influence on the background because the strength of the transverse focusing changes by varying the post acceleration, i.e., beam energy [19]. To check this aspect the source settings were not changed but the post acceleration was varied between 25 and 60 keV, shown in Figure 6. As a starting point, a 35 keV beam was used, where the signal minimized as good as possible (+1800 V acceleration sheath, +300 V cup bias, 800V grid potential, magnet 0.8A).

Keeping the detector constant, the background signal depends on the post-acceleration, but only low energies show a clear result where a mismatched beam produces a huge positive signal, an indication of positive residual gas ion created by beam losses. Higher beam energies show a change more at the beginning; towards the end of the ion source pulse, the influence is very small. The two peaks within the first 100 μs may have to do with the rise time of the ion source extraction power supply, [19] but that need more quantified investigations.

Note the smaller signal towards the end of the ion source pulse compared to the ringing during the first 80-100μs. Regarding the photodetached electrons, the non-continuous operation mode of the ADC helps to avoid overloading the input capacitance of the charge integrator.

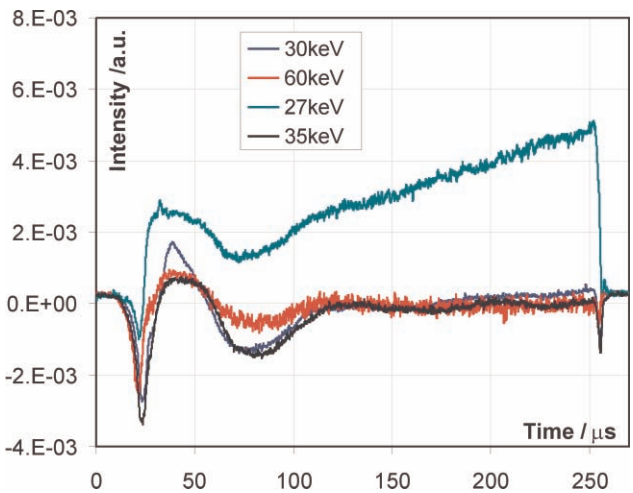

Fig. 6: The background signal was minimised for 35keV beam keeping the detector settings constant. Then, the beam energy was varied:

SUMMARY AND OUTLOOK

First tests of the detector, laser and optics took place in late summer 2009 (summarized in [16,17]) and demonstrated functionality of the detector, but also identified several problems, which need to be addressed.

One outcome of this work is a need for increased laser power to prove the principle of photodetachment with this experiment. Thankfully, the Goethe-University Frankfurt, IAP, supports this project with a suitable cw laser. Several changes in the electronics, optics and mechanical set-up have been performed to adapt the new laser and to simplify the experiment.

At the moment the focus is on principle demonstration experiments without scanning the laser through the ion beam. This demonstration of photo detachment should be achieved in the very near future. Further steps, with better alignment feedback, beam profile measurements should be possible in horizontal direction.

Still, the final aim is to integrate rotatable mirrors to make accessible the full 2D beam distribution. Measurements will be combined with computational algorithms like the Algebraic Reconstruction Method (ART) or possibly Maximum Entropy (MaxEn)t [20].

A strong argument for photodetachment is the renunciation of mechanical parts inside the beam, i.e., having a non-invasive technique to minimize the influence on beam transportation. In the long term the beam losses shown in Figure 5 caused, by the acceleration potential of the detector, are not acceptable and need to be addressed as well.

One solution could be to move the detector to a more suitable position at the beamline with a smaller beam radius. That may imply a higher beam energy further downstream of the RFQ. Radius and divergence angles are typically smaller than at the ion source energy but the photodetached electrons also have higher energy. The latter means that the potential of the acceleration sheath can be reduced, since the detached electrons of a 3 MeV H- beam are at 1.6 keV, compared to the ~40 eV of photodetached electrons from a 65 keV ion beam.

ACKNOWLEDGEMENT

This diagnostics work benefits greatly from the laser loan from the Goethe-University of Frankfurt, Institute of Applied Physics. The author wants to thank the whole FETS team and all its members for comprehensive support, but in particular D. Faircloth and S. Lawrie for running the ion source and P. Savage for mechanical engineering. Grahame Blair made the fruitful cooperation between RHUL and RAL possible. The initial experimental set-up was designed and built mainly by D.A. Lee and J.K. Pozimski.

REFERENCES

[1] T.R. Edgecock, 6th Int. Workshop on Neutrino Factories and Superbeams (NuFact 2004), July/ August 2004, Osaka.

[2] R. Maier, High power proton LINACs: Application and design concepts, Proc. of EPAC, 2002, pp.174–178, Paris, France.

[3] D.J.S. Findlay, M.A. Clarke–Gayther, D.C. Faircloth, et al., The RAL Front End Test Stand, Proc. of NuFact 2004, Osaka University, Japan, pp. 323–325.

[4] D.C. Faircloth, S.R. Lawrie, M. Whitehead, T. Wood, A. P. Letchford, C. Gabor, P. Wise, M. Perkins, M. Bates, M.E. Westall, J.K. Pozimski, P.J. Savage, D. Lee, "Initial results from the Front End Test Stand high performance H- ion source at RAL", MO6RFP040, PAC09, Vancouver, Canada, May 2009.

[5] S.R. Lawrie, D.C. Faircloth, A.P. Letchford, C. Gabor, J.K. Pozimski, "Plasma meniscus and extraction electrode studies of the Isis H-ion source ", Rev. Sci. Instr., Feb. 2010, Part II. Vol. 81, 2, Proc. of the 13th Int. Conf. on Ion Sources, Sept. 2009, 02A707.

[6] D.C. Faircloth, S.R. Lawrie, A.P. Letchford, C. Gabor, P. Wise, M. Whitehead, T. Wood, M.E. Westall, D. Findlay, M. Perkins, P. Savage, D.A. Lee, J.K. Pozimski, "The front end test stand high performance H- ion source at RAL",Rev. Sci. Instr., Feb. 2010, Part II. Vol. 81, 2, Proc. of the 13th Int. Conf. on Ion Sources, Sept. 2009, 02A721

[7] J.T. Broad, W.P. Reinhardt, One and two photo ejection from H-: A multichannel J-matrix calculation, Phys. Rev., 14, 6(A), 1976.

[8] M. Daskhan, Photo-detachment cross section of the negative hydrogen ion, Phys. Rev., 28, 5(A), 1983.

[9] M.P. Ajmera, K.T. Chung, Photodetachment of negative hydrogen ions, Phys. Rev., 12, 2(A), 1975.

[10] C. Gabor, O. Meusel, J.K. Pozimski, Status report of the Frankfurt H- LEBT including a non-destructive emittance measurement device, Proc. of 9th Internat. Sym. of PNNIB, 2002, CEA/ Saclay, Paris, France.

[11] W.B. Cottingame, G.P. Boicourt, J.H. Cortez, W.W. Higgings, O.R. Sander, D.P. Sandoval, Non-interceptive Techniques for the Measurement of Longitudinal Parameters for Intense H-, IEEE Trans. Nucl. Sci., NS-32, 1985, p.1871, Proc. Particle Accelerator Conference, PAC 1985.

[12] C. Gabor, D.A. Lee, J.K. Pozimski, A. Letchford, "Laser based beam diagnostics for the front end test stand (FETS) at RAL", TUPCH019, EPAC06, Edinburgh, Scotland, UK, June 2006.

[13] D.A. Lee, J.K. Pozimski, C. Gabor, P. Savage, "A laserwire beam profile measuring device for the RAL front end test stand", TUPB11, DIPAC07, Venice, Italy, May 2007.

[14] D.Rapira, et al. " The Algebraic Reconstruction Technique (ART)", 2P057, PAC97, Vancouver, Canada, May 1997.

[15] D.A. Lee, C. Gabor, J.K. Pozimski, "Laser-based beam diagnostics for the front end test stand at RAL", TUPC058, EPAC08, Genoa, Italy, June 2008.

[16] D.A. Lee, P. Savage, J.K. Pozimski, C.Gabor, "A laser-based beam profile measuring instrument for the front end test stand", PAC09, Vancouver, Canada, May 2009.

[17] David A. Lee, Ph.D., December 2009, "A laser-based beam profile monitor for the RAL front end test stand", London Imperial College, London, UK.

[18] C. Gabor, H.Klein, O.Meusel, U.Ratzinger, J.K.Pozimski, " Experimental results of a non-destructive emittance measurement device for H- beams", PAC05, Knoxville, Tennessee, USA, May 2005, RPAT001.

[19] C. Gabor, D.C. Faircloth, D.A. Lee, S.R. Lawrie, A.P. Letchford, J.K. Pozimski, "Diagnostic experiments at a 3MeV test stand at Rutherford laboratory (UK)", Rev. Sci. Instr., Feb. 2010, Part II. Vol. 81, 2, Proc. of the 13th Int. Conf. on Ion Sources, Sept. 2009, 02B718.

[20] C. Gabor, C.R. Prior, A.P. Letchford, J.K. Pozimski, "Emittance measurement instrument for a high brilliance H- ion beam", LINAC08, Vicorioa, British Columbia, Canada, 2008, TUP084.

MULTI-CHANNELTRON BASED PROFILE MONITOR AT THE ISIS PROTON SYNCHROTRON

S.A. Whitehead, P.G. Barnes, G.M. Cross, S.J. Payne, A. Pertica
STFC, ISIS Facility, Rutherford Appleton Laboratory, UK

Abstract

The gas ionisation beam profile monitor is a well established piece of diagnostic hardware. The use of active devices such as Microchannel Plates (MCPs) and Channeltrons within such a diagnostic can present problems with gain differences between channels. At the Rutherford Appleton Laboratory we have produced a beam profile monitor that uses an array of 40 individually powered Channeltrons; these devices were chosen over the MCP for their robustness and longer lifetimes. These Channeltron devices (like MCPs across their surface) can suffer from large variations in gain at the desired operating voltage. We have successfully shown that an additional in-built calibration system using a single, motorised, Channeltron can overcome these issues. We report on the work to build the calibration system, and the 40 Channeltron array. The PXI (National Instruments) system used to control the motor drive and provide the data acquisition is also covered. Also we report on the new high voltage drift field to reduce space charge effects on the beam profile. Ongoing work on understanding how the drift field as well the beam field affects the measured profile is also discussed.

INTRODUCTION

The ISIS facility at the Rutherford Appleton Laboratory is currently the world's most productive neutron spallation source. The rapid-cycling proton synchrotron operates at 50 Hz and accelerates two proton bunches (total of ~3.5×10^{13} protons) from 70 MeV to 800 MeV within the 10 ms acceleration period, delivering a total beam power of ~0.24 MW to the target. Accurate determination of the beam profile is important for improving injection and acceleration efficiencies as well as helping to reduce beam loss. Recent major upgrades to ISIS, like the 2nd harmonic system and Target Station 2, have resulted in higher beam currents within the accelerator ring. This increase in beam intensity has placed even more emphasis on the need for faster, more accurate profile monitors. This need has led to our current upgrade programme aimed at improving the ISIS profile monitoring systems.

ISIS RING PROFILE MONITORS

The original, and still used, gas ionisation profile monitors installed in the ISIS accelerator ring employ a single electron multiplier (Channeltron) to measure the +ion current produced from the interactions between the proton beam and the residual gas in the beam pipe. The single Channeltron profile monitor (SCPM) measures the beam profile in one plane only. The Channeltron is either stepped horizontally across the top of the proton beam or moved vertically up one side of the monitor. In each case the Channeltron covers a total distance of 240 mm in 5 mm steps. A high voltage drift field (30 kV) sweeps the +ions into the Channeltron device. At present we have five of these SCPMs, three measuring the horizontal plane and two measuring the vertical plane. Using these devices real-time profiles cannot be obtained because the mechanical system takes several minutes to complete each scan. The desire to obtain real-time profiles for setting up the synchrotron and carrying out machine physics studies of the ISIS beam has prompted the development of a new multi-channel profile monitor. This new monitor has an array of 40 fixed Channeltrons spanning 240 mm across the beam thereby allowing it to simultaneously collect beam profile information.

EVOLUTION OF THE MULTI-CHANNEL PROFILE MONITOR

The Channeltrons are manufactured by the company Photonis [1] (previously Burle Industries) and are their standard 4800 series device. These Channeltrons have a collection aperture of 15.75 mm × 4.5 mm and a gain of ~10^4 when biased with -1300 V (our normal operating voltage). An example of a 4800 device is shown in Figure 1.

Figure 1: Channeltron on left is the 4800 series of the Channeltron array. On the right is the 4700 series still used in the old SCPM.

The decision to use Channeltrons rather than a Microchannel Plate was influenced by a number of factors. As the existing single-channel profile monitor already used a Channeltron (Photonis type 4700 device, shown in Figure 1) we already had a good working knowledge of this technology. The 4800 series device is

small enough to assemble into an array giving a 6 mm centre to centre spacing, which is similar to the 5 mm step size of the existing motorised system. The smaller device also offered the same electrical characteristics as the older 4700 and therefore we could use the same front end electronics as our DAQ system. We also considered the fact that Channeltrons are easier to handle than MCPs, they are more robust and have a greater lifetime, (roughly 10 times). Also, as the beam at ISIS is relatively large where the profile monitor is positioned (~100 mm) this means we have sufficient data points using a Channeltron array (with 6 mm spacing) and do not require the finer resolution that can be achieved using an MCP and custom anode assembly.

This first multi-channel profile monitor (MCPM) was a horizontal plane monitor and the design consisted of 4 Macor (machine-able ceramic) blocks, each housing 10 Channeltrons to form a 40 detector array [2, 3]. The completed monitor can be seen in Figure 2. All 40 Channeltrons were powered from the same 0-2.5 kV power supply. Initial measurements with this design highlighted significant variation in the gains of individual Channeltrons, shown in Figure 3. This meant that the MCPM would need to be calibrated in order to recover the true beam profile.

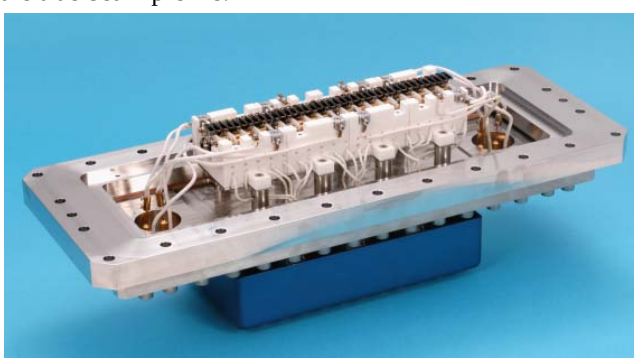

Figure 2: First generation multi-channel profile monitor using a (40) Channeltron array.

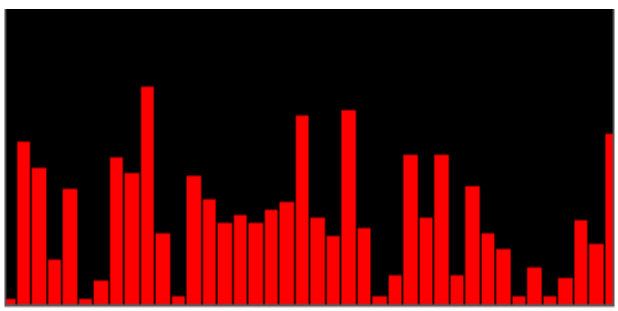

Figure 3: Raw beam profile data.

The calibration of the multi-channel array is achieved using an original motorised profile monitor which is located in the same stainless steel vacuum vessel as the new MCPM. This calibration relies on the fact that the single Channeltron in this system does not suffer from any gain variation during a profile scan. Figure 4 shows beam profile data after calibration.

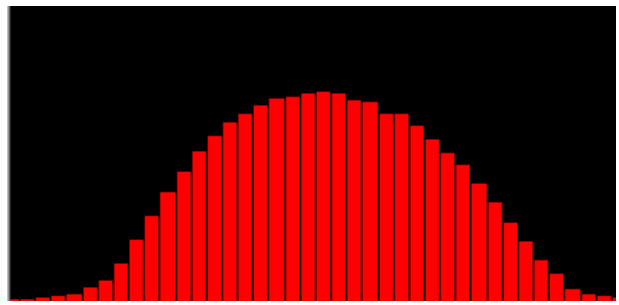

Figure 4: Calibrated beam profile data.

In an attempt to solve the gain variations found in the original MCPM, the second design split the 40 detectors into 10 blocks of 4 Channeltrons. The 4 Channeltrons in each block had been ‘gain matched’ at the Photonis factory and each block was given its own power supply to allow adjustment of gain between blocks. Unfortunately the gain matching of the detectors appeared not to hold within the synchrotron environment and we found that the individual gains of the Channeltron devices were as mismatched as on the first MCPM. Figure 5 shows the ‘improved’ profile monitor in position in the ISIS synchrotron. This monitor measures the beam profile in the vertical plane.

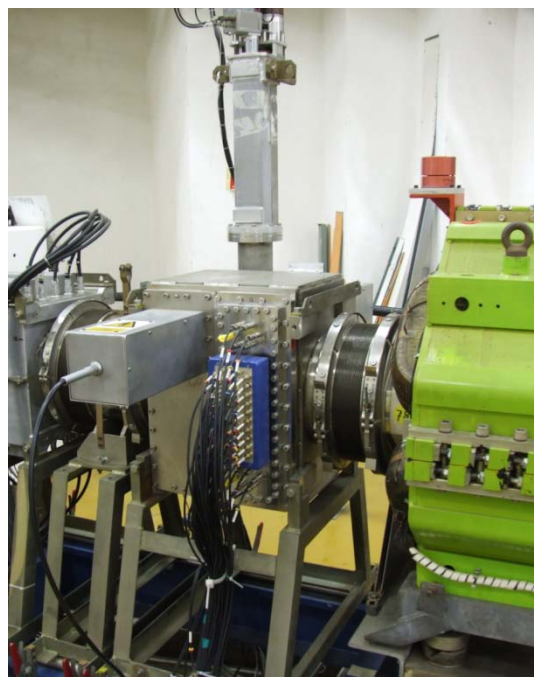

Figure 5: Second generation multi-channel profile monitor installed in the ISIS synchrotron. The motor drive of the SCPM can be seen diagonally opposite.

In a second attempt to reduce the effects of Channeltron gain variation on the system, a third generation design is currently under construction and consists of 40 Channeltrons, still arranged in 10 blocks of 4, but with each Channeltron having its own individual power supply (shown in Figure 6). This design will allow the gains of each Channeltron to be closely matched by varying the individual power supply voltages. This third generation

MCPM is scheduled to be installed in the ISIS synchrotron in the autumn of 2010.

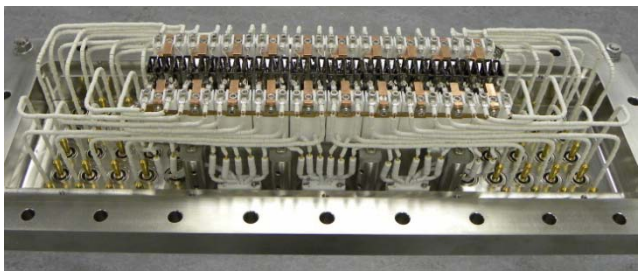

Figure 6: Third generation multi-channel profile monitor.

DATA ACQUISITION AND CALIBRATION

The data acquisition system consists of a National Instruments PXI controller and chassis and five 8-channel analogue input cards which are sampled simultaneously using a timing and synchronisation card [4]. On every 50Hz pulse of ISIS each of the 40 channels are read for 10ms at an interval selected by the user, down to 10us. From the LabVIEW user interface the user can view the profile of the beam at a selected time, view graphs that display the 90% beam widths and centres over the acceleration cycle and view a 3D plot of all the profiles (Figure 7). The user can also choose to subtract background data and save data. The saved data can be loaded and superimposed over the currently selected profile.

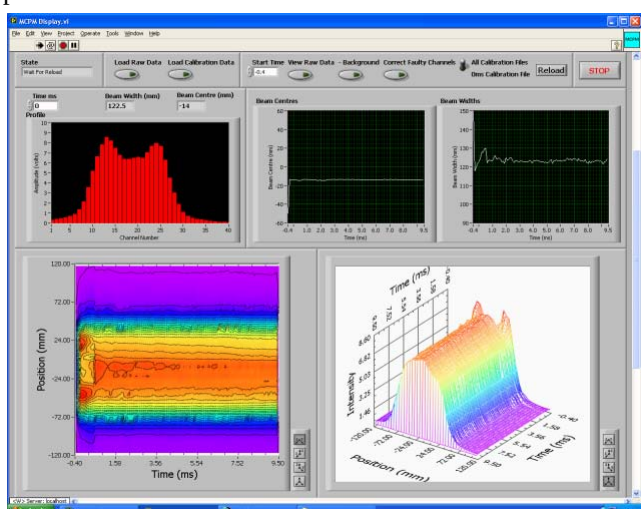

Figure 7: LabVIEW User Interface

During the calibration procedure the SCPM moves across the beam using a step size that aligns it to the transverse positions of the 40 Channeltrons in the MCPM. The data is saved to a database. Using the LabVIEW HTTP server the MCPM program can access the data and use it to create a calibration file which is then applied to the raw data from the MCPM. The PXI system has made the process of simultaneously collecting and analysing large amounts of data from each of the 40 channels relatively simple.

BEAM PROFILE SIMULATION

A beam profile simulator has been developed so that all the electronics and computer hardware and software can be tested in the absence of the ISIS proton beam. The simulator is a microcontroller which can be switched into the circuit using a digital line on a PXI card. Different profiles are preloaded to the microcontroller and selected using a digital I/O card. A signal generator card provides a waveform equivalent to the intensity fall off that occurs during the acceleration cycle. This waveform is applied to potentiometers which adjust the output level of each channel.

SINGLE-CHANNEL UPGRADE

The old motor driven single channel profile monitors (SCPM), have now taken on a new role with the development of the MCPM. Their new function, as a calibration tool for the MCPM has meant that their accuracy, reliability and longevity are vital. To ensure that this is the case, the mechanics of the SCPMs are being re-designed using high quality linear stages with radiation hard motors and wiring.

To ensure accurate calibrations, the new stepper motor driven Channeltron will be pre-aligned with the 40 set locations of the Channeltron array in the MCPM diagnostic. This alignment will be carried out in the lab prior to installation of the monitors. Every new MCPM will have an upgraded SCPM as its calibration system.

FUTURE WORK

The accuracy of the beam profile measurements obtained from a gas ionisation profile monitor are largely dependent on the electric field that drives the +ions and the space charge properties of the proton beam [5]. Both can cause large inaccuracies in the measured profile.

At ISIS, space charge levels are highest during injection into the synchrotron and beam bunching. For the MCPM to provide accurate beam profiles linear ion trajectories between generation point and detection must be assumed. In reality the electric field of the beam itself, which acts radially outwards from the centre of the beam, will deflect the ions and widen the detected beam width.

Measurements on the current system, using drift field voltages from 10 kV to 30 kV have shown a significant change in measured beam width with voltage [6], as shown in Figure 8. Looking at one specific time during the acceleration cycle, in this case 0 ms, Figure 9 shows the measured points fitted to a curve and extrapolated. This highlights the possible increase of accuracy that could be achieved with increasing drift field. The measured beam width at 30 kV is 120 mm, this is reduced to 114 mm at 60 kV and reduced further still to 112 mm at 80 kV. Looking at these results it was decided that a bias field of 60 kV provided a worthwhile increase in accuracy without the cost and technical challenges that would be faced with higher voltages.

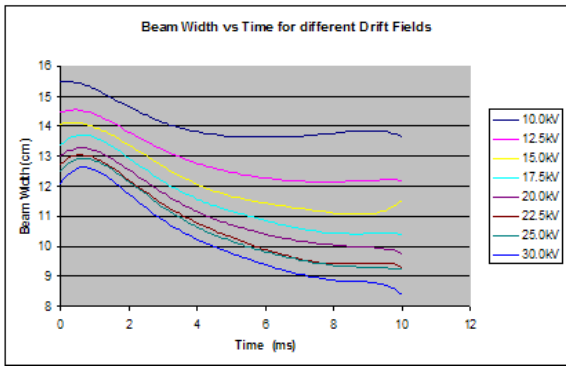

Figure 8: Measured beam width for different drift field voltages over the ISIS acceleration cycle.

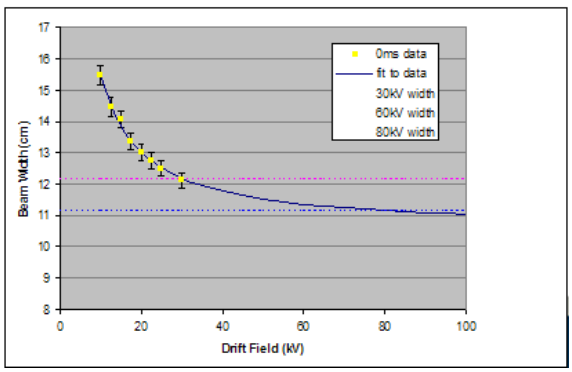

Figure 9: Beam width measurements at 0ms.

This 0-60 kV bias field voltage will allow the opportunity to study the effects of space charge on the profile measurement in greater detail and allow our current space charge models to be checked.

A model of the profile monitor showing electrostatic potential distributions caused by the drift field and space charge effects is currently being developed using the finite element modelling package CST Studio Suite [7]. The potential distributions in the longitudinal plane are shown in Figure 10 and in the transverse plane are shown in Figure 11. It is clear that the curved electric field distribution shown in the transverse plane would have a distorting effect on the beam profile. The distortion is due to the lack of shaping field electrodes within the monitor which were never part of the original design. The CST work will help determine by how much shaping field electrodes could improve the profile monitor data.

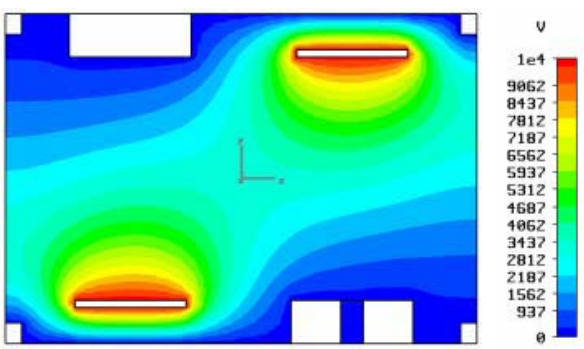

Figure 10: Longitudinal electrostatic potential distributions in the ISIS ring profile monitors.

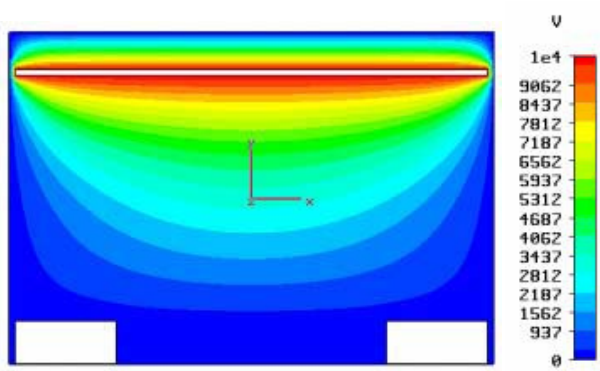

Figure 11: Transverse electrostatic potential distributions in the ISIS ring profile monitors.

SUMMARY

We have shown the effectiveness of the new Channeltron based gas-ionisation profile monitor used in the ISIS accelerator ring. Issues regarding calibration affect profile monitor systems that use active devices like Channeltrons or Microchannel Plates. The use of a separate single Channeltron device that can be driven across the beam to provide calibration for the Channeltron array has proved very effective in our application. Issues regarding space charge effects will be addressed using the new 60 kV variable drift field. Electrostatic simulation work of the drift field, plus work proposed using particle tracking software is being carried out with the aim of improving the profile data. This work might also lead to the installation of shaping field electrodes.

Further research into profile monitor distortions due to the drift field will be carried out in the extracted proton beam line (EPB) to Target Station 1. We are proposing to install an MCPM device in the EPB at a point where there are three harp style wire profile monitors and no quadrupole magnets. Comparison between the harp monitors and the MCPM will yield information on the inaccuracies produced by the high voltage drift field of our present gas ionisation system.

REFERENCES

[1] See 'Channeltron Electron Multiplier handbook', BURLE industries, www.burle.com

[2] S.J.Payne *et.al* 'A self calibrating real time multi-channel profile monitor for the ISIS proton synchrotron., DIPAC'07, Venice, Italy, 2007, p364

[3] S.J.Payne *et.al* 'Beam Diagnostics at ISIS' HB2008 conference, Nashville, TN, 2008

[4] For examples of PXI DAQ systems see National Instruments, http://www.ni.com.

[5] B. G. Pine *et al*, 'Modelling of Diagnostics for Space Charge Studies on the ISIS Synchrotron', EPAC '06, Edinburgh, August 2006, p1082, (2006)

[6] S J Payne *et al*, 'Investigation into the relationship between the drift field voltage and measured beam width on the ISIS ring profile monitor system',

Rutherford Appleton Laboratory ISIS Machine Physics Report, IADM/MPS/2.1/03 (2003).

[7] R. E. Williamson *et al*, 'Analysis of measurement errors in residual gas ionisation profile monitors in a high intensity proton beam', EPAC '08, Genoa, June 2008, p.1317 (2008).

OPERATIONAL USE OF IONIZATION PROFILE MONITORS AT FERMILAB*

James Zagel, Andreas Jansson, Thomas Meyer, Denton K Morris, David Slimmer, Todd Sullivan, Ming-Jen Yang, Fermilab, Batavia, IL 60439, U.S.A.

Abstract

Ionization profile monitors (IPMs) are installed in the Fermilab Booster, Main Injector and Tevatron. They are used routinely for injection matching measurements. For emittance measurements the IPMs have played a secondary role to the Flying Wires, with the exception of the Booster (where it is the only profile diagnostics). As Fermilab is refocusing its attention on the intensity frontier, non-intercepting diagnostics such as IPMs are expected to become even more important. This paper gives an overview of the operational use of IPMs for emittance and injection matching measurements at Fermilab, and summarizes the future plans.

INSTALLATION LOCATIONS AND OPERATING CONDITIONS

IPMs are used in three accelerators at Fermilab. Booster and Main Injector IPMs are designed to collect a data sample once per machine revolution. The Booster has two electrostatic units that collect ions using an 8 KV clearing field. These units collect data in the Booster throughout its complete operating cycle of about 20,000 turns. At injection (400 MeV) the revolution period is 2.25 μsec. At extraction (8 GeV) this period drops to 1.5 μsec. The Main Injector has two electrostatic units, one horizontal and one vertical, operating at 28 KV, collecting ions and producing data each 11.1 μsec. An additional horizontal unit was installed with a 1 KGauss magnetic field, and 10 KV clearing field which allows the collection of electrons,. The magnetic field confines liberated electrons to orbits smaller than the anode pick-up strips which minimizes the deleterious effect of space charge from the beam. The Main Injector IPMs are limited to the 65K samples of the current digitizer, however by skipping turns during acquisition, the full cycle can be measured. The Tevatron has two magnetic units of 1KGauss and a 10 KV clearing field. As explained later, these units are capable of sampling 36 proton and 36 antiprotons (pbars) bunches, turn by turn, for up to 1000 turns.

FRONT END INTERFACE

LabVIEW was chosen as the environment for the front end program because of its facilities for easily tying together different types of hardware (GPIB, VME, Ethernet) and software (Accelerator Control Network (ACNET), .dlls). The LabVIEW built-in graphical environment has also proved to be a significant help in debugging and commissioning the IPM systems. In normal operation, the system is controlled remotely through ACNET, but the front-end program provides complete functionality for running the system locally. Beam measurements are configured with a set of file based measurement specifications that include trigger and event types, timing delays, high voltage settings, analysis parameters, and logging preference. Measurements are initiated by activating a specification number through ACNET to the front end, which then configures the system hardware and waits for the specified trigger clock event. The triggering phase occurs in two parts. A pre-trigger is generated which initiates the hardware setup. and turns on the micro channel plate high voltage, This is followed by the event trigger, which starts the data acquisition. Data is collected using a beam synchronous clock. After acquisition, the front end analyzes the data using the selected parameters (turn by turn, averaging, start turn for analysis, and number of turns to analyze), and then returns the selected data and measurement parameters through ACNET. Raw data and measurement conditions are saved in binary files on the front end, and can be recalled into the front end program and reanalyzed.

The front-end code makes use of parallelism to take advantage of multi-core processors. There are three major tasks running: an event loop to detect front panel activity and handle ACNET commands, a monitor loop to track high voltage and receive remote commands, and a state machine to execute measurements and all other program functions. State machine functions are driven by a dynamically created command queue which can contain single or multiple commands. After the queued commands are executed, the state machine returns to an idle state. A second state machine was added to one of the IPM systems that does frequent measurements so that the front end could respond to select remote commands while it is waiting for a pre-trigger or trigger. The queue driven state machine design pattern has proved to be very flexible and efficient in operation, as well as easy to diagnose and debug system issues.

A significant benefit of using commercial PC's running LabVIEW is that it has enabled us to retain the front end hardware unchanged while being able to realize overall system performance improvements as faster PCs have become available.

ACNET CONSOLE INTERFACE

The ACNET user interface is comprised of two distinct parts, the console application page, and the pre-existing data collection engines.

*Operated by Fermi Research Alliance, LLC under Contract No. DE-AC02-07CH11359 with the United States Department of Energy.

The application page for the IPMs, as well as for most LabVIEW front-ends, is largely an attempt at duplicating the format and function of the LabVIEW front-end's own interface. From this application you can modify typical measurement parameters such as the start event, number of skipped turns per sample, and micro-channel plate high voltage levels for normal operations.

The ACNET console raw data plot, Fig.1, is a read back of the front-end data for a single Main Injector cycle measurement. It uses the Y axis to show intensity dots instead of false color used on the front-end. This results in a mountain range plot, which is more easily readable. A green dot marking the calculated center and red dots marking the sigma are added for clarity.

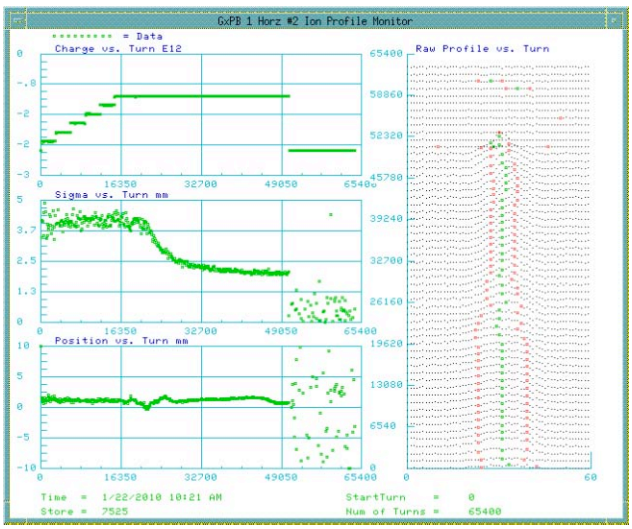

Figure 1: IPM application page plot showing (from top left) beam intensity, beam sigma vs. turn, beam position vs. turn, and on the right, the raw data vs. turn. Beam is extracted at turn ~50,000.

This plot shows sigma and position data during an 8 GeV to 120 GeV MI cycle. The reduction in sigma corresponds to the acceleration of the particles. Measurements are taken for each pbar transfer from the Accumulator to the Recycler Ring, and for each proton and pbar injection into the Tevatron. Fig. 2 shows a typical front end interface, albeit this one for Booster.

There are two types of logging engines, Shot Data Analysis (SDA), and the data logger called the Lumberjack. The SDA and Lumberjack systems are used to collect scalar data in four different situations:

- On a regular interval (once/minute)
- At some accelerator clock event plus delay
- At an accelerator sequence point i.e. HEP shot setup or pbar transfer
- On a state change generated by the front-end itself. (data ready)

These data collection engines allow the recall of any stored data, to be plotted over any time period of interest, for debugging of accelerator issues and system performance.

BOOSTER

The Fermilab Booster is a rapid cycling, 15Hz alternating gradient synchrotron accelerating 400MeV proton beam to 8GeV. Typically High Energy Physics (HEP) requires 4-5e12 particles per pulse. The practical minimum for a good measurement is 1e12.

The Booster IPM [1] is the only non-destructive tool for measuring its transverse beam profiles. The width of the distribution is determined from a fit to a Gaussian plus a linear background, and was calibrated to the crawling wire on the injection girder [2].

A typical beam width display measured throughout the entire Booster cycle is shown in Fig. 2, Fig. 3, and Fig. 4.

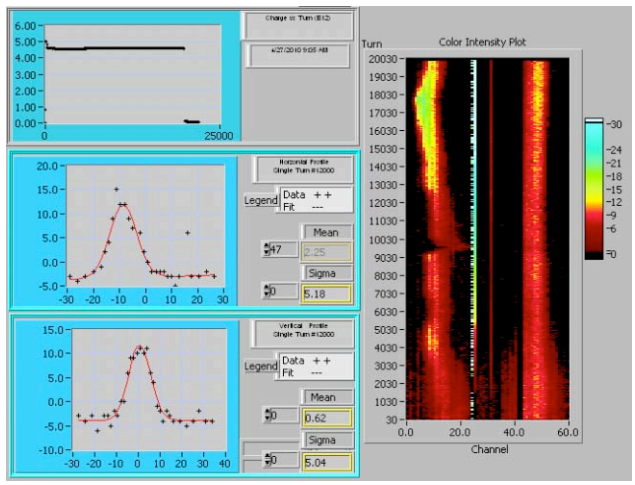

Figure 2: Front End interface to operate Booster IPM.

This data is a useful reference tool when comparing good running periods with changing efficiencies and/or beam intensities. Once a good reference set of beam profiles is taken, they are compared to the current conditions to observe if any changes have taken place. If the profiles differ during the current running period this leads to investigating what machine parameters may have changed. By comparing magnet settings and ramps during these periods of change a problem can be corrected.

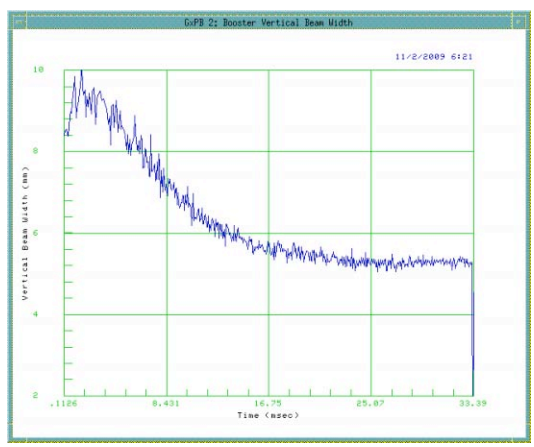

Figure 3: Booster beam Vertical Sigma vs Turn.

The IPM is used to better understand the increase in transverse emittance with its relation to beam intensity. The emittance growth is thought to be due to space charge effects [4]. The IPM is limited by beam variations that can make interpreting the data inconsistent from day-to-day. Some of this disparity can be caused by position changes in the beam due to tuning the beam or cycle-to-cycle variations. The beam can undergo RF manipulations on different beam cycles and in some cases the same beam cycle.

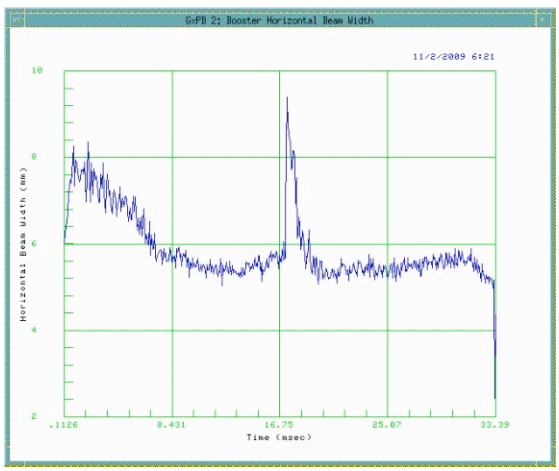

Figure 4: Booster beam Horizontal Sigma vs Turn. The spike is due to transition at about 5.2 GeV.

MAIN INJECTOR

The Fermilab Main Injector (MI) is a very dynamic machine used to accelerate both protons and pbars from 8 GeV to 120 GeV or 150 GeV with intensities from $5x10^8$ to $5x10^{10}$ particles per bunch and a peak total intensity of $5x10^{13}$ particles in the ring. At the current peak intensities the flying wires would be damaged if used so the IPM system[4] is the only method to measure sigma parameters in the Main Injector on high intensity cycles.

The injected 8 GeV protons and pbars can come from either the Proton Source via the MI-8 transfer line, the Accumulator storage ring via the P1 injection line, or from the Recycler Ring via the RR800 transfer line.

To monitor the lattice matching between the various transfer lines and the MI ring, the MI IPMs are configured to acquire data on the various transfer events associated with each type of transfer. The data is logged on every transfer and recorded in the SDA system described earlier.

With the data from the IPM we are able to track changes in the sigma/emittance and measure oscillations in the sigma, which is indicative of a lattice mismatch.

In November 2009 the MI IPMs showed an oscillation of ~1.3 mm on the sigma for protons injected into MI from the Booster, via the MI-8 line. Fig. 5 shows how increasing the quad magnet current by 9 Amps (5%) improved the lattice match resulting in sigma oscillations being reduced to less than 0.4 mm.

Correcting the match between the MI-8 injection line and the MI lattice reduced the beam spot size on the NUMI target after extraction at 120 GeV by almost 5%.

Automated data collected from the pbar injections into the MI from the Accumulator ring showed similar oscillations on the injected sigma which led us to adjust one of the transfer line quadruple magnet power supply currents by 3 Amps (0.8%). This reduced the sigma oscillations from 1.3 mm to 0.5 mm and resulted in a slightly smaller sigma and a 1% increase in pbar transfer efficiency.

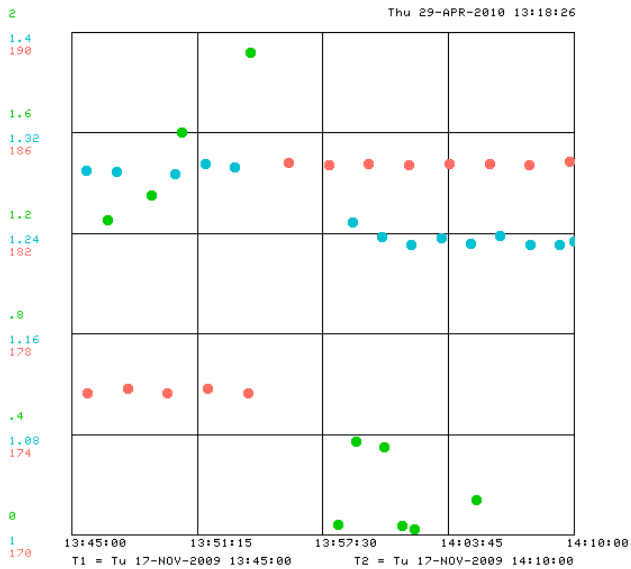

Figure 5: I:Q847 current (red data points) optimization reduces the sigma oscillations (green data points) at injection and results in smaller beam spot size on the NUMI target (cyan data points) after extraction at 120 GeV.

In addition to the automated monitoring of the injected beam, the IPMs are used to measure beam parameters for studies and to diagnose transverse beam instabilities. They can be configured to do a detailed analysis of 500 turns of the collected data, at any point in the cycle.

The IPM systems provide sigma data independent of our flying wires and can be used to verify suspect measurements at intensities low enough to use the wire system without damage.

Table 1: Listing results of simultaneous measurements from both Flying-wire and IPM, with a 25 turn average.

	Flying wire		IPM	
	sigma	Emittance	sigma	Emittance
8-GeV Pbar from Accumulator	2.37	6.6	2.25	5.4
8-GeV Pbar from RR	1.22	1.7	1.3	1.8
150 GeV Pbar to TEV	0.37	3.1	0.6	5.7
8-GeV Proton from Booster	3.75	16.4	4.2	18.8
150 GeV proton to TEV	0.81	15.0	1.2	22.8

IPM and Flying-wire data have been taken consistently for beam monitoring and diagnostics. Table 1 lists results from various modes of MI operation for both instruments. Fig. 6 shows the IPM measured sigma compared to expected sigma, i.e. sigma from Flying-wire adjusted for differences in lattice beta function. Fig. 7 shows the

comparison of their measured normalized emittances. The results for 8 GeV beam are very comparable. At 150 GeV we see higher measured emittances from the IPM, for both proton and pbar. This may be signaling the limitation of IPM sensitivity for small beam size.

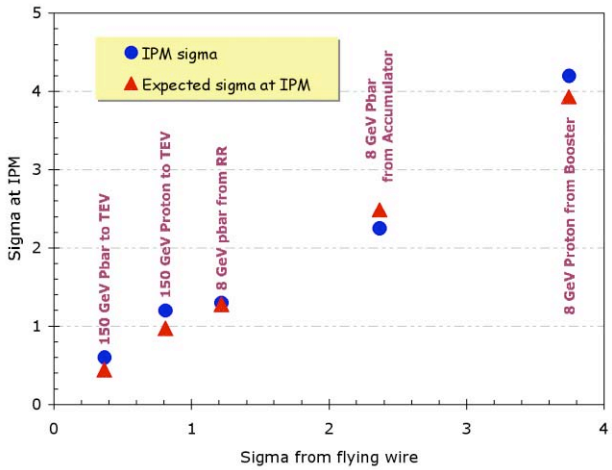

Figure 6: Comparing measured IPM profile sigma to that of Flying-wire. Blue dots are IPM sigmas. The red triangles are sigmas calculated from Flying-wire data with adjustment for difference in lattice beta function between the instrument locations.

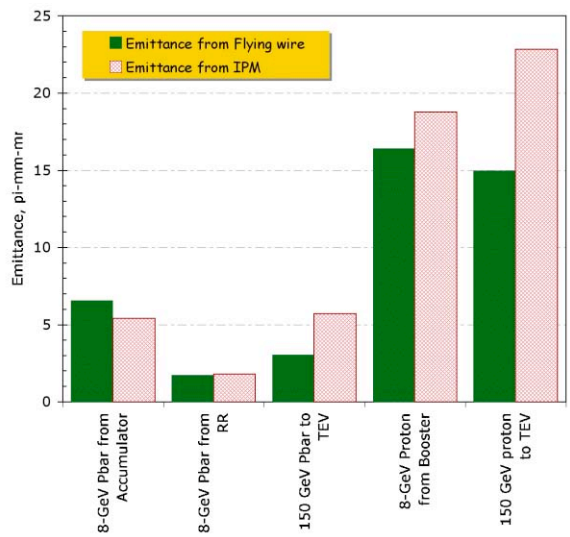

Figure 7: Comparison of measured normalized emittance from Flying-wire and IPM for different beams.

TEVATRON

The Tevatron IPMs [5,6] were developed primarily to measure injection beam size oscillations due to mismatch, in particular for pbars. Early in the Tevatron Run II there were indications of relatively large antiproton emittance blow-up between the Main Injector and Tevatron, The IPMs were installed as part of a campaign to eliminate any such sources of Luminosity loss.

To measure antiproton injections in the presence of a circulating proton beam, the Tevatron DAQ system is significantly different from the other machines. Instead of using a low pass filter with a time constant of the order of a turn followed by a regular ADC, the signal of each anode strip is continuously integrated in intervals of approximately 60 ns using a chip developed for the CMS experiment. One full revolution corresponds to 318 such intervals. The location of the IPMs and the integration interval (3.5 T_{rf}) were chosen in such a way that proton and pbar signal end up in separate integration intervals. Fig. 8 shows one turn of Tevatron IPM data, where proton and pbar bunches can be clearly identified. The measured profile for each bunch can be analyzed either turn-by-turn for injection measurements, or averaged over many turns in order to improve the signals for coasting beam.

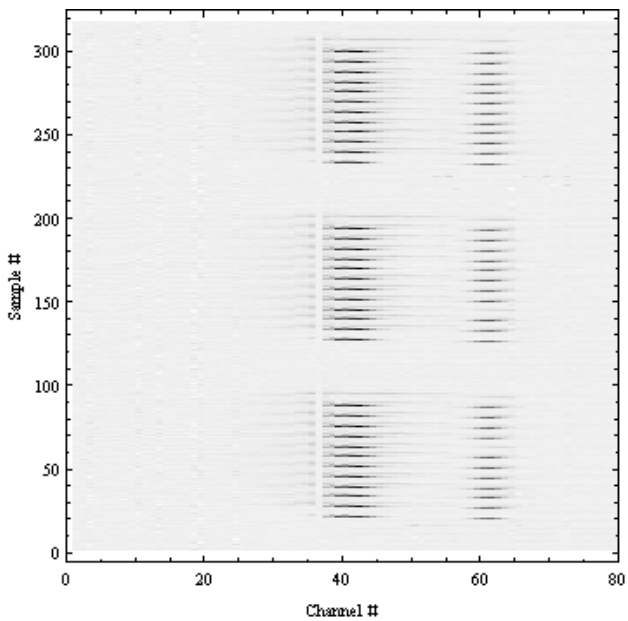

Figure 8: One machine revolution (318 samples) of Tevatron IPM data, showing the 36 protons (center) and 36 pbar (right) bunches. Proton and pbar separation due to the open helix orbit. (Channel 36 is a dead channel that is ignored by fitting routines.)

With the incorporation of the Recycler as an intermediate storage ring for pbars, and the routine operational use of high-energy electron cooling, antiproton emittance blow-up due to injection mismatch is no longer a concern. In fact, it has been found that too small a pbar emittance has an adverse effect on proton lifetime and losses. Therefore, the pbars delivered by the Recycler are typically first injected into the Tevatron with an intentional offset in order to increase its emittance, and then further blown up at flat top by injecting noise through a directional coupler (pbar jacking.)

The IPMs are used to monitor the process of blowing up the pbar emittance at flat top. For this, the system is run at the maximum measurement rate, which is a bit less than 1 Hz. This rate is limited by the time it takes to turn the HV voltage on/off. Fig. 9 shows an example of such a measurement.

Despite the decreased focus on injection matching, the

IPMs are set to monitor every injection event. They are also used to measure the coasting beam at regular intervals during HEP stores. Figure 10 shows the evolution of the beam sizes as measured by IPM and Flying Wires.

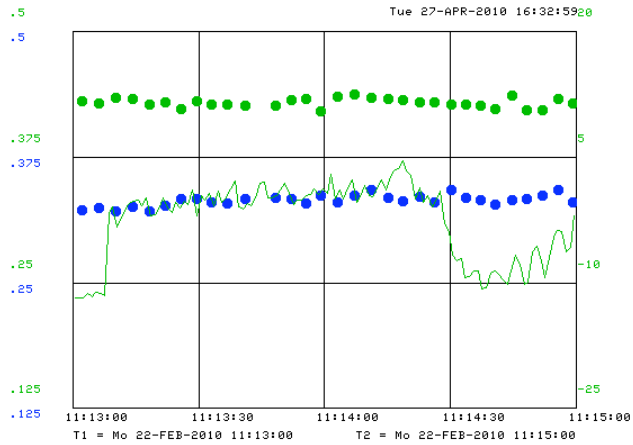

Figure 9: Tevatron IPM pbar beam size measurement during 'jacking' (intentional increase of pbar emittance at flat-top to improve proton lifetime and limit losses in the low beta squeeze). Green dots indicate vertical proton sigma, and blue dots vertical pbar sigma. The green solid line shows the Schottky power, which increases during jacking.

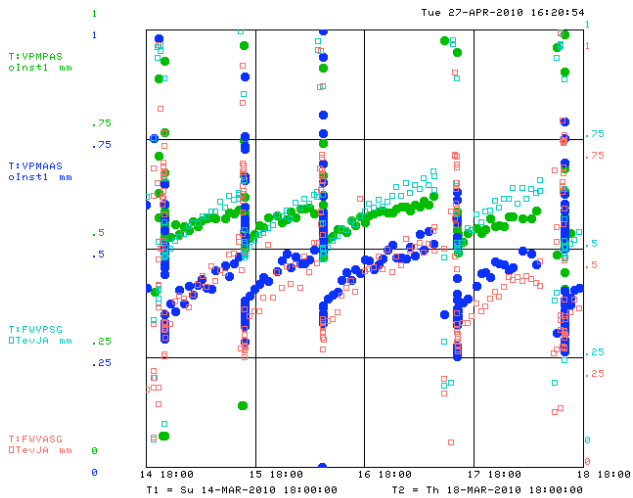

Figure 10: Tevatron IPM and Flying Wire beam size measurement during 4 typical stores. Green and blue dots are proton and pbar IPM measurements, while blue and red squares are the corresponding Flying Wire measurements. All measurements are in the vertical plane.

MICROCHANNEL PLATE LIFETIME

The MI IPMs are taking data for each pbar transfer that occur about every 40 minutes and typically include 3 batches each. Tevatron shots occur approximately once per day and include about 100 proton injections, and exactly 9 pbar injections. This results in about 220 measurements per day plus any physics study measurements. The micro-channel plates show signal degradation that can be compensated for only slightly by increasing gain or using another position on the plate. Eventual replacement on at least a yearly basis is required.

SUMMARY - THE INTENSITY FRONTIER

The IPMs are incorporated into the daily operations of the Fermilab Accelerators. They provide direct measurements of sigma oscillations during normal operation. As particle intensity increases, traditional intercepting profile monitors cannot be used. IPMs will certainly fill this need. Micro-channel plates do require regular replacement to maintain good signal integrity due to lifetime issues.

REFERENCES

[1] J. Amundson, J. Lackey, P. Spentzouris, G. Jungman and L. Spentzouris, "Calibration of the Fermilab Booster ionization profile monitor", Phys. Rev. ST Accel. Beams 6, 102801 (2003).

[2] J.R. Zagel, D. Chen., and J. Crisp, "Fermilab Booster Ion Profile monitor System Using LabView." BIW1994, Vancouver B.C., October 1994, AIP Conf. Proc. 333, pp 385-390.

[3] Xiaobiao Huang, Beam Diagnosis and Lattice Modeling of the Fermilab Booster.

[4] J.R. Zagel, D.J. Harding, B.C. Brown, H.D. Glass, L.R. Kozien, S.M. Pruss, J.T. Volk, "Permanent Magnet Ion Profile Monitor at the Fermilab Main Injector." PAC2001, June 2001, pp1303-1305.

[5] A. Jansson, K. Bowie, T. Fitzpatrick, R. Kwarciany, C. Lundberg, D. Slimmer, L. Valerio, and J. Zagel, "The Tevatron Ionization Profile Monitors," BIW2006, AIP Conf. Proc. 868 (2006) pp. 159-167.

[6]] A. Jansson, K. Bowie, T. Fitzpatrick, R. Kwarciany, C. Lundberg, D. Slimmer, L. Valerio, and J. Zagel, "IPM Measurements in the Tevatron," PAC07, Albuquerque, N.M., (2007)

RESIDUAL-GAS-IONIZATION BEAM PROFILE MONITORS IN RHIC*

R. Connolly, J. Fite, S. Jao, S. Tepikian and C. Trabocchi,
Brookhaven National Lab, Upton, NY, USA

Abstract

Four ionization profile monitors (IPMs) in RHIC measure vertical and horizontal beam profiles in the two rings (yellow and blue). These work by measuring the distribution of electrons produced by beam ionization of residual gas. In 2007 a prototype of a new design was installed in the yellow ring. During the 2007-2008 run it proved to be almost completely free from backgrounds from rf coupling, electron clouds and x-rays from upstream beam loss. In 2009 four new IPMs were built based on the prototype. During the 2009 shutdown two of these IPMs were installed. This paper describes the new IPMs and shows data from the 2010 beam run. The new IPMs have been extremely important in the commissioning of the RHIC stochastic cooling system.

INTRODUCTION

The Relativistic Heavy-Ion Collider (RHIC) at Brookhaven National Laboratory is a pair of concentric synchrotrons in which counter-rotating beams intersect at six points [1]. Beams ranging in mass from protons (E_{max}=250 GeV) to fully-stripped gold (E_{max}=100 GeV/nucleon) are accelerated and stored for several hours. There are detectors at two of the six intersection points for physics experiments with colliding beams.

Transverse beam profiles in RHIC are measured with ionization profile monitors (IPMs)[2,3,4,5]. An IPM collects the electrons in the beamline resulting from residual gas ionization during a bunch passage. The electrons are swept transversely from the beamline and collected on 64 strip anodes oriented parallel to the beam axis. After each bunch passes through the detector, the charge pulses are amplified, integrated, and digitized to give the bunch profile. Four IPMs are installed in RHIC to measure vertical and horizontal profiles in the two rings. Similar detectors are used at Fermi National Lab [6], DESY [7], and CERN [8].

The beam profile is measured primarily to find the transverse beam emittance which is the area occupied by the beam in transverse phase space, ie. (x,p_x) [3]. The beam radius at the IPM is equal to the square root of the betatron function, $\beta(s)$, times the emittance where s is the azimuthal coordinate of the IPM. The value of $\beta(s)$ is either calculated or measured and the beam radius is determined by profile measurements.

DETECTOR

Figure 1 is a schematic of the detector and its associated electronics in the accelerator tunnel. Figure 2 is a cutaway drawing and fig. 3 is a photo of the transducer. The detector chamber is located in a section of 10x15cm rectangular pipe. In an 18-cm-long section of this beam pipe half of the pipe has been removed and a saddle piece inserted. This saddle piece is biased at -6kV producing an accurate transverse electric field of $6x10^4$V/m.

A screen-covered rectangular opening in the grounded half of the beam pipe allows the signal electrons to pass through the image-current path to the detection assembly. The detection assembly is a 8x10cm microchannel plate (MCP) with a 64-channel anode etched on a ceramic circuit board. The collector board with attached MCP is located in an rf enclosure to prevent coupling to the beam. The only opening to this enclosure, which the signal electrons pass through, is a grounded aluminum honeycomb which attenuates rf by 80dB. Between the image-current bypass screen and the rf honeycomb window is a wire-screen control grid for gating the signal electrons off between measurements.

Each channel is connected via vacuum feedthrough to a preamplifier which drives a shielded twisted-pair transmission line to a 10MSPS VME digitizer.

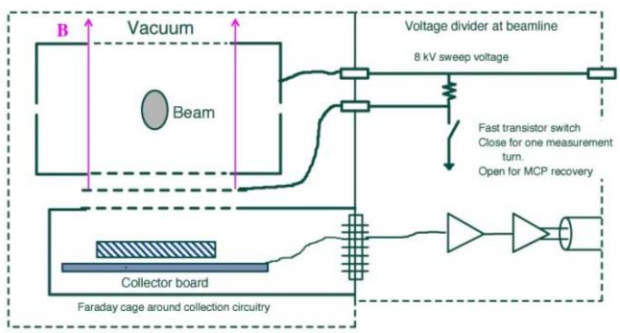

Figure 1: Schematic of detector and electronics located at the beamline.

In routine operation the signal-gating grid is biased at the sweep voltage of -6kV which prevents the signal electrons from passing. It is pulled to ground for a single turn (12μs) for measurement and returned to the off voltage. During this turn the digitizers are triggered. Each channel of an MCP has a dead time of about 1ms after firing. The intense heavy-ion beams of RHIC create such a large signal flux that the MCP becomes charge depleted very quickly. After a single measurement turn the grid is returned to -6kV for about 100 machine revolution periods for the MCP to recover. This is repeated 100 times and the data are averaged.

*Work performed by employees of Brookhaven Science Associates, LLC under Contract No. DE-AC02-98CH10886 with the U.S. Department of Energy.

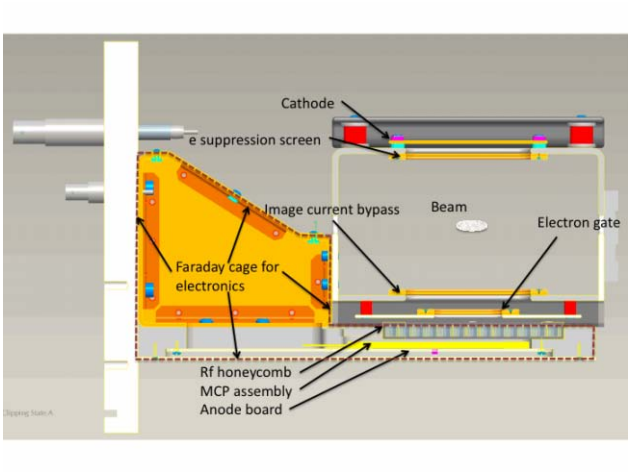

Figure 2. Cutaway drawing of the IPM. The HV sweep electrode is on top and MCP and anode board on bottom.

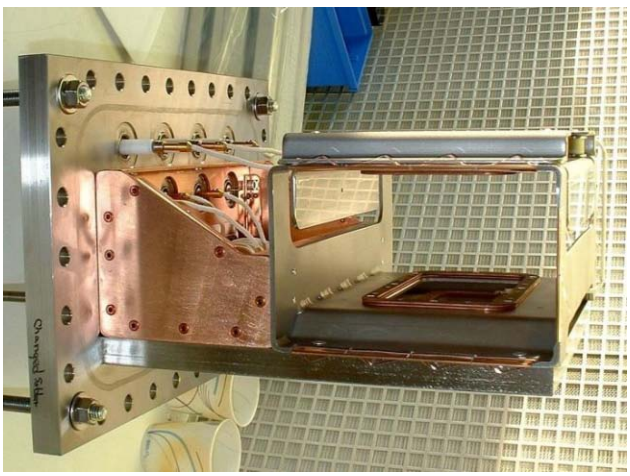

Figure 3. Assembled IPM transducer.

BEAM MEASUREMENTS

In 2009-10, RHIC ran gold beams, and the IPMs were set up for single-bunch measurements. In this mode the digitizers can be triggered on any of the buckets desired. During most of the beam run we monitored the bunch in bucket 121. This bucket has beam in all fill patterns and is not affected by the tune measurements or gap cleaning. Figure 4 is the display page of the IPM application showing the data, Gaussian fits and calculated widths and emittances.

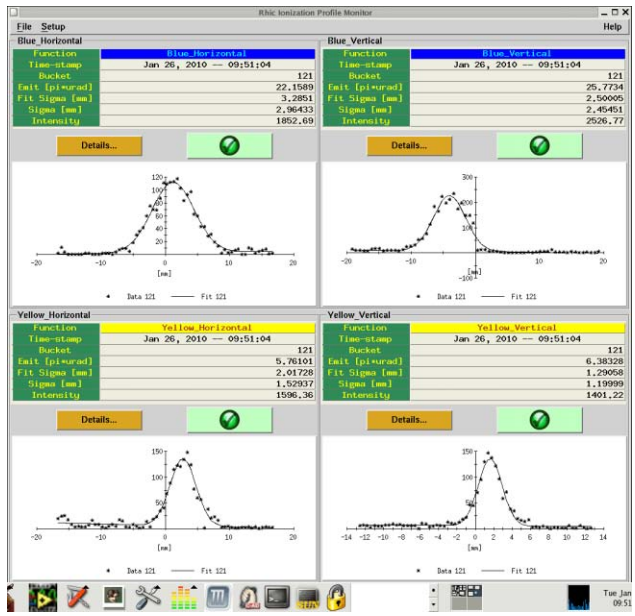

Figure 4. The IPM display page.

The most interesting development of this beam run was the commissioning of the RHIC stochastic cooling system[9,10]. The yellow-ring system was the first to operate and ran more consistently than the blue ring system. Figure 5 is a four-hour emittance record from the IPMs showing the effect the cooling system had on the beam in the yellow ring. Yellow cooling is turned on shortly after 18:20 and reduces the emittances in both planes of yellow from (13π)μm to (5π)μm in about an hour. Emittances in blue continue to grow during this time. The profiles shown in fig. 4 were taken with yellow cooling on and show dramatically smaller beams in the yellow ring. Figure 6 is the log entry from the first time cooling was done in the blue ring. At 17:30 yellow cooling was turned off and at 18:00 blue cooling is turned on.

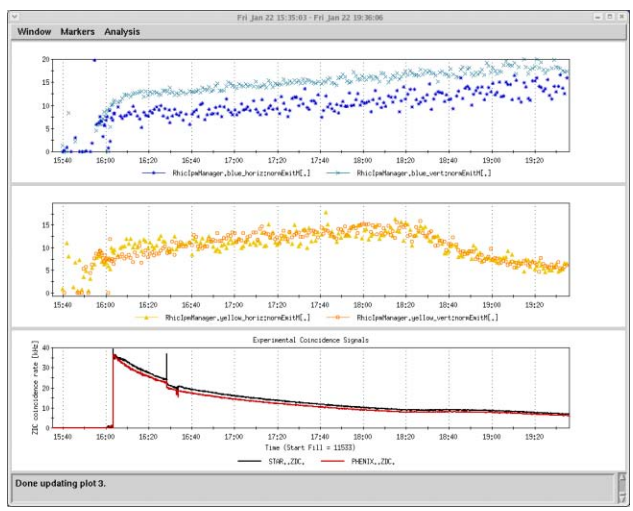

Figure 5. IPM record showing yellow-ring cooling.

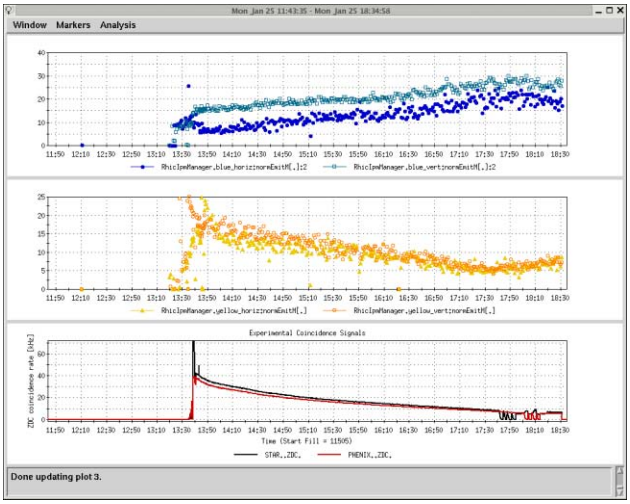

Figure 6. IPM record of first blue-ring cooling.

The IPMs are turned on at each machine fill. They take measurements at 30s intervals during the acceleration ramp and at 1minute intervals during the store. All beam and system parameters are recorded at each measurement. Figure 7 is a log entry showing the IPM records over a weekend. The top plot shows the IPM data and the bottom plot is the beam current record. During this weekend the blue-ring emittances were nearly constant but the yellow emittances fluctuated over a range of (20π)μm to (40π)μm.

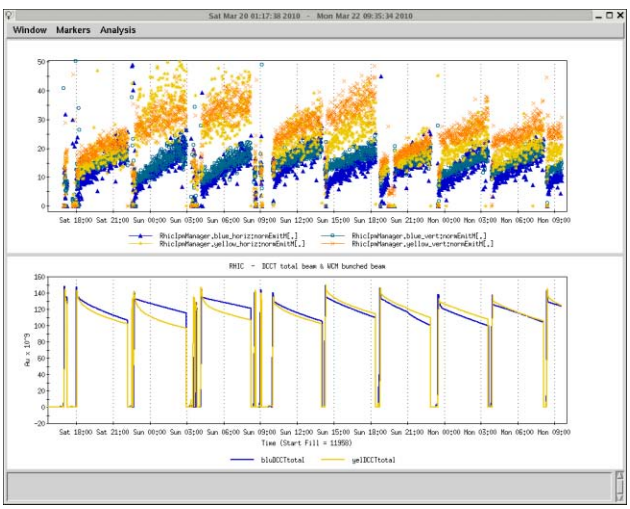

Figure 7. IPM emittance records over a weekend.

DISCUSSION

The last paper on the RHIC IPMs, presented at the 2005 PAC [2], reported issues with the electron-control grid coupling to the beam and rf noise from the beam coupling into the detection electronics. Since that paper was written we have moved the control grid outside of the beam image-current path and placed the MCP and collector inside an rf enclosure inside the vacuum chamber. These improvements have almost completely eliminated backgrounds.

Also since the last paper, emittance measurements have been implemented on RHIC using a movable Schottky cavity [11]. A resonant cavity is moved transversely on the beam line. At each position the ratio of the power in the revolution line to the sum of the powers in the two betatron sidebands is measured. A parabola is fitted to the data to find the rms beam size, σ, and the dispersion offset. These measurements agree exactly with the IPMs.

ACKNOWLEDGEMENTS

The prototype of the new IPM was built by Dave Kipp. Tom Russo developed the procedure for soldering the signal wires to the ceramic circuit boards.

REFERENCES

[1] http://www.rhic.bnl.gov/
[2] R. Connolly, R. Michnoff and S. Tepikian, "Residual-gas-ionization Beam Profile Monitors in RHIC," Proc. 2005 PAC, Knoxville, TN.
[3] R. Connolly, R. Michnoff, T. Moore, T. Shea, and S. Tepikian, Nucl. Instr. and Meth. A 443 (2000) 215-222.
[4] Connolly, R., Cameron, P., Michnoff, R., and Tepikian, S., *Performance of the RHIC IPM*, Proc. 2001 PAC, Chicago.
[5] R. Connolly, M. Grau, R. Michnoff and S. Tepikian, "The IPM as a Halo Measurement and Prevention Diagnostic," Halo '03, ICFA Advanced Beam Dynamic Workshop, Montauk, NY, USA (2003).
[6] J. R. Zagel, D. J. Harding, B. C. Brown, H. D. Glass, L. R. Kozien, S. M. Pruss, J. T. Volk, "Permanent Magnet Ion Profile Monitor at the Fermilab Main Injector." TPAH036, Proc. 2001 PAC., Chicago.
[7] K. Wittenburg, "Experience with the Residual Gas Ionization Beam Profile Monitors at the DESY Proton Accelerators," Proc. 1992 EPAC., 24.3.-28.3, Berlin, Germany and DESY HERA 92-12
[8] C. Fischer, "Results on Prototype Measurements for LHC Beam Instruments," Proc. 2001 DIPAC, Grenoble, France.
[9] M. Blaskiewicz, J.M. Brennan and F. Severino, Phys. Rev. Let. **100**, 174802 (2008).
[10] J.M. Brennan and M. Blaskiewicz, "Stochastic Cooling in RHIC," Proc. 2009 PAC, Vanouver, BC, Canada.
[11] K.A. Brown, M. Blaskiewicz, C. Degen and A. Della Penna, Phys. Rev. Spec. Topics-Accel. and Beams, **12**, 012801 (2009).

BEAM-ENERGY AND LASER BEAM-PROFILE MONITOR AT THE BNL LINAC*

R. Connolly, B. Briscoe, C. Degen, L. DeSanto, W. Meng, R. Michnoff, M. Minty, S. Nayak, D. Raparia and T. Russo, Brookhaven National Lab, Upton, NY, USA

Abstract

We are developing a non-interceptive beam profile and energy monitor for H^- beams in the high energy beam transport (HEBT) line at the Brookhaven National Lab linac. Electrons that are removed from the beam ions either by laser photodetachment or stripping by background gas are deflected into a Faraday cup. The beam profile is measured by stepping a narrow laser beam across the ion beam and measuring the electron charge vs. transverse laser position. There is a grid in front of the collector that can be biased up to 125 kV. The beam energy spectrum is determined by measuring the electron charge vs. grid voltage. Beam electrons have the same velocity as the beam and so have an energy of 1/1836 of the beam protons. A 200 MeV H^- beam yields 109keV electrons. Energy measurements can be made with either laser-stripped or gas-stripped electrons.

INTRODUCTION

In 2002 we reported on a project at BNL to develop a beam profile monitor for H^- beams using photoneutralization by a laser beam directed perpendicular to the ion beam [1]. That effort was in support of the Spallation Neutron Source being built at Oak Ridge National Lab [2]. In 2008 we reported on a prototype profile and energy monitor developed at BNL for Fermi National Lab [3] to use on the High Intensity Neutrino Source project [4]. Based on the success of the Fermi device we received funding from the BNL Linac Isotope Producer (BLIP) facility [5] to build a detector to measure beam energy and transverse profiles in the linac HEBT.

An H^- ion has a first ionization potential of 0.75 eV and can be neutralized by the 1eV photons from a Nd:YAG laser (λ=1064nm). To measure beam profiles, a narrow laser beam is stepped across the ion beam, removing electrons from the portion of the H^- beam intercepted by the laser. These electrons are deflected into a Faraday cup by a magnetic field. To measure the energy distribution of the electrons, the laser position is fixed and the voltage on a screen in front of the Faraday cup is raised in small steps.

*Work performed under Contract #DE-AC02-98CH10886 under the auspices of the US Department of Energy.

At the time of this writing, the laser platform is not yet installed. However we found that accurate energy measurements can be made on high-current beams (>5mA) by measuring the electrons stripped from the beam by background gas. Electrons are stripped by the residual gas in the beamline at a rate of ~1.5×10^{-8}/cm at 1×10^{-7} torr. In this detector a 30 mA beam produces about 40 nA of electron current.

In this paper we describe the detector and show results from the gas-stripped energy measurements.

DETECTOR

Figure 1 is a cutaway diagram of the detector from the side showing the signal-electron path. The neutralization chamber is a six-way cross with the laser beam passing through viewports either horizontally or vertically. An optics plate with the laser head and scanning optics is mounted on this chamber. The 100mJ/pulse, Q-switched Nd:YAG laser neutralizes 70% of the beam it intercepts during the 10ns pulse. The laser beam is scanned across the ion beam by reflecting it from a 45° mirror mounted on a linear translation stage.

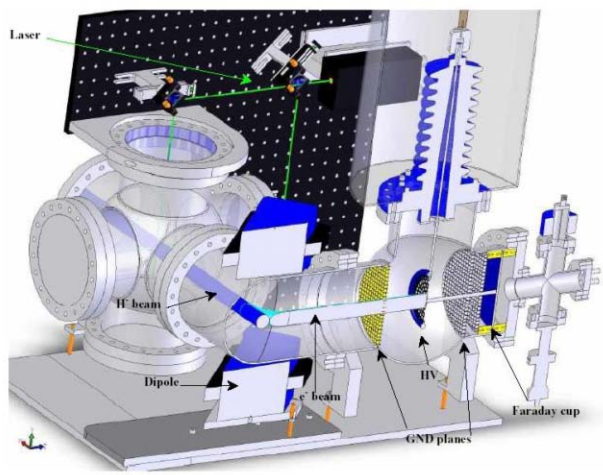

Figure 1: Cutaway schematic. Electrons from the H^- beam are deflected by a magnet through a HV grid into the Faraday collector.

Downstream a dipole magnet deflects the signal electrons 90° into the retarding grid and Faraday cup assembly. A corrector magnet upstream keeps the ion beam straight. A voltage grid in front of the collector

provides secondary-electron suppression. The electron signal is transported from the tunnel over 1/4" heliax cable and digitized by a LeCroy LT584L oscilloscope. Figure 2 shows the detector installed in the HEBT beamline.

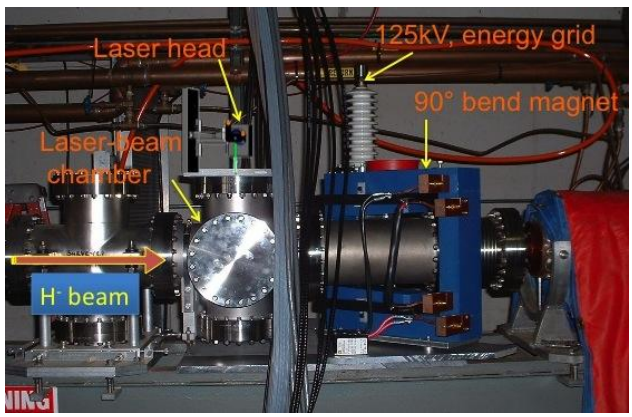

Figure 2: HEBT installation. The ion beam travels left to right. The laser chamber is left of the cable bundle and the deflector magnet is right. Electrons are deflected back through the grid and into the electron collector.

The control system is a Labview program running on a dedicated PC with digital and analog I/O through a National Instruments USB-6229 BNC. The maximum firing rate of the laser is 20 Hz so only one data point can be obtained per linac cycle (6.6 Hz). A measurement cycle is initiated by a timing pulse from the linac, which triggers the laser. The laser outputs a Q-switch synchronous pulse, which triggers the scope. The signal pulse from the Faraday cup is passed through a 10 MHz low-pass filter into the scope, which does a baseline subtraction and integrates the pulse. Upon completion of this process, the scope signals the computer, which reads the pulse.

ENERGY MEASUREMENTS

When the 2009-10 beam run started, the optics plate and enclosure were not finished. The high radiation level in the HEBT during the run prevents us from completing installation until the 2010 summer shutdown. However the BLIP program is primarily interested in beam-energy measurements, which we provide without the laser by using the gas-stripped-electron signal.

We estimate from ref. 6 a gas-stripping cross section of $\sigma \approx 4 \times 10^{-18}$ cm^2/atom. At the HEBT pressure of $\sim 1 \times 10^{-7}$ torr, the one meter drift from the upstream quad to our chamber produces about 40nA of electron current from a 30mA beam. About half of this current is lost to the four grids the signal electrons pass through. The signal current is amplified by 10^7V/A resulting in a full-beam signal of ~200 mV into the oscilloscope.

An energy measurement starts with a scan of the deflector magnet current to center the electron beam on the collector. The electron signal is integrated over each linac pulse of 400 μs, which gives data in units of volt*second. Figure 3 is the Labview screen showing the results of a magnet scan done with a 117 MeV beam.

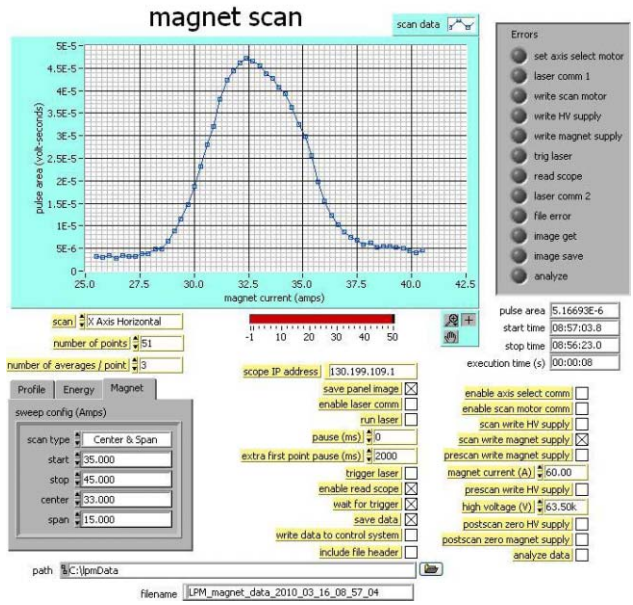

Figure 3: A magnet scan showing electron signal vs. deflector magnet current.

Figure 4 shows an energy scan that resulted in a measured beam energy of 117.06 MeV. This data set was produced by sampling 51 grid voltages over a range of 62.0 to 63.8 kV. Each point is averaged over 3 machine pulses. A sigmoid function is fitted to the data and the half-value point is taken as the electron center energy. Here the center electron energy is E_e=63.760 keV.

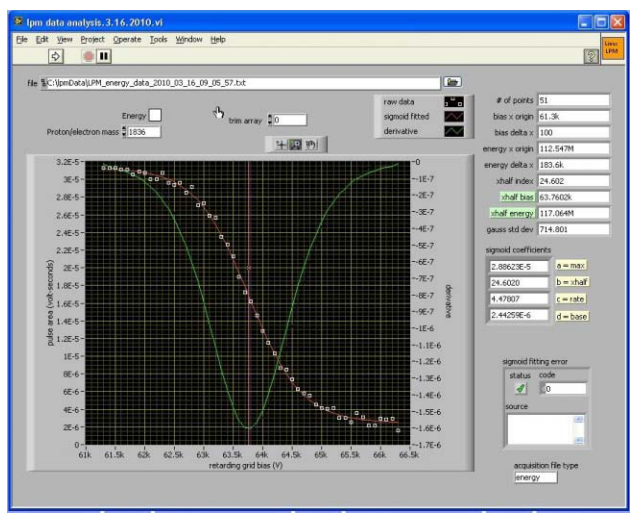

Figure 4: The analyzed data from an energy scan with a 117.06 MeV beam.

The Gaussian-like curve is the derivative of the sigmoid. From this we get the energy spread of the electrons. Most of this energy spread is from the space-charge potential spread in the bunched beam (Figure 5).

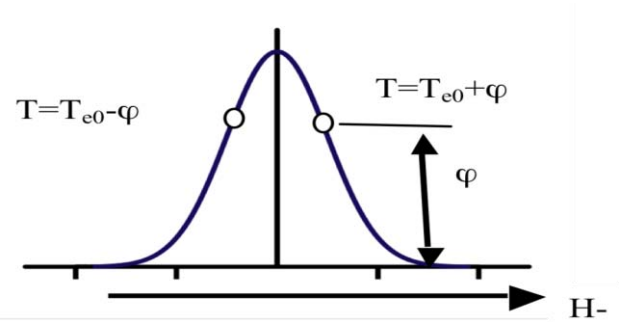

Figure 5: Illustration showing space-charge energy spread. Electrons in back of bunch lose the space-charge potential, φ, and those in front gain φ.

We did a series of energy measurements over one hour at five different beam currents (Table 1). Several measurements made at each current are averaged showing an rms measurement repeatability of about 0.03%.

Table 1. Results of energy measurements over one hour at five different beam currents.

BEAM CURRENT	FILE	MEASURED ENERGY (MeV)
40mA	09-03-43	116.99
	09-05-57	117.06
	09-07-11	117.06
	09-08-29	117.1
	09-10-20	117.01
	Average	117.04±0.04
35mA	9-16-05	117.12
	9-17-31	117.11
	9-18-59	117.11
	9-20-19	117.07
	Average	117.10±0.02
25mA	09-24-27	117.14
	09-25-38	117.14
	09-26-51	117.13
	09-28-01	117.07
	Average	117.12±0.03
15mA	09-42-01	117.17
	09-43-46	117.11
	09-45-21	117.21
	Average	117.16±0.05
5mA	09-52-54	117.01
	09-54-34	117.3
	09-56-07	117.04
	Average	117.12±0.16

DISCUSSION

When completed this detector will provide both energy and transverse-profile measurements of H^- beams with energies up to 200MeV and beam currents of 0.2-40 mA. During this beam run we are getting accurate energy measurements from the beam electrons produced by background-gas stripping. The gas-stripped-electron measurement has been demonstrated with beam currents as low as 5mA. Measurements on the 200μA polarized proton beam will probably require the laser, but we are testing new amplifier schemes.

ACKNOWLEDGEMENTS

The authors thank Cyrus Biscardi, Tony Curcio, and Vinnie LoDestro for their many contributions.

REFERENCES

[1] R. Connolly *et. al*., "Laser Beam-Profile Monitor Development at BNL for SNS," Proc. 2002 Linac Conf., Gyeongju.
[2] S. Assadi *et. al*., "SNS Transverse and Longitudinal Laser Profile Monitors Design, Implementation and Results," EPAC 2006, Edinburgh.
[3] R. Connolly, *et.al*., "Laser-based Profile and Energy Monitor for H- Beams," Proc. 2008 Linac Conf., Vancouver.
[4] http://www-td.fnal.gov/projects/hins.html
[5] http://www.bnl.gov/medical/Isotope_Distribution/Isodistoff.htm
[6] George H. Gillespie, Phys. Rev. A., Vol. **16**, No. 3, 1977.

DATA AND ANALYSIS FROM A TIME-RESOLVED TOMOGRAPHIC OPTICAL BEAM DIAGNOSTIC*

Daniel K. Frayer#, Douglas Johnson, National Security Technologies, LLC,
Los Alamos, NM 87544, U.S.A.
Carl Ekdahl, Los Alamos National Laboratory, Los Alamos, NM 87545, U.S.A.

Abstract

An optical tomographic diagnostic instrument developed for the acquisition of high-speed time-resolved images has been fielded at the Dual-Axis Radiographic Hydrodynamic Test (DARHT) Facility at Los Alamos National Laboratory. The instrument was developed for the creation of time histories of electron-beam cross section through the collection of Cerenkov light. Four optical lines of sight optically collapse an image and relay projections via an optical fiber relay to recording instruments; a tomographic reconstruction algorithm creates the time history. Because the instrument may be operated in an adverse environment, it may be operated, adjusted, and calibrated remotely. The instrument was operated over the course of various activities during and after DARHT commissioning, and tomographic reconstructions reported verifiable beam characteristics. Results from the collected data and reconstructions and analysis of the data are discussed.

INTRODUCTION

Kaufman et al. (2006) [1] describe design considerations for the development of a time-resolved diagnostic system for use at the Dual-Axis Radiographic Hydrodynamic Test (DARHT) Facility at Los Alamos National Laboratory. This design was finalized and the diagnostic instrument was fabricated, calibrated, and fielded. Frayer et al. (2008) [2] give the final system description and discuss characterization, qualification, integration, and preliminary experimental results.

In brief, the DARHT facility is designed to record high-speed radiographic images of explosively driven hydrodynamic events. This is accomplished by the illumination of a test object with x-ray pulses that occur within a 2 μs envelope and the recording of the resulting radiographic images. The x-ray pulses are generated by illuminating x-ray converter targets with high-power electron beams along two orthogonal axes.

The tomographic instrument was developed to create time histories of the DARHT electron beam when the DARHT second axis was being commissioned. Four discrete optical subsystems with distinct lines of sight view, through a 6-inch window in a pump cross, Cerenkov light generated by the beam incident upon a inside the vacuum envelope. Each subsystem employs cylindrical optics to image light in one direction and collapse light in the orthogonal direction. Each of the four images and collapses in unique axes, thereby capturing information as a projection. Light along the imaging axes is relayed via optical fiber arrays and is recorded by streak cameras coupled to CCDs, resulting in temporal resolution of 2 ns over a recording window of 2 μs. Computer software then reconstructs a two-dimensional time history of the electron beam from the four optically collapsed one-dimensional (1-D) histories.

Two versions of this diagnostic have been built and fielded: a system with two lines of sight, as described by Bender et al. (2007) [3] and used in early stages of DARHT commissioning [4] and an earlier four-view system [5]. Both systems were fielded at DARHT in easily accessible, low-environmental-risk areas. This third-generation diagnostic was designed to be fielded in an area with restricted access and higher environmental risk, and to have the ability to change optical parameters during experiments. Although the optical design is similar to that of its predecessors, this instrument is necessarily more advanced as it offers remote calibration and remote control of optical magnification, focus, and aperture. This version of the instrument was fielded at DARHT in February, 2008, and has been operational since.

Figure 1: The DARHT tomographic instrument.

We first provide a brief treatment of the methodology used in reconstructing time-resolved images from the individual datasets. We give requirements upon the system for results of such reconstruction, as well as

*This work was done by National Security Technologies, LLC, under Contract No. DE-AC62-06NA25946 with the U.S. Department of Energy.
#frayerdk@nv.doe.gov

qualification data proving system performance under the required condition. Finally, we analyze and discuss data from reconstructions of actual beam data.

TOMOGRAPHIC RECONSTRUCTION ALGORITHM

Given an image such as that given in Figure 2, a single-dimensional projection can be found at a given angle *k* by integrating in one direction at that angle. To simplify the notation, we can work in a rotated coordinate system:

$$s_k = x \cdot cos(\theta_k) + y \cdot sin(\theta_k) \quad (1)$$

$$t_k = y \cdot cos(\theta_k) - x \cdot sin(\theta_k) \quad (2)$$

The image then becomes the function $f(s_k, t_k)$, while the projection becomes

$$P_k(s_k) = \int f(s_k, t_k) \cdot dt_k \quad (3)$$

In the case of the discussed system the actual image is unknown, and collected data consist of a number of projections at various angles. As such, the algorithm must proceed from the real data to a reconstruction of the original image. However, with a small number of projections there is no single solution. Given the smooth datasets expected from the accelerator, the maximum entropy constraint is added to force a unique solution:

$$H(f) = \iint f(x,y) \cdot ln\big(f(x,y)\big) \cdot dx \cdot dy$$
$$\Psi(f,\lambda) = H(f) + \sum_k \lambda_k(s_k) \cdot \left[P_k(s_k) - \int f(s_k, t_k) \cdot dt_k\right] \quad (4)$$

with the function H(f) defined as the entropy of the image f(x,y). This entropy can be combined with the projection functions using LaGrange multipliers, λ_k, to form the functions Ψ_k. Differentiating with respect to the LaGrange multipliers and setting the result to zero returns the original definition of the projections:

$$\frac{d\Psi}{d\lambda} = \sum_k \left[P_k(s_k) - \int f(s_k, t_k) \cdot dt_k\right] = 0$$
$$P_k(s_k) = \int f(s_k, t_k) \cdot dt_k \quad (5)$$

Differentiating with respect to the image defines the image in relation to the LaGrange multipliers:

$$\frac{d\Psi}{d\lambda} = 1 + ln\big(f(x,y)\big) - \sum_k \lambda_k(s_k) = 0$$
$$f(x,y) = \epsilon \cdot e^{\sum_k \lambda_k(s_k)} \quad (6)$$

Since the LaGrange multipliers are unknown, their exponentials are also unknown. We can simplify the result as:

$$f(x,y) = \prod_k h_k(s_k) \quad (7)$$

This indicates that any given pixel in the reconstructed image is a product of the corresponding points in the h-functions. The h-functions have a one-to-one relationship to the projections as shown in Figure 3.

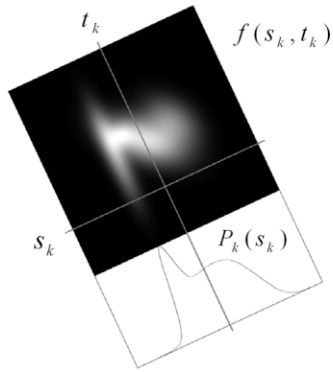

Figure 2: A sample image and projection.

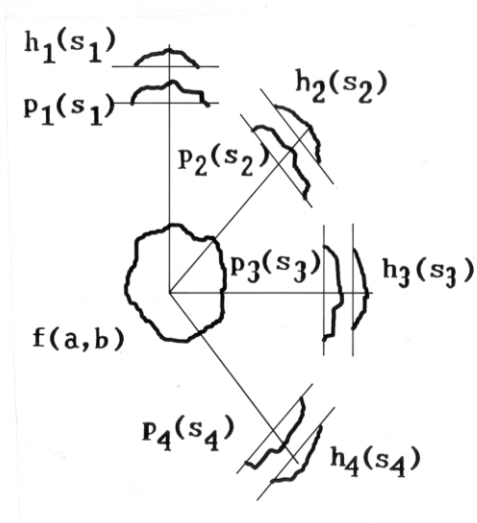

Figure 3: A sample image and projection.

The projection data are collected as a series of discrete points. The h-functions are found as a matching series of points. We can solve for the h-functions iteratively by starting with assumed values and adjusting them by comparing calculated projections with the data projections. Initially, all of the points in the h-functions are set equal to 1. An image is calculated from these and integrated to produce the calculated projections:

$$f(a,b) = \prod_k h_k\big(s_k(a,b)\big)$$
$$P_{k,calc}(s_k) = \int f(s_k, t_k) \cdot dt_k \quad (8)$$

New h-function values are then determined from the difference between the calculated and data projections:

$$h_{k,new}(s_k) = h_{k,old}(s_k) - \frac{g \cdot h_{k,old}(s_k) \cdot \left[P_{k,calc}(s_k) - P_{k,data}(s_k)\right]}{P_{k,calc}(s_k)} \quad (9)$$

The variable g is a gain factor that is adjusted between 0 and 1. If set too high, the iterations become unstable and head towards infinity. If it is too low, the algorithm fails to converge. Iterations are manually repeated while gain factor is adjusted so that the difference between the calculated and data projections decreases sufficiently. Ideally the difference would converge to zero; in reality they will converge to some finite number, with the magnitude reflecting quality of the data.

Operationally, the reconstruction software has as inputs calibration images: per camera, a dark-field image with timing marks, a flat-field image and a resolution pattern; and two data files, one from each streak camera. As outputs, it produces the time-resolved series of images; each image or integrated set of images comes with calculated centroid position, RMS radius, skew, and kurtosis, each in x and y; and angle and ellipticity.

SYSTEM REQUIREMENTS AND QUALIFICATION

Initial customer requirements for the measurement of a beam profile elliptical in cross section and Gaussian in illumination profile to have the following accuracies [2]: 1) Centroid position to ±10% of radius for beam radii of 1 to 5 cm; 2) RMS radius to ±10% of radius for beam radii of 1 to 5 cm; and 3) Ellipticity (defined here as the ratio of minor and major axes) to ±10% of actual value for discernibly noncircular ellipses.

Optical requirements were determined by the system requirements [2]; the built instrument has a range of magnification, allowing a full field of view from 55.3 mm to more than 180 mm while operating at a distance of 0.5 m, with a resolution of 2.1 lp/mm in the high-magnification configuration. The functioning instrument was characterized in the laboratory with an illumination source as given in the requirements: namely, elliptical in cross section and with a Gaussian exitance profile. Calibrations were performed and five sets of data were taken of the ellipse while operating in a zoomed-in configuration. The tomographic reconstruction algorithm was applied to the data; results of ellipticity calculations are given in Figure 4, while an image of the original juxtaposed with a reconstruction is given in Figure 5.

RMS x and y radius calculations, based on five qualification runs and calculated with a 5% background, were 95.6% and 95.1% accurate, with standard deviations of 3.3% and 3.0%, respectively. Ellipticity calculations, based on the same reconstruction set, were 91.8% accurate, with a standard deviation of 0.97%. No absolute reference for centroid position was present, but x and y centroid position calculations had standard deviations of 0.72% and 12.0%, relative to RMS radius, respectively. Based on the results, the instrument received qualification and was fielded at DARHT in February, 2008.

BEAM DATA

The instrument operated during beam shots from February 2008 through February 2010. Data sets were

Reconstructions Zoomed In 10-26-07	RMS Radius x-y Background 5% of Peak Excluded	RMS Radius x-y Background 10% of Peak Excluded	2D Gaussian Fit Ratio of Minor to Major Axes
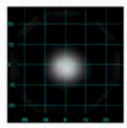	Reconstruction 01		
	width = 5.306 height = 4.429 h/w = 0.83	width = 3.719 height = 3.360 h/w = 0.90	major = 24.7200 minor = 22.2342 ratio = 0.90
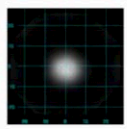	Reconstruction 02		
	width = 4.497 height = 3.845 h/w = 0.86	width = 3.617 height = 3.268 h/w = 0.90	major = 24.7090 minor = 22.2327 ratio = 0.90
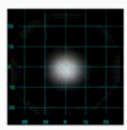	Reconstruction 03		
	width = 3.851 height = 3.490 h/w = 0.91	width = 3.335 height = 3.005 h/w = 0.90	major = 24.6606 minor = 22.1878 ratio = 0.90
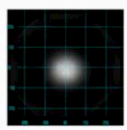	Reconstruction 04		
	width = 4.545 height = 3.855 h/w = 0.85	width = 3.617 height = 3.266 h/w = 0.90	major = 24.6299 minor = 22.1641 ratio = 0.90
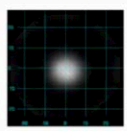	Reconstruction 05		
	width = 4.920 height = 4.136 h/w = 0.84	width = 3.692 height = 3.347 h/w = 0.91	major = 24.6246 minor = 22.1875 ratio = 0.90

Figure 4: Reconstructed ellipses for system qualification.

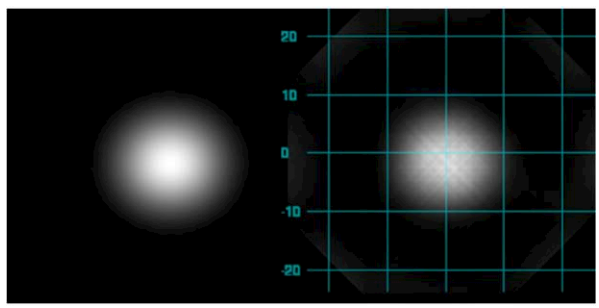

Figure 5: The illumination target (left) and reconstruction (right).

captured during 138 shots, and reconstructions were used in real-time to tune the DARHT beam line. Of these images, 44 were captured a) during shots in which the target was inserted into the beam line and b) simultaneously recorded by a PI-MAX single-frame camera imaging the reverse side of the beam target. Although data captured solely by the tomographic instrument are of value, for purposes of analyzing fidelity of capture and reconstruction, only data captured by both the tomographic instrument and the single-frame camera are useful. As such, only results from these 44 shots are analyzed here. As the majority of beam profiles were complex and highly nonelliptical, the assumption of ellipticity and Gaussian shape does not hold and quantitative error is expected. Also, as comparisons are being made to calculations from the PI-MAX images and such calculations are made with software that makes similar assumptions, the baseline numbers are themselves not expected to be entirely meaningful.

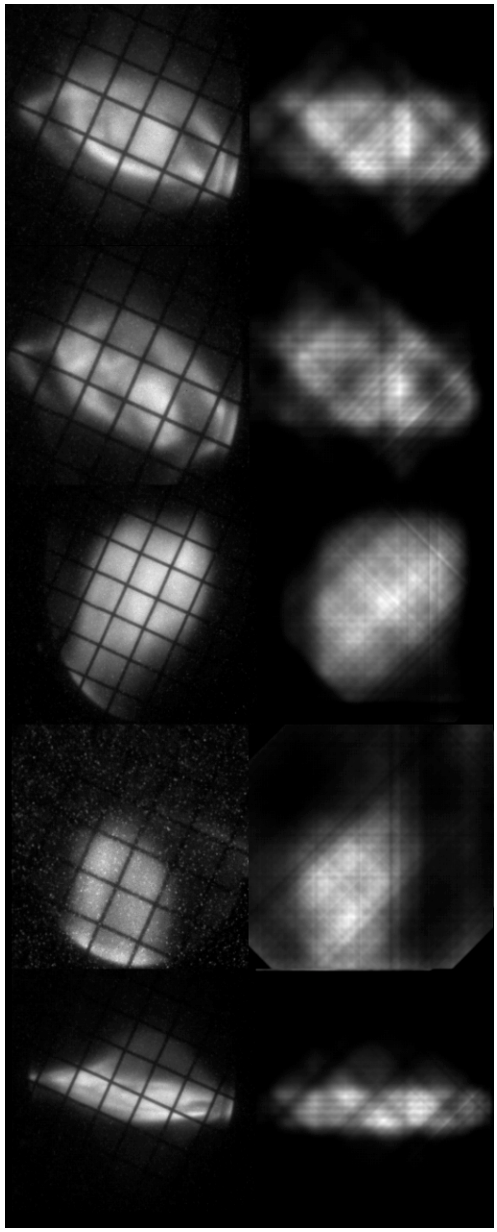

Figure 6: Selected correlated PI-MAX images (left) and tomographic reconstructions (right).

For each time record produced by the algorithm, images were integrated over the same temporal window, i.e., with the same initial time and duration, as that over which the PI-MAX recorded images in order to compare algorithmically produced measurements of centroid position (x and y), RMS radius (x and y) and ellipticity (here defined as the ratio between the difference in major and minor axes to the sum of the axes) for both images. Additionally, for each data set in which some pixels were saturated, an estimate for the ratio of saturated pixels to data pixels was made. This was done for the purpose of correlating error with saturation level, and was determined by counting pixels above an observable saturation threshold and those above a rough estimate of the background level. Representative pairs of temporally correlated PI-MAX images and reconstructed integrated images are shown in Figure 6. Shown in Figures 7 through 9 are measured values of x centroid (Table 1), y centroid (2), x and y RMS radius (3) and ellipticity (4), respectively, along with calculated best fits.

ANALYSIS AND CONCLUSION

For all collected data, the tomographic instrument was fixed but the PI-MAX underwent several configuration changes, resulting in several subsets for both x and y centroid position with varying offsets. The data presented in Figure 7 have had these subtracted. For the charted datasets, best fits for x and y centroids were obtained by forcing equal slopes equal across data subsets while allowing offsets to vary. Those for x and y RMS radius were obtained by allowing the slopes to vary while maintaining offsets of zero. Both slope and offset were allowed to vary for ellipticity. Information derived from these figures is given in Table 1.

Several sources of error contaminate the original data and reconstructions. Background light affects both the PI-MAX camera and the tomographic system, although environmental and instrument configurations result in different levels seen by both in each correlated set, and changes in these configurations over the course of the entire dataset result in changes in background in a single instrument. Background is subtracted when making calculations from both raw images and reconstructions, but this process is not deterministic for the mentioned reasons. Additionally, light is generated in the fiber sub-arrays due to proximity to the beam line, in varying amounts due to relative placement. Finally, two current-return grids are present in the beam line, as can be seen in the left column of Figure 6, one seen by each system. These grids have different relative orientations, but more importantly, the one seen by the tomographic system is spatially separated from the beam target such that the four projections are contaminated with four different superpositions of the grid upon the target via parallax.

As can be seen in Table 1, the slopes for x and y centroid position, x and y RMS radius, and ellipticity are below unity such that lines with unity slopes are outside

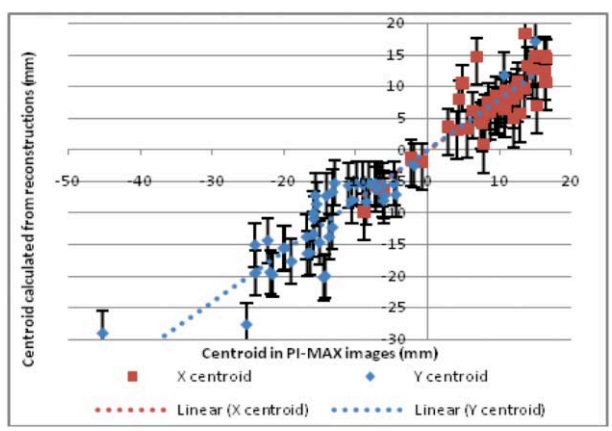

Figure 7: Centroid x and y position with best fits.

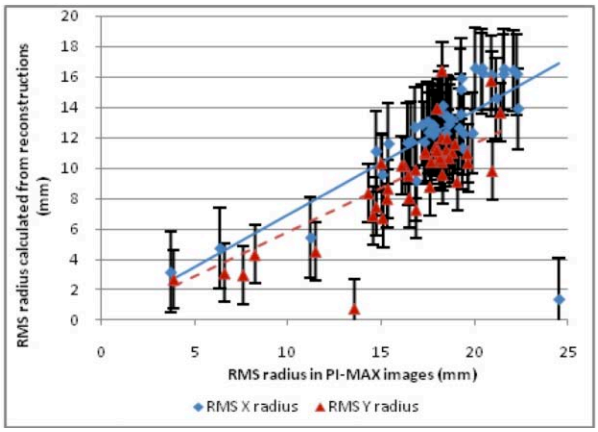

Figure 8: RMS radius in x and y with best fits.

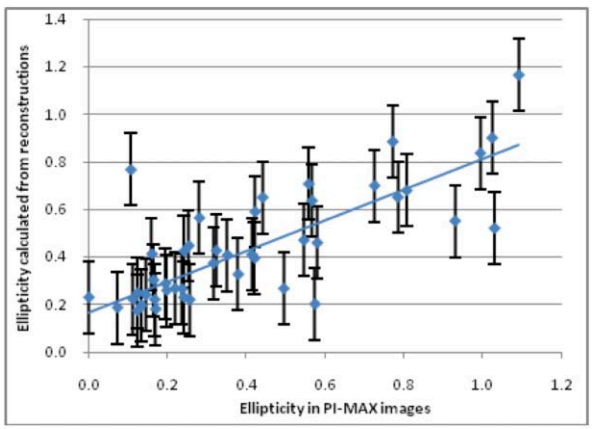

Figure 9: Ellipticity and best fit.

of the error bars for the calculations. As those calculated from datasets taken from elliptical sources are accurate, it is unclear whence the consistent inaccuracy in calculated radius of non-elliptical sources comes.

Compromise of data by saturation of pixels in one or more projections places the reconstruction in question. The convergence factor was found to correlate inversely with the ratio of data pixels saturated. However, error in any of the values listed in Table 1 was not found to correlate at all with this ratio. Unexpectedly, this was found to hold true even in severe cases of saturation, when blooming was induced on the streak-coupled CCD cameras, or when a large percentage of data pixels was compromised in multiple views. This implies a degree of robustness that is highly desirable in dynamic beam-tuning sequences, when it is not possible to predict light levels coming from the beam target and adjust the instrument accordingly ahead of time.

Table 1: Derived values from Figures 7−10

Figure	Datum	Value
7	X centroid slope	0.800
	X centroid offsets	2.89 mm
	X centroid standard deviation	0.801
8	X RMS radius slope	3.52
	X RMS radius standard deviation	0.689
	Y RMS radius slope	2.7 mm
	Y RMS radius standard deviation	0.582
9	Ellipticity slope	0.648
	Ellipticity offset	0.166
	Ellipticity standard deviation	0.2

The described instrument and reconstruction software has proven a valuable tool in determining qualitative beam parameters such as temporally resolved movement, changes in shape, and note of features such as filamentation. It is expected that to be of value in determining quantitative values as the beam in DARHT second axis converges to the expected form. Future work on the tomographic instrument includes determination of consistent inaccuracy in calculated parameters in reconstructions of highly non-elliptical, non-Gaussian beam profiles relative to those calculated from imaged captured by the PI-MAX single-frame camera.

REFERENCES

[1] Kaufman, M., Frayer, D., Dreesen, W., Johnson, D., and Meidinger, A., “Design considerations for a time-resolved tomographic diagnostic at DARHT,” Proc. SPIE 6289, 2006.

[2] Frayer, D., Cox, B., Dreesen, W., Johnson, D., Jones, M., Kaufman, M., “Fielding of a time-resolved tomographic diagnostic,” Proc. SPIE 7061, 2008.

[3] Bender, H., Carlson, C., Frayer, D., Johnson, D., Jones, K., Meidinger A., Ekdahl, C., “Quasianamorphic optical imaging system with tomographic reconstruction for electron beam imaging,” Rev. Sci. Instrum. 78(1), 013301 (2007).

[4] Ekdahl, E., Abeyta, O., Bender, H., Broste, W., Carlson, C., Caudill, L., Chan, K. C. D., Chen, Y. J., Dalmas, D., Durtschi, G., Eversole, S., Eylon, S., Fawley, W., Frayer, D., Gallegos, R., Harrison, J., Henestroza, E., Holzscheiter, M., Houck, T., Hughes, T., Jacquez, E., Johnson, D., Johnson, J., Jones, K., McCuistan, B. Trent, Meidinger, A., Montoya, N., Mostrom, C., Moy, K., Nielsen, K., Oro, D., Rodriguez, L., Rodriguez, P., Sanchez, M., Schauer, M., Simmons, D., Smith, H. V., Studebaker, J., Sturges, R., Sullivan, G., Swinney, C., Temple, R., Tom, C. Y., and Yu, S. S., “First beam at DARHT-II,” Proc. of the 2004 Particle Accelerator Conference, 558–562 (2003).

[5] Ekdahl, E., Abeyta, E. O., Aragon, P., Archuleta, R., Bartsch, R., Bender, H., Broste, W., Carlson, C., Dalmas, D., Eversole, S., Frayer, D., Gallegos, R., Harrison, J., Jacquez, E., Johnson, D., Johnson, J., McCuistan, B. Trent, Montoya, N., Nath, S., Oro, D., Rowton, L., Sanchez, M., Scarpetti, R., Schauer, M., Seitz, G., Tipton, A., and Tom, C. Y., “Commissioning the DARHT-II scaled accelerator,” Proc. of the 2007 Particle Accelerator Conference, 2373–5 (2007).

LANSCE WIRE SCANNING DIAGNOSTICS DEVICE MECHANICAL DESIGN

Sergio Rodriguez Esparza, Los Alamos National Laboratory, Los Alamos, NM USA

INTRODUCTION

The Los Alamos Neutron Science Center (LANSCE) is one of the major experimental science facilities at the Los Alamos National Laboratory (LANL). The core of LANSCE's work lies in the operation of a powerful linear accelerator, which accelerates protons up to 84% the speed of light. These protons are used for a variety of purposes, including materials testing, weapons research and isotopes production. To assist in guiding the proton beam, a series of over one hundred wire scanners are used to measure the beam profile at various locations along the half-mile length of the particle accelerator. A wire scanner is an electro-mechanical device that moves a set of wires through a particle beam and measures the secondary emissions of electrons from the resulting beam-wire interaction to obtain beam intensity information. When supplemented with data from a position sensor, this information is used to determine the cross-sectional profile of the beam. This measurement allows beam operators to adjust parameters such as acceleration, beam steering, and focus to ensure that the beam reaches its destination as effectively as possible. Some of the current wire scanners are nearly forty years old and are becoming obsolete. The problem with current wire scanners comes in the difficulty of maintenance and reliability. The designs of these wire scanners vary making it difficult to keep spare parts that would work on all designs. Also many of the components are custom built or out-dated technology and are no longer in production.

DESIGN CRITERIA

The first design criterion is that the wire scanner should be constructed with as many commercially available off-the-shelf components as possible. This will facilitate having spare parts that can fit multiple wire scanners. This is similar to the wire scanner design of the Oak Ridge National Laboratory (ORNL) Spallation Neutron Source (SNS) wire scanner. The second criterion is that the wire scanner should be capable of 1mm movements at 4Hz (1mm in 250ms) with a triangular velocity profile as illustrated in Figure 1. Notice that for the area under the curve to be 1mm, the peak velocity must be 8mm/s half way through the motion. This yields an acceleration of 64mm/s² (Note: 1g = 9807mm/s^2). Third, the position of the wires at the end of the "fork" must be known within ±1mm with respect to an external monument. Also, the repeatability of the system must be within ±0.1mm. Fourth, the motor must be powered off while taking a measurement at each bin location. Lastly, the wire scanner should be designed to accommodate as many existing beam structures as possible.

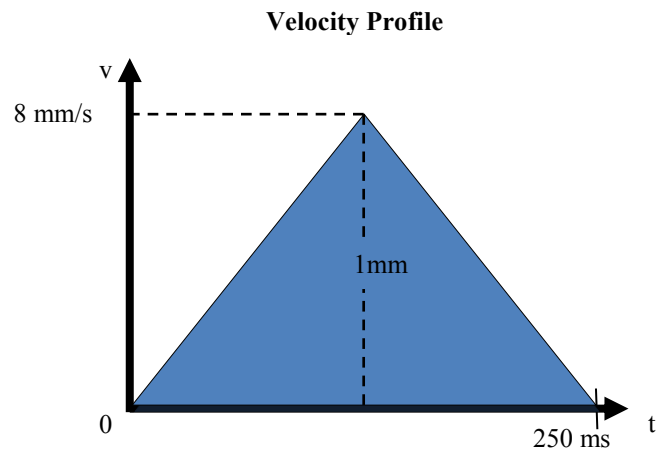

Figure 1: Velocity profile for the wire scanner.

MECHANICAL DESIGN

As mentioned above, the first design criterion resembles that used by ORNL and likewise does so the mechanical design. Figure 2 shows the ORNL wire scanner design.

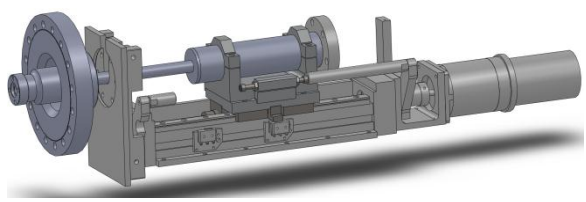

Figure 2: ORNL SNS wire scanner design.

The ORNL SNS wire scanner design has been modified to fit our current beam structures and our design specifications. Figure 3 shows the LANSCE future wire scanner design.

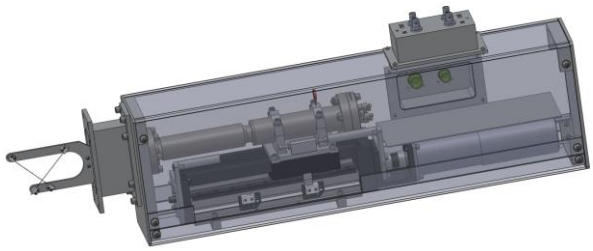

Figure 3: LANSCE wire scanner.

The first difference to notice is the mounting interface between the wire scanner and the beam structures; ORNL uses a circular pattern while LANSCE uses a rectangular pattern. Second, ORNL uses a one-piece rectangular frame with removable side and top panels while the LANSCE wire scanner design is a two-piece, top and bottom, frame with removable front and rear plates. The LANSCE wire scanner can be broken down into 6 sub components or sub assemblies: frame, drive system, arm assembly, fork, accessories, and motor. These will be further discussed in the following sections.

Frame

The frame provides structural support to the wire scanner. Additionally, the frame has been designed to house all of the wire scanner's components internally and thus protecting them from dust and debris. As mentioned above, the frame is composed of four components: the front plate, back plate, top of the frame, and bottom of the frame; all made from 6061 aluminum alloy. The front plate has three sets of tapped holes; the outer holes are used to mount the garage to the wire scanner. The inner set of holes is used to mount the bellows and thus creating a vacuum seal. The holes on the sides are used to hold together the top and bottom of the frame. The back plate also has a set of tapped holes to increase the rigidity of the system. The top and bottom of the frame have been designed in such a way that the top of the frame can be removed to gain access to the internal components while maintaining the bottom of the frame in place.

Drive System

The drive system converts the rotational input of the motor into linear motion. A Lintech 100-series linear stage with a 10-mm-lead ball screw and 6 inches of available travel was selected. It comes fully assembled with a NEMA 23 motor mount and motor coupling. The slide table travels on two rails with two linear bearings per rail. Each bearing has a dynamic load capacity of 775 lbs rated for 2 million inches of travel; the table is estimated to only travel 36,000 inches in 20 years, with a load of 7 lbs at most. The maximum acceleration of these bearings is 19.6 m/s² (2 g's). Some additional features are two mounts for limit switches and a cover plate to protect the ball screw from dust and debris.

Arm Assembly

The arm assembly acts as support for the fork as well as a vacuum boundary with an electrical feedthrough for the signal wires. The fork adapter has two threaded holes where the fork assembly bolts onto. The arm is a hollow ½ inch stainless steel tube, this allows for the signal wires from the fork to travel through it and gain access to the electrical feedthrough. This is welded to the fork adapter and the tube bushing. The bellows allows motion while maintaining vacuum on the inside. This is also welded to the tube bushing as well as to a Conflat (CF) 2.75 flange that bolts onto the front plate. The bellows and flange assembly is provided by Metal Flex Welded Bellows Inc. part number 13783AA-10. The larger tube in this assembly acts as the sole support for this assembly. On one end it is welded to the tube bushing, on the other it is welded to a CF 2.75 flange. This tube is supported by a carriage and clamp assembly that mounts onto the linear stage. Finally, the electrical feedthrough is composed of 4 double-ended SMA connectors built into a CF 2.75 flange. This allows for the signal to travel from the wires on the fork to the outside while maintaining vacuum on the inside. This feedthrough is from Accu-Glass Products, Inc. Model Number 2SMA-GS4-275.

Fork

The fork assembly is designed such that two wires, positioned perpendicular from each other, act as X and Y beam profile indicators when mounted at ±45° from the horizontal. This assembly allows for the current to travel from the wires through the arm and exit through the electrical feedthrough. The fork and fork bracket are made from aluminum while the wire mounts are made from macor. The wire itself is typically 0.1mm diameter of tungsten, silicon carbide, or carbon fibers.

Accessories

Accessories for the wire scanner include the mounting interface, limit switches, hard stops, carriage, connectors, and cable guard. The mounting interface supplies extra room the fork when it is fully retracted. The limit switches indicate the system when it has reached it inward and outward limit. The hard stops act as protection in the case that the wire scanner does not stop at the in or out limit switch positions. The carriage is the mounting point for the arm assembly and moves with the linear stage. The connectors allow for both the retrieval of the current from the signal wires as well as connections for the motor, resolver, and limit switches. Lastly, the cable guard protects the signal cables from getting tangled with any other component(s).

Mounting Interface

As mentioned above, the mounting interface serves as extra room for the fork to retrieve into away from the beam line. Additionally, the mounting interface, serves as

the mounting interface between the beam structure and the rest of the wire scanner. This component is a solid rectangular piece of aluminum 6061 with two flanges on its ends. The flange that interfaces with the beam structure is flat while the one that interfaces with the rest of the wire scanner has a groove for a 0.040in diameter aluminum 1100 wire seal.

Limit switches

For this design we will be using three limit switches, one for the in-limit and two on the out-limit. On the out-limit, one of the switches lets the operators know that the wire scanner is ready to perform while the second limit switch simply indicates when the wire scanner has fully retrieved from the beam line. The first out-limit switch to engage is the one that indicates that the wire scanner is fully retrieved, the other lets the operators know that the wire scanner is ready to run or if it is done.

Hard Stops

The hard stops act as mechanical precautions in the case that the stage does not stop when the trigger engages the limit switches. These hard stops mainly protect the fork from over travel into the beam structure. Additionally, it protects the bellows from over extending or over compressing which may cause tearing and leaks.

Carriage

The purpose of the carriage is to hold the arm assembly to move with the linear stage. Additionally, this carriage has two tapped holes for screws to act as the impacting surface with the hard stops in the case of over travel.

Connectors

Connectors are needed to transfer signals from the wires intercepting the beam and also to interface with the motor, resolver, and limit switches. For the signal wires, four BNC bulkhead connectors are used in this design. These four connectors mount to the mounting case via D-shaped holes. The mounting case is engraved with indications of which connections belong to which set of wires depending on the orientation that the wire scanner is mounted. The 90° wires indicate the X-profile of the beam while the 0° wires indicate the Y-profile of the beam. For the motor, resolver, and limit switches, two MS connectors are needed. One is a 19-pin connector and the other a 10-pin connector. The motor requires 8 wires which would go on the 10-pin connector. The limit switches require a total of 9 wires and the resolver requires 6; these 15 wires would go onto the 19-pin connector. The mounting cases for these connectors are made from aluminum-6061 stock machined to specifications and bolted to the top and side of the frame.

Cable Guard

The cable guard is designed to protect the signal wires that run from the electrical vacuum feedthrough to the BNC connectors. This cable guard allows for the wires to rest on it while the actuator is in its fully retracted position thus protecting them from getting tangled on any other component and at the same time preventing contact with the motor which may be hot. The cable guard is manufactured with 14-gauge aluminum sheet metal bent at 90 degrees and mounts along with the out-limit hard stop mount and motor mount onto the linear stage.

Motor

Because of the velocity requirements for the movements made by the wire scanner, the motor had to be sized correctly in order to achieve the specifications. In the process of sizing the motor we compared two types of motors; stepper and servo motors. Both motors have their advantages over the other and these are discussed in this section of this document. The motors being compared are from Empire Magnetics Inc. (EMI) since it is one of the few manufacturers that offer radiation-hardened motors.

As you will see in Figure 4 and Figure 5, servo motors have more torque available than stepper motors for the same rotational speed. As shown in Figure 1, a 1 mm movement in 250 ms would require a maximum velocity of 8 mm/sec assuming a triangular velocity profile. If we use a 10 mm lead ball screw this speed translates to 0.8 revolutions per second (RPS) or 0.048 kilo revolutions per minute (krpm).

Figure 4 shows that at this velocity the stepper motor has an available 400 oz-in of torque. Figure 5 shows that at this velocity the servo motor has an available 40 in-lbs of torque which convert to 640 oz-in. Additionally, servo motors have lower rotor inertia than a stepper motor for motors of the same frame size. An advantage over the servo motor is that the stepper motor has a detent torque that helps prevent back driving of the system. Since the wire scanner is mounted in a vacuum environment at a ±45° angle from the horizontal axis, it is prone to back drive due to gravity and vacuum forces. The equations below were used to correctly size the motors.

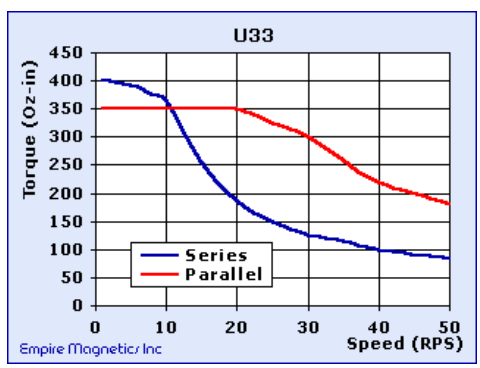

Figure 4: EMI U33 stepper motor speed vs. torque curves.

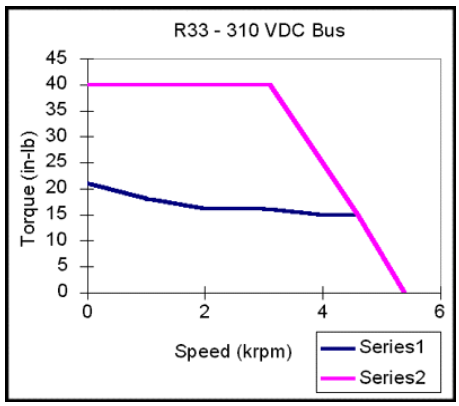

Figure 5: EMI R33 servo motor speed vs. torque curves.

In order to determine if the desired velocity will be reached, the torque required to perform such action must be calculated. To do so, the following equations have been used. The torque required for this task is composed of three parts, the torque to overcome axial loads, the torque to overcome frictional loads, and the torque needed to accelerate the ball screw to the desired velocity. The axial loads in this case would be the vacuum force, gravitational force, and the spring force due to the bellows.

$$\tau = \tau_{friction} + \tau_{axial} + \tau_{accelerate}$$

$$\tau_{friction} = \frac{\mu W sin(45) \times Lead}{2\pi e}$$

$$\tau_{axial} = \frac{(F_{vac} + Wcos45 + F_{spring}) \times Lead}{2\pi e}$$

$$F_{vac} = P_{atm}A$$

$$F_{spring} = kx$$

$$\tau_{accelerate} = (J_{load} + J_{screw} + J_{motor})\frac{\omega}{t}$$

$$J_{load} = \frac{W}{g(\frac{2\pi}{Lead})^2}$$

$$J_{screw} = \frac{\pi r^4 \times L \times \rho}{2g}$$

$$\omega = \frac{2\pi v}{Lead}$$

Table 1 shows the given values for the variables on the equations listed above. From these values and these equations the following results have been tabulated to compare stepper motors with servo motors and different size motors in each of those classes. All of the motors listed are from Empire Magnetics Inc. (EMI).

Table 1: Given values

μ	Friction coefficient between ball screw and nut = 0.01
W	Load carried by linear stage = 7lbs
Lead	Linear distance per revolutions of the ball screw = 10mm/rev
e	Efficiency of the screw = 90%
P_{atm}	Atmospheric pressure (at 7,200 ft elevation) = 78.19 kPa
A	Area where vacuum pressure is applied = 4.383 x 10^{-4} m²
k	Spring Coefficient = 2.5 lbf/in
X	Bellows compression distance (stroke length) = 3.5 in
J	Moment of Inertia (J_{motor} depends on motor)
ω	Maximum angular velocity = 5.03 rad/s
t	Time to reach peak velocity on triangular velocity profile = 125ms
r	Ball screw radius = 8mm
L	Length of ball screw = 330mm
ρ	Density of ball screw (stainless steel) = 8 g/cm^3
v	Maximum linear velocity = 8mm/s

Table 2 lists the EMI stepper motors with their respective required and available torque values.

Table 2: Stepper motor torques

Motor Model#	Torque Available in Series (oz-in)	Torque Available in Parallel (oz-in)	Total Torque Required (oz-in)	Ratio of Torque Available/ Required
U43	1545	2278	12.47	123.92
U42	1161	774	10.18	114.08
U41	385	308	7.89	48.82
U33	443	402	6.67	66.44
U32	294	247	6.29	46.72
U31	143	161	5.96	24.00
U23	146	90	5.78	25.27
U22	98	49	5.73	17.11
U21	55	52	5.64	9.74

Table 3 lists the EMI servo motors with their respective required and available torque values. From Tables 2 & 3, all the motors, both stepper and servo, have enough torque available to complete the required task of 1mm in 0.250ms. Because all of these motors have enough torque, the more desirable are the smaller motors since this simplifies the overall design of the wire scanner. This led us to concentrate on stepper motors U21-23 and servo motors R32-34.

Table 3: Servo motor torques

Motor Model#	Continuous Torque Available (oz-in)	Intermittent Torque Available (oz-in)	Total Torque Required (oz-in)	Ratio of Torque Available/ Required
R32	224	480	6.00	31.33
R33	336	640	6.12	44.43
R34	432	960	6.24	66.69
R43	560	1120	6.87	81.53
R45	768	1680	7.38	104.03
R46	960	2240	7.90	121.55
R63	1024	2400	10.23	100.13
R65	1840	3840	12.80	143.75
R67	2480	2480	15.37	161.32

An additional consideration that needs to be taken is the possibility of the system back driving. In this system, when powered off, vacuum forces as well as gravitational forces induce a torque on the ball screw. If this torque is greater than the frictional torque between the screw and nut, then the screw will rotate causing unwanted movement of the system. This affects servo motors differently than stepper motors due to the servo's free spinning rotors and the stepper's detent torque. A stepper motor's detent torque can be enough to prevent back drive. From the equations above, the total back driving torque is 11.417 oz-in. Table 4 lists the stepper motors in the NEMA 23 frame from EMI and their respective detent torques.

Table 4: Stepper motor detent torques

Stepper Motor	Detent Torque (oz-in)
U21	6
U22	15
U23	21

From this table we can see that the U22 and U23 motors have enough torque to prevent back drive. However, the U22 only has 31% more torque than the back driving torque. For reliability purposes, the U23 is a much better choice with almost twice the torque required to prevent back driving of the system. Servo motors provide more torque than the stepper motors; however they have a free spinning rotor that does not prevent back driving. If a servo motor were to be used in this system, a brake would need to be implemented adding complexity to the system. The chosen stepper motor has over 20 times the torque required and therefore it is the chosen motor for this design.

CONCLUSION

This wire scanner is designed with the intent to perform all of its duties as well as possible while maintaining the design simple and easy to maintain. Most of the main components are available off the shelf which makes replacing parts easier and faster. Current wire scanners along the linear accelerator (linac) consist of many custom parts and vary in design. Another goal of this project is to standardize the design of the wire scanners in order to have interchangeable parts that fit wire scanners at different locations along the linac. By doing so, we are able to have spare parts that can be used on different wire scanners as opposed to just a handful.

LANSCE HARP UPGRADE: ANALYSIS, DESIGN, FABRICATION, AND INSTALLATION*

J. Douglas Gilpatrick#, Phillip Chacon, Derwin Martinez, John F. Power, Brian G. Smith, Mark A. Taylor, LANL, Los Alamos, NM 87545, U.S.A., and

M. Gruchalla, EG&G Albuquerque Operations, Albuquerque, NM 87107, U.S.A.

Abstract

The primary goal of this newly installed beam profile measurement is to provide the facility operators and physicists with a reliable horizontal and vertical projected beam distribution and location with respect to the proton beam target and beam aperture. During a 3000-hour annual run cycle, 5 μC of charge is delivered every 50 milliseconds through this harp to the downstream TRMS Mark III target. The resulting radioactive annual dose near this harp is at least 6 MGy. Because of this harsh environment, the new harp design has been further optimized for robustness. For example, compared to an earlier design, this harp has half of the sensing wires and utilizes only a single bias plane. The sensing fibers are 0.079-mm diameter SiC fibers. To hold these fibers to a rigid ceramic structure, a collet fiber-clamping device accomplishes the three goals of maintaining a mechanical fiber clamp, holding the sense fibers under a slight tensile force, and providing a sense-fiber electrical connection. This paper describes the harp analysis and design, and provides fabrication, assembly, and some installation information, and discusses wiring alterations.

INTRODUCTION

The Los Alamos Neutron Science Center (LANSCE) facility primary beam target, TRMS Mark III, has been replaced [1]. This target's primary goal is to convert 800-MeV protons to various energetic neutrons. In order to perform this conversion efficiently, the incoming proton beam position and width are measured using a common measurement device known as the "harp" that samples the transverse profile with respect to the beam pipe aperture. The interesting aspect of this particular harp is that due to its location, inside the TRMS Mark III target, it is in a very harsh environment. For a single 3000-hour annual run cycle, this particular harp is expected to receive 6 MGy of absorbed dosage [2]. Since the expected target lifetime is at least 5 years, the harp will receive at least 30 MGy. Therefore, its design should be sufficiently robust to withstand this harsh environment.

1L HARP THEORY

The 1L harp's principle of operation is very basic (Figure 1). Fibers sample the projected beam charge distribution in two orthogonal planes. An intervening plane of fibers between the two signal planes is biased such that secondary electrons emitted from one signal plane are not allowed to impinge on the second signal plane. Generally, a small amount of the proton beam's energy deposited into the fiber and is converted to emitted secondary electrons (SE). The current flow of these SE leaving the fiber is measured by external electronics to produce a series of amplitudes for each projected beam distribution.

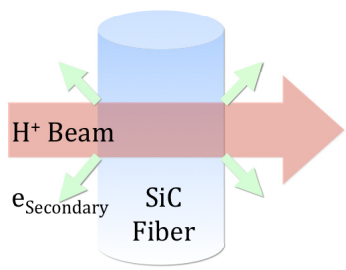

Figure 1: The 800-MeV beam passing completely through the SiC fiber and depositing a small amount of the beam's energy. A subsequent amount of the deposited beam energy is converted to SE emission.

*Work supported by US Department of Energy
#gilpatrick@lanl.gov

The Sternglass theory states that the SE emitted electron yield is

$$\mathrm{Y} = \frac{Pd}{\varepsilon}\frac{dE}{dx} = (0.002\,cm/MeV)\frac{dE}{dx}, \qquad (1)$$

where Y is the SE yield from a proton beam current impinging on the SiC fiber, P is the probability that an electron will escape from the SiC fiber material (typically, ~0.5), d is the average depth from which electron escape from the SiC fiber material (typically, ~ 1 nm), and ε is the average amount of kinetic energy lost by an ion per ionization in material (typically, ~25 eV) [3,4]. For an 800-MeV proton beam, the energy loss in SiC, dE/dx, is 1.98 MeV/g/cm^2, and the density of SiC is 3.0 g/cm^3 resulting in a SE yield of 0.0119.

The secondary electron emission current, i_{SE}, from a proton beam impinging on a fiber is

$$i_{SE} = \mathrm{Y} i_b, \qquad (2)$$

where i_b is the proton beam current impinging on the 0.079-mm SiC fiber.

A typical 12.5-mm by 14.5-mm transverse rms beam has an integrated charge of 5 μC. This beam bunch is 300-ns long and has roughly a triangular longitudinal distribution. The integrated proton beam charge impinging on a central vertical fiber is 12.6 nC. Using Sternglass's theory, the calculated peak SE emitted current from this central vertical wire is 1 mA.

To reduce the number of "shadow" electrons that may impinge upon the downstream signal SiC fibers, a bias plane between the two transverse signal planes is biased positively so as to attract SE. Furthermore, to optimize emitted SE, each of the transverse signal plane fibers is biased negatively.

Since each fiber's emitted SE current is proportional to the quantity of impinging beam current, the SE integrated charge during a single pulse for each signal fibers provides a sampled transverse beam distribution.

The peak SiC fiber temperature was calculated at the center of the beam distribution. This calculation assumes 1-dimensional geometry with no conduction along the fiber, i.e., radiative cooling only. The energy lost from the 300-ns long, 20-Hz pulsed beam provides an energy input into the fiber, and fiber radiative cooling throughout all time provides an energy output term.

With production quality beams and a 12.5-mm by 14.5-mm transverse rms beam has an integrated charge of 5 μC, attains steady state equilibrium within ~ 60 seconds and reaches peak temperatures of ~ 1480 K.

1L HARP DESIGN

Since one of the goals for this particular harp replacement was to simplify its construction, this TRMS Mark III harp consists of three individual planes, two transverse signal planes and a single intervening bias plane. Figure 2 shows an exploded view of these three planes.

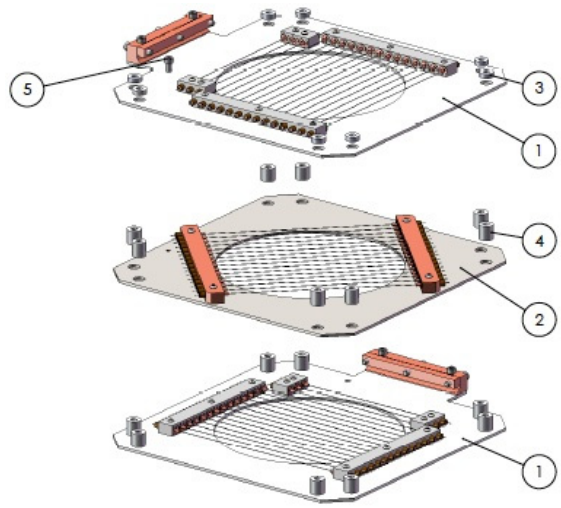

Figure 2: The exploded perspective drawing of the TRMS Mark III harp shows the two signal planes (#1), the bias plane (#2), various Macor spacers (#3 and #4), and the bias plane potential circuit trace connection (#5).

The transverse signal planes each have 17 SiC fibers extending across the 101.6-mm (4-inch) beam aperture. The TRMS Mark III harp design also has increased the distance between distribution bins, or fiber pitch, to 6 mm, for two reasons: (1) it does not require a spacing of 3 mm between fibers, and (2) simplicity. The Macor circuit board material is 1.52 mm thick, with the circuit traces initially flashed with Ni

and then covered with a Au plating [5]. The intervening bias plane is constructed in the same manner, except that the circuit board is fabricated from a 1.52-mm thick 304 SS card, such that each wire takes on the same bias potential as the supporting metal card. The seventeen bias-plane wires are clocked at a $\pi/4$ radian angle with respect to the two signal plane fibers.

The connections, first developed for the wire scanners for the Low Energy Development Accelerator and further used at the Spallation Neutron Source, use a collet-style fiber holding mechanism that simultaneously accomplishes three goals. The collet mechanisms hold each fiber mechanically rigid, yet provide a slight tensile force on each fiber to account for a slight change in length due to local heating, and maintain electrical connections to each fiber. Furthermore, this collet system holds and tensions the signal fibers in a manner that is believed to impart less stress in the filament and give better stress uniformity than could be expected from the crimping system used in the TRMS Mark II harp.

Figure 3 shows the schematic of each projected signal plane. There are seventeen 10-pF capacitors that provide a way to verify that each fiber is properly connected via the collet clamps.

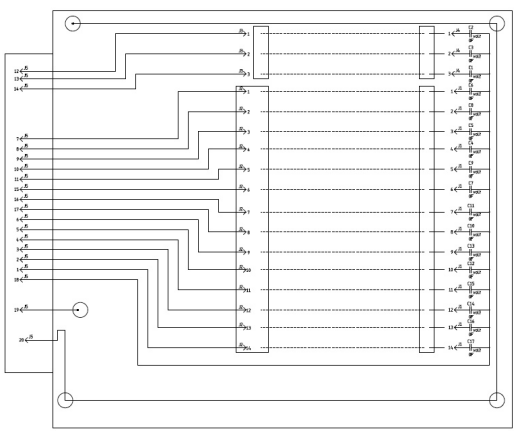

Figure 3: A single projected signal plane that has 17 capacitors that isolate the incoming "integrity" signal from the fiber signals.

Figure 4 shows an "integrity" drive and fiber sense signal. With this technique, we will detect a fiber misconnection independent of beam delivery.

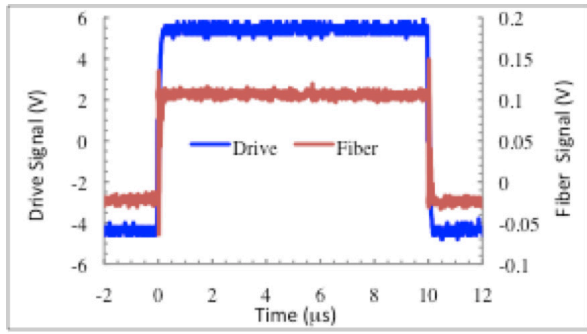

Figure 4: Two oscilloscope traces consisting of an "integrity" drive signal (blue) and an intact-fiber signal (red).

Figure 5: Three planes of 1L Harp with 0.079-mm SiC fibers attached using a collet style of clamp.

The Cu collets, pictured in Figure 6, clamp a fiber with two jaws and use a spring under compression to both force the ring collar to provide force to the clamping jaws and to the fiber. As the fiber is heated by beam impingement, the slightly expanding fiber will still maintain its alignment due to these compressed springs. Figures 7 and 8 show the

1L harp mounted in its instrument carrier, which bolts on the end of the insert beam pipe within the TRMS target assembly.

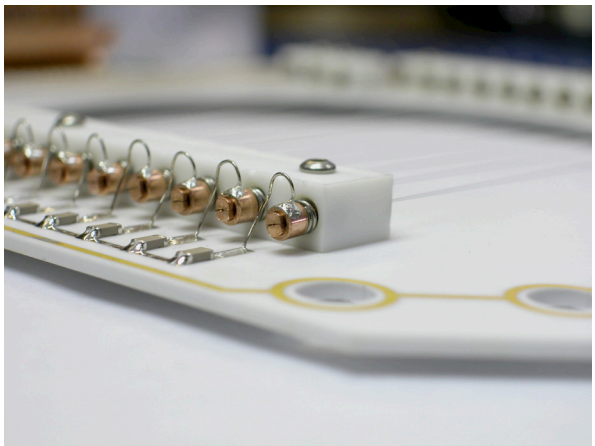

Figure 6: The clamp side of the collet and the 10-pF capacitors that provide some isolation for an injected "integrity" signal.

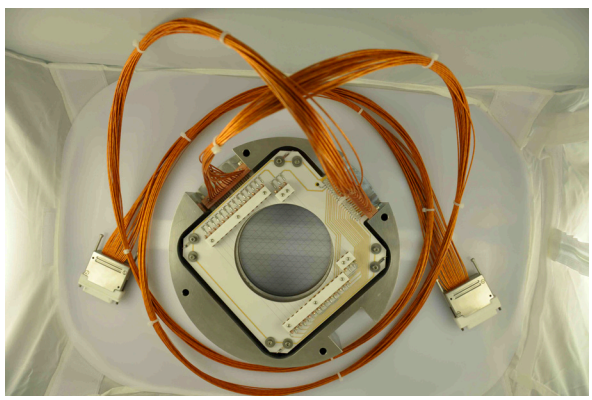

Figure 7: The harp in its instrument carrier prior to installation on the bottom of the insert.

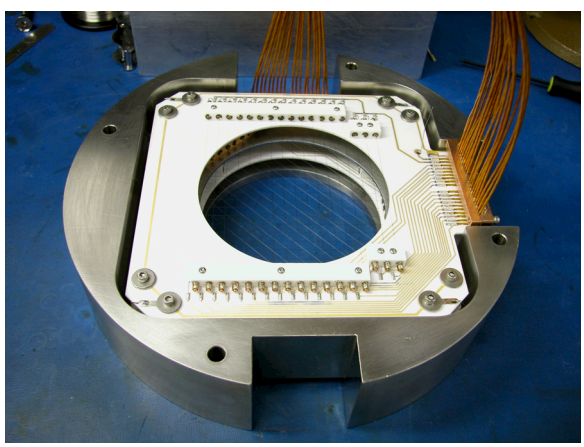

Figure 8. A closer view of the 3-plane harp installed in its instrument carrier.

1L HARP FABRICATION & INSTALLATION

The fabrication of the harps was initiated by manufacturing the ceramic printed circuit boards. These printed circuit boards were first designed by a mechanical and electronics designer. The mechanical designer defined the circuit board dimensions and the electronics designer laid out the circuit traces on the circuit board design. After the circuit boards were fabricated without circuit traces and then Ni traces as defined by the electronics designer was initially placed on the ceramic circuit boards. A 13-micron Au layer was plated on the traces to avoid radioactive mixed waste.

Figure 9 is a drawing showing the collet style anchorage system of the Mark III harp. Figure 10 shows one of the anchorage and tensioning collets used in the Mark III harp. The collets are made UNS C10100 full hard copper, and were difficult to machine because of the ductile nature of the copper combined with the relatively long length and small diameter of the collet. The manufacturer, Model Products of Albuquerque, NM, suffered a high loss ratio during turning of the collet shafts. The slots in the end of the collets were cut using EDM wire cutting performed by Excel Manufacturing, also of Albuquerque. The collets are drilled through to an internal diameter of 0.38 mm.

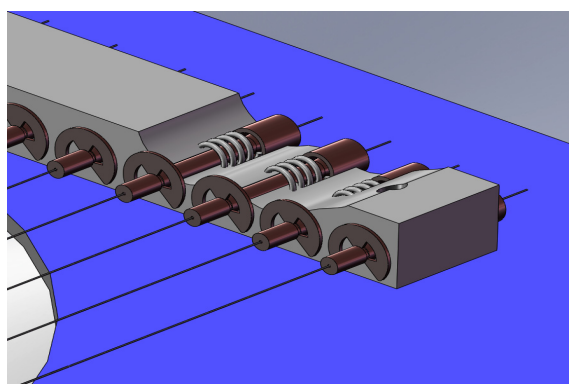

Figure 9. The cut-away drawing above shows copper collets placed in a Macor dielectric holder.

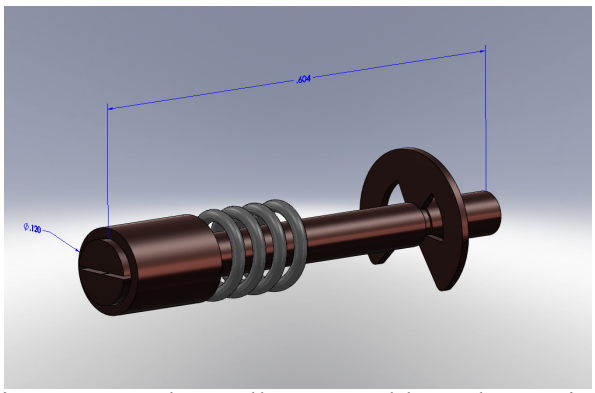

Figure 10. The collet assembly. The spring pushes against the Macor block and the collet collar, causing the collet to clamp and tension the signal wire simultaneously.

A special set of kapton coaxial cables was purchased and installed on the individual signal-plane circuit boards [6]. One set of in-vacuum cables reaches from the signal plane circuit board strain reliefs to its associated conflat flange D-connector feedthrough (see Figures 7 & 8) [6]. Another special set of equivalent coaxial cables on the air-side cable mates to this same D-connector feedthrough and makes the proper connections to an existing MS connector [6]. The rest of the existing cable plant is used.

The TRMS Mark III harp was installed into the instrument carrier and then both were attached to the beam pipe insert. With the appropriate bore sighting tools, the harp's alignment offset was measured and recorded.

FUTURE PLANS FOR ELECTRONICS

Presently, each fiber's signal is sent to a CAMAC 7166D QDC (charge integrating digitizer). In the coming year, we hope to install another, more recent set of electronics that will digitize the integrated charge and will be capable of providing the distribution and position of this measurement for the horizontal and vertical projected planes.

SUMMARY

The new harp implements a simple, robust technique for measuring a simple beam distribution for two orthogonal planes for the beam within the TRMS Mark III target. It was further simplified from the TRMS Mark II target harp. Some of these simplifications included 50% fewer fibers in the harp and a single bias plane. The improvement also includes the addition of isolating capacitors that provide a method of testing fiber integrity.

REFERENCES

[1] J. O'Toole, et al., "TMRS MK III Engineering Design," IEEE Nuclear Science Symposium and Medical Imaging Conference, Orlando, FL, October 23-31 2009.

[2] Private communication with Charles Kelsey (LANSCE Division) and his discussions with radiation protection personnel.

[3] S. J. Sternglass, "Theory of Secondary Electron Emission by High-Speed Ions," The Physical Review, published by the American Physical Society, Second Series, Vol. 108, No. 1, October 1, 1957.

[4] M. Plum, "Interceptive Beam Diagnostics - Signal Creation and Materials Interactions," 2004 Beam Instrumentation Workshop, Tutorial, May 3 – 6, 2004.

[5] Manufacturer of the Macor circuit boards were manufactured Cetek Technologies, Inc., 19 Commerce Street, Poughkeepsie, NY 12603, Tel. 845-452-3510. The printed circuit boards were plated by Elcon, Inc., 1009 Timothy Drive, San Hose, CA 95133, Tel. 408-292-7800.

[6] AccuGlass Vacuum Cable information can be obtained from http://www.accuglassproducts.com/home.php?cat=307.

RESOLVER-BASED, CLOSED-LOOP POSITION AND VELOCITY CONTROL FOR THE LANSCE-R WIRE SCANNER*

J. Sedillo, LANL, Los Alamos, NM 87545, U.S.A.

Abstract

This study evaluates a technique for the closed-loop position and velocity control of a wire scanner actuator. The focus of this technique is to drive a stepper motor-driven actuator through a 1-mm move using a combination of velocity feedback control and position feedback control. More specifically, the velocity feedback control will be utilized to provide a smooth motion as the controller drives the actuator through a pre-planned motion profile. Once the controller has positioned the actuator within a certain distance of the target position, the controller will transition to position-based feedback control, bringing the actuator to its target position and completing the move. Position and velocity data is presented detailing how the actuator performed relative to its commanded movement. Finally, the layout of, and algorithms employed by the wire scanner control system are presented.

INTRODUCTION

A goal of the LANSCE-R wire scanner design is that it possess the ability to utilize closed-loop feedback for the positioning of the wire scanner actuator. The focus of this study is to describe a controller that utilizes a velocity controller to provide smooth acceleration, cruise, and deceleration motions until finally handing-over control to the position controller to bring the actuator position to within some distance of the desired position.

For this evaluation, a LEDA wire scanner was used. This wire scanner is driven by a Parker OS22B stepper motor coupled to a Moog resolver. A National Instruments compact RIO 9074 was used as the controller. As is typical in general for closed-loop control systems; in order to position the actuator, the controller reads the sensor data of the resolver, compares the resolver data with a commanded set point, and then acts on the drive mechanism (i.e. motor) to drive the actuator to the commanded set point. The drive pulse rate was limited to any frequency within the range of 15.2 Hz to 2.5 kHz.

POSITION AND VELOCITY CONTROLLER

Position Controller

The position controller (algorithm shown in figure 1) reads the actuator position data from the RDK 9314 (resolver-to-digital converter) module and subtracts that position from the commanded position resulting in a position error e(t). This error is then fed into a proportional, integral, and derivative controller. The proportional controller simply multiplies the position error by a constant known as the proportional control constant K_p (unitless). The proportional control constant has the effect of driving the actuator at a higher rate of speed if the position error is large, and a lower rate of speed if the position error is small. The derivative portion of the controller subtracts the present value of the position by the previous position value. This result is then multiplied by the derivative control constant K_d (μseconds).

Generally, the derivative controller is beneficial for command tracking since it detects deviations in the rate of change between the commanded and measured positions (a.k.a. position error). The larger the deviation in the rate of change of the error, the more severely it acts to correct the error. Finally, an integral controller simply sums the position error over time.

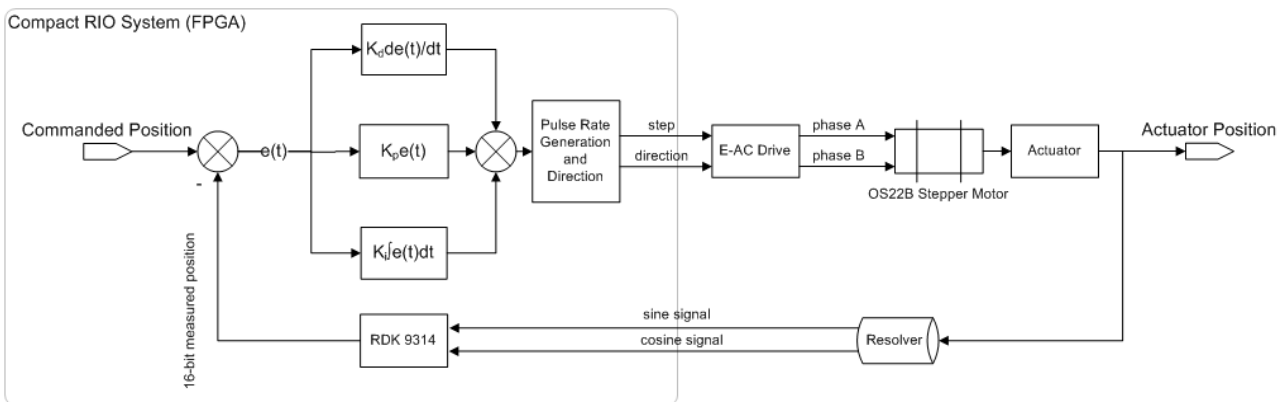

Figure 1: Position Controller Algorithm.

*Work supported by U.S. Department of Energy

As with proportional and derivative control, the effect of the integral error is reduced or magnified by the integral constant K_i ($\mu seconds^{-1}$). Integral control has the benefit of driving the system to zero steady-state error.

The results of the proportional (P), integral (I), and derivative (D) controllers are then summed to form the control output. In the case of the system implemented here, the results of the PID controller act upon the step-rate of the stepper motor. Positive errors drive the stepper motor counter-clockwise (actuator forward) while negative errors drive the stepper motor clockwise (actuator backward). The larger the error, the faster the motor turns. The summed result of each controller (P, I, and D) is input to the pulse rate generator.

In this case, the summed result passes through the following relations:

$$PRF_{\text{stepper}} = K_{\text{clock}} \times \alpha \qquad (1)$$

$$Direction = \begin{cases} \text{forward } a \geq 0 \\ \text{backward } a < 0 \end{cases} \qquad (2)$$

where $PRF_{stepper}$ is the pulse rate applied to the stepper driver, K_{clock} is the clock rate of the FPGA, and is the resolver angular measurement of position in radians. The summed resolver angle error value may vary anywhere from $380x10^{-9}$ to $62.5x10^{-6}$ radians; corresponding to a controller-induced pulse rate from 15.2 Hz to 2.5 kHz. The error's effect on step rate keeps the system operation equivalent to servo motor systems since the step-rate is linearly related to the angular velocity of the stepper motor and is a parameter which can be changed rapidly.

Velocity Controller

The velocity controller (algorithm depicted in figure 2) behaves in much the same way as the position controller. However, in this case, the velocity controller acts upon the velocity error; not the position error. In this case, proportional-only control is utilized since the velocity data attained from the stepper motor motion has a high degree of high-frequency noise.

In order to provide smooth motion, the velocity controller must first have a filtered velocity signal obtained from the resolver. This filtering is necessary because the step-like nature of the stepper motor introduces high frequency noise into the position measurement. The effect of this noise is exacerbated once its derivative is taken to compute the velocity. This noise is reduced through the use of an 8-point running average filter. The second method utilized to smooth the motion is the use of a pulse-code modulation technique to modulate the stepper pulse frequency. This technique causes positive error to increase the pulse rate and negative error to decrease the pulse rate. It prevents the motor from being driven in reverse in order to slow it down.

The overall operation of the position and velocity controller is summarized in the flow diagram of Figure 3. It summarizes how the two controllers (velocity and position) are coordinated in order to accomplish a move. In this scheme, the velocity controller acts first, following a motion profile until the actuator's position resides within a specified distance of the target position. Once within this target position, the position controller takes over and positions the actuator to within a smaller distance of the target position. Finally, when the actuator has been adequately positioned, both controllers quit operating on the actuator in order to prevent dithering and lock the actuator position in place.

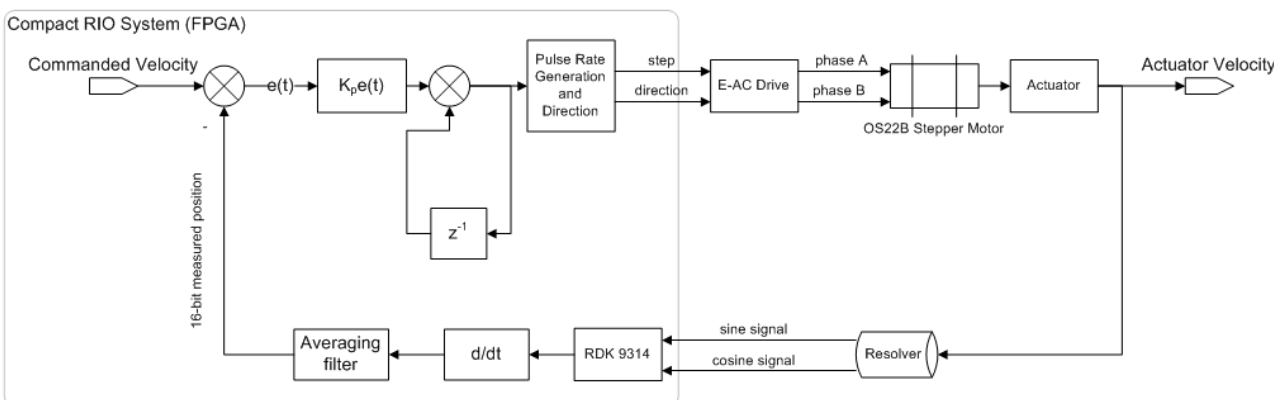

Figure 2: Velocity Controller Algorithm

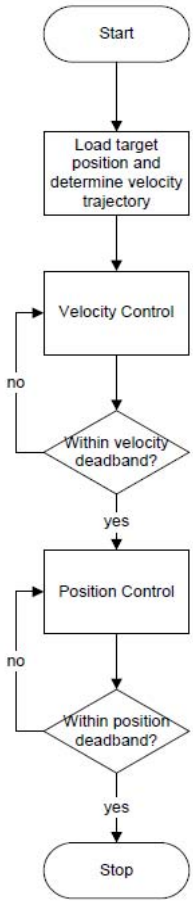

Figure 3: Velocity and Position Controller Switching.

POSITION AND VELOCITY CONTROLLER PERFORMANCE

The following plots detail the motion of this control system for 1-, 3-, and 5-mm moves. The resolver resolution was set for 12 bits with a 16-bit readback resulting in a position resolution of 1.9 micrometers.

Figure 4: Plot of position of 1-mm move.

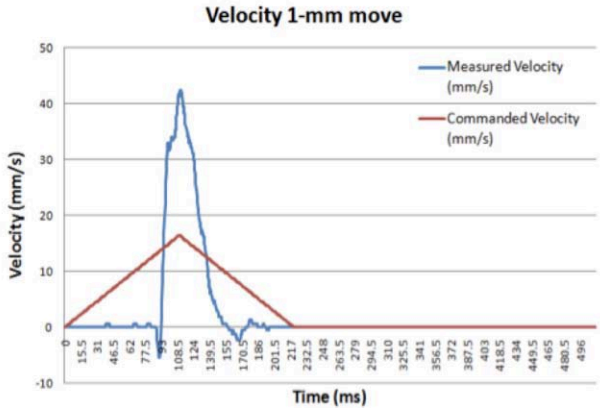

Figure 5: Plot of velocity of 1mm move.

Figure 6: Plot of position of 3mm move.

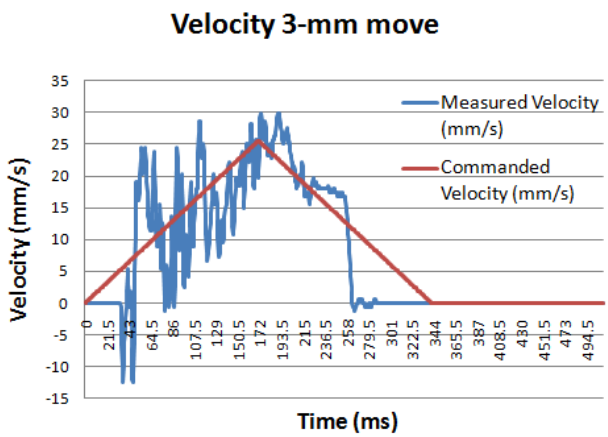

Figure 7: Plot of velocity of 3mm move.

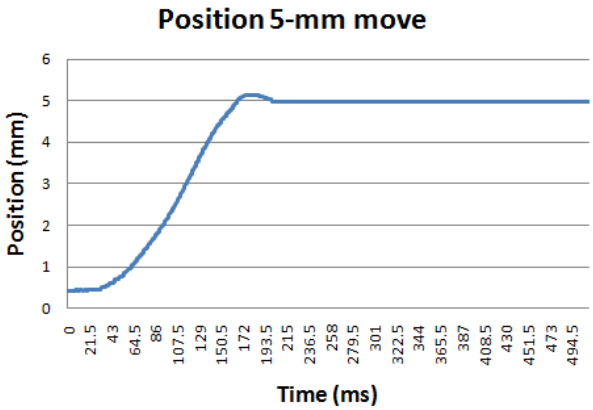

Figure 8: Plot of position of 5mm move.

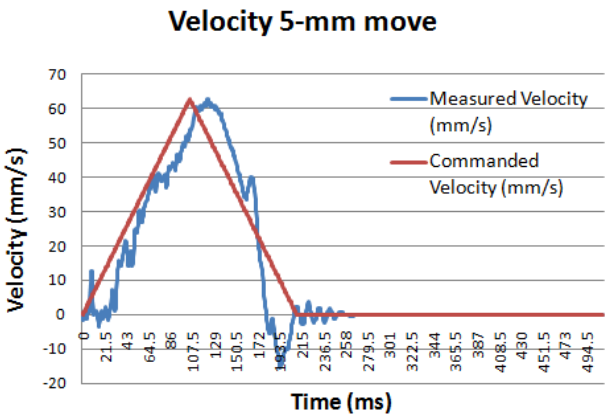

Figure 9: Plot of velocity of 5mm move.

The data suggests that the combined velocity and position controller is quite affective for larger moves, while performance is decreased for smaller moves. This may be due to a few factors. First of all, movement resolution (i.e. motor steps per move) is reduced for smaller moves, thus the ability to make these moves "smooth" is reduced. This is evidenced by the granularity of figure 4. Secondly, smaller moves either require higher proportional gain, or increased velocity setpoint values to alleviate the initial lag in response indicated by figures 5 and 7. The 5-mm move of figure 8 shows the smoothest motion in position.

SUMMARY

All in all, it is evident that a reasonable degree of position smoothness can be attained by the use of this velocity control method generally in moves that are larger than a millimeter.

Improvements in performance may be attained with decreased step size, improved PID tuning, and improved low-pass sensor noise filtering. However, the tradeoff associated with decreased step size will be a decrease in applied motor torque whereas the tradeoff associated with lower-bandwidth sensor noise filtering will be decreased controller bandwidth. Future studies of brushless and dc servo motor systems may improve the tracking capabilities of wire scanner actuator systems. Furthermore, others [1] have shown that full-state estimation and PID control techniques of stepper-based systems are possible through the use of a linearization controller and a stepper motor driver capable to driving the individual stepper phase windings in an analog fashion.

REFERENCES

[1] R. Rekowski, "Implementation of an Exact Linearization Controller for a Permanent Magnet Stepping Motor Using Only Optical Encoder Feedback." Master's thesis, Univ. Pittsburg, 1991.

LANSCE WIRE SCANNER AFE: ANALYSIS, DESIGN, AND FABRICATION*

M. Gruchalla#, EG&G Albuquerque Operations, Albuquerque, NM 87107, U.S.A.

P. Chacon, J. D. Gilpatrick, D. Martinez, J. Power, B. Smith,

Los Alamos National Laboratory, Los Alamos, NM 87545, U.S.A.

Abstract

The goal of the design LANSCE-R Wire-Scanner Analog Front-end Electronics is to develop a high-performance, dual-axis wire-scanner analog front-end system implemented in a single cRIO module. This new design accommodates macropulse widths as wide as 700μs at a maximum pulse rate of 120Hz. A lossey integrator is utilized as the integration element to eliminate the requirement for providing gating signals to each wire scanner. The long macropulse and the high repetition rate present conflicting requirements for the design of the integrator. The long macropulse requires a long integration time constant to assure minimum integrator droop for accurate charge integration, and the high repetition rate requires a short time constant to assure adequate integrator reset between macropulses. Also, grounding is a serious concern due to the small signal levels. This paper reviews the basic Wire Scanner AFE system design implemented in the cRIO-module form factor to capture the charge information from the wire sensors and the grounding topology to assure minimum noise contamination of the wire signals.

INTRODUCTION

One element of the LANSCE-R task is to replace a number of the aging wire-scanner systems. Both the mechanical components and the electronics are to be replaced.

The National Instruments cRIO system has been selected as the basic platform for the wire-scanner electronics [1]. To the extent feasible, commercial of-the-shelf (COTS) cRIO modules are being utilized with custom modules for specific tasks designed specifically for the LANSCE-R application. The Wire-Scanner Analog Front-end Electronics (WS AFE) is a custom cRIO module.

The WS AFE independently collects and integrates the charge from two orthogonal sensing wires and delivers the processed analog signal to cRIO digitizers. The goal for the LANSCE-R application is to provide the ability to capture macropulses as long as 700μs at a maximum macropulse rate of 120Hz. The long macropulse and the short inter-pulse period present a unique challenge in the design of the integration function of the WS AFE.

The small signal levels expected at the extremes of the beam distribution require careful attention to minimizing noise encroachment into the WS AFE signal paths. It is reasonably expected that there will be a substantial potential difference between the beam-line equipment ground and the electronics equipment ground. This represents a nuisance potential that could corrupt the wire-scanner data. Therefore, management of the grounding between the beam line and the instrumentation is critical.

DESIGN STRATEGIES

The LANSCE accelerator is a production system, as compared to a purely experimental accelerator, and the wire scanners are diagnostic tools used to manage system operation. In comparison to typical experimental venues, the magnitude and spectrum of the wire-scanner signals expected in the LANSCE accelerator are very-well bounded. This relieves some of the complexity of the WS AFE by allowing functions typically required in the wire scanner to be moved into other elements of the system. Several of the more critical design challenges are reviewed below.

Measurement Dynamic Range

The maximum total collected charge in a macropulse is a function of the wire-scanner location in the LANSCE accelerator. The dynamic range of collected charge across all locations at the distribution center is less than nominally 100. The dynamic range required in the measurement at any specific position has been set at nominally 100. Therefore, a total dynamic range of 10,000 is required in the WS AFE system so that any WS AFE unit may be utilized at any position [2].

Normally, the WS AFE would include analog gain switching to accommodate a very wide operational dynamic range. Since only a nominal 10,000 dynamic range is required in the LANSCE-R application, this may be totally provided in the cRIO digitizers. A National Instruments NI 9205 cRIO digitizer is utilized to digitize the WS AFE analog signals. The NI 9205 is a 16-bit plus sign digitizer and provides four full-scale sensitivities: ±10V, ±5V, ±1V and ±200mV. This unit provides a theoretical dynamic range of 3e6 with a basic precision of 3μV.

Measurement Sensitivity

The measurement sensitivity required is a function of how far down in the distribution data is desired at the position in the accelerator providing the lowest signals.

*Work supported by US Department of Energy

#gruch@lanl.gov

Based on historical wire-scanner data at LANSCE, a noise-limited sensitivity of nominally 100pC is adequate. The design goal is a noise-limited sensitivity of less than 1pC in the WS AFE alone [3], and better than 10pC overall.

Charge Integration

In a typical wire-scanner application, the charge collected from the wire-scanner sense wire is integrated directly in the analog electronics. A simple lossey integrator is contraindicated in the LANSCE-R application due to the long macropulse length of 700μs and the high PRF of 120Hz (8.33ms pulse period). The integrator time constant required for acceptable integrator droop and the integrator time constant required for adequate integrator reset between macropulses are conflicting.

An integrator reset signal specific for each wire scanner would normally be required to provide both high-quality macropulse charge integration and adequate inter-pulse integrator reset. However, providing separate unique timing signals for each wire scanner would substantially increase the command and control complexity of the overall accelerator wire-scanner system.

A hybrid approach for charge integration is used in the LANSCE-R WS AFE. The AFE provides a lossey analog integrator having a comparatively short integration time constant to provide adequate integrator reset between macropulses, and numeric integration is provided in the cRIO FPGA to provide integration of the total charge collected during each macropulse.

Grounding

Grounding is always a challenge in low-noise instrumentation systems. And, due to the numerous high-level devices, such as RF sources, magnets, kickers, etc., high-quality low-level instrumentation grounding in accelerator facilities is a unique challenge. In general, it must be expected that there will be substantial nuisance potentials between the beam line and the electronics.

The nature of the sensor in a wire scanner also presents a unique grounding challenge. The sense wire presents as virtually a true current source. Therefore, it has no ground reference. A simple coaxial cable from the beam line to the electronics will not provide a high-performance ground where there are significant nuisance potentials between the ends of the coaxial path.

A combination of conventional grounding and shielding is utilized with a guard system to provide a high-quality shielding of the sense-wire signal.

Sense-Wire Bias

A DC bias potential is required to optimise the charge signal. The bias magnitude and polarity are a function of the beam energy, particle species, wire material, etc. A bias range of zero to ±50V has been specified for the LANSCE-R wire scanners. The wire bias is provided through the WS AFE from an external power supply.

Wire Integrity Validation

An important element of a wire-scanner system is a means to validate the integrity of each sense wire. It is also useful to have means to validate the integrity of the wire-validation system to assure that a failure in the integrity system does not falsely indicate a broken wire and subsequent unnecessary removal of a wire scanner from the beam line.

The integrity of the sense wire is provided by simply driving a test signal through the wire and sensing the resulting signal with the data-acquisition electronics.

CIRCUIT DESCRIPTION

A simplified schematic diagram of one WS AFE signal channel is shown in Figure 1. Two independent signal channels are implemented in a single cRIO module to allow instrumentation of both wires of a typical two-wire wire-scanner system in a single cRIO module.

Sense-Wire Interface

Access to both ends of the sense wire is necessary to allow the wire integrity to be validated. Referring to Figure 1, both ends of the sense wire are instrumented separately and the signals summed. It is important to note that this configuration is not a differential measurement since the wire is not a differential source.

The signals from each end of the sense wire are communicated to the vacuum interface on coaxial cables. Since this path is very short, and is inside the beam pipe, grounding is much less critical than the long cable path to the instrumentation. Therefore, this short length of coax is simply grounded to the beam-line equipment ground inside the beam pipe. This allows the use of standard radiation-tolerant coax and standard vacuum feed-through connectors.

From the vacuum interface to the instrumentation, the two wire signals are carried on separate triaxial coax. The use of a triaxial cable configuration allows the signal path to be both shielded and guarded.

Some RF signal is expected to be collected by the sense wires. The frequencies of these RF components are well beyond the bandwidth needed in the WS AFE. This RF energy could corrupt the operation of the WS AFE input circuitry if allowed to enter the sensitive inputs of the

amplifiers. Therefore, RF energy with spectral components outside the operational bandwidth of the analog circuitry is filtered out by the R1-C1 pole at 100kHz.

There is also a concern that the AFE input circuitry could be damaged by electrostatic discharge (ESD) events. For example, if the instrumentation cable were disconnected during beam operations, charge collected by the sense wire could charge the cable capacitance to high enough potentials to damage the AFE input circuitry when reconnected. To protect the AFE input, a transient-protection network is provided immediately at the input to the first amplifier as shown in Figure 1. Resistor R2 provides a current-limiting impedance to protect the transient-protection network and to improve the effectiveness of the protection provided.

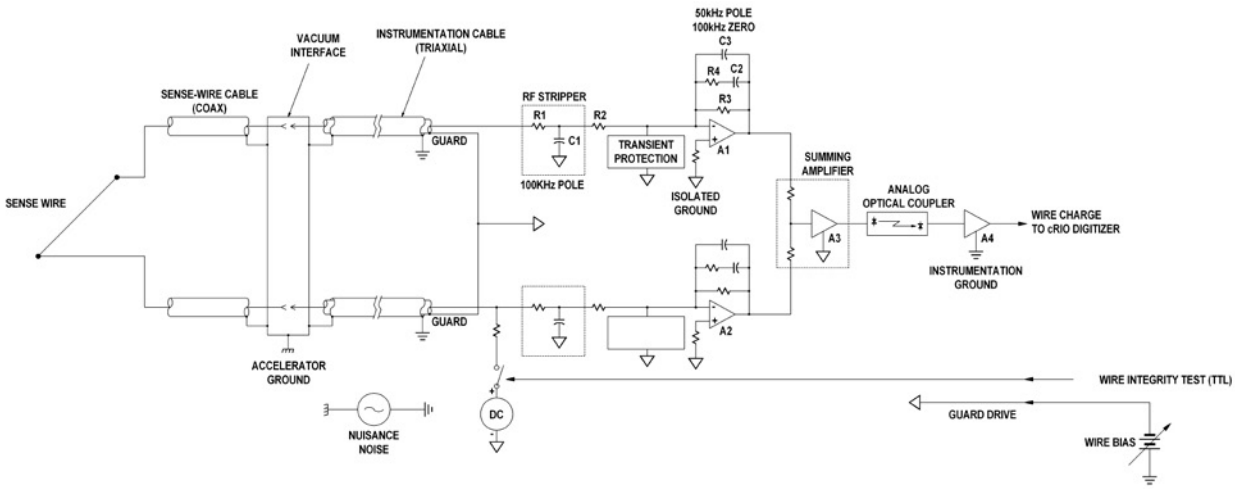

Figure 1: Single Channel of the LANSCE-R Wire Scanner-Analog Front-end Electronics

A second network pole is introduced by the time constant of R2 and the capacitance of the protection network. The value of R2 is selected to place that pole at nominally 500kHz to limit the input noise bandwidth.

Input-Amplifier Configuration

The wire signal current is delivered to the input to amplifier A1 configured as a transimpedance amplifier. The DC gain of this configuration is equal to R3. Capacitor C2 introduces a dominant network pole at 50kHz. This is the basic response bandwidth of the AFE. Resistor R4 and Capacitor C2 introduce a network zero at 100kHz to cancel the pole of the RF stripper. This provides a true integral response above 50kHz. Capacitor C3 provides a final high-frequency pole to define the overall noise bandwidth of the first AFE stage.

Two identical signal paths are utilized to sense both ends of the sense wire. As noted above, this is not differential sensing. When charge is collected, the charge is divided between the two signal paths and each charge component is processed in the corresponding input stage.

The two wire signals are simply summed in the summing amplifier A3. The output signal of A3 represents the total charge collected by the wire sensor.

Dielectric Isolation

Dielectric isolation of the input circuitry is provided by a high-performance analog optical coupler. The coupler utilized (HCNR200) provides 5kV RMS isolation (recognized under UL-1577). The -3dB bandwidth of the isolator was measured to be in excess of nominally 3MHz, The specified transfer error and nonlinearity is 0.01%. All these parameters are well within the requirements of the WS AFE.

Output Stage

The optical isolation is followed by a buffer amplifier referenced to the cRIO instrumentation ground. For LANSCE-R, since the overall dynamic range required is well within the signal-to-noise ratio of the AFE at full-scale output, and well within the capabilities of the digitizers, the gain of the WS AFE is fixed to provide a ±5V full-scale output for the largest wire signal expected within the LANSCE accelerator.

Bias

Typically, a bias electric field must be provided to minimize recapture of secondary electrons radiated from the wire. For the LANSCE-R system, the most straight-

forward approach to providing this bias is to bias the sense wire itself. This is accomplished in the LANSCE-R WS AFE by elevating the entire input circuitry to the desired bias potential. Since the input amplifiers are of a transimpedance configuration, the input node of the amplifier is forced to the reference ground of the input stages. By elevating this input-circuit reference-ground net to the desired bias potential, that bias potential is delivered directly to the sense wire. This is shown in Figure 1. The bias potential is delivered externally to the WS AFE cRIO module and is applied directly to the reference ground of the input stage.

Frequency Response and Charge Integration

The overall response of the basic WS AFE is flat from DC to 50kHz, and then breaks with a true first-order pole to nominally 1MHz. Above 1MHz, a second pole is introduced to limit the system noise bandwidth. Therefore, above the 50kHz pole, the WS AFE is self integrating to 1MHz. A complete integral response of the wire signal is achieved by providing numeric integration with a numeric zero at 50kHz to cancel the hardware pole at 50kHz. Since the DC component is not typically of interest in a wire-scanner system, the DC component is numerically removed prior to integration.

Data are collected over the entire macropulse, and numeric integration of the wire signal above 50kHz is provided real time in the cRIO native VIRTEX 5 FPGA and cRIO Power PC. This allows both the temporal characteristics of each macropulse (with 50kHz bandwidth) as well as the overall macropulse integrated charge to be recorded and displayed on a pulse-by-pulse basis.

Wire-Integrity Verification

Sense-wire integrity is provided by passing a test current through the wire and recording the response through the normal data-acquisition path.

In Figure 1, a DC potential of nominally 100mV is switched into the input path of the WS AFE by means of an external TTL signal. When this potential is applied, the two input amplifiers operate as voltage amplifiers having a nominal gain of R3/R2 with a 50kHz bandwidth.

The test signal is delivered directly to Amplifier A2, and in turn to the summing amplifier A3. If the sense wire is intact, this test signal is also delivered to amplifier A1 through the sense wire, and to the summing amplifier.

The output signal level with an intact wire is the sum of the two signals of amplifiers A1 and A2 respectively. However, if the sense wire is broken, no signal is delivered to amplifier A1. The resulting sum is then nominally one half that seen with an intact wire.

This method of wire-integrity validation not only provides verification of the sense-wire continuity, but also provides verification that the wire-integrity circuitry is operational. This assures that a failure in the wire-integrity system will not be interpreted as a wire failure.

Grounding and Shielding

High-quality grounding is critical due to the small signal levels expected at the extremes of the beam distribution and particularly at the accelerator locations having the lowest peak signal levels. This is further complicated by the fact that the sense wire presents as virtually a true current source with no reference to a signal ground. But, the AFE input stage must measure the input signals with respect to its own ground reference.

The instrumentation alcoves are approximately 50m from the beam line. It is reasonably expected that there will be a potential comprised of various signals between the beam-line equipment ground and the instrumentation equipment ground. This potential is shown as the “Nuisance Noise” source in Figure 1. One of the known nuisance noise sources is the motor-drive signal to the wire-scanner actuator mechanism.

When a coax is utilized to carry the sense-wire signal, and its shield is connected to the beam-pipe and the instrumentation equipment grounds respectively, the nuisance potential between the beam pipe and the instrumentation grounds presents this nuisance potential across the shield which introduces a nuisance current in the shield of the coax.

The shielding-effectiveness transfer function of the coax results in a potential on center conductor, and the capacitive coupling between the shield and center conductor results in a capacitive coupling of shield potentials to the center conductor. These effects can produce substantial noise on the center conductor.

The noise performance may be improved by guarding the input signal node along the entire signal path from the wire sensor to the AFE. A guarding system is utilized in the LANSCE-R wire-scanner system to provide a high-level of noise rejection. A triaxial coax is utilized with the outer shield connected between the beam-line and instrumentation equipment grounds in a conventional fashion. This outer shield provides protection from radiated fields. The inner shield of the triax is driven by the guard-drive signal in the WS AFE.

The guard drive is a low-impedance source that effectively forces the guard shield to the same potential as the input-signal potential. Since this inner shield is forced to the same potential as the signal conductor, the signal conductor is protected, e.g., shielded from, coupling from the outer shield to the inner shield.

The transimpedance input-stage configuration of the WS AFE shown in Figure 1 forces its input node to the amplifier reference potential, e.g., the virtual ground of the input-stage. Since the input-node potential is at the input-stage ground reference potential, the guards must be driven to that same reference potential. In Figure 1, the guard shields of the triax s are connected to the input stage isolated reference ground. This isolated ground is driven by the bias source.

The bias source is a low-impedance source which effectively holds the guard shield of the triax at the bias potential. This guarding configuration shields the center conductor of the triaxial cable from conducted and radiated noise impressed on the outer shield.

SUMMARY

The design of the new analog front-end electronics for the LANCE-R wire scanner has been provided in this work. Details of a wide-bandwidth transimpedance input stage with numeric charge integration to meet the macropulse width and PRF requirements has been described. The method of providing bias directly on the sense wires was reviewed. The grounding and guarding topology to provide low-noise charge collection was detailed.

REFRENCES

[1] National Instruments, Inc., Austin, TX 78759-3504, www.ni.com/compactrio.

[2] J. D. Gilpatrick, D. Barr, L. Day, D. Kerstiens, M. Stettler, R. Valdiviez, M. Gruchalla, J. O'Hara, J. Kamperschroer, "Beam-Profile Instrumentation for a Beam-Halo Measurement: Overall Description, Operation, and Beam Data," DIPAC'01, Grenoble, May, 2001 CT05, p. 76 (2001); http://www.JACoW.org.

[3] M. E. Gruchalla, J. O'Hara, D. Barr, T. Cote, L. Day, D. Gilpatrick, M. Stettler, D. Martinez, "Beam Profile Wire-Scanner/Halo-Scraper Sensor Analog Interface Electronics," PAC'01, Chicago, June, 2001, WPAH098-3, p. 2314 (2001); http://www.JACoW.org.

A STATISTICAL ANALYSIS OF THE BEAM POSITION MEASUREMENT IN THE LOS ALAMOS PROTON STORAGE RING*!

J. Kolski#, R. Macek, R. McCrady, LANL, Los Alamos, NM 87545, U.S.A.

Abstract

The beam position monitors (BPMs) are the main diagnostic in the Los Alamos Proton Storage Ring (PSR). They are used in several applications during operations and tuning including orbit bumps and measurements of the tune, closed orbit (CO), and injection offset. However, the BPM data acquisition system makes use of older technologies, such as matrix switches, that could lead to faulty measurements. This is the first statistical study of the PSR BPM performance using BPM measurements. In this study, 101 consecutive CO measurements are analyzed. Reported here are the results of the statistical analysis, tune and CO measurement spreads, the BPM single turn measurement error, and examples of observed data acquisition errors.

INTRODUCTION

A PSR BPM is a collection of four stripline electrodes located in the beam pipe and situated top, bottom, left, and right. The BPM diameters are 4″ and 6″. They are tuned to the 201.25 MHz longitudinal structure of the beam and are a 201.25 MHz quarter wavelength long, ~37 cm. A mechanical relay matrix switch (MUX) selects the BPM for measurement. There are four MUXs to interface with each of the four BPM electrodes. Beam signals from the selected BPM pass the MUX to the analog front end (AFE) where the signals are converted from AM to PM. The AFE outputs a voltage proportional to the power ratio deposited on opposing BPM electrodes [1]. The voltages are digitized by a 12-bit analog to digital converter (ADC). The intrinsic BPM resolutions (defined as the BPM diameter divided by 2 to the power of the bit depth, $d/2^b$) are .0124 mm and .0186 mm for the 4″ and 6″ BPMs respectively. The ADC is triggered to digitize data by a beam present trigger. The digitized voltages are read to the input/output controller (IOC) where they are converted back to beam positions using geometric coefficients and AM-PM theory [2, 3]. The position data is lastly read by EPICS.

There are 18 real and two "missing" BPMs in the PSR. The missing BPMs do not exist, but data is still collected. The missing BPMs are included in the analysis because they possess information about the data acquisition errors. For the convenience of analysis, an orbit response matrix (ORM) BPM naming convention is employed. This convention distinguishes the two dimensions of a single BPM, dividing a bi-directional BPM into two different BPMs, a horizontal and vertical BPM. The convention then gathers all BPMs of the same direction and numbers them consecutively. Thus, the 20 BPMs in the PSR are divided into 40 different BPMs. BPMs 1-20 are the horizontal BPMs and BPMs 21-40 are the vertical BPMs such that BPM 1 and BPM 21 are the horizontal and vertical division of SRPM01, BPMs 2 and 22 are the horizontal and vertical parts of SRPM02, and so on. The missing BPMs are indexed as BPMs 10, 15, 30, and 35.

MEASUREMENT SETUP AND DATA ANALYSIS

The PSR was set up for single turn injection and after ~1800 turns, extraction to the tune up beam stop (TUBS) at 20 Hz. The vertical bump magnets and the harmonic buncher that respectively allow phase space painting in the vertical and keep the beam bunched longitudinally were turned off. The CO was centered. The beam was injected near-on-axis ([-0.72 mm, 0.31 mradian] in the horizontal and [1.99 mm, -0.168 mradian] in the vertical) to avoid scraping and BPM saturation. Injecting near-on-axis allowed for 40 turns of turn-by-turn beam positions to be collected before the 201.25 MHz longitudinal structure of the beam washed out due to momentum variation in the mircopulses. The energy of the beam was corrected using the time of flight for 1100 turns.

One hundred one consecutive CO measurements were taken for the same PSR configuration. Each CO measurement consists of 40 turns of turn-by-turn beam position data at each BPM. Since a MUX is employed to select the BPMs, data from only one BPM can be recorded per machine cycle. The CO is measured at each BPM on a different pulse with slightly different central momentum (different CO) due to the pulse-to-pulse momentum variations in the linac. It took 7.5 minutes to take 101 CO measurements.

As the beam circulates around the ring, it performs harmonic (betatron) oscillation about the CO. Thus, the turn-by-turn BPM data is then fit to a cosine wave,

$$y_n = A\cos(2\pi\nu n + \phi) + O_{offset}, \qquad (1)$$

where y_n is the turn-by-turn BPM data, n ranges from 1 to 40; A, ν, ϕ, and O_{offset} are the amplitude, betatron tune, phase, and CO respectively. A nonlinear least squares fitting routine was used to fit for A, ν, ϕ, and O_{offset}. The sum of squares of residuals per degree of freedom (SSR/DOF) was used as the goodness of fit quality factor. A maximum likelihood (ML) error analysis was applied to calculate the fitting error on the fitting parameters, the single turn BPM measurement error, and the covariance and correlation matrices relating the fitting parameters. Aside from the tune and the phase, the fitting parameters were found to be uncorrelated. The tune and the phase

*Work supported by the US DOE under contracts DE-AC52-06NA25396 and DE-FG02-92ER40747 and the NSF under contract NSF PHY-0852368.
! LA-UR 10-02364
jkolski@lanl.gov

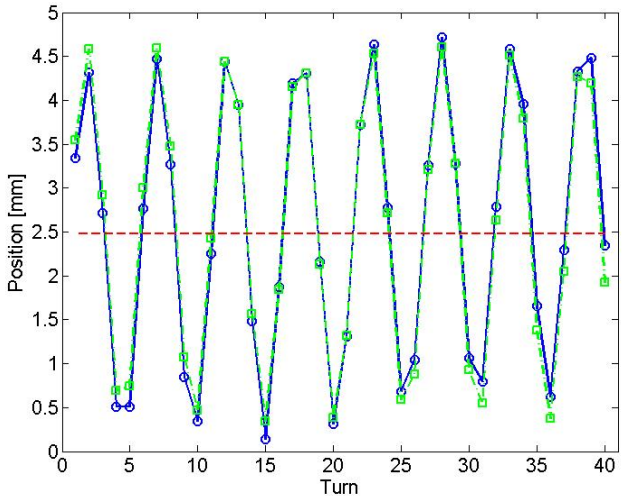

Figure 1: (Color) A typical scan. The blue circles are the BPM data, the green squares are the cosine wave fit, and the red line is the value of the extracted CO from the cosine wave fit of Eq. (1).

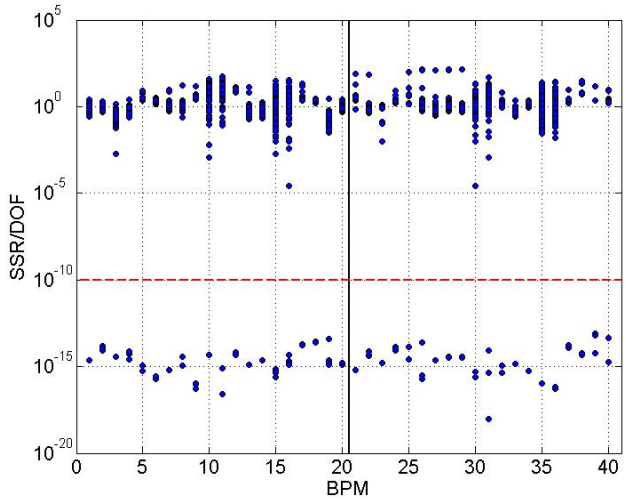

Figure 2: The SSR/DOF comparing the power ratios from one scan with the preceding scan for all scans at all BPMs. The horizontal line shows the threshold value of 10^{-10}. The vertical line divides horizontal and vertical BPMs. Note that some scans from the missing BPMs (BPMs 10, 15, 30, and 35) also have BPM selection errors.

had a correlation of ~-.86. This correlation comes from the fact that the first derivatives of the fitting function, Eq. (1), with respect to the tune and phase differ by a constant $2\pi n$. The ML error analysis assumes mean zero random errors. The average residual for each fit was found to be < 6e-8 mm, satisfying the ML requirement. A typical scan and fit are shown in Fig. 1.

When the turn-by-turn BPM data is fit using Eq. (1), it is assumed that there is no nonlinear motion induced by higher order multipole magnets (such as sextupole and octupole), or nonlinearities in the BPM measurement. This assumption is justified because the beam is injected near-on-axis where the nonlinearities are the smallest. Nonlinearities in the beam position measurement are observed in BPM data when the beam is injected at production injection offsets (~[-3 mm, .6 mradian] in the horizontal and ~[17 mm, 3 mradian] in the vertical) for phase space painting.

DATA ACQUISITION ERRORS

Although the turn-by-turn data is expected to follow Eq. (1), sometimes there are errors in the way that the BPM data is collected or handled and the recorded beam positions are not sinusoidal. Eleven different data acquisition errors were observed in the PSR BPMs [4]. The three most common errors are reported here.

BPM Selection Errors

BPM selection errors look like cosine waves, and fit cosine waves very well because they are cosine waves! BPM selection errors are the most insidious errors. However finding them is not difficult. This error is x-y symmetric i.e. if the error occurs in the horizontal, it also occurs in the vertical.

Normally the ADC buffer, where the digitized voltages are stored, is cleared between machine cycles. When the ADC buffer is not cleared, the IOC reads the same digitized voltages multiple times. However, the IOC "thinks" the data is from the MUX selected BPM which is not the BPM where the digitized voltages originated. The IOC analyzes the same digitized voltages using the different coefficients of the MUX selected BPM. The same data can be used four times and even in different CO measurements.

BPM selection errors are identified and removed from the data set by comparing the power ratios of a scan with the scan taken immediately before it. If the ADC buffer is not cleared, the digitized voltages are used again to calculate the same power ratios for both scans. An SSR/DOF of the difference of the power ratios for both scans can be computed. This value for all scans is plotted in Fig. 2. An SSR/DOF of less than 10^{-10} indicates a BPM selection error.

Of the 3636 scans taken for the CO reproducibility measurement, 78 scans were removed because they possessed a BPM selection error (2.15%), and eight CO measurements of the 101 in the reproducibility dataset had BPM selection errors, 7.95%. This error does not affect the tune, but does yield a fitted phase equal to previous BPM. It is most likely that a BPM selection error will yield faulty amplitude and offset results.

Flat Line Errors

At first glance, flat line errors are obvious errors, and thus easily identified and removed from the dataset. This error is also x-y symmetric. A typical flat line error is shown Fig. 3.

Flat line errors have only been observed in BPMs that immediately follow the missing BPMs. The scan structure of Fig. 3 is consistent with all flat line errors, six or seven points of random noise with significant amplitude and the rest of the data equal to zero. The noise is similar to BPM

data collected with both MUX outputs unplugged and unterminated.

The zeros are easy to understand. The IOC will "fill" the scan with zeros if it receives less digitized turns from the ADC than the user requested number of turns [5].

To understand why there are always six or seven turns of random noise, one needs to look at data recorded from the previous, missing BPM. Data from the missing BPMs always consists of one or two points of random noise. The first point can be attributed to a digitization triggered by noise from the ADC disarm trigger, which fires ~1 ms after T_0, long after the beam has been extracted from the PSR [6]. If there is a second point, it seems to be a digitization ~100 μs after the disarm trigger. This could be a result of the software flushing the ADC pipeline (where three turns of digitized data are stored before being saved to the buffer to increase the ADC sampling speed) before reading the buffer. The power ratios of the first (and/or second) non-zero point from the missing BPM are the same as the power ratios of the first one or two points of the scan with the flat line error. This means that the ADC buffer did not clear properly and the same data is used for both scans. The addition of five points of random noise to the data from the missing BPM is presumably a digitization triggered by noise from the ADC arm and disarm triggers and three points from flushing the pipeline.

Flat line errors are identified as scans that have matching power ratios and more points of turn-by-turn BPM data compared the previous scan. Flat line errors were found in ten of the 3636 scans (.28%) and in five of the 101 CO measurements, 4.95%. If left in the data set, a flat line error will result in bad measurements for all of the fitted parameters.

Missing Turn Errors

A missing turn error occurs when the ADC digitizes the AFE output voltage as normal, but then for some turn, the beam present trigger does not trigger the ADC to digitize data. The beam passes by the BPM and no data is taken. The following beam present triggers prompt the ADC to digitize data like normal.

A typical scan with a missing turn error is plotted in Fig. 4. The missed turn is observed by comparing the BPM data with the initial cosine wave fit guess. Although the initial cosine guess is not perfect, it does have a constant frequency that in the beginning of the scan matches up well with the BPM data. At turn 24, the cosine guess indicates a maximum in the oscillation, but the BPM data goes down from the previous turn. After turn 24, the turn-by-turn data is one turn ahead of the initial cosine guess. However, if the BPM data was delayed a turn for turns after 24, all traces lie on top of each other until a turn is missed, and then the BPM data with the added turn and the initial cosine guess match for the rest scan.

In the CO reproducibility measurement, 106 turns were missed out of 145440 (.073%), 96 scans out 3636 were removed from the data set because they had missing turn

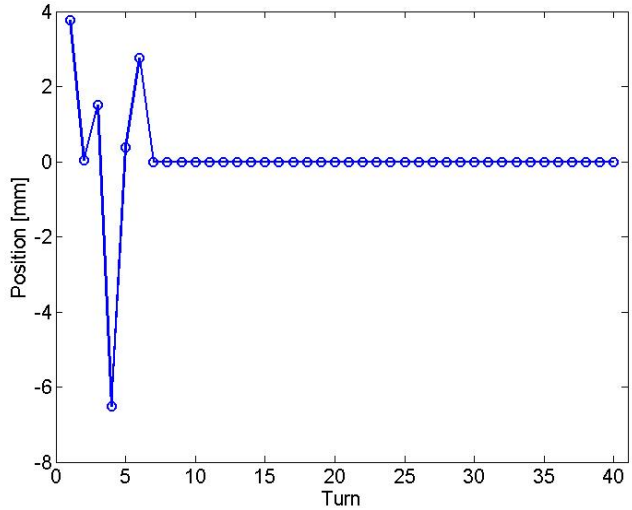

Figure 3: A typical flat line error.

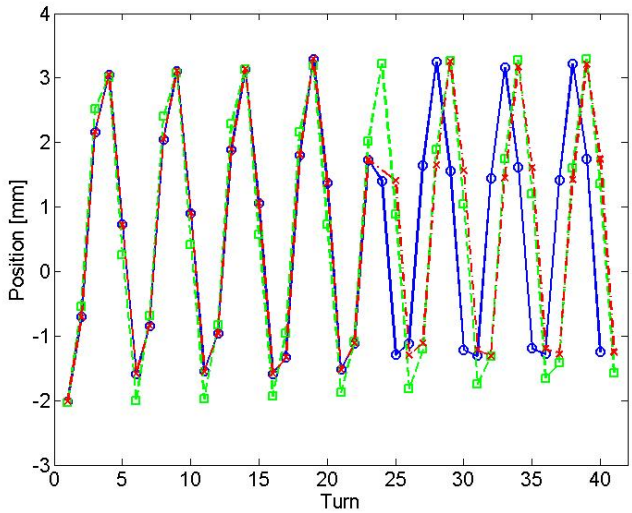

Figure 4: (Color) A typical missing turn error. The blue circles are BPM data, the green squares are points for an initial cosine wave guess fit, and the red x's are BPM data with a turn added at turn 24.

errors (2.64%, 10 scans were observed to have two missing turns), and 42 out of 101 CO measurements contained a scan with a missing turn error, 41.58%. If left in the data set, the missing turn error will compromise the tune measurement and the phase through correlation in the cosine fit, but the amplitude and offset are unaffected.

RESULTS

After the BPM data is fit to a cosine wave and all data acquisition errors have been identified and removed, the resulting good scans are left describing the reproducibility of the beam position measurement. The results for the fitted tune and offset parameters and the BPM single turn measurement error are summarized in this section.

The Fitted Tune

The tune is the frequency of the cosine wave fit. The tune fit is better with more turns of data. Since the tune is

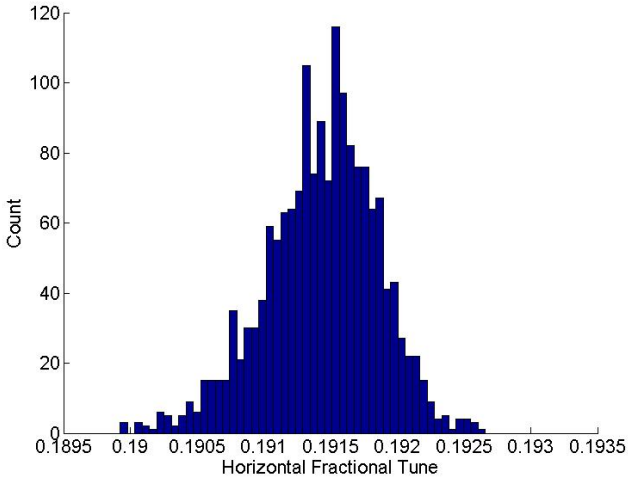

Figure 5: Histogram of final horizontal tune distribution.

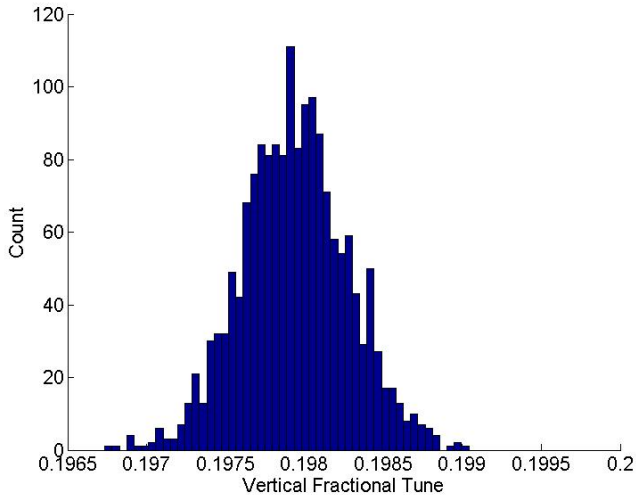

Figure 6: Histogram of final vertical tune distribution.

~.2, 40 turns of data is eight betatron oscillations and yields a good fit. The tune is multiplied by 2π in Eq. (1), so only the fractional tune can be fit. The integer part of the tune will only contribute to other betatron oscillations in between turns and will not be observed in the discrete time measurement of the BPM, $\cos 2\pi = \cos 2\pi i$ where i = 1, 2, 3...

All of the BPMs in one direction measure the same tune, so the final quoted tune measurement is actually the average of all scans in that direction. Histograms of the total horizontal and vertical fitted fractional tune distributions are shown in Figs. 5 and 6. The *rms* standard deviation of these profiles is about 10 times smaller than the expected error using the current operations method, 4.2e-4 (.22%) in the horizontal and 3.4e-4 (.17% of the fitted fractional tune) in the vertical. The tune averages are .191432 in the horizontal and .197938 for the vertical.

The Fitted Offset

The fitted offset is the CO. The fitting error on the offset calculated from the ML error analysis for each scan is fairly constant across all BPMs, Fig. 7. The fitting error

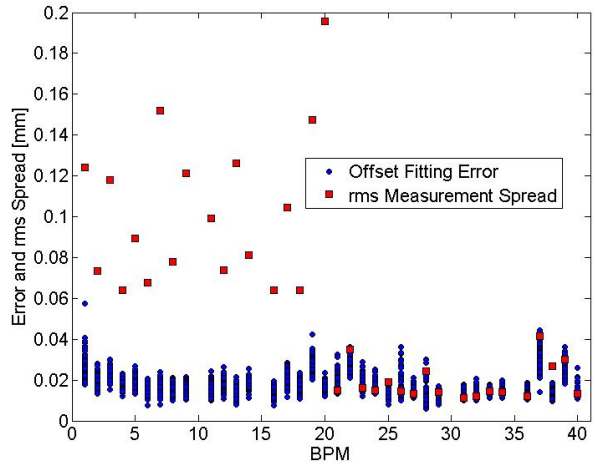

Figure 7: (Color) The fitting error on the offset parameter for all scans without data acquisition errors (blue circles) and the measurement spread at each BPM, red squares.

on the offset is only slightly larger than the intrinsic resolution of the BPM. The fitting errors for the vertical BPMs match the spread in the measurement distribution. Thus the precision of vertical CO measurement is limited by the intrinsic resolution of the BPM measurement. The difference between the horizontal fitting error and the offset *rms* measurement spread is a clue pointing to the pulse-to-pulse momentum variations influencing the horizontal offset measurement spread. The horizontal measurement spread is ~5 times larger than the fitting error. The pulse-to-pulse momentum variations do not influence the vertical CO measurement

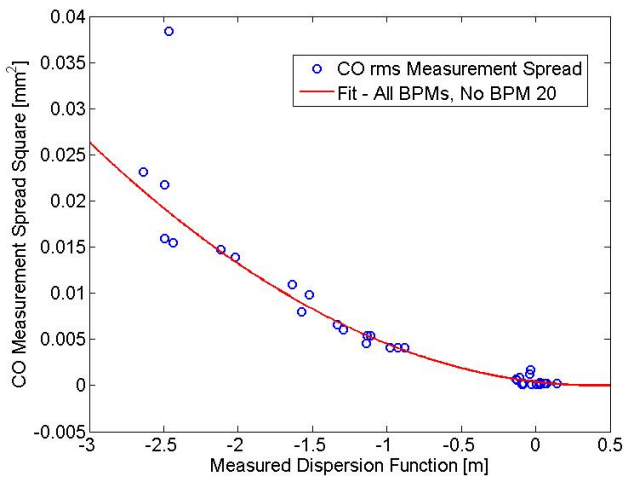

Figure 8: (Color) The square of the CO measurement spread (blue circles) fit (red line) to $\sigma_{CO}^2 = \sigma_{BPM}^2 + 2\langle \varepsilon_\delta, \varepsilon_{BPM} \rangle D + \sigma_\delta^2 D^2$, where σ is an *rms* error, ε is the absolute error, <...> is a covariance, D is the measured dispersion function, and BPM and δ indicate errors due to the BPM measurement and pulse-to-pulse momentum variations respectively [4], shows the dependence of the CO measurement spread to the pulse-to-pulse momentum variations.

because the vertical dispersion function is small. Interestingly, the horizontal CO measurement spread tracks the measured dispersion function well, yielding a calculated correlation of .97. This is because the CO change at a BPM is equal to the relative momentum change multiplied by the dispersion function, $\Delta x_{CO} = D\delta$. The dependence of the CO measurement spread on the dispersion is shown in Fig. 8. The fit in Fig. 8 is derived from assuming that there are only two contributions to the CO measurement error: an error in the BPM measurement and changes to the CO due to errors in the momentum, the pulse-to-pulse momentum variations.

The error on the average CO can be calculated using the offset measurement spreads and Eq. (2). The error on the average CO for 101 CO measurements is less than the intrinsic resolution of the BPMs. At this scale the discrete nature of the digitization in the ADC is prominent. Thus the accuracy of the CO measurement is limited by the intrinsic resolution of the BPM measurement.

$$\sigma_{ave} = \frac{\sigma_{meas}}{\sqrt{M}} \qquad (2)$$

The Single Turn Measurement Error, Sigma

The single turn measurement error (sigma) is the *rms* standard deviation of the gaussian residual distribution. Every turn of data taken at one BPM should have the same measurement error. The single turn measurement error for all scans is shown in Fig. 9. All BPMs have about the same measurement error, between .1 and .2 mm. This is much smaller than expected for the PSR BPMs. Analyzing the residuals as a function of turn it becomes apparent that the main contributor to sigma is a constant offset drift across all scans of turn-by-turn BPM data. The average drift of the offset in a scan of 40 turns is ~.4 mm. This creates a residual distribution with a larger *rms* standard deviation.

CONCLUSIONS

One hundred one consecutive CO measurements were taken for the same PSR configuration. A CO measurement consists of 40 turns of turn-by-turn BPM data at each of the 20 BPMs. The turn-by-turn BPM data was fit to a cosine wave using Eq. (1). Three of the 11 data acquisition errors found were discussed. These errors yield bad fitted parameters. Two hundred sixty four scans out of the 3636 scans in the CO reproducibility measurement were observed to have data acquisition errors, 7.26%. But 62 CO measurements of the 101 in the dataset possessed a data acquisition error, 61.38%. After these scans were removed, the fitted parameters from the remaining good data scans were analyzed.

All scans of one dimension were used to calculate the overall tune value. The tune measurement was [.191432, .197938] with an *rms* measurement spread of 4.2e-4 (.22%) in the horizontal and 3.4e-4 (.17% of the fitted fractional tune) in the vertical.

The CO measurement spreads were found to be ~.1 mm in the horizontal and ~.02 mm in the vertical. The CO measurement spread in the vertical is minimum and limited by the intrinsic resolution of the BPM measurement. The pulse-to-pulse momentum variations are the cause of the much larger CO measurement spread in the horizontal. The correlation between the horizontal CO measurement spread and the measured dispersion function is .97. The error on the average CO for 101 CO measurements is less than the intrinsic resolution of the BPMs. Thus the accuracy of the CO measurement is also limited by the intrinsic resolution of the BPM measurement.

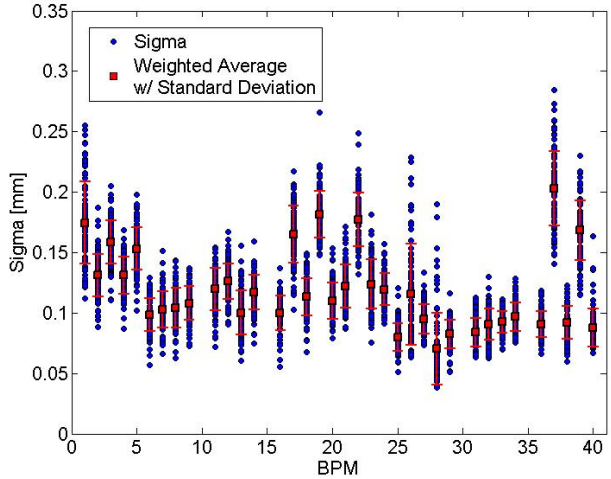

Figure 9: (Color) The calculated single turn measurement error (sigma) for all scans without data acquisition errors (blue circles) and the average with one *rms* standard deviation, red squares.

The single turn measurement error (sigma) was found to be between .1 and .2 mm. A constant offset drift in each scan is the main contributing factor to sigma.

ACKNOWLEDGEMENTS

Special thanks to S.Y. Lee of Indiana University.

REFERENCES

[1] J. Gilpatrick, Hardek, "Known Problems and Solutions of the RI Beam Position Measurement Systems," PSR-95-013, AOT-1 Tech Note 95-98.
[2] J. Gilpatrick, "Derivation of the LANSCE BPM Nonlinear Beam Position Response", PSR-97-003.
[3] R. McCrady, "Pedigree of Data and Formulas used in the PSR BPM Data Processing", (Unpublished).
[4] J. Kolski, R. Macek, R. McCrady, "A RingScan Reproducibility Measurement in the Los Alamos Proton Storage Ring", LA-UR-10-01237, PSR-10-001, AOT-ABS 10-006.
[5] J. Faucett, private communication.
[6] E. Bjorklund, private communication.

LIGHT YIELD, IMAGING PROPERTIES AND SPECTRAL RESPONSE OF INORGANIC SCINTILLATORS UNDER INTENSE ION IRRADIATION

E. Gütlich, W. Ensinger, Technical University Darmstadt, Germany
P. Forck, R. Haseitl, B. Walasek-Höhne, GSI Helmholtz Centre for Heavy Ion Research GmbH, Darmstadt, Germany

Abstract

Scintillating screens are widely used for transverse beam profile monitoring and pepper-pot emittance measurements at accelerator facilities.
For high current beam operations at the GSI heavy ion UNILAC, several inorganic scintillators were investigated under different ion beam conditions. The imaging properties of various materials were studied with respect to light yield and imaged beam width.
The measured properties show a strong dependence on the scintillating material and change significantly with screen temperature. The spectral response of the materials was mapped for different temperature levels, using a spectrometer in the visible and near UV range. The results clearly demonstrate that their temperature behaviour and scintillating properties are critical issues for high current operations and have to be taken into account for correct beam profile reading.

INTRODUCTION

Scintillating screens are a direct but intercepting method to observe an ion beam. Profile measurements are important for controlling the spatial distribution of the ion beam, as well as the matching of the different parts of the accelerator from the ion source to the experimental area. Depending on beam current and energy, a large variety of scintillating materials can be used.
Additionally scintillating screens are an essential part of a single shot pepper-pot emittance measurement system used for the determination of the width of 'beamlets' created by a plate with several small holes. The realization at GSI used for the high current operation of UNILAC is described in [1]. The angular distribution within the phase space can be calculated from the intensity distribution of the 'beamlets'. The precise measurement of the spot's light distribution requires a linear light output without saturation effects from the scintillating material and has to match the optical sensitivity of the CCD camera. To observe possible (time dependent) variations of the beam size a short decay time is necessary. The scintillating material has to be radiation hard and it is necessary to ensure that the material is not destroyed by ion beam irradiation during high current operation (see Fig. 1). For precise profile reading the heating of the scintillating material due to the energy loss has to be considered [2].

Several scintillating materials (Table 1) were investigated with different ion beams from protons up to Uranium at energies between 4.8 and 11.4 MeV/u and different beam currents as delivered by the GSI linear accelerator. Standard scintillators like YAG:Ce or BGO could only be used for low beam currents in the range of some nA [4]. For the high intensity ion beams, ceramic materials and quartz glass have to be applied [2].

Table 1: Investigated materials

Type	Material	Supplier
Crystal scintillator	YAG:Ce, BGO, $CdWO_4$, CaF_2:Eu	Saint Gobain Crystals
Powder	ZnS:Ag	HLW
Ceramics	ZrO_2:Al, ZrO_2:Y (YSZ), ZrO_2:Mg, BN, SiN, SiC, AlN, Al_2O_3, Al_2O_3: Cr	BCE Special Ceramics
Quartz glass	Herasil 102, SiO_2:Ce (M382)	Heraeus Quarzglas

EXPERIMENTAL SETUP

For systematic measurements a movable target ladder (see Fig. 1) with six different scintillating materials was used. This experimental setup allowed to test different materials under identical beam conditions without breaking the vacuum (typical $5 \cdot 10^{-7}$mbar).

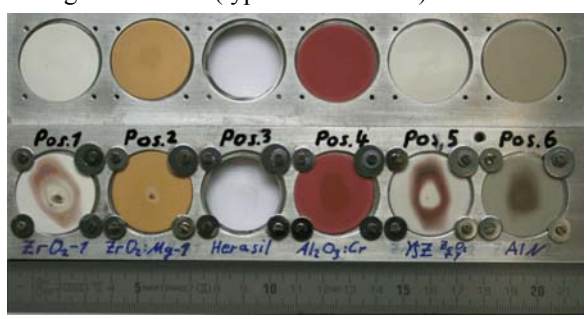

Figure 1: Target ladder with six different scintillating materials before (upper row) and after 100 pulses of U^{28+} ion beam (lower row). Beam parameters: $5.2 \cdot 10^{10}$ particles per pulse (ppp) at 4.8 MeV/u, 0.8 ms pulse length and 0.5 Hz repetition rate. Target modifications after irradiation are visible.

The scintillating screens were monitored with a monochrome CCD camera (AVT Stingray F033B, 8-bit ADC and VGA resolution). Due to the material dependent light yield a lens system with remote controlled iris (Pentax, 25 mm focal length) was implemented. With this experimental setup a resolution of 10 px/mm was achieved. The software BeamView [5] was used for data acquisition. The camera was connected to a PC which runs the server part of BeamView. The images were

recorded and sent to a client application via Ethernet. The reading from an upstream beam current transformer was sent to the client and saved together with the according image for offline analysis.

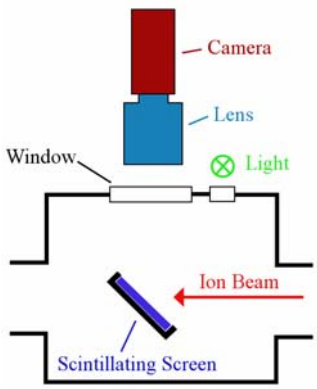

Figure 2: Experimental setup for transverse beam profile monitoring. The target ladder with six scintillating screens is tilted by 45^0 with respect to the beam and is movable perpendicular to the displayed plane.

The recorded image of the beam spot was projected to both the horizontal and the vertical plane and a quantitative analysis was performed. For the characterisation of the projected beam spots their centre μ (1^{st} moment) and standard deviation σ (square root of 2^{nd} moment which describes beam width) were calculated. The higher statistical moments were also taken into account but are not discussed in this paper [2].

To obtain a reference beam profile with a higher resolution than a Secondary Electron Monitor grid (SEM-grid), a scraper scan (Fig. 3) was implemented in the experimental area.

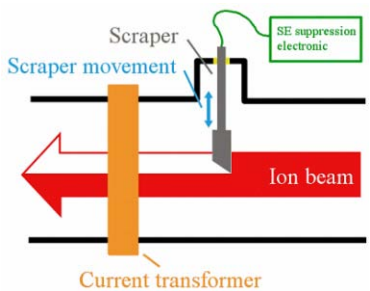

Figure 3: Scheme of the transverse beam profile measurement system based on scraper scan. The scraper is moving through the ion beam and the beam current is measured for each position of the scraper.

Furthermore, spectroscopic studies on the light emitted by the scintillating screens were performed.

The experimental setup (Fig. 4) consists of an imaging spectrograph (Horiba Jobin Yvon CP140-202) coupled to an area scan CCD camera (pco1600). For an object distance of 230 mm, a chromatically corrected UV lens (Linos inspec.x) with a focal length of 50 mm and f/2.8 was chosen. The key issue of this experiment is to have both, the spectral information of the optical transition and the spatial information about the beam profile along the imaging axis.

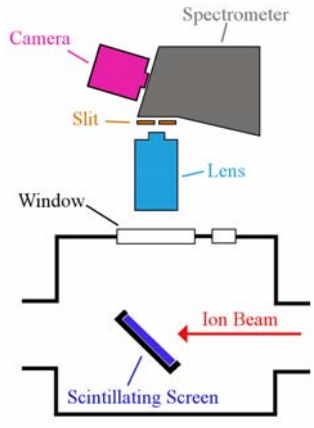

Figure 4: Experimental setup for spectroscopic studies on the light emitted from scintillating materials.

The example in Fig. 5 shows the obtained spectral information for a U^{28+} ion beam. The AlN sample emits light at 390 nm and the beam profile, along the imaging axis, has a width of approximately 10 mm.

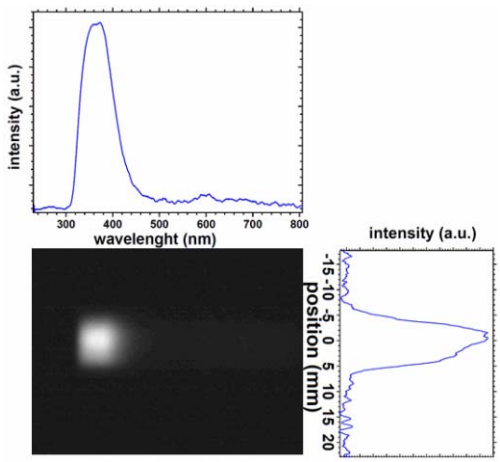

Figure 5: Example of the spectroscopic beam image obtained with U^{28+} for the AlN sample at 1^{st} pulse. Beam parameters: $5.2 \cdot 10^{10}$ ppp at 4.8 MeV/u and 0.8 ms pulse length.

RESULTS AND DISCUSSION

Systematic measurements

For high current operation with an Ar^{10+} ion beam at 11.4 MeV/u the light yield and beam width were investigated for several materials (Fig. 6).

During irradiation the light yield of AlN, ZrO_2:Mg and Herasil drops significantly with the integrated particle number. Additionally, the light yield of ZrO_2:M_g decreases coincidently with the beam width, but with a different time constant. As reported in [2] the change of the parameters in ZrO_2:Al is mainly due to the increase of the sample temperature. For Al_2O_3 the light yield and the beam width increase during the irradiation process but

these changes are smaller than for all other investigated materials. The increase of beam width and light yield for Al_2O_3 might be due to the heating process.

Most emphasized but difficult to understand are the changes observed for Al doped ZrO_2 and ZrO_2:Y. As shown in Fig 6. the beam width varies within a factor of two and the major changes of beam width readings are observed for Al and Y doped ZrO_2 samples. The Herasil sample shows the smallest imaged beam width, whereas AlN shows the maximum width.

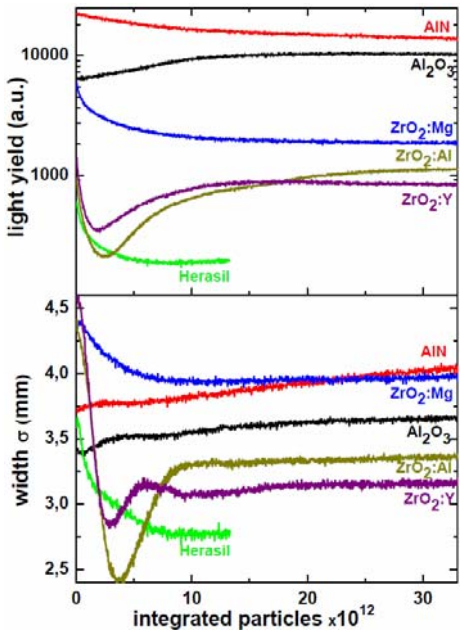

Figure 6: Light yield and beam width over the accumulated ion dose. Each point represents the value for one macro-pulse for different materials irradiated by Ar^{10+}. Beam parameters: $3.3 \cdot 10^{10}$ ppp at 11.4 MeV/u, 0.2 ms pulse length and 1.5 Hz repetition rate.

Comparison of the methods

Three different transverse profile measurement methods: Al_2O_3 screen, SEM-grid and the scraper scan were compared. The SEM-grid and the scraper were installed 25 cm in front of the scintillating screens holder.

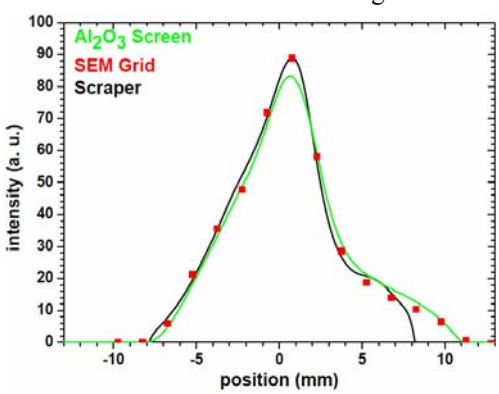

Figure 7: Comparison of the beam profile width for the three different beam diagnostic methods: first macro pulse irradiated on Al_2O_3 screen (blue), SEM-grid (red) and scraper scan (black) (beam parameters as Fig. 6).

The beam profiles obtained with the three different methods are in good agreement (Fig. 7). For the scraper scan, the difference in the profile is the result of the used smoothing algorithm (Gaussian FFT) and beam fluctuations during the measurements. To reduce this error measurements with more stable ion beam conditions have to be performed.

The calculated σ (in the ±7 mm region) is comparable for the Al_2O_3 screen (σ=2.82mm) and the scraper scan (σ=2.81mm). The difference for the SEM-grid (σ=3.0mm) might be correlated to the poor spatial resolution of this method (1.5mm).

Spectroscopic studies

The luminescence spectra of the six different scintillation screens (Al_2O_3, ZrO_2:Mg, Herasil, Al_2O_3:Cr, ZrO_2:Y, AlN) were studied using a high intensity U^{28+} ion beam (up to 100 macro pulses). In the following section we will concentrate on the spectroscopic changes during irradiation of Herasil, AlN and Al_2O_3:Cr scintillating screens.

The most prominent changes in the emitted light occur in the quartz glass (Herasil). The obtained spectra (Fig. 8 and Fig. 9) change significantly with the increasing number of macro pulses irradiated on the sample.

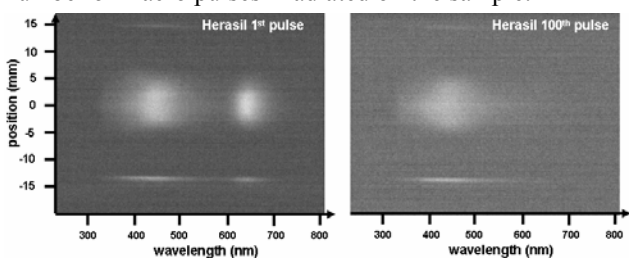

Figure 8. Spectroscopic beam image obtained for Herasil sample at 1st and 100th pulse of the high current U^{28+} ion beam. Beam parameters: $5.2 \cdot 10^{10}$ ppp at 4.8 MeV/u, 0.8 ms pulse length and 0.5 Hz repetition rate. Due to the low intensity of the right image, the brightness was adjusted.

The intensity of the broad band around 440 nm decreases with irradiation time, while the band at around 640 nm completely vanishes after ten pulses.

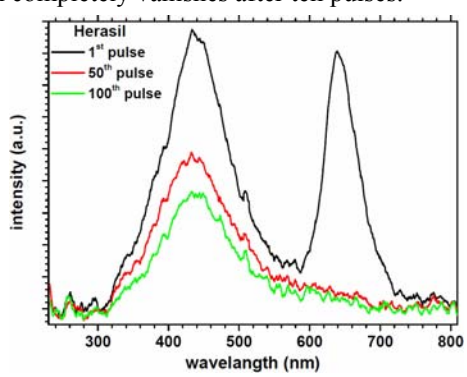

Figure 9: Luminescence spectra of Herasil obtained for the 1st (black), 50th (red) and 100th (green) macro pulse (beam parameters as Fig. 8).

Also for the AlN sample significant changes occurred in the emitted light spectra. The luminescence spectra (Fig. 10) show a broad band emission with the centre at 370 nm which can be related to imperfections in the sample created during its growth as discussed in [6]. The intensity of the peak rapidly decreases with the successive pulses.

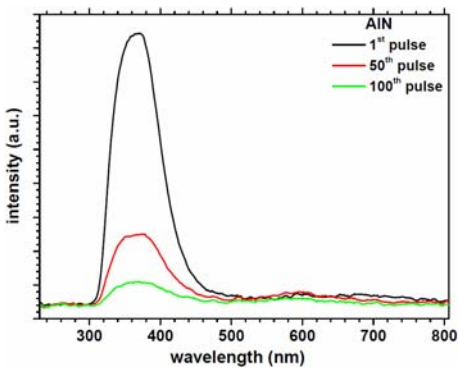

Figure 10: Luminescence spectra of AlN recorded during the 1st (black), 50th (red) and 100th (green) macro pulse (beam parameters as Fig. 8).

After several macro pulses the spectroscopic picture shows that no more transitions are detected from the middle part of the sample (Fig. 11). This suggests strong and permanent damages of the sample due to irradiation (e.g. heating of the sample) as shown in Fig 1.

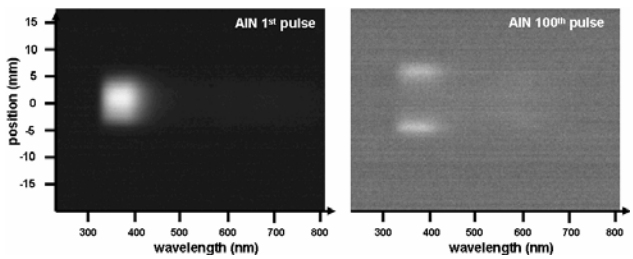

Figure 11. Spectroscopic pictures of AlN sample at 1st (left) and the 100th (right) pulse. Due to the low intensity of the right image, the brightness was adjusted (beam parameters as Fig. 8).

The projected beam profiles for AlN, obtained along imaging axes, change dramatically with the integrated particle number and can lead to wrong profile measurements (see Fig. 12).

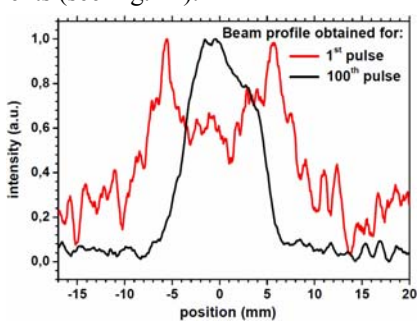

Figure 12: Beam profile obtained along imaging axis for AlN recorded during the 1st (black) and 100th (red) macro pulse (beam parameters as Fig. 8).

Cr doped Al_2O_3 is often used for the adjustment of the ion beam at accelerating facilities.

The luminescence spectra show (Fig. 13) a clear and sharp line at 693 nm. This transition can be attributed to the relaxation from the exited ^{2}E-state of the Cr^{3+} ions which produce R-line emission in this spectral region [7]. The intensity of the observed peak strongly decreases with the successive pulses and surface modification occurs (see Fig. 1).

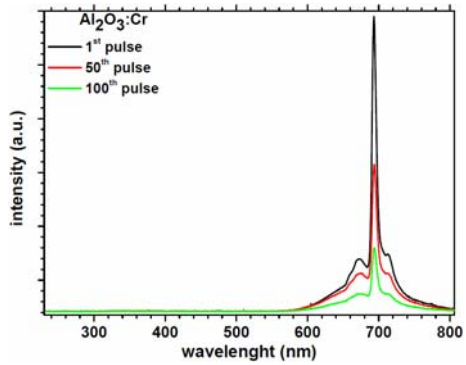

Figure 13: Luminescence spectra of Al_2O_3:Cr recorded during the 1st (black), 50th (red) and 100th (green) macro pulse (beam parameters as Fig. 8).

CONCLUSION

Several scintillating materials were investigated under irradiation with high current ion beams. The obtained beam width differs by a factor of two for different materials. The investigated properties are influenced by the temperature of the applied material. This knowledge is essential for choosing a well suited material for the precise emittance measurements with the pepper-pot method.

In the case of Al_2O_3 comparison of the obtained beam profile width for three different diagnostic methods show a good agreement. The advantage of the optical method is that it provides a big amount of detailed information on the beam particle distribution with much higher spatial resolution.

Spectroscopic studies performed on inorganic scintillators show that damages, generated during ion irradiation, lead to significant changes in the emitted light spectra. Additionally, the beam profile may vary strongly with the number of macro pulses as shown in Fig. 6 and Fig. 12. Both effects limit the performance of the detectors over operation time and more detailed investigations on these topics have to be performed. For high current ion beams the radiation resistance of the sample is critical.

ACKNOWLEDGMENT

The authors would like to thank Walter Tutsch from PCO AG, Germany for the possibility to use a high performance CCD camera and Klaus Höhne for useful discussion.

REFERENCES

[1] T. Hoffmann et al., "Emittance measurements at the new UNILAC pre-stripper using a pepper-pot with a PC-controlled CCD camera"; http://www-bd.gsi.de.

[2] E. Gütlich et al., "Scintillation screen investigations for high current ion beams", IEEE Transactions on Nuclear Science (accepted for publication in June 2010).

[3] P. Forck, "Lecture notes on Beam Instrumentation and Diagnostics", Joint Universities Accelerator School (JUAS 2010); http://www-bd.gsi.de.

[4] E. Gütlich et al., "High current ion beam investigation on inorganic scintillation screens", DIPAC'09; http://www.pcapacworkshop.org.

[5] R. Haseitl et al., "BeamView – A Data Acquisition System for Optical Beam Instrumentation", PC@PAC'08; http://www.JACoW.org.

[6] S. W. Choi et al., "Emission spectra from AlN and GaN doped with rare earth elements", Journal of Alloys and Compounds 408-412 (2006).

[7] S. W. S. McKeever et al., "Characterisation of Al_2O_3 for use in thermally and optically stimulated luminescence dosimetry", Radiation Protection Dosimetry 84 (1999).

BEAM INDUCED FLUORESCENCE MONITOR - SPECTROSCOPY IN NITROGEN, HELIUM, ARGON, KRYPTON AND XENON GAS

F. Becker*, P. Forck, T. Giacomini, R. Haseitl, B. Walasek-Hoehne, GSI, Darmstadt, Germany

F.M. Bieniosek, P.A. Ni, LBNL, Berkeley, California, D.H.H. Hoffmann, TU-Darmstadt, Germany

Abstract

As conventional intercepting diagnostics will not withstand high intensity ion beams, Beam Induced Fluorescence (BIF) profile monitors constitute a pre-eminent alternative for non-intercepting profile measurements [1]. This diagnostic technique makes use of the optical fluorescence emission of beam-excited gases. Recently BIF became an important diagnostic tool for transversal beam profile measurements with applicability in beam tuning over a wide range of beams and accelerator conditions [2]. In this paper optical VIS-spectroscopy with an imaging spectrograph for 5 MeV/u proton, S^{6+} and Ta^{24+} beams in nitrogen, Xe, Kr, Ar, Ne and He at 10^{-3} mbar gas pressure is presented. Atomic physics processes are a major performance issue, since they determine transition intensities and lifetimes of excited states. Further investigations are required to improve the detector performance and increase its range of application.

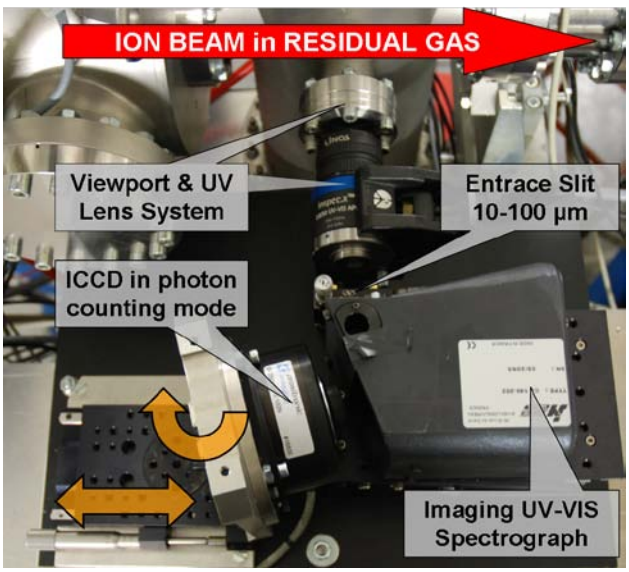

Figure 1: Top-view of the optical setup looking onto the diffractive plane. Length of spectrum in the image plane is 10 mm. 1:1 imaging from slit to image plane. All refractive optics adapted to UV-VIS [4]. ICCD performs single photon detection including a Ø 25 mm UV-enhanced photocathode with a V-stack MCP [5] and digital VGA 8-bit greyscale camera [6].

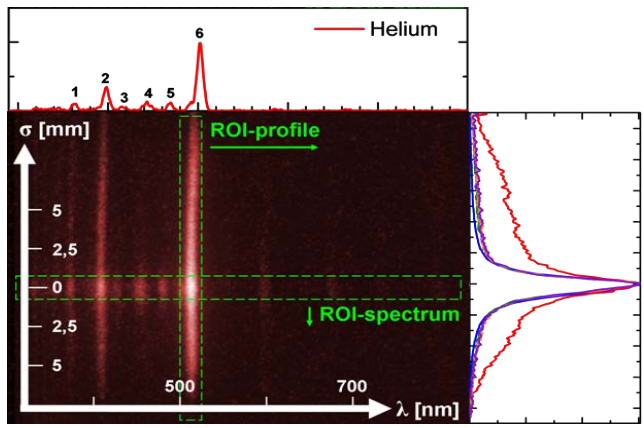

Figure 2: Spectrographic average image of n=2000 pulses of $3{\cdot}10^{11}$ S^{6+} ions @ 5.16 MeV/u in 10^{-3} mbar helium gas, σ_w=1.8 mm. Log colour-scale for better illustration. Projections yield either spectra (upper) or profiles (right).

EXPERIMENTAL SETUP

Key issue of this experimental layout using an imaging spectrograph with an area scan intensified CCD (ICCD) camera (Fig. 1) was to have both, the spectral information of specific beam induced gas transitions along the diffraction axis and the spatial information about the beam profile width, transition wise along the imaging axis, see Figure 2. For 150 mm object distance, a chromatically corrected UV-lens of f = 50 mm and f/2.8 was chosen. A CCD height of 4.9 mm and a total reproduction scale β_{tot} = 0.42 yield a 19.5 mm field of view, covering ~ $5{\cdot}\,\sigma_w$.

Imaging Spectrograph & Gas Composition

The spherical mirror (Ø 70 mm) with 140 mm focal length is holographically etched and astigmatism corrected. 140 sinusoidal grooves per mm produce a spectral dispersion of 50 nm/mm and an image field of 8x12 mm on the vertical imaging axis and the horizontal dispersive axis, respectively. With an optical resolution of 33 lp/mm the ICCD limits the spectral resolution to 1.5 nm for an entrance slit ≤ 30 µm. The total spectral system efficiency includes all single component efficiencies as a convolution, see Fig. 3 (upper plot). Most limiting factors for increasing wavelength ≥ 600 nm are the tri-alkali $(Na_2KSb)Cs$ photocathode and the decreasing grating-efficiency. Investigation of optical gas spectra relies on a

* Frank.Becker@gsi.de

sufficient purity of the actual gas species.

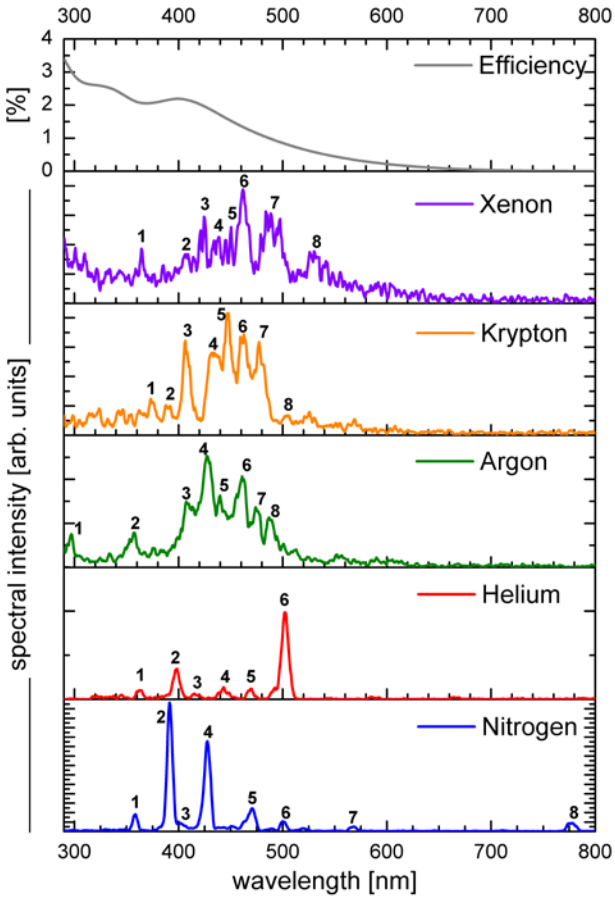

Figure 3: Optical Beam Induced Fluorescence spectra of $3{\cdot}10^{11}$ S^{6+} ions @ 5.16 MeV/u in 10^{-3} mbar residual gases (Xe, Kr, Ar, He, N_2). Most prominent transitions are indicated and described in Table 1. The total spectral efficiency in the upper plot is determined by single efficiencies of the lens, grating and photocathode.

In order to measure and control impurities, a residual gas analyzer (RGA) 'quadrupole mass spectrometer'-type was used [7]. Base pressure of the unbaked vacuum system was 10^{-7} mbar, with the typical fingerprint of hydrogen, water, nitrogen and traces of the previously introduced rare gas species like krypton in an argon atmosphere. Although the gas leak system was flushed carefully after each gas exchange, a significant source of residuals was gas contamination the pressure reducing regulator. In order to keep relative impurities below 5 %, the working pressure for all experiments had to be set to 10^{-3} mbar N_2-equivalent. More details about that in [9].

DATA ANALYSIS – RESULTS

All optical spectra were recorded during 2000 beam pulses for constant accelerator settings. Each single image was recorded as 8-bit bitmap, using the ICCD in photon counting mode. To maintain the dynamic range, the average images were 32-bit float tiffs, see Fig. 2. Further resolution improvement by a factor of ~ 4 was achieved with a cognitive algorithm that determined barycenters of single photon spots and added them as single counts to the VGA-sized matrix [8]. To discriminate spectral peaks against spiky shot noise, Savitzky-Golay fits were applied. Regions of interest (ROI) were chosen like 10 pixel or 40 µm at the beam center for the BIF-spectra in Fig. 3 and like 20 pixel or 16 nm for the transitions specific profile plots in Fig. 4 (mid & bottom).

Table 1: Residual gases (block-wise), observed charge states, observed integral intensity I_{meas}, I_{gas} normalized to p_{eff} and $I_{gas\&Z}$ normalized to p_{eff} and Z (upper block line). Corresponding transitions as indicated in Figure 3, central wavelength and relative intensity with respect to the integral intensity (lower block line). Peaks indicated with No.)* are superpositions of several transition-lines.

gas species	**Charge state**	**I_{meas} I_{gas} $I_{gas\&Z}$**
No.) central-wavelength [nm], *relative intensity [%]*		
Xenon	**Xe^+/Xe**	**41; 86; 22**
1) 363, *4*; **2)*** 407, *4*; **3)*** 424, *6*; **4)*** 438, *5*		
5) 450, *2*; **6)*** 462, *12*; **7)*** 484, *16*; **8)*** 530, *5*		
Krypton	**Kr^+/Kr**	**45; 63; 25**
1) 373, *4*; **2)*** 388, *3*; **3)** 407, *10*; **4)*** 434, *14*		
5) 447, *12*; **6)*** 463, *12*; **7)*** 477, *13*; **8)*** 505, *2*		
Argon	**Ar^+**	**50; 38; 30**
1) 297, *3*; **2)**_ 357, *5*; **3)**_ 407, *11*; **4)** 427, *19*		
5)* 440, *8*; **6)*** 461, *15*; **7)*** 474, *8*; **8)*** 487, *7*		
Helium	**He**	**21; 4; 26**
1) 364, *4*; **2)** 398, *16*; **3)*** 415, *3*; **4)*** 443, *7*		
5)* 470, *5*; **6)** 502, *48*		
Nitrogen	**N_2^+/N^+**	**100; 100; 100**
1) 358, *4*; **2)*** 391, *45*; **3)*** 428, *29*; **4)*** 470, *9*		
5) 501, *3*; **6)** 560, *1*; **7)*** 776, *3*		

BIF-Spectra

All spectra were first calibrated to an Hg-Ar-standard and then refined step by step adding identified transitions of the recorded BIF-spectra. The accuracy for the central wavelength is ≤ 1 nm. The investigations were performed with 5 ms long beam pulses of $3{\cdot}10^{11}$ S^{6+} ions at 5.16 MeV/u, focused to a σ_w = 1.8 mm. Obtained BIF spectra are depicted in Fig. 3. Actual spectra have not been normalized to the spectral efficiency of the optical components, which is therefore given in Fig. 3 as well (upper-plot). In Table 1 the observed charge states, relative integral intensities and most prominent transitions are listed. Different signal-to-noise ratios for the gas species are determined by the observed integral intensity I. Spectral lines of optical transitions in nitrogen and helium are pronounced and more clearly separated as compared to the heavier rare gas species, showing many clustered lines of lower intensities. Although nitrogen shows the brightest transitions, e.g. xenon and krypton

show similar integral intensities I_{gas}, normalized with respect to effective gas pressure p_{eff}.

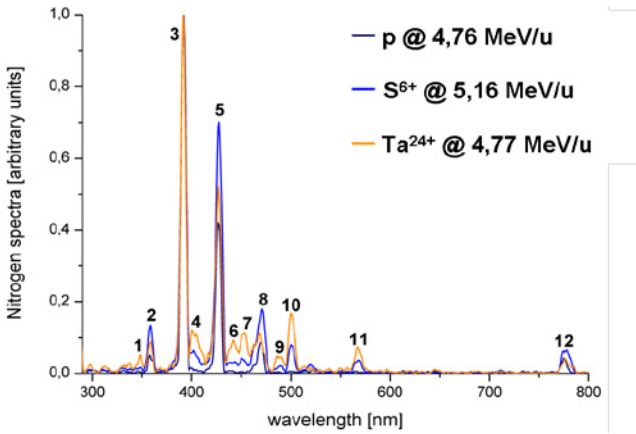

Figure 4: Comparison of nitrogen spectra induced by different ion species (p, S^{6+}, Ta^{24+}) of the same energy. The heavier the ion (Ta^{24+}), the more intense transitions of singly dissociated singly charged nitrogen atoms appear.

To account for the electronic stopping power, integral intensities $I_{gas\&Z}$ were furthermore normalized to Z. This intensity represents a fluorescence-efficiency normalized to the differential energy loss -dE/dx. $I_{gas\&Z}$ of all rare gas species is similar, except for nitrogen having a four times higher fluorescence-efficiency. In contrast to the other gases with ionic transitions, He-fluorescence is caused by transitions of the neutral atom, see Tab. 1. Ion species and charge states influence the dissociation probability of N_2, since additional atomic lines appear for heavy ions, see Fig. 4. When the ROI was moved from the profile center to the beam fringes, spectral intensity decreased for all gases in the same way, except for helium that showes an unequal decrease for different transitions.

Transition dependent Profile Data

Motivated by the abnormality of He-spectra, profile plots were recorded for beam conditions of Figure 3, as spectrally integrated profiles (see Fig. 5), or transition-wise [13]. To be able to compare the profiles, they have been normalized to their maximum specific intensity. All gas-species show similar profile widths σ_w besides helium, showing a factor of 2.5 larger σ_w. Assuming that neutral He atoms might have large cross-sections for electron excitation, an 8 mm beam halo is reasonable, as the mean free path of secondary electrons is in the order of 10 mm, for $p_{eff} = 4 \cdot 10^{-3}$ mbar. For proton beams as well as for Ta and U beams, similar spectra and profiles were obtained.

CONCLUSION

Optical spectra of nitrogen, xenon, krypton, argon and helium were successfully recorded. They excellently agree with measurements at lower beam energies ≤ 10 MeV/u in the case of nitrogen [10, 11] and higher beam energies in the range of 50 MeV/u to 25 GeV/u for nitrogen and xenon [12]. The present experiments show hat nitrogen is the most appropriate residual gas for BIF applications, because of its spectral concentration between 390 and 430 nm, fitting typical S20-cathode efficiencies. In addition, nitrogen shows the highest integral intensity. Especially the four times higher fluorescence-efficiency $I_{gas\&Z}$ makes it the right choice, if stopping power is an issue. Intense ion beams can generate electric fields in the order of 10 kV/mm, so that trajectories of excited charged molecules like N_2^+, are influenced by the beam's space charge and perturb the profile reading [13]. Therefore different selection criteria come into play, like e.g. larger molecule masses and shorter transition-lifetimes, provided by rare gases like Xe and Kr. Helium is no alternative due to its wrong profile image in the considered pressure range. Once a residual gas is selected, optical components like lenses or photo-cathodes have to be further optimized. However, the outcome of our experiment is, that for most beam parameters N_2 is the optimal choice.

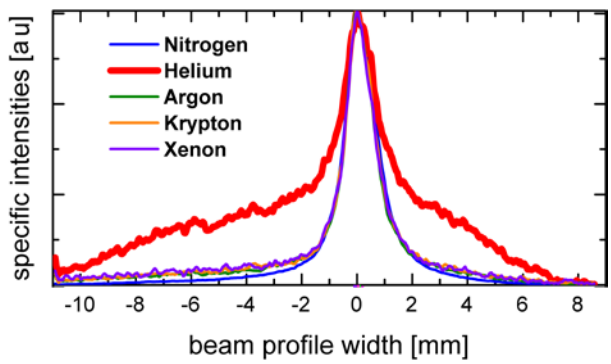

Figure 5: Optical Beam Induced Fluorescence spectra of $3 \cdot 10^{11}$ S^{6+} ions @ 5.16 MeV/u in 10^{-3} mbar residual gases (Xe, Kr, Ar, He, N2). Most prominent transitions are indicated and described in Table 1. The total spectral efficiency in the upper plot is determined by the lens, grating, and photocathode.

REFERENCES

[1] P. Forck et al., DIPAC'05, ITTA01, 2005.
[2] F. Becker et al., DIPAC'07, MOO3A02, 2007.
[3] Company: www.horiba.com, CP140202 spectrograph.
[4] Company: www.linos.com, inspec.x 2.8/50 UV-VIS apochromatically corrected lens system.
[5] Company: www.proxitronic.de, BV-2581 QYV 100N.
[6] Company: www.baslerweb.com, Type 311-f VGA Sony ICX414AL Sensor.
[7] Company: www.pfeiffer-vacuum.de, Gauge PKR-261, Valve EVR-116, Controller RVC-300, Calibration-Gauge CMR-264, RGA PrismaPlus.
[8] Software: http://rsbweb.nih.gov/ij/, Image-J package.
[9] F. Becker, "Non-destructive Profile Measurement of intense Ion Beams", PhD-thesis, Darmstadt, 2009.
[10] R.H. Hughes et al., Phys. Rev., 123, 2084 (1961)
[11] C. S. Lee et al., "Study of N2+ first negative system" Nucl. Instrum. Meth. B 140, p. 273-280, 1998.

[12] M. A. Plum et al., “N2 and Xe gas scintilliation @ Cern PS and Booster”, Nucl. Instrum. Meth. A 492, p. 74-91, 2002.
[13] F. Becker et al., BIW’08, California , 2008.

PHOTON BEAM POSITION MEASUREMENTS BY LIBERA PHOTON USING COPPER BLADE SENSORS AT SOLEIL SYNCHROTRON

P. Leban, D.Tinta, Instrumentation Technologies, Solkan, Slovenia
N. Hubert, J.C. Denard, SOLEIL Synchrotron, Gif-sur-Yvette, France

Abstract

Libera Photon is the new Photon Beam Position processor (PBPM) from the Instrumentation Technologies. First measurements on real beam have been done at SOLEIL Synchrotron. The module was connected to a PBPM installed on the DIFFABS bending magnet beam line. Three different beam position experiments were done: measurement of position at beam bump (+/- 500 µm), beam current dependence and filling pattern dependence. Measurements were done with internal BIAS voltage source set to -70 V. Measured current was in the range up to 250 µA on the sensor. Measurements were done on standard 100 kS/s, 10 kS/s and 10 S/s data flows with different bandwidths. The article discusses the results and consequential improvements of the device.

INSTRUMENTATION

Libera Photon is a photon beam position processor, which features current-to-voltage conversion, digitalization and signal processing. The output data flows are delivered with different rates (100 kS/s, 10 kS/s and 10 S/s) and can be accessed simultaneously. The acquisition can be performed using Matlab, Tango or EPICS clients.

Input currents were in the range up to 200-250 µA per input. Libera Photon features Automatic Range Control (ARC) with 7 ranges: ±2 nA, ±20 nA, ±200 nA, ±2 µA, ±20 µA, ±200 µA and ±1,85 mA. ARC adapts the I/U converter values automatically according to the input signal level. During our tests, the measurement range was set manually.

Blade sensors were copper type. It requires BIAS voltage to extract the photons. BIAS voltage was supplied by the Libera Photon unit and was set to -70 V. There were 2 XBPM sensors placed in the storage ring front-end: Libera Photon unit was connected to the first one (XBPM1), whereas Soleil analog device was used on the second one (XBPM2) to be used as a comparison. XBPM1 sensor is placed 4,7 metres from the source point, XBPM2 is placed 7,73 metres from the source point.

MEASUREMENTS

The following measurements were done on the beamline: beam bump measurement, beam current dependence measurement, filling pattern dependence measurement and noise measurement. Beside tests in the beamline, beam current dependence and noise measurements were done also under laboratory conditions.

All data, presented in this paper, were acquired at 10 kS/s (DD buffer) or at 10 S/s (SA) data rates.

Beam bump measurement

Slow orbit feedback and Fast orbit feedback in the storage ring were disabled in order to be able to displace the photon beam. Transverse feedback was enabled all the time. Filling pattern was multi bunch 4/4. Photon beam was displaced from -500 µm to +500 µm by steps of 100 µm using correctors to create a bump on the electron beam. Position was read by Libera Photon on XBPM1 and analog device on XBPM2 and compared to the position at source point using electron BPM. Results are presented in Figure 1.

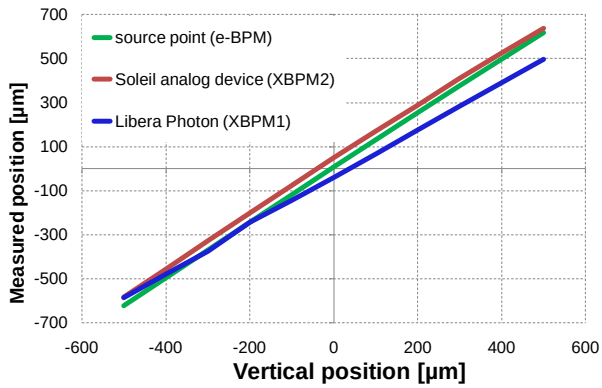

Figure 1: Beam bump measurement.

The analog device shows good correlation with the source point. Libera Photon, however, shows different slope in the measurement. There was no calibration or compensation used in Libera Photon. The slope and the offset can be set for each input channel individually. This must be done during instrument set up and then saved to the configuration file.

Beam current dependence measurement

With orbit feedbacks ON, the current in the storage ring was increased from 0 to 400 mA by steps of 50 mA (injections) and then scrapped down to 0. Measuring range used on Libera Photon was ±200 µA.

Both instruments (Libera Photon and Soleil analog device) measured changes in the position for several microns. The beam was really moving because of the machine current dependence (thermalization, eBPM beam current dependence,...). So this method could not be used to measure the beam current dependence of the Libera Photon electronics.

The current dependence measurements were done also under laboratory conditions. Both centered and off-

centered beam positions were simulated. The test setup consisted of 4 resistors with same (centered beam) and different (off-centered beam) resistance values. Current through resistors was changed by using external voltage supply. Libera Photon unit was configured with maximum range (n° 6) to cover the range up to 1800 µA for both measurements.

With a simulated centered beam, results were 0,1 µm in horizontal and 0,25 µm in vertical direction.

With a simulated off-centered beam, the highest average current measured was 1,28 mA. One of the inputs was already in saturation if the current was raised even more. The current dependence was 4 µm in horizontal and approximately 3 µm in vertical direction. Results are presented in Figure 2.

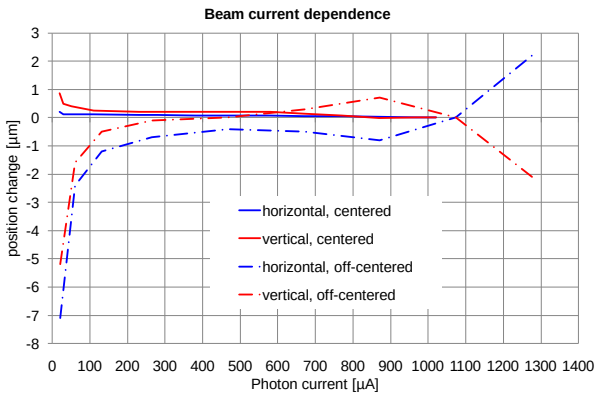

Figure 2. Beam current dependence measurement in the laboratory.

The current dependence at off-centered beam did not reach the specification as for centered beam (< 1 µm). Therefore, more investigation will be done to understand the phenomena and achieve better results.

Bunch pattern dependence measurement

Orbit feedbacks in the storage ring were enabled during the measurement. Storage ring current was set to approximately 50 mA. Amplitudes and position were read for 2 different filling patterns: multi bunch with 4/4 filling and 8-bunches. Data from Libera Photon was acquired at 10 kS/s data rate. Mean positions of both acquisitions are the average of 10 second measurement (100 kSamples) and are presented in Table 1.

Table 1: Fill pattern dependence.

Fill pattern	Vertical position
Multi bunch 4/4	-61529 nm
8-bunch	-60999 nm

The measured filling pattern dependence is around 500 nm, which is very satisfying. Moreover, we can not certify that the measured movement was not really on the beam. Indeed, the machine has its own filling pattern dependence (mainly caused by e-BPMs). So the filling pattern dependence of the Libera Photon is probably below 500 nm.

Results are presented in Figure 3.

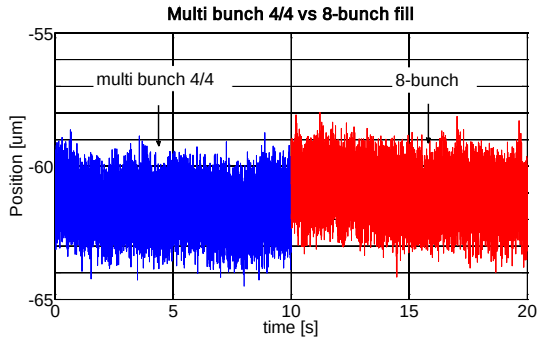

Figure 3: Multi bunch vs 8-bunch fill pattern.

Resolution measurement

At first, the noise in the position measurement was measured in the beamline. Data at 10 kS/s was analyzed. Measured noise was in the range of 700 nm. By analysing the data using a FFT, it was clearly seen that the main component was in the 50 Hz spectrum line (~500 nm). Results are presented in Figure 4. In parallel, SA data was acquired. Noise was lower for approximately a decade. Results are presented in Table 2.

Table 2: Noise measurement in the beamline.

Acquisition type	Position noise (RMS)
DD buffer	702 nm
SA data	57 nm

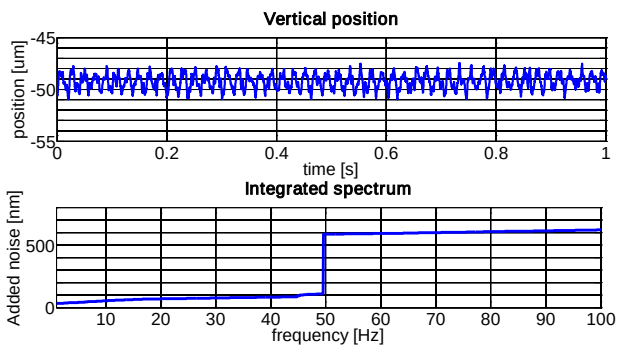

Figure 4: Noise measurement in the beamline.

Then, Libera Photon noise was also measured in the laboratory environment. Test setup consisted of 4 resistors which simulated approximately 350 µm off-centered beam and a voltage generator. Measurements were done

in steady conditions. Data at 10 kS/s and 10 S/s was acquired. We can notice that the 50 Hz component is no more present, so it was not introduced by the electronics. Please see Figure 5 and Table 3.

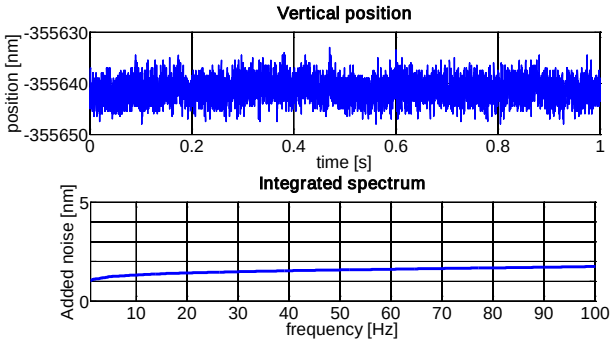

Figure 5: Noise measurement in laboratory conditions.

Results show very low noise on both, the DD buffer data and SA data. The FFT analysis did not show any specific component which would introduce significant noise to the measurement. Noise is not dependent on the absolute position.

Table 3: Noise measurements in laboratory conditions.

Acquisition type	Position noise (RMS)
DD buffer	4,2 nm
SA data	1,7 nm

Issues discovered

There were two issues discovered during the testing on the real beam which could lead to malfunctioning of the unit.

If charged cables are connected to the unit, the energy in the cable can stick the contacts of input relays. The measurements with the unit are still possible but the calibration can not be done anymore. The occurrence of the failure is not high, but may happen if cables are often disconnected/connected. It is suggested at the moment that the cables are connected while the photon current is not present. Anyway, for this case, the input protection is under investigation and will be implemented in the unit shortly.

The second issue is related to unit's restart, reboot or turn OFF. If the bias voltage is used and the unit is restarted, rebooted or turned OFF while the bias voltage is set to some value, the contacts of the switching relay stick. As the consequence, the bias voltage source sees the short circuit and can not provide the voltage. The issue has been already fixed.

CONCLUSION

The first Libera Photon units have been tested with a current source at Instrumentation Technologies and on a real beam at SOLEIL.

During the tests, some problems related to instrument reboot were discovered. These problems have been fixed.

The current dependence is within specification for a centered beam but not yet for a beam off-centered by 0,35 mm in both directions (< 1 µm required). This is going to be fixed very soon.

The other measurements showed good results. The resolution of the position measurement is in the range of nm on DD buffer and SA data. The very low noise, in the nm range, should allow a precise angle monitoring, within a feq nrad, between two XBPMs separated by only a couple of meters.

THE DIAGNOSTICS' BACK END SYSTEM BASED ON THE IN HOUSE DEVELOPED A|DA| AND A|D|O BOARDS

A. O. Borga#, R. De Monte, M. Ferianis, L. Pavlovic, M. Predonzani, ELETTRA, Trieste, Italy

Abstract

Several diagnostic instruments for the FERMI@Elettra FEL, among them the Bunch Arrival Monitor (BAM) [1] and the Cavity Beam Position Monitor (C-BPM), require accurate readout, processing, and control electronics integrated within the main machine control system. The back end platform, based on the MicroTCA standard [2], provides a robust environment for accommodating such electronics, including reliable infrastructure features. Two types of Advanced Mezzanine Cards (AMC) had been developed in-house and manufactured for meeting the demanding performance requirements. The first is a fast (160 MSps) and high-resolution (16 bits) Analog to Digital and Digital to Analog (A|D|A) Convert Board, hosting 2 A-D and 2 D-A converters controlled by a large FPGA (Virtex-5). The FPGA is also responsible for service and host interface handling. The latter board is Analog to Digital Only (A|D|O) Converter, derived from the A|D|A, with an analog front side stage made of four A-D converters. The overall systems' architectures, together with the specific AMCs' functionalities, are described. Results on performance measurements are also presented.

BACK END OVERVIEW

Figure 1 shows a block diagram of the general architecture of the high-bandwidth, real-time diagnostics back end. Three sub-systems can be identified according to their installation location:

Tunnel area: hosting the *monitors* and the monitors' *front-end electronics* responsible for signal pick-up, conditioning, and transmission to the back-end.

Service area: *back-end* and *A|D|A* and *A|D|O boards*, the system fulcrum where further signal conditioning, data processing, analysis, and computations are performed before data are sent back to users in the control room.

Control room: the users' control and monitor Linux/Tango PC, for data storage, further off-line analysis, and visualization.

The sub-systems are interfaced through transmission media chosen according to the different sections' specific needs. From the tunnel area to the service area the **A-B interface** carries signals via shielded coaxial or optical cables, for noise immunity. The cabling of the A-B interface is a task left to the monitors and front-end designers. The **E-F interface** connects the back-end crates to the control room's PC through standard Ethernet CAT6 cables and doesn't require particular attention. In the service area inside the back-end system, flexibility is more of a concern, so boards are connected through the **C-D interface** with SMA coaxial cables (for analog signals) or flat ribbon cables (in the case of digital signals).

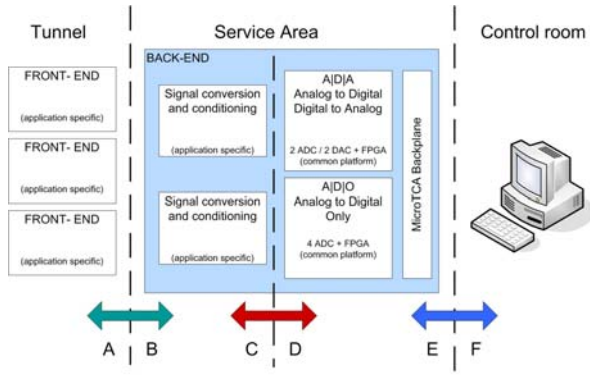

Figure 1: Block diagram of a diagnostic system based on µTCA and A|D|A and A|D|O AMCs

The C-D interface inside the back-end system's crate is used to interface three types of modules:

A|D|A and A|D|O AMCs: Advanced Mezzanine Cards (AMCs) for digital processing; FPGA based.

Custom Passive AMCs: interface transition cards that adapt front-end signals to the inputs of A|D|A and A|D|O.

Custom Active AMCs: standalone modules, for application-specific tasks not strictly related to diagnostics, that might not require an interface with A|D|A or A|D|O (e.g. timing and trigger cards, storage devices, processor cards, etc).

The whole electronics is based on the Micro Telecommunications Computing Architecture, which is beyond the scope of this paper but is described in, for example, [2]. For the C-BPM diagnostics case a 3D mock-up of a hypothetical system is shown in Figure .

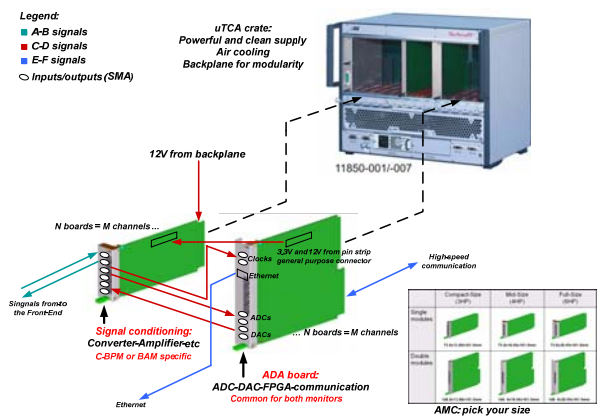

Figure 2: Example 3D mock-up of a system

A|D|A MODULE ARCHITECTURE

Block diagram

The main purpose of the Analog to Digital and Digital to Analog (A|D|A) [3] converter Advanced Mezzanine Card (AMC) is acquisition, processing, and generation of fast analog signals. The architecture is based on a large Xilinx Virtex-5 FPGA responsible for the data handling of all the external inputs, the data processing, and the interface to users. A block diagram of A|D|A is shown in Figure 3.

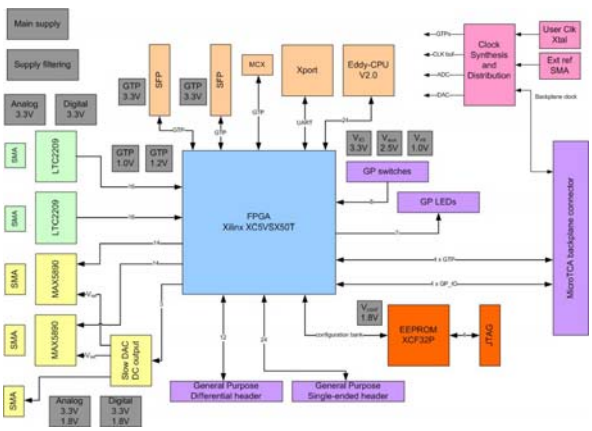

Figure 3: A|D|A AMC module block diagram

It has the following seven major subsystems:

1. **Power section:** from the backplane 12V all local voltages are derived by means of Point Of Load (POL) switching (for digital sections) and Low Drop Out (LDO, for analog sections).
2. **Clock distribution:** a programmable and configurable clock tree provides precise timing to on board devices with the freedom to choose between several internal or external references Figure 4.
3. **Configuration section:** the logic can be programmed with direct access through an onboard JTAG chain, or remotely via the backplane or via Ethernet.
4. **Analog inputs and outputs:**

- 2 LTC2209 ADC inputs 160 Msps 16 bits, electrically isolated with Bandwidth 50 – 700 MHz of the input filter and Amplitude range V_{p-p} 2.5V
- 2 MAX5890 DAC outputs 600 Msps 14 bits, AC coupled with Bandwidth 0.130 – 425 MHz of the output filter and Amplitude range V_{p-p} 1V
- 1 LTC2602 dual DAC output 16 bits, DC coupled with Bandwidth DC – 1 KHz and Amplitude range 0 – +3.3 V

5. **Computational core:** the whole board's activity swings around a Xilinx Virtex-5 SX50T FPGA. All external signals to and from the board are directed to the logic device
6. **Remote access:** access to the logic is granted in several ways

- *Lantronix*: 1Mbps Ethernet (TCP/IP or UDP/IP)
- *Eddy-CPU:* 100Mbps Ethernet (TCP/IP or UDP/IP)
- *Small Form-factor Pluggable (SFP) ser-des:* 1Gbps custom link based on ISO/OSI layer 0 and 1 from the Ethernet standard.
- *uTCA Backplane via Gigabit Transceiver Pairs (GTPs):* 4 x 1Gbps custom protocol links
- *uTCA Backplane via standard IOs:* 4 x 200Mbps custom protocol links

7. **General purpose inputs and outputs:** 24 single ended and 12 differential lines, directly interfaced to the FPGA, are available through two standard 1.27 mm pitch pin strip connectors for users' custom requirements. These connectors also provide +3.3V (500 mA) and +12V (1A) users supplies.

Clock distribution

A fully configurable and programmable clock tree is available onboard (Figure 4). The ADC (4.5 – 160 MHz) and DAC (4.5 – 600 MHz) stages can be independently supplied with external clock sources through SMA inputs on the front panel. The FPGA can be clocked off of the same external clock either from the DAC or ADC inputs; or timed independently from one of the onboard clock sources. Alternatively the whole board can be timed by high-accuracy (tens of pico-seconds range) frequency synthesizers starting from a low frequency (14 – 37.78 MHz). Frequency selection and tree setup are accomplished by setting jumpers. The backplane and other data transfer and communication sections (e.g. Gigabit links) are timed independently having other clocking requirements.

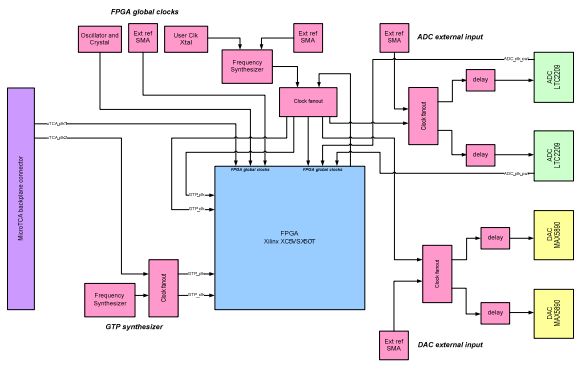

Figure 4: A|D|A Clock generation and distribution

Firmware top level diagram

The idea behind the firmware architecture depicted in Figure 5 is to provide black box core logic to support a **user's space** containing application specific algorithms. Three blocks can be then identified and developed separately: **control and monitoring**, **interface layer**, and **clock and timing**. The control and monitoring is a portion of the chip devoted to interfaces to/from the communication world, i.e. the Lantronix, the Eddy-CPU, and the backplane.

Data to the rest of the logic is stored inside a memory mapped RAM based area, providing a fully asynchronous, independent and well defined separation between different blocks.

The interface layer consists of a series of buffers controlled by state machines whose purpose is to collect and store the data to and from the ADCs and DACs. Their key role is then to absorb possible read/write delays and synchronize the readout to the internal logic's speed.

The clock and timing contains all the logic necessary for providing clocks to the different sections described above: it includes PLL, DLL, dividers, multipliers, etc.

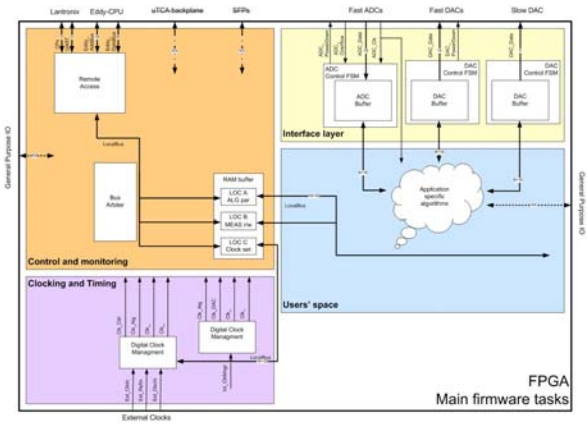

Figure 5: block diagram of the firmware sub-modules

A|D|O MODULE ARCHITECTURE

Block diagram

The Analog to Digital Only (A|D|O) converter Advanced Mezzanine Card (AMC) is derived directly from A|D|A. Like its predecessor, it is based on a large Xilinx Virtex-5 FPGA responsible for the data handling of all the external inputs, the data processing, and the interface to users. A block diagram of A|D|O is shown in Figure 6.

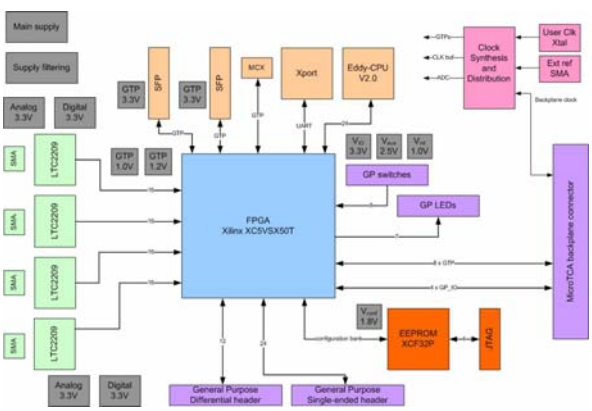

Figure 6: A|D|O AMC module block diagram

The main difference between the two cards is the front-end that in the A|D|O case in made of 4 A-D converters. The backplane connectivity had been enhanced and improved, as well as the clocking architecture.

Clock distribution

Based on the experience gained measuring with A|D|A new solutions for further adding flexibility to the clock distribution tree of A|D|O (Figure 4) had been adopted. The ADC (4.5 – 160 MHz) stage can still be independently supplied with an external clock source through SMA inputs on the front panel. The FPGA can run clocked off of the same external clock for the ADC inputs, as well as being timed independently. Providing more clock capabilities via the backplane allows future development of a dedicated uTCA timing card. Thus a small 3x3 cross point switch had been added in-between the backplane and the rest of the clocks. Still available on board are high-accuracy (tens of pico-seconds range) frequency synthesizers starting from a low frequency (14 – 37.78 MHz). Frequency and tree setup are accomplished by setting jumpers.

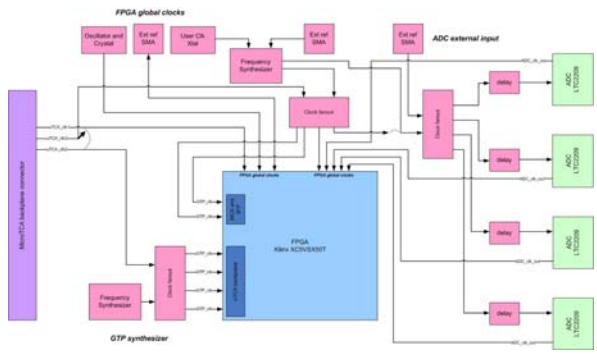

Figure 7: A|D|O Clock generation and distribution

Firmware top level diagram

As for most of the hardware design, the firmware architecture for A|D|O was ported from A|D|A. Tweaks for the light differences still need to be done, but the basic functions had been successfully ported from the previous card.

MEASUREMENTS ON A|D|A

Three main features of the board were identified as fundamental for guaranteeing the minimum board functioning:

1. Data generation through the DACs
2. Data acquisition through the ADCs
3. Remote access via the Lantronix XPort

DACs tests

Two types of periodic waves were synthesized using the two DACs present on the A|D|A board for testing the digital to analog conversion section. Results are shown in Figure 8 and Figure 9.

The first waveform was a plane sine wave at 60 MHz using a 120 MHz logic clock for the FPGA and a 240 MHz sampling clock for the DAC.

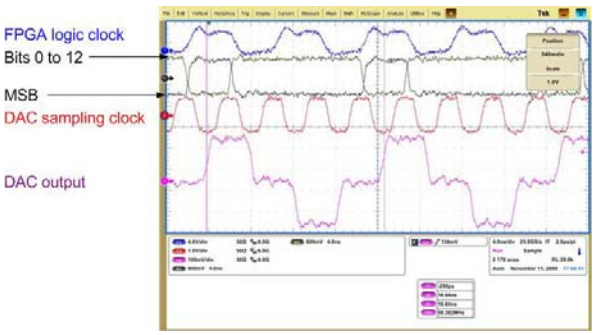

Figure 8: DAC synthesized pure sine at 60 MHz

The second waveform was a damped sine wave at 80 MHz using a 160 MHz logic clock for the FPGA and a 320 MHz sampling clock for the DAC.

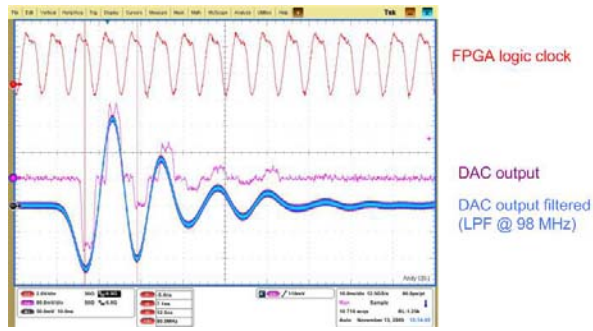

Figure 9: DAC synthesized damped sine at 80 MHz

ADCs tests

The ADCs were tested using two methods:

1. Loopback through the FPGA of the two inputs to the two DAC outputs.
2. Burst data transfer to a basic acquisition and display software

The results of the measurements are shown in Figure 10 through Figure 13. The sampling rate of the ADCs was set at their maximum (160 MHz). Though the DAC had been proven to run faster, the same frequency of the ADCs was chosen in order to avoid synchronicity issues.

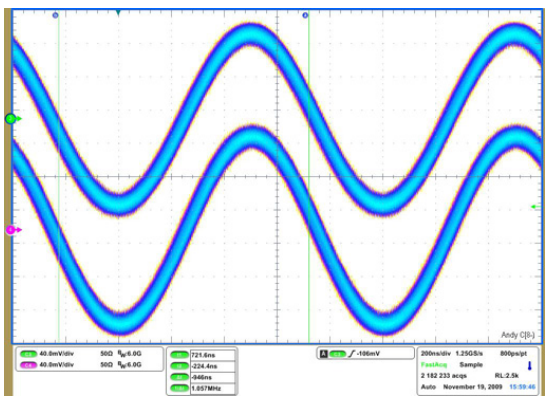

Figure 10: ADC1 and ADC2 acquisition of 1MHz sine wave redirected to DAC1 and DAC 2 outputs used as monitors

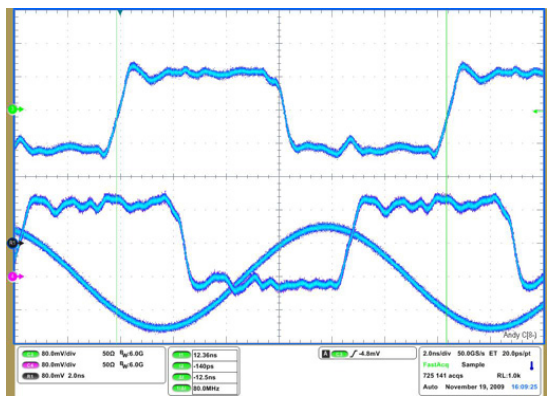

Figure 11: ADC1 and ADC2 acquisition of 80MHz sine wave redirected to DAC1 and DAC 2 outputs used as monitors

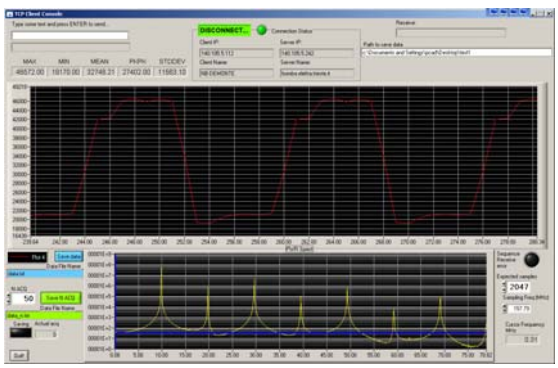

Figure 12: FFT on a 10MHz trapezoidal wave

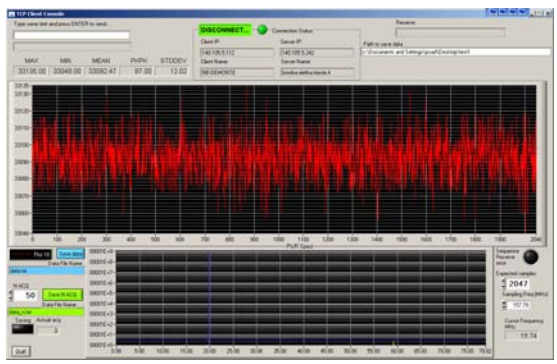

Figure 13: 34 values Std. Dev. on a 160MHz sine

Software communication interface

Several subsequent steps of software refinement led to the realization of a basic GUI, based on National Instruments' CVI, of fundamental utility for debugging. Capable of acquiring data from an open TCP/IP socket, it can either display them real time in both the time and frequency domain, as well as dumping acquisitions onto text files. A picture of the GUI is shown in Figure 12.

MEASUREMENTS ON A|D|O

ADCs tests

Data acquisition of one of the four ADC channels is shown below (Figure 14). All the other channels have equivalent performance on the whole range of frequencies tested 100 KHz to 160 MHz.

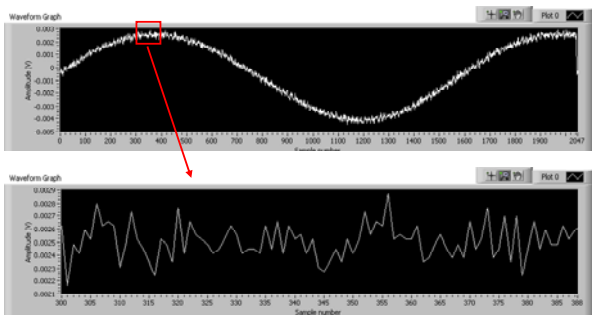

Figure 14: 700 µV noise on a 100 KHz 50 mV_{p-p} sine

As measured on the LTC2209 evaluation kit the noise of the input of the ADC is 5 LSB (Figure 15).

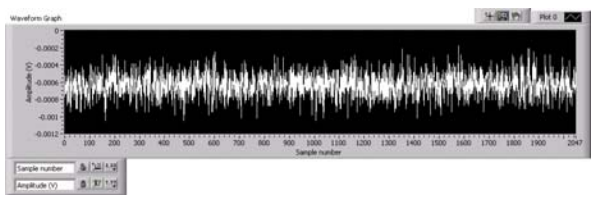

Figure 15: 5 LSB noise on 50Ω terminated input

Software communication interface

In order to debug at least the basic functionalities of the module, the analog front-end of the card with its four ADCs had been tested using the first control interface used for A|D|A: data stored in the ADC RAM buffer are transferred to the PC via ChipScope and the analyzed with a LabView GUI. Figure 14 and Figure 15 show the result of one acquisition with this technique.

DEVELOPMENT FRAMEWORK

The A|D|A project is a brave step toward an ambitious and far-seeing final goal: leading the road toward uTCA based systems at Elettra. Moreover as the general trend in the scientific community suggests, it aims at contributing for the spread of this promising technology among particle physics laboratories. It is therefore crucial to foster discussions within the scientific community to promote the development and growth of the innovative idea. As a step toward openness, the best candidate for boosting the finalization of many aspects of the card is the *Open Hardware Repository* (*OHR*, www.ohwr.org). The current manpower devoted to the project is too limited for a prompt coverage and fast reaction time to both the users' specific requirements, and the developer's technology related needs for enhancing the design. The OHR natural inclination toward diversified and parallel developments aiming at a common goal perfectly suits the "needs and wishes" of the A|D|A developers. Profiting from peer review and community based shared developments will bring prompt support, fast feedback, together with a sure visibility of the laboratory's activity.

CONCLUSION AND OUTLOOK

Presently both modules' prototypes (4 boards each) had been successfully tested and debugged, showing performances well within specifications. The A|D|A modules (Figure 16) are in the process of a mini-series production of 20 pieces, expected to be delivered by June. While the A|D|O modules (Figure 17) production will start later this summer. The development of the firmware is continuously growing, including both infrastructural features' improvement and application specific algorithm implementation. Moreover the usage of such cards in other interesting fields of application is being fostered.

Figure 16: A|D|A Prototype Components/Top side

Figure 17: A|D|O Prototype Components/Top side

ACKNOWLEDGMENT

The Author thanks all the Colleagues from the Timing and Diagnostics group at Elettra for the great professional collaboration and the pleasant social company.

REFERENCES

[1] The MictoTCA specifications page MTCA.0 R1.0 http://www.picmg.org/v2internal/microTCA.htm

[2] L. Pavlovic, A. O. Borga, M. Ferianis, M. Predonzani, F. Rossi, "Bunch Arrival Monitor at FERMI@ELETTRA", BIW'10, Santa Fe, May 2010, TUPSM086

[3] A. Borga, "Back-end system and A|D|A module concepts for FERMI's diagnostics", FERMI@ELTTRA, ST/F-TN-09/14, November 2009

SIMULATION OF A CAVITY BPM FOR HIGH RESOLUTION SINGLE-PASS BEAM POSITION MEASUREMENTS

A. Morgan, G. Rehm, Diamond Light Source, UK
A. Lyapin, University College London , UK
S. Boogert, N. Joshi, S. Molloy, Royal Holloway University London, UK

Abstract

This paper describes the design of a cavity BPM for use in single pass machines. The design was modelled using a number of different EM codes to allow cross comparison of the simulation results. Furthermore, in addition to existing designs, the geometry has been modified to introduce a frequency separation between the horizontal and vertical dipole signals, as well as a reduction of the sensitivity of the position monitor to the monopole sum signal. The next stage of this project will be the manufacture of a prototype for tests in the transfer path at Diamond Light Source.

DESIGN REQUIREMENTS

Modern and future single-pass machines such as Free Electron Lasers and Linear Colliders require fast and sensitive beam position monitors (BPMs) able to do precision beam position measurements of individual bunches.

Cavity BPMs have been shown to provide nanometre level resolutions [1], while stability studies resulted in micrometre and even sub-micrometre drifts over a few hours [2].

Several methods of improving the time resolution of cavity BPMs allow for bunches separated by 10s of nanoseconds to be resolved.

Basing on the previous works we wanted to take advantage of the simple cylindrical geometry and the inherent filtering effects of the slot-coupled design in order to better select out the desired dipole mode, while simultaneously suppressing the signals from the unwanted modes.

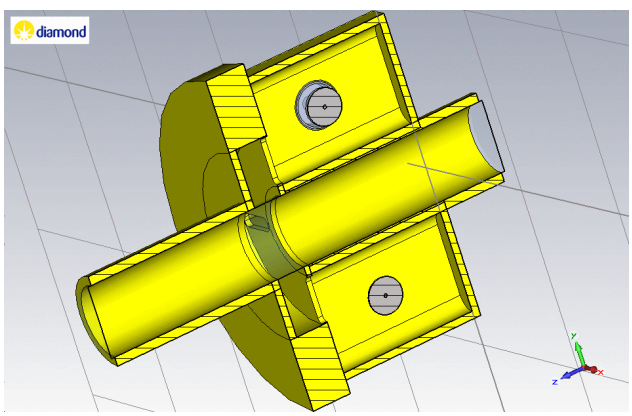

Figure 1: Full cavity BPM geometry

We also aim at simplifying the design flow, making the BPM easy and hence inexpensive to manufacture, and also fixing the remaining problems of cavity BPMs, such as the cross-coupling of the horizontal and the vertical signals.

As with many other recent cavity BPMs[3,4,5], this design comprises of a resonant cavity with coupling slots leading into waveguides. Each waveguide has a pickup in it to transmit the signal down a coaxial line for signal processing. (See figure 1)

Resonant cavity

The radius of the resonant cavity is determined by the frequency we are interested in. In the longer term we want to use the Diamond RF system (running at 499.654 MHz) to deliver local oscillator (LO) signals for down conversion. We chose the 13th harmonic, which gave us an initial target of 6.495 GHz. The dipole mode frequency has to be slightly offset from the peak so once the signal is down converted it sits near the centre of the IF bandwidth. A 100Msample ADC gives 50MHz bandwidth so a 20 MHz offset downwards was included, bringing the target to 6.475 GHz.

The longer the cavity the stronger it couples to the beam. On the other hand, the cavity becomes sensitive to the beam incline while the sensitivity increase with the length drops due to the signal in the cavity and the beam becoming asynchronous. 8 mm length was found to provide enough coupling while keeping the timing effects to a minimum.

Waveguide

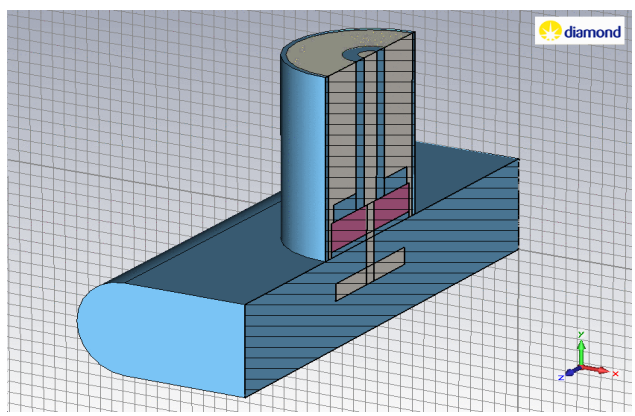

Figure 2: waveguide and coaxial port geometry

The dimensions of the waveguides are such that the first monopole mode is below the waveguide cut-off for the lowest odd mode TE_{01}, so that the monopole mode signal leaking due to asymmetries is suppressed, while the dipole mode is the first mode transmitted by the TE_{01}.

Although the other modes can be present near the slots they do not propagate. Therefore the length of the

waveguide can determine the amount of filtering seen by unwanted modes coupled through the slots.

The location of the coaxial port on the waveguide, and the location of the coupling plate in the waveguide is such to maximise the coupling from waveguide to coaxial modes.

Coupling slots

The width of the coupling slots in the two planes is different (4mm for x and 3mm for y).

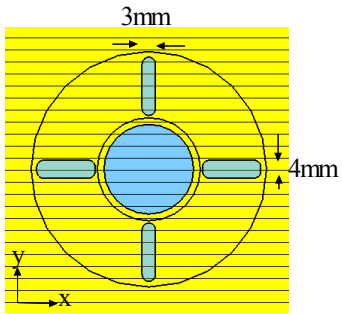

Figure 3: Coupling slot geometry

This achieves some frequency separation between the horizontal and vertical polarisations of the dipole mode which allows us to improve the rejection of the cross coupled signal once the signal is digitised.

This is because we do digital down conversion using different frequencies for x and y. The signals are then passed through a filter with a passband small enough that the cross-coupled signals fall outside and so are suppressed .

CODE COMPARISONS

Several different EM modelling codes were used in parallel for this design (CST studio, GdfidL[6], Omega3P). This gave us an idea of the amount of confidence we should give to a particular result. Once all three codes converged we could be sure we had a representative result.

In order to find out the different codes' strengths and weaknesses, some simpler simulations were done. The idea of this was to get an understanding of the mesh densities required to get good results for the cylindrical geometry using cartesian geometry codes. This is because once the details of the full design are added, radial symmetry is broken and you need a cartesian model to fully represent the desired geometry.

Pillbox cavity

The first was a simple pill box cavity of the dimensions of the main resonance cavity of the CBPM. This allowed us to not only compare the codes against each other, but also with the theoretical predictions for this geometry.

The theoretical frequency results were generated from this analytical formula[7].

$$f_{(mnp)} = \frac{c}{2\pi}\sqrt{\left(\frac{j_{mn}}{b}\right)^2 + \left(\frac{p\pi}{l}\right)^2}$$

Where f is the frequency and j are zeros of the bessel function J_m in a cylindrical coordinate system, while b and l are the radius and length of the cavity respectively. Under the assumption of no modes in the z direction p is always 0. Also we are mainly interested the lowest radial mode, so n is always 1. So the frequencies of the monopole, dipole and quadrupole modes are where j_{nm} is j_{01}, j_{11} and j_{21} respectively.

In order to find the theoretical Q values, we first needed to calculate the skin depth, using

$$\delta = \frac{1}{\sqrt{\pi \sigma \mu f}}$$

which we can then use with

$$Q = \frac{1}{\delta}\frac{l}{1+\frac{l}{b}}$$

Where b and l have the same meaning as before. f is the frequency of interest, μ is the magnetic permeability of the cavity wall material, while σ is the electrical conductivity of the cavity material.

To within 2.3MHz all the codes agree with the theoretical expectation of the frequency (Table 1). The spread of results between the codes is also of the same order, with the monopole mode having the closest agreement and the quadrupole mode diverging the most.

The increasing divergence between the codes as you move from monopole to dipole to quadrupole is due to the fact that the mesh is unable to describe the higher frequency modes as accurately .

Table 1:Eigenmode frequency results for the pillbox.

Pill box cavity (Frequencies (GHz))					
		Difference from theory (MHz)			
Mode	Theory	CST	GdfidL	Omega 3P	Spread (MHz)
Monopole	4.3414	-0.2	0.0	1.0	1.2
Dipole	6.9173	-0.5	0.0	1.6	2.1
Quadrupole	9.2712	-1.2	1.1	2.3	3.5

The Q factors also agree well with the theoretical prediction (see table 2).

Table 2:Eigenmode Q_0 results for the pillbox.

Pill box cavity (Q factors)					
		Difference from theory			
Mode	Theory	CST	GdfidL	Omega 3P	Spread
Monopole	6123	0	55	-7	62
Dipole	7729	2	75	-15	90
Quadrupole	8948	2	55	-24	79

Pillbox cavity with beam pipe

The next step was to do the same analysis on a pillbox cavity on a beam pipe. Again, with the same dimensions as the full design.

Again the codes showed good agreement on the frequencies with the dipole being within 3MHz (see table3).

Table 3: Frequency results for pillbox on beam pipe

Pill box cavity with beam pipe (Frequencies (GHz))				
Mode	CST	GdfidL	Omega3P	Spread (MHz)
Monopole	4.7071	4.7111	4.7030	8.1
Dipole	6.4750	6.4764	6.4734	3
Quadrupole	9.0025	9.0030	9.0045	2

The Q values broadly agreed but the reduced ability of the mesh to describe the higher frequency modes is more pronounced (see table 4).

Table 4:Eigenmode Q_0 results for pillbox on beam pipe.

Pill box cavity with beam pipe (Q factors)				
Mode	CST	GdfidL	Omega3P	Spread
Monopole	6272	6373	6266	107
Dipole	7144	7612	7687	543
Quadrupole	8425	9864	9077	1439

These studies allowed us to develop an understanding of the limits of the codes and to spot indicators of poor convergence which was vital when dealing with the more complex cavity BPM model.

RESULTS FOR THE CBPM MODEL

For reasons of computational time and memory, the coaxial pick-ups were omitted from the model.

S parameter results

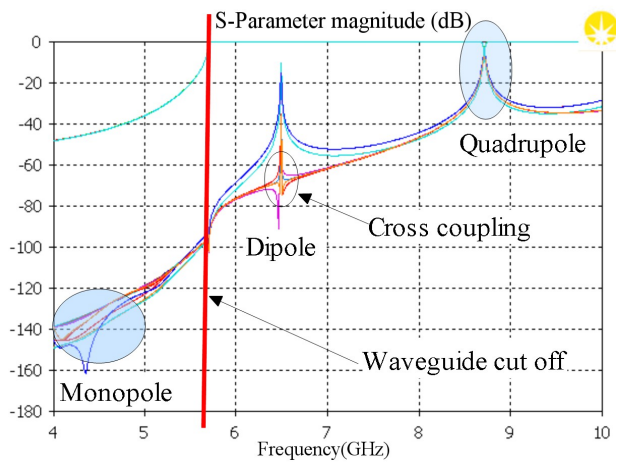

Figure 4: S-parameter response of CBPM

Figure 4 shows a typical S parameter response for the CBPM model.

It can be clearly seen that the residual monopole mode signal is suppressed because it is below the waveguide cut off frequency. Strong resonances can be seen at the dipole and quadrupole frequencies, with the dipole signal being split into coupling in the same plane, and cross coupling between x and y.

Figure 5 shows the ~5MHz frequency separation we get by using the different coupling slot widths for x and y, as described earlier. The blue curves show the transmission from one port to it's pair on the same axis. All the other curves are cross coupling terms and their absolute values are largely determined by the mesh density of the model.

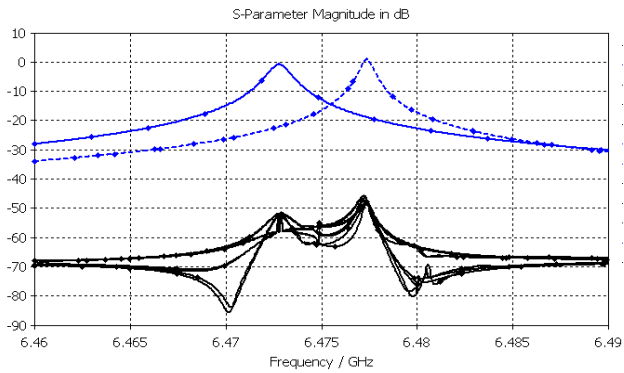

Figure 5: S-parameter response of the dipole mode

As expected, the transmission curves have one well defined peak corresponding to the geometry of the coupling slots in each plane. The cross terms show both peaks as the signals are always passing through one of each type of coupling slot.

Wakefield results

Using a wakefield solver has enabled us to simulate the cavity's response to an excitation with a charged particle bunch travelling through the beam pipe, as compared to the excitation on the ports as used in the S-parameter simulation.

By doing both lossless and lossy simulations we could retrieve both the external and loaded Q values.

Both CST and GdfidL were used for the lossless simulations to check for consistency of the results. Both codes gave very similar results, giving us confidence that they are accurate.

The beam simulated was a 3mm long gaussian pulse containing 1nC of charge. By moving the position of the beam in the beam pipe we could determine the effect of an asymmetric input on the structure. The centred position was used to judge what level of signal could be attributed to meshing artefacts.

Figure 6 shows the typical signal coming out of one of the ports, with a 1mm beam offset in both x and y. It is clear that the signals are comprised by different modes with different amplitudes, decaying at different rates.

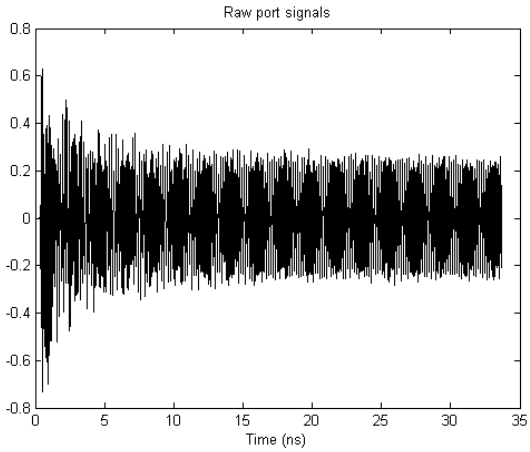

Figure 6: Raw port signals

Indeed, taking the FFT of the port signals we can see that two modes dominate the output (figure 7). For all offsets the dominant mode frequency was 6.47GHz, corresponding to the lowest order dipole mode.

When beam was only offset in either x or y it was the only significant signal. However, when the beam was off axis in both dimensions then an additional peak at 8.85GHz appeared.

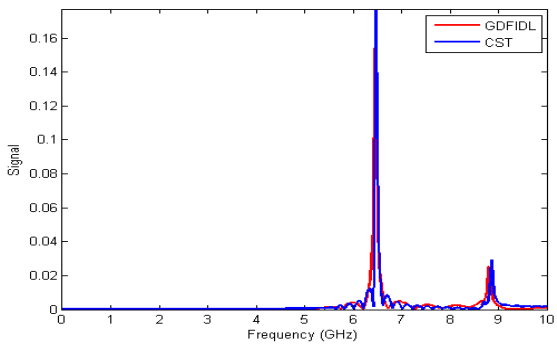

Figure 7: FFT of the port signals

This behaviour is a signature of the quadrupole mode: a beam offset in x or y only produces a field that is symmetric with respect to the slots, and so does not couple into the waveguide. However, when the beam is offset in both x and y, the symmetry gets broken, and the quadrupole mode is generated, some of which is able to couple out into the waveguide. The maximum coupling is achieved when when the beam is equally offset in x and y, so the field is antisymmetric with respect to the slots.

Knowing the peak frequencies in the signal's spectrum, it is possible to demodulate the port signals to find the time domain magnitude evolution of the two modes. Figure 8 shows the decay of the dipole mode (shown in black) and the quadrupole mode (shown in blue) for all 4 output ports. The split between the dipole traces is due to the asymmetry in the coupling slots, the wider slots providing lower external quality factor and shorter decay time.

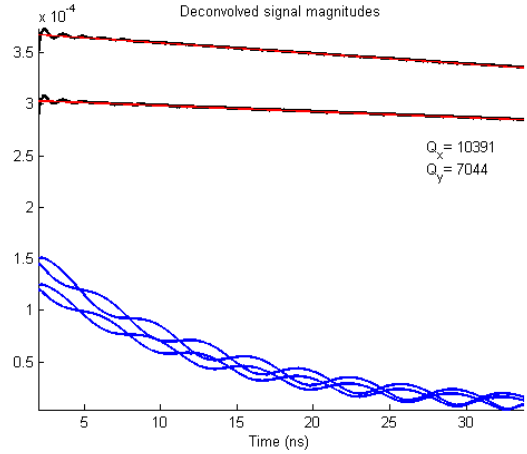

Figure 8: demodulated output signals

From figure 8 it can be seen that the quadrupole component contributes a ~30% early, short term enhancement of the output signals, which can explain the initial shape of the trace seen in figure 6.

By taking the gradient of the initial part of the dipole curve the Q factor can be extracted. Depending on whether material losses are applied to the model this give us either the external or the loaded Q.

The external Q values were ~10,000 and ~7,000 for x and y respectively, while the loaded Q values were ~4,000 and ~3,500 for x and y respectively.

From the loaded Q values we obtained ring down times to 1/e of 0.63us in x, and 0.55us in y. Assuming we want the residual signal to be no more than 5% of the original, this implies 3 ring down periods giving us a maximum bunch repetition frequency of ~500KHz. Of course, by accepting a larger residual signal we could increase the repetition frequency. This is largely determined by the accuracy of the signal subtraction in the digital processing.

By taking the output power integrated over the port geometry, and assuming perfect conversion from waveguide to coaxial transmission the expected signal seen on the 50Ω transmission line can be deduced.

Figure 9 shows the amplitude of the output signal for a 1 mm offset in only one plane. One can see a short pulse peaking to just under 4V and a much slower signal at around 1.3V. The initial pulse is a combination of the signals of all short-live modes that are above the beam pipe cut-off frequency, such as higher order dipole modes etc. These modes decay very quickly as the energy escapes through the beam pipe. Although the pulse looks high compared to the dipole slower decaying signal of the first dipole mode, it can be reduced by orders of magnitude by a band-pass filter in the front-end of the processing electronics.

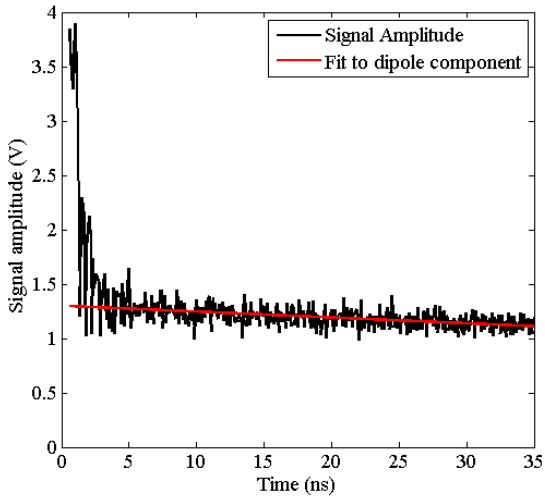

Figure 9: Calculated output signal for 1mm offset

Due to the high Q factor the peak signal for the dipole mode is relatively low, but the energy is spread out over a longer time and in a narrow frequency band. This allows us to use narrow-band filters on the signal in order to get better discrimination between the wanted position signal and the unwanted signals from cross coupling, other cavity modes, and noise. Furthermore, a longer piece of the waveform (compared to the low-Q case) fits into the dynamic range of the electronics and digitisers, and so can be used for digital down-conversion or even fitting analysis.

Consistency check

By using the results of different simulations to get internal Q, the external Q, and the loaded Q (Q_0 ,Q_{ext} and Q_L respectively). A cross check can be done by combining Q_0, Q_{ext} in order to predict Q_L. This value can then be compared against the value for Q_L taken from the wakefield simulation with material losses included.

The Q values are combined in the following way.

$$\frac{1}{Q_L} = \frac{1}{Q_0} + \frac{1}{Q_{ext}}$$

Where Q_0 is the eigenmode result, which include cavity losses. Q_{ext} is the wakefield result with no losses, while Q_L is the wakefield result including losses.

The predicted results show good agreement with the simulated values. The remaining discrepancy can be explained by the fact that the predictions do not take into account any losses of the parts of the structure not covered by the eigenmode models.

Table 5: Comparison of Q values

	Q_0	Q_{ext}	Predicted Q_L	Simulated Q_L	Difference
Using the pillbox with beam pipe eigenmode result					
Q_x	7144	10391	4233	4071	4%
Q_y	7144	7044	3547	3439	3%

SUMMARY

Our design uses proved to work cylindrical cavity with four waveguides coupled via slots for monopole mode reduction. We introduced a frequency split for the two polarisations of the dipole mode making the slots in x and y different. We hope that the isolation between the x and y couplers we observe in the simulations will be confirmed on the prototypes that will be manufactured in the late 2010.

For benchmarking purposes we compared three different EM simulation codes; CST, GdfidL and Omega3P, all of which showed very good agreement between each other and the theory.

The key values we obtained from the simulations include the external Q values: ~10,000 and ~ 7,000 for the x and y axis respectively; and the loaded Q-values of 4071 and 3543. A cross check with internal Q factors showed a the correct relationship with an error less than 5%.

At a bunch repetition frequency of 500kHz the bunch to bunch signal spillover is about 5%, which is low enough for most cases. Much lower spillover can be achieved by subtraction of the digitised signals.

The wakefield simulation gave us an estimate of the output signal of 1.3V for the dipole mode at 1 mm beam offset for a 1 nC bunch charge. An additional short-lived signal initially peaking to 4V was also observed, which, although, is produced by higher order modes and is expected to be strongly suppressed in the electronics.

We are planning to build and test a few prototype cavities in a transfer line of the Diamond light source. We are also looking into involving industrial partners in the manufacturing process, so that if any demand arises for a large scale project, this design can be mass-produced on demand.

REFERENCES

[1] S. Walston et al., Performance of a high resolution cavity beam position monitor system, Nuclear Instruments and Methods, 2007, 10.1016/j.nima.2007.04.162

[2] M. Slater et al., Cavity BPM system tests for the ILC energy spectrometer, Nuclear instruments and Methods, 2008, 10.1016/j.nima.2008.04.033

[3] D. Lipka et. al. Orthogonal coupling in cavity BPM with slots, Proceedings of DIPAC 09, p44

[4] H. Maesaka et. Al Development of the RF cavity BPM of XFEL/SPRING-8, Proceedings of DIPAC 09, p56

[5] S. Smith et. al. LCLS cavity position monitors, Proceedings of DIPAC 09, p285

[6] W. Bruns, Improved GdfidL with Generalized Diagonal Fillings and Reduced Memory and CPU Requirements, Proceedings of the 1998 International Computational Accelerator Physics Conference (ICAP '98)

[7] S. Y.Lee Accelerator Physics, World scientific publishing, 2004

NEW BEAM MONITORING INSTRUMENTATION AT ATF2, KEK*

E. Medvedko, R. Johnson, S. Smith, G. White
SLAC National Accelerator Laboratory, Menlo Park, CA 94025, U.S.A.

Abstract

A new stripline beam position monitoring (BPM) readout and processing system was installed and successfully tested over a two-week period at the Accelerator Test Facility (ATF2), at KEK, Japan during February 2010. The core analog processing board used in the system is a duplicate of that developed for, and in use at, the Linac Coherent Light Source (LCLS) at SLAC. The digitization, processing and control front-end were custom designed for ATF2 using a 14-bit 100-MHz VME digitizer and an EPICS Input / Output Controller (IOC) running on the VME controller. Control of the analog boards is via EPICS, which controls a serial-over-TCP / IP port server. Hardware for the readout of up to 14 BPMs with 3 spare analog boards was delivered. The goal of this installation was to provide better than 10 microns resolution, non-charge-dependent readout of the ATF2 electron beam with long-term gain stability compensation. These criteria were tested and successfully met. This design was found to be highly effective and to have many advantages, especially that it required minimal installation effort at ATF2.

INTRODUCTION

Twelve analog processing chassis are connected with cables to ATF2 stripline electrodes (Fig. 1). Each chassis has four inputs from Y+/- and X+/- striplines.

The 140 MHz output signals go to the VME 14-bit digitizers which have a 100 MHz sampling frequency. An EPICS IOC on a VME controller (Motorola MVME3100) receives and analyses the digitizer data, controls the analog processor gain, and calibrates signal power and calibration tone pulse width.

The port server communicates with the analog processing board via RS232 protocol. One trigger pulse initiates the calibration cycle in the time gap between the beam pulses. Another trigger synchronizes the digitizer's data conversion.

REQUIREMENTS

The main requirements:

- Resolution better than 10 microns.
- The measured beam position independent of beam charge. Operational ranges are ~ 0.15-1.5 nC (single bunch) with a dynamic range of +/- 3mm.
- Long-term gain stability 5%-10% over month timescales. The actual gain stability performance is still to be assessed.

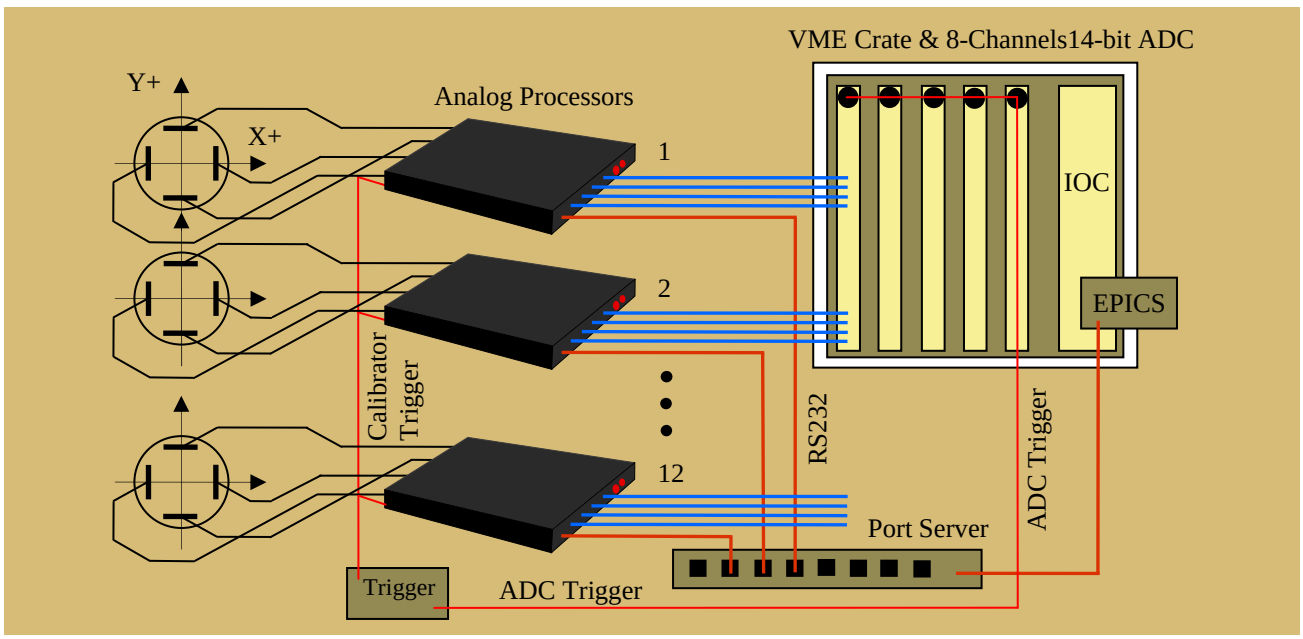

Figure 1: The ATF2 BPM processing system block diagram.

* Work supported by U.S. Department of Energy contract DE-AC02-76SF00515

BPM READOUT AND PROCESSING SYSTEM

The analog processing board or Analog Front-End board (AFE) originates from LCLS [1]. High resolution beam position monitoring processor electronics were designed a few years ago for LCLS for a single bunch of 0.08-8.0 nC charge. The LCLS processor consists of the AFE and 16-bit Analog-to-Digital Converter (ADC) boards, packed into 19-in rack mount chassis, 1U high. The ADC board has a microprocessor (IOC) and requires three network ports for communications. Fourteen chassis with the AFE but without the ADCs were built for ATF2. This design has many advantages.

Analog Processing Board

The AFE board has four analog processing channels, with three low-noise amplifies, three band-pass filters, two programmable attenuators of maximum attenuation 15 dB and 31 dB, a fast comparator and a switch at the end of the analog channel for overvoltage protection of an external ADC.

Input bandpass filters are centered at a frequency of 140 MHz with a processing bandwidth of 7 MHz. The analog channels input noise is very low, approximately 3 microV rms. The maximum gain is 34 dB with programmable attenuation of up to 46 dB in 1 dB steps. The calibrator (CL) sends short 140 MHz tone-bursts between the beam pulses alternately to the Y+ and X- striplines. The signal ratio of the two adjacent striplines calibrates the processing channels gain and cable loss. The programmable attenuator can vary CL amplitude over 31 dB in steps of 1 dB. The maximum power output is close to 2 W. The CL tone-burst duration is typically between 260 and 300 ns. The CL requires an external trigger pulse synchronized with the beam.

The fast comparators and a switch at the end of the channels (limiter) shut down the outputs if an overvoltage approaches, and prevents damage to the ADCs.

The LCLS processors show an average position resolution of 5 microns rms at a bunch charge of 220 pC in a stripline pickup of 1 inch diameter.

A Xilinx FPGA controls the programmable attenuators, CL and limiter. The FPGA supports two types of communications: RS232 and Queued Serial Peripheral Interface (QSPI). RS232 is used for the ATF2 BPM chassis.

ATF2 BPM Chassis Construction

The ATF2 BPM chassis is a 19” rack-mount unit, 1 U high. The enclosure size is 17” x 17”. AC Power input is 100-240 VAC, 47-63 Hz. On the rear panel there are four input SMA and two LEMO connectors, two fans and a power plug. The front panel has four output SMA connectors, “power on” LEDs, an RJ45 communication port and three fans. The enclosures are made by Protocase, Inc [2].

Digitizer

Eight-channel, 14-bit, 100-MHz VME digitizers (SIS3301) from Struck Innovative Systeme (Hamburg, Germany) are used in ATF2 for BPM signals processing [3]. With 140 MHz input signals and a 100 MHz sampling frequency, the digitizer under-samples the input waveform and the data aliases to 40 MHz. The advantages of using the external ADC are: flexibility of ADC selection, the ADC could later be replaced with a better one, for example one with more bits, a higher sampling rate, or higher analog bandwidth. The IOC runs in the local controller (VME for ATF2) and it requires only one network connection.

The SIS3301 has an analog input bandwidth of 70 MHz. At 140 MHz, the input signal is attenuated by 17 dB. This adds additional noise to the noise budget. As set up at ATF2, the corresponding digitiser 1-bit noise represents a resolution limit of about 2 microns. This is sufficient for the planned operation and can be improved in future by using digitizers with a higher bit-count or with increased input analog bandwidth.

Port Server

The RS232 port interface was used in preference to the QSPI one as readily available and easy to use commercial distribution hardware exists for this protocol. The Digi Port Server (TS 16) has 16 RS232 ports / serial-to-Ethernet [4]. These are used for programming the AFE, for setup, monitoring and control of the VME processor and for remote reboot control of the VME crate.

The AFE board has DB-9 connectors for RS232. Only three pins are used: Receive Data (RD) - pin 2; Transmit Data (TD) - pin 3; Ground is pin 5, so the AFE is Data Terminal Equipment (DTE) type.

EPICS Control Display

All setup, control and monitoring is done through a single Matlab Graphical User Interface (GUI) panel.

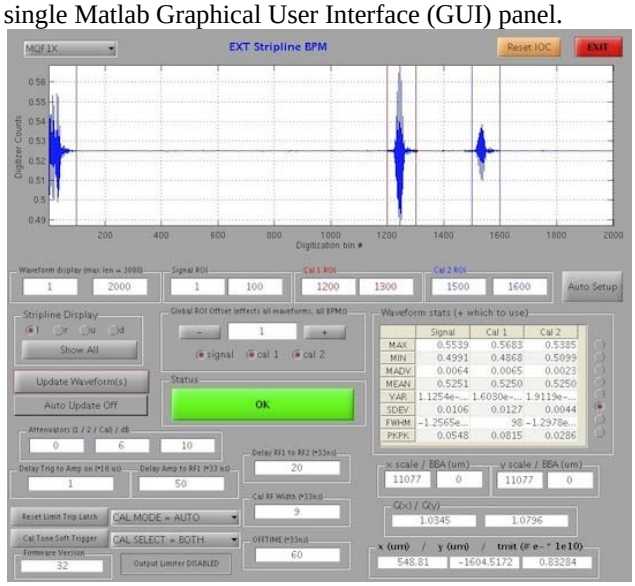

Figure 2: EPICS Control Display.

This principally allows for the selection of regions of interest for the main stripline signals and calibration signals. It also allows all other parameters supported by the AFE to be examined and changed. It displays the statistical analysis of the waveforms for use by the position algorithm and allows user selection of different ones. A simple standard deviation calculation for each waveform was found to give the best performance.

MEASUREMENTS AND DATA ANALYSIS

The BPMs were calibrated using dipole corrector magnets through the ATF2 beamline. To investigate resolutions, gain stability and charge sensitivity, one thousand continuous stable pulses were taken.

Resolution

The resolution was calculated for each BPM chassis. Y resolution is 6 microns or better, X resolution is 10 microns or better (Fig. 3). The resolution data below was calculated from a 1000 pulse run. A model-independent analysis technique using Singular Value Decomposition (SVD) was used to subtract the coherent pulse-pulse jitter from the accelerator, leaving the resolution-related jitter of the BPMs shown below. The horizontal BPMs in regions of the machine with large design horizontal dispersion show the worst resolutions, meaning that the applied technique did not succeed in completely removing all energy-related jitter. Hence the below should be considered as an upper-estimate of the resolution. The achieved resolution meets requirements and the best shown meets the expectation of 2-5 microns of jitter.

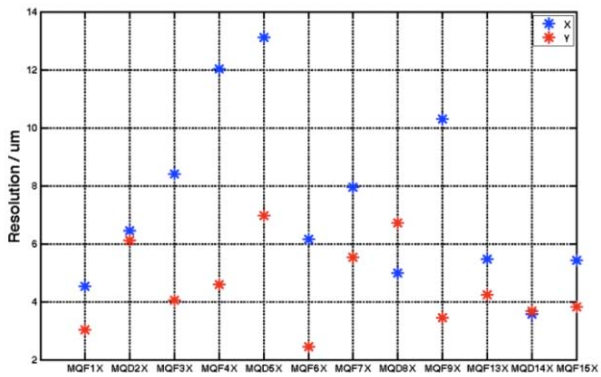

Figure 3: Estimate of the resolution for 12 BPMs.

Gain

Gain is stable. It was monitored over 24 hours (Fig. 4). The MQD5X BPM has a large gain imbalance due to a defective cable, it also exhibits far more gain drift than the other BPMs. The gain monitoring analysis system nicely deals with this however.

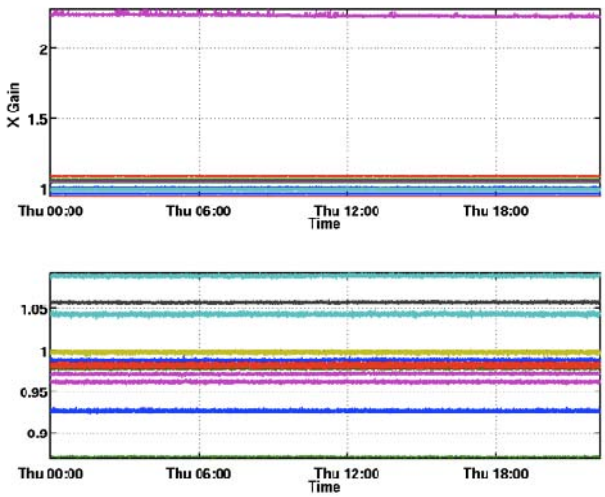

Figure 4: X and Y gains over 24 hours.

Beam Charge versus position

The position is mostly insensitive to the beam charge. Fig. 5 and 6 below show the data from two of twelve processors. The X and Y spreads are distributed horizontally. There is a very small tilt on the charge-versus-Y-position plot of MQD2X.

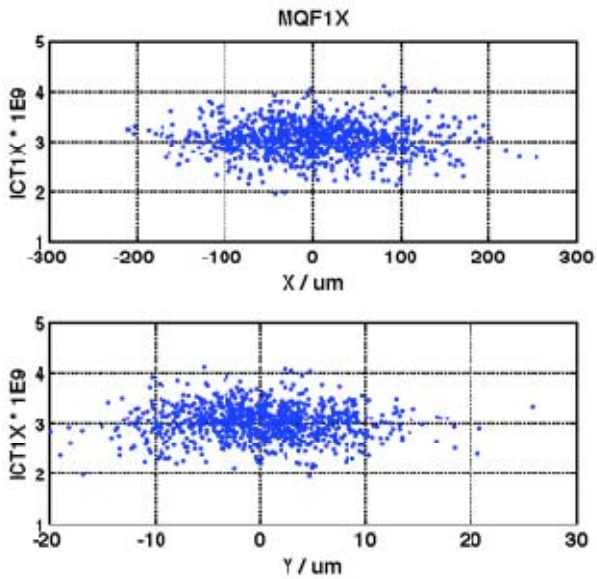

Figure 5: BPM MQF1X beam charge versus position, X and Y data spreads are distributed horizontally. There is no charge-position sensitivity.

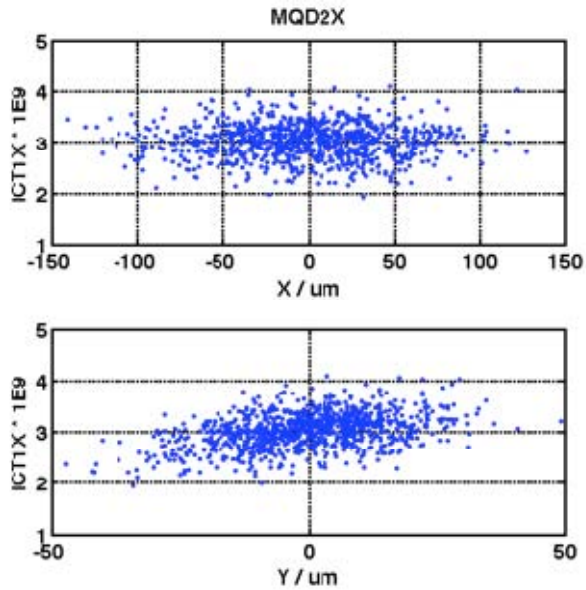

Figure 6: BPM MQD2X-Y has a charge-position tilt, negligibly small deviation.

Beam Based Alignment

Each BPM is attached to one of the quadrupole magnets in the extraction line of the ATF2. Quadrupole-shunting beam-based alignment (BBA) was used to align the BPM readout with the magnetic center of its associated quadrupole. This entails sweeping the beam across the magnet using an upstream corrector with the magnet at full and 80% of nominal strengths. The center of the magnet can be found from the crossing of the two orbits on a downstream BPM.

An example is shown in Fig. 7. It is hoped that the stability of this BPM system will allow for this BBA data to be valid for a long period of time enabling "golden orbit" restoration at the start of beam tuning shifts.

SUMMARY

- A new BPM readout and processing system was installed at ATF2, tested and available for use.
- Resolution 10 microns or better satisfies the requirements.
- Gain is stable over 24 hours.
- The measured beam position is insensitive to the beam charge.
- This design is very effective, required minimal installation effort. Each unit could be replaced relatively easily. A digitizer already supported by the existing control system was used.

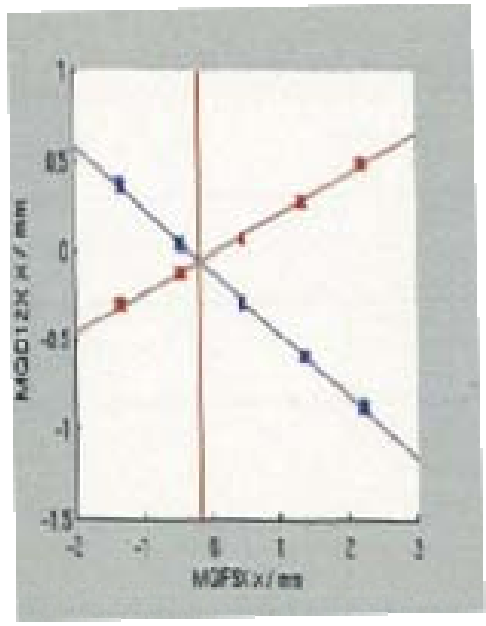

Figure 7: BBA results of QF9X quadrupole using MQF9X BPM and downstream MQD12X BPM and a quad shunting method.

ACKNOWLEDGEMENTS

We would like to thank the KEK staff at ATF for their help and assistance during the installation of the BPM system. Especially N. Terunuma for his enormous help co-ordinating this international collaborative effort.

REFERENCES

[1] E. Medvedko, R. Johnson, S. Smith, R. Akre, D. Anderson, J. Olsen, T. Straumann, A. Young "Stripline Beam Position Monitors for LCLS", BIW08, Tahoe City, CA, USA May 2008, TUPTPF037, p. 285.
[2] http://www.protocase.com/index.php
[3] http://www.struck.de/sis3301.htm
[4] http://www.digi.com/products/serialservers/portserverts816.jsp#overview

LCLS RESONANT CAVITY BEAM POSITION MONITORS *

Andrew Young, Ronald G. Johnson, Stephen Smith
SLAC National Accelerator Laboratory, Menlo Park, CA 94025, U.S.A.
Robert M. Lill Argonne National Laboratory, Argonne, IL 60439, U.S.A.

Abstract

The Linac Coherent Light Source (LCLS) is a free-electron laser (FEL) at SLAC producing coherent 1.5 Å x-rays. This requires precise, stable alignment of the electron and photon beams in the undulator. We describe construction and operational experience of the beam position monitor (BPM) system which allows the required alignment to be established and maintained. Each X-band cavity BPM employs a TM_{010} monopole reference cavity and a single TM_{110} dipole cavity detecting both horizontal and vertical beam position. The processing electronics feature low-noise single-stage three-channel heterodyne receivers with selectable gain and a phase-locked local oscillator. Sub-micron position resolution is required for a single-bunch beam of 200 pC. We discuss the specifications, commissioning and performance of 36 installed BPMs. Single shot resolutions have been measured to be about 200 nm rms at a beam charge of 200 pC.

FEL COMMISSIONING

LCLS photocathode RF gun and injector systems were commissioned in 2007, followed by linac and bunch compressor systems in 2008. Beam was first taken through the undulator beamline (with no undulators installed) in December, 2008. After aligning each undulator segment individually, 21 undulator magnets were inserted in April 2009. We observed lasing at 1.5 Angstroms essentially immediately [1].

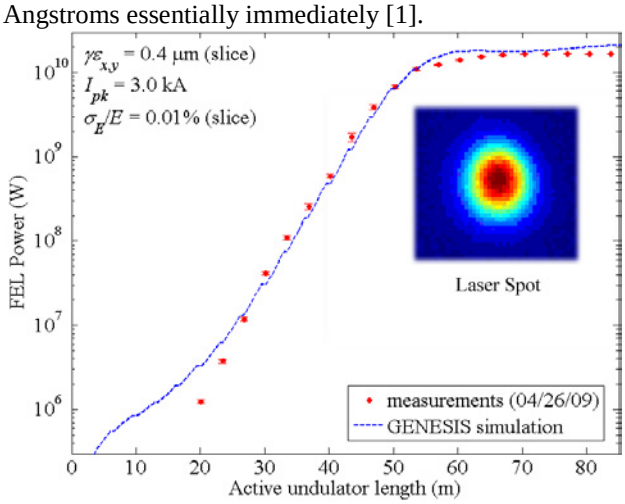

Figure 1: FEL gain length measurement at 1.5 Å made by kicking the beam after each undulator sequentially (red points), prediction (blue line) and YAG screen laser spot.

*Work supported by U.S. Department of Energy under Contract Numbers DE-AC02-06CH11357 and DE-AC02-76SF00515.

BPM REQUIREMENTS

Laser saturation in the LCLS FEL requires the electron and photon beams be collinear in the 131 meter-long undulator to about 10% of the 37 μm rms transverse beam spot size over scales of the FEL amplitude gain length (~4m) [2,3]. BPM system requirements include centering accuracy, reproducibility, small physical size, radiation hardness, and sub-micron resolution at 200 pC.

SYSTEM DESIGN

The major subsystems for the LCLS undulator BPM system are the cavity BPM, receiver, and data acquisition components. The cavity BPM and downconverter reside in the tunnel while the analog-to-digital converters (ADC) and processing electronics are in surface buildings.

Thirty-four BPMs are installed on undulator girders while two are placed in the linac-to-undulator (LTU) transport line. The BPMs provide stable and repeatable beam position data for both planes on a pulse-to-pulse basis for up to a 120-Hz repetition rate.

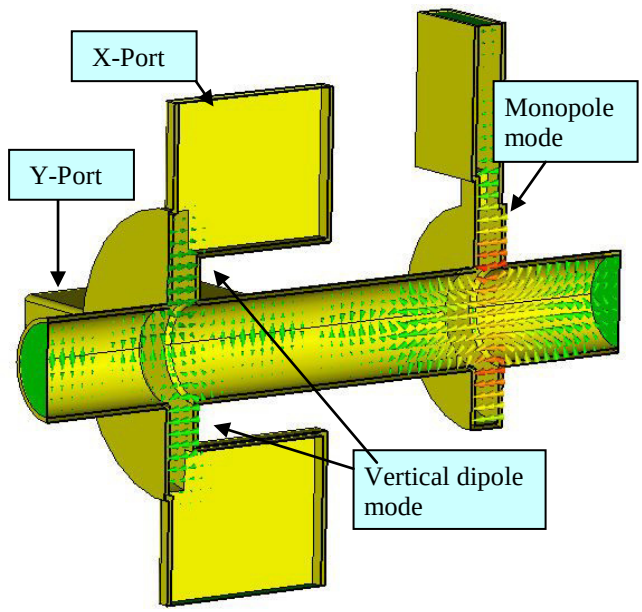

Figure 2: BPM Cavity schematic with electric fields of position (dipole) and reference (monopole) cavities.

X-Band Cavity

Figure 2 shows the electric field vectors in the cavity BPM simulated when the beam is offset[4,5]. Beam passes through the monopole reference cavity on the right, exciting the TM_{010} monopole mode signal resonant

at 11.384 GHz. The TM_{110} dipole cavity is located 36 mm downstream through the 10-mm-diameter beam pipe. Monopole-dipole isolation is 130 dB, due to a below-cutoff beampipe, copper losses, and poor coupling of the TM beampipe mode to the cavity dipole mode.

The position cavity dipole mode is resonant at 11.384 GHz, its output proportional to the product of beam position and bunch charge. The X and Y position modes are nominally degenerate in frequency, with the appropriate component chosen by the geometry of the couplers. The dipole coupler geometry is chosen to reject (the generally larger) monopole modes[4-8].

Iris couplers are precisely electrical discharge machined (EDM) into a solid copper block to ensure repeatable and accurate coupling. This technique ensures that the waveguide braze has little or no effect on the cavity performance. The dipole cavity was designed as a 4-port device with two opposing X couplers orthogonal to two opposing Y couplers. This is useful for cold testing and preserves symmetry. Unused ports are terminated with the potential for using them for future diagnostics.

Forty BPMs were built to a tolerance of ±10 MHz of design frequency. Accomplishing this without demanding unrealistic machining tolerances requires tuning. First, parts are inspected and cleaned. End caps are fitted to the body and clamped to a test fixture. Frequency and bandwidths are measured, then endcap beam pipe inner diameters are micro-machined as needed. BPMs are reassembled and checked to ensure the cavities are within the tolerance of +0, -10 MHz to compensate for frequency shift in the brazing process. End cap brazing was strictly controlled and a 10 MHz frequency shift was typically measured after the braze.

Dipole cavity final tuning was done with a sliding hammer in up to eight boss locations in the endcap to dimple the wall of the cavity. Four tuners in-line with the iris couplers are used for frequency adjustment. Four cross-talk tuners on the dipole cavity end cap are located at 45 degrees to the couplers. They reorient the dipole mode such that the modes are symmetric about the vertical and horizontal planes. These tuners are used to set the symmetry of the modes and optimize the isolation between planes.

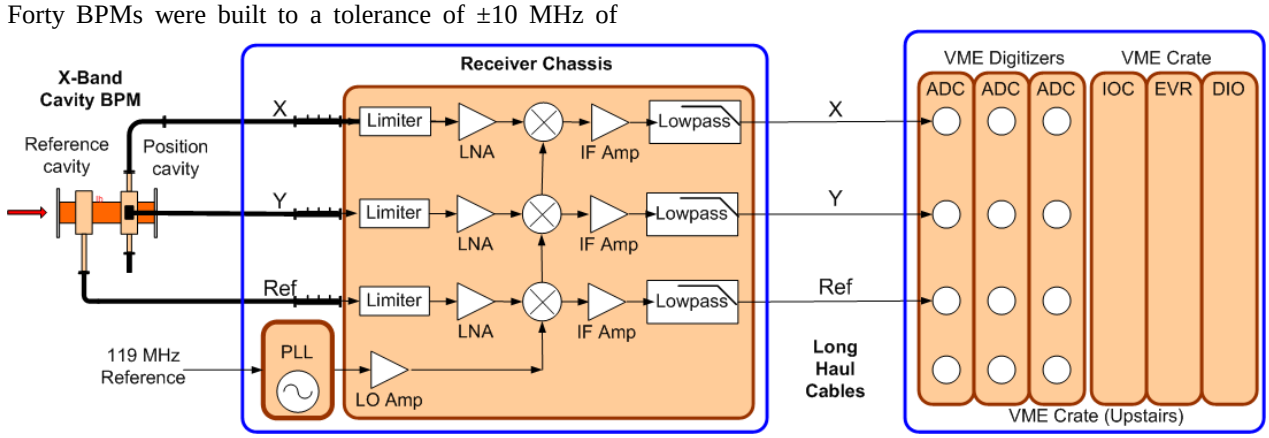

Figure 3: System block diagram. The receiver is mounted on the undulator stand while the digitizers are upstairs.

Receiver

A three-channel heterodyne receiver (Figure 3) mixes incoming X-band signals to a 25-50 MHz intermediate (IF) frequency. Each receiver input is limited to a 35 MHz bandwidth around 11.384 GHz. Filters also provide a broadband -10 dB return loss match to the cavities. Out-of-band filtering of -60 dB prevents higher modes from saturating the receiver input. Signals are first amplified in a low noise stage (LNA), then translated to the lower IF by mixing with a local oscillator (LO). The LNA is protected against high-power surges by a limiter that is rated at 50 W peak. The dynamic range of the electronics is extended by switching the gain of the receiver. Overall conversion gain/loss is +10 dB in the high gain mode and -15 dB in low gain. The LO is a low noise phase-locked dielectric resonant oscillator (PDRO) locked to the 119-MHz timing reference [9].

Digitizer

The X, Y, and Reference signals are digitized to 16 bits at a 119 MHz sampling rate in 4-channel VME digitizers designed and built at SLAC. Waveforms are transmitted over the backplane to a VME processor which reduces raw waveforms to beam position and charge.

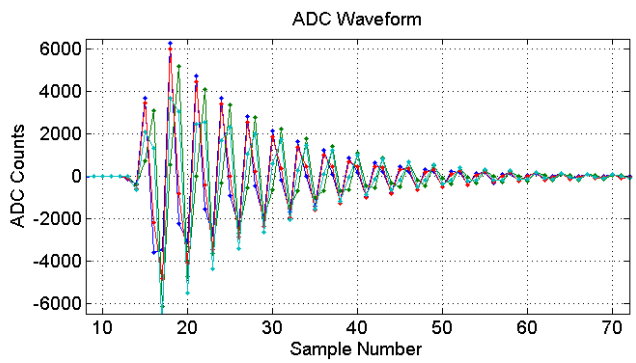

Figure 4: BPM raw waveforms sampled at 119 MHz.

ALGORITHM

Beam charge at each BPM is estimated by scaling the amplitude of the reference cavity. Each position

waveform is reduced to amplitude and phase in an appropriate bandwidth around the cavity frequency. Normalized amplitudes are formed by dividing by the amplitude of the reference cavity and rotating by its phase. Position is estimated by rotating this complex normalized amplitude by a phase established with beam calibration, projecting out the position component, and scaling to microns. Finally a linear transformation accounts for potential physical rotations of the BPM, non-orthogonality of the X and Y ports, and coupling between the ports.

CALIBRATION

Recovering beam position and charge from the digitized cavity waveforms requires knowledge of cavity phases and scales. Undulator BPMs are calibrated by mechanically moving the girder on which the BPM is fixed, fitting the phase and amplitude of the position signals normalized in phase and amplitude to the reference. Presently production BPM code calibrates by moving BPMs in 100 micron steps, much larger than typical 10 to 20 micron beam jitter. In principle we can use uncalibrated measurements from nearby BPMs to remove beam jitter during calibration, and calibrate with motion below alignment tolerances. The results of such a small-move calibration are shown in Figure 5. Transfer line BPMs, which are not mounted on movers, are calibrated by moving the beam on the BPM with a corrector.

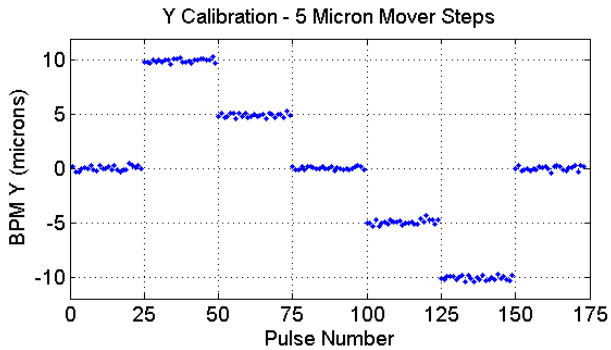

Figure 5: Calibration moving BPM in 5 micron steps.

PERFORMANCE

Resolution

We evaluate BPM resolution in the presence of >10 micron beam jitter by acquiring beam position synchronously over many beam pulses from many BPMs. A least-squares fit predicts position in each BPM as a linear combination of position measured in neighboring BPMs. Figure 6 shows this procedure applied to the 26th cavity BPM. It shows Y measured 120 times in 3 adjacent BPMs, Y versus that predicted from four closest neighbors, and the fit residual, or difference between measurement and prediction. The scatter of fit residual is an estimate of BPM resolution. Also plotted is a histogram of Y resolutions for 33 BPMs.

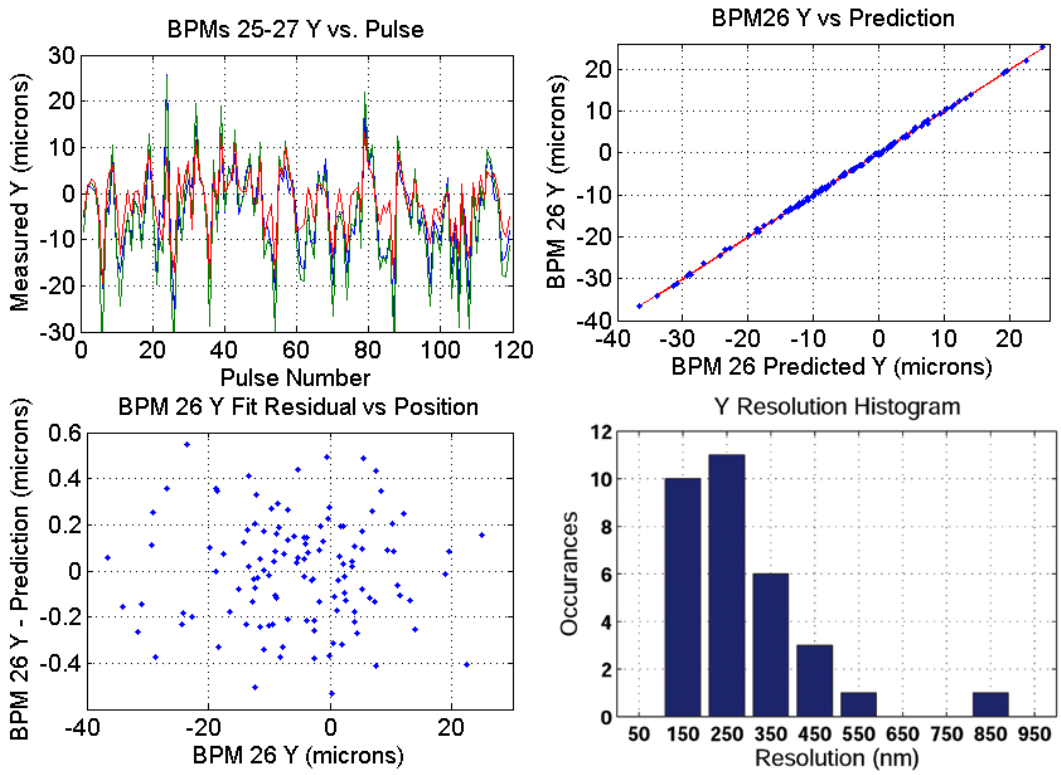

Figure 6: Upper-left: Y position measured at adjacent BPMs for 120 pulses. Upper right: Y at BPM26 vs. best fit prediction from its neighbors. Lower left: Fit residual, Lower right: Histogram of measured BPM resolutions.

Stability

We evaluate two aspects of BPM stability. Calibration stability is evaluated by repeatedly calibrating about once a shift over three days. We find the scale drifting by less than 0.5% in 24 hours and the phase stable to 0.1 degree. Secondly we record groups of about 100 beam pulses every 20 minutes over a 3.5 day period using a single calibration. Using adjacent BPMs to remove beam jitter, we plot measured beam position at each BPM. Typical stability is better than 1 micron drift over 24 hours.

Gain Drifts

Since LCLS turn-on the cavity BPM receivers have been losing gain. Figure 7 shows gains of all the BPMs as of April 20th. There were several theories why the gain was changing: radiation, over-voltage, beam excursion, higher-order modes (HOM), or hydrogen poisoning of the GaAs MMIC and mixers. Radiation damage seems unlikely; the dose rate was measured to be less than 0.1R/week. GaAs devices are radiation hard to ~10kR. The receiver sits below the beam pipe. The damage units are not correlated with high dose areas. Likewise over-voltage damage seems unlikely, as both the reference and position channel saw damage. The reference channel is sensitive to charge not position. With extremely short bunches in the LCLS, this excites HOMs in the THz region. It is important to note, that the reference cavity channel has a 12dB pad on it input and it was getting damaged.

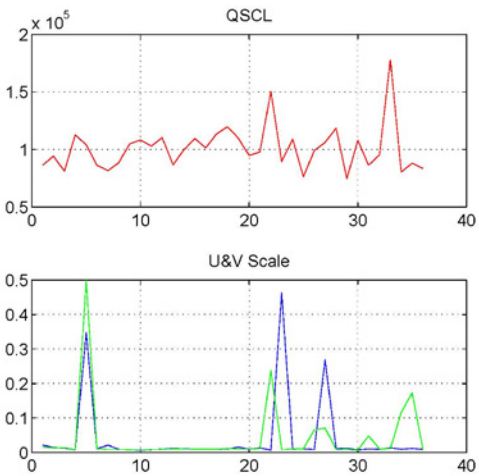

Figure 7: After ten receivers were modified this is the gains of all BPMs. The red curve is the gain of the reference channel and the blue and green are the gain of the position channels.

The most likely scenarios have the GaAs MMIC amplifiers getting damaged due to hydrogen poisoning. The front-end receiver was made by MITEQ using a GaAs MMIC low-noise amplifier (LNA) from Hittite. The datasheet warns that if these amplifiers are installed in a hermetically sealed package then hydrogen getter material should be incorporated [10]. Figure 8 is a picture of the front-end receiver with the covers off the LNA.

Figure 8: Cavity BPM recevier module

The belief is that molecular hydrogen is converted to atomic hydrogen through a catalytic reaction with platinum or palladium in the gate structure and diffuses into the Schottky metal and channel. There have been at least eighteen receivers affected so far. Some of the LNA amplifiers have had the drain source current change as much as 20%. With the use of GaAs devices on the rise due to the higher speed performance and low power consumption, the reliability of GaAS devices have been analyzed [11]. The Hittite GaAs MMIC has a structure shown in figure 9. The gate width of the device is 0.2um and a length of 0.4mm with a noise figure of 1.75dB. The gate length is what set the high frequency limit while the gate width defines the gain and the drain source current. Thus the hydrogen affects the gate width which changes the gain and the drain source current. The Isolation implant maximizes the gate isolation.

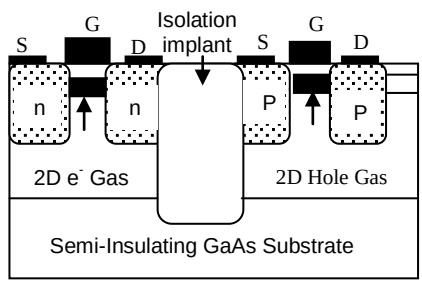

Figure 9: Block Diagram of the GaAs Structure

Before the 2010 downtime, we recorded the gain change on BPM17 and is illustrated in figure 9. In the 180days the gain changed by a factor of 6.

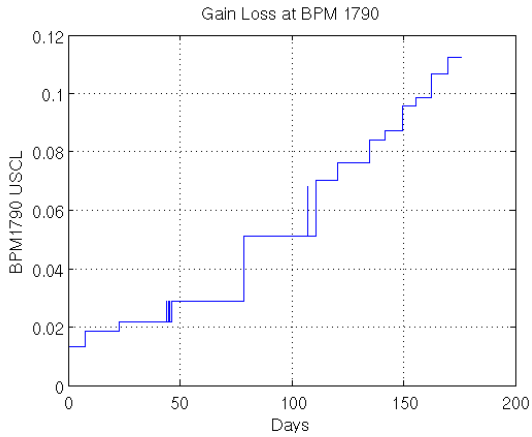

Figure 10: Gain variation over 180 days for BPM17

The solution to the hydrogen poisoning problem that was chosen was to replace the all of the LNA that have shown a decrease in gain in ten RF receivers. To lower the Hydrogen level trapped in the enclosure by baking the enclosure at 100 degree C for 100 hours in a dry nitrogen environment. After the enclosures were baked, the Hydrogen getter material was adhered to the enclosure lid. Finally the RF circuit was assembled to the housing. The LNA was tested before the getter material was activated. Due to the delayed turn on of the LCLS and the completion of CD4 we have not been able to do long time gain studies of the repaired receivers. We hope to accomplish this in the near future.

REFERENCES

[1] P. Emma, "First Lasing of the LCLS X-Ray FEL at 1.5 A", to be published in Proceedings of PAC09, May, 2009.

[2] R. Hettel, et al, "Investigation of Beam Alignment Monitor Technologies for the LCLS FEL Undulator," BIW98, Stanford CA, May 1998, p. 413.

[3] P. Emma, J. Wu, "Trajectory Stability Modelling and Tolerances in the LCLS," EPAC06, Edinburgh, Scotland, June 2006, p. 151.

[4] R. Lill, et al, "Linac Coherent Light Source Undulator RF BPM System," FEL06, Berlin, Germany, July 2006, p. 706.

[5] G. Waldschmidt, R. Lill, L. Morrison, "Electromagnetic Design of the RF Cavity Beam Position Monitor for the LCLS", PAC 07, Albuquerque NM, May 2007, p. 1153.

[6] V. Balakin, "Experimental Results From a Microwave Cavity Beam Position Monitor", PAC99, New York, May 1999, p. 461.

[7] Z. Li, et al "Cavity BPM with Dipole-Mode-Selective Coupler", PAC03, Portland OR, May 2003, http://accelconf.web.cern.ch/AccelConf/p03/PAPERS/ROAB004.PDF

[8] S. Walston, et al, "Performance of a High Resolution Cavity Beam Position Monitor System." NIM A578, 2007.

[9] R. Lill, G. Waldschmidt, D. Walters, L. Morrison, S. Smith, "Design and Performance of the LCLS Cavity BPM System", PAC07, Albuquerque NM, p. 1153.

[10] Hittite application note: Hydrogen Effects On GaAs pHEMT Devices: v00.010

[11] S. Kayali, "Hydrogen Effects on GaAs Device Reliability,"Int. Conf. On GaAs Manufacturing Technology, San Diego,CA, 1996, pp. 80-82.

DESIGN AND PERFORMANCE OF SSRL BEAM POSITION ELECTRONICS*

J. Sebek#, D. Martin, T. Straumann, J. Wachter, SSRL/SLAC, Menlo Park, CA 94025, U.S.A.

Abstract

SSRL designed and built beam position electronics for its SPEAR storage ring. We designed the electronics, using digital receiver technology, for highly accurate turn by turn measurements of both the position and arrival time of the beam, allowing us to use this system to measure the betatron and synchrotron tunes of the beam. The dynamic range of the system allows us to measure the properties of the beam at currents ranging from those of single bunch injection to those of the full SPEAR stored beam. This paper discusses the architecture of the electronics, presents their performance specifications, and shows a range of applications of this system for accelerator physics experiments.

SPEAR PARAMETERS

SPEAR is a 3 GeV electron storage ring used for synchrotron radiation. The operational beam current is now 200 mA; the ring will run at 500 mA after all of the beamline optics have been commissioned. The beam emittance is 10 nm, the vertical beam size is 30 μm, and the bunch length is 5 mm. The radio frequency (RF) of the SPEAR klystron is 476.316 MHz and the ring circumference is 234.3 meters; the harmonic number of SPEAR is 372 and its revolution frequency is 1.28 MHz.

ORBIT FEEDBACK BPM ELECTRONICS

We use a modified version of the Bergoz MX-BPM processor [1] to measure the beam position monitor (BPM) signals for our orbit feedback system. We use 60 BPM processors to monitor the beam position and 60 steering magnets to correct the orbit. Our feedback algorithm updates at a rate of approximately 4 kHz. Our target orbit stability is 3 μm in a 1 Hz bandwidth, 10% of the nominal vertical beam size. Our orbit feedback system achieves a stability of a few hundred nm, an order of magnitude better than our requirements.

SINGLE TURN BPM ELECTRONICS

We also wanted a high performance BPM processor that was optimized for machine physics applications. Therefore it needed to produce highly accurate turn by turn data of the beam from which we could extract the dynamics of the machine. We have 18 of these electronics, one for each sector of the ring.

Machine physics use requires the electronics to work over a large dynamic range, from injected beam to stored beam at full current and it needs to work for all potential fill patterns, ranging from the standard fill pattern, when almost all buckets are full, to single bunch studies. In particular we need to be able to use this processor to measure the betatron and synchrotron oscillations of the beam, both when we are driving the beam and the oscillations are strong, as well as when the beam is quiet.

*Work supported by the U.S. Department of Energy under contract number DE-AC02-76SF00515

#sebek@slac.stanford.edu

BEAM SPECTRUM

Ideal Bunch

In order to motivate our system architecture, we first briefly review the properties of a relativistic beam in a storage ring. The ideal beam circles the ring at the revolution period T. If the bunch were ultra-relativistic, a point particle, and the BPM button had infinite bandwidth, the signal would be a series of delta functions

$$i(t) = \sum_{n=-\infty}^{\infty} Q\delta(t - nT),$$

where Q is the bunch charge. Because of its periodic nature the current can be expressed in a Fourier series

$$i(t) = \sum_{k=-\infty}^{\infty} Qe^{ik\omega_0 t},$$

where $\omega_0 = 2\pi/T$, showing that the spectrum consists only of the harmonics of the revolution frequency. Even though there are an infinite number of harmonics, they all carry the same information about the bunch. Finite size of the bunch and finite bandwidth of the pickup give Q a dependence on the frequency ω.

The ring may have up to h bunches, where h is the harmonic number of the ring. The beam spectrum is still composed of the harmonics of ω_0, but now the amplitude of the various harmonics depends on the fill pattern of the ring. For example, if h is even, and every other bunch is equally filled, only the coefficients of the even harmonics are non-zero; one cannot distinguish between this situation and one in which the ring is half as large (with twice the revolution frequency) but in which every bunch is filled. But even though there are an infinite number of harmonics, the number of independent terms is finite. In fact, since there are h bunches, there are only h independent coefficients Q_k. The coefficient corresponding to the klystron RF frequency ω_{RF}, and all of its multiples, is the same as the DC coefficient. In order to obtain a signal independent of bunch pattern, one needs to process the signal at a harmonic of ω_{RF}.

Dynamic Bunch

We can see what happens to a dynamic bunch by making a slowly varying approximation to the Fourier expansion. A beam executing transverse motion about its nominal trajectory will have a time-varying amplitude; a

beam executing longitudinal motion will have a time-varying phase. Therefore our Fourier expansion for a dynamic beam is

$$i(t) = \sum_{k=-\infty}^{\infty} Q_k(t) e^{i\theta_k(t)}$$

where

$$\theta_k(t) = k\omega_0(T_0 + \tau(t))$$

and $\tau(t)$is the deviation in arrival time from the nominal particle. Note that $\tau(t) \ll T_0$. We can therefore find a mode of the beam motion by measuring the slowly varying amplitude and phase of the beam. Betatron oscillations are characterized as sinusoidal variations of $Q_k(t)$, corresponding to amplitude modulation, and synchrotron oscillations are sinusoidal variations of $\tau(t)$, corresponding to phase modulation.

A beam with *n* bunches has *n* degrees of freedom. Therefore, in order to measure all possible motions of the beam, one needs to measure either *n* bunches in the time domain or n harmonics (modes) in the frequency domain. These are the methods used in feedback systems. However, one can investigate the dynamics of a system by driving one mode, the common mode $(n = 0)$ in which all bunches have the same motion, and observing the beam response. The harmonics of ω_{RF} correspond to this common mode.

SIGNAL PROCESSING

We now know that we can obtain the information that we want by extracting the information at ω_{RF} and measuring its slowly varying amplitude and phase. We will digitize our data, resulting in a stream of digital data to process. We now describe the signal processing algorithm that we use on this data to achieve our goal.

Since we deal with a finite number of samples, our processing involves a discrete filtering process. With the appropriate choice of frequencies, and the appropriate choice of our hardware architecture, we will see that this filtering process is accomplished with a discrete Fourier transform (DFT).

In general, it is very difficult to obtain the exact information about one frequency from a DFT. This is because a DFT has only finite resolution. It samples a finite section of a waveform at *N* discrete, usually equally spaced, times T_S. The DFT assumes that this section of length NT_S repeats periodically. Therefore, since even a pure sinusoid, in general, does not have an integral number of periods during these *N* samples, the DFT does not interpret this signal as a sinusoid, but rather as a concatenation of identical sinusoidal segments. If the sinusoid is not continuous in amplitude and slope, a cusp arises in this infinite waveform. The DFT interprets this cusp as higher frequencies that alias into a measured frequency.

Only for a select set of problems can one construct the system to avoid these problems and exactly measure the frequency of interest. The beam signal from a storage ring belongs to this set. As seen above, all of the frequencies of interest are multiples of the revolution harmonic ω_0. If we sample for a period of time that is exactly one revolution period, $NT_S = T_0$, then all of the revolution harmonics have an integral number of wavelengths during this period. The equally spaced revolution harmonics are the orthogonal basis vectors of the DFT.

In the frequency domain, the response of the DFT is a series of sinc functions centered on the revolution harmonics. The sinc amplitudes are unity at their central harmonics and zero at the other harmonics. The DFT separates out the different revolution harmonics to the arithmetic precision of the digital processor.

The DFT produces a complex amplitude

$$Q_k(t) e^{ik\omega_0\tau(t)}$$

for each harmonic during each revolution period; the real part is the in-phase (I) signal component and the imaginary part is the quadrature (Q) component. On each revolution we use I and Q to calculate the magnitude

$$|Q_k(t)| = \sqrt{I^2 + Q^2}$$

and the phase

$$\mathrm{k}\omega_0\tau(\mathrm{t}) = \tan^{-1}\frac{Q}{I}$$

of the revolution harmonic.

HARDWARE CONSIDERATIONS

Timing

In order to implement our system, we needed to assemble a synchronous timing system that could support the required timing infrastructure. Our system clock, f_{RF}, comes from a PTS-500 programmable frequency source [2]. In addition to its low noise specifications, the PTS-500 is phase continuous when its frequency is changed. We need this property since f_{RF} is part of our orbit feedback system, we change it to correct for the diurnal dispersion component of our orbit.

We then specified a frequency distribution chassis [3] that generates from f_{RF} all of our synchronous system clocks. For the purposes of this article, the two frequencies of interest are a local oscillator (LO) used in the down-converter of the BPM and a digitizer clock. The LO frequency, f_{LO}, is exactly 359 times the revolution frequency f_0, so that our intermediate frequency (IF) will be exactly $13f_0$. The system clock is $50f_0$. We use 50 samples per revolution to measure exactly 13 periods of f_{IF}.

(We also note that the sampling of our orbit feedback BPM electronics is also synchronous with f_{RF}. We sample each of the multiplexed BPM buttons for exactly $80T_0$; a complete module of four buttons is sampled every $320T_0$ which is almost exactly 250 μs. This is also the rate at which our orbit feedback system calculates corrections and at which the steering magnets update their corrections.)

BPM Electronics Design

We designed, specified, and procured our hardware for this system before the December, 2003 commissioning of

SPEAR3. At that time, 14 bit, 65 MSPS digitizers were at the leading edge of commercial digitizers. The easiest way to implement our DFT algorithm was to use a commercially available digital receiver chip (subsequent improvements in technology may now make the preferred filter element an FPGA). We specified and purchased a digital receiver (DR) board [4] and designed our own RF-IF down converter.

The DR board supports eight channels of input, enough for two BPM modules. Two programmable DR chips are devoted to each channel. There is also on-board memory that holds 128k samples for each channel; this corresponds to approximately 100 ms of data capture, much longer than the time of any beam phenomenon.

RF-IF Converter

Although the digitizers used in our DR board are capable of direct RF sampling, there are many technical advantages to first down-converting the RF signal to an IF.

First, although the performance of the digitizer is still good at f_{RF}, the performance is even better at lower frequencies (our $f_{IF} \cong 16.645$ MHz). Second, since there are technical limitations on the quality factors of inexpensive band-pass filters, it is easier to construct analog band-pass filters of the appropriate width at f_{IF} than at f_{RF}. Finally, the accuracy of the phase measurement depends on the relative jitter of each clock sample as measured in radians of the frequency to be measured. By decreasing the frequency we process by a factor of almost 30, we improve the phase accuracy of our measurements by more than an order of magnitude.

Analog Signal Processing

Although we finally digitally process our signal, we still need an analog signal processing stage to optimize the system performance. We use a dielectric resonator band-pass filter at f_{RF} [5] to limit the peak voltage into our electronics. Such commercial filters can achieve about a 1% bandwidth, so the length of the impulse response is shorter than desired. These filters are periodic structures, so although they reject very well frequencies near their center frequency f_C, they also pass higher harmonics of f_C. To reject these frequencies, we added a coaxial 600 MHz low pass filter upstream of the electronics.

We performed our desired filtering at the IF, where we built a Gaussian response filter with a bandwidth of 2 MHz. The response and bandwidth were chosen so that an impulse response of a single bunch would provide signal over the entire 50 samples of a single period T_0 yet decay without ringing before the next period. Lengthening the impulse response also reduces the peak amplitude seen by the digitizer.

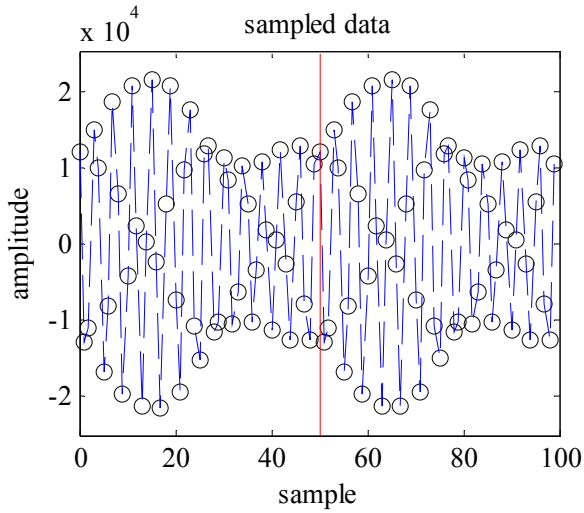

Figure 1: Two turns of IF samples

We used several stages of amplification. The gain block in the RF stage was chosen for its low noise figure; the one in the IF stage was chosen for its low distortion. The RF gain block is used to amplify the signal for low beam current applications. Both the RF gain block and the IF filter are switchable so that the electronics can be optimized for different applications.

Calibration

We chose to calibrate our system using a constant calibration tone. We have combiners [6] located inside of our ring, near the BPM modules, and there combine the calibration tone with the signals from the beam. The continuous signal allows us to avoid switches, so that we do not have to skip data or compensate for switching transients.

Our calibration frequency is chosen to be $1/2f_0$ below f_{RF}, well within the bandwidth of our analog stages. For technical reasons, it is generated by a second frequency synthesizer that is locked to the master synthesizer. (For stability reasons, the tunes in a light source are always far away from the half-integer.) In this mode, we have both DR chips run on each channel and instead of producing a measurement each revolution, we output data every second turn. This allows the two signals to be orthogonal to each other in the two DRs.

The calibration is only used during normal operation of the BPM electronics with stored beam. It is turned off during machine physics studies.

RESULTS

Accuracy

We first measure the accuracy of the BPM electronics by examining the data for nominal user beam with a standard fill. Figure 1 shows 100 samples, two complete turns of data; the periodicity of the system is evident.

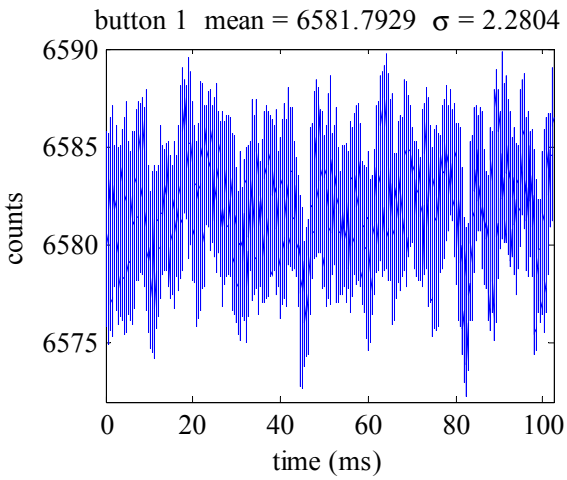

Figure 2: Turn by turn data for one button.

The data in Figure 2 is taken on a vacuum chamber with a 17 mm half height. The standard deviation measured for this 100 ms of data gives an accuracy of about 7 μm per turn (781 ns).

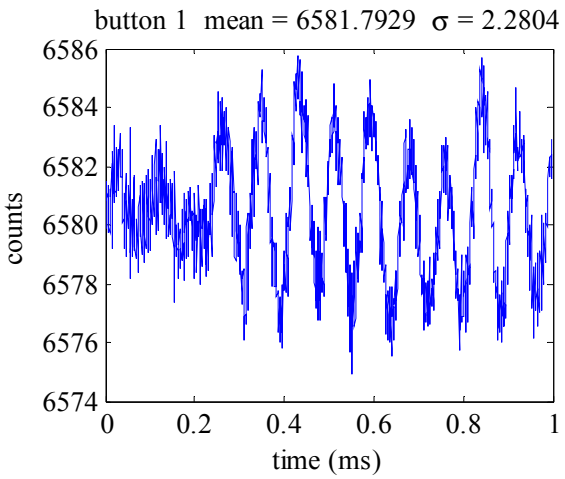

Figure 3: First 1 ms of turn by turn data.

However the standard deviation includes contributions from beam motion, including synchrotron oscillations (in dispersive regions) driven by transients in the klystron high voltage power supply. If one instead measures σ from the noise on the peaks of the synchrotron oscillations in Figure 3, the resolution of each button, before the position is calculated, is seen to be approximately 1.4 μm per turn on a 34 mm high chamber.

We calculate the beam position using the standard difference over sum calculation using the four buttons. Figure 4, which shows the first ms of data shows that this calculation improves the sensitivity of the measurement.

The phase measurement is also very accurate. Figure 5 shows that the standard deviation of the phase over 100 ms corresponds to 1.4 ps at ω_{RF}. However, estimating the σ from the noise at the top of the oscillations shows that our accuracy is better than 100 fs. Note that, as expected, the energy oscillations in Figure 4 are in quadrature with the phase oscillations in Figure 5.

Spectral Purity

The spectral resolution of the horizontal beam position measurement is displayed by the Fourier transform of the turn by turn data displayed in Figure 5. The noise floor of the measurement is approximately 115 dB below the carrier, with spurs about 20 dB above this floor. All of the tunes for a normal, quiet beam are clearly visible. Again we see that the synchrotron tune is visible in the horizontal beam spectrum; this is due to the BPM location in a dispersive section of the ring.

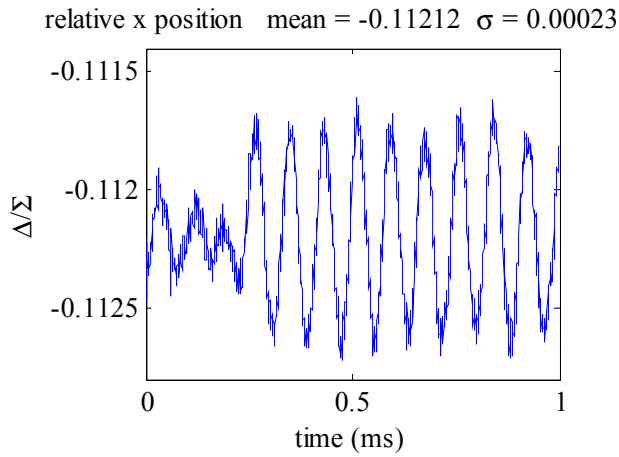

Figure 4: First 1 ms of horizontal position.

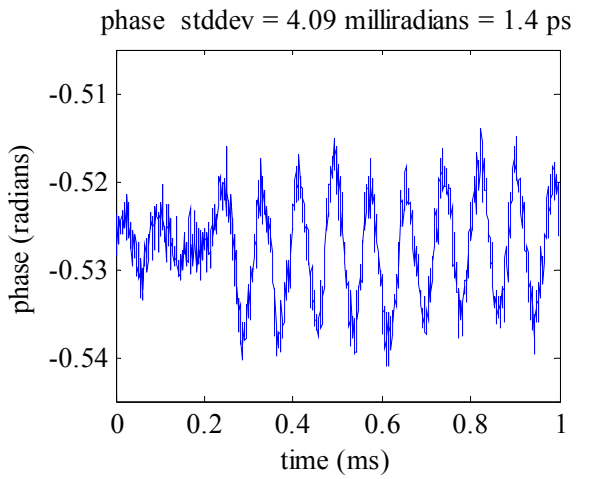

Figure 5: First 1 ms of bunch phase.

The horizontal tune line, only slightly visible in the dense spectrum in Figure 6, is about 25dB above the noise floor of the electronics, as seen in Figure 7. The vertical and synchrotron tune lines are also very visible from the spectra.

Low Current Injection Studies

Finally we look at data from low current injection studies. A single bunch of current is injected into SPEAR every 100 ms. In order to optimize injection, one needs to determine that the phase delay between the injector and SPEAR is correct and that the energy of the injected beam matches the SPEAR energy [7].

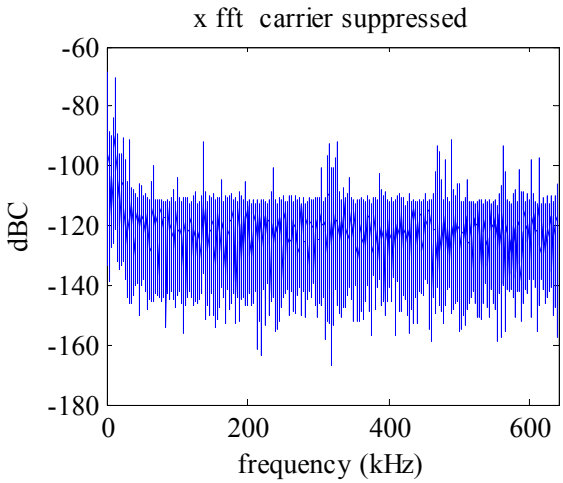

Figure 6: Spectrum of horizontal position.

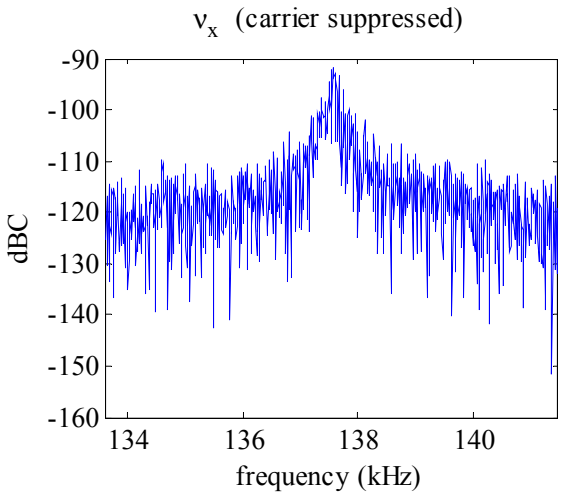

Figure 7: Horizontal tune.

The injected current is only 50 μA per pulse, four orders of magnitude lower than the maximum current in the ring. One cannot measure this low current in the presence of a stored beam, but the injected beam can be stored and then kicked out before the next injection cycle. At these currents, the digitizer is at its bit resolution, but the signal is still well above the noise floor. By averaging multiple injections, in this case sixteen cycles were averaged, the effective resolution of the digitizer increases and the desired signals can be accurately measured.

Figures 8a and 8b show the horizontal position and phase, respectively of a mis-timed injected beam. The position signal executes expected betatron oscillations due to the injection kickers. Both signals execute synchrotron oscillations. Since the position signal is sine-like and the phase signal is cosine-like, the injected beam has the proper energy, but the incorrect phase. Proper tuning of the injector phase reduces the measured phase oscillation to ± 0.1 radians.

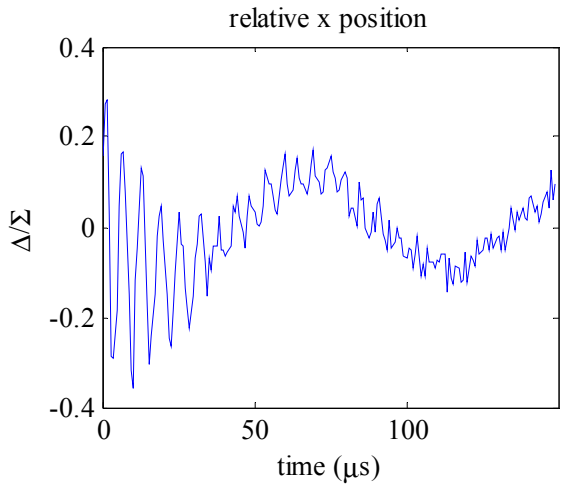

Figure 8a: Horizontal position of mis-timed injected beam.

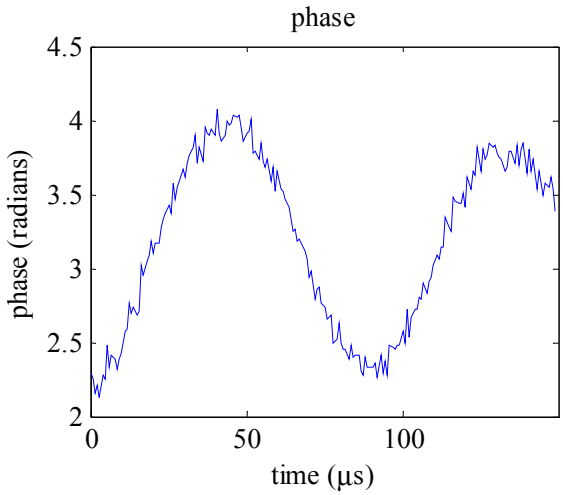

Figure 8b: Phase of mis-timed injected beam.

REFERENCES

[1] MX-BPM User's Manual Spear-3 options, Bergoz Instrumentation, Saint Genis Pouilly, France; http://www.bergoz.com.

[2] Programmed Test Sources, Inc., Littleton, MA; http://www.programmedtest.com.

[3] Wenzel Associates, Inc., Austin, TX; http://www.wenzel.com.

[4] Echotek Division of Mercury Computer Systems, Huntsville, AL; http://www.mc.com.

[5] Integrated Microwave, San Diego, CA; http://www.imcsd.com

[6] Mac Technology, Inc., Klamath Falls, OR; http://www.mactechnology.com

[7] X. Huang, et al., "Optimization of the Booster to Spear Transport Line for Top-Off Injection," PAC'09, Vancouver, May 2009, TU6RFP043.

A WIRE POSITION MONITOR SYSTEM FOR SUPERCONDUCTING CRYOMODULES AT FERMILAB*

D. Zhang#, N. Eddy, B. Fellenz, J. A. Fitzgerald, O. Lysenko, P. Prieto, A. Saewert, A. Semenov, D. C. Voy, M. Wendt, FNAL, Batavia, IL 60510, U.S.A.

Abstract

Fermilab is jointly developing capabilities in high gradient and high Q superconducting accelerator structures. Based on the 1.3 GHz INFN/TESLA design [1-4], a wire-position-monitor (WPM) system is integrated to monitor cavity alignment and cold mass vibrations. The system consists of a reference wire carrying a 325 MHz signal, 7 stripline pickups (per cryomodule, 12-m long), and read-out electronics using direct digital signal down-conversion techniques. We present technical details of the system, and preliminary results on resolution and stability measured at a mock-up test stand.

Figure 1: The first cryomodule being moved to the cave.

WPM PRINCIPLE

Fermilab is building up a SCRF test facility. It consists 3 INFN/TESLA style cryomodules (see Figure 1), each incorporates 7 WPMs, at each end, at the three posts and between the posts.

Figure 2: Picture of the WPM at one end.

As shown in Figure 2, a WPM is a coaxial tube with four 50-Ω microstrip pickups spaced 90° apart. The IF wave on the center wire induces signals on the pickups through space coupling. While the wire's position in space is determined by its two ends, a WPM may move or vibrate with the cryomodule body. This relative displacement (in the transverse plane) between a WPM and the center wire manifests as imbalances between the strengths of the four induced signals, and can be deducted by iterations according to:

$$I_x = \frac{V_B - V_D}{V_B + V_D}, I_y = \frac{V_A - V_C}{V_A + V_C}$$

$$x = a_{10} I_x + a_{30} I_x^3 + a_{12} y^2 I_x + \ldots, y = a_{01} I_y + a_{03} I_y^3 + a_{21} x^2 I_y + \ldots$$

where A through D denote the pickups at the top, left, bottom and right.

READOUT SYSTEM

The readout electronics is housed in a VME crate. It includes a MVME-5500 PPC processor board, a timing board and a few digital receiver boards. The timing board generates a 325 MHz CW signal and 8 clock signals, using either an external RF or an internal oscillator. The 325 MHz CW is amplified and feed to the center wire. The 8 clock signals are divided down from the 325 MHz by either 4, 8, 16 or 32. They are used to clock the digital receiver boards and can be individually phase adjusted at 8.6 ps steps. Each digital receiver board has 8 channels, handling 2 WPMs. The digital receiver boards sample the induced signals from the pickups at 40.625 MHz. Every 9918 samples are grouped to get one average making the data output rate of 4096.09 Hz. For each cycle, the system takes 16384 data samples in about 4 seconds. It then processes the data and self trigger again.

The frequency of 325 MHz is chosen for good coupling between the center wire and the pickups, and for easy handling.

The DAQ software is in C++ under VxWorks. It incorporates a client-server tool to communicate with host machines. A LabVIEW package is used to control the system and visualize the results.

TEST STAND

A test stand is set up to test the readout electronics and DAQ software (see Figure 3). It uses a thinner CuBe alloy wire, 0.5 mm diameter, about 1.1 m long. The tension is 9.07 kg. The fundamental vibrating frequency of the wire is calculated to be 104.5 Hz.

To verify the long term stability of the electronics, one average position was recorded every ~ 4 seconds over a period of about 8 hours, with the inputs to the digital receiver boards connected to test signals. It showed that the system is stable to within ~ 1 um. Over another similar period, the system clearly showed the instability of the amplifiers for the test signals (see Figure 4).

To verify the capability of the system as a detector for microphonic vibrations, the support table were struck, and

*Operated by Fermi Research Alliance, LLC under Contract No. DE-AC02-07CH11359 with the United States Department of Energy.

#dhzhang@fnal.gov

FFTs were performed over the position data, 16384 samples for every 4 seconds (see above), with the digital receiver board inputs connected to the pickups. The 104.5 Hz fundamental frequency and the 2nd harmonic are clearly shown (see Figures 5 and 6).

Figure 3: The test stand.

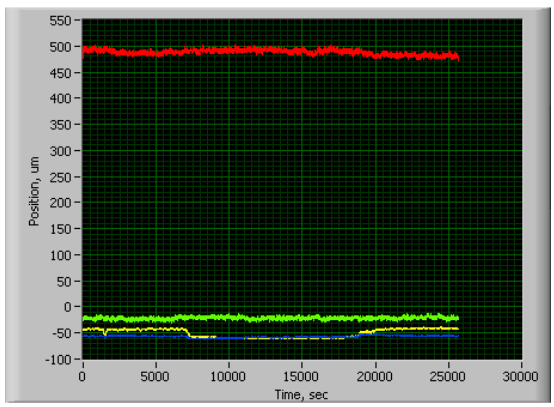

Figure 4: Positions from test signals over 7 hours.

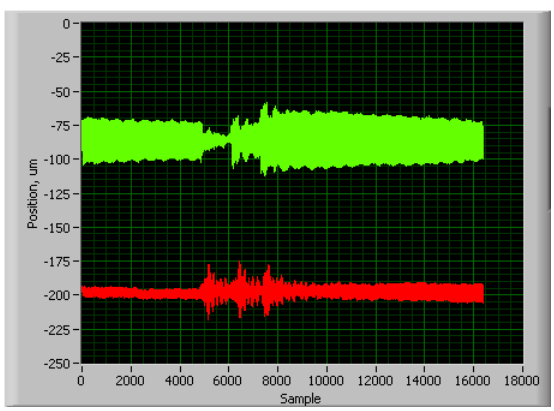

Figure 5: Positions from pickups after mechanic excitation.

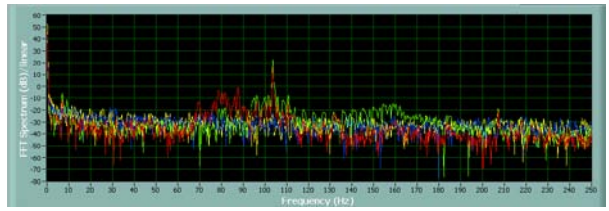

Figure 6: FFTs of the positions from pickups after mechanic excitation.

In Figure 6, 0 dB corresponds to wire displacement of 1 um, 20 dB corresponds to 10 um, -20 dB corresponds to 100 nm and so on. As can be seen the noise floor is below -20 dB, indicating the system has a special resolution of ~ 100 nm.

CONCLUSIONS

The readout electronics and software are thoroughly tested and working. The system is able to track slow drifts over long period of time with a resolution of about 1 um, and detect microphonic vibrations with a resolution of ~ 100 nm.

REFERENCES

[1] W. R. Rawnsley et al., “A wire position monitor system for the ISAC-2 cryomodule components alignment”, Proc. LINAC 2004, Lubeck, Germany.

[2] D. Giove, A. Bosotti, C. Pagani and G. Varisco, “A wire position monitor (WPM) system to control the cold mass movements inside the TTF cryomodule”, INFN Milano, LASA, Via F. lli Cervi 201, Segrate (Mi), Italy.

[3] W.R. Rawnsley, Y. Bylinski, K. Fong, R.E. Laxdal, G. Dutto, D. Giove, “Alignment of the ISAC-2 Medium Beta Cryomodule with a Wire Monitoring System”, TRIUMF, 4004 Wesbrook Mall, Vancouver, BC, Canada.

[4] A. Bosotti, C. Pagani, R. Paparella, P. Piereni, D. Sertore, “The wire position monitor (WPM) as a senser for mechanical vibration or the TTF cryomodules”, INFN LASA, Milano, Italy.

A HIGH-RESOLUTION CAVITY BPM FOR THE CLIC TEST FACILITY*

N. Chritin, H. Schmickler, L. Soby, CERN, Geneva, Switzerland
A. Lunin, N. Solyak, M. Wendt#, V. Yakovlev, Fermilab, Batavia, IL 60510, U.S.A.

Abstract

In frame of the development of a high resolution BPM system for the CLIC Main Linac we present the design of a cavity BPM prototype. It consists of a waveguide loaded dipole mode resonator and a monopole mode reference cavity, both operating at 15 GHz, to be compatible with the bunch frequencies at the CLIC Test Facility. Requirements, design concept, numerical analysis, and practical considerations are discussed.

INTRODUCTION

The next high energy physics (HEP) lepton collider, operating at the energy frontier (CM > 500 GeV) needs to accelerate the particles along a straight line, to avoid too high losses caused by synchrotron radiation. For both concepts, the superconducting RF technology based International Linear Collider (ILC) [1], as well as for the two-beam acceleration Compact LInear Collider (CLIC) [2], generation and preservation of beams with ultra-low transverse emittance is mandatory to achieve the luminosity goals. A "golden" trajectory path has to be established, steering the beam with sub-micrometer precision through the magnetic centres of the quadrupoles, avoiding a beam blow-up due to non-linear fields.

Table 1: CLIC / CTF Main Linac BPM specifications.

	CLIC	CTF CALIFES
Nominal bunch charge [nC]	0.6	0.6
Bunch length (RMS) [μm]	44	225
Batch length [nsec]	156	1-150
Bunch spacing [nsec]	0.5	0.6667
Beam pipe radius [mm]	4	4
BPM time resolution [nsec]	<50	<50
BPM spatial resolution [nm]	<50	<50
BPM stability [nm]	<100	<100
BPM accuracy [μm]	<5	<5
BPM dynamic range [μm]	±100	±100
BPM resonator frequency [GHz]	14	14.98962

To discover and minimize unwanted dispersion effects along the Main Linac beam-line, an energy chirp modulation within the bunch train is proposed for the CLIC beam commissioning. Therefore the beam position monitors (BPM) have to have both, high spatial and high time resolution. We propose a low-Q waveguide loaded TM_{110} dipole mode cavity as BPM, which is complemented by a TM_{010} monopole mode resonator of same resonant frequency for reference signal purposes.

Table 1 gives the basic requirements for the BPM, however, as the bunch frequencies at the CLIC Test Facility (CTF) are different from the proposed CLIC linear collider, the nominal resonant frequencies (f_{110} for the dipole mode cavity, f_{010} for the reference cavity) are not the same for the CTF prototype BPM, and the CLIC Main Linac BPMs:

- CLIC: 14 GHz
- CTF: 15 GHz

Choosing a rather high operating frequency $n\ f_{\text{bunch}}$ has several advantages, e.g. most higher-order modes (HOM) are damped by the beam pipe cut-off frequency, and higher shunt impedances can be achieved (better sensitivity, higher resolution potential). However, as dipole mode and reference cavity operate at the same frequency, we have to ensure that they do not couple by evanescence fields leaking into the beam pipe.

With a time resolution of <50 nsec we will be able to acquire three beam position samples within the 156 nsec long bunch train (batch). Because of dynamic range limitations in the read-out system, the high 50 nm spatial resolution can only be accomplished within a small range of ±100 μm beam displacement from the BPM center, however a moderate resolution (some μm) will be achievable over the full aperture (±4 mm).

Each of the two ~20 km long CLIC Main Linacs will be equipped with ~2000 BPMs, therefore a simple, cost-effective design with minimum maintenance and calibration requirements is important. The longitudinal expansion of the two BPM resonators should not exceed 95 mm, including flanges. A simple analog down-converter has to be placed in close proximity to the BPM detector; no external reference or timing signals are required.

CAVITY BPM PRINCIPLE

A cylindrical "pillbox" having conductive (metal) walls of dimensions radius R and length l resonates at eigenfrequencies:

$$f_{\text{mnp}} = \frac{1}{2\pi\sqrt{\mu_0\varepsilon_0}}\sqrt{\left(\frac{j_{mn}}{R}\right)^2 + \left(\frac{p\pi}{l}\right)^2} \qquad (1)$$

This resonator can be utilized as passive, beam driven cavity BPM by assembling it into the vacuum beam pipe. A subset of these eigenmodes is excited by the bunched

*Work supported by the Fermi National Accelerator laboratory, operated by Fermi Research Alliance LLC, under contract No. DE-AC02-07CH11359 with the US Department of Energy.
#manfred@fnal.gov

beam, for use as BPM the lowest transverse-magnetic dipole mode TM_{110} is of interest ($n f_{bunch} = f_{110}$). Its

$$E_z = C J_1 \frac{j_{11} r}{R} \cos\phi e^{i\omega} \qquad (2)$$

field component couples to the beam, with almost linear dependence to the beam displacement r, and beam intensity (hidden in the constant C).

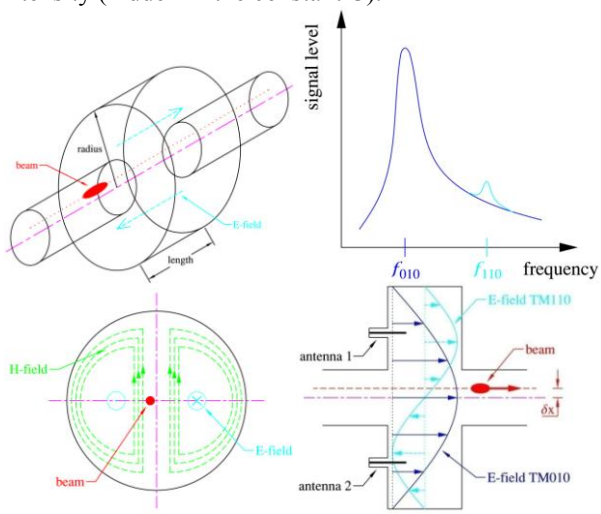

Figure 1: Cavity BPM principle.

As Fig. 1 illustrates, the TM_{110} dipole mode vanishes as the beam moves exactly through the center of the cavity pickup ($r = 0$). A set of capacitive coupling pin-antennas or other coupling schemas can be used to sense the dipole mode displacement signal of frequency f_{110}. Compared to broadband BPM pickups, e.g. button- or stripline style, the strength of the beam excited eigenmode is due to the cavity shape. For a simple cylindrical cavity BPM the corresponding R/Q (shunt impedance / quality factor) typically has much higher values when compared to the transfer impedance of a broadband BPM, one achieves a higher beam displacement sensitivity and therefore a greater potential to operate as "high resolution" BPM.

"CM-FREE", LOW-Q CLIC BPM

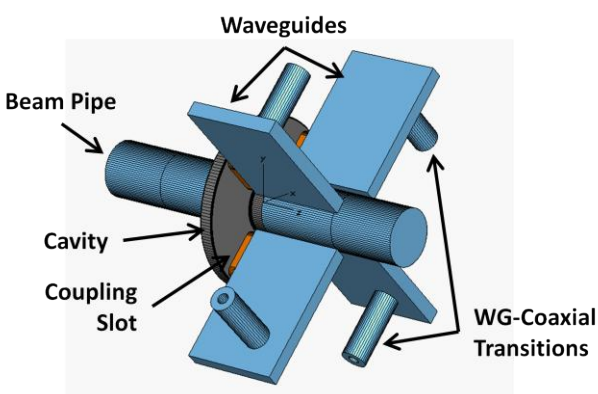

Figure 2: CLIC cavity BPM.

Figure 2 shows the proposed CLIC cavity BPM. A set of four, symmetrically arranged waveguides are slot-coupled to the dipole mode resonator. The TE_{10} cut-off frequency of the rectangular waveguide is choosen between the first monopole and dipole mode of the cavity,

$$f_{TM010(Cav)} < f_{TE10(WG)} = \frac{1}{2a\sqrt{\varepsilon\mu}} < f_{TM110(Cav)} \qquad (3)$$

and acts like a high-pass filter to suppress the strong monopole mode signal. The four narrow slots between cavity and waveguides sets the TM_{110} polarization axes in the resonator to the horizontal, respectively vertical plane, and provide magnetic coupling of the beam displacement signal to the waveguides. A feedthrough pin antenna is used for the waveguide-to-coaxial transition of 50 Ω characteristic impedance. Figure 3 illustrates an *Ansoft* HFSS simulation, showing the broadband behaviour of the WG-coaxial transition, BW~1 GHz for -30 dB return loss. We plan to read-out all four coaxial ports, using a hybrid combiner may further improve the suppression of higher-order modes (phase filtering). We also can utilize the 2nd ports for calibration and redundancy purposes.

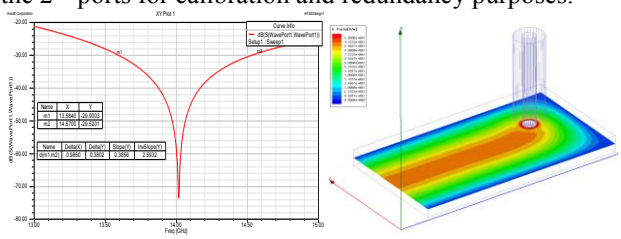

Figure 3: Matching of the WG-to-coaxial transition.

When excited with a beam bunch, the resonant BPM cavity behaves like a damped oscillator, with an impulse response voltage signal:

$$v(t) \propto v_0 e^{-t/\tau} \cos(\omega_0 t) \qquad (4)$$

where $\tau = 2Q_l/\omega_0$ is the resonator time constant, and Q_l is the loaded quality factor. The required BPM time resolution (<50 nsec) and dynamic range (±100μm) limits the maximum loaded quality factor of the cavity. The amplitude of the TM_{110} dipole mode should decay 10^3 times within 50 nsec in order to achieve the required resolution. Thus, the maximum loaded Q-factor is given by:

$$Q_{max} = \frac{t_{max}\omega_0}{2\ln(1000)} \approx 320 \qquad (5)$$

Keeping the cavity dimensions reasonable and applying the waveguide load impedance is not sufficient to achieve this rather low Q-value, thus the resonator has to be manufactured out of a more lossy material, i.e. stainless steel.

BEAM SPECTRUM ESTIMATION

The BPM cavity, with its four slot-coupled waveguides, terminated by WG-coaxial transition ports, and beam pipe ports is a complex resonant system. A single beam bunch will excite most eigenmodes, from which only the TM_{110} cavity dipole mode is of interest for our beam position measurement, Figure 4 illustrates the coupling mechanism.

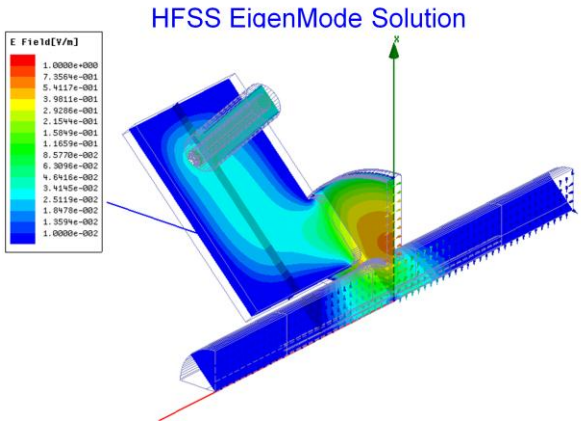

Figure 4: E-field of the TM_{110} eigenmode.

However, unwanted modes, even though they have different resonance frequencies, will perturb the TM_{110} dipole mode because their energy is spread over a wide range of frequencies, due to their limited Q-value (mode leakage). For each mode below the beam pipe cut-off frequency (22 GHz) we estimated the signal voltage (at t=0) at the coaxial output port:

$$\mathrm{v} = q\,\omega\sqrt{\frac{Z_0\,(R/Q)}{Q_{ext}}} \tag{6}$$

where q is the bunch charge, Z_0=50 Ω is the characteristic impedance of the coaxial port, and R/Q is the characteristic impedance of the cavity for a specific mode. In (6) the signals of all coaxial ports are summed, to report monopole mode signals, V_{0mp} has to be divided by 2, for the dipole modes divide V_{1mp} by √2. Table 2 lists the results for the relevant eigenmodes.

The computed output voltage for each mode (CLIC BPM frequencies) in Table 2 has to be multiplied by the expected rejection coefficients, i.e. frequency selectivity, phase filtering and multi-bunch rejection. The frequency filter rejection KF_{nmp} is simply the normalized signal intensity of an unwanted mode TM_{nmp} leaking into the TM_{110} dipole mode (at f_{110}):

$$\mathrm{KF}_{nmp} = \frac{\mathrm{V}_{nmp}(\omega_{110})}{\mathrm{V}_{nmp}(\omega_{nmp})} \tag{7}$$

By summing the two opposite port signals we can benefit in additional ~20 dB (0.1) phase filter rejection for the TM_{210} mode.

In the practical application, the cavity BPM will not be excited by a single bunch, but by a train of typically k=312 bunches, spaced by 0.5 nsec. Therefore the output signal is a superposition of the single bunch responses of all modes, assuming the same intensity of all bunches:

$$\mathrm{V}_{\mathrm{sum}}(t,k) = \sum_{1}^{k}\mathrm{V}_{010}\,e^{-\beta_{010}(t-t_b k)}\cos[\omega_{010}(t-t_b k)] + \sum_{1}^{k}\mathrm{V}_{110}\,e^{-\beta_{110}(t-t_b k)}\cos[\omega_{110}(t-t_b k)] + \ldots \tag{8}$$

While f_{110} is in phase with the bunch frequency $1/t_b$, resulting in a positive signal pile-up, the unwanted modes receive a "random" multi-bunch excitation, which leads to a rejection with respect to the beam position signal:

$$\mathrm{KM}_{010} = \frac{\int_0^{t_{\max}}\sum_{1}^{k}\mathrm{V}_{110}\,e^{-\beta_{110}(t-t_b k)}\cos[\omega_{110}(t-t_b k)]}{\int_0^{t_{\max}}\sum_{1}^{k}\mathrm{V}_{010}\,e^{-\beta_{010}(t-t_b k)}\cos[\omega_{010}(t-t_b k)]} \tag{9}$$

Table 2: Results of the modal analysis of the CLIC cavity BPM.

Mode Type		**Freq.** [GHz]	Q_{tot}[1], (Q_l)	***R/Q*** [Ω], [Ω/mm^2], [Ω/mm^4]	**Output Voltage**[2,3] [V], [V/mm], [V/mm^2]	**Frequency Filter Rejection**	**Phase Filter Rejection**[4]	**Multi-bunch Regime Rejection**
TM_{010}		10.385	380, (>10^9)	45	<0.001	0.005	-	0.1
TM_{110}		13.999	250, (540)	3	17	-	-	-
TM_{210}		18.465	80, (100)	0.05	5	0.025	0.1	0.1
TM_{020}		24.300	680, (>10^9)	12	<0.001	0.001	-	0.05
WG1	TM_{11}	12.285	6	-	3	-	-	-
	TM_{21}	12.285	6	-	0.3	-	-	-
WG2	TM_{11}	15.878	4	-	5	-	-	-
	TM_{21}	15.880	4	-	1.2	-	-	-
WG3	TM_{21}	21.610	7	-	-	-	-	-

[1] - Stainless steel resonator material.
[2] – RMS value; normalized to 1 nC charge.
[3] - Signals are from a single coaxial output at the eigenmode frequency. Multipole modes are normalized to 1 mm off-axis shift.
[4] – For TM_{210} only.

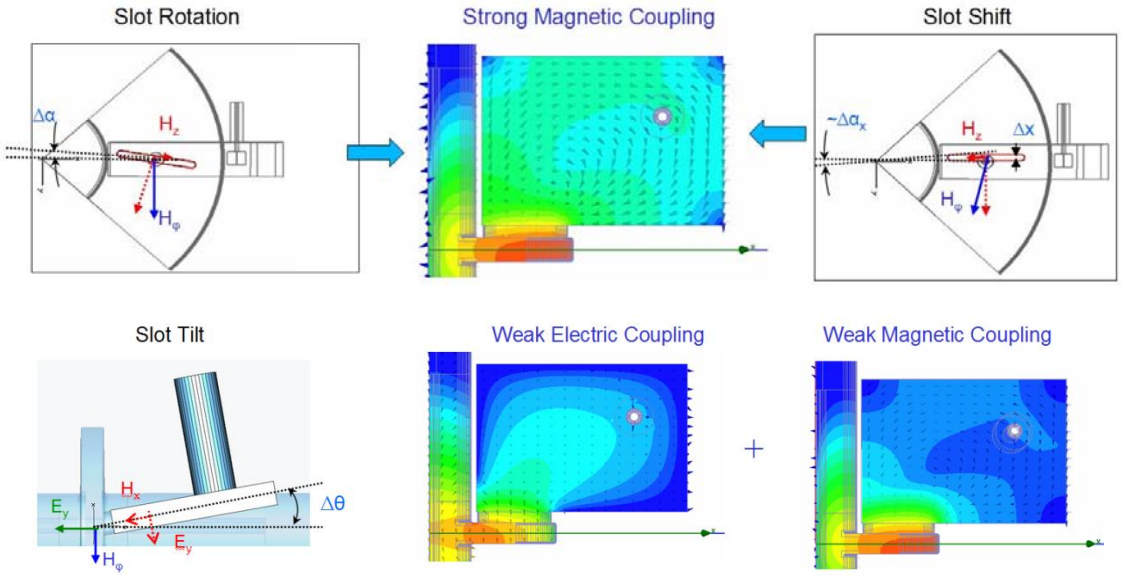

Figure 5: Investigation of tolerances on the cavity-waveguide coupling slot.

SPATIAL RESOLUTION LIMITS

Table 3: Limitations of the BPM resolution due to TM_{010} & TM_{210} mode leakage.

Mode Type	Freq. [GHz]	Q_{tot} [1]	Beam shift [µm]	Output voltage [2] [mV]	BPM Resolution [nm]	
					SB	MB
TM_{010}	10.385	380	0	<1	40	4
TM_{110}	13.999	250	0.1	2.4	-	-
TM_{210}	18.465	80	100	<0.18	8	1
TM_{210}	18.465	80	500	<4	200	20

1 – Stainless steel material was used.
2 – RMS value of the sum signal of two opposite coaxial ports at the 14 GHz operating frequency after all filters applied; signals are normalized to 1 nC charge.

The spatial resolution of the cavity BPM is defined as the smallest change of the beam position, which can be resolved. Beside the mode leakage effects, we also have to investigate consequences of practical imperfections, like mechanical tolerances from the manufacturing process, and other imperfections. It turns out, that the alignment of the coupling slot windows between cavity resonator and waveguides are most critical. In detailed EM-simulations we studied the effects of asymmetries due to shift, rotation and tilt of these slots, which causes additional leakage of the higher-order modes (see Figure 5). Also a shift between beam pipe and cavity centers will cause a degradation of the spatial resolution. In summary, limiting the slot shift to <5 µm, and the slot rotation to <0.05 deg, we can expect the cross coupling between horizontal and vertical plane to be >40 dB, while achieving a ±100 µm dynamic range at maximum resolution. This resolution is dominated by the TM_{010} mode leakage, and is ~40 nm for a single bunch (SB) excitation, and ~4 nm for a multi-bunch (MB) beam batch (see Table 3). At large beam displacements >0.5 mm, the TM_{210} mode leakage dominates and limits the theoretical achievable resolution, however, in practice the limited dynamic range of the read-out receiver will further reduce the BPM resolution for this case.

CAVITY BPM PROTOTYPE FOR CTF

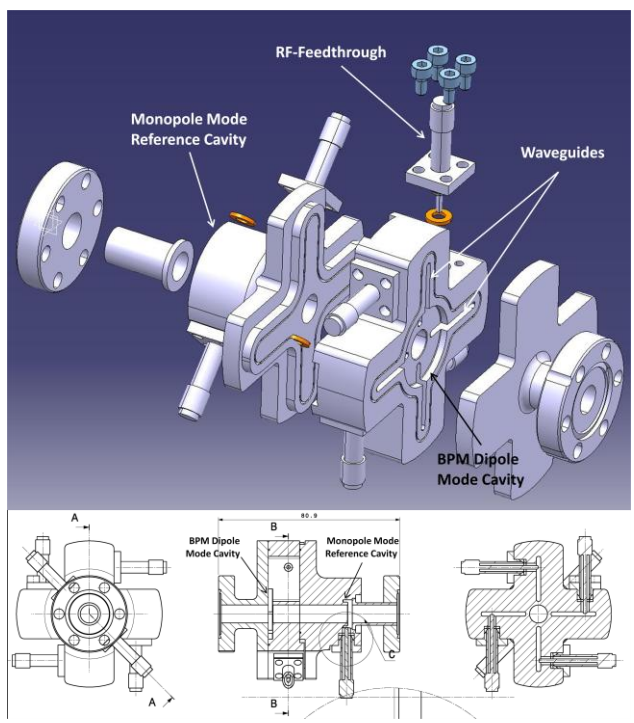

Figure 6: Layout of the CTF cavity BPM prototype.

Figure 6 shows an early draft of the mechanical layout of the CTF cavity BPM prototype. It consists out of four major parts, all milled / EDM out of type 304 stainless steel:

- The central section with the BPM resonator and waveguides. The waveguide structures can be manufactured using a wire-EDM process, the cavity will be milled.
- A section with the reference cavity and a cover for the waveguides
- Two cover sections with transitions for the beam pipes

The manufacturing tolerances on the critical structures have to be <±5 μm. We will use four RF-feedthroughs with capacitive pin coupling for the waveguide-coaxial transition of the BPM signals, and additional two RF-feedthroughs with magnetic coupling, extracting the signal of the reference cavity. The tolerances of the capacitive pin coupling are very tight, for the prototype we consider tuning dimples. We plan to use a commercial microwave UHV-feedthrough with minor custom modifications (*Meggitt*); some details still have to be worked out.

The total length of the cavity BPM detector including flanges measures 80.9 mm, BPM and reference cavities are separated ~50 mm. Both resonators operate at the same frequency (~15 GHz) and have very similar loaded Q-values (~300). The signal from the reference cavity can be used directly (no external frequency or clock signals required), and provides

- A phase reference for the dipole mode signal, to distinguish the beam position is up or down, respectively left or right.
- A magnitude reference, as the dipole mode signal is proportional to beam displacement and intensity.

A set of three CTF prototype cavity BPMs have to be manufactured, tested and installed into the CTF beam-line to fully exploit beam based studies on the BPM characteristics and measurement capabilities. The presented cavity BPM detector has to be complemented by a read-out system, utilizing microwave and digital signal processing technologies.

SUMMARY

A simple, straightforward design of a cavity BPM with high spatial (50 nm) and temporal (50 nsec) resolution is proposed for the CLIC Main Linac. In depth EM-simulations and optimizations include the analysis of mechanical tolerances. A prototype with a slightly different operation frequency, to be tested at the CLIC Test Facility (CTF), is currently under development.

REFERENCES

[1] C. Phinney, N. Toge, N. Walker, “International Linear Collider Reference Design Report”, Volume 3: Accelerator, August 2007.

[2] The CLIC Study Team, “A 3 TeV e^+e^- Linear Collider based on CLIC Technology”, CERN 2000-008, Proton Synchrotron Division, July 28, 2000

ROGUE MODE SHIELDING IN NSLS-II MULTIPOLE VACUUM CHAMBERS*

A. Blednykh#, B. Bacha, A. Borrelli, M. Ferreira, H.-C. Hseuh, B. Kosciuk, S. Krinsky, O. Singh, K. Vetter, BNL, NSLS-II, NY 11973-5000, U.S.A.

Abstract

Modes with transverse electric field (TE-modes) in the NSLS-II multipole vacuum chamber can be generated at frequencies above 450MHz due to its geometric dimensions. Since the NSLS-II BPM system monitors signals within 10 MHz band at RF frequency of 500 MHz, frequencies of higher-order modes (HOM) can be generated within the transmission band of the band pass filter. In order to avoid systematic errors in the NSLS-II BPM system, we introduced frequency shift of HOMs by using RF metal shielding located in the antechamber slot.

INTRODUCTION

A new 3GeV NSLS-II storage ring is under construction at Brookhaven National Laboratory. The ring has a 30 cell double-bend achromatic (DBA) lattice [1]. Six beam position monitors (button type) per cell are going to be located on multipole vacuum chambers to control electron beam trajectory. Each vacuum chamber in each cell is numerated in according to girder location. Five types of multipole vacuum chambers are going to be used in the NSLS-II storage ring [1]. They have the same cross-section profile and differ mostly in length. Multipole vacuum chambers S2, S4 and S6 are shown in Figure 1 with location of BPM Buttons.

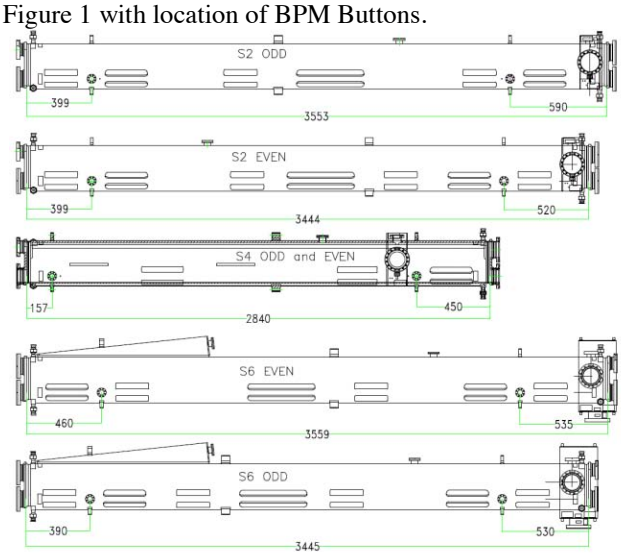

Figure 1: Types of NSLS-II multipole vacuum chambers.

The NSLS-II multipole vacuum chamber profile is shown in Figure 2. The full horizontal and vertical aperture of the beam channel is *76mm* x *25mm* respectively. The antechamber slot with a gap of 10mm is extended up to a trapezoidal area with a vertical aperture of 44mm. The NSLS-II cross-section profile has a complex geometry and looks similar to APS chamber design, except a difference in geometric dimensions. There is a concern that existence of rogue modes observed in vacuum chambers with antechamber slot [2] can affect precision of the NSLS-II BPM diagnostic system. As in APS, the NSLS-II BPM buttons are located on top and bottom of multipole vacuum chambers, which have an antechamber slot (Fig. 2). Rogue modes, which are classified as modes with Transverse Electric field (H-mode) in a ridged waveguide, can couple to the BPM buttons at frequencies near to the RF. It can produce a noise in BPM system and difficulties in monitoring of beam position in the ring.

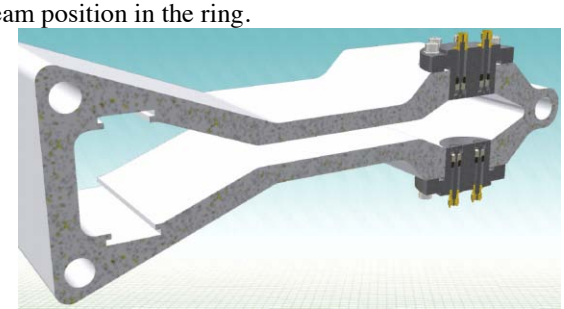

Figure 2: NSLS-II multipole vacuum chamber profile.

Since the NSLS-II multipole vacuum chamber profile has a complex geometry, the cutoff wavelength has been simulated numerically using the GdfidL code [3]

$$\lambda_c = 0.695m\,.$$

Since the cutoff wave length is known a set of resonance modes can be generated in a chamber at frequencies

$$f^H_{mnp} = \frac{c}{2\pi}\sqrt{\left(\frac{2\pi}{\lambda_c}\right)^2 + \left(\frac{p\pi}{L}\right)^2}\,,$$

where c is the velocity of light, λ_c is the cutoff wavelength, $p=1,2,\ldots k$ and L is the chamber length. Based on Maxwell's equations the first lowest mode like in a ridged cavity depends on the structure length (H_{101}-mode). Index p cannot be equal zero ($p \neq 0$). For a length of $L=3553mm$ (length of the S2-chamber), the first resonant frequency is $f^H_{101} = 434MHz$. It agrees well with the frequency of the dominant mode obtained due to numerical simulations and microwave measurements (Table 1). Frequencies of the first six H_{mnp}-modes are shown in Table 1. The frequency of H_{106}-mode is almost equal to the RF frequency. In order to avoid interference of H-modes (TE-modes) with the BPM signal, the RF shielding is required.

*Work supported by DOE contract No: DE-AC02-98CH10886
#blednykh@bnl.gov

Table 1: Frequency comparison of the H_{10p}-modes for the multipole vacuum chamber with a length of 3553mm

Mode	Measurements f, MHz	GdfidL f, MHz	Equation f, MHz
H_{101}	430	434	434
H_{102}	436	440	440
H_{103}	446	450	450
H_{104}	458	463	464
H_{105}	478	480	481
H_{106}	496	500	501
H_{107}	518	523	523

ROGUE MODES SHIELDING REQUIREMENTS

The NSLS-II RF BPM electronics [4] employ a sub-sampling architecture whereby the fundamental 500MHz RF signal is under-sampled at ~117MHz utilizing 16b ADC's. The short pulses produced by the button pickups are passed through the high-band of a diplexer located 1m from the pickup. The resultant high-band diplexer output corresponds to the 5th-order Bessel impulse response centered at 500MHz. The low-band of the diplexer centered at 470MHz is used to inject a calibration tone.

The BPM spectral region of concern illustrating the desired rogue mode attenuation profile derived from an RF BPM signal processing perspective is shown below in Fig. 3. The horizontal axis is frequency in MHz, the left vertical axis is power relative to milliwatt (dBm), and the right vertical axis is power relative to the BPM pickup port seen by the RF BPM (i.e. dB_pu).

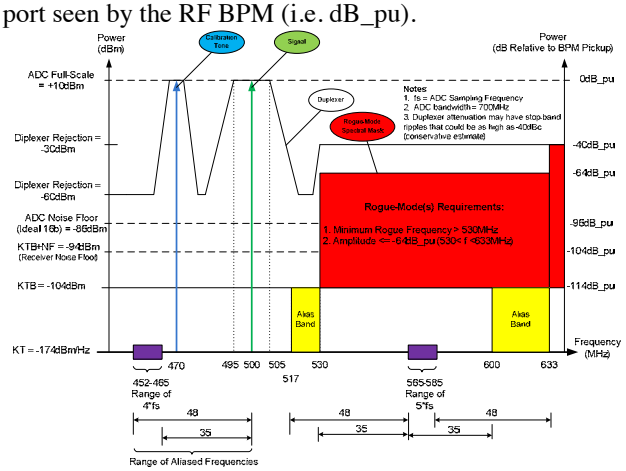

Figure 3: Rogue-Mode RF BPM Requirements.

The horizontal axis also illustrates two harmonic sampling regions (452-465, and 565-585MHz). These regions correspond to the 4th and 5th harmonics of the sampling clock of the ADC. The baseband digital signal processing operates on an intermediate frequency resulting from aliasing of the 500MHz signal with the 4th sampling harmonic. The fundamental sampling frequency of the ADC can range from 113MHz to 117MHz. As a result of bandpass sampling two alias regions of concern relative to the 5th sampling harmonic exist. These two regions are illustrated in yellow (517MHz – 530MHz, and 600MHz – 633MHz).

The desired rogue mode spectral mask has been defined in red considering the aliasing regions, finite attenuation of the diplexer, and the system noise floor. For the first requirement it would be desirable that no rogue modes exist below 530MHz. Rogue mode energy below 530MHz could potentially result in inter-modulation distortion (IMD) products that fall in-band. These in-band IMD products could either bias the position measurement, or add a time-varying component to the position measurement. The 2nd requirement would be for the BPM Pickup signal power to be less than -64dB_pu for the region between 530MHz to 633MHz. For a mode at -64dB_pu the 40dB of attenuation introduced by the diplexer high-band will push the mode down to the noise floor of -104dB_pu (-94dBm at receiver input). The rogue mode power above 633MHz is less of a concern as a result of the ADC response roll off starting at 700MHz combined with an anti-aliasing low pass filter with a cutoff frequency of 550MHz.

BASIC CONCEPT OF ROGUE MODE SHIELDING

All dimensions of the NSLS-II multipole vacuum chamber are already fixed and cannot be changed. The RF frequency is chosen to be 499.68MHz. Due to user requirements, we cannot keep a fixed fill pattern with bunch frequency less than 400MHz. To protect the NSLS-II BPM Buttons from the electric field of H_{mnp}-modes the RF shielding will be installed in each multipole vacuum chamber.

One way to avoid signal interference with frequencies of rogue modes is a wideband frequency shift due to insertion of RF metal shielding into the chamber. Since the cutoff frequency f_c of the H_{10}-mode depends on geometric parameters such as a, a', b and b' the width of the chamber can be reduced by introducing the RF shielding at a distance D as is shown in Fig. 4. It gives an opportunity to shift frequencies of H-modes above required frequency of 530 MHz.

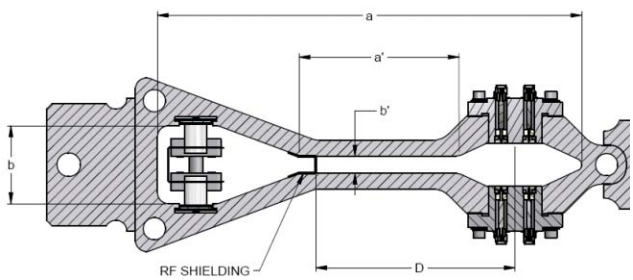

Figure 4: NSLS-II multipole vacuum chamber profile.

Vacuum requirements dictate that RF shielding should not significantly affect the performance of the getter strips located in the antechamber. A simple RF shielding design was chosen with a cross section shaped such that it could be inserted into the aft section of the 10mm extraction slot

adjacent to the anti-chamber (Fig. 5). This is an ideal location in part because in five out of six BPM locations, ray tracings revealed no radiation here that could damage the shield. Beryllium copper (BeCu) was chosen for it's high elastic modulus, giving the shield adequate spring force to retain it in the extraction slot. To satisfy the pumping requirement, it was necessary to perforate the face of the shield with roughly 50 percent transparency. This resulted in an array of 6.6mm square apertures spaced on 7.5mm intervals, small enough so the fields could not penetrate but large enough for adequate pumping. Notching the wings of the shield every 25mm allowed it to be produced using traditional progressive tool stamping technology which in turn allowed the shields to be produced in a continuous length then cut to the size needed for each chamber.

Installation is achieved by first positioning the shield inside the vacuum chamber against the back of the extraction slot. An insertion tool which is guided by the NEG slots is then pulled down the length of the chamber, seating the shield to the appropriate depth.

Figure 5: Flexible BeCu RF shielding with 50% of opening space inside of the multipole vacuum chamber. The thickness of the RF shielding is 0.25mm.

MICROWAVE MODE MEASUMENTS IN CHAMBERS WITH RF SHIEDFING

Three types of the multipole vacuum chamber have been measured; S2, S4 and S6 chambers with the length of 3553mm, 2840mm and 3445mm respectively. The S21-parameter has been measured through loop antennas installed on one side of the chamber and BPM buttons located on both sides of the chamber. Loop antennas can generate the whole frequency spectrum of H_{10p}-modes, whereas the BPM buttons can miss some of the mode, which have minimum electric field at the point of the BPM button location.

S4-Vacuum Chamber (L=2840mm)

S4 vacuum chamber has been loaded with flexible BeCu RF shielding at a distance D=114mm from the beam pipe center. Two separate RF shields of 2.2m and 460mm length are required in order to provide shielding before and after the stick absorber (Fig. 1). Two loop antennas are mounted on a side of the vacuum chamber to generate fields of H_{10p}-modes. Transmission coefficients (S21-parameter) using two loop antennas, from button to button and from loop to button have been measured for frequency cross checking.

Figs. 6 and 7 present measured results of the transmission coefficients in S4 chamber. Since the stick absorber splits the chamber into two sections with different lengths we measured S21-parameter in each of the sections. In the long-length section the first resonant peak of H_{101}-mode is generated at frequency *923MHz* (Fig. 6). In the short-length section the first lowest frequency is *929MHz* (Fig. 7). The proposed shield works properly, effectively shifting the frequencies sufficiently higher than required.

Since S4 chamber has been extruded with a small difference in gap along longitudinal direction we had some difficulties to install RF shielding properly, using a brand new installation tool designed by B. Kosciuk. The gap is a bit smaller in the middle of the chamber than required. The RF shielding was installed manually and it can have some wave-form along the chamber. In this case first several peaks can correspond to H_{101}-mode at first few frequencies. In order to be sure, we measured the electric field distribution along the chamber at frequency *978MHz* (Fig. 8, bead-pull measurements) using a thin metal disk. The horizontal axis in Fig. 8 corresponds to a chamber length of *L=2840mm*. As can be seen the electric field occurs at the beginning of the structure, on the length equivalent to one-eight of the structure.

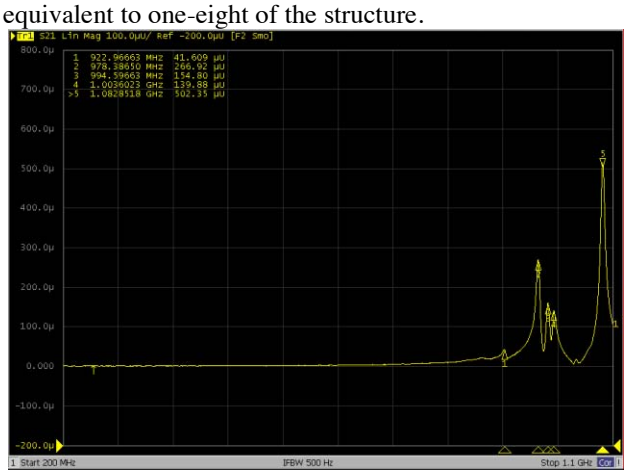

Figure 6: Measured S21-parameter in the long-length section of the S4 multipole vacuum chamber with RF shielding inside (linear scale). Loop to button.

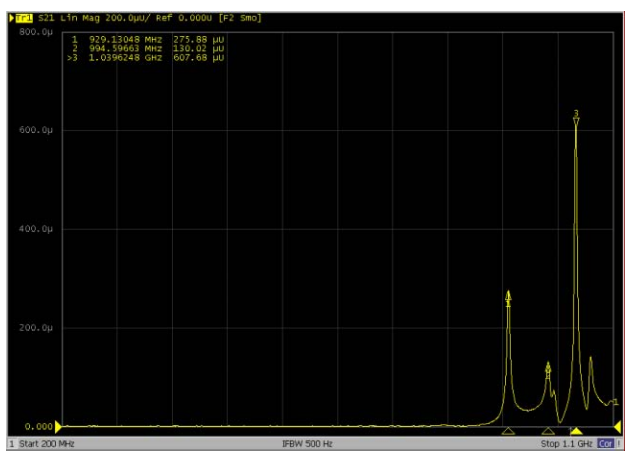

Figure 7: Measured S21-parameter in the short-length section of the S4 multipole vacuum chamber with RF shielding inside (linear scale). Loop to button.

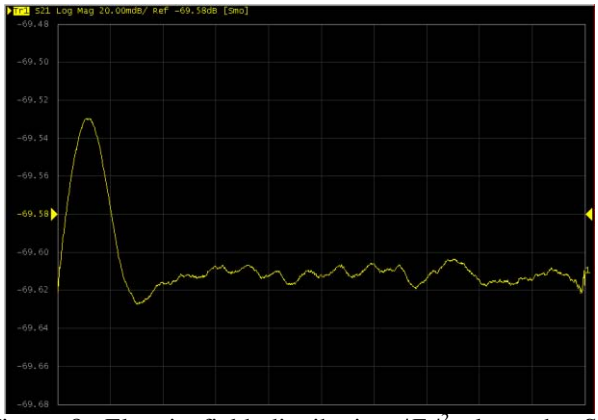

Figure 8: Electric field distribution $|E_y|^2$ along the S4 chamber at frequency 978MHz in long-length section. Vertical field measured in the middle of the chamber.

S2-Vacuum Chamber (L=3553mm)

S2 odd chamber has been measured in the same manner as S4 chamber. Since the stick absorber is located close to end of the chamber, only one RF shield with a length of ~3.5m has been loaded. In this case we applied an installation tool and based on measurement results no unexpected frequencies were found as in a case with S4 chamber. The lowest frequency measured in the chamber with RF shielding is 939MHz (Fig. 9). Measured electric field distribution at frequencies 939MHz and 948MHz is shown in Figs. 10a and 10b respectively.

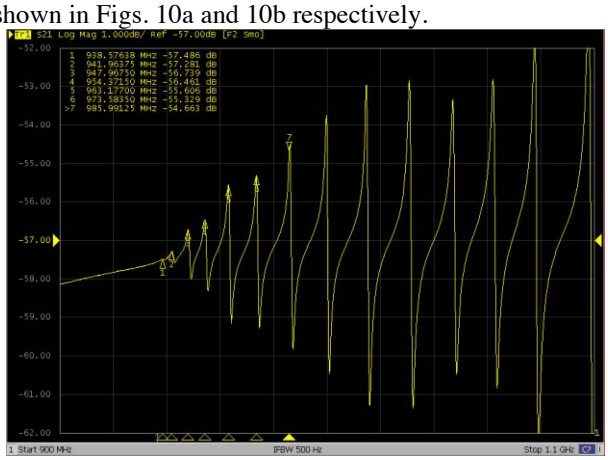

Figure 9: Measured S21-parameter in the S2 multipole vacuum chamber with RF shielding inside (logarithmic scale). Input and output signals are taken from loop antennas located on one side of the chamber.

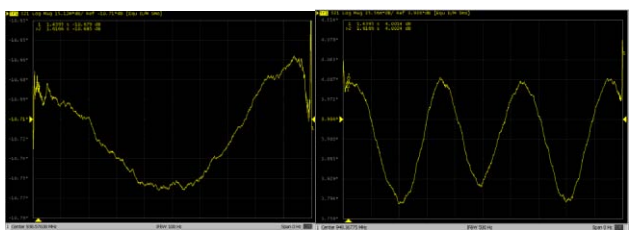

(a) (b)

Figure 10: Measured electric field distribution $|E_y|^2$ along the S2 chamber at frequencies 939MHz (a) and 948MHz (b). Frequencies correspond to H_{101}-mode and H_{103}-mode respectively.

In Table 2 we compare measured frequencies versus numerically simulated. These results show that there is a slight difference between frequencies. It can be explained due to strong frequency dependence on D parameter. A bit larger/smaller pressure by installation can move RF shielding that can bring frequencies higher/lower.

The RF shielding was installed properly. Measured and simulated frequencies correspond to a different H_{10p}-mode. In Fig. 11 we plot electric field distribution simulated for the first few values of p (p *=1, 2 and 3*). The red line is the field distribution $|E_y(L)|$ at frequency f=954MHz. It corresponds to H_{101}-mode. The blue dashed line is $|E_y(L)|$ at frequency f=957MHz. It corresponds to H_{102}-mode. The vertical field component E_y varies in the longitudinal direction depends on p-value.

Table 2: Frequencies of H_{10p}-modes in 3553m multipole vacuum chamber with the RF shielding inside

Mode	Measurements f, MHz	GdfidL f, MHz
H_{101}	939	954
H_{102}	942	957
H_{103}	948	962
H_{104}	954	968

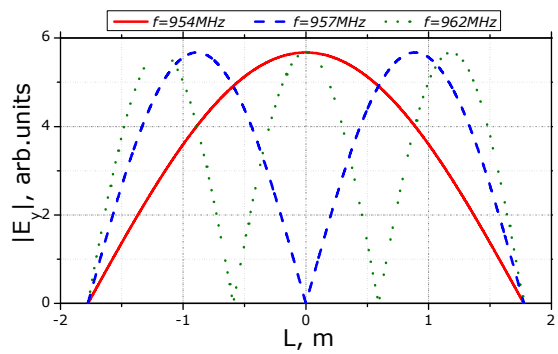

Figure 11: Numerically simulated electric field distribution inside the S2 chamber with RF shielding for first three values of p (p*=1,2 and 3*). We show the results of $|E_y|$ as a function of chamber length L simulated in the middle of the chamber.

S6-Vacuum Chamber (L=3445mm)

The RF shielding length inside the S6 chamber has to stay clear of synchrotron radiation (red shaded color in Fig. 13) from downstream magnets. The emission angle in the horizontal direction at downstream of each S6 chamber is pretty large. The RF shielding has to be loaded at a distance of ~2m away from the right side of the chamber (keeping the same horizontal distance of D=114mm) to avoid its heating and damage due to synchrotron radiation. The total inner length of the S6 even and odd chambers are 3559mm and 3445mm, respectively. It makes it hard to protect each downstream BPM Button in each S6 chamber with ~2m of unshielded space.

We are considering two possibilities. First, the length of the RF shielding can be optimized so that 500MHz frequency can be centered between two neighboring frequencies of H_{10p}-modes, which are generated in the empty space.

Measurements of the transmission coefficient using the downstream BPM buttons show that with a length of 2.1m unshielded space two neighboring peaks are seen at frequencies of 483MHz and 521MHz (Marker 3 and Marker 5 in Fig. 12). Marker 4 set up manually at frequency 500MHz. Perhaps tens of MHz criterion will be sufficient.

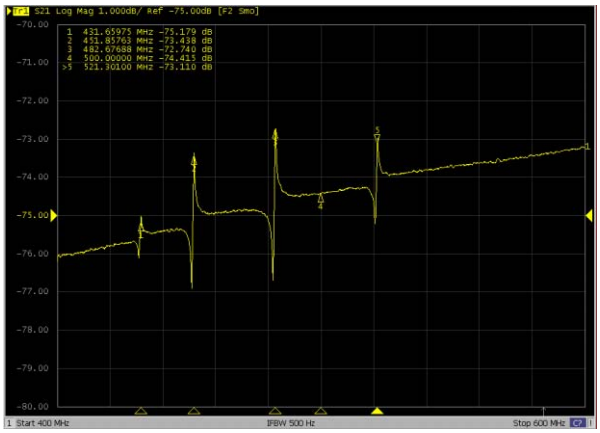

Figure 12: Measured S21-parameter in the S6 even multipole vacuum chamber with RF shielding inside (logarithmic scale). Location of the RF shielding is shown in Fig. 13. Input and output signals are taken from the downstream BPM button.

Second, if ±15MHz frequency shift from 500MHz is not sufficient, then there is a risk to lose one BPM in each S6 chamber. To compensate it, ID BPM or high stability BPM are going to be located right after each S6 chamber in each straight section.

Measurements through the upstream BPM button (shielded area) show that the lowest frequency can be generated at ~830 MHz. Electromagnetic fields generated in unshielded space (Fig. 12) at frequencies 432MHz, 451MHz and etc. are not seen by the upstream BPM button.

CONCLUSION

We demonstrated numerical modeling and experimental studies of the spurious TE modes in the NSLS-II vacuum chambers with antechamber slot. Calculated frequencies of TE-modes in considered chambers with and without RF shielding were verified experimentally. Flexible BeCu RF shielding inside each chamber at proper location shifts frequencies of H_{10p}-modes above ~900MHz, except chambers S6 odd and even. These chambers need special attention because of synchrotron radiation from downstream magnets.

S6 odd multipole vacuum chamber needs to be measured and the RF shielding length has to be optimized.

RF shielding looks adequate for baseline design. Fifty percent of open space provides adequate pumping speed.

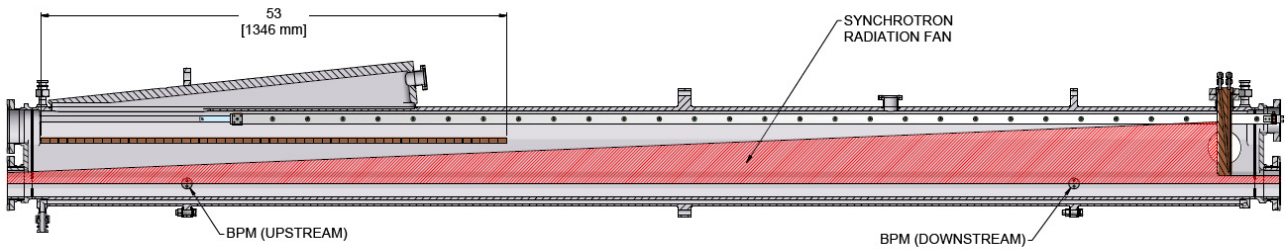

Figure 13: S6 even multipole vacuum chamber with RF shielding inside. The red shaded region represents the synchrotron radiation fan. Flexible BeCu RF shielding is 1346mm long.

ACKNOWLEDGEMENT

We thank Glenn Decker (APS/ANL), John Hoyt (APS/ANL), Bob Lill (APS/ANL), Mike Blaskiewicz (CAD/BNL) and Sushil Sharma (NSLS-II/BNL) for participating in review of the RF shielding for the rogue modes in the NSLS-II vacuum chamber and for their expertise and contribution to the design process.

REFERENCES

[1] NSLS-II Preliminary Design Report, 2008; http://www.bnl.gov/nsls2/project/PDR/

[2] Y. Kang, G. Decker and J. Song, "Damping spurious harmonic resonances in the APS storage ring beam chamber," EPAC'96, Sitges, June 1996, p. 7984.

[3] W. Bruns, GdfidL code; http://www.gdfidl.de

[4] K.Vetter et al., "NSLS-II RF Beam Position Monitor", BIW10, Sante Fe, NM. Current proceedings.

OPTIMIZATION OF SMALL APERTURE BEAM POSITION MONITORS FOR NSLS-II PROJECT*

I. Pinayev #, A. Blednykh, B. Kosciuk, O. Singh, BNL, Upton, NY 11973, U.S.A.

Abstract

The NSLS-II Light Source is being built at Brookhaven National Laboratory. It will provide users with ultimate brightness beam and full realization of its capabilities requires corresponding stability of the beam orbit. The small aperture beam position monitors (BPMs) will provide better sensitivity to the beam position but also requires thorough design. In this paper we present the results of the optimization including signal power levels and button heating.

INTRODUCTION

The standard beam position monitors for the NSLS-II storage ring is be mounted on an aluminum multipole vacuum chamber [1, 2]. The vertical gap is 25 mm and the distance between the button centers is 16 mm.

Small aperture BPMs will be installed in the straights around the insertion devices (ID). The ID beamlines are the most demanding for the beam stability, therefore, most of the small aperture BPMs will be installed on the special supports providing high mechanical stability [3]. The vertical gap is expected to be around 15 mm. Therefore the design of the small aperture BPMs will differ from the regular assemblies.

GEOMETRY OPTIMIZATION

The MATLAB script similar to [4] was used for optimization of the distance between centers of the buttons.

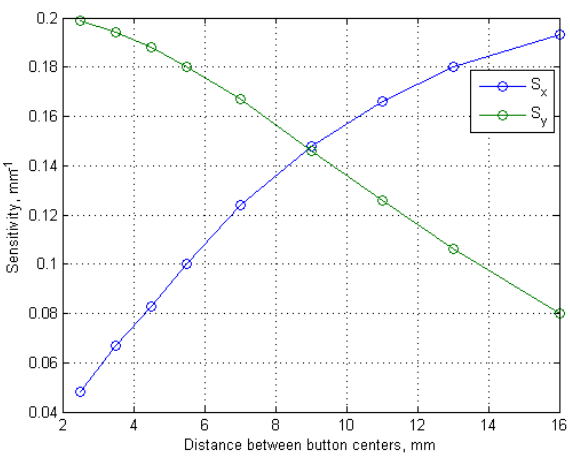

Figure 1: Dependence of sensitivity coefficients on the distance between the centers of the 4.5 mm buttons.

The results of the simulations are shown in Fig. 1. Based on the numerical the calculations we specified 4.5 mm separation between the button centers. In this case sensitivity to the vertical motion doubles in comparison with the standard BPMs when horizontal is not changed. The rational for such choice is that the vertical beam size is much smaller and requirement for beam stability in the vertical plane are stricter. The dependence of difference over the sum signal for the chosen button separation is shown in Fig.2.

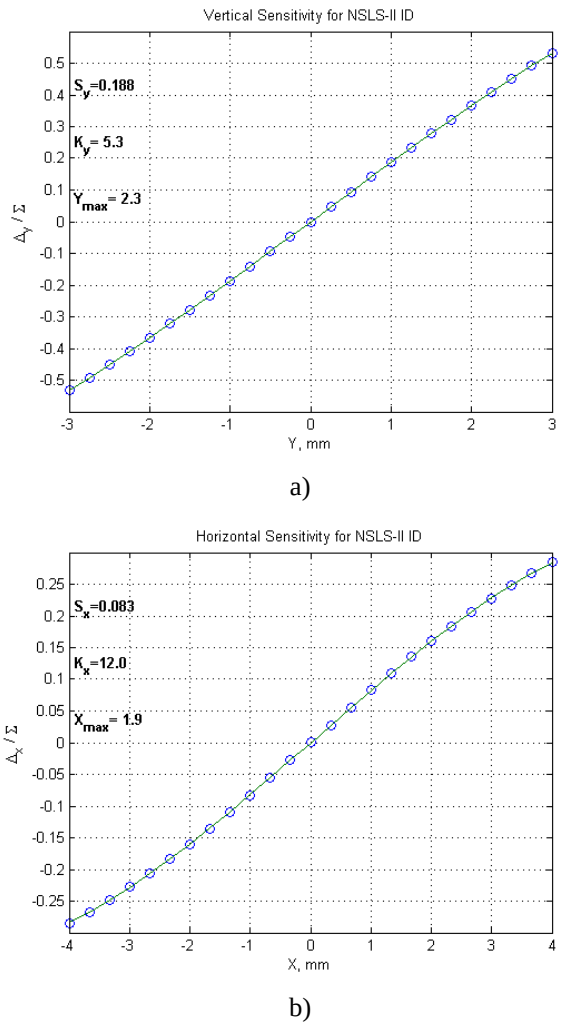

Figure 2: Dependencies of difference over sum signal for the geometry with 4.5 mm distance between button centers: a) for the vertical plane, b) for the horizontal plane.

The standard BPMs has separation of 16 mm and it is possible to reduce the distance down to the 9.6 mm. Further reduction is limited by the size of the SMA connector. However, it is possible to reduce the effective

*Work supported by U.S. Department of Energy, Office of Science, Office of Basic Energy Sciences, under Contract No. DE-AC02-98CH10886.

#pinayev@bnl.gov

distance by rotation of the BPM assembly as it was done at APS [5].

SIGNAL LEVEL ESTIMATION

The MATLAB script, has been used for a geometry optimization, also performs the evaluation of signal power for the on axis beam. With 500 mA circulating current will induce -8.2 dBm signal (at the RF frequency of 499.68 MHz) on the 4.5 mm diameter buttons installed on a vacuum chamber with 15 mm vertical gap. For a vacuum chamber with a 10 mm gap the power rises to -6.8 dBm. These signal levels are in line with standard BPMs. The trace of the BPM signal is shown in Fig. 3.

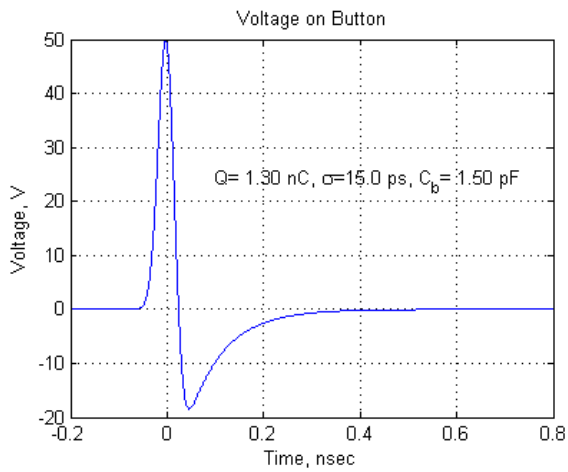

Figure 3: Trace of the signal from the button with 500 mA circulating beam.

IMPEDANCE OF THE BPM ASSEMBLY

Since the small aperture BPM buttons are closer to the beam than the standard ones there is a concern of heating due to wakefields induced by the travelling bunch. As it was proposed in [6] figure-of-merit has been uses to estimate power dissipated in a button. Its value depends on vacuum chamber vertical gap, button diameter, bunch length, circulating current, number of bunches and the revolution frequency. The regular BPMs have FOM=809 with nominal beam (500 mA in 1000 bunches). The small aperture BPM with 4.5 mm diameter buttons has FOM=204 (460 for a 10 mm vacuum chamber) for the same conditions. So, the SA BPMs are operating in milder conditions mostly due to the smaller button diameter.

The final design will be performed according to the rules described in [7]. The button diameter was set to 4.47 mm. With 0.25 mm annular gap the frequency of the trapped mode will be between harmonics of RF frequency. The longitudinal impedance has been simulated using GdfidL code [8] and the results are shown in Fig. 4. The loss factor simulated for a 4.5 mm bunch length is 3 mV/pC and the expected power loss is 1.5 W.

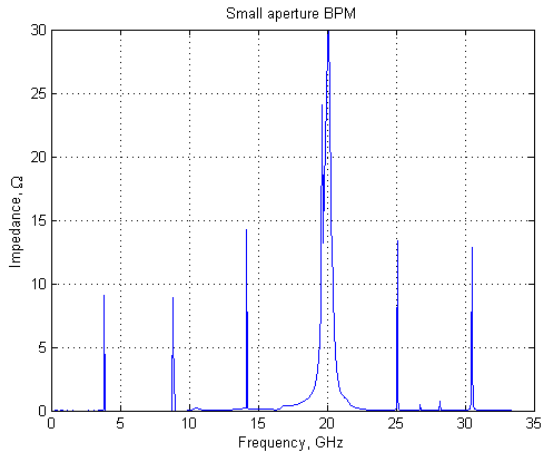

Figure 4: Real part of the longitudinal impedance of the small aperture BPM. The trapped mode resonance frequency is at 20.24 GHz. The small narrow peaks are due to the reflections from the unmatched ports.

CONCLUSIONS

The optimized small aperture beam position monitors provide required sensitivity to the beam motion with signal level as regular BPMs.

REFERENCES

[1] I. Pinayev, O. Singh, R. Alforque, A. Blednykh, P. Cameron, V. Ravindranath, and S. Sharma, “Research and Development Program on Beam Position Monitors for NSLS-II Project,” EPAC’08, Genoa, June 2008, TUPCC082, p. 1245 (2008); http://www.JACoW.org.

[2] O. Singh et al., “NSLS-II Beam Diagnostics Overview”, PAC’09, Vancouver, May 2009, TU3GRI03.

[3] B. Kosciuk et al., “Development of High Stability Supports for NSLS-II RF BPMs”, PAC’09, Vancouver, May 2009, TH5RFP012.

[4] A. Olmos, F. Perez, G. Rehm, “MATLAB Code for BPM Button Geometry Computation”, DIPAC’07, Venice, May 2007, TUPC19, p. 186 (2007); http://www.JACoW.org.

[5] G. Decker, “Beam Stability in Synchrotron Light Sources”, DIPAC’05, Lyon, June 2005, ITWM01, p.233 (2005); http://www.JACoW.org.

[6] P. Cameron and O. Singh, “Comparative Study of Button BPM Trapped Mode Heating” PAC’09, Vancouver, May 2009, TH5PFP081.

[7] P. Cameron, A. Blednykh, B. Kosciuk, I. Pinayev, V. Ravindranath, and O. Singh, “BPM Button Optimization To Minimize Distortion Due To Trapped Mode Heating”, PAC’09, Vancouver, May 2009, TH5RFP011.

[8] W. Bruns, GdfidL code; http://www.gdfidl.de

CONCEPT OF BEAM POSITION MONITOR WITH FREQUENCY MULTIPLEXING*

I. Pinayev#, P. Cameron, BNL, Upton, NY 11793, U.S.A.

Abstract

Two most widely used beam position monitor (BPM) systems (manufactured by Bergoz [1] and Instrumentation Technologies [2]) implement switching technique to eliminate errors associated with drifts in the channel gains. High stability is achieved by an alternative routing of signals from all pick-up electrodes (PUE) through the same chain. Such an approach creates problems with turn-by-turn acquisition as well as measurement noise. In this paper, basing on the advances of digital signal processing that allow identical gains for the wide frequency ranges, we propose separating signals in the frequency domain. The experimental set-up and test results are presented. Practical realization of the beam position monitors is also discussed.

INTRODUCTION

Development of ultra-bright synchrotron radiation sources and high luminosity colliders requires unprecedented levels of beam stability. To achieve needed steadiness one can use a channel switching technique [1, 2] or utilize a pilot tone [3, 4]. The channel switching produces very low drifts but also manifests itself as narrow band measurement noise at the switching frequency. Another disadvantage is lack of the turn-by-turn (TbT) capabilities. Pilot tone technique can provide both stable long-term beam position monitoring and TbT data: however it requires extra hardware to be placed inside an accelerator tunnel.

In this paper we propose a new approach based on the separation of the signals from different pick-up electrodes (PUE) in the frequency domain combined with digital processing. Processing in the digital chain is a key element, because it provides stable and equal gain in the wide frequency range.

EXPERIMENTAL SETUP

The proposed signal processing scheme is shown in Fig. 1. For simplicity the scheme with two pick-up electrodes, A and B, is used (four-PUE implementation will be discussed later). Signal from each pick-up is divided into the two channels with equal amplitudes by splitters S_1 and S_2. Two local oscillators Osc 1 and Osc 2 set the intermediate frequencies (IF). Signals from each PUE are down-converted with mixers M_1-M_4 and cross combined with combiners C_1-C_2. The first analog-to-digital converter (ADC) processes signal A at the first intermediate frequency and signal B with the second IF; the second ADC processes signal A at the second IF and signal B with the first IF.

Due to symmetry of the processing chain the first-order errors from the splitters and combiners (such as inequality of division and summation) and the amplitude variations of the local oscillators are cancelled; only the second-order terms remain. For the analysis purpose the variation of mixers insertion losses are included into the corresponding errors in splitters and/or combiners.

Components characterization

The tests were performed utilizing a LeCroy WavePro 7300A digital oscilloscope, ZFSC-2-4-S+ splitters/combiners, ZX05-10-S+ mixers by Mini-Circuits, two N5181A RF signal generators by Agilent were used as local oscillators, and an RF and Clock Generator by Instrumentation Technologies for the signal source. The carrier frequency was suppressed by the low-pass filters with cut-off frequency depending on the chosen IF. The carrier frequency was set to 481.57 MHz to minimize the effect of reflected wave from the mixers.

First, the splitters and ADC were verified with two measurements in which signal after splitter goes directly and then is crossed to the two channels of the oscilloscope. The measured waveforms were fit with sine, and obtained amplitudes were used to calculate unevenness of the splitters and the gain inequalities of the ADCs. The channel gains were different by 6×10^{-3} and the splitter was found to have 1.4×10^{-3} unbalance.

Beam offset was simulated by insertion a 1 dB attenuator (theoretical transmission of 0.8913) into position A or position B. The measured transmission was 0.885.

Tests with Low IF

The initial measurements were performed with low IF, where the reduced sampling rate allows ADCs to have less noise and more effective bits. The local oscillators were set to 478.93 MHz (IF_1=2.64 MHz) and 478.01 MHz (IF_2=3.56 MHz). The SLP-5+ low-pass filters by Mini-Circuits have cut-off frequency of 5 MHz. The sequence of 10 μs duration was recorded with 1 Gs/sec rate. The recorded signals ware fitted with a two-tone sine waveform:

$$y = y_0 + A\cos\omega_1 t + B\sin\omega_1 t + C\cos\omega_2 t + D\sin\omega_2 t \quad (1)$$

The obtained amplitudes were used to calculate the ratio of levels:

*Work supported by U.S. Department of Energy, Office of Science, Office of Basic Energy Sciences, under Contract No. DE-AC02-98CH10886.

#pinayev@bnl.gov

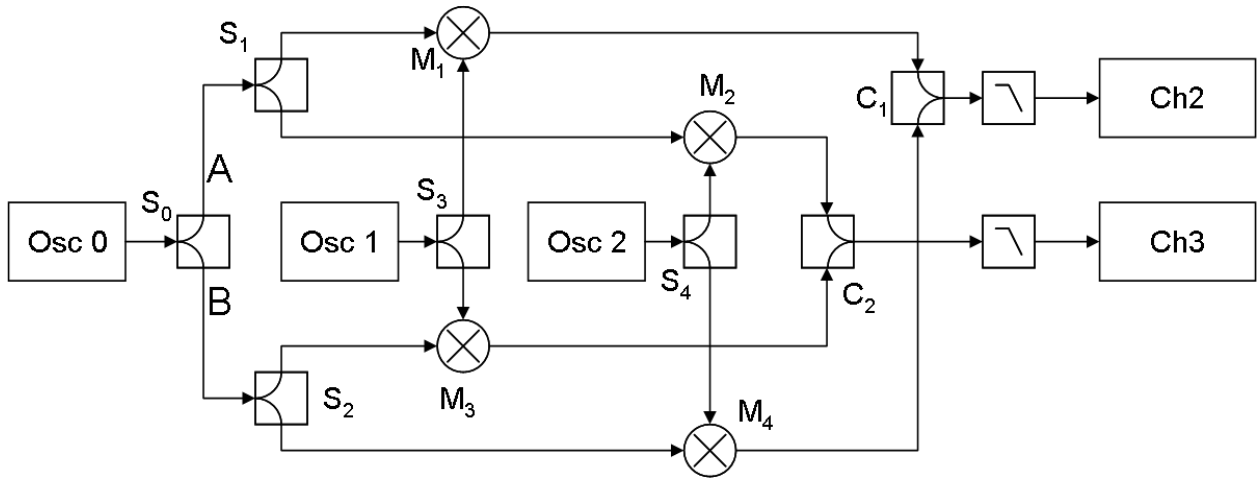

Figure 1: Test set-up for beam position monitor with frequency multiplexing.

$$R = \frac{\sqrt{A_2^2 + B_2^2} + \sqrt{C_3^2 + D_3^2}}{\sqrt{A_3^2 + B_3^2} + \sqrt{C_2^2 + D_2^2}} \qquad (2)$$

For the direct connection (without any attenuators) the ratio of the signals was R=1.0206±9.6×10^{-5}, with the attenuator in chain A 1.1467±1.8×10^{-4} and in chain B 0.9130±1.6×10^{-4}. Sensitivity to the ADC gain was verified by installation of another 1 dB attenuator before the Ch3 oscilloscope input. Direct measurements gave R=1.0195±1.1×10^{-4}; with attenuator in chain A R= 1.1457±1.7×10^{-4}.

The effect of local oscillator power variations was studied by varying Osc 2 amplitude. The obtained results are shown in Table 1.

Fig. 2 shows the observed ratio depending on the input signal level. During these measurements gain of the oscilloscope channels was adjusted accordingly. The legend shows the utilized scales. At low signal levels the ratio stays unchanged; when the mixers are overloaded the ratio changes substantially.

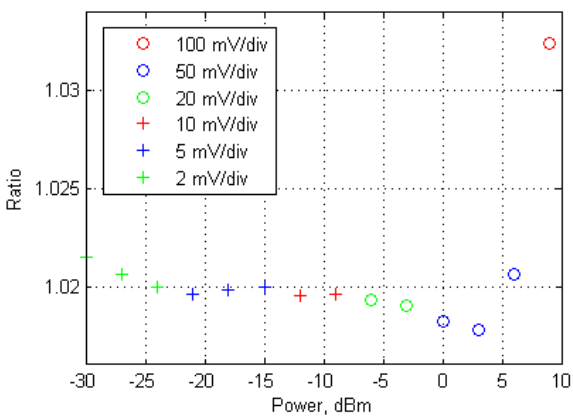

Figure 2: Dependence of measured ratio vs. Osc 0 power.

Table 1: Effect of local oscillator power for low IF

Osc 2 Power	R without attenuator	R with attenuator in position A
7 dBm	1.0232±1.6×10^{-4}	1.1488±2.0×10^{-4}
10 dBm	1.0204±1.8×10^{-4}	1.1470±1.7×10^{-4}
13 dBm	1.0164±1.4×10^{-4}	1.1437±1.3×10^{-4}

The storage rings usually operate with partial fill and spectrum of the beam signal has sidebands around RF frequency, which are separated by the revolution frequency F_{rev}. Fig. 2 shows spectrum of the signal for 80% fill with revolution frequency of the NSLS-II storage ring (378 kHz). The separation between two intermediate frequencies was chosen in such way that spectral content does not overlap.

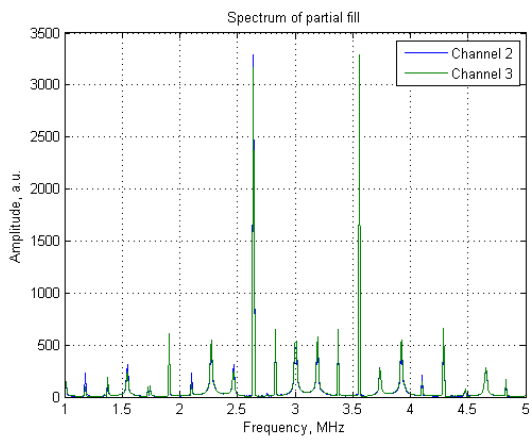

Figure 3: Spectrum of the beam with 80% partial fill.

For the reduction of the fill duty factor the main line decreases and sidebands amplitudes grows. In order to improve signal-to-noise ratio the energy in the sidebands should accounted as well. Therefore, to evaluate

capabilities with TbT data the fit with N sidebands was utilized:

$$y = y_0 + \sum_{i=-N}^{N} A_i \cos\left[(\omega_1 + i\omega_{rev})t + \phi_i\right] + \sum_{i=-N}^{N} B_i \cos\left[(\omega_2 + i\omega_{rev})t + \varphi_i\right] \quad (3)$$

Tests with High IF

In order to have TbT resolution, higher intermediate frequencies are required. For this purpose frequencies of local oscillators were set to 446.06 MHz and 451.41 MHz (IF_1= 35.51 MHz, IF_2=30.16 MHz). The low-pass filters used were SLP-50+ by Mini-Circuits with cut-off frequency of 48 MHz.

The tests similar to the ones done for low IF were performed. The results are shown in the Tables 2 and 3, and Figs. 3 and 4.

Table 2: Effect of ADC mismatch

Connection	R without attenuator	R with 1dB attenuator in Ch3
Direct	$1.0578\pm2.3\times10^{-4}$	$1.0583\pm4.1\times10^{-4}$
A	$1.1881\pm1.1\times10^{-4}$	$1.1889\pm3.5\times10^{-4}$
B	$0.9554\pm1.1\times10^{-4}$	$0.9472\pm2.2\times10^{-4}$

Table 3: Effect of local oscillator power for high IF

Osc 2 Power	Ratio with attenuator in position B
7 dBm	0.9491
8 dBm	0.9490
9 dBm	0.9477
10 dBm	0.9459
11 dBm	0.9434
12 dBm	0.9406
13 dBm	0.9382

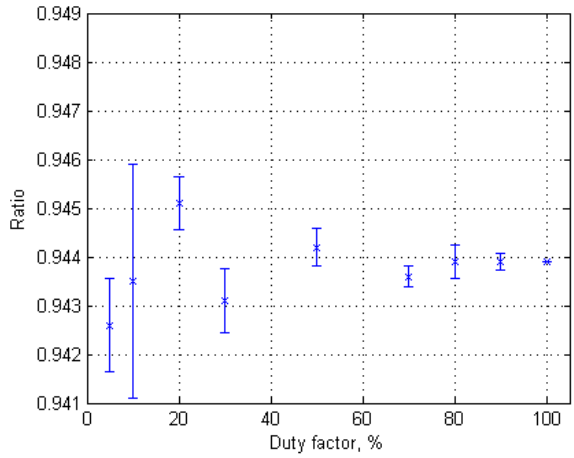

Figure 3: Turn-by-turn measurements with different fills.

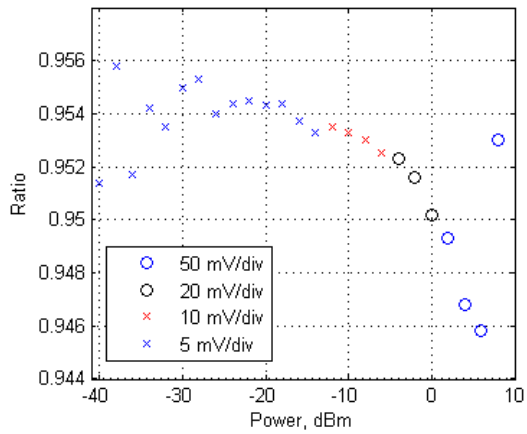

Figure 4: Ratio vs. signal level.

OTHER CONFIGURATIONS

A simpler configuration can be achieved when the frequency of one of the local oscillators is set to zero, i.e., no frequency conversion. A low-pass filter installed after a mixer can suppress the upper sideband as well as the carrier line. The amplitudes of the signals in both paths can be equalized with attenuators.

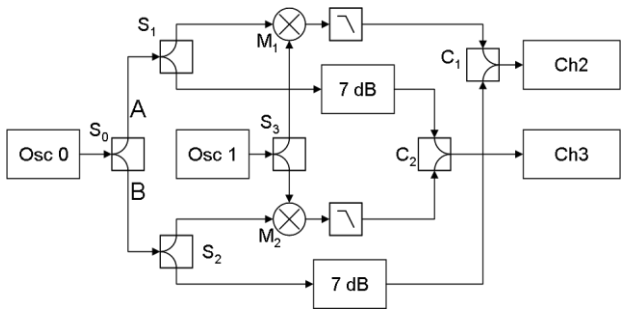

Figure 5: Layout of the signal processing chain with single local oscillator and two mixers.

It is possible to build a receiver without mixers by utilizing the higher harmonics of the beam signal. For example one channel will be used for the measurement of the 1st harmonic of signal form button A and second

harmonic from button B, when the other channel will monitor 2nd harmonic from button A and the first harmonic from button B. The scheme can build using four diplexers as shown in Fig. 6.

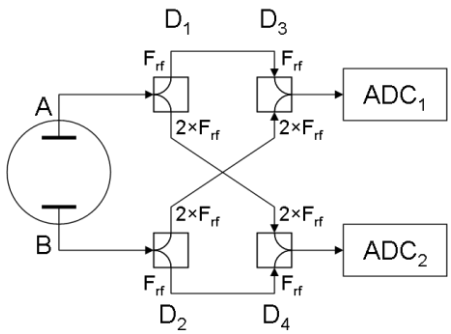

Figure 6: Set-up with four diplexers. The bandwidth of the system is defined by diplexers bandwidth.

FOUR PUE IMPLEMENTATION

In principle, the proposed set-up can be easily expanded for case of four pick-up electrodes. The signals should be split by four 4-way splitters, mixed into the four IF (four local oscillators required), combined and processed with four ADCs. More cumbersome but straightforward analysis similar to the two PUE case shows that all first order errors are suppressed as well.

But there is a possibility to utilize two double-channel devices connected to the diagonally located PUE (Fig. 7).

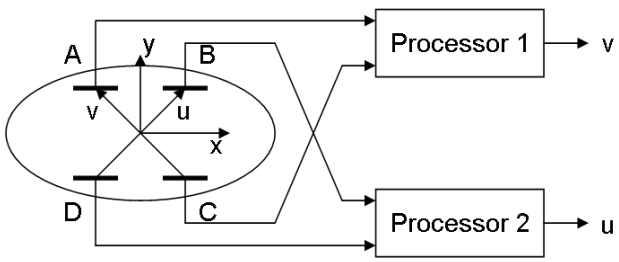

Figure 7: Usage of two receivers for 4 pick-up electrodes.

In this case two variables u and v are found and the beam position can be found by coordinate transformation:

$$\begin{pmatrix} x \\ y \end{pmatrix} = \begin{bmatrix} a & -a \\ b & b \end{bmatrix} \begin{pmatrix} u \\ v \end{pmatrix} \qquad (5)$$

CONCLUSIONS

Measurements confirmed the expected benefits of RF BPM with frequency multiplexing in the wide dynamic range:

- A 10% variation of ADC "gain" changes the observed ratio within error margins;
- Sensitivity to local oscillator power is most likely due to the changing impedance mismatch and circuit asymmetry (different length of cables);
- The device is capable of processing signals from a beam with a partial fill;
- The scheme used is capable of turn-by-turn measurements (more study is needed for low fill modes).

Four buttons signals can be processed, as well.

REFERENCES

[1] R. Biscardi, J.W. Bittner, "Switched Detector for Beam Position Monitor", PAC'89 Chicago, March 1989, p. 1516; http://www.JACoW.org.

[2] R. Ursic, R. De Monte "Digital Receivers Offer New Solutions for Beam Instrumentation" PAC'99 New York, March 1999, p. 2253; http://www.JACoW.org.

[3] P. Prieto et al., "High Resolution Upgrade of the ATF Damping Ring BPM System", BIW'08, Tahoe City, May 2008, p. 200; http://www.JACoW.org.

[4] K. Vetter, "NSLS-II RF Beam Position Monitor", these proceedings

NSLS-II RF BEAM POSITION MONITOR*

Kurt Vetter#, Al Joseph Della Penna, Joseph DeLong, Bernard Kosciuk, Joe Mead, Igor Pinayev, Om Singh, Yuke Tian, Kiman Ha BNL, NSLS-II, NY 11973, U.S.A.

Abstract

An internal R&D program has been undertaken at BNL to develop an RF BPM to meet all requirements of both the injection system and storage ring. The RF BPM architecture consists of an Analog Front-End (AFE) board and a Digital Front-End board (DFE) contained in a 1U 19" chassis. An external passive RF signal processor has been developed that will be located near the RF BPM pickups. The partitioning into two boards enables a flexible Software Defined Instrument. A model-based design flow has been adopted utilizing AWR VSS, Simulink, and Xilinx System Generator for algorithm development and AFE impairment performance analysis. The DFE architecture consists of a Virtex-5 with MicroBlaze embedded processor. An optional Intel Atom SBC is also supported. The AFE is based on a bandpass sampling architecture utilizing 16-bit ADCs. Long-term drift is corrected by inclusion of an out-of-band calibration tone. An RF BPM Calibration Tool is being developed for removal of systematic errors and performance verification. In this contribution we will present a detailed overview of the architecture, then compare simulation results to laboratory performance.

INTRODUCTION

An internal R&D program was started in August 2009 to develop an RF BPM for the 3GeV NSLS-II currently under construction at Brookhaven National Laboratory for the Injection System and Storage Ring. Since the start of the BPM R&D program was after the Critical Decision 3 award, the development timeline is aggressive. The development schedule mandates a proof-of-principle demonstrated August 2010.

As a state-of-the-art 3rd generation light source designed to deliver world-leading intensity and brightness, beam stability will be of utmost importance. The most stringent BPM stability requirement [1] is for the multi-bunch stored beam condition where vertical resolution, horizontal resolution, and long-term stability must be less than 200nm rms. It is well known that the most challenging requirement is the sub-micron long-term stability. The sub-micron horizontal, and vertical resolution correlate to the intrinsic signal-to-noise (SNR) of the pickup geometry [4] which can be met by proper analysis and design of the analog and digital processing.

The NSLS-II RF BPMs utilized in the Storage Ring are housed in thermally stabilized racks, regulated to +-0.1° C of the preset operational temperature. Based on tests of existing BPM technology in the NSLS-II thermally controlled racks it is possible to achieve sub-micron long-term gain drift without calibration. However, a dynamic calibration scheme has been incorporated to achieve long-term (i.e., 8 h) gain stability to meet the required 200 nm objective [4] over the operational range of 50-500 mA.

*Work supported by DOE contract No: DE-AC02-98CH10886

#kvetter@bnl.gov

SYSTEM ARCHITECTURE

The NSLS-II RF BPM architecture consists of a passive RF Processor box located in the tunnel, the AFE, and DFE. Shown below in Figure 1 is the prototype BPM consisting of both AFE and DFE.

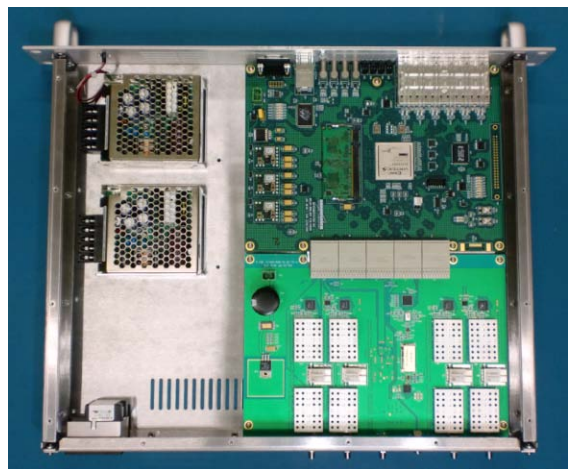

Figure 1: NSLS-II Prototype RF BPM.

The RF Processor box consists of a custom Diplexer designed by K&L Microwave, isolator, and 4-way power splitter. An illustration of the Passive RF Processor is illustrated below in Figure 2. The RF Processor is shown located on the girder directly below the BPM pickups. Four 1 m SiO_2 cables are connected from the pickup assembly to the RF Processor.

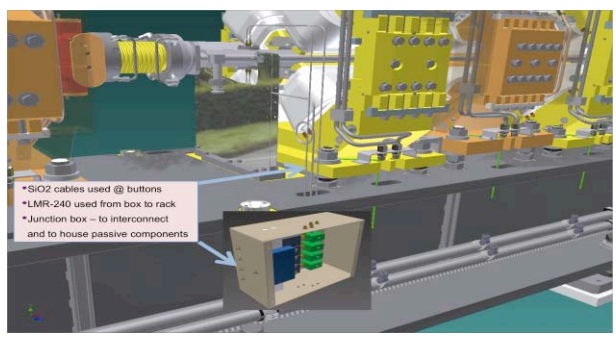

Figure 2: Passive RF Processor.

A detailed illustration of the RF Processor is illustrated below in Figure 3. One m of SiO_2 is used to connect the BPM pickup to the RF Processor. The RF Processor consists of an isolator and custom diplexer. The isolator presents a return loss of 18 dB over a 150 MHz

bandwidth centred at the RF fundamental frequency of 500 MHz. The custom diplexer is used to combine an out-of-band calibration tone with the pickup signal. The prototype diplexer design consists of four independent diplexers used to process each channel. It is intended that the production design will incorporate all four diplexers into a single four channel monolithic design. The high band of the diplexer centred at 500 MHz consists of a 5th-order Bessel response. The low band of the diplexer passes a calibration tone over a 35MHz band centred at 465 MHz utilizing a Chebyshev response.

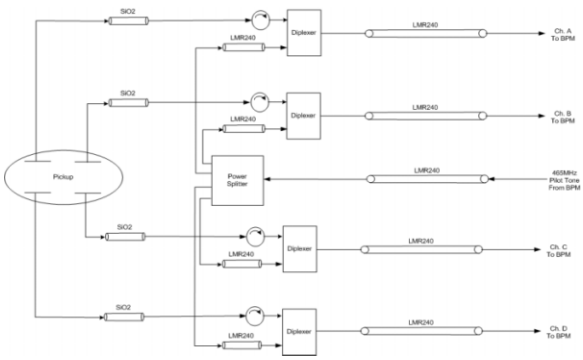

Figure 3: Tunnel Configuration - Passive RF Processing. RF Passive elements include Isolators, Diplexer, and 4-way Power Splitter.

An illustration of the prototype single-channel custom diplexer is shown below in Figure 4. A suspended microstrip topology is used to maximize Q while maintaining minimum insertion loss.

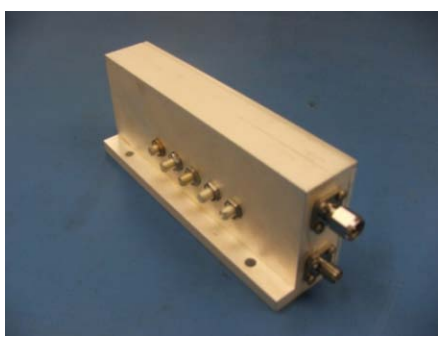

Figure 4: Prototype single-channel diplexer.

The measured 5th-order order Bessel response is shown below in Figure 5. The measured bandwidth is 8.5MHz, 3.8dB insertion loss, and maximum group delay of 83ns. The 5th -order diplexer high-band response was chosen to provide good pulse response characteristic which include minimal group delay distortion, linear in-band phase, and rapid decay of stored impulse energy measured in terms of "Time-Sidelobe" decay.

The Time-Sidelobe decay is illustrated below in Figure 6. The Bessel filter has a -40 dBc first Time-Sidelobe response compared to -10 dBc for the Chebyshev filter response. The composite output signal of the diplexer is transmitted to the RF BPM electronics via LMR200FR cable. Each RF BPM consists of an AFE and DFE that process four BPM channels. Slow Acquisition (i.e. 10Hz) and data on demand are transmitted to and EPICS IOC via Gigabit Ethernet. The Fast Orbit FeedBack (FOFB) is transmitted via a custom Serial Data Interface (SDI) link developed at BNL.

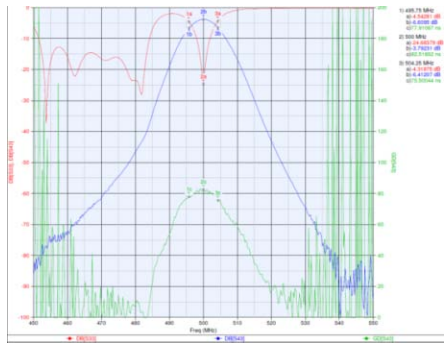

Figure 5. Measured Diplexer high-band response.

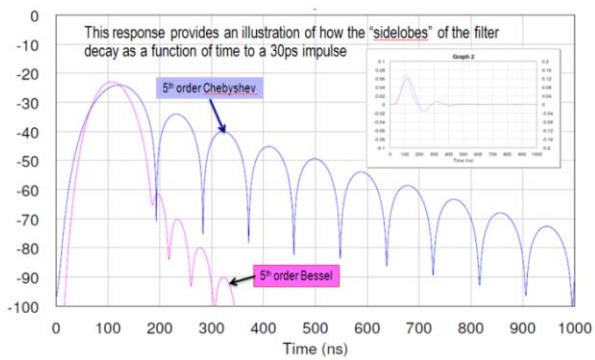

Figure 6: Diplexer high-band time-sidelobe response.

ANALOG FRONT END

The AFE employs a bandpass sampling architecture for the Storage Ring and Booster. The composite RF signal from the diplexer consisting of the BPM signal centred at 500MHz contained in a 8.5 MHz bandwidth along with a narrowband pilot tone approximately 25 MHz below the 500 MHz BPM signal are under-sampled at approximately 117 Msps by four independent 16-b ADCs. An alternate heterodyne architecture is currently under investigation to yield higher spatial resolution for the Injection system.

Careful consideration has been given to the design of the AFE to meet the long-term sub-micron gain drift requirement while achieving maximum dynamic range, and minimum distortion. Each of the four identical AFE receivers consists of two identical low-noise amplifiers, and two identical digital attenuators. Systematic gain variation is minimized by utilizing a minimal number of different components with each different component selected from the same die for each individual BPM. Each receiver also incorporates an inter-stage bandpass filter to minimize noise and distortion with sufficient bandwidth to pass the composite RF signal from the diplexer. A

drop-in compatible narrow band interstage bandpass filter is used for the injection system.

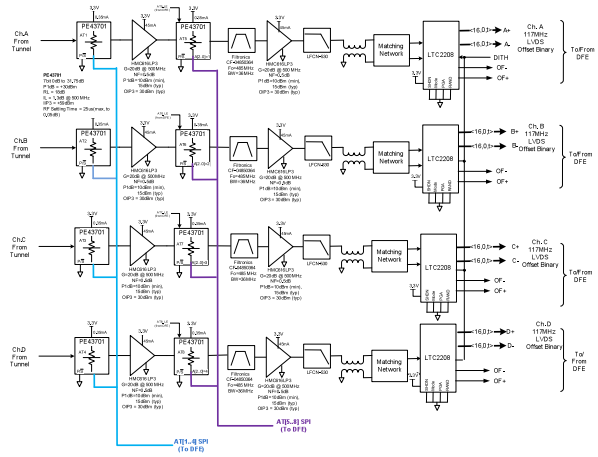

Figure 7: AFE functional block diagram.

The two Peregrine PE43701 Ultra CMOS digital attenuators provide 31dB of dynamic range with 0.25 dB resolution with an IIP3 of +59 dBm. The HMC616 amplifiers are tuned to operate over a band of 400-600 MHz, produce 20 dB of gain at 500 MHz, have an OIP3 of +37 dBm and a noise figure of 0.5 dB. The HMC616 amplifiers have a specified thermal gain dependence of 0.0003dB/0.1° C. Thermal gain dependence measurements of the HMC616 were conducted at BNL yielding a thermal gain dependence of 0.00016 dB/0.1° C, approximately a factor of four lower than the allotted gain variation to maintain 200 nm stability. The thermal gain stability of the HMC616 also revealed perfect thermal tracking at the maximum pilot tone offset frequency of 465 MHz, and the BPM signal frequency of 500MHz.

The AFE has been constructed using Rogers RO4350B RF laminate in conjunction with Rogers RO4450 bonding material. The AFE consists of 6 layers with an overall thickness of 0.93 inch. The AFE board thickness was chosen to match the DFE board thickness to ensure proper connection of the co-planer high speed inter-board connector.

AFE Simulation

An analysis of the AFE performance was first performed utilizing AWR VSS. The goal of the analysis was to design the RF BPM receiver to maximize dynamic range by simultaneous optimization of minimal noise figure, and maximum IP3 at the ADC input. Simulation results demonstrate an overall gain of approximately 22 dB, and a cascaded noise figure of 12 dB including cable losses. The simulated gain satisfies the theoretical gain required to translate the system noise floor to the lower limit of the ADC dynamic range in order to maximize the instantaneous SNR. Instantaneous dynamic range is more of an important factor for single-pass, and TbT processing since only minimal digital processing gain can be realized for these two conditions.

The simulated 1dB compression point of +14dBm ensures linear operation over the full-scale dynamic range of the ADC. The simulated IP3 at the ADC input is +36dBm. It is important to maximize the IP3 at the ADC input to simultaneously maximize immunity to intermodulation distortion at the ADC output.

AFE Laboratory Characterization

The entire RF BPM receiver was prototyped and characterized at BNL utilizing evaluation boards in conjunction with AFE layout development. The measured AFE performance is illustrated below in Figure 8.

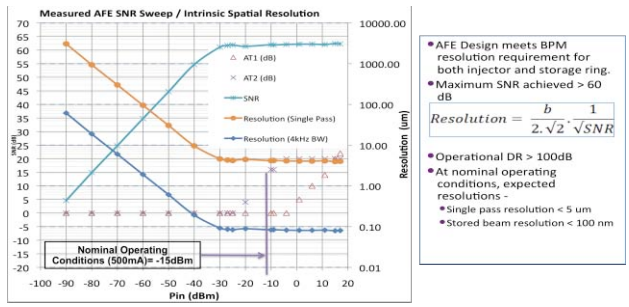

Figure 8: Measured AFE performance.

Data obtained by sweeping RF input using Agilent N5181A RF Signal Generator. The Rhode & Schwarz SMA100A RF Signal Generator was used to provide a 117MHz CW signal to the ADC with a measured RMS jitter of 72fs. Tests conducted with ADC clock synthesizer implemented on the AFE yielding a 312 fs RMS jitter resulted in negligible performance degradation.

The plot in Figure 8 illustrates the intrinsic RF BPM resolution for the case of instantaneous signal processing (e.g. no averaging, single-pass), and for the case of stored beam where an estimated 28 dB of processing gain will be realized. The measured AFE performance demonstrates >100 dB of dynamic range, 100 nm stored beam resolution, and 5um single-pass resolution over the operational dynamic range of 50-500 mA.

AFE Calibration

AFE calibration consists of two parts, a systematic gain normalization performed on each unit prior to installation, and a dynamic calibration utilizing an out-of-band continuous pilot tone inject at approximately -30 dBc at the ADC input. A preliminary assessment of the diplexer which combines the pilot tone and BPM signal exhibits a gain variation of approximately 1ppm/°C, yielding nearly an order of magnitude gain variation margin considering the 200 nm limit.

DIGITAL FRONT END

The digital half of the beam position monitor electronics is referred to as the Digital Front End (DFE) and is responsible for all digital signal processing of the button signals and communication of the results with the control system.

The DFE is shown below in Figure 9. It measures 9.5 by 7.5 inches and sits in the front half of the BPM chassis.

The main component of the DFE is a Xilinx Virtex-5 XCSX95T Field Programmable Gate Array (FPGA). The DFE will be iterated to incorporate a Virtex-6 for the production build. The FPGA handles the digital signal processing chain which will be discussed in the next section. The FPGA also instantiates a soft-core Microblaze processor, which is responsible for all communications with the control system and also coordinates all on-board functionality. Memory for the board is provided with a 256 Mbyte SO-DIMM DDR2 memory module.

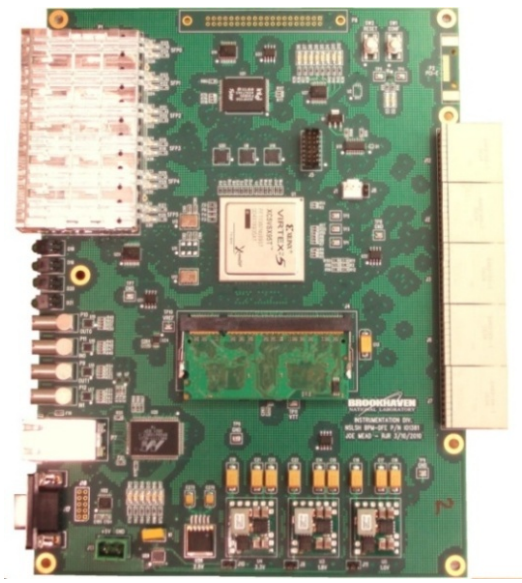

Figure 9: Digital Front End.

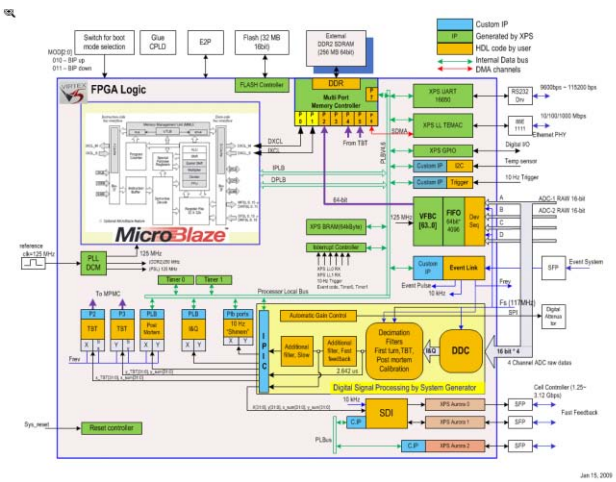

Figure 10: DFE architecture.

This memory provides the program memory space for the Microblaze as well as a large buffer for raw ADC data and turn-by-turn data. The total throughput of the memory is 4 GBytes/sec, which is enough to store continuous bursts of raw ADC data, turn-by-turn data, and provide program and data memory for the Microblaze.

For non-volatile memory the DFE has a single 256 Mbit FLASH memory. This FLASH memory stores the FPGA bitstream as well as the program data for the Microblaze. On power-up the FPGA configures itself from the FLASH memory. When the Microblaze comes out of reset it executes a small boot-loader program from internal memory. This boot-loader fetches the final program from FLASH and copies it to the DDR memory, from which it is executed.

Slow Acquisition and Control

For slow controls, communication with the control system is provided by a gigabit Ethernet interface. Using the Microblaze processor a TCP/IP stack is implemented for robust communication. This interface provides 10 Hz position data as well as on demand requests and configuration settings.

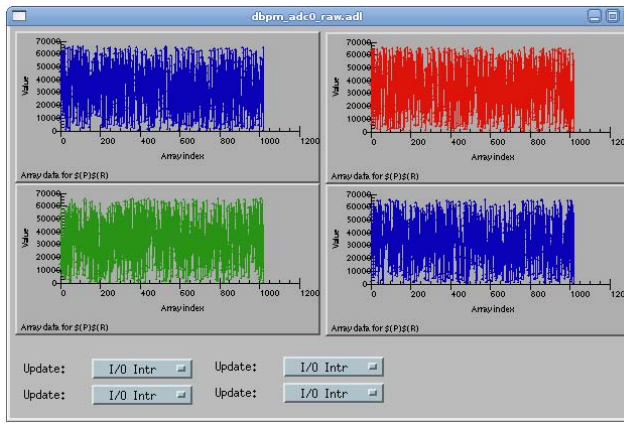

Figure 11: EPICS acquisition of raw ADC data via BPM SA port.

Fast Orbit Feedback

For other communications including fast-orbit feedback data the DFE provides 6 SFP modules, which supports data rates of up 3.2 Gbit/sec. For fast orbit feedback the data needs to be low latency and highly deterministic. This 10 khz updated data therefore bypasses the Microblaze and connects directly from the FPGA fabric to the high speed SERDES section of the FPGA. This data is transmitted to dedicated cell-controllers which can process the data and provide deterministic low-latency updates to the fast magnet power supplies.

AFE Interface

Finally, is the interface with the AFE, which is via five high speed differential Tyco Hm-Zd style connectors. All high speed connections are done via LVDS signalling levels. Four of the connectors are used for the four ADCs, which are 16 bit and run at 117 MHz. The fifth connector is used for configuration and status signals between the two boards.

Digital Signal Processing

The main signal processing element is the FPGA. It is here that all digital signal processing occurs. The FPGA that was chosen was the SX95T, which is rich in hard multipliers to allow for the complex filtering that is

needed. To implement the signal processing, the MATLAB/Simulink environment along with the Xilinx System Generator toolbox is used. This method allows for easy modeling and simulation of the system at a level higher then HDL code. The top level block diagram of the signal processing chain is shown below in Figure 12.

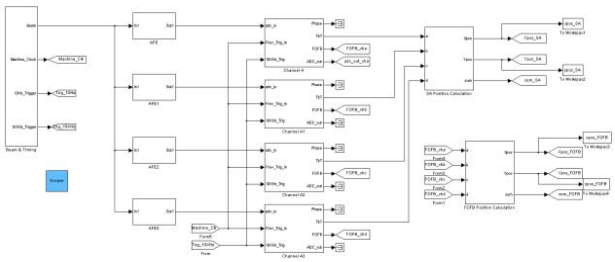

Figure 12: Simulink top-level system simulation model.

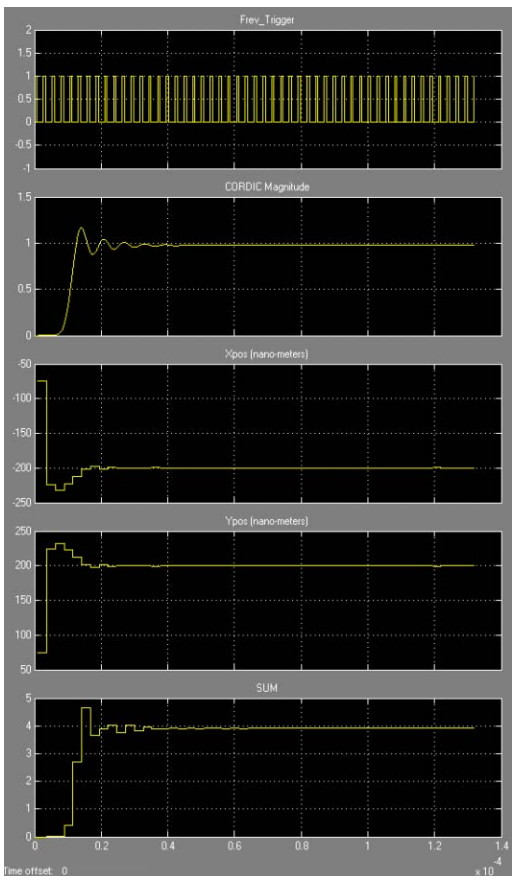

Figure 13: Slow Acquisition System impulse response.

RF BPM CALIBRATION TOOL

The RF BPM Calibration Tool is a Matlab-based program used to measure, and normalize the AFE systematic gains of the four channels prior to installation. Post calibration verification is also performed.

Systematic gain calibration will be performed in a laboratory setting on each BPM prior to installation using the "RF BPM Calibration Tool" (Figure 14). The Factory Calibration consists of a Rhode & Schwarz SMA 100A RF Signal Generator, general purpose computer running the calibration software, and the RF.

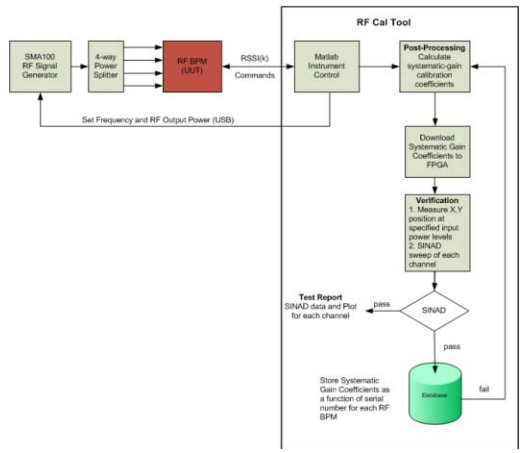

Figure 14: RF BPM calibration tool architecture.

STATUS

Two DFE units have been tested to be 100% functional. Six more DFE units have been received. Ten AFE boards have been received. Five AFE boards are currently being assembled for testing. Ten chassis have been fabricated. Five diplexers will be received in early May. System integration will commence at the end of April 2010. Performance measurements of the diplexer will be conducted on live beam in May. The first system objective is to quantify performance in terms of resolution and drift in the NSLS-II thermally stable racks in the late May-June timeframe. TbT and Single-Pass characterization will follow.

ACKNOWLEDGEMENT

We thank Bacha Belkacem (BNL), Marshall Maggipinto (BNL) for their technical support. We also thank Jonah Webber (ALS) for his assistance in the development of the Multi-Port Memory Controller. Jim Sebak (SLAC), and Mike Chin (ALS) for insightful technical discussions.

REFERENCES

[1] "NSLS-II Preliminary Design Report, 2008"; http://www.bnl.gov/nsls2/project/PDR/
[2] A.Blednykh et al., "Rogue Mode Shielding in NSLS-II Multipole Vacuum Chambers," these Proceedings.
[3] Al DellaPenna Jr, "ADC Considerations and Analysis for Bandpass Sampling Systems", Proceedings of the 2010 Beam Instrumentation Workshop, Santa Fe, NM.
[4] R. Shafer, "Beam Position Monitoring", 1990 AIP.

STATUS OF THE RE-ENTRANT CAVITY BEAM POSITION MONITOR FOR THE EUROPEAN XFEL PROJECT

C. Simon#, O. Napoly, CEA-Saclay/DSM/Irfu, Gif sur Yvette, France
J-P. Prestel, N. Rouvière, CNRS-IN2P3-IPN, Orsay, France.

Abstract

The European XFEL is a research facility, currently under construction in Germany. It is based on a superconducting electron linac including about 100 cryomodules based on the TESLA technology. Each cryomodule is equipped with a beam position monitor connected to a quadrupole at the high-energy end of the cavity string. Around one third of cold BPMs will be re-entrant RF cavities. This contribution describes the present status of the cold re-entrant cavity BPM and presents the measurements performed with BPM pickup and electronics prototypes.

INTRODUCTION

The European XFEL (E-XFEL) is a project to construct an X-ray Free-Electron-Laser international user facility close to DESY in Hamburg [1]. This machine, which is based on the TESLA superconducting RF technology, will accelerate electron beams up to 17.5 GeV at a repetition rate of 10 Hz. The first beam is expected in 2014.

To provide position and charge information along the linac, about 450 Beam Position Monitors (BPM) will be installed. Depending on the BPM location and the performance requirements, different BPM types will be used. In the accelerator modules, two types of BPMs will be installed: button BPMs [2] and re-entrant cavity BPMs. These latest represent 30 % of the cold BPMs. Independent of the type of BPM, they will have a common mechanical interface and the same specifications shown in table1.

Table 1: Cold BPM parameters

Parameter	Value
Beam pipe diameter	78 mm
Length	170 mm
Single bunch resolution (RMS)	50 µm
Operation range for maximum resolution	± 3 mm
Transverse Alignment Tolerance (RMS)	300 μm

One re-entrant BPM is already installed in a warm section of the FLASH linac [3], and achieves 4 µm resolution over a dynamic range of ± 5 mm [4].

In this paper, the status of the XFEL cold re-entrant BPM is presented. A prototype has been manufactured to be installed in an XFEL prototype cryomodule and an electronics based on a Printed Circuit Board (PCB) will be discussed.

#claire.simon@cea.fr

RE-ENTRANT BPM MECHANICS

The length of the re-entrant cavity is 170 mm to respect the constraints imposed by the cryomodule and its aperture is 78 mm (see Fig. 1). It is composed of two parts, in stainless steel, welded together by an electron beam. Flanges are manufactured in the same blocks to get the alignment tolerances. The alignment of the BPM is done by dowel pins with respect to the cold magnet.

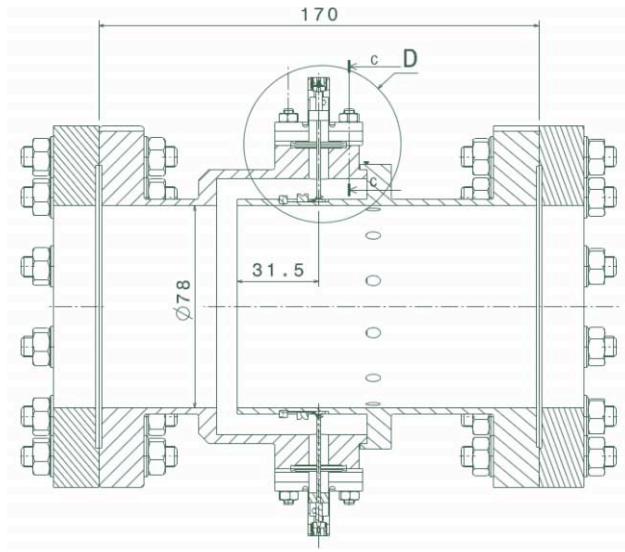

Figure 1: Drawing of the re-entrant cavity BPM.

In order to avoid hydrogen out-gassing, a heat treatment at 950 °C for 2 hours is applied to the BPM cavity. Since it is connected to a cold magnet, the BPM will be at a temperature close to the 4 K level and will be mounted in a clean room. For an effective cleaning, twelve holes of 5 mm diameter are drilled at the end of the re-entrant part.

To reduce the cryo-losses, a 12 µm thick copper coating is deposited on the inner beam pipe. Then, a heat treatment at 400 °C is done to check the copper surface and test the contact of copper and steel.

Each antenna, which is a combination of stainless steel, molybdenum and alumina Al2O3 ceramic brazed, is mounted on the cavity via a CF16 flange. They have to pass cryogenic shocks and to fulfil the conditions of Ultra High Vacuum (UHV). Four copper-beryllium radio-frequency contacts are also welded in the inner cylinder of the cavity to ensure the electrical conduction between the feedthrough inner conductors and the cavity.

RE-ENTRANT BPM INSTALLED IN A XFEL CRYMODULE

The re-entrant BPM will be mounted in an XFEL cryomodule and connected to a cold quadrupole at the high-energy end of the cavity string as shown in Fig. 2.

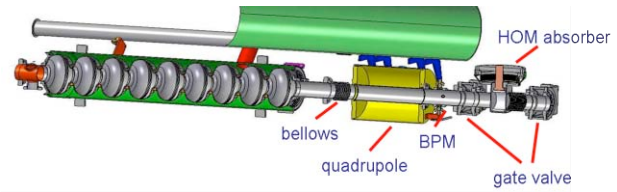

Figure 2: Layout of the downstream end of the XFEL cryomodule.

In 2009, one prototype of re-entrant BPM with copper coating has been manufactured and installed in a prototype cryomodule. Transverse alignment of two parts composing the cavity was measured around 74 µm and the leak rate measured at 4.10^{-10} mbar.l/s. During the fabrication process, a few manufacturing, welding and, copper coating problems appeared. A severe control has to be carried out for the different steps.

The RF measurements were done in laboratory and are presented in Table 2.

Table 2: BPM RF characteristics.

	Frequency (MHz)	**Q_{ext}**
	Measured in lab.	Measured in lab.
Monopole mode	1272	22.3
Dipole mode	1732	47

Frequencies shifted by around 10 MHz in comparison with the simulation results and the measurements done on the re-entrant BPM installed on the FLASH linac [5]. This difference could be due to the cavity geometry. For the next prototype, tolerances were tightened. Cross-talk was measured around 31.8 dB. These RF measurements can be used in the quality control process of the series.

This prototype has been sent to DESY, connected in a clean room to the quadrupole and mounted in an XFEL prototype cryomodule (see Fig. 3).

SIGNAL PROCESSING ELECTRONICS

Electronics concept

The signal processing of the re-entrant BPM uses a single stage down conversion to obtain Δ/Σ. As shown Fig. 4, the difference Δ and sum Σ signals are obtained from a passive 4- ports 180° hybrid which will be installed in a box mounted at the side of the cryomodule. Each coupler is connected to each pair of opposite antennas and transmits the signals to the radio-frequency front-end electronics via some 30 m long semi-rigid cables. The Radio-Frequency front-end (RFFE) electronics is based on a PCB with surface mount components. Because of the low external quality factor, the single bunch response of the cavity has to be broadened before its acquisition.

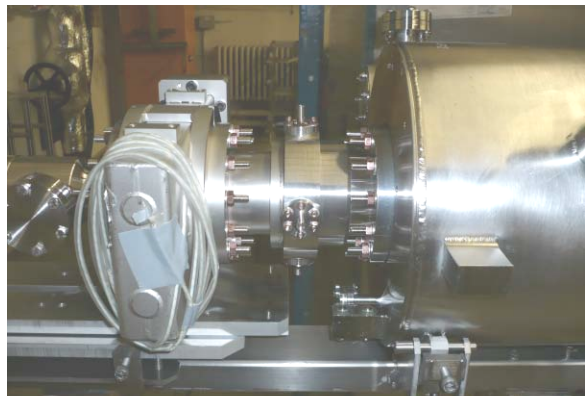

Figure 3: Re-entrant BPM mounted in the XFEL prototype cryomodule.

On the Δ channel, the rejection of the monopole mode signal, which does not depend on the beam position, is produced by a hybrid coupler, a band-pass filter centred at the dipole mode frequency and an in-phase/quadrature-phase (I/Q) demodulation of the dipole mode signal. A reference signal from the linac machine system is combined with a phase-locked loop (PLL) to generate a local oscillator (LO) signal to the mixers around the dipole mode frequency. The I/Q demodulator is composed of mixers used for systems with a high dynamic range, and of 90 ° hybrids couplers chosen for their good phase and amplitude unbalances.

To protect the downstream active electronics from possible high output power from the antennae, an RF limiter is used on each channel.

The Σ signal, which depends on the beam intensity, is measured by a direct detection using a Schottky diode detector.

On each channel, the gain is adjusted thanks to variable attenuators to avoid saturation from ADCs in different operating modes of the accelerator.

The output Σ signal and I/Q IF signals: Ix, Qx, Iy and Qy, detected by the signal processing electronics are differential signals. They deliver to ADCs a pulsed signal of width around 40 ns with a shape close to a Gaussian shape [5] and should have amplitude in the range ± 1.25 V.

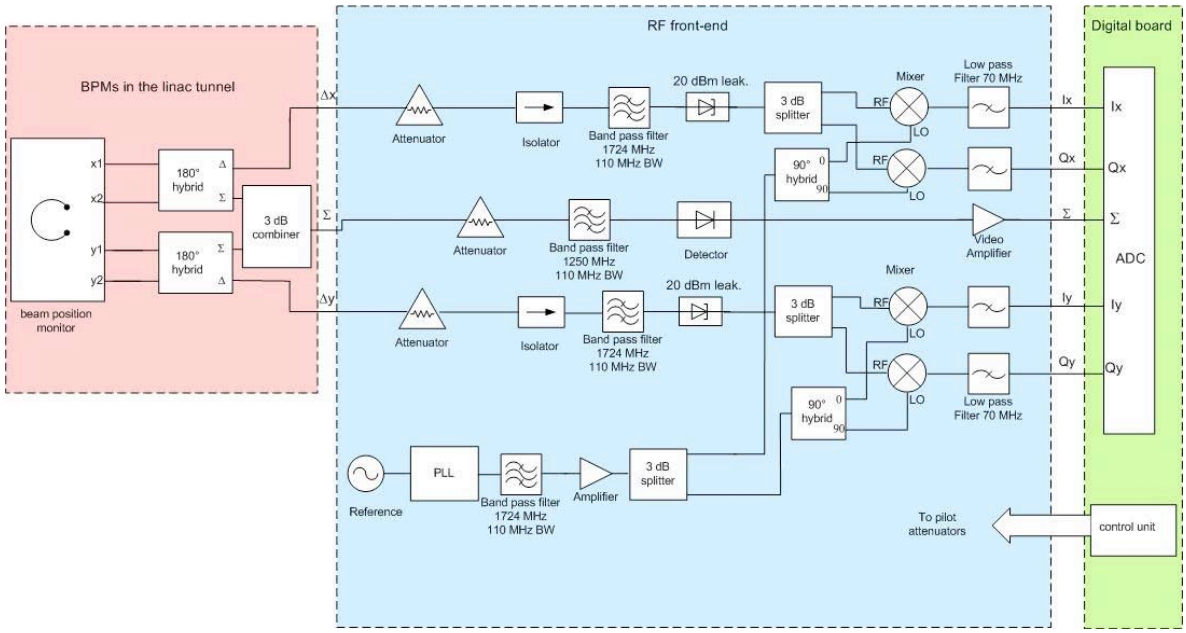

Figure 4: RF signal processing electronics.

The sampling and the interface to the control-system are carried by 16 bits ADCs digital electronics operating at 160 Msps designed by PSI. The phase of the ADC sample clock has to be carefully adjusted to input signals to get correct measurements of a pulsed signal and to determine the peak values of the output signals from the RFFE.

A modular system called Modular BPM Unit (MBU) [6] contains two re-entrant BPM RFFE electronics which occupies one slot each; two additional slots in the MBU are foreseen for theGeneric PSI ADC Carrier Board (GPAC) with its ADC mezzanines. The mechanical form of the re-entrant RFFE is compatible to VME64x.

Preliminary test of the electronics

A re-entrant RFFE printed circuit board (Fig. 5) has been designed in 2009, with a particular attention to the design of the IQ demodulator.

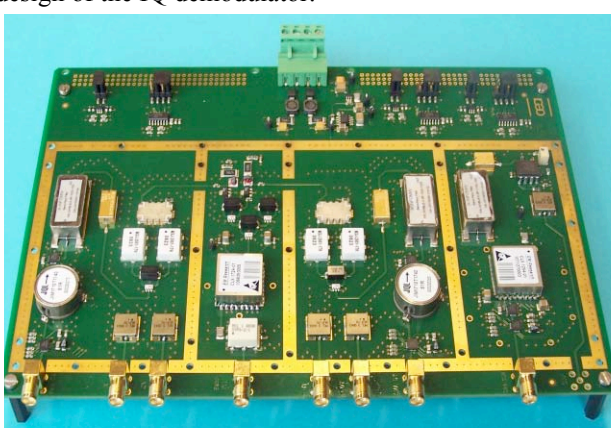

Figure 5: Re-entrant RFFE board.

To test this RFFE electronics prototype, first measurements have been carried out in laboratory. A test bench is created with a pulse generator. Pulsed signals at the monopole and dipole mode frequencies were injected to the RFFE board with amplitude corresponding to an offset of 0.5 mm. The output signals Ix, Qx, Iy, Qy and Σ deliver information to ADCs and the amplitude is determined by the following equation (see Eq 1).

$$A_n = \sqrt{(I_n - I_{ADC})^2 + (Q_n - Q_{ADC})^2} \qquad (1)$$

where n is the sample and I_{ADC} and Q_{ADC} are the offsets of ADCs. The RMS jitter calculated by the standard deviation is around 0.68 µm on the X channel, and around 0.91 µm on the Y channel.

CONCLUSION

The status of the re-entrant BPM is presented in this paper. On the last prototype, the RF frequencies being shifted of a few MHz, tolerances of the cavity were tightened. A better quality control will be done to check each step of the fabrication process.

First lab test results of the RFFE board are promising for the resolution that needs to be achieved. However, this electronics was designed with a reference frequency of 9.028 MHz while 216 MHz should be used for the XFEL machine. Some components will be therefore, changed. Moreover, the lab test does not include the environment noise which is generally predominant. Beam tests with the re-entrant cavity, RFFE electronics and digital back-end electronics in their final version are required in order to

check the impact of that environment on the beam position.

ACKNOWLEDGMENTS

We thank our colleagues from DESY and PSI: D. Nölle, S. Vilcins, B. Keil, R. Kramert for their support and the fruitful discussions on the BPMs. We wish to acknowledge MDI, MKS and MVS teams at DESY for the installation of BPM in the XFEL prototype cryomodule. Finally, we would like to thank all our colleagues from CEA Saclay for their advices and their help on this project.

REFERENCES

[1] "XFEL Technical Design Report", DESY 2006-097, http://xfel.desy.de.
[2] D. Nölle et al, "BPMs for the XFEL cryomodule", DIPAC07, Venice.
[3] V. Ayvazyan et al., Eur. Phys. J. D 37, 297 (2006).
[4] C. Simon et al, "Beam position monitors using a re-entrant cavity", DIPAC07, Venice.
[5] C. Simon, et al., "Performance of a reentrant cavity beam position monitor", Physical review special topics – accelerators and beams 11, 082802 (2008).
[6] B. Keil, "Infrastructure Requirements for the European XFEL Beam Position Monitor and Intra-Bunch Train Feedback System Electronics."

MAGNETIC COUPLED BEAM POSITION MONITOR FOR THE FLASH DUMP LINE

N. Baboi, A. Brenger, D. Lipka#, J. Lund-Nielsen, K. Wittenburg, DESY, Hamburg, Germany.

Abstract

To measure the beam position at the entrance of the FLASH dump a position monitor has been installed outside of the vacuum in a nitrogen atmosphere. When a charged particle travels through the gas it ionizes the atoms. Therefore the signal from a capacitive button BPM would be contaminated by high backgrounds. To avoid this a magnetic coupled monitor has been designed. The monitor consists of four longitudinal loops symmetrically arranged in the pipe wall. An analytical expression of the signal for this monitor is derived and compared with simulations. Measured data are compared with predictions.

INTRODUCTION

A new diagnostics section before the beam dump has been installed at FLASH [1]. A major component is a new beam position monitor (BPM). The beam exits the vacuum system through a special window before reaching the dump. Its position must be measured here to verify the proper absorption of the beam in the dump. A beam-pipe here connects the exit window to the dump.

The charged particles of the beam ionize the N_2 gas volume between the window and the dump. A 1 GeV electron has an ionization loss of 3 keV/cm in nitrogen. The effective ionization length is the distance between the window and the dump (l = 15 cm). The energy loss over this length is 45 keV. According to the production yield [2] this corresponds to about 1300 electron-ion pairs per beam-electron. In the absence of an electric field most of the pairs recombine but some would reach the electrodes of a BPM. In this case the signals of an electric coupled button or stripline BPM would be strongly influenced by the electron-ion pairs [3]. The influence can be drastically reduced by measuring not the electric but the magnetic field of the fast moving charge.

The coupling has been realized with a thin metallic wire forming an electric loop in the pipe. The normal direction of the area of the loop is parallel to the magnetic field of the beam to maximize the signal amplitude. In Figure 1 a sketch of the magnetic coupling is shown. This paper discusses the derivation of analytic expressions for the signal of this BPM and the results are compared with simulations and with measured signals.

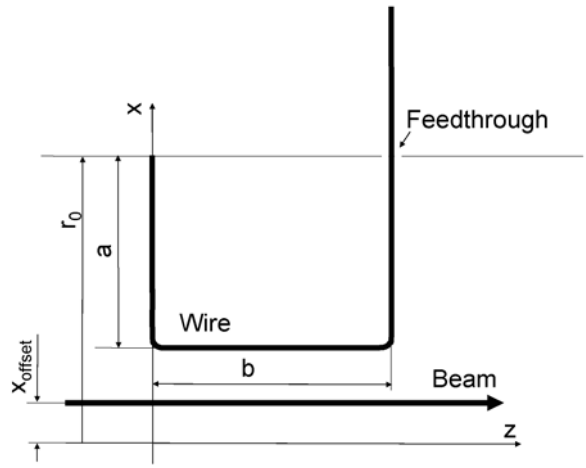

Figure 1: A sketch of one quarter of the detector. A wire forms a loop in the pipe with radius r_0=61.5 mm in the y plane and surrounds an area $A = a \times b$, with a=12 mm and b=10 mm. The signal is transferred with a feedthrough.

ANALYTICAL SOLUTION

The magnetic field of a beam with current $I(t)$ is given by the Biot-Savart rule as

$$\vec{B}(\vec{r},t)=\frac{\mu_0 I(t)}{2\pi\rho}\vec{e}_\phi,$$

with μ_0 the vacuum permeability and ρ the distance to the z-axis in cylindrical coordinates. The beam current can be expressed as

$$I(t)=q_0\frac{1}{\sigma\sqrt{2\pi}}e^{-\frac{1}{2}\frac{t^2}{\sigma^2}},$$

with q_0 the beam charge and σ the bunch length in units of time. In Cartesian coordinates the magnetic field is

$$\vec{B}(x',y',t)=\frac{\mu_0 I(t)}{2\pi\left(x'^2+y'^2\right)}\begin{pmatrix}-y'\\ x'\\ 0\end{pmatrix}.$$

The magnetic field with a horizontal offset can be described by a coordinate transformation: $x'=x_{offset}-x$, $y'=y$, $z'=z$, resulting in

$$\vec{B}_1(x_{offset},x,y,t)=\frac{\mu_0 I(t)}{2\pi\left(\left(x_{offset}-x\right)^2+y^2\right)}\begin{pmatrix}-y\\ x_{offset0}-x\\ 0\end{pmatrix}.$$

This field is valid without the beam pipe. To include it a second current is introduced with $I_2(t)=-I(t)$. The direction

#dirk.lipka@desy.de

of this current is parallel to the *z* axis. The distance x_2 to the pipe has to satisfy the following boundary conditions:

- for $x_{offset}=0$: $x_2=\infty$
- for $x_{offset}=r_0$: $x_2=r_0$.

This results in

$$x_2 = \frac{r_0^2}{x_{offset}}.$$

The offset x_2 can be used as a coordinate transformation for a second magnetic field component $\vec{B}_2$:

$$\vec{B}_2\left(x_{offset},x,y,t\right)=\frac{-\mu_0 I(t)}{2\pi\left(\left(\frac{r_0^2}{x_{offset}}-x\right)^2+y^2\right)}\begin{pmatrix}-y\\ \frac{r_0^2}{x_{offset}}-x\\ 0\end{pmatrix}.$$

The resulting magnetic field is

$$\vec{B}\left(x_{offset},x,y,t\right)=\vec{B}_1\left(x_{offset},x,y,t\right)+\vec{B}_2\left(x_{offset},x,y,t\right)$$

for the range $x_{offset}\in\{-r_0+a, r_0-a\}$ and $y=0$. For an offset in the vertical plane one can exchange *x* and *y* accordingly.

The magnetic flux is given by

$$\Phi\left(x_{offset},t\right)=\int\vec{B}\left(x_{offset},x,y,t\right)\cdot d\vec{A},$$

with the area $d\vec{A}=dxdz\vec{e}_y$, see Figure 1. Here only the vertical component of the magnetic field contributes to the flux which results in

$$\Phi\left(x_{offset},t\right)=\frac{\mu_0 I(t)}{2\pi}\int_{x=r_0-a}^{r_0}\int_{z=0}^{b}\left(\frac{1}{x_{offset}-x}-\frac{1}{\frac{r_0^2}{x_{offset}}-x}\right)dxdz$$

$$=\frac{\mu_0 I(t)b}{2\pi}\left[E\left(x_{offset}\right)-F\left(x_{offset}\right)\right]$$

with $E\left(x_{offset}\right)=\ln\left(\frac{x_{offset}-r_0+a}{x_{offset}-r_0}\right)$

and $F\left(x_{offset}\right)=\ln\left(\frac{r_0^2-r_0x_{offset}+ax_{offset}}{r_0^2-r_0x_{offset}}\right)$.

Here the beam offset has been removed from the numerator so that the equation can also be used for $x_{offset}=0$. The induced voltage is

$$U\left(x_{offset},t\right)=-\frac{d\Phi}{dt}$$

$$=-\frac{\mu_0 b}{2\pi}\left[E\left(x_{offset}\right)-F\left(x_{offset}\right)\right]\frac{dI(t)}{dt}$$

with

$$\frac{dI(t)}{dt}=-q_0\frac{1}{\sigma^3\sqrt{2\pi}}te^{-\frac{1}{2}\frac{t^2}{\sigma^2}}.$$

One can see that the voltage strongly depends on the bunch length. The amplitude is located at the bunch length $t=\pm\sigma$ and depends linearly on the area *A*.

To measure the position in a plane, introduce two opposite wires and calculate the individual amplitudes

$$U_1=U\left(x_{offset},\sigma\right)=D\frac{q_0}{\sigma^2}\left[E\left(x_{offset}\right)-F\left(x_{offset}\right)\right],$$

with $D=\mu_0 be^{-1/2}/\left(2\pi\sqrt{2\pi}\right)$ and

$$U_2=U\left(-x_{offset},\sigma\right)=D\frac{q_0}{\sigma^2}\left[E\left(-x_{offset}\right)-F\left(-x_{offset}\right)\right].$$

When the offset tends to be zero the second term (*F*) also approaches zero. Using the difference-over-sum-method one gets:

$$Q=\frac{\Delta}{\Sigma}=\frac{U_1-U_2}{U_1+U_2}.$$

Here the dependencies of the bunch length and charge are eliminated. Applying this method one can measure the beam offset. The sensitivity *S* depends only on the radius r_0:

$$S=\left.\frac{dQ\left(x_{offset}\right)}{dx_{offset}}\right|_{x_{offset}=0}$$

Note that the above equations for the voltage are only applicable for an offset in one plane.

SIMULATIONS

The cross section of the beam-pipe in front of the beam dump is an octagon, as shown in Figure 2. The distance between two opposite planes is 123 mm. Each wire forms a loop with an area of A=120 mm^2. The wire has a diameter of 1 mm. The design has been transferred to the simulation tool CST [4]. The beam is simulated longitudinally as a Gaussian distribution, a total charge of 2.5 nC and a bunch length of 660 ps; these parameters are chosen to compare with the measurement. Figure 3 shows the shape of the voltage of two opposite sensors from the calculation and the simulation with an offset of 10 mm. The analytical expressions clearly agree very well with the results of the simulations.

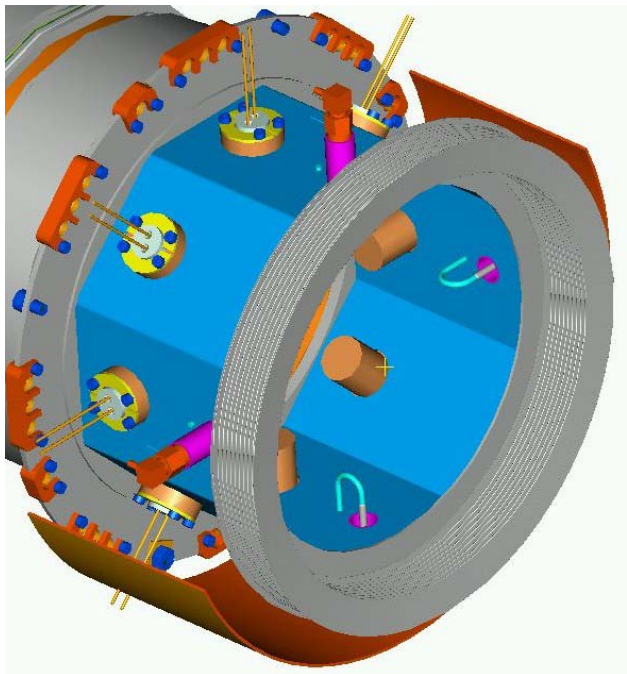

Figure 2: Construction view of the end of the beam-pipe in front of the dump. Two wire-loops are visible.

In addition the difference-over-sum-method has been calculated analytically and simulated and the results are shown in Figure 4. They are in very good agreement; the calculation describes even the non-linearity at large offsets. The slope at x_{offset}=0 gives the sensitivity to be S=0.032/mm. This is comparable to a button BPM with the same pipe diameter and a button diameter of 20 mm, (which results in S_{button}=0.022/mm [5]).

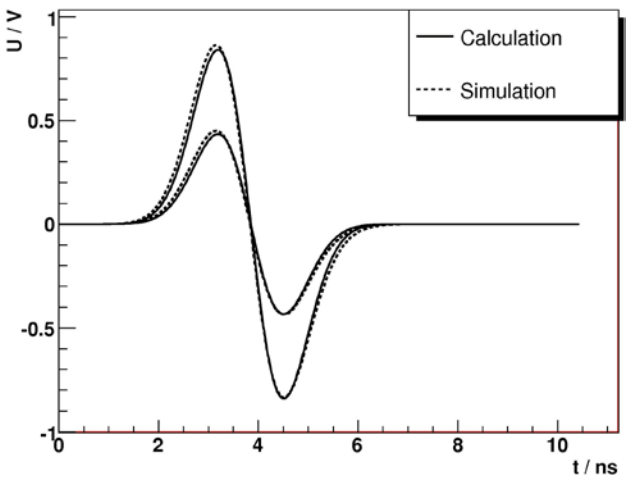

Figure 3: The time response from the analytic calculations and from the simulations for the magnetic coupled BPM for a charge of 2.5 nC, bunch length of σ_z=660 ps and an offset of 10 mm for two opposing sensors.

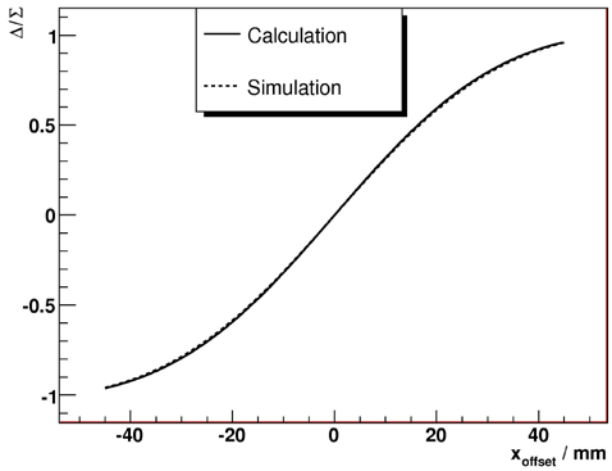

Figure 4: The difference-over-sum as a function of beam offset for the analytic and simulation methods. The results are in very good agreement; so much so that it is difficult to distinguish the lines. The slope at x_{offset}=0 corresponds to the sensitivity.

MEASUREMENTS

The new diagnostics section in front of the dump was built and installed at FLASH before the start of a 9 mA study-run in Sept. 2009. In Figure 5 the beam-pipe with the BPM is shown.

Figure 5: The end of the diagnostics beam line with the wire-loops. The 8 cylinders upstream of the wire loops contain beam halo monitors [1].

The beam measurements were done during the 9 mA study-run. During this time the bunch-charge was not the typical value of 1 nC, but 2 to 3 nC; for this measurement it was 2.5 nC. The actual bunch length is much shorter than 660 ps, which was taken for the calculations and simulations. But the cable between the BPM and the rack room acts as a low-pass filter such that higher frequency components are attenuated. In addition a low-pass filter with 200 MHz threshold (with 3 dB attenuation) was used to filter the first TEM mode of the beam-pipe, which is approximately 1.71 GHz. (This is lower than the corresponding frequency for a round tube of 1.75 GHz due to the octagonal shape). The longer bunch length

assumed in the calculations and simulations corresponds to the signal after the cable and low-pass filter.

The measurements of the signals from all four wires of the BPM are compared with the simulation in Figure 6 (the analytical solution is not shown because the beam has large offsets in both planes). The measurements were taken with a Tektronix TDS 6604 oscilloscope. The attenuation of the cables and the low-pass filter has been corrected in the measurement. Therefore one can see the low-pass filtered amplitude of the beam at the exit of the BPM. The measurement corresponds to a horizontal beam offset of 39 mm and a vertical offset of 16 mm. In the positive branch of the amplitudes there is good agreement between measurement and simulation. The negative amplitudes of the measurement are smeared out due to the cables and low-pass filter. Nevertheless, the simulation results predict well the voltage distribution for all beam positions. The good agreement also indicates a negligible influence of the ionization products on the BPM readings.

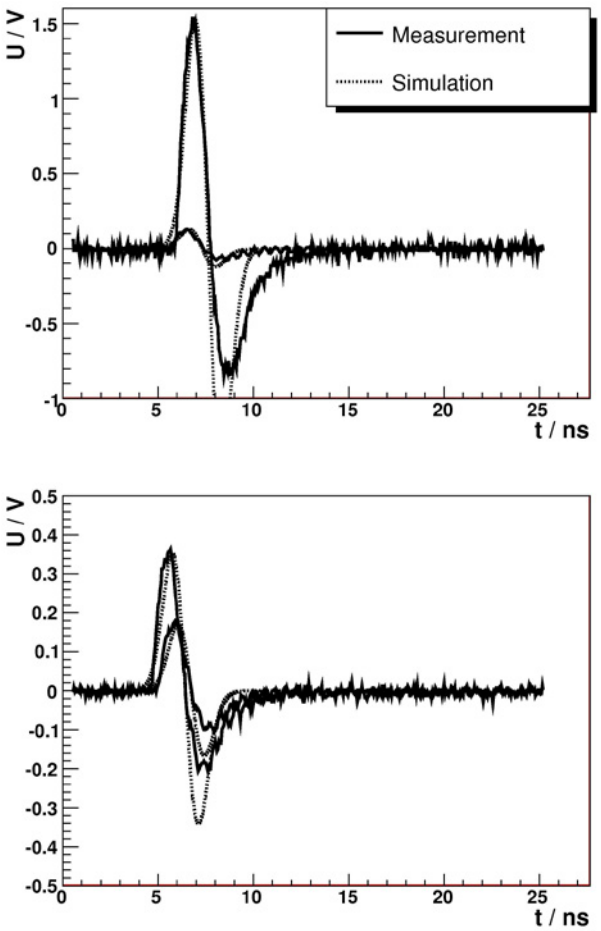

Figure 6: The signal voltage as a function of time from all wires of the BPM. The upper diagram shows the two opposing wire for the horizontal plane, the lower diagram shows the corresponding wires for the vertical plane The amplitudes are corrected for the attenuation of the cables and low-pass filter. The results of the simulations are included with a bunch length of σ_z=660 ps and a bunch charge of 2.5 nC.

SUMMARY

A BPM is introduced directly in front of the FLASH beam dump. The BPM is positioned outside of the vacuum system in a nitrogen atmosphere. A magnetic coupled BPM has been chosen to avoid the distortion of the signals from the ionized electron-ion pairs. The derivation of analytic expressions of the voltage as a function of time from a magnetic coupled BPM is presented and the results compared with simulations. Both are in good agreement. The sensitivity is comparable to that of a button BPM. The device has been manufactured at DESY and installed in the dump line. The first measurements show good agreement with the simulations. No influence of the ionization products on the signals could be detected.

ACKNOWLEDGEMENT

Thanks to M. Dohlus for the idea of superimposing two fields to satisfy the boundary condition of a pipe. B. Lorbeer performed the measurements of the attenuation of the cables.

REFERENCES

[1] N. Baboi et al., „New electron beam diagnostics in the FLASH dump line", these proceedings: TUPSM093.
[2] C. Grupen, "Teilchendetektoren", BI-Wiss.-Verl.,ISBN 3-411-16571-5, 1993.
[3] Rh. Jones, "CNGS Target Area Beam Position Monitors", talk at NBI2003.
[4] Computer Simulation Technology (CST), http://www.cst.com.
[5] G. Kube, "Sensitivity estimation for the PETRA-III beam position monitors based on a Boundary Element Method", DESY technical note 07-01, 2007.

COMMISSIONING RESULTS AND IMPROVEMENTS OF THE MACHINE PROTECTION SYTEM FOR PETRA III

T. Lensch#, M. Werner, DESY, Hamburg, Germany

Abstract

PETRA III is a high brilliant synchrotron light-source operating at 6GeV. The commissioning of the machine had started in April 2009 [1]. In the first months of operation the Machine Protection System (MPS) ran on basic MPS requirements to protect absorbers and vacuum chambers in the damping wiggler section and the undulator section against synchrotron light. Therefore several alarms distributed along the machine are identified and within 100µs a dump command is created. The beam is dumped within 400µs by switching off the RF system [2]. Prior to the first user runs different improvements increasing the reliability and availability were planned and partly implemented in the MPS. This paper presents commissioning results of the system and gives an overview of these new implementations as well as a more detailed discussion of some alarm conditions and the dump procedure. Additionally some key aspects of the Temperature Interlock as one major alarm deliverer are described.

INTRODUCTION

Starting in June 2007 the former preaccelerator PETRA II was rebuilt to a high brilliant 3rd generation synchrotron light source operating at 6 GeV. In seven eights of the 2.3km long accelerator tunnel all installations were removed, modernized and reinstalled. In one eight an experimental hall was built which houses 14 undulator beamlines, experimental hutches and laboratories. In two straight sections of the machine damping wigglers are installed to reduce the horizontal emittance to the designed value of 1 nm rad [1]. A Machine Protection System (MPS) is required to protect absorbers against too high impact of synchrotron light and wigglers and undulators against losses of the electron beam. The MPS needs to dump the beam within several hundreds microseconds in case of unsafe conditions, detected from several alarm deliverers located around the machine [2].

The commissioning of the PETRA III machine as well as the MPS started in March 2009, the first beam was stored in April 2009. In the first months of operation with low beam currents the MPS ran on basic requirements to prevent the machine from damage. Since then diverse functionalities for increasing the availability and reliability of the system were implemented as well as upgrades for diagnostic purposes.

timmy.lensch@desy.de

MPS CONFIGURATION

The MPS is distributed in nine PETRA III halls in 19" crates. A connection to the control system is made via the in-house fieldbus SEDAC. At one position (east hall) the beam current (DC) is measured and digitally distributed by a redundant optical fibre loop which transmits both beam current information and dump information to all crates in the system. 24 alarm modules are shared in 10 crates. Each alarm module features 16 inputs for several alarm deliverers (e.g. beam position monitors (BPM), temperature interlock, etc.).

Every alarm input can be masked by an individual beam current threshold. There are three types of alarms connected to the MPS:

- To protect the machine against damaging by synchrotron radiation or the electron beam about 170 alarms can create a trigger which dumps the beam.
- Further 16 alarms are used to mask other inputs.
- Additionally 50 alarms from magnet power supplies, the RF system and kickers are connected to the MPS which are not triggering a dump but allow a first alarm detection. This can help operators finding the reasons of beam losses and dumps [2].

Figure 1 shows the connections of the MPS; figure 2 shows the topology of the MPS.

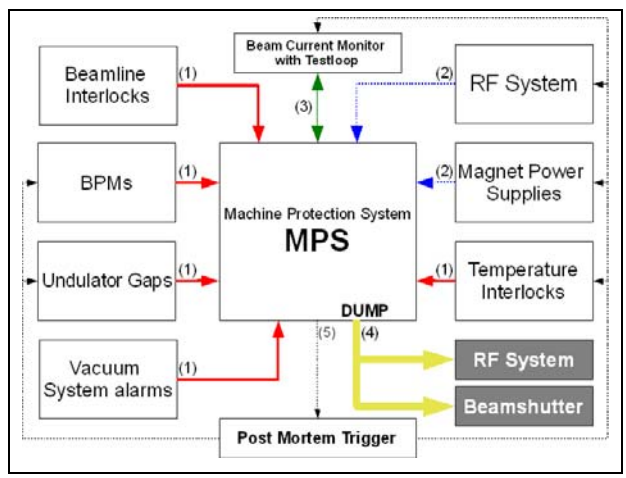

Figure 1: Connections of the MPS. Diverse alarm deliverers are connected to the MPS: red (1) Alarms generate a beam dump; blue (2) alarms are used for the first alarm detection. The MPS compares the measured beam current (green, 3) with an individual beam current threshold for each alarm input. The RF system and beam-stoppers are used for a beam dump (yellow, 4). A post mortem trigger (black, 5) is sent to several systems (e.g. RF system, BPM system).

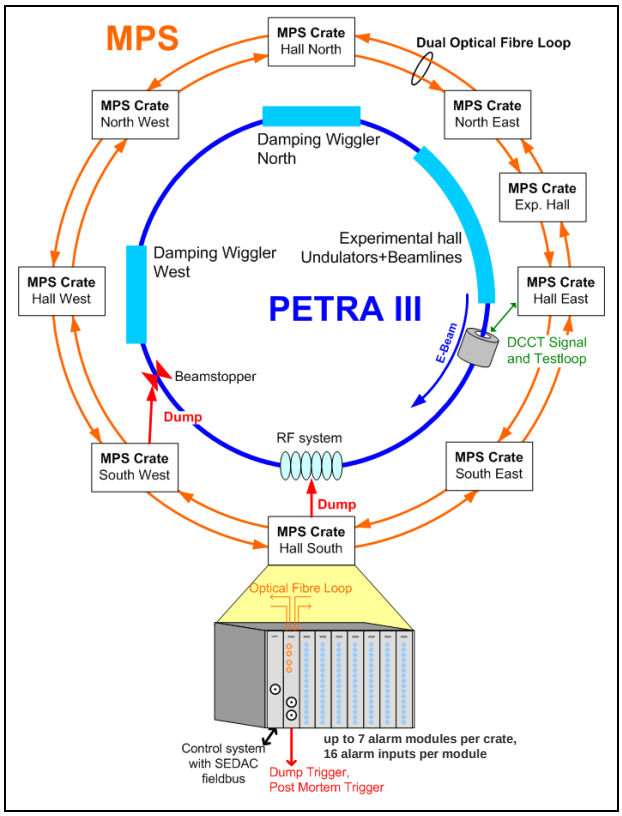

Figure 2: Topology of the Machine Protection System. The inner circle demonstrates the scheme of PETRA III.

Dumping the Beam

If a dump trigger is created due to fulfilled alarm conditions, a 5ms inhibit pulse is send to the RF system. The RF system then stops delivering power to the beam. Within approximately 400µs the beam is lost on a dedicated scraper [8]. As a slow fallback two beam-stoppers are driven into the beam aperture, which inhibits also a new injection of beam into the machine until the operator resets the MPS manually.

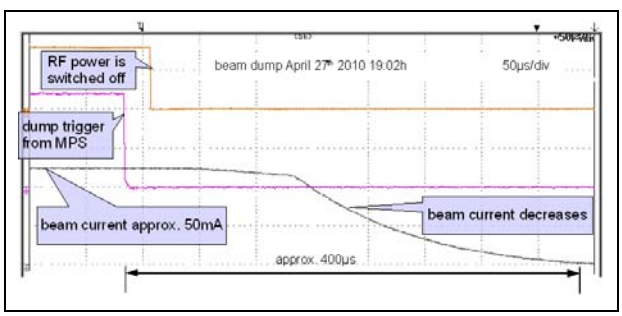

Figure 3: The falling edge of the MPS dump trigger (magenta) switches off the klystron power (orange). The beam (grey) is lost in approx. 400µs after the dump trigger. (courtesy of R.Onken, DESY)

Post Mortem Trigger

The MPS detects a beam loss by a fast drop in the measured beam current. This event is distributed through the optical fibre loop to all MPS crates from where the post mortem trigger is sent to several external systems, such as BPM system, RF system and magnet power supplies. The collected post mortem datasets can be used for time correlated analysis.

ALARM DELIVERERS

A dump can be triggered by the following systems:

Beam Position Monitors

A total number of 227 BPMs are installed in PETRA III for orbit monitoring, feedback and machine protection. The system is based on the Libera Brilliance electronics [3].

95 of these BPMs are connected to the MPS. They are placed mainly in the two damping wiggler sections (12 BPMs each) and in the experimental hall between the undulators. The alarm trigger of the BPMs in the undulator and damping wiggler sections are partly masked (disabled) by the “open” status of undulator or wiggler gaps [2] because then they do not limit the aperture.

Damping Wiggler Section and BPMs

After the first weeks of commissioning all damping wigglers where closed by hand around the beam pipe. Since then the permanent magnets of the wigglers had to be protected against the electron beam, and the absorbers placed between each wiggler had to be protected against synchrotron radiation. The power of several absorbers was limited to 26kW and 100kW respectively 120kW at that time. This corresponded to a beam current of 35 mA [8]. If at least two BPMs send an alarm and the beam current is above the threshold of 35mA the MPS dumps the beam. The BPM itself detects critical states by an orbit deviation of approximately +/-10mm in horizontal or +/-2mm in vertical direction to send an alarm to the MPS [5].

Undulator Section and BPMs

In the undulator section a set of two (single undulator) or three (double undulator) BPM alarms are masked/disabled by the corresponding “open” undulator gap [2]. The power of the synchrotron radiation without correct orbit (BPM) must not exceed 30W. An undulator gap of 12mm with a beam current of 1mA gives a power of approximately 15W in the beamline [6, 7]. Based on this, gaps closer than 35mm and a beam current exceeding 1mA in combination with BPM or other beamline alarms (e.g. fast vacuum shutters in the beamline) cause a dump trigger through the MPS. In the undulator section the BPM alarms are enabled by orbit distortions of approximately +/-0.5mm in horizontal and +/-0.2mm in vertical direction [5].

Temperature Interlock

The temperature interlock modules are an in-house development. Each module concentrates up to 8 PT100 sensors connected in 4-wire technique. Via a fieldbus connection temperatures can be read-out and individual temperature thresholds for each sensor can be configured to enable an alarm signal.

About 1.800 temperature sensors are located at certain locations such as absorbers and the beam chamber in the undulator and damping wiggler sections. Further sensors are placed on magnets and water cooling components for absorbers. 440 of these sensors are placed at sensitive locations and can generate an alarm for the MPS if a sensor exceeds a temperature threshold. 23 sensor groups are composed, each activated if at least one sensor of the group generates an alarm, to reduce the number of necessary MPS alarm inputs by a factor of 20.

The remaining sensors are used for information as shown in the temperature Interlock GUI in figure 4.

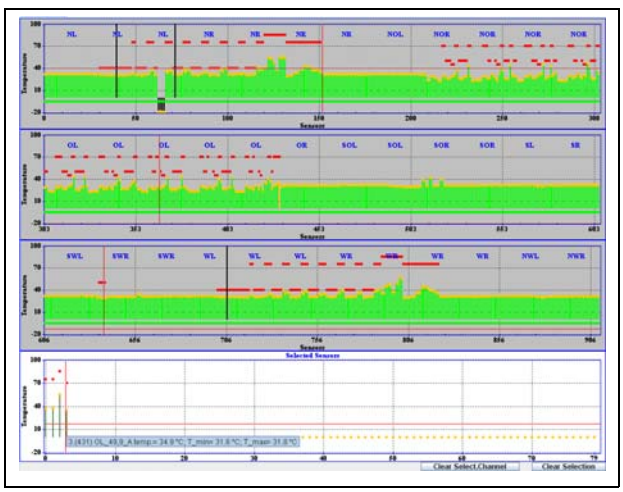

Figure 4: Temperature Interlock Console program. All sensors around the machine are displayed on one screen. Each sensor is represented by a vertical green bar. If the sensor is configured with a threshold, this is displayed by a horizontal red line. A horizontal yellow line at each sensor shows a maximum temperature of the sensor, updated every 60s.

Other Alarms

Beside undulator and wiggler gaps, BPMs and temperatures there are several other alarm sources such as vacuum shutters, getter pumps, a screen monitor, beamline interlock sensors and water flow sensors (absorber cooling) connected to the MPS for generating a beam dump in case of unsafe conditions. Also alarms from the RF system, the magnet power supplies, feedback systems and kickers are connected to the MPS to enable a detailed first alarm detection [2]. An important example are alarms generated by the RF system in case of RF-glitches and -failures which causes a beam loss itself. Together with the timestamps of the alarms, the beam current behaviour and the post mortem trigger one can sample a lot of information for a detailed analysis of the beam loss.

COMMISSIONING OF THE MPS

In the first months of PETRA III operation the MPS ran with basic requirements. During this time the major task was to protect the machine running at low beam currents. Not all functionalities to achieve a high availability were implemented. Observing the MPS hard- and software also led to ideas of suggestive, needful improvements and fine tuning for the system.

Step by step more alarm deliverers where connected to the MPS. With increasing beam current and better understanding of the machine some beam current thresholds in the MPS where also changed to higher values. As well temperature thresholds were increased and new sensors were installed at some new locations.

Due to extensive tests in the laboratory before installation the hardware worked without any problems from the very first beginning.

Since features like first alarm detection and beam loss analysis were not implemented from the beginning, this sometimes had to be done by hand. The first undulator operations took place with beam currents below 1mA. Since high accuracy for such small currents was not foreseen in the MPS requirements some improvements were implemented.

Beside the main goal of protecting the machine from damage, the MPS can serve another important purpose: with its connections to a number of other systems it can support the operators with important information about the chronological order of alarms to derive the reason of a beam loss or beam dump.

FIRMWARE IMPROVEMENTS

The hardware configuration of the MPS mostly remained unchanged since the beginning of the commissioning. Due to the flexibility of FPGAs as the heart of the modules important improvements for several functionalities such as beam loss detection or averaging mechanisms for the measured beam current can be made.

Beam Current Measurement

The MPS measures the beam current with a dedicated beam current monitor (BERGOZ MPCT) [2]. Regarding to the basic requirements the necessary resolution was 1mA. Just at the beginning of the commissioning a more accurate beam current measurement was required to operate with undulators below 1mA. To satisfy this requirement, an averaging of 100ms was implemented in the firmware what still guarantees a safe machine operation. To ensure still a fast tracking of the beam current in the MPS after a beam loss, the averaging mechanism has to be handled dynamically. Therefore the averaging is switched off after detecting a beam loss and is subsequently switched back to the 100ms averaging algorithm. This implementation works very well and

provides both a stable beam current measurement with a resolution of 0.1mA and a fast tracking of the beam current in case of a beam loss.

Beam Loss Detection and Post Mortem Data

The new firmware detects beam losses and then triggers an FPGA internal post mortem recorder which stores the 83kS/s beam current values (12 bit) and the dump trigger signal over a total time of 24ms (+/- 12ms relative to the beam loss). This information is displayed in the MPS console GUI and helps the operator to interpret a beam loss by time relation between a beam loss and a dump trigger and the shape of the beam current decrease during the beam loss. Figure 5 shows a detected beam loss without a dump trigger. In figure 6 a dump was generated after a beam loss. Figure 7 shows a dump trigger generated by the MPS with the subsequent beam loss.

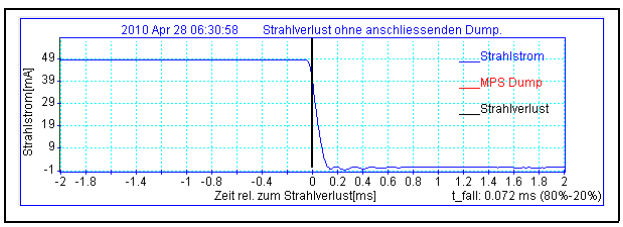

Figure 5: A beam loss occurred (e.g. by RF fail). No dump trigger was generated. The inwards circulating beam causes no dump trigger by BPMs after the beam loss due to the dynamic averaging in the MPS.

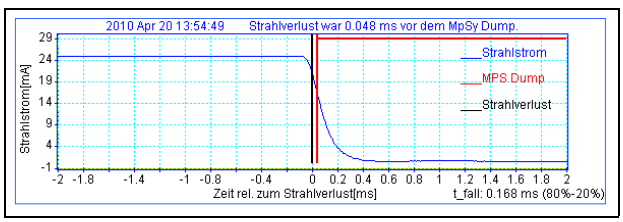

Figure 6: As a result of beam loss a dump is generated just after by the MPS. Due to an inwards circulating beam detected by undulator BPM with small horizontal orbit thresholds the dynamic averaging in the MPS reacts too slow.

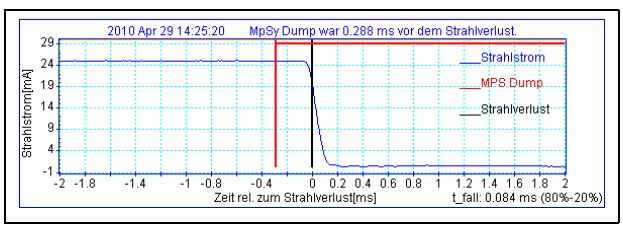

Figure 7: The MPS generates a dump trigger in consequence of fulfilled conditions (e.g. BPM alarms, temperature interlock) resulting in a beam loss.

First Alarm Detection

Preliminary first alarm detection is established in the firmware. This feature points to the alarm input(s) which first fulfilled the dump conditions. The module wide accuracy is approximately 100ns. The system wide accuracy (approximately 30µs) is only given by the delay of the optical loop which is used to send a dump condition among other things to all modules in the MPS.

In a later version more accurate first alarm detection supports timestamps to get a system wide resolution better than one turn (approximately 2µs).

Redundancy of the Optical Fibre Loop

The optical fibre loop is used for transmitting beam current information, dump trigger and synchronisation information in the MPS [2]. For the first time only one of the loops was used. By implementing the second loop the correct operation of the MPS is guaranteed even if one fibre breaks.

SOFTWARE IMPROVEMENTS

In the MPS console program (see figure 8) each alarm input is represented by an icon which shows the state of the input (e.g. alarm/no alarm, dump, disabled input).

One of the first improvements in the software was a simple archiving functionality. With this tool all alarm inputs can be viewed later and support both operators and designers detecting failures and the specific time of events with a resolution of 0.5s. The new implemented first alarm detection in the hardware is displayed by a special icon in the MPS console program so that the operator's attention is directly lead to the correct alarm and therefore to the faulty condition. Post mortem data from the MPS beam current monitor is displayed after beam losses occur (see figure 5 – 7). In figure 8 alarm inputs which are disabled are invisible.

Figure 8: GUI of the MPS console program. Disabled alarm inputs are invisible. The chart on the bottom shows a dump (red bar) following a beam loss (blue curve).

FUTURE EXTENSIONS

In the next steps the firmware will be extended by a function check of the beam current monitor by using a testloop [2]. Therefore a periodic test signal (frequency approximately 120Hz, amplitude 5V, trapezoidal shape) is sent through the test loop. In the measured beam current the test signal is digitally subtracted. By looking for the test loop frequency a defect beam current monitor electronic or toroid can be recognized. This is important since a defect beam current monitor can automatically disable all alarm inputs with a beam current threshold above 0mA (e.g. BPMs, beamline alarms)

The synchronisation of all MPS modules using the redundant optical loop to achieve a synchronous post mortem trigger and timestamps for alarms is going to be implemented. The target time resolution is 2µs.

The software will be extended by a more detailed alarm analysis to give more help to the operator by showing the exact involved alarms as a text string after a beam loss. This includes alarms which do not dump the beam through the MPS such as RF system or magnet power supplies. The concept of this is described in detail in [4]. The archiving function of the MPS will be enhanced by filters since in some cases a large number of entries were generated for a day. Further the post mortem data of the beam current measured by the MPS is going to be archived.

In the next years PETRA III is going to be upgraded by up to 10 undulator beamlines. Therefore MPS extensions are necessary, e.g. a number of new alarm inputs and possibly new functionality. Due to the modularity of the hardware and the flexibility of the FPGA there are many options to match upcoming requirements.

CONCLUSIONS

During the last months improvements to the MPS were implemented in the firmware and the software. Experiences during the commissioning led to new ideas and requirements which were partly installed. During one year of operation – from the starting of commissioning to the first user runs in spring 2010 no faults of the MPS with negative effects to the machine operation were observed, so that the availability of PETRAIII was not limited by the MPS. On the other hand the MPS handles faulty conditions with very high efficiency and provides a secure operation of the machine.

REFERENCES

[1] K.Balewski et al., “Commissioning Results of Beam Diagnostic for the PETRA III Light Source”, DIPAC09, Basel, Switzerland, May 2009

[2] T.Lensch, M.Werner, “Machine Protection System for PETRA III”, DIPAC09, Basel, Switzerland, May 2009

[3] I.Krouptchenkov et al., “Experience with the commissioning of the Libera Brilliance BPM Electronics at PETRA III”, DIPAC09, Basel, Switzerland, May 2009

[4] M.Werner, “A Concept to improve the availability of PETRA III by correlation of alarms, timestamps and Post Mortem Analysis”, DIPAC09, Basel, Switzerland, May 2009

[5] F.Schmidt-Föhre, private communication

[6] M.Degenhardt, private communication

[7] A.Schöps, private communication

[8] K.Balewski, private communication

[9] R.Susen, private communication

DEVELOPMENT OF BUTTON ELECTRODES FOR SUPERKEKB RINGS

M. Tobiyama*, H. Fukuma, K. Shibata, M. Tejima, S. Hiramatsu, K. Mori, H. Ishii, T. Obina
KEK Accelerator Laboratory, 1-1 Oho, Tsukuba 305-0801, Japan

Abstract

Button-type beam position monitors for SuperKEKB rings have been designed. The RF characteristics such as beam response, trapped modes or wake functions have been simulated using 3-D E-M codes such as GdfidL and HFSS. The estimated instability threshold from the trapped modes was much higher than the radiation damping time. The prototype units have been tested in the prototype-antechambers installed in KEKB rings. The mechanical reliability and the beam responses are also reported.

INTRODUCTION

The KEKB B-Factory has been operating since 1998, keeping the world highest luminosity and accumulating integrated luminosity more than 1 ab^{-1} up to now. To investigate the flavour physics with the aid of huge integrated luminosity, improvement of the KEKB to SuperKEKB has been proposed. In SuperKEKB rings, we almost double the stored current, reduce the emittance about 1/10, squeeze betatron functions at the interaction point to achieve about 40 times larger luminosity. To reduce the beam size of the injected beam, we will construct a positron damping ring. Most of vacuum chambers around arc sections will be replaced with new antechambers to reduce the electron cloud effect in LER (4 GeV positron ring), and to overcome huge heat load from SR in HER (7 GeV electron ring). In the positron ring, the inner surface will be coated with TiN to reduce secondary emission yield (SEY) of electron clouds. The interaction region (IR) will be completely re-designed with much more complicated structure. Since all of the modifications shown above change the requirements for beam position monitors, it is necessary to evaluate and re-design the BPM electrodes.

We have designed N-type feedthroughs (FTs) with the button electrode of diameter of 12 mm for KEKB rings[1]. Those FTs were brazed to a vacuum chamber of Cu directly with good precision except several special region such as IR or a monitor test section which are made of aluminium vacuum chambers. Up to now, no major trouble was found on the FTs. However, for the SuperKEKB, the original N-type BPM will have the following difficulties:

- Since the FTs are already assembled under blazing process, the second blazing process to the vacuum chamber needs to be controlled with great care not to break the FTs with exceed temperature. We will need huge trials before establishing the final procedure.
- It is fairly difficult to repair the electrodes even if the case of the FT are fairly suspicious to such as shorted circuit or deformed output. The minimum unit of replacement is a quadrupole vacuum chamber unit; not realistic in most cases.
- Because of the large structure, a center frequency of the trapped mode (HOM) around a button-head stays rather lower frequency, around 5 GHz. The threshold beam current of the longitudinal coupled bunch instability caused by this HOM is estimated to be near the present maximum beam current of KEKB[2].

We have developed a BPM electrode with a vacuum flange-connection which will be used for most of a new vacuum chamber and the new damping ring, and an IR special electrode capable for very tight space and large beam power. The RF characteristics, beam response, wake function and beam impedance have been evaluated using 3D electromagnetic codes such as HFSS[3] and GdfidL[4]. The trial pieces of the electrodes have been installed in a vacuum chamber as a position monitor and been checked with the beam. The main parameters of SuperKEKB rings including damping ring are shown in Table 1.

Table 1. Main parameters of SuperKEKB rings (HER: electron, LER: positron, DR: positron damping ring)

	LER	HER	DR	
Energy	4.0	7.0	1.05	GeV
Circumference	3016		135	m
RF frequency		508.886		MHz
Beam current	3.8	2.6	0.08	A
Bunch number	2503		4	
Bunch length	6	5	5	mm
No. of BPM	~450	~450	84	
H emittance	3	5	13	nm rad
Coupling	0.4	0.3	10	%

NORMAL BPM ELECTRODE

Mechanical structure

A button electrode for SuperKEKB rings needs to have enough mechanical precision, at least the position error of the BPM to the level comparable to the errors coming from the gain or loss error of other components such as cables. Also the structure should be capable to the beam power much larger than KEKB. An RF connector should have full reliability on long term operation. Longitudinal coupling impedance of the BPM needs to be reduced lower enough not to cause coupled bunch instability with maximum beam current. Since the vacuum chambers of the LER and the damping ring (DR), including monitor section will be coated with TiN to reduce the SEY, it is necessary to assemble the BPM heads after the coating

*makoto.tobiyama@kek.jp

process; in the present plan, this will be made in KEK by ourselves. This require us to design the BPM heads to be connected with vacuum-sealing flange to the monitor chambers. To satisfy the requirements given above, we will have the following design principles as:

- The electrode and the FT will be assembled to the vacuum chamber with the vacuum-sealing flange with enough mechanical precision. This also gives us easy accessibility of the electrode after the assemble.
- To reduce the coupling impedance and to increase the frequency of the trapped mode higher than bunch form factor, the button size and the vacuum seal should be reduced by about the half of the present KEKB button.
- The inner conductor of the RF connector should be pin with jack structure to keep good electrical contact with long term operation.

To satisfy the requirements, we have designed the button electrode based on the SMA-type FT used for the bunch feedback system[5] and interaction region (IR) special BPM on KEKB as shown in Fig. 1. The diameter of a button head is 6 mm with thickness of 3mm. The inner conductor is supported and sealed with an alumina ceramics of ε_r=9.7. In the air side, a reverse-type SMA connector is designed to keep the good electrical contact under long term operation.

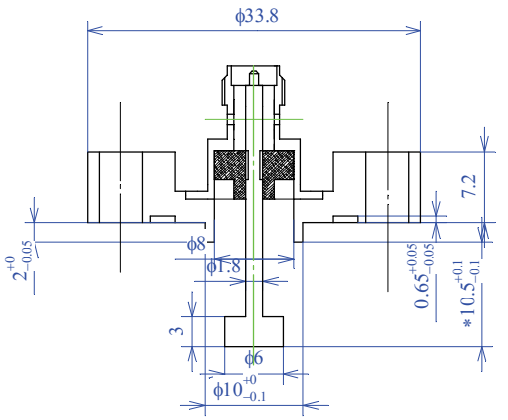

Figure 1. Drawing (top) and the photo (bottom) of a normal BPM electrode for SuperKEKB.

It has a circular flange of diameter of 34 mm made of low carbon stainless steel to connect the vacuum chamber using Helicoflex seal. The metal part for the FT including inner conductor and the button are made of Kover. It is blazed to the flange simultaneously during assemble of the FT. We have also manufactured a non-magnetic BPMs using Ti for the FT and the button for use under larger magnetic field such as very near to the quadrupole magnets. The position of the button will be fixed with the precisely defined projection of the BPM flange and the notch of the vacuum chamber within 0.1 mm. Figure 2 shows the monitor chamber in wiggler section.

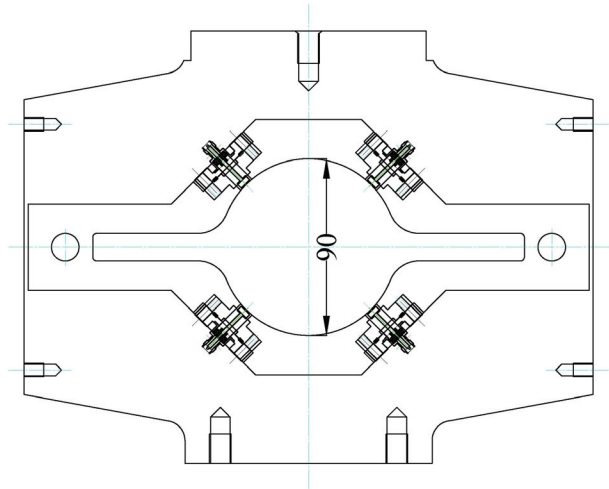

Figure 2. LER monitor chamber in wiggler section. The cut off frequency of the lowest waveguide mode is 930 MHz.

Frequency-domain simulations

We have simulated the frequency response of the button using HFSS. Both the boundary condition of the button and the RF connector were defined as impedance matched ports. Figure 3 shows the S-parameter with the comparison of N-type KEKB-LER BPM where mode 1 is the lowest coaxial mode.

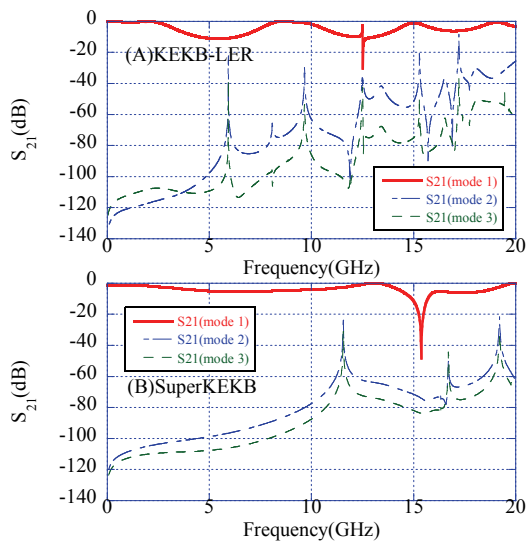

Figure 3. Simulated S-parameter of KEKB LER BPM (A) and SuperKEKB BPM (B).

With the better impedance matching around the ceramics, and with the smaller structure, S_{21} response of the SuperKEKB BPM is much smoother than the N-type BPM. The frequency of the lowest trapped mode around the button (TE-mode) increases from 6 GHz to 12.5 GHz, and the trapped mode around ceramics also increases from 12 GHz to 16 GHz. With the bunch length of 6 mm, the frequency shift reduces the coupling impedance and the risk of possible damage due to HOM.

Time-domain simulation

We have estimated the output of the BPM, longitudinal and transverse wake function and the coupling impedance using GdfidL. Figure 4 shows the cut plot of GdfidL model of 1/4 structure where the size is 111 mm, 109 mm and 50 mm in horizontal, vertical and longitudinal, respectively. With the isotropic mesh size of 0.2 mm and the bunch length of 6 mm, it needed about 5h30min to get the wake function up to 5 m using 32 cores of Opteron. Figure 5 shows the simulated output of the BPM in both time domain (A) and the frequency domain (B).

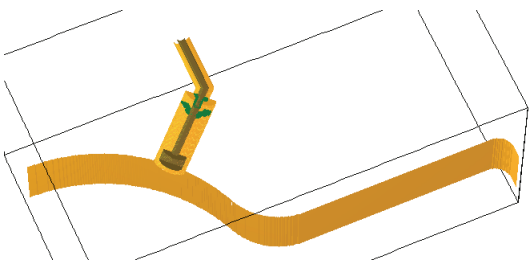

Figure 4. Cut plot of GdfidL 1/4 model of LER BPM.

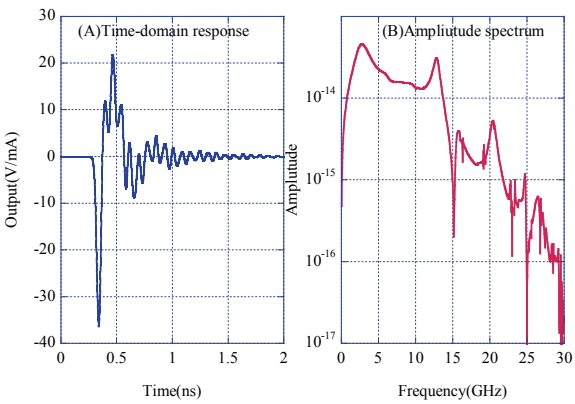

Figure 5. Simulated output of SuperKEKB LER BPM in time-domain (A) and the frequency-domain (B).

The estimated longitudinal loss factor was 0.16 mV/pC per a BPM chamber. The coupling impedance is shown in Fig. 6. By fitting the result, we obtained the Rsh~2 Ω, Q~38 and the center frequency (CF) of 14.8 GHz. The estimated growth time of the longitudinal coupled-bunch instability in the worst case is slower than 120 ms with maximum beam current; it is much longer than the radiation damping time of 37 ms. In the case of present N-type BPM, the estimated impedance by MAFIA T3 were Rsh~10 Ω, Q~48 at 7.3 GHz. The worst growth rate is around 7 ms [2] with the beam current of 3.8 A and will not be safe for use of SuperKEKB. The wake field of ultra short bunch (0.5 mm) was also calculated using windowwake mode of GdfidL to estimate the threshold current of the microwave instability. The contribution of the BPM was much smaller than other impedance sources such as vacuum components.

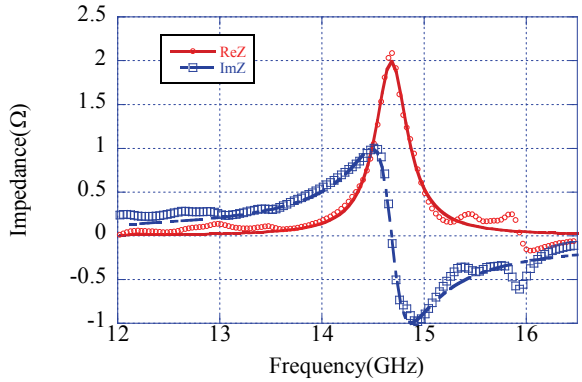

Figure 6. Estimated longitudinal coupling impedance of the SuperKEKB LER BPM.

BPM for positron damping ring (DR)

The positron damping ring (DR) will be constructed to reduce the beam size of positron beam at injection. For the position monitor, we plan to use the same BPM FT as main rings for the DR. To suppress the electron cloud effect it is planned to use an antechamber with TiN coating. Since the size of the vacuum chamber is much smaller, about 34 mm in diameter, than that of the main rings, the impedance of the BPM might affect the beam. We have made the GdfidL simulations and obtained the longitudinal coupling impedance, transverse kick factor and the wake function for ultra-short bunch beam. Figure 7 shows the 1/2 GdfidL model of DR BPM.

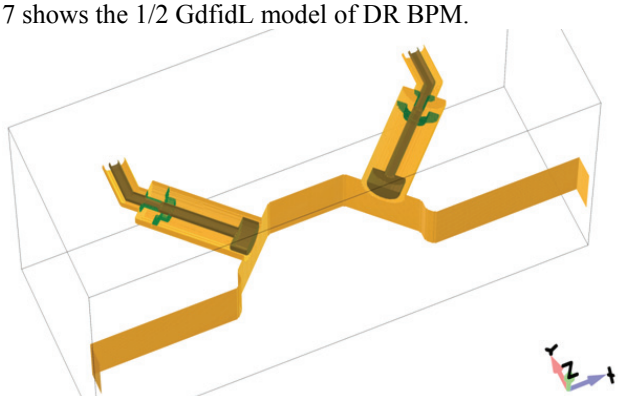

Figure 7. DR BPM 1/2 model for GdfidL.

By fitting the result, we obtained the impedance of Rsh~38 Ω, Q~104 at 14.8 GHz, and the longitudinal loss factor of 2.6 mV/pC for bunch length of 5 mm. Though the impedance itself is larger than that of SuperKEKB LER, the threshold current of the longitudinal coupled bunch instability is much larger than the maximum beam current. The transverse kick factors and wideband wake from ultra-short bunch were also calculated and confirmed to be negligibly small[6].

IR SPECIAL BUTTON ELECTRODE

Mechanical structure

Since the design beam size at interaction point (IP) of SuperKEKB is much smaller than that of KEKB, monitoring the beam position around IR and making fast position feedback is essential to keep good collision. Among the position monitors of IR, monitors between IP and the final focusing quadrupole magnets have much importance because it reflects pure beam position not affected by the error of strong magnets around IP. It is however not easy to install the position monitors there because of fairly tight space, terribly difficult accessibility and the strong magnetic field of superconducting solenoid of the Belle II detector. The inner-diameter of the vacuum chamber is 20 mm so the output power from the beam will be much larger than the normal BPM placed at the monitor chamber of diameter of about 90 mm. Figure 8 shows the designed special FT for nearest IP.

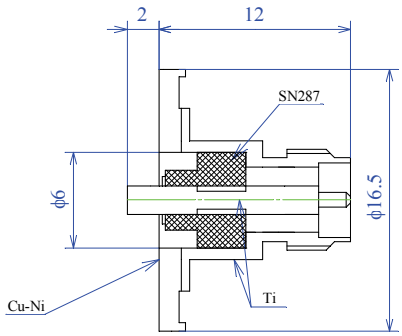

Figure 8. Drawing of a IR special feedthrough.

The button head is a simple rod of diameter of 1.8 mm to reduce the beam power. The sealing and supporting ceramics is made of silicon nitride with the dielectric constant of 7.9 that has lower dielectric loss than alumina ceramics. The body and the rod are made of titanium and blazed to the flange made of CuNi. Since the vacuum chamber will be made of Cu, the button block will be welded using electron beam as shown in Fig. 9

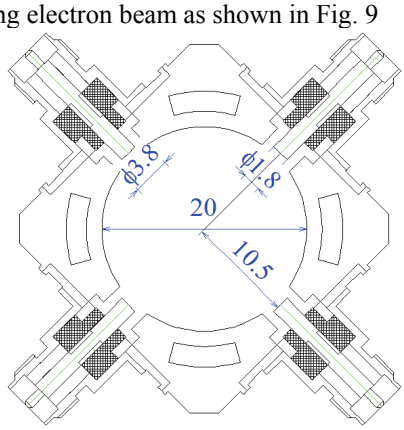

Figure 9. Nearest IP BPM.

We have manufactured several trial FTs and examined the breaking strength of the center rod to the ceramics. The results was about 120 N, much weaker than normal SMA FTs of around 1 kN. Though the strength satisfy the minimum requirement, we will try to improve the strength. Figure 10 shows the photo of the feedthrough.

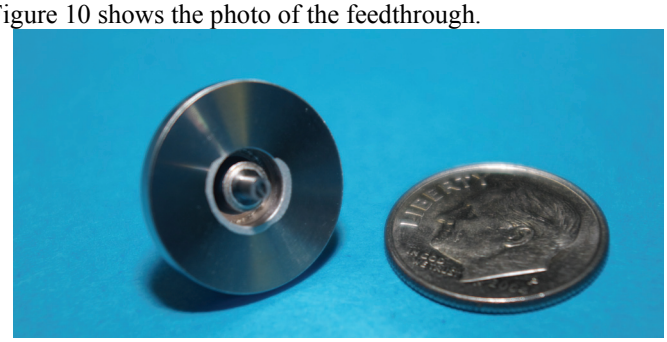

Figure 10. Photo of the nearest IP BPM FT.

3D electromagnetic simulation

The frequency response of the button was simulated using HFSS. As shown in Fig. 11, the frequency of the trapped mode both around the head and around ceramics became much higher frequency where almost no beam spectrum exist.

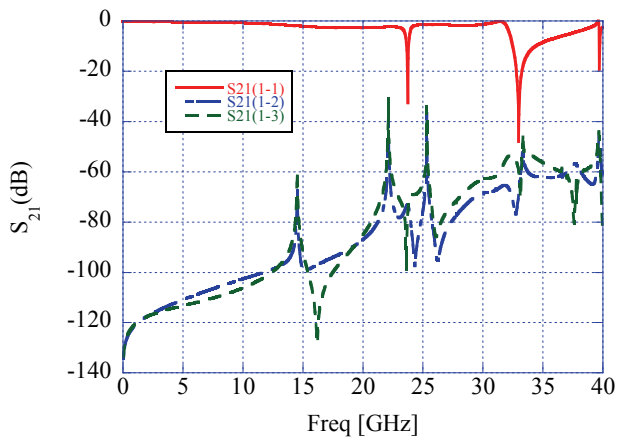

Figure 11. Frequency response of the IR special BPM.

With GdfidL, we have simulated the output of the BPM as shown in Fig. 12 where the bunch length was 5 mm and the bunch charge was 10 nC.

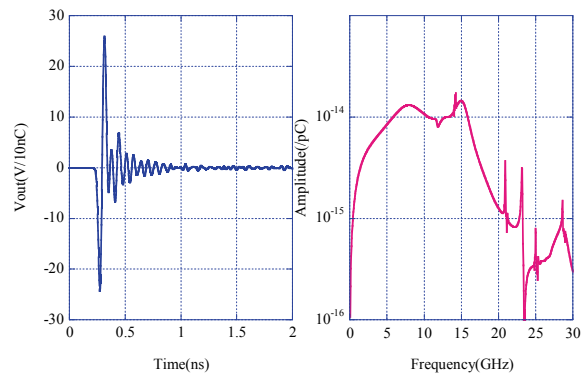

Figure 12. Simulated BPM output for IR special BPM.

The impedance was also estimated from the wake simulation of the GdfidL. The fitted result was Rsh~0.3 Ω with Q~200 at 14.3 GHz, which were negligibly small.

By summing the BPM output for the nominal bunch filling pattern, we obtain the total beam power passing through the FT, and the power level of detection frequency of 508 MHz. With the maximum beam current of 3.8 A, the estimated power level of 508 MHz will be around 6 dBm and the total beam power will be around 10 W, which is similar power at the FT near IR BPMs in KEKB where both HER and LER beam pass in the same BPM chamber with large horizontal offset.

BEAM RESPONSE WITH THE REAL KEKB BEAM

We have installed two sets of test BPM chambers with the new BPMs at Nikko straight section and south arc of KEKB-LER, then observed the raw BPM output and the beam positions. Figure 13 shows a photo of BPM chamber installed at south arc of KEKB-LER. By the gain

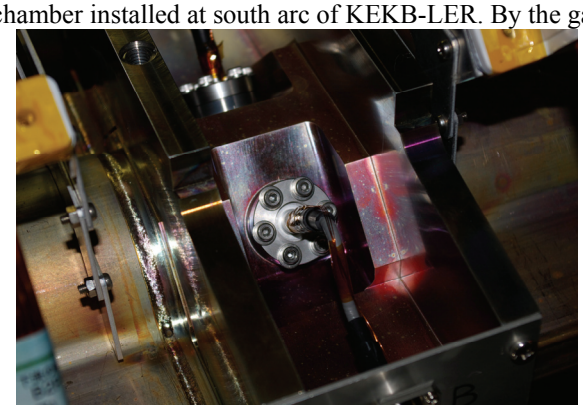

Figure 13. Test BPM chamber installed in KEKB-LER.

mapping using beam, we have found rather larger gain deviations up to 10% than those of the present BPMs. By observing the flange connection, we have found rather larger gaps (~0.2 mm) on several flanges even though no vacuum leak were found. To check the possibility that the Helicoflex gasket might be stiff enough to prevent the touch of the projection to the notch, we have made a simple test flange of ICF152 with BPM interface. With this test set, we have checked the gap changing the torque of the bolt with and without the gasket. The gap difference with and without the gasket was less than 0.01 mm when fasten with 6 Nm of torque. Therefore, we have tried to tighten the bolt much more on the real BPM and measured the gain difference again and found the resulting gain deviation has been reduced. This concludes that if we could control the torque of the bolt, we will be able to set the BPM flange to the correct position.

Figure 14 shows an example of observed raw beam signal with the bunch current of around 1 mA where bunch spacing was about 6 ns. Though it is not so easy to compare the result with the electromagnetic simulation of GdfidL due to the long cable and the insufficient bandwidth of the oscilloscope, the signal level was as expected. The beam spectrum was also observed with a spectrum analyzer and was almost in good agreement with the simulation.

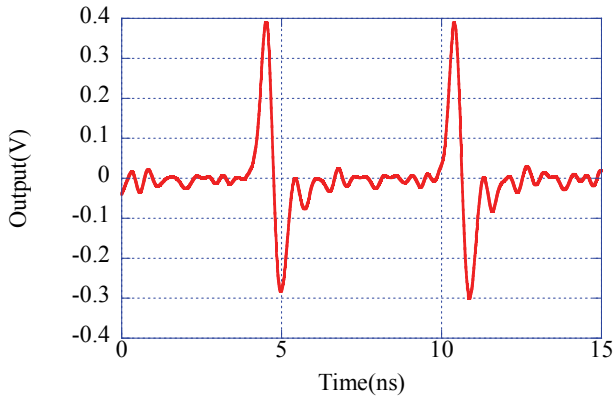

Figure 14. The raw BPM signal observed with a 1.5 GHz real-time oscilloscope. The length of a thick, low-loss cable from BPM to the oscilloscope was about 50 m.

SUMMARY

We have designed the BPM heads for SuperKEKB rings in normal section and the damping ring, and the special BPM for the IR nearest position monitor. The RF and beam coupled response such as frequency response and coupling impedance are estimated using 3D electro-magnetic simulation codes such as HFSS or GdfidL. The impedance was low enough not to cause the coupled-bunch instability. The broad band characteristics was also calculated using much shorter bunch and the broad band impedance was confirmed small enough. Simulated signal output showed enough level for detection frequency and safe level for total pass power of the feedthrough.

The prototype monitor chamber was installed in KEKB-LER and the beam response was observed. The response was as expected and no major difficulty was found up to now.

We will replace most of the BPM chamber with the new BPM unit on SuperKEKB. The new damping ring for positron beam will also use the same type of BPM.

REFERENCES

[1] M. Arinaga et.al., Nucl. Instrum. Meth. Phys. Res. A499 (2003) 100-137.
[2] K. Shibata et.al., in proceedings of PAC 97, Albuquerque, p.4048-p.4050, 2007.
[3] Ansoft HFSS ver.11.
[4] GdfidL http://www.gdfidl.de/
[5] M. Tobiyama et. al, in proceedings of APAC98, KEK, 1998.
[6] H. Ikeda, private communication.

BEAM MEASUREMENTS OF A LARGE SOLID-ANGLE BEAM LOSS MONITOR IN THE APS*

B.X.Yang, W. Berg, J. Dooling, A. Pietryla, A. Brill, and L. Erwin
Advanced Photon Source, Argonne National Laboratory, Argonne, IL 60439, USA.

Abstract

For reliable radiation dosimetry of undulator magnets, a beam loss monitor (BLM) covering a large solid angle from the point of beam losses is highly desirable. A BLM that uses a Cherenkov radiator plate wrapping around the beam pipe is utilized in the Linac Coherent Light Source (LCLS) undulators, and a similar BLM geometry has been tested for the Advanced Photon Source (APS) undulators. We report on measurements made with these BLMs recently installed in the APS storage ring and the booster-to-storage-ring transfer line. A two-order-of-magnitude variation in the relative sensitivity of the Cherenkov detector is observed as a function of incident electron position in the quartz radiator. A factor of 10 variation in signal sensitivity was observed with the change of particle entry angle. The introduction of tungsten and lead shields enhances count rates by 30 – 40%. When the detector is moved along the insertion device chamber, the signal intensity peaks 1 m from the chamber entrance. The measured data are compared with numerical simulation of the beam loss processes.

INTRODUCTION

At the APS, a large area beam loss monitor (BLM) was developed for the LCLS to measure radiation dose rates at the FEL undulator magnets [1]. The BLM detects Cherenkov radiation generated by high-energy electrons in an aluminum-coated, quartz radiator. The radiator is placed just upstream of each LCLS undulator magnet. Ray-tracing analyses and numerical simulations show that the optical efficiency varies by at least 2 orders of magnitude as a function of electron position in the radiator [2]. In this work, we present detector efficiency measurements using APS high-energy radiation beams.

BEAM LOSS MONITOR DESIGN

Figure 1 shows the tuning-fork-shaped LCLS-BLM radiator design. The electron beam passes into the paper at the location of the small cross in the figure. The radiator wraps around the beam pipe and covers the entire area of the undulator magnets. Shower particles from high-energy, lost electrons are expected to deviate only slightly from the incoming beam direction and enter the radiator approximately normal to the surface of the paper.

Figure 2 shows the enlarged top view of the coupling area between the radiator and the photomultiplier tube (PMT). The Cherenkov radiation is emitted in a cone with a half cone angle determined by $\cos\theta_C = 1/n\beta \approx 1/n$, where $n \approx 1.47$ is the refractive index of the radiator material. In our case, where the PMT is mounted 90º from the direction of the electron beam, $\theta_{PMT} = \pi/2 - \theta_C$, and $\sin\theta_{PMT} \approx 1/n$, which is the same condition of total internal reflection at the PMT coupling surface, implying a very low coupling efficiency with the PMT. We note that the condition of total internal reflection can be broken if the radiator is rotated.

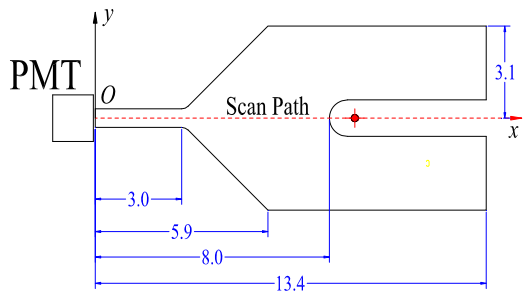

Figure 1: BLM radiator (units in cm). The dashed line shows the scan path of the gas bremsstruhlung beam.

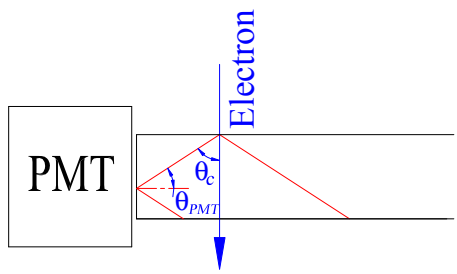

Figure 2: Top view of the radiator showing the Cherenkov radiation cone and the total internal reflection.

GAS BREMSSTRUHLUNG SOURCE

Undulators occupy many long straight sections in synchrotron radiation sources. As stored electrons traverse through the residual gas in these straight sections, gas bremsstruhlung (GB) photons are generated with energies up to the electron energy of the machine [3-6]. During normal operations, the GB photon beam is stable with a well-defined direction, size, and intensity. Accessibility to experimental stations makes it possible to perform experiments with high-energy, gamma-ray and electron detectors with great flexibility and convenience. We hope to demonstrate the advantages of this gamma-ray source for testing radiation detectors using, for example, pair-production electrons and photoneutrons.

Simulated Angular Distribution

To characterize the GB radiation in the 35-IDA hutch, realistic beamline geometry is simulated using the

* Work supported by U.S. Department of Energy, Office of Science, Office of Basic Energy Sciences, under Contract No. DE-AC02-06CH11357

particle tracking code MARS [7,8]. Since the scattering angle $1/\gamma$ dominates the size of the GB photon beam in the x-ray hutch, a circular electron beam was assumed for simplicity the left side of Figure 3 shows a scatter plot of (right) simulated photon distributions. The adjacent plot shows the distribution of photons with a 0.8-cm-thick tungsten block placed just upstream. From these data sets, intensity profiles can be calculated.

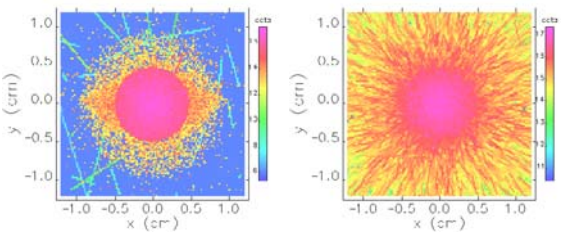

Figure 3: Left: MARS-simulated GB photon plot; Right: GB plot with a 0.8-cm-thick tungsten block.

Measured Spatial Distribution GB Beam Source

The transverse GB radiation profiles are measured using two additional reference detectors of different design located 38 m from the center of the straight section: 1) a Bergos PIN diode beam loss monitor [9] and 2) a lead-encased Cherenkov detector (CD) [10,11]. Both detectors are running in pulse-counting mode.

Figure 4 shows the horizontal and vertical intensity profiles acquired with the Bergos diode. The spatial distribution of MARS-simulated gamma-ray fluence is plotted for comparison, after normalization at the peak. While the FWHM of the Bergos profiles measure 3 mm horizontally and 2.3 mm vertically, the FWHM of simulated profile measures 4.2 mm. The simulation is not detector-specific; therefore, the agreement between these data sets is considered reasonable.

Figure 5 shows the horizontal and vertical intensity profiles acquired with the reference CD. The spatial distribution of the MARS-simulated gamma-ray fluence with the 0.8-cm-thick tungsten block just upstream of the detector is plotted for comparison, after normalization at the peak. The FWHM of the Cherenkov profiles are measured to be 13 mm in both directions; whereas, the FWHM of the simulated profile measures only 5 mm. We note that the reference CD uses a cylindrical radiator, 8 mm in diameter and 10 mm in length, shielded by a lead cylinder 15 mm thick. The size of this CD radiator is large compared to that of the beam, which contributes to the poor spatial resolution. We note that since the PMT is mounted on top of the radiator [11], the asymmetric profile shows the transport efficiency of Cherenkov radiation is reduced as the GB beam is scanned away from the PMT ($x < 0$).

Figure 6 shows a vertical scan of the CD over a wider spatial range. We can see that the measured radiation has long exponential tails away from the central peak. This broad wing appears to be related to the additional beam losses associated with APS storage ring top-up injection.

GB RADIATION MEASUREMENT

The LCLS BLM was mounted on an XYθ stage to map out the detector efficiency as a function of the electron entry point coordinates and entry angle. The BLM is rotated along the vertical axis, y in Figure 1. The PMT rotates downstream of the axis when $\theta > 0$.

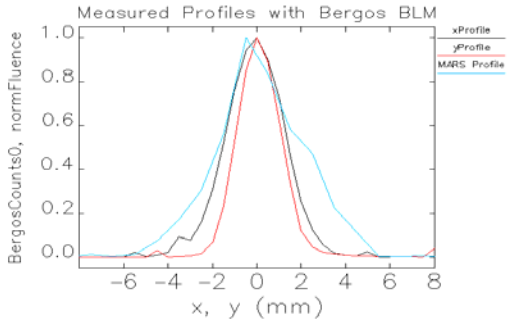

Figure 4: Measured horizontal and vertical profiles using a Bergos BLM, along with a MARS-calculated gamma-ray fluence profile for comparison.

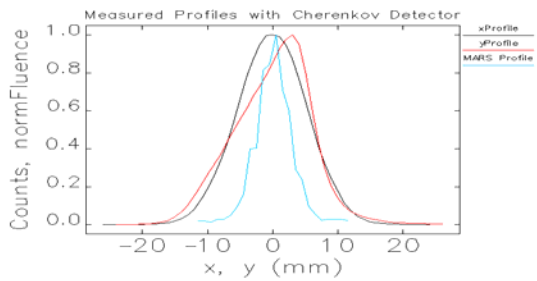

Figure 5: Measured horizontal and vertical profiles using a Cherenkov detector, along with a MARS-calculated gamma-ray fluence profile for comparison.

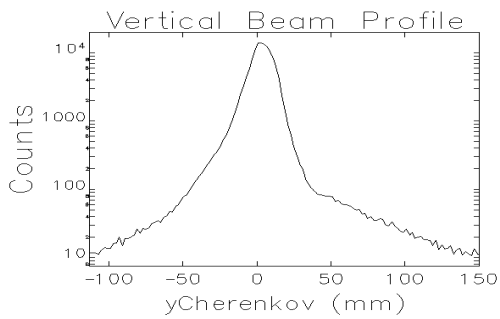

Figure 6: Measured vertical profile over an increased spatial range using a Cherenkov detector.

Measured Angle Dependence

Figure 7 shows the count rate as a function of x when the entry point is scanned along the path shown in Figure 1. A 12.5-mm brass plate was placed 15 cm upstream of the detector to enhance the shower. We observe the following features in the data: (1) The change in slope at x = 30 mm correspond to the end of the narrow neck in the radiator; (2) the slope variation at x = 80 mm corresponds to the cut-out for beam pipe; (3)

counts beyond $x = 80$ mm are likely a result of scattering from the brass enhancer. We can see that the collection efficiency is a very sensitive function of the entry position. It decreases by a factor of 200 when the entry point is scanned horizontally from the PMT to the beam pipe. The collection efficiency is also a sensitive function of beam entry angle. Outside of the narrow neck, it increases over 20 times when the radiator is rotated by +39 degrees.

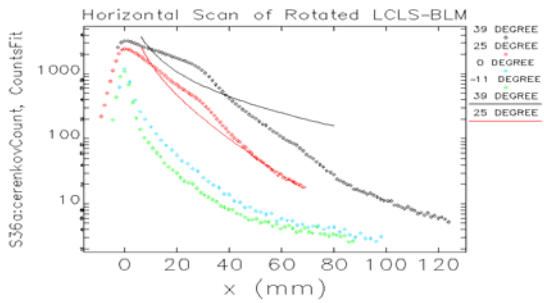

Figure 7: BLM sensitivity along the horizontal scan path for differing rotation angles (diamonds). Also shown are fits to a parallel plate model for the two larger angles with fit parameter $R = 0.45$.

Parallel Plate Approximation

Next we apply the parallel plate model [2] for the experimental geometry. Figure 8 shows an electron entering the radiator at an incident angle θ_i and generating a Cherenkov light cone around the particle trajectory. We trace the Cherenkov rays propagating towards the PMT through multiple reflections Q-R-S-T. To calculate the length, we reflect the radiator boundary planes several times to obtain a virtual quartz stack R0-R1-R2-R3-R4, although the Cherenkov light is only generated in R0. We extend the original light ray to intercept the virtual radiator exit aperture at P-Q-R'-S'-T'-U'. By the time the ray reaches the end of the radiator, the Cherenkov cone radius is $x' = x - \frac{d}{2}\sin\theta_i \approx x$, where $x >> d\sin\theta_i$. The height of the cone is given by $y' = x'\cot(\theta_i + \theta_C)$ and the number of reflections is given by $n_R = \left[\frac{y'}{d} + \frac{1}{2}\right] \approx \frac{y'}{d}$, where d is the thickness of the radiator, and the fraction of light cone intercepted by the PMT is $D/2\pi x'$, where D is the PMT diameter. For surface reflectivity R, the light intensity at the PMT is $I(\theta) \propto \frac{DT_{PMT}}{2\pi x'\cos\theta_i} R^{n_R}$, which accounts for the increased length of the oblique path and the transmittance for in-plane polarized light at the exit aperture [12], $T_{PMT} = \frac{4n\sin(\theta_i+\theta_c)\cos\theta_t}{\left[\sin(\theta_i+\theta_c)+n\cos\theta_t\right]^2}$.

Hence

$$I(\theta) \approx I_0 \frac{T_{PMT}}{x\cos\theta_i} R^{x/d\tan(\theta_i+\theta_c)}. \quad (1)$$

The two parameters, I_0 and R, can be adjusted to measured data fit in this expression. We found that low values of $R < 0.6$ are needed to account for the steep slopes in Figure 7. We acknowledge that this reflection coefficient is unrealistically low. Further refinement of the model to correlate the fluence with count rate is required.

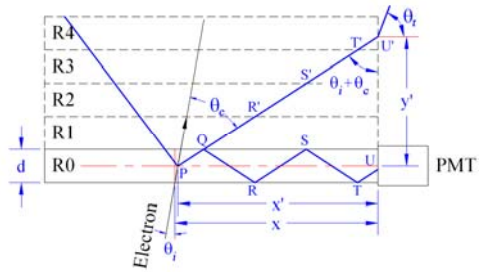

Figure 8: Parallel plate approximation of the transport of Cherenkov light.

STORED BEAM LOSSES

The tuning fork design was considered an attractive candidate for APS undulator magnet dosimeters because of the radiator's large solid angle. A larger fork fitting the APS insertion device (ID) chamber has been built and installed at Sector 33. The detector is configured in pulse-counting mode, recording single electron losses due to Touschek scattering, as well as injection losses at the chamber entrance. A CD next to the ID chamber is used to monitor the local electron losses (flux monitor). The data are averaged over five-day-long user runs. Only 24-bunch fill patterns are used since different magnetic lattices give slightly different loss profiles, likely from different spatial distribution of the lost electrons.

Shielding Dependence

A 10-mm-thick tungsten shielding plate and another 3-mm lead plate, are installed upstream of the BLM to increase the production of electrons in the electromagnetic shower. Table 1 lists the count rate of the detector N_{TF}, that of the CD N_{CD}, and their ratio N_{TF}/N_{CD} for three different shielding configurations. We see that the 3-mm lead plate enhanced the count rate by ~ 30%; and the 10-mm tungsten plate enhances by ~ 40%.

Table 1: Tungsten Enhancer Effect on BLM Sensitivity

Shielding	N_{CD} (c/s)	N_{TF} (c/s)	N_{TF}/N_{CD}
No Shielding	54.9	405	6.0 (baseline)
3-mm lead plate	51.2	339	7.9 (+30%)
10-mm tungsten	60.1	501	8.3 (+40%)

Distance Dependence

The BLM, with a 10-mm tungsten shield, was positioned at four different locations along the ID chamber over the course of 3 months. Table 2 compares the measured ratio N_{TF}/N_{CD} at four different locations;

the distance was measured from the ID chamber entrance. While the flux monitor shows that the loss rate is stable within ±20%, the TF-BLM signal changed over ±100%. The TF-BLM count rate reaches a maximum at 0.86 m and then starts to decrease; indicating that a significant number of particles emerge from the ID chamber at angles greater than 30 mrad. These electrons could then possibly pass over the BLM located at z = 1.3 m.

Table 2: BLM Count Rate as Function of Position

Location (m)	N_{CD} (c/s)	N_{TF} (c/s)	N_{TF}/N_{CD}
0.00	47.5	308	6.5
0.86	66.8	1642	24.6
1.30	70.3	1276	18.1
1.73	56.3	633	11.3

MARS simulations were performed using Sector 33 geometry without the undulator. Since we had no prior knowledge on the lost electron distribution, two cases were modeled: (1) a "thick beam," $\sigma_x = 1.5$ cm, $\sigma_y = 0.5$ cm, and (2) a "thin beam," $\sigma_x = 1.5$ cm, $\sigma_y = 0.1$ cm. Figure 9 shows the integrated electron fluence in the BLM radiator as a function of radiator position z. While both profiles peak in the first meter, the thin beam has the more pronounced peak. Near the chamber entrance, the shower cone is small, so the lower efficiency of the detector could suppress the measured count rate. As z increases, the shower expands and more particles hit the BLM near the PMT end, thus increasing the count rate. This could partly explain the difference between Figure 9 and Table 1.

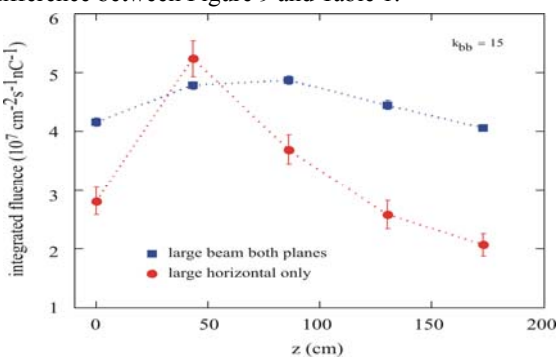

Figure 9: Simulated axial profiles of electron fluence in the BLM radiator versus position along the ID vacuum chamber. Tungsten enhancer is presented.

Figure 10 shows the enhancement ratio of the tungsten plate at different locations. At the chamber entrance, when the average electron energy is low, the tungsten plate actually reduces the electron fluence in the BLM. As z increases, more energetic electrons emerge from the chamber after smaller-angle scattering, and the fluence downstream of the tungsten plate increases dramatically. At z = 1.73 m, the electron fluence is 150% higher with the tungsten plate than without it. This compares with the observed count rate enhancement of 40% in Table 1. At this time, it is not clear to us how the fluence enhancement translates to a pulse count rate increase, and the direct comparison is difficult.

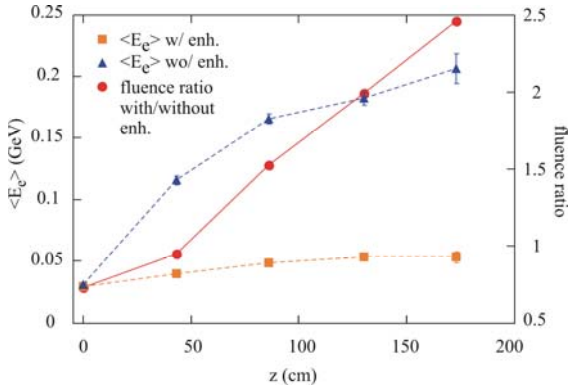

Figure 10: Fluence enhancement ratio by a 10-mm tungsten plate (circle); Electron fluence in BLM with W-plate (triangle) and without it (square).

BTS MEASUREMENTS

Two 0.5-mm thick chromium-doped alumina flags (Chromox screen) are employed to generate localized loss in the 7-GeV transport line from the booster synchrotron to the storage ring (BTS). Depending on which of the two flags are inserted, the loss point occurs either 12 or 20 m upstream of the BLM. As shown in Figure 11, the BLM is mounted on a pneumatically-driven linear slide that raises and lowers the detector out of a lead-brick shield for exposure to scattered electrons. Assuming linear operation of the photomultiplier tube (PMT) we expect the BLM's PMT, current to follow a power law of applied voltage V_{PMT},

$$G(V_{PMT}) = G_o \left(\frac{V_{PMT}}{V_o} \right)^{n_p}, \qquad (2)$$

where n_p = 7.2 for the 7-stage R7400-04 tube used here. The output charge of the BLM PMT as a function of high voltage bias is shown in Figure 12, along with the power law extrapolation of the charge measured at V_{PMT} = 300 V.

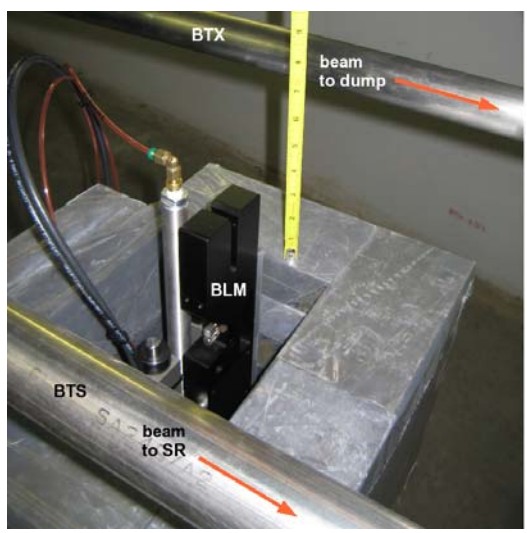

Figure 11: LCLS BLM in the raised position between BTS and BTS beamlines.

MARS simulation was performed for the two scattering geometries, including the quadrupoles fields

upstream of the radiator. To estimate absolute signal intensity, we used the measured charge from the booster synchrotron, the known thickness of the flag, and the small-current PMT gain at 400 V bias, where the PMT appears to be in the linear range. For simplicity, we used a uniform optical coupling of 3.5×10^{-3}, consistent with a reflectivity $R = 0.9$. As shown in Figure 12, the results are within a factor of 3 of the measured data. Unfortunately, due to the non uniformity of the BLM response, the result was a large error bar. While the good agreement strengthens our confidence in using MARS as a tool to study APS beam losses and shielding, we note that discrepancies still exist. For example, the simulation is unable to predict the ratio of lost charge at the two flags.

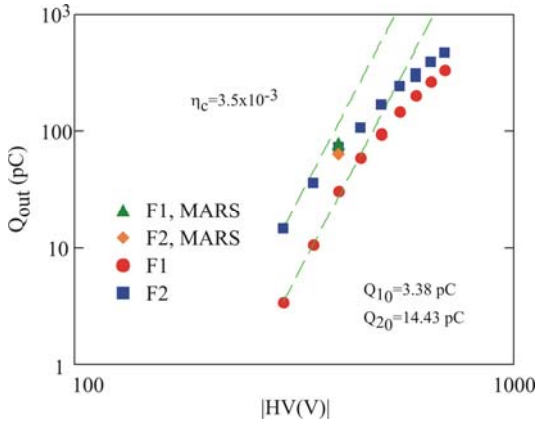

Figure 12: LCLS BLM integrated current signal output as a function of PMT bias voltage. Dashed lines represent power law extrapolation of data at 300 V. It also includes predicted PMT charge for PMT voltage of 400 V, using MARS simulations (diamond and triangle).

SUMMARY

We measured a tuning-fork shaped, large solid angle BLM at the APS using gas bremsstruhlung beam from the 15-m straight section, Touschek-scattered electrons from the ID chamber, and flag-scattered electrons in the BTS. We found that the TF-BLM efficiency may vary by a factor of 200 for different electron entry points. The count rate is also sensitive to particle entry angle, varying nearly two orders of magnitude over the angle range of ±40º.

We also performed BLM calibration at the BTS transport line with radiation dosimetry. Despite the complex geometry of the BTS, the MARS simulation predicted an absolute signal level within a factor of three.

The GB photon beam at the APS is shown to be a gamma ray source with well-defined size and small divergence and may prove a useful tool for the development and calibration of radiation detectors in the APS accelerators.

We would like to thank Glenn Decker and Louis Emery for their enthusiastic support for this project. We would also like to thank Heinz-Dieter Nuhn, Alan Fisher, and Mario Santana of the LCLS group for stimulating discussions.

REFERENCES

[1] W. Berg, J. C. Dooling, A. Pietryla, and B.-X. Yang, "Development of a Beam Loss Monitor System for the LCLS Undulator Beamline," LINAC'08, p. 492, 2008; http://www.JACoW.org.
[2] J. Dooling, these proceedings.
[3] N. Ipe, D.R. Haeffner, E.E. Alp. S.C. Davey, R.J. Dejus, U. Hahn, B. Lai, K.J.Randall, and D. Shu, "Guide to Radiation Beamline Shielding Design at the APS," ANL/APS/TB-7 (1993).
[4] P. K. Job, et al. "Guidelines for Beamline and Front-End Radiation Shielding Design at the Advanced Photon Source," ANL/APS/TB-44, Rev. 3, September 2008.
[5] M. Pisharody, E. Semones, and P. K. Job, "Dose Measurements of Bremsstrahlung-Produced Neutrons at the Advance Photon Source," ANL/APS/LS-269 (1998); Nucl. Instrum. Meth. A, 430, 542 (1999).
[6] J. C. Dooling, "Dose Calculations Using MARS For Bremsstrahlung Beam-Stops and Collimators in APS Beamline Stations", ANL/APS/TB-54, 2010.
[7] N. V. Mokhov and S. I. Striganov, "MARS15 overview," Technical Report Fermilab-Conf-07/008-AD, 2007.
[8] N. V. Mokhov et al., "Physics models in the MARS15 code for accelerator and space applications," in Int. Conf. on Nuclear Data for Science and Technology, AIP Conf. Proc. 769, pp. 1618-1623, 2004.
[9] K. Wittehburg, "Beam Loss Monitor for the HERA proton Ring," EPAC'90, p. 789, (1990); http://www.JACoW.org.
[10] A. Fischer et al., "Diagnostics Development for the PEP-II B Factory", AIP Conf. Proc. 390, BIW'96, p. 248 (1996).
[11] A. Pietryla, W. Berg, "A Cerenkov Radiation Detection System for the Advanced Photon Source Storage Ring," PAC'01, p. 1622, (2001).
[12] P. Lorrain and D. Corson, *Electromagnetic Fields and Waves*, 2nd ed., Freeman, San Francisco, 1970.

HIGH-POWER HARD X-RAY BEAM POSITION MONITOR DEVELOPMENT AT THE APS*

B.X.Yang, G. Decker, S. H. Lee, and P. Den Hartog
Advanced Photon Source, Argonne National Laboratory, Argonne, IL 60439, USA

Abstract

Accurate and stable x-ray beam position monitors (XBPMs) are key elements in a feedback control system for good x-ray beam stability. For the low-emittance mode of operation of the Advanced Photon Source (APS), the cross sections of the undulator x-ray beams are not upright ellipses, and the effective beam sizes in the horizontal and vertical planes depend on the undulator gaps. These beam characteristics introduce strong gap dependence in photo-emission blade-type XBPMs designed for upright elliptical beams. A center-of-mass XBPM will significantly reduce the gap dependence of the BPM readings. We report the development status of a high-power center-of-mass XBPM at the APS. We note that users often discard more than 50% of the undulator beam power outside of the monochromatic beam. These photons can be intercepted by the limiting aperture of the beamline, and their x-ray fluorescence footprint can be imaged onto a detector. The position of the x-ray beam can be read out using position-sensitive photodiodes. Thermal analyses show that the XBPM can be used for the measurement of beam with a total power up to 21 kW for the 7-GeV APS beam.

INTRODUCTION

X-ray beam stability is an important requirement from the Advanced Photon Source (APS) users. X-ray beam position monitors (XBPMs) are at the heart of the control system delivering the required stability. As the stability requirements become increasingly demanding, XBPMs are asked to deliver increasingly precise information about the x-ray beam. In this work, we propose a design concept that combines the function of a high-heat-load photon collimator and the beam position monitor. We will present a thermal analysis of the collimator, an optical design of the readout detector, and the results of preliminary tests.

XBPM Challenge

Table 1 shows properties of typical APS undulator sources, as well as the beam stability currently achieved and planned for the future upgrade [1].

Since its commissioning, the APS has used the photoemission blade-based XBPM [2]. It is located well away from the undulator beam core and does not have to handle the full power of the undulator under normal conditions. The thermal distortion of its blades has not been measured experimentally. The dependence of its calibration on undulator gap is its main weakness. To understand the gap dependence, let us consider a vertical XBPM using Gaussian beam approximation: We assume that the spatial distribution of the photoelectron is given by:

$$J_{PE}(y) = J_{PE0} e^{-(y-y_0)^2/2\sigma_y^2}, \quad (1)$$

where y_0 is the center of the x-ray beam. We further assume that the upper blade covers b to $+\infty$, and its signal is given by $I_{PE+} = \int_b^{\infty} J_{PE}(y)\,dy$. A similar expression can be written for the lower blade, $I_{PE-} = \int_{-\infty}^{-b} J_{PE}(y)\,dy$.

Table 1: XBPM Characteristics

Location (m)	Current	Planed
Maximum beam current	100	200
No. of Undulator A	1	2
Maximum power	6 kW	21 kW
Maximum power density	183 kW/mr^2	630 kW/mr^2
RMS stability, Horizontal (0.1 – 200 Hz) Vertical	5 μm/0.85μr 2 μm/0.8 μr	3 μm/0.53μr 0.4 μm/0.2 μr

The BPM ratio signal is defined as the ratio of the difference over sum of these two signals,

$$R_{PE}(y_0) = \frac{erfc\left(\frac{b-y_0}{\sqrt{2}\sigma_y}\right) - erfc\left(\frac{b+y_0}{\sqrt{2}\sigma_y}\right)}{erfc\left(\frac{b-y_0}{\sqrt{2}\sigma_y}\right) + erfc\left(\frac{b+y_0}{\sqrt{2}\sigma_y}\right)}, \quad (2)$$

where $erfc(u) = \frac{2}{\sqrt{\pi}} \int_u^{\infty} e^{-t^2} dt$ is the complementary error function. The readout of the BPM is given by $Y = l_y R_{PE}$, where the calibration length,

$$l_y = \sqrt{\frac{\pi}{2}} \sigma_y e^{\frac{b^2}{2\sigma_y^2}} erfc\left(\frac{b}{\sqrt{2}\sigma_y}\right), \quad (3)$$

is chosen so $Y \approx y_0$ for small displacement. Figure 1 plots the calibration length l_y as a function of the beam size σ_y, for b = 2, …, and 6 (mm). For fixed blade spacing, l_y depends on beam sizes: the larger the beam size, the larger is l_y, and the less sensitive the XBPM becomes.

When undulator harmonic energies are away from Au absorption edges, the broadband excitation can be approximated using bend magnet (BM) spectra. The total electron yield (TEY) from the gold surface can be estimated using Henke approximation [3] with x-ray spectra calculated with XOP [4]. We found that, as shown in Figure 2, the vertical TEY profile fits well to a pseudo-Student distribution function,

$$S_e = S_{e0}\left(1 + \frac{1}{\nu}\left|\frac{y_0}{\sigma_s}\right|^m\right)^{-\frac{\nu+1}{2}}, \quad (4)$$

* Work supported by U.S. Department of Energy, Office of Science, Office of Basic Energy Sciences, under Contract No. DE-AC02-06CH11357.

where m, ν, σ_s are parameters dependent on the critical energy of the BM source. This function gives the standard Student distribution when $m = 2$ [5].

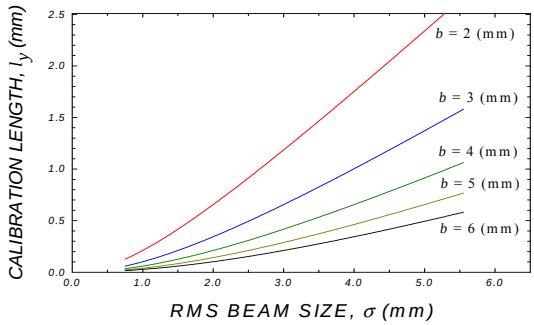

Figure 1: The BPM calibration length vs. Gaussian beam size σ_y for $b = 2, \ldots, 6$ (mm).

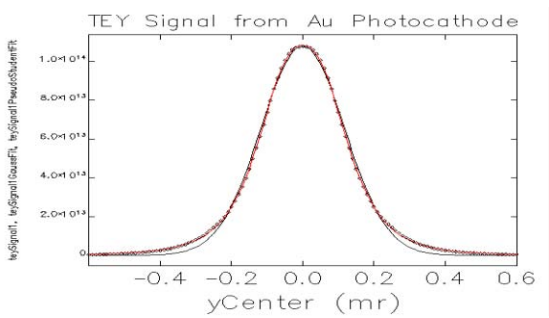

Figure 2: Calculated vertical gold TEY profile of BM source (circles), and a pseudo-Student fit (red line).

As an undulator gap changes, its effective critical energy changes, causing the width and shape of the vertical x-ray beam profile to change. As a consequence, the calibration length of the XBPM changes with the undulator gap. These changes are even more dramatic when one of the harmonics is near an absorption edge. Since the beam size is several mm, even a 1% change of the beam size is in the range of several tens of μm.

Figure 1 also reveals that for fixed beam sizes, the larger the blade spacing, the shorter the calibration length, and the BPM is more sensitive to beam movements. This encourages the practice to place blades away from the beam core, $b > \sigma_y$. As a result, the signal is significantly reduced (note that erfc(1) = 16% and erfc(2) = 0.5%) and the background from bend magnet is significantly increased. At the APS, clean blade signals are hard to obtain for gaps wider than 30 mm.

Finally, the low-emittance lattice at the APS introduces horizontal and vertical dispersions and dispersion slopes within insertion devices. When the electron beam with energy spread passes through the undulator, it generates an x-ray beam with tilted cross sections, making the vertical TEY signal depend on the horizontal offset of the blades from the beam center.

GRAZING INCIDENCE XBPM

Discussions in the last section leads us to conclude that the best way to increase the signal-to-noise ratio is to maximize the undulator x-ray flux intercepted and minimize the background radiation received. This naturally leads to the solution of combining the XBPM with the limiting aperture of the front end. Most collimator designs use copper alloys, hence copper K-edge x-ray fluorescence (Cu-K XRF) may be used for XBPM readout. Since the XRF footprint size is usually about half of TEY's, the XRF-XBPM is more sensitive to beam position changes. Figure 3 shows the vertical XRF profile measured at the APS diagnostics undulator [6] using a pair of slits and a silicon PIN diode monitoring the XRF from the beam dump. The profile fits well to a pseudo-Gaussian form,

$$S_f = S_{f0} e^{-\frac{1}{2}\left|\frac{y_0}{\sigma_m}\right|^m}, \qquad (5)$$

with σ_m = 1.6 mm and m = 2.73. This functional form agrees well with calculations using a bend magnet source, where the parameters σ_m and m depend on the critical energy of the source. For undulators, they depend on the undulator gap.

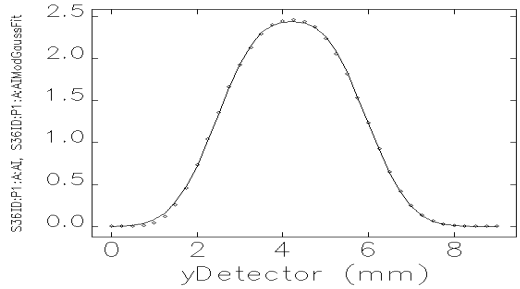

Figure 3: Measured vertical XRF profile of the APS diagnostics undulator from a Cu beam dump (circles) with a pseudo-Gaussian fit (line).

Table 2: RMS Beam Sizes for Diagnostics Undulator

Parameter	Location	Horizontal	Vertical
E-beam size	0 m	270 μm	12 μm
E-beam divergence	0 m	11.5 μr	4 μr
Mono x-ray beam size	20 m	0.36 mm	0.11 mm
	30 m	0.45 mm*	0.17 mm*
Cu XRF footprint size	20 m	0.9 mm	0.8 mm
	40 m	1.7 mm	1.6 mm**
Au TEY footprint	20 m	1.84 mm	1.82 mm
Power envelope	20 m	0.88 mm	0.84 mm

* Measured at 30 m from APS diagnostics undulator [6].
** Measured at 40 m from APS diagnostics undulator.

Table 2 lists the electron and x-ray beam sizes of the APS diagnostics undulator. The x-ray beam sizes of the monochromatic APS diagnostics undulator are measured using an x-ray wire scanner [7] at 30 m. They are consistent with the electron beam size and divergence derived from the lattice model. The measured values are extrapolated to the XBPM located at 20 m. The TEY and total power profile sizes are calculated using XOP.

Choice of Limiting Aperture for Undulator A

Table 3 lists the estimated x-ray beam sizes at 20 m from an APS Undulator A with a fully closed gap (K = 2.6). The properties of the e-beam are from Table 2. If the beam is centered in an aperture of 4-σ in both the horizontal and vertical sides, 1.6 mm (H) × 0.5 mm (V), 99% of the monochromatic photons in the central zone would pass through the aperture. We choose 2 mm (H) ×

1 mm (V) to allow 0.5 mm missteering in both planes. Since the power and XRF envelopes are much wider than the mono beam size, the aperture intercepts about 75% of the total power and 70% of the total XRF intensity.

Table 3: Maximum Beam Sizes for Undulator A*

Parameter	Horizontal	Vertical
RMS Mono x-ray beam	0.36 mm	0.12 mm
RMS Cu XRF footprint	~ 2.2 mm	0.9 mm
RMS Au TEY footprint	~ 5.0 mm	2.0 mm
RMS X-ray power envelope	~ 2.4 mm	0.9 mm
Full x-ray aperture	2.0 mm	1.0 mm

* $K = 2.6$, $z = 20$ mm

Thermal Analysis

From Table 3, we can see that the power profile spreads wider horizontally than vertically. It was shown in studies of APS front end components that vertical surfaces of shutters and collimators are better for higher total power load applications [8]. Table 4 lists the design parameters of a new grazing incidence XBPM. Its active surface is made of cold-rolled GlidCop AL-15. ANSYS was used for the finite element thermal stress-strain analysis: Figure 4 shows the stress distribution over the GlidCop active surface. The temperature distribution looks similar. Figure 5 shows the temperature distribution over the cooling channel. Under operating conditions, the maximum cooling channel temperature, active surface temperature and Von-Mises stress will reach 77ºC, 184ºC and 296 MPa, respectively. Under the worst missteering conditions studied, they will reach 101ºC, 229ºC and 384 MPa, respectively. These values are well within our engineering limits of 150ºC, 300ºC and 455 MPa.

Table 4: Design Parameters for XBPM

Parameter	Value
Electron beam current	200 mA @ 7 GeV
Insertion device	2 Undulator A
Power load	21 kW
Max beam power density	1.68 kW/mm^2
X-ray grazing incidence angle	0.8º
Peak surface power density	23.5 W/mm^2
Heat transfer coefficient	0.010 W/mm^2/ºC

Vertical beam position readout

The vertical position of the footprint is read out using a split silicon PIN diode and a slit-camera geometry, shown in Figure 6. The fluorescence signal produced by a source point at y in the lower diode is proportional to the illuminated area, $J_-(y) = C(a + My)$, where $M = S'/S$ is the magnification. For a distributed fluorescence source with an intensity distribution $\rho(y)$, we have $I_- = C\int \rho(y)(a + My)\,dy$. Similarly, we can write $I_+ = C\int \rho(y)(a - My)\,dy$. The BPM ratio is proportional to the center of mass (CM) coordinate of the distribution,

$$R(\bar{y}) = -\frac{I_+ - I_-}{I_+ + I_-} = \frac{M}{a}\frac{\int \rho(y)\,y\,dy}{\int \rho(y)\,dy} = \frac{M}{a}\bar{y}. \quad (6)$$

We note that the calibration length $l_y = a/M$. The higher the magnification, the more sensitive the XBPM is.

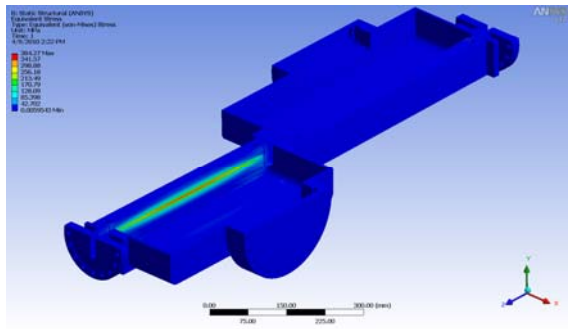

Figure 4: Stress distribution over the XBPM.

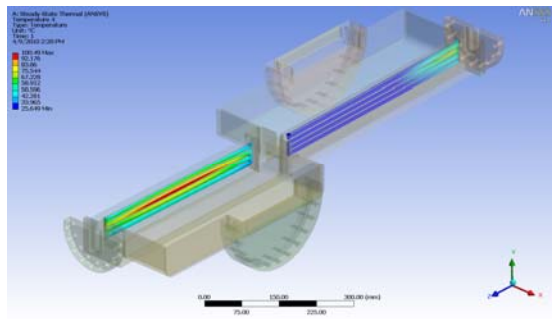

Figure 5: Cooling channel temperature distribution.

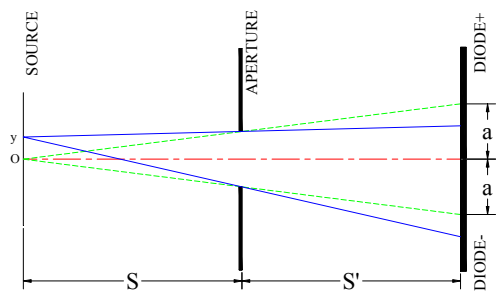

Figure 6: Vertical position readout: CM detector.

Horizontal Beam Position Readout

Due to artifacts we will discuss in the next section, it is more robust to derive the horizontal position from the total signal intensity from the left and right collimator plates. As discussed in the introduction, the horizontal ratio signal will depend on the effective beam size measured using XRF, which may be compensated using the following algorithm: Since the undulator beam size does not change when one reverses the magnetic field, we can write $\sigma_y^2 = \sigma_{y0}^2\left(1 + b_2K^2 + \ldots\right)$. The signal intensity depends on undulator power, $I = I_0K^2\left(1 + c_2K^2 + \ldots\right)$. Combining the above expressions, we have

$$\sigma_y = \sigma_{y0}\sqrt{1 + a_2\frac{I}{I_0} + a_4\left(\frac{I}{I_0}\right)^2 + \ldots}. \quad (7)$$

This expression can be used to determine the vertical calibration length using Eq. (1), where b is the half aperture width. Other parameter, σ_{y0}, I_0, a_2, …, can be determined empirically from gap scan measurements.

MINIMIZING ARTIFACTS

The grazing incidence XBPM is susceptible to a number of known artifacts and others from imperfections.

Bend Magnet Radiation

The fringe of the bend magnet (BM) radiation reaches the XRF-XBPM, just as in the TEY-XBPM. However, due to higher threshold of excitation, ε_K = 8.98 keV, soft x-ray radiation does not contribute to the XRF-XBPM signals, as long as the detector is properly filtered to block low-energy x-ray photons. A smaller acceptance aperture also helps to reduce BM background signal.

Powder Diffraction

Figure 7 shows measured powder diffraction peaks from the copper absorber, recorded with a narrow silicon PIN diode scanning above the water-cooled Cu beam stop. The x-ray beam was delivered by the APS diagnostics undulator (~24 keV) through a small aperture. Significant powder diffraction peaks (rings) can be seen at small angles. At lower photon energies from Undulator A, these peaks shift to higher angles and may enter the split PIN diode. When this happens, the additional photons make the source area of the diffraction peak appear to the detector as bright vertical stripes. Since the diffraction ring intensity varies little near the orbit plane, these stripes are uniform along the vertical direction and do not pose a big problem for vertical position readout. However they may shift the horizontal center of mass slightly as a diffraction ring enters or leaves the diode. On the other hand, using the intensity signal for horizontal position readout reduces the impact of powder diffraction rings. Further reduction may be achieved by modifying the edge of the detector and letting the diffraction ring gradually reach its maximum intensity.

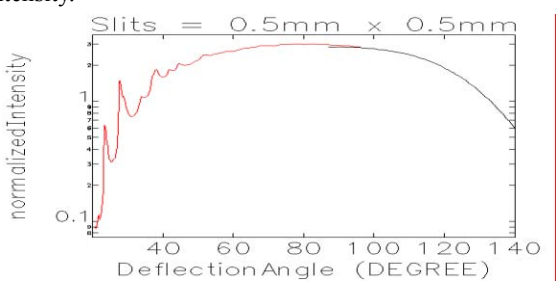

Figure 7: Power diffraction peak off the Cu absorber at 24 keV.

Compton Scattering

Compton scattering intensity from copper is strong. But its angular distribution is smooth and does not vary azimuthally. Hence its impact on position readouts is similar but less than powder diffraction.

Thermal bump

Figure 8 shows the thermal directional deformation of the active surface in the horizontal axis. We note overall deformation as well as longitudinal stretch of the collimator since the structure was supported via three kinematic points on the base surface, causing the asymmetric displacements around the baseline. In addition, the raised surface intercepts the x-ray photons further upstream than the ideal planar surface, causing the center of weight to shift upstream, thus inducing error in CM measurements. If we use the intensity asymmetry as the position signal, the total intensity intercepted by the upstream plate determines the upstream signal, while the remainder is the downstream signal. In this scheme, maintaining the position of the edge of the upstream plate is critical. In Figure 8, –21 μm of the total edge displacement of –25 μm comes from the thermal and vacuum loads. If we instead support the collimator at its middle, the thermal bump would be dramatically reduced for the full 21 kW power load. We note that a horizontal missteering of 0.5 mm shifts the edge further by –12 μm. In practice, the latter appears as a horizontal calibration change of 12/500 and can be absorbed in Eq. (7). In summary, we expect the thermal bump to shift the origin at a level of ~0.2 μm/kW, which can be compensated with the diode signal.

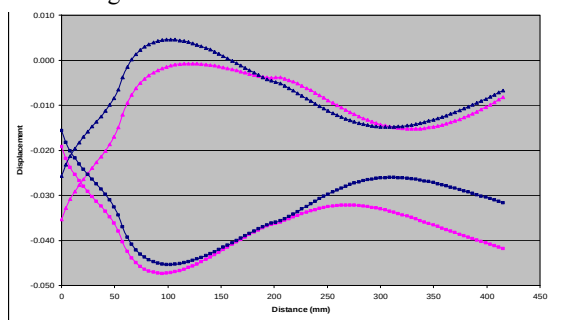

Figure 8: Thermally induced surface displacement.

Alignment Error

Due to the small grazing incidence angle, a minor misalignment may change the angle by a noticeable fraction, thus moving the fluorescence CM towards the mid-plane if the grazing incidence angle is increased, or away from it otherwise. This causes systematic errors if the CM was used for the horizontal signal. On the other hand, the fluorescence signal intensity is not very sensitive to the incidence angle, especially in a grazing geometry. The minor impact on the detected intensity of shifting XRF distribution can be further minimized if we use two or more split PIN diodes and position them along the z-direction at appropriate locations.

EXPERIMENTAL TEST

Figures 9 shows a schematic of the XBPM and figure 10 shows an in-air test setup for demonstrating the principle of the grazing incidence XBPM. It consists of a water-cooled copper split collimator as the absorber and two imaging detectors made of a horizontal slot and a silicon PIN diode assembly. The APS diagnostics undulator beamline, designed to accept the full undulator beam, was used to test the XBPM. The transverse calibration was performed by scanning the XY stages built in the XBPM support. Figure 11 shows vertical scan data for different undulator gaps. It can be seen that the gap dependence is well below ±25 μm in these tests. Figure 12 shows horizontal scan data for different undulator gaps, showing a stronger gap-dependence, as expected from a sampling XBPM. Since the diagnostics undulator is a high-energy low-power device, these tests are limited in scope. We are

not able to quantify the effect for an undulator harmonic to cross the Cu K-edge, nor can we study the impact for a major power diffraction ring to pass the PIN diode. Furthermore, the permanent distortion due to thermal expansion hysteresis will not be studied until the XBPM is installed in an Undulator A front end.

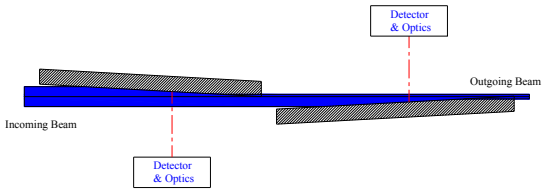

Figure 9: Schematic of the grazing incidence XBPM.

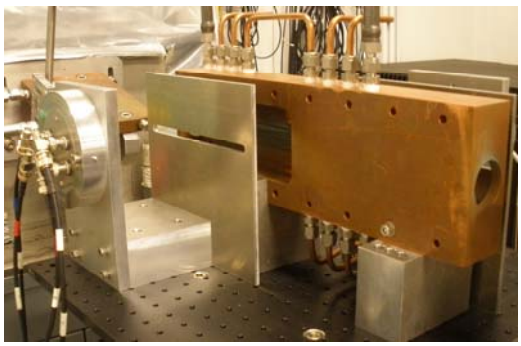

Figure 10: A test setup to demonstrate the grazing incidence XBPM sign principle.

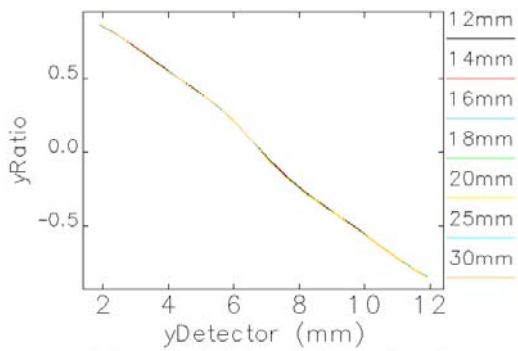

Figure 11: Vertical XBPM scan data for several undulator gaps.

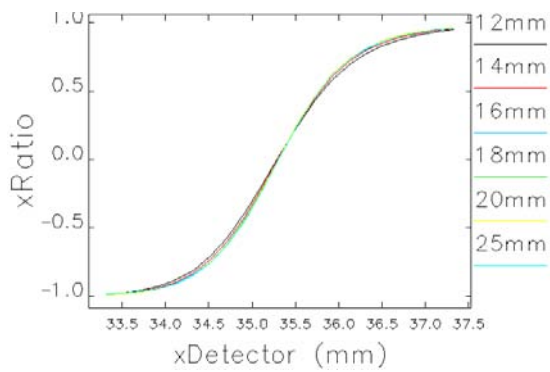

Figure 12: Horizontal XBPM scan data for several undulator gaps.

SUMMARY

We propose to combine the functions of the limiting aperture and an XBPM in the APS ID front ends and discuss one design to illustrate the concept. A vertical wall absorber was chosen for its power-bearing capacities; slit-camera geometry was chosen to read the vertical CM position of the fluorescence footprint. The horizontal position is derived from signal imbalance between two opposing absorbers to minimize the impacts of angular alignment error, thermal bumps, and x-ray powder diffraction. Gap-dependent compensation for horizontal readout is discussed. A preliminary test successfully demonstrated the validity of the principle.

REFERENCES

[1] G. Decker, "APS beam Stability Studies at the 100-nanoradian Level," these preceedings.

[2] D. Shu, B. Rodricks, J. Barraza, T. Sanchez, and T. M. Kuzay, "The APS x-ray undulator photon beam position monitor and tests at CHESS and NSLS," Nucl. Instrum. Methods, A 319, 56 (1992).

[3] B. L. Henke, J. A. Smith, and D. T. Attwood, "0.1-10-keV x-ray-induced electron emissions from solids-Models and secondary electron measurements," J. Appl. Phys. 1852 (48) 1977.

[4] M. Sanchez del Rio and R. J. Dejus, "Status of XOP: an x-ray optics software toolkit," SPIE Proceedings Vol. 5536 (2004) pp.171-174.

[5] Jay L. Devore, *Probability and Statistics for Engineering and the Sciences*, 7th ed. Brooks and Cole, Belmont, CA, (2007).

[6] B. X. Yang, A. H. Lumpkin, G. A. Goeppner, S. Sharma, E. Rotela, I. C. Sheng, E. Moog, "Status of the APS Diagnostics Undulator Beamline," PAC'97, 8P045, p. 2207 (1997); http://www.JACoW.org.

[7] B. Yang, E. E. Norum, S. Shoaf, and J. Stevens, "X-ray Wire Scanner," these proceedings.

[8] Y. Jaski, "New front-end design for multiple in-line undulators at the Advanced Photon Source," AIP Conf. Proc. 705, 356 (2004).

BUNCH-BY-BUNCH DIAGNOSTICS AT THE APS USING TIME-CORRELATED SINGLE-PHOTON COUNTING TECHNIQUES*

B. X. Yang, W. E. Norum, S. Shoaf, and J. Stevens
Advanced Photon Source, Argonne National Laboratory, Argonne, IL 60439, USA.

Abstract

Time-correlated single-photon counting (TCSPC) techniques have been used for bunch purity measurement since the Advanced Photon Source (APS) started operations. Recent improvements of the monitor have increased the signal-to-noise ratio and dynamic range to about 100 billion. Resolution improvements of commercial TCSPC components to under 50 ps FWHM allowed us to measure the longitudinal profile of individual bunches in the APS storage ring using a single-photon avalanche photodiode and a PicoHarp 300 TCSPC unit. Due to its robustness, the system operates continuously and measures the average longitudinal profile of the stored beam, updating the process variables for bunch phases and bunch lengths every 8 seconds. In a third application, using a TCSPC x-ray detector with an x-ray wire scanner in the monochromatic beam of the diagnostics undulator, measurements of transverse profiles of individual bunches can be completed in less than 4 minutes. It showed that, due to energy losses to the storage ring impedance, the high-current bunch clearly travels a different trajectory from low-current bunches. These bunch-by-bunch diagnostics provide valuable beam information to users performing timing experiments.

INTRODUCTION

Time-correlated single photon counting (TCSPC), a technique for measuring arrival time of the photon pulses against a clock pulse train, is a well-established technique for studying time-resolved phenomena in physics, chemistry and biology [1,2]. At the Advance Photon Source (APS), this technique has been used for bunch purity measurement since 1999 [3].

Figure 1 shows a conventional TCSPC instrument. It uses a time-to-amplitude converter (TAC) to produce a pulse with its amplitude proportional to the interval of time between the signal pulse (START) and the clock pulse (STOP), and an analogue-to-digital converter (ADC) to measure the pulse height. Since only one signal pulse can be processed during the interval between two clock pulses, the dead time may be as long as a clock period, and obtaining a high count rate and long time-scale at the same time is difficult. Modern TCSPC instrument, however, digitizes the event time using time-to-digital converters (TDC). Figure 2 shows the timing diagram of a TDC: A high-frequency clock and one or more lower-frequency timing signals establish a timing grid. Internally, the TDC generates higher-frequency ticks to make finer timing divisions. When a signal pulse (event) triggers the counter, the number of ticks since the last clock pulse, $\tau(k)$, the number of clock pulses since the last timing marker, $t(j)$, and the number of timing markers since the instrument are enabled, $T(i)$, are recorded by the internal circuitry, giving the complete timing information of the event. In the time-tagged time-resolved (TTTR) mode, the complete set of event timing information, (i, j, k), is recorded for user processing. In histogram mode, these events are collected and made into frequency of occurrence within designated intervals by an internal program. Using the TDC, more than one event can be recorded between two clock pulses, and a high count rate of several Mc/s is not in conflict with a long time scale of μs or even ms. In the following examples, we will show how the TDC-based TCSPC techniques are used at the APS for accelerator diagnostics.

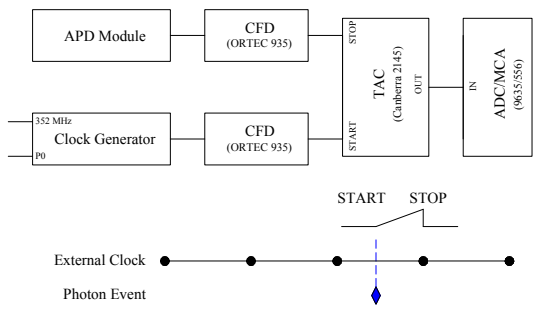

Figure 1: Conventional TCSPS and timing diagram.

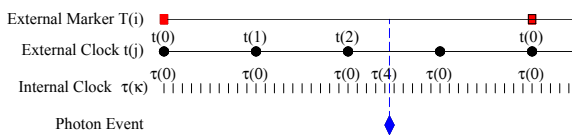

Figure 2: Digital TCSPS timing diagram.

BUNCH PURITY MONITOR UPGRADE

The original APS bunch purity monitor used the conventional TAC-ADC technique. It was used 2–3 times daily and provided bunch purity data typically at the 10^{-6} – 10^{-7} level [3]. Our upgrade effort included redesign of the fluorescence-target; improvement of the detector and analogue electronics operations, and implementation of an field-programmable gate array (FPGA) based TDC [4].

Redesign of the fluorescence target chamber

Figure 3 shows the redesigned fluorescence target

* Work supported by U.S. Department of Energy, Office of Science, Office of Basic Energy Sciences, under Contract No. DE-AC02-06CH11357

chamber. The chamber is made of thick brass alloy, which contains 3% Pb to provide effective shielding from scattered x-rays in the hutch. The target chamber is 1 cm in diameter, 2.5 cm long. The entrance path was shielded by a long, narrow tube to reduce solid angles of back-scattered x-rays. By shortening the multiple-scattering time to well below the accelerator bucket length of 2.84 ns (80 cm), we make the backscattered x-ray pulses appear under the main peak, instead of several ns later. Furthermore, the upstream white x-ray slits are opened wider to improve the signal-to-noise ratio.

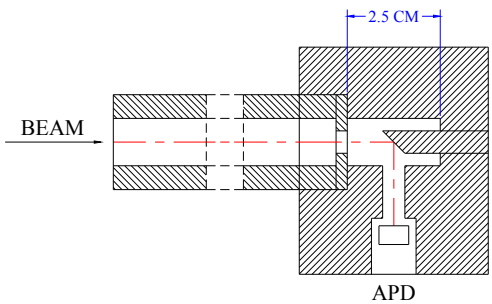

Figure 3: A compact target chamber design.

Fpga-based time-to-digital converter

A fast TDC was implemented on an Altera Stratix II fpga [4], using the storage ring revolution clock (P0) as the coarse timing marker and the 44-MHz subharmonic of the storage ring rf frequency as the external clock. Inside the fpga, the external clock frequency was quadrupled to provide a 352 MHz bunch clock; and it is further multiplied 16 times to make internal clock ticks. Due to a limitation of the FPGA, only six accumulators can be implemented per bucket, allowing 7776 accumulators per revolution of electrons in the ring. In the experiment, we found that the FPGA system may handle count rate well above 1 Mc/s while maintaining the range of 3.68 μs to cover the entire ring. However, we were unable to test the system's theoretical 176 MHz burst count rate limit. As we will see in the next paragraph, the TDC provided additional timing information for trouble-shooting the bunch purity monitor detectors and electronics.

Improved operation of detector electronics

In the old configuration, the APD detector module is connected to a constant fraction discriminator (CFD) located outside of the x-ray enclosure via a coaxial cable over 40 m long, which significantly attenuated the 2-ns signal pulse and picked up substantial rf noise from the accelerator components located nearby. To characterize the source of the noise, we moved the APD detector away from the target to reduce the signal and collected counts continuously for 5 hours. Figure 4 shows a histogram as a function of bucket numbers, where a significant level of noise can be seen between buckets Nos. 800 and 900. Figure 5 shows the integrated counts between bucket numbers 845 and 890, plotted as a function of time. We can see that the noise counts are recorded only during top-up injections when the stored current increases. We concluded that the long signal cable was picking up injection kicker pulses from the storage ring.

To reduce the noise pickup, we installed a CFD within 1 m from the APD detector module, and its threshold was set higher to match the unattenuated signal amplitude. This immediately improved the measured bunch purity to down around the 10^{-10} level, as can be seen in Figure 6. At this level, after-pulsing of the APD detector [5] appeared to be the main contributor of the background. We discovered that, if the applied high voltage on the APD is turned off for one minute every few hours and the accumulated charges are drained through a 10-Mohm resister bypassing the APD, the background counts can be significantly reduced, as shown in Figure 7. This power cycle is performed automatically by the EPICS IOC controlling the pulse processor.

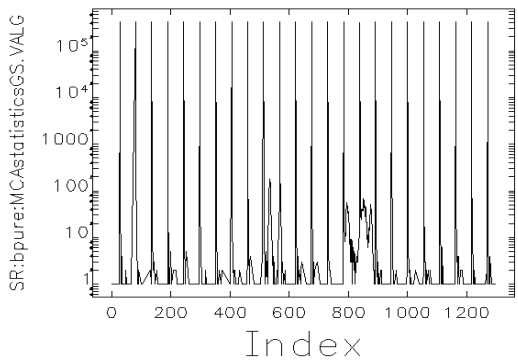

Figure 4: Noise picked up by long cables of APD module: The horizontal axis shows the rf bucket number; the vertical axis shows the counts per bucket.

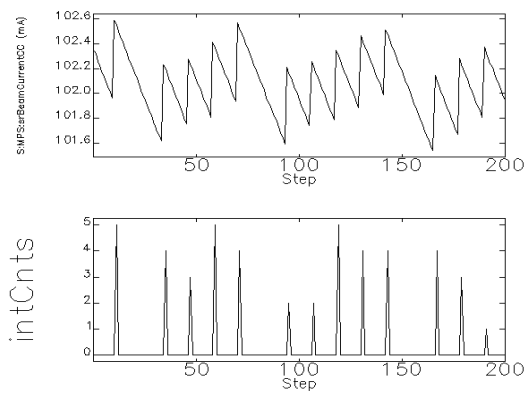

Figure 5: Integrated counts between bucket numbers 845 and 890. The bottom plot shows correlation with top-up injection as indicated by current increase in the top plot.

Figure 7 also shows a typical bunch purity histogram: while the main peak exceeds 10^{11} counts cumulated over 5 days, there are few counts between 20th and 30th buckets after the main bunch. The impurity bunch profile shows

the electron halo density in the fundamental bucket of the APS injector Particle Accumulator Ring (PAR), with more pronounced peaks at ±3 buckets due to the 12-th harmonic (117.3 MHz) rf compressor. A broad peak below 10 counts can be seen around bucket No. 36, which originates from the rare event when a few electrons are extracted in the second turn and survived through the booster synchrotron. All these impurity peaks are carefully monitored during user operations so they do not increase out of specifications.

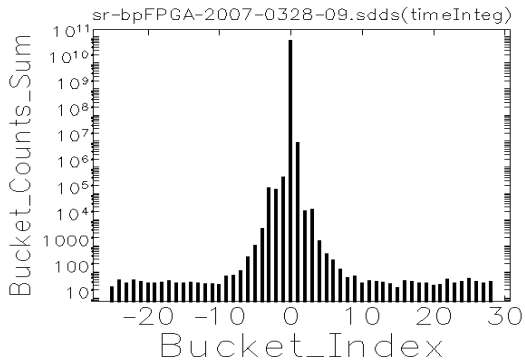

Figure 6: Bunch purity histogram using a CFD near the APD. The background is likely from afterpulsing.

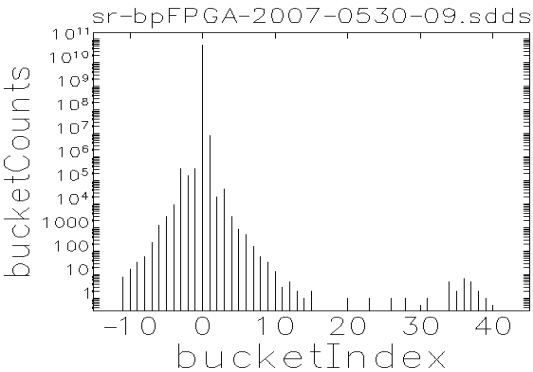

Figure 7: Bunch purity histogram with periodic automatic power cycling of the APD.

BUNCH LENGTH MONITOR

Since 1997, streak camera has been used to measure the bunch length and longitudinal bunch profiles at the APS. As users require more detailed timing information for their increasingly sophisticated experiments, a reliable diagnostics needs to be developed to continuously provide longitudinal bunch profile information. Due to our experience with the robust operation of the bunch purity monitor, the TCSPC technique became our first candidate for this bunch length monitor.

The temporal resolution of the commercial TSCPC electronics has improved continuously and reached a few ps rms in the last decade. At the same time, fast single-photon avalanche photodiodes (SPAD) with advertised time resolution better than 50 ps FWHM and maximum count rate exceeding 1 Mc/s have become commercially available. Their resolution compares favourably with the ~ 50 ps rms width of the 16-mA bunch for hybrid fill operations, and ~ 40 ps rms width of the 24-bunch normal operations of the APS storage ring. Figure 8 shows the setup of our TCSPC bunch length monitor: The visible synchrotron light is focused on an SPAD, id100-20 from IDQ [6]. The output pulse of the detector was inverted, attenuated and fed to a TCSPC pulse counter, PicoHarp 300 from PicoQuant [7], which operated in the histogram mode. When tested with two bunch clock generators, one connected to the clock input (0) and another to the event pulse input (1), the combined electronic resolution was found to be 9 ps rms. To estimate the overall system resolution, we used the short electron bunches with a bunch current ~ 0.3 mA, during the 324-bunch beam operations.

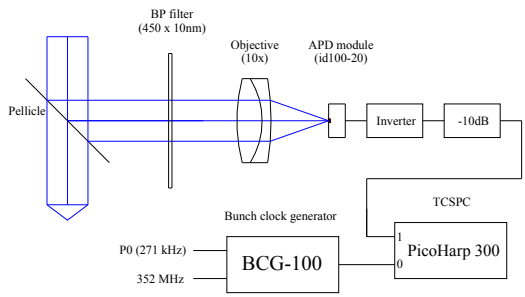

Figure 8: Schematic of the TCSPC bunch-length measurement system.

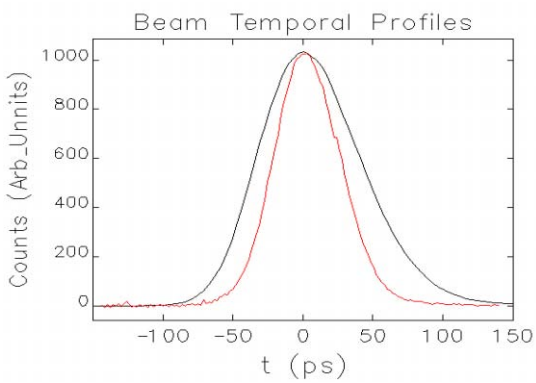

Figure 9: Acquired temporal profile for short bunches using a streak camera (red) and the TCSPC technique (black).

Figure 9 shows the temporal profiles acquired at the same time by both the TCSPC system and the streak camera. While the streak profile fits well with a Gaussian function with an rms width of 23.4 ps, the fit to the TCSPC profile gives an rms width of 35.7 ps. We concluded that the TCSPC system using id100-20 has an effective rms resolution of 27 ps, which is dominated by the contribution from the SPAD. While the short electron bunches are useful for calibration of the TCSPC system,

they are not being used by APS users for time-resolved experiments due to the short bunch spacing of 11 ns. Figure 10 shows the temporal profiles taken with TCSPC technique the using id100-20, PDM-50CT, another SPAD from Micro Photon Device [8], and a micro channel plate photomultiplier (MCP-PMT) from Hamamatsu, with a 4-mA bunch current, during 24-bunch operation. The profiles are compared with one acquired with a streak camera. While other TCSPC detectors have better resolution than the id100-20, as evidenced by the sharp front edges, their profiles contain significant tails. The figure also shows that the TCSPC profile is reasonably close to the true temporal profile of the bunch.

The histogram has 64 K channels, covering 260 ns at the highest resolution of 4 ps/bin. Since the storage ring revolution time is 3.68 μs, we need to set three clock pulses per revolution to fit all bunches in the histogram for hybrid fill, as shown in Figure 11. The bunches are, from left to right, Bucket 0 (16 mA), Groups 5, 1, 6, 2, 7, 3, 8, and 4. Each group contains seven 1.5-mA bunches.

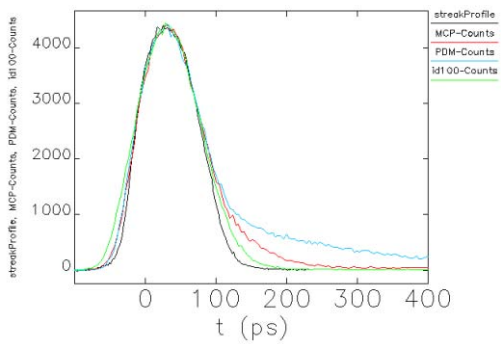

Figure 10: Comparison of the longitudinal profiles acquired with SPAD modules id100-20 (green) and PDM-50CT (blue), MCP-PMT R3809U-50 (red), and the Hamamatsu streak camera (black).

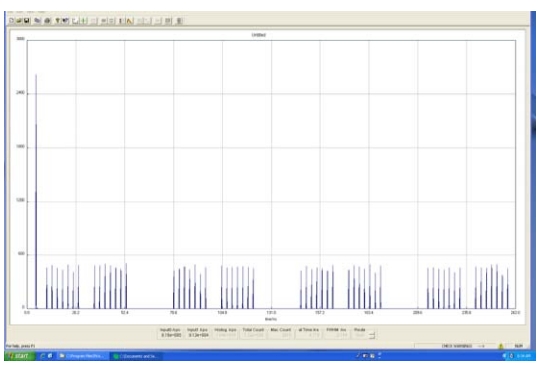

Figure 11: PicoHarp 300 control screen for profile measurement of hybrid fill.

A PC running Red Hat Enterprise Linux (RHEL) was used to control the PicoHarp through its USB interface. A histogram is accumulated every 8 seconds and transferred to the Linux PC, where it was sorted and the longitudinal time coordinates were added using the internal clock and the storage ring rf frequency at the time. The longitudinal profiles are fitted to a Gaussian function to obtain phase and width information. These profiles and fit parameters are made available online as process variables. Figure 12 shows a sample MEDM screen for the temporal profile of the 16-mA bunch during the hybrid fill operation.

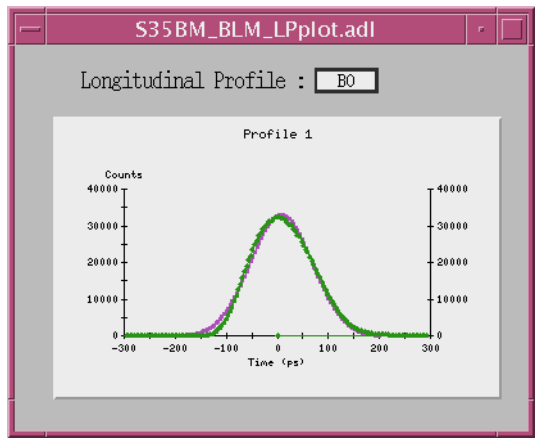

Figure 12: MEDM screen showing the acquired temporal profile of the 16-mA bunch (green) along with a Gaussian fit to the profile curve (purple).

X-RAY WIRE SCANNER

During the beam operations with hybrid fill, electron bunches with very different bunch currents are circulating in the ring at the same time. It is natural to ask whether these bunches have different energies and travel in different trajectories, and whether their differences impact user experiments. Measurement of the bunch properties can be performed using gated optical (gated camera) or electrical (BPM) detectors. However, the intensity dependence of these detectors often complicates the quantitative interpretation of the data. The TCSPC technique, while measuring only average properties, has a large dynamic range and collects data simultaneously for all bunches, significantly reducing potential ambiguities.

For a high S/N ratio, a scanning slits measurement is optimal, as shown in the discussions of the bunch purity monitor. But it also intercepts the entire beam. An x-ray wire scanner, on the other hand, minimizes its disturbance on the x-ray beam. Figure 13 shows such a scanner design. A copper wire with a diameter less than $\sigma/3$, where σ is the rms size of the x-ray beam, scans through the monochromatic x-ray beam at 30 m from the undulator source. The Cu-*K* x-ray fluorescence (XRF) photons from the wire are detected by an x-ray APD mounted nearby. A FPGA-based TCSPC pulse counter is used to determine the bunch number that excites the XRF. After completing the transverse scan, a computer program resorts the data and generates the transverse intensity profiles of individual x-ray bunches. Figures 14 and 15 show the horizontal and vertical bunch profiles, respectively for the hybrid fill pattern after normalizing them at the peaks.

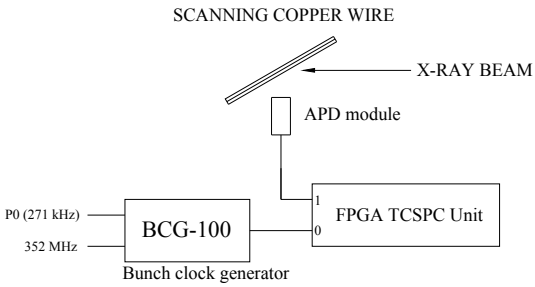

Figure 13: Schematic of the x-ray wire scanner.

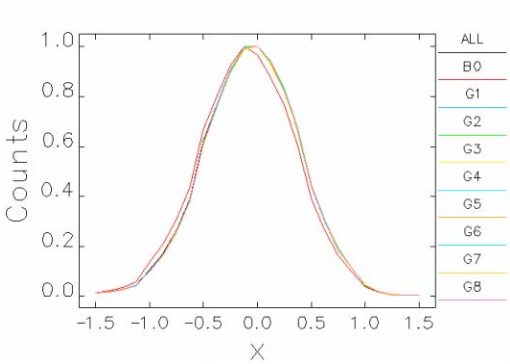

Figure 14: Normalized x-ray beam profiles for hybrid fills in the horizontal direction. The high-current bunch is offset from other low-current bunches by 50 µm.

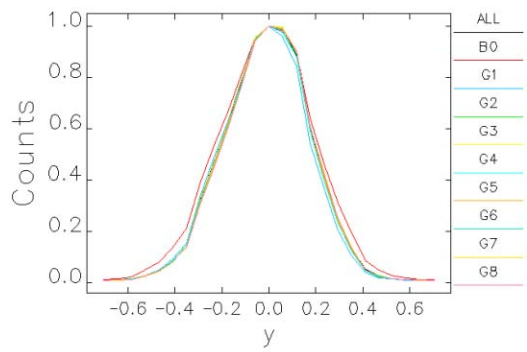

Figure 15: Normalized x-ray beam profiles for hybrid fills in the vertical direction. The high-current bunch is larger than the low-current bunches by about 20%.

Figure 14 shows that the horizontal x-ray profile of the high-current bunch is shifted by 50 µm compared to low-current bunches at 30 m from the undulator. This is likely due to the energy losses to the storage ring impedance: A high-current bunch loses more energy per turn in the storage ring. To maintain the same average energy as the low-current bunches, it acquires more energy from the rf cavity. Hence the electrons in the high-current bunch have higher energy at Sector 1 coming out of the rf cavities, and lower energy at Sector 35 before re-entering the rf cavities. As a result, the x-ray spectra of the high-current bunch are shifted higher in Sector 1 but shifted lower in Sector 35. At locations with non-zero dispersions / dispersion slopes, the x-ray source / beam directions from the high-current bunch differ from those from the low-current bunches. In Figure 4, the dispersion slope is likely the main contributor for the x-ray beam offset. Figures 14 and 15 also show that the high-current bunch has larger beam sizes than do the low-current bunches, likely due to its higher energy spread and the dispersions at the source point.

SUMMARY

The TCSPC technique has been used for bunch-by-bunch diagnostics of the stored beam in the APS storage ring. For bunch purity monitors, the new TDC and improved detector and electronics have made significant performance improvement possible. We demonstrated that it is possible to use TCSPC technique for measuring the longitudinal and transverse profiles. We note that significant improvement of resolution is not only possible but also probable as we test other hardware and software tools. For example, developing a proper treatment for the tails in the detector response curve would allow us to use detectors with better temporal resolution, thus improving the system resolution. We would like to thank Glenn Decker and Louis Emery for stimulating discussions for the interpretations of the data. We would also like to thank Om Singh for his strong support of bunch purity system upgrade.

REFERENCES

[1] O. V. Desmond, and D. Phillips, “Time-Correlated Single Photon Counting,” Academic Press, London, 1984.
[2] W. Becker, “Advanced Time-Correlated Single-Photon Counting Techniques,” Springer, Berlin, 2005.
[3] A.H. Lumpkin, C.-Y. Yao, B.X. Yang, and T. Toellner, “Bunch Purity Evolution During APS Storage Ring Top-up Operations,” PAC’03, p. 2411 (2003); http://www.JACoW.org.
[4] W. E. Norum and B. Yang, Eric Norum, “A Novel FPGA-based Bunch Purity Monitor System at the APS Storage Ring,” PAC’07, p. 4384 (2007); http://www.JACoW.org.
[5] Y. Kang, et al, “Dark Count Probability and Quantum Efficiency of Avalanche Photodiodes for Single-Photon Detection,” Appl. Phys. Lett., Vol. 83, p. 2955, 2003.
[6] Datasheet for id100, IDQ, www.idquantique.com.
[7] Datasheet for PicoHarp 300, PicoQuant GmbH, www.picoquant.com.
[8] Datasheet for PDM Series, Micro Photon Devices, www.microphotondevices.com.

NUMERICAL STUDIES OF CURTAIN GAS JET GENERATION FOR BEAM PROFILE MONITORING APPLICATIONS IN THE ULTRA LOW ENERGY STORAGE RING*

M. Putignano†, C.P. Welsch, Cockcroft Institute and University of Liverpool, UK.

Abstract

For beam profile monitoring applications where low beam perturbation together with bi-dimensional imaging is required, ionization monitors based on neutral gas-jet targets shaped into a thin curtain are an interesting option. When integrated in ultra-high vacuum systems, such as in the Ultra-low energy Storage Ring (USR), where local vacuum preservation is of primary concern, such systems present severe difficulties linked to the creation and proper shaping of a high quality gas-jet curtain. In this contribution, investigations into the generation and evolution of the jet with the Gas Dynamics Tool (GDT) software and purpose-written C++ analysis modules are presented. By means of extensive numerical analysis the advantages of a novel nozzle-skimmer system in terms of curtain quality are summarized when compared to traditional axisymmetric gas-jet creation and curtain shaping by means of scrapers. It is also shown that variable nozzle-skimmer geometries allow for modifying the gas-jet characteristics in a wide range, including jet splitting and local density modulation. Finally, the layout of a test stand that will be used for an experimental benchmark of these studies is shown.

INTRODUCTION

Low-energy physics and storage rings are recently attracting growing interest in the scientific community, as remarkable characteristics of quantum systems are most conveniently studied at low projectiles energies in the keV range [1,2]. Development of low-energy storage rings causes widespread beam diagnostic technologies to become obsolete. In particular preservation of the beam lifetime causes perturbing profile monitoring, like e.g. interceptive foils, to be ruled out [3]. Furthermore, existing non-perturbing techniques such as residual gas monitors can take up to about 100 ms [4] to make meaningful measurements, due to the low residual gas pressure, at the expected operating pressure of around 10^{-11} mbar. A possible solution around these limitations is constituted by a neutral supersonic gas jet target shaped into a thin curtain and bi-dimensional imaging of the gas ions created by impact with the projectiles. If the curtain is kept at a 45° angle from the impinging direction of the projectiles, and the ions extracted perpendicularly to this direction on a position sensitive detector, an image of the projectile beam transverse section is formed on the detector, much like a mirror reflection [5], as shown in Fig. 1.

Such monitor, as compared to those based on residual gas, allows injection of additional gas, in order to increase the ionization rate, together with efficient evacuation to keep the required vacuum level elsewhere in the storage ring, due to the high directionality of the supersonic jet [6]; furthermore, it allows simultaneous determination of both transversal profiles and beam imaging. At the same time, it is possible to use it also as a current and beam position monitor.

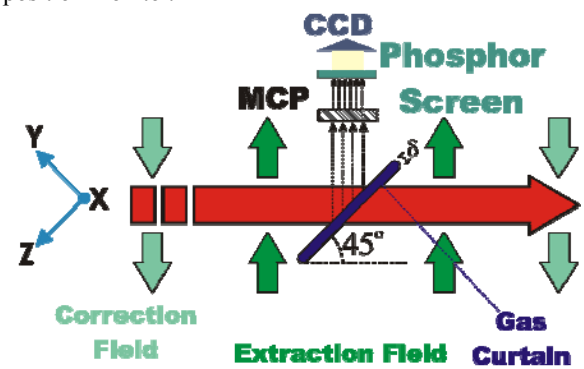

Figure 1: Jet-curtain profile monitor operation principle: the large horizontal arrow shows the projectiles path.

This monitor becomes hence the monitor of choice for multi-pass, low-energy, ultra-high vacuum storage rings such as the Ultra-Low Energy Storage Ring (USR), to be installed at the Facility for Low Energy Antiproton and Ion Research (FLAIR), in the FAIR facility planned to be built at GSI, Darmstadt, Germany.

Crucial to such monitor is the generation and control of the gas-jet in terms of achieved density and directionality. In order to prove that optimization of the jet performance can be obtained through suitable engineering of the nozzle-skimmer system for the jet generation, we have run a detailed numerical study of the fluid dynamic system.

NUMERICAL SIMULATIONS

Software Description

The software used for our simulations was a well-established commercial code, the Gas Dynamic Tool, GDT, developed by the CFD group of A. Medvedev in Tula, Russia. The code has been widely benchmarked against known flows, proving very reliable in dealing with high compressibility effects such as shock waves.

*Work supported by the EU under contract PITN-GA-2008-215080, by the Helmholtz Association of National Research Centers (HGF) under contract number VH-NG-328 and GSI Helmholtzzentrum für Schwerionenforshung GmbH.
†corresponding author: massimiliano.putignano@quasar-group.org

Indeed, most of our benchmarking cases dealt with very rarefied gases at supersonic velocities.

In order to select the optimum set of equations for the solver, we considered that the initial expansion stages of a typical beam diagnostics gas-jet apparatus are housed in vacuum vessels which are kept at relatively high pressures of $10^{-2}\div10^{-4}$ mbar, while the jet itself has a typical pressure of 1÷0.1 mbar. At room temperature, this equates to mean free paths in the sub-millimeter range, hence still compatible with the continuum description of the flow (Knudsen number < 0.2), allowing the use of the Navier-Stokes equations as opposed to a full molecular description of the gas behavior. In turn, these reduce to the Euler equations as it has been shown that the gas-jet expansion is a quasi-isentropic process [7], and viscosity effects can be neglected. Hence, we have used the GDT continuum flow solver based on the Euler equations.

The boundary conditions have proved to be a crucial point in the simulations. Differently from a standard approach to supersonic flows, the boundary conditions have been set to constant pressure in the regions less exposed to supersonic flow, in order to stabilize the results; whilst only in the regions where supersonic flow is not negligible, mainly downstream the expansion, standard floating value boundary conditions have been kept, to avoid reflection of artifact shock waves formed at the interface between the flow and the constant pressure boundary. In fig. 2-3 it is shown how this choice of boundary conditions leads to a much more stable solution as compared to indiscriminately assigning floating boundary conditions on all sides.

Given the output of GDT in the form of a value matrix, shown on screen by the GDT Visualizer Package, we then completed the code with our own C++ purpose-written analysis modules which import the data from the GDT output matrix, compute the variables of interest and organize them in suitable plots and tables.

Description of the Quality Factors

Differently from most other applications, which aim to low temperature jets, for application to beam diagnostics, there are different characteristics of interest in the curtain by which it is possible to assess its performance.

Firstly, the Mach Number reached downstream the skimmer at the designed point of interaction with the projectile beam (M), which gives an indication of the efficiency of the expansion: it is linked to the efficiency of transferring thermal energy into kinetic directional motion and hence directly relates to the directionality of the jet. Secondly, the geometrical dimensions of the gas curtain: width and depth (W and D respectively), which affect the resolution of the monitor [6].

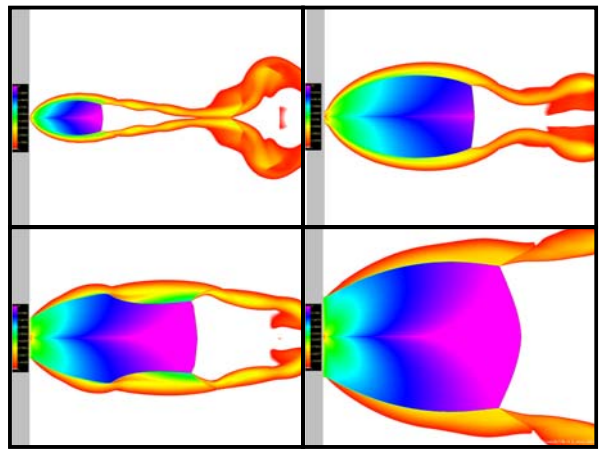

Figure 2: subsequent stages (top line 0.5 ms; 1 ms; bottom line 1.5 ms; 3 ms) of the free expansion of an axissymmetric gas jet computed by GDT using open boundary conditions on all boundaries. Time instability of the equilibrium pattern is shown. The flow reaches a first condition of equilibrium (top left); then expands further and reaches a second position of equilibrium (top right); only to show some instabilities (bottom left) and finally blowing up (bottom right) until it eventually exceeds the simulation domain (not shown).

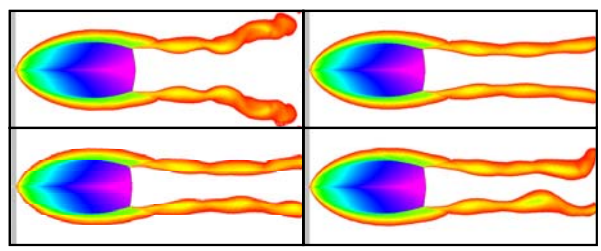

Figure 3: subsequent stages (5 ms, 10 ms, 300 ms, 650 ms) of the free expansion of an axissymmetric gas jet computed by GDT using the optimized boundary conditions discussed in the text. An equilibrium pattern is visible in the region of interest upstream the main Mach Disk shock wave .

To show the importance of the geometry of the nozzle-skimmer system for the curtain characteristics, we run several set of simulations, varying 5 geometric parameters, which we will refer from now on as variables.

The variables are: the skimmer aperture angles in the direction parallel (α), and perpendicular (β) to the curtain expansion, the width of the skimmer slit (SW), the depth of the skimmer structure (SD) and the nozzle-skimmer distance (Dist), as shown in Fig.4.

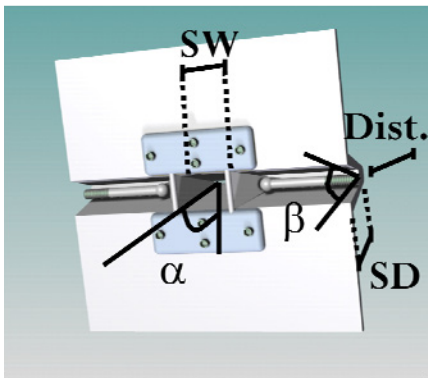

Figure 4: Geometric variables of the skimmer.

Results

We have run about 5000 simulations using different geometrical parameters for the nozzle-skimmer system, automating the numerical investigation through our own purpose written c++ code, which also took care of the computation of the three quality factors.

When analysing this system we are confronted with 5 variables, resulting in an exceedingly complex set of results, whose mathematical description needs a detailed treatment which goes beyond the scope of this paper. Our results are hence best expressed in the form of qualitative behavioural trends of each observable as a function of each variable, obtained by varying that variable alone while leaving the others constant.

A trend is intended to be found when the form of the functional relationship between the observable and the variable under investigation is preserved in the simulations regardless of the actual values of the other variables. This way, we are able to draw a table, shown in Fig.5, which summarises the simulated behaviour of each observable (column entry) when the respective variable is increased (row entry).

We identify linear relationships (straight arrows), parabolic relationships (curved arrows), and more complex relationships (circles), where even the form of the functional relationship depends on the value of some secondary variables (indicated inside the circle), and hence, according to our previous definition, a trend is not found.

This last one is a qualitatively different behaviour as compared to the first two cases, where the shape of the trend does not depend on the remaining variables, while still the details of the trend, such as the gradient for the linear relationships, will depend on the values of the remaining variables.

In the table the bold orange lines represent the very clear trends, defined as those trends where the average over all points of the best fit Pearson value lies above 90%, while the slim, black lines represents less evident trends, where the average best fit Pearson value lies between 75% and 90%.

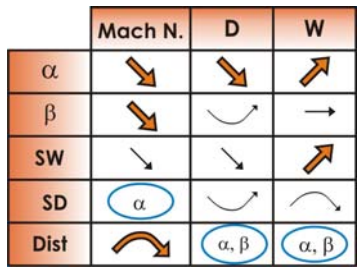

Figure 5: Table of simulated trends.

This table gives an indication of how sensitive the gas jet is to the geometry of the nozzle-skimmer system, hence providing strong evidence in favor of the need of a detailed study for the goal of proper optimization. Furthermore, it also gives an insight as to which variables have a stronger impact on the performance of the jet in terms of directionality (namely α, β and Dist) and curtain width to depth ratio (α and SW).

Two important examples of the plots from which the above table was deduced are shown in Fig.6-7. These two plots express the trade-off needed in choosing the angle α: indeed, while increasing α brings about an improvement in the width/depth ratio, crucial for resolution, it also decreases the efficiency of expansion at the expenses of directionality; furthermore, too high a value of alpha appears to bring instability in the response of the system to slight nozzle-skimmer distance variation. This could potentially become a problem as vibrations in the apparatus, slightly modifying the nozzle-skimmer distance could sensibly change the performance of the monitor.

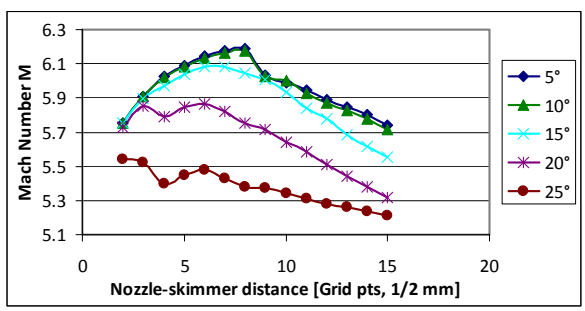

Figure 6: Mach number plotted as a function of nozzle-skimmer distance, with the aperture angle α as parameter. It is seen how increasing α brings about a decrease in Mach number, and hence decreases the expansion efficiency, worsening the directionality of the jet.

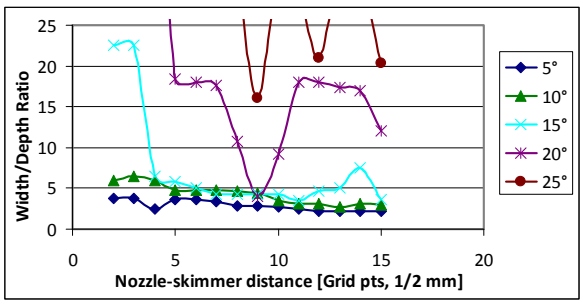

Figure 7: Geometric width/depth ratio plotted as a function of nozzle-skimmer distance, with the aperture angle α as parameter. Increasing values of α improve the width/depth ratio, hence increasing monitor resolution. However, the system becomes more unstable with respect to the nozzle-skimmer distance.

On the other hand, the examples also show how the nozzle-skimmer distance can be used to maximize the Mach Number without negatively affecting the geometric width/depth ratio.

It must be also mentioned that suitable modifications of the nozzle-skimmer geometric parameters, namely large α/β ratios, and small nozzle-skimmer distance, together with high pressure ratios bring about a peculiar "split" behavior in the formed jet curtain, illustrated in Fig.8. Such form of the curtain could be exploited for beam halo monitoring (where its peculiar density distribution could be exploited for decreasing the count rate in the high density core of the beam, avoiding detector saturation effects), or, in storage rings, where multi-pass operation is envisaged, even for halo scraping applications.

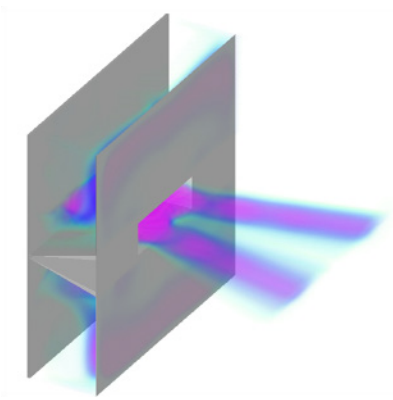

Figure 8: Simulated split curtain operation of the gas jet.

OUTLOOK

Experiments tailored to benchmarking the results described in this contribution are currently in preparation in our laboratories.

The vacuum vessels, the signal acquisition electronics and the detectors needed for the experiments were designed and are in the final stage of manufacturing, while the experimental stand which will hold the system has been already mounted in our laboratory (Fig.9).

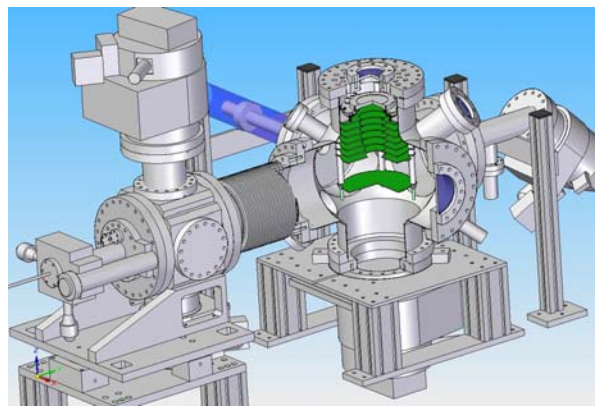

Figure 9: CAD of the experimental setup.

First experimental tests, which will characterize the created Argon and Nitrogen jet curtains density-wise, are expected to be performed before the end of 2010.

REFERENCES

[1] C.P.Welsch *et al*, "FLAIR – A facility for low-energy antiproton and ion research", Hyperf. Inter., 172, 71 (2006).

[2] L.H. Andersen *et al*, "Physics with electrostatic rings and traps", J. Phys. B: At. Mol. Opt. Phys., 37, p. R57-R88 (2004).

[3] J. Harasimowicz *et al*, "Beam instrumentation for the future ultra-low energy electrostatic storage ring at FLAIR", Hyperfine Interact (2009) 194:177-181.

[4] T. Honma *et al*, "Design and performance of a non-destructive beam-profile monitor utilizing charge-division method at HIMAC", Nucl. Instr. and Meth. A, 490 (3), p. 435-443 (2002).

[5] Y. Hashimoto *et al*, "Oxygen gas-sheet beam profile monitor for the synchrotron and storage ring", Nucl. Instr. Meth. Phys. Res. A, 527 (3), 289-300 (2004).

[6] M. Putignano *et al*, "A Fast, Low Perturbation Ionization Beam Profile Monitor Based on a Gas-jet Curtain for the Ultra Low Energy Storage Ring.", Hyperfine Interact (2009) 194:189-193.

[7] M. Jugroot *et al*, "Numerical Investigation of interface region flows in mass spectrometers: neutral gas transport.", J. Phys. D: Appl. Phys. (2004) 37:1289-1300.

INFLUENCE OF DARK COUNT ON THE PERFORMANCE OF SILICON PHOTOMULTIPLIERS

A. Intermite#, M. Putignano, C.P. Welsch, The Cockcroft Institute, Warrington WA4 4AD, UK,
Department of Physics, University of Liverpool, Liverpool L69 7ZE, UK

Abstract

The introduction of Silicon Photomultipliers (SiPMs) as single photon sensitive detectors represents a promising alternative to traditional photomultiplier tubes. This is especially true in applications in which it is compulsory to attain magnetic field insensitivity, low photon flux detection, quantum efficiency in the blue region that is comparable to standard photomultipliers, high timing resolution, dimensions comparable to the dimensions of an optical fiber diameters, and low costs. The structure of the SiPM is based on an array of independent Avalanche Photodiodes (APDs) working in Geiger-mode at a low bias voltage with a high gain. The output signal is proportional to the number of pixels "fired" by impacting photons. The detection efficiency for state-of-the-art devices is in the order of 20% at 500 nm. In this contribution, the measured dark count rates of different SiPMs are compared and the signal shape and statistical spectrum of this noise analyzed. A characterization of the effects on the noise of the bias voltage is performed as part of the study to determine the optimized working parameters for a future beam loss monitor at CTF3/CLIC.

INTRODUCTION

Sensors capable of detecting single photons have found different applications in fields as astronomy [1] laser ranging [2], Optical Time Domain Reflectometry (OTDR) [3] and beam loss detection [4], replacing in such applications the former use of photomultiplier tubes (PMTs). The need to reduce the detector dimensions and to produce marketable nanotechnology applications require the use of small area, highly sensitive detectors that combine integrated readout circuitry functionality in a cheap fabrication process. In addition, small area detectors can be easily integrated in a dense array, be coupled with optical fibers, and reach high sensitivities.

Due to their high quantum efficiency, magnetic field immunity, robustness, low costs, possibility to operate at non-cryogenic temperatures and single photon detection capability, SiPMs are considered a suitable candidate for the readout of optical fibers in a beam loss detection system [4].

In this contribution, the operation principle of the beam loss monitor that will be used at CLEX/CLIC is introduced before a noise study for the SiPM, providing both a theoretical description and a set of experimental data, is described in detail. Within the analysis the behaviour of the noise with respect to the bias voltage applied to the SiPM by the user and to the quality of the manufacturing features dependent on the supplier are explored.

BEAM LOSS DETECTION

For detecting and localizing beam losses in an accelerator, it is possible to exploit the generation of Cerenkov light inside optical fibers generated by impinging charged relativistic particles. At the locations where particles are lost from the main beam in the accelerator, these are likely to generate secondary particles through interaction with material, such as the beam pipe. These secondary charged particles are typically moving at relativistic velocities, hence, when they cross a medium with high enough dielectric constant, such as an optical fiber, they generate photons by the so-called *Cerenkov Effect* [5]. In such a configuration the fiber can be used to guide these photons to a SiPM, optically coupled to the fiber end [6]. In order to detect the beam losses at CTF3/CLIC, a system consisting of two parallel fibers connected to two identical SiPMs with an active surface matched to the fiber core of 1 mm^2 is under consideration.

The first fiber is used to carry a reference signal, and is chosen to be a low attenuation multimode fiber with a large core diameter. This maximizes the length of interaction with the escaping particles and thus the production of Cerenkov photons. The second arm is instead a composite sensor, realized by separating equally long sections of a fiber identical to the one in the first arm by splicing in between them equally long section of a different fiber with larger attenuation. This way, the number of Cerenkov photons reaching the SiPM at the end of the second arm will be smaller than the number reaching the SiPM in the first arm by a factor depending on how many section of the more attenuating fiber were crossed and, therefore, on the position of the loss.

Simulation studies indicate that this sensor has the ability to achieve a resolution of down to a few centimeters, depending mainly on the length of the spliced fiber sections in the second sensor. In addition, each signal is read independently and the absolute position is then calculated from the intensity ratio in the two branches. This guarantees that there is no overlap of the signals and it becomes possible to detect multiple signals without using clock triggers.

The high spatial resolution of the monitor is particularly relevant when there is the need to monitor losses in narrow spaces as for example in the CLIC Experimental

#Corresponding author : angela.intermite@quasar-group.org

area (CLEX). In this test facility, two beams run parallel to each other: the drive beam and the probe beam.

The accelerator hall of the CLEX building, shown in Fig. 1, measures 42.5 m by 8 m, and the distance between the two beams is about 0.75 m.

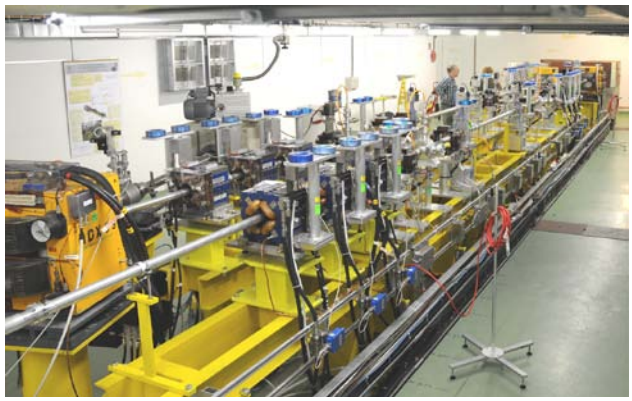

Figure 1: Photo of the CLEX area, showing the two beam pipes running parallel to each other.

This contribution will focus on the characterization of the photon detector used for this project, the SiPM.

SiPM Structure and working principle

A SiPM is composed of an array of Single Photon Avalanche Diode (SPAD) cells, combined to form a macroscopic unit. In most of the SiPMs that have been studied in the frame of this work, about 500 cells are used to cover an area of 1 mm^2. Each cell operates in limited Geiger mode, a few Volts above the breakdown voltage. In this working mode, the device can remain in a steady state until a free carrier such as an incident photon enters into the depletion zone. This photon generates an electron/hole pair, acting as a charge carrier that is accelerated by the electric field set by the bias voltage provided, releasing other carriers by impact ionization. Being the bias voltage above breakdown, the liberated carriers acquire enough energy to ionize more carriers in turn, resulting in triggering a self-sustaining avalanche. The avalanche is then quenched by suitable external circuitry, which includes a large load resistance for the current and hence limits the current flow in the detector. Limiting the current flow turns off the avalanche and allows the detector to recover and be able to detect another photon [7, 8].

The general features that are required to ensure detection of most incident photons are:

- Low dark count;
- Low pixel to pixel optical coupling;
- High photo detection probability;
- Fast time response;
- Low after pulsing;

Depending on the device structure, recovery times ranging from 3 ns to 50 ns can be observed. A typical SiPM signal is shown in Fig. 2.

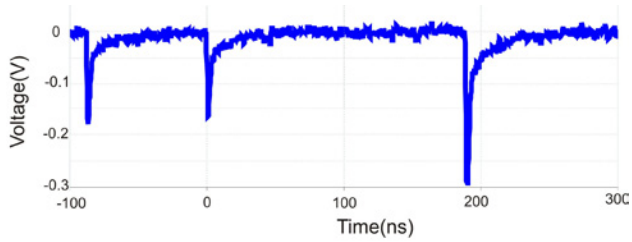

Figure 2: Example of a typical SiPM signal that illustrates the recovery time of a single cell after a signal peak.

Dark Noise

In addition to the real signal, electron/hole pairs can also be generated in the depletion region of a SiPM by thermal generation of carriers through Shockley-Read-Hall (SRH) recombination-generation centers or by bulk diffusion of minority carriers from the quasi-neutral region. The generation of electron/hole pairs and thermal bulk diffusion represents the characteristic noise of this type of detectors and, being undistinguishable from the real signal, sets a limit for the ultimate sensitivity of these devices. In the absence of light, the electrical effect of these mechanisms is referred to as dark count rate and determines the number of noise counts generated in the detector per second.

In a SiPM the instantaneous current that is conserved everywhere in the circuit is given by [9]:

$$i(t) = \frac{A}{V}\sum_{n} - q v_{xn} = - q \frac{N}{L} < v_x >_N$$

Where A, V and L refer, respectively, to the area, the volume and the length of the SiPM and the sum over n is performed for all N carriers in the device. v_x is the carrier velocity along the x axis.

The average instantaneous current is zero. However, since the velocity and the number of carriers can fluctuate, $i(t)$ generally is not exactly zero at any given time. This small deviation from zero is responsible for the so-called *current noise*.

Two sources of noise coexist in this last equation for the *current noise*:

- Thermal or Johnson/Nyquist noise: the velocity of each carrier fluctuates due to scattering during thermal motion.
- Generation-recombination noise: the number of carriers fluctuates because of generation-recombination processes.

When it comes to the application, the dark noise influences the performance of the detector depending on the specific light intensity level to be monitored.

When the photon flux is high, provided the detector is not saturated, i.e. when the number of photons per nanosecond is larger than 1 and smaller than about 250 for a 500 cells SiPM, one has a considerable increase in the number of cells firing within the time scale that is typical for the development of the avalanche; 1÷5 ns in optimum operating conditions. This results in an overlap of the signals of different cells, thus producing

proportionally higher signal peaks. This allows to clearly distinguish these events from the peaks caused by noise, which are mainly single cell events, by setting a discrimination threshold. On the other hand, when the photon flux is low enough that the probability of more cells firing in a window of few nanosecond is small (<50 photons per μs), one must resort to count single cell peaks. This makes it difficult to easily discriminate the dark counts from the signal of interest and hence results in an error added to the measurement. Therefore, it sets a limit to the minimum photon rate detectable.

Other Sources of Noise

There are several other sources of noise that can contribute to the total noise in the SiPM signal. Depending on the respective working conditions these can become dominant and should therefore always be carefully considered:

- *Gain noise* is specific to avalanche detectors. All avalanche photodiode generate excess noise due to the statistical nature of the avalanche process. This noise results in varying the amount of charge created in the avalanche from time to time, producing a broadening of the signal peak spectrum. The gain noise factor is a function of the carrier ionization ratio *k*. *k* increases strongly with the electric field across the structure, i.e. with the bias voltage provided, and also depends on the doping profile. In the Geiger mode, where the SiPM is biased above the breakdown voltage for operation at very high gain, this noise becomes particularly relevant, leading to rather broad peaks in the signal spectrum (see Fig.6). It can be reduced by cooling.
- *Cross-talk* due to the migration of photons towards neighboring pixels. Hot carriers in avalanche p-n junction can emit photons even in the visible range, which then fall in the detection range of other pixels. There are 3 different ways of cross talk, differing in the way the created photon reaches the neighboring pixel: direct, inside the depletion layer and through reflection. A solution to avoid the first way of cross-talk is to isolate pixels optically by trenches filled with an opaque material, whilst the others can be reduced by improving the purity of the material used and especially during the manufacturing process, where it is essential to avoid defects. All of this depends on the manufacturer and influences the choice of the supplier. In later sections it will be shown how drastically the cross talk depends indeed on the actual SiPM model tested.
- *After pulsing* caused by trapping centers in the depletion layer. Traps may result from the damage caused by an implantation in the fabrication process of the SiPM. These centers appear as deep levels in the energy gap of the semiconductor. They trap some avalanche carriers and release them with a statistical delay. If the delay is greater than the dead time after the previous avalanche pulse, a released carrier can re-trigger an avalanche and cause a statistically correlated pulse. The probability that an afterpulse occurs increases with the amount of charge that flows through the diode during a Geiger discharge. Thus, the afterpulsing probability increases with the increase of the bias voltage.

EXPERIMENTAL SETUP

Detailed studies of different SiPMs were carried out in an optical lab at the Cockcroft Institute. The setup illustrated in Fig. 3 was installed inside an optical black box to shield the ambient light.

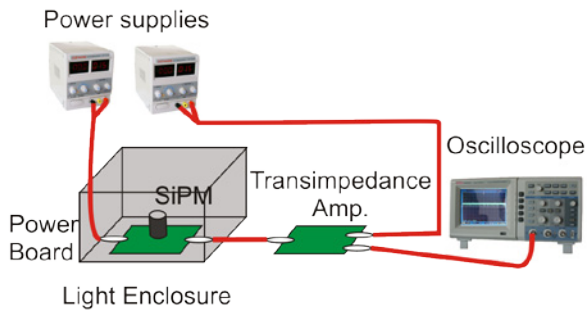

Figure 3: Illustration of the experimental setup used to characterize the SiPM dark noise.

The active surface of every tested SiPM was 1 mm^2. The number of cells ranged from 400 to 500 pixels. All models are equipped with an antireflective coating layer on every pixel. In addition, the quasi-neutral region thickness above the thin junction depletion layer is reduced to enhance the spectral response in the blue and near-ultraviolet wavelength ranges. Finally, each elementary cell is surrounded by a suitable trench filled with opaque material to drastically reduce the probability of optical crosstalk between neighbouring cells.

All SiPMs are not cooled and measurements were taken at room temperature.

Results

Tests measurements were done for the SiPMs of three different suppliers (ST-Microelctronics, Photonique, SensL), measuring the dark count rate and the peak height spectrum for each of them as a function of the bias voltage. In addition, 8 prototype detectors, which have yet to be released for commercial use, were tested.

It is important to study the behaviour of the noise when modifying the bias voltage since increasing the bias voltage is the main way to increase the sensitivity of the detector and the signal to noise ratio.

To illustrate this, Fig. 4 indicates the behaviour of a typical signal as a function of the bias voltage for a selection of the samples considered in this study: by increasing the bias voltage, the peak height increases, as it is expected: A higher bias voltage leads to more energetic carriers able to produce more ionizations. The same effect

also influences the dark noise signals, which are also described by plots identical to the one in Fig.4.

Bringing the bias voltage up by 3V produces an increase in the signal by a factor of 3. However, it must be noted that the signal rise time also increases by a similar factor.

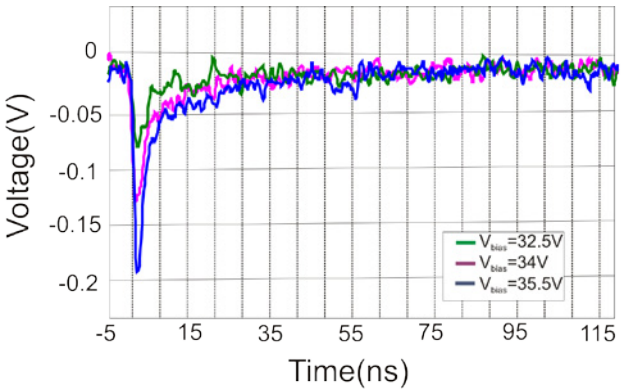

Figure 4: Variation of the dark count signal as a function of the bias voltage.

On the other hand, increasing the bias voltage also increases the probability of thermal generation of electron/hole pairs in the depletion region, resulting in an increase in the overall dark count rate. Fig. 5 shows measurements of the dark count rate for different SiPMs. All models have a breakdown voltage of about 29.5 V. A typical value of dark count rate for these devices is 1 MHz/mm^2, measured at a bias voltage of 32 V. Increasing the bias voltage by 3 V also produces an increase of the overall dark count rate of a factor 3.

Since the dark count rate is very high and depends on the temperature as well as on the overvoltage, a possible solution for reducing the noise is using a thermoelectric cooler (TEC) to guarantee temperature stability [10]. On the other hand, the trap lifetime in the depletion layer increases with lower temperatures, resulting in an increased after pulsing.

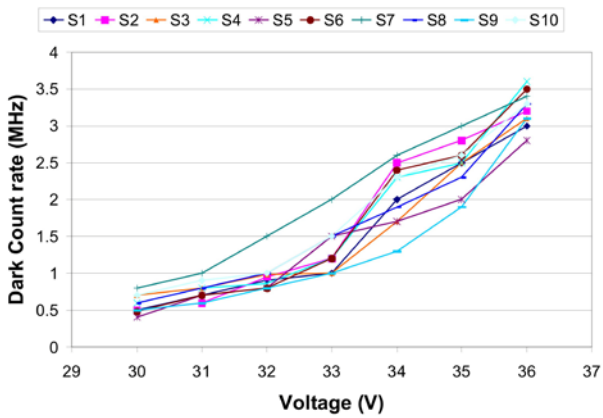

Figure 5: Variation of the dark count rate as a function of the bias voltage for 10 different SiPMs

To assess the contribution of rising the bias voltage on cross-talk noise, a more detailed analysis of the dark noise peak height spectra has been carried out.

If cross-talk was not present at all, the occurrence of double peaks, i.e. when two pixels fire simultaneously, and hence when the SiPM produces a voltage drop twice as high, should be only a statistical effect. This would lead to a spectrum following a Poissonian distribution. Any deviation from this spectral shape, in which higher voltage drops occur more frequently, can be safely attributed to cross-talk contribution to the dark noise.

Figure 6 shows 2 cross-talk spectra corresponding to the same SiPM sample for 2 different bias voltages. It can be seen how the peak amplitude moves rightwards, increasing with increasing bias voltage, in accordance with Fig. 4. The peak height ratio between the first and the second peak also increases by a factor of 1.7 when increasing the bias voltage by 3V, showing how the bias voltage increases the cross-talk effect, even though this contribution to noise is slightly less severe than the one on the overall count rate described in the previous paragraph.

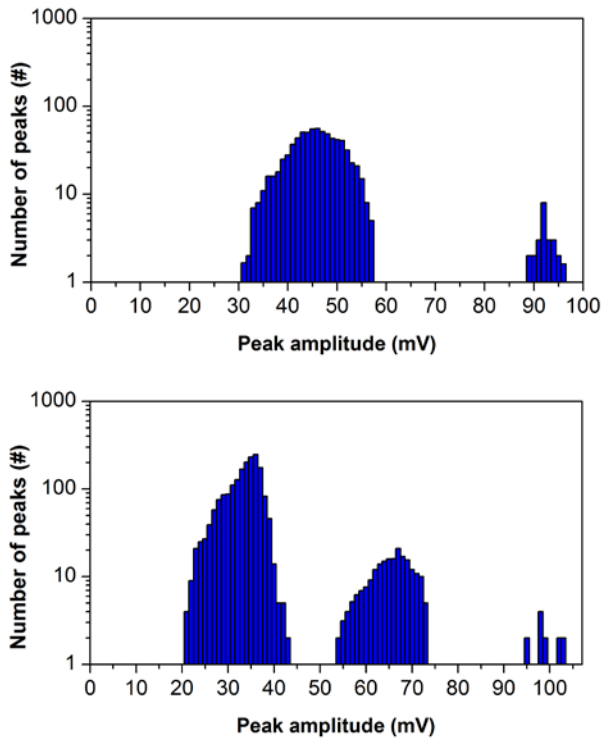

Figure 6: Peak height spectra for the same SiPM sample with two different bias voltages of 29.5V and 32.5V.

Finally, to show the importance of manufacturing techniques on the occurrence of cross-talk, peak height spectra at the same bias voltage of 32V for different SiPM samples were acquired, three examples are shown in Figure 7.

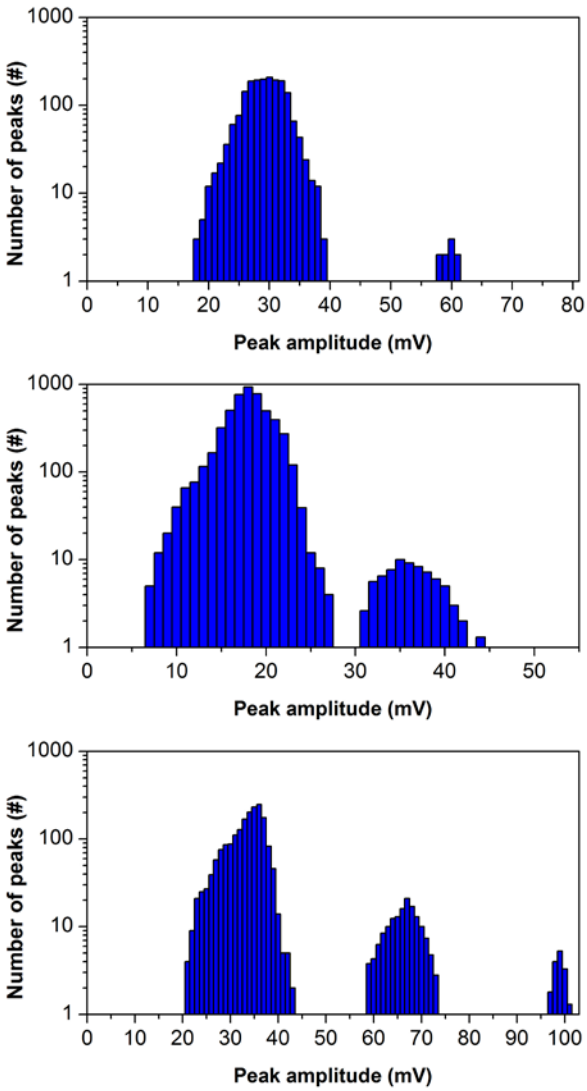

Figure 7: Plots of dark noise spectra at a bias voltage of 32 V for different SiPM samples.

Three different behaviors were observed. In the first and second plot 2 peaks were measured: the highest one, occurring at lower peak amplitude, is due to a single pixel firing, whilst the shortest is due to two different pixels firing in parallel. The last plot shows a different characteristics were even three different pixels were activated in parallel. The height ratio between the first two peaks shows an increasing occurrence of cross-talk in the three samples, differing by a factor of 1.3 between the first and the second sample, and even by a factor of 8 between the first and the third, showing how better manufacturing can improve the cross-talk performance by an order of magnitude.

These measurements allow thus to characterize the quality of different samples in terms of the cross-talk signal.

CONCLUSION

In this contribution the main sources of dark noise, i.e. the thermal generation of electron-hole pairs in the depletion layer and the optical crosstalk, which limit the performances of SiPM were analyzed and characterized, describing their response to different bias voltages and manufacturing techniques.

Experimental tests on several commercial and pre-release samples yielded a typical dark count rate of about 1 MHz/mm^2 for a bias voltage of about 2V above the breakdown value for essentially all samples. Increasing the bias voltage was shown to proportionally increase the signal peak height and overall dark count rate by similar factors of about 3 for a 3V increase, while showing a slighter effect on increasing the cross-talk by a factor of 1.7 for the same voltage increase.

The influence of manufacturing techniques on the cross talk was instead found to be severe, with spectra from different samples showing a difference in cross-talk occurrence by almost an order of magnitude.

Further tests and data acquisition are currently been carried out to improve the characterization of these devices and to select the best commercially available sample for a future beam loss monitor at CTF3/CLIC.

REFERENCES

[1] N. Nightingale, “A new silicon avalanche photodiode counting detector module for astronomy,” Experimental Astronomy 1, pp. 407-422, 1991.

[2] F. Zappa, G. Ripamonti, A. Lacaita, S.Cova and C. Samori, ”Tracking capabilities of SPADs for laser ranging,” 8th International Workshop on Laser Ranging Instrumentation, Annapolis, MD, USA, pp. 25-30, May 1992.

[3] G. Ripamonti, M. Ghioni and S. Vanoli, “Photon timing OTDR: A multiphoton backscattered pulse approach,” Electronics Letters 26, pp. 1569-1572, December 1990.

[4] F. Wulf, M. Korfer, “Local beam losses and beam profile monitoring with optical fibers,” Proceedings of DIPCA09, Basel, Switzerland.

[5] J. V. Jelley, “Cerenkov Effect and Its Applications”, British J. of Appl. Phys. 6, 1955, p. 227-232.

[6] P. Gorodetsky et al, “Quartz Fiber calorimetry”, Phys. Rev. Lett. 25 (1997), 56.

[7] P. Finocchiaro et al, “Characterization of a Novel 100-Channel Silicon Photomultiplier-Part 1: Noise”, IEEE Trans. On Electron Devices 55 (10), October. 2008, p. 2757 - 2762.80

[8] P. Finocchiaro et al, “Characterization of a Novel 100-Channel Silicon Photomultiplier-Part 2: Charge and Time”, IEEE Trans. On Electron Devices 55 (10), October. 2008, p. 2765 – 2772.

[9] E. Rosencher and B. Vinter, “Optoelectronics,” Cambridge University Press 2002.

[10] P K Lightfoot, G J Barker, K Mavrokoridis, Y A Ramachers and N J C Spooner , “Characterisation of a silicon photomultiplier device for applications in liquid argon based neutrino physics and dark matter searches,” Journal of Instrumentation, Vol. 3, 2008.

BEAM POSITION MONITOR DEVELOPMENT FOR THE USR*

J. Harasimowicz#, C. P. Welsch, Cockcroft Institute, Warrington WA4 4AD, UK,
and Department of Physics, University of Liverpool, Liverpool L69 7ZE, UK.

Abstract

Capacitive pick-ups for closed-orbit measurements are presently under development for an Ultra-low energy Storage Ring (USR) at the future Facility for Low-energy Antiproton and Ion Research (FLAIR). Low-intensity, low-energy antiprotons impose challenging demands on the sensitivity of the monitoring system. The non-destructive beam position monitors (BPMs) should be able to measure about 10^7 particles and give sufficient information on the beam trajectory. This contribution presents the status of the BPM project development. Main goals of the investigation include optimization of the mechanical design and preparation of a narrowband signal processing system.

INTRODUCTION

A diagonal-cut capacitive pick-up (PU) is a device of choice for beam diagnostics in hadron machines due to its highly linear response and large sensitivity. This beam position monitor (BPM) consists of four isolated and equally distributed metal plates formed to surround the beam. It provides information on beam offset by means of non-destructive measurements of electric field produced by passing bunches: by comparing the signals generated at each electrode, it is possible to determine the position of the beam centre. PU linearity, important for beams of non-negligible diameter, is assured by a diagonal cut of the plates. Their length is typically of 10-20 cm per plane, but still much less than the bunch longitudinal profile, and results in high signal strength. On the other hand, bulky dimensions might be a problem when only limited space is available. Also the capacitive coupling between the large electrodes should not be neglected and its reduction may lead to a complex mechanical design. Nevertheless, an optimised diagonal-cut PU can be a powerful tool for a variety of measurements, like beam position, Q-value or closed orbit determination [1].

The application of BPMs for low intensity, low energy beam diagnostics requires additional considerations. The signal-to-noise (S/N) ratio drops down with the decreasing beam current and becomes a dominating problem for beams with only few particles per bunch. In order to improve PU sensitivity, the signal U_S has to be amplified while the noise U_N needs to be significantly reduced. Since U_N is proportional to $\sqrt{(\Delta f)}$, where Δf is the bandwidth of the system, a narrowband signal processing is required for low intensity beam diagnostics. Further complications can be caused by low velocities. For $\beta < 0.1$, the beam can no longer be approximated by a TEM wave and deviations from a relativistic case should be taken into account. The field distribution becomes dependent on the beam displacement and the PU response may be affected [2].

* Work supported by the EU under contract PITN-GA-2008-215080, by the Helmholtz Association of National Research Centers (HGF) under contract number VH-NG-328, and GSI Helmholtz Centre for Heavy Ion Research.

#Janusz.Harasimowicz@quasar-group.org

BEAM PARAMETERS

The boundary conditions of a novel electrostatic Ultra-low energy Storage Ring (USR) [3] at the future Facility for Low-energy Antiproton and Ion Research (FLAIR) [4] put challenging demands on its beam instrumentation. The USR will store and decelerate antiproton beams from 300 keV to 20 keV, corresponding to β values of only 0.025 and 0.006 respectively. At such low energies the total number of particles is restricted by space charge limitations to about $2 \cdot 10^7$ antiprotons. With the ring circumference of 42.6 m, their revolution frequency f_{rev} will vary from 178 kHz to 46 kHz in the given energy range. To achieve bunch lengths of the order of 100 ns required in the standard operation of the USR, an RF field $f_{RF} = h \cdot f_{rev}$ with harmonic number $h = 10$ will be applied. The resulting frequencies and related beam parameters are summarized in Table 1. Since bunches will be at least 1 m long, a diagonal-cut capacitive pick-up will be an ideal tool for beam position monitoring. However, few particles per bunch as well as low β values have to be considered when designing the BPM system.

Table 1: USR beam parameters

Energy	300 keV → 20 keV
Relativistic β	0.025 → 0.006
Revolution frequency	178 kHz → 46 kHz
Revolution time	5.6 µs → 21.8 µs
RF frequency (h = 10)	1.78 MHz → 459 kHz
Bunch repetition time (h = 10)	560 ns → 2.2 µs
RF bucket length (h = 10)	4.4 m
Charge per bunch (h = 10)	0.3 pC ($2 \cdot 10^6$ pbars)

MECHANICAL DESIGN

The initial proposal for the diagonal-cut capacitive pick-up for the USR was already discussed in [5], but its final design includes several important modifications.

In order to avoid distortion of the electric field in the vicinity of the monitor edges, the inner diameter of the cylindrical PU is the same as of the straight section vacuum pipe of the USR. Initially, it had been assumed to

be as large as 250 mm, but this resulted in large dimensions of the vacuum vessel enclosing the BPM and in reduced signal strength. For this reason, the diameter was decreased to 100 mm. In addition, grounded guard rings were introduced at both ends and in the middle of the PU. The outer will help to minimize the effect of transition between the BPM and the vacuum chamber walls, while the inner will reduce coupling capacitance between X and Y planes. Approximate deviations from the idealized case with edge effects ignored were calculated in accordance with [6] and are presented in Figure 1. As a rule of thumb, guard rings of length equal to the beam tube diameter eliminate unwanted distortions. However, the rings length was limited to 40 mm in order to preserve space in the USR. With such a configuration, the discrepancies introduced by the boundary conditions will not be more than 2% for the image charge and scaling factor, and 0.2 mm for the centre displacement.

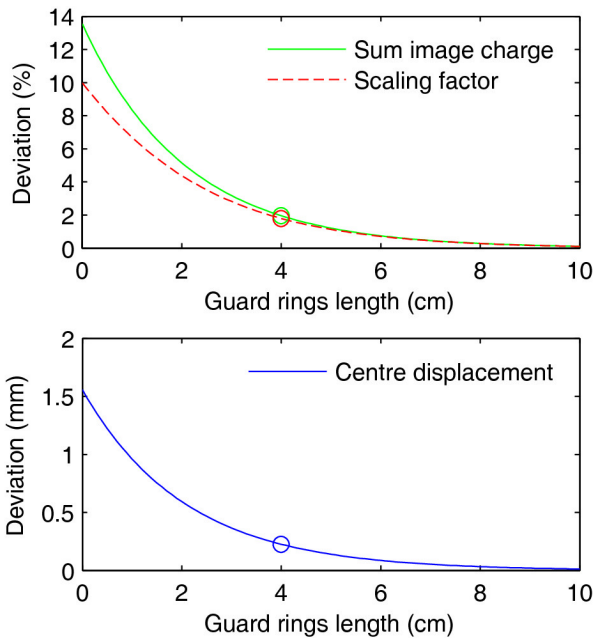

Figure 1: Discrepancies introduced by edge effects to total image charge induced on the PU plates, scaling factor and centre displacement as a function of the guard rings length for a beam tube diameter of 100 mm.

The new BPM design is presented in Figure 2. The electrodes of 100 mm length are shown in blue and green (for "left" and "right") as well as in red and yellow (for "up" and "down"). In violet are the grounded diagonal electrodes introduced to reduce cross-talk between opposite signal plates [5,7]. A version of the BPM without the separating rings will be also tested. The outer casing of 150 mm inner diameter is to ensure shielding against electromagnetic noise. It is on a separate "clean" ground and is electrically isolated from the vacuum vessel in which the monitor will be installed. The setup can be considered as a coaxial capacitor with capacitance-to-ground C:

$$C \propto \frac{L}{\ln(d_{SHIELD}/d_{PU})} \quad (1)$$

Here L is the cylinder length, d_{SHIELD} and d_{PU} are casing inner diameter and PU outer diameter respectively. In the given geometry, C can be estimated to about 20 pF. The real value will differ due to a more complex setup and will be increased by feedthroughs, connectors and the preamplifier.

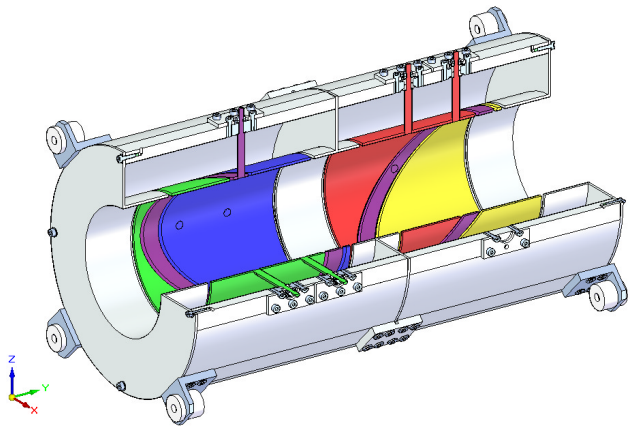

Figure 2: CAD model of the BPM.

SIGNAL PROCESSING

Signal estimation

For a BPM system equipped with a high input resistance (1 MΩ) preamplifier, the total signal U_S is a direct image of the bunch time structure and can be calculated as discussed in [8]:

$$U_S = \frac{1}{\beta c} \cdot \frac{1}{C} \cdot L \cdot I_{BEAM} \quad (2)$$

Like previously, L and C are length and capacitance-to-ground of the PU, while βc is beam velocity and I_{BEAM} is beam current. For L = 10 cm and C = 100 pF, a 300 keV antiproton beam expected in the USR will result in the average sum signal $\Sigma U = 2 \cdot U_S = 150$ µV. The difference signal ΔU for a small beam displacement x sensed by two opposite electrodes is assumed to be linear and can be estimated as:

$$\Delta U = \frac{x}{k} \cdot \Sigma U \quad (3)$$

Here k is a scaling factor. With coupling capacitance C_C between the electrodes taken into account it is:

$$k = (1 + 2 \cdot \frac{C_C}{C}) \cdot r \quad (4)$$

As can be seen, k is equal to the PU radius r when no coupling is present. For the discussed BPM, C_C was assumed to be 5 pF resulting in k = 55 mm. Consequently, the average ΔU signal expected for x = 0.1 mm is about 270 nV. This value will be compared with noise present in the system and used for S/N ratio calculations.

Noise estimation

For a beam position monitor with a high input resistance FET amplifier connected to the signal plate, the noise is determined mainly by amplifier voltage noise density $U_{N,amp}$ [9]. However, the contribution of thermal noise $U_{N,th}$ and amplifier current noise density $I_{N,amp}$ will also be considered. The total noise can be calculated as [10,11]:

$$U_N = \sqrt{(4k_B T \,\mathrm{Re}(Z) + |Z|^2 {I_{N,amp}}^2 + {U_{N,amp}}^2)\Delta f} \quad (5)$$

k_B and T are Boltzman constant and temperature, while Z is the impedance of the equivalent RC circuit:

$$Z = (R^{-1} + i\omega C)^{-1} \quad (6)$$

In order to minimise the total noise, commercially available low-noise FET amplifiers SA-220F5 from NF Corporation were bought. Their parameters are summarized in Table 2. With these preamplifiers, a gain of 46 dB is achievable, while voltage, current and thermal noise densities contributing to equation (5) are 0.5 nV/√Hz, 0.2 nV/√Hz and 0.1 nV/√Hz respectively.

Table 2: SA-220F5 amplifier parameters

Frequency band	300 Hz to 100 MHz
Input impedance	1 MΩ
Input voltage noise density	0.5 nV/√Hz (0.01-1 MHz)
Input current noise density	200 fA/√Hz (100 kHz)
Voltage gain	46 dB

With equation (5), it is possible to plot the signal-to-noise ratio as a function of bandwidth Δf. Figure 3 shows the corresponding graph. It is clear that neither bunch-by-bunch (Δf = 20 MHz) nor turn-by-turn (Δf = 2 MHz) measurements are possible in the USR if resolution better than 1 mm is expected. However, closed orbit determination is still feasible with a bandwidth restricted to less than 200 kHz.

Beam position determination

Further signal processing, including filtering and position calculation, will be done in a digital manner. The signals measured by the PU will be fed into an analogue-to-digital converter (ADC) at an early stage and processed with dedicated software. Digitization will lead to a granularity of values, which might limit the accuracy.

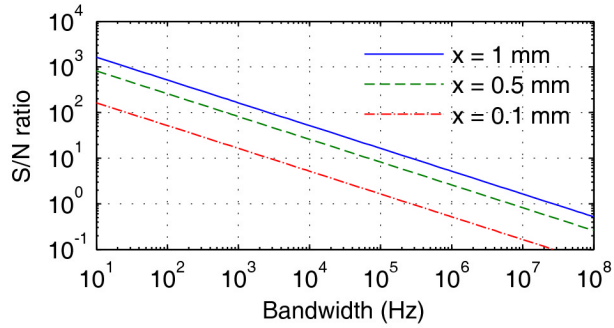

Figure 3: Signal-to-noise ratio as a function of bandwidth for different resolution requirements.

The achievable granularity for different numbers of bits and maximum input voltage settings of an ADC is summarized in Table 3. The PU signal will be amplified 200 times before digitization, which means ΔU = 54 µV for x = 0.1 mm. It should be kept in mind that this is an average signal and the peak value will be higher, yet the granularity requirements are discussed for the conservative estimation. For a bandwidth of only 100 Hz, the noise contribution will be 1.1 µV after amplification, which is much less than the granularity of the ADC configurations presented in Table 3. Therefore, it can be expected that the uncertainty of beam position determination will be dominated by analogue noise for larger Δf and by granularity for smaller Δf. This is reflected in Figure 4 presenting the beam position measurement error as a function of bandwidth for a 12-bit ADC with a 200 mV input voltage range. Figure 5 shows the S/N ratio for a digital system with a finite granularity.

Table 3: Signal granularity as a function of an ADC input voltage range (peak-to-peak)

ADC	**100 mV**	**200 mV**	**400 mV**	**1 V**
10 bit	98 µV	190 µV	390 µV	980 µV
12 bit	24 µV	48 µV	98 µV	240 µV
14 bit	6.1 µV	12 µV	24 µV	61 µV
16 bit	1.5 µV	3.0 µV	6.1 µV	15 uV

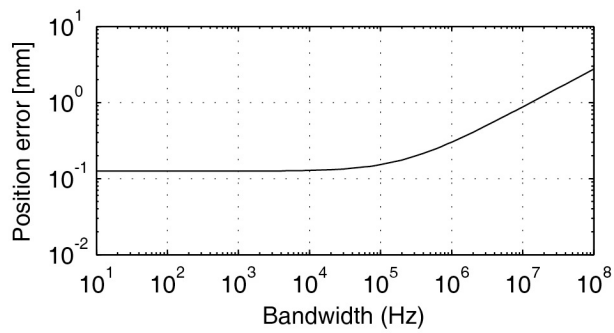

Figure 4: Beam position uncertainty as a function of bandwidth for a 12-bit ADC with a 200 mV input range.

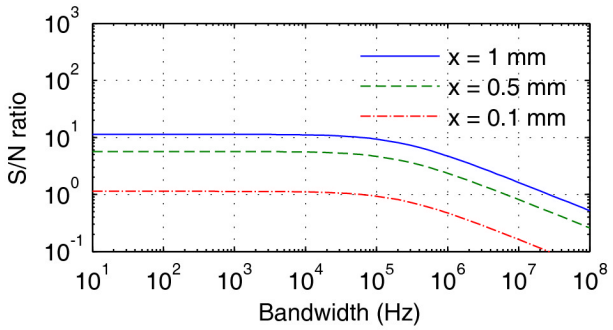

Figure 5: Signal-to-noise ratio as a function of bandwidth for different resolution requirements for a 12-bit ADC with a 200 mV input range.

The estimated uncertainty plotted in Figure 4 is for on-axis beams. However, it increases by at least 30% for off-centred beams passing a few mm from a PU electrode. This is reflected in the next plot in Figure 6.

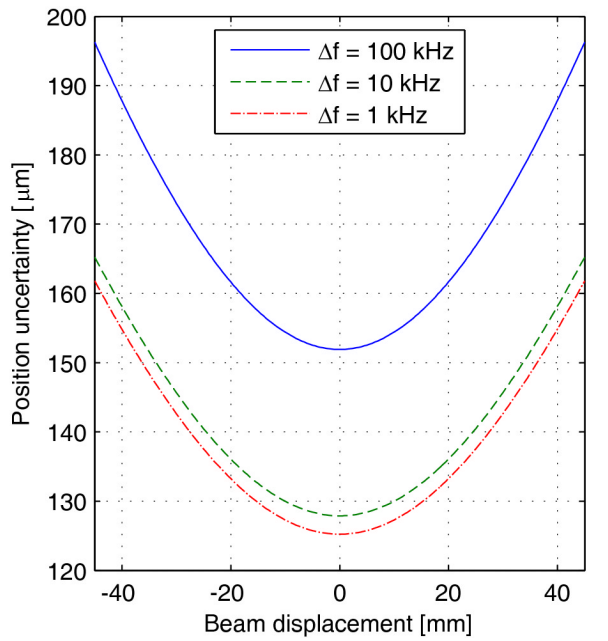

Figure 6: Calculated position read-out uncertainty.

Finally, a more realistic model of the signal expected in the USR was studied. A $\cos^2$-like bunch distribution was assumed which resulted in ΣU = 600 $\mu V_{p\text{-}p}$ and ΔU = 1 $\mu V_{p\text{-}p}$ peak-to-peak values. The noise calculated according to equation (5) was added. The signal was simulated with MATLAB [12] for a low-pass filter with the upper cut-off frequency of 10 MHz and no narrowband filtering was applied at this stage. The granularity was introduced to the signal like it would have happened with a 12-bit ADC with a 200 mV input voltage range. The sampling rate was 100 MS/s which for a 32 MSamples memory per channel means a resolution of 3.1 Hz. The results converted to values before amplification are presented in Figure 7. Although the sum signal appears to be quite clear, the difference signal for x = 0.1 mm is buried in noise as expected for a wide bandwidth Δf = 10 MHz. However, amplitude spectra taken over 1 ms, i.e. for roughly 1800 bunches which corresponds to 180 beam revolutions, exhibits visible peaks for the difference signal as can be seen in Figure 8. With further signal conditioning, it should be possible to achieve sub-mm resolution for closed-orbit measurements.

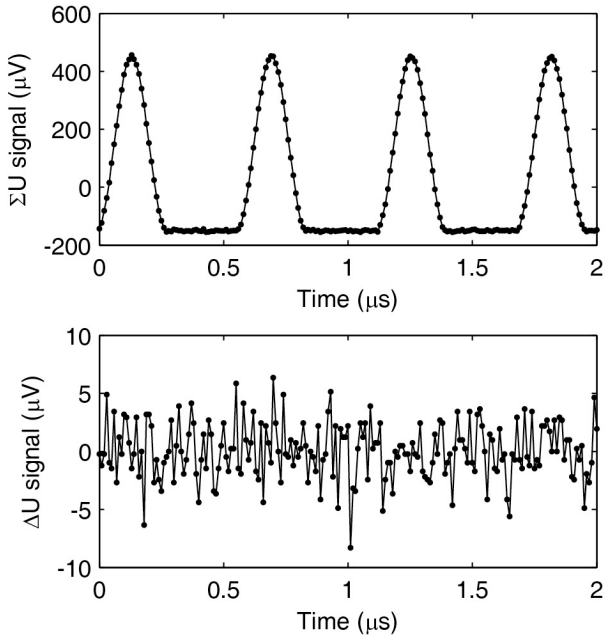

Figure 7: Sum (top) and difference (bottom) signals simulated for 0.1 mm of beam displacement with 100 MS/s sampling rate and 10 MHz bandwidth.

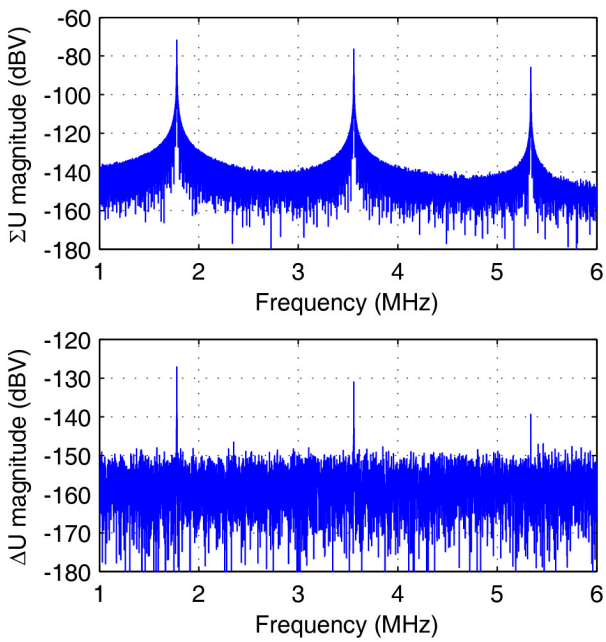

Figure 8: Sum (top) and difference (bottom) spectra for the signals shown in Figure 7 averaged over 1 ms.

Resonant amplification

With a flexible signal processing system, a resonant amplification could be added to increase the overall position sensitivity [5,10]. Should a lower S/N ratio be expected in the final BPM system, the pick-up can be built as a part of a resonant circuit with a matched inductance coil. Problems related to this solution as well as ideas how to overcome them were already discussed elsewhere [5,10,13]. In the light of the results presented in this contribution, the resonant amplification does not seem to be a necessity for the USR and will not be discussed in details.

LOW VELOCITY BEAMS

Since the USR will provide beams in the ultra-low energy regime, the influence of $\beta << 1$ on the pick-up response should not be neglected. With several assumptions discussed in [14], it is possible to estimate the PU response curve, calculated as $(\Delta U)/(\Sigma U)$, as a function of beam displacement x and harmonic number h. As can be seen in Figure 9, the approximately linear curve becomes strongly distorted for higher harmonic numbers when $\beta = 0.025$ and 0.006 is considered. Therefore, a low harmonic number should be chosen to minimise the non-relativistic effects [10]. This is the case of the standard operation of the USR for which $h = 10$ is planned to be used.

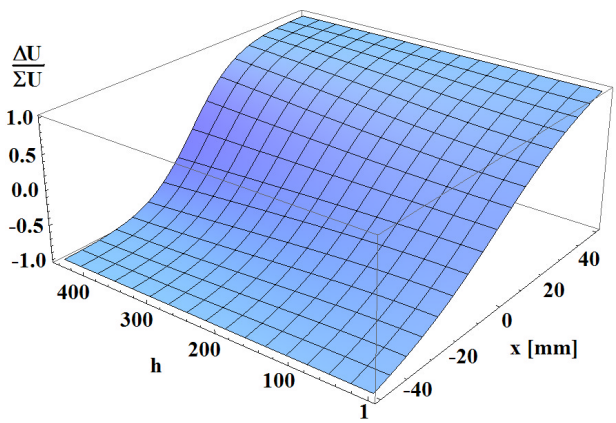

Figure 9: Theoretical response of a pick-up to the USR beams with $\beta = 0.025$ and 0.006 for a range of positions and harmonic numbers as calculated according to [11,14].

OUTLOOK

The beam position monitor is planned to be used with low energy, low intensity beams. It will be manufactured in mid 2010 and tested thereafter. It is planned to realise measurements with a "stretched wire" method in close collaboration with the Cockcroft Institute and the Daresbury Laboratory staff. Also a fully operational, flexible processing system for the close-orbit determination will be prepared in the near future.

ACKNOWLEDGMENTS

The authors would like to thank Felix Laux from the Max-Planck Institute for Nuclear Physics in Heidelberg for extremely helpful and inspiring discussions on the coupling capacitance, noise and low β beams calculations for capacitive pick-ups in the low energy, low intensity regime.

REFERENCES

[1] P. Strehl, "Beam Instrumentation and Diagnostics", Springer (2006).
[2] P. Kowina et al., "FEM Simulations - a Powerful Tool for BPM Design", DIPAC'09, Basel (2009).
[3] C. P. Welsch et al., "An Ultra-low-energy Storage Ring at FLAIR", Nucl. Instrum. Meth. A 546(3) p. 405-417 (2005).
[4] C. P. Welsch et al., "FLAIR Project at GSI", AIP Conf. Proc. 821, p. 85-94 (2006).
[5] J. Harasimowicz et al., "Optimisation Studies of a Resonant Capacitive Pick-Up for Beam Position Monitoring of Low Intensity, Low Velocity Antiproton Beams at FLAIR", DIPAC'09, Basel (2009).
[6] J. H. Cuperus, "Edge Effects in Beam Monitors", Nucl. Instrum. Meth. 145(2), p. 233-243 (1977).
[7] P. Kowina, "BPM simulations for the FAIR SIS100 synchrotron using Microwave Studio", 4th CARE-HHH-ABI Workshop Proc., Lüneburg, p. 4-17 (2006).
[8] P. Forck et al., "Beam Position Monitors", CERN Accelerator School on Beam Diagnostics, p. 187-228 (2008).
[9] M. Le Gras et al., "The Closed-Orbit Measurement System for the CERN Antiproton Decelerator", DIPAC'99, Chester (1999).
[10] F. Laux et al., "Position Pickups for the Cryogenic Storage Ring CSR", 1st DITANET Topical Workshop Proc., Hirschberg-Großsachsen, p. 85-89 (2009).
[11] F. Laux, private communication (2010).
[12] MATLAB R2009a, http://www.matlab.com.
[13] P. J. Chou et al., "Transverse Schottky Detectors for the Fermilab Main Ring", Fermilab Report (1994).
[14] R.E. Shafer, "Beam Position Monitor Sensitivity for Low-β Beams", AIP Conf. Proc. 319, p. 303-308 (1994).

FARADAY CUP FOR LOW-ENERGY, LOW-INTENSITY BEAM MEASUREMENTS AT THE USR*

J. Harasimowicz#, C. P. Welsch, Cockcroft Institute, Warrington WA4 4AD, UK,
and Department of Physics, University of Liverpool, Liverpool L69 7ZE, UK.

Abstract

For destructive beam intensity measurements, electrostatic Faraday cups will be incorporated into the Ultra-low energy Storage Ring (USR) and its transfer lines at the Facility for Low-energy Antiproton and Ion Research (FLAIR). This multi-purpose machine will offer both slow and fast extracted beams resulting in a wide range of intensities and varying time structure of the beam. In this contribution, we present the particular challenges of measuring the beam intensity in the USR, results from numerical optimization studies, as well as the design of the cup.

INTRODUCTION

Faraday cups are commonly used for beam intensity monitoring due to their simplicity and reliability. Despite a destructive character of the measurements, they can provide accurate information on the beam current in a very straightforward manner: a conductive beam stopper is introduced in the beam path and the total charge carried by the particles is collected and measured by means of an ammeter connected to the device.

A number of issues need to be considered when designing a Faraday cup: the heat load together with a proper cooling system, a suitable current meter, and finally, the emission of secondary charged particles which could escape from the cup and affect the results. This is normally not a problem for most accelerators, but very important when an existing design needs to be optimised to specific beam parameters.

BEAM INTENSITIES AT THE USR

A novel electrostatic Ultra-low energy Storage Ring (USR) [1], being under development for the future Facility for Low-energy Antiproton and Ion Research (FLAIR) [2], will require ultra-sensitive instrumentation for its proper operation. The USR will store antiprotons and decelerate them from 300 keV to 20 keV. Due to the space charge limitations at such low energies, the expected total number of single-charge particles is about $2 \cdot 10^7$ corresponding to only 3.2 pC. In order to make a wide range of external experiments possible, the beam will be extracted in two modes: in a single shot lasting a few microseconds and in a quasi-DC manner with the particles released over a longer time scale [3]. The latter will result in as few as $5 \cdot 10^5$ - 10^6 particles per second. Consequently, a Faraday cup planned for the USR will have to cover intensities from about 1 μA down to the fA range.

SECONDARY PARTICLES

Whilst antiprotons are of the main interest at the USR, other particles, like protons or H^- ions, will be used for the initial commissioning of the machine. Ideally, all beams would be monitored with one device, but this may not be possible. Given that the Faraday cup accuracy will depend on the collection efficiency of the total charge carried by the beam, the secondary charged particles emission processes need to be well understood and no charge should be allowed to escape the detector.

In the case of a proton beam, only secondary electrons will be emitted from the surface of the beam stopper. The total electron yield varies proportionally to the inelastic stopping power of the projectiles in the target material. It increases with increasing proton energy, then reaches a maximum in the 100 keV range and decreases thereafter. The yield scales with the incident angle α, measured with respect to the surface normal, by a factor $1/\cos(\alpha)$ for protons [4]. The energy spectrum of the secondary electrons has a peak at a few eV with a spread at half height of the same order of magnitude, thus about 85% of emitted particles are below 50 eV [4]. The emission of these low energy electrons is a result of a cascade process, while the higher energy tail of the spectrum is due to direct energy transfer from the impinging particle to an electron of a solid body. However, the most energetic δ-electrons are expected to be emitted mostly in the forward direction. Electrons emitted backwards can be stopped by means of an electric field applied at the entrance of the monitor.

In the case of an antiproton beam, the use of the Faraday cup will be strongly limited. The reason for this is the creation of highly energetic charged particles being able to escape the device very easily. Following the annihilation of antiprotons on protons or neutrons, various combinations of pions will emerge at 100-MeV-scale energies. Due to momentum conservation, a nuclear recoil of a few tens of MeV, depending on the target material, will be also observed. In addition, a fraction of annihilations will induce the production of an unstable nucleus; the nuclear breakup will result in fragments emitted in all directions and ionizing surrounding atoms. All in all, many annihilation products will have energy hundreds of times higher than the primary keV beam, thus their stopping in the detector will be extremely difficult. Consequently, the MeV-scale pions and recoiling ions will leave the monitor and the charge measured will not reflect the absolute beam current. Despite this limitation, the cup

* Work supported by the EU under contract PITN-GA-2008-215080, by the Helmholtz Association of National Research Centers (HGF) under contract number VH-NG-328, and GSI Helmholtz Centre for Heavy Ion Research.
#Janusz.Harasimowicz@quasar-group.org

will be very useful for the commissioning stage with protons or ions. In addition, it will be used for a comparison of the response to both protons and antiprotons of similar intensities.

MECHANICAL DESIGN OPTIMISATION

The initial design proposed for the Faraday cup is presented in Figure 1 [5]. The monitor consists of a cylindrical beam stopper with a conical cut-out, and a suppressing ring electrode. Both are electrically isolated from each other and shielded against external influences by means of a grounded casing. The primary proton beam, not shown in the picture, approaches from right to left. The colour-coded curves drawn in the figure are randomly generated tracks of secondary electrons emitted in the backward direction from different points of the cup. Due to insufficient suppressing voltage applied to the electrode in this illustration, some charge may eventually leave the monitor in its central part.

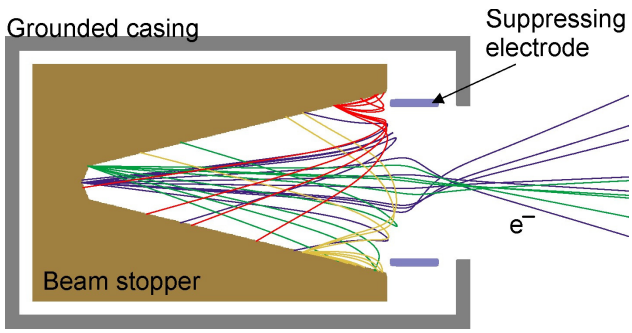

Figure 1: Simplified model of the Faraday cup produced with SIMION [6] (a cylindrical symmetry of the device around its horizontal axis is assumed).

The shape of the beam stopper was chosen in order to optimise the secondary electrons collection efficiency. Since they are not simply emitted from a surface perpendicular to the primary beam, their escape solid angle is greatly reduced in the proposed geometry. In addition, a larger area of the material is exposed to the incident beam, therefore the heat load per mm is lowered. However, the heat performance as such is not a problem in the USR due to low intensities and low energies of the available beams. Considering the energy of 300 keV and the instantaneous beam current of 1 μA, the peak beam power will not exceed 300 mW. This corresponds to 14.5 mW/mm for a 28° cut-out cone surface and a beam of 5 mm diameter, and is 15 times smaller for a 20 keV beam. As for the material, the oxygen-free high thermal conductivity (OFHC) copper was chosen. It is suitable for vacuum and has medium atomic number which is important since backscatter increases with Z. The thickness of the beam stopper is much larger than the sub-mm penetration depth of 300 keV protons.

The suppressing electrode made of stainless steel is used to prevent secondary electrons from leaving the monitor. A ring shape instead of a grid was chosen in order to avoid losses of the already few primary particles hitting anything else than the beam stopper. In the given geometry, protons can freely enter the cup and their energy is low enough not to produce very high energy electrons which could be difficult to stop afterwards. The shape of the ring was optimised as compared to the setup in Figure 1. By increasing the length of the electrode by only a few mm, the potential on the axis of the suppressor was decreased by about 20%.

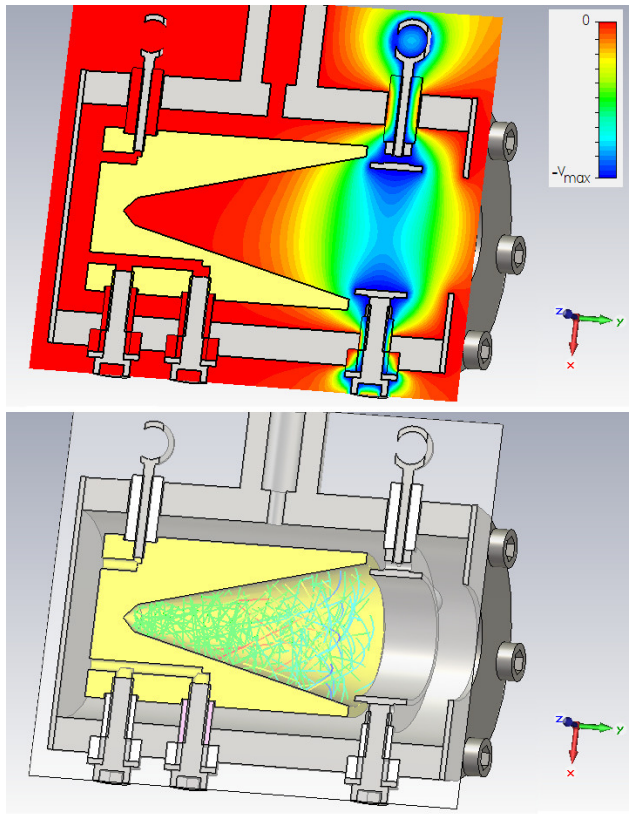

Figure 2: Simulations of the field distribution (top) and the secondary electron emission (bottom).

A more detailed model of the Faraday cup was prepared and studied in terms of electric field distribution and electron collection efficiency. Figure 2 shows numerical calculations made with the CST Studio package [7]. As expected, the critical point of the cup is at the central axis of the electrode where the electric field is reduced due to the finite length of the suppressor. By implementing the known secondary electrons emission model, it was shown that the majority of the particles are kept inside the monitor. Only high energetic electrons emitted in a very narrow solid angle covering the central axis of the suppressor may be able to escape the cup. Due to small probability, this will have only a minor effect on the measurement accuracy.

The outer grounded casing is made of stainless steel and additional ceramic insulators ensure the electric isolation of the cup components. The entrance bore is 21 mm in diameter which also determines the maximum beam size that can be measured. The whole device is about 8 cm in length and about 5 cm in diameter. It will

be mounted on a pneumatic actuator with a 75 mm stroke, and will fit into a DN100 CF cross chamber. The final design of the Faraday cup is presented in Figure 3.

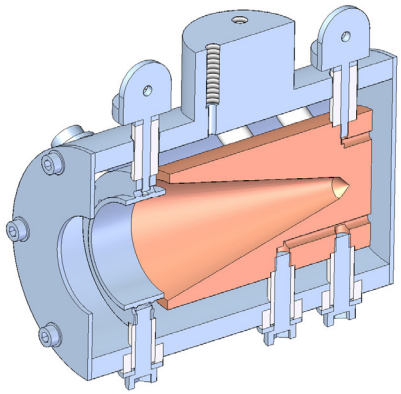

Figure 3: Section view of a CAD model of the cup.

LOW CURRENT MEASUREMENTS

Beam current monitoring in the USR will be a challenging task. Intensities in the fA range are extremely difficult to measure already in the simplest setups due to theoretical and practical noise limitations. The situation is far more complicated in a real accelerator where many noise sources, like vacuum-to-air feedthroughs, long cables or vibrating vacuum pumps, cannot be eliminated. In addition, the USR extraction schemes will lead to a variable time structure and different peak beam intensities.

To overcome the difficulties with measurements under the different beam delivery schemes, a variable gain transimpedance amplifier DLPCA-200 from FEMTO was bought. It offers several gain and bandwidth settings of which three are summarized in Table 1. The gain of either 10^6 or 10^7 V/A is sufficiently high for sub-μA bunches while the rise/fall time is short enough to sample the inner bunch structure. For sub-pA quasi-DC beams, the highest sensitivity can be achieved with 10^{11} V/A and an internal low-pass filter with the upper cut-off frequency of 10 Hz. The two possibilities are presented in Table 1 as the fast and slow mode respectively.

Table 1: Transimpedance amplifier parameters

Parameter	Fast mode		Slow mode
Gain setting [V/A]	10^6	10^7	10^{11}
Upper cut-off [kHz]	500	400	1.1 (0.01)
Rise/fall time [μs]	0.7	0.9	300
Input noise [fA/√Hz]	1800	450	4.3

For ultra-low current measurements, low noise triaxial cables should be used. Double screening reduces noise caused by ground loops and other parasitic effects. Such cables and feedthroughs, however, are not available for the ultra-high vacuum (UHV) of about 10^{-11} mbar under which the Faraday cup will be operated. For this reason, a custom-made 50 Ω Kapton-coated cable with an additional stainless steel screen was prepared. It includes a special connector for a floating BNC vacuum feedthrough. The components are presented together with the assembled cup in Figure 4.

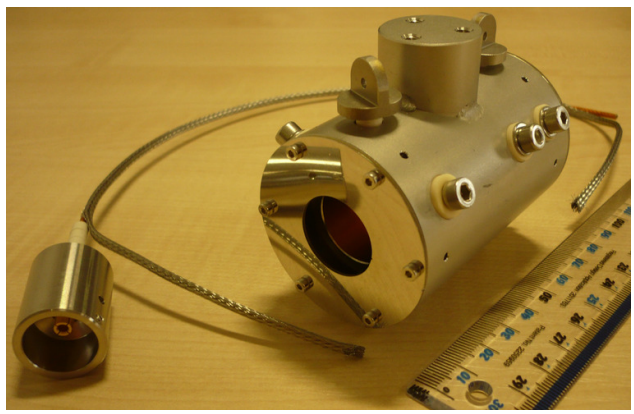

Figure 4: Assembled Faraday cup together with a double shielded cable equipped with a floating shield connector.

OUTLOOK

The Faraday cup will be incorporated into the USR as a reference monitor for a range of beam currents. A compact UHV test bench will soon be built and initial detector tests will be run with an electron gun. Should the variable gain current-to-voltage converter DLPCA-200 be not sensitive enough for the lowest intensities, a separate narrowband amplifier dedicated for sub-fA DC measurements will be used.

The flexible design of the cup and the wide operating range of the amplifier triggered collaboration with the Clatterbridge Centre for Oncology where the Faraday cup will be tested with 62 MeV protons.

REFERENCES

[1] C. P. Welsch et al., “An Ultra-low-energy Storage Ring at FLAIR”, Nucl. Instrum. Meth. A 546(3) p. 405-417 (2005).
[2] C. P. Welsch et al., “FLAIR Project at GSI”, AIP Conf. Proc. 821, p. 85-94 (2006).
[3] Ph. Schmid et al., “Preliminary Design Studies of an Extraction of the USR”, Hyperfine Interactions 194, p. 183-187 (2009).
[4] D. Hasselkamp et al., “Particle Induced Electron Emission 2”, Springer-Verlag (1992).
[5] J. Harasimowicz et al., “Beam Diagnostics for the USR”, PAC’09, Vancouver (2009).
[6] SIMION 8.0, http://www.simion.com.
[7] CST Studio 2009, http://www.cst.com.

MEASUREMENT, SIMULATION, AND SUPPRESSION OF APS STORAGE RING VACUUM CHAMBER TE MODES IMPACTING VERTICAL BPM READINGS *

R. Lill, G. Decker, J. Hoyt, X. Sun
Advanced Photon Source, Argonne National Laboratory, Argonne, IL 60439
J. Wang
CST of America, Inc., 492 Old Connecticut Path, Framingham, MA 01701

Abstract

The Advanced Photon Source (APS) storage ring rf beam position monitors (BPMs) are impacted by the presence of beam-excited transverse electric (TE) modes. These modes are excited in large-aperture vacuum chambers and become trapped between the bellow end flanges. The TE modes are vertically oriented and are superimposed on the TEM beam position signals, corrupting the BPM measurements. Erroneous step changes in beam position measurements and systematic intensity dependence in the vertical plane have been traced to these modes, placing a fundamental limitation on vertical beam position stabilization. Experiments were conducted suppressing these modes on a test vacuum chamber. These experiments were simulated with Mafia [1] and Microwave Studio [2], confirming experimental results. We will describe the measurements, simulations, and prototype test results.

INTRODUCTION

As the Advanced Photon Source (APS) prepares for a large-scale upgrade, many of the fundamental limitations on beam stability are being studied. The APS storage ring vacuum chambers presently suffer from transverse electric (TE) longitudinal resonances trapped in the beam vacuum chamber. These TE-like modes are excited in the large-aperture sections of the vacuum chambers and become trapped between the bellow end flanges. The modes are vertically oriented and are superimposed on the beam position signals. These modes were identified and reported in 1998 when a network analyzer was used to measure the transmission of rf power from one beam position monitor (BPM) to an adjacent BPM on the same vacuum chamber section [3].

VACUUM CHAMBER DESCRIPTION

The Advanced Photon Source (APS) storage ring has 40 sectors each having 5 sections of vacuum chambers for a total of 200 individual sections. There are 80 curved and 120 straight sections of vacuum chambers that make up the 1104-meter-diameter APS storage ring. The storage ring vacuum chamber geometry shown in figure 1 has an oval beam chamber (left), connected to the antechamber by a small gap in the area between the two sections. The 0.426-inch gap section between the beam and antechamber sections shown in figure 1 introduces large capacitive loading that effectively lowers the cut-off frequency for TE01-like modes of the chamber.

The wavelength in a hollow waveguide satisfies the relationship:

$$F = \frac{c\sqrt{\left(1+\left(\lambda_g/\lambda_c\right)^2\right)}}{\lambda_g} .$$

Where c is the speed of light in free space, λ_c is the cut-off wavelength, and λ_g is waveguide wavelength. Using chamber length L = 4.81 m and λ_g = 2L/N (N=1, 2, 3….), the resonance frequencies can be estimated. The first resonance is the one closest to the cutoff frequency of the waveguide. The waveguide wavelengths for these lower-order modes are much longer than free space wavelengths.

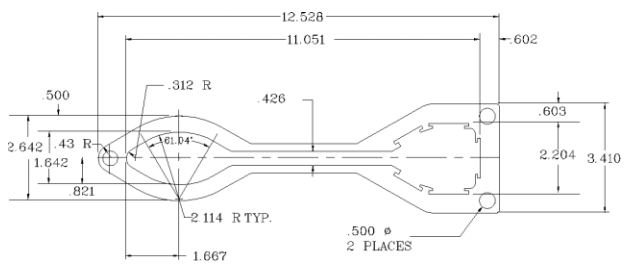

Figure 1: Storage ring vacuum chamber cross section (dimensions shown are inches).

MEASUREMENTS

Figure 2 illustrates the measurements that led to the discovery that these TE-like modes were corrupting

*Work supported by U.S. Department of Energy, Office of Science, Office of Basic Energy Sciences, under Contract No. DE-AC02-06CH11357.

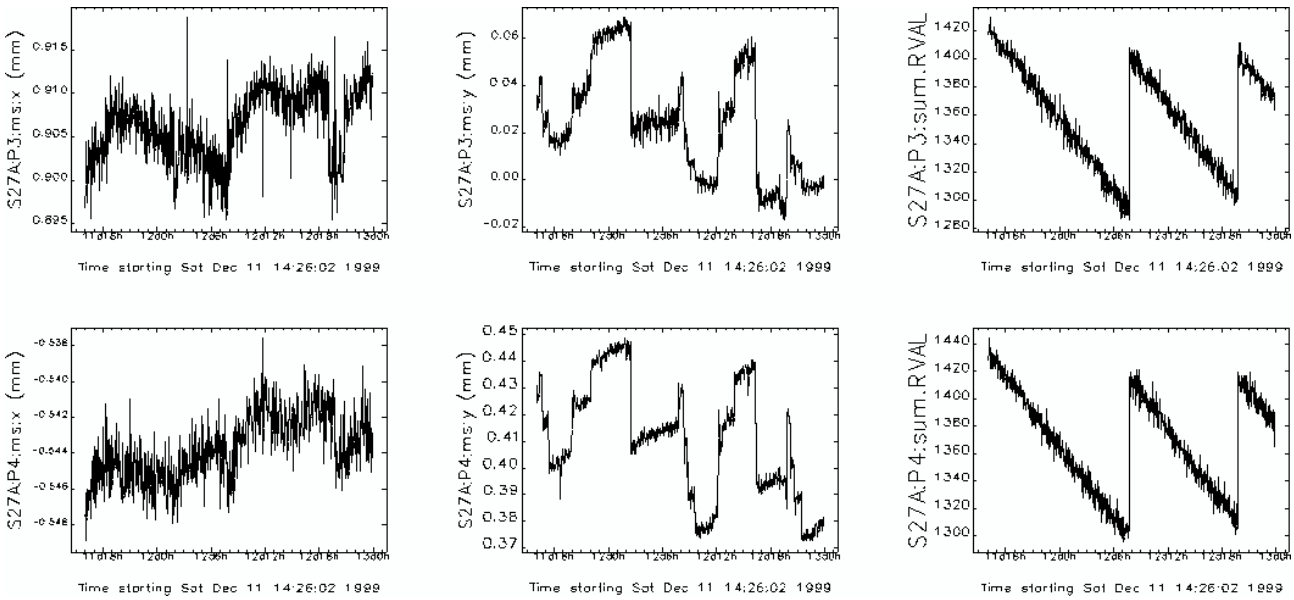

Figure 2: Systematic error measurements that led to the discovery of these TE-like modes. Horizontal position, far left plots; vertical position, center plots; and beam current, far right plots.

vertical BPM readings. The curved chamber (section 2) in sector 27 has two BPMs, S27:AP3 and S27:AP4 that are strongly effected by this mode. The beam current is represented in the far right plots labeled "sum RVAL," which is the sum of four button electrodes. As the beam decays as a function of time, the vertical position shown in the center plots exhibits a step-like function in two different positions along a single section of the curved vacuum chamber. At the same beam charge, the horizontal position does not show the step-like position change. The vertically orientated TE-like modes depend on the stored current and change as the current decays. This might be explained by source points of the TE mode, being heated and cooled as the beam intensity decays.

The electronics were closely examined and the chamber physically monitored for evidence of these step changes. The conclusion of this examination showed no signs of problems that could explain the step-like systematic errors. This led to the measurements of the BPM coupling from the upstream BPM to the downstream BPM on the same section of vacuum chamber. A network analyzer was used to make this transmission measurement and confirmed there was a weak coupling one from one button BPM to the downstream button BPM.

Early investigations to solve this problem included the use of lossy ceramics and shorting plungers to damp or otherwise modify the modes [3]. These ideas were never implemented since they required breaking vacuum for each of the 200 vacuum chambers affected. The solution to date has been to rely on rf BPMs attached to the insertion device vacuum chambers which do not have this problem. In addition, bending magnet and insertion device photon BPMS are used for vertical DC orbit correction.

RF Bench Measurements

The APS upgrade will include an extensive effort to improve beam stability. This opportunity has enabled us to revisit many of the fundamental limitations on beam stability. An R&D effort started last fall to study and write a proposal to reduce or eliminated this rogue TE mode. A spare curved vacuum chamber was set up on the bench and historic measurements of the chamber resonances were revisited. The first measurement was a simple transmission measurement from one button to a downstream button. This was similar to the measurement that was made in the discovery phase on this problem. The coupling is weak from button to button, but there is evidence that the vacuum chamber is not in cut-off at the BPM center frequency of 351.927 MHz. The next set of measurements was made using an electric field probe launch. The electric field probe launches a vertically polarized signal from one end of the chamber to a downstream BPM button used to receive the signal. Figure 3 shows the result of a measurement of microwave transmission using this arrangement. The cut-off frequency measured is about 331 MHz and the first resonance is 335.5 MHz. Table 1 shows the measured resonant peaks and the calculated eigenmodes [1] for a simplified geometry of the chamber.

Table 1: Measured and Calculated Resonances

Eigen mode Mode number	Measured (MHz)	Calculated (MHz)
1	335.5	330.2
2	341.0	336.5
3	345.5	346.8
4	356.4	360.7
5	369.4	377.8
6	384.6	384.6

These data demonstrate that the resonances fall in the operating band of the BPMs: 351.927 MHz with a 10 MHz, -3 dB bandwidth. The TE modes are vertically oriented, corrupting only the vertical BPM measurements. These data were compared with historical data taken for the chamber measured showing similar results. The measurements were also made using a magnetic field probe to launch a signal into the antechamber and showed similar results.

Mode Suppression Measurements

A new approach that effectively alters the geometry of the vacuum chamber by periodically shorting the high field region in the small gap was tested. The vacuum chamber was probed to determine if the cut-off frequency could be increased by shorting the small gap areas closest to antechamber, where getter vacuum pumping strips are mounted. The basic idea is to short the small gap region closest to the antechamber to avoid intercepting stray x-rays and increase the cut-off frequency. To demonstrate that the cut-off frequency could be shifted to a frequency higher than the BPM processing frequency, low-resistance shorting material was installed in the gap at 3 locations. The shorts were inserted about halfway into the small gap region in three different locations through antechamber pumping ports at about quarter length intervals. Figure 4 shows the results when the 10 mm gap is shorted. The resonances that were previously measured in figure 3 were greatly reduced or eliminated. This was encouraging and prompted a full investigation of ray tracing through each of the chambers to determine the optimal placement of shorts inserted into the small gap.

MODE SUPPRESSION REQUIREMENTS

The most critical requirement for implementing the mode suppressor is that the shorting device does not intercept the x-ray beam. To determine this, careful ray tracing plots have been generated for each chamber under worst-case steering conditions. The arrangement used for the data in figure 4 violates this requirement and could not be implemented because the short would intercept the x-rays.

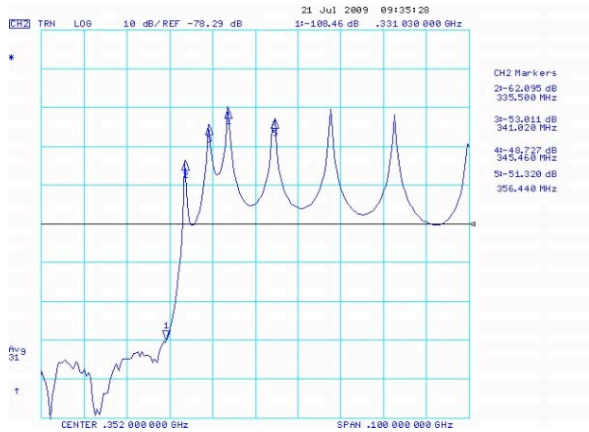

Figure 3: Vacuum chamber rf transmission as built.

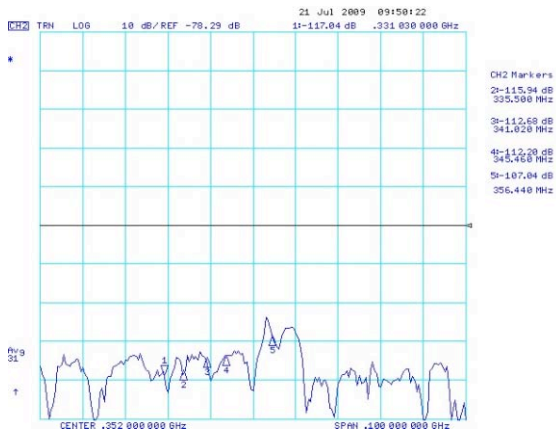

Figure 4: Vacuum chamber rf transmission with three shorts installed in gap area.

The short or snubber circuit must provide low resistivity at UHF frequencies and provide reliable and complete grounding of high-field areas. The installation must be accomplished by access of the vacuum flanges on each end of the chamber. It should be installed similar to the getter strips, which slide in tracks along the antechamber shown in figure 1. There are a total of five tracks in the antechamber, but only two are presently being used. This facilitates the use of the inside tracks closest to the small gap. It is critical that the installation of these snubber circuits does not damage the chamber.

SIMULATIONS

Simulations have been conducted on a simplified straight section model of vacuum chamber with Mafia [1] and Microwave Studio [2]. The source was modeled as a vertical 50 ohm S-parameter discrete port, which produces a TE mode signal at the upstream port. The receiver probes were located close to the downstream end of the chamber. Shown in figure 5 are simulation results with longitudinal magnetic field Hz vs. frequency. First a transient progress was simulated in a 158-inch straight smooth vacuum chamber without shorting snubbers. Then

a series of 3, 6, 9 and 12 rf shorts were added in the small gap one inch from the antechamber. The short height was 10-mm which is the same as the small gap between the beam and the antechamber. The first short shown in figure 6 is located 6 inches from the source. The following two snubbers are 12 inches apart. Each new sequence adds 3 addition shorts separated by 12 inches. Figure 5 shows the simulation results without short and with 3, 6, 9, 12 shorts starting from the upstream port. Similar to the bench measurements in figures 3 and 4, the resonances without shorts were suppressed over 50 dB when the small gap was shorted by different numbers of shorts. The more shorts, the greater the resonances were reduced and the higher the cut-off frequency was shifted.

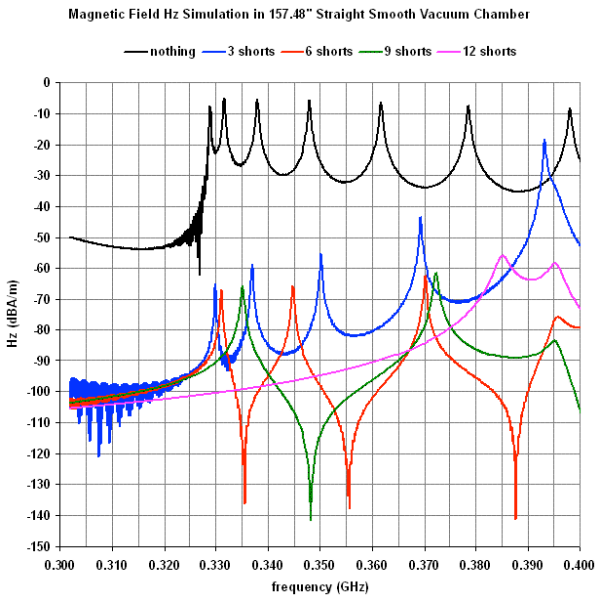

Figure 5: Simulation results without short and with 3, 6, 9, 12 shorts installed in the gap area.

MODE SUPPRESSION PROTOTYPE SNUBBER

The snubber prototypes feature an off-the-shelf longitudinal grounding strip to short the top to bottom of the chamber in the small gap region shown in figure 6. The grounding strip is designed to provide a low impedance path from the top to bottom of the small gap and can be readily inserted into the vacuum chamber. The material is beryllium copper giving it excellent spring features and resistance to compression set. The grounding strips are mounted in stainless steel carriers that can be linked together as shown in figure 7. Installation is similar to that of installing the vacuum chamber getter strips.

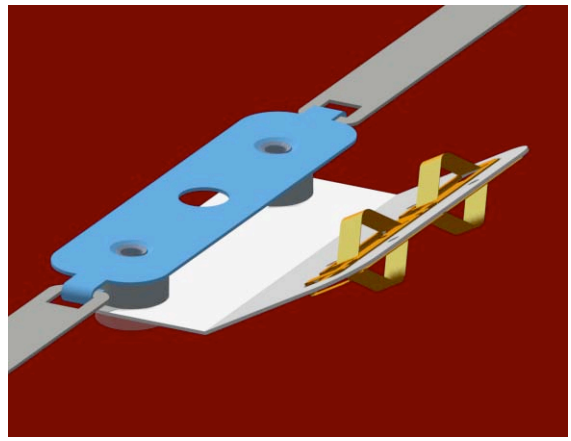

Figure 6: Snubber prototype

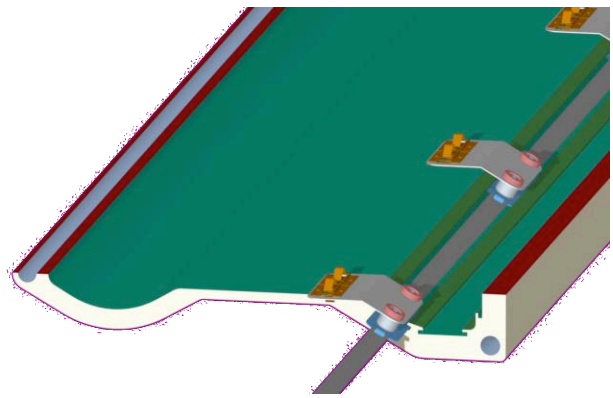

Figure 7: Storage ring vacuum chamber cross section with snubbers installed.

PROTOTYPE SNUBBER SIMULATION

Only eight snubbers can be used on the curved vacuum chamber to avoid x-ray interception. For the convenience of simulation, a straight simplified chamber geometry was assumed. A diagonal 50Ω S-parameter discrete port worked as a source at the upstream port. The adjacent two snubbers were 15.6 inches apart, and the first one started at 6.4 inches away from the upstream port. A vertical cylinder through the chamber was considered, but the x-ray absorber and rf screens installed in this cylinder were ignored. The probes were located at the downstream BPM's position. The simulated structure is shown in figure 8. Figure 9 shows the simulated results for the simplified straight chamber and the measured results in the APS curved chamber without snubbers. The simulated and measured resonances were similar, especially at the ring RF frequency of 351.93 MHz. The difference between the simulation and measurement may come from the simplification of the chamber and snubbers.

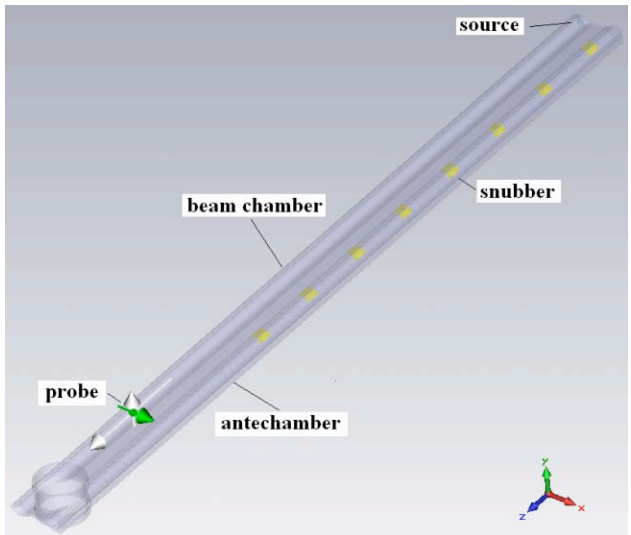

Figure 8: Straight APS vacuum chamber without x-ray absorber and rf screens.

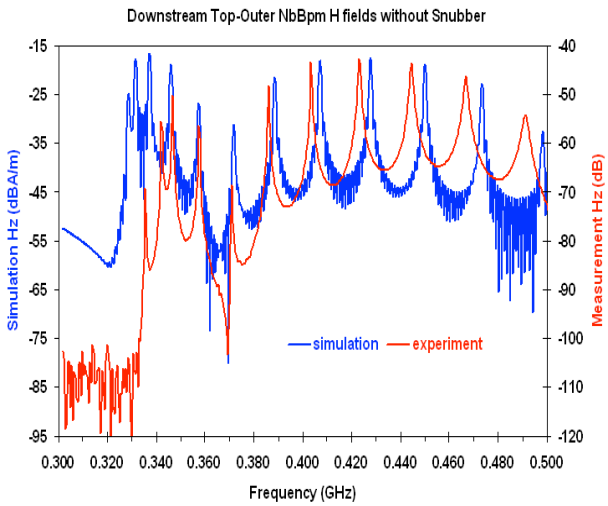

Figure 9: Comparison of the simulated and measured results without snubbers.

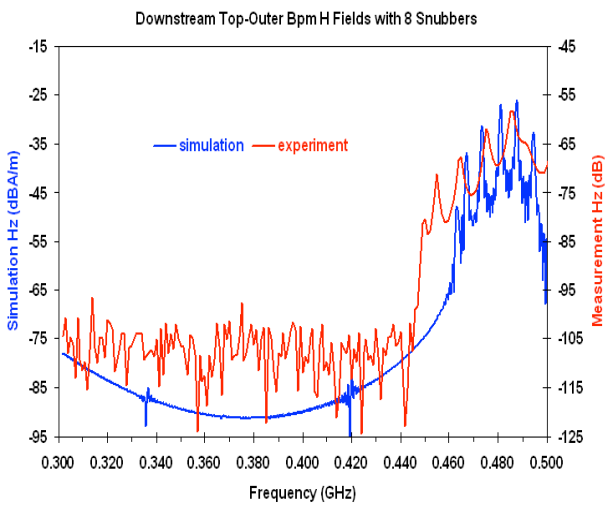

Figure 10 shows the simulated results in a straight simplified chamber and the measured results in the APS curved chamber with 8 snubbers installed. The cut-off frequencies were shifted much higher than the ring rf frequency of 351.93 MHz in both simulation and measurement.

CONCLUSION

The snubber design will reduce or eliminate the trapped TE mode resonances in the APS storage ring vacuum chambers. This solution will work for all but two of the nine BPMs. The two curved vacuum chambers present a new challenge. The ray-tracing studies indicate that the x-ray stay-clear area of the two downstream BPMs would inhibit installation of the snubbers. The snubbers as designed cannot be subjected to high-power x-rays. Additional measurements and simulations to suppress the sources from the downstream port, such as the crotch absorber, have to be considered. This effort could involve a more robust snubber design or a stick absorber that is water cooled for these two BPMs.

Figure 10: Comparison of the simulated and measured results in with 8 snubbers.

REFERENCES

[1] MAFIA Version 4.106, Computer Simulation Technology, www.cst.com.

[2] CST Studio Suite 2010, Computer Simulation Technology, www.cst.com.

[3] Y. Kang, G. Decker, and J. Song, "Damping Spurious Harmonic Resonances in the APS Storage Ring Beam Chamber," PAC '99, New York, NY March 1999, THP61, p. 3092 (1999); http://www.JACoW.org

STUDIES OF APS STORAGE RING VACUUM CHAMBER THERMAL MECHANICAL EFFECTS AND THEIR IMPACT ON BEAM STABILITY*

R. Lill, B. Yang, G. Decker, L. Erwin, J. Xu, J. Collins
Advanced Photon Source, Argonne National Laboratory, Argonne, IL 60439 USA

Abstract

As the Advanced Photon Source (APS) prepares for a large-scale upgrade, many of the fundamental limitations on beam stability have to be identified. We report on measurements of thermal mechanical effects of both the water, and air-handling systems impacting insertion device vacuum chambers (IDVCs). Mechanical stability of beam position monitor pickup electrodes mounted on these small-gap IDVCs places a fundamental limitation on long-term x-ray beam stability for insertion device beamlines. Experiments conducted on an insertion device vacuum chamber indicates that the beam position monitor blocks are moving with water temperature cycles at the level of 10 microns / degree C perpendicular to the beam direction. Measurements and potential engineering solutions will be described.

INTRODUCTION

The Advanced Photon Source (APS) is preparing for a large-scale upgrade and many of the fundamental limits on beam stability are being studied. One of the most critical locations for beam stability is at the insertion device (ID) points. The insertion device vacuum chambers (IDVC) are extruded aluminum with integrated beam position monitors (BPM) electrode housings machined out at each end of the IDVC. Three different versions of the vacuum chamber have vertical apertures of 12 mm, 8 mm, and 5 mm. The chambers are fabricated by extruding 6063 aluminum alloy to form a tube with the desired internal shape shown in figure 1. The exterior details, such as the BPM electrode housing, are machined to the finished dimensions. The IDVC have a pumping antechamber with non-evaporable getter strips. The wall thickness of the completed chamber at the beam orbit position is 1 mm. The design uses a rigid strongback that limits deflection of the chamber under vacuum despite the thin wall. Alignment of the vacuum chamber on its support is routinely accomplished with a precision of 75 microns over the entire surface, allowing minimum ID pole gaps.

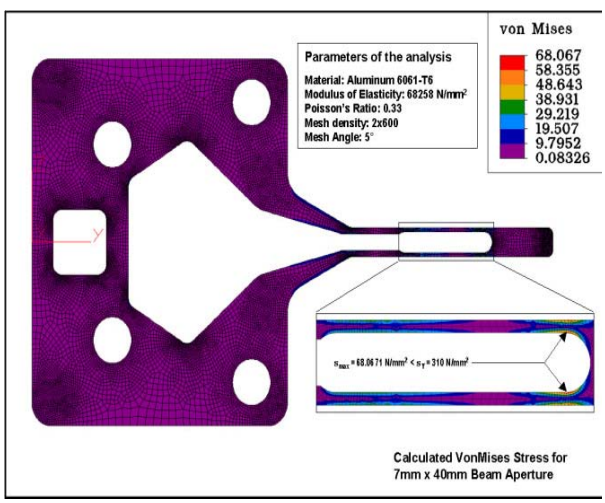

Figure 1: Storage ring IDVC cross section

ID BPM MEASUREMENTS

The IDVC BPMs provide the critical steering data necessary to maintain beam stability through the ID. The BPMs are machined in precise platforms on each end of the IDVC. In figure 2 the BPM is shown on the far left of the picture. The BPM button electrodes mounted in the machined platforms have a 4 mm diameter. There are two button electrodes mounted on a single miniature vacuum flange. The horizontal separation of the buttons is 9.6 mm center-to-center, with vertical apertures of 12 mm, 8 mm, and 5 mm. The button signals are cabled out to the electronics racks located above the tunnel. Narrowband Bergoz switching-type receivers are connected to the IDVC buttons. Narrow-band (300 Hz) BPM electronics are used to reduce beam intensity dependence and long-term drift. The long-term (one week) drift associated with the BPMs at this time is 7 microns horizontally and 5 microns vertically peak-to-peak. Plans to improve this will also include upgrading the electronics in the future.

BPM Measurements

As the noise sources are eliminated and BPM improvements are made, new noise sources can be discovered. During the operations period October 2009, an elevated noise level was reported on several IDVC BPMs. The plot in figure 3 shows beam position and vacuum chamber water temperature as a function of time. It was determine at this time that the beam position measurement was correlated to the water cycle of the aluminium vacuum chamber. The period of the water cycle is about 15 minutes with a 2.8 microns/degree Fahrenheit (5.2 microns/degree Celsius) change in the vertical position.

*Work supported by U.S. Department of Energy, Office of Science, Office of Basic Energy Sciences, under Contract No. DE-AC02-06CH11357.

Figure 2: Sector 32 ID vacuum chamber.

Water Cooling System for Aluminum ID Chambers

Many improvements have been made to the water temperature regulation system over the years from the original requirement of 78 +/- 1 degree Fahrenheit. Currently, the aluminium IDVC water system typically regulates the IDVC temperature at 78 +/- 0.05 degrees Fahrenheit peak to peak during normal operation. The cooling systems for the IDVCs are divided into twenty cooling skids with each skid containing two pumps [2]. One skid is responsible for supplying water to two of the forty sectors of the storage ring. This system has its own set of dedicated heat exchangers and a temperature controlling system. Chilled water is used to bring down the warm water temperature to 78° F ± 0.05° F. Flow rate is 50 gpm at a supply pressure of 50 psig.

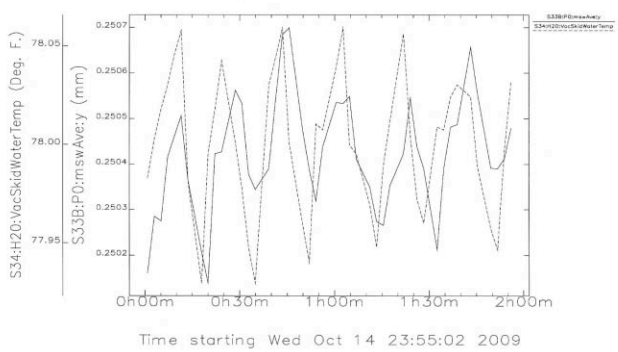

Figure 3: Sector 34 IDVC BPM readback and chamber water temperature variation over a two-hour period.

Chamber Measurements

During the December 2009 shut down period, the IDVC shown in figure 2 was instrumented to study the effects of the tunnel air and vacuum chamber water temperatures on mechanical stability. Two Keyence LK-G37 laser displacement sensors were used to measure the IDVC vertical positions as functions of air temperature and water cooling temperature. The Keyence sensors have a resolution limit of 0.05 microns. The BPM shown in figure 2 was instrumented with a laser sensor measuring vertical deflection and a second laser sensor was installed near the center of the five meter IDVC, also measuring vertical deflection. Five temperatures were recorded with the two vertical position measurements. Figure 4 shows recorded data during a period of three hours when the water temperature was deliberately changed in a controlled fashion over a range of 2.7˚ C. We can make the following observations from the data: (1) While the temperature of the vacuum chamber follows closely the temperature of the water flowing through it, the change in surrounding air temperature is only about one-tenth of the change in water temperature. Such a small change in air temperature did not affect the temperature of the stand within our measurement accuracy. (2) At the first temperature cycle, the vertical position of the BPM block appears to be a linear function of the water temperature: The higher the temperature, the lower the chamber height. It moves ~ 19 μm from peak to peak. (3) It is the vertical position of the center of the IDVC that exhibits a complex behavior: As we reduced water temperature from 23˚C, it moves up at a level of 10 microns/degree Celsius. However, when the water temperature reached 21.5˚C, the IDVC center reversed its motion and started moving down as the water temperature continues to decrease. This behaviour appears to be reproducible in the next two phases when

the temperature is increased and decreased again. (4) Reexamination of the position of the BPM block shows that a small slope change existed in the temperature region where the IDVC reversed its direction of motion.

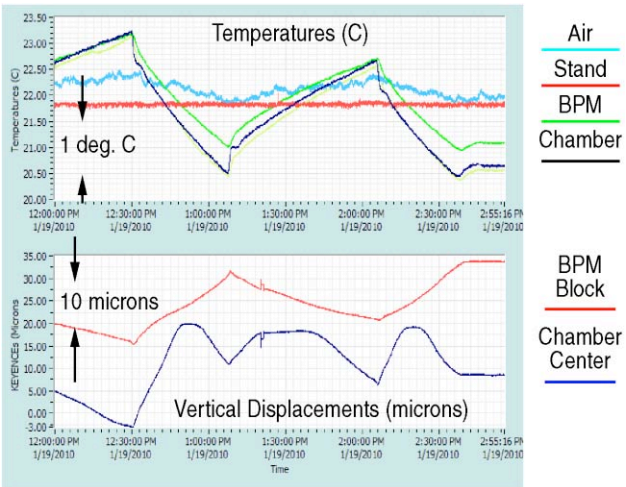

Figure 4: Variation of IDVC and BPM mechanical position with vacuum chamber water temperature.

We note that the IDVC strongbacks need not only provide stable support to the chamber, they also need to supply adequate torques in two planes to correct residual twisting and bending of the chamber and maintain its shape within specifications. During the temperature swing experiment, the floor, the strongbacks and the chamber, being made of different materials and at different temperatures, expanded differently, which changes the torques and the axial compression of the chamber. This results in a complex distribution of forces and torque in the over-constrained chamber. It is thus not surprising that the IDVC and BPM block expansion/contraction cycle is not a linear function of water temperature. Since the forces and torques applied to the chamber depends on the initial distortion of the ID chamber, they are not the same for different installations. This helps explain why the correlation of measured temperature dependence is stronger in some sectors but not in others. The horizontal movement of the BPM block was also measured but was less severe.

BEAM STABILITY

BPM Positioning

The experiments described in the last section clearly confirmed that the thermal distortion of the vacuum chamber leads to movements of the BPMs up to 10 μm/˚C, or a 0.5 μm peak-peak for a temperature change of 0.05˚C peak-peak. This is incompatible with the new stability requirements for the planned APS upgrade. To meet these requirements, we may request upgrades to the water temperature regulation and a new strongback design, but these changes are unlikely to be the whole solution. Our past experience shows that new sources of error will be discovered with increasing accuracy and precision of the BPM. We need to look at the issue differently: Now that the water system and strongbacks have been thoroughly worked on, and their thermal motion is well below the original stability tolerance, it is best that we measure these errors and compensate for them using the BPM electronics. We will measure the BPM position relative to the floor, and the beam position relative to the BPM, the sum of the two numbers gives the position of the beam relative to the floor, the reference system for the purpose of this paper. The contribution of the BPM movements to the beam position error is now reduced from the thermal movements to the measurement error of that movement. This approach will also address many other sources of error in addition to the two discussed here, such as beam heating transients from stored current changes, heating pattern changes due to fill pattern change, etc.

BPM Position Monitor Design

Figure 5 shows a conceptual design for a real-time BPM position monitoring system. The BPM is connected to a pair of Invar/Super-Invar rods, which are connected to swivels on the floor through precision distance meters. The distance meters are mounted on precision slides allowing free expansion along its length but rigid in all other degrees of freedom. The position of the BPM can be determined by elementary trigonometry using the parameters in the figure. Specifically, the change in horizontal (x) and vertical (y) coordinates can be given by measured changes of two distance meters:

$$\Delta x = \frac{\Delta L_1 \sin\theta_2 - \Delta L_2 \sin\theta_1}{\sin(\theta_1 + \theta_2)}, \quad (1)$$

and

$$\Delta y = \frac{\Delta L_1 \cos\theta_2 + \Delta L_2 \cos\theta_1}{\sin(\theta_1 + \theta_2)}, \quad (2)$$

where ΔL_1 and ΔL_2 are measured increments by the distance meters. This conceptual design has the following features: (1) The distance meters are located far away from the beam, reducing the possibility of radiation damage. (If needed, it is also easier to shield at the floor level.) (2) Mounting the distance meter at the floor level also makes it easier to design support and swivel since the sagging of rod is minimized. (3) Last but not least, it provides a reliable horizontal position measurement without resorting to an expensive support stand with strong horizontal stability.

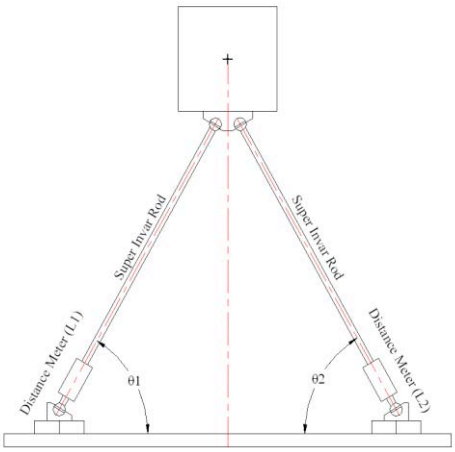

Figure 5: BPM position monitor concept.

Table 1 lists a number of candidates for the distance meter. Since this approach is applicable to rf BPMs and x-ray BPMs [3], each distance meter [4] will need to be evaluated and tested for each application before a final decision is made regarding its adoption. The radiation hardness of each of the following technologies will be evaluated before a final decision can be made.

Table 1: Characteristics of Distance Meters for a BPM Position Monitor

Technology	Resolution	Measurement Range	Cost
Potentiometer	200 nm	2 – 12 mm	Low
Optical Encoder	10 nm	5 - 500 mm	Medium
Capacitive Sensor	2 - 10 nm	0.1 – 0.5 mm	High-medium
Inductive Sensor	0.5 - 5 nm	0.5 – 5 mm	High
Optical Interferometer	10 nm	1 – 100 mm	High-medium

SUMMARY

We observed strong correlation of measured beam position signal with the ID chamber water temperature in several sectors during user beam operations. In beam-off, IN-SITU experiments, we observed a BPM position change at a rate up to 10 μm/°C. A nonlinear, complex behavior was observed in the chamber shape changed with water temperature changes. We propose to monitor the position of the BPM in real time during user beam operations to compensate for the distortion of the ID vacuum chamber. We presented a conceptual design to monitor the vertical as well as horizontal position change of the BPM and discussed a development plan based on this concept.

REFERENCES

[1] E. Trakhtenberg, E. Gluskin, P. Den Hartog, T. Klippert, G.Wiemerslage, and S. Xu, "The Vacuum System for Insertion Devices at the Advanced Photon," PAC'95, Dallas, TX. May 1995, MPP16, P. 2072 (1996); http://www.JACoW.org.
[2] Private Communication
[3] B.X. Yang, G. Decker, S. H. Lee, and P. Den Hartog, "High-Power Hard X-ray Beam Position Monitor Development at the APS," these proceedings.
[4] Renishaw, http://www.renishaw.com, Lion Precision, http://www.lionprecision.com/, Micro-Epsilon, http://www.micro-epsilon.com/

THE LHC FAST BCT SYSTEM: A COMPARISON OF DESIGN PARAMETERS WITH INITIAL PERFORMANCE

D. Belohrad#, L. K. Jensen, O. R. Jones, M. Ludwig, J. J. Savioz, CERN, Geneva, Switzerland

Abstract

The fast beam current transformers (FBCTs) for the Large Hadron Collider (LHC) were designed to provide bunch to bunch and turn by turn intensity measurements. The required bunch to bunch measurements together with a large machine circumference call for stringent control of the transmission bandwidth, droop and DC offsets in the front-end electronics. In addition, two measurement dynamic ranges are needed to achieve the required measurement precision, increasing the complexity of the calibration. This paper reports on the analysis of the measurement and calibration methods, discusses theoretical precision limits and system limitations and provides a comparison of the theoretical results with the real data measured during the LHC start-up.

INTRODUCTION

The FBCT measurement system (Fig. 1) is composed of the measurement device [1], front-end electronics, an acquisition system [2], and a software control system. The system was designed to comply to the measurement specification [3].

The beam current is measured using 1:40 toroid transformer from Bergoz Instrumentation. The signal is split in the RF distributor into two dynamic ranges, each of them providing measurements in two bandwidths: 200 MHz for bunch by bunch measurements and ~2 MHz for turn based measurements. The four measurement signals are independently integrated using the LHCb2002 analogue integrator ASIC, and sampled using 14 bit ADCs clocked synchronously with the beam. The entire measurement process is driven in the hardware by two Digital Acquisition Boards (DABs) [4]. Each DAB processes two integrated signals of the same bandwidth using an FPGA. The measured data are stored either in the FPGA on-chip memory, or in the external synchronous SRAM for large-volume measurements. The real-time software running in the front-end controller (FEC) provides the necessary system control, calibration procedure, conversion of the stored measurements to the number of charges, and a data publishing.

Four measurement modes are provided:

- **Capture** – a snapshot of the intensity measurement in each bunch slot for a specified number of turns
- **Turn Sum** – a total intensity measured over single LHC turn (3564 bunch measurement slot)
- **Slot Sum** – a sum of bunch slot intensities measured over specified number of turns
- **Sum Sum** – a measurement of *Turn Sum* over specified number of turns.

Each FBCT system is calibrated by 5 µs long current pulses of specific amplitudes. The calibration pulses are generated in a calibrator, implemented into a VME64x 6U board, and they are transported to the calibration circuit installed in the measurement device using 7/8" Heliflex cables.

MEASUREMENT ERROR

According to [3], the measurement error is specified in terms of absolute accuracy and resolution. Two LHC operational modes relevant to the measurement error are discussed in this article: the LHC pilot bunch injection, and the LHC ultimate SPS batch injection. The required turn-based measurement precision for both scenarios is summarised in Tab. 1.

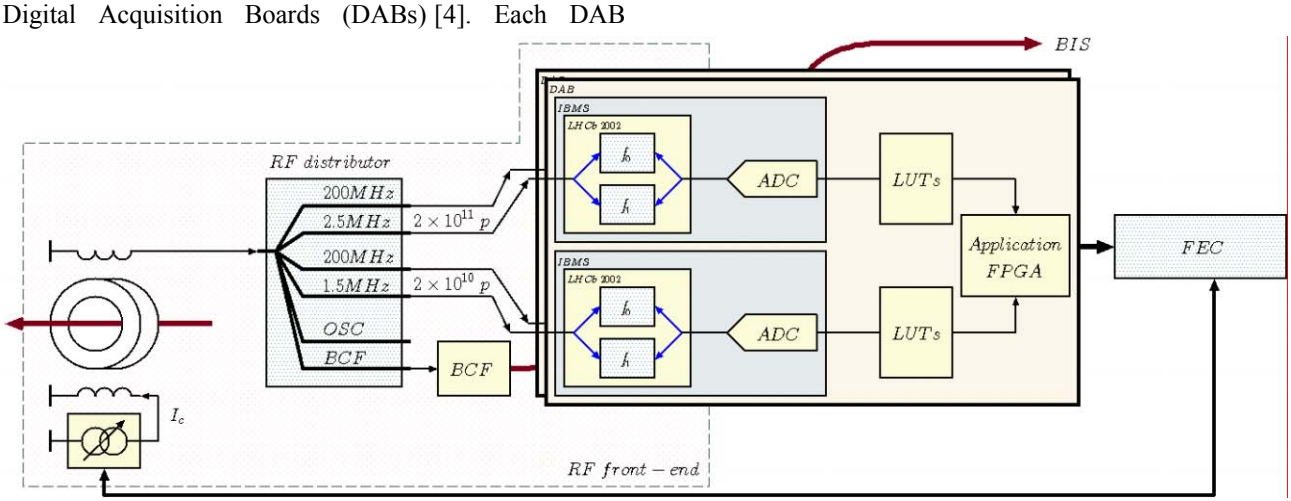

Figure 1: Block schematic of the FBCT measurement system

#david.belohrad@cern.ch

Instrumentation

Table 1:Required measurement precision

Operational mode	Number of charges per bunch	Absolute accuracy per bunch	Resolution
LHC pilot	5×10^9	±20% ±10^9 ch.	±20% ±10^9 ch.
Ultimate SPS batch	1.7×10^{11}	±2% ±2×10^9 ch.	±1% ±10^9 ch.

In order to fulfil such stringent measurement requirements the FBCT system blocks were evaluated individually, minimising the measurement error of each signal treatment stage. Following measurement error contributors were identified:

- droop of the measured beam current signal
- offsets in the front-end electronics
- calibration algorithm and accuracy of the generated calibration current
- transmission of the calibration current from the calibrator to the FBCT measurement winding

MEASUREMENT ERROR CONTRIBUTORS

Beam Current Signal Droop

The FBCT transfer function for a toroid transformer having N_s turns is defined as:

$$I_s = \frac{s\tau}{s\tau+1}\cdot\frac{I_b}{N_s}, \qquad (1)$$

where $\tau = L_s/R_s$ determines the low-frequency (LF) cut-off and I_b is the beam current. L_s and R_s define the inductance and resistance of the measurement winding. The first term of Eq. (1) describes a high-pass filter. Hence the FBCT does not transfer the DC signal component and the measured signal I_s exhibits a droop. When the beam circulates in the LHC, the droop can be actively suppressed using a base-line restoration (BLR) algorithm, however the BLR is of no use at injection. This case was identified to be critical for the measurement error caused by the droop.

In order to calculate the absolute droop error for each LHC bunch slot an analytical droop model was constructed. The model uses a convolution of the transfer function Eq. (1) with a base function, defined as:

$$f(t)=\begin{cases} a[\cos(b(t-kT_0))^2-1]^2 & t\in\langle kT_0; kT_0+\frac{\pi}{b}\rangle \\ 0 & t\in\langle kT_0+\frac{\pi}{b}; (k+1)T_0\rangle \end{cases} \qquad (2)$$

The base function describes a bunch train spaced by T_0, where each bunch is defined using constants a and b derived from the LHC longitudinal bunch size σ.

The convolved signal (Fig. 2) is used to determine the measurement error in each bunch slot of the LHC machine as a difference between the convolved signal and the original signal. The model analysis reveals, that for the case of the LHC pilot bunch, a 1% droop error is achieved using an FBCT with LF cut-off of 100 kHz.

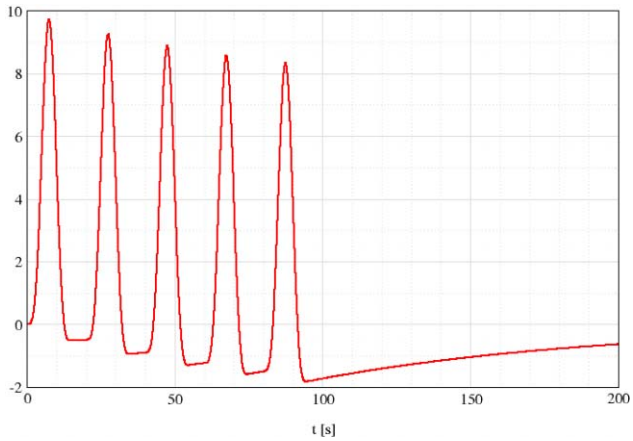

Figure 2: Result of the convolution calculation for five bunch slots and arbitrarily chosen parameters to emphasize the effect of the signal droop

Such model was applied as well to determine the required LF cut-off in case of an injection of a maximum of four SPS batches. The worst-case error exhibits at the end of the injection, and its absolute value can be determined using following generic equation:

$$E_e(k)=N_p e\cdot\frac{24\tau^5 b^4 a\left(e^{\frac{KT_0}{\tau}}-e^{\frac{KbT_0+\pi}{b\tau}}+\frac{\pi}{b\tau}-1\right)e^{-\frac{(k+1)T_0}{\tau}}}{64b^4\tau^4+20b^2\tau^2+1}, \qquad (3)$$

where N_p is the number of charges, e is the elementary charge, K is number of injected bunches and τ is the FBCT LF cut-off. Lower-case k denotes the bunch slot number for which the error is calculated (k > K).

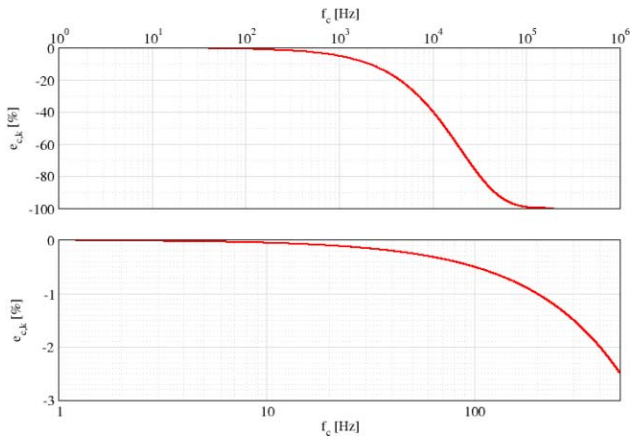

Figure 3: Relative error caused by the signal droop at the end of 4 SPS batch (288 bunches, ~8μs) injection into the LHC as a function of the FBCT LF cut-off

The result of the calculation of the relative error caused by the signal droop at the end of four-batch SPS LHC injection is shown in Fig. 3. Should the droop error be kept under 2% an FBCT having a LF cut-off lower than 400Hz is required. The toroids in the LHC have a LF cut-off approximately 200 Hz so the droop error lowers to 1%.

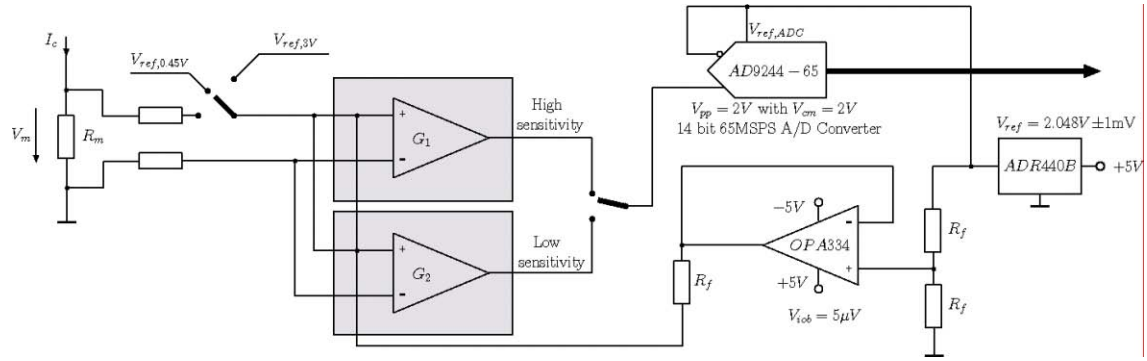

Figure 4: Acquisition system implemented into the calibrator to measure the amplitude of the current pulse sent to the calibration winding of the FBCT

Calibration algorithm

The FBCT calibration is based on a linear fit of the values measured to associated reference signals. Reference signals are provided by a calibrator generating a current pulse of a known amplitude. The pulse is sent into the FBCT calibration winding, and appropriate reference values are measured. Four measurement ranges require totally three calibration currents, as shown in Tab. 2.

Table 2:Required calibration currents

	Low bandwidth	**High bandwidth**
Low gain	650mA	650mA
High gain	12mA	40mA

Each measurement channel is calibrated using an averaged offset and a reference current measurement. 32 sample-averaging is used to reduce the noise imposed on the measured data.

The important measurement error contributor is the accuracy of the generated calibration pulse. Accuracy of the current amplitude setting is limited by the on-board amplifiers offset and gain errors as well as by the precision of the resistors. The amplifiers have high bandwidth and high slew rate, and contribute significantly to the current setting uncertainty. The actual calibrator implementation exhibits a current setting uncertainty of 1.9 mA. This is not sufficient to calibrate properly the high gain (HIGAIN) measurement channels and hence a system to measure the current sent to the calibration winding was included into the calibration pulse generator.

The current measurement is based on sampling and conversion of a voltage developed across a shunt resistor installed in the feedback of the current source amplifier (R_m). The measurement method is shown in Fig 4. The measured voltage is amplified by two fast Voltage-feedback Operational Amplifiers (VFOA). The amplifiers amplify the input signal using different gains and provide two sensitivity ranges: the high-sensitivity range performs measurements of generated currents not exceeding 150 mA in amplitude, the low-sensitivity range provides measurement of full 800 mA current span. The amplified voltage is then sampled using a 14-bit AD9244 ADC clocked synchronously with the beam.

The reference voltage for the ADC is generated by a precision 2.048±0.05% voltage source. The ADC is set up to give a reading for a positive voltage of 1 to 3 volts. The OPA334 injects into the gain blocks a DC voltage shifting the measured voltage V_m to the operational range of the ADC. It adds as well a small positive offset so that in all possible cases the ADC generates non-zero positive response when performing offset measurements.

Two references are used to calculate on-fly a linear fit of the ADC measured data to the calibration current.

Estimation of the measurement uncertainty is based on an idea of uncertainty propagation for indirect measurements of current. The type B uncertainty [5] of the measured current $I_c = V_m / R_m$ is determined using following equation:

$$u_{B,I_c} = \sqrt{\frac{u_{V_m}^2}{R_m^2} + \frac{V_m^2 u_{R_m}^2}{R_m^4}}, \quad (4)$$

where V_m is the measured voltage, R_m the reference shunt resistor, u_{Rm} is the type B uncertainty of the resistance used and u_{Vm} is the type B uncertainty of the measured voltage.

The resistance value uncertainty is determined using widely accepted $\sqrt{3}$ rule:

$$u_{R_m} = \frac{1}{100} \cdot \frac{R_m \cdot \delta_{R_m}}{\sqrt{3}}, \quad (5)$$

where δ_{R_m} denotes the resistance tolerance (%).

The unknown in Eq. (4) is the uncertainty of the voltage measured u_{Vm}. This value is determined from a linearisation function implemented in the calibrator's FPGA:

$$V_m = (V_{ref,1} - V_{ref,2}) \cdot \frac{ADC_m - ADC_{ref,2}}{ADC_{ref,1} - ADC_{ref,2}} + V_{ref,2} \quad (6)$$

The uncertainty propagation function Eq. (7) is applied to all the terms of Eq. (6) for both measurement ranges to determine the linearisation uncertainty u_{Vm}:

$$u_f = \sqrt{\sum_i \left(\frac{\partial f(x_0, x_1, \ldots, x_i)}{\partial x_i} \cdot u_{x_i} \right)^2} \quad (7)$$

The used reference voltages in Eq.(6) differ for each measurement range (Tab. 3), their uncertainties were determined using Eq. (7) applied on the references' transfer functions. Corresponding ADC values were measured on a real system.

Table 3:Used references for both sensitivity ranges

	High Sensitivity	Low Sensitivity
$V_{ref,1}$	0.45 V	3 V
$V_{ref,2}$	0 V (offset)	0.45 V

Uncertainty of the ADC measurements was determined using Eq. (8) as only integral non-linearity and resolution are major error contributors.

$$u_{ADC} = \frac{\sqrt{3}}{3} \frac{INL \cdot FSR}{2^N - 1}, \quad (8)$$

where INL is the integral non-linearity of the ADC used and FSR is its full-scale reading.

Type A uncertainty was evaluated on the real system for both measurement ranges and all generated currents, and only the worst-case estimations of $u_{A,h}$=12.4 µA for high sensitivity, and $u_{A,l}$=84.9 µA for low sensitivity were considered (32 samples were used to estimate the uncertainty). The total uncertainty was determined using geometrical sum of both uncertainty types. Extended relative uncertainty was calculated using inclusion factor 2. The results are shown in Fig. 5. Detailed analysis can be found in [6].

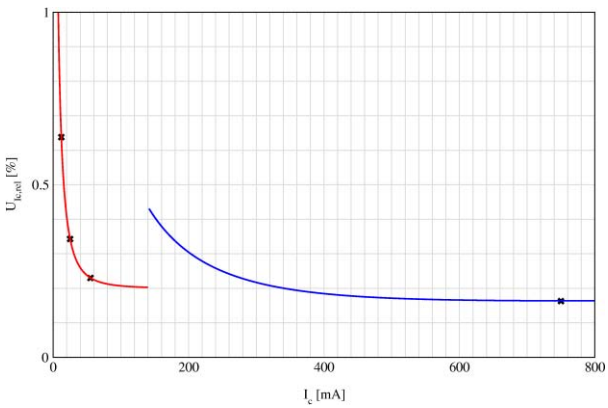

Figure 5: Relative extended uncertainty of the calibration current pulse measurement

Transmission of the calibration current from the calibrator to the measurement winding

Special attention was paid to create a well matched transmission line to transport the calibration pulse to the measurement device, and to assure a minimum signal loss due to electromagnetic coupling. Achieving this requires the calibration current generated electromagnetic field to be homogeneously distributed in the volume of the toroid. To find the best possible calibration turn winding arrangement a set of them were tested.

The schematic drawing of the winning candidate is shown in Fig. 6. The test calibration turns were fabricated using 0.381 mm thick NY9220 RF substrate. Four connection types, dividing the current to 4, 6, 8 and 16 parallel branches were tested.

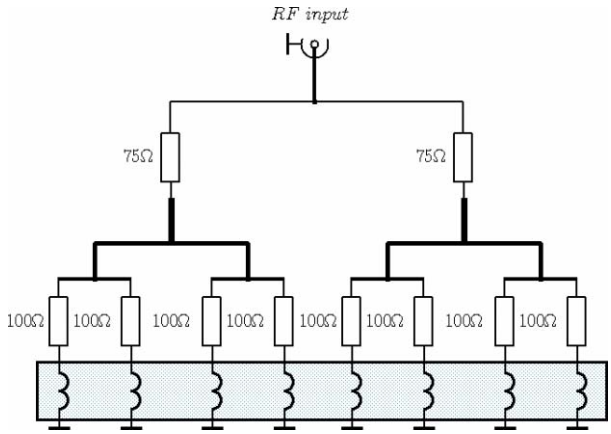

Figure 6: The LHC FBCT calibration turn

The charge transmission ratio was calculated comparing the charge measured at the FBCT output to the value calculated from the charge measured at the input of the calibration turn. Summary of the results is shown in Tab 4. Mechanical constraints did not permit to use the 16 branches, hence a compromise 8 branch version was used.

Table 4:Transmission ratio for tested calibration circuits

Number of branches	Coefficient of transmission [%]
4	87.2
6	95.2
8	99.3
16	99.8

Offsets in the Front-end electronics

The used analogue integrator works with input voltages of approximately 2 V and provides full-scale (FS) charge measurement of 62pC. Any DC signal present at its input represents an error signal at its output. In extreme case the DC input signal would saturate the integrator and the useful signal would be lost. Although the DC signal can be calibrated away, it lessens the dynamic range of the used integrator.

The RF distributor generates the signals for the measurement channels integrators. As each channel provides measurement using different gain and bandwidth, the provided signals may exhibit output DC offsets in range of hundreds of millivolts. This is especially case of low-bandwidth high-gain measurement channel, which must heavily amplify (+30dB) the low mean value LHC pilot beam signal. An active output offset suppression was developed to minimise the effect of the DC voltage [2]. As shown in Fig. 7, the offsets are limited to theoretical 500 µV, however much better mean offset of 47 µV was measured on a lot of 20 fabricated RF

distributors. This corresponds to 0.05% of the available dynamic range.

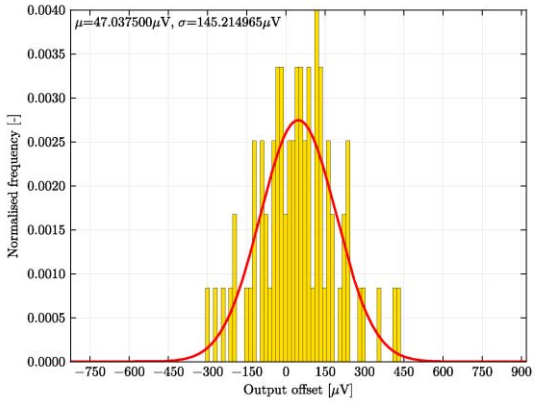

Figure 7: Normalised histogram of DC offsets measured at all outputs of RF distributor fabrication batch

MEASUREMENT RESULTS

In order to evaluate the performance of the measurement method the implemented FBCT systems were calibrated, and their measurements were compared to the independently calibrated DC current transformers (DCCTs). One such comparison is shown in Fig.8.

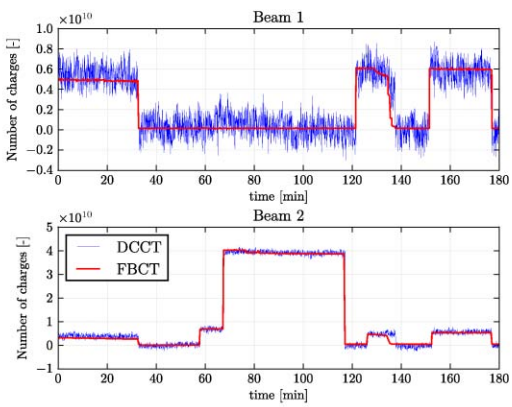

Figure 8: Comparison of independently calibrated measurements of the DCCTs and FBCTs installed in the LHC rings

The red traces correspond to the FBCTs measurements, the blue traces depict the DCCTs measurements. Top graph shows measurement of the single LHC pilot bunch, circulating in *beam 1*, bottom graph is the measurement of cumulated intensity of ≈4×10^{10} charges circulated in *beam 2*. The two independent measurement systems exhibit high degree of match. Further analysis reveals the measurement difference better than 0.5%

Table 5 summarises the noise floor measurements. As expected, the noise mean value is close to zero due to calibration and offset suppression. Its standard deviation, measured using 3564x10 samples (corresponds to ten LHC revolution periods) sets the resolution limits for future fast dI/dt measurements.

Table 5:No-beam measurements of single FBCT measurement system installed in the LHC ring

Channel	*Mean value* [# charges]	*Standard deviation* [# charges]	*STD relative to FS* [%]
HIGAIN HIBW	-0.7×10^6	1.3×10^7	0.09
HIGAIN LOBW	0.6×10^6	6.2×10^7	0.42
LOGAIN HIBW	10.3×10^6	1.6×10^8	0.1
LOGAIN LOBW	-1.7×10^6	1.4×10^8	0.1

CONCLUSION

The FBCTs installed in the LHC were designed to satisfy the specification [3]. Although the devices were not fully tested with all possible variants of the beams, the achieved measurement accuracy on currently used LHC beams is in accordance with the specifications. This is proven as well by long-term match of the DCCT and FBCT measurements.

The noise figures measured on all measurement channels assure an optimal data source for the fast dI/dt measurement, which is currently being implemented.

The FBCT system is constantly improving as more experience is gained during the LHC operation. Its functionality was so far verified only using limited LHC injection patterns and the 'ultimate' proof of functionality will be obtained when more complex injection and acceleration scenarios are measured.

ACKNOWLEDGEMENT

The authors wish to thank to Assoc. Prof. P. Kaspar from Czech Technical University in Prague for his fruitful hints and help with the uncertainty calculus.

REFERENCES

[1] D. Belohrad, P. Odier, S. Thoulet, S. Longo: "Mechanical Design of the Intensity Measurement Devices for the LHC", DIPAC'07, Venice, Italy, March 2007

[2] D. Belohrad, O. R. Jones, M. Ludwig, J. J. Savioz: "Implementation of the electronics chain for the Bunch by Bunch Intensity Measurement devices for the LHC", DIPAC'09, Basel, Switzerland, May 2009

[3] C. Fischer, R. Schmidt: "On the measurements of the beam current, lifetime and decay rate in the LHC rings", LHC-BCT-ES-0001, EDMS 359172, CERN, Geneva, Switzerland, January 2005

[4] Jones, O. R.: "VME64x Digital Acquisition Board for the LHC Trajectory and Closed orbit System", LHC-BP-ES-0002, EDMS 410295, CERN, Geneva, Switzerland, March 2004

[5] JCGM 100:2008: "Evaluation of measurement data – Guide to the expression of uncertainty in measurement", Joint Committee for Guides in Metrology, September 2008

[6] Belohrad, D.: "Fast Beam Intensity Measurements for the LHC", Doctoral Thesis, to be published at Czech Technical University in Prague, 2010

ANALYTICAL METHOD FOR DETERMINING ERRORS IN CURRENT MEASUREMENTS WITH A ROGOWSKI COIL

M. J. Hagmann, NewPath Research L.L.C., P. O. Box 3863, Salt Lake City, UT 84110, U.S.A.

Abstract

Algebraic expressions are derived for the open-circuit voltage induced on a toroidal coil with unevenly spaced turns, by a sinusoidal current through its aperture. The derivation requires that the winding layer is thin, the number of turns is large, and the cross-section of the winding is rectangular. These expressions are used to determine the effects of the gap between the ends of the coil and other irregularities in the spacing of the turns on the position sensitivity, defined as the dependence of the induced voltage on the location of the current. This technique may be used to define the criteria to meet a specified upper limit for the positional sensitivity.

INTRODUCTION

A Rogowski Coil [1] is a non-ferrous current probe in which a uniformly wound helix with a constant cross-sectional area follows a closed curve of arbitrary shape. Faraday's law of induction, with Ampere's law [2], requires that the open circuit voltage V induced on the coil is given by

$$V = \mu_0 N' A \frac{dI}{dt} \quad (1)$$

where N' is the number of turns per unit length of the helix, A is the cross-sectional area of the helix, and dI/dt is the rate of change of the current passing through the area enclosed by the closed curve.

An ideal Rogowski coil would provide equal sensitivity to currents that are located anywhere within the aperture and would not be sensitive to currents outside of the aperture. However, the derivation of Eq. (1) requires that (1) The winding is uniform; (2) The radius of the winding is much less than the distance from the current to the coil; (3) N' is large so the helix may be approximated by a large number of evenly-spaced coils that are each normal to the curved axis of the helix; and (4) The frequency is low enough that displacement current and transit time may be neglected.

Measurements show that Rogowski coils have "position sensitivity" in that the induced voltage depends on the location of the current within the aperture [3]. Conventional methods of winding coils generally cause a positional sensitivity greater than 1%. A position sensitivity of less than 0.1% has been obtained by machining coils to a precision of 25-50 μm and reducing the gap where the two ends of the coil are adjacent to each other.

In the following sections of this paper we examine the effects of unevenly spaced turns in a toroidal Rogowski coil on the induced voltage when the cross-section of the winding is uniform and rectangular with arbitrary size. However, it is necessary to assume that the winding has zero thickness, so the present analysis does not show changes in the sensitivity when the distance of the current to the coil is comparable to the thickness of the winding. The number of turns per unit length is assumed to be large enough that the winding may be approximated by a group of closely-spaced coils in planes having constant θ (azimuthal coordinate about the axis through the center of the aperture). Otherwise the incremental advancement of each turn would create an undesirable one-turn loop to cause the coil to be sensitive to magnetic fields parallel to the axis. However, the latter effect may be mitigated by adding a one-turn return loop [4] or other methods which are not considered here. The present analysis is limited to frequencies that are low enough so the current probe is much smaller than a wavelength.

Our objective is to provide a tool to determine limits for the nonuniformity in the winding to satisfy a specified upper limit for the positional sensitivity. Others have used numerical integration to model these effects [5], but we have derived algebraic expressions that are intended to be simpler to implement and provide greater understanding.

ANALYSIS

Figure 1 shows the configuration used for the analysis of induction with a non-ferrous toroidal coil that may have a nonuniform winding. We consider the induction in an incremental winding of length $R_1 d\theta$, centered at (R_1,θ) that is caused by current I intersecting the plane at point $P(R_2,\Phi)$. Lines L_1 and L_2 are normal to the plane of the incremental winding, and parallel to the magnetic field caused by the current, respectively, and the angle between these two lines is α.

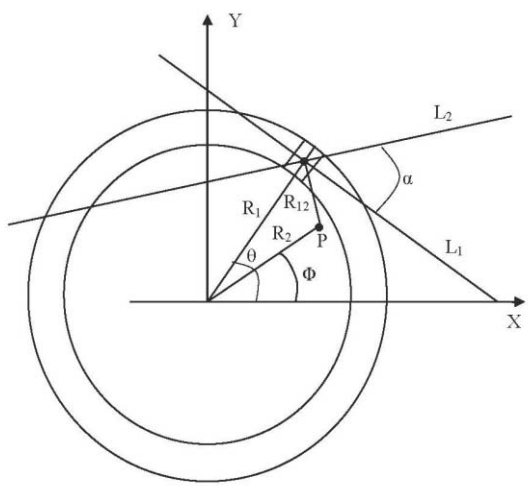

Fig. 1. Diagram for analysis.

The increment of winding has $dN = N'(\theta)R_1 d\theta$ turns, where $N'(\theta)$ is the turn density, defined as the number of turns per unit length of the toroid. Thus, the open-circuit voltage induced on the coil is given by

$$V_{OC} = \int_0^h dz \int_{r_1}^{r_2} dr \int_0^{2\pi} \frac{j\omega\mu_0 R_1 I_0 \cos(\alpha) N'(\theta) d\theta}{2\pi\sqrt{R_2^2 + r^2 - 2R_2 r\cos(\theta - \Phi)}} \quad (2)$$

The limits for integration over the cross-section of the winding are 0, h, r_1, and r_2; r is a dummy variable in place of R_1, and the cosine of α is given by

$$\cos(\alpha) = \frac{r - R_2\cos(\theta - \Phi)}{\sqrt{R_2^2 + r^2 - 2R_2 r\cos(\theta - \Phi)}} \quad (3)$$

Thus, combining Eqs. (2) and (3), the open-circuit voltage is given by

$$V_{OC} = \frac{j\omega\mu_0 R_1 I_0}{2\pi} \int_0^h dz \int_{r_1}^{r_2} \frac{dr}{r} \int_0^{2\pi} \frac{\left[r^2 - R_2 r\cos(\theta - \Phi)\right] N'(\theta) d\theta}{\left[R_2^2 + r^2 - 2R_2 r\cos(\theta - \Phi)\right]} \quad (4)$$

The turn density is given by the following Fourier series:

$$N'(\theta) = N_0' + \sum_{J=1}^{\infty} N_{JC}'\cos(J\theta) + N_{JS}'\sin(J\theta) \quad (5)$$

Substituting Eq. (5) into Eq. (4), and evaluating the integrals [6] gives the following expression for the open-circuit voltage on the Rogowski coil:

$$\begin{aligned} V_{OC} &= j\omega\mu_0 h \ln\left(\frac{r_2}{r_1}\right) R_1 N_0' I_0 \\ &+ \frac{j\omega\mu_0 h R_1 I_0}{2} \sum_{J=1}^{\infty} \frac{N_{JC}'\cos(J\Phi)}{J} \left[\left(\frac{R_2}{r_1}\right)^J - \left(\frac{R_2}{r_2}\right)^J\right] \\ &+ \frac{j\omega\mu_0 h R_1 I_0}{2} \sum_{J=1}^{\infty} \frac{N_{JS}'\sin(J\Phi)}{J} \left[\left(\frac{R_2}{r_1}\right)^J - \left(\frac{R_2}{r_2}\right)^J\right] \end{aligned} \quad (6)$$

For the special case of a thin toroid, so that $r_1 = R_1 - \Delta/2$ and $r_2 = R_1 + \Delta/2$ where $\Delta << R_1$, Eq. (6) may be simplified to give the following expression:

$$\begin{aligned} V_{OC} &\approx j\omega\mu_0 h \Delta N_0' I_0 \\ &+ \frac{j\omega\mu_0 h \Delta I_0}{2} \sum_{J=1}^{\infty} \left[\begin{array}{l} N_{JC}'\left(\frac{R_2}{R_1}\right)^J \cos(J\Phi) \\ + N_{JS}'\left(\frac{R_2}{R_1}\right)^J \sin(J\Phi) \end{array}\right] \end{aligned} \quad (7)$$

When given a specified turn density N'(θ), the coefficients in the Fourier series of Eq. (5) may be determined using the following equations:

$$N_0' = \frac{1}{2\pi}\int_0^{2\pi} N'(\theta) d\theta \quad (8A)$$

$$N_{JC}' = \frac{1}{\pi}\int_0^{2\pi} N'(\theta)\cos(J\theta) d\theta \quad (8B)$$

$$N_{JS}' = \frac{1}{\pi}\int_0^{2\pi} N'(\theta)\sin(J\theta) d\theta \quad (8C)$$

EXAMPLES

1. Effect of a gap in the winding

Consider a coil having a gap over a fraction f of the total circumference, such as between the two adjacent ends of the coil. The gap is located from $-\pi f < \Phi < \pi f$ in a coil which elsewhere has a uniform turn density $N'(\theta) = N_0'$. The Fourier coefficients are determined with Eqs. (8A)-(8C), and then Eq. (6) gives the following expression for the fractional error in the open-circuit voltage:

$$\frac{\Delta V_{OC}}{V_{OC0}} = -f - \frac{1}{\pi\ln(\gamma)} \sum_{J=1}^{\infty} \frac{\sin(fJ\pi)}{J^2} \left(\frac{R_2}{r_1}\right)^J \left(1 - \frac{1}{\gamma^J}\right)\cos(J\Phi) \quad (9)$$

where V_{OC0} is the value for the case where the width of the gap is zero and the relative width of the coil, $\gamma = r_2/r_1 > 1$. Equation (9) shows that the position sensitivity which is caused by a gap can always be reduced by increasing γ, as others have noted from their specific numerical solutions [5]. For the case of a thin toroid, Eq. (9) may be simplified to give the following expression:

$$\frac{\Delta V_{OC}}{V_{OC0}} = -f - \frac{1}{\pi} \sum_{J=1}^{\infty} \frac{\sin(fJ\pi)}{J} \left(\frac{R_2}{R_1}\right)^J \cos(J\Phi) \quad (10)$$

Figures 2 and 3 show the fractional error in the open-circuit voltage as a function of the angle Φ for a coil with a gap having a width of 1° (f = 1/360), determined with Eq. (14). These two figures also show the effect of the radial location of the current, with R_2/r_1 = 0.1, 0.2, 0.3, 0.4, 0.5, 0.6, 0.7, 8.8, and 0.9 from the top curve to the lowest curve, respectively. Figures 2 (γ = 1.25) and 3 (γ = 3.0) show that the position sensitivity increases sharply as the current is moved closer to the gap, both azimuthally and radially, and it may be reduced by increasing the thickness of the coil.

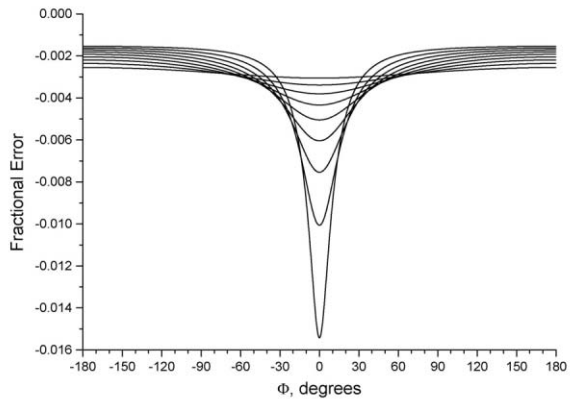

Fig. 2. Fractional error vs. the angle Φ for a coil with γ = 1.25, having a gap having a width of 1°.

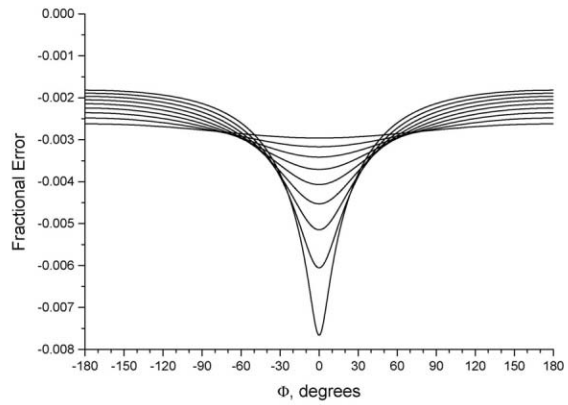

Fig. 3. Fractional error vs. the angle Φ for a coil with γ = 3.0, having a gap having a width of 1°.

2. Effect of a sinusoidal perturbation in winding the coil

When a single sinusoidal term from the Fourier series in Eq. (5) is added as a perturbation to a uniformly-wound coil, Eq. (6) shows that the peak value of the fractional error in the open-circuit voltage is given by

$$\frac{\Delta V_{OC}}{V_{OC0}} = F\left(J, \gamma, \frac{R_2}{r_1}\right)\frac{N_{JC}'}{N_0'} \qquad (11A)$$

$$\text{where } F\left(J, \gamma, \frac{R_2}{r_1}\right) \equiv \frac{1}{2J\ln(\gamma)}\left(\frac{R_2}{r_1}\right)^J\left(1-\frac{1}{\gamma^J}\right) \qquad (11B)$$

Figure 4 shows the value of the coefficient $F(J, \gamma, R_2/r_1)$ from Eq. (11B) as a function of the normalized radial coordinate of the current (R_2/r_1) for a coil with $\gamma = 1.25$, having a sinusoidal perturbation with J = 1, 2, 3, 4, 5, 6, 8, and 10, from the top to the lowest curve, respectively. The fractional error in the open-circuit voltage is proportional to the Jth power of R_2/r_1, so terms with higher spatial frequency would have a small effect unless the current is close to the surface of the coil. As seen in the first example for a gap in the winding, the error that is caused by a single sinusoidal term from the Fourier series may also be reduced by increasing the relative width of the coil.

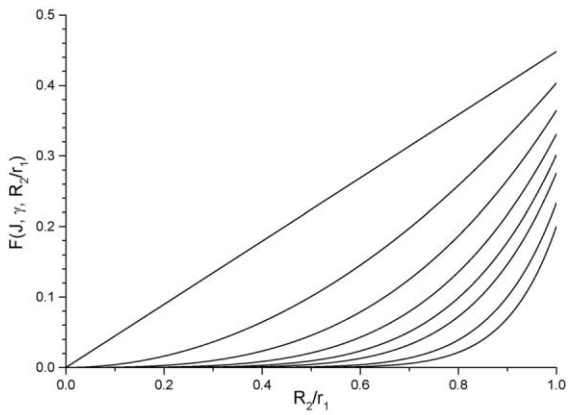

Fig. 4. Function $F(J, \gamma, R_2/r_1)$ vs. normalized radial coordinate of the current, R_2/r_1, for a coil with $\gamma = 1.25$

3. Effect of random errors in the winding on the position sensitivity

Others have made measurements with different types of Rogowski coils to show that the position sensitivity may be mitigated by reducing random errors in the winding and reducing the gap between the two ends of the coil [3]. They developed techniques to prepare coils with a precision of 50 μm to reduce the position sensitivity to as low as 0.1%, whereas commercial Rogowski coils generally have a position sensitivity greater than 1%. One of their techniques is laser machining of a thin layer of conductive material that is fired onto a core that is made from a machinable ceramic [4]. One coil that was made in this manner has 130 turns with the dimensions r_1 = 5.1 cm and r_2 = 7.6 cm (γ = 1.49). The criterion for a precision of 50 μm with this coil would correspond to 0.1 % of r_1 for this device.

We have extended the present analysis to develop the following method for determining the effects of random errors in the fabrication on the position sensitivity of a Rogowski coil:

1. N points are specified which are evenly spaced on a circle with radius $r = r_1$, corresponding to the ends of each of the N turns of a uniformly wound coil.
2. Each of the N points is displaced by adding Gaussian-distributed random errors to the angular coordinate θ, so the positions at the ends of each turn are displaced by distances having an rms value that is approximately 0.1% of r_1.
3. This array of points is used to determine local values of the turn density N'(θ) for a nonuniformly wound coil.
4. The Fourier coefficients for Eq. (5) are determined by using the local values of N'(θ) with numerical integration with Eqs. (8A)-(8C).
5. The Fourier coefficients are used in the following equation, derived from Eq. (6), to determine the fractional error in the open-circuit induced voltage when the current is located at each of a large number of points on a ring with radius R_2, and then the rms variation of these voltages is calculated as a measure of the position sensitivity.

$$\frac{\Delta V_{OC}}{V_{OC0}} = \frac{1}{2N_0'\ln(\gamma)} \bullet \sum_{J=1}^{\infty}\left[\frac{\left[N_{JC}'\cos(J\Phi)+N_{JS}'\sin(J\Phi)\right]}{J} \bullet \left(\frac{R_2}{r_1}\right)^J\left[1-\frac{1}{\gamma^J}\right]\right] \qquad (12)$$

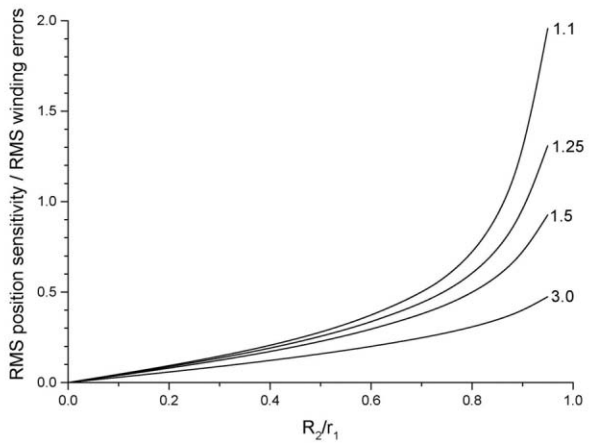

Fig. 5. Ratio of rms variation of the errors from position sensitivity to rms fractional errors in the coil vs. normalized radial coordinate of the current.

Figure 5 shows the effect of random errors in the winding on the position sensitivity. When the errors are small, the variation that is caused by position sensitivity is proportional to the errors in the locations of the points in the winding. Thus, the ordinate in Fig. 5 is the ratio of the rms variation of the errors caused by position

sensitivity, to the rms fractional errors in placing the end points of the turns of the coil. This quantity is plotted as a function of the normalized radial coordinate of the current, R_2/r_1, for coils having a relative width, $\gamma = 1.10$, 1.25, 1.50, and 3.00.

SUMMARY AND CONCLUSIONS

Figures 2 and 3 in the first example are consistent with numerical solutions [5] and measurements [3,5] by others. These two figures show that the position sensitivity becomes large when the current is in a small wire or particle beam that is far from the axis of the toroid. However, the full magnitude of this effect would not be seen in some practical applications of Rogowski coils such as when the current is in a bus bar that occupies 56% of the cross-sectional area of the aperture of the coil [3]. Manufacturers of Rogowski coils generally suggest that the aperture should not be much larger than the size of the conductor. However, this is not possible in measurements with particle beams so such measurements are subject to position sensitivity.

Others have previously noted that increasing the relative width of the coil reduces the position sensitivity that is caused by a gap in the winding [5], and Eq. (9) in the first example shows that this is the case. Furthermore, Eqs. (11A) and (11B) in the second example show that increasing the relative width of the coil also reduces the position sensitivity which is caused by a sinusoidal perturbation in the winding. Furthermore, Eq. (12) in the third example shows that the position sensitivity which is caused by random errors in the winding is also reduced by increasing the relative width of the coil. Figure 5 in the third example shows that with coils that are wound with a specified degree of precision, when the current is located at $R_2/r_1 = 0.8$, the position sensitivity may be reduced by a factor of 2 by increasing γ ($r_2/_{r1}$) from 1.25 to 3.0.

REFERENCES

[1] W. Rogowski and W. Steinhaus, “Die messung der magnetischen spannung,” Arch. Electrotech, 1 (1912) 141-150.

[2] A.G. Klein, “Demonstration of Ampere’s circuital law using a Rogowski coil,” Am. J. Phys. 43 (1975) 368-370.

[3] A. Andersson, D. Destefan, J.D. Ramboz, S. Weiss and J.M. DeHaan, “Unique EHV current probe for calibration and monitoring,” IEEE/PS Transmission and Distribution Conference, Vol. 1 (2001) 379-384.

[4] J.D. Ramboz, “Machinable Rogowski coil, design, and calibration,” IEEE Trans. Instrum. Meas. 45 (1996) 511-51

[5] L. Ferkovic, D. Ilic and R. Malaric, “Analysis of the mutual inductance of a precise Rogowski coil,” Instrumentation and Measurement Technology Conference, IMTC-2007, No. 7685 on the CD for the Conference Proceedings.

[6] W. Grobner and N. Hofreiter, *Integraltafel Zweiter Teil Bestimmte Integrale*, Vienna, Springer-Verlag, 1966, p. 112.

MONITORING TRANSVERSE BEAM PROFILE WITH NONUNIFORMLY-WOUND TOROIDAL COILS

M. J. Hagmann, NewPath Research L.L.C., P. O. Box 3863, Salt Lake City, UT 84110, U.S.A.

Abstract

Others have shown that the voltages induced on one uniformly-wound toroidal coil and two sinusoidally-wound toroidal coils may be used to determine the current in a single filament and its coordinates. We have extended this technique to show that the voltages measured on a group of sinusoidally-wound toroidal coils may be used to approximate the transverse distribution of the current that passes through their common aperture. This is possible because each measured voltage is proportional to the product of unique functions of the radial and azimuthal coordinates of each increment of the current. We have developed matrix methods to determine the transverse distribution of the current and determined the sensitivity of these calculations to measurement errors. Shielded sinusoidally-wound coils with a precision of 0.02 cm have been prepared using rapid prototyping, and methods to prepare the next generation of these coils, which will have a precision of 0.001 cm, by using an engraving tool with the 4th axis of a vertical milling machine have been defined.

INTRODUCTION

A number of different techniques have been used to monitor the transverse distribution of the beam current in accelerators, including secondary emission monitors, wire scanners, multi-wire chambers, gas curtains or jets, residual gas monitors, scintillator screens, scrapers and measurement targets, synchrotron radiation, and Laser-Compton scattering [1], as well as optical transition radiation [2] and the deflection of a probe beam of electrons [3].

A Rogowski Coil is a non-ferrous current probe which is generally wound as a toroid, but may also be made by bending a uniformly wound helical coil to follow a closed curve having arbitrary shape [4-6]. A time-dependent current passing through the aperture of a Rogowski Coil induces a voltage on the coil, and for an ideal coil this voltage would be independent of the location of the current within the aperture, and zero for currents outside of the aperture.

Great care is taken to limit the deviations from a perfectly uniform winding because these errors cause a Rogowski Coil to have "position sensitivity" so that the induced voltage depends on the location of the current within the aperture and may be non-zero when the current is outside of the aperture [7-8]. However, others have shown that the position sensitivity of non-uniformly wound coils may be used advantageously to determine the location of a single current that passes through the aperture [9-11].

SUMMARY OF THE ANALYSIS

We have previously derived exact closed-form expressions for the open-circuit voltage that is induced on a non-ferrous toroidal coil by a time-dependent current passing through the aperture when the turn density of the coil varies sinusoidally as a function of θ, which is the angle about the axis of the toroid [12-13]. To illustrate the configuration, Fig. 1 is a design drawing that was used in fabricating one of our toroids which has a total of 268 turns in which N'(θ), the number of turns per unit length at the mean radius R_1, is proportional to sin(θ). Thus, it may be seen that there is a reverse in the direction of the winding at the midpoint of the coil.

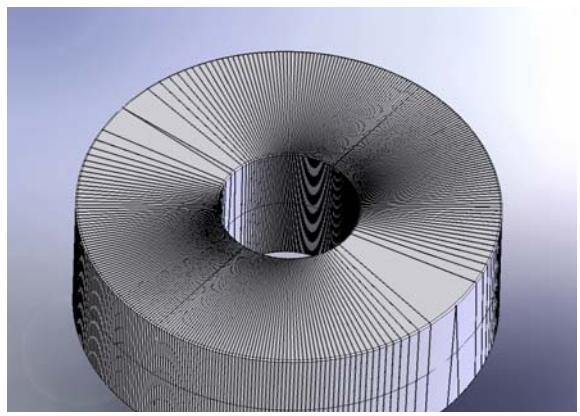

Fig. 1. Design drawing for sin(θ) toroid.

Each coil has a rectangular cross-section with height h, inner radius r_1, and outer radius r_2. To begin with we determine the open-circuit voltage induced on the coil by a filament of current I_0 which is located at the coordinates (R_2, Φ) where $R_2 < r_1$ to be inside of the aperture. The current is assumed to have harmonic time-dependence of $e^{j\omega t}$, but Fourier analysis may be used to extend the analysis to pulses or other functions of time. If the turn density is given by N_0', $N_{JC}\cos(J\theta)$, or $N_{JS}\sin(J\theta)$, it may be shown that the open-circuit voltage is given respectively, by the following three expressions:

$$V_{oc} = j\omega\mu_0 h R_1 N_0' I_0 \ln\left(\frac{r_2}{r_1}\right) \qquad (1A)$$

$$V_{oc} = \frac{j\omega\mu_0 h R_1 N_{JC}' I_0 \cos(J\Phi)}{2J}\left[\left(\frac{R_2}{r_1}\right)^J - \left(\frac{R_2}{r_2}\right)^J\right] \qquad (1B)$$

$$V_{oc} = \frac{j\omega\mu_0 h R_1 N_{JS}' I_0 \sin(J\Phi)}{2J}\left[\left(\frac{R_2}{r_1}\right)^J - \left(\frac{R_2}{r_2}\right)^J\right] \qquad (1C)$$

For the special case of a thin toroid, where $r_2 - r_1 << R_1$, these three expressions simplify to give those which were

reported earlier [12-13]. Nonuniformly wound coils are also sensitive to other currents which may be located outside of the aperture so it is necessary to shield the coils to limit the effects of this interference.

We have previously reported simulations which show that a group of sinusoidally-wound toroidal coils may be used to approximate the transverse distribution of the current that passes through their common aperture [12], or the current and position of one or two filaments [13]. This may be understood because Eqs. (1A), (1B), and (1C) show that the voltage measurements are related to the distribution of the current through orthogonal sine and cosine functions of the azimuthal angle θ, as well as radial functions which are unique for each coil in the group.

EXPERIMENTAL COILS

Three different coils have been fabricated for laboratory measurements; a 300 turn coil with a uniform winding, a 268 turn coil with a turn density proportional to sin(θ), and a 264 turn coil with a turn density proportional to sin(2θ). Each coil was wound on a toroidal form with the dimensions $r_1 = 4.0$ cm, $r_2 = 12.0$ cm, and $h = 8.0$ cm.

The coil forms were prepared by rapid prototyping through stereo lithography (SLA) in which 0.10 mm thick layers of DMX-SL100 resin (similar to ABS plastic) are deposited with a specified tolerance of 0.050 mm. Data files were prepared to define the location and shape for grooves to hold the wire, but the tolerance was not met on the vertical faces of the coil forms where the minimum center-to-center spacing of the wires is as small as 0.60 mm. Thus, it was necessary to prepare inserts for the inner and outer vertical faces of the coil forms.

Each coil was wound from a single piece of wire with no splices, by passing a spool through the aperture. The coils were made of No. 30 tin-plated copper wire (O.D. = 0.254 mm) to provide some additional rigidity for the small wire and also simplify connections to the coil. The total resistance of each coil is approximately 30 Ω. Kapton tape was used to hold the coil in each groove.

Each toroidal form was made in two parts, with a groove for an additional turn that passes along the center of the tube of the toroid. This turn is connected in series with the toroidal coil as a compensating turn to correct for the effects of the single turn that the coil itself makes in the toroidal winding [8]. Figure 2 is a design drawing that shows the bottom half of the coil form, including the groove which holds the compensating turn.

Each coil has a metal shield to limit interference by currents that may be outside of the aperture as well as electric fields. Figure 3 is a design drawing that shows the coil with a uniform winding, including the plastic ribs on the coil form which are used to hold the coil in place within the shield. Figure 4 is a design drawing showing the shield, in which the top and base were machined from a single piece of aluminum. The two halves are in electrical contact at the outer surface, but there is a circumferential gap on the inner surface to allow the coil to be sensitive to the effects of currents that are within the aperture. All of the construction of each current probe is non-ferrous.

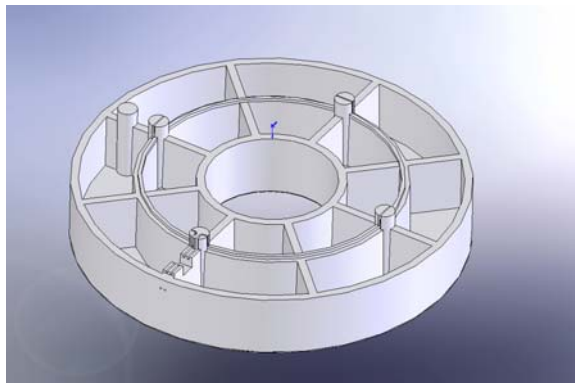

Fig. 2. Design drawing showing the inside of the bottom half of the coil form.

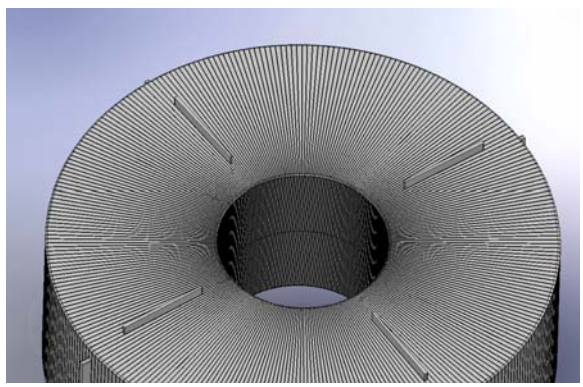

Fig. 3. Design drawing showing the coil with a uniform winding, including the ribs which secure the coil.

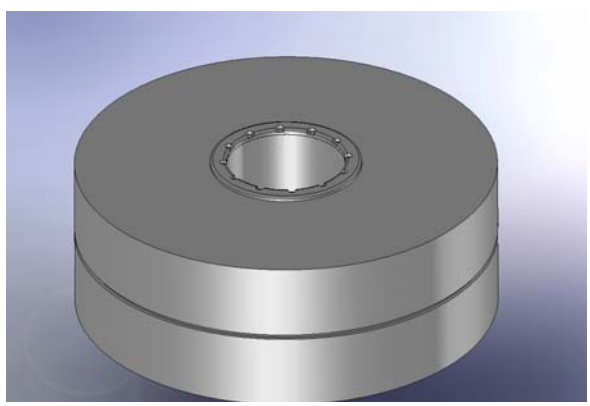

Fig. 4. Design drawing showing a coil with a shield.

The precision of the winding on these coils, which have been prepared by rapid prototyping supplemented by machined inserts, is approximately 0.02 cm, and we are prepared to make the next generation of coils, which will have a precision of 0.001 cm, by using an engraving tool with the 4th axis of a vertical milling machine. A test fixture has been prepared which will enable highly accurate measurements to be made in order to determine

the precision that is required for the coils to be used for determining the transverse distribution of the current that passes through their common aperture.

DESCRIPTION OF TEST FIXTURE

A Rogowski coil is generally calibrated by placing it in a metal box and passing a wire with a known current through the aperture. However, the box must be much larger than the coil and the box must also be much smaller than the wavelength to prevent higher modes. In order to simplify the calibration and make it possible to use higher frequencies we have generally used the metal shield for the coil as the outer conductor to form a coaxial calibration cell [6]. Metal plates cover the top and base of the shield, and coaxial connectors in these plates are connected to a metal cylinder which serves as the inner conductor of the cell. The ratio of the inner radius of the shield to the radius of the cylinder is equal to 2.30 so the coaxial calibration cell has a characteristic impedance of 50 Ω. A signal generator and a 50 Ω load are attached to the two coaxial connectors to complete the test circuit.

Figure 5 illustrates the concept for the precision test fixture which is used to calibrate and measure the position sensitivity for these coils. Two plates with coaxial connectors are used with a central cylinder to provide a coaxial calibration cell as was done earlier [6]. However, now two track systems are used to slide the current probe relative to the cylinder in order to scan the position of the current through the full area of the aperture. Two gauges are used to measure this movement along two axes to an accuracy of 0.001 inch (0.0254 mm).

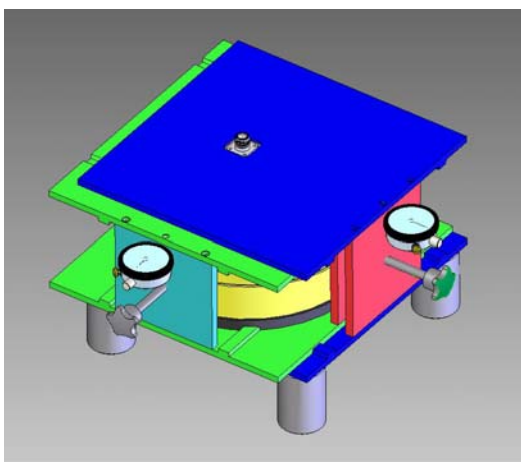

Fig. 5. Concept for the test fixture.

Figures 6 and 7 are photographs of the completed test fixture with one of the three shielded toroids. We have verified the accuracy of positioning with the test fixture and also determined that it has a low standing-wave ratio, and we believe that similar instruments would be useful to others for determining the position sensitivity of Rogowski coils as well as other types of current probes. However, measurements with our three current probes having uniform, sin(θ) and sin(2θ) turn densities are still in progress.

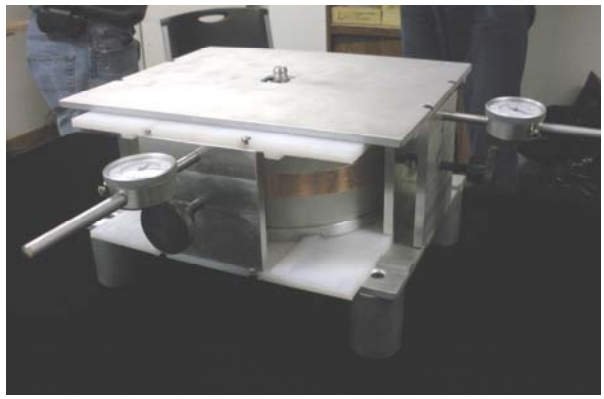

Fig. 6. First picture of the test fixture with a current probe.

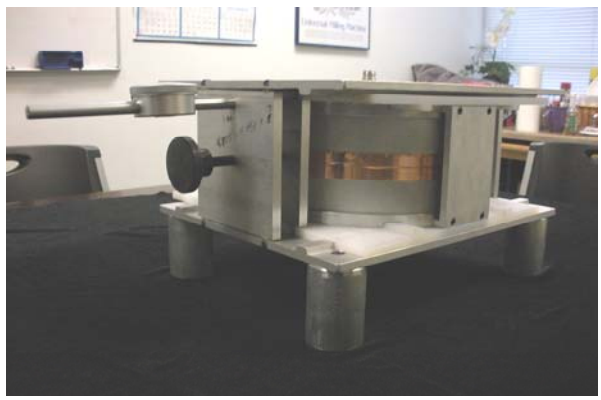

Fig. 7. Second picture of test fixture with a current probe.

SUMMARY AND CONCLUSIONS

- Exact closed-form expressions have been derived for the open-circuit voltage induced on a non-ferrous toroidal coil by a time-dependent current when the turn density of the coil varies sinusoidally as a function of the angle θ about the axis of the toroid.
- These expressions show that the voltages that are measured on a group of such coils are related to the distribution of the current through orthogonal sine and cosine functions of θ, as well as radial functions that are unique for each coil.
- Simulations show that it is possible to determine the traverse distribution of a current, or the current and position of one or two filaments, by this method.
- We have fabricated three different precision toroidal coils having turn densities that are uniform, and proportional to sin(θ) and sin(2θ), as well as a test fixture which can be used to determine the response of these coils to currents at precise locations within their apertures.

- We have verified the accuracy of positioning the current within the test fixture and also determined that this fixture has a low standing-wave ratio.

- Simulations suggest that the three coils have sufficient precision to enable determining the transverse distribution of a current, or the current and position of one or two filaments. Measurements with the three current probes are still in progress.

REFERENCES

[1] H. Koziol, "Beam diagnostics for accelerators," Proceedings of the CERN Accelerator School, Fifth General Accelerator Physics Course, ed. S. Turner (1992).

[2] V. A. Verzilov, "Spatial resolution in optical transition radiation beam diagnostics," Phys. Rev. Special Topics –Accelerators and Beams 1 (1998) 062801.

[3] J. A. Pasour and M. T. Ngo, "Nonperturbing electron beam probe to diagnose charged-particle beams," Rev. Sci. Instrum. 63 (1992) 3027-3039.

[4] W. Rogowski and W. Steinhaus, "Die messung der magnetischen spannung," Arch. Electrotech. 1 (1912) 141-150.

[5] A. G. Klein, "Demonstration of Ampere's circuital law using a Rogowski coil," Am. J. Phys. 43 (1975) 368-370.

[6] M. J. Hagmann and T. M. Babij, "Non-invasive measurement of current in the human body for electromagnetic dosimetry," IEEE Trans. Biomed. Eng. 40 (1993) 418-423.

[7] A. Andersson, D. Destefan, J.D. Ramboz, S. Weiss and J.M. DeHaan, "Unique EHV current probe for calibration and monitoring," IEEE/PS Transmission and Distribution Conference, Vol. 1 (2001) 379-384.

[8] J.D. Ramboz, "Machinable Rogowski coil, design, and calibration," IEEE Trans. Instrum. Meas. 45 (1996) 511-515.

[9] D. Berners and L. Reginato, "Beam position and total current monitor for heavy ion fusion beams," Accelerator Instrumentation Fourth Workshop, AIP Conference Proceedings No. 281 (1993) 168-174.

[10] P. Adderley, W. Barry, J. Heefner, P. Kloeppel, R. Rossmanith and M. Wise, "A beam position monitor for low current DC beams," Proceedings of the 1989 Particle Accelerator Conference (1989) 1602-1604.

[11] P. N. Murgatroyd and D. N. Woodland, "Geometrical properties of Rogowski sensors," IEE Colloquium on Low Frequency Power Measurement and Analysis 9 (1994) 1-10.

[12] M.J. Hagmann, "New method to monitor the transverse distribution of current in particle beams," Proceedings of the 13th Beam Instrumentation Workshop, F. Sannibale and J. Chew Eds., 2009, pp. 161-164.

[13] M.J. Hagmann, "New method to monitor the current and position of one or two particle beams," Proceedings of the 13th Beam Instrumentation Workshop, F. Sannibale and J. Chew Eds., 2009, pp. 165-167.

EMITTANCE MEASUREMENT WIZARD AT PITZ

A.Shapovalov(1) and L.Staykov(2), DESY, Zeuthen, Germany

Abstract

The Photo Injector Test Facility at DESY, Zeuthen site (PITZ) develops electron sources of high brightness beams, required for linac based free electron lasers (FELs) like FLASH or the European XFEL. One of the key issues in electron beam optimization is the minimization of the transverse emittance. The main method to measure emittance at PITZ is a single slit scan technique, implying local beam divergence measurement by insertion of the slit mask at a definite location within the beam and measurements of the transmitted beamlet profile downstream of the slit station. "Emittance Measurement Wizard" (EMWiz) is the program used by PITZ operators for automated emittance measurements. EMWiz combines an acquisition program for beam and beamlet image recording and a postprocessing tool for the analysis of the measured transverse phase space of the electron beam. It provides a way to execute the difficult emittance measurements in an automatic mode and to get a calculated emittance result.

INTRODUCTION

At the PITZ facility, the electron source optimization process is conducted. The goal is to reach the XFEL specifications of 0.9 mm mrad at a bunch charge of 1 nC. The research activities at PITZ include the production, optimization and characterization of electron sources with a small normalized projected transverse emittance. The transverse emittance is a key property of high brightness electron sources and the key value for the measurements at PITZ [1]. This task of emittance measuring is organized at PITZ through the emittance measurement wizard (EMWiz) software. This advanced high-level software application interacts through a Qt [2] graphical user interface with the DOOCS [3] and TINE [4] systems for machine control and ROOT [5] for data analysis and visualization. For communication with the video system and acquiring images from cameras at several screen stations, a set of video kernel libraries have been created [6]. In this paper, details about the Emittance Measurement System for both hardware and software parts are described.

shapovalov.mephi@yandex.ru
[1] On leave from NiYaU MEPhI, Moscow Russia

lazaraza@ifh.de
[2] On leave from INRNE, Sofia, Bulgaria

EMITTANCE MEASUREMENT HARDWARE

The transverse emittance and phase space distribution are measured at PITZ using the single slit scan technique [7, 8]. The Emittance Measurement SYstem (EMSY) consists of horizontal and vertical actuators with 10 and 50 μm slits masks and YAG/OTR screens for the beam size measurement. The slit mask angle can be precisely adjusted for the optimum angular acceptance of the system (Figure 1). Three EMSY stations are located in the current setup as shown in Figure 2. The first EMSY station (EMSY1) behind the exit of the booster cavity is used in the standard emittance measurement procedure. It is at 5.74 m downstream of the photocathode corresponding to the expected minimum emittance location. For this technique, the local divergence is estimated by transversely cutting the electron beam into thin slices. Then, the size of the beamlets created by the slits is measured at the YAG screen at some distance downstream the EMSY station. The 10 μm slit and a distance between the slit mask and the beamlet observation screen of 2.64 m are used in the standard emittance measurement. Stepper motors are applied to move each one of the four axes separately. They give the precise spatial positioning and orientation of the components. On each of the actuators, either a YAG or OTR screen is mounted to observe the beam distribution. A single and a multi slit masks are mounted consecutive to take samples from the transverse phase space of the electron beam. A CCD camera is used to observe the images on the screens (see Figure 1).

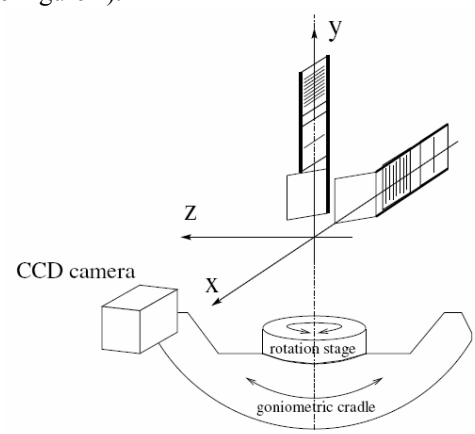

Figure 1: Layout of the Emittance Measurement System.

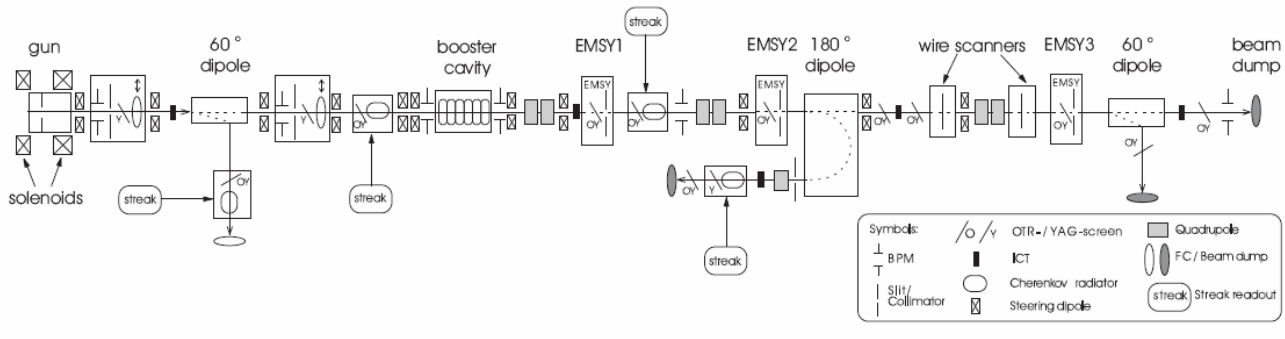

Figure 2: Layout of the Photo Injector Test facility at DESY, Zeuthen site (PITZ).

EMITTANCE MEASUREMENT ANALYSIS

A schematic representation of the single slit technique is shown in Figure 3. For this technique the local divergence is estimated by transversely cutting the electron beam into thin slices and measuring their size on a screen after propagation in a drift space. The so called 2D-scaled emittance is then calculated using the following definition [1]:

$$\varepsilon_n = \beta\gamma \frac{\sigma_x}{\sqrt{\langle x^2 \rangle}} \sqrt{\langle x^2 \rangle \cdot \langle x'^2 \rangle - \langle xx' \rangle^2} \qquad (1)$$

Here $\langle x^2 \rangle$ and $\langle x'^2 \rangle$ are the second central moments of the electron beam distribution in the trace phase space obtained from the slit scan, where $x' = p_x / p_z$ represents the angle of a single electron trajectory with respect to the whole beam trajectory. The RMS beam size is measured on an additional YAG screen at the position of the slit. The local divergence is obtained by analyzing the profiles of the beamlets produced from the slit at some distance downstream. There, the spatial distribution of the beamlets corresponds to the local divergence $\langle x'^2 \rangle_{local}$, which can be derived from the size of the beamlet using:

$$\sqrt{\langle x'^2 \rangle_{local}} = \frac{\sqrt{\langle x^2{}_b \rangle}}{L_d} \qquad (2)$$

Here $\sqrt{\langle x^2{}_b \rangle}$ is the RMS size of the beamlet on the screen after the distance L_d. The total uncorrelated divergence of the beam is estimated by a weighted average of several measurements of the local divergence $\langle x'^2 \rangle_i$ taken from different locations across the beam:

$$\langle x'^2 \rangle = \sum_{i=1}^{N} \omega_i \cdot \langle x'^2 \rangle_i \qquad (3)$$

Here weights ω_i are based on a ratio of pixel sum of the i[th] beamlet to the pixel sum of all beamlets. The Lorentz factor $\beta\gamma$ is measured using a dispersive section downstream of EMSY.

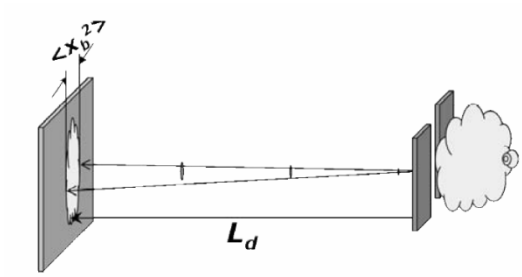

Figure 3: Schematic representation of the single slit scan technique.

The factor $\sigma_x / \sqrt{\langle x^2 \rangle}$ is applied to correct for possible sensitivity limitation of low intensity beamlets, where σ_x is the rms whole beam size measured at the slit location. In the emittance measurement setup and procedure, intrinsic cuts have been minimized by e.g. using highly sensitive screens, a 12 bit signal resolution CCD-camera and a large area of interest to cover the whole beam distribution. Therefore, emittance value is called 100% rms emittance. The measurement system was optimized to measure emittance as low as 1 mm mrad for 1 nC charge per bunch with precision about 10 %.

EMITTANCE MEASUREMENT WIZARD

This wizard is a multithread, multiprocessor, multiwindow application with user-friendly interface, flexible design which based on XML-config-file. It is created for 64 bits Scientific Linux CERN version 5.0.

Before using the wizard for measurement, the machine parameters have to be adjusted. Some necessary values, e.g. gun and booster energy, laser beam rms size are measured by other tools and put in the corresponding proper field of EMWiz. In principle the wizard is a set of tools and automatic procedures for emittance measurements, to collect experimental data and to analyze the data.

The video system at PITZ has 24 digital cameras with 8 and 12 effective bits per pixel and 7 video servers [6]. The video part (Figure 4) of EMWiz manages the cameras by reading properties, changing settings and connecting to a video server. The client makes it possible to get the video image, to apply filters, to grab and to save video images.

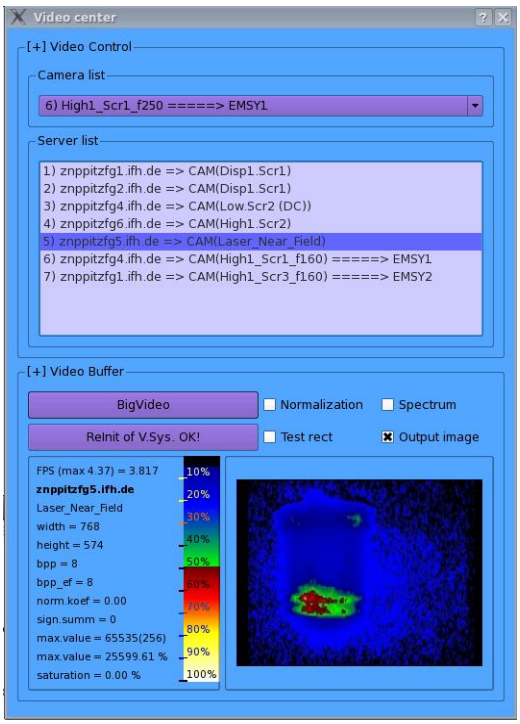

Figure 4: Video component of EMWiz.

Calculation of important values is going simultaneously with the drawing process. Control of saturation is one important criteria for obtaining good data quality. The calculated saturation parameter gives more reliable results than visual observation on the video image.

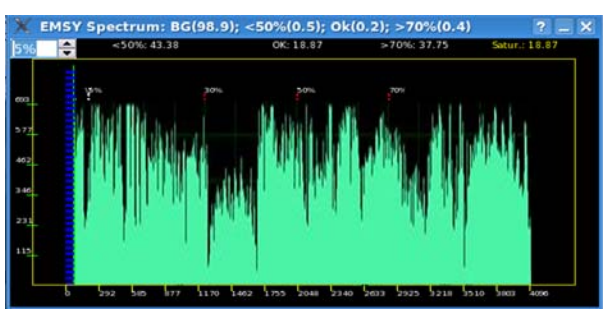

Figure 5: Spectrum tool.

Currently, the following instruments are available: spectrum, find best angle and prescan. The spectrum tool shows the number of pixels in the image with a given intensity (Figure 5). Major part of image pixels should have intensity between 50% and 70% of maximum intensity.

The tool “Find best angle” helps to find an optimum angle between the slit opening and the YAG screen in automatic mode. The total intensity signal depends on the angle between the slit opening and the beam axis. The maximum intensity is the desirable angular orientation.

The most complex tool is “PreScan”. It is a hands-off procedure for signal quality testing and finding the scan limits of emittance measurements. In the past an operator did all measurements manually and the human factor could strongly affect on the result. The PreScan tool moves the EMSY slit between some selected limits and collects sets of image frames from a chosen camera.

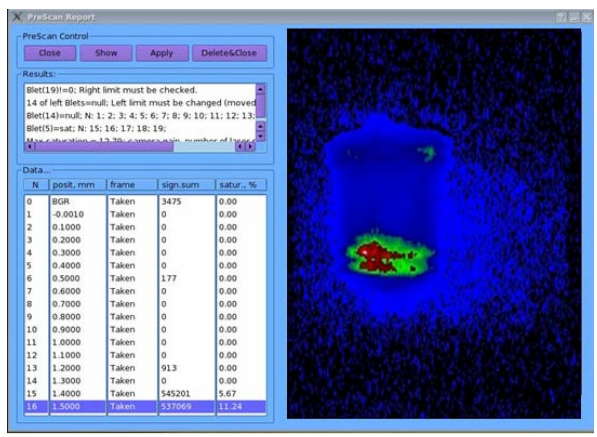

Figure 6: PreScan tool of EMWiz.

The next step is background frame collecting via controlling of the laser shutter. The wizard changes some parameters of the machine system and scan limits. In the final analysis, the tool generates a report with recommended settings for the EMWiz e.g. scan range, and the machine parameters (Figure 6). An operator has a choice to apply these settings or to make own corrections in difficult cases.

EMITTANCE MEASUREMENT PROCEDURE USING EMWIZ

At beginning, an operator chooses an EMSY station (EMSY1, EMSY2, EMSY3) and an axis (x or y axis) in the scan “Info center” panel (Figure 7). The step is the beamsize measurement at the slit and the beamlet observation screen locations using the YAG/OTR screen. The transverse beam images and background

frames at the slit location (EMSY) and at the beamlet screen (MOI) are recorded using the "Grab&Save" tool (Figure 8). These images are required for the emittance

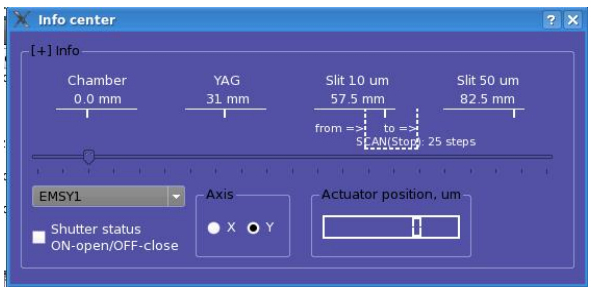

Figure 7: Scan info panel.

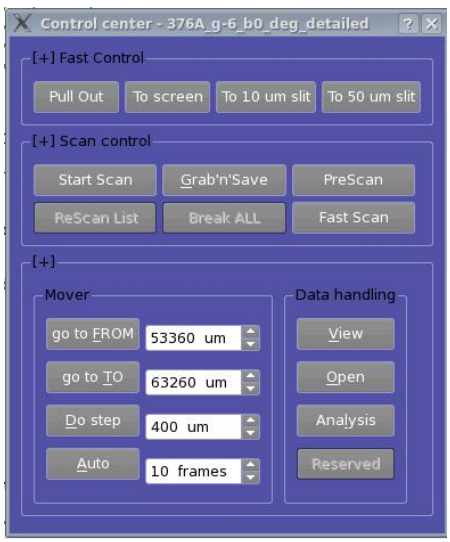

Figure 8: Scan & Grab control.

calculation using formula (1). Then, then beamlet scan procedure can be started. Presently, the algorithms are available:

a) The slit is moved through the beam within the scan limit and selected step (Figure 8). Video images and background frames are grabbed at each scan step. An operator changes the solenoid current and repeats the scan, including the procedure "PreScan". The measurement time for one given solenoid setting is about 30 minutes.

b) A new method "Fast Scan" improved the measurement time. This method was also implemented to EMWiz. Firstly, background statistics is collected. Next step, the slit is moved continuously with slow constant speed from the left to the right within the scan limit. At the same time, the selected CCD camera saves the image frames from the beamlet observation screen with fixed rate. The operator repeats the scan for all main solenoid current values of interest. The measurement time for one solenoid setting is about 20 seconds.

The process of data collection in EMWiz stores all machine parameters continuously and informs the operator about critical fluctuations of controlled parameters (Figure 9), which can influence the measurement reliability. The data is recorded with cross-reference to the number of the grabbed frame. That means the actuator position, RF-power and gun temperature are known for each video frame. This gives possibility to process and explore data with more precision. The list of the parameters can be changed via an XML-config file. This GUI is based on a config file and can be easily transformed with new demands.

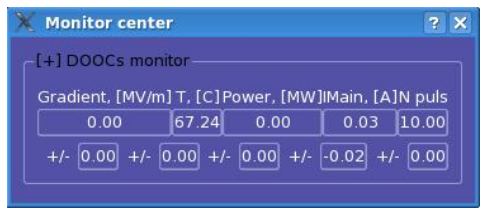

Figure 9: System monitoring.

The EMWiz has a black box feature. All actions of the operator to the program and machine, system status, error events and alarms with time-stamp are stored to a log-file. With help of an expert, one can open a hidden window (Figure 10), to support the shift crew remotely for fixing of a problem.

The last step in the measurement is to calculate the emittance using the "calculator" tool. The operator sets a folder with saved data, and then the tool checks the data in this folder and shows only good data sets. A lot of data processing is ongoing during calculation. Different filters, formulas etc. can be applied to the data.

A user can select plotting options for to plot all intermediate results after each complex process. At the end of the calculation the emittance plot is shown by default (Figure 11). For the plotting ROOT was integrated to EMWiz.

Currently, the wizard consists of separated programs for each logical task. Communication between program components is realized by a shared memory. This approach gives the possibility to use EMWiz components on different user stations with starting on one host. This increases graphics productivity and decreases the CPU loading. In the future it is planned to add network communication to give possibility for using parts of the wizard on different machines.

The PITZ facility is updated continuously and development of EMWiz is also ongoing. The work with EMWiz is going in the directions of complete automation of the measurement process, improving the quality of the experimental data and calculation

algorithms for taking into account changing machine parameters during the measurement.

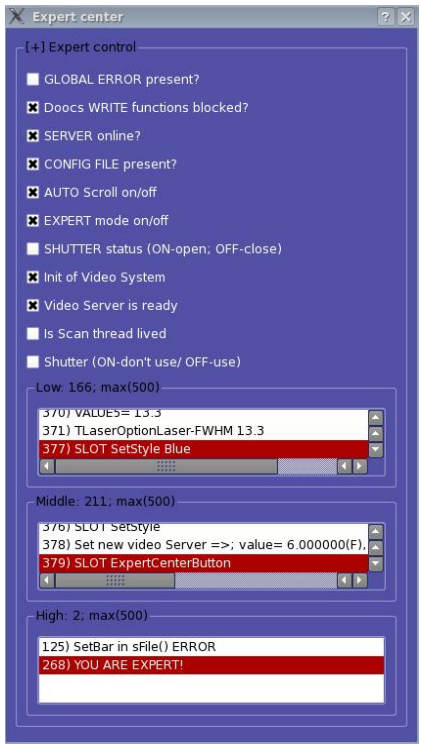

Figure 10: Expert window.

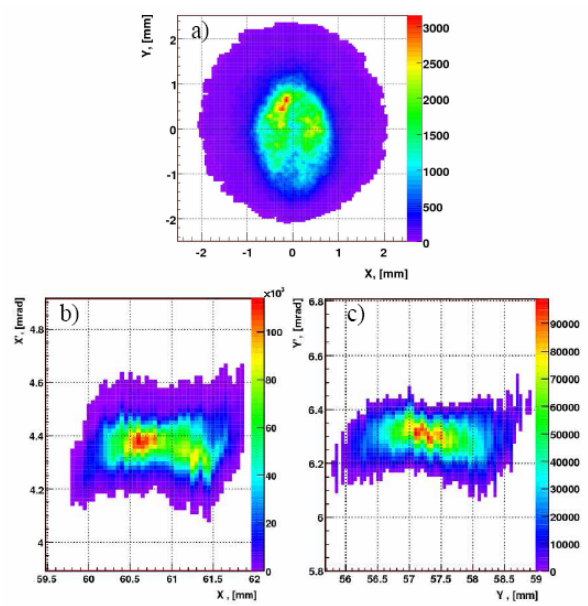

Figure 11: Transverse distribution (a), horizontal (b), and vertical (c) phase space for a give machine setup. The measured maximum mean longitudinal momentum of the beam for this point was 6.61 MeV/c after the gun acceleration and 14.6 MeV/c after the booster acceleration [1].

CONCLUSIONS

The Emittance Measurement Wizard (EMWiz), a semiautomatic emittance measurement client application. It strongly interfaces with the machine control and video system. EMWiz is one of the main measurement tools at PITZ. With the help of this program, the final emittance value can be measured much faster, more reliable, less attention requirement and user-interaction by operators. This is a big step forward in comparison to the emittance measurement solutions which have been used before. The majority of wizard components are universal and can be used for others tasks, not only for emittance measurement. Further development of this wizard will give new features for automatic data collection and analysis, which will result in decreasing of measurement time and increasing of measurement quality.

REFERENCES

[1] S. Rimjaem et al., “Recent emittance measurement results for the upgraded PITZ facility”, Proceedings of FEL09, Liverpool, UK.

[2] http://qt.nokia.com

[3] http://tesla.desy.de/doocs/doocs.html

[4] http://adweb.desy.de/mcs/tine/

[5] http://root.cern.ch/drupal/

[6] Stefan Weisse et al., “TINE video system: proceedings on redesign”. Proceedings of ICALEPCS 2009, Kobe, Japan.

[7] L. Staykov et al., Proceeding of the 29th International FEL Conference, Novosibirsk, Russia, 2007, MOPPH055, p. 138.

[8] F. Stephan, C.H. Boulware, M. Krasilnikov, J. Bahr et al.,“Detailed characterization of electron sources at PITZ yielding first demonstration of European X-ray Free-Electron Laser beam quality”, Phy. Rev. St Accel. Beams 13, 020704 (2010)

COMPARISON OF EXTRACTION AND BEAM TRANSPORT SIMULATIONS WITH EMITTANCE MEASUREMENTS FROM THE ECR ION SOURCE VENUS*

D. Winklehner#, D. Todd, LBNL, Berkeley, CA 94704, USA
D. Grote, LLNL, Livermore, CA 94551, USA
D. Leitner, J. Benitez, M. Strohmeier, LBNL, Berkeley, CA 94704, USA
F. Aumayr, Vienna University of Technology, Vienna, Austria

Abstract

The versatility of ECR (Electron Cyclotron Resonance) ion sources makes them the injector of choice for many heavy ion accelerators. However, the design of the LEBT (Low Energy Beam Transport) systems for these devices is challenging, because it has to be matched for a wide variety of ions. In addition, due to the magnetic confinement fields, the ion density distribution across the extraction aperture is inhomogeneous and charge state dependent. In addition, the ion beam is extracted from a region of high axial magnetic field, which adds a rotational component to the beam. In this paper the development of a simulation model (in particular the initial conditions at the extraction aperture) for ECR ion source beams is described. Extraction from the plasma and transport through the beam line are then simulated with the particle-in-cell code WARP. Simulations of the multispecies beam containing Uranium ions of charge state 18+ to 42+ and oxygen ions extracted from the VENUS ECR ion source are presented and compared to experimentally obtained emittance values.

INTRODUCTION

The superconducting Versatile ECR ion source for NUclear Science (VENUS) [1, 2], was developed as the prototype injector for the Facility for Rare Isotope Beams (FRIB) and as injector ion source for the 88-Inch Cyclotron at Lawrence Berkeley National Laboratory [3, 4]. Like most ECR ion sources VENUS operates in a minimum B field configuration which means that a magnetic sextupolar field for radial confinement is superimposed with a magnetic mirror field for axial confinement. Consequently:

- Ions are extracted out of a region with high axial magnetic field (in VENUS typically 2 T) which then continuously decreases as the ions move along in axial direction, adding a rotational component to the beam.
- Due to the sextupolar field, the total magnetic field inside the source is not rotationally symmetric and thus the spatial distribution of ions at extraction resembles a triangle rather than a circle. This is also confirmed by beam imaging of single- or few-species ion beams (e.g. Figure 1) [4].

Furthermore, the extracted beam often consists of more than 30 different ion species with different mass-to-charge ratios which makes modeling even more complicated. At the moment, several groups are developing versatile extraction codes that are able to handle the complex initial conditions presented by ECR ion source plasmas. The main goals are:

- To better understand the underlying plasma physics that leads to these initial conditions.
- To create a design tool for future ECR injection systems.

The work described here represents the current status of a long-term effort to create a highly adaptable, advanced simulation code utilizing the well-established PIC (particle-in-cell) code WARP [5].

Figure 1: Tantalum imaging of a triangular He^+ beam, 80 cm after extraction [4].

Many of the issues regarding the extraction simulation and the beam transport through the beam line have been addressed in earlier work by D. Todd et al. [4, 6] and will be reviewed briefly in the following sections respectively. Results of a Uranium beam simulation using an improved way to obtain the initial conditions will then be presented and compared to emittance measurements.

SIMULATIONS

The simulation of a multispecies ion beam from plasma extraction to the position of the diagnostics box can be divided into three separate simulations (see Figure 2), each employing different simulation methods which are discussed in the following subsections.

* This research was conducted at LBNL and was supported by the U.S. Department of Energy under Contract DE-AC02-05CH11231.
# dwinklehner@lbl.gov

Initial Conditions

(See Figure 2, region I: Inside the plasma) The initial particle spatial- and velocity-distributions of each species on the plasma side of the extraction simulation are a vital part of any extraction simulation. These initial conditions are not known for ECR plasmas and are subject to debate. Different approaches exist, including:

- Considering effects within the plasma such as negative potentials forming along the axis which would increase the density of highly charged ions near the axis [7, 8]
- Requiring the ions to be created at points inside the source which a.) exhibit higher or equal magnetic flux density than the extraction region and are b.) connected to the aperture via a field line, along which the ions can travel [9].

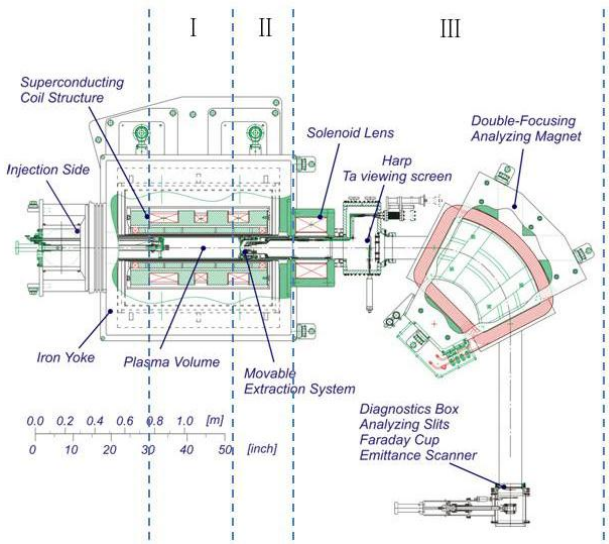

Figure 2: Layout of VENUS and its beam transport system. Initial conditions, extraction simulation and beam line transport correspond to regions I, II and III respectively.

For this work, a semi-empirical approach was taken: VENUS, similar to most ECR ion sources, operates with a negatively biased metal plate (biased disk) on the injection side of the source to enhance the flux of low energy electrons into the plasma. The biased disk is kept at a voltage of -50 V to -100 , thus providing the ions with enough kinetic energy to sputter the surface. As seen in Figure 3, upper left, this disk exhibits two kinds of sputter-marks:

- A large triangular discoloration: Plasma marks which match the magnetic field lines crossing the ECR resonance zone.
- A smaller triangle of about 4 mm height that is etched deeply into the disk and seems to have sharp edges.

The same discoloration can be found on the extraction plate (see Figure 3, upper right) and seeing how the smaller, brighter triangle on the extraction plate fills the extraction aperture completely, one could presume that ions are extracted evenly distributed over the whole surface of the aperture. This, however, contradicts the triangular beam cross-section image seen in Figure 1 as well as emittance measurements indicating that higher charge states are emitted from a "virtual" extraction aperture of smaller size than the actual one [10]. Clearly, requiring ions to be created on the ECR resonance surface and following field lines to the extraction aperture alone is not enough.

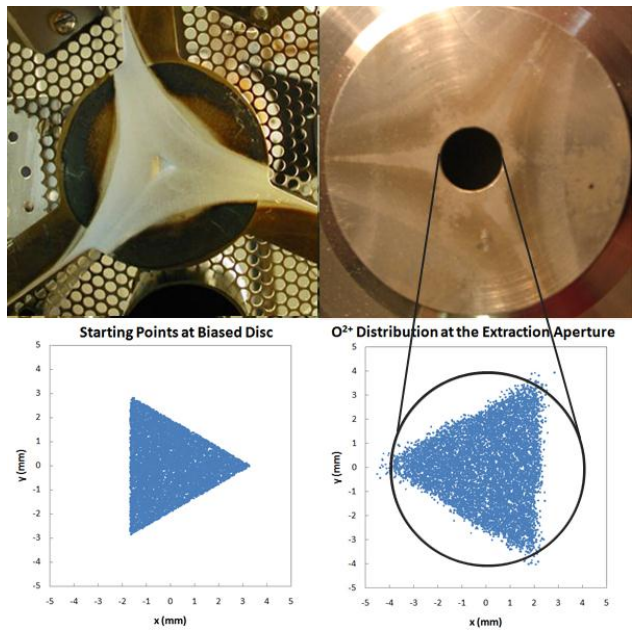

Figure 3: Sputter marks on biased disk (upper left), marks on extraction aperture (upper right), initial particle distribution on biased disk matching sputter marks (lower left) and particle spatial distribution after tracking through the source, shortly before extraction aperture (lower right).

So the small sputtered triangle on the biased disk was examined further. The small triangle's depth and sharp edges indicate a higher ion density near the axis and also give rise to the assumption that "collisions which cause radial diffusion must be a secondary effect between the resonance zone and the biased disk" [6]. Because the ions are cold (a few eV) resulting in small Larmor radii it is reasonable to assume that they mainly follow the magnetic field lines. In addition, there is no reason why the direction towards the biased disk should be preferred, thus it can be argued that a similar ion beam distribution can be found on the extraction side of the source.

The initial (and direct) approach for producing the starting conditions for the sheath extraction simulation was the following: Ions are randomly distributed on a triangle corresponding to the sputtered triangle and given a random velocity corresponding to a Boltzmann distribution with a peak temperature of 2 eV. Subsequently, these ions are tracked through the magnetic field of the source to the extraction aperture by means of a Leapfrog algorithm. Collisions are neglected assuming low plasma

density and small Larmor radii. However, obtaining a statistically relevant number of ~10000 ions per species (~30) is a very time-consuming process and so an alternative (faster) method has been developed.

In this alternate method, particles are still initialized the same way, but instead of tracking them through the source, each particle's respective gyro-motion guiding-centre is calculated and only the field-line originating at that point is tracked through the source. At the respective end-point, an appropriately scaled Larmor radius is applied and the particle is put on a random point on a circle with this scaled radius around the guiding-centre. Because travelling through the source's magnetic field leads to a shift from the ion's transversal velocity to the longitudinal velocity component, velocities are recalculated from the scaled Larmor-radius in the end. As an example, starting points at the biased disk as well as the derived (spatial) initial conditions at the extraction aperture for O^{2+} can be seen in the lower part of Figure 3. Testing both methods against each other with selected ion species showed very good agreement.

One of the limitations of this model for the initial conditions at the plasma interface is that it assumes the same initial spatial distribution of the ions at the bias disk for all charge states. As this assumption might not be valid for the highest charge states the model might need further refinement.

Extraction Simulation

(See Figure 2, region II: The extraction system) WARP includes both a two-dimensional, axially symmetric plasma sheath extraction model similar to IGUN [11] and a three-dimensional sheath extraction model comparable to KOBRA [12]. In order to allow for sufficient resolution at the plasma sheath while keeping the simulation time reasonable, the following two-step approach has been taken:

1. An axially symmetric beam with the same species parameters, currents and energies as the triangular beam is extracted using the two-dimensional model. The beam is tracked through the simulation several times, until a relaxation of the combined potential of applied fields and self-fields has been reached.
2. The obtained potential is stored and used as an applied field in the second step, where the beam is initialized with the obtained triangular particle distributions and the simulation is run in three-dimensional mode.

Previous tests against a full 3D simulation have confirmed the validity of this approach [4].

Beam line Transport Simulation

(See Figure 2, region III: The beam line) Since the longitudinal velocity in the remaining beam line is much higher than the transverse, a two-dimensional Poisson solver can be used to simulate the beam line transport (slice mode). The longitudinal self-fields are neglected but the motion through the three dimensional analyzing magnet fields is simulated [4].

The beam-influencing components in the beam transport simulation are (see Figure 2):

- The solenoid field of the source
- The solenoid lens
- The dipole analyzing magnet

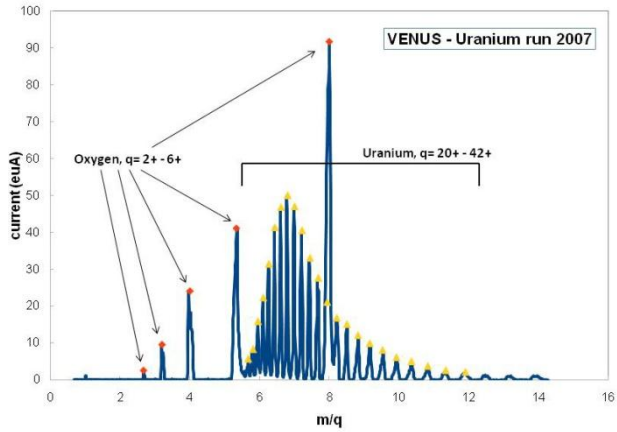

Figure 4: Spectrum of a Uranium beam from VENUS used for the initial species and current distribution in the extraction simulation.

RESULTS

One of the most important beams for FRIB are high intensity medium charge state uranium beams [13]. Uranium beam data from VENUS is thus available and benchmarking this data against simulations is of particular interest. This simulation was run with 28 different ion species, namely Oxygen (as support gas) with charge states 2+ to 6+ and Uranium with charge states 20+ to 42+. The species distribution and respective currents in eμA were obtained from the VENUS spectrum which was optimized for U^{35+} as shown in Figure 4. The key initial parameters of the simulation are listed in Table 1. While source and puller voltages, drain current and magnetic fields are known, the other parameters have to be chosen due to the theoretical model of ECR plasmas. Choosing these initial parameters differently can change the simulation and will have to be studied in more detail. The total drain current of 1 mA (as opposed to the measured beam drain current of 1.6 mA) was chosen due to its rather good plasma meniscus and reasonable simulation time and is believed to be close enough to the real current to do a cautious comparison of the results.

Table 1: Initial simulation parameters (E_{kin} is added to the longitudinal Temperature in order to account for pre-sheath acceleration and the current distribution from the spectrum is normalized to the total drain current)

Parameter	Value
Ion mean Temperature	2 eV
Uranium E_{kin} (longitudinal)	~3 eV
Electron Temperature (in sheath)	5 eV
Source Voltage	20 kV
Puller Voltage	-2 kV
Total drain current	1 mA
Max. mag. flux density at extraction	2.1 T

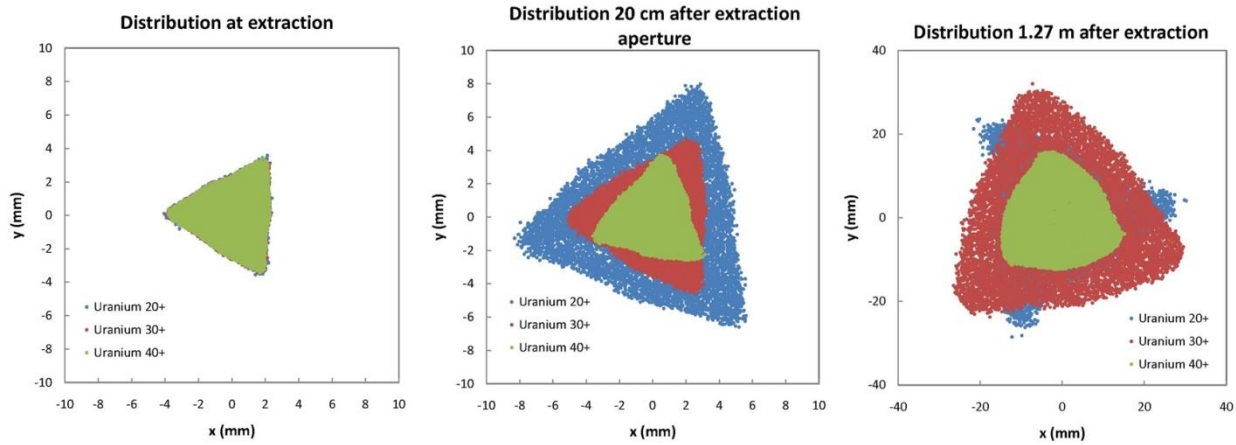

Figure 5: Spatial distributions for U^{20+}, U^{30+} and U^{40+} at the extraction aperture (left), 20 cm after (middle) and 127 cm after (right). Note the different scale for x and y in the last plot, this is the z-position right before the analyzing magnet (the third simulation was done with a neutralization of 70% and the focusing magnet was set for U^{36+}, hence the over-focusing of U^{20+}).

Results from Simulations

The influence of the source solenoid on the extraction end can be seen in Figure 5. The spatial distributions of three different charge states of Uranium (q = 20+, 30+ and 40+) are plotted before extraction and 20 cm after the extraction aperture (where the particles are handed over to the beam line transport simulation) as well as shortly before the dipole magnet. A noticeable difference in rotation and focusing for different charge states can be seen. Emittances for U^{30+} to U^{40+}, both horizontal and vertical, are plotted in Figure 6 for different levels of neutralization due to rest gas ionization in the beam line (0%, 70%, 80% and 90%). Surprisingly it was experimentally observed that although the beam is not pulsed, the extracted ion beams are not fully neutralized [14]. Therefore different neutralization levels were tested in the model.

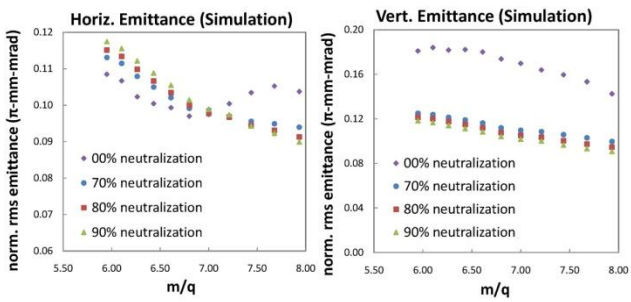

Figure 6: Comparison of horizontal and vertical emittances for U^{20+} to U^{40+} for different neutralization factors.

As expected, Figure 6 generally shows a decrease of emittance with increasing neutralization. The horizontal emittances show additional structures which can't be explained at this moment and will be further investigated.

Comparison to emittance measurements.

The experimental data were taken with Allison type emittance scanners [15] at the position labeled "Diagnostics Box", seen in Figure 2. Figure 7 shows a comparison of U^{36+} phase space plots between experiment and simulation. Though there is no 1:1 resemblance, certain features (like the region of maximum beam current) seem to be reproduced by the simulations and the overall size of the phase space plots is in good agreement.

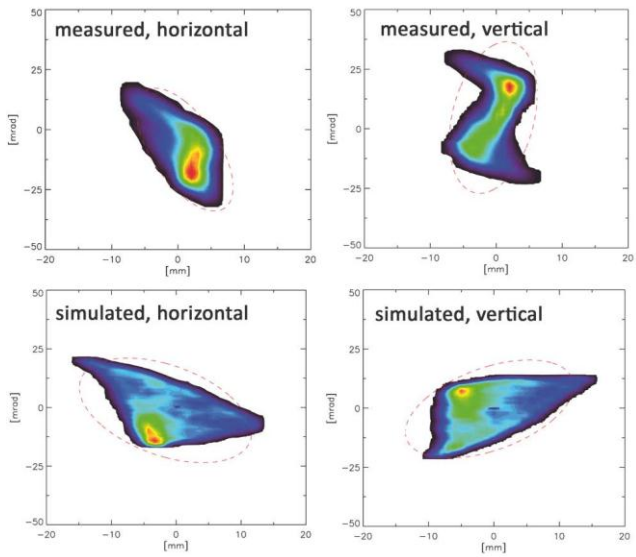

Figure 7: Comparison of U^{36+} phase space plots 3.3 m after extraction and after the analyzing magnet (position of the diagnostics box). The simulation was done with 70% neutralization and optimal focusing for U^{36+}.

Figure 8 shows horizontal and vertical emittances from the simulation compared to measurements. The trend of increasing emittance for decreasing m/q is clearly seen in both simulation and measurement. The overall higher emittances in simulation can be attributed to slightly off initial assumptions about e.g. ion temperature, electron temperature or the radial density distribution of the ions.

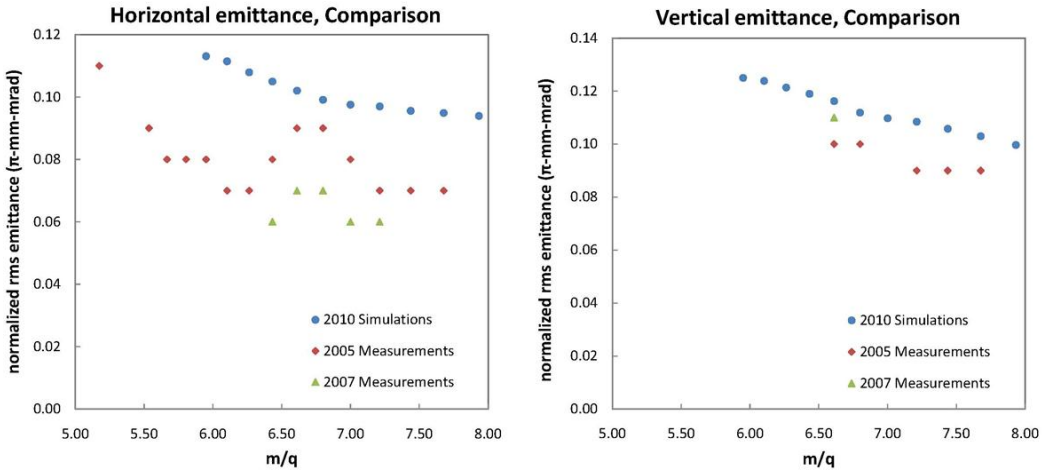

Figure 8: Comparison of emittances for U^{30+} to U^{43+} obtained by simulations and by experiment. Simulations were run with 70% neutralization.

CONCLUSION

The status of the efforts to create an adaptable simulation code for beam extraction from an ECR ion source using WARP has been presented. It is now possible to simulate multispecies beams with more realistic initial particle distributions and a high number of species in 3D mode with a high grid resolution. Emittance values are reproduced within reasonable margins by the simulations. Future work will aim to better understand the physics leading to the initial conditions and beam neutralization.

ACKNOWLEDGEMENTS

This work was supported by the Director, Office for Energy Research, Office of High Energy and Nuclear Physics, Nuclear Physics Division of the U.S. Department of Energy under Contract DE-AC02-05CH11231.

REFERENCES

[1] C.M. Lyneis et al., New results with the superconducting ECR Ion Source VENUS, Review of Scientific Instruments **75** (2004).

[2] D. Leitner et al., Next generation ECR ion sources: First results of the superconducting 28 GHz ECRIS - VENUS, Nuclear Instruments and Methods in Physics Research Section B **235**, 486 (2005).

[3] R.C. Pardo et al., Heavy-Ion Beams Required for the RIA Accelerator, Review of Scientific Instruments **75**, 1427 (2004).

[4] D.S. Todd et al., Comparison of particle-in-cell simulation with experiment for the transport system of the superconducting electron cyclotron resonance ion source VENUS, Review of Scientific Instruments **77** (2006).

[5] David P. Grote et al., The WARP Code: Modeling High Intensity Ion Beams, in 16th Intern. Workshop on ECR Ion Sources, edited by M. Leitner (AIP, Berkeley, CA, 2004).

[6] D.S. Todd et al., Simulation and beamline experiments for the superconducting electron cyclotron resonance ion source VENUS (AIP, 2008), p. 02A316.

[7] M. Cavenago et al., Model of accumulation, multi-ionization, and extraction of ions in ECR ion sources (AIP, 2002), pp. 537.

[8] T. Thuillier et al., High current beam transport with Phoenix 28 GHz: experiment and simulation, in 16th International Workshop on ECR Ion Sources, edited by M. Leitner (AIP Conference Proceedings, Berkeley, CA, 2004), pp. 41.

[9] P. Spädtke et al., Prospects of ion beam extraction and transport simulations (invited), Review of Scientific Instruments **79**, 02B716 (2008).

[10] M. A. Leitner, D. C. Wutte, and C. M. Lyneis, Design Of The extraction system of the Superconducting ECR Ion Source VENUS, in Particle Accelerator Conference (PAC'01) (The American Physical Society, IEEE, Chicago, 2001).

[11] R. Becker, and W. B. Herrmannsfeldt, Igun - A program for the simulation of positive ion extraction including magnetic fields (AIP, 1992), pp. 2756.

[12] INP, KOBRA3-INP (INP, Junkernstr. 99, 65205 Wiesbaden, Germany.

[13] D. Leitner et al., High intensity production of high and medium charge state uranium and other heavy ion beams with VENUS, (AIP, 2008), p. 02C710.

[14] D.S. Todd, D .Leitner, and M. Strohmeier, Low Energy Beam Diagnostics at the VENUS ECR Ion Source, in BIW 2008 (Tahoe City, CA, 2008).

[15] P.W. Allison, J.D. Sherman, and D.B. Holtkamp, An Emittance Scanner for Intense Low-Energy Ion Beams, IEEE Transactions on Nuclear Science **NS-30** (1983).

ESTIMATION OF PROFILE WIDTH IN HYBRID ION BEAM TOMOGRAPHY

H.Reichau*, O. Meusel, U. Ratzinger, C. Wagner, IAP, JWG University, Frankfurt, Germany

Abstract

In beam diagnostics, optical techniques had become increasingly important as they provide information with the advantage of minimal effect on the beam. The planned Frankfurt Neutron Source will consist of a proton driver linac providing beam energies up to 2.0 MeV. The rotatable diagnosis tank hybrid ion beam tomography tank HIBTT will be placed at the end of the low energy beam transport section (LEBT) to provide beam tomography based on the visible radiation of the ion beam in front of the RFQ. The beam energy in this section will be 120 keV and the current 200 mA. Additional to the CCD camera that takes optical data for the tomography, other non-interceptive devices could be used to gain additional information. The question behind this hybrid approach to non invasive beam diagnostics is: what and how much information can be extracted from an ion beam without disturbing or destroying it? The actual contribution deals with the information of profile width in beam profile measurements. The presentation introduces a definition and an information sensitive method for profile width determination and verifies them using experimental and numerical data.

INTRODUCTION

Beam diagnosis systems that provide knowledge about beam properties and behavior of an ion beam serve as a source of potential controllability through attained information. What one could actually learn about an ion beam, or rather, which and how much information can be extracted from it without disturbing or destroying it, essentially influences the extent of possible control over the beam. Based on a theory of information, an extended diagnosis pipeline was derived that forms the basis for a beam diagnostic system for HIBT (hybrid ion beam tomography), consisting of a flexible measurement device and an associated, modular software agent. The hardware device is the hybrid ion beam tomography tank (HIBTT) that was developed to serve as a multi-measurement device (Figure 1). It consists of a rotatable vacuum chamber with four 100 mm adapter flanges sthat everal non-invasive measuring equipment could be plugged into. HIBTT rotates within a maximum angle of 270 degrees in $>$5000 steps of angle encoding driven by a pecking motor and drive belts. The seal was constructed to resist vacuum pressures up to 10^{-7}mbar. Accordingly the software agent for data analysis has to be built in a modular manner. This permits analysis of data from several measurement devices without adjusting the basic structure. To analyze the measured data, an interface module for the software agent might be implemented if not contained in the default assembly. Furthermore, collective phenomena that arise from intense beams or non neutral plasma can be identified. In the first section of this contribution a suitable theory of information for beam diagnostics will be introduced. The second section deals with an information sensitive approach to profile width in optical beam measurements by giving a general definition of profile width, an error estimation and a first algorithm that will be implemented and proved in relation to the introduced error estimation.

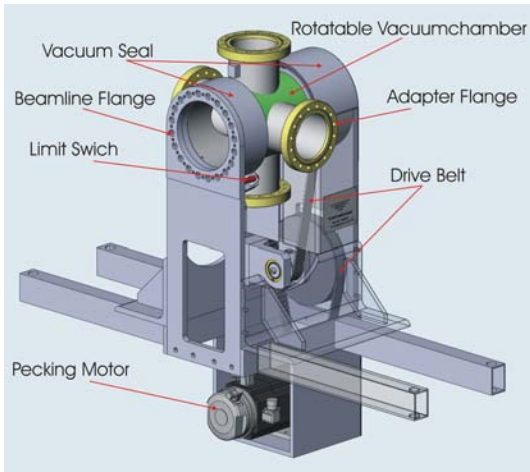

Figure 1: HIBTT is designed to serve as a multi measurement device for non- invasive beam diagnostics.

INFORMATION AND BEAM DIAGNOSTICS

Unfortunately no consistent theory of information in general exists, so one has to specify what has to be understood by the term *information* as the case arises. Consider a definition for beam diagnosis:

Let the term beam diagnosis be considered as ascertainment of distinctive properties called information for the evaluation of beam quality.

Then one has to point out the meaning of *information* in this context. In [1] three dimensions of information are introduced. The syntactical dimension of information, where the information theory of Shannon [2] resides, deals with relations between individual symbols, e.g., single particles or a beam in this case. Around this dimension lies the semantical dimension of information, which assigns a

* reichau@iap.uni-frankfurt.de

meaning to the relations taken from the first dimension. In this dimension information always arises between two reference layers, e.g. the information of emittance arises between the micro layer of n particles and the macro layer of a 6n-dimensional phase space. The syntactical dimension provides the necessary syntax in the form of Liouville's Theorem. The third dimension containing the previous two is the pragmatical dimension, which is the point of origin of the diagnosis, since it permits one to distinguish relevant data from non-relevant data in matters of a predefined aim or question. Based on this dimension a concept of data is needed, since the data basis is the source of information retrieval. A general definition of information (GDI) that comprises a proper definition of data and its correlation to information defines an instance of information σ as a semantic content, iff it consists of n data for $n \geq 1$, the data is well-formed in terms of a syntax in form of constraints that cluster data correctly, and the well-formed data is meaningful[3],[4]. That means the data must comply with the semantics of the system at hand.

The implementation of beam diagnosis in order to explore what information could be gained demands a careful acquisition and analysis of a large amount of data, out of which the distinctive properties could be mined. A multi-functional measurement device and information-sensitive algorithms are needed. Additionally a preferably precise definition of the information that has to be extracted. Otherwise one will meet with the dt-problem: achieving an answer that could not explicitly interpreted, since the underlying question is not unambiguously determined.

SENSITIVE INFORMATION MINING IN BEAM DIAGNOSTICS

With HIBT, established methods as well as new ideas of information mining shall be analyzed with regard to information acquisition. In a first approach data will be provided by a CCD camera, that was tested before on exposure behavior, noise, exposure time in relation to intensity, intensity in relation to residual gas composition and other inquiries to ensure a nearly all-over view on the data provided by this measurement device. Several optical methods for the determination of emittance use the parameter of profile width, e.g., [5],[6],[7]. The error propagation of this methods is seriously influenced by the exactness with that the profile width could be specified. For instance, the determination of emittance from beam profile measurements [7] evidences that an abberation of 1% from the exact profile width results in a maximal error in the range of 12 % - 14% for a determination of emittace out of three profile widths. An abberation of 5% even causes a maximal error of about 25% [6]. Therefore an exact determination of profile width is essencial for the accuracy of methods using optical beam profile measurements to determine the emittance.

Theoretical derivation

Initially a definition of profile width will be presented, that enables to define an error estimation for the exactness of a profile width.

Definition 1 (Isolumen)
Two lines $g_1^{I_l}, g_2^{I_l}$ with:

$$g_{1,2}^{I_l}(x) = m_{1,2}^{I_l} \cdot x + b_{1,2}^{I_l} \tag{1}$$

are called *isolumen* for intensity I_l, iff
$\forall p_x^{(0,0)}(x) \in g_1^{I_l}, g_2^{I_l}$:

$$min_P\{\overline{\overline{I_p^{(i,j)}(x) - I_l}}\} \tag{2}$$

where P is an optical beam measurement, e.g. a CCD camera picture, $p_x^{(0,0)}(x)$ a pixel at position (x,$g_{1,2}^{I_l}(x)$) of P, $I_p^{(0,0)}(x)$ is the intensity of pixel $p_x^{(0,0)}(x)$, N_r is the neighborhood of $p_x^{(0,0)}(x)$ of size r, such that:
$N_r =$

$$\begin{pmatrix} p_x^{(-r,-r)} & \cdots & p_x^{(-r,-0)} & \cdots & p_x^{(-r,r)} \\ \vdots & & \vdots & & \vdots \\ p_x^{(0,-r)} & \cdots & p_x^{(0,0)} & \cdots & p_x^{(0,-r)} \\ \vdots & & \vdots & & \vdots \\ p_x^{(r,-r)} & \cdots & p_x^{(r,0)} & \cdots & p_x^{(r,r)} \end{pmatrix} \tag{3}$$

$I_p^{(i,j)}(x)$ then is the intensity of $p_x^{(i,j)}(x)$ at position $(x + j, g_{1,2}^{I_l}(x) + i)$ for i,j = -r,...,0,...+r

Two lines thus are called isolumens for an intensity I_l, iff they fit in the area along an optical beam measurement P, where the mean overall distances between the mean intensity of the defined neighborhood and intensity I_l is minimal. Out of Definition 1 one could specify:

Definition 2 (profile width)
The profile width at position x $x_{prof}(x)$ for intensity I_l in an optical beam measurement P is defined as:

$$x_{prof}(x) := |g_1^{I_l}(x) - g_2^{I_l}(x)| \cdot \frac{l}{N} \tag{4}$$

where l is the width of P in [mm] N the width of P in pixel, and $g_{1,2}^{I_l}(x)$ are the vertical coordinate of the isolumen $g_{1,2}^{I_l}$ for I_l

Next, an error quantity will be introduced, that helps to compare isolumens found by different algorithms, to get a quality criterion relating to the exactness of profile width. For all algorithms that take a given optical measurement, size and quantification have to be the same in order to compare them. W.l.o.g the optical measurement is a picture from a CCD camera taken along the drift. Therefore only the distance between two isolumens could be consulted to

implement an error quantity for profile width viz. the error depends on the correctness with which the isolumens are determined. To proof how exactly an isolumen is determined, the deviation of the proximity of the line from the exact intensity value I_l has to be computed. The mean x_k over all $p_x^{(i,j)}$ and its aberration from I_l has to be considered:

$$x_k = \frac{1}{(2 \cdot r + 1)^2} \sum_{j=-r}^{r} \sum_{i=-r}^{r} I_p^{(i,j)}(x) \tag{5}$$

The error could then be determined by the root mean square error between all x_k and I_l as follows:

$$\chi = \sqrt{\frac{1}{N^2} \sum_{k=1}^{N} (x_k - I_l)^2} \tag{6}$$

IRF-Method for isolumen determination

In the following an information sensitive algorithm based on the previous considerations will be presented. By a simple smoothing of the whole data by filtering, e.g., with a Gaussian filter, inclosed information will be erased or blurred. Therefore an information sensitive filter will be introduced. The intensity range filter takes an intensity I_l and a confidence interval $\pm\Delta\kappa$ to separate relevant information. An overview of the IRF-Method is given in Figure 2.

The algorithm works as follows:
The input for the algorithm is a picture taken from a CCD camera, the desired intensity level I_l and $\Delta\kappa$

1. *Normalization:* The original picture P is normalized colum by colum to value 1. Therewith intensity levels I_l could be implemented as percentage values. Result of this step is P^1

2. *IRF:* all values that are not in the defined confidence interval will be set to zero:

   $$\{\forall p_x \in P^1 | I_l - \Delta\kappa > p_x \vee I_l + \Delta\kappa < p_x\} = 0 \tag{7}$$

   The result of this step is P^1_{IRF}.

3. *Divide:* The centroid line of P^1_{IRF} is computed. Along this line the picture is divided in two pictures $P^{1,T}_{IRF}$ and $P^{1,B}_{IRF}$, where in $P^{1,T}_{IRF}(P^{1,B}_{IRF})$ are all values under(over) the centroid line will be set to zero. With $P^{1,T}_{IRF}(P^{1,B}_{IRF})$ the top(bottom) isolumen is computed.

4. *Balance:* The intensity distribution within the intensity range will be balanced around I_l by their distance. As a consequence of this the distribution will be approximated to a Gaussian distribution. This balancing is done by:

   $$\forall I_p(x) \in P^{1,T/B}_{IRF} : I_p(x) = I_l - |I_p(x) - I_l| \tag{8}$$

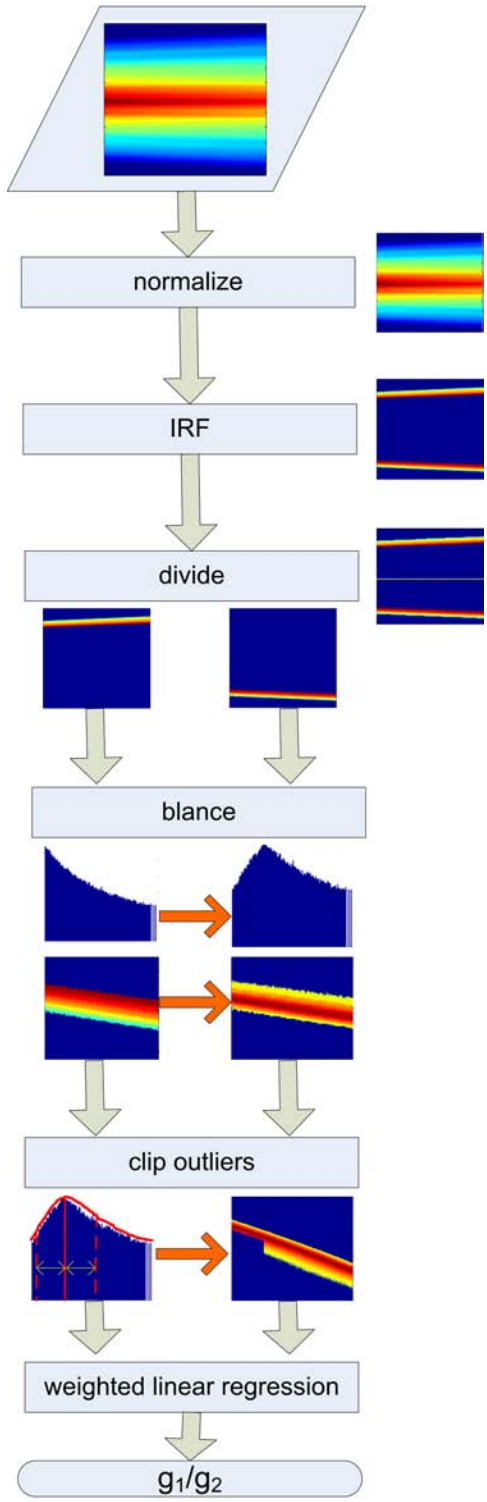

Figure 2: The IRF-method determines isolumens sensitive to information.

   The result of this step are the two pictures $P^{1,T}_{bal}$ and $P^{1,B}_{bal}$

5. *Clip outliers:* All relevant data for a proper determination of the desired information viz. all values

that are part of the chosen confidence interval are untouched up to now. If desired, one can skip to the next step. In case of a beam where single intensity points are widespread within the picture, outliers could adversely influence the determination of the isolumen. This might be the case within data with a bad signal to noise ratio. The accuracy of the isolumen also in this cases could be increased by clipping outliers. Therefore, in a defined window the expectancy μ of the position of intensities in the confidence interval and the standard deviation σ is computed. The vertical distribution then is clipped (Figure 3) with $n \cdot \sigma$ to both sides(top and bottom). The results of this step are $P_{cut}^{1,T}$ and $P_{cut}^{1,B}$

6. *weighted linear regression:* A weighted linear regression is performed on $P_{cut}^{1,T}$ and $P_{cut}^{1,B}$ to gain the isolumen $g_1^{I_l}$ and $g_2^{I_l}$.

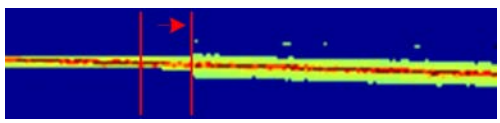

Figure 3: Clipping outliers in step 5 of the IRF-Method. Outliers are pixels with an intensity value that fits the chosen confidence interval but do not lie in the expected position for this intensity

Results and discussion of IRF-Method

The IRF-Method was performed on numerical computed pictures of different shapes as well as on a measured picture without noise reduction, to imitate a kind of worst case scenario. The measured picture is taken by a CCD camera in a test assembly, which was constructed to have the possibility of prior analysis, since HIBTT is under construction. Picture 10 shows a H^{1+} beam at a current of 20 keV, 1.3 mA and a residual gas pressure of about 10^{-5}mbar Intensities from 0.0 to 1.0 were tested in steps of 0.1 (Figure 4).

For picture 1 (Figure 5) and 2 the error constantly rises from 0% up to a maximum of 2%.

Concerning that with higher intensities the fluctuations within the beam are declining one might expect an oppositional behaviour, but the beam becomes more dense in direction to the beam axis; therefore single intensity levels close ranks, such that the neighbourhood around an isolumen has to be chosen to be very small. This effect is amplified in the next pictures, where the overall beam is densely focussed (Figure 6).

Additionaly numerical effects cause an irregular ascent in the direction of the beam-axis, which also disturbs neighborhood estimation. Pictures 8 (figure 7) and 9 show the same effects. Additionally, for intensity one an error peak of about 4 % was computed, which is not remarkable, since intensity level 1.0 is ambigious because of the already mentioned numerical effects, seen as dark lines (figure 8). .

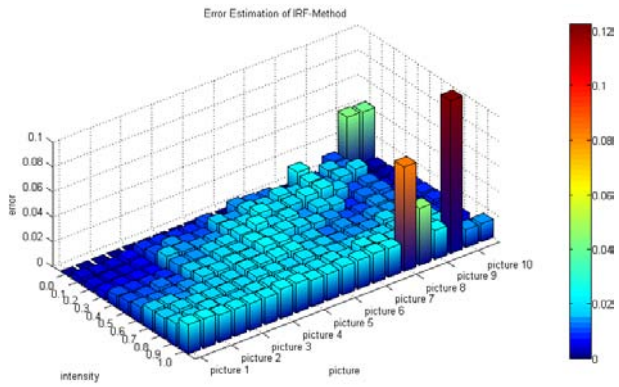

Figure 4: Error Estimation of the IRF-Method on nine numerical and one measured picture. For every picture the upper and the lower isolumens were computed and estimated with χ.

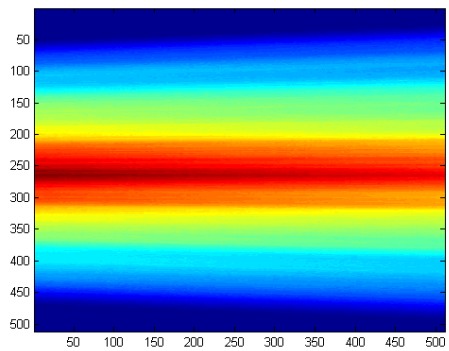

Figure 5: Picture 1 shows a slightly defocused beam that was computed numerically.

Picture 10 (CCD) first shows a significant difference within intensity level 0.0. This is caused by noise effects. The isolumen for 0.0 lies at the borders of the picture. Within the numerical pictures in this range all intensities are 0, so that the error at this level also is 0.0 for all pictures from 1 to 9. In picture 10 noise is spread to the edges of the whole picture and influences the error in this area. For intensity level 1.0 the error also rises but only to a maximum of about 1%. As one could see for intensities in the range of 0.1-0.9 the error is $>1\%$. The beam in picture 10 is free of numerical artifacts and shows a continously ascending intensity level. That is why intensities in the neighbourhood of an isolumen do not differ too much for reliable isolumens to be found.

EVALUATION

The IRF-Method determines isolumens with a good approximation as far as numerical effects as well as noise effects could be suppressed. To determine the profile width on the basis of isolumen one has to make sure, that always only two isolumen are determined for one intensity level.

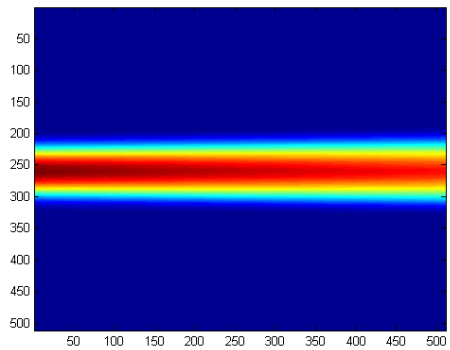

Figure 6: Picture 3 shows a highly focused beam that was computed numerically. Higher intensity levels are very dense.

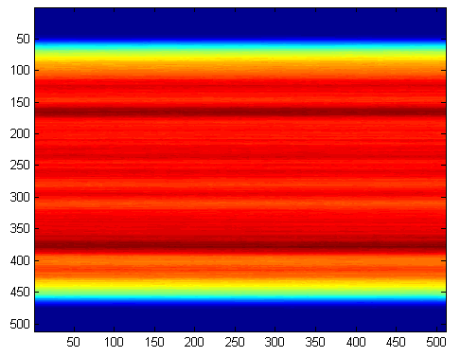

Figure 7: Picture 8 shows a strongly defocused beam that was computed numerically. Dark lines in the middle are numerical artifacts, which significantly could disturb the proper determination of isolumens, because unambiguousness gets lost.

Some other differences analysis have to be made, e.g., influence of unequal picture size, difference with noisy and filtered pictures. The error estimation provides a possibility of comparison for isolumens computed by different algorithms, but does not prove if the two isolumen are minimal for a picture, as is claimed in the definition for an isolumen. This constraint has to be ensured by the algorithms themselves.

REFERENCES

[1] B-O. Küppers, "Information and the Origin of Life," MIT Press, 1990.

[2] C.E. Shannon and W. Weaver, "The Mathematical Theory of Communication," University of Illinois Press , 1963.

[3] L. Floridi, "Philosophy and Computing," Routledge, London, 1999.

[4] J. Mingers, "The nature of information and its relationship to meaning," in I.R.Winder et al. (eds.), Philosophical Aspects of Information Systems, London, 1997.

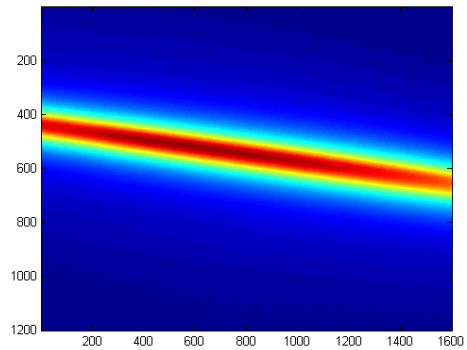

Figure 8: Picture 10 shows a H^{1+} beam, taken by a CCD camera.

[5] J. Pozimski, O. Meusel, A. Jakob, A. Lakatos, H. Klein, "Non destructive determination of beam emittance for low energy ion beams using CCD camera measurements. Proc. 7 th EPAC, 2000, Vienna, Austria,

[6] F. Sittinger, "Untersuchungen zu optischen Profil- und Emittanzmessungen an niederenergetischen intensiven Ionenstrahlen," Dissertation IAP, University of Frankfurt, Germany, 1995.

[7] P. Strehl, "Beam Instrumentation and Diagnostics," Springer, Berlin, 2006.

A LOW ENERGY ION BEAM PEPPER POT EMITTANCE DEVICE

M. Ripert, A.Buechel, A. Peters, J.Schreiner, T.Winkelmann, HIT, Heidelberg, Germany

Abstract

The transverse emittance of the ion beam at the Heidelberg Ion Therapy Center (HIT) will be measured within the Low Energy Beam Transport (LEBT) using a pepper-pot measurement system. At HIT, two ECR sources produce ions (H, He, C and O) at an energy of 8keV/u with different beam currents from about 80 µA to 2mA. The functionality and components of the pepper-pot device is reviewed as well as the final design and the choice of the scintillator. For that, results from recent beam test at the Max Planck Institute für Kernphysik at Heidelberg are presented. The material investigation was focused on inorganic doped crystal, inorganic undoped crystal, borosilicate glass and quartz glass with the following characteristics: availability, prior use in beam diagnostics, radiation hardness, transparency, fast response, spectral matching to CCD detectors.

PEPPER POT DEVICE

Location

The Pepper-Pot Scintillator Screen system should fit within the existing beam line components (vacuum boxes already used with beam diagnostics equipment like Faraday cups, profile grids and slits). The N1DK1 vacuum box will be equipped with a fast iris shutter, a pepper-pot mask and a scintillator screen. The N1DK2 vacuum box will contain a 45 degrees tilted mirror inside and a CCD camera outside. (Figure 1)

The pepper-pot principle

The pepper-pot mask, which is perpendicular to the beam and contains a regular array of identical holes, splits the beam into beamlets. The scintillator is used to create a photographic image of the beamlets with pixel intensity corresponding to the charge concentration of beam particles striking the transparent scintillator. A CCD camera with a mirror placed behind at 45 degrees will record single and multi-shots.

Why use a pepper-pot device?

We want to measure both x-y components of the beam emittance simultaneously in one shot and to obtain data in real time. Four methods [1-2] can be used and all utilize a slit or mask to select a portion of the beam for analysis:

1. The two-slit scanner method uses a second slit which can be scanned through the direction parallel to the first. The cut out beam current is normally measured by a Faraday cup.
   However, this method is really slow because the second slit has to be scanned through the range for every position of the first slit.
2. With the multi-wire collector method, each wire collects the beam particles that pass through the slit. The disadvantage of this method is that it requires an amplifier for every wire in the collector.
3. The Allison-type emittance scanner is faster than the multi-wire collector method but slower than the pepper –pot method [2]
4. The Pepper-pot.

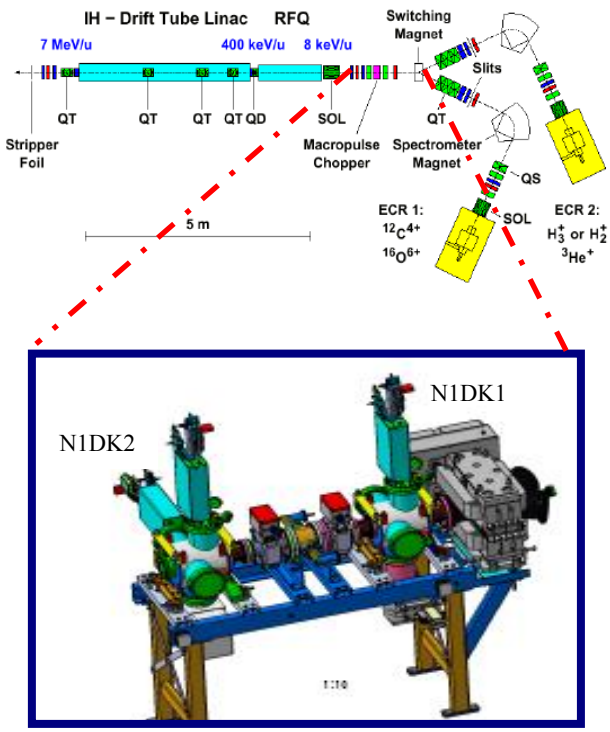

Figure 1: The Low Energy Beam Transport at HIT and the position of the Pepper-Pot Scintillator Screen device within the LEBT (Low Energy Beam Transfer).

Pepper pot measurement sequence and necessary components

Once the beam is tuned into the Faraday cup and a beam current measurement is acquired, the shutter (1) is released and the beam travels down to the pepper pot (2) mask (ideal case), and then to the scintillator screen (3).

The vacuum shutter UNIBLITZ VS35 [3] will be used. It has stainless steel blades, 35 mm aperture with a time to open of 13 ms. The pepper pot mask (60×60 mm×0.1mm) is made of tungsten and should contain a 40×40 array hole with 50 μm to 100 μm holes diameter and 1 mm pitch). Since the range of 8 keV ions in tungsten is approximately 100 Å, the tungsten will stop over 90% of the ions. The holes will allow an ion beamlet to pass which then propagates through a distance of 15-100 mm. The beamlets then impinge on a scintillator screen (4). The screen should be 80×80 mm and resides on a fixed sample holder. Whereas the pepper pot mask resides on a sample holder driven by a linear rail. The mask should be movable from 15 mm to 100 mm (with respect to the screen). The mechanical design (figure 2) of the pepper–pot system is a collaboration between GSI and HIT.

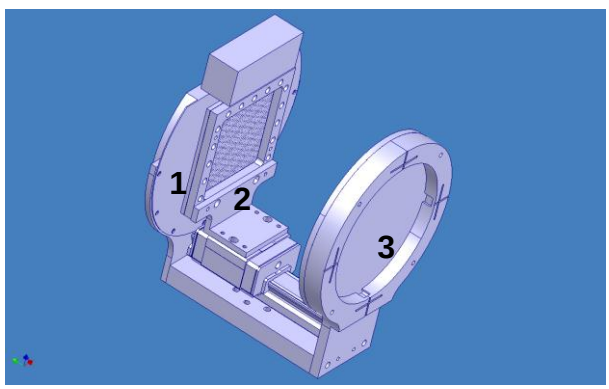

Figure 2: The Pepper-Pot Scintillator Screen bench. From left to right; (1) shutter (2) pepper-pot mask (3) scintillator screen.

SCINTILLATOR

The pepper pot mask and the measurement screen will be aligned perpendicularly to the beam. The beam images will be thus produced by a transparent scintillator and will be captured by a suitable CCD camera.

Why is the screen so important?

When the ion source delivers the beam to the pepper-pot, ideally, we would like the screen material to trap all coming particles and preserve the initial distribution over (x, x´, y, y´, E). Could this information be corrupted while the material transmits photons?

The screen visualizes the beamlets. The dimension and the intensity distribution of the beamlets will then be correlated to the angular distribution. To enable high spatial resolution, the screen material should trap particles uniformly from a very broad distribution over x ´and y´. In general, in most materials, particles are trapped uniformly.

The position coordinates (x, y) of the particles are generally preserved. The accuracy of the transmission in angles (x', y') should be one major point. Different type of scintillators could be used. Some of them have better light yield. That's why an experiment was performed with the collaboration of MPI-K to test the light output, damage and reproducibility.

Properties

The materials, selected because of their availability, radiation hardness, transparency, fast response, prior use in beam diagnostics, or spectral matching to detectors (CCDs,...) are

- Inorganic Doped Crystal : YAG:Ce, YAP:Ce, Caf2:Eu (Crytur Inc.). [4]
- Inorganic Undoped Crystal : Sapphire, YAG (Focteck Inc). [5]
- Quartz: Herasil 3 & 102, Infrasil 301 & 302, Suprasil 1 & 300 (Aachener Quarz-Glas Technologie Heinrich). [6]
- Borosilicate Glass D 263 T (Präzisions Glas & Optik). [7]

One of the most important properties of fused quartz is its extremely low coefficient of expansion: 5.5×10^-7 mm °C. Its coefficient is 1/34 that of copper and only 1/7 of borosilicate glass. This makes the material particularly useful for applications which require local and minimum sensitivity to thermal changes.

Experiment at the Max Planck Institute - Heidelberg

These tests were made on the first week of November 2009. During these runs, the scintillator plate was placed in the beam path at a 45 degree angle and a CCD camera was recording images. Three scintillators could be placed on a holder and be tested with the same conditions in one machine run before breaking vacuum and replacing materials with three non-irradiated samples.
The ion beam parameters used in this experiment are the following:

- Ion Beam: protons.
- Energy: 8 keV/u.
- Beam Current: 10 μA.
- Particles per pulse: 9.4×10^{11}– 3×10^{13}.
- Variable Pulse Length: 15 ms – 500 ms.
- Frequency: 1 Hz.

Each material is irradiated with 3 macro pulses of 15 ms, 20 ms, ….until 500 ms (or less if the light output intensity became constant) with a frequency of 1 Hz. At the end of the test a total irradiation time of 1.5 sec to 2 sec have been applied to each material.

The ion beam is first passing through a collimation entrance slits. Once the beam is tuned into the Faraday cup and a beam current measurement is acquired, the chopper is released and the beam travels down to the screen material situated in front of the Faraday Cup. In this way a flux up to 3×10^{13} pps for protons was achieved.

Three samples to be irradiated reside on a sample holder driven by a manual actuator (figure 3). The target is heated to below the melting point by the beam energy. The aim of this test was to evaluate the time dependence of the scintillating response of various scintillators.

Signal formation

The signal formation [8-9] of the scintillator light output consists of the following steps:

- Energy transfer from incident particles to secondary charged particles within the material. Charged particles being formed by the interaction of incident particles with the material.
- Energy transfer by secondary charged particles to luminescence centers [10].
- De-excitation of photons by excited luminescence centers which can lead to delayed fluorescence or phosphorescence (afterglow).
- Collection of photons by a CCD camera.

Only a part of the incident energy lost within the material by the charged particles will become the excitation energy of the luminescence centers which will emit photons. Some multiple electronic excitations (electron–hole pairs) will be formed along the ion track. The electron-hole pairs resulting from the ionization process form separated charge defects that cause the surroundings atoms to rearrange themselves (relax). To reach electro-neutrality, holes and electrons will capture charge carriers. If the concentration of electrons and holes is inferior to the concentration of activator atoms, both holes and electrons will have a large probability to be captured by different charge carriers. This recombination could generate electron centers (called F centers), hole centers (called H centers) and also self-trapped-hole centers (called V centers). For example, electrons in an F center will tend to absorb light in the visible such that the material becomes colored (“color center defect”) which is defined a slow recombination due to trapping (~ ms). However, if an activator atom first captures one carrier, the result may be an electronic states of the activator atom or exciton which will be a considered a fast recombination.

The density of these defects (excitons, color centers) increases until large clusters of defects are formed which diffuse to the surface.

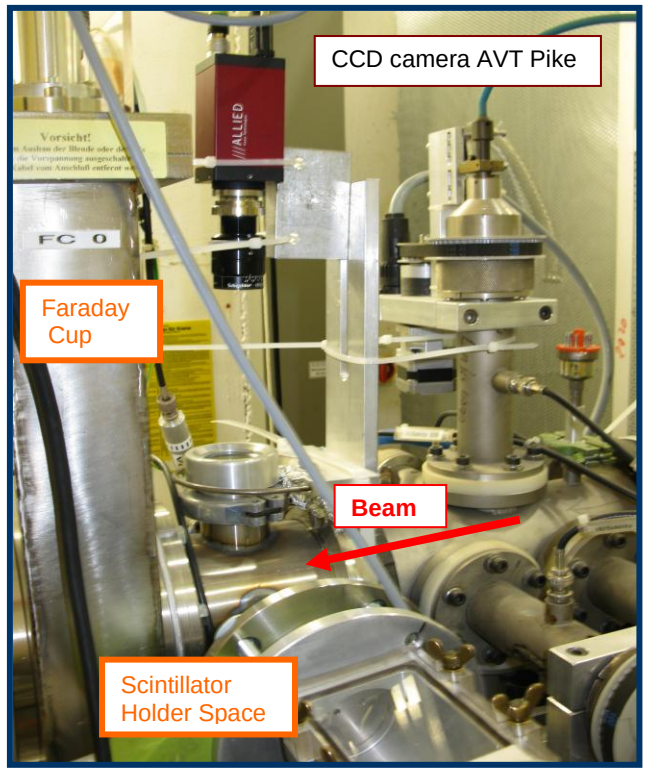

Figure 3: Ion Beam-Material Irradiation Test Setup at the Max- Planck Institute in Heidelberg.

Results

Matlab was used to process the images and to compute the intensity pixel values along the horizontal and vertical components. Two groups can be categorized:

- One with higher intensity values
- One with lower intensity values, two times lower than the first group.

The first group is primarily composed of the doped Inorganic Crystal: YAG:Ce, YAP:Ce and CaF2:Eu. These crystals saturate from the beginning of the irradiation and show some damage after being totally irradiated. Since the effect of saturation is intensity dependent, the use of YAG:Ce as a beam profile monitor should be limited to lower current densities for future experiment.

To gain high temporal resolution, doped (Ce3+) scintillators with fast decay of light output and intensive fluorescence have been chosen. However, a fraction of scintillation light is still present a certain time after the excitation stops, which can be explained by two phenomena: delayed fluorescence or afterglow. Another fraction can also be seen before the intensive fluorescence making really inconvenient the possibility to measure the light output for a specific irradiation time (and for the total irradiation) and the repeatability of the measurement. As seen in figure 5 A-B, the intensity profile for 40 ms

shows some large discrepancy in the repeatability of the light output.

A decrease of the optical transmission which causes a decrease in the intensity distribution can also deteriorate the spatial resolution. An example of this damage can be seen in figure 5-A where a part of the horizontal intensity profile of YAG:Ce disappears slowly with time. In Figure 4-B, the damage "blackened" area has been revealed thanks to a 10 pA beam current. After a total irradiation of 2000 ms, one part of YAG:Ce cannot scintillate anymore due to some degradation. However, a standard microscope does not show any damage (burning bubbles, changes in colour...)

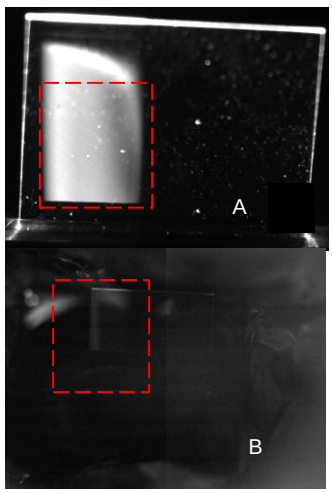

Figure 4 A-B: The degradation of YAG:Ce after a total irradiation of 2000 ms (which is equivalent to 1.4 *10^14 particle per pulse) can be seen in picture B.

The second group shows also some materials with some distorted Gaussian beam profile over the horizontal axis and some saturation effect over the y axis.

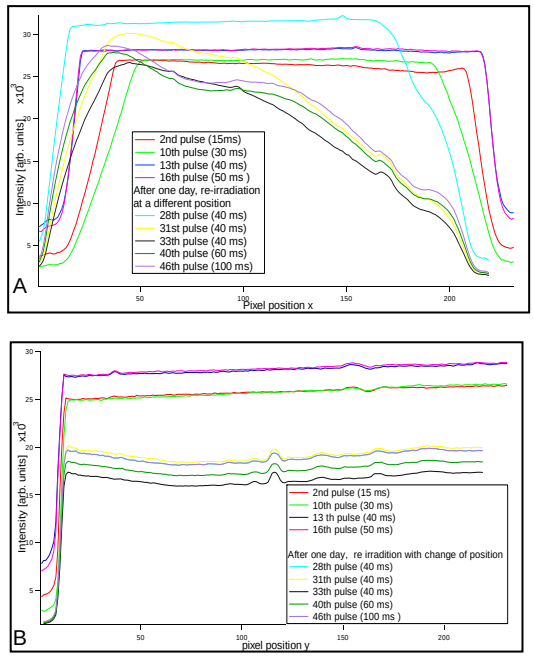

Figure 5 A-B: The intensity distribution of image 4 A is plotted over the horizontal (A) and vertical (B).

For sapphire, the light output increases with the integrated beam pulse but still lead to some damaging effect "blackening". The YAG undoped shows some similar behaviour which results in some damage after a total irradiation time of 1.3 seconds. (Figure 6). This picture confirms that undoped material cannot be used anymore. Only a small part of the material scintillates, a big part (corresponding to the irradiated beam width of the previous day) does not scintillate at all.

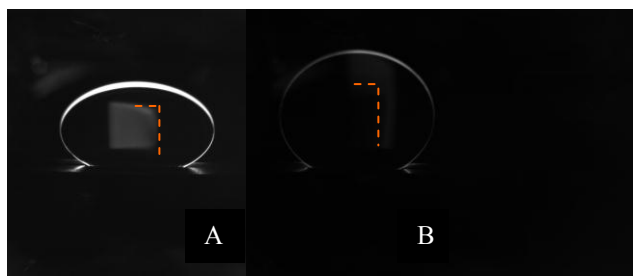

Figure 6: Degradation effects of undoped YAG after an integrated irradiation time of 1.3 seconds.

Borosilicate glass and Suprasil 300 demonstrate some really low light output and some fluctuations in the intensity distribution with respect to the beam pulse. Consequently, repeatability of the measurement could not be achieved.

Between this two groups, Herasil 3, Infrasil 302 and Suprasil 1 could be of some interest. The light output of these scintillators is sufficient and increases with the beam pulses (Figure 7).

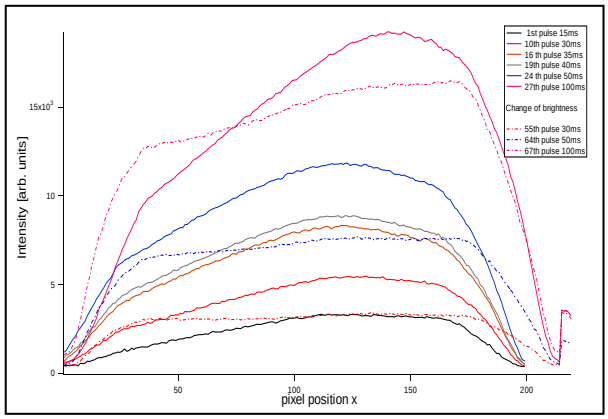

Figure 7: The repeatability of the intensity distribution over 65 beam pulse of Herasil 3 (which is equivalent to a integrated time of ~ 2000 ms) and the degradation effects after changing the CCD camera set-up to a lower brightness

In the experiment, an image was taken of the material irradiation every 1 Hz (for three beam macro pulses). The beam pulse is then increased until 200 ms. Afterwards, a change in the CCD parameters (lowering brightness level) lead to another set of images taken with the same beam parameter setting (energy, current ...) and without breaking the vacuum. The repeatability of these measurements was shown in Figure 6. The light output distribution for Herasil 3 is shown from the 1st to the 65th pulses. The new set of data (after the change of parameters of the CCD camera) for different beam pulse shows the same phenomenon: their corresponding intensity distribution follows the "previous" data curve until the distribution broke. The "flat top" appearing after ~100 ms of integrated irradiation can be due to saturation of activator centers, slow decay processes (slow recombination due to trapping), or some non- visible damage. The same behavior can be seen for Suprasil 1 and Infrasil 302.

Most of the materials except the doped inorganic crystal have a "flat top" distribution in the vertical axis and a "broken" non Gaussian distribution in the horizontal axis from the beginning of the irradiation. This distribution is not homogeneous and this pattern was also observed when increasing the irradiation time. A longer irradiation time did not lead to a more homogeneous intensity distribution for most of them. These heterogeneities can be due to the beam delivery or to the non-homogeneity of the crystal. Such effects should be investigated by studying the relationships between the beam parameters and the achieved effects.

The decrease of light output can be due to the saturation of activation centers, the slow decay processes, and also some damage. Due to the existence of slow decay processes which are mainly caused by charge carrier re-trapping at shallow traps, the light output does not increase with respect to the integration time. Additionally, some large fluctuation of the intensity distribution has been observed. However, in order to explain the slower scintillation process in the timescale of ms and these large fluctuations, such effects should be investigated.

CONCLUSION

The design of the pepper pot mechanics is completed and is under construction. The pepper pot device will be implemented at HIT in a new research and development test bench available in September 2010.

The inorganic doped scintillators have a greater light output than the inorganic undoped scintillator and the quartz material. However, some aspects of their scintillation behaviour (large fluctuations of their light output, non-repeatability of measurement) have not been explained satisfactorily and need further investigation.

ACKNOWLEDGMENTS

I would like to thank Manfred Köning of MPI-K for the assistance in running the accelerator, and to Christoph Dorn of GSI for the mechanical design. Thanks also go to Tim Winkelmann for assistance in running the test at MPI-K. It is a pleasure to acknowledge helpful discussions with Christophe Dujardin, Ayman S. El-Said, Rainer Haseitl, Simon Jolly, Erik Ritter, Markus Strohmeier, and Richard Wihelm. This work is funded by the European commission as part of the FP7 Marie Curie Actions under contract number PITN-GA-215080.

REFERENCES

[1] T.Hoffmann, W.Barth, P.Forck, A.Peters, P.Strehl, Emittance Measurements of High Current Heavy Ion Beams Using a Single Shot Pepper Pot System
[2] M.P.Stockli et al, Measuring and Analysing Transverse Emittances of Charged Particle Beams, BIW'06, Batavia, IL, 2006, AIP Conf. Proc.868, p.25.
[3] Uniblitz Inc, from http://www.uniblitz.com/
[4] Crytur Ltd, from http://www.crytur.com/
[5] Foctek Photonics Inc, from http://www.foctek.net/
[6] Aachener Quarz-Glas Technologie Heinrich, from http://www.quarzglas-heinrich.de/
[7] Präzisions Glas & Optik, from http://www.pgo-online.com/intl/
[8] R.B.Murray; A.Meyer, Phys.Rev. 122(1961) 815
[9] J.A.Mares et al.,IEEE transactions on nuclear science, vol 55, No.3, June 2008.
[10] T. J. Renk et al., Proceedings of the IEEE, 92, No. 7, 1057–1081 (2004) .

EMITTANCE MEASUREMENTS AT THE LBNL ECR AND AECR-U ION SOURCE USING A PEPPER-POT EMITTANCE SCANNER *

M.Strohmeier#,1,2, J.Y.Benitez[1], D.Leitner[1], D.Winklehner[1], D.S.Todd[1], C.M.Lyneis[1], M.Bantel[2]

[1] Lawrence Berkeley National Laboratory, 1 Cyclotron Road, Berkeley, CA, 94720, U.S.A.
[2] University of Applied Science Karlsruhe, Moltkestrasse 30, 76133 Karlsruhe, Germany

Abstract

Two Electron Cyclotron Resonance (ECR) ion sources are currently available to inject beams into the 88-Inch Cyclotron at Lawrence Berkeley National Lab (LBNL). Ion beam emittances for various ion species of both sources were measured using a recently commissioned pepper-pot emittance scanner[1] and are discussed in this paper. Pepper-pot scanners[1,2,3] are capable of extracting the full four-dimensional transverse phase space of the beam, allowing for the calculation of the cross coupled emittances xy' and yx'. This is especially of interest for ECR ion sources, where asymmetric beams are extracted in the presence of a strong solenoidal field. The axial field adds a rotational momentum to the extracted beam resulting in a transverse emittance growth, which depends on the magnetic stiffness of the extracted species. In this paper, the pepper-pot software is described and emittance data from both LBNL ECR sources are presented and compared. The data confirm a strong mass dependence of the normalized emittance for ions with the same mass-to-charge-state ratio, as previously also observed by other groups. This dependence indicates different particle distributions at the extraction aperture for different ion species.

INTRODUCTION

Electron cyclotron resonance (ECR) ion sources are widely used in the particle accelerator community because they are capable of producing high current beams of highly charged ions. Their operation relies on magnetically confined plasmas in which the electrons are resonantly heated with microwave radiation. They can reach energies of several hundred keV and ionize the gas in a step-by-step ionization process. In order to achieve high charge states, long confinement times (milliseconds) are needed which are achieved by the superposition of an axial mirror field and a radial multi-pole field, resulting in a minimum B-field configuration. Since the extraction aperture of most ECR sources is located near the center of the extraction solenoid coil, particles are extracted and accelerated in a decreasing magnetic field, which increaes the transverse emittance. Two different types of emittance scanners are currently in operation at LBNL to measure the beam emittance: an Allison type slit scanner[4] and a pepper-pot scanner[1]. The slit scanner can provide a better spatial and angular resolution than the pepper-pot, but measurements take a few minutes. Additionally, the slit scanners can only extract one-dimensional data sets, since the intensities are integrated over the whole slit while stepping through the beam. Scintillator based pepper-pot scanners capture the image data in just a fraction of a second, making it less vulnerable to emittance changes caused by plasma instabilities or other transitions. Furthermore, the image array of a pepper-pot scanner provides two dimensional data sets from which the xx' and yy' as well as the cross coupled xy' and yx' phase spaces can be extracted.

The principle of the pepper-pot scanner[1,2,3] is to image the beam as it passes through a hole mask and creates a light pattern on a scintillator behind the mask. By knowing the absolute locations of the holes in the mask and relating them to the light pattern on the scintillator, one can obtain the transverse angular distribution of the particles in the ion beam. Since the pepper-pot scanner uses a camera (typically a CCD camera) to capture the light pattern on the scintillator, it is important to investigate the influence of the optical parameters on the emittance. These parameters can greatly influence the final emittance values and have to be chosen carefully in order to minimize and define the induced error stemming from the respective parameters[2]. For the scintillator, the absolute light yield, its linearity and the lattice degradation as a function of the integrated beam exposure are crucial parameters [1, 2]. Camera settings that influence the emittance value are the exposure time of the charge coupled device CCD chip to the scene, the gain and the brightness.

NOISE PROCESSING

The noise treatment consists of the following three steps, which are described in this section in detail:

1. Detecting faulty pixels.
2. Smoothing the data.
3. Threshold cut of the data.

1) Detecting fault pixels

As CCD cameras age, the pixel array degrades, and the number of faulty pixels increases. If the camera is additionally mounted in a radiation environment, this degradation is even more accelerated. Unfortunately, the gray scale values of these damaged pixels show a random distribution rather than a constant value of “255” or “0”. Neglecting these pixels for the emittance evaluation would introduce a large error in the calculation. Therefore, before calculating the emittance value the analyzing software needs to locate and replace those pixels with approximated values. In order to locate the faulty pixels, a reference image without beam has to be

* This research was conducted at LBNL and was supported by the Director, Office of Energy Research, Office of High Energy and Nuclear Physics, Nuclear Physics Division of the U.S. Department of Energy under Contract No. DE-AC02-05CH11231.
# MMStrohmeier@lbl.gov

recorded where the faulty pixels are clearly visible. Empirically, a gray scale value of about 80 was found to be an appropriate threshold to decide which pixels are damaged. Once those pixels are identified, they are substituted in the real image with the average of the eight intermediate neighbors.

2) Smoothing the data

In the next step a 3x3 smoothing filter is applied to the data. While this simple smoothing filter turns out to work well, future tests will compare more filter types such as low-pass filters, Gaussian filters or median filters.

3) Threshold cut of the data

In the last step, a threshold cut is applied to the image with a value that can be set online via a slider on the GUI (graphical user interface) to eliminate electrical noise in the image. The GUI gives the user an immediate visual feedback of how the threshold level affects the data. The value of the threshold cut has to be chosen carefully since it is a measure of how much beam intensity is neglected and will be discussed later in this paper. Typical threshold values are in the order of 10 to 15 gray scale units (which is less than 5% of the full dynamic range). Figure 1 shows two profile plots of the same image slice before and after the noise processing steps described above were applied.

Influence of noise threshold on the emittance

In this section, the influence of the value for the threshold cut which is applied to the raw data on the obtained emittance number is discussed. The threshold cut is problematic since the "real" emittance of the beam is not known and the border regions of the spots greatly influence the obtained emittance value. By applying a threshold cut, these border regions are disregarded and the emittance becomes artificially smaller. The neglected portion of the beamlet increases with the value for that threshold cut. The black curve in Figure 1 shows that without a threshold cut, the beamlets cannot be separated, which is essential for the pepper-pot evaluation software[1].

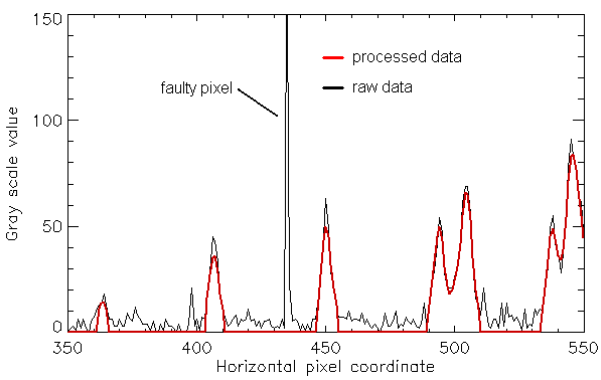

Figure 1: Plot of the same image slice before and after the noise processing steps were applied. BLACK: raw data, RED: after eliminating the faulty pixels, smoothing and thresholding the data.

Curve-fitting to each of the spots would eventually make the threshold cut obsolete; this software improvement will be implemented in the future. Figure 2 shows the emittance curves for an oxygen spectrum with different threshold values applied to the data.

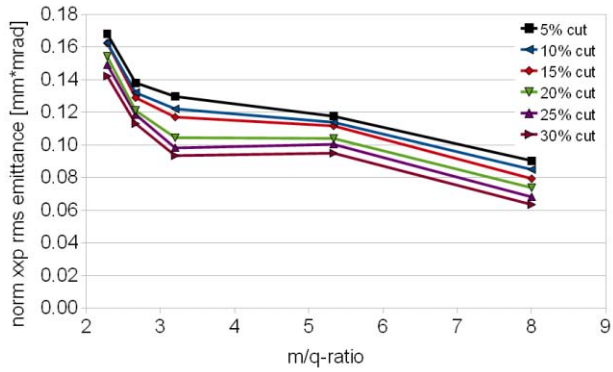

Figure 2: The emittance decreases as the noise threshold is increased and a greater portion of the spots is neglected. This change is different for every charge state and cannot be generalized.

For the top curve in figure 2 a 5% threshold was set, such that the spots on the pepper-pot image could just be separated and assigned to the corresponding holes. It can be clearly seen that for an increasing value of the threshold, the emittance becomes smaller.

Figure 3 shows the change of the emittance value for each charge state as the threshold is increased. The individual change for each charge state can be due to the fact that the intensity distribution in bigger spots is more diluted which results in a bigger intensity as the threshold cut is applied. As mentioned before, for future analysis the threshold cut must be replaced by a fitting routine in order to obtain even more realistic emittance values.

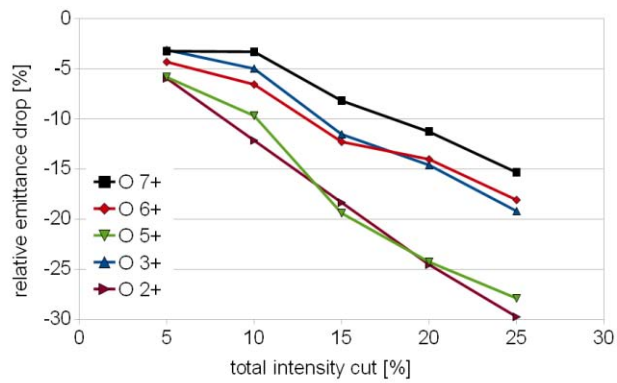

Figure 3: The difference in change of the emittance value for each charge state with different threshold values means that for bigger spots are the intensities are more diluted, resulting in a bigger decrease through the threshold cut.

DEVICE CALIBRATION

Since a pepper-pot scanner method is based on an optical data acquisition system, it is essential to investigate the influence of optical parameters such as the light response of the scintillating surface, the shutter time of the camera, the camera gain and the noise threshold on the obtained emittance values. Both the light yield of the scintillating surface as well as the shutter time of the camera determine the amount of light that falls onto the CCD chip. Therefore, these parameters play an important role for the sensitivity of the device. Previous measurements[1] have demonstrated that the light yield increases linearly with the deposited particle current and that the scintillator does not saturate in the tested current range. The next parameter to be considered is the camera gain. After the emittance pattern has been captured the gain is simply a multiplication of the image with a constant value. Generally, the gain and the shutter time should be chosen such that the CCD chip is close to its saturation in order to maximize the sensitivity of the measurement. The influence of each value is discussed in the following paragraphs.

The influence of the shutter time on the emittance value is shown in Figure 4, in which the emittance value is plotted as a function of the exposure time of the CCD chip. The data were taken with the same ion beam (33 μA, O^{5+}, 10 keV), while the ion source and beam line settings were kept constant for the measurement. Obviously, the shutter time has to be chosen to fall in the flat region of Figure 4 in order to measure realistic emittance values. On the other hand, the shutter time must be small enough to avoid saturation of the the chip, which would cut off the top of the spots.

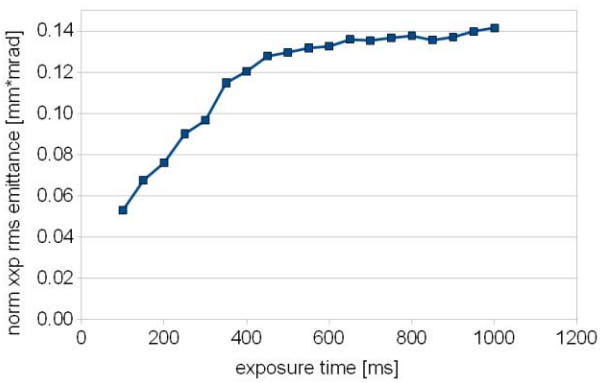

Figure 4: Generally, the spots become bigger as the shutter time increases. This induces a larger angular spread, which leads to a higher emittance.

As mentioned before, the gain of the camera is a constant value by which each pixel value is multiplied after the image has been captured. This increases image contrast, and the faint border regions of every spot become more visible as the gain is increased. However, this simple multiplication does not improve the signal-to-noise ratio (SNR). Figure 5 shows how the 1 rms normalized emittance of an O^{2+} beam (10 keV) behaves as the gain is increased while all other beam line and acquisition parameters remained the same. Again, measurements should be performed in the flat region of the curve.

As can be seen from Figures 4 and 5, the gain and shutter time have to be chosen carefully so that the CCD chip is close to its saturation in order to maximize the sensitivity and the signal-to-noise ratio. In addition, it is useful to combine pepper-pot measurements with an electrostatic type of emittance measurement such as the Allison scanner to have an independent cross check. By combining the higher resolution and better dynamic range of an electrostatic scanner with the 4D pepper-pot emittance scanner, the maximum information about the beam emittance can be obtained.

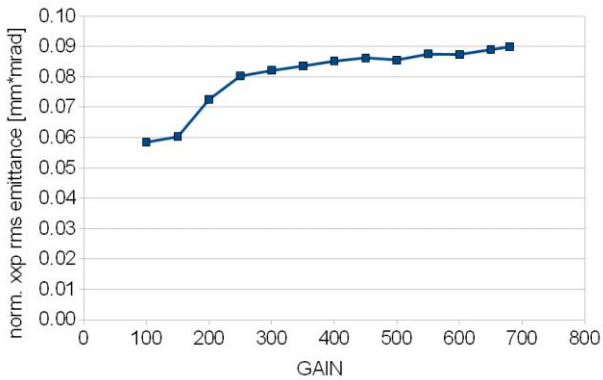

Figure 5: For small values of gain, the emittance appears to be very sensitive to changes in the camera gain. For a reliable measurement, the emittance value has to be evaluated from data taken in the flat region.

EMITTANCE VALUES OF ION BEAMS EXTRACTED FROM ECR ION SOURCES

The emittance of an ion beam extracted from an ECR source consists of two components: the magnetic emittance and the thermal emittance. For ECR sources, the magnetic influence is usually the main contribution to the total emittance and is influenced by the charge state of the ions and the axial field strength at the extraction aperture[5]. The ion temperature determines the thermal contribution to the emittance and is given by:

$$\varepsilon_{ther} = 0.016 \cdot R_{extr} \cdot \sqrt{\frac{kT_i}{M/Q}} \qquad (1)$$

where R_{extr}*[mm]* is the radius of the extraction aperture, kT_i *[eV]* is the ion energy and *M/Q* the mass-to-charge ratio. Accordingly, the magnetic contribution to the emittance can be calculated by:

$$\varepsilon_{mag} = 0.032 \cdot \left(R_{extr}\right)^2 \cdot \left(\frac{B_{extr}}{M/Q}\right) \qquad (2)$$

where B_{extr} *[T]* is the maximum magnetic field at the extraction region of the source. For most ECR ion sources the magnetic component dominates over the thermal component [5].

EMITTANCE DATA

First emittance measurements with the new pepper-pot device were performed using the LBNL 6.4 GHz ECR and the 14 GHz AECR-U ion source.

1) Emittance change for different RF powers and beam intensities

As a first test, the beam emittance was measured as a function of the beam intensity. If more microwave power is coupled into the plasma, its density and consequently the beam intensity are increased, as long as the plasma remains stable. As an example, Figures 6 and 7 show a summary of a data series taken during a high intensity sulfur production run, where ECR source was optimized for S^{7+} through S^{10+}. The emittance values increase with increasing microwave power since the beam intensity for all charge states increases.

The average relative beam current increase of 30-40% between the different power levels is about the same as the increase in the absolute emittance values. Additionally, the plasma might be less stable at high power operation, which could lead to a higher emittance as well due to increasing transverse temperature. These two effects are difficult to decouple, but will be further investigated in the future.

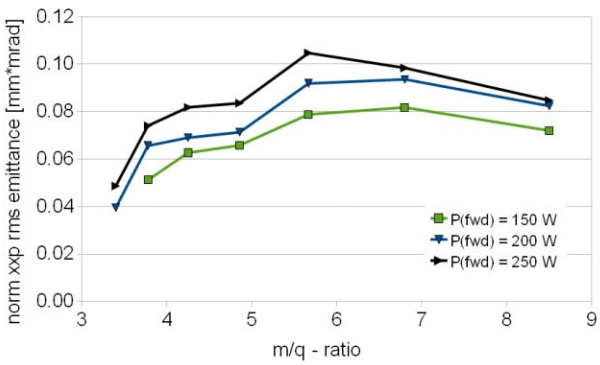

Figure 6: Coupling more RF power into the plasma increases the total extracted power and leads to an emittance growth.

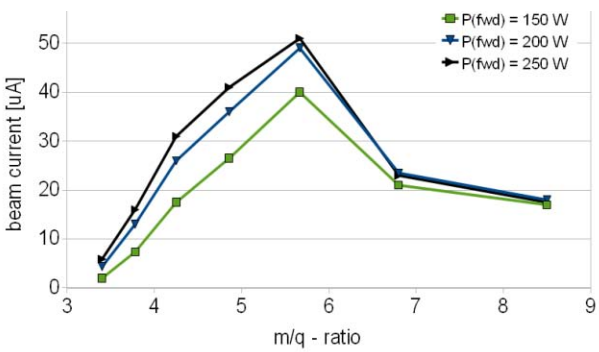

Figure 7: For high charge states the extracted current decreases, which makes the spots smaller, leading to a decreasing emittance number (see Fig. 6).

2) Emittance measurements at the ECR source

Figure 8 shows the result of a series of emittance measurements performed at the LBNL ECR ion source for oxygen, argon, sulfur and krypton beams extracted at 10 kV as a function of the mass-to-charge state ratio (m/q-ratio). For all data, the 1 rms normalized emittance values are plotted after an intensity threshold cut of approximately 5%. It can be seen that for the same m/q-ratio heavier ions have a lower emittance than lighter ions, which is consistent with previous measurements[4]. This experimental result cannot be explained by equation 2 and might indicate that the particle distributions for heavier and lighter ions differ at the extraction aperture.

In addition, the measurements indicate a decreasing emittance for the higher charge states (e.g., Kr ions in figure 8). This could be an optical artifact since lower intensities are extracted for the higher charge states and the scanner might not be sensitive enough to measure the outer regions of the spots which would lead to smaller emittances. However, similar dependencies have been measured with Allison type slit scanners by various groups making the following interpretation possible as well. Due to the better confinement of the high charge states, the high charge state ions might be created closer to the axis of the source and would be extracted from a smaller region reducing the effect of the magnetic field on the transverse emittance.

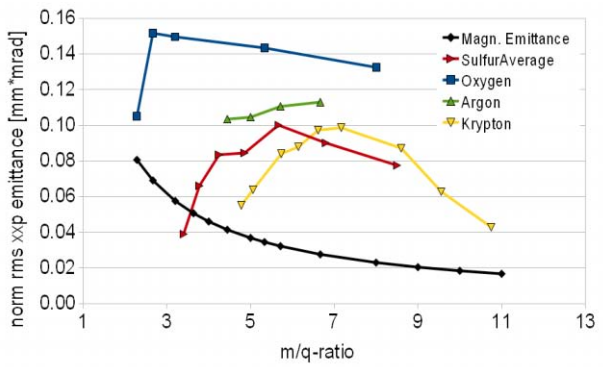

Figure 8: The data from the ECR source reveals that ions with a high mass have a lower emittance. This indicates a lower transverse ion temperature in the plasma.

3) Emittance measurements at the AECR-U source

A similar measurement series as described above for the LBNL ECR ion source was performed using the LBNL AECR-U ion source. Figure 9 shows the 1 rms normalized emittance for several species after an intensity threshold cut of about 5% was applied to the raw data. The extraction voltage was set to 12.5 kV and the maximum axial field strength in the extraction region is 0.9 T (about three times higher than the LBNL ECR ion source extraction field).

Contrary to the LBNL ECR source, most emittance values are well below the value predicted by the magnetic contribution (Equation 2), which indicates that the ion beam does not completely fill the extraction aperture. Similar to the ECR data, heavier masses have lower emittance values than lighter masses with the same magnetic rigidity. When the LBNL ECR ion beam emittance values are plotted together with the numbers obtained at the AECR-U ion source, the emittance values do not scale with the magnetic field as expected.

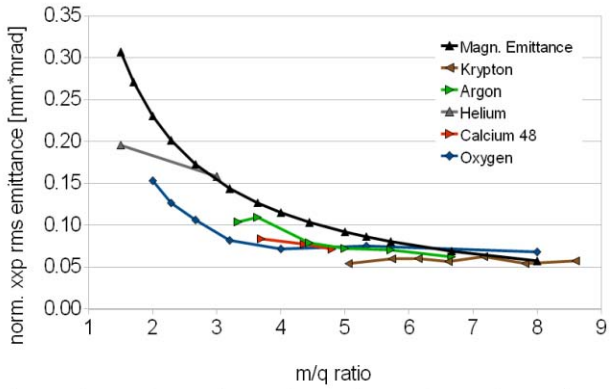

Figure 9: Especially for oxygen, the emittance grows clearly with the charge state and shows the same trend as the (theoretical) magnetic emittance.

Since the two analyzing beam lines are identical, any differences in the emittance values of the ion beams extracted from the two sources should only stem from the different magnetic field present at the extraction region. The maximum axial magnetic fields at extraction are 0.3 T for the LBNL ECR and 0.9 T for the LBNL AECR-U. The LBNL ECR emittance numbers should be three times smaller if the numbers would scale as predicted by Equation 2. The higher emittance measured at the LBNL ECR might be due to misalignment of the beam line or less stable plasma conditions and will be further investigated.

OUTLOOK

Future work with the LBNL pepper-pot emittance scanner will focus on comparing the results with an Allison type slit scanner and on further improvements of the analyzing software.

ACKNOWLEDGEMENTS

This research was conducted at LBNL and was supported by the Director, Office of Energy Research, Office of High Energy and Nuclear Physics, Nuclear Physics Division of the U.S. Department of Energy under Contract No. DE-AC02-05CH11231.

REFERENCES

[1] M. Strohmeier, J. Y. Benitez, D. Leitner, C. M. Lyneis, D. S. Todd, and M. Bantel. Rev. of Scientific Instruments, **81**, 02B710 (2010).

[2] S. A. Kondrashev, A. Barcikowski, B. Mustapha, P. N. Ostroumov, and N. Vinogradov, Nucl. Instrum. Methods Phys. Res. A **606**, 296 2009.

[3] H. R. Kremers, J. P. M Beijers, and S. Brandenburg, *A Versatile Emittance Meter and Profile Monitor* KVI, Groningen, 2007.

[4] D. Wutte, M. A. Leitner, and C. M. Lyneis, Phys. Scr. **T92**, 247 2001.

[5] M.A. Leitner, D.C. Wutte and C.M. Lyneis, *Design of the Extraction System of the Superconducting ECR Ion Source VENUS,* PAC2001 Proceedings, Chicago.

BUNCH-LENGTH MEASUREMENTS AT SCSS TEST ACCELERATOR TOWARD XFEL/SPRING-8

Y. Otake#, S. Matsubara, H. Maesaka, K. Tamasaku, T. Togashi, K. Togawa, and H. Tanaka
RIKEN/SPring-8, 1-1-1, Kouto, Sayo-cho, Sayo-gun, Hyogo, 679-5148, Japan
M. Goto, Hamamatsu Photonics K.K., 812 Joko-cho, Higashi-ku, Hamamatsu-shi,
Shizuoka, 431-3196, Japan

Abstract

The SCSS test accelerator, which was constructed to check the feasibility of XFEL/SPring-8, is being operated for user experiments using stable EUV (Extreme Ultra-violet) SASE. This accelerator provides a high-quality electron beam with parameters, such as a bunch length of 300 fs and a peak current of 700 A, for power saturation of the EUV SASE. Evaluating the parameters is very important to ensure the stable generation of SASE. Bunch-length measurement systems to evaluate the parameters have been developed. The systems use the rf zero-phase crossing method, the EO sampling method with temporal decoding and an 800 nm laser, and a method for observing OTR (near the infrared region) by a streak camera (fesca-200), which is mature technology. All of the measured bunch lengths were about 300 fs (FWHM), which is consistent with the individual methods. The most important result is that the streak camera with optimum tuning directly measured the temporal structure with femto-second resolution, and the reliabilities of these systems were mutually checked.

INTRODUCTION

Constantly keeping the peak currents of the electron bunches of a free electron laser at SPring-8 (XFEL/SPring-8) [1] and the SCSS test accelerator to check the feasibility of the XFEL/Spring-8 [2.3], which are used to generate coherent and extremely intense x-rays and extreme ultra-violet (EUV) light, respectively, is one of the most important points to ensure stable generation of their lasers. In the present technology, the charge amount of a bunch can only be reliably measured by a current transformer with a reasonable accuracy of 1~5%. Therefore, measurements of the bunch shape, which determines the peak current, are very important. Furthermore, we introduced the SCSS concept [2] for the XFEL and the SCSS test accelerator. The SCSS concept employs a velocity bunching process using multi sub-harmonic bunchers (SHB) for an injector and a magnetic bunching process using a chicane bunch compressor (BC) comprising four bending magnets after the injector. For the SCSS test accelerator, a single BC is used, and for the XFEL three-stage BCs are employed after the injector. For this reason, the individual bunch compression processes have different bunch lengths; the bunch width of the velocity bunching is from 1 ns to 10 ps (1~20 A in peak current), the bunch length after the 1st BC is 2~3 ps (~70 A), the bunch length after the 2nd BC is around 150 fs (~600 A), and the bunch width after the 3rd BC is about 30 fs (~3 kA). Since the stability of the laser is extremely dependent on their bunch lengths, evaluating and properly adjusting the bunch lengths at each process are very important to ensure a stable laser. To establish the measurement reliability and adapt measurements with the different bunch lengths, different kinds of bunch-length measurement methods are employed for the XFEL and the SCSS test accelerator, even through the methods almost cover the same temporal resolution and range. Because the temporal accuracy of the individual bunch length methods in the case of a measurement with a resolution under 1ps, such as a streak camera for observing optical transition radiation (OTR) and an rf zero-crossing [4], still has some ambiguity caused by measurement errors. For example, the errors are sensitivity dependent on the wavelength, where the streak camera is used [5], and the aberration of an electron beam optical system, where rf zero-crossing is employed. Therefore, we think that the reliability on the temporal resolution of the bunch-length measurements in a femto-second region is not yet established at the present time.

Six kinds of bunch-length measurement systems, as mentioned below, to guarantee the reliability of the beam-monitor system of the XFEL have been developed, or are under development. In this paper, we report on the already developed bunch-length measurement systems using a streak-camera method, an rf zero-phase crossing method, and an EO sampling method [6] selected from the bunch-length monitors for the XFEL, which are described blow. These methods cover a temporal measurement range of several hundred femto-seconds. This time range can adapt observing the electron bunch of the 1st BC and the 2nd BC.

To check the reliability of the developed methods, and to evade any ambiguity of the measurement accuracy, the electron bunch length of the SCSS test accelerator was measured by the developed systems, and the data taken by the systems were compared. The test accelerator uses multi- SHBs of 238 MHz and 476 MHz for velocity bunching and a BC for magnetic bunching. A schematic layout of the test accelerator is illustrated in Fig. 1. The electron bunch length of the accelerator is compressed from 1 ns to a spiky lasing part of 300 fs with the 750 A peak current by the bunching process, while the final whole compressed bunch length is about 1ps, including the spiky lasing part. These bunch compression processes were numerically simulated, and their performances were experimentally confirmed by measurements.[3]

otake@spring8.or.jp

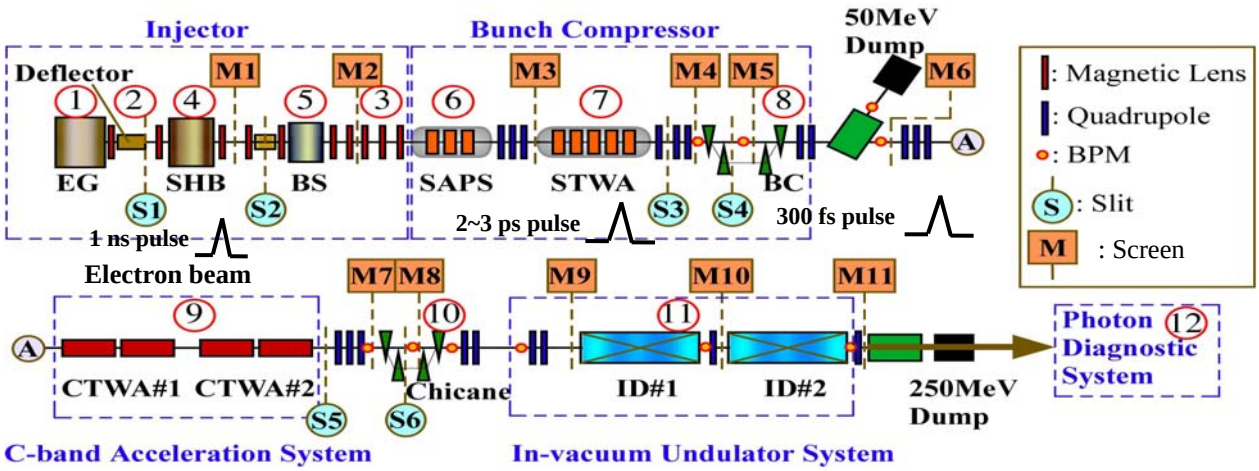

Figure 1. Schematic layout of the SCSS test accelerator. 1 EG, electron gun; 4 SHB, sub-harmonic buncher; 5 BS, booster cavity; 6 SAPS, S-band APS cavity; 7 STWA, S-band travelling wave accelerator; 9 CTWA, C-band travelling-wave accelerator; 11 ID, insertion device (undulator).

Table 1. Number of beam monitors for the XFEL and the SCSS test accelerator.

Kinds of Monitor	Number of Monitors (XFEL/SPring-8)	Number of Monitors (SCSS test accelerator)
RF cavity BPM	56	10
Screen Monitor	43	11
Current Transformer	30	12
Transverse rf Deflector	1	0
Streak Camera using OTR	3	1
EO Sampling	1	1
Waveguide Spectrometer	4 ~ 5	2 ~ 3
CSR Pyro-detector	3	1

In this paper, we firstly show a brief overview of the beam-diagnostic system of the XFEL/SPring-8, and then the experimental set-ups of the developed bunch-length measurement systems used to monitor the bunch characteristic of the test accelerator, as previously mentioned, are described and their experimental results are also reported.

OVERVIEW OF THE BEAM DIAGNOSTIC-SYSTEM FOR XFEL/SPRING-8

The beam-diagnostic system for the XFEL [7] mainly comprises rf cavity-type beam position monitors (RF-BPM), precise screen monitors (SCM), and high-speed differential current transformers (CT). Furthermore, for bunch-length measurements used to evaluate the individual bunch compression process placed along the stream of the accelerator, as mentioned above, the following instruments are used: a CT to measure a bunch length from 1ns to 500 ps at the electron gun and the 238 MHz SHB, a waveguide spectrometer [8] to detect coherent transition radiation (CTR) emitted from the SCM and to measure an electron bunch length of up to 10 ps for velocity bunching, a streak-camera (Hamamatsu Photonics, Fesca-200) system to observe optical transition radiation (OTR) emitted from the SCM and to monitor an electron bunch with a width from 10 ps to 300 fs, a pyro-detector [9] to monitor coherent synchrotron radiation (CSR) emitted from an electron bunch with a 30~1000 fs pulse passing through the bending magnet of the BC, an EO sampling system to monitor the relativistic electric field of an electron bunch and to measure up to a 100 fs bunch length, and a transverse rf deflector system [7] to measure a bunch width of less than 30 fs after all the bunch compression. The quantities of these monitors are tabulated in Table 1. The test accelerator also has some of the same beam monitors as shown in Table 1.

EXPERIMENTAL SET-UPS FOR THE DEVELOPED THREE BUNCH-LENGTH MESUREMENT SYSTEMS

To fulfill the requirements of electron bunch-length measurements for the XFEL, as mentioned above, the three measurement systems described below have been developed by using the SCSS test accelerator.

Streak camera system

Figure 2 shows a developed bunch length measurement system using a streak camera and an OTR screen (SCM). The SCM of M9 is placed just after the chicane, as shown in Fig. 1. The OTR light emitted from M9 is guided along an optical system using mirrors to feed into the streak camera. To reduce the effect due to an optical group delay

along the optical pass and energy dispersion on the photoelectric surface of the streak camera dependent on a wavelength, which deteriorates the temporal resolution of this system, an optical low–pass filter is employed. The cut-off wavelength, λ_c, of the filter is 640 nm. The wavelength sensitivity of the streak camera is limited to over about 850 nm. Therefore, the wavelength sensitivity of this bunch-length measurement system is from 850 nm to 640 nm. To obtain sufficient optical intensity, which reflects an improvement of the signal-to-noise (S/N) ratio, a focusing lens placed near the streak camera is employed.

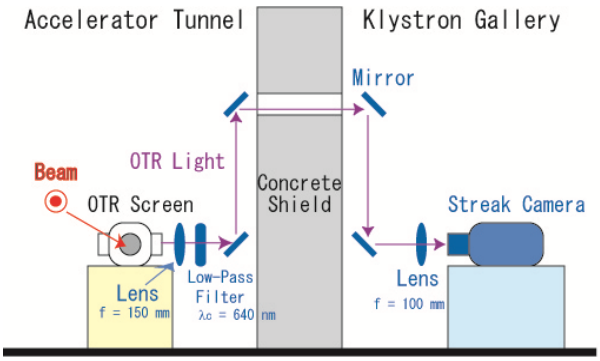

Figure 2. Experimental set-up of an electron bunch-length measurement using OTR light and a streak camera.

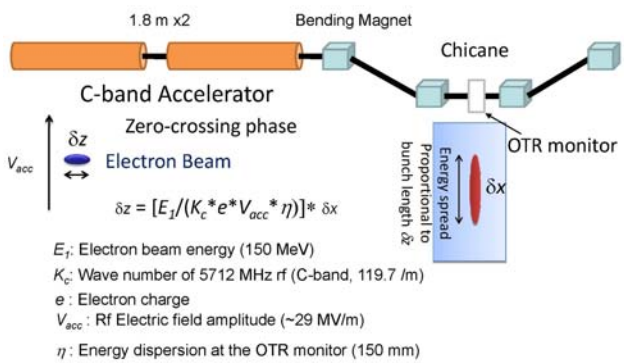

Figure 3. Measurement instrumentation configuration of the rf zero-crossing method.

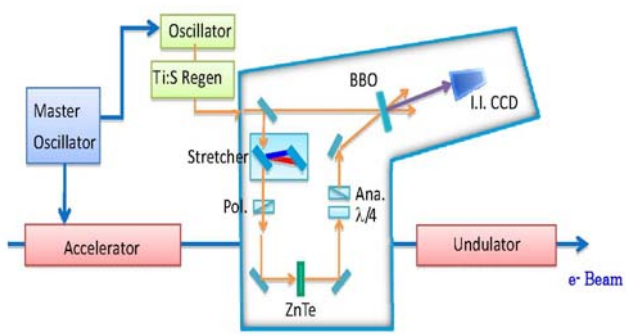

Figure 4. Experimental set-up for E/O sampling using a Zinc Telluride, ZnTe, crystal. This schematic shows the temporal decoding method.

Rf zero-phase crossing system

For measuring a bunch length by the rf zero-phase crossing method, as shown in Fig. 3, the SCM (M8 in Fig. 1) at the energy dispersive section of the chicane and the 2nd C-band traveling-wave accelerator #2 (CTWA#2) were used. When the timing of the electron bunch centroid is settled at a zero-crossing point of the acceleration rf electric field of the CTWA#2, the energy of the electron bunch is proportionally modulated along the bunch direction (Z axis) by the quasi-linear rf electric field around the zero-crossing point. Then, the beam passes through a bending magnet, and reaches M8 of the dispersive point. In this case, the beam image on the screen shows the intensity distribution of the electron bunch along a temporal direction. The bunch length, δz, is calculated from the equation of $\delta z=[E_1/(k_c*e*V_{acc}*\eta)]*\delta x$ from the length, δx, of the observed beam image, where E_1 is the acceleration energy of the electron, k_c is the wave number of a C-band rf, 5712 MHz, e is the electron charge, V_{acc} is the acceleration voltage, η is the energy dispersion at the M8.

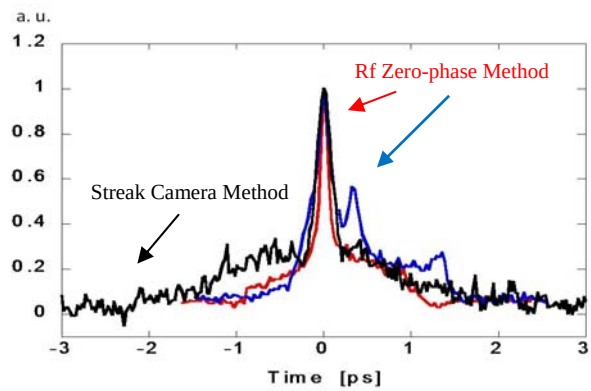

Figure. 5. Bunch-length data taken by the streak camera and the SCM, and the rf zero-phase crossing method. Red is at a bunching phase. Blue is at a debunching phase.

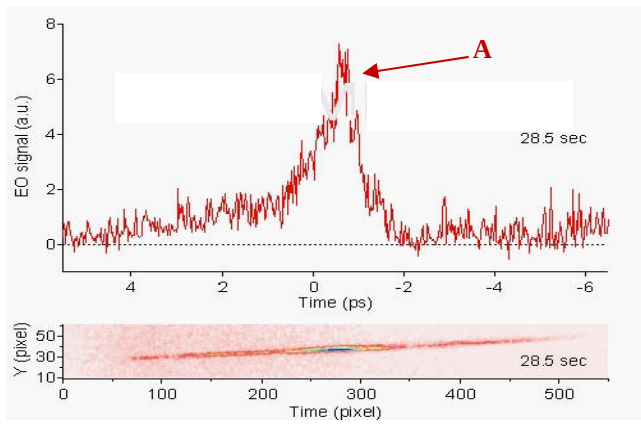

Figure. 6. Experimental result by E/O sampling with temporal decoding. The “A” could be the spiky lasing part.

EO sampling system

Figure 4 shows an electron bunch-length measurement system using the EO sampling method. EO sampling uses an optical polarizer and an electro-optical crystal, such as ZnTe, which detects the relativistic electric field of an electron beam. When the electron beam passes nearby the crystal, the electric field rotates the polarization axis of the crystal. Then, the combination of the polarization orientation between the polarizer and crystal picks up some part of an incident laser pulse of 800 nm TiSapphire to the crystal. The pulse length of this part corresponds to the electron bunch length. To detect this part, a temporal decoding method [6] using a BBO (β-BaB204) crystal as a correlator and a CCD camera with an image intensifier was used.

BUNCH-LENGTH MEASUEMENT RESULTS

Streak-camera and rf zero-phase crossing systems

Figure 5 shows the results of electron bunch-length measurements using the steak-camera method and the rf zero-phase crossing method. The bunch lengths observed by both methods were about 300 fs (FWHM), which corresponds to the spiky lasing part in the ID section, while the whole electron bunch length is about 1 ps. The bunch shape taken by the streak camera was obtained by superimposing 10 shots with which the individual bunch shapes were normalized at each peak point. The waveform measured by the rf zero-phase crossing method was single-shot data.

EO sampling system

The measured bunch length by EO sampling is shown in Fig. 6. The electron bunch length of a single-shot image in the figure is about 300 fs (FWHM), if we look at the spiky part, “A”, of the bunch shape, which could correspond to the lasing part. The whole bunch length is also 1~ 2 ps.

SUMMARY

The bunch length of the SCSS test accelerator was measured by three methods: the streak-camera method, an rf zero-phase crossing method, and an EO sampling method. The results of bunch length experiments using these methods were consistent; the measured bunch lengths were about 300 fs. This consistency mutually proved reliability of the measurement accuracy of the methods. Furthermore, the most important result is that the streak camera is mature technology with the optimum tuning, which directly measured the temporal structure of an electron beam bunch with femto-second resolution. We believe that our data taken around 300 fs (FWHM) bunch lengths by the systems are the first experimental results in the world, because of comparing these data.

The authors thank the members of the XFEL/SPring-8 project for their help.

REFERENCES

[1] T. Shintake *et al.*, Status of X-ray FEL/SPring-8 Machine Construction, Proc. of EPAC’08, (2008).
[2] T. Tanaka and T. Shintake (Eds.), SCSS X-FEL Conceptual Design Report, (2005).
[3] T. Shintake et al., *Nature Photonics* **2**, 555 (2008).
[4] D. X. Wang, *et al.*, Phys. Rev. E **57**, 2283 (1998).
[5] Streak camera catalog, Hamamatsu Phtonics K.K. (2009).
[6] G. Berden, *et al.*, Phys. Rev. Lett. **99**, (2007) 164801.
[7] Y. Otake *et al.*, Development Status of Beam Monitor System at XFEL/SPring-8, Proc. of PAC’09 (2009).
[8] H. Maesaka *et al.*, Development of The Microwave Spectrometer for The Bunch Length Measurement using Coherent Transition Radiation at The SCSS Test Accelerator, Proc. of the 6th Meeting of the PASJ (2006), in Japanese.
[9] H. Delsim-Hashemi *et al.*, Broadband Single Short Spectrometer, Proc. of FEL’05 (2005).

BEAM LIFETIME MEASUREMENTS WITH LIBERA BRILLIANCE

A. Kosicek, P. Leban, Instrumentation Technologies, Solkan, Slovenia
B.K. Scheidt, ESRF, Grenoble, France.

Abstract

The lifetime of the electron beam in a Synchrotron Light Source is an important parameter. Its precise measurement within a short time is an essential tool to evaluate properties and stability of a storage ring. In some cases, for example during short gas outbursts in the UHV vacuum chamber leading to rapid lifetime drops, it can be used as a useful diagnostic tool as well. Traditionally, dedicated PCTs (Parametric Current Transformers) are mostly used for this purpose. The idea to use Libera Brilliance Beam Position Processor instead came after the excellent quality of its sum signal was observed. Moreover, the measurement accuracy is greatly increased by averaging the lifetime measurements of all the individual stations, bearing in mind that there are typically more than hundred BPMs positioned around the ring. First measurements were performed on ESRF, showing very good performance potential. The article discusses the measurements, their results, the comparison with more classical methods, and the implementation of this feature in the Libera Brilliance software.

INSTRUMENTATION

Libera Brilliance is widely used as a beam position processor at third generation synchrotron light sources around the world. Its flexibility allows very fast wideband measurements on one side, fast feedback operation, and narrowband monitoring of the signals on the other. All this data is available simultaneously, enabling complete characterization of the accelerator system.

The native purpose of such instrumentation is of course the beam position measurement at different bandwidths. It was however noticed that the sum signal is very useful as well as it is proportional to the stored current in the ring. Specifically, the Slow Acquisition (SA) dataflow is used for slow monitoring of the position and comes at 10 Sps. It consists of four amplitudes, the derived Δ/Σ position and the derived sum value of four amplitudes.

MEASUREMENTS

All measurements were performed in the ESRF storage ring, where a total of 224 Libera Brilliance units are routinely used for the beam position monitoring. The injection at ESRF is scheduled twice a day, at 9 AM at 9 PM. The typical current in the ring is ~200 mA immediately after the injection, decreasing to a minimum value at ~150 mA before the next injection. A typical graph of sum value of one Libera Brilliance can be seen in Figure 1.

It can be assessed immediately that a single Libera Brilliance unit is already capable of a precise and reproducible beam lifetime measurement. Theoretically, all Libera Brilliances around the storage ring should of course measure the same beam lifetime.

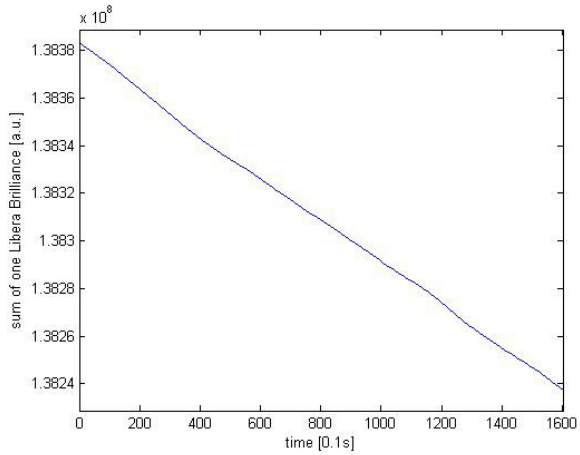

Figure 1: Decrease of the sum value on one Libera Brilliance through 160 s.

However, when reading the data from all units around the storage ring at the same time, few random units reported significantly different beam lifetime from time to time. Jumps in the lifetime value are just short spikes and are not really related to the beam lifetime change. The most frequent reason for them is a change in the fans speed due to temperature control loop inside Libera Brilliance. This phenomenon is depicted in Figure 2.

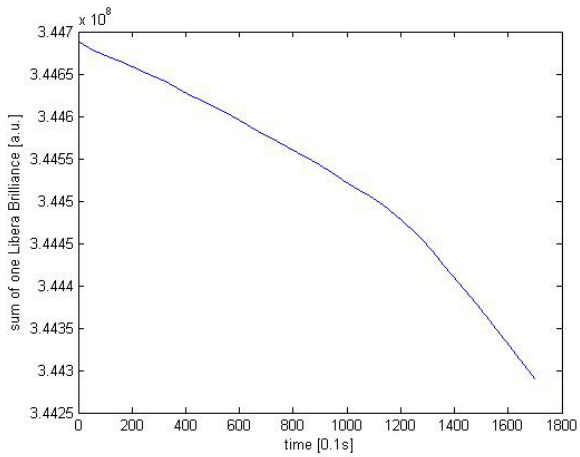

Figure 2: Decrease of sum value on this Libera was affected by the fans speed change.

This actually shows how sensitive the beam lifetime measurement is. The effect of the fans speed change can be even better observed on Figure 3. Six Libera Brilliances lifetime calculations are directly compared to recorded fans speed. Same colour denotes the same

Libera Brilliance unit. At certain point in time, the health daemon, which is controlling temperature inside Libera Brilliances, was stopped. The fans speed was manually set to 4600 rpm at that point. The effect of this change can be seen as a spike in lifetime measurement. Moreover, the Libera Brilliance, marked with red colour, had an oscillation in fan speed prior to daemon's stop. It can be directly seen that its lifetime calculation is not valid in such conditions.

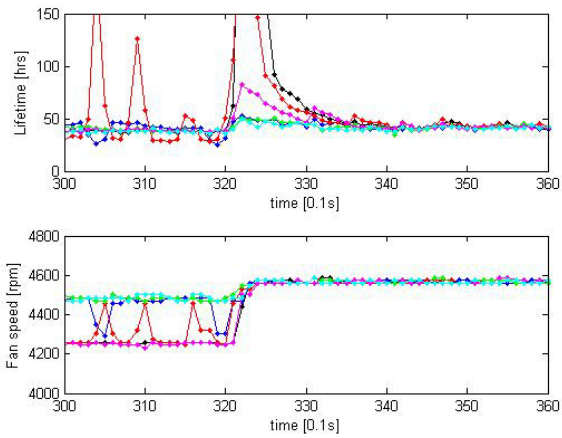

Figure 3: Fans speed fluctuation (below), affecting beam lifetime measurement (above).

In Figure 4, the sum value from all 224 Libera Brilliance units around the storage ring is normalized and plotted together:

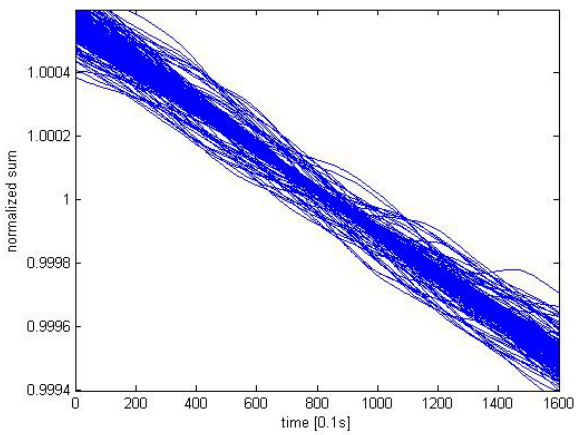

Figure 4: Normalized sum value from all 224 Libera Brilliance units around the storage ring.

It can be observed that majority of Libera Brilliance units report the sum values that are consistant, however, some are fluctuating around. The beam lifetime calculation, based on this data is given in Figure 5. It can be seen here even more easily how some calculated beam lifetime values are not stable. However, the big advantage of having a large number of instruments, each calculating the beam lifetime value, is that it can be easily determined which measurements are not valid.

Validity of data can be defined by setting the criteria. Individual values, which are considered as invalid, are discarded. Typically, beam lifetime value is useful for more than 3/4 of Libera Brilliance units around the storage ring. With ¾ of 224 units (=168) the improvement factor because of averaging is 13.

The beam lifetime measurements after this clean-up is shown in Figure 6, and after averaging in Figure 7.

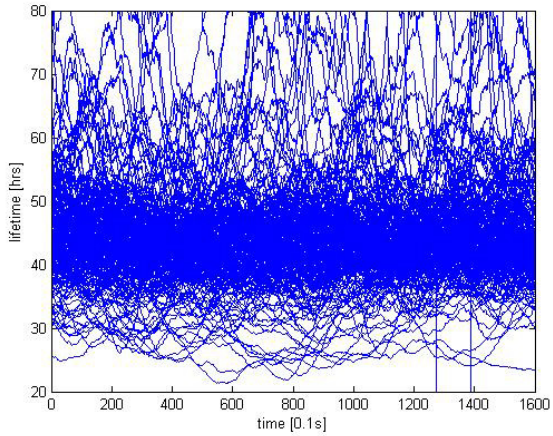

Figure 5: The lifetime from all 224 Libera Brilliance units, calculated from data on Figure 3.

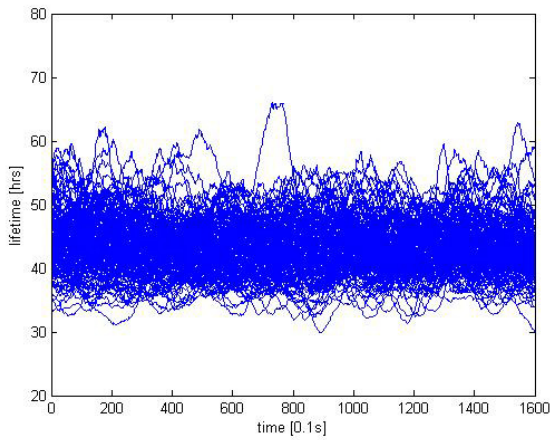

Figure 6: The beam lifetime measurements after the unstable ones are discarded.

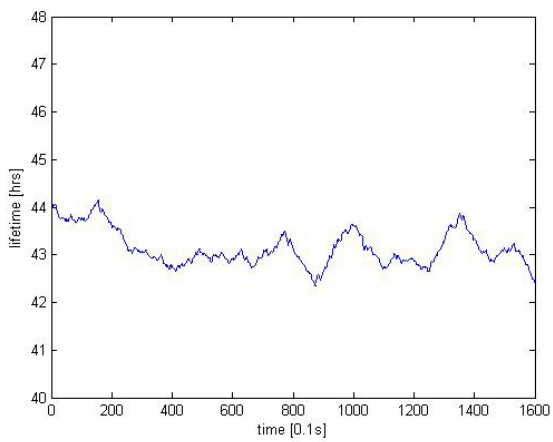

Figure 7: Accurate beam lifetime as the final result. Note: vertical scale is zoomed compared to Figures 5 and 6.

Comparison with existing current monitors

ESRF storage ring is equipped with three current monitors (PCTs). The comparison of the beam lifetime measurements with both systems was the next step. On Figure 8, the three PCTs are compared to Libera Brilliance units, separated into three groups [1]:

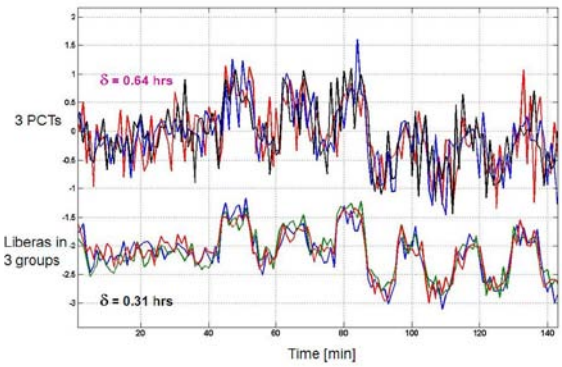

Figure 8: The comparison of three PCTs with Libera Brilliance units in three groups.

It can be seen that after averaging, the RMS of the measurement is lower with Libera Brilliance units. The long term performance was compared as well (see Figure 9), showing good matching of two instruments [1]:

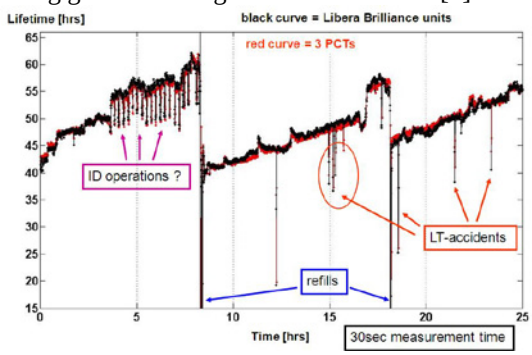

Figure 9: The measurements from both systems match and reveal the same phenomena.

Closer look at the beam lifetime accidents show that the measurement from Libera Brilliance units is a bit faster than the one from the PCTs [1]:

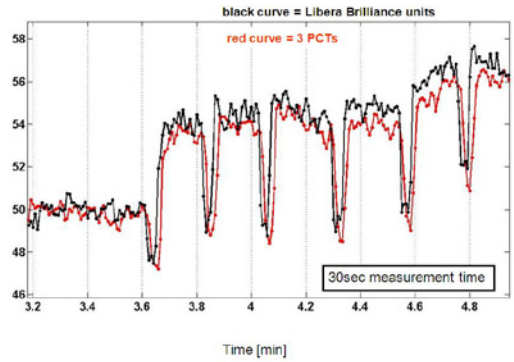

Figure 10: The zoom into real beam lifetime measurements.

The speed of measurements is important since it directly indicates the quality of the vacuum and the nature of so-called lifetime accidents. Such lifetime accidents are of serious concern for the ESRF, which is an aging Ring (20 years old) with many UHV chambers & components.

IMPLEMENTATION ON LIBERA BRILLIANCE

All the measurements and analysis above were done outside Libera Brilliance, based on the SA sum data, in Matlab®. It is however clear that by doing the calculation of beam lifetime on Libera Brilliance one could save a lot of data transport and network bandwidth. The measurement is faster and more reliable as well.

The implementation was done recently and is being tested on ESRF. Calculation is done continuously on latest SA samples (moving window). Beam lifetime value is calculated using the following equation [2]:

LT = (-1 *dt / ln (S(p) / S(p-dt))) / 3600 [hrs]

Where:
LT ... lifetime;
N ... window for calculation [SA samples];
n ... current SA sample;
dt ... time interval over which the LT is calculated [sec];
S(p) ... mean(S(n : n-N));
S(p-dt) ... mean(S(n-N-1 : n-N-N-1));
dt ... N * Tsa;
Tsa ... FREV / (SA_dec * DFA);
FREV ... revolution frequency in Hz;
SA_dec ... SA decimation factor, always 1024;
DFA ... FA decimation factor;

Most of the parameters are of course fixed because they are accelerator specific. The only parameter which can be set for beam lifetime calculation is the time window for calculation. It can be set runtime. The correct setting of this window is a compromise between resolution and response time. For all the measurements in this article the window of 30 s was used.

CONCLUSION

The use of the Sum signals of the numerous Libera Brilliance units in a Ring is shown to be very suitable for highly accurate beam lifetime calculations and of better resolution and response time than with PCT current monitors. This Lifetime measurement output is now added in the Libera Brillianc's functionality.

REFERENCES

[1] K. B. Scheidt, Status of ESRF BPM system, ppt presentation, Solkan, November 2009

[2] Instrumentation Technologies, Libera Brilliance User Manual v2.10, Solkan, February 2010

AN FPGA-BASED BUNCH-BY-BUNCH TUNE MEASUREMENT SYSTEM FOR THE APS STORAGE RING*

C.-Y. Yao#, Y.-C. Chae

Advanced Photon Source, Argonne National Laboratory, Argonne, IL 60439, USA

W.E. Norum

Lawrence Berkeley Laboratory, Berkeley, CA 94720, USA

Abstract

A bunch-by-bunch tune measurement system was developed for beam diagnostics and machine studies of Advanced Photon Source (APS) storage ring. It can be applied to such machine physics studies as characterization of transverse impedance, observation and identification of coupled-mode instabilities, and electron cloud effects. The system has a single-bunch and a multibunch operation mode. In single bunch mode tunes are processed with FFT. In multibunch mode the system excites a set of driven bunches with a frequency sweep signal, samples a set of monitored bunches, and extracts amplitude and phase information from sampled data using digital demodulation method. We report its hardware and software design, performance, and recent experimental results on the APS storage ring beam.

SYSTEM DESCRIPTION

The bunch-by-bunch tune measurement system was originally developed as a diagnostics tool for a transverse feedback system at the APS [1]. It now serves as an alternative of the original storage ring tune measurement system that uses spectrum analyzers.

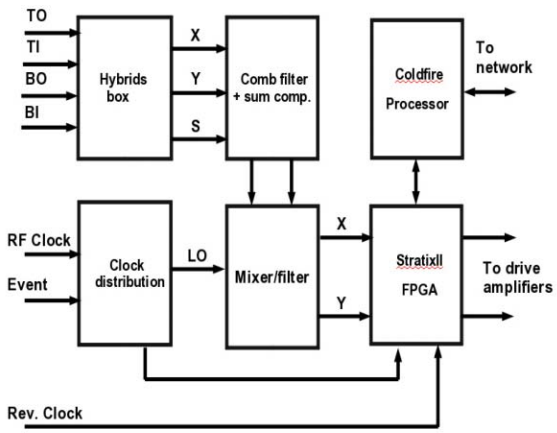

Figure 1: Block diagram of the tune measurement system.

Figure 1 shows a diagram of the system. The front-end circuit consists of a hybrid input box, a 3-tap comb filter and sum compensation circuit, and a down converter mixer. The LO input of the mixer is a 352 MHz clock signal directly derived from main rf source. The front-end and pickup stripline are shared by the tune measurement system and a transverse feedback system [2]. The tune measurement module consists of a StratixII DSP development board [3] for data conversion and processing, a ColdFire uCDIMM card as EPICS IOC, and a small daughter card for receiving timing synchronization signals from the APS even system. Other than this small daughter card, all components are commercial, off-the-shelf.

Two 12-bit 125 MHz ADCs on the FPGA board are used for beam position acquisition, one for each transverse plane. Two 14-bit 175 MHz DACs are used for generating chirp signals for both planes. Two trigger output channels provide synchronization with external excitation sources.

FIRMWARE PROCESSES

Figure 2 shows a block diagram of the tune measurement firmware. The ADC block acquires input beam signals at a rate of 117 MHz, or 1/3 of the storage ring rf frequency.

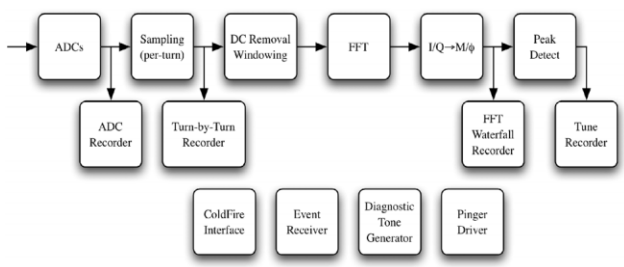

Figure 2: Block diagram of the tune measurement firmware.

The system has two operations modes: a single-bunch mode that provides tune measurement of any single bunch of the storage ring, and a multibunch mode that chirps a train of selected driven bunches and acquires tune data on another train of monitored bunches.

*Work supported by U.S. Department of Energy, Offices of Science, Office of Basic Energy Sciences, under contract No. DE-AC02-06-CH11357

#cyao@aps.anl.gov

In single-bunch mode operation fast Fourier transform (FFT) is performed on records of 2048 turn-by-turn samples. The FFT and rectangular-to-polar conversion are accomplished in less than 20 μsec. The FFT results are presented as an EPICS [4] waveform record. A waveform record contains magnitude components up to 128 FFT measurements of 1024 frequency points each. With typical pinging excitation patterns, this corresponds to an acquisition time of about 1 second.

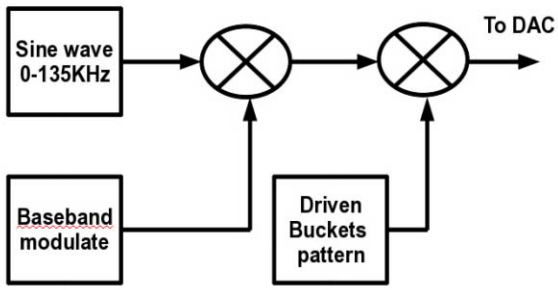

Figure 3: Block diagram of the chirping signal generator program.

A turn-by-turn waveform is available for recording raw ADC samples of beam position of up to 262144 turns. It is mainly used for offline tune processing, system diagnostics, and capturing of transient beam motions.

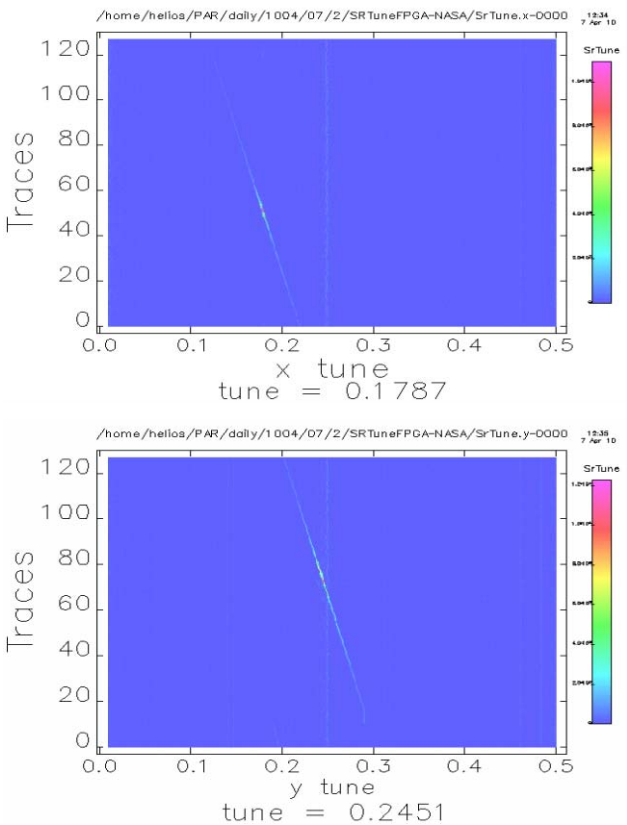

Figure 4: Contour plots of APS storage ring tune measurement results. The vertical axis is the trace number. Each trace represents about 8 ms. The vertical line in the middle of the plot is an unidentified noise sideband.

TUNE MEASUREMENT

The APS storage ring normally operates with high chromaticity in both planes and strong sextupole currents. The beam has a large tune spread. Centroid beam motion dissolves within 100 turns of a perturbation. This is mainly due to the de-coherence effect of a large tune spread. In order to achieve good tune measurement results, continuous chirping is necessary.

Figure 3 shows a block diagram of the chirping generator. A sine waveform tune frequency signal is first modulated with a DC (baseband) or a ±1 pulse (modulated). It is then modulated with a driven-bucket pattern pulse train. The modulated mode is necessary to avoid an AC coupling effect of the DAC output and amplifiers.

In single-bunch mode, the beam is excited by an external source -- a HP6396A network analyzer. Sampled data are FFT processed with a tune resolution of 0.001. The FFT result can be shown both in an amplitude versus tune plot or in a spectrograph. In the latter case, the time variation of spectrum can be reviewed easily. Figure 4 shows spectrographs of both the x and y tunes.

In the multibunch mode digital demodulation method is used to derive tune peaks. A chirping signal, which consists of a sequence of frequency points with each point lasting 2048 revolution periods, is generated by the FPGA and sent to the drive stripline to excite the beam. The digital waveform data of the same chirping signal is digitally demodulated with the beam position signal to produce amplitude and phase for each frequency point. Only amplitude data are further processed, and one data point is generated for each bunch and each frequency point. The driven buckets and monitored buckets are selectable.

A graphic interface application was developed to simplify operation of the system.

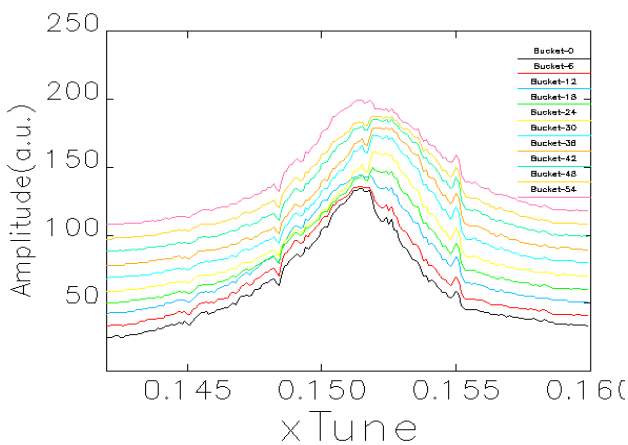

Figure 5: A plot of multibunch horizontal tune results with 6-bucket spacing showing a maximum tune shift of 0.001 in this case.

APPLICATION TO BEAM STUDIES

The multibunch mode is used to investigate possible ion trapping or electron cloud effects in the APS storage ring. In this case, a train of buckets is filled, and tunes of each buckets were measured. We have observed a horizontal tune shift of 0.001 to 0.004 between the leading and trailing bunches. Further study is needed to fully characterize the phenomenon. Figure 5 shows a plot of horizontal tune versus bucket number for a 6-bucket spacing bunch train.

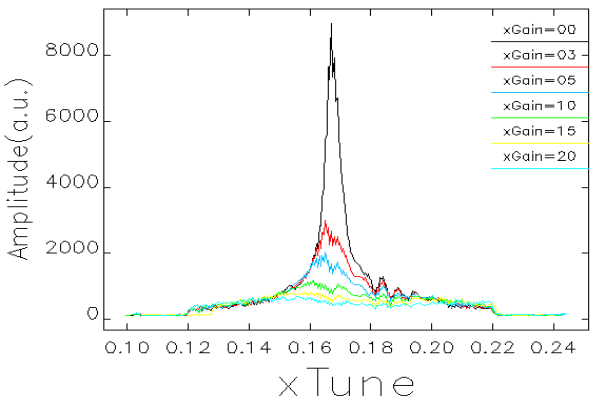

Figure 6: Horizontal feedback gain scan result.

The system is used to measure the damping time of the feedback system. Beam is excited by the tune measurement drive signal, and we scanned the gain of the transverse feedback system. The amplitude response of a damped oscillation excited at resonance frequency is proportional to damping time τ. A relative damping time can be estimated from the gain scan. Figure 6 shows a result of a horizontal gain scan.

Using the tune measurement system we successfully identified a 40 kHz noise that is generated by the switching power supplies of the vertical and horizontal faster correctors, which has an effect on the storage beam motion and impacts the function of feedback system. The noise was eliminated by installing additional filters on all fast corrector supplies.

The system can also be used to record injection transients. Figure 7 shows recorded horizontal beam motions. In the first plot, due to the strong amplitude dependency of tunes, the centroid beam motion of stored beam de-coheres within only 30 turns. In the second plot beams with different chromaticity are kicked with a 1 kV kicker pulse. Damping time increases as chromaticity decreases.

FUTURE UPGRADE PLAN

The current version of the hardware limits sample rate to 117 MHz, or sampling every third storage bucket. We plan to upgrade the front-end electronics and the ADCs to a sample rate of 352 MHz so it can measure arbitrary fill patterns, which is important for many study subjects.

We also plan to add a mode detection feature so the system can be used to monitor couple-bunch mode instabilities for equally-spaced fill patterns.

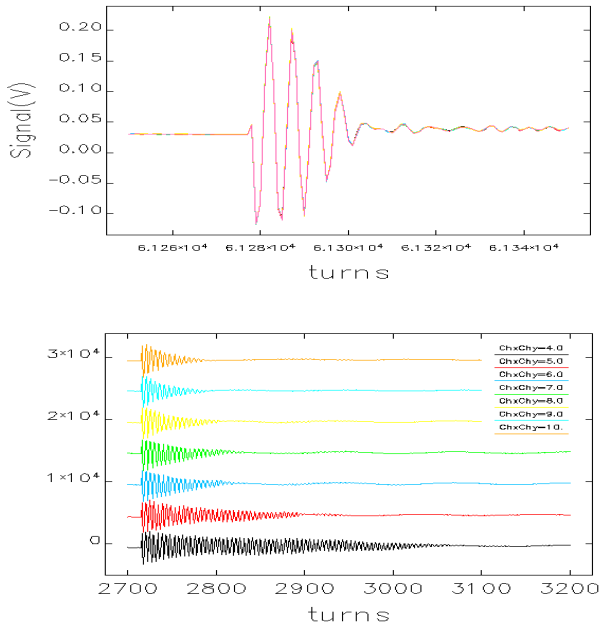

Figure 7: Top: storage ring injection transient. Bottom: horizontal beam motion after a kicker pulse with 1 kV amplitude with different chromaticity. Legend are chromaticity in both x and y planes.

CONCLUSIONS

We developed a bunch-by-bunch tune measurement system. It is a powerful tool for investigating beam instabilities, diagnosing feedback system, and for studying ion trapping, ion cloud effects, and injection transient.

ACKNOWLEDGMENTS

The authors acknowledge Hairong Shang, Louis Emery, Frank Lenkszus, Bob Laird, Chuck Gold, Randall Zabel and Pat Dombrowski for their contribution, discussions, and assistance for this work. We also thank APS operations staff for their support.

REFERENCES

[1] C.Y. Yao et al., "An FPGA-based Tune Measurement System for the APS Booster Synchrotron," Proc of BIW08.

[2] C.Y. Yao et al., "An FPGA-based Bunch-to-bunch Feedback System at the Advanced Photon Source," proc of PAC07.

[3] "Stratix II EP2S60 DSP Development Board Data Sheet," http://www.altera.com/products/devkits/altera/kit-dsp-2S60.html#documentation.

[4] "Experimental Physics and Industrial Control System," http://www.aps.anl.gov/epics/index.php

INJECTION BEAM DYNAMICS IN SPEAR3*

J. Corbett[1], W. Cheng[2], A.S. Fisher[1], X. Huang[1], W. Mok[3], J. Safranek[1] and S. Westerman[1]
[1]SLAC National Accelerator Laboratory, Menlo Park, CA 94025
[2]Brookhaven National Laboratory, Upton, NY 11973
[3]Life Imaging Technology, Palo Alto, CA 94301

Abstract

For the top-off operation it is important to understand the time evolution of charge injected into the storage ring. The large-amplitude horizontal oscillation quickly filaments and decoheres, and in some cases exhibits non-linear x-y coupling before damping to the stored orbit. Similarly, in the longitudinal dimension, any mismatch in beam arrival time, beam energy or phase-space results in damped, non-linear synchrotron oscillations. In this paper we report on measurements of injection beam dynamics in the transverse and longitudinal planes using turn-by-turn BPMs, a fast-gated, image-intensified CCD camera and a Hamamatsu C5680 streak camera.

INTRODUCTION

SPEAR3 is a 3rd generation, 3GeV storage ring light source with nominal emittance ε_x=10nm-radian. Single-bunch top-off injection occurs at either 8 hr or 10 min intervals with photon beamline shutters open [1]. Since the injector and BTS transport line were not specifically designed for top-off, it is particularly important to measure and understand dynamics of the injected beam in order to minimize perturbations seen by the users and to protect sensitive ID magnets in the lattice.

The injection system consists of a 10Hz booster synchrotron with single-bunch filling capability. Under nominal I=200mA operating conditions each stored bunch contains ~550pC (700uA) and each injected pulse contains ~30pC (40uA). The contrast makes measurement of the injected pulse difficult. A vertically-deflecting Lambertson septum brings the beam to SPEAR3 with the injected beam at x=-13mm. Several key parameters related to injection are listed in Table 1.

A number of diagnostic instruments are used to measure the injected beam dynamics. Centroid motion is monitored with fast turn-by-turn BPMs developed specifically for SPEAR3 [2]. Optical imaging of the charge distribution is possible at a diagnostic beam line which directs 3.5 x 6mrad of unfocused visible/UV light to an optical bench. After passing through a 6" diameter, f=2m collection lens the light is relayed to one of several diagnostic stations. An intensified, fast-gated camera can image the transverse beam profile at each turn [3] but the light intensity is low and in most cases must be averaged over consecutive injection events [4]. Similarly, in the longitudinal direction, a dual-axis streak camera can be used to image the injected beam profile by integrating over a series of injection pulses [5]. For a detailed analysis of the transient response of the injected beam into a storage ring see references [6,7].

*Work sponsored by U.S. Department of Energy Contract DE-AC03-76SF00515 and Office of Basic Energy Sciences.
[1]corbett@slac.stanford.edu

Table 1: SPEAR3 injection parameters

Injection amplitude	x=-13 mm
Stored beam size	310x20 μm, 20 ps
Stored beam, dp/p	0.1%
Damping times	4.2, 5.1, 2.8 ms
Injected beam size	~1.0x0.8 mm at SLM
Injected dp/p	0.07%

BTS TUNING AND TURN-BY-TURN BPMS

As reported in [8], a systematic program was carried out to optimize electron beam steering and lattice optics through the booster-to-SPEAR (BTS) transport line. Important elements of this work included removal of stainless steel windows intercepting the beam path and application of response-matrix analysis to correct the beam optics.

The injection kicker waveforms were then carefully matched and 6-D phase-space coordinates of the incoming beam adjusted by monitoring the bunch centroid motion on turn-by-turn BPMs. For these measurements, specially-designed Ecotek BPM receivers [2] mix the raw BPM signals down to an intermediate frequency $f_{IF} = 13f_0$ that is band-pass filtered and allowed to electronically ring several times while being digitized by high quality commercial digitizers. In order to monitor and compensate for changes in gain, a low-level calibration signal at $f_{cal} = f_{RF} - f_0/2$, is combined into the BPM long haul cables. Parallel digital receivers tuned to both f_{RF} and f_{cal} respectively allow for the calibration. The resulting digitally-processed data yields low-distortion, highly-accurate measurements of beam position on a turn-by-turn basis. For nominal stored-beam conditions the beam centroid resolution is of order 1μm.

For injected-beam measurements, the incoming single-bunch charge is only ~30pC so the BPM signals are relatively weak, -85dBm after cable loss, and the position resolution is only about 1mm. As a result, horizontal injection oscillations can be resolved but small amplitude vertical motion and synchrotron oscillations require averaging. In order to measure individual injection pulses, at each injection cycle injection kicker #3 (downstream of the injection septum) is triggered at the nominal injection time while injection kickers #1 and #2 (upstream of the septum) are mismatched and triggered 50ms late to kick out the stored beam [8].

Of particular interest, the synchrotron oscillation component was extracted via FFT processing and the initial phase-space coordinates of the motion used to match injected beam energy and timing. An example

where the injection beam is phase mismatched is illustrated in Fig. 1. In this case the synchrotron

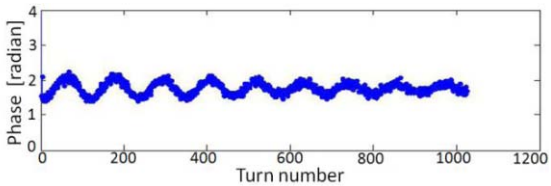

Figure 1: Synchrotron oscillations on the beam centroid due to booster/SPEAR timing mismatch.

oscillation amplitude is large, about 1 radian in rf phase. At 781ns per turn, the ~125 oscillation period agrees well with the nominal 10kHz synchrotron oscillation frequency. Although the beam arrival time can be adjusted manually, the phase drift typically requires adjustment several times per day. The source of error lies in temperature variation of the long-haul cable connecting the 476MHz SPEAR3 master oscillator to the 358MHz booster master oscillator. Various ways to automatically correct the phase error are being investigated including installation of a transmission line interferometer and direct measurement of the low-amplitude synchrotron oscillations on the injected pulse in the presence of stored beam. Once the injected beam energy has been optimized it typically remains stable over the course of several months [8].

TRANSVERSE BEAM DYNAMICS

A fast-gated, MCP-intensified PiMax camera was used to image the transverse profile of the beam at injection. Visible light focused through a commercial 1:5 lens onto the front-end photocathode yields a net de-magnification of M=0.59. A parallel optical path uses a combination of single-plane cylindrical lenses to yield a net de-magnification of M_x=0.7 and M_y=0.2 in the x/y planes, respectively [4,9]. In both cases the SR light passes through a vertical corner-periscope to create a 90 degree coordinate rotation. The horizontal beam axis and horizontal betatron motion are then oriented perpendicular to the optical bench and along the vertical axis of the camera CCD.

With the cylindrical lens system, the beam image has a tall, narrow orientation so that a fast, rotating mirror can sweep the image horizontally across the face of the camera. A series of spatially separated images can then be acquired in a single CCD exposure [9]. An example of data taken with the rotating mirror is illustrated in Figure 2. In this case a single stored-bunch is subject to an impulsive horizontal kick and beam distribution is imaged for all turns over the 10ms interval of mirror rotation. The betatron damping time agrees well with calculations and turn-by-turn BPM measurements. The rotated image of a single-pass to the right in Fig. 2 shows the effect of charge filamentation in phase space at t=120μs.

In principle single-bunch imaging within a full bunch train is possible using the 2ns photocathode gate but the

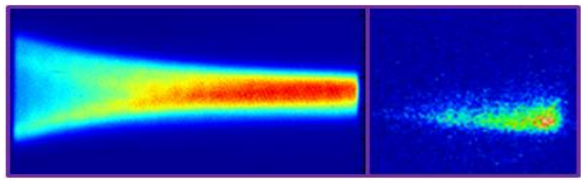

Figure 2: Damped horizontal betatron oscillation of stored beam, 10ms exposure & single turn at t=120μs.

images suffer from bleed-through of photons radiated by the rest of the beam. The camera gate extinction ratio is 10^6 [3], so a 3ms mechanical shutter is required to reject light arriving before and after the exposure to achieve clear images with ~10^8 extinction ratio.

Similar to the BPM system, turn-by-turn imaging of the injected beam is complicated by low signal levels. In this case, with all filters removed, each turn yields a few thousand photons per pass across the UV/visible camera detection bandwidth [10]. When the electron beam is well focused, light from a single injection pulse on a single turn can be amplified by the MCP to yield only a feint image even under darkroom conditions. As the beam filaments the photon flux is spread out over more pixels and the image becomes increasingly difficult to detect.

To enhance contrast, the PiMax software is configured to take multiple exposures of a single turn over a series of injection pulses. Starting from a t=-320μs pre-trigger pulse, light from ten's of separate injection events is integrated on the CCD chip to produce a single camera 'frame' before readout and advance to the next frame. The software *sequence* mode is used to set the frame exposure count and advance from turn-to-turn as the booster injects beam into SPEAR3. As described above, the charge from each injected pulse is ejected using mis-timed kickers prior to the next injection cycle.

Figure 3 shows an example of the multi-exposure,

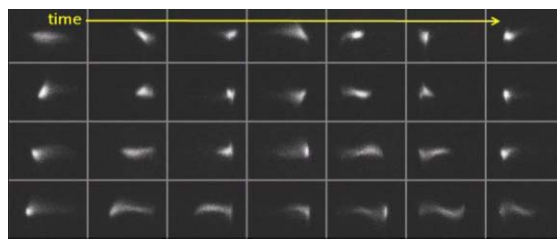

Figure 3: Transverse images of injected beam on consecutive turns. Coordinate rotations corrected.

multi-turn imaging technique utilizing the 1:5 lens branch line (no rotating mirror). The left/right motion is due to the inherent horizontal betatron oscillation in the injected beam and up/down motion indicates some degree of coupling. Each image represents a transverse projection of the charge distribution on consecutive turns. At the extremes in horizontal position the charge distribution appears as a relatively tight spot while exposures taken as the charge passes across the center of the screen generate 'comet-like' images. As sketched in Fig. 4, one plausible

explanation is that tune shift with betatron amplitude leads to charge filamentation. Other possible causes include chromaticity with energy spread and tumbling of a mismatched beam as it rotates in phase-space. Either way, the camera only sees images projected onto the x-axis from the full x-x' phase space distribution.

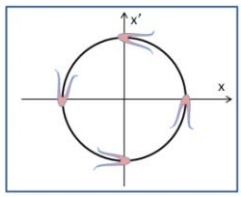

Figure 4:Charge filamentation in x-x' phase-space.

In a more complete scenario each image can be viewed as an x-y projection of the 3-D bunch structure or 'snake' of injected charge moving toward the observer. A full account of the transverse turn-by-turn images must then take into account evolution of the vertical and longitudinal charge distribution in time. The potential to image the beam in the x-t and y-t planes and thereby resolve the full snake-like 3-D charge distribution is discussed in the next section.

One consequence of charge filamentation is the appearance of rapid damping of the beam centroid as seen by the BPMs. Hence, as illustrated in Fig. 5, the nominal 3500-turn damping time can be masked by non-linear filamentation of the injected charge.

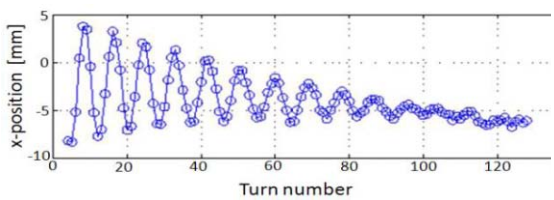

Figure 5: BPM measurement of the injected beam centroid in the horizontal plane.

Interestingly, the pulse-to-pulse beam dynamics, although complicated, is reproducible. The image of turn #28 shown in Fig. 6(a) was reproduced over many independent measurements despite the strong x/y coupling. In this case, it is likely the bunch has 3-D structure directed perpendicular to the page. In Fig. 6(b), a high-field wiggler field is removed and the same turn #28 demonstrates a different, reproducible distribution. Figure 6(c) shows yet another example of turn #28 when the SPEAR3 lattice is adjusted to low-alpha optics. Clearly the dynamical evolution of the injected charge distribution is a complicated function of subtle changes in the magnetic field distribution within the storage ring.

Further into the injection process, the charge distribution continues to smear in the x-y plane until the photon flux density becomes so low that details are difficult to resolve. The time sequence displayed in Fig. 7 shows how after a several damping times, the injected charge re-coalesces to the closed-orbit beam axis. Here, starting at t=100μs, the time evolution of injected charge is captured every 2ms, and the rf voltage was lowered to

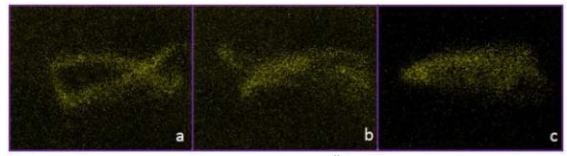

Figure 6: Comparison of turn #28 for three different magnetic lattice configurations

the level where only a few μA of charge remains to mark the stored beam axis but does not accumulate. For each exposure the camera gate was held open for 5μs. Although the charge couples into the vertical plane the injected charge capture efficiency is known to approach 100% under optimal injection conditions.

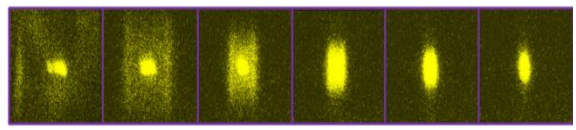

Figure 7: Injected charge distribution every 2ms.

LONGITUDINAL BEAM DYNAMICS

In terms of longitudinal coordinates, the injected beam is captured and damped in the non-linear potential of the rf system. Ideally the injected charge is matched in arrival time (synchronous phase), distribution in arrival time, average beam energy and energy spread. This section investigates injected beam dynamics in the longitudinal plane for long- and short timescales. In each case the Hamamatsu C5680 streak camera is used to collect data in dual-scan mode. By way of review, the streak camera reveals the longitudinal beam profile along the fast, vertical camera axis while the slower horizontal axis captures the evolution of time-dependent beam dynamics.

Since precise measurements of bunch length are not required here and the radiated light intensity is often low, no optical filters or color attenuators are used. For low intensity measurements the signal is integrated on the camera CCD using the inject/kickout scheme described above. The vertical time scale for the R2 synchroscan is 704ps full scale or 0.69ps-per-pixel.

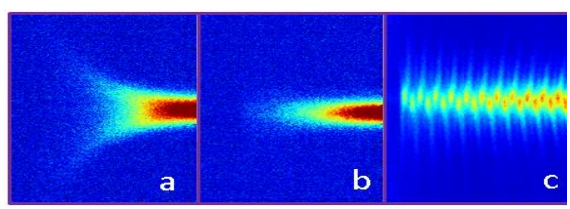

Figure 8: Dual-scan streak camera image of injected beam on 10ms and 1ms time scales.

Starting with long time scale injection phenomena, Fig. 8 shows beam capture during the first 10ms of beam capture with (a) injection phase mismatch and (b) correct timing during the first 10ms of injection ($\tau_{||,damp}$=2.8ms). The initial large-amplitude oscillations are not visible with correct timing. Figure 8(c) zooms in to the 1ms time

scale to illustrate the presence of 10kHz synchrotron oscillations, even with accurate injection timing.

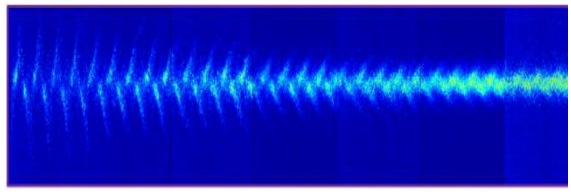

Figure 9: Evolution of longitudinal bunch distribution during first 3.5ms after injection.

Figure 9 shows the same injected charge sequence during the first 3.5ms, in this case rendered from a series of seven 500μs horizontal-sweep images stacked together in software. Similar to motion in the transverse plane, time evolution of the bunch in the longitudinal dimension can be influenced by filamentation and/or tumbling of the bunch in phase-space. In this case filamentation is caused by synchrotron tune shift with amplitude in the non-linear rf potential. The motion, however, maintains a relatively coherent structure as charge damps to the synchronous phase. In the damped condition the stored beam typically executes ~1ps rms coherent synchrotron oscillations.

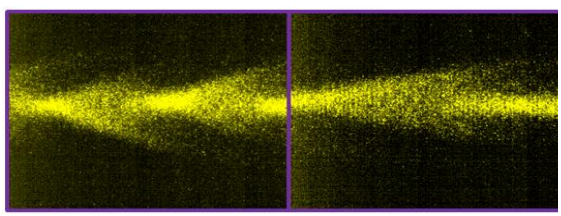

Figure 10: Evolution of injected charge distribution on 100μs and 50μs time scales at t=1.27ms.

Moving to later-time injection dynamics, Fig. 10 shows evolution of the charge distribution on the 100 μs and 50μs time scales after 1.27ms into the process. The tails observed in the images can be correlated with a highly-filamented time/energy phase-space structure projected to the time axis [11].

If we now zoom in to short-time dynamics, Fig. 11(a) shows clear evidence of phase-space mismatch in the injected beam. The projected charge density as seen by the streak camera periodically appears as a 'condensed' image and a 'diffuse' image alternating at twice the synchrotron frequency as the distribution rotates in phase-space. In the 'diffuse' projection the bunch length is found to be several hundred ps long. The corresponding energy spread can be extracted from the 'condensed' state. A good description of these phenomena with a comparison to simulation is given in [11].

In Fig. 11(b) the horizontal time scale is further reduced to 50μs so that initially the injected bunch can be resolved on a turn-by-turn basis in 2-D x-t coordinates. The small tilt or x-t correlation is indicative of charge dispersion in the horizontal plane as seen on the PiMax camera. After about 10 turns, a more complete de-coherence is evident.

Of note, the images in Fig. 11 were integrated over 30 injection pulses, again demonstrating a high level of injector stability over short time intervals. This is consistent with the turn-by-turn PiMax data shown above.

In order to further resolve turn-by-turn beam dynamics the optical beam transport line leading to the streak camera was modified to incorporate cylindrical lenses. The nominal streak camera configuration utilizes a Leice Acro 10/0.25 objective lens to produce a small focus at the entrance the slit of the streak camera. In the cylindrical lens configuration, a weak horizontal lens was used in conjunction with a strong vertical lens to produce

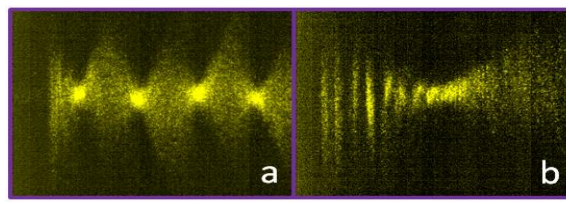

Figure 11: Evolution of charge injected bunch distribution on (a) 200μs and (b) 50μs time scales.

magnification in the horizontal direction and de-magnification in the vertical direction. The small vertical spot size is necessary for good time resolution.

The camera is then operated with a 500ns horizontal time base to capture single turns during injection. Similarly, by rotating the incoming beam with a dove prism, the bunch can be imaged in the y-t plane. In conjunction with the PiMax camera, the object was to capture a full rendering of the injected bunch in x-y-t coordinates. Unfortunately the initial results were ambiguous, in part because the horizontal magnification was too high and in part because the large amplitude betatron motion is hard to capture a turn-by-turn basis.

Variable RF Voltage

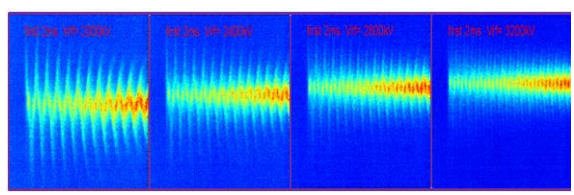

Figure 12: Variation of injection oscillations with increasing rf voltage (2.0, 2.4, 2.8 and 3.2MV).

Since the injected bunch is captured in the potential of the rf system, it is interesting to investigate time evolution of the injected beam dynamics with variable rf voltage. The effect is shown in Fig. 12 where the rf voltage is increased from 2.0MV to 3.2MV in steps of 400kV. Under matched timing conditions, the charge distribution is seen to extend from about +/-200ps in the low-voltage case to only about +/-50ps in the high-voltage case. As expected the synchrotron oscillation frequency and synchronous phase scale with $\sqrt{V_{rf}}$.

Injection Timing Errors

By adjusting the injected beam arrival time, one can see the longitudinal beam dynamics with timing mismatch, as shown in Fig. 13. In first four plots to the left the horizontal sweep time is 1ms, vertical synchroscan range is R2 (704ps) and the delay times are 0, 20, 30 and 45ps relative to synchronous injection. From these images it is clear that filamentation and/or phase-space mismatch cause the charge to disperse over a range of time much greater than the bunch centroid delay time. The motion shown furthest to the right was taken in R4 synchroscan mode has 150ps injection delay. In this case the vertical time scale is 1687ps and the injected bunch exhibits coherent dipole-mode oscillations.

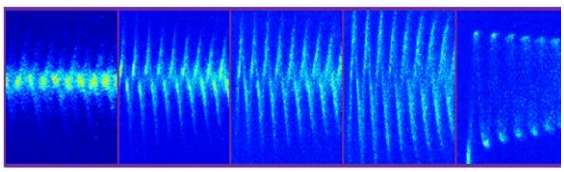

Figure 13: Longitudinal injection oscillations with arrival time error Δt=0, 20, 30, 45 and 150ps (R4).

SUMMARY

SPEAR3 is presently moving toward top-off operation at 10 min injection intervals. The incident charge must be well matched in the transverse and longitudinal dimensions for efficient capture, radiological concerns and ID protection. Turn-by-turn BPMs are used to control the 6-D launch conditions into the storage ring. Synchrotron light diagnostics are used to monitor different projections of the charge distribution. The fast-gated camera shows evidence of filamentation in the horizontal plane caused by tune shift with betatron amplitude and/or optical mismatch. In the longitudinal plane the correct timing, beam energy and phase-space distribution are needed to minimize turbulence in the rf bucket. Future studies will concentrate on reconstruction of the 3-D structure of the inject pulse at early times to understand and improve matching conditions.

ACKNOWLEDGEMENTS

We gratefully acknowledge the advice and assistance of Bill Cieslik, the SPEAR3 operations staff and the SLAC radiation physics department.

REFERENCES

[1] J. Schmerge, et al, “Summary Report on SPEAR3 top-off injection safety”, SSRL-AP-007, 2009.
[2] J. Sebek, “BPM system electronics design”, SSRL-ENG-NOTE M594, and J. Sebek, *et al*, “Design and performance of SSRL beam position electronics”, these proceedings.
[3] Roper Scientific, PiMax Camera, UV enhanced, www.princetoninstruments.com.
[4] W. Cheng, et al, “Fast-gated camera measurements in SPEAR3”, PAC09, Vancouver, Canada, 2009.
[5] W.Cheng, A.S.Fisher and J.Corbett, “Streak camera measurements in PEP-II and variable optics in SPEAR3”, BIW08, Lake Tahoe, CA (2008).
[6] H. Moshammer, ‘Transient response of the beam after injection in a storage ring”, NIMA 323, (1992).
[7] H. Moshammer, “Moments and characteristic function of a nonstationary particle distribution after injection”, Phys. Rev. E, Vol. 48, 3 (1993).
[8] J. Safranek, *et al*, “Optimization of the booster to SPEAR3 transport line for top-off injection”, PAC09, Vancouver Canada, 4-8 May, 2009.
[9] A.S. Fisher *et al.*, “Turn-by-turn imaging of the transverse beam profile in PEP-II”, BIW06, Batavia, IL, 1–4 May 2006.
[10] J. Corbett, et al, “Visible light diagnostics at SPEAR3”, SRI09, Melbourne, Australia, 2009.
[11] J. Byrd and S. De Santis, “Longitudinal injection transients in an electron storage ring”, PRST-AB, Vol. 4, 024401 (2001).

LHC BEAM STABILITY AND PERFORMANCE OF THE Q/Q' DIAGNOSTIC INSTRUMENTATION

R.J. Steinhagen, A. Boccardi, M. Gasior, O.R. Jones, S. Jackson (CERN, Geneva, Switzerland)

Abstract

The BBQ tune (Q) and chromaticity (Q') diagnostic systems played a crucial role during the LHC commissioning while establishing circulating beam and first ramps. Early on, they allowed to identify issues such as residual tune stability, beam spectrum interferences and beam-beam effects – all of which may impact beam life-times and thus are being addressed in view of nominal LHC operation. This contribution discusses the initial beam stability in relation to the achieved instrumentation sensitivity, corresponding tune frequency and Q' resolution.

INTRODUCTION

The LHC requires excellent control of particle loss which – with the tunes being in the vicinity of third-order resonances – implies an excellent control of tune, coupling and chromaticity effects. Relying on the Base-Band Tune meter (BBQ, [1]), the base-line Q/Q' diagnostics chain was widely considered to be a 'work-horse' from Day 1 of LHC commissioning and could since be operated with no hardware-, minimal software- and only a few beam-dynamics related issues. While the general system overview is given in [2], this contribution focuses on the system's performance and issues that arose during initial beam operation.

BBQ PERFORMANCE

Due to the BBQ's nm-level sensitivity, most of the tune and corresponding chromaticity measurements could be done with residual beam excitation using one of the two Fourier analysis-based systems per beam. Figure 1 shows a typical non-excited LHC beam oscillation magnitude spectrum that has been calibrated against the LHC BPM system. The spectrum is based on an acquisition of 8192 turns (corresonding bin bandwidth is about 0.72 Hz) and normalised so that the spectral amplitude has a one-to-one relation with the r.m.s. amplitudes in time-domain for single-tone frequencies. The corresponding amplitude of broad-band perturbations require an integration over the given bandwidth using this scheme. Thus, the residual tune oscillations at $q_h \approx 0.292$ and $q_v \approx 0.277$ have r.m.s. oscillation amplitudes between 0.1 and 1 μm in the time domain. The vertical tune oscillations being typically ten times stronger than the horizontal ones are typically also visible in the horizontal plane. A number of additional lines and a broad-band excitation around 0.31 f_{rev} are also visible in the spectrum.

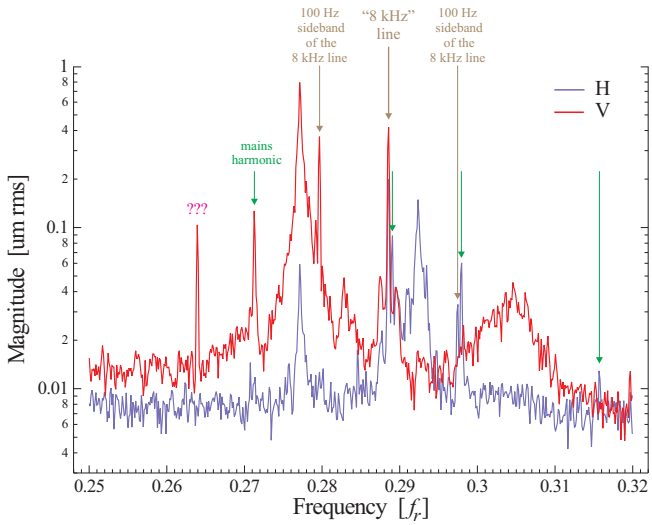

Figure 1: Typical LHC beam spectrum zoomed-in around the tune working points.

Based on this measurement, the BBQ turn-by-turn resolution is estimated to be better than 1 μm. Nevertheless, a full set of tune beam exciters (tune kickers, transverse damper exciters and an experimental strip-line based, low-amplitude and low-noise exciter) were commissioned.

FFT-based Q-Tracking

The BBQ oscillation data is typically processed using Fourier-analysis (FFT) and Phase-Locked-Loop (PLL) based systems described in [3, 4]. Figure 2 shows an exemplary FFT-based measurement of the tune and intensity evolution during the third LHC ramp with the tune feedback being switched 'off'.

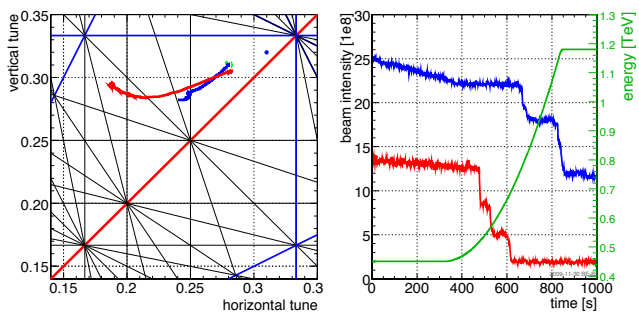

Figure 2: Tune and intensity evolution during the third ramp (2009-11-30).

The intensity and tunes of 'Beam 1' (B1) and 'Beam 2' (B2) are indicated in blue and red, respectively. The resonance lines are indicated in the tune diagram up to the sixth order, with the first and second orders drawn in red, the third order in blue, and higher orders in black with decreasing line width with increasing order. The intensity losses are correlated with the tunes crossing the fourth and fifth order resonances. The source for these drifts remains to be identified.

The tune data of the inital ramps was used as feed-forward corrections for the successive ramps and – for a well pre-cycled machine – reached fill-to-fill tune reproducibilities of about $\pm 3 \cdot 10^{-3}$. However, this limit was frequently exceeded due to varying magnetic pre-cycles, for instance, after an access or magnet quench that caused tune perturbations up to ± 0.02 during the following ramp that was not well described and thus not compensated for by the magnetic field description model, within the desired tolerances. Thus the tune feedback was routinely deployed during almost every ramp to compensate for these residual non-reproducibilities [6]. Figures 3 show two horizontal BBQ ramp spectra with feed-forward corrections only and with tune feedback being switched 'on'. Tune stability both without and with tune feedback around the nominal working points ($Q_h = 64.28$ & $Q_v = 59.31$) is visible. The tune stability with feedback is typically 10^{-3} during the snap-back, better than 10^{-4} during the rest of the ramp, and essentially limited by the residual tune ripple at injection and effective feedback bandwidth.

The FFT based system further facilitated the fast commissioning of the β^* squeeze within a few days. Figure 4 shows an exemplary evolution of the tune eigenmodes and corresponding unperturbed tunes taken during first squeeze attempt. The multiple crossing of the unperturbed tunes –

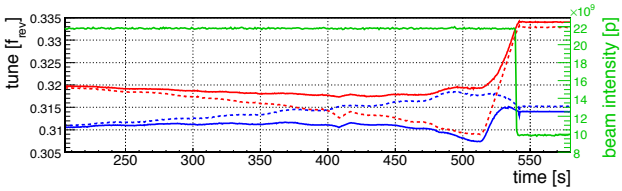

Figure 4: Tune evolution during the first squeeze to $\beta^* = 2\,\mathrm{m}$. The eigenmodes (solid lines) and tunes (dashed lines) are indicated in blue for the horizontal plane, and in red for the vertical plane.

which are the tunes in the absence of betatron coupling.– and the crossing of the third order resonance causing particle loss are visible. The same tune and coupling measurements were used as corrections, leading to the next squeeze that successfully reached a β^* of 2 m in all interaction points

An extraordinary tune measurement resolution of 10^{-6} has been achieved, which is illustrated in Figure 5, showing the tune evolution during the first long physics fill with colliding beams and squeezed optics at 3.5 TeV. In this particular example, the residual tune oscillation is dominated by energy fluctuations driven by tidal changes of the machine circumference causing energy modulations, and in turn is propagated to the tune via chromaticity. The maximum momentum amplitude of $\Delta p/p \approx 3 \cdot 10^{-5}$ and modulation period of about 12 hours makes this measurement probably one of the the slowest high-precision chromaticity measurements achieved in any accelerator to date.

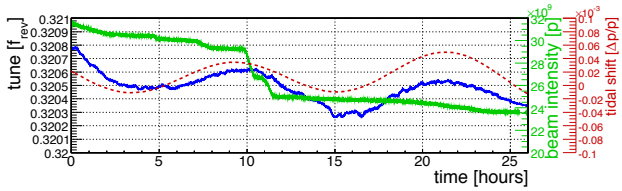

Figure 5: Vertical tune evolution and tidal-driven energy changes during the first long physics collisions.

PLL-based Q-Tracking

The tune phase-locked-loop systems were also commissioned for both beams. The Q-PLL was designed for beam scenarios when the residual tune oscillations do not allow sufficient diagnostics with the FFT-based system, and is a prerequisite for continuous chromaticity tracking, particularly during the ramp. A typical beam-transfer-function (BTF) measurement is shown in Figure 6. With the given

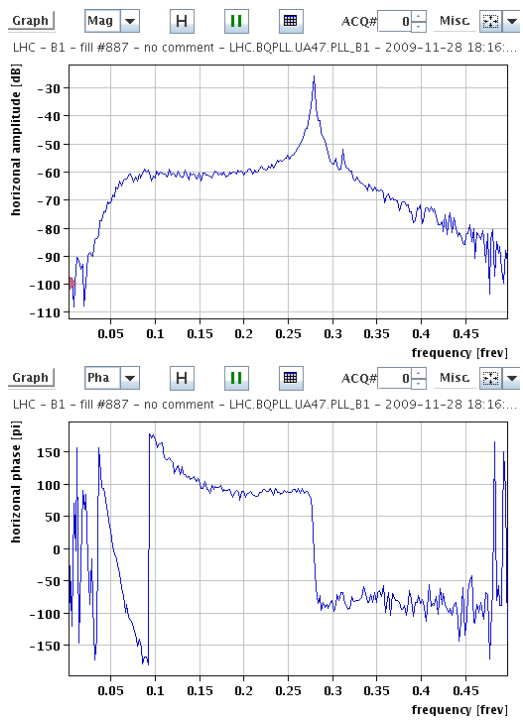

Figure 6: Full-range horizontal Q-PLL BTF example.

phase compensation, the measured BTF response is sufficiently linear and corresponds to model expectations that allow tune tracking operation within the frequency range of about 0.15 and 0.45 f_{rev}. Besides depending on the machine tune itself, the BTF is also an indicator of high-order beam physics effects. The loop gains and phase compensation established with the BTF taken during the initial commissioning may need to be re-verified for higher bunch in-

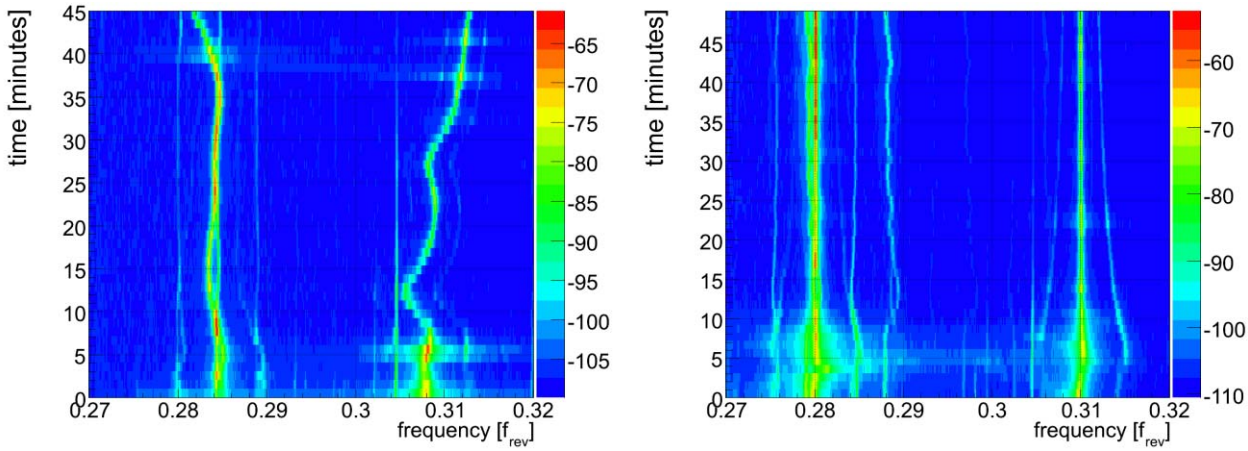

(a) Feed-forward (Q-FB 'off')

(b) Q-FB 'on'

Figure 3: Horizontal tune spectra taken during the ramps without and with tune feedback being switched 'on'. The magnitude of the residual oscillations has been colour-coded in a 'dB' scale.

tensities, other bunch configurations, and machine settings.

A Q'-Tracker measurement based on momentum modulation induced tune changes is shown in Figure 7. The induced tune modulation and amplitude reduction before and after the chromaticity trim of 10 units is visible. The momentum has been modulated with an amplitude of about $\Delta p/p = 10^{-4}$ and a frequency of 1.0 Hz. The measured loop-gain response relation agree to first order with the underlying theoretic model assumptions and the loop was thus able to track these fast tune changes. For the initial tracking tests, the driven excitation amplitudes were comparable or only slightly larger than the residual tune oscillations, thus resulting in a comparable frequency tracking resolution as for the FFT-based system.

CHROMATICITY TRACKING

The baseline Q' diagnostics essentially relies on the classic dependence of small $\Delta p/p$ momentum-driven tune modulations on the machine chromaticity and was prototyped at the CERN SPS [7]. The inital LHC baseline Q/Q' diagnostic chain foresaw the PLL as a tracker of these tune oscillations. However, its operation was impractical due the strong residual tune oscillations that would require larger PLL-driven beam excursions. Since the FFT-based tracking provided sufficient tune tracking, chromaticity was thus mostly measured by demodulation of the FFT-based tune tracking data. Figure 8 shows a typical chromaticity tracking example during an LHC ramp. Due to residual errors in the magnetic field description model, the chromaticity snap-back is only partially compensated, causing Q'_H to drop and Q'_V to rise by about 10 units at the start of the ramp. For the time being, these Q' transients are mitigated by raising and lowering the corresponding component at injection, and the data primarily used to re-fit and improve the magnetic field model. While the initial Q' was designed for momentum modulations of $\Delta p/p = 10^{-5}$ and modulation frequencies of 2.5 Hz, the FFT-based chromaticity tracker achieved the targeted Q' resolution of better than one unit, with the chosen momentum modulation of $\Delta p/p = 10^{-4}$ and modulation frequency of 0.2 Hz . Once accelerating higher beam intensities that require more precise chromaticity control, it is planned to use this chromaticity tracker as an input to the chromaticity feedback.

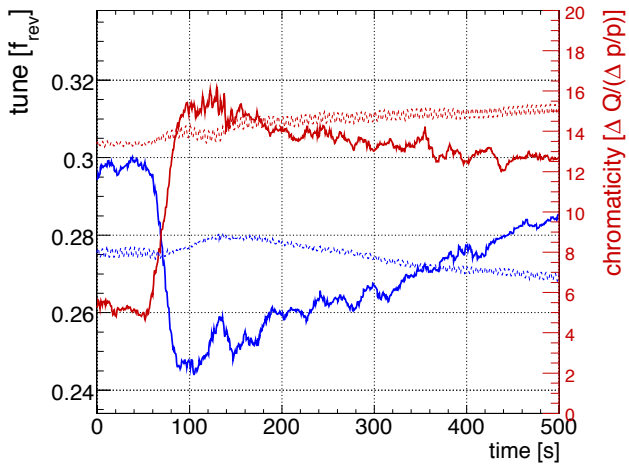

Figure 8: Chromaticity tracking during the energy ramp. The chromaticities (solid lines) and modulated tune signals (dashed lines) are indicated in blue for the horizontal and in red for the vertical plane.

Q/Q' DIAGNOSTICS OPERATION AND BEAM STABILITY ISSUES

Since any feedback performance is tightly linked to the underlying model and instrumentation performance, much time was spent on verifying the Q/Q' beam instrumentation systematics and residual beam stability. During early commissioning, some effects that could impact beam performance and that affect tune and chromaticity diagnostics operation were identified:

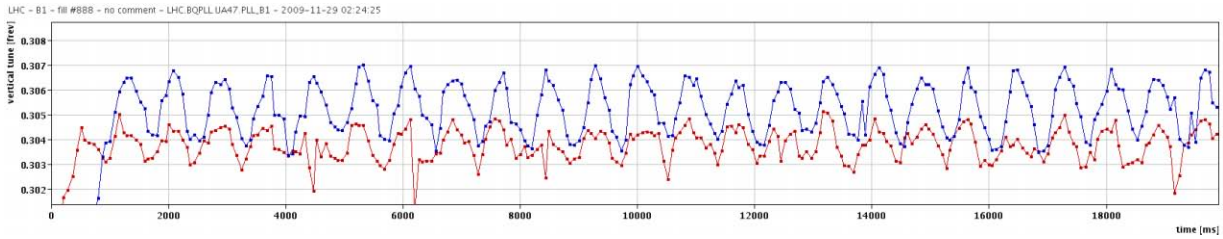

Figure 7: PLL tracking of momentum-induced tune modulation before (blue) and after a $\Delta Q' = 10$ trim (red).

- residual amplitude tune oscillations,
- residual tune jitter, and
- various spectra perturbations

deteriorating beam emittances and life-time.

Residual Tune Oscillations

Most tune measurements could be performed without any explicit beam excitations due to the residual um-level tune oscillations by the beam. In addition to the tunes, a number of non-tune beam signals are visible in Figure 1: a broad-band excitation signal around the nominal vertical tune working point (0.31), colloquially referred to by the operational crew as 'The Hump', a narrow-band excitation at a constant frequency of 8 kHz or $Q = 0.2886$, and various smaller-amplitude discrete interference lines mostly believed to be related to mains harmonics. In this particular example, the vertical tune was deliberately set below the horizontal tune working point to investigate and mitigate the effect of the broad-band excitation source, discussed in subsequent sections.

While these tune oscillations are beneficial with respect to the FFT-based tune diagnostics, they contribute to an increase in beam size, reduction of beam life-time and reduced performance of the Q-PLL system. The latter implicitly relies on the assumption that the main excitation and amplitude contribution to the tune resonance is driven by the PLL. Since the observed residual oscillations are not (systematically) correlated to the PLL excitation, they de-facto translate to an effective rise of the beam noise floor as seen by the PLL, and thus causes either a reduced PLL measurement resolution or necessitates increased excitation amplitudes. While the transverse damper operation would likely attenuate the base-band oscillations, this will also make a reliable tune diagnostic more challenging, as the PLL's closed-loop response would, in this case, not only depend on the beam but also on the entire transverse damper closed-loop transfer function.

Tune Stability

In order to be transparent for regular operation, momentum modulations in the order of 10^{-5} were initially envisaged. With the desired Q' resolution of one unit, this corresponds to a required tune measurement resolution of also about 10^{-5}. While the given BBQ signal-to-noise ratio supported tune resolutions down to 10^{-6}, the residual measured tune stability was several orders of magnitude larger at injection, as illustrated in Figure 9, which shows the relative tune changes during the third LHC ramp. Filtering

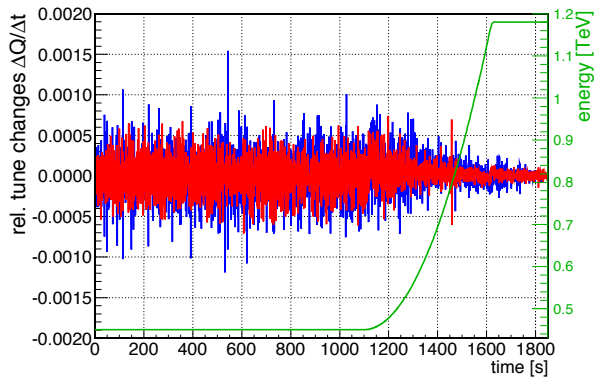

Figure 9: Residual tune noise during injection and ramp.

slow tune drifts below 0.1 Hz, the residual short-term stability was typically about $\pm 5 \cdot 10^{-4}$. This tune frequency noise proved to have little or no particular frequency or chromaticity dependence, but was rather 'white noise'-like. While this random tune modulation is believed to have less impact on life-time or beam-beam effects, it implies larger required $\Delta p/p$ modulations in the order of 10^{-4} for the Q'-tracker operation, which may be impractical for everyday operation and limits its usage to ramp diagnostics and boot-strapping of selected ramps. Though the tune frequency stability improved significantly as the beams are accelerated, the Q'-tracker is most needed at injection energies to allow snapback diagnostics during the start of the ramp. The tune trim quadrupoles may be one of the perturbation sources as they are usually used with very small milli-Ampere-level currents, while their maximum current rating is 600 A. The corresponding typical current to tune trim relation is given by Equation 1:

$$\begin{pmatrix} \Delta I_{QTD}\,[\mathrm{A}] \\ \Delta I_{QTF}\,[\mathrm{A}] \end{pmatrix} \approx \frac{p\,[\mathrm{GeV}]}{450\,\mathrm{GeV}} \cdot \begin{pmatrix} +4.3 & +22.2 \\ +22.7 & +3.9 \end{pmatrix} \cdot \begin{pmatrix} \Delta Q_H \\ \Delta Q_V \end{pmatrix} \quad (1)$$

While a small, horizontal tune shift of $\Delta Q_H = 10^{-4}$ at 450 GeV causes current changes in the order of 2.2 and 0.4 mA for the focusing (RQTF) and defocusing (RQTD) trim quadrupoles, the measured current stability ranged between 1 and 10 mA for some corrector circuits, which could possibly explain the measured effect. Individually powered strong quadrupoles such as the warm insertion or triplet

quadrupoles could be also sources for these tune perturbations. Further studies are required to fully assess these effects.

Spectral Perturbations

Besides the residual tune oscillations, the beam spectrum also contains other strong non-tune excitation lines, as visible in Figure 1. In case the beam tune is close or on these excitations, it gets resonantly excited, leading to emittance blow-up and reduced beam life-times. These additional lines are particularly problematic for the FFT-based tune diagnostics that relies on the fact that the tune line is the strongest spectral component within the given search window. However, in this case, the Q-PLL is less affected by these lines as these are not strictly phase coherent with the PLL excitation.

The narrow-band 8 kHz line was caused by the UPS switching power-supplies and, among other systems, was propagated by the transverse damper exciter (ADT) via its input to the beam. Yet, even with the ADT being switched 'off' and these perturbations being filtered within the ADT, a small portion of the 8 kHz component prevailed, which is being further investigated. In any case, their effect is expected to pose less problems as the 8 kHz and other mains harmonics are fixed in frequency and not in the vicinity of the nominal tune working points.

The source of the broad-band excitation signal around the nominal vertical tune working point (0.31) visible in Figure 1 remains elusive. Similar to the 8 kHz lines, once this perturbation is in the vicinity of the tune, the beam gets resonantly excited, subsequently decreasing beam lifetime. While the effect has been observed on both beams, it is more dominant in the vertical plane of B2. A higher temporal analysis revealed that the broad-frequency distribution is actually caused by a narrow-band single frequency with the same shifting mean frequency for both beams, as shown in Figure 10. The central frequency of the hump shifted typically between 0.15 and 0.45 f_{rev} over a duration of a few minutes to hours. The B1 to B2 hump

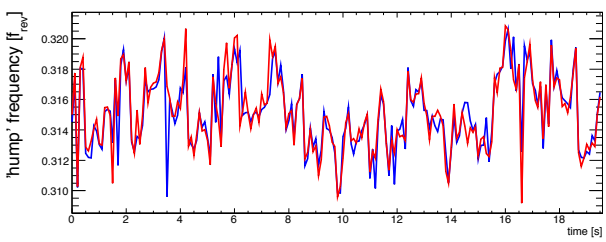

Figure 10: Beam 1 (blue) and Beam 2 (red) 'hump' frequency change.

frequency correlation factor is about 0.896. Nevertheless, the 'hump' is visible independent of whether there are one or two beams circulating in the machine. The magnitude spectrum of the hump frequency shift as a function of time revealed a $1/f$ dependence. As visible in Figure 1, the amplitude of the 'hump' corresponding to a few hundred nano-metre is extremely small and – provided it is caused by a single dipolar-type kick – corresponds to a deflection angle in the order of a few nano-rads. Due to the huge number of elements in the machine that a priori could potentially create these minuscule deflections, the identification and location of the true perturbation source proved to be extremely difficult. Based on switching 'off' given accelerator elements, the orbit correctors, transverse damper exciter, injection septa, transfer lines, pre-injector accelerators, experimental magnets and higher-order magnets could be ruled out as the cause for the 'hump'. Despite a series of investigations, the true source of the 'hump' remains unknown, and its investigation and mitigation is a priority of the ongoing LHC commissioning.

CONCLUSIONS

The commissioning of the tune and chromaticity diagnostic chain advanced well, and facilitated a fast and reliable establishing of ramps, β^* squeeze, and the identification of potential beam stability issues early on such as residual tune oscillations, tune frequency ripples, and spectral interferences. Due to the BBQ's high sensitivity for small beam oscillations, the FFT- and PLL-based tune systems system could achieve measurement resolutions between 10^{-4} and 10^{-6} depending on energy and mainly limited by the available signal-to-noise ratio of the tune peaks. Derived from the tune trackers, the chromaticity tracker achieved a chromaticity resolution of about 1 units on a regular basis facilitating. While the initial performance is sufficient for present operation, some effects such as the residual un-explained tune oscillations, the large tune jitter during injection and the 'hump' will need to be addressed in view of nominal LHC operation.

REFERENCES

[1] M. Gasior, O.R. Jones, "The Principle and First Results of Betatron Tune Measurement by Direct Diode Detection", CERN-LHC-Project-Report-853, 2005.

[2] A. Boccardi et al., "An overview of the LHC Transverse Diagnostics Systems", CERN-BE-2009-002

[3] A. Boccardi et al., "The FPGA-based Continuous FFT Tune Measurement System [..]", CERN-AB-2007-062, 2007

[4] R.J. Steinhagen, "Influence of Varying Tune Width on the Robustness of the LHC Tune PLL and its Application for Continuous Chromaticity Measurement", CERN LHC Project Report 1027, 2007

[5] A. Boccardi, "The LHC PLL System for Q, Q' [..]", CARE-Workshop, Chamonix, December, 2007

[6] R.J. Steinhagen, "Feedbacks on Tune and Chromaticity", DIPAC'07, 2007

[7] R.J. Steinhagen et al., "Results of the LHC Prototype Chromaticity Measurement System Studies in the CERN-SPS", EPAC'08, 2008

HIGH RESOLUTION BEAM ORBIT MEASUREMENT ELECTRONICS BASED ON COMPENSATED DIODE DETECTORS

M. Gasior, R. J. Steinhagen, CERN, Geneva, Switzerland

Abstract

A high resolution beam position monitor (BPM) electronics based on diode peak detectors has been developed at CERN. The circuit processes the BPM electrode signals independently, converting the short beam pulses into slowly varying signals which can be digitized with high resolution ADCs operating in the kHz range or even measured with a DC voltmeter. For signals with peak amplitudes larger than some hundred mV the non-linear forward voltage of the diodes is compensated by a simple network using signals from two peak detectors, one with a single and the second with two diodes in series. This contribution presents results obtained with the first prototype in the laboratory and with the CERN-SPS beam. Ongoing development and possible future applications of the technique are also discussed.

INTRODUCTION

Diode peak detectors have been used at CERN for processing BPM signals in tune measurement systems [1] and recently for observing beam motion of very small amplitude [2]. For these applications the detector DC components related to beam position are rejected and only AC beam motion signals are processed. Diode detectors allow direct conversion of the fast beam pulses from BPM electrodes to signals in the kHz range, which can be efficiently digitised with high resolution ADCs. These benefits allow a very high amplitude resolution to be achieved with simple and robust hardware.

The main difficulty in using a similar scheme for measuring beam position is the diode forward voltage. This voltage causes the detector output voltage to be smaller than the true peak of the input signal, introducing an important error. In the ideal case the beam position p_{AB} in the plane of BPM electrodes A and B can be evaluated from the electrode peak voltages V_A and V_B as

$$p_{AB} = c_{AB}\frac{V_A - V_B}{V_A + V_B} \qquad (1)$$

where c_{AB} is the BPM conversion factor, for simplicity assumed to be a constant equal to the BPM half aperture. If beam position is estimated from the output voltages of the diode peak detectors of electrodes A and B, which are smaller than V_A and V_B by the diode forward voltage V_d, then (1) can be rewritten as

$$p_{AB} = c_{AB}\frac{V_A - V_B}{V_A + V_B - 2V_d} \qquad (2)$$

Thus, V_d causes large beam position errors for small V_A and V_B. In reality V_d is not a constant, but varies with the detector input signal amplitude, its slew rate, temperature, making the beam position error a complex function.

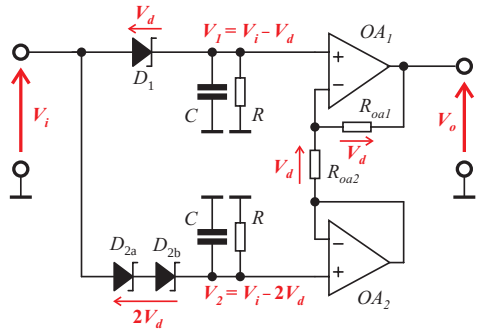

Figure 1: A compensated diode detector

The dream of the authors was to find a circuit with self-compensation of the diode forward voltage, in order to profit from the benefits of the peak detector scheme also for beam orbit measurement. The simplest and most promising scheme found is shown schematically in Fig. 1. Such a circuit diagram was published in [3], and mentioned in a popular electronics textbook [4].

The compensation scheme is based on two peak detectors, one with a single and the second with two diodes in series. The signals from two such detectors are processed with a simple network with two operational amplifiers, allowing the input peak voltage to be restored. The voltage values at circuit nodes explain the compensation scheme. The difference of the output voltages from both peak detectors is equal to the drop on one diode, V_d. As the voltage between the inverting and non-inverting inputs of the operational amplifiers is practically zero, V_d is converted into current V_d/R_{oa1} and, as the current of the non-inverting input of OA_1 is practically zero, the current V_d/R_{oa1} is converted again into V_d with $R_{oa2} = R_{oa1}$. In this way $2V_d$ is added to the output of OA_2, compensating the $2V_d$ drop on the two diodes D_{2a}, D_{2b}.

Identical voltage drops across each diode require the diode currents for both detectors to be equal, also during transients when the parallel capacitors are being charged. This is not possible with small input signal amplitudes, for which the current of the two-diode detector is smaller. Hence, the compensation mechanism does not work for small input signals. This limitation cannot be removed for pulse signals by biasing the diodes with DC current, as the symmetry of the detector pulse currents is required.

THE PROTOTYPE

The first prototype of the diode orbit measurement electronics was built as a simple circuit to test the performance of the compensated diode detectors. It was built using the PCB, power supply and mechanical parts of a diode tune measurement front-end [5]. For simplicity

it has only two channels foreseen for two BPM electrodes. The prototype is built as follows:

- The compensated diode detectors (of positive polarity for proton beams) are almost as simple as the circuit of Fig. 1 and are based on small signal Schottky diodes. The three diodes of each compensated detector are in one single package for good forward voltage symmetry and thermal coupling.
- The time constant of the detectors can be increased by adding two additional parallel capacitors. Larger capacitors filter more efficiently noise of the parallel resistors [5], improving noise performance of the detectors at the expense of increasing their time constants.
- A small diode bias current can be switched on and off. This was used to study the effect of the bias current on the performance of the detectors for small input signals.
- The two prototype inputs are connected to the two compensated detectors through a simple two-by-two multiplexer built with 4 reed relays. The multiplexer is foreseen to multiplex the inputs to improve absolute measurement accuracy.
- The outputs of both compensation circuits are connected directly to the prototype outputs.
- The prototype is built from components “as they come” and there was no component selection or adjusting.
- The prototype does not have any temperature stabilisation.
- The prototype does not have any adjustable elements.

LAB MEASUREMENTS

The performance of the compensation scheme was first verified by applying a sine wave of variable amplitude on the prototype input and measuring the output voltage with a laboratory voltmeter. Both of the prototype compensated detectors were connected to one input through a relay multiplexer and this input was driven by a generator. The input matching was conserved, as the termination is done before the multiplexer and the diode detectors have high impedance inputs (in the steady state with the capacitors charged). To minimise measurement errors the output voltages of both channels were measured one after the other with the same voltmeter.

The measured conversion characteristics of a 1 MHz sine wave into DC voltage is shown in Fig. 2. A large nonlinearity is present only for input amplitudes below some 50 mVp (mV peak). The characteristics above 0.5 Vp are very linear.

The linearity error from a fit for the input signals of amplitude larger than 0.5 Vp is shown in Fig. 3. Four error curves are presented, one for each channel with the diode bias current off and on. It is seen that the measurement points for both channels are very close, indicating that the majority of the observed linearity errors come from the generator itself. The plot therefore shows the upper error bounds set by the generator. The bounds are smaller than 1 mV for input amplitudes larger than 0.5 Vp and are still smaller than 2 mV for amplitudes

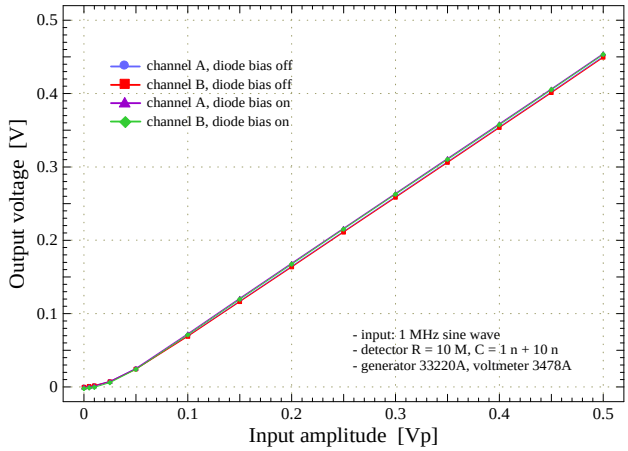

Figure 2: Prototype conversion characteristics.

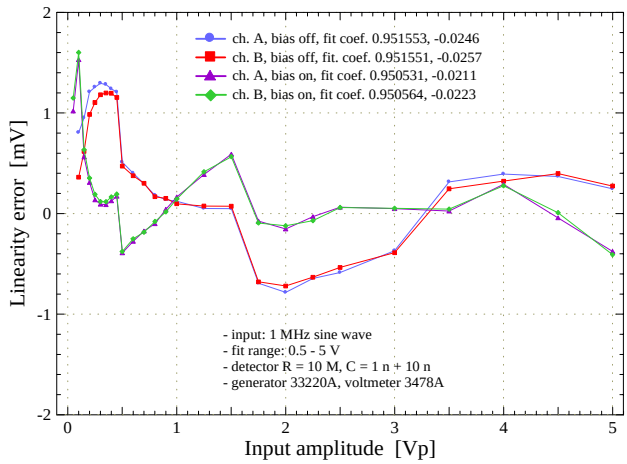

Figure 3: Linearity errors of the prototype.

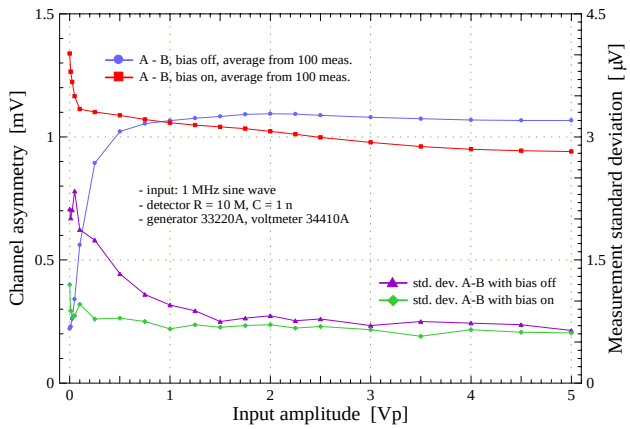

Figure 4: Asymmetry between both prototype channels.

below 0.5 Vp and larger than the voltages at which the curves start, i.e. 100 mVp and 50 mVp for bias current off and on, respectively. Note that the fit coefficients listed in Fig. 3 are remarkably close for both channels, especially the slope coefficient for the measurement with the bias current off (difference of 2 ppm). This is possible because the steady-state capacitor voltage depends little on the capacitor and resistor values. It was not the case with the

Table 1. Statistics of long-term measurement of the difference of the output voltages from both channels. Input signal: 1 MHz sine wave, 2 Vp.

observation time [h]	average [mV]	peak-peak [μV]	standard dev. [μV]
1	1.056	8	1.1
2.5	1.060	13	1.9
24	1.051	60	17
60	1.044	55	11

presence of the bias current, which in the prototype was not optimised for stability.

In order to be more independent of the limited accuracy of the input amplitude readings the following measurements were performed in a differential way, namely by measuring the difference in response of both channels to the same input stimulus. Results of such measurements taken at the 10 Hz rate are shown in Fig. 4. The measurements were carried out with a voltmeter which allowed a programmed number of acquisitions to be made and whose statistics were then calculated. The standard deviation form 100 measurements is shown, with the scale on the right hand axis. It can be seen that the channel asymmetry is close to 1 mV and changes little for amplitudes larger than 0.5 Vp. The standard deviation used to estimate the measurement resolution is extremely small in all cases, in the order of 1 μV, and go significantly lower for input amplitudes above 1 Vp. The average standard deviation for amplitudes higher than 1 Vp are 0.8 μV and 0.7 μV for the bias current off and on, respectively.

In order to determine noise of a single channel one has to take into account the fact that the above results are standard deviations of a difference of output voltages from both channels and that the voltmeter itself introduces some measurement noise. To estimate this noise the voltmeter input was shunted and the same measurements were performed, giving the standard deviation of about 0.5 μV. With these contributions taken into account, the upper bound of 1 μV of the measurements of Fig. 4 shrinks to 0.5 μV of noise on one channel.

The fact that both channels were driven from the same generator makes the measurements of Fig. 4 independent of the generator signal noise. For the output voltages from each input measured individually the standard deviations were in the order of 30 μV.

Assuming that the compensated detectors are used for the input amplitudes larger than 0.5 Vp the noise of 0.5 μV introduced by the detectors gives the measurement resolution of 1 ppm for a detector time constant of 10 ms and a measurement rate of 10 Hz. This resolution still improves by an order of magnitude if the input amplitude is increased to give 5 V at the compensated detector outputs, which can be considered as the largest value acceptable by modern high resolution ADCs.

If this 0.1 ppm resolution of the electrode peak voltage measurement could be translated into a resolution of the beam orbit measurement in the order of 1 ppm, then for a BPM with a 100 mm aperture the achievable orbit resolution would be in the order of 100 nm.

The measurement of long term stability of the symmetry of the compensated detectors is summarised in Table 1. The one hour and 60-hour peak-peak variations are in the order of 10 μV and 60 μV, respectively. This would be equivalent to an orbit measurement error in the order of 1 μm and 6 μm, respectively, for an input signal of 1 Vp and 100 mm BPM aperture.

MEASUREMENTS WITH BEAM

Typical signals from the prototype compensated diode detectors installed in the CERN-SPS are shown in Fig. 5. The beam signals came from two horizontal electrodes of a stripline BPM through some 300 m long cables. As the bandwidth of the diode detectors extends down to DC, the signals went through RF transformers in order to break ground loops and remove potential low frequency interference captured by long input cables. The detector output signals were digitised with a sampling oscilloscope operated in a high resolution mode.

A record of three SPS cycles with different total beam intensities is shown. The detector output signals are BPM electrode peak voltages, which depend not only on the beam position, but also on beam intensity and bunch length. The corresponding normalised horizontal beam position calculated according to (1) is shown in Fig. 6. It can be seen that the beam position variations along each of the cycles are quite reproducible, in spite of the fact that the overall beam intensity from the different cycles vary significantly, which is compatible with the detector good linearity observed during laboratory measurements.

Small beam excursions different for each of the cycles can be observed before beam ejection. They are related to beam orbit changes caused by RF frequency adjustments during SPS to LHC injection phase matching.

The rising and falling detector signals of the first cycle are shown in Fig. 7. For better channel comparison the DC offset voltages (mostly of the oscilloscope) were removed and the signals were normalised.

The decay of the signals is determined by the discharge of the detector parallel capacitor (1 nF) through the parallel resistor (10 MΩ), giving the 10 ms time constant. The signal rising is faster and depends on the charging speed of the parallel capacitor, which depends in addition to the capacitor value (i.e. the conversion factor of charge into voltage), also on the signal amplitude, the number of bunches present and the charging resistance, an important part of which is the dynamic resistance of the diodes.

It can be seen that the rising edge signals are very similar for both channels. This symmetry can be explored for potential orbit measurement just after beam injection, before the capacitor voltages reach their steady state values. If the symmetry is confirmed with more detailed beam measurements, then this would allow such a diode based orbit system to be used for cycling machines, like the SPS.

The quality of the presented beam measurements is determined by limited resolution of the oscilloscope acquisition (i.e. some 8 bits from the hardware and 3 bits from signal averaging). A more adequate, 24-bit acquisition system was built, but unfortunately, it could not be used with beam signals, as there have not been SPS high intensity runs since the system was ready. Such measurements will be performed as soon as adequate beam is available.

The dedicated 24-bit acquisition is based on digitisers used in the tune measurement systems [6] and modified for DC measurements. The digitisers sample at rates up to 50 kHz with signal-to-noise radio of some 110 dB for full scale signals (5 V). If the detector voltages are measured only at the 10 Hz rate, then each 5000 samples can be replaced by their average, resulting in the signal-to-noise increase by some 37 dB, resulting in the overall signal-to-noise ratio of 147 dB. This noise performance would make it possible to measure signal from the compensated diode detectors with resolution in the order of 0.2 μV, which still can be an important contribution to the overall noise performance of the whole beam orbit measurement system.

ONGOING DEVELOPMENT

The development leading to the results presented in this paper was initially targeted for the system of BPMs looking to be integrated into the next generation LHC collimator jaws. In this system signals from small button BPMs placed at the extremities of the collimator jaws will be used to position the jaws symmetrically with respect to the beam. Signals of exactly the same amplitude are expected from the opposing BPM buttons, therefore linearity of the electronics processing these signals is not that important if both signals are treated with the same multiplexed electronics chain. As a 1 μm resolution with 1 Hz reading is expected from this system, the authors, encouraged by very positive experience with sensitive diode-based tune measurement systems, started looking for a similar solution for measuring beam orbits. The compensated diode detector scheme presented here was found to have excellent resolution and very good linearity, much better than anticipated. For this reason the initial concept of diode-based orbit electronics for the LHC collimator BPMs was extended and now the development is targeted at a high resolution general purpose BPM electronics for measuring beam orbits. Its first application is still LHC collimator BPMs, but if the expected performance of the final diode electronics is confirmed, then this solution can be used for other applications requiring orbit measurement with very high resolution.

Another potential application of the compensated diode detectors is the new BPM system for the SPS. This machine requires both, trajectory and orbit measurements, therefore the idea would be to build a system containing two dedicated sub-systems, one for fast measurements with limited resolution, and the second dedicated for high resolution orbit measurements. This solution would allow

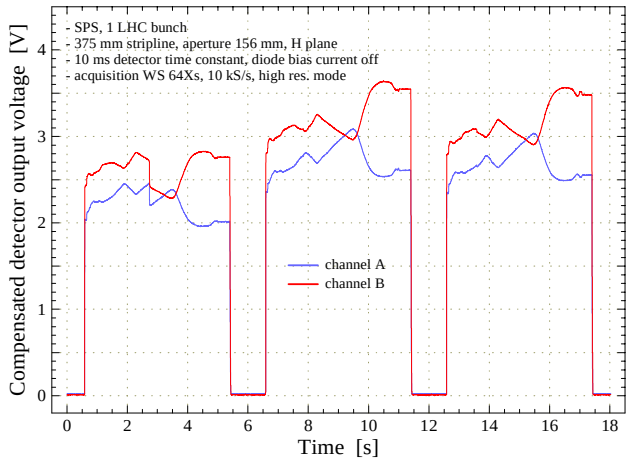

Figure 5: Compensated detector voltages for three SPS cycles with a LHC type beam.

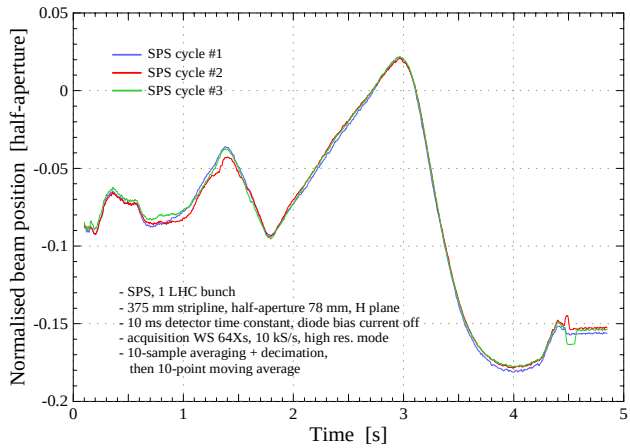

Figure 6: Beam position calculated from the detector signals of Fig. 5.

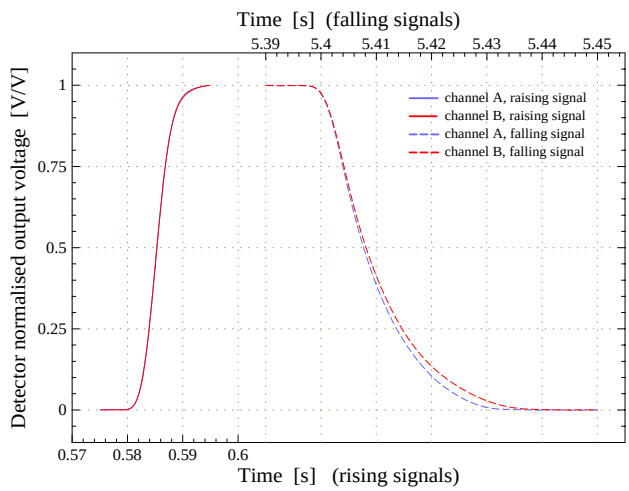

Figure 7: Normalised rising and falling signals of the first SPS cycle shown in Fig. 5.

calibration of the fast trajectory system operated in the orbit mode against the precise high resolution orbit system based on compensated diode detectors. As the diode orbit measurement circuitry is very simple and

inexpensive, adding it to a more complex trajectory system would not drastically change the overall cost and complexity.

The ongoing development has to address the issue of processing low amplitude signals. Compensated diode detectors work nicely for input amplitudes larger than some hundred mVp, therefore an amplification is required if the BPM electrode signals are smaller. As the amplitude of the detector input signals should be kept between some 0.5 Vp and 5 Vp, variable gain amplifiers (VGAs) need to be used for this signal amplification. Since the gains of VGAs can be matched only to a percent level, which would be a limiting factor for the overall system accuracy, the processing channels should be multiplexed before the VGAs.

To evaluate the benefits of the multiplexing, assume that each of the peak voltages V_A and V_B from opposing BPM electrodes is measured with each of the two processing channels A and B, having gains g_a, g_b, and offsets o_a, o_b, respectively. The resulting voltages V_{m1a} and V_{m1b} measured at the same time during the first measurement and V_{m2a} and V_{m2b} from the corresponding second measurement are

$$V_{m1a} = g_a V_A + o_a\,, \quad V_{m1b} = g_b V_B + o_b \qquad \text{(3a, 3b)}$$

$$V_{m2a} = g_a V_B + o_a\,, \quad V_{m2b} = g_b V_A + o_b \qquad \text{(3c, 3d)}$$

Performing a third measurement with no signal at the channel inputs, one can evaluate the offset voltages

$$V_{m0a} = o_a\,, \quad V_{m0b} = o_b \qquad \text{(4a, 4b)}$$

If the beam position is calculated similarly to (1) but using signals from all three measurements according to

$$p_{AB} = c_{AB}\frac{\left(V_{m1a} - V_{m1b}\right) + \left(V_{m2b} - V_{m2a}\right)}{V_{m1a} + V_{m1b} + V_{m2a} + V_{m2b} - 2V_{m0a} - 2V_{m0b}} \qquad (5)$$

then substituting (3) and (4) into (5) results in

$$p_{AB} = c_{AB}\frac{\left(g_a + g_b\right)\left(V_A - V_b\right)}{\left(g_a + g_b\right)\left(V_A + V_b\right)} = c_{AB}\frac{V_A - V_b}{V_A + V_b} \qquad (6)$$

making the beam position independent of the channel gains and offsets, assuming only that they do not vary between the two measurements.

The difficulty in using (5) for compensated diode detectors is that the offset voltages of the processing channels cannot be evaluated from a simple measurement without input signals because the detector conversion characteristic is highly nonlinear for small signals. As the VGA outputs will be AC-coupled to the inputs of the compensated diode detectors, the detectors will determine the overall channel offsets. The offsets can be evaluated by extrapolating to zero the conversion characteristic measured at least with two known input amplitudes (see fit coefficients in Fig. 3). Whether this procedure has to be done only once in the laboratory or needs to be repeated as an online calibration depends on the time scale of offset variations and required measurement accuracy. This is being addressed in the ongoing development.

The VGAs currently on the market as integrated circuits and which would be suitable for the project have bandwidths in the order of 100 MHz. To work with nanosecond pulses such VGAs require low-pass filtering on the input, which reduces the signal peak voltages. This in turn requires more gain from the VGAs. The low-pass filters will be in the processing chain after the multiplexer, so the limited match of the filter attenuation will be removed by the multiplexing.

CONCLUSIONS

Laboratory measurements show that the compensated diode peak detectors work very well with signals of amplitudes larger than some hundred mV, achieving a channel match of about 1 mV and measurement resolution better than 1 μV for a 10 ms detector time constant and 100 ms measurement time. The measurement noise introduced by the detectors and a 6-digit laboratory voltmeter were of a similar order.

The initial results from prototype testing in the CERN-SPS are encouraging. Further studies with dedicated beam time will now be required to fully characterise this high resolution technique under varying beam configurations.

If these beam measurements confirm those of the laboratory, then a general purpose beam orbit measurement electronics based on the diode compensated detectors will be developed. Resolutions in the order of 1 ppm of BPM aperture are expected with measurement rates in the Hz range. The largest development challenge is addressing the linearity degradation for small input signals.

The first application of the diode orbit measurement system will be for the BPMs integrated into the next generation LHC collimator jaws.

With the potential that this technique could be used to measure beam orbits at Hz rates using readings from a high resolution DC voltmeter, the authors decided to publish these first results of the diode orbit measurement development at an early stage. The hope being to encourage the beam instrumentation community to study this technique in parallel to the CERN efforts.

The compensated diode detectors may find application in systems with fast signals, whose slow varying amplitudes should be measured with very high resolution.

REFERENCES

[1] M. Gasior, R. Jones, “High Sensitivity Tune Measurement by Direct Diode Detection”, DIPAC‘05.

[2] A. Gasior et al., “Sub-nm beam motion analysis using a standard BPM with high resolution electronics”, this conference.

[3] V. McOmber, “A Voltmeter for a universal counter”, HP Journal 9/80, pp 28-29.

[4] P. Horowitz, W. Hill, “The Art of Electronics”, Cambridge University Press, 1989.

[5] M. Gasior, R. Jones, “The Principle and First Results of Betatron Tune Measurement by Direct Diode Detection”, CERN LHC Project Report 853, 2005.

[6] A. Boccardi, M. Gasior, “High dynamic range spectral analysis in the kHz band”, DIPAC‘09.

IMPROVEMENTS FOR OPERATIONAL BASEBAND TUNE AND COUPLING MEASUREMENTS AND FEEDBACK AT RHIC*

M. Wilinski, W.C. Dawson, C. Degen, A. Marusic, K. Mernick, M. Minty, T. Russo, BNL, Upton, NY, USA

Abstract

Throughout RHIC Run-9 (polarized protons) and Run-10 (gold), numerous modifications to the Baseband Tune (BBQ) system were made. Hardware and software improvements resulted in improved resolution and control, allowing the system to overcome challenges from competing 60Hz mains harmonics, other spectral content, and other beam issues. Test points from the Analog Front End (AFE) were added and connected to diagnostics that allow us to view signals, such as frequency spectra on a Sr785 dynamic signal analyser (DSA), in real time. Also, additional data can now be logged using a National Instruments DAQ (NI-DAQ). Development time using tune feedback to obtain full-energy beams at RHIC has been significantly reduced from many ramps over a few weeks, to just a few ramps over several hours. For many years BBQ was an expert-only system, but the many improvements allowed BBQ to finally be handed over to the Operations Staff for routine control.

INTRODUCTION

Tune measurement and feedback [1, 2, 3] in RHIC was first begun during the 2004 RHIC gold run as part of the US LHC Accelerator Research Program (LARP). Development of the system has continued since then with the present installation consisting of a pickup and kicker in each of the 1 and 2 o'clock sectors in the RHIC tunnel. The remainder of the system is installed in Service Building 1002A and consists of direct diode detection (3D), and analog front end (AFE), a kicker chassis, various VME/controls modules (such as Numerically Controlled Oscillators (NCO), digitizers, and timing), and several diagnostics packages including Stanford Research Systems Sr785 Dynamic Signal Analyzers and National Instruments PCI-6143S Multifunction DAQ PCI cards.

From the 2004 run through the 2008 run, a good amount of progress was made, but an expert was still required to operate the BBQ system. Various problems were encountered [4] such as mains interference, 'anomalous' beam transfer functions, and 'tune scalloping' which often interfered with acquiring a successful tune lock on the beam. Prototype boards and chassis were fabricated to try to help solve some of these problems.

Prior to the 2009 run (Run-9), a new team of people took over responsibility for BBQ [5]. During this time, nearly 50 issues involving tune measurement hardware items were addressed, along with numerous software enhancements that significantly improved resolution of the measured tunes. Modifications were also made to allow for exploration of near integer working points, as well as working points near 1/3.

*Work performed by employees of Brookhaven Science Associates, LLC under Contract No. DE-AC02-98CH10886 with the U.S. Department of Energy

HARDWARE MODIFICATIONS

General Modifications for Operations

Among the first major tasks were massive cleanups of the tunnel areas and Service Building 1002A. Both areas contained a great deal of clutter (old cables, connectors, clamps, etc). A number of old, unused prototype chassis were still installed in the racks, some with cables connected only at one end. Once all of the extraneous equipment was removed, the remaining equipment was adjusted such that the racks for the blue and yellow rings were identical in layout. Blank panels were added to racks as needed to cover up empty areas and improve shielding.

Next, attention was focused on improving the AFEs. Several voltage under-rated capacitors were replaced with properly rated capacitors. Transfer functions of the AFE were simulated and measured, and upon comparison of the results were found to match well. A driver board was added to each AFE to get the pickup +/- signals into the controls system so a dB-to-mm position calculation would be available. The addition of the test signals allow the BBQ pickups to be easily centered on the beam, rather than the beamline.

The most significant effort on the AFE was adding additional test points to observe internal signal levels. Small daughter cards were added to monitor the following signals: +/- input signals from the pickups, the input difference signal, and the filtered signal. All of these signals can be observed via several methods: a local scope, an Sr785 DSA, or the NI-DAQ. Two, 2-channel DSA units are installed, one each for the blue and yellow rings. Typically the difference signals of the blue horizontal (BH), blue vertical (BV), yellow horizontal (YH), and yellow vertical (YV) planes are monitored and logged through the controls system, but signals can be changed locally if necessary. The NI-DAQ system consists of two computers, each with two 8-channel PCI-6143S cards that sample at 250kSamples/second. All four test point signals from each plane (BH, BV, YH, and YV) along with several kicker diagnostic signals are input into the cards. The DAQ is triggered automatically at the start

of every RHIC ramp and collects five minutes of data. The data is stored in .tdms format which can be read and analyzed using LabVIEW or MATLAB.

As with the AFE, several modifications were made to the kicker amplifiers. A Hall Effect current transducer was added to each output of the kicker amps, as well as a voltage output to one side of each bridge amplifier. An RMS-to-DC converter was added to the amplifier current signal, which was input into an MADC for logging in the controls system. Additional power supply filtering was added to solve the problem of ripple on both +/-15V power supplies. The output of the kicker amplifiers were calibrated to determine the output current for each kicker setting in dB.

Several smaller pieces of the hardware were also altered for increased reliability. All spare diode boxes were modified to be identical, and the end connectors were changed to avoid the use of adaptors. The Khronhite filters and transformers were removed and replaced with passive low pass filters. Mechanical bracing was then added to support the diode boxes and filters. Bracing rods were also attached to the NCO daughter cards so they make a robust connection and do not flex. Front panels for the NCOs were machined and installed. Finally, the NCO outputs were connected to a VME 3123 digitizer to allow software to determine the phase of the NCO relative to the ADC sample buffer.

There are a myriad of interconnects in this system, and signal quality is only as good as the worst cable. Tests were performed with a network analyzer to check the integrity of the kicker cables going into the tunnel. Shortly after that, it was noticed that eight feedthroughs on the BBQ pickups needed to be repaired. Extra adaptors were eliminated where possible, and all interconnect points were wrench tightened. Several broken SMA "T"s were discovered, as well as four ¼" Heliax cables that needed to be re-terminated. Where appropriate, cables were re-routed to better paths and strain-relieved properly. New cable assemblies were made for the AFE-to-MADC paths as some cables were showing signs of wear.

Near-Integer Tune Modifications

During RHIC Run-9, several Accelerator Physics Experiments (APEX) sessions were devoted to the investigation of near-integer betatron tunes as a possibility for future runs. The tunes were expected to be Q_x=0.88 and Q_y=0.97, yielding aliased sidebands of f_x=9.4kHz and f_y=2.3kHz. The filter characteristics of the AFE were such that the horizontal sideband would be in the passband (-3dB low frequency cutoff was about 8kHz), but the vertical sideband would be outside of the passband and therefore attenuated by approximately 20-30dB. Simulations were run using MATLAB to extend the passband and several AFE components were changed to lower the cutoff frequency to around 1kHz, see figure 1.

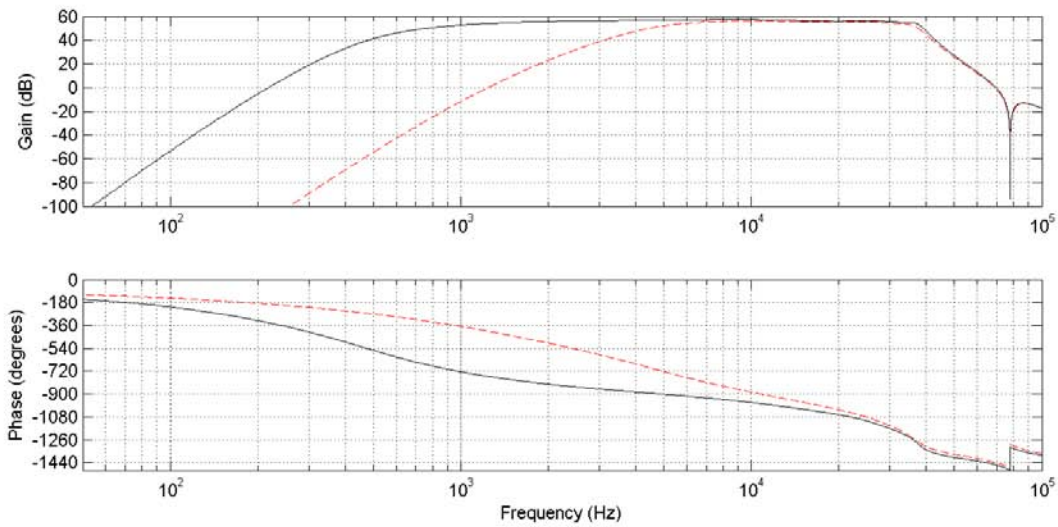

Figure 1: Frequency and phase response of the original (red dashed line) and modified (black solid line) AFE.

One-Third Tune Modifications

Many APEX sessions during Run-10 were dedicated to the exploration of Q=1/3 tunes for use during future polarized proton operations. The VME 3123 digitizers that were installed had a maximum scan frequency of 100kHz. However, based on the revolution frequency and energies expected, tunes above 0.3197 and below 0.68 require scan frequencies greater than 100kHz. We were able to take advantage of the VME 3123 "channel doubling" mode to extend the sampling frequency to 200kHz by using two digitizer channels per signal. To use the channel doubling, a signal must be split and input to a channel pair: Channel 0 and 8, Channel 1 and 9, etc. Preliminary testing on the split-signal setup was done in the lab, and then first implemented in the blue ring, followed by the yellow ring. Minor software modifications needed to be made to correctly read the

data from the digitizer. At around a tune of 0.42, the interrupt rate starts to oscillate, which is interpreted as reaching the limit of the CPU in the VME. Therefore, by using the channel doubling mode, we have extended the range of tunes that are possible to measure, and have a small deadband for tunes between 0.42 – 0.58.

SOFTWARE MODIFICATIONS

General Modifications for Operations

One of the main problems with tune feedback involved noisy tune data. The previous algorithm only used the last data point out of every sixteen data points. The code was changed to use the average of the last sixteen samples.

Various diagnostic parameters were added to the code, and the parameter which displays the number of interrupts processed per second revealed that not all scans were being processed. This was diagnosed as a competition for CPU time from another process. The other process would periodically corrupt beam transfer function data, was determined to be unnecessary, and therefore removed from the code.

Other changes include modifying the software to be more deterministic in the processing of data. Previously, if the code was not waiting to process data when new data arrived, the new data was never processed. A programming error was found and fixed in which digital filter parameters used for one application were overwriting those of another application. Also, precision phase optimisation and frequency-dependent phase correction were implemented.

The magnet control software for tune feedback was also improved. The code which is used to save feedback data for subsequent ramp replay was modified to save cached data to be immune to occasional delays in writing data to a file. Prior to this change, gaps and corruption of data would occur at the start of a ramp, presumably because of network slowdown at that time. The code was also modified to stop the control loop from delivering data to magnets when beam was lost from the machine. This change prevents the control loop from sending unphysical corrections to magnets which could ultimately result in a quench link interlock.

Two user-selectable digital filters labelled 40Hz and 20Hz were implemented in software, but their characteristics were not documented. Simulations were performed to determine their response; with a 25kHz input signal, the full width half max (FWHM) of the passbands of the output with no filter, 40Hz, and 20Hz filters were found to be 2310Hz, 820Hz, and 420Hz respectively. The BBQ system traditionally operates using the 20Hz filter, which is specified as a sequence of 11 taps and therefore its characteristics change in proportion to the scan frequency. This feature turned out to be beneficial for the near-integer operation because at lower frequencies, the filter passband becomes narrower. For example, at a scan frequency of 5kHz, the FWHM of the passband is 85Hz, which in turn reduces the interference of 60Hz harmonics.

Near-Integer Tune Modifications

For near-integer tune operations, further modifications were necessary to the software for tune measurements and magnet control. In normal operations, the PID control algorithm had coefficients depending on the sampling frequency that scales with betatron frequency. The sampling frequency changed by a factor of ten at the near-integer tune. The PID loop was modified to use coefficients based on the given data rate such that the control becomes independent of the sampling frequency.

The dependence of the NCO phase on NCO frequency was previously defined in software as a hard-coded coefficient yielding linear dependence between NCO phase and the tune. This was changed to allow a user-specified linear coefficient instead.

The most critical and extensive modification for this mode of operation concerned the requirements for the magnet control code. In near-integer mode the data rate for sending tune corrections to the magnet power supplies were reduced by a factor of 10 or more, resulting in less frequent and larger requested changes. The amplitude of the requested correction often exceeded the capabilities of the power supplies. To resolve this issue, the magnet control code was modified to keep the setpoint generation rate above 180Hz.

One-Third Tune Modifications

As mentioned in the corresponding hardware section, channel doubling of the digitizers was required for this operating mode. Therefore the software that handles the data acquisition needed to be modified to interleave the data coming from the digitzer. No other software modifications were necessary.

RESULTS

During both Run-9 and Run-10, the BBQ system modifications and upgrades resulted in much success. Measurements were taken after most of the improvements had been implemented using frequency resonators to determine the resolution of the BBQ system. Using a linear fit between the vertical lines depicted in Figure 2, it was determined that the instrumental resolution was (1.9 +/- 0.1) x 10^{-6}, or 0.05Hz. This measurement was also performed prior to many of the hardware and software changes, and the resolution at that time was calculated to be (4.3 +/- 0.2) x 10^{-6}. Clearly the efforts to modify the system resulted in significant improvements to tune measurement resolution.

While 60Hz harmonics continue to be present on the signals, the BBQ system is now robust enough to “ignore” mains contributions and only lock on the correct tune value. Polarized proton operation at 100GeV includes a tune swing of approximately 0.05 during the ramp, which encompasses about 65 harmonics of 60Hz. Tune measurements and tune feedback worked

successfully during these tune swings, with no user intervention.

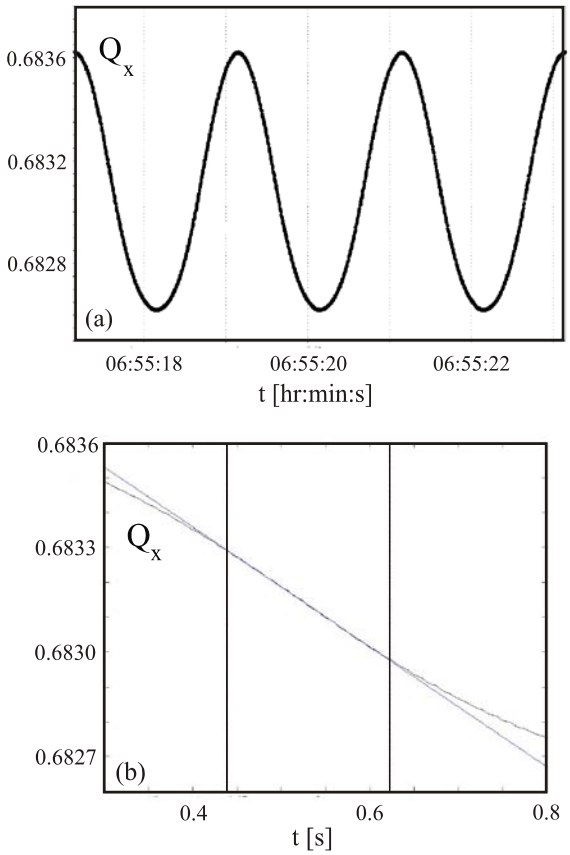

Figure 2: Measured tune in the blue ring with resonator input (a) with expanded axis scale showing linear fit (b) to determine resolution

Vibration of triplet quadrupoles in RHIC cause beam orbits to be perturbed at frequencies close to 10Hz [6]. Not long after establishing beam at full energies during Run-9, tune modulations at a 10Hz rate could be seen for the first time as seen in Figure 3. The oscillations between planes are observed to be out of phase thereby suggesting the modulation is not instrumental. Further comparisons between FFT signals from a BPM and BBQ indicate common dominant frequency contributions around 10Hz, see Figure 4 [5]. While the BBQ system was able to maintain a lock on the proper tune value, the 10Hz modulations were a limiting factor in resolution. For applications where precision tune measurements are required, digital filtering of the 10Hz modulations is implemented. Throughout Run-10, a 10Hz Global Orbit Feedback system is being tested in six RHIC locations in an effort to correct the 10Hz perturbations. Testing has gone well, and it is expected that the system will be fully deployed during the summer shutdown maintenance period.

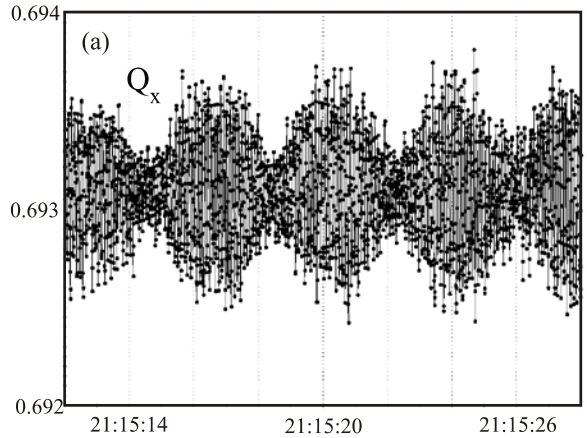

Figure 3: Horizontal tune data from blue ring at store during Run-9 with 10Hz modulation.

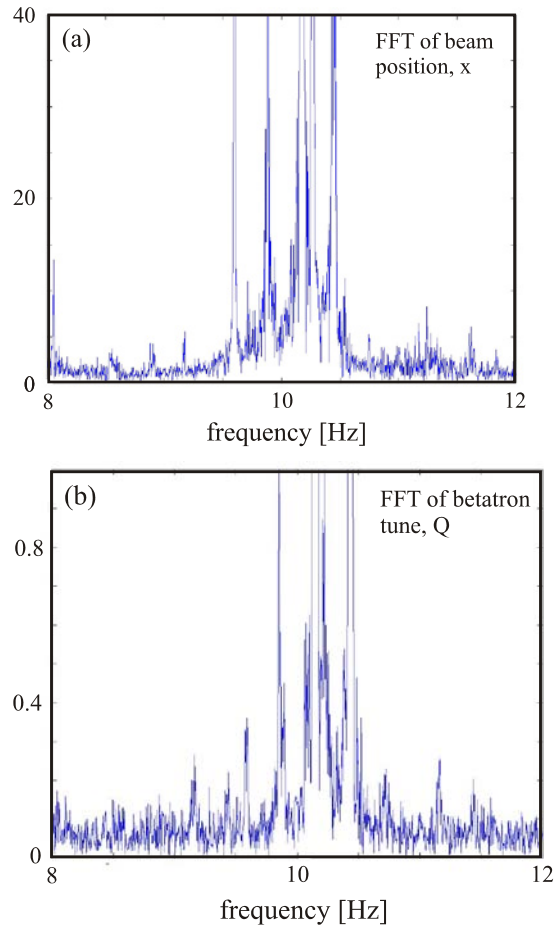

Figure 4: Fourier transforms of the horizontal beam position (a) and horizontal tune (b) showing similar frequency contributions from the ~10Hz perturbations

Whereas development time used to take many shifts over many days to ramp RHIC to desired top energies, development time during Run-9 took at most 6 hours to obtain proper tune feedback data for "replay"; see Table 1. (Replay is a setup that will reuse previously obtained tune feedback data to control magnet corrections during a ramp.) Prior to the upgrades, many ramps were lost as a result of the system losing a lock on the tunes. This

changed during Run-9 as only one lost ramp could be attributed to the BBQ system, and that was because of a bad connector. No ramps were lost because of poor or no tune lock. The ramp failure rate decreased even further in Run-10 with only one failure attributed to BBQ as a result of improperly entered tune range scan values.

Table 1: Run-9 Ramp Development

Ramp Type	Commissioning Hrs. to First Replay Ramp	# Ramps to First Replay Ramp
250GeV 0.7m beta*	6 (blue ring only) 5 (blue & yellow rings)	12
100GeV 0.7m beta*	3 (blue & yellow)	4
100GeV 20m beta*	3 (blue & yellow)	5

After obtaining experience with both polarized proton and gold beams, and discovering that prior runs' observed ill-effects were no longer occurring, BBQ was no longer declared an "expert-only" system. Main Control Room Operations Staff were trained in a "classroom" as well as in a "hands-on, with beam" environment on how to use the system. Typically operations staff handle the day-to-day measurements, and experts are present during setup for different operating modes (i.e. APEX or energy change). Operators ran the tune and coupling feedback during Run-10 ramp development up through the physics handoff on December 31, 2009. Procedures and other reference documents are made available to operations staff at the Instrumentation Wiki site.

Coupling feedback is regularly used and has also seen improvements as a result of the hardware and software improvements. Prior to ramp development, the coupling of each beam is minimized at injection energy. If the measure of the coupling control is defined to be the rms of the signal strength in the orthogonal plane, it has been demonstrated that the precision on the decoupling control was reduced from +/-0.0414 during Run-8 to +/-0.0035 in Run-9 [5]. As with tune feedback, coupling feedback was automated and required no human intervention starting with Run-9.

ACKNOWLEDGEMENTS

Many people have made contributions to the modifications, installation, and operation of this system and we thank: A. Curcio, L. Hoff, J. Laster, G. Marr, B. Martin, P. Oddo, C. Rhein, V. Schoefer, R. Schroeder, C. Schultheiss, A. Weston, & P. Ziminski

REFERENCES

[1] M. Gasior, R. Jones, LHC Project Report 853.
[2] M. Gasior, R. Jones, "High Sensitivity Tune Measurement By Direct Diode Detection", DIPAC'05, Lyon, France, 2005, p. 312-314.
[3] R. Jones, P. Cameron, Y. Luo, "Towards a Robust Phase Locked Loop Tune Feedback System", DIPAC'05, Lyon, France, 2005, p. 298-300.
[4] P. Cameron, et al, "Progress in Tune, Coupling, and Chromaticity Measurement and Feedback During RHIC Run-7", PAC'07, Albuquerque, NM, 2007, p. 886-888.
[5] M. Minty, et al, "High Precision Tune and Coupling Measurements and Tune/Coupling Feedback in RHIC", BNL C-AD AP Note 366 (2010).
[6] C. Montag, et al, "Measurements of Mechanical Triplet Vibrations in RHIC", EPAC '02, Paris, France, 2002, p.1267-1269.

DYNAMICALLY TUNED HIGH-Q AC-DIPOLE IMPLEMENTATION*

P. Oddo, M. Bai, W. C. Dawson, W. Meng, K. Mernick, C. Pai, T. Roser, T. Russo, Brookhaven National Laboratory, Upton, NY 11973, USA

Abstract

AC-dipole magnets are typically implemented as a parallel LC resonant circuit. To maximize efficiency, it's beneficial to operate at a high Q. This, however, limits the magnet to a narrow frequency range. Current designs therefore operate at a low Q to provide a wider bandwidth at the cost of efficiency. Dynamically tuning a high Q resonant circuit tries to maintain a high efficiency while providing a wide frequency range. The results of ongoing efforts at BNL to implement dynamically tuned high-Q AC dipoles will be presented.

INTRODUCTION

Work on a new spin flipper for RHIC (Relativistic Heavy Ion Collider) incorporating multiple dynamically tuned high-Q AC-dipoles has been developed for RHIC spin-physics experiments. A spin flipper is needed to cancel systematic errors by reversing the spin direction of the two colliding beams multiple times during a store [1]. The spin flipper system currently consists of four DC magnets and three AC-dipoles and will go to five AC-dipoles. Multiple AC-dipoles are needed to localize the driven coherent betatron oscillation inside the spin flipper. Having multiple AC-dipoles that require precise control over amplitude and phase makes it necessary to implement them as dynamically tuned high-Q resonant circuits. One of the major challenges was to design of a new magnet and the proper topology to drive it. The topology is required to be both efficient and serviceable.

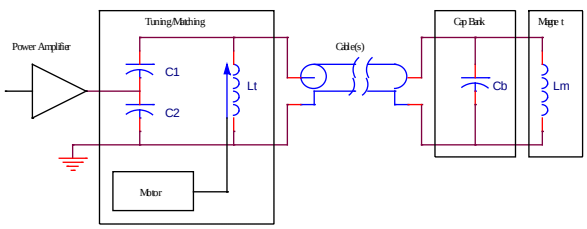

Figure 1: RHIC High-Q AC-dipole simplified schematic.

HIGH-Q AC-DIPOLE SYSTEM

Figure 1 is a simplified schematic of the present implementation. This topology places the bulk of the capacitance at the magnet. A pair of heliax coaxial cables connects the capacitor bank to the tuning chassis in the service building. Tuning is accomplished via a motor driven variable air-gap inductor. A servo loop adjusts the air gap to maintain the system at resonance.

This topology was initially chosen to support solid state (switched capacitor) tuning which required the tuning to be done outside of the ring in order to protect the semiconductor (MOSFET) switches from radiation damage. However, due to scheduling and concerns over switching distortion, solid state tuning was not implemented.

Existing AC-dipole systems

For comparison, figure 2 is a simplified schematic of the existing RHIC AC-dipoles [2] and figure 3 of the CERN LHC [3] and the FNAL Tevatron [4] AC-dipoles. For clarity, these schematics only illustrate the location of major components. In all cases the transmission line is the dividing line between the components in the service building and in the ring. The placement and use of the transmission line is a key difference between approaches.

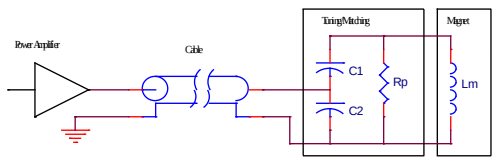

Figure 2: RHIC AC-dipole simplified schematic.

RHIC AC-dipoles

The RHIC AC-dipoles matches and tunes the AC-dipoles at the magnet. This approach tries to terminate the transmission line with its characteristic impedance. Although the magnet was designed as a high-Q air-core, the Q is deliberately spoiled (Rp). Since the resonant impedance is greater than amplifier/transmission line impedance, a capacitive step-up matching network was used (C1, C2).

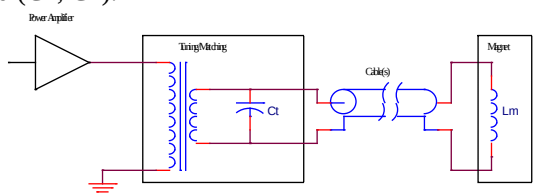

Figure 3: LHC/Tevatron AC-dipole simplified schematic

LHC and Tevatron AC-dipoles

The LHC/Tevatron approach does the tuning and matching at the service building. For this approach the transmission line current is the magnet current. Furthermore, since low impedance kicker magnets are used, the transmission line is terminated with an impedance that's much lower than its characteristic impedance; the transmission line therefore forms a parasitic series inductance. This inductance increases the peak energy stored.

Key difference

The RHIC High-Q AC-dipoles also do not terminate the transmission line with its characteristic impedance. However, since the capacitor-bank and magnet parallel impedance is a lot greater than the transmission line's characteristic impedance, the transmission line looks capacitive. This capacitance is not harmful and actually reduces the amount of capacitance that has to be added to from the resonant circuit. It's this difference that allows the tuning chassis to be separated from the magnet by long (400ft or 122m long) cables and have a minimal effect on efficiency. The cable capacitance makes up about 10% of the total system capacitance and can be viewed as a stretched out capacitor bank. The cable current is not uniform and the peak is at different locations based on frequency.

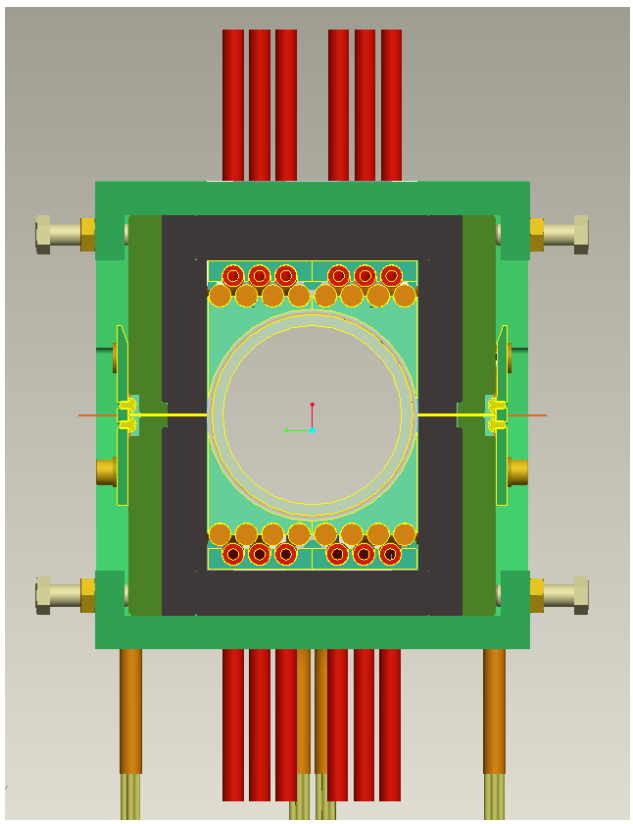

Figure 4: RHIC Spin Flipper high-Q AC-dipole magnet cross sectional view

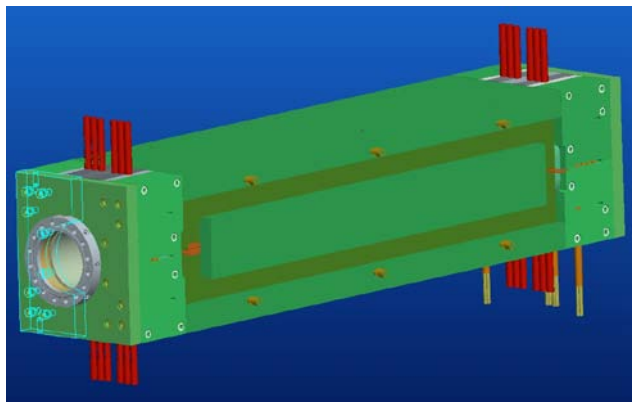

Figure 5: RHIC Spin Flipper high-Q AC-dipole 3D view

MAGNET DESIGN

Referring to figures 4 and 5, the magnet is an eight-turn litz-wire wound ferrite core window frame magnet build around a ceramic beam pipe. This geometry was chosen over the air-core geometry used for the existing RHIC AC-dipoles because it can accommodate a larger aperture with a shorter effective path length (l_e). This shorter path length translates into less stored energy, less reactive power and therefore less power loss. This geometry also more easily satisfies the field-fidelity requirements.

TUNING CHASSIS

The tuning chassis houses the tuning coil and capacitive matching network (C1 and C2 in figure 1) that form a parallel LC circuit. When the tuning coil gap is set to minimum (maximum inductance) this LC circuit looks capacitive and pulls the frequency lower. As the gap increases the circuit becomes inductive and starts pulling the frequency higher.

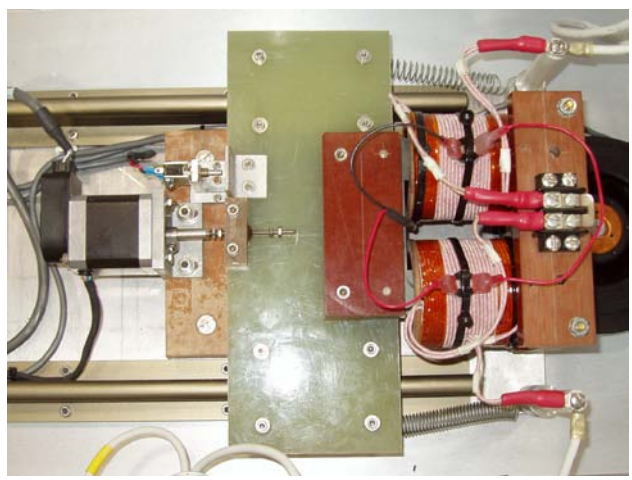

Figure 6: Tuning coil assembly

TUNING COIL

The tuning coil is composed of two litz-wire wound coils mounted on the legs of two U-shaped cores. One core is fixed (right side of figure 6) and the other movable by the stepper motor (left side of figure 6) and thus

* Work performed by employees of Brookhaven Science Associates, LLC under Contract No. DE-AC02-98CH10886 with the U.S. Department of Energy and RIKEN Japan.

produces a variable air gap. As implemented, the relationship between the air gap size and center frequency is nearly linear.

CONTROLS

The prototype control system was based on commercial Xilinx development boards. This initial version runs two servo loops per magnet. The first loop keeps the magnet at the resonant frequency by comparing the magnet current to amplifier drive current phase and adjusting the tuning coil air-gap to keep these in quadrature. The second loop operates as an automatic gain control (AGC) and adjusts the amplifier drive to maintain the magnet current amplitude. The control system is being overhauled to become more capable and scalable. One planed change is to replace the relatively slow AGC with a fast feedback that tries to match the magnet current to a reference waveform. This change will allow much tighter control over phase and will use the amplifier's headroom to fine-tune the magnet frequency until the slower frequency loop settles.

CONCLUSION

Testing has validated this dynamically tuned high-Q AC-dipole design. The basic requirements of tuning range and magnet current were easily met. Beam based measurements showed the AC-dipoles to be well matched. However, continuing development is ongoing.

REFERENCES

[1] M. Bai et al, "RHIC Spin Flipper," Proc. 2007 IEEE U.S. Part. Accel. Conf., 2007

[2] M. Bai et al, "RHIC AC Dipole Design and Construction," Proc. 2001 IEEE U.S. Part. Accel. Conf., 2001

[3] J. Serrano, "The AC Dipole system for LHC," LHCCWG meeting, 2007

[4] R. Miyamoto S. Kopp, A. Jansson, M. Syphers, "Tevatron AC Dipole System," Proc. 2007 IEEE U.S. Part. Accel. Conf., 2007

DIGITAL BASE-BAND TUNE DETERMINATION

P. Kowina [1], U. Springer [1,2], P. Forck [1], P. Hülsmann [1,2] and P. Moritz [1]

[1] GSI, Darmstadt Germany, [2] Goethe University, Frankfurt, Germany

Abstract

To avoid beam losses of intense beams stored at the GSI heavy ion synchrotron SIS18 a precise tune measurement during a whole acceleration cycle is required. This contribution presents a sensitive method of tune determination using data of Beam Position Monitor (BPM) measured in bunch-by-bunch manner. The signals induced in the BPM electrodes were digitized by 125 MS/s and integrated for each individual bunch. The tune was determined by Fourier transformation of the position data for typically 512 subsequent turns. Coherent betatron oscillations were excited with bandwidth-limited white noise. The presented method allows for tune measurements with satisfactory signal-to-noise ratio already at relatively low beam excitation i.e. without significant increase of transverse beam emittance. In parallel the evolution of transverse beam emittance was monitored by means of an Ionization Profile Monitor. The system for online tune measurement is an integral part of the new digital BPM System, presently under commissioning.

INTRODUCTION

Unlike other beam parameters, e.g. beam current, position, transversal beam profile etc., the tune is a crucial beam parameter that can not be obtained in a single individual measurement. A most fundamental technique is based on the excitation of coherent transversal beam motions with a known perturbation source and post-processing of the beam response using beam position monitors (BPM).

The GSI heavy ion synchrotron SIS18 has some particular machine parameters, which make tune diagnostics challenging. Namely the comparatively long bunches, the injection at non-relativistic velocity β = 15.5% and the fast ramping of the acceleration frequency from 0.8 to 5 MHz within 400 ms. Since tune measurement during a whole acceleration cycle is required, other methods of tune determination using e.g. passive monitoring of the residual beam oscillation (like observation of Schottky noise) or active techniques based on phase-locked-loop systems are either to slow or require a lot of manpower during implementation. For an overview see e.g. [1] and references therein.

On the other hand, a new data acquisition system for BPMs at SIS18 presently under commissioning [2] opens new possibilities for tune determination. Since the beam position is measured in bunch-by-bunch manner it was evident to investigate if the tune can be determined by appropriate post-processing of anyhow existing beam position data. The results of these investigations are presented and discussed in the following sections.

For a stable beam consisting of a large but finite number of particles a movement of the centre-of-mass is the incoherent sum of individual particle oscillations effected by random phases and frequency spread. This so called *Landau damping* [3] makes the betatron motions of individual particles inaccessible. Usually the residual coherent particle motions are too weak to be detected and the beam needs to be slightly excited. There are three methods of the beam excitation available at SIS18:

- One-turn kick-type excitation using a pulsed magnet that applies its full power within a single revolution period. However, the transversal motions decay within some hundreds of turns due to Landau damping which excludes the possibility of tune observation over the whole acceleration cycle.
- Frequency sweep excitation: generated using a sinusoidal-type signal with time-varying frequency. However, for fast ramping accelerators like SIS18 the increase of the SIS rf frequency is faster compared to the sweeps performed by the exciter which does not allow for tune diagnostics on the acceleration ramp.
- Noise excitation which considers an excitation with a broadband noise covering the expected frequency range.

For the investigation presented in this contribution the last method was used.

METHODS AND RESULTS

Fig.1 shows schematically the detection setup. The beam was excited using a noise applied to the exciter plates installed at SIS18. The noise signal with adjustable bandwidth around the side bands of the carrier frequency

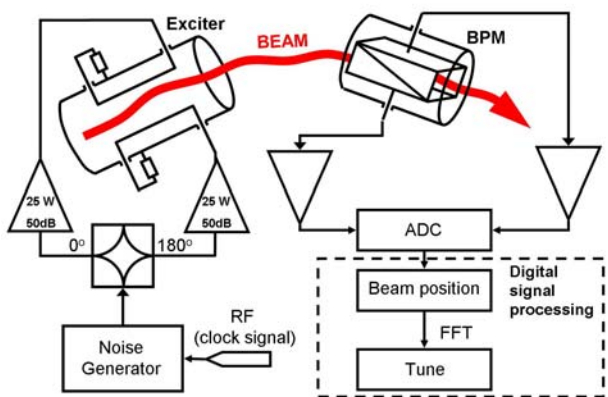

Figure 1: Detection setup (see description in text).

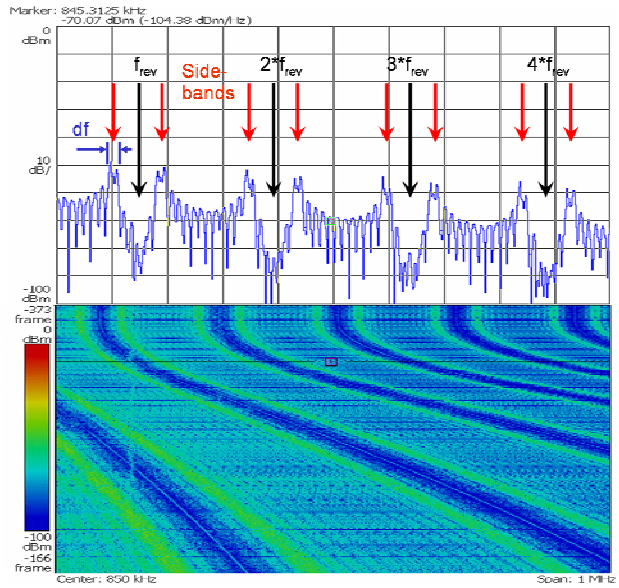

Figure 2: Frequency spectrum of the pseudo random noise generator. The first four harmonic frequencies are seen (top). The noise bandwidth df corresponds to Δq=0.05. The carrier frequency is locked to the SIS18 acceleration frequency (bottom).

was produced by means of Digital Pseudo Random Noise generator [4]. The frequency spectrum of the noise signal is shown in Fig.2. The carrier frequency follows the acceleration rf by using a frequency tracker. The noise bandwidth df is chosen to be broad enough to cover the maximum expected tune deviation from the set value which, in the particular case of SIS18, usually does not exceed Δq=0.05. The signal of the noise generator was split using a 180^{O} hybrid, amplified up to a maximal power of 2*25 W and fed to a 750 mm long stripline exciter having horizontal/vertical apertures of 200x70 mm^2, respectively. Note that Fig.1 shows only one half of the system, e.g. for the vertical tune measurement; analogical system components are used independently for the measurement of the horizontal tune.

The beam response was observed using one of the 12 regular BPMs. The broadband analog signals from all four plates of a diagonal-cut type pick-up [5] were fed to an amplifier with high input impedance and digitized by a 14 bit ADC with a sampling rate of 125 MSa/s. For typical SIS18 beam parameters this corresponds to about 140 Sa/bunch at injection and about 20 Sa/bunch at extraction, respectively. In a digital signal processing, after restitution of base line shift [6], the signals are integrated bunch-by-bunch within the integration windows. The integration windows are generated from the input signal itself as described i.e. in [7]. The output of this beam position algorithm was one value for the vertical and one for horizontal beam position, calculated for each individual bunch using the delta-over-sum method [8].

The fractional tune is calculated by Fast Fourier Transformation (FFT) of position values for the given bunch typically over 512 turns. In FFT computation subsequent bunch positions are treated as equidistant. This implies that the obtained frequency spectrum is per definition normalized to the revolution frequency f_{rev} of the ions within the synchrotron i.e. is automatically transformed into a base-band. The resulting fractional tune spectrum is expressed in units of f_{rev} and ranges from $0 < q < 0.5$ (see Fig. 3). Typically more than one bunch is circulating in SIS18 (usually 4 bunches). In this case the number of calculated FFTs is equal to the number of circulating bunches. A final spectrum (as the one shown in Fig. 3) represents an average of all FFT results.

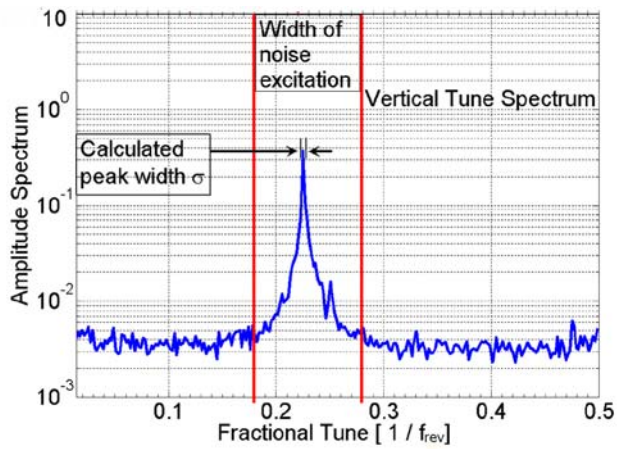

Figure 3: Typical vertical tune spectrum for a beam of 6.5 x 10^9 Ar^{18+} ions obtained in FFT over 512 turns. The red lines depict the bandwidth of the excitation signal.

Fig. 4 presents results obtained for a complete acceleration cycle. A beam of 6.5 x 10^9 Ar^{18+} ions was accelerated from 11.4 MeV/u to 300 MeV/u within 400 ms, which corresponds to 220.000 turns. The upper part of Fig. 4 shows the vertical beam position over the whole acceleration cycle. To increase the resolution of position read-out an average over 1000 turns is calculated.

For each block of 512 subsequent turns the FFT is calculated resulting in the tune distribution over the acceleration cycle shown in Fig. 4 (bottom). For each point of this curve the mean position of the peak in FFT spectrum was determined. For the beam parameters mentioned above one obtains about 400 points per second. A measured tune diverges from the preset one. While the value for the vertical tune was preset to 3.23 the measured mean fractional tune is 0.221 and varies over the acceleration cycle within ±0.005.

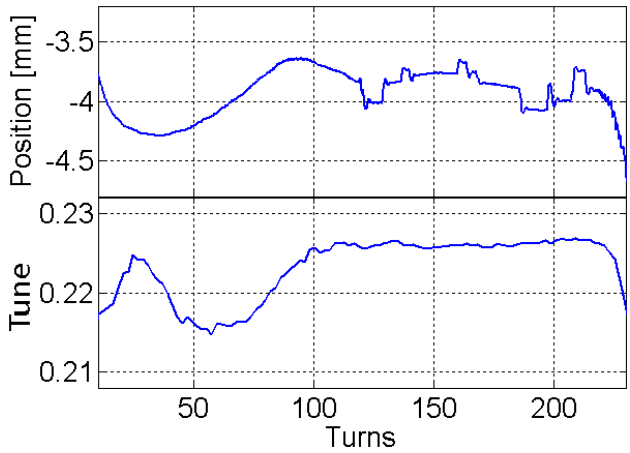

Figure 4: Vertical beam position (top) and vertical fractional tune (bottom), see text for beam parameters. Excitation at q_{ex} = 0.23 ± 0.05 with amplitude of P_{ex} = 3.5 W.

Determination of optimal excitation strength

The above mentioned Landau damping is actually the main mechanism leading to transversal emittance blow-up: While the observed centre-of-mass motion decays, the sum of the individual particle energies is preserved. In hadron accelerators such as SIS18, that are practically unaffected by synchrotron radiation losses, there is no mechanism that could lead to damping of the incoherent oscillations of the individual particles. Therefore it's necessary to avoid excessive excitation of the beam as it leads directly to emittance blow-up and, in consequence, to particle losses. On the other hand there is a certain excitation strength needed for proper tune measurements. In order to determine the ideal range of excitation power a series of measurements was performed with different excitation strength, whereas all other beam parameters remained unchanged. The exciter power was increased from zero to the maximum possible excitation power of 50 W (this value corresponds to a power spectral density (PSD) of 0.72 mW/Hz).

The signal-to-noise ratio presented in Fig. 5 (top) was calculated by comparison of the integral underneath the tune peak in the Fourier amplitude spectrum (Fig.2) to the same width of the noise flour i.e. a part of the spectrum of equal width but outside the resonance. Each data point in Fig. 5 (top) is an average of 26 acceleration cycles. The fluctuations are represented in the error bars.

Simultaneously to the tune measurements the beam intensity and the beam profiles were recorded. The influence of beam excitation on the transversal emittance was observed by measurements of the horizontal and vertical beam profiles using an Ionization Profile Monitor (IPM) [9]. The dependency of the beam width on the beam excitation strength is shown in Fig.5 (bottom). Each data point is an average of 60 acceleration cycles, whereas the error bars indicate a maximum deviation of the single measurement from the mean value. Starting from a beam excitation of about 8 W a measurable beam broadening is observed. In addition data from the DC Current Transformer (DCCT) were analyzed in order to detect the beam losses, see Fig. 5 (middle). For the DCCT data an average of 100 measurements is taken.

A 'working area' can be defined as follows: For an exciter power of about 2 W (PSD = 0.029 mW/Hz) the S/N ratio reaches a factor of three which is sufficient for stable tune determination. On the other hand no significant beam loss exceeding 2 % was observed for excitation levels below 8.5 W (PSD = 0.12 mW/Hz). Hence, the working area can be defined to the range 2-8.5 W. Of course these values are only valid for the SIS18 beam parameters listed above since they depend on charge state, ion mass and energy ranges. However, similar measurements can be done for other ion species and energy ranges almost online.

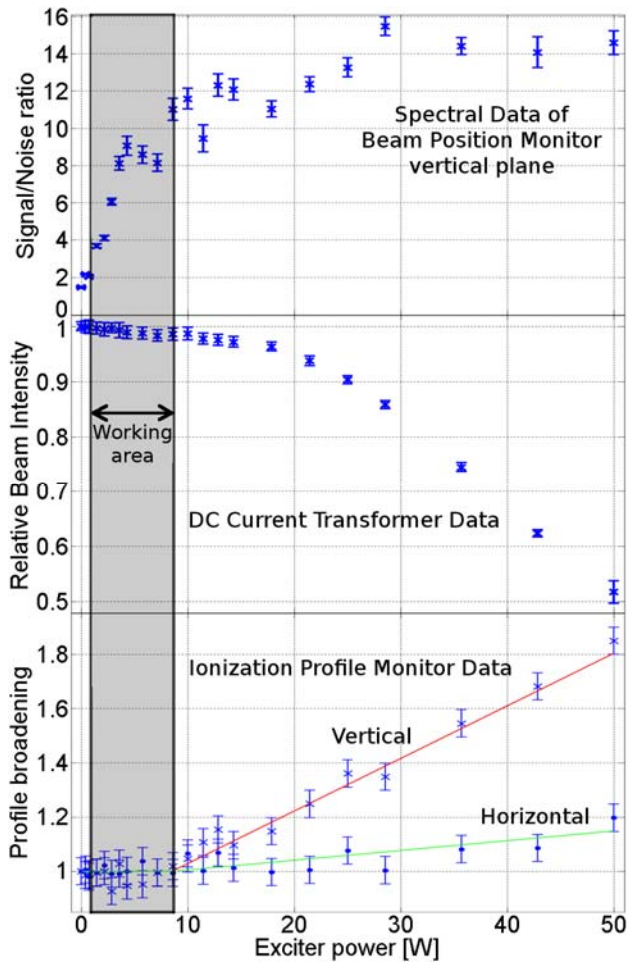

Figure 5: Influence of beam excitation using band limited noise on the signal–to-noise ratio of the tune signal (top), beam loss (middle) and beam profile (bottom). For measurement parameters see text.

Another interesting issue can be pointed out, when analyzing the bottom part of Fig. 5: Though, the beam was excited in vertical direction only, there is a

measurable response in the horizontal plane. This coupling is commonly referred to a betatron coupling and is an evidence of the skew quadrupole components caused by e.g. tilts of lattice quadrupole magnets or offsets in lattice sextupole magnets.

SUMMARY AND OUTLOOK

The base-band digitization of BPM signals together with band-limited white noise excitation of the beam allows precise tune determination on the synchrotron ramp. The measurements yield reproducible results on a low excitation level using a PSD of below 0.1 mW/Hz, thus defining the right working range for tune measurements and preventing detrimental emittance blow-up. Displaying the measured machine tune with a resolution of $\Delta q < 2*10\text{-}3$ next to a precise beam position with a resolution below 30 µm gives a powerful tool for machine operation and is a good alternative for the analog based high sensitive base-band tune detection system [10].

The advantage of the digital system is fourfold:

- Integration of each individual bunch over many samples does not only increase the effective ADC granularity but also reduces contributions of stochastically distributed perturbations like thermal or digitization noise.
- An integration of bunch signal is performed within the windows generated on the signal itself. The window width is optimally adjusted to the width of the bunch, which acts as a filter with optimal and variable bandwidth. This is extremely advantageous especially for accelerators like SIS18 with long bunches and acceleration frequency changes exceeding a factor of 5.
- Since the tune is calculated as FFT of the position data that are treated as equidistant, the tune is automatically normalized to the base-band without any additional external parameter.
- In the particular case of SIS18, where four bunches are present in the cycle, the purely digital signal treatment allows for easy selection of one single bunch. This allows removing tune signal smearing due to the eventual difference in the phase of betatron motions between the accumulated bunches. It corresponds to the gating as used in analog tune measurement systems [11].

The tune measurement presented here requires a very cautious procedure of bunch recognition: Losing even one single bunch introduces a phase offset that diminishes the measurement resolution.

The presented system is a promising prototype for tune measurements at FAIR and is actually being implemented at SIS18.

REFERENCES

[1] R. Steinhagen, CAS ”Beam Diagnostics”, Dourdan (2008) ed. by D. Brandt, CERN-2009-005, p. 317.

[2] K. Lang et al, Proc. of PCaPAC '08, Ljubljana (2008) p79.

[3] A. Hofmann, CAS - Course on Accelerator Physics, Zeuthen, (2003) ed. by D.Brandt, CERN-2006-002, p. 271.

[4] K. Blasche et al, “SIS Status Report”, GSI Scientific Report 2000, p.184

[5] P. Kowina et al, Proc. of DIPAC'05, Lyon (2005) p.114.

[6] A. Galatis et al., Proc. of EPAC06, Edinburgh (2006) p.1019.

[7] U. Rauch et al, Proc. of 5th Care-HHH-ABI workshop, Chamonix (2007), http://adweb.desy.de/mdi/CARE/chamonix/Care-Proceedings-Chamonix.pdf. and U. Springer et al. Proc. of DIPAC2009, Basel (2009) p. 324.

[8] P. Forck et al., CAS ”Beam Diagnostics”, Dourdan (2008) ed. by D.Brandt, CERN-2009-005, p.187

[9] T.Giacomini, Proc. of BIW '04, Knoxville, USA, 2004

[10] M.Gasior, Proc. of DIPAC'05, Lyon (2005) p312.

[11] M. Gasior, Proc. of 5th Care-HHH-ABI workshop, Chamonix (2007).

A SHIELDED PICK-UP DETECTOR FOR ELECTRON CLOUD MEASUREMENTS IN THE CESR-TA RING*

J. Sikora#, Y. Li, M. Palmer, Cornell University, Ithaca, NY 14850, U.S.A.
S. De Santis, D. Munson, LBNL, Berkeley, CA 94720, U.S.A.

Abstract

The experimental study of the electron cloud dynamics and mitigation techniques is one of the main objectives of the CESR Damping Ring Test Accelerator (Cesr-TA) program. Shielded pick-up buttons are a relatively simple diagnostic device for obtaining time-resolved information on the electron cloud density. They have been already successfully employed on the SPS at CERN [1], although with different resolution parameters due to the different type of beams. We present the initial results obtained using such a detector in the Cesr-TA electron/positron ring. By carefully designing the read-out electronics we were able to resolve the individual bunch contribution to the electron cloud formation process along a bunch train and gain useful information on its decay time. Alternatively, by increasing the electronics integration time, we could use our device as a sensitive detector of the average electron cloud density level generated by the passage of a bunch train.

INTRODUCTION

One of the leading R&D issues for the positron damping ring of a future linear collider is to ensure that the density of electron cloud (EC) build-up in the vacuum chambers can be kept below the levels at which beam instabilities and incoherent emittance growth will occur. In the present ILC damping rings (ILCDR) design, the presence of the EC in the positron ring limits the maximum current that can be stored and hence the minimum circumference of the ring that can be employed. As such, it is a significant cost driver for this accelerator system as well as being a major source of concern for whether the design can reach its performance goals.

Characterization and mitigation of the electron cloud effect constitutes one of the main activities in the Cesr-TA research program [2]. Several methods have been developed to experimentally study electron clouds such as retarding field analyzers (RFA) [3], TE wave based method [4], tune shift measurements with a witness bunch [5]. All these methods complement each other in that each one of them is best suited to study some particular aspects of the electron cloud dynamics.

Shielded pickups (SPU) are especially useful for measuring the time properties of the electron cloud formation and decay process at a given location in the accelerator. Their small size and relatively simple electronics also makes them a good choice as monitoring devices for the electron cloud density at multiple points around the accelerator ring. The SPU voltage V_{PU} is a function of the electron cloud density in the beampipe region close by. An estimate is given by the following formula [1]:

$$\lambda_{EC} = \frac{V_{PU}}{F_g t \cdot f_b \cdot Z_{PU} G_{sys}} \qquad (1)$$

where λ_{EC} is the electron cloud linear density, F_g a geometric factor that takes into account the SPU electrode and the beampipe size, t the shielding grid transparency, f_b the bunch frequency and Z_{PU} the pickup input impedance, and G_{sys} the system's gain.

In this paper we present our studies of the electron cloud in the Cesr-TA synchrotron ring using SPUs discussing their hardware and showing experimental results with both positrons and electrons beams.

HARDWARE DESCRIPTION

An SPU is conceptually an electrode placed on the beampipe wall, which collects low-energy electrons present in that portion of vacuum chamber and is shielded from the beam wakefield. By applying a DC bias voltage to the electrode, with respect to the pipe ground, it is

*Work supported by the US National Science Foundation, the US Department of Energy, and the Japan/US Cooperation Program.

possible to attract, or repel, electrons depending on their energy. This can be used to maximize the SPU current, when measuring the average electron cloud density, and help eliminate any residual contribution from direct coupling to the beam wakefield. Alternatively, varying the bias voltage, together with the time analysis from fast read-out electronics, can give information about the special and energy distribution of the electron cloud.

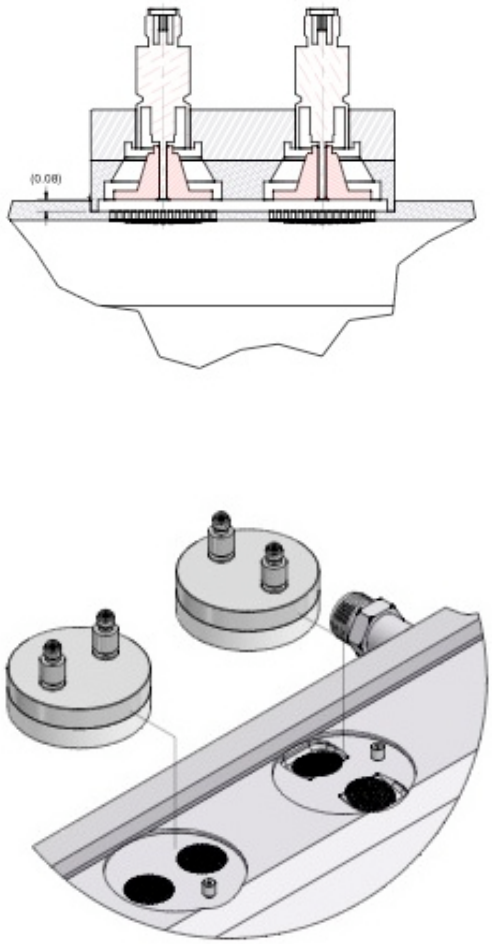

Figure 1: Section drawings of the Cesr-TA shielded pickup buttons (SPU1) and their assembly on the vacuum chamber.

To study the electron cloud in Cesr-TA and complement measurements obtained by the other methods listed in the introduction, we began installing SPUs on the ring during the Fall of 2009. The machine standard BPM buttons were used as a basis for the design of the first four units which were commissioned during the November-December 2009 experimental run.

These SPUs, shown in Fig.1, where realized by recessing standard BPM buttons 80 mils inside the pipe to allow the placement of an RF shield with a 23% transparency and circular holes with a 30 mils diameter. The electrodes diameter was a little reduced down to 680 mils to increase the gap with the vacuum chamber, thus increasing the maximum bias voltage. Connectors are standard SMA in-vacuum feedthroughs. Two pairs of SPU were initially installed on a section of straight pipe (Q15E) coated with TiN. As shown, one pair has both SPUs on the pipe axis, while in the other they are offset to the right and to the left by 550 mils. Following encouraging initial results another pair of on-axis SPU was installed on an identical straight section (Q15W), which was coated with amorphous carbon instead. After collecting data, those sections were recoated in April 2010 and are now uncoated aluminium (Q15W) and amorphous carbon (Q15E).

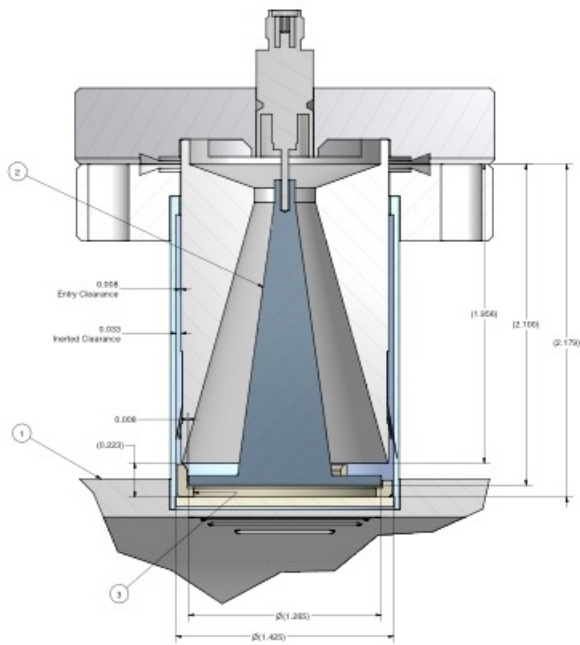

Figure 2: Drawings of the L3 shielded pickup (SPU2). Dimensions in inches.

In March 2010 it was decided to instrument the NEG coated chamber about to be installed in the L3 region with one additional SPU. A larger port, initially designed for an RFA, was made available allowing for a substantially larger SPU electrode.

A section of the new SPU, with dimensions in inches, is shown in Fig.2. The RF shield is the one originally designed for the RFA and is composed of circular holes with a diameter of 63 mils for a transparency around 15%. Due to larger gaps between the electrode and the vacuum chamber this newer SPU can support a larger bias voltage, although at present we have limited ourselves to use +50 to -50 V in all SPUs.

Several solution for the readout electronics have been implemented. For maximizing the SPU signal we have used an integrating capacitor driving a buffer amplifier, followed by a low-noise amplifier when required (Fig.3).

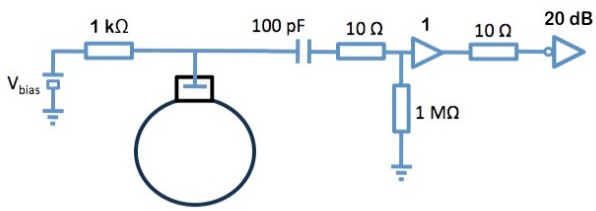

Figure 3: Integrating readout electronics. Rise time ~140 ns.

The operational amplifier used as a buffer is a National Semiconductors CLC409 with a 350 MHz bandwidth [6].

For faster applications, when we want to discriminate the contribution of each individual bunch, we use an AC-coupled cascade of two low-noise amplifiers, as shown in Fig.4.

The amplifier used is a Microcircuits ZFL-500 [7] with a 500 MHz bandwidth.

Half-inch Heliax cables are used to transmit the signal from the SPU locations to the amplifiers and scopes. Signal attenuation is of the order of a few dB.

The 2 GHz Agilent scopes used for signal analysis are linked to the accelerator control system, so that it is possible to take data remotely from the control room in manual mode or automatically whenever beam conditions change.

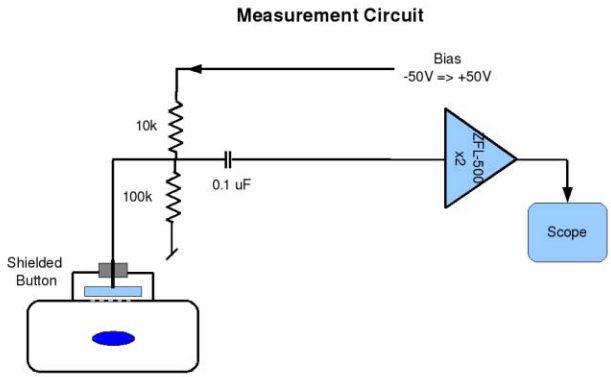

Figure 4: Fast readout electronics with sub-nanosecond response time.

CESR-TA PARAMETERS

Table 1: CesrTA Beam and SPU Parameters

Energy [GeV]	2, 4, or 5
Bunch spacing [ns]	14 or multiples of 4
Bunch current [mA]	up to 8
Bunch length [ps]	30
Beam species	electrons or positrons
Beam pipe height (in.)	1.9 (SPU1) 3.5 (SPU2)
SPU $F_g \cdot t$ [m]	$7.4 \cdot 10^{-5}$ (SPU1) $4.4 \cdot 10^{-4}$ (SPU2)

The Cesr-TA main beam parameters during our measurements are summarized in Tab.1. The machine can circulate either electrons or positron beams at three different energies. The feedback system allows for a minimum spacing between bunches of either 4 or 14 ns. Typically trains of 10, 20 or 45 bunches are used. Although many other fill configurations are possible. In particular, we have used a 2-bunch fill, with the two bunches at many different distances, to study the electron cloud formation and decay dynamics.

The beampipe in Q15E and Q15W has a quasi-elliptical shape with a 2 in. vertical

aperture and a 4 in. horizontal, while is circular in L3, with a 3.5 in. diameter.

EXPERIMENTAL RESULTS

In this section we show some interesting results from SPU measurements in the Q15E and Q15W regions. The commissioning of the SPU in L3 has just started and we are not showing results from that unit. The aluminium chamber presently in Q15W has the highest electron cloud levels and therefore offers the clearest signals.

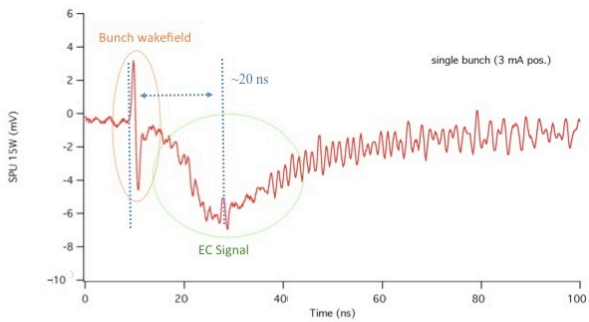

Figure 5: Single positron bunch at 2 GeV. Wakefield and electron cloud signal on the SPU in the aluminium vacuum chamber (bias +50V).

Figure 5 shows the signal from a single 3 mA positron bunch at 2 GeV in the aluminium pipe. A residual direct signal from the bunch wakefield is clearly visible on the left. This is useful as it gives a precise timing reference for the electron cloud signal, which is visible as a much broader peak following the bunch by about 20 ns. The spread in this time lag is due to electrons being generated with different energies and at different distances from the SPU.

The effect of changing bias voltage is exemplified in Fig.6: signal from two electron bunches separated by 8 ns is shown for three different bias settings. The wakefield signal for the trailing bunch is partially masked by the electron cloud signal and it is obviously independent on the bias voltage. Comparing results for different voltages we have concluded that +50V is generally a bias large enough to capture all the electrons that reach the shielding grid and using higher voltages wouldn't be particularly beneficial. We have not performed a similar assessment for the SPU in L3.

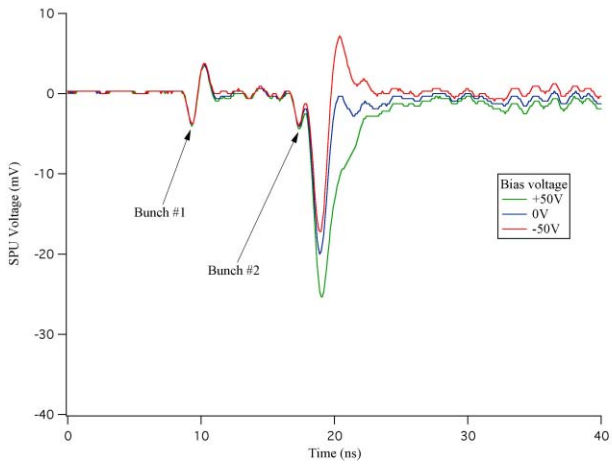

Figure 6: Effect of SPU bias voltage. 2 electron bunches (3 mA/bunch) separated by 8 ns at 2 GeV in the aluminium vacuum chamber.

A trailing bunch not only generates its own primary photoelectrons, which would generate a signal identical to the first bunch, but also kicks those electrons from the first bunch "trapped" in the pipe and slowly dissipating. These electrons can reach directly the SPU, or can generate secondary electrons by impacting the pipe walls. This is evident in Fig.7: The trailing bunch generates an electron cloud signal that can be more than ten times larger than the single bunch cloud. The signal is maximum with the second bunch trailing the first by 24 ns. Not shown in Fig.6, we can increase the bunch separation until the second bunch generates a signal identical to the first one.

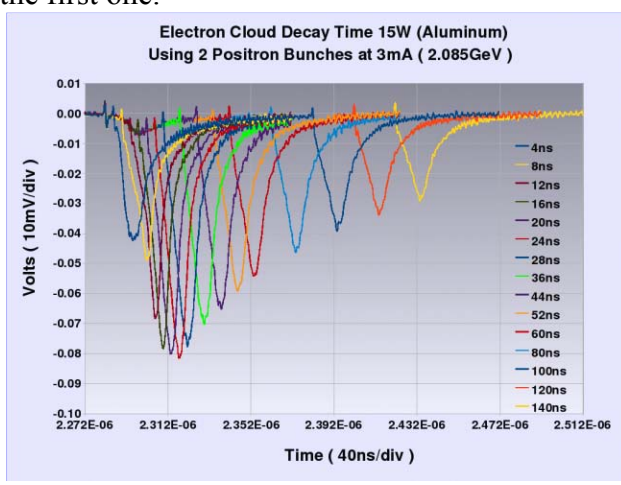

Figure 7: 2-bunch measurement, with different distances between bunches (bias +50V).

This means that the two bunches generate electron cloud independently, or that the

electron cloud generated by the first bunch has completely decayed by the time the second bunch comes around. Furthermore we can extract the electron cloud decay time to be around 100 ns by observing the reduction of the signal as distance between the two bunches increases. This figure is consistent with theoretical data for aluminium.

The effect of clearing solenoids was studied in the amorphous carbon beampipe using the integrating electronics shown in Fig.3.

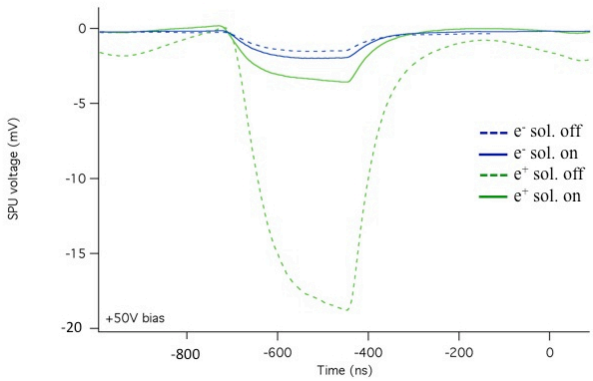

Figure 8: Clearing solenoid in Q15W. Amorphous carbon beampipe. 20-bunch train, 14 ns. 4 mA/bunch (positrons), 2 mA/bunch (electrons).

The results shown in Fig.8 show a substantial reduction of the electron cloud with a positron beam, but the effect is opposite with an electron beam. More recently, we have observed an increase in the electron cloud signal, when the solenoid is turned on, also with a single circulating positron bunch. This apparently surprising behaviour could be due to the combination of SPU and solenoid acting as a energy/mass spectrometers. We are planning to investigate this phenomenon in depth.

CONCLUSIONS

In this paper we have shown a selection of the many experimental results obtained when measuring the electron cloud using SPU in the Cesr-TA electron/positron ring. From the results shown it is apparent that SPUs are flexible diagnostic devices, which can offer useful insight for the characterization of the electron cloud in specific points of an accelerator. Average measurements of the cloud density can be performed with a high sensitivity. By using fast electronics it is possible to investigate in detail the electron cloud growth and decay process, with a resolution time shorter than the bunch spacing, thus identifying the contribution from primary photoelectrons and the beam-driven secondary emission.

REFERENCES

[1] E. Mahner, T. Kroyer, and F. Caspers, Phys. Rev. ST-AB 11, 094401 (2008).
[2] M. Palmer, et al. “The Conversion and Operations of the Cornell Electron Storage Ring As a Test Accelerator (CESRTA) For Damping Rings Research and Development”, in Proc. of PAC 2009, Vancouver (2009).
[3] R. Rosenberg and K. Harkay, NIM-A 453, 507 (2000).
[4] S. De Santis, J. M. Byrd, et al. Phys. Rev. Lett. 100, 094801 (2008).
[5] K. Ohmi, et al. “Study of the Coherent Tune Shift Caused By Electron Cloud in Positron Storage Rings”, in Proc. of 2nd APAC, Beijing (2001).
[6] www.national.com/opf/CL/CLC409.html
[7] www.minicircuits.com/pdfs/ZFL-500LN.pdf

TUNE MEASUREMENT SYSTEM AT THE ALBA BOOSTER

U. Iriso*, F. Pérez, and A. Salom.
CELLS, Ctra BP-1413 Km 3.3, Cerdanyola - 08290 (Barcelona), Spain

Abstract

The ALBA Booster synchrotron is designed to ramp electron beams of 5 mA from 100MeV to 3GeV in a 3Hz cycle. The Booster is equipped with two common $\lambda/4$ striplines for tune excitation and precise beam position measurement. Beam excitation along the cycle requires the amplitude kick to increase in synchronism with the energy ramp. This paper shows the excitation and measurement system at the ALBA Booster, including both mechanical and hardware instrumentation. First results during the 2 weeks of Booster pre-commissioning are shown.

INTRODUCTION

ALBA is a third generation light source whose injection system is composed by a 100MeV Linac followed by a full energy Booster synchrotron, which ramps the electron beams up to 3GeV in a 3Hz cycle. More details about the Booster are given in Table 1 and Ref. [1].

Table 1: Booster design main parameters.

Parameter	Injection	Extraction
energy, E [GeV]	0.1	3.0
hor. emittance, ε_x [nm-rad]	150	9
max. current, I [mA]	5.0	
circumference, C [m]	249.6	
rf freq., f_{rf} [MHz]	499.6	
hor / ver tunes, ν_x/ν_y	12.42 / 7.38	

In order to properly monitorize the betatron tunes along the ramp, two identical $\lambda/4$ stripline BPMs are installed. The first stripline is devoted to excite the beam, while the second one is used to precisely measure the beam position. Their acronyms are SEXC and SMES, respectively.

Horizontal and vertical beam excitation are done with an electrick kick whose amplitude increases in synchronism with the energy ramp. An excessively strong kick will induce beam losses at low energy, while a too weak one will not allow the measurement at full energy [2]. Two weeks of Booster pre-commissioning were scheduled during January 2010 [3]. This paper present as well the first results obtained during this pre-commissioning.

MECHANICAL DESIGN

Two pictures of the Booster stripline are shown in Fig. 1. The same setup is used for excitation and measurements, and so we used $\lambda/4$ electrodes, matched to 50Ω for tune excitation, and shorted for tune measurements (being $\lambda = c/f_{\mathrm{rf}}$ the rf wavelength).

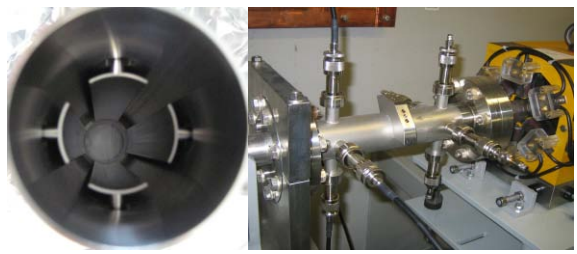

Figure 1: Picture of the stripline transverse geometry (left), and stripline as installed in the ALBA Booster. The electrode covering angle is 60°.

The electrode surface has been maximized as much as possible to increase kick efficiency when used as excitation device, and pick-up detection when used as measurement device. SUPERFISH simulations have been carried out to match the electrodes to 50 Ω. Figure 2 shows the S-parameters measured with the NA, which shows optimum results for both reflection (S11) and electrodes coupling (S12).

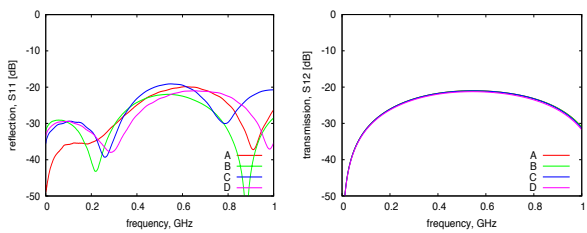

Figure 2: Stripline S-parameters as measured with the Network Analyser (NA): S11 (left) and S12 (right).

TUNE EXCITATION LAYOUT

The shunt impedance Z_{sh} of a kicker made out of two electrodes of length l and spaced with a distance d is [4]

$$Z_{\mathrm{sh}} = 2Z_0\left(\frac{2g\beta c}{d\omega}\right)^2 \sin^2\left(\frac{\omega l}{c}\right), \qquad (1)$$

where Z_0 is the vacuum impedance, ω refers to the kick angular frequency, c is the speed of light, and g is the geometrical factor. Assuming a pessimistic case of a flat electrode of $w = R \times (\pi/3)$ spaced by a distance $d = 2 \times R$ (with R the chamber radius), this is inferred as [4]:

$$g = \tanh\frac{\pi w}{2d}. \qquad (2)$$

* ubaldo.iriso@cells.es

The shunt impedance is $Z_{sh} = 4.23$ kΩ for the frequency range in which we are interested ($\omega \to 0$, since the excitation frequency is much smaller than rf frequency). With a $P = 50$ W, the angular kick is then calculated as

$$\Delta\theta = \frac{e}{E\beta^2}\sqrt{2PZ_{sh}}\,. \qquad (3)$$

For an energy $E = 3$ GeV, this is $\Delta\theta$ =0.22 μrad. Although the amplifier IFI-ML50 ensures the linearity to 50 W, it can provide up to 250 W in a non linear regime – for which the kick angle is then ∼1 μrad.

In order to excite the beam with the same angle all along the ramp, the excitation signal is ramped in synchronism with the energy increase. This is achieved with the setup described in Fig. 3.

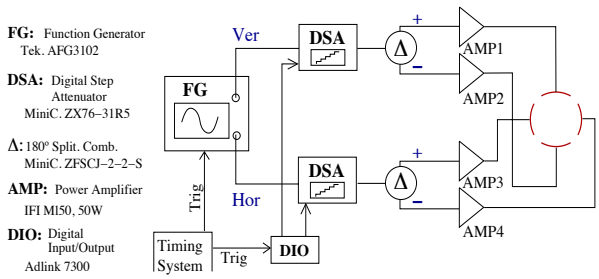

Figure 3: Block diagram of the tune excitation.

The source of the excitation signal is the Function Generator (FG, Tektronix AFG3102), which produces the white noise signal (set with a central frequency plus a frequency range). The signal is then inputed at the Digital Step Attenuator (DSA), which offers an attenuation range up to 31.5dB in 0.5dB steps. The excitation signal is later splitted using a 180° passive splitter-combiner (Δ). The two identical signals (only differing by 180° phase difference) are each amplified by the power amplifier before polarizing the two horizontal (or vertical) SEXC electrodes.

The DSA has a parallel control interface, which allows a fast switching speed up to 1 μs. It is controlled by a fast I/O module with 32 digital channels (Adlink cPCI-7300), which allows to change the DSA attenuation in 64 steps for both hor and ver planes. The timing signal triggers everything in synchronism with the energy ramp. Figure 4 shows the output of the DSA before the 180° SC.

TUNE MEASUREMENT LAYOUT

The signal picked up by an electrode is directly proportional to the electrode's surface, whence the use of a stripline BPM instead of a button BPM. This is specially useful in the early phases of the Booster commissioning (with about 0.1 mA in the machine). In the ALBA Booster, the surface ratio between both electrodes is 15.2.

Figure 5 shows the sum signal of the SMES with respect to that of a button BPM nearby over 16 kturns. The measured ratio between both signals is 6.98±0.16, which is in a good agreement with the expected value (7.6) if we also

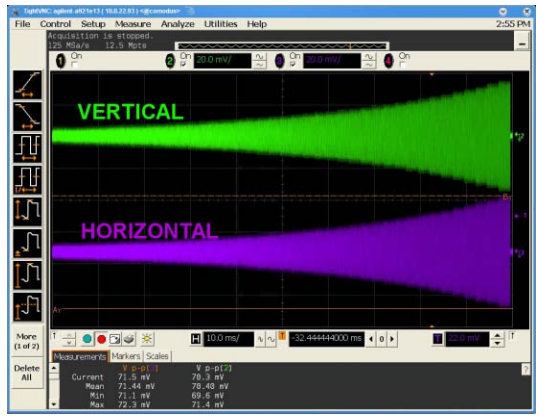

Figure 4: Vertical (green top) and horizontal (violet bottom) tune excitation signals coming from the DSA.

take into account the 3 dB provided by the splitters. It is worth mentioning that its location was in a high dispersion region and so the betatron tunes had also synchrotron sidebands (this is why the SMES signal in Fig. 5 seems noiser).

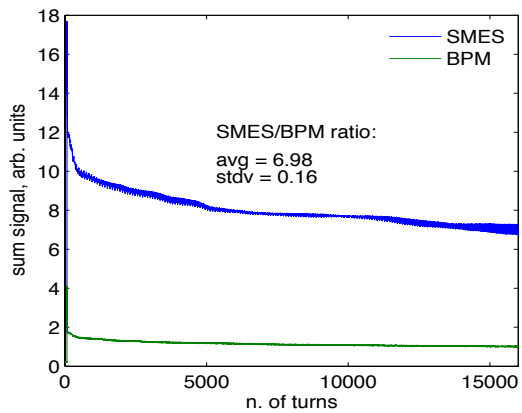

Figure 5: Sum signals of the SMES (blue) compared to the sum signal of a button BPM nearby (green).

The signal coming from the SMES electrodes is splitted in two in order to analyze it through both the BPM read-out electronics (I-Tech Libera Brilliance) and the Real Time Spectrum Analyzer (RTSA, Tektronix RSA3303A). Figure 6 shows the layout of the system that splits the signal coming from the SMES electrodes. Tunes are computed using the FFT from the Libera turn-by-turn position measurements, and the Δ signals proportional to the horizontal and vertical beam offsets.

The Libera electronics have been working on the *Data on Demand* mode in order to capture turn-by-turn data during the ∼190 kturns of the ramp. See more details about the read-out electronics in Ref. [3].

The RTSA is a fast sampling instrument with built-in FFT algorithm and data presentation. The RTSA allows a spectrum measurement every 6.4ms, which corresponds to a total of 25 measurements during the 160 ms ramp. The accuracy of this measurement is $<10^{-3}$ [5].

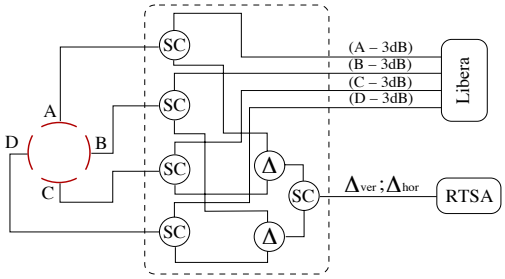

Figure 6: Block diagram of the system that splits the stripline signal for the Libera electronics and the RTSA.

RESULTS

The goal of the Booster pre-commissioning was to check that all subsystems performed according to specifications. We almost reach the full energy in one specific day (we stayed at 2.7 GeV), but in general we stayed below that to get a thorough knowledge of the machine for the next commissioning (July 2010).

Figure 7 shows an example of the tune measurement at injection, using the FFT of the hor turn-by-turn data, averaging over 10 shots. The abovementioned synchrotron sidebands are visible. We can also see that because of the coupling, both ver and hor tunes are visible.

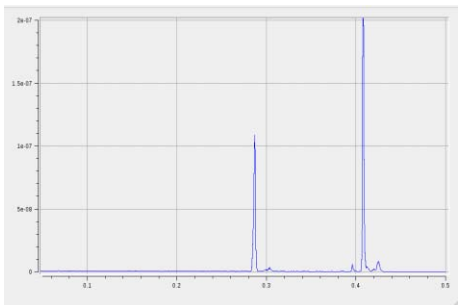

Figure 7: Tune measurement at injection.

The tune excitation application performed according to expectations. However, we would like to carry out more beam studies to perform a fine tuning of our amplifiers and evaluate the effect of the kick amplitude into the beam.

The best tune measurements along the ramp were based on the FFT calculations of the turn-by-turn data provided by the Libera electronics, which is done using the Matlab Middle Layer (MML). With this purpose, a especial GUI has been developed by Beam Dynamics group. Figure 8 shows an example of the tune measurement performed over a ramp from 0.1 to about 1GeV. In this case, the beam was lost after about 70 kturns.

During these two weeks of Booster pre-commissioning, the tune measurement system using the Real Time Spectrum Analyzer (RTSA) could not be set operational. The tune measurement based on the RTSA requires a transformation of the amplitude modulated 500 MHz - signal component as delivered by the beam to the base band. This will

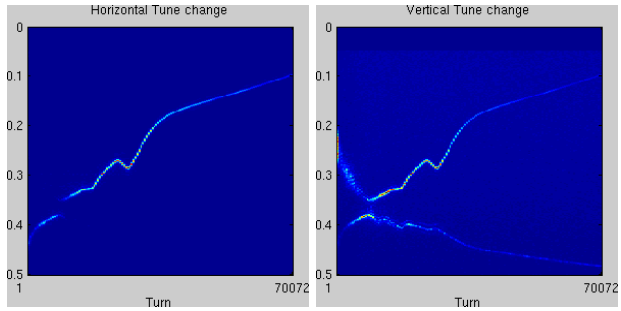

Figure 8: Tune measurement along the ramp in the hor (left) and ver (right) planes.

be done by mixing the stripline signal with the frequency of the master oscillator, or even simpler with a diode. We hope to implement this solution for the next Booster commissioning in order to produce an alternative to the MML.

SUMMARY

The use of the DSA allows to linearly increase the excitation signal with the energy gain, so as to produce the same angular kick throughout the ramp. The kick amplitude can be fixed in a range between 0.25 to 1 μrad.

The use of the SMES in the Booster produces a signal 7 times larger than the button BPMs signal. The signal from this stripline is then analyzed through two methods: FFT analysis of the beam position measurements, and through the RTSA.

The turn-by-turn data collection and FFT-analysis has been the most useful way to determine the tunes during the ramp, and so far, the only method. Further work is needed in order to properly set the tune measurement through the RTSA.

ACKNOWLEDGMENTS

We are very grateful to the Cinel colleagues for the stripline mechanical manufacturing, the Controls Group for their computing work, and M. Muñoz (Beam Dynamics Group) for the MML tune development.

REFERENCES

[1] G. Benedetti, D. Einfeld, Z. Marti, M. Munoz, M.Pont. *Optics for the ALBA Booster Synchrotron*, Proc. of EPAC'08. Genoa (Italy), 2008.

[2] J.M. Koch, J. Meyer and E. Plouviez. *New tune measurement system for the ESRF Booster*, Proc. of EPAC'08. Genoa (Italy), 2008.

[3] U. Iriso, M. Alvarez, R. Muñoz, A. Olmos and F. Pérez. *Diagnostics during the ALBA Booster*, in these Proceedings.

[4] A.W. Chao and M. Tigner (Ed.). *Handbook of Accelerator Physics and Engineering*, 2nd printing, 1998. Ch.7.

[5] S. Bassanese, M. Ferianis, F. Iazzourene. *Fast Tune Measurement System for the ELETTRA Booster*, Proc. of DIPAC03, Mainz (Germany), 2003.

DIAGNOSTICS DURING THE ALBA BOOSTER COMMISSIONING

U. Iriso*, M. Alvarez, R. Muñoz, A. Olmos, and F. Pérez.
CELLS, Ctra. BP-1413 km 3.3, Cerdanyola - 08290 (Barcelona), Spain

Abstract

The ALBA Booster is a synchrotron designed to accelerate electron beams from 100 MeV to 3GeV in a 3Hz cycle. The maximum pulse coming from the ALBA Linac provides 5 mA in the Booster. In order to check all the Booster sub-systems, a Booster pre-commissioning took place during two weeks in January 2010. This paper presents the Diagnostics elements installed in the ALBA Booster and our experience during the Booster pre-commissioning.

INTRODUCTION

The ALBA Booster installation finished in November 2009. In order to find out unexpected problems at an early stage, a short Booster pre-commissioning was scheduled for January 2010. It lasted only two weeks so as not to interfere excessively with the installation of the Storage Ring and beamlines.

The electron beam at the Booster comes from the Linac, which can work in Single and Multi Bunch Mode and was commissioned in Autumn 2008 [1]. The maximum Linac pulse charge is 4 nC, which represents a current of 5 mA at the Booster. The beam is then accelerated in the Booster synchrotron from 100 MeV to 3 GeV in a 3Hz cycle. The Booster consists of a 4-fold symmetry FODO lattice with 40 combined function dipoles [2]. The basic parameters of the ALBA Booster are listed in Table 1.

Table 1: Booster design main parameters.

Parameter	Injection	Extraction
energy, E [GeV]	0.1	3.0
hor emittance, ε_x [nm-rad]	150	9
max. current, I [mA]	4.0	
circumference, C [m]	249.6	
rf freq., $f_{\rm rf}$ [MHz]	499.6	
hor / ver tunes, ν_x/ν_y	12.42 / 8.37	
dipole field, B [T]	0.168	0.873
hor size (at dipole), σ_x [mm]	< 1.8	< 0.3
ver size (at dipole), σ_y [mm]	< 1.8	< 0.10

In order to properly check the Booster synchrotron performance, the set of Diagnostics equipment described in Fig. 1 is installed in the machine. Next, we present the Diagnostics elements installed in the Booster and our experience during the pre-commissioning.

SCREEN MONITORS

The FSOTR is the acronym used to describe the setup that allows to insert either a Fluorescent Screen (YAG:Ce) or an Optical Transition Radiaton plate. The YAG screen is used for moderate intensity beams, the OTR is devoted for high intensity beams (which typically saturate the YAG emission). The setup includes a manually controled focus and zoom optics got *off-the-shelf* from EHD-Imaging and a Gigabit Ethernet CCD camera (Basler Scout, 12-bit resolution, 1034x779 pixels, with a square pixel size of 4.65μm). More information about this setup is shown in [3].

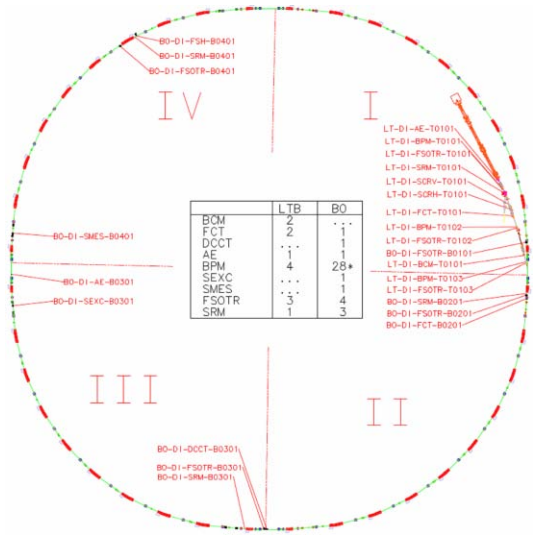

Figure 1: Linac, LTB, and Booster sketch with the location of the Diagnostics components.

We placed 3 FSOTRs to monitor the beam path along the transfer line from the Linac to Booster (LTB), while 4 more are installed in the Booster to ease the first commissioning goals (first injection, first quadrant, first turn).

In order to avoid undesirable image reflections with the YAG screen, it is convenient to make YAG plates optically non-transparent. We did so by attaching a sandblasted plate downstream the YAG. Moreover, reference marks have been added to this plate to provide in-situ calibration and centering position. Figure 2 shows an example of an image taken with the YAG screens.

BPM SYSTEM

The Booster is equipped with 44 hor and 28 ver correctors, and 44 button type BPMs. For economical reasons, it was decided to equip only 28 BPMs with the read out electronics (I-Tech Libera Brilliance). Simulations showed that the horizontal orbit correction with 28 BPMs allows an rms residual of 0.5 mm at BPMs, with a maximum of 4.5 mm

* ubaldo.iriso@cells.es

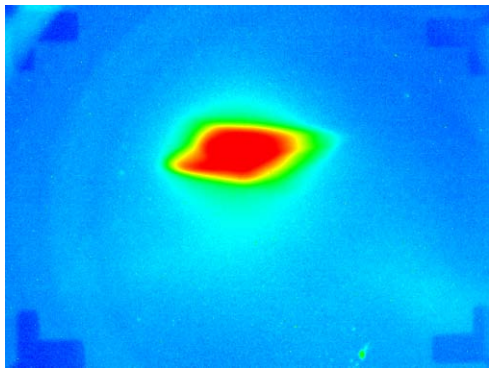

Figure 2: Example of a beam image at LTB transfer line with the YAG screen.

in the hor plane [4].

We found that the orbit correction was not efficient enough to correct the orbit on the horizontal plane, and orbits with ±4mm (at BPMs) in injection conditions were found (see Fig. 3). To improve the Booster commissioning efficiency, we are currently taking Libera electronics from the Storage Ring for all the existing Booster BPMs, so as to equip (at least temporarly) all the 44 BPMs with read-out electronics.

We typically used the Liberas on *Data on Demand Mode* (DD), which allows to obtain 200 ms of turn by turn data. Although the same trigger on all units is delivered by the ALBA timing system, data retrieval from all Libera units before the next trigger is not guaranteed. However, we did not find any trigger discrepancy. We have been using this mode to monitor the orbit along the ramp and perform tune measurements [5].

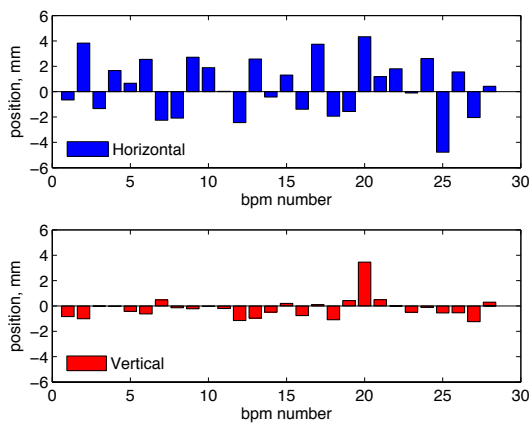

Figure 3: Example of a closed orbit measurement.

Orbit correction was performed using the *Slow Acquisition Mode* (SA), which performs an average on a 10 Hz period. Figure 3 shows an example of an orbit measurement in the hor and ver planes. A suspicious BPM (#20) was found to have too high vertical readings and higher XY coupling than the others. This BPM and its electronics are currently under investigation. The accuracy for a 0.2 mA beam was ∼4 μm on SA mode and 70 μm in DD mode, which agrees with the previous studies [7].

Tune monitoring

Two stripline BPM are installed in the ALBA Booster for tune measurements. One of the striplines excites the beam around the tune frequency (referred to SEXC in Fig. 1), while the other is connected to the electronics that compute the tune measurement (referred to SMES in Fig. 1). Details about this system are throughly given in Ref. [5].

CURRENT MONITORS

Linac, LTB and Booster are equipped with three different type of current monitors: Fast Current Transformers (FCT), DC Current Transformers (DCCT) and Beam Charge Monitors (BCM). The only worth reporting problem in all cases is the noise produced by the nearby components such as klystrons or pulsed magnets.

The Linac beam pulse charge is precisely measured with the Beam Charge Monitors (BCM). These monitors are Bergoz *off-the-shelf* components, and as reported previously, we had to struggle the noise produced by the Linac klystrons [6].

We extensively use the in-flange Fast Current Transformer (FCT) along the Linac (6 units), and Linac to Booster transfer line (2). This allows to easily monitorize transmission efficiency along the transfer line by comparing the scope signals. We did not encounter major problems with them, except for the FCT at the Booster, which picks up the noise produced by the attached Booster injection kicker – see Fig. 4.

Figure 4: Scope signal with the 2 last FCTs on the transfer line (green and violet traces), kicker pulse (yellow) and the Booster FCT signal (pink trace). The Booster FCT baseline is significantly affected by the kicker pulse.

The most precise Booster current measure is done with the DCCT, whose specifications are ±1.7μA (rms, averaging over 1ms), with a temperature drift of 10μA / °C. Figure 5 shows the current offset drift along 48 hours. It oscil-

lates with an amplitude of 40μA, consistent with the temperature evolution measured on a quadrupole yoke (temperature oscillation amplitude of 3.3 °C) and less consistent with the temperature logged in the tunnel.

During non-commissioning periods, the oscillation amplitude (no beam, tunnel open) increased to 50μA, which points towards a thermal effect. In any case, we plan to install a thermocouple at the DCCT to further study this effect.

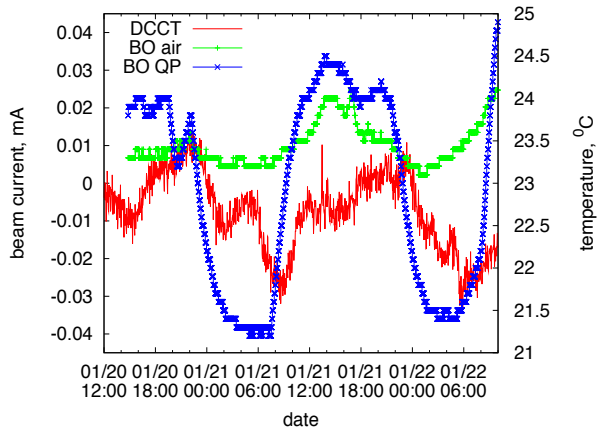

Figure 5: DCCT offset drift evolution during two days (red trace), and temperature evolution at a quadrupole yoke (blue trace) and tunnel ambient temperature (green).

SYNCHROTRON RADIATION MONITORS

The Synchrotron Radiation Monitors (SRM) infers the beam size using the synchrotron radiation produced when the beam traverses a bending magnet. The SRM setup includes optomechanics components from Thorlabs, a commercial telephoto lens (Sigma 70-300, with manual zoom and focus) and the CCD camera (same model as the FSOTR ones). These components are holded using ad-hoc mechanical supports designed in-house.

The fine image alignment is performed using the beam itself through an orientable mirror, which compensates all other mechanical misalignments through two position knobs, which is not an inmediate task: one needs several restricted tunnel accesses to move the knobs. This is not always possible during a commissioning period.

A peculiar SRM image is shown in Fig. 6, which shows two different spots. These spots slightly move when the upstream vertical corrector is powered to two different values: +0.05 A (left), and -0.05 A (right).

The reason for these two spots stems in the SRM design itself, which is limited by the available space. The SRM not only receives the radiation fan from the dipole where it is located, but also from the upstream dipole (5 m away). Therefore, we are having two images: one focused image (corresponding to the beam crossing the dipole where the SRM is located), and one unfocused image (corresponding to the upstream dipole).

The influence of the upstream dipole will be finally assessed during the next commissioning. In the other two SRM, the final image could not be evaluated because we did not have time to properly align the system.

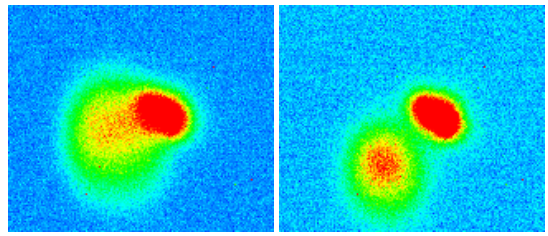

Figure 6: Images of the two beams with the SRM when the vertical corrector upstream the dipole is powered to +0.05 A (left), and -0.05 A (right).

SUMMARY

The set of diagnostics described in this report performed satisfactorily and allowed a successful Booster precommissioning. Nonetheless, few aspects are being addressed to improve the diagnostics performance.

We need to address the noise produced at the FCT by the nearby kicker. The DCCT is performing without worrying problems, and the 40μA oscillation drift is within the thermal specifications.

To improve the orbit correction, we are equipping all the 44 button BPMs with the read-out electronics for the next commissioning.

The SRM design provides two beam images in the CCD camera: one focused and one unfocused image due to the influence of the upstream dipole. Its influence will be finally assessed during the next commissioning.

ACKNOWLEDGMENTS

We are very grateful to the Controls and Beam Dynamics Group.

REFERENCES

[1] G. Benedetti, U. Iriso, and A. Olmos. *Beam measurements at the ALBA Linac*, Proc. of PAC09. Vancouver (Canada), 2009.

[2] G. Benedetti, D. Einfeld, Z. Marti, M. Munoz, M.Pont. *Optics for the ALBA Booster Synchrotron*, Proc. of EPAC08. Genoa (Italy), 2008.

[3] U. Iriso, G. Benedetti, and F. Pérez. *Experience with YAG and OTR screens at ALBA*, Proc. of DIPAC09, Basel (Switzerland), 2009.

[4] G. Benedetti. Closed orbit correction in the ALBA Booster, CELLS Tech. Note AAD-BO-BD-AN-0186, 2007.

[5] U. Iriso, F. Pérez and A. Salom. *Tune measurements at the ALBA Booster*, Proc. of BIW10, Santa Fe (USA), 2010.

[6] U. Iriso, F. Pérez and A. Olmos. *Beam diagnostics at the ALBA Linac*, Proc. of DIPAC09, Basel (Switzerland), 2009.

[7] A. Olmos, F. Pérez and T. Günzel. *BPM design for the ALBA Synchrotron*, Proc. of EPAC06, Edinburgh, Scotland (2006).

BEAM POSITION MONITORS CHARACTERIZATION FOR ALBA

A. Olmos*, M. Álvarez and F. Pérez. ALBA-CELLS, Cerdanyola del Vallès, Barcelona, Spain

Abstract

Beam position monitors (BPM) characterization has been widely studied at ALBA Synchrotron Light Source. Special care has been taken on the analysis of their electrical offset in order to achieve submicron beam stabilities. This paper shows the results of the BPM offset study for Booster and Storage Ring. The electrical effect of the different vacuum vessels housing the BPMs is also reported.

INTRODUCTION

Beam position monitoring at ALBA synchrotron will be performed using a total of 177 button type BPMs, 172 of them dedicated to pure orbit measurements; 3 will be used to do machine studies and 2 for multi-bunch instabilities measurement.

Table 1: BPM Distribution at ALBA

# BPMs	Machine	Purpose
1	Linac	Position
3	LTB	Position
44	Booster	Position
2	Booster	Machine Studies
4	BTS	Position
120	Storage Ring	Position
1	Storage Ring	Machine Studies
2	Storage Ring	Multi-Bunch

Intensive measurements of the feedthroughs during their manufacturing process have been done at the factory on the Booster and Storage Ring BPMs. Electrical tests have been done at ALBA for final manufacturing checking and electrical offset calculation of the BPMs.

BUTTONS CHECKING AND SORTING

Feedthrough capacitance has been measured at different stages during the manufacturing process of the BPM blocks in order to analyze their deviation from specifications. These tests also allow tracking of the BPM quality during the manufacturing. ALBA BPM blocks are directly welded on the vacuum chamber and any defect on the BPM block will require complete chamber replacement. For that reason, intense checking of the feedthrough quality at each stage was almost mandatory.

Measurement of button capacitance

Capacitance was measured using a TDR device [1,2]:

- After button manufacturing
- After button welding on the BPM block
- After BPM block bake-out

The plots in Figure 1 show the results of the capacitance measurement of the 204 buttons of Booster and Booster to Storage Transfer line (BTS) before and after the manufacturing process of the complete vacuum chamber. Design capacitance value was 3.2 pF. The buttons capacitance deviation from specs remained in all cases below +-10% (the tender requirement), with an absolute average value of 3.2%, maximum change on a button of +8% and -5.3%.

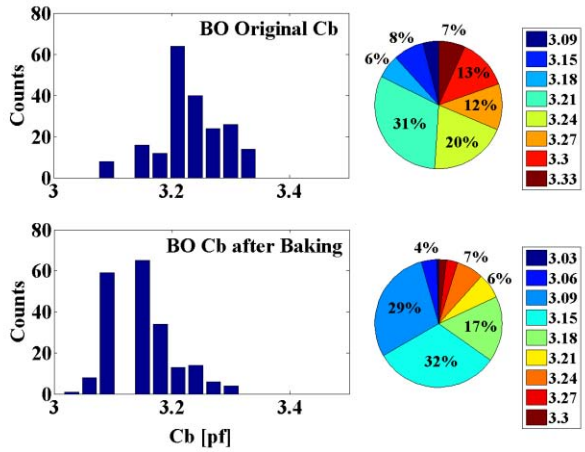

Figure 1: Capacitance deviation on Booster and BTS buttons after vacuum chamber manufacturing.

All these variations of capacitance led to an electrical offset effect on the BPMs (only due to the buttons difference). An extra effect was introduced by the relative positioning of each button on the BPM block (measured later using a network analyzer test).

Button sorting

A sorting of all buttons was done before welding in order to reduce their effect on the electrical offset of the BPMs. Figure 2 shows the calculated offset on the Storage Ring BPMs before and after welding. Buttons were sorted for closer capacitance, so the obtained offset before welding is negligible. Offset after manufacturing remains well below +-50 μm.

ELECTRICAL OFFSET MEASUREMENTS

Once the BPMs were welded and baked on the vacuum chambers and delivered to ALBA, an electrical offset measurement on all of them was performed before installation.

Electrical offset must be known in order to improve the absolute beam position readings, especially on the first days of the accelerator commissioning and operation.

*angel.olmos@cells.es

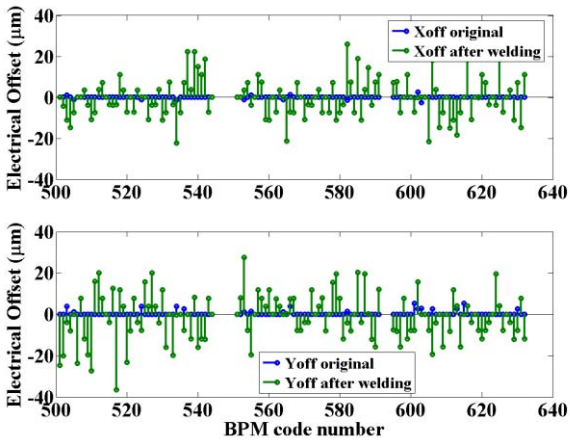

Figure 2: Calculated offset of Storage Ring BPMs before and after welding (only due to buttons imperfections).

Later, the Beam Based Alignment (BBA) technique will better determine the final settings for the correction of the offsets [3].

One of the main obstacles to overcome on the offset measurements was the fact that the BPM blocks welded on the chamber didn't allow for an antenna or wire-through based measurement. The so-called Lambertson method was used instead [4].

Laboratory setup

Pictures in Figure 3 show the measurement setup for Booster and Storage Ring BPM offset characterization.

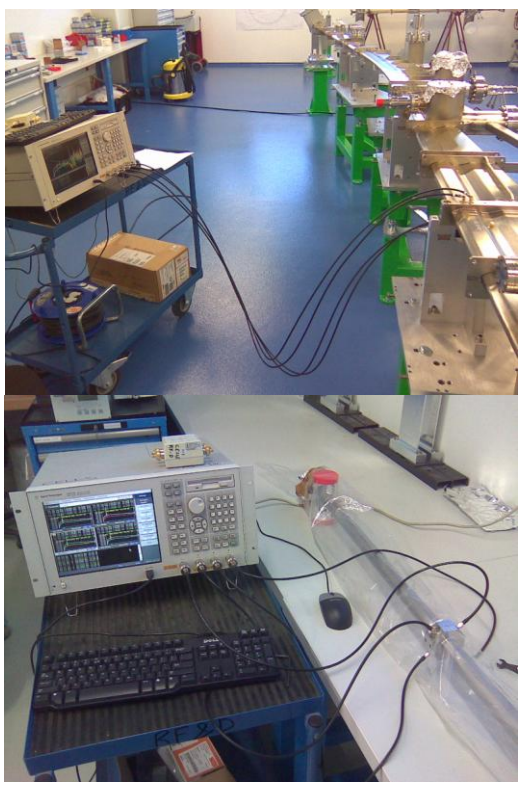

Figure 3: Measurement setup for Storage Ring (top) and Booster (bottom) BPM electrical offset.

The easurement method is based on the use of a network analyzer (NA) for scattering parameters calculation on the 4 buttons of a BPM. Output signal from the NA is injected through one button and the S-parameters to the other buttons are measured. Repeating the process on all buttons an S-parameters matrix is obtained. Ideally the reflection coefficients should be 0 and the transmission ones should be symmetric (S12=S21, S13=S31...). Transmission coefficients will determine the electrical offset value, while their non-equal value gives a figure of the differences in the feedthroughs' quality. Figure 4 shows a snapshot of the S-parameters measurement on a Booster BPM. As the BPM has a 45º symmetry, the distance from buttons 1-to-4 and 1-to-2 is the same and so S41 curve (green) is hidden by S21 (blue).

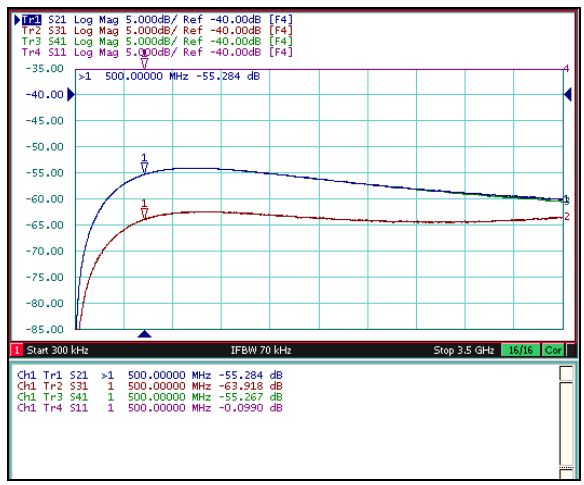

Figure 4: Snapshot of a Booster BPM S-parameters measurement

ALBA BPMs electrical offset

The electrical offset of a BPM will be determined by two effects: the non-equal electrical behaviour of the feedthroughs and the buttons positioning in the BPM block during the welding process. Due to the sorting performed prior the welding, the asymmetry of the resulting BPM block is the dominant contributor to the offset.

The electrical offset of the BPMs is computed on a Matlab based application according to the S-parameters measured in the laboratory [5]. Figures 5 and 6 show the obtained electrical offset on the BPMs finally installed in Booster and Storage Ring respectively. Comparing the results shown in Figures 2 and 6 it can be seen that main contribution to the BPM offset is determined by the errors in the positioning of the feedthroughs and the asymmetry of the resulting BPM block.

Effect of the vacuum vessel

During the measurements of the electrical offset performed on the Storage Ring BPM blocks it was seen that the ante-chamber had a high influence on the data obtained by the network analyzer device.

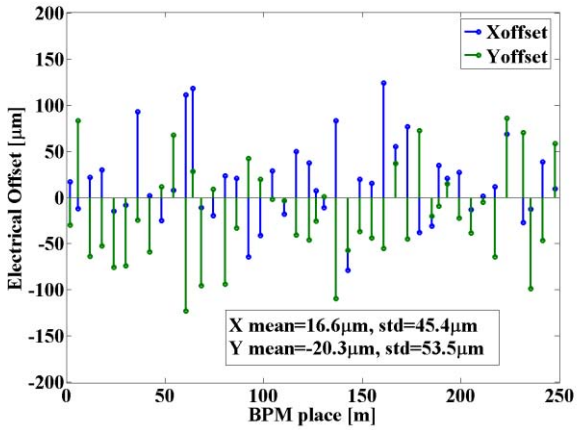

Figure 5: Electrical offset distribution for ALBA Booster BPMs.

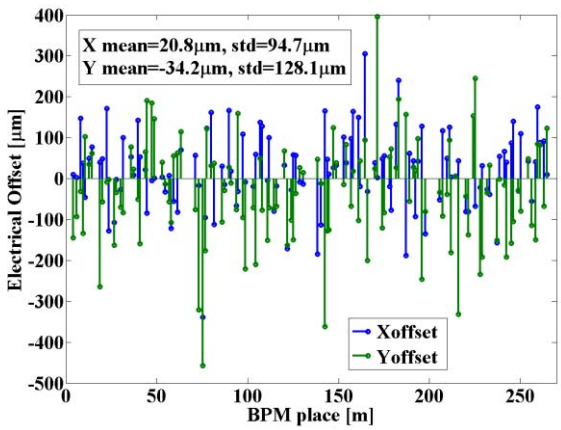

Figure 6: Electrical offset distribution for ALBA Storage Ring BPMs.

Storage Ring BPM blocks have 6 different cross sections because of the antechamber, depending on the place in the machine (see Figure 7). Cross section at the feedthroughs side is kept the same in the entire machine.

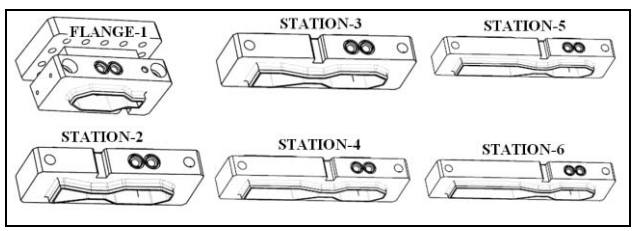

Figure 7: ALBA Storage Ring BPMs cross sections.

Figure 8 shows the data obtained when measuring the electrical offset on 4 different BPM blocks of the same vacuum chamber sector (S05 in this case).

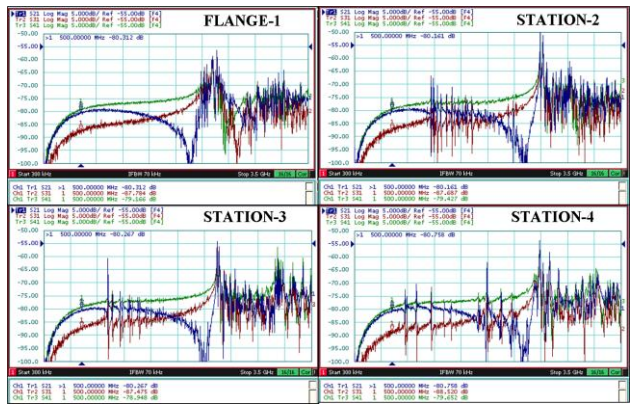

Figure 8: S-parameters on 4 different types of BPMs.

There is no ante-chamber on the Flage-1 type, whereas the length of the antei-chamber of Station type BPMs changes from one to the other, and so the transmission signals from one to another button is affected.

Increase of peaks on the S-parameters spectra is due to the extra resonance modes created by the ante-chamber of the BPM block.

Higher noise in the transmission curves compared to the ones showed for Booster (see Figure 4) is due to the smaller size of the feedthroughs electrodes. Storage Ring buttons are closer to each other than the Booster ones, but they are almost half the diameter (7 mm for Storage versus 14.3 mm for Booster).

CONCLUSIONS

Characterization of all the buttons and BPMs during manufacturing and later test on the laboratory gave us a good tracking of BPMs quality control. Electrical offset measurement was also performed on all machine BPMs in order to have a first estimation of the offset correction needed on day one. Offsets will stay between ±150 μm and ≠±400 μm for Booster and Storage Ring, respectively.

REFERENCES

[1] G. Decker, Y. Chung, “Progress on the Development of the APS Beam Position Monitoring System”, Proceedings of 1991 PAC.

[2] A. Olmos, “Sorting of the first batch of Booster buttons”, CELLS internal document AAD-BODIEBPM-A-0001, July 2007.

.[3] J. Niedziela , C. Montag, T. Satogata, “Quadrupole Beam-Based Alignment at RHIC”, Proceedings of 2005 PAC.

[4] Y. Chung, G. Decker, “Offset calibration of the Beam Position Monitor Using External Means”, Proceedings of 1991 Accelerator Instrumentation Workshop.

[5] http://www.cells.es/Divisions/Accelerators/RF_Diagnostics/Diagnostics/OrbitPosition/Tools/Offset.

FIRST BEAM MEASUREMENTS OF THE FNAL HINS RFQ*

V. Scarpine#, R. Webber, J. Steimel, S. Chaurize, D. Wildman, B. Hanna, D. Zhang, FNAL, Batavia, IL 60510, U.S.A.

Abstract

The High Intensity Neutrino Source (HINS) is a research project to address accelerator physics and technology questions for a new-concept, low-energy, high-intensity, long-pulse H^- superconducting linac. HINS will consist of a 50 kKeV ion source, a 2.5 MeV Radiofrequency Quadrupole (RFQ), and a 10 MeV room temperature spoke resonator acceleration section, followed by superconducting spoke resonator acceleration sections. To date a proton ion source and the RFQ module have operated with beam. This paper presents the results of first beam measurements through the HINS RFQ.

INTRODUCTION

The HINS accelerator project is a DOE approved and funded avenue to pursue advanced low-energy linac technologies. HINS has undergone various changes, as its development is vital for the testing and design of Project-X [1]. Details of the HINS program can be found in [2].

The HINS project has identified four basic goals [2]:

1. Demonstrate beam acceleration using superconducting spoke type cavity structures.
2. Demonstrate the use of high power RF vector modulators to control multiple RF cavities by a single high power klystron for acceleration of a non-relativistic beam.
3. Demonstrate beam halo and emittance growth control by the use of solenoidal focusing.
4. Demonstrate a fast 325 MHz bunch-by-bunch beam chopper.

Figure 1 shows an early block diagram of a 60 MeV version of the HINS accelerator. This version of HINS consists of an ion source, a 2.5 MeV RFQ, a medium energy beam transport (MEBT), a room temperature acceleration section and a series of superconducting single spoke resonator cyromodules. For this paper, only a proton ion source and RFQ have operated with beam.

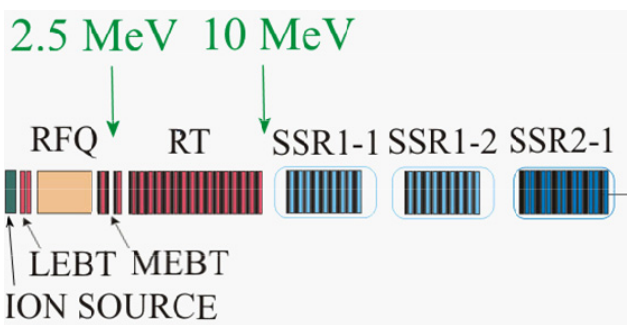

Figure 1: An early proposed HINS layout for a 60 MeV beam line and three superconducting cryomodules.

RFQ BEAMLINE

Figure 2 shows a block diagram of the present HINS beamline with its 2.5 MeV diagnostics section. This section consists of a pair of BPMs, a toroid, three transverse wire scanners and a water cooled beam dump. Figure 3 is a photograph of this 2.5 MeV diagnostic section used for the measurements in this paper.

Ion Source

The present HINS ion source is a 50 keV proton source and a low energy beam transport line (LEBT) with solenoid focusing. This proton source is capable of up to 30 mA beam in 3 ms pulses at a rate of 5 Hz [3].

RFQ

The HINS RFQ is designed to accept 50 keV beam and accelerator it to 2.5 MeV. The RFQ operates at 325 MHz and has been tested to a peak power of 450 kW, without beam, for up to 1 ms [2]. Details of the RFQ design can be found in [4].

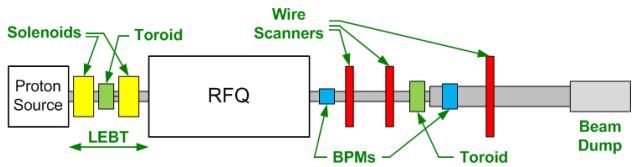

Figure 2: Original HINS proposal from 2006 showing a 90 MeV beam line and four cryomodules.

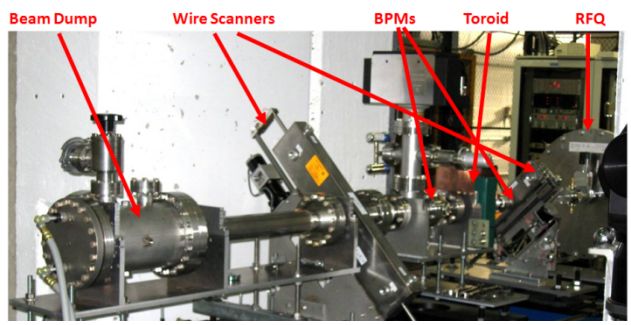

Figure 3: Original HINS proposal from 2006 showing a 90M eV beam line and four cryomodules.

RFQ BEAM MEASUREMENTS

RFQ Beam Current and Transmission Efficiency

RFQ beam current measurements were taken with a toroid in the 2.5 MeV diagnostic line. The maximum current measured was 4 mA for an input source current of 20 mA. However, these current values cannot give a measure of the RFQ transmission efficiency for two

reasons. First, the present proton source consists of an unknown percentage of other charged species, i.e., H_2^+, etc. Second, beam emerging from the RFQ rapidly expands transversely, such that beam is lost before reaching the downstream toroid.

A number of beamline improvements are being implemented in order to improve the measurement of the RFQ transmission efficiency. First, the present ion source species will be characterized to determine the percentage of protons. Second, the downstream toroid will be moved to the output flange of the RFQ. This will allow measurement of the entire RFQ beam current.

Beam Transverse Size

Beam profile measurements are made with three wire scanners in diagnostics line. These wire scanners obtain horizontal, vertical and diagonal beam profiles over many ion source beam pulses. Figure 4 shows a typical set of horizontal wire scans at a beam current of 4 mA. The data points are fitted with Gaussian profiles. The bottom right plot in this figure shows data and fits for all three wire scanners.

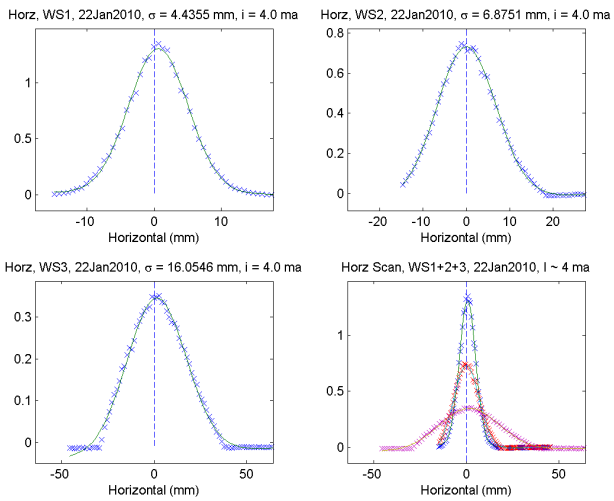

Figure 4: Typical horizontal profile measurements for all three wire scanners. Bottom right is an overlay of all three scanner measurements on one plot.

Initially, the three wire scanners were to give a measure of the RFQ beam transverse emittance. Figure 5 shows the horizontal, vertical and diagonal profile sizes as a function of beamline location. The figure also shows a linear best fit and extrapolated beam sizes at the exit of the RFQ. However, it appears that there is significant beam loss after the first wire scanner position. Table 1 gives the beam profile Gaussian-fitted sigma values and the integrals of these profiles. The integral values show that there is beam loss after the first wire scanner. This beam loss does not allow a measure of the RFQ beam emittance from the three wire scan measurements.

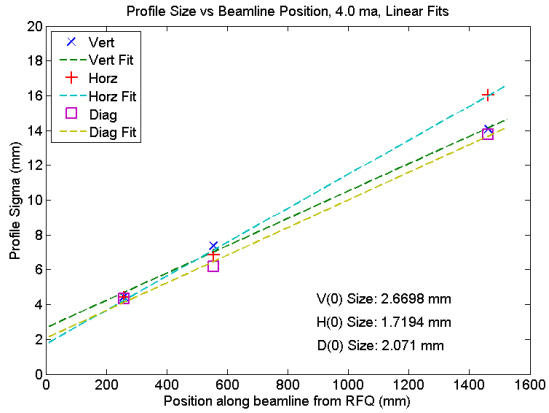

Figure 5: Beam profile sizes versus wire scanner position. The data are overlaid with linear best fit.

Table 1: Beam profile sizes and integrated areas for 4 mA beam current.

Sigmas	Horizontal	Vertical	Diagonal
Scanner 1	4.5 mm	4.2 mm	4.3 mm
Scanner 2	7.0 mm	6.8 mm	6.2 mm
Scanner 3	16.2 mm	13.2 mm	13.4 mm

Integrals	Horizontal	Vertical	Diagonal
Scanner 1	14.8 V*mm	14.9 V*mm	14.7 V*mm
Scanner 2	11.8 V*mm	10.5 V*mm	10.2 V*mm
Scanner 3	11.6 V*mm	10.1 V*mm	10.7 V*mm

Beam Energy

Initial RFQ beam energy measurements were intended to come from the time-of-flight between two BPMs in the diagnostics line. Calculations show that, for protons, a 43.9 ns time-of-flight would indicate a 2.5 MeV beam energy. However, because of the continuous nature of the beam through the RFQ, it is impossible to determine the same beam feature in both BPMs. In order to get a measure of the beam energy, we purposely sparked the RFQ to kill the beam quickly, thus generating a sharp beam edge that could be seen in both BPMs. Figure 6 shows these BPM signals and the time-of-flight difference. These data show that the RFQ beam energy is ~2.5 MeV.

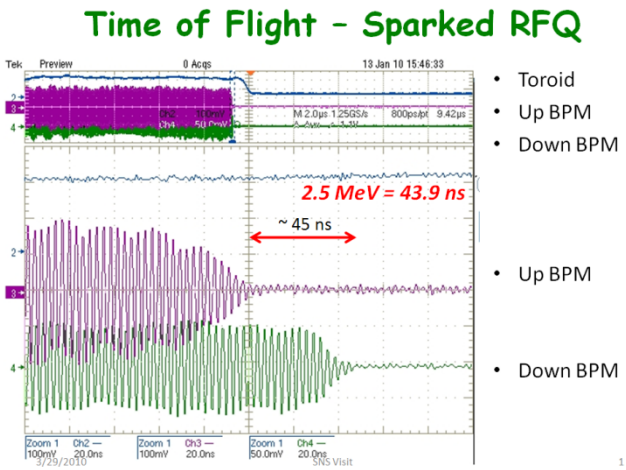

Figure 6: BPM signals showing time-of-flight time difference. Time-of-flight is consistent with 2.5 MeV beam energy.

RF Measurements

We tested the RFQ under different RF conditions in order to characterize it. Figure 7 shows the beam energy stability over a 50 µs RF pulse. The energy variation, measured by the phase difference between the two BPMs in the diagnostics beamline, is less than 8 keV, or ~0.3%, after the RFQ turn-on.

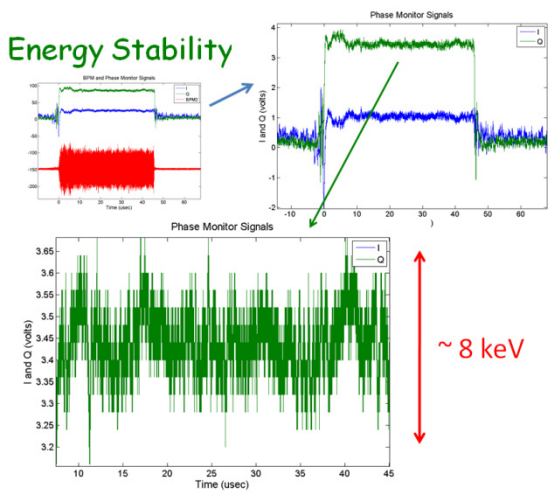

Figure 7: A measure of the beam energy stability from the BPM phase monitor I and Q values.

We also measured the RFQ efficiency versus RF power. Figure 8 shows the downstream toroid beam current as well as the magnitude of the 325 MHz frequency component of the first BPM signal as a function of RF power. The plot shows that the RFQ turns on at approximately 270 kW. In addition, the plot shows that the RFQ starts to transmit beam at a lower power, but that it has less 325 MHz bunch structure than at higher RF power levels.

We measured the change in beam transverse profile size as a function of RF power. Figure 9 shows that there is little change in the beam size when the RF power is above the 270 kW turn-on power.

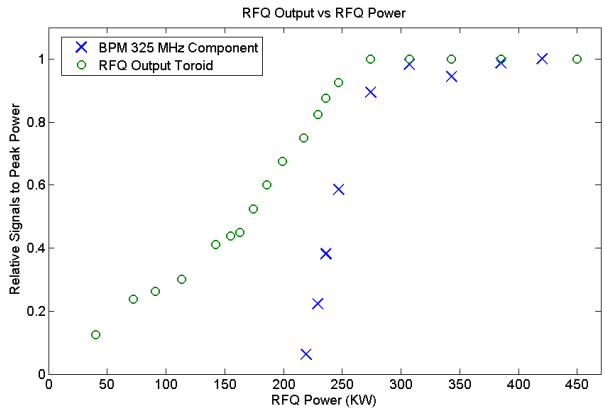

Figure 8: Relative RFQ beam output versus RFQ power.

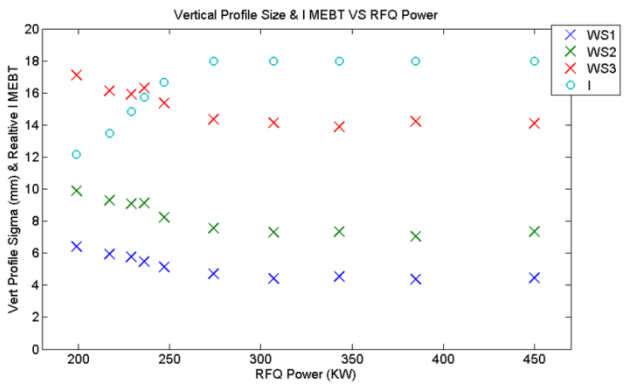

Figure 9: Vertical beam profile size at each wire scanner position versus RFQ power. The figure also shows the relative RFQ beam output current.

MEASUREMENT IMPROVEMENTS

From this initial set of beam measurements, it is apparent that improvements are needed to fully characterize the RFQ and any future HINS configurations. A number of improvements and new instruments are being implemented for HINS [5]. Figure 10 shows a schematic of a proposed new diagnostics beamline.

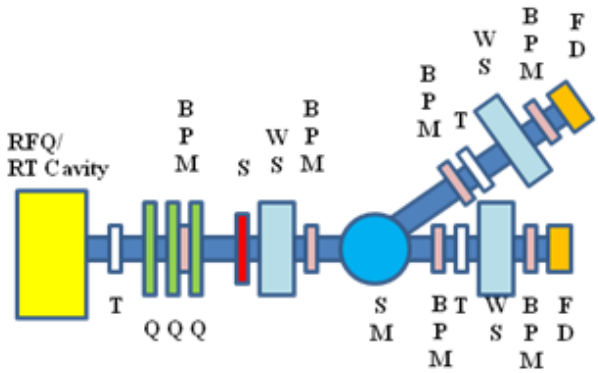

Figure 10: A schematic of an improved diagnostics beamline for HINS beam measurements. (Q) quadrupole, (T) toroid, (S) slit scanner, (WS) wire scanner, (SM) spectrometer magnet, (FD) Faraday cup/beam dump.

RFQ Efficiency

A measure of the RFQ transmission efficiency suffers from the unknown input ion source species content and the output beam loss. The present ion source is undergoing additional characterization to determine its species content. Also, a toroid is being integrated into the output flange of the RFQ to measure its output current properly.

Beam Energy

In order to measure the HINS beam energy, a magnetic spectrometer will be added to the diagnostics beamline along with downstream wire scanners. This will allow for an absolute energy measurement and a measure of the energy spread of the HINS beam.

Transverse Emittance Beam Measurements

The present diagnostics beamline has no transverse focusing and suffers from beam loss. Quadrupole focusing magnets are being added to reduce this beam loss. This focusing will also allow for transverse beam emittance measurements from quadrupole scans and a wire scan profile monitor. In addition, a slit scanner will be installed to allow for direct emittance measurements.

Longitudinal Beam Measurements

Initial beam measurements did not include any measure of the longitudinal structure of the RFQ output beam. Although not shown in figure 10, a longitudinal wire monitor, to measure bunch shape, will be added to the diagnostics beamline. In addition a high-bandwidth fast Faraday cup will also be tested to measure the longitudinal structure of the beam pulses.

CONCLUSION

Initial beam measurements have been made on the new HINS RFQ. These basic measurements indicate that the RFQ is operating within the design specifications. However, additional improved measurements will be needed to characterize fully the RFQ.

REFERENCES

[1] S. Holmes, “Project X at Fermilab: Prospects and Plans”, PAC09, Vancouver, BC, Canada, May 2009.

[2] R. C. Webber et al., “Overview of the High Intensity Neutrino Source Linac R&D Program at Fermilab”, LINAC08, Victoria, BC, Canada, September 2008, pp. 36-40.

[3] W.M. Tam et al., “Fermilab HINS Proton Ion Source Beam Measurements”, PAC09, Vancouver, BC, Canada, May 2009.

[4] G. Romanov et al., “Complete Design of the HINS RFQ with CST MWS and HFSS”, LINAC08, Victoria, BC, Canada, September 2008.

[5] J. Steimel et al., “Beam Instrumentation Requirements for the HINS Program at Fermilab”, these proceedings.

BUNCH-BY-BUNCH DETECTION OF COHERENT TRANSVERSE MODES FROM DIGITIZED SINGLE-BPM SIGNALS IN THE TEVATRON*

G. Stancari#†, A. Valishev, and A. Semenov, FNAL, Batavia, IL 60510, U.S.A.

Abstract

A system was developed for bunch-by-bunch detection of transverse proton and antiproton coherent oscillations based on the signal from a single beam-position monitor (BPM) located in a region of the ring with large amplitude functions. The signal is digitized over a large number of turns and Fourier-analyzed offline with a dedicated algorithm. To enhance the signal, the beam is excited with band-limited noise for about one second, and this was shown not to significantly affect the circulating beams even at high luminosity. The system is used to measure betatron tunes of individual bunches and to study beam-beam effects. In particular, it is one of the main diagnostic tools in an ongoing study of nonlinear beam-beam compensation studies with Gaussian electron lenses. We present the design and operation of this tool, together with results obtained with proton and antiproton bunches.

INTRODUCTION

In the Tevatron, 36 proton bunches collide with 36 antiproton bunches at the center-of-momentum energy of 1.96 TeV. Each species is arranged in 3 trains of 12 bunches, circulating at a revolution frequency of 47.7 kHz. The bunch spacing within a train is 396 ns, corresponding to 21 53-MHz rf buckets. The bunch trains are separated by 2.6-μs abort gaps. The synchrotron frequency is around 30 Hz, or 7×10^{-4} times the revolution frequency. The machine operates with betatron tunes near 20.58.

The betatron tunes and tune spreads of individual bunches are affected by the head-on and long-range beam-beam interaction. These phenomena are among the limiting factors of modern colliders. For optimal machine performance, knowledge of bunch-by-bunch tune distributions is crucial. Three systems are currently used in the Tevatron to measure incoherent tune distributions: the 21.4-MHz Schottky detectors, the 1.7-GHz Schottky detectors, and the direct diode detection base band tune (3D-BBQ). The latter two can be gated on single bunches.

Detection of transverse coherent modes can complement these three systems. The relationship between coherent oscillation frequencies and betatron tunes is indirect, and therefore a systematic uncertainty arises from the beam-beam model when extracting the lattice tunes and the beam-beam parameter. Still, the method is appealing because of its high frequency resolution.

*Work supported by the United States Department of Energy under contract No. DE-AC02-07CH11359.

#stancari@fnal.gov

†On leave from Istituto Nazionale di Fisica Nucleare, Sezione di Ferrara, Italy.

Another motivation for measuring coherent modes is our study of nonlinear beam-beam compensation with Gaussian electron lenses [1-3]. Due to their high brightness compared with protons, an improvement in antiproton lifetime from beam-beam compensation is not foreseen. The goal of this project is a proof-of-principle observation of tune shifts induced by the electron lens and the associated changes in tune spread and beam-beam parameter. This may benefit the Relativistic Heavy Ion Collider, where electron lenses are being built, and possibly the Large Hadron Collider. Also in the case of beam-beam compensation, the spectrum of coherent modes complements the observation of Schottky signals in terms of frequency resolution.

In this paper, we present the detection technique and the measured spectra of proton and antiproton bunches under various experimental conditions.

TRANSVERSE COHERENT MODES

Transverse coherent modes carry information about lattice tunes and the beam-beam parameter [4-8]. In the simplest case, when two identical bunches collide head-on in one interaction region, two modes appear: a σ-mode at the lattice tune, where bunches oscillate transversely in phase, and a π-mode, separated from the σ-mode by a shift slightly larger than the beam-beam parameter, in which bunches are out of phase.

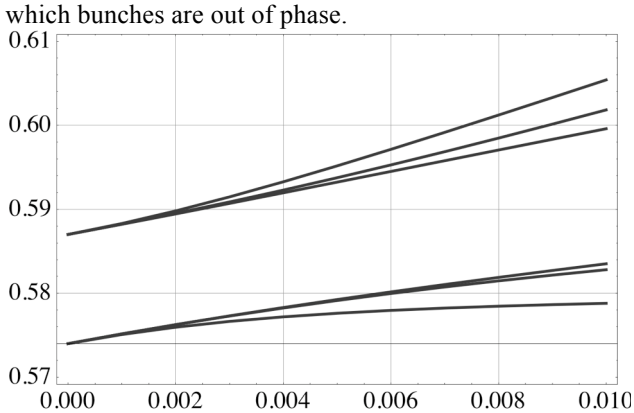

Figure 1: Sample calculation of coherent mode frequencies vs. beam-beam parameter per interaction point for 3×3 rigid round bunches with different lattice tunes.

In general, the frequency and number of these modes depend on the number of bunches and interaction regions, on the tune separation between the two beams, on beam sizes and relative intensities. Figure 1 shows how the mode frequencies evolve as a function of the beam-beam parameter, in the case of 3 rigid round bunches colliding with 3 bunches with different lattice tune at 2 head-on

crossings. This simplified model captures the essential features of collisions at the Tevatron.

Coherent beam-beam modes were observed in several electron machines, including PETRA, LEP, and VEPP-2M [4,9,10]. Although their observation in hadron machines is made more difficult by the lack of strong damping mechanisms, they were seen both at the ISR and at RHIC [11,12].

APPARATUS

The system (Figure 2) is based on the signal from a single vertical BPM (VB11) located near the B0 interaction point, in a region where the amplitude function at collisions is 900 m. It is a stripline pickup, with two plate outputs (A and B) for both protons and antiprotons. While observing the proton signal, the outputs can be split, sending half of the signal to the Tevatron BPM system and orbit stabilization and half to the present system. Antiproton signal are a factor three weaker and are usually not used for orbit feedback, so the splitter is not necessary and the full signal can be analyzed. Switching between proton and antiproton signals presently requires physically swapping cables.

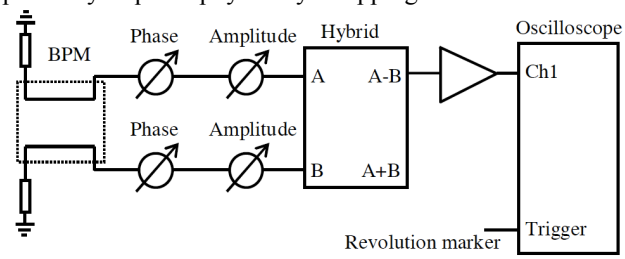

Figure 2: Schematic diagram of the apparatus.

Before processing, it is necessary to equalize the A and B signals to take advantage of the full dynamic range of the digitizer without saturating it. Equalization also reduces false transverse signals due to trigger jitter, as discussed below. The phase and attenuation of each signal is manually adjusted before feeding it to the hybrid by looking at the A–B output. If necessary, fine-tuning is done by displacing the beam with a small orbit bump. Orbits at collisions are stable over a time scale of weeks, and this adjustment does not need to be repeated often. To automate the task in the case of changing orbits and intensities (e.g., for observations at top energy between the squeeze and initiating collisions, or for observing both proton and antiproton bunches), a circuit board is being designed with self-calibrating gains and offsets.

The difference signal from the hybrid is amplified by 23 dB and sent to the digitizer. We use a 1-channel, 1-V full range, 10-bit digitizer (Agilent Acqiris series) with time-interleaved ADCs that can sample at 8 GS/s and store a maximum of 1024 MS or 125,000 segments (due to a firmware problem, only half of the memory could be used). The 47.7-kHz Tevatron revolution marker is used as trigger, so we will refer to 'segments' or 'turns' interchangeably. Typically, we sample at 8 GS/s (sample period of 125 ps), which corresponds to 150 slices for each 19 ns rf bucket. A C++ program running under Windows on the front-end computer controls the digitizer.

To enhance the signal, the beam is excited with a few watts of band-limited noise ('tickling') for about 1 s during the measurement, which simply consists of digitizer setup, tickler turn-on, acquisition start, tickler turn-off, and acquisition stop. The cycle takes a few seconds. The procedure is parasitical and it was shown not to affect the circulating beams even at high luminosity (3.5×10^{32} cm^{-2} s^{-1}). When repeating the procedure several times continuously, the 21.4-MHz Schottky spectrum showed some activity, but no beam loss was observed.

DATA ANALYSIS

Data analysis is performed offline using the multi-platform, open-source R package [13] running on the front-end computer or wherever is convenient. Data is written in binary format. It contains the raw ADC data together with trigger time stamps and delays of the first sample with respect to the trigger. Timing information has an accuracy of about 15 ps, and it is extremely important for the synchronization of samples.

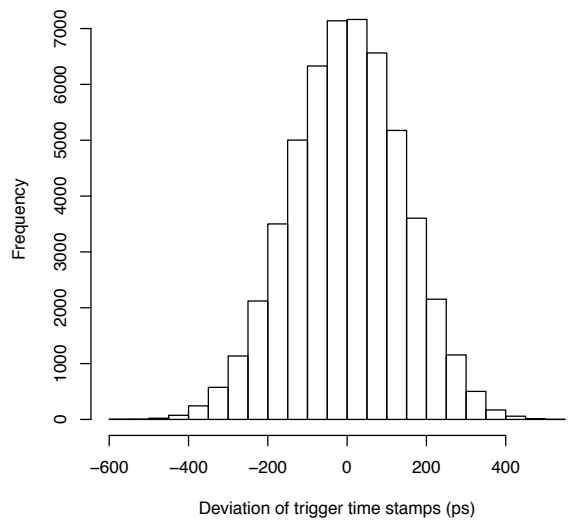

Figure 3: Distribution of the deviations of the trigger time stamp from the ideal trigger time for all 52,707 turns in a measurement.

From the distribution of differences between consecutive trigger time stamps, the average revolution frequency is calculated and, from it, the ideal trigger time stamps for each turn. The distribution of the difference between measured and ideal time stamps (Figure 3) is a measure of the jitter in the revolution marker, and its rms is typically 0.2 ns. The sum of trigger offset and sample delay is the correction by which each sample in a segment is to be shifted in time to be aligned with the other segments. For each turn and each bunch, the signal is interpolated with a natural spline and shifted according to the correction. The only side effect of this procedure is that a few slices at the edges become unusable, as they cannot be replaced with real data. The synchronization of turns is extremely important, as the jitter in trigger

translates into a false transverse oscillation where the signal has a slope. If the BPM signals are not well balanced, jitter of even a fraction of a nanosecond can raise the noise floor by several dB and compromise the measurement.

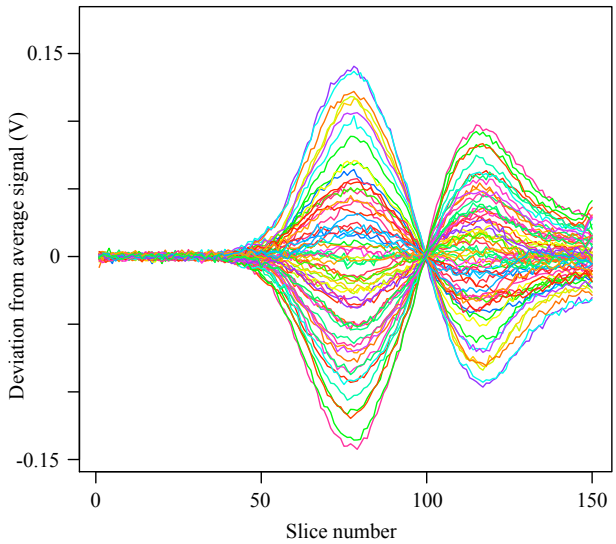

Figure 4: Example of digitized antiproton signal.

Figure 4 shows an example of digitized data for an antiproton bunch after synchronization and offset subtraction. Each slice corresponds to 125 ps. The full vertical scale represents a displacement of the beam centroid of about 20 µm. 64 randomly chosen turns are plotted out of the recorded 52,707.

For each bunch, the signal of each individual slice vs. turn number is Fourier transformed. The number of bins in the FFT vector is chosen according to the desired frequency resolution, 10^{-4} of the revolution frequency being a typical choice. The data is multiplied by a Slepian window of rank 2 to confine leakage to the adjacent bins and suppress it below 10^{-5} in farther bins. To reduce data loss from windowing, the FFT vectors are overlapped and averaged.

The noise level was estimated by observing the spectra without beam. They show several sharp lines. These are attributed to gain and offset differences between the time-interleaved ADCs themselves and to timing skew of their clocks [14-16]. The same spurious lines are also present in the Fourier spectrum of the time stamps, and this corroborates their attribution to digitizer noise.

To improve the signal-to-noise ratio, and to suppress backgrounds unrelated to the beam, such as the spurious lines from the digitizer, a set of signal slices (near the signal peaks) and a set of background slices (before the arrival of the beam) are defined. Power spectrums are extracted for both signal and background, and their ratio is calculated. The ratios are very clean, with some additional variance at the frequencies corresponding to the narrow noise spikes.

Data analysis takes about 50 s per bunch for 62,500 turns, its duration being dominated by the synchronization algorithm, which is interpreted within the R environment. Of course, it can be compiled, if necessary, and linked for faster response.

RESULTS

In preparation for our studies on beam-beam effects, the system was tested on both proton and antiproton bunches under different experimental conditions.

Beam position variations are dominated by long-term drifts, which are compensated by the orbit-stabilization program, and by low-frequency jitter, related to ground motion and other sources [17-20]. This low-frequency jitter does not affect the measurements directly, but it reduces the available dynamic range. (A high-pass filter and more amplification are being considered to improve the system.)

At injection (150 GeV), while antiprotons are being loaded into the machine on a different orbit, the proton signal shows a single main peak at the lattice tune, even without tickling (Figure 5, top). At collisions (Figure 5, bottom), a complex pattern of beam-beam modes with synchrotron sidebands appears, showing some dependence on longitudinal position in the bunch.

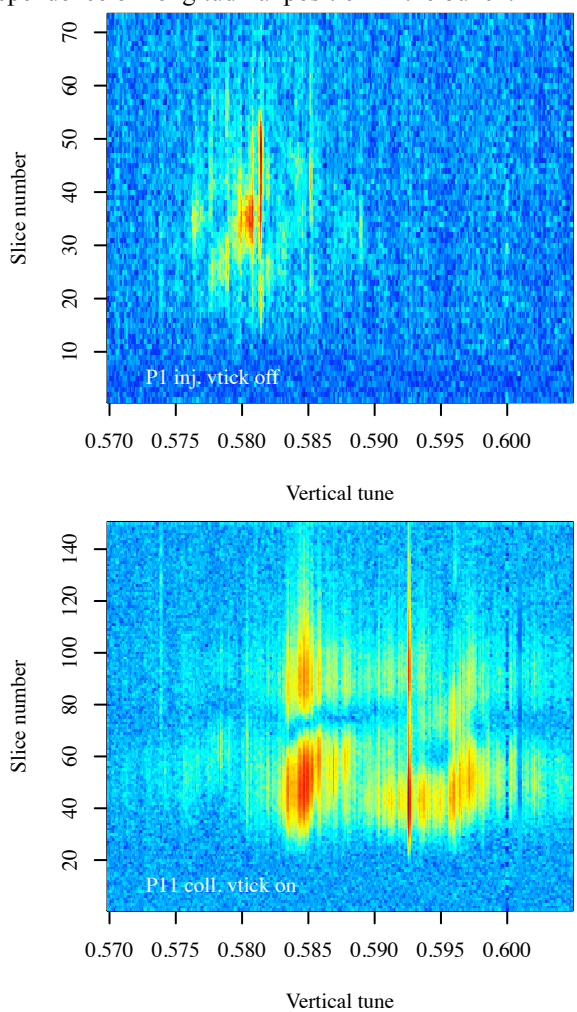

Figure 5: Comparison between the spectra of protons at injection (top) and after initiating collisions (bottom)

It was also verified that the mode frequencies respond to changes in tunes, and that the π-mode gets stronger as the tunes of the two beams are brought closer together.

The evolution of transverse coherent modes in the vertical plane over a complete store was studied with antiprotons (Figure 6). The lattice tune was intentionally changed between the last three measurements to keep the average Schottky tune constant. A decrease in mode separation can be observed, in agreement with the decrease of beam-beam forces. One can also appreciate the large ratio between signal level and background variance.

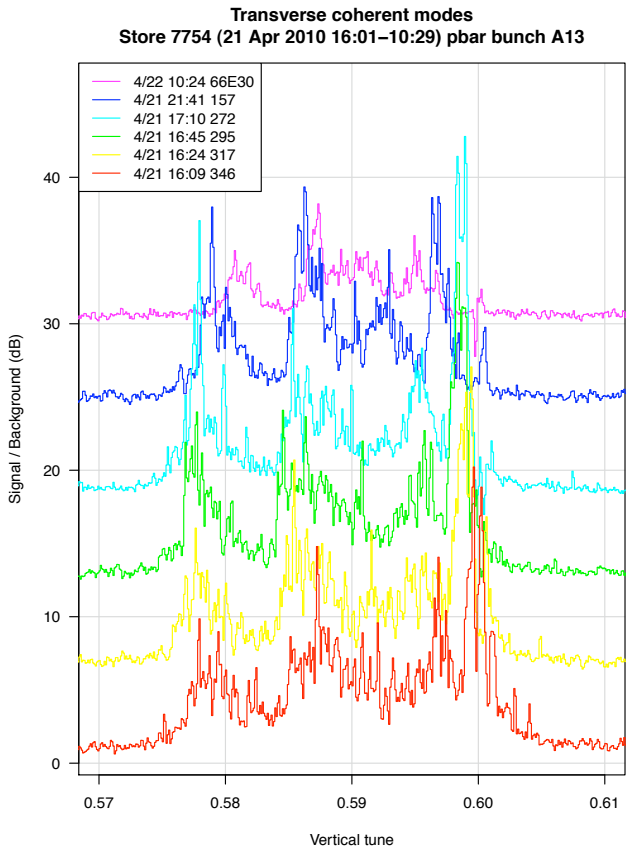

Figure 6: Evolution of vertical coherent modes over the course of a store.

CONCLUSIONS

We have implemented a system to cleanly detect transverse coherent modes of individual proton and antiproton bunches in the Tevatron. The device is used for measurements of the lattice tune and to independently estimate the beam-beam parameter. We plan to employ in our ongoing studies of compensation of nonlinear beam-beam forces with Gaussian electron lenses.

ACKNOWLEDGEMENTS

We would like to thank Y. Alexahin, B. Fellenz, G. Saewert, V. Scarpine, and V. Shiltsev (Fermilab) for their help and insights.

REFERENCES

[1] V. Shiltsev et al., New J. Phys. 10 (2008) 043042.
[2] V. Shiltsev et al., Phys. Rev. ST AB 11 (2008) 103501.
[3] V. Kamerdzhiev et al., Proc. EPAC08 (2008) 3500, http://www.jacow.org.
[4] A. Piwinski, IEEE Trans. Nucl. Sci. 26 (1979) 4268.
[5] R. E. Meller et al., IEEE Trans. Nucl. Sci. 28 (1981) 2431.
[6] K. Yokoya et al., Part. Accel. 27 (1990) 27.
[7] Y. Alexahin, Nucl. Instrum. Meth. Phys. Res. A480 (2002) 253.
[8] W. Herr, CERN-2006-002 (2006) 379.
[9] E. Keil et al., Proc. 15th International Conference on High Energy Accelerators (1992) 1106, http://cdsweb.cern.ch/record/239617.
[10] I. N. Nesterenko et al., Phys. Rev. E 65 (2002) 056502.
[11] J. P. Koutchouk, CERN ISR-OP/JPK-bm (1982).
[12] W. Fischer et al., BNL C-AD/AP/75 (2002).
[13] R Development Core Team, R: A language and environment for statistical computing. R Foundation for Statistical Computing, Vienna, Austria. ISBN 3-900051-07-0, URL http://www.R-project.org.
[14] T. Ieiri et al., Nucl. Instrum. and Meth. Phys. Res. A265 (1988) 364.
[15] N. Kurosawa et al., IEEE Proc. Instrum. Meas. Tech. Conf. 2 (2000) 763.
[16] J. Elbornsson et al., IEEE Trans. Sig. Proc. 53 (2005) 1413.
[17] J.-P. Carneiro et al., Beams-doc-1911-v1, http://beamdocs.fnal.gov.
[18] A. Semenov et al., Proc. PAC07 (2007) 3877, http://www.jacow.org.
[19] V. Kamerdzhiev et al., Proc. BIW08 (2008) 300, http://www.jacow.org.
[20] A. Valishev et al., Proc. EPAC08 (2008) 3158, http://www.jacow.org.

11.424 GHZ STRIPLINE TRANSVERSAL FILTER FOR SUB-PICOSECOND BUNCH TIMING MEASUREMENTS*

D. Van Winkle, A. Young, J. D. Fox SLAC National Accelerator Laboratory, Menlo Park, CA

Abstract

Measurement of time-of-arrival or instantaneous longitudinal position is a fundamental beam diagnostic. We present results from a stripline transversal periodic coupler structure which forms the heart of a sub-ps beam timing detector. This filter structure approximates a sinx/x response in the frequency domain which corresponds to a limited pulse length response in the time domain. These techniques have been used extensively in beam feedback systems at 3 GHz center frequencies with operational single-shot resolutions of 200 fs [1]. We present a new design, based on a 11.424 GHz center frequency, which is intended to offer a factor of four improvement in time resolution. Two-dimensional electromagnetic simulation results are shown, and the design optimization approach leading to the final circuit implementation is illustrated. The prototype circuit has been fabricated on 64mil Rogers 4003 and lab frequency domain and time domain data are compared to the 2-D simulation results. Performance of the prototype circuit is shown with applicability to sub-ps beam measurements in LINAC and FEL applications.

INTRODUCTION

In this paper, we discuss the general application of using these transversal filters for longitudinal position and phase detection in comparison to other potential schemes, followed by a brief discussion of why increasing the frequency could potentially increase the resolution, we then move on to details regarding the design of the filter and discussion of simulated vs. Measurement results. We finally discuss a demo phase detection system we simulated and have preliminarily built and close with conclusions and potential follow on work.

Application

Techniques to measure time-of-arrival or relative phase of a particle bunch are fundamental diagnostics. A bunch can be detected from the signals it generates in pick-up devices, though direct measurements in the time domain can be limited in time resolution due to the difficultly of processing very wideband signals. Some techniques use the bunch passing to resonate a high-frequency resonator as part of the beam vacuum structure, or an external resonator driven from a wideband BPM. This resonator can be a high frequency (GHz), and a phase detection technique can give high resolution in the measurement of the arrival phase. These external resonator techniques [2], [3] require adequate separation of bunches so that the excitation can decay away before the next measurement (a high-Q resonator also offers a narrower measurement bandwidth which can help improve resolution). Another approach samples the beam signals in an electro-optic sampler, which allows very high-resolution time measurements [4], [5]. However this approach is limited to sampling rates of the sampling mode-locked laser, which is typically in the 100 MHz range.

For measurements of closely spaced bunches, these resonator or electro-optic techniques are not useful (for example in bunch-by-bunch longitudinal feedback systems sampling at 500 MHz rates). For these measurement needs, a technique using short periodic coupled microwave circuits was developed [6]. The heart of this technique is a microwave circuit with a sin(x)/x frequency response, so that in the time domain the excited signal has a rect(t) envelope, and ends cleanly after a few cycles of a defined frequency. Systems of this sort have been developed at 1 - 3 GHz in several applications with resolutions of 160 - 200 fs [1]. This paper extends the technique to 11.424 GHz, and potentially improves the measurement resolution by a factor of 4.

Higher Resolution

As timing requirements become more and more stringent for various accelerator facilities, the resolution requirements for timing detection systems continue to increase. It follows logically that to detect finer and finer time scales (sub-ps), the bandwidths and frequencies of the detection electronics need to increase.

The idea for extending this technique to higher frequencies comes from the fact that if we do phase comparisons at X-Band instead of S-Band, we should see a four times increase in phase sensitivity by comparing to a frequency 4 times previous. In the case of the PEP-II longitudinal feedback system receiver noise analysis shows an effective resolution of 200 fs at 2856 MHz [6]. Extrapolation to 11.424 GHz could imply resolutions on the order of 50 fs.

In the real world, things simply don't scale quite so easily, so the authors set out to begin work on an actual demonstration system which could potentially show the aforementioned resolutions. The first step in the process is to design the transversal filter. At this stage, we are still working on the estimation of the actual resolution.

TRANSVERSAL FILTER DESIGN

General Considerations

The basic structure of this filter is that of microwave couplers connected together by quarter wave transmission

*Work supported by Department of Energy contract DE–AC03–76SF00515 and the US-Japan High Luminosity Collaboration

lines. A plot showing how the filter shape changes based upon the number of sections is shown in figure 1.

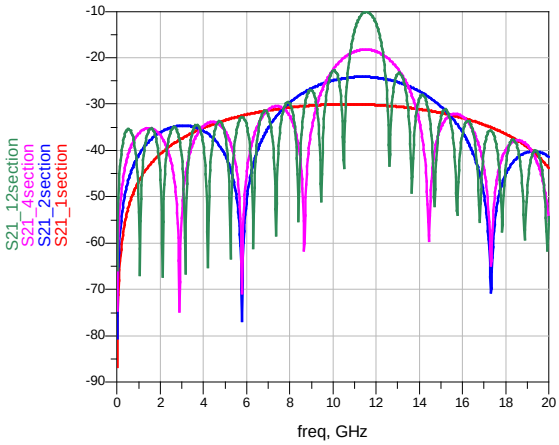

Figure 1: Plots of various numbers of sections of transversal filter

As with any design, it is important to start with design goals and key parameters. The key deign parameters for the filter we designed are shown in Table 1.

Table 1: Filter Design Parameters

Parameter	Value
Number of Taps	12
Center Frequency	11.424 GHz
Board Thickness	64 mils
Board Material	Rogers 4003
Technology	stipline
Coupling per section	30 dB

12 taps were chosen so that the effective output pulse would have a length of approximately 1 ns at a center frequency of 11.424 GHz. The center frequency of 11.424 GHz was chosen because it is a convenient multiple of the 2856 MHz which is main line frequency at the SLAC linac. A board thickness was chosen at 64 mils because on the Rogers material, the line thicknesses were quite well matched to the available stripline launches. The Rogers board material was chosen because it has been shown to work quite well at these frequencies in numerous other projects. Stripline was chosen over microstrip due to its inherent shielding.

In choosing the coupling factor, the design trades-off several constraints. A very low coupling factor is undesirable in the total output signal, but is useful in that the energy removed along the line is a small fraction of the incident pulse, and the coupling does not have to be varied down the line to have constant output pulse amplitude vs. time. Additionally, a strongly coupled line means that small mismatches and imperfections between the sections are more significant in their impact in the time structure of the output pulse. We have experience building these stripline generators at 3 GHz with coupling factors from 10 through 40 dB, and based on our experience at 3 GHz we chose 30 dB as a reasonable starting point for this 11.424 GHz evaluation.

Detailed Design

To begin the design, rather than just simulate the entire 12 coupler filter, we simulate a single section a single set of connecting lines. The main goal of this is to set the overall through path length to 180 electrical degrees while centering the coupled section at the desired center frequency. This would be seemingly easy since the coupled section, when centered, is naturally 90 degrees long. Then it would just be a matter of adding a 90 degree transmission line to connect to the next coupled section. Unfortunately, you cannot just connect to the next section with a straight line or you will end up with two staggered couplers which are not what we desire. In essence, you want a coupled section followed by a non coupled section. One way to do this would be to offset the connecting lines from the coupler so that they form a coupled section with less coupling. An idea like this is shown in Figure 2

Figure 2: Potential idea for offset connecting lines.

Unfortunately, this did not work well because of the discontinuity between the two lines resulted in a large VSWR. Since we are connecting multiple sections together, the VSWR between sections can become so significant as to render the structure. The structure finally used in the design is as shown in Figure 3.

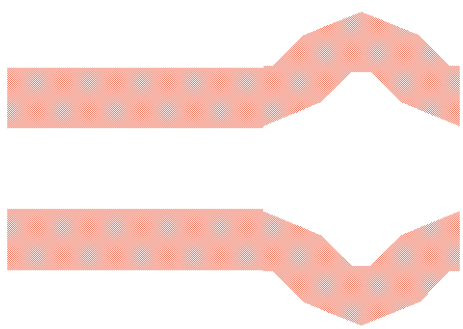

Figure 3: Realized coupler and connecting lines

The Agilent Analog Design System (ADS) used to simulate these structures has two main components useful for this type of design. One uses a model based circuit type simulator for a starting point in the design. While

these models are typically very good, as designs are pushed higher in frequency, it becomes necessary to use the momentum 2.5D field solver which has shown excellent accuracy in the past. Once the single section has been fully optimized so that good return loss and proper phase delay and coupling is achieved then the overall circuit can be combined into the 12 section filter design.

In much the same way as the single section, the twelve section filter is analyzed using a combination of the linear modelling simulation and momentum 2.5D simulations. Because the single section was so well analyzed before the combining, very little iteration was required. A 3D visualization of the circuit as simulated is shown in Figure 4.

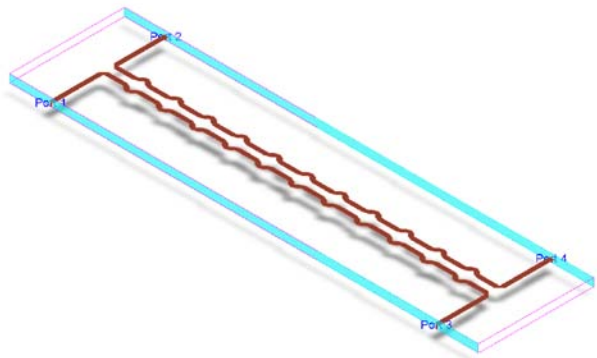

Figure 4: 3D visualization of final 12 coupler filter.

For illustrative purposes, a plot showing the difference between the model based and field solver based solutions is shown in figure 5.

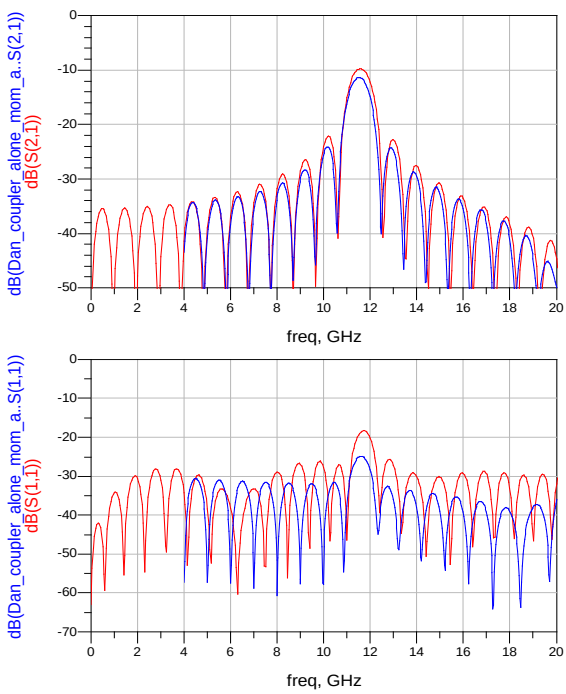

Figure 5: Difference between model and field solver simulations. These differences can be mostly attributed to small errors of the model based simulation. In addition, coupling in the "non-coupled" sections is ignored in the model based simulation.

FABRICATION AND MEASUREMENT RESULTS

Fabrication

The circuit was fabricated on Rogers 4003 material in two halves to allow for easy attachment of input and output connectors. This immediately introduces some error into the overall design since a small gap of air dielectric could be present between the two halves of the board due to the thickness of the circuit metallization. We chose to ignore this in the original design.

Figure 6 shows a photograph of the board as fabricated. In addition to the board, two gold plated aluminium plates were fabricated to ensure that the boards were held tightly together and to create a stable mount point for the sma stripline launch connectors.

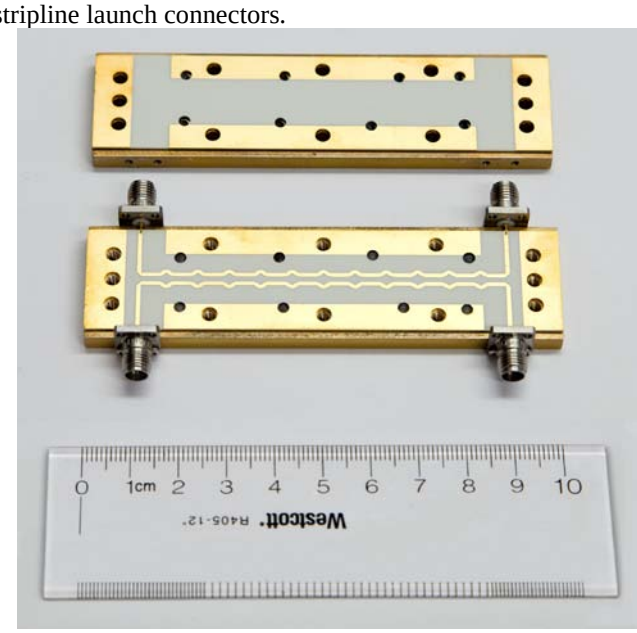

Figure 6: Fabricated board and plates with sma connectors

Measurement

The filters were measured on an Agilent 8720 network analyzer to verify the performance against the simulations. Figure 7 shows the measured response of the filter contrasted with the momentum simulation results. As is clearly seen in this plot there is a frequency error of the center frequency of the filter of about 466 MHz or 4%. This is not a surprise to author DVW, and what is typically done is another turn is done with a new design centered 4% lower in frequency. One revision on the board is usually enough to resolve this type of error. The good news is that the circuit will still behave as expected but with a slightly different frequency of operation. With the 1 ns pulse length, the impact of this 466 MHz error is to introduce a tilt in the phase detected baseband pulse output (instead of mixing the signal to DC, the phase error is really the difference frequency at 466 MHz). Since

each pulse starts off as a unique impulse signal, if the phase detector is set to sine-like detection (nominally zero output) the error signal follows a cosine-like amplitude, and the initial error voltage starts to assume a cosine at 466 MHz For a 1 ns length pulse, for tilts of less than 50% (cosine of 60 degrees) the frequency error should be less than 170 Mhz. The actual measured phase error from sampling this pulse is related to the sampling time jitter and the slope of the output baseband pulse.

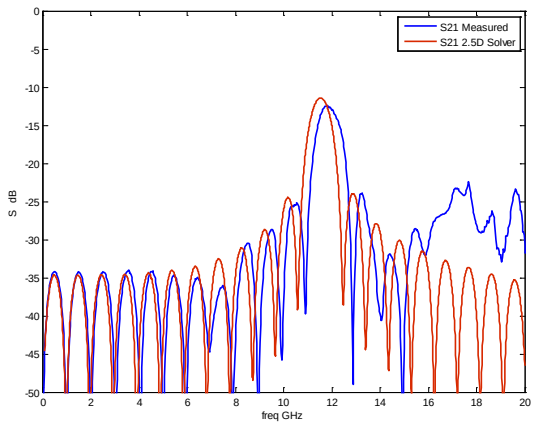

Figure 7: Measured S21 of measured and simulated filter

Testing the circuit in the time domain requires an "impulse" or delta function signal generator. In actual practice, signals from bunched beams serve as excellent impulse generators, and lab generators often have slower rise times and are not as clean. It is possible to test the generator with step-recovery diodes, which produce 100 - 200 ps impulses, though they have shapes which are not Gaussian, and the signals have significant "tail" components after the initial impulse. These generators have served to test our 3 GHz generators, but we observed strange responses using them to excite this 11.424 GHz circuit.

For our initial measurements we injected an approximately 120 ps wide impulse signal generated by a 119 MHz driven step recovery diode. The response was measured using an Agilent 86108 Precision Waveform Analyzer. The obtained response was very surprising to us and led us to return to simulation to see if what we were seeing made sense in comparison to what we actually measured. To do this, we used the time domain SPICE based simulator built into ADS which allows us to combine S-parameter data into a time domain simulation. We used the S-parameter data from the 2.5D solver and for an input as shown in figure 8, we obtained an output as shown in figure 9. Both figures 8 and 9 show the simulated and measured responses. The surprise we observed was the very large spikes at the beginning and end of the pulse train, and the relatively insignificant signal we were seeing at the desired frequency.

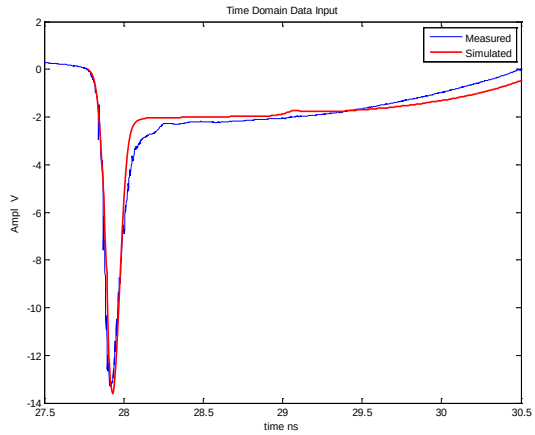

Figure8: Simulated and measured input impulse

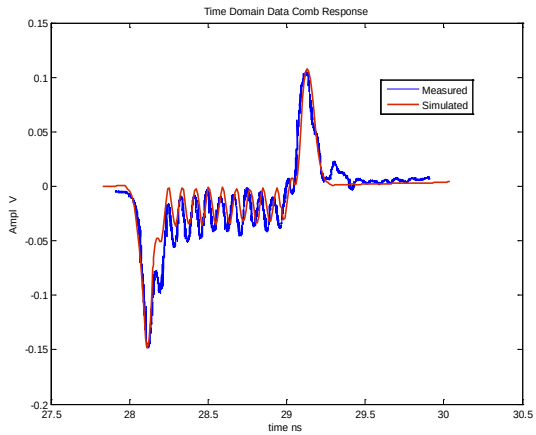

Figure 9: Simulated and measured filter time domain response to 120 ps impulse

Upon further investigation in the simulation, we began to realize that the width of the impulse has a profound impact on the “overshoot” at either end of the response. We were able to use a picoseconds pulse labs 3500C 60 ps impulse generator to further verify this and the results from that measurement are shown in Figure 10.

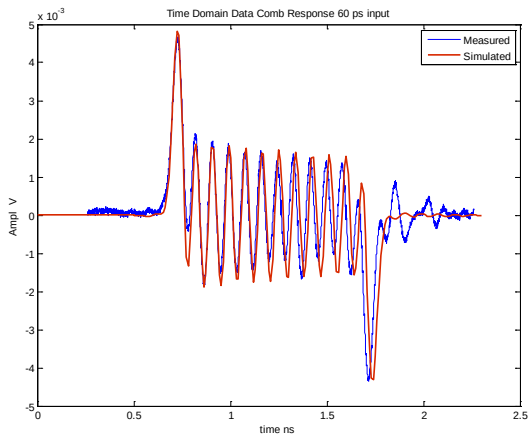

Figure 10: 60 ps impulse response

As a further investigation into this phenomenon, we simulated the ideal circuit using SPICE over a wide range of pulse widths and calculated the “% overshoot” using

the difference of heights between the first overshot impulse and the amplitude of the next peak divided by the amplitude of the first peak. These results are shown in figure 11.

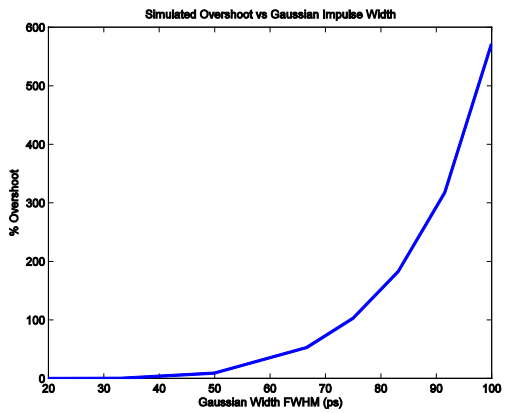

Figure 11: % Overshoot vs. Gaussian impulse width at FWHM

PHASE DETECTION EXAMPLE

As a way to demonstrate this technique, a simple phase detection scheme was simulated and built using our filter. The essential idea is to generate impulses at some sub-multiple of the center frequency of the filter and then use a mixer and low pass Bessel filter to detect the "DC" component of the phase detection. Figure 12 shows the simulation block diagram which is very similar to the actual circuit we built and tested. This type of phase detector has a sinusoidal output vs. Phase shift and the simulation shows this clearly. The system we build contained a variable phase shifter which allowed us to vary the LO phase (unlike what is shown in the simulation diagram).

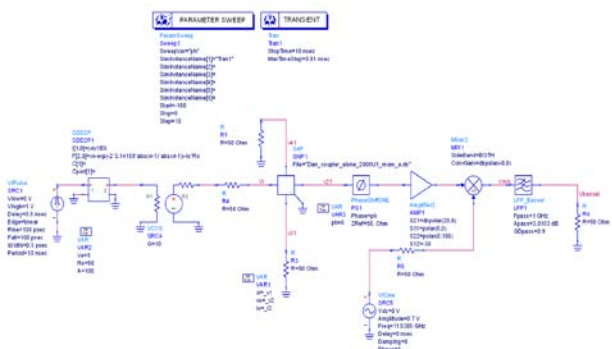

Figure 12: Simple phase detection scheme

We obtained screen captures from the phase detection hardware but were having trouble maintaining constant phase due to variations in temperature. The results from those measurements are shown in Figure 13. A strange asymmetry is occurring; at this point we have not yet had time to fully explain.

Further work is required to verify our estimate of a 4X increase in sensitivity..

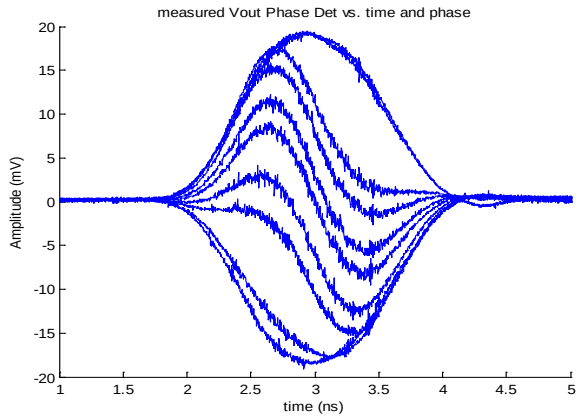

Figure 13: Time domain response of test phase detector

CONCLUSIONS AND FOLLOW ON IDEAS

One interesting aspect of this work with the 11.424 GHz comb generator is the recognition that at these frequencies, the generation of a clean beam-derived signal to drive the comb is a special concern. If one wants to use this technique at higher frequencies, the generation of the beam input signal requires special care to get the clean short tone burst signal at full amplitude. The best use of this comb circuit might be as a part of a pick-up electrode or vacuum structure itself, as this would allow the highest fidelity coupling to the bunched beam signal. This approach also is attractive in that it reduces the bandwidth requirements on associated feedthroughs and cable assemblies. Such an integrated processing electrode combining pickups and comb generators would be a very challenging and interesting microwave circuit design.

ACKNOWLEDGEMENTS

The authors would like to personally acknowledge Dr. Makoto Tobiyama of the Beam Monitor Group at KEK for his longstanding support, thoughtful collaboration and enthusiasm for lab demonstration projects." He is great guy.

REFERENCES

[1] Stripline Transversal Filter Techniques for Sub-picosecond Bunch Timing Measurements. J.D. Fox et al. DIPAC 2007, Venice, Italy, 20-23 May 2007.

[2] Performances of the SPARC Laser and RF Synchronization Systems. A. Gallo, D. Alesini, M. Bellaveglia, G. Gatti, C. Vicario, (Frascati) EPAC08-THPC156, Jun 26, 2008. 3pp.

[3] LCLS Beam Phase Cavity and Detection, Internal design review, SLAC Joe Frisch

[4] F. Loehl et al. EPAC08-THPC158, Jun 26, 2008.

[5] S. Schulz et al. EPAC08-THPC160, Jun 26, 2008.

[6] D. Briggs, P.L. Corredoura, J.D. Fox, A. Gioumousis, W. Hosseini, L. Klaisner, J.L. Pellegrin, K. Thompson, (SLAC) , G.G. Lambertson, (LBL, Berkeley) . PAC-1991-1404, May 1991. 3pp.

STABLE TRANSMISSION OF RADIO FREQUENCY SIGNALS ON FIBER LINKS USING INTERFEROMETRIC DELAY SENSING*

R. Wilcox, J. M. Byrd, L. R. Doolittle, G. Huang#, J. W. Staples,
Lawrence Berkeley National Laboratory, One Cyclotron Road, Berkeley, CA 94720, USA

Abstract

We demonstrate distribution of a 2850 MHz radio frequency signal over stabilized optical fiber links. For a 2.2 km link we measure an RMS drift of 19.4 fs over 60 hours and for a 200 m link an RMS drift of 8.4 fs over 20 hours. RF signals are transmitted as amplitude modulation on a continuous optical carrier. Variations in the delay length are sensed using heterodyne interferometry and used to correct the RF phase. The system uses standard fiber telecommunications components.

INTRODUCTION

The next generation of accelerator-driven light sources will produce sub-100 fs high brightness x-ray pulses [1]. Pump-probe experiments at these facilities require synchronization of pulsed lasers and RF accelerating fields on sub-100 fs time scales over distances of a few hundred meters to several kilometers. Several approaches have been implemented to send stable signals over fiber optics, with average uncertainties of a few hundred femtoseconds to under 10 fs[2, 3, 4, 5, 6].

We describe a system for stable radio frequency distribution which has demonstrated less than 20 fs RMS jitter and drift over 2.2 km of optical fiber for 60 hours, and less than 10 fs over a 200 m fiber, using common fiber telecommunications components and microwave electronics

The system is easily manufacturable and low cost. It is straightforward to expand to many channels, because all delay control is done electronically in the receiver rather than by mechanical delays at the transmitter. Eliminating commonly-used mechanical delays also improves reliability and provides an arbitrarily large delay correction range, limited only by software. Because delay sensing is done using a continuous optical carrier, rapid delay changes beyond the control bandwidth are tracked continuously without jumping fringes. Standard fiber is used, requiring no dispersion compensation. Signal processing in the receiver is done digitally, so all key parameters are inherently controllable. Any frequency or combination of frequencies can be transmitted, in contrast to a fixed set of harmonics available in pulsed schemes.

A schematic diagram of a single-channel RF transmission and delay stabilization link is shown in Fig. 1 (a dual-channel variant is shown in Fig. 2). In our scheme, the optical phase delay through a fiber is precisely measured using a heterodyne interferometer. This measurement is used to correct the phase error of an RF signal which is transmitted on that fiber. We can derive simplified equations for propagation of optical and RF signals through the link, assuming that the small and constant delays within the temperature controlled boxes are zero.

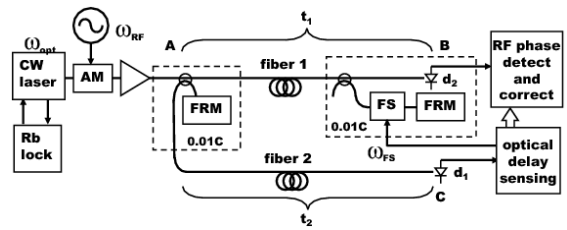

Figure 1: Schematic layout of a single channel RF transmission over an optical link. RF frequency is 2850 MHz. AM: Amplitude modulator; FRM: Faraday rotator mirror; FS: optical frequency shifter. Dotted rectangles indicate components temperature controlled to ±0.01° C.

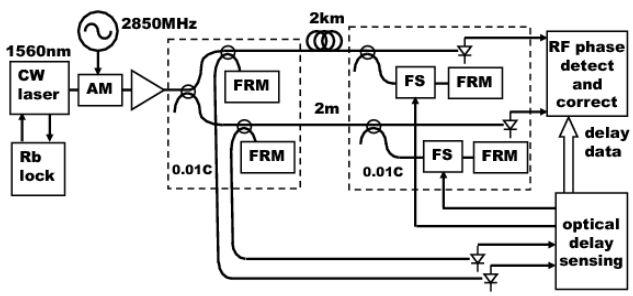

Figure 2: Dual channel RF transmission experiment. RF frequency is 2850 MHz.

To understand the operation of the interferometer, consider an optical wave starting at A and propagating through fiber 1 with delay t_1. At B, it is shifted in frequency by ω_{FS} by the optical frequency shifter (FS), retroreflected by the Faraday rotator mirror (FRM) and shifted in frequency again. It goes back through fiber 1 with delay t_1 to A, through a directional coupler, and through fiber 2 with delay t_2 to C. This is the "long" path. A second path through the interferometer is from A to the Faraday rotator mirror in the box at A, back through the directional coupler, and through fiber 2 to C. This is the "short" path. These two waves can be represented by their electric fields at C, which contain information as to the phase shifts each has encountered along its path. The fields can be expressed as

$$E_{long} = \cos(\omega_{op}((t - t_1 - t_1 - t_2) + 2\omega_{FS}(t - t_1 - t_2) + \phi_{FS})) \quad (1)$$

$$E_{short} = \cos(\omega_{op}((t - t_2)) \quad (2)$$

*Work supported by the U.S. Department of Energy under Contract No. DE-AC02-05CH11231
#ghuang@lbl.gov

where ω_{op} is the optical frequency (2π200THz), ω_{FS} is the frequency shifter RF frequency(2π50MHz), and $_{FS}$ is a phase that can be added to ω_{FS} for control. Calculating the intensity incident on detector d_1 at C, low pass filtering the AC component to remove ω_{op}, and mixing the resultant RF with a local oscillator at $2\omega_{FS}$ yields the phase of the detected RF.

$$\phi_{det} = -2\omega_{op}t_1 - 2\omega_{FS}\ t_1 + t_2\ + 2\phi_{FS} \quad (3)$$

Note that $2\omega_{FS}$ is 2×10^{-6} smaller than ω_{op}, so the second term is negligible. If we can adjust ϕ_{FS} so that ϕ_{det} is held constant, ϕ_{FS} will directly indicate changes in t_1, given ω_{op} held constant also (as explained below). Thus we can determine changes in the optical phase delay in fiber 1, t_1, to high precision since it is measured optically.

A control loop holds ϕ_{det} constant, and the information from ϕ_{FS} is used to correct the phase of RF received on diode d_2. The phase of the output RF from the link at ω_{RF} is given by

$$\phi_{RF_out}\ t\ = \omega_{RF}t - \omega_{RF}t_1 + \frac{\omega_{RF}}{\omega_{op}}\phi_{FS} \cdot k_{group_phase} \quad (4)$$

The first two factors on the right side are the detected RF, while the third is the correction. Ideally, the phase Φ_{RF_OUT} would be just ω_{RF} t, as it is at the transmitter. The additional changes due to $\omega_{RF}\ t_1$ are cancelled by controlling Φ_{FS}. There is a factor k_{group_phase} which has to be included, to correct for the difference between group delay (of the RF) and phase delay (of the carrier) through the fiber due to chromatic dispersion. Chromatic dispersion in the fiber shifts the phase of the AM sidebands compared to their original phase with respect to the carrier at the modulator. This results in a slippage of modulated RF phase with respect to the optical carrier phase as the signal travels, and a difference in group delay. In practice, we measure this factor in a loop-back experiment where two channels are compared, then add it to the single-channel control software.

The operation of the interferometric optical phase control provides constant optical frequency and phase at the receiver, which has been the goal of previous transmission systems using a frequency shifter[7]. Our scheme differs from [7] in that phase sensing and frequency control is done at the receiver, making multiple channels easier to implement.

The stability of our optical phase controller was verified by constructing a Mach-Zehnder interferometer out of two such heterodyne interferometers. One 2 km fiber was exposed to ambient temperature variation and a short 2 m fiber was in a temperature controlled environment. Diurnal temperature variations caused up to 2ns delay changes in the 2km fiber. After correction, the overall differential phase error between two stabilized links was six optical waves peak-to-peak over ten days[8].

For stable RF transmission, the CW laser used in the interferometer must have a fractional frequency stability less than the desired fractional temporal stability of the transmission delay. For a 2 km link with 10 fs stability, this corresponds to $\Delta\lambda/\lambda = 1 \times 10^{-9}$. The CW laser frequency is locked to a hyperfine absorption line in Rb vapor, achieving 5×10^{-10} when two independent lasers are beat together [9, 10].

A 2850 MHz RF signal is amplitude modulated onto the optical carrier by a lithium niobate modulator. The bias point is stabilized by detecting the second harmonic of the 2850 MHz modulation in a phase-locked loop. Amplitude modulation depth is typically 70%, detected by a photodiode.

One issue with photodiode detection is AM-to-PM conversion, where changes in the average optical power modulate the phase of the detected RF signal. This is usually explained as a variation in junction capacitance due to changes in peak carrier density. In our photodiodes (Discovery Semiconductor DSC50) we observe a nonmonotonic AM-to-PM response, in contrast to the monotonic response found in[11]. The optical power level is set to a local maximum in the AM-to-PM photodiode response, where there is zero slope and minimal sensitivity to fluctuations in optical power. At this peak, a ±10% variation in average photocurrent causes less than 10 fs delay variation in the detected RF signal

The receiver is a digital RF phase comparator used to compare the transmitted RF signal with a local signal to be controlled. Since the delay through coax cables and other RF components is temperature dependent, variations are corrected by subtracting a local calibration signal sent through both comparison paths. Critical RF and optical components are temperature stabilized to ±0.01° C, while RF mixers and amplifiers are stabilized to ±0.1° C. All processing of RF signals is done at an intermediate frequency of 50 MHz, after mixing down with a 2800 MHz local oscillator.

Due to the continuous nature of the signal, retro reflections anywhere in the fiber optic signal path can cause random fluctuations of the received RF signal phase. The measured RF signal is the vector sum of the desired signal and an interference vector whose relative angle is determined by the physical spacing of the reflections, and whose amplitude is determined by the relative optical phase of the signal and retroreflection. This relative optical phase varies rapidly with temperature, in the case of widely spaced reflections. As the amplitude of the interference vector changes, the received RF phase and amplitude varies. To suppress these effects to the less than 10 fs, all optical reflection losses need to be greater than 40 dB, so APC connectors and high return loss components are used.

Measured relative time differences between long and short stabilized links are shown in Fig. 3 for a 2.2 km and for a 200 m fiber in one of the two channels, and 2 m in the other. There is a 2-hour fluctuation correlation with temperature, possibly due to the rubidium frequency locker. The uncorrected time difference is shown for the case of the 2.2 km fiber (divided by 1000 and offset). This variation diminishes with decreasing fiber length, as expected if the wavelength were changing. The resultant RMS variation in delay of 2850 MHz RF signal between the two arms is 19.4 fs with a 2.2 km fiber, and 8.4 fs with a 200 m fiber.

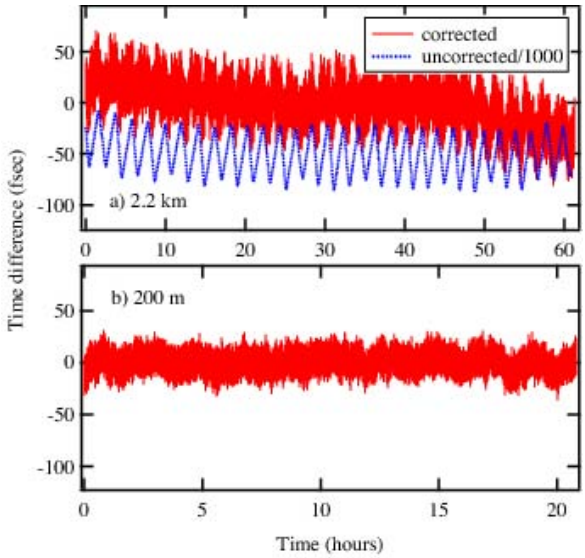

Figure 3: Relative drift of a 2850 MHz signal transmitted over a long and short (2 m) fiber. a) 2.2 km long fiber. The relative time difference has an RMS deviation of 19.4 fsec over 60 hours. The relative time difference (/1000) without the correction is also shown. b) A 200 m fiber has an 8.4 fsec RMS deviation over 20 hours.

Figure 4 shows the Allan deviation of the relative phase of the 2850 MHz RF signal for the 2.2 km fiber with and without the correction. Note that the periodic 2-hour variations evident in Fig. 3a appear in the Allan deviation and the correction results in three orders of magnitude improvement in relative time stability.

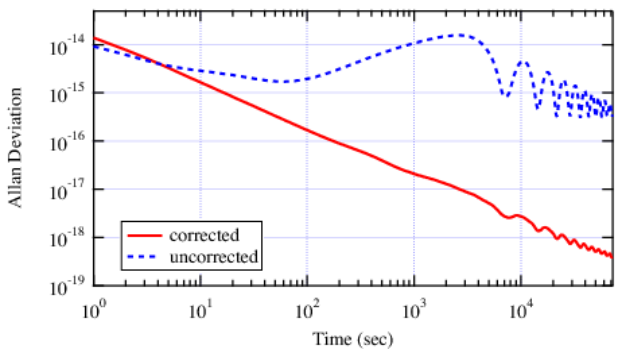

Figure 4: Allan deviation of the relative timing of a 2 m and a 2.2 km link. Dotted line: uncorrected RF delay. Solid line: corrected RF delay.

In conclusion, we have demonstrated a robust RF distribution system based on common fiber and RF components, capable of low jitter operation. It is easily expandable to multiple channels, requiring only an increase in transmitter optical power and the addition of fiber optic splitters and mirrors. This system will be of use in FEL light sources and other applications requiring sub-100 fs synchronization of RF and/or lasers.

REFERENCES

[1] C. Pellegrini, "Overview Of Single Pass Free Electron Lasers," in Proceedings of the 10th European Particle Accelerator Conference (EPAC 06), Edinburgh, Scotland, 26-30 Jun 2006

[2] O. Lopez, A. Amy-Klein, C. Daussy, Ch. Chardonnet, F.Narbonneau, M. Lours, and G. Santarelli, "86-km optical link with a resolution of 2x10-18 for RF frequency transfer," Euro. Phys. J. D 48, 35 (2008).

[3] P. A. Williams, W. C. Swann, N. R. Newbury, "Highstability transfer of an optical frequency over long fiberoptic links," J. Opt. Soc. Am. B 25 1284 (2008).

[4] H. Kiuchi, "Highly Stable Millimeter-Wave Signal Distribution With an Optical Round-Trip Phase Stabilizer" IEEE Trans. Microwave Theory and Tech., 56, 1493 (2008).

[5] D. D. Hudson, S. M. Foreman, S. T. Cundiff and J. Ye, Opt. Lett. 31, 1951 (2006).

[6] J. Kim, J. A. Cox, J. Chen, F. X. Kartner, "Drift-free femtosecond timing synchronization of remote optical and microwave sources," Nature Photonics 2, 733 (2008).

[7] J. Ye, J.-L. Peng, R. Jason-Jones, K. W. Holman, J. L. Hall, D. J. Jones, S. A. Diddams, J. Kitching, S. Bize, J. C. Bergquist, L. W. Holberg, L. Robertsson, and L.S. Ma, "Delivery of high-stability optical and microwave frequency standards over an optical fiber network" J. Opt. Soc. Am. B 20, 1459 (2003).

[8] J. W. Staples, J. M. Byrd, L. Doolittle, G. Huang, and R. Wilcox, "A Femtosecond-Level Fiber-Optics Timing Distribution System Using Frequency-Offset Interferometry," Proceedings of the 2008 Linear Accelerator Conference, M. Comryn, ed. (IEEE, 2008).

[9] A. Bruner, V. Mahal, I. Kiryuschev, A. Arie, M. A. Arbore, M. M. Fejer, "Frequency stability at the kilohertz level of a rubidium-locked diode laser at 192.114 THz" Appl. Opt. 37, 6410 (1998).

[10] S. Masuda, A. Seki, S. Niki, "Optical frequency standard by using a 1560 nm diode laser locked to saturated absorption lines of rubidium vapor," Appl. Opt. 46, 4780 (2007).

[11] F. X. Kartner, H. Byun, J. Chen, F. J. Grawert, F. O. Ilday, J. Kim, and A.Winter, "Progress in Large-Scale Femtosecond Timing Distribution and RF-Synchronization," in Proceedings of the 2005 Particle Accelerator Conference, C. Horak, ed. (IEEE, 2005).

SIGNAL PROCESSING FOR HIGH PRECISION PHASE MEASUREMENTS*

G. Huang#, L.R. Doolittle, J. W. Staples, R. Wilcox, J.M. Byrd,
LBNL, Berkeley, CA 94720, U.S.A.

Abstract

High precision phase measurement is important for many areas of accelerator operation. In a heterodyne digital receiver, one source of phase error is the thermal variation of the input stage. We have developed a technique to calibrate this drift. A CW calibration signal is sent through the same components together with the RF signal to measure and compensate the component drift. At intermediate frequency (IF), we use FPGA based digital signal processing to measure and reconstruct the RF signal after applying appropriate correction. Using this technique, we can measure the phase of a 2856 MHz signal with an accuracy of 15 milli-degrees. We describe how this approach is applied to the femtosecond timing distribution system.

INTRODUCTION

We developed a high precision phase measurement technique by using a live calibration signal to compensate for the thermal effect on the input stage of heterodyne receiver. This technique can be applied in a timing system, a low-level RF controller, and potentially other accelerator subsystems. We used this technique in a femto-second timing distribution system and achieved ~20 fs timing jitter and drift between two RF receivers[1].

A simplified block diagram of the femtosecond timing distribution system is given in Figure 1.

An RF signal is distributed as a phase reference over the fiber link. At each end station, a receiver reconstructs the RF signal and maintains the jitter between two end stations at the tens-of-fs level.

At the transmitter side, we amplitude modulate the RF source onto the carrier light, which is from a CW laser in our case. The modulated light is transmitted through a single-mode fiber link to the end station. The phase delay variation of the signal on the fiber is measured by a frequency shifted Michelson interferometer.

At the receiver side, the RF signal is detected by a photodiode. As soon as the RF signal is peeled off from the light and enters components, including cables, mixers, etc., the thermal variation effect becomes significant.

We measure the RF signal phase by downconverting it to IF, then digitize the IF signal, and process it with an FPGA based signal process board. The LLRF4 board we are using was developed for the SNS low level RF system[2]. We describe the signal processing for the phase measurement in this paper.

A CW double sideband suppressed carrier (DSB-SC) signal is added onto the RF signal as a common mode

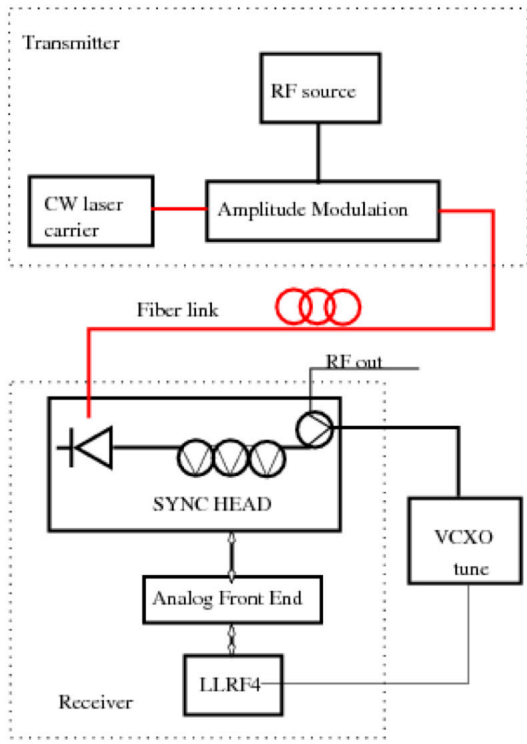

Figure 1: Simplified block diagram of the timing distribution system.

among both channels; we call it the calibration signal. The cable from the photodiode to the combiner is not included in the calibrated path, so that part needs to be temperature stabilized.

Physically, we split our receiver into a sync head, close to the device under control, and a stabilizer chassis, in a rack. The variation of the cable between them can be calibrated out. In the stabilizer chassis, an analog front end circuit downconverts the RF signal and upconverts the calibration signal. There is another bandpass filter on the LLRF4 board in front of the fast ADC.

After the signal is digitized, we measure the phase of each spectrum line in the signal and calculate the corrected RF phase accordingly.

We set up a simplified experiment to evaluate the out-of-loop error of our phase measurement, and the result was 15 mdeg at a 250 kHz sample rate.

ANALOG FRONT END CIRCUITS

We measure the phase difference between two signals: reference (REF) and signal (SIG).

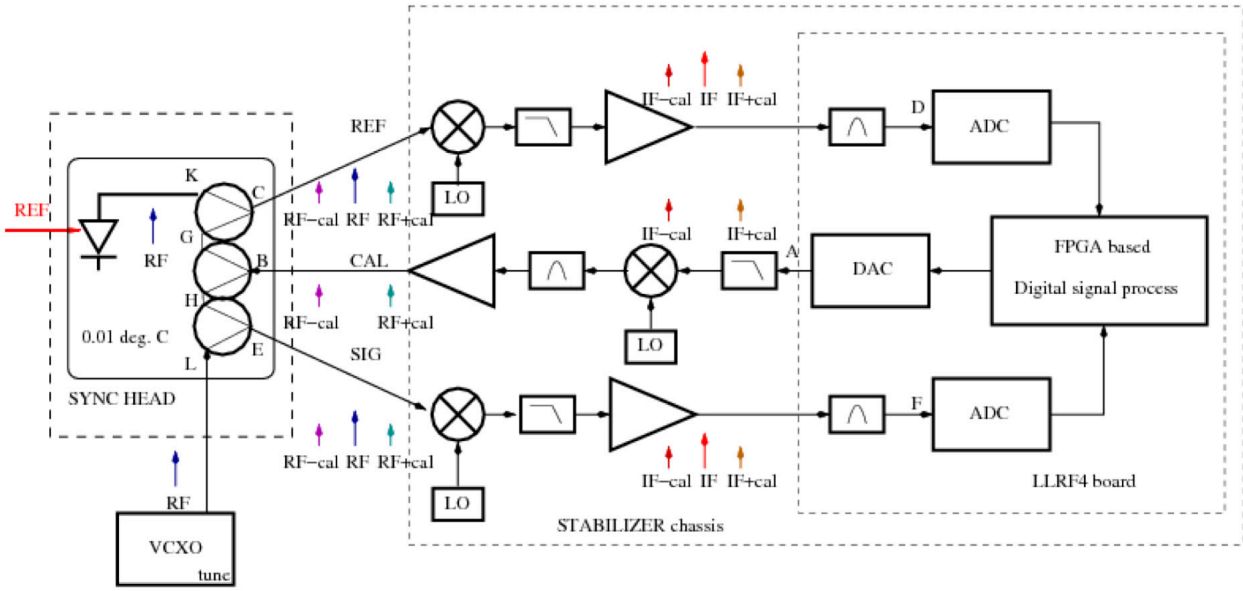

Figure 2: Analog front end circuits.

The analog front end circuit (Figure 2) contains two downconverter channels (REF and SIG) and one upconverter channel (CAL). The reference comes from the fiber link and the signal comes from a VCXO. We can further control the VCXO to follow the reference signal while we have the phase difference.

In the sync head, we have the RF detection photodiode and a combiner/splitter circuit to add the calibration signal onto the RF signal.

The photodiode output and the VCXO output contain only the RF signal. These RF signals are downconverted to IF by the mixer and filters as usual. A DSB-SC calibration signal co-propagated with the RF signal from point C to D as well as E to F. The DSB-SC signal is synthesized by the DAC and upconverted by the mixer. The phase delay from A to B is common to both the REF channel and the SIG channel.

The phase delay on the path BGC-BHE-KC-LE cannot be canceled, so we put them in a temperature controlled box to keep their phase delay variations as small as possible. The in-loop temperature error of our control loop is less than 0.01˚ C.

After the combination of RF signal and calibration signal, we have 3 spectrum lines propagating through the cable, mixer, amplifiers and filters. The intermodulation among them by the nonlinear effects of components will generate a new spectrum line. To minimize this effect, we select high-IP3 components in our system, and lower the signal power going to the mixer as much as possible and boost it up later. We also scan the whole spectrum in software to make sure the intermodulation products are low enough. Temperature control of all the analog front end circuit was added at first, but eventually we found that is not really necessary for meeting our specifications.

The LO phase noise is not critical here, since it is common to both channels and the differential calculation process eliminates it.

After the mixer and low pass filter, the signal contains IF and two sidebands separated by the calibration frequency. The IF power level is adjusted to a range appropriate for the ADC.

DIGITAL SIGNAL PROCESSING

The digital signal processing in phase measurement detects the phase of each spectrum line and then calculates the phase difference between REF and SIG.

The signal being digitized contains multiple frequencies. They are sent to a series of mixers to detect the phase of each spectrum line relative to the LO.

Each phase detector contains a mixer and a low pass filter as shown in Figure 3. The mixer can be implemented directly by a multiplier or by a Coordinate Rotation Digital Computer (CORDIC). The low pass filter (LPF) is implemented by a Cascaded Integrator

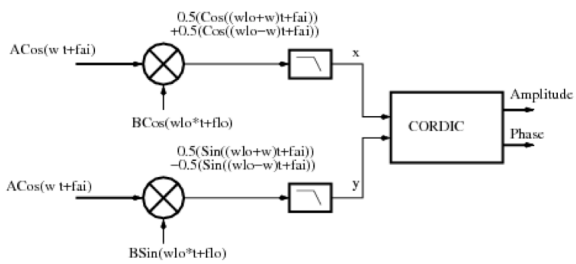

Figure 2: Unit circuit to detect signal phase relative to LO

Comb (CIC) filter. The mixer LO port is used to select the spectrum line to be measured. Ideally, only when the $w=w_{lo}$ does the LPF have nonzero output.

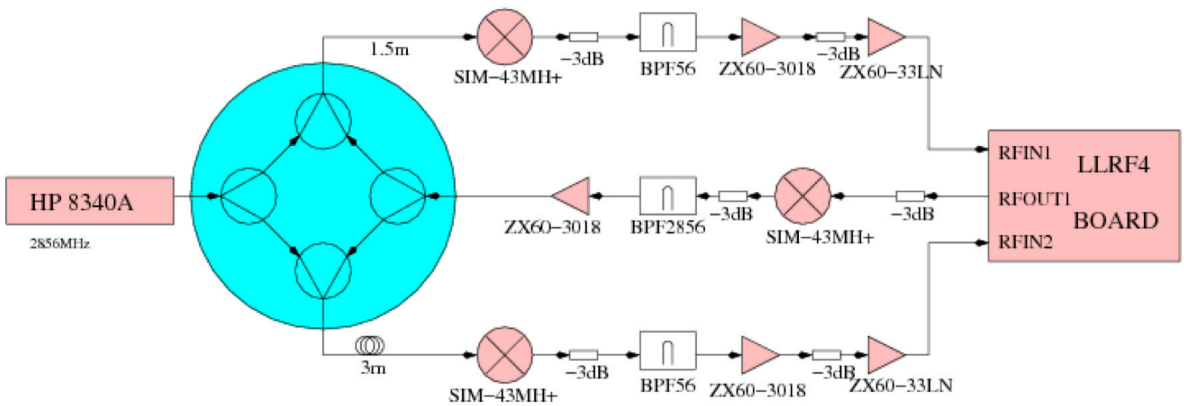

Figure 3: Out of loop test experiment setup.

After the mixer and LPF, the x and y values of each spectrum line are converted to amplitude and phase by another CORDIC. To achieve higher accuracy, the x and y are shifted together to make their MSBs are not all zero. Then we feed the result into the CORDIC. The shift does not affect the phase calculation, but for the amplitude calculation, we need to shift it back afterward.

The phases of the two calibration sidebands are detected independently; the amplitude of those spectrum lines does not affect the phase result.

When we have the phase of sideband calibration signals and RF signal for both the REF and the SIG channels, we can calculate the phase difference by

$$\phi_{REF,SIG} = (\phi_{RF,REF} - \phi_{RF,SIG}) - (\phi_{CALU,REF} - \phi_{CALU,SIG})/2 - (\phi_{CALL,REF} - \phi_{CALL,SIG})/2$$

where REF and SIG represent two channels, CALU represents the RF, and CALL represent the RF signal and upper and lower calibration sideband.

Considering a linear phase system, the phase delay of the RF is equal to the average phase delay of the two sidebands. Since the all the phase wrap around 2π, there is a π ambiguity when averaging two phases. We can resolve that by checking the phase difference of the upper and lower sidebands.

Here we assume the electric path from the photodiode to the ADC does not change by an extent comparable to a half wavelength of the calibration signal.

OUT OF LOOP TEST

We set up an experiment as shown in Figure 4 to test the phase detector out-of-loop error. A simplified sync head containing only 3 splitters is temperature controlled to 0.01˚ C (in loop temperature error). A 2856 MHz RF signal is split in the same temperature controlled box and fed the input of the sync head.

The cable lengths between the sync head and the analog front end circuit are different for the two channels (1.5 and 3 m) so as to be able to pick up some thermal expansion on the cable. The cable is in a room where an air conditioner regulates room temperature every 2 hours, and the peak to peak temperature variation is about 2˚ C.

The test is measuring the out of loop phase difference before and after we apply the calibration signal. We are trying to measure the difference of the same signal split to two channels. Ideally, we should get, as the result, zero phase difference between two channels.

The test result is shown in Figure 5. The red line is the uncorrected phase difference between the two detected RF signal, which followed the room temperature variation. The green line is the corrected phase difference between the two detected RF signals, which flattened all the temperature related fluctuations.

The live calibration process suppressed the rms value of the phase difference between the two channels from 0.142˚ to 0.015˚, which limited our phase detection accuracy.

If we did 128 more averages, which implies decreasing our sample rate from 250 kHz to 1.95 kHz, the rms value could even decrease to 0.003˚.

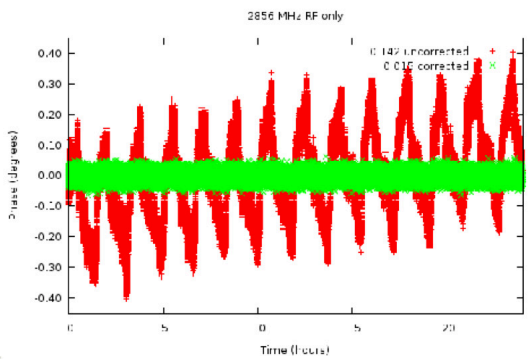

Figure 4: Out of loop test experiment data.

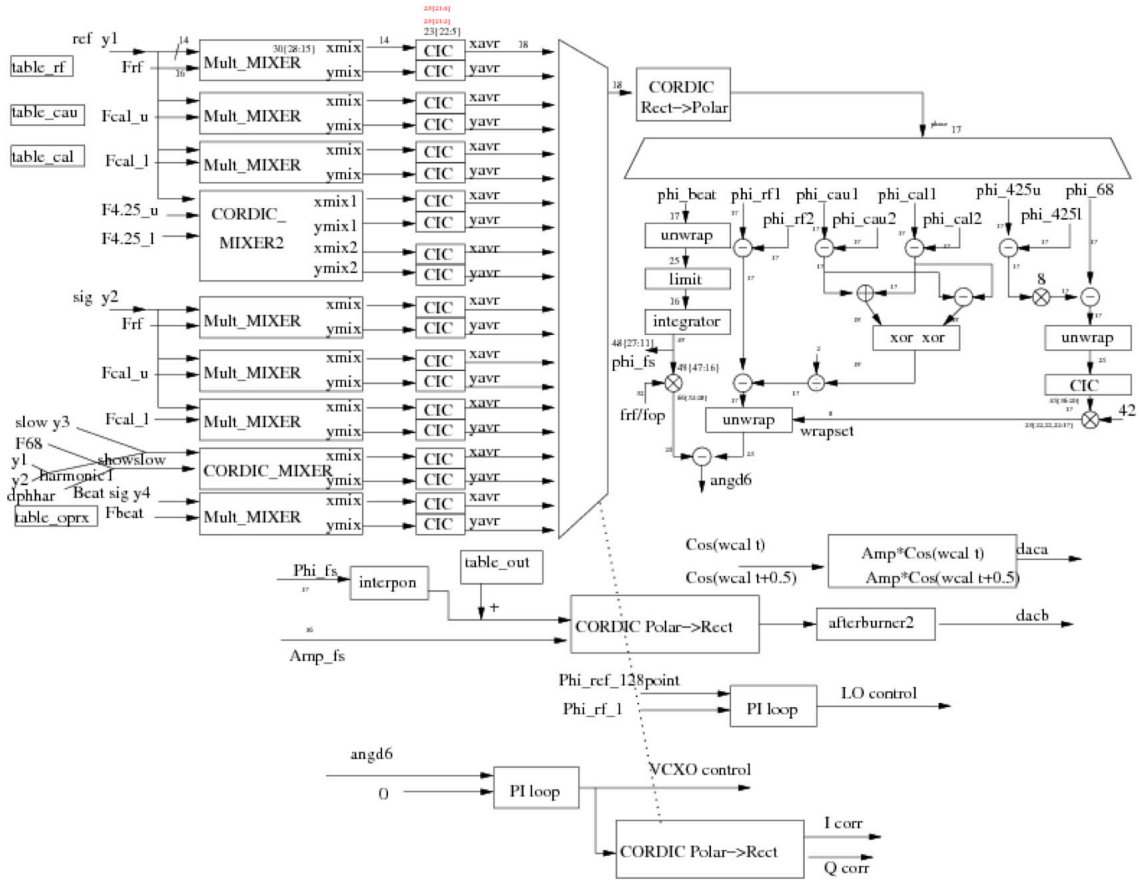

Figure 5: DSP for fs timing distribution system at LCLS.

APPLICATION IN FEMTOSECOND TIMING DISTRIBUTION SYSTEM

This high precision phase measurement technique is applied in the femtosecond timing distribution system.

The phase difference between the reference coming from the fiber and the harmonic signal coming from the laser is detected by the phase measurement system. The the error signal is sent to a PI loop to control the pico motor and piezo transformer [3].

Figure 6 shows the block diagram of digital signal processing for the timing distribution system.

Y1 is the reference signal. Beside the RF signal and calibration signal, it has another pair of sidebands, which are used to transfer another lower frequency (4.25 MHz) clock. By using this frequency, we can resolve the bucket ambiguity.

We tested such a timing distribution system at LCLS in SLAC. The jitter and drift from the out of loop test is about 20 fs.

REFERENCES

[1] R. Wilcox, J. M. Byrd, L. Doolittle, G. Huang, J. Staples, Optics Letters, Vol. 34, No. 20, 2009 (3050).

[2] http://recycle.lbl.gov/llrf4.

[3] J. Byrd, L. Doolittle, J. Arthur etc. Femtosecond Synchronization of Laser Systems for the LCLS, these Proceedings.

THE LCLS TIMNG EVENT SYSTEM*

J. Dusatko#, S. Allison, M. Browne, P. Krejcik,
SLAC National Accelerator Laboratory, Menlo Park, CA 94025 U.S.A.

Abstract

The Linac Coherent Light Source requires precision timing trigger signals for various accelerator diagnostics and controls at SLAC-NAL. A new timing system has been developed that meets these requirements. This system is based on COTS hardware with a mixture of custom-designed units. An added challenge has been the requirement that the LCLS Timing System must co-exist and "know" about the existing SLC Timing System. This paper describes the architecture, construction and performance of the LCLS timing event system.

INTRODUCTON

The Linac Coherent Light Source (LCLS) at the SLAC National Accelerator Laboratory is a fourth generation X-ray light source. It uses the last 1/3rd of the SLAC Linac to create 4.6 to 13.6 GeV, electron bunches at a nominal charge of 0.05 to 1.0 nC which are sent into a single-pass permanent magnet undulator FEL. Through the Self-Amplified Spontaneous Emission (SASE) process, the undulator produces tuneable 1.5 to 15 Angstrom hard X-rays. A precision timing system is required to coordinate the acceleration process, as well as the triggering of diagnostics to measure beam performance. In addition, experimental data acquisition systems require precision timing reference and triggers to properly coordinate their measurements in coincidence with the LCLS beam.

The comprehensive LCLS Timing System consists of three levels of timing and synchronization, correlating to three different, but interlinked timing subsystems [1]. The first is a precision RF phase reference generation and distribution system needed to drive the injector gun and acceleration klystrons as well as the gun laser system and keep the phase within few fractions of a degree of S-band. The second is an ultra-stable timing phase reference distribution system that is used to synchronize the LCLS electron beam with experiment pump-probe laser systems to a level of 10fs at the photon end of the machine [2]. The third is the timing trigger generation and distribution system which produces precision timed triggers for use by acceleration, diagnostic and experimental DAQ subsystems. This has been designated the Timing Event System to distinguish it from the other two timing subsystems, and is the focus of this paper.

SYSTEM OVERVIEW AND DESIGN

The Timing Event System was developed to meet the requirements of the LCLS [3]; table 1 lists these requirements. It should be noted that the original trigger jitter requirement was specified as 2ps rms. This requirement was driven by the bunch length measurement. The requirement was later relaxed to the 10-ps value after it was determined that level of trigger jitter was not needed and would require a larger effort in the system design to achieve.

Table 1: LCLS Timing Trigger System Requirements

Requirement	Value
Maximum trigger rate	360 Hz
Clock frequency	119 MHz
Clock Precision	20 ps
Coarse step size	8.4 ns ± 20 ps
Delay range	>1 sec
Fine step size	20 ps
Maximum timing jitter (w.r.t. clock)	10 ps rms
Differential error, location to location	8 ns
Long term stability	20 ps

The previous generation SLAC Linac timing trigger system is CAMAC based and developed in the 1980s for the Stanford Linear Collider (SLC) [4]. This system had served the machine well for many years, but was not extensible for LCLS from a requirements, HW obsolescence and SW development point of view. It was not practical to replace the entire SLC timing system (where existing system requirements were sufficient) for LCLS from a cost and retrofitting effort standpoint. Thus, the LCLS Timing Event System had to be layered on top of and function alongside the SLC Timing System; at least for the initial running of LCLS. Because of this, certain architectural tradeoffs were made and the LCLS event timing system was slaved to the SLC system, receiving reference and synchronization signals from it, which are ultimately used to form the LCLS timing triggers.

During the design phase of the LCLS Timing System, several timing trigger solutions were considered including COTS (Commercial Off The Shelf) units. COTS was emphasized as a implementation solution for LCLS controls as a way of cost savings by leveraging industrial solutions that could meet system requirements. An accelerator timing component supplier, MicroResearch Finland (MRF) [5], was identified and selected. MRF had developed the Event System, originally for the Swiss Light Source and later commercialized it. The MRF Event

*Work supported by U.S. Department of Energy under Contract Nos. DE-AC02-06CH11357 and DE-AC02-76SF00515.
#jedu@slac.stanford.edu

System design was conceptually based on the ANL APS Event System, but upgraded and improved.

The EVG and EVR

The MRF hardware is central to LCLS Event Timing, and is now described in detail. The Event System consists of one or more EVent Generator (EVG) timing masters, capable of being daisy-chained to send data in a priority-encoded manner. The EVG broadcasts serialized timing data, along with an embedded clock to multiple EVent Receiver (EVR) timing clients. The system uses the 8b10b linecode standard to broadcast serial timing data over fiber optic links. The timing data consists of a 16-bit word, which is further divided into two bytes. The upper byte contains timing trigger bytes called event codes, giving 256 distinct combinations. The event codes are used to create triggers in the EVR. The value of the event codes broadcast depends on certain pre-defined conditions setup by external information and triggers into the EVG. The event codes are received by the EVR and, depending on the setup, certain selected codes are used to generate triggers. The other half of the 16-bit timing word sent across the serial link contains two multiplexed data streams. The first contains the distributed databus data, and the second contains the EVG data buffer data. The distributed databus provides an 8-bit HW signalling interface between the EVG and EVRs; it is not used for LCLS. The EVG contains a 2K data buffer, whose contents can be sent to a receiving data buffer in the EVRs. The transmission of the buffer is triggered by software. The EVG is a 6U VME module, which is setup and controlled via a VME CPU.

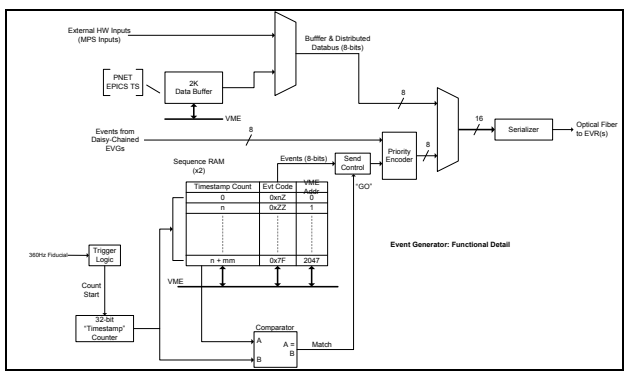

Figure 1: EVG block diagram.

A detailed block diagram of the EVG is shown in Fig 1. At the core of the EVG is the Sequence RAM. This RAM contains the event codes which get broadcast to the EVRs. Each event code in the sequence RAM is associated with a timestamp value. This timestamp is not to be confused with the EPICS timestamp. One sequence RAM timestamp is a value associated with one event code. The timestamp value is 32-bits wide. When the EVG receives a trigger telling it to begin sending out event codes, said trigger actually starts the timestamp counter running. The counter value is presented to the sequence RAM and when a match between the counter value and the event code's associated timestamp value is made, that event code is sent out. This mechanism allows the user to have temporal control over when the event code is sent out following a trigger. There are two sequence RAMs, permitting one to used for actively broadcasting while the other is being setup for the next trigger. The Sequence RAM is 2K deep and can be setup to either broadcast the full contents per trigger, or continuously loop, sending out the same event codes after one trigger has been received. The EVR requires a system clock for timing and sequencing its operation, this is typically the accelerator system reference clock. This clock is used for all internal logic and is multiplied up by serialization hardware for the serial bit stream. The clock is embedded into the serial data stream sent to the EVRs from the EVG. The EVG logic and serializer are implemented in a Xilinx FPGA.

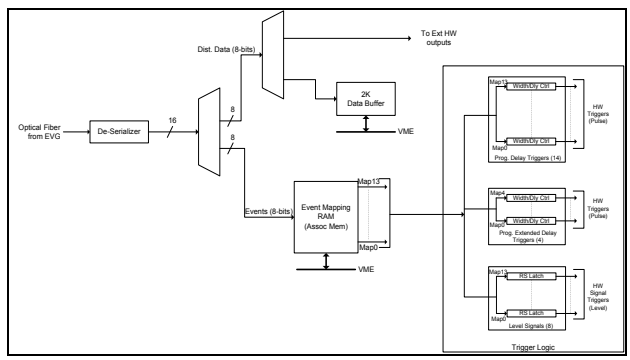

Figure 2: EVR block diagram.

A block diagram of the EVR is shown in Figure 2. The EVR's logic is also implemented in a Xilinx FPGA. The EVR contains an associative memory, called the Mapping RAM. The mapping RAM is programmed with a desired event code associated with one of fourteen mapping bits. The mapping bits are used to form individual hardware triggers. When the event code broadcast by the EVG is received and de-serialized, it is presented to the mapping RAM. If the event code matches a location in the mapping RAM, a hit is generated on the associated map bit. This map bit generates a trigger. The triggers are fully programmable in delay (from the assertion of the map bit), width and polarity. The EVG clock embedded into the serial data stream is recovered and used to clock all of the EVR trigger logic. Thus, the triggers are synchronous with the system reference clock. The EVR also contains a 2K data buffer which receives the EVG's buffer. The buffer data, once received, can signal this condition by sending an interrupt to the EVR's controlling CPU. EVRs are available in VME and PMC formfactors. Each type can supply 14 output triggers with several configurable signalling levels. LCLS uses TTL level triggers for all client subsystems. MRF also supplies a special version EVR (VME-EVR-RF230) which will supply the recovered system clock to external applications.

System Architecture

A block diagram of the LCLS Timing Event System is shown in Fig 3. The MRF EVG and EVRs are arranged in a star topology with one EVG broadcasting timing data to multiple EVR subsystem clients across the accelerator complex. When triggered, the EVG broadcasts these event codes serially at 2.38Gb/s to the EVRs over a fiber optic distribution system. The items in Fig 3 connected to the EVG support the forming of the event codes and generation of the clock and trigger needed to broadcast them. The EVG receives special timing data in the form of a 128-bit timing pattern from the SLC Master Pattern Generator (MPG). The pattern data is broadcast over a dedicated network at SLAC called PNET. The PNET data contains information about the machine rate, beam states, and so on. When a PNET is pattern is received, the PNET module generates an interrupt to the VME CPU located in the EVG crate. This CPU loads the PNET data along with data from the EPICS control system and forms the event codes which get loaded into the EVG's sequence RAM. PNET data is broadcast in a pipelined fashion, with data for three up coming machine cycles being sent. Once the data is loaded into the sequence RAM, it can be sent out when the 360Hz trigger is received. The other hardware provides a clock and trigger for the EVG. LCLS runs at a maximum of 120Hz, with sub-multiple rates being available. The Linac timing system broadcasts a *Fiducial* pulse at 360Hz. The Fiducial is the fundamental metronome of the entire timing system complex. The 360Hz fiducial is derived from the AC mains, and is used to sequence the firing of various accelerator systems in a consistent manner so as not to perturb the AC line. This pulse is amplitude-modulated onto the accelerator 476Mhz phase reference carrier that is driven onto the Main Drive Line that runs the entire 3000 meters of the Linac. The MDL is tapped off at the LCLS Linac Sector 20 RF hut and the Fiducial is demodulated by an SLC Timing FIDO (FIducial DetectOr) chassis. The raw 360Hz fiducial is passed into the Sync/Div chassis which was designed for LCLS. This chassis re-synchronizes and conditions the fiducial and outputs it to the EVG. The fiducial triggers the EVG to broadcast the event codes in its sequence RAM to the EVRs. At SLAC, the 360Hz fiducial is divided down into six 60Hz "timelslots", which correspond to different beam types. LCLS, running at 120Hz occupies timeslots 1 & 4 (the MPG keeps track of the timeslots and sends out special codes corresponding to each one). Other timeslots in the system were reserved for legacy systems such as PEP-II, SLC and others. The timeslots provide a way of intermixing different beam types in the machine.

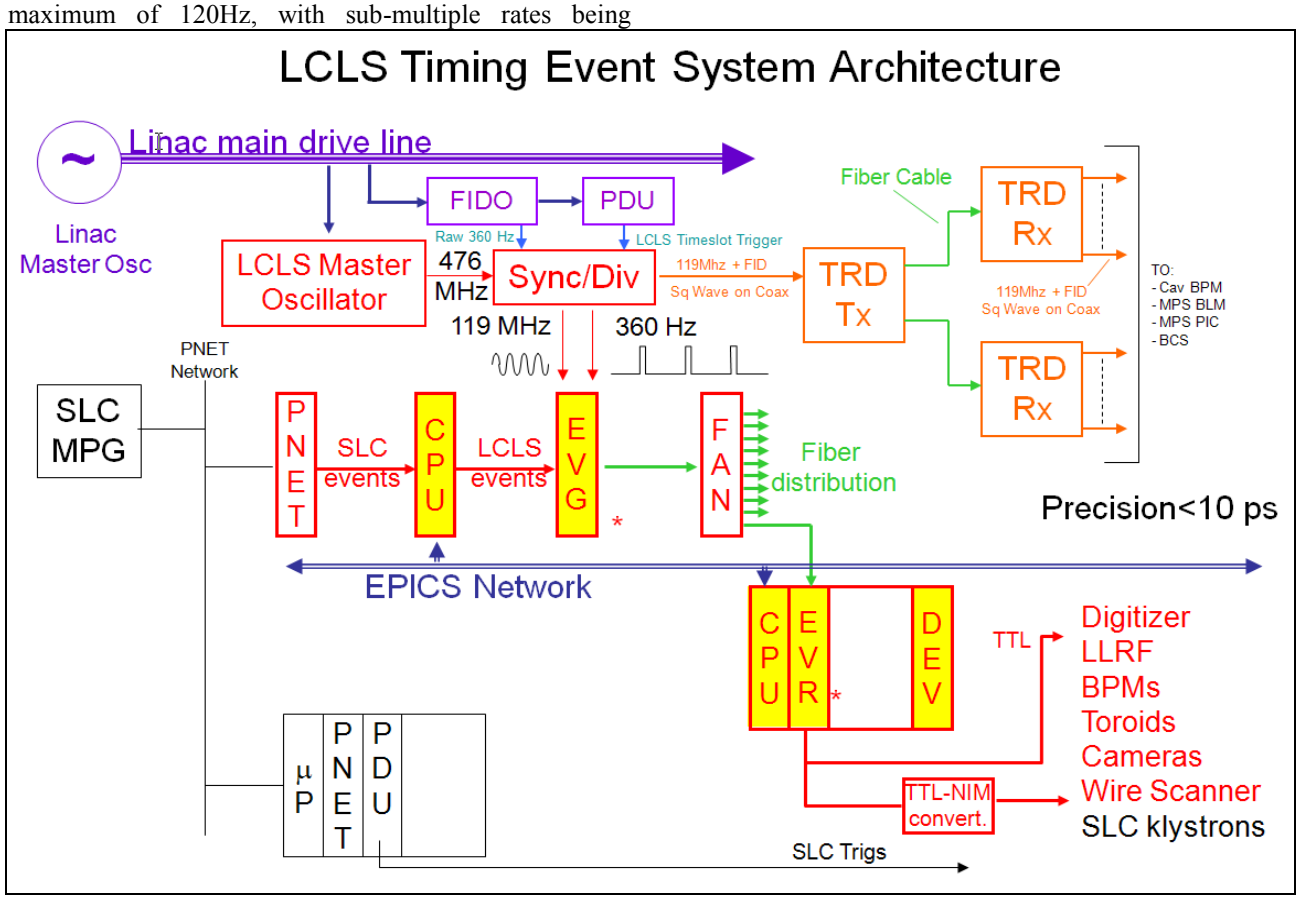

Figure 3: LCLS Timing Event System diagram.

The EVG also receives a 119Mhz system clock from the Sync/Chassis. This clock is a divided-by-4 version of the 476Mhz accelerator clock. This clock comes from the LCLS master oscillator which performs two important operations: 1) It provides a very low phase noise clock phase-locked to the MDL clock for the LCLS RF system.

And 2) It provided a stable clock source that masked the +/-720 deg phase shift present on the MDL for PEP-II storage ring injection. Item 2 is no longer relevant since PEP-II has been shut down, but was important when LCLS first began operation. Although the EVG could receive the 476Mhz clock and divide it down directly, there is no way to synchronize the clock division process so that is consistently occurs on a fixed phase of the 119MHz. This is necessary to ensure a fixed phase relationship between the Fiducial (which is synchronous to the 476MHz), the 476MHz and output triggers of the EVRs. Without this fixed phase relationship, the phase of the EVR triggers could vary by several 8.4ns steps depending upon which phase the system was initialized at and could differ from initialization to initialization (e.g. power cycles of the system components). The division process is synchronized by a 120Hz trigger, running on timeslots 1 & 4 from the PDU (SLC Programmable Delay Unit) going into the Sync/Div chassis. The EVG uses the 119Mhz clock to generate the 2.38Gb/s serial data link clock, which is embedded into the data stream.

TRD Subsystem

Another component of the timing system, is the Timing Reference Distribution (TRD) system. This is located in the upper right hand corner of Fig 3. This system distributes the 119Mhz clock with a phase-modulated 360Hz fiducial encoded onto it. This timing signal is provided for systems requiring a basic timing reference clock and trigger without the overhead of the EVR. The LCLS Undulator Cavity BPM, Toroid Charge Monitor, Beam Containment and Machine Protection systems use this signal for clocking and/or trigger sequencing. The TRD timing signal is generated by the Sync/Div chassis. The phase modulation consists of one “missing” 119MHz clock cycle and is easily demodulated using purely digital techniques. The TRD signal is distributed over fiber optic links, using spare dark fibers from the timing cable plant. It should be noted that this signal is not phase-stabilized. The goal of this system was simplicity and it takes advantage of commodity Small Formfactor Pluggable (SFP) electrical to optical transceiver modules for signal transmission and reception. The outputs from the TRD chassis are TTL-level for all client subsystems.

System Software

The LCLS Timing Event system is controlled by 360hz high priority software tasks running on the RTEMS real-time operating system. The user interface and diagnostics for these tasks are implemented using EPICS. On the EVG side, the system software coordinates receiving the 360hz PNET pattern as well as other pulse-unique information, including the EPICS timestamp. It determines which event codes need to go out for the pulse and loads them into the sequence RAM. In addition, it determines if the pulse applies to any beam-synchronous-acquisition (BSA) user request and sets BSA flags appropriately. It then immediately sends 360hz data, consisting of the PNET pattern, EPICS timestamp, BSA flags, and other pulse-unique information, using the EVG data buffer. At reception of a fiducial trigger (about 2 ms later), the sequence RAM is sent over the link to awaiting EVRs.

On the EVR side, the 360hz software task, which is activated on the fiducial trigger (about 1 msec before beam), processes the buffer data received from the EVG and makes it available in memory for other data acquisition tasks on the CPU, i.e. to timestamp the data and determine if there is beam on this pulse. The BSA flags are also stored and used by data acquisition tasks, later on the same pulse, to update BSA arrays. At a lower priority and on user request, the EVR EPICS software controls the mapping of event codes to HW triggers and the set up of the trigger parameters.

The BSA software allows a user to gather beam-dependent scalars across multiple CPUs over multiple pulses up to 120Hz. The data is gathered in BSA arrays (maximum of 2800 values) on each CPU, where each array is assigned to a user. Each value in the array can be an average of up to 1000 values. The user can specify the machine conditions of interest and only pulses that satisfy those conditions will be updated in that user's BSA arrays. The user interface for reserving, releasing, setting up, and activating BSAs is done by EPICS on the EVG CPU. The EVG 360hz task determines if the pulse matches each user request and sends flags to the EVR 360hz tasks for data gathering. The EVR CPU data acquisition tasks look at the BSA flags and update the appropriate data arrays, with optional averaging. Once the BSA is finished, the EPICS software on the EVG CPU notifies the user. The user then reads the assigned data arrays on all CPUs of interest and then releases the BSA slot for another user.

Trigger Generation Process

The following sequence of operations occurs in the formation of a trigger:

1) The PNET message is broadcast by the master pattern generator (MPG) following a fiducial. The PNET message is for 3 cycles ahead which requires all software to pipeline the data.
2) The VME PNET receiver in LCLS master timing crate receives the PNET broadcast and interrupts the VME CPU.
3) The master timing VME CPU takes the PNET data and uses it to assign proper event codes in the sequence RAM which is then ready for the next fiducial.
4) The external fiducial signal (at 360hz) is received by the VME EVG.
5) The EVG begins to send out the event codes in its Sequence RAM.
6) The event codes get sent across the serial fiber links to the EVRs.

7) When the event code matches the same value in the mapping RAM, a hit is generated and after a programmed delay, a HW trigger is output from the EVR to the device.

SYSTEM IMPLEMENTATION

The system was designed for integration within the LCLS control system framework; which is based on the VME-64x bus platform, running EPICS. A key design decision was that each accelerator control and diagnostic subsystem would have its own CPU and VME crate. Thus, each subsystem has its own EVR. The EVG, along with the CPU, PNET receiver and fiber Fanout modules reside in the master timing crate. This, along with the other supporting hardware, occupy one 19inch rack in the Linac sector 20 RF Hut, adjacent to the LCLS injector. All subsystems use PMC-EVRs, with the exception of Low-Level RF and Beam Position Monitors, which use VME EVRs (which have lower jitter). Physical connection of the triggers to subsystem units are typically made using RG-174 lemo cables going from either the EVR front panel or the rear trigger transition module. A dedicated fiber distribution system was designed and implemented to supply timing over the full 2KM of the LCLS machine. Cost was a significant factor in designing the cable plant. One key design requirement was that no more than four layers of timing fanout could be used, in order to keep within the system jitter budget. For the Linac, timing had to be distributed to ten Linac sectors (Sectors 20…30). Beyond the end of the Linac (sector 30) timing was required in the Beam Switchyard, the Linac to Undulator line, the Undulator, Main Dump, the X-ray Line and finally, the Near and Far Experimental Halls. Due to the distances involved, multi-mode Fiber could not be used (at 2.38Gb/s the maximum distance is ~300meters) and required the use of single-mode fiber and transceivers. The system uses Single-Mode fibers for all long-haul distribution trunks and Multi-Mode for all local distribution (e.g. connections to EVRs within one service building). The decision to use mixed fiber types was based on cost, with single-mode being higher. The MRF components use industry-standard Small Formfactor Pluggable (SFP) fiber optical transceivers. A single-mode SFP transceiver was identified (Avago AFCT-57R5APZ), evaluated and used. One item to note is that the fiber distribution system is currently uncompensated for fiber phase drifts due to temperature. While this was not a fundamental requirement, it may become important for future applications.

PERFORMANCE

The trigger jitter of the system was measured using the EVG fiducial input as a reference and measuring multiple time intervals between it and an EVR (MRF VME-EVR-200) output trigger (setup to trigger at the same rate at the fiducial). This measurement was performed using an Agilent model 54845A Infinium digital oscilloscope in time interval histogram mode. The resulting measurement showed the trigger jitter to be better than 10ps rms, over thirty minutes. Factoring out the instrument's internal jitter, the measured jitter is closer to 7ps rms.

FUTURE DIRECTIONS

The LCLS Event Timing System has performed satisfactorily to date over the run of LCLS. Some future upgrades of the system are being planned. The largest of which is the eventual separation of the LCLS Timing Event system from the legacy SLC Timing System. This mainly involves no longer slaving LCLS timing to the SLC MPG. A project is underway to make the EVG operate stand-alone from the MPG. This work involves implementing software and hardware to determine various timing conditions based on machine states and timeslots for formation of the EVG Event Codes. Additional upgrades are planned including the eventual replacement of SLC/CAMAC controls and timing across the accelerator complex. In addition, some work and planning is underway to implement a phase stabilization mechanism to deliver stabilized triggers for experiments.

ACKNOWLEDGEMENTS

The authors would like to thank the following for their contributions in making this system a success: Thanks to Jukka Pietarinen of MicroResearch Finland, OY for support and assistance with our implementation of the MRF HW. Thanks to Bob Dalesio and Dayle Kotturi who were the initial system developers and adopted the MRF units for LCLS timing. Thanks to Dave Brown for developing the VME PNET module and Sync/Div chassis. Thanks to Debbie Rogind and Mike Zelazny for their development of the BSA software. Thanks to Vern Smith and Bob Traller for their hard work and diligence with the system cable plant and installation of the system components.

REFERENCES

[1] P. Krejcik et.al., "Timing and Synchronization at the LCLS" DIPAC 2007, Venice, Italy May 2007, SLAC-PUB-12593

[2] J. Byrd. "Development of a Sub-Picosecond Timing and Synchronization System for LCLS", Project Overview Slides, LCLS Laser Synchronization Preliminary Design Review, Feb 13, 2008.

[3] P. Krejcik, "LCLS Timing System Requirements", LCLS Physics Requirement Document #1.1-305-r0

[4] L. Paffrath, et.al., "A New Timing System for the Stanford Linear Collider", IEEE-NSS, Orlando, FL October 31, 1984; SLAC-PUB-3508.

[5] MicroResearch Finland Oy, http://www.mrf.fi

THE LCLS UNDULATOR BEAM LOSS MONITOR READOUT SYSTEM*

J. Dusatko#, M. Browne, A. S. Fisher, D. Kotturi, S. Norum, J. Olsen
SLAC National Accelerator Laboratory, Menlo Park, CA 94025, U.S.A.

Abstract

The LCLS Undulator Beam Loss Monitor System is required to detect any loss radiation seen by the FEL undulators. The undulator segments consist of permanent magnets which are very sensitive to radiation damage. The operational goal is to keep demagnetization below 0.01% over the life of the LCLS. The BLM system is designed to help achieve this goal by detecting any loss radiation and indicating a fault condition if the radiation level exceeds a certain threshold. Upon reception of this fault signal, the LCLS Machine Protection System takes appropriate action by either halting or rate limiting the beam. The BLM detector consists of a PMT coupled to a Cherenkov radiator located near the upstream end of each undulator segment. There are 33 BLMs in the system, one per segment. The detectors are read out by a dedicated system that is integrated directly into the LCLS MPS. The BLM readout system provides monitoring of radiation levels, computation of integrated doses, detection of radiation excursions beyond set thresholds, fault reporting and control of BLM system functions. This paper describes the design, construction and operational performance of the BLM readout system.

INTRODUCTION

SLAC National Accelerator Laboratory's Linac Coherent Light Source (LCLS) is a Free Electron Laser which produces tuneable hard X-Rays in the 1.5 to 15 Angstrom range. The X-rays are produced by passing 4.6 to 13.6 GeV, 0.05 to 1.0 nC single bunches of electrons from the last third of the SLAC Linac through a newly constructed undulator line. The undulator line consists of 33, 3.42 meter long permanent magnet segments. Each segment contains 226 NdFeB magnets with vanadium permendur poles arranged with 30mm period [1]. These materials can be demagnetized by radiation induced by beam loss. The Beam Loss Monitor (BLM) system has been developed based on system requirements [2] to detect this loss before it reaches an appreciable level.

The BLM system was developed in collaboration with Argonne National Laboratory. ANL had the responsibility of developing the BLM detectors and detector signal conditioning electronics. SLAC had the responsibility for developing the readout electronics system, integration into the LCLS Machine Protection System, and system commissioning.

The system design requires 33 BLM detectors, one for each undulator segment. Due to initial budget limitations, only five ANL BLM detectors and associated electronics were produced. As a interim solution, re-purposed PEP-II BLM detectors, available after the shutdown of the B-factory, were installed on the remaining 28 undulators plus some additional locations.

BEAM LOSS DETECTORS

The ANL BLM detectors consist of a fused silica Cherenkov radiator optically mated to a PMT [3]. The complex geometry of the radiator was chosen in order to cover the undulator magnets, while propagating the resultant output light to a single PMT. Signal conditioning, high voltage and a test signal are provided by a local BLM Interface Module (BLM-IM) on a per detector basis. The detectors are mounted at the upstream end of each undulator segment, with the companion BLM-IM mounted nearby on the undulator girder in the undulator hall tunnel. The BLM-IM contains an adjustable high-voltage power supply with a range of 0…-1KV, as well as a charge-sensitive preamp which converts the PMT charge pulse into a time-shaped (tc=50μs) voltage signal with a maximum output voltage of -1.5V in 50 ohms. Additionally, the BLM-IM contains an LED pulse generator whose 600ns light signal is optically connected to the detector head. This allows the detector and electronics chain to be stimulated with a test pulse during non-beam time as a built-in self check.

The PEP-II detectors [4] are similar in their materials (quartz Cherenkov radiator mated to a PMT) but have a different geometry: cylindrical radiator mounted in a cylindrical housing. The housing contains a lead shield to attenuate the storage ring synchrotron radiation and enhance beam-loss showers, and also the dynode resistive divider chain. The PEP-II detectors are mounted near the original locations of the ANL units, but a 10cm away due to their incompatible geometry. High voltage is supplied to a string of PEP-II tubes from one of two supplies, serving approximately 15 tubes each. The raw charge pulse from the PMTs is sent directly, following a 1dB attenuator, to the readout system. Thus the readout system has to accommodate mixed-mode detector signals. Note that the PEP-II units have no provision for an LED test signal input. In addition to the undulator, additional PEP-II BLM detectors were installed near upstream collimators and the Undulator tune-up dump in the Linac-To-Undulator beamline.

SYSTEM OVERVIEW AND DESIGN

The original system design accommodated the ANL detector systems exclusively. This design was modified in

*Work supported by U.S. Department of Energy under Contract Nos. DE-AC02-06CH11357 and DE-AC02-76SF00515.
#jedu@slac.stanford.edu

order to include the PEP-II units. Figure 1 shows the system diagram with ANL detectors. The PEP-II installation differs in that there in no BLM-IB, and the PEP-II high voltage power supply is located upstairs. In both cases, the detectors are located in the undulator hall tunnel, along with the BLM-IM for the ANL units, and the readout systems are located in service buildings, which are located at the beginning and end of the undulator line.

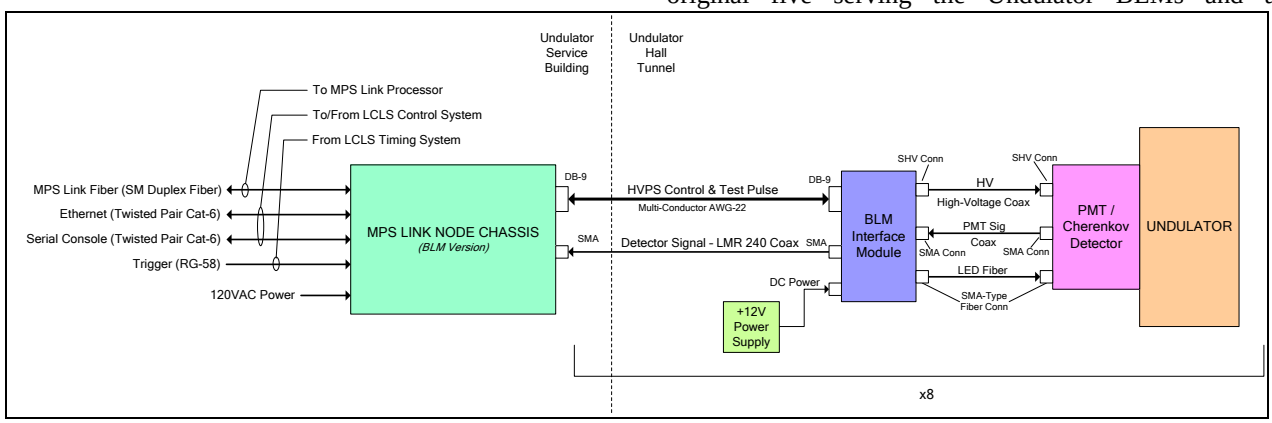

Figure 1: LCLS Undulator Beam Loss Monitor system block diagram – ANL detectors

A system design goal was to keep as much of the readout electronics out of the tunnel as possible. This is for serviceability as well as to avoid additional heat loads in the tunnel, which must be kept at +20 deg Celsius ±1deg C for the undulator magnets.

The longest cable run from tunnel to service building is approximately 100 meters. The detector signals are transmitted over high-quality LMR-240 coax cable, with SMA connectors at each end. The BLM-IM control signals are transmitted over a multiconductor cable consisting of four individually shielded (only three are used), AWG22 twisted pair cables with foil shield and drain wire, wrapped by an overall foil shield which is encased in a low-smoke non-halogenated jacket. This cable is terminated with DB-9 connectors at each end. The controls signals present are the analog HVPS set and readback, both driven differentially on the cable, and a digital RS-485 level test pulse that drives the test LED, also differential. Grounding and shielding of the differential pairs is handled carefully, with only one end of each individual shield connected to ground at the sending end. Local +12VDC power is supplied to each BML-IB by standard "wall-wart" power supply units that have been carefully chosen and evaluated.

The PEP-II HVPS voltage is carried down to the PMTs using Type-C high voltage coax. In the tunnel, this HV is daisy-chained to the string of PMTs, with standard SHV connectors on RG-59 cables. The PEP-II HVPS units receive power and control from the readout system. These power supply units are also re-purposed from PEP-II and have an added signal conditioning unit, designed to match the control and readback voltage levels of the ANL units. This allows direct connection to the readout system.

The MPS BLM Link-Node

Readout and control of the BLM detectors and support electronics is accomplished by the LCLS Machine Protection System (MPS) BLM Link-Node (L-N) chassis. One BLM L-N can serve eight BLM detector channels. There are a total of six BLM L-Ns in the system: the original five serving the Undulator BLMs and an additional chassis installed to serve the added LTU BLMs. The L-N is a component of the LCLS MPS [5]. The MPS consists of an array of Link-Node chassis which connect to various status and mitigation devices. The L-Ns are connected to a central Link Processor via Gigabit Ethernet links in a star topology, over a private fiber optical network. A commodity GigE switch connects the Link-Nodes to the Link Processor. The Link-Processor, a VME CPU, runs the MPS algorithm, polling all L-Ns on the network for status at 360Hz. The LP is connected to the LCLS Timing Event system and receives a 360Hz interrupt from it. This invokes the message passing / status checking / fault mitigation operation between the LP and individual L-Ns. The MPS is capable of responding to a fault condition within 1/360th of a second by either halting or rate-limiting the beam.

A block diagram of the BLM Link-Node is shown in Figure 2. The MotherBoard (MB), common to every type of L-N, contains a Xilinx XC4VFX20, Virtex-4 FPGA. This FPGA implements the core MPS function of fault detection and reporting. The FPGA's Multi-Gigabit Transceiver and MAC core implement the Ethernet interface to the LP. The FPGA contains a fault memory which is then read out over Ethernet. A USB 1.1 interface port is included on the MB as a local diagnostics and control port. When connected to a host system, the unit's full fault memory, control, status and diagnostics functions are available. Additionally, an embedded ColdFire CPU (Arcturus Networks uC-528XF) has been integrated into the MB. This CPU is used for the EPICS interface and provides control, status, diagnostic and housekeeping functions between the L-N and the LCLS control system. It should be noted that the actual fault handling mechanism is separate and isolated from EPICS.

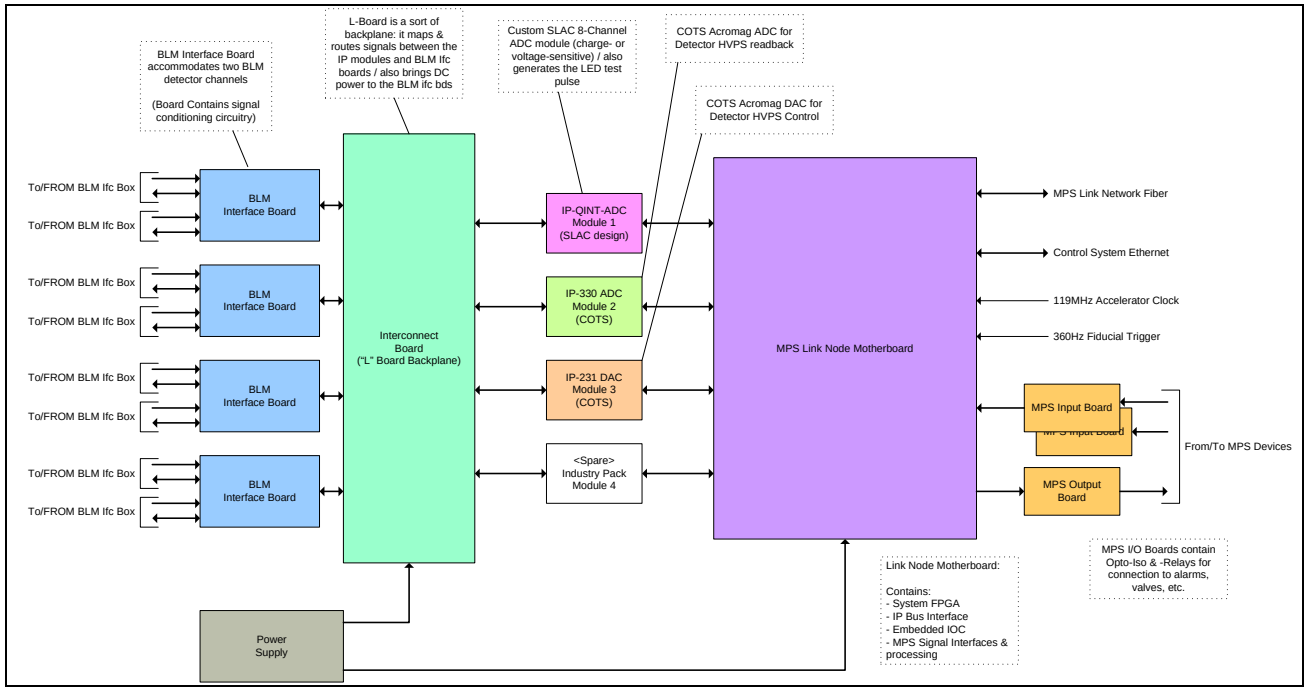

Figure 2: The BLM Link-Node Block Diagram

The BLM L-Ns serve standard digital MPS input and output devices. Inputs are connected to the motherboard by plug-in boards. MPS Input boards contain 16 optical isolators for interface with devices, typically at +24V levels. The MPS input signals are debounced digitally with a 100us minimum time constant. The MB has provision for six input boards, giving a total of 96 inputs. One MPS digital output board is also available to provide outputs to mitigation devices. Eight channels of optically isolated solid-state relays are provided.

The BLM version L-N adds some more hardware to the base L-N. The HW added to the Link-Node for the BLM version is shown in the left-hand side of Fig. 3. These items implement the data acquisition and control functions of the BLM system and interface with the BLM detectors and front-end electronics.

The MB was also designed with a general-purpose Industry Pack [6] interface, capable of supporting up to four IP modules. The IP interface logic is implemented in the FPGA. The BLM readout and control is handled by three individual Industry Pack (IP) modules inside the Link Node. One of these is custom (the IP-QINT-ADC) while the other two are commercial off the shelf (COTS). The two COTS modules consist of an Acromag IP-231 16-channel, 16-bit DAC and an IP-330A 16-channel, 16-bit ADC. These two modules are used to set and read back the system high voltage power supplies, respectively.

The signals from the IP modules are routed to the BLM Interface Boards by way of the Interconnect Board L-board (called L board because of its shape); the L-board also provides power the BLM Interface boards. This board is passive except for some buffer devices for the LED Test pulse.

The BLM interface boards contain interface and signal conditioning circuitry for the physical interface to the BLM detectors. This board contains an analog differential driver and receiver for the HVPS control and readback, and a differential RS-485 driver for the LED test pulse. The PMT signal is not processed or conditioned on this board (other than an input overvoltage protection circuit) and is passed directly to the IP-QINT-ADC module. Careful routing and shielding of the detector signals is done to minimize noise and crosstalk. This interface board serves two detector channels. Four are required for a complete BLM Link-Node.

Triggering and Data Acquisition

The BLM L-N also receives a 119Mhz clock with phase-modulated 360Hz fiducial from the LCLS Timing Reference Distribution system [7]. The motherboard processes this signal and extracts the 360Hz fiducial to form the BLM system trigger. The delay of this trigger is settable from EPICS. The system triggers at 360Hz, performing its BLM acquisition, signal processing and fault checking operations. Note that the maximum LCLS beam rate is 120Hz. Three measurements occur at each trigger: Beam, Test and Pedestal. A timing diagram is shown in Fig. 3. The Beam measurement interval acquires the actual BLM detector data. Timing is adjusted so that the detector signal arrives within the Beam gate. Approximately 900us later, the Test acquisition interval sends the LED test pulse to the detector and acquires the resultant detector signal. At 900us after this interval, during the system "quiet time", the Pedestal measurement acquires any offset voltage present in the detector and front end electronics. In charge integrating mode, a 2.5us gate is opened at the start of each measurement interval.

Charge is collected for 2us, and the resultant integrated voltage is sampled 500ns before the close of the gate.

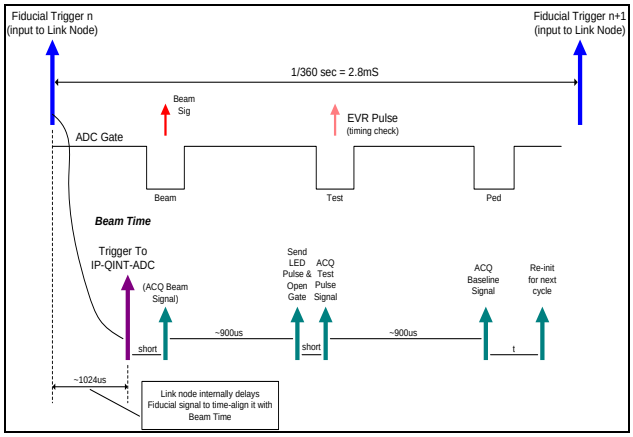

Figure 3: BLM System Data Acquisition Timing

For voltage-sensitive mode, the gate signals are still present and timing relationships are the same except that a voltage signal is sampled.

Since the various timing delays in the acquisition subsystem are SW programmable, there exists the possibility that a wrong setting could cause the beam signal to get missed, never indicating a fault. A separate fault checking mechanism was employed using the LCLS timing system Event Receiver to inject a 360Hz trigger pulse into the analog front end (via an RF directional coupler) during the Test acquisition interval of a non-ANL channel. This produces a signal that could be thresholded. If timing changes the level of this signal varies, exceeding the thresholds and indicating a fault.

IP-QINT-ADC

The IP-QINT-ADC is the functional core of the BLM readout system. This module (called the QADC) was custom-designed for MPS BLM and Protection Ion Chamber (PIC) applications. It consists of eight HW programmable charge-integrating or voltage-sensitive ADC channels and a signal processing and fault checking subsystem implemented in a local FPGA. The BLM version QADC also generates the LED test pulse for the ANL BLMs. The programming of input sensitivity type is set by four resistors per channel. All analog inputs are terminated into 50 ohms at the QADC. For each channel, the analog front end consists of a single opamp integrator with a 100pF integration capacitor. Integration is controlled by the gate signal, generated by the QADC FPGA. When the gate is closed, the integration capacitor is shorted. The integrator is followed by a shaping amplifier with a gain of +3.74 and a 1.24us shaping time constant. The gain was chosen so that the maximum output of the ANL preamp (+1.5V) will present a near full-scale input to the ADC. For the integrator, the corresponding maximum charge input is 134pC. When in voltage mode, the integrator is bypassed and the input is connected directly to the shaping amplifier. In voltage sensitive mode, the maximum charge (via the charge-sensitive preamp in the BML-IM) that the system can read is 200pC per channel. The ADC is an Analog Devices AD7656 16-bit successive approximation device configured with a +/-5V bipolar input. All eight input channels are sampled simultaneously.

Special signal processing is done on the sampled data. The sampled pedestal data is summed for 360 samples and its average taken. The averaged pedestal is used to subtract of the offset present on the Beam and Test data samples. The pedestal-corrected most recent Beam and Test data samples are integrated over several different intervals to provide integrated dose measurements. The integration is performed digitally on a sample x[n], according to the relation:

$$y[n] = y[n-1] + x[n] - y[n-k]$$

The first two terms form the integration function, with the last being the leakage term; subtracting off the k^{th} sample in the array, limiting the integration to a fixed rate. These rates are 1Hz, 10Hz, 30Hz and 60Hz. These sums are also used for rate limiting and recovery. The most recent and integrated data are then presented to a fault checking block inside the same FPGA that compares them with a windowed threshold. If outside, a fault bit is set.

Fault Reporting

The L-N MB polls the QADC at 360Hz and stores this fault data in its local fault memory, which is then sent to the LP. A done/ready handshake is employed between the QADC and L-N MB FPGA state machine, ensuring that valid fault data is read. The BLM faults are copied into the L-N MB FPGA fault memory by that FPGA's state machine. The MB FPGA also applies window thresholds to the HVPS readback values on each channel. Any excursions outside the fault windows are indicated and sent to the LP, along with the BLM faults. Additionally, the most recent and accumulated data values are made available for read out over EPICS.

System Software

The control of the IP modules, setting of fault thresholds, trigger delays, and other housekeeping functions are controlled via EPICS with the embedded CPU running the RTEMS real-time operating system. A set of EPICS EDM GUIs have been created for system control, status and diagnostic functions. The fault reporting is handled by a separate set of MPS software, with faulted conditions being mirrored in the EDM GUIs. BLM faults are individually bypassable in the global MPS application.

OPERATIONAL EXPERIENCE AND PERFORMANCE

The BLM System was commissioned in the winter of 2009. Overall, the system has performed well in its primary MPS function. Many things were learned during

the commissioning process, which led to fixes and improvements in the system.

Several channels exhibited large noise signatures. After some effort, the noise sources were identified to be AC power in one case and signal transmission from a klystron modulator through a cable in the same tray as the BLM detectors in another. The noise sources were mitigated by shielding, grounding and isolation.

Studies were performed to determine the sensitivity of the detectors, both PEP-II and ANL. The results of these studies showed that the ANL units were more sensitive.

Another study was undertaken to understand the noise contributions of the electronics since it was noticed that the voltage-sensitive channels tended to be quieter than the charge-sensitive ones. The study showed that the analog integrator circuit was susceptible to noise pickup and crosstalk from clocks and other signals within the BLM Link-Node chassis. While able to perform its primary Machine Protection well, this noise has limited the ability to make meaningful radiation dosage measurements. Work continues in understanding the various radiation mechanisms seen by the detectors as well as the differences between measured versus expected loss levels.

Figure 4 plots the one-second sums of several BLM channels while a beam finder wire is inserted. The figure is an EPICS stripchart plot showing the loss signal induced when beam finder wire 26 was inserted. The beam is running at a rate of 10Hz and the gaps between peaks is due to the beam being toggled on and off with BYKIK, the upstream undulator beam kicker magnet. The largest loss signal seen is on the BLM on girder 33, as expected, because the loss radiation peaks approximately 10 girders beyond the inserted finder wire.

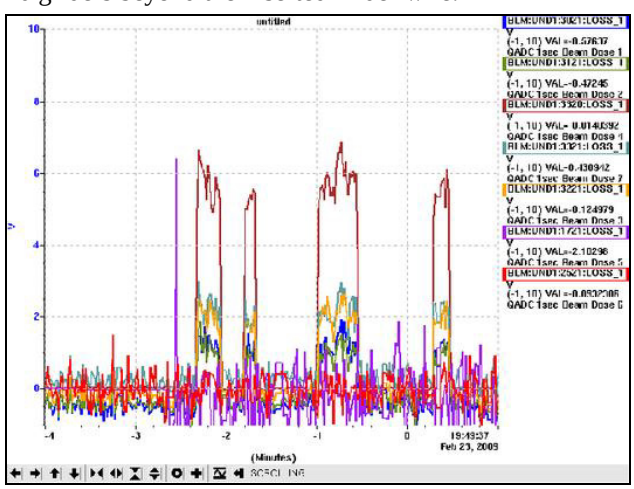

Figure 4: Measured Beam Loss from inserted BFW.

UPGRADES AND FUTURE PLANS

In its current configuration the system contains only five ANL BLM detectors. In late 2009, funding was secured to construct the remaining ANL-type BLM detectors and interface modules. These new units will replace the PEP-II units in all locations along the undulator. Construction is progressing and at the time of this writing, with full delivery of the ANL units is expected by summer 2010.

In anticipation of these units, the timing check mechanism for the BLM L-Ns was modified into a more permanent configuration: the directional coupler will not be usable when all channels are occupied with ANL units. Instead a hardware modification was made to the Link-Node's L-board that will allow the LED test pulse to be directly driven by an EVR trigger, instead of the QADC. The change was implemented during the 2009/2010 winter downtime, tested and shown to work. The checking mechanism is sensitive to within ±200ns.

Other feature enhancement upgrades to the MotherBoard and QADC FPGAs have been implemented, along with the supporting software and are currently in the integration testing phase. These improvements include added watchdog timers to guard against system failures, extended integrated sum readouts, extended threshold setting ranges and individual threshold settings on all accumulated sums and most recent data values. The latter is required for the MPS rate recovery feature, which is scheduled to be commissioned in 2010.

Longer term plans in implement Beam-Synchronous Acquisition (BSA) in the BLM system to allow recording of loss data coincident with beam events. This will be very useful for loss radiation studies.

REFERENCES

[1] "Linac Coherent Light Source (LCLS) Conceptual Design Report", Chapter 8, SLAC-R-593, UC-414, April, 2002; http://ssrl.slac.stanford.edu/lcls/cdr/.

[2] H-D Nuhn, "Undulator Beam Loss Monitor", LCLS Physics Requirement Document #1.4-005-r0.

[3] W. Berg et.al., "Development of a beam Loss Monitor System for the LCLS Undulator Beamline", LINAC08, September 29, 2008, Victoria, BC, Canada, TUP043.

[4] A. Fisher, "Instrumentation and Diagnostics for PEP-II", BIW98, AIP Conf. Proc. 451, 95-109 (1998)

[5] S. Norum et.al., "The Machine Protection System for the Linac Coherent Light Source", PAC09, Vancouver B.C. Canada, FR5REP039.

[6] VITA, "American National Standard for IP Modules", VMEbus International Trade Association, ANSI/VITA 4-1995 (R2002).

[7] J. Dusatko et.al., "The LCLS Timing Event System", This conference, TUPSM083.

MICROWAVE LINK PHASE COMPENSATION FOR LONGITUDINAL STOCHASTIC COOLING IN RHIC*

K. Mernick#, M. Blaskiewicz, J.M. Brennan, B. Johnson, F. Severino, BNL, Upton, NY 11973, U.S.A.

Abstract

A new microwave link has been developed for the longitudinal stochastic cooling system, replacing the fiber optic link used for the transmission of the beam signal from the pickup to the kicker. This new link reduces the pickup to kicker delay from 2/3 of a turn to 1/6 of a turn, which greatly improves the phase margin of the system and allows operation at higher frequencies. The microwave link also introduces phase modulation on the transmitted signal due to variations in the local oscillators and time of flight. A phase locked loop tracks a pilot tone generated at a frequency outside the bandwidth of the cooling system. Information from the PLL is used to calculate real-time corrections to the cooling system at a 10 kHz rate. The design of the pilot tone system is discussed and results from commissioning are described.

INTRODUCTION

In the Relativistic Heavy Ion Collider (RHIC), intra-beam scattering (IBS) is a primary cause of emittance growth of the gold beam. The stochastic cooling system is a wide band feedback loop designed to combat IBS and reduce the emittance of the beam.

A longitudinal stochastic cooling system was commissioned in the Yellow ring at RHIC in 2007 [1] and used during the FY07 and FY08 runs. The pickup for this system was in the 12 o'clock straight section, and the kicker was in the 4 o'clock straight section. As the beam travelled counter-clockwise, the pickup signal was transmitted on an analog fiber optic link through the tunnel. The pickup to kicker delay was 2/3 of a turn.

Prior to the FY09 run, a new longitudinal system was installed in the Blue ring. This system had the pickup located in the 2 o'clock region and the kicker at 4 o'clock. A microwave link connected them, with the transmitter installed on the berm above the beamline and the receiver located on the roof of the RF service building. The Blue beam travels clockwise, so the delay from pickup to kicker is 1/6 of a turn. The FY09 run was dedicated to polarized protons, so while important R&D work was completed, the new longitudinal cooling system was not made operational.

During the 2009 summer shutdown, the existing longitudinal cooling system in the Yellow ring was removed, and an upgraded system using the microwave link was reinstalled. The pickup was now located in the 2 o'clock straight section, with the kicker in the 12 o'clock region. Systems for vertical cooling were also installed in both rings. The vertical cooling systems use fiber optic links to transmit the signal from the pickups to the kickers.

The Blue and Yellow longitudinal stochastic cooling systems were both successfully commissioned during the FY10 100 GeV/nucleon gold run. Blue cooling was used in routine operation. Yellow cooling was successfully tested, but a series of mechanical problems with the kicker prevented routine operation. A schematic representation of the locations of the system components, along with the links between them, is shown in figure 1.

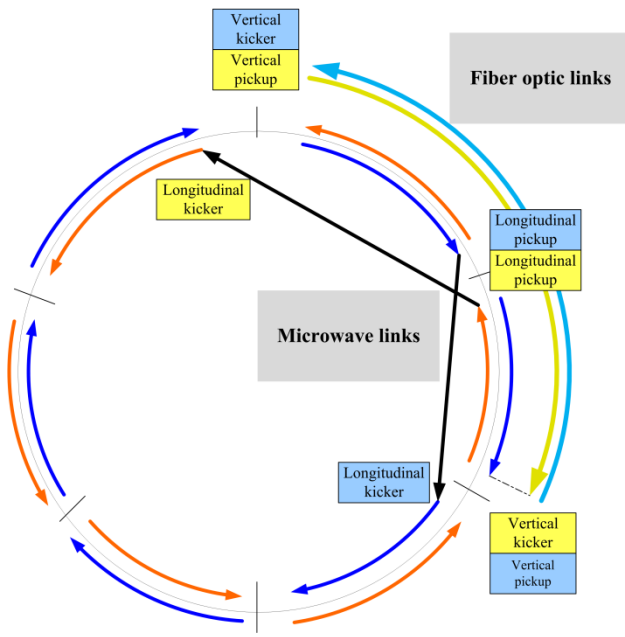

Figure 1: Locations of pickups and kickers (blue and yellow boxes), longitudinal system microwave links (black arrows), and vertical system fiber optic links (light blue and yellow arrows). The dark blue and orange arrows indicate the direction the beams travel.

EFFECT OF PICKUP TO KICKER DELAY

The longitudinal cooling system uses a one-turn delay notch filter to determine the kick necessary for cooling. The signal from the previous turn is subtracted from the current signal. This filter has the transfer function $G_1(f) = [1 - \exp(2\pi i \Delta f T_0)]\exp(2\pi i \Delta f T_d)$, where T_0 is the revolution period, T_d is the pickup to kicker delay, and Δf is the difference between the drive frequency and the nearest revolution line.

With the 2/3 of a turn delay of the fiber optic link and the one-turn filter, the cooling force has the correct sign for $|\Delta f| \leq 16.5$ kHz [2]. For gold beam with γ = 107 and 4 MV on the RF storage cavities at h = 2520 the

*Work performed by employees of Brookhaven Science Associates, LLC under Contract No. DE-AC02-98CH10886 with the U.S. Department of Energy.
#kmernick@bnl.gov

frequency spread at the edge of the bucket is

$$\frac{\Delta f}{f_{sys}} = \eta \frac{\Delta p}{p} = \pm 2.8 \times 10^{-6}$$

where f_{sys} is the operating frequency of the cooling system, $\Delta p/p$ equals $\pm 1.5 \times 10^{-3}$ is the momentum spread, and η equals 1.82×10^{-3} is the frequency slip parameter. This would have limited a one-turn delay cooling system to an upper frequency of 5.9 GHz. Instead, the previous system used a two-turn delay filter [3] to extend the stable part of the cooling force to a larger frequency spread, at the expense of reduced cooling in the center of the bunch. The maximum stable frequency for this system was 8.3 GHz, and the highest kicker frequency used was 8.0 GHz.

By reducing the pickup to kicker delay to 1/6 of a turn, the cooling force has the correct sign for $|\Delta f| \leq 29.3$ kHz. This increases the maximum stable frequency to 10.4 GHz. The highest kicker frequency used in the current system is 9.0 GHz. The cooling force for the different pickup to kicker delays and filters are compared in figure 2.

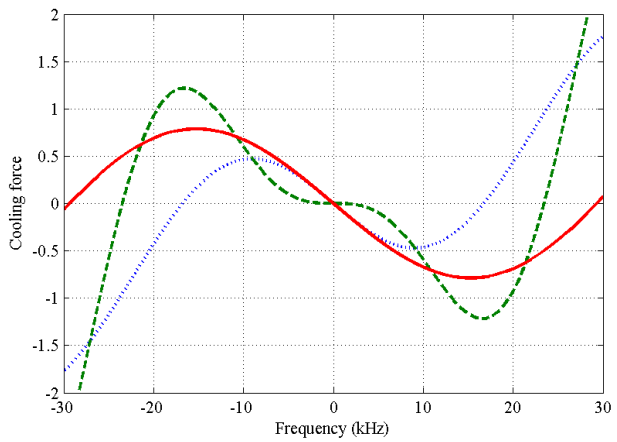

Figure 2: Cooling force for one-turn (blue dots) and two-turn (green dashes) filters with 2/3 turn pickup to kicker delay and for one-turn (red solid) filter with 1/6 turn pickup to kicker delay

THE MICROWAVE LINK

The microwave link is adapted from a commercial product for point-to-point wireless links for Gigabit Ethernet [4]. It operates via amplitude modulation in the 70 GHz E-band, with synchronous up and down conversions at the transmitter and receiver. The local oscillator is generated in an alcove in the tunnel at approximately the midpoint between the transmitter and receiver. The signal is distributed by fiber optics to both ends of the link.

New longitudinal pickups were installed during the 2009 shutdown. These pickups consist of ceramic windows in the beam pipe with waveguide to coax adapters. Previously, we had used planar array pickup devices built for stochastic cooling tests in the Tevatron [5]. The new pickups do not have any moving parts inside the vacuum, greatly simplifying their mechanical design

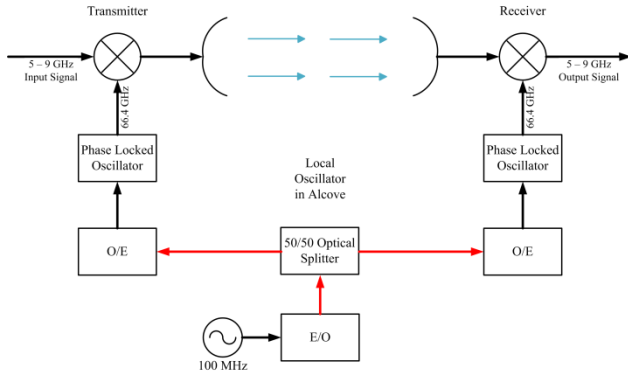

Figure 3: Microwave link signal distribution

and reducing the possibility of vacuum leaks. The signals from the inside and outside waveguide adapters are summed and routed directly to an electronics rack suspended from the ceiling of the tunnel. This rack contains a digitally controlled step attenuator, preamplifier, and the traversal filter [3]. The fiber optic receiver for the local oscillator is also located in this rack. The signal and local oscillator are then routed through a port in the roof of the tunnel to the microwave transmitter. The microwave signal is down converted by the receiver and fed to the input of the notch filter. The cable lengths for all of these connections are kept as short as possible to minimize delay. After optimizing the rack layouts and cable and fiber lengths, the signal arrives at the kicker within 10 ns of the optimal time. The traversal filter stretches the bunch signal to 80 ns, so the small extra delay is acceptable.

Microwave Link Phase Modulation

The microwave link introduces variations in the phase of the signal at the receiver. One source of phase modulation is variations in the time of flight from the transmitter to the receiver. A pure time delay of the received signal is modelled as $G_p(\omega) = \exp\left(iT_p\omega\right)$, where T_p is the propagation delay of the link. This results in a phase shift that increases linearly with frequency. Another source is phase shift of the local oscillators. The up conversion and down conversion can be modelled as

$$x_r(t) = x_t(t)\exp\left(i(\omega_{LO}t + \varphi_t)\right)\exp\left(-i(\omega_{LO}t + \varphi_r)\right)$$
$$= x_t(t)\exp\left(i(\varphi_t - \varphi_r)\right)$$

where $x_t(t)$ is the transmitted signal, $x_r(t)$ is the received signal, and φ_t and φ_r are the local oscillator phases at the transmitter and receiver. This results in a phase shift that is constant at all frequencies.

Fluctuations in the phase of the kicker signal reduce the phase margin of the system and can decrease the efficiency of the cooling. An out of band pilot tone is generated, and a phase locked loop (PLL) is used to compensate the fluctuations in the link.

THE PILOT TONE

A CW 5.075 GHz tone is generated in the service building that houses the electronics at the receiving end of the microwave link. The operating frequency of the pilot tone was selected to align with one of the nulls of the traversal filter at the pickup in order to reduce interference. This signal is split and one branch is connected to an electrical to optical converter. This signal is sent over a fiber optic link to the pickup electronics in the tunnel, where it is converted back to an electrical signal, amplified and added to the pickup signal with a directional coupler. This combined signal is then transmitted by the radio.

The received signal is passed through a 20 dB directional coupler, with the main branch connected to the input of the one-turn delay notch filter. The coupled signal is connected to a preamplifier with a bandpass filter centered at the pilot tone frequency. The signal is phase shifted by an I/Q vector modulator, and connected back to the module that generates the pilot tone.

The pilot tone module contains a mixer and low-pass filter which detect the phase difference between the received pilot tone signal and the signal split from the generator. The bandwidth of the phase detector is 15 kHz. A block diagram of the RF hardware is shown in figure 4.

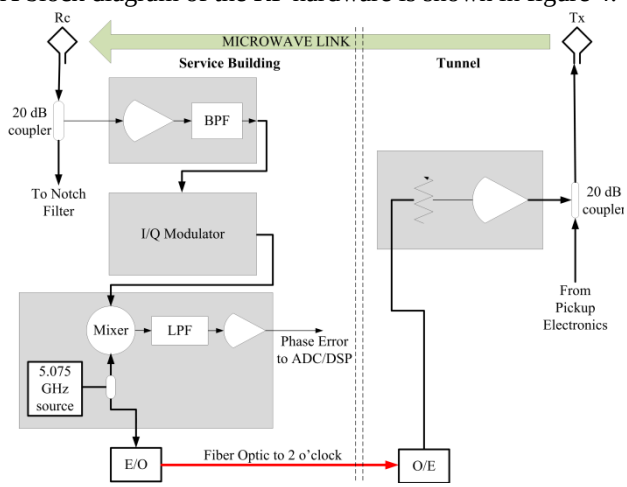

Figure 4: Block diagram of pilot tone RF hardware

The phase detector output is connected to a DSP carrier board in the VME chassis that contains the front-end computer (FEC) for the low-level control of the system. This DSP carrier board was originally designed for the AGS Booster [6], and was modified for this application.

The DSP carrier board contains an Analog Devices ADSP-21160, logic for the VME bus interface, local RAM that is shared with the VME bus master, and two daughter card sites. One of these sites is populated with a 4 channel ADC daughter card, which contains 4 AD9245 14-bit analog to digital converters and an Altera Stratix FPGA.

The FPGA acquires the phase detector data from the ADC at 40 MSPS, and filters it with a first-order IIR filter with 3 kHz bandwidth. The DSP reads the phase data from the FPGA at 10 kHz, and calculates a phase

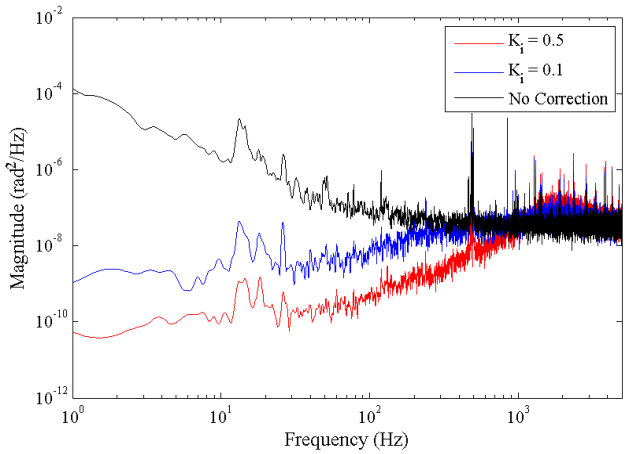

Figure 5: Power spectral density of phase error signal with pilot tone correction off (black) and on with integral gains of 0.1 (blue) and 0.5 (red)

correction with a PID loop. The normal configuration for the system only uses integral gain, and sets the proportional and derivative gains to zero. The pilot tone PLL is stable with a bandwidth up to approximately 1 kHz. The performance of the PLL is shown in figure 5.

System Corrections

The PLL applies a phase shift to the received pilot tone signal to cancel the phase shift from the link, but in order to improve the performance of the cooling system a correction must be applied to the drive signal for each of the 16 kicker cavities.

The low level system contains an I/Q modulator for each of the cavities. The settings for these modulators are determined by measuring the beam transfer function (BTF), and correcting the amplitude and phase to match a reference response [7]. This correction is performed every 10 to 15 minutes. These corrections are calculated by the FEC.

The I/Q modulator settings are distributed over a local serial bus. This bus, known as the NIM Link, originates from the Stratix FPGA on the ADC daughter card. The 10

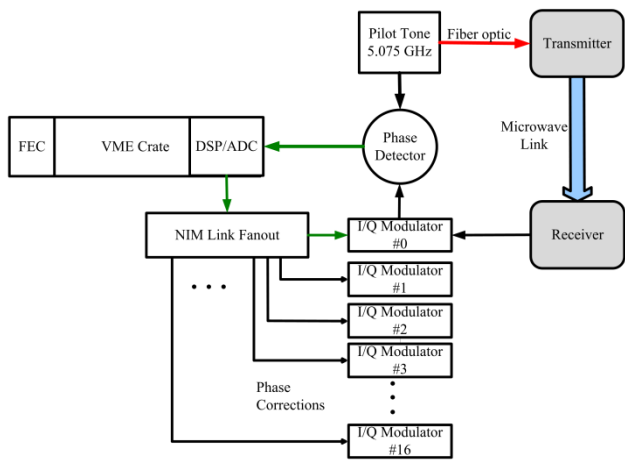

Figure 6: Block diagram of pilot tone phase compensation system

Mbps, biphase mark protocol is similar to the Real Time Data Link (RTDL) used throughout the RHIC complex, and the daughter card was modified to include a differential line driver so that the same fanout hardware and type of cabling can be used.

The initial belief was that the dominant source of phase shift would be the time of flight variation in the link. The initial DSP implementation calculated a frequency dependent phase shift $\varphi(f_{cav}) = (f_{cav}/f_{pilot})\varphi_{pilot}$ where f_{cav} and f_{pilot} are the cavity and pilot tone frequencies, and φ_{pilot} is the phase shift resulting from the pilot tone PLL. During testing before the start of the FY10 run, we found that this method overcorrected at the cavity frequencies, and was worse for the high cavity frequencies that were farther away from the pilot tone frequency.

Additional testing confirmed that the phase shift due to the microwave link local oscillator was the dominant factor. The DSP software was modified so that it applies the same phase shift, the result from the PLL, at all frequencies.

To summarize the data flow, the FEC calculates periodic updates to the I/Q modulator settings based on the BTF measurements and writes amplitude and phase settings for each cavity to the shared memory on the DSP carrier board. The DSP reads the amplitude and phase from the shared memory, calculates and applies the additional phase shift based on the pilot tone PLL, converts the amplitude and phase to real and imaginary components, and writes these values to the FPGA on the ADC daughter card. These adjustments are performed at the same 10 kHz update rate as the PLL calculations. The FPGA generates the NIM Link data frames and sends them over the serial link to the I/Q modulators.

RESULTS

The pilot tone correction at the cavity frequencies was tested prior to the run with a synthetic beam signal. A signal from the network analyzer was transmitted over a fiber optic link to the pickup electronics and then back to the analyzer over the microwave link. The network analyzer was configured for zero span, and the phase of the received signal was monitored with the pilot tone corrections enabled and disabled. We were able to determine that applying the single phase correction at all

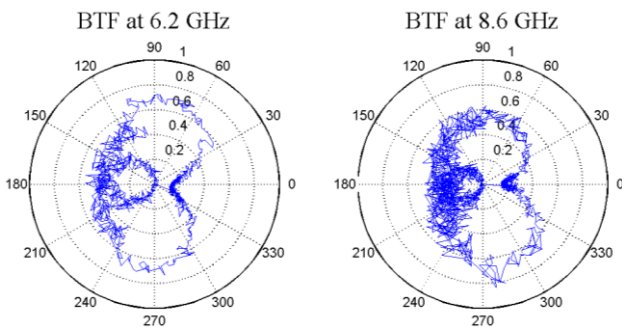

Figure 7: Beam transfer functions for 6.2 GHz and 8.6 GHz cavities.

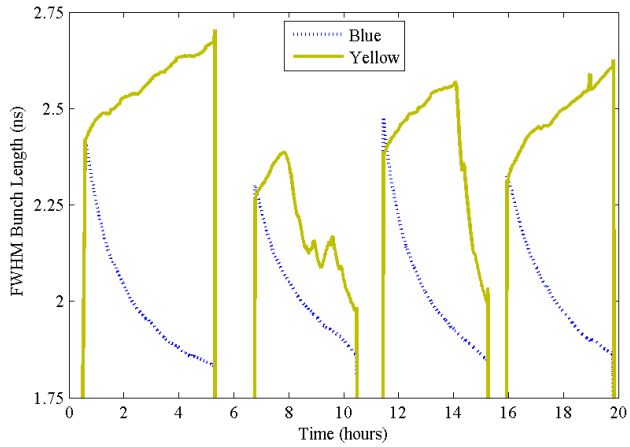

Figure 8: Evolution of the full width at half maximum bunch length in Blue and Yellow for four RHIC stores.

cavity frequencies significantly reduced the phase variation of the received signal. However, performance was degraded at the higher cavity frequencies. This indicates that there is some phase variation caused by the time of flight which is not currently compensated.

The phase compensation performance with beam was acceptable. The BTF measurements at the higher cavity frequencies exhibit more noise, consistent with the pre-run testing. This behavior is illustrated in figure 7. An additional test used the kicker to put a CW tone on the beam and measure the phase of the received signal after the phase correction was applied. The results of this test were consistent with the prior tests using the fiber optic link.

Figure 8 shows the performance of the longitudinal cooling system with the microwave link and pilot tone phase correction. Blue longitudinal cooling was on for all stores. Yellow longitudinal cooling was off for the first and last stores, and was being setup during the middle two stores. The shortened bunches improved the total luminosity and also increased the percentage of collisions in the center of the detectors, which enhances the efficiency of the PHENIX detector.

CONCLUSIONS

The microwave link allowed higher frequency operation of the longitudinal stochastic cooling system with better phase margin. A phase locked loop was successfully used to track an out of band pilot tone and apply phase corrections to the individual kicker cavity signals to compensate the phase modulation added by the link. We are developing an upgrade to the system to use tones at two frequencies to improve performance further.

ACKNOWLEDGEMENTS

We thank the members of the Controls, Operations, RF, and Beam Components groups of the Collider-Accelerator Department for their hard work and support. In particular, we would like to thank Rob Michnoff for his help understanding the DSP hardware, Roger Lee for his

help with the interface to the RHIC control system software, and Craig Dawson and Peter Oddo for the NIM Link implementation.

REFERENCES

[1] M. Blaskiewicz, J.M. Brennan, F. Severino, *Phys. Rev. Lett.* 100, 174802 (2008).
[2] M. Blaskiewicz, J.M. Brennan, F. Severino, Stochastic Cooling of High-Energy Bunched Beams, PAC 2007, p 2014 (2007).
[3] J.M. Brennan, M. Blaskiewicz, Bunched Beam Stochastic Cooling at RHIC, COOL 2007, p 25 (2007).
[4] HXI Millimeter Wave Products, 22 Parkridge Rd, Haverhill MA 01835, www.hxi.com.
[5] D. McGinnis, et al. PAC 1991, p1389 and P. Hurh and G. Jackson,PAC 1993, p. 2148.
[6] J. Delong, et al, Topology for a DSP Based Beam Control System in the AGS Booster, PAC 2003, p 3338 (2003).
[7] J.M. Brennan, M. Blaskiewicz, Stochastic Cooling in RHIC, PAC 2009

BUNCH ARRIVAL MONITOR AT FERMI@ELETTRA

L. Pavlovic, University of Ljubljana, Ljubljana, Slovenia
A. O. Borga, M. Ferianis, M. Predonzani, F. Rossi, Sincrotrone Trieste ELETTRA, Trieste, Italy

Abstract

The bunch arrival monitor (BAM) for the IV generation synchrotron light source FERMI@Elettra is presented. It is based on an original idea developed at FLASH/DESY, specifically designed and built in-house for FERMI@Elettra. Each BAM station consists of a front-end module, located in the machine tunnel, and of a back-end unit located in the service area. It makes use of the pulsed optical phase reference along with the stabilized fiber link. The front end converts the bunch arrival times into amplitude variations of the optical phase reference pulses distributed over the link. The analogue signal is generated at the e-beam's passage in a broadband pick-up and is sent to the modulation input of an electro-optical modulator (EOM). The back end acquires, synchronously, the amplitude modulated pulses, using a broadband photodiode and a fast analog-to-digital converter. The digitized data is sent to the machine control system for further processing. The dedicated analog-to-digital conversion, processing and communication board, part of the monitor back end, is also briefly described.

INTRODUCTION

New 4th Generation Light Sources (4GLS) currently in operation, construction or design at several National Laboratories are posing demanding requirements on the associated Timing and Synchronization (T&S) systems, identified as femto-second (fsec) T&S systems. 4GLS are typically Free Electron Lasers (FEL) driven by single pass Linear Accelerators (LINAC). Such demanding requirements on jitter (<10fsec$_{RMS}$), and drift, originate from the adopted scheme for the generation of the electron beam and the FEL radiation.

The typical bunch length (τ_B<50fsec$_{FWHM}$), achievable in single pass accelerators thanks to the beam longitudinal manipulation techniques, the required beam quality (6-D emittance) and the radiation generation (seeding) and exploitation (time resolved / pump-probe experiments) schemes call for an ultimate jitter of <10fsec$_{RMS}$. This ultra-low jitter value is typically required either between the electron bunch and the seed laser pulse or between the FEL pulse and the User laser pulse. To achieve this goal, the whole accelerator components need to share a Phase Reference with <10fsec$_{RMS}$ jitter and drift.

BUNCH ARRIVAL MONITOR

In 4GLS, the time position of the bunch is identified by the combination of the timing pulse (as a reference) and the slope of the electrical signal produced by the bunch passage through the pick up mounted on the beam line. This scheme was first proposed by the Desy group [1]. The pick up signal is fed to an Electro-Optical Modulator (Mach-Zehnder modulator - MZM) and modulates the optical pulses of the optical master oscillator (OMO) as a reference. The timing jitter of the bunch shifts the temporal position of the slope and thus amplitude modulates the optical pulses. Therefore the amplitude variations correlate to the timing jitter of bunches. The BAM system consists of two main parts, the front end installed in the tunnel close to the beam pick up and the back end installed in the service area for the readout of the modulated pulses and further processing.

BAM Front End

The BAM front end does the timing comparison between the reference's optical pulses and the electron bunches in the accelerator. Due to the very high resolution requirement, the BAM front end is mainly an optical system. The time comparison is done by a MZM, which converts the time difference into an amplitude difference. The modulated optical pulses from the MZM are fed to the photodiode in the BAM back end. The front end is shown in Figure 1.

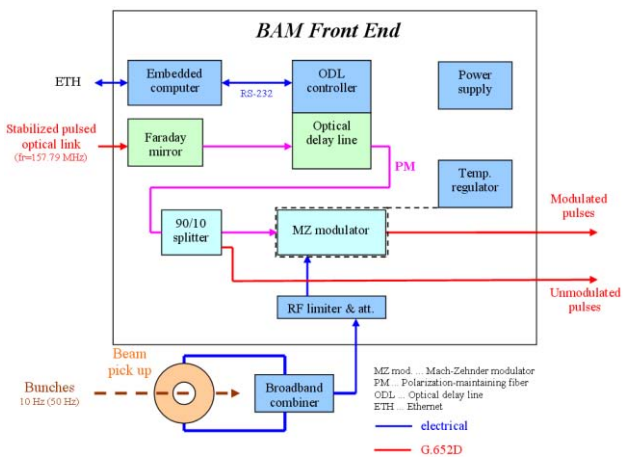

Figure 1: Block diagram of the BAM front end.

The front end has two inputs, the optical pulses from the OMO, distributed via a stabilized link, and the electrical signal from the pick up. The Faraday mirror is part of the stabilized link and needs to be close to the MZM, since short pulses provide better timing resolution. The optical delay line compensates slow drifts of the link and enables the calibration of the system at the beginning of the operation. The splitter passes 90% of the optical power to the MZM, while the 10% is left un-modulated for the ADC clock extraction at the back end. The polarization from the stabilized link needs to be controlled. Optionally, there is a need for a limiter after the pick up for the protection of the MZM's RF input. Since the MZM's transfer characteristic is temperature dependent, the MZM is temperature stabilized by a

regulated heat-pump. The delay line and some diagnostic parameters are remotely controlled via the Ethernet connection.

BAM Back End

The BAM back end is in charge of the readout and processing of the timing comparison made in the BAM front end. The modulated pulses are digitized by a dedicated analog-digital-analog (ADA) board based on the uTCA platform [2]. Beside the ADA the BAM back end includes also the signal-conditioning board (SCB) which extracts the ADC clock signal and provides a low phase-noise phase shifter. Two high-speed photodiodes are required for the opto-electrical conversion. The BAM back end is depicted in Figure 2.

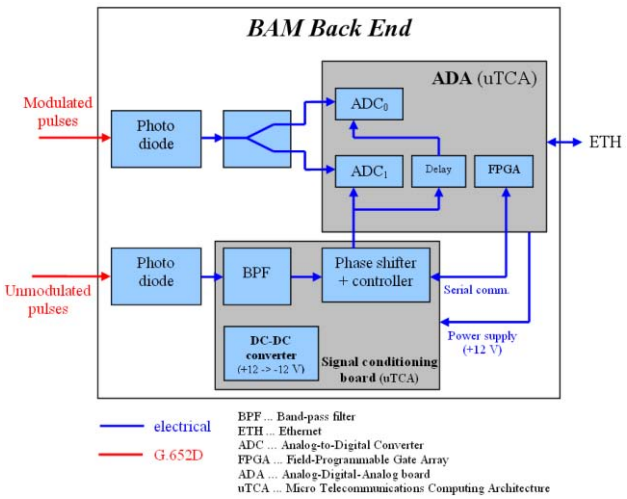

Figure 2: Block diagram of the BAM back end.

Two ADCs are used for the acquisition of the modulated optical pulses, first one for pulses and the second one for the baseline. In this way the noise present on the baseline can be used for the pulse amplitude normalization. The delay between the ADC sampling times is few hundreds of ps. The ADA is described in more detail in a later section. The low phase-noise electrically-adjustable phase shifter is based on a passive IQ modulator and features an automatic gain control for the incoming signal. It is controlled via a serial interface through the FPGA, connected to the Ethernet.

PHASE REFERENCE FOR THE BAM

The BAM stations need a phase reference signal for their operation. It is obtained from the pulsed sub-system of the FERMI optical timing system [3]. Each BAM front end in the machine tunnel has a dedicated stabilized fiber optical link. The scheme of the timing distribution and optical cabling related to the BAM diagnostic is represented in the Figure 3.

The optical master oscillator (OMO) is a soliton fiber laser working with a repetition rate of 157.790 MHz. The optical pulses are distributed to the BAM front ends by the fiber-link stabilization (FLS) units. The link receiver (RX) is composed of an Erbium-doped fiber amplifier and a Faraday rotator mirror. The latter is integrated into the BAM front end, so the link stabilization is done as close as possible to the point where the optical pulses are effectively used. The modulated (bunch timing) and the un-modulated (OMO clock) pulses are distributed to the back end via (non-stabilized) optical fibers for the data processing (bunch-arrival time and jitter).

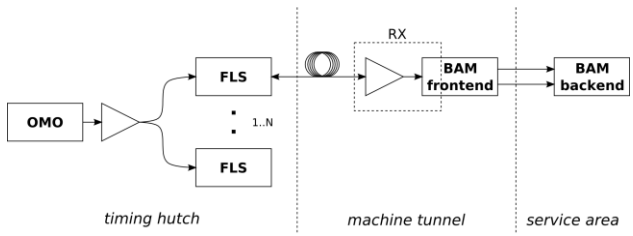

Figure 3: Optical distribution used for the BAM.

The optical pulses, used to sample the pick-up signal generated by the e-beam, are dispersion compensated and have a duration of about 200 fs FWHM at the output of the link. It is important to have short pulses at the input of the modulator but they are stretched before the input of the Mach-Zehnder Modulator because of the extra fiber path. The latter is therefore kept as short as possible.

ACQUISITION AND PROCESSING BOARD

For the BAM and other high-performance systems at FERMI@ELETTRA a dedicated data-processing platform (analog-digital-analog - ADA) has been designed [3]. It is based on the MicroTCA standard and is implemented as an Advanced Mezzanine Card (AMC). The main features of the platform are high-speed signal acquisition, generation, data processing and communication towards the control system. The architecture is based on the Xilinx Virtex-5 FPGA responsible for the data handling of all the external inputs, the processing and the interface to users. The block diagram of the ADA is shown in Figure 4.

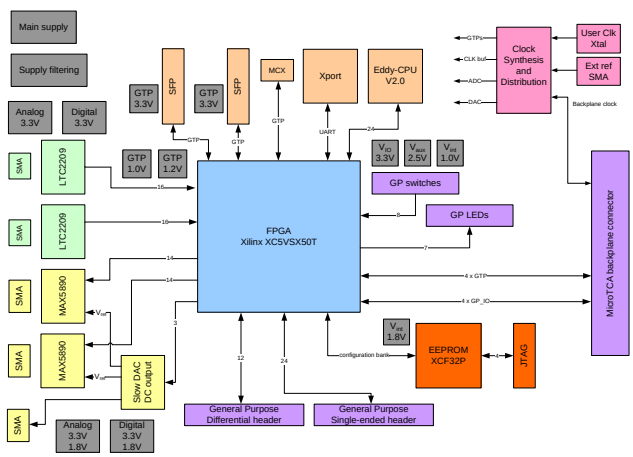

Figure 4: Data-processing platform for the BAM.

The ADA platform is divided in the following subsystems:

1. Power-supply section
2. Clock distribution: a programmable and configurable clock tree provides precise timing to on board devices with the freedom to choose between several internal or external references
3. Configuration section: the logic can be programmed choosing between direct access through an onboard JTAG chain or remotely either via the backplane or the Ethernet through the microcontroller
4. Analog inputs and outputs:
   2 LTC2209 ADC inputs, 160 Msps, 16 bits
   2 MAX5890 DAC outputs, 600 Msps, 14 bits
   1 LTC2602 slow dual DAC output, 16 bits
5. Computational core: Xilinx Virtex-5 SX50T FPGA
6. Remote access:
   Lantronix: 1 Mbps Ethernet link
   Eddy-CPU: 100 Mbps Ethernet link
   Small Form-factor Pluggable (SFP) ser-des: 1Gbps custom link
   uTCA Backplane via Gigabit Transceiver Pairs (GTPs): 4 x 1Gbps custom protocol links
   uTCA Backplane via standard IOs: 4 x 200Mbps custom protocol links
7. General purpose inputs and outputs: 24 single ended and 12 differential lines

The ADA supports various fully-configurable and programmable clock possibilities. The ADC and DAC stages can be independently driven by external clock sources through SMA inputs on the front panel. Since the BAM acquisition is critical the latter clock option is used. The ultra-low phase-noise clock is provided by the un-modulated optical pulsed link to the back end via the signal-conditioning board. In addition, the FPGA can be clocked off of the same external clock either from the DAC or ADC inputs, as well as being timed independently from one of the onboard clock sources. Alternatively the whole board can be timed by high-accuracy (tens of pico-seconds range) frequency synthesizers starting from a low frequency (14 – 37.78 MHz). The selection of the various frequencies and tree setup is accomplished by setting jumpers. The backplane and other data transfer and communication sections (e.g. Gigabit links) are timed independently having other clocking requirements.

PRELIMINARY RESULTS

The e-beam pick up, shown in Figure 5, provides an electrical signal which incorporates the bunch timing (jitter) information. The pick up is a 4-electrode open coax-line type (SMA connectors), having extremely wide bandwidth (few tens of GHz) required for the needed steep slope of the voltage-to-time conversion. Important property of the pick up is also the coupling factor between the beam and the electrodes. The latter must be optimally chosen, not to provide too high nor too low voltages at the output SMA ports. The optimal output voltage needs to match the Mach-Zehnder modulator drive voltage (i.e. 5 Vpp).

Figure 5: BAM 4-electrode (open coax-line type) pick up.

The signal from the pick up was measured by a real-time high-bandwidth (12 GHz) oscilloscope with only 1 m of coax cable between the pick up and the oscilloscope. The signal was measured at 100 pC charge and is shown in Figure 6. The signal has a typical mono-pulse shape, with the central (the steepest) slope being used for the timing information. The slope's rise time is limited mainly by the oscilloscope's bandwidth. With further increase of the charge (to few hundred pC), suitable amplitude for the Mach-Zehnder modulator will be achieved (few Vpp).

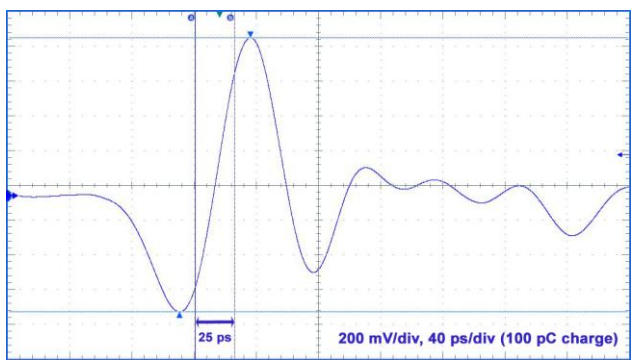

Figure 6: BAM pick-up signal measured on a 12 GHz scope.

The un-modulated optical link from the BAM front end to the back end provides the low phase-noise clock for the ADCs. The signal-conditioning board (SCB) extracts the first harmonic (157.79 MHz) and features a 360-degree electrically-adjustable phase-shift capability. The preliminary OMO-output measurement in the 10 Hz to 10 MHz integration range show about 258 fs of timing jitter. The SCB-output jitter, shown in Figure 7, is about 287 fs. The additive jitter of the SCB is therefore in the order of 130 fs. The noise between the 50 Hz and 10 kHz of the preliminary measurement is coming from the OMO (mainly due to the loose power-supply filtering), while the noise between 10 kHz and 1 MHz is generated in the SCB. With further reduction of the OMO phase noise (better power-supply filtering) the total timing jitter below

200 fs is expected which is adequate for a high-resolution acquisition of the ADCs in the back end.

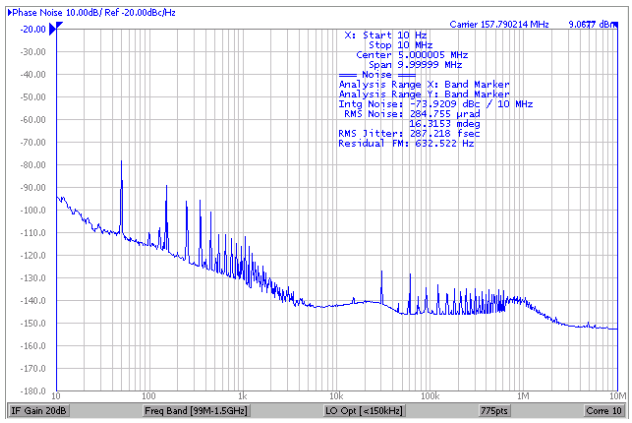

Figure 7: Preliminary phase-noise measurement of the extracted clock for the ADC.

The prototype of the BAM front end has been built. Using some commercial solutions (i.e. optical delay line, Peltier driver) and several custom-made electrical circuits a fully-functional and remotely-controlled standalone unit was assembled. The aluminium box is 250 x 250 x 100 mm in size and includes all blocks shown in Figure 1. It features a temperature-stabilized chamber for the Mach-Zehnder modulator, an embedded computer for the remote control via Ethernet, a diagnostic board for several important parameter readout, a 560 ps optical delay line with controller and some additional circuits. The BAM prototype box (with the Faraday-mirror module removed) is shown in Figure 8.

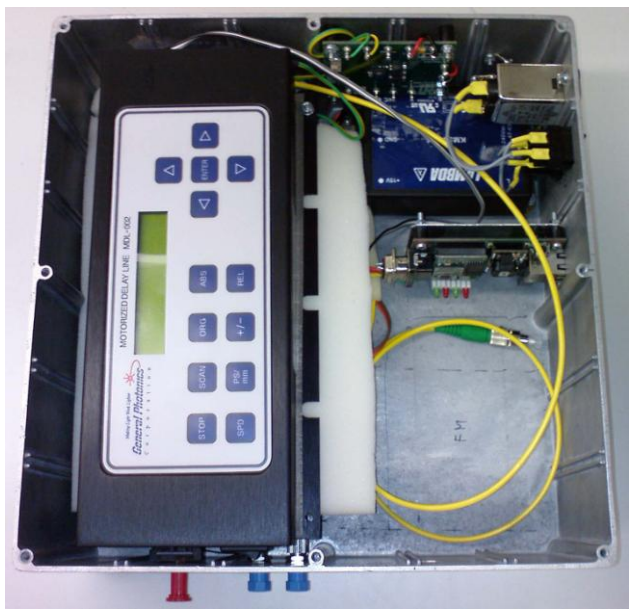

Figure 8: BAM front-end prototype. The Faraday-mirror module of the stabilized link is not installed in the box (lower right area).

The preliminary measurements of the complete BAM system (front end and back end) without the beam have been carried out. Assessment of the optical and electrical power levels throughout the system has been made. The most critical are the optimal Mach-Zehnder RF drive level and the optical power levels at the two photodiodes in the back end. The amplitude noise of the OMO pulses has been evaluated with real-time measurements using the ADA acquisition board. The amplitude RMS noise measured was 0.37 %, which seems a little bit too high, but the input power and voltage levels of various devices and components were not optimally set at this point.

FUTURE WORK

An integration of the complete system (front end and back end) is planned in June/July 2010. The first bunch timing jitter measurements will be performed. The prototype units will be used at first, but will be later replaced with the (first) industrially-manufactured series. The final BAM system with the complete integration into the FERMI@Elettra control system will be done in autumn.

CONCLUSION

The bunch-arrival-time monitor developments have been described. Up to now working front end and back end prototype units have been manufactured and tested. The measurements of the pick-up signal show a slope of about 50 mV/ps (at 100 pC charge), which is limited by the measurement equipment. Normally, the machine will operate at several hundreds of pC charge, so the slope will be appropriately steeper. Although the first acquisition measurements show relatively large OMO's amplitude noise, optimization of levels throughout the system will greatly improve the readout resolution.

ACKNOWLEDGMENT

The authors wish to thank all the colleagues from the Timing and Diagnostics group at Elettra and also the Desy team for the help and advice.

REFERENCES

[1] F. Loehl et al., "A sub 100 fs electron bunch arrival-time monitor system for FLASH", Proceedings of EPAC 2006, Edinburgh, Scotland, 2006, pp. 2781–2783.

[2] A. O. Borga et al., "The Diagnostics' Back-End Platform Based on the In-House-Developed A|D|A And A|D|O Boards", this conference, TUPSM025.

[3] M. Ferianis et al., "The copper free Fermi Timing System: implementation and results", this conference, TUPSM087.

THE COPPER FREE FERMI TIMING SYSTEM: IMPLEMENTATION AND RESULTS

M. Ferianis, A. Bucconi, G. Gaio, G. Mian, M. Predonzani, F. Rossi
Sincrotrone Trieste S.C.p.A. ELETTRA, Trieste, Italy

Abstract

With respect to its timing system, FERMI@Elettra is the first "copper free" FEL facility. Having been conceived during the FERMI Technical Optimization Study (TOS), the FERMI timing system is based on the original ideas developed at MIT/DESY and at LBNL, which have been demonstrated also with the significant support of Sincrotrone Trieste. Since then, at FERMI, a young though strong team has been growing in time and is now running the system on the facility. As for the trigger distribution we have adopted the COTS solution by Micro-Research Finland Oy, the main original contribution to the Community is found in the phase reference generation and distribution. The huge engineering effort afforded by the FERMI@Elettra project in the last twelve months has produced a unique system that is now ready to assure a stable seeded FEL operation. The current system implementation is presented here along with the obtained performances, at the few tens of femto-second (fs) level (jitter and drifts).

INTRODUCTION

FERMI@Elettra is the fourth generation synchrotron light source currently under commissioning in Trieste [1,2], Italy. Being based on a seeded Free Electron Laser (FEL), it requires state of art timing and synchronization.

Given the electron bunch length and seed laser pulse duration, both in the tens of fs range, the specifications of the timing system are very demanding as the whole machine stability requirements are. When the FERMI@Elettra project officially started, back in 2006, there were laboratory experiments on optical timing systems showing possible solutions to meet these challenging small values, jitter having been addressed first. It was common believe that only newly developed optical techniques could meet the target jitter (<<100fs).

Collaborations were started in 2006 and 2008, with the Research Laboratory of Electronic (RLE) at MIT [3], Cambridge MA-USA, and with the Center for Beam Physics at the LBNL, Berkeley CA-USA, respectively.

Furthermore, a European expert group on fs timing systems [5] also grew during the FP6 EUROFEL Design Study [6], coordinated by DESY. In this joint effort, 16 European organisations developed some of the key technologies required for the design and construction of next generation free electron laser (FEL) sources.

After having analyzed the timing system specifications for a single bunch FEL, the *hybrid* timing system has been proposed for FERMI@elettra, adopting both the *pulsed* and *continuous wave* (CW) optical timing [2].

The rationale for this original approach is in that the synchronization schemes, adopted to phase lock different systems, are some based on an optical pulsed phase reference (like an optical cross-correlator or an electro-optical bunch arrival monitor) and some based on a CW one (like the low level radio frequency system). A fs jitter measurement laboratory has been also set-up as well as demonstrators of both pulsed and CW systems.

THE FERMI TIMING SYSTEM

In figure 1, the basic block diagram of the FERMI@elettra timing system is presented.

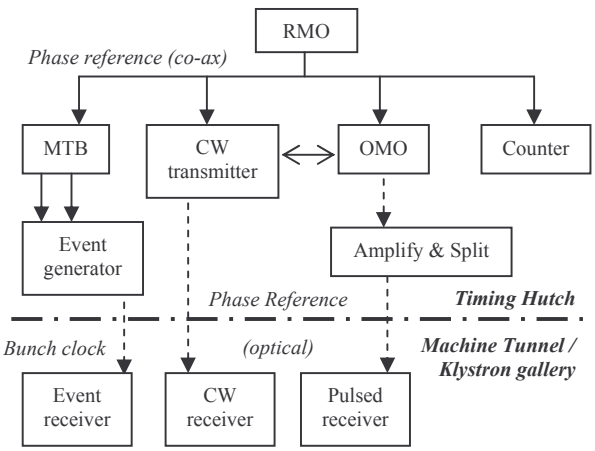

Figure 1: basic block diagram of the FERMI timing system. Solid lines indicate coaxial cables; dashed lines, optical fibres.

Primarily, the FERMI@elettra timing system generates and distributes throughout the facility the phase reference signal which all synchronized sub-systems (*timing clients*) are locked to. The frequency of the phase reference master oscillator is the same of the S-band accelerating structures in the linear accelerator (Linac). The phase reference information is transferred to the *clients*, either using an optical pulse train, generated in the Optical Master Oscillator (OMO) or a CW signal encoded onto an optical carrier (CW optical transmitter), actively stabilized fibre optics links being used for both systems.

The FERMI@elettra timing system also generates the bunch clock (up to 50Hz) and the laser *coincidence* clock (f_{COIN}=S-band÷38=78.895MHz) which is used to align the pulses from the different laser oscillators in the facility. The master time base (MTB) is implementing this task.

The bunch clock is then distributed throughout the whole facility, over fibre optics cables, by means of the *Event system* of Micro Research Finland Oy [7].

As a result, both the phase reference and the auxiliary signals are distributed using fibre optics (*copper free* timing system) which to our knowledge is a world premiere for synchrotron radiation facilities.

The timing hutch

The FERMI@elettra timing system presents a star topology. The centre of the star is the *timing hutch*, a dedicated laboratory where all the timing system equipments are located and where the optical cables start from. The timing hutch is next door to the photo-injector laser, on the same level of the Linac tunnel.

The main equipments located in the timing hutch are:

- the reference microwave oscillator (**RMO**)
- the pulsed optical master oscillator (**OMO**)
- the pulsed optical amplifier and splitter
- the pulsed links stabilization system
- the CW phase reference sender
- the master time base (**MTB**)
- the Event generator (**EVG**)
- the patch panels of the fibre cabling

The timing hutch has started operation in July 2009, for the 1st commissioning period of FERMI@elettra.

The reference microwave oscillator

The reference micro-wave oscillator is a 3GHz oscillator (f_{RMO}=2,998010GHz) specifically developed for FERMI@elettra by the German company Inwave [8]. The outputs of 4 locked 125MHz oscillators are multiplied to provide 1GHz signal which is then multiplied times three. The 3GHz signal is amplified and filtered; a passive splitter provides the six RF outputs, with +15dBm each.

Due to the aging of the crystals, some tunings of the RMO have been carried out during first operation period

PHASE REFERENCE SYSTEMS

In a Linac-based FEL facility, the main systems calling for fs synchronization are:

- the Linac (klystrons and accel. structures);
- the lasers: photo-injector, seed and user's ones;
- the longitudinal diagnostics;

The phase reference generation and distribution systems are responsible for remotely providing the phase reference at the femto-second level.

The optimum phase reference system depends, to some extent, on the synchronization schemes to be adopted for the above cited systems. The radio frequency (RF) amplifiers (klystrons), used to feed the accelerating structures of the Linac, are phase and amplitude stabilized by means of Low Lever RF (LLRF) systems. These systems are quasi-CW and adopt a CW phase reference. On the other hand, optical cross-correlators normally phase lock at the fs level two laser oscillators. These systems adopt as a phase reference signal a train of optical pulses [9]. Furthermore, new longitudinal diagnostics techniques have been proposed and on-field demonstrated, again based on the pulsed optical phase reference [10].

It is also worth mentioning here how the required phase noise may differ for the cited systems; for FERMI [11], the values range from the <70fs_{RMS} of the Linac accelerating voltage to the <15fs_{RMS} of the seed and user lasers; same applies for the drift (8h.).

Phase noise integration interval

When specifying and measuring the phase noise, the offset frequency integration interval needs to be carefully chosen [12]. Typically, different intervals are appropriate for different machines, being primarily related to the time structure of the beams. The time structure (single bunch or pulse train, repetition rate) together with the total (gun to experimental station) physical extension of the facility defines its *time of flight*, i.e. the minimum time interval over which the phase needs to be ultra-stable.

Plugging in the numbers of FERMI, a single bunch machine with a 50Hz maximum repetition rate and a total extension (gun-to-experimental station) of <300 meters, the time of flight results to be <1μs. Therefore, including some margin for the stabilization loops, any variation of the phase reference slower than 1ms is not relevant. As a consequence the phase noise integration interval has been set from 100Hz to 10MHz of the offset frequency.

The pulsed optical phase reference system

The pulsed optical phase reference system is represented in figure 2. The optical master oscillator (**OMO**) is a *soliton* fibre laser [13] working at a repetition rate of 157.790MHz (S-band÷19). Two modules are provided for its phase locking to the phase reference signal: a conventional *Fast Photo-Diode-Phase Detector* (**FPD-PD**), used also to select the OMO relative phase respect the RMO, and an innovative *Balanced Optical Micro-wave-Phase Detector* (**BOM-PD**), designed by the group at MIT [14], specifically engineered for FERMI by MENLOSYSTEMS gmbh [15]. To minimize the system downtime, a redundant easy-to-swap pump diode has been included. The optical signal of the OMO, amplified by an Er-doped Fibre Amplifier (EDFA), is split (8 ways) to feed the link stabilization (FLS) units (6). One output goes to the CW to pulsed locking units.

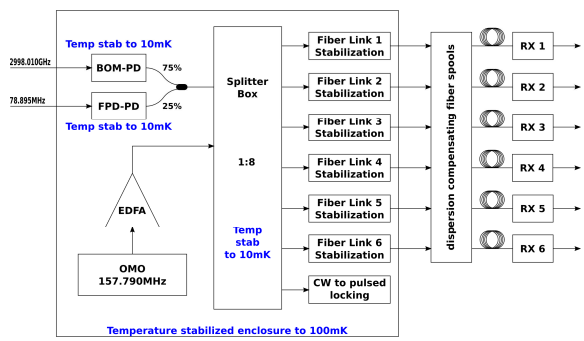

Figure 2: pulsed optical phase reference system; the components, inside the box on the left, are temperature stabilized to 0.1°K (the splitter box down to 0.01°K).

The path between the OMO and each FLS is entirely in fibre; the dispersion compensation assures the shortest pulses in front of the link cross-correlators. Each splitter output port provides ≈40mW of power with an average FWHM of 165fs (figure 3) and 30nm of bandwidth.

Each FLS unit implements a link stabilization scheme based on a single type-II phase-matched PPKTP crystal

[16] which is used as a phase detector. The path length variations are actively compensated by the combined action of a piezo-mirror, on the short time scale, and a motorized translation stage, for the drifts.

The system components, up to the FLS units, are installed in the timing hutch in a temperature controlled box, stable to 0.1°K; the *splitter box*, inside the same box, is stable down to 10mK.

The loop electronics implements a PID controller, interfaced to the control system, driven by the error signal generated from the pulse overlap.

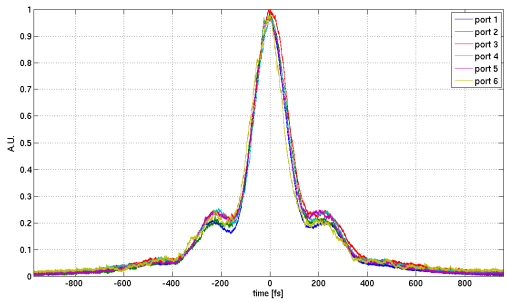

Figure 3: autocorrelation traces at the splitter ports.

At the remote end of the stabilized link there is the receiver composed of an electro-optic module, containing the link amplifier used to overcome the losses along the link, and a separate passive reference-head where a 10% reflecting *Faraday Rotator Mirror* is installed. The link stabilization is performed up to this point, resulting in a highly flexibility and compact solution.

The clients of the optical pulsed phase reference system are the lasers and the longitudinal diagnostics. The optical pulse train is used to synchronize a remote laser oscillator either by direct conversion (coarse locking) or using optical techniques (fine locking).

In the Bunch Arrival Monitor (BAM) [10, 17], the pick-up signal generated by the electron beam amplitude modulates the distributed OMO pulses used. In the Electro-Optical Sampling (EOS) station the local fibre laser oscillator is also phase locked to the OMO pulses.

As of today, the foreseen pulsed timing clients are:

- Photo-injector laser oscillator;
- Seed laser oscillator;
- EOS fibre laser oscillator;
- User laser oscillator;
- two BAM stations (at Laser Heater and BC1);

An increase of the client number is possible and it has been considered as a future option.

The Continuous Wave (CW) phase reference

The relative time stability of the different RF plants of the Linac is a key element to the overall stability of the accelerator i.e. to the quality (energy spread) of the electron beam. Such a relative stability is achieved by adopting a specifically designed LLRF system, typically one station for each klystron, and by feeding the LLRF stations with an ultra stable phase reference signal.

At FERMI, the LLRF system based on the original LBNL design [18] has been tested in March; tests have been performed on a FERMI klystron to cross-check the performances of the whole system.

In the LBNL system, the distribution of the phase reference is accomplished by means of CW optical links [19] where the phase reference signal is encoded onto an optical carrier. Peculiar to this design, a novel concept has been adopted where the drift of the link is measured with fs accuracy, but is not compensated for. Rather, the measured drift value is periodically added as a digital delay in the LLRF loop. By doing so, any moving part has been omitted for improved reliability.

The CW to pulsed phase locking system

To cancel out any possible residual slow phase drift between the OMO and the Linac accelerating voltage, a slow phase-lock system is foreseen lo have the 3GHz of the Linac tracking any residual OMO slow phase drift.

DAY-ZERO PHASE REFERENCE

The FERMI@elettra commissioning started back in August 2009; an in-house optical CW phase reference distribution system has been designed and installed.

The in-house CW system

The in-house CW phase reference system is based on COTS components [20] with excellent jitter performance. The FO transmitter (based on a DFB laser) modulates its optical carrier at 1550nm with the RF signal. The FO receiver extracts the modulation and converts the optical signal into and electrical one. Thanks to the transmitter power and the low attenuation of the links, the transmitter output is optically split 1-to-4, feeding up to four links. Two Miteq DFB lasers are housed in a single transmitter unit (fig. 4) which can drive up to 8 optical links.

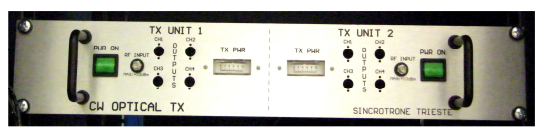

Figure 4: the in-house CW dual optical transmitter unit.

The receiver unit is equipped with the Miteq receiver and an RF amplifier to match the RF output level.

The "Event" system

The bunch clock is distributed to the clients by the Event system, a VME commercial solution developed at Micro-Research Finland Oy [7].

The “event system” is based on:

- an optical fibre network with star configuration;
- a VME FPGA board, installed in the timing hutch (Event Generator, EVG, VME-EVG-230);
- a series of VME boards located atthe different clients (Event Receiver, EVR,VME-EVR-230RF
- a series of optical fan-out modules

The EVG receives the laser coincidence clock (78.895MHz) and the bunch clock (10-50 Hz) from the

Master time base. The series of EVR boards connected to the EVG through VME optical fan-outs, distribute the trigger with different optical (HFBR-1414/HFBR-1528) and electrical (TTL/NIM/LVPECL) levels. According to the specifications, a jitter of ~20ps$_{RMS}$ has been measured for a TTL output signal at the EVR on a remote station.

The Master time base

The Master time base (MTB) generates the bunch clock (10Hz) and the laser coincidence clock (78MHz); both pre-bunch and post-bunch clocks are available.

The actual version of the Master time base is based on two evaluation boards: the AD9516EVAL from Analog Devices (synchronous division of the RMO frequency) and the XUP VIRTEX II PRO Development System to accomplish the bunch clock generation, the synchronization with the mains (220V AC) voltage zero-crossing and the communication link to the Timing system Computer.

The bunch clock parameters (repetition rate, pulse width and delay between pre-bunch and post-bunch) may be changed. The remote control the Master time base is implemented using the FPGA registers and RS-232. The FPGA circuits are synchronous with the input frequency to keep the jitter as low as possible.

The Master time base outputs interface to coaxial cables by means of fan-out buffer modules; TTL level signals are generated with additional LVDS buffers soon being provided.

FERMI OPTICAL CABLING

The optical fibres adopted by the FERMI timing system have been chosen to fulfil the following requirements:

- optical quality
- mechanical stability
- ease of installation and maintenance

The blown fibre solution has been adopted.

The Sirocco blown fibre system

The Prysmian Sirocco "blown fibre" system [21] has been identified as suitable for FERMI as it allows for improved flexibility, both in terms of maintenance and upgradability. These are key issues for a 24 hour / 7 days user facility. The optical fibres are compliant with the ITU-T G652.D telecom standard [22]. The fibres have been optically tested [23], paying special attention to the polarization mode dispersion (PMD), which may be an issue on long time scales where drift effects dominates the performance.

Each timing system client is served by an 8 single mode fibre bundle.

The installation of the FERMI fibre cabling

Two batches have been identified to lay down the optical fibres throughout the whole facility. The blowing fibre system is well suited to the FERMI progressive installation. All the fibres are laid down in the machine tunnel to exploit its temperature stability.

MEASUREMENT RESULTS

The FERMI timing system started its operation in July 2009; by then, the photo-injector and the first two accelerating sections were first put into operation. The phase reference was provided to the photo-injector laser and to K1 and K2 klystrons. The RMO, the master time base and the Event system were running. The measured RMO phase noise (fig. 5) has been measured to be less than 12fs$_{RMS}$.

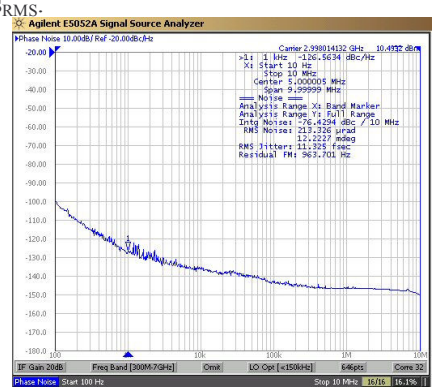

Figure 5: phase noise of the RMO measured in the 100Hz 10MHz offset frequency bandwidth.

As in the July 09 time frame, the pulsed optical phase reference system was under delivery, the phase reference has been temporarily routed to the laser by means of a phase stable coaxial cable instead. Thanks to the short distance between the laser and the timing hutch and to the good internal temperature stability of the building, also considering the jitter and drift specification of the photo-injector laser (≈100fs$_{RMS}$), this solution proved to be adequate for the first commissioning runs.

The first batch of fibre cables have been routed in 2009, the second batch being scheduled for May 2010.

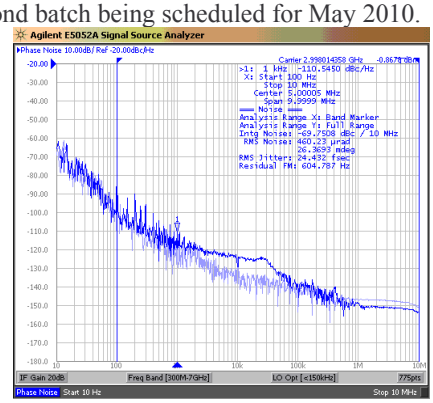

Figure 6: OMO locked (dark trace) to the RMO (light trace): phase noise profiles.

The installation of the pulsed phase reference system started also in July 2009. In figure 6, the measured phase noise of the OMO, when locked to the RMO using the BOM-PD, is presented. By the end of the year the stabilized link prototype has been installed as well.

Recently, the commissioning of the engineered link stabilization units has also started; the installation of the first three links (dedicated to the photo-injector laser, the

laser heater and bunch compressor BAMs) is scheduled for June 2010. Preliminary measurements of the out-of-loop (OOL) drift between a stabilized link and an output port of the splitter gave 8.6fs$_{RMS}$ jitter over 80 hours.

The in-house developed CW phase reference system has been on-line through commissioning runs 1 and 2 to feed up to four RF plants. The jitter of the 3GHz phase reference signal as delivered in the klystron gallery, including a low noise RF amplifier, has been measured to be 18fs$_{RMS}$ (fig. 7). Given the RMO phase noise (12fs$_{RMS}$) the contribution of the CW link is equal to 13fs$_{RMS}$.

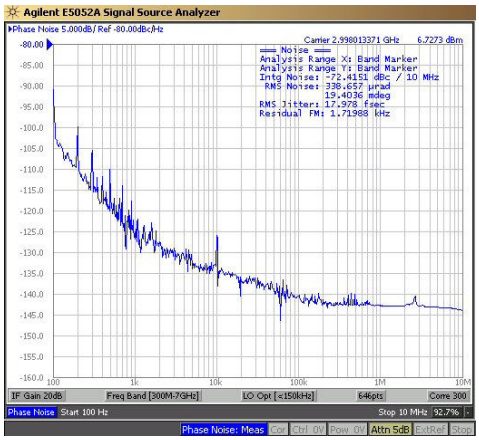

Figure 7: jitter measured on the 3GHZ phase reference signal at the end of the CW in-house link in klystron gallery by the RF plant K2.

A series of EVR boards have been used to drive the RF pulse for the klystrons; other EVR boards are used to trigger the BPM system, the Current Monitors, the Multi Screen, the bunch length monitor, the laser diagnostics and the Machine Protection system.

Polarization issues

Slow polarization fluctuations in the fibres show up as amplitude variations in the extracted optical pulses at the remote end, possibly causing unwanted drifts of the synchronized client. A State of Polarization (SOP) measurement set-up has been implemented on one FERMI fibre bundle. Polarization values have been logged over 96 hours, showing a peak-to-peak variation of ±2degree of the vectors on the Poincare' Sphere.

To cure the polarization issue, a polarization locker could be adopted. A polarization locker, by Thorlabs, has been tested in-field on a link fed by optical pulses at 157MHz. The polarization locker reduces by a factor of 10 the polarization fluctuations, whose effects on a phase locked client are now being quantified.

Temperature monitoring

The temperature of the timing hutch is kept constant at 22±0.2^{o}C; the temperature of the machine tunnel (first section, L=70m) has been measured to be constant at the same level over 4 months, a fundamental ingredient to the overall machine stability.

ACKNOWLEDGMENTS

The Authors wish to thank all the Colleagues at Sincrotrone Trieste who helped us in setting up the whole system, especially: R. Marizza, F. Debiasi, D. Baron, M. Miculin, I. Cudin and S. Noe'.

REFERENCES

[1] E. Allaria et al. "FERMI@Elettra: a seeded FEL facility for EUV and soft x-rays" FEL 2006, Berlin
[2] FERMI@Elettra Conceptual Design Report 2007
[3] RLE, Optics and Quantum Electronics Group; http://www.rle.mit.edu/oqe
[4] CBP, Electro-dynamics group, http://cbp.lbl.gov
[5] A.Winter et al "Layout of the Optical Synchronization system for FLASH", EPAC '06, Edinburgh, Scotland.
[6] EUROFEL FP6, http://www.eurofel.de
[7] Micro Research Finland Oy, http://www.mrf.fi/
[8] INWAVE gmbh, http://www.inwave-gmbh.de/
[9] J. Kim et al. "Drift-free femtosecond timing synchronization of remote optical and microwave sources", Nature Photonics 2, 733 - 736 (2008).
[10] F. Loehl, "Optical Synchronization of a Free Electron Laser with femto-second precision", Ph.D. Thesis at Hamburg University, 2009
[11] P. Craievich: FERMI Physics Requirement Document FPRD #005 "FERMI LInac Stability Requirements for the MLB mode"
[12] M. Ferianis "State of the Art in High-Stability Timing, Phase Reference Distribution and Synchronization Systems", PAC '09 Vancouver, Canada
[13] A. Winter et al. , "High-precision Laser Master Oscillators for Optical Timing Distribution Systems in Future Light Sources", EPAC '06, Edinburgh.
[14] J. Kim et all, "A Balanced Optical-RF Phase Detector", CLEO 2006
[15] Menlosystems gmbh, http://www.menlosystems.com
[16] J. Kim et all, "Long-term femtosecond timing link stabilization using a single-crystal balanced cross correlator",Optics Letters,Vol.32,pp.1044-1046, 2007
[17] Leon Pavlovic et al., "Bunch Arrival Monitor at FERMI@Elettra", this conference
[18] J. M. Byrd, "Plans for precision RF controls for FERMI@elettra", PAC 07 Albuquerque, NM, USA
[19] J. M. Byrd et al., "Timing distribution in accelerators via stabilized optical fiber links" LINAC 2006 Knoxville, USA.
[20] p/n: LBL-50K3G Miteq, http://www.miteq.com/
[21] Sirocco Blown fibre system www.prysmian.com.
[22] ITU-T G.652: Characteristics of a single-mode optical fibre cable. http://www.itu.int/ITU-T/publications/recs.html
[23] A. Galtarossa "Relazione Tecnica alle misure di dispersione di Polarizzazione", Technical Note of the Photonics Group, Uni. Padua, http://peg.dei.unipd.it

SIGNAL DELAY MEASUREMENT METHOD FOR TIMING SYSTEMS

M. Bousonville*, GSI, Darmstadt, Germany
J. Rausch, Technische Universität Darmstadt, Germany

Abstract

In this paper, a method for measuring the absolute signal delays of active optical transmission lines will be presented. This measurement method is an essential part of the timing system for FAIR (Facility for Antiproton and Ion Research).

To prevent interference of the timing signals whose delays are to be measured with the measurement signal sequence, the latter is transmitted on a separate optical carrier in the same fibre. By using a wavelength selective mirror at the end of the transmission line, the optical measurement signals are reflected and led back to the measurement unit. The measurement sequence consists of a number of sinusoidal signals with different frequencies that are modulated one by one on the optical carrier. For each frequency a phase comparison of the outgoing and returning signal is performed. In the last step, the absolute delay is calculated from the obtained phase values by using an algorithm.

It will be shown that this method enables cost efficient delay measurements with an accuracy of better than 100 fs.

INTRODUCTION

Different methods are used to provide phase stable reference signals e.g. for cavity synchronisation. All methods deliver one or more reference signals [1-12], mostly sinusoidal clock signals, to several points of the facility. To transmit the reference signal, standard single mode fibres (SMFs) are used. The transmission process should add as little as possible disturbances, like noise and variation of the signal delay, to the reference signals. Noise leads to fast phase fluctuations (jitter) and the variation of the signal delay causes slow phase shifts (drift) [13]. Many timing systems measure the delay changes and compensate them with phase shifter or delay devices, either optical [6-9] or electrical [10-12]. A common basic principle [6-12] is sketched in Fig. 1. For observation of the delay changes, a phase comparison of the outgoing and returning signal is performed.

A disadvantage of this functional principle is the high attenuation (about 15 dB [6], page 14), having effect on both the part of the signal that reaches the receiver (*Rx*) and the part of the signal that is reflected. Caused by the high attenuation, the signal power fed to the receivers is lower than in an optimal case [1], page 5. This results in a lower signal-to-noise ratio (SNR) and thus in more phase jitter. On the one hand, this affects the phase stability of the transmitted reference signal, on the other hand the phase comparison is less precise. The latter leads to disturbances while compensating the delay change in the fibre. These disturbances cause delay correction errors and therefore additional phase instabilities.

A further disadvantage is the fact that the signal for detection of the delay changes and the reference signal have the same frequency. Since the accuracy of the phase measurement, by approximation, is not depending on the frequency used, an accurate reading of the delay changes is more easily achieved with a higher frequency than with a lower one. Normally the frequencies of the reference signals are specified by other boundary conditions. Therefore within the basic principle of Fig. 1 it is not possible to increase the frequency to get a better delay observation.

DWDM

Relatively low frequencies (between 100 kHz and 200 MHz) are used in the FAIR timing system. Therefore the idea arose to determine the delay by other means. Using the *dense wavelength division multiplex* (DWDM) method, it is possible to transmit both signals on different optical carriers of different wavelengths over a shared fibre. In this way the two clock signals and the measurement signal can be sent independently of one another (Fig. 2).

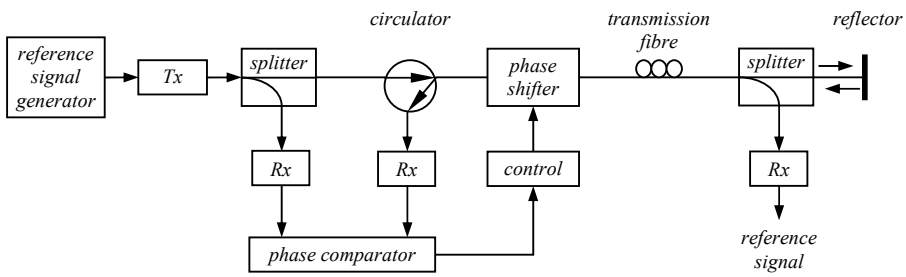

Figure 1: Basic principle of a frequently used timing system. High attenuation, reference signal = measurement signal.

*M.Bousonville@gsi.de

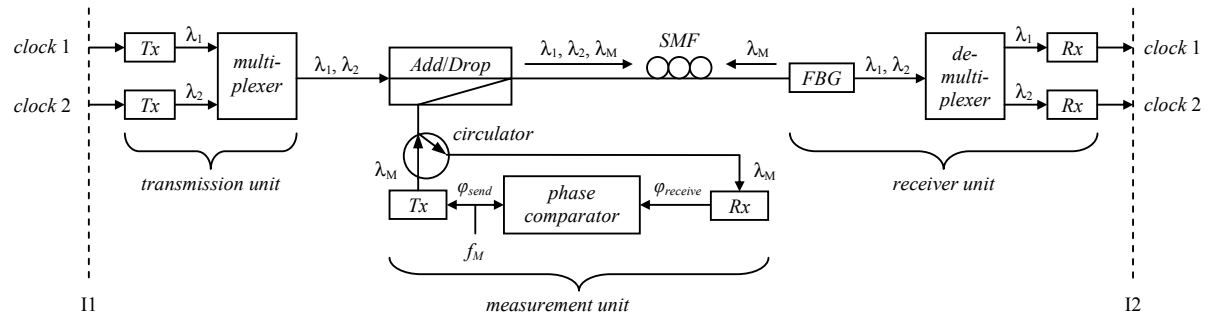

Figure 2: A single optical transmission branch of the FAIR timing system with DWDM: Two transmission channels and one separate measurement channel. Low attenuation, reference signal ≠ measurement signal.

The two clocks are optically multiplexed, i.e. they are modulated to two different optical wavelengths λ_1 and λ_2 in the transmitters (*Tx*) and combined into a single fibre in a multiplexer (Fig. 2). The two optical signals then pass through an add/drop multiplexer, the transmission line (SMF ≤ 1 km) and an FBG (fibre Bragg grating). In the demultiplexer, the wavelengths are separated again and fed to two separate receivers (*Rx*).

The delay changes on the transmission fibre are compensated in a next step in two other components called the Reference Generators [1-4]. Therefore the Reference Generators need information about the absolute clock signal delay. This is determined by the measurement unit and provided to the Reference Generators. The measurement signal for determining the delay is modulated to a third optical carrier λ_M. Via a circulator, the measurement signal is delivered to the add/drop multiplexer which combines the signals λ_1, λ_2 and λ_M. After passing through the SMF, all signals meet the FBG, which represents a wavelength-selective reflector that exclusively reflects λ_M while letting through the other two signals. The measurement signal now returns, is decoupled in the add/drop multiplexer and fed to the measurement receiver via the circulator.

In contrast to the conventional method in Fig. 1, the attenuation between the transmitter and the receiver in both the measurement channel and the transmission channel is less than 4 dB, instead of 15 dB.

MEASUREMENT METHOD

After creation of the basic conditions in Fig. 2, the following measurement method can be applied.

Step 1

In step 1, a sinusoidal oscillation with the frequency $f_{M,1}$ is modulated in the transmitter (*Tx*) to the optical wavelength λ_M (Fig. 2). After the signal had passed through the transmission fibre, it is reflected, runs back and is fed to the receiver of the measurement unit. In the receiver, the optical signal is converted to in an electrical signal and delivered to the phase comparator. A phase comparison of the outgoing and returning signal is performed. The delay is determined in step 1 with the measured phase difference $\Delta\varphi_{M,1}$ (Fig. 3) and the first value can be calculated

$$\tau_{M,1} = \frac{\Delta\varphi_{M,1}}{2 \cdot 360°} \cdot T_{M,1} \,. \tag{1}$$

It is mandatory that the period of the sinusoidal oscillation $T_{M,1}$ shows the following relation to the true value of delay τ

$$\frac{1}{f_{M,1}} = T_{M,1} > 2\tau \tag{2}$$

to achieve an unambiguous result. This first determination of the delay $\tau_{M,1}$ is relatively inaccurate. The accuracy of the delay determination depends on the period of the measurement frequency and on the precision of the phase comparator $\Delta\varphi_{accu,step}$. The following equation is valid for all 1 to N steps

$$\tau_{accu,step} = \frac{\Delta\varphi_{accu,step}}{2 \cdot 360°} \cdot T_{M,step} \,. \tag{3}$$

Step 2 to N

To improve the accuracy of the first delay determination, in step 2 a measurement signal 10 to 100 times higher in frequency is used and a second phase comparison is performed. Now the frequency is so high that inequality (2) is not fulfilled anymore. As a consequence, the delay determination becomes ambiguous (Fig. 4)

$$\tau_{M,step} = \underbrace{\frac{K_{step}}{2}}_{\substack{\text{indeter-}\\\text{minate}}} \cdot T_{M,step} + \frac{\Delta\varphi_{M,step}}{2 \cdot 360°} \cdot T_{M,step} \,, \tag{4}$$

if the integer factor K_2 is not known. But this factor can be determined by using $\tau_{M,1}$ from the first delay determination

$$K_{step} = \left\lfloor \frac{2\tau_{M,step-1}}{T_{M,step}} \right\rfloor, \tag{5}$$

so an unambiguousness result is achieved again. Since K_{step} is rounded down, the phase difference $\Delta\varphi_{M,step}$ must

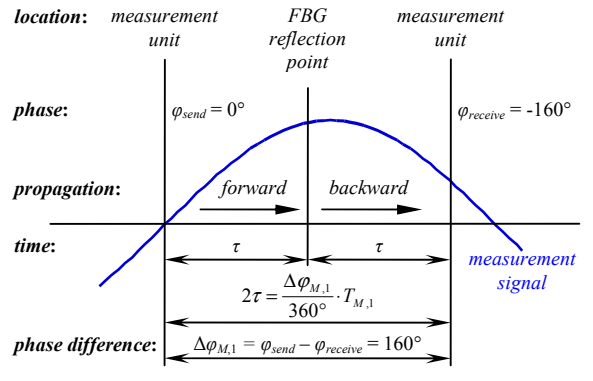

Figure 3: Signal delay measurement – Step 1.

be positive and this is always true when using the following definition† (see Fig. 2)

$$\Delta\varphi_{M,step} = (\varphi_{send} - \varphi_{receive}) \bmod 360°. \quad (6)$$

To prevent an incorrect determination of the factor K_{step} with Eq. (5), note that the error of the first measurement $\tau_{accu,1}$ needs to be significantly smaller than the period of the second measurement frequency. This is also valid for all further phase measurements

$$\tau_{accu,step-1} << T_{M,step} \quad (7)$$

In step 3, the next phase measurement with a still higher frequency is performed and the delay is determined again with Eq. (4) and (5). Thus, the accuracy is further improved according to Eq. (3). By approximation, it can be assumed that the phase measurement accuracy is independent of the frequency

$$\Delta\varphi_{accu,1} = \Delta\varphi_{accu,2} = \ldots = \Delta\varphi_{accu,N} = \Delta\varphi_{accu} \quad (8)$$

and therefore the accuracy of the delay determination is rising with the measurement frequency.

MEASUREMENT ACCURACY

In order to identify how precise the absolute delay can be measured, at first additive noise due to transmission will be considered and which effect it had on the accuracy. Afterwards the need of a permanent calibration of the measurement unit and finally the effect of the time base will be described.

Signal Quality

To generate the measurement signal and carry out the phase comparison, a network analyser is used. The network analyser passes the measurement signal to the transmitter and is fed with the returning signal via the receiver to perform the phase comparison (Fig. 2).

† Modulo definition : $a \bmod b := a - \left\lfloor \frac{a}{m} \right\rfloor m$

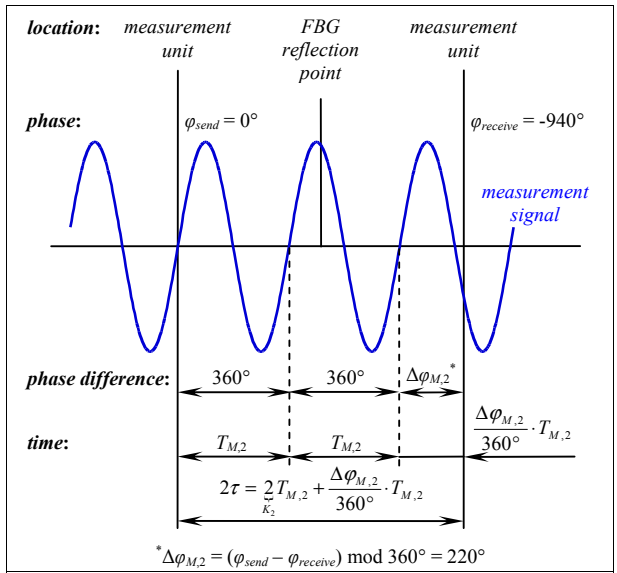

Figure 4: Signal delay measurement – Step 2.

The use of sinusoidal measurement signals pays off now. Thus the measurement bandwidth can be reduced to 10 Hz and this is how a large SNR of ≥ 90.6 dB‡ has been achieved in the prototype of the FAIR timing system [1], page 7. As a consequence, the phase jitter of the measurement signal is ≤ 0.0012° and therefore negligible compared with the measurement accuracy of the network analyser. The quality of the measurement signal transmission is so good that the accuracy of the measured phase difference $\Delta\varphi_{accu}$ only depends on the phase comparator in the measurement unit which is specified as < 0.4° in the prototype.

Principle of Permanent Calibration

The specification of measurement accuracy of < 0.4° is only valid within a short time frame after calibration§. So it is not sufficient to calibrate the measurement unit only once before operation, because a sustained continuous operation over months must be possible without decrease of the measurement accuracy. For that reason, a calibration routine for the operating system has been developed. Fig. 5 shows how in the FAIR timing system the measurement unit can be connected with all transmission branches and a mirror via an optical switch. This configuration enables a sequential measurement of all branches with only one measurement unit. Thus the costs are reduced significantly. Once per measurement cycle, for all frequencies the phase differences that occur upon reflection on the special mirror are measured. The mirror is placed nearby the optical switch (< 1 m) for calibration. Thus the measurement unit is fed with calibration data for correction of the measured phase differences during delay determination.

‡ For fibre lengths of L > 1 km, the dominant Rayleigh noise increases slightly (SNR ≥ 80 dB) [1], page 6.

§ The output value of the phase comparator depends e.g. on the temperature [6], page 46.

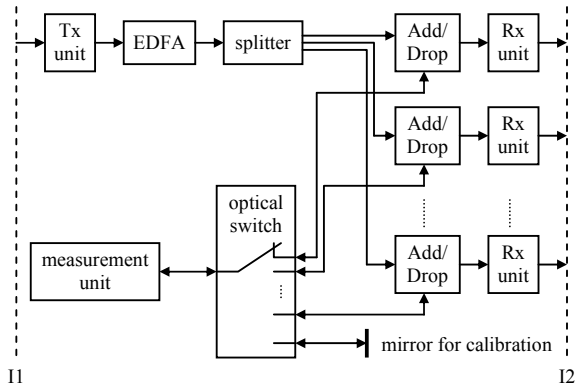

Figure 5: Permanent Calibration.

Not only the phase comparator, but the complete measurement unit is calibrated. This is in particular necessary because of the anticipated delay drifts of the optical transmitter and receiver caused by temperature changes [6, 10] as well as their generally not linear phase responses. From literature, no calibration method of this kind is known.

Absolute Measurement Accuracy

The absolute accuracy of the delay measurement depends, other than in Eq. (3), not only on the accuracy of the phase measurement $\Delta\varphi_{accu}$, but also on the deviation of the time base $(\Delta T/T)_M$

$$\tau_{accu,abs} = \frac{1}{f_{M,\max}} \frac{\Delta\varphi_{accu}}{2 \cdot 360°} + \underbrace{\frac{L \cdot N_g}{c}}_{\tau} \left(\frac{\Delta T}{T}\right)_M . \qquad (9)$$

This means for the prototype, with the following values $f_{M,\max}$ = 6 GHz, $\Delta\varphi_{accu} < 0.4°$, the fibre length L = 1 km, their group index N_g = 1.47, the speed of light c = $2.9979 \cdot 10^8$ m/s and $(\Delta T/T)_M = 5 \cdot 10^{-9}$ an absolute accuracy of $\tau_{accu,abs} < 117$ fs can be achieved.

Elimination of Time Base Deviation

The real purpose of the delay measurement is to determine the change of the phase at the end of the transmission line, enabling corrections in order to stabilize the overall transmission delay. When this is done without particular precautionary measures, another error occurs, caused by the deviation of the clock signal time base $(\Delta T/T)_{clock}$. The resulting relative accuracy

$$\tau_{accu,rel} = \frac{1}{f_{M,\max}} \frac{\Delta\varphi_{accu}}{2 \cdot 360°} + \frac{L \cdot N_g}{c} \left| \left(\frac{\Delta T}{T}\right)_M - \left(\frac{\Delta T}{T}\right)_{clock} \right| \qquad (10)$$

depends on the difference between the time base deviations. Since in the prototype both the measurement and clock signals are derived from the same time base, their time deviations are of the same magnitude

$$\left(\frac{\Delta T}{T}\right)_M = \left(\frac{\Delta T}{T}\right)_{clock} \qquad (11)$$

and thus, the second summand in Eq. (10) and therefore the error caused by the deviation of the time bases is cancelled out. As a consequence, the relevant relative delay measurement accuracy depends only on the precision of the phase comparator. Instead of Eq. (10), the following is valid

$$\tau_{accu} = \frac{1}{f_{M,\max}} \frac{\Delta\varphi_{accu}}{2 \cdot 360°} . \qquad (12)$$

With the parameters $\Delta\varphi_{accu} < 0.4°$ and $f_{M,\max}$ = 6 GHz, the delay measurement accuracy of the prototype amounts to $\tau_{accu} < 92.6\,fs$[**].

Dispersion

Owing to dispersion in the SMF, the delay in the measurement channel deviates from the delay in the transmission channel. With the known dispersion properties of the fibre, the delay deviation can easily be calculated[††] [2], page 113, and the delay in the transmission channels can be determined.

PRACTICAL MEASUREMENT

Now a practical example of the functionality of the measurement method will be presented. The delay in a transmission fibre with L = 1 km, N_g = 1.47 and c = $2.9979 \cdot 10^8$ m/s is about

$$\tau = \frac{L \cdot N_g}{c} \approx 4.9\mu s . \qquad (13)$$

According to Eq. (2), in the beginning the first measurement frequency $f_{M,1}$ must be < 100 kHz. Supposing that the accuracy of the phase comparison is $\Delta\varphi_{accu} < 0.4°$ and taking into account the condition in Eq. (7), the measurement frequency can be increased by a factor of << 1800 in each step. For experimental purpose, the 4 measurement frequencies in Tab. 1 have been chosen. After performing these 4 phase comparisons, from the phase differences $\Delta\varphi_{M,step}$ obtained with Eq. (6), the delay for each step is determined according to Eq. (4) and (5). The measurement period per transmission branch amounts to 1 s in the prototype.

Verification

As a first functional test to verify the measurement method, the delay $\tau_{M,4}$ is defined as the true value and the absolute deviation from $\tau_{M,step}$ is calculated. Tab. 1 shows that the measurement accuracy τ_{accu} calculated with Eq. (3) is maintained in each step.

Under to the same assumption that $\tau_{M,4}$ is the true value and using the deviations $|\tau_{M,step}-\tau_{M,4}|$, the phase comparison error $\Delta\varphi_{M,error,step}$ can be calculated. Tab. 1 shows

[**] This value is valid for the delay of the transmission line up to the FBG (Fig. 2). Delay changes in the receiver unit cannot be observed. Special measures must be taken for stabilisation of the delays in the receiver unit.

[††] The difference between λ_1 = 15551.721 nm and λ_M = 1548.515 nm is about 50 ps/km.

Table 1: Practical delay determination – specification of phase measurement accuracy: $\Delta\varphi_{accu} < 0.4°$.

step	$f_{M,\text{step}}$ [MHz]	$\Delta\varphi_{M,step}$ [°]	K_{step} [ ]	$\tau_{M,step}$ [ps]	$\lvert\tau_{M,step}-\tau_{M,4}\rvert$ [ps]	$\tau_{accu,step}$ [ps]	$\Delta\varphi_{M,error,step}$ [°]
1	0.05	175.98	0	4888333.333	277.778	11111.111	0.010
2	0.5	319.73	2	4888133.333	75.000	1111.111	0.027
3	50	289.98	244	4888055.000	2.472	11.111	0.089
4	5000	206.88	24440	4888057.467	:= 0	0.111	:= 0

that the phase comparison error stays below the specified value of $< 0.4°$ in each step as well.

These results led to the assumption that this measurement accuracy will also be achieved at the highest frequency. To examine this, a maximum frequency of $f_{M,\text{max}} = 6$ GHz has been used. Applying Eq. (12) the measurement accuracy is $\tau_{accu} < 92.6$ fs. By means of a test setup specifically developed for this problem, this value has been verified and confirmed [1], page 8.

SUMMARY

A measurement method for determination of the absolute delay in standard single mode fibres with an accuracy of better than 92.6 fs has been presented. This accuracy was verified in practice.

For each measuring, 4 sinusoidal signals are sent sequentially on a separate optical channel through the fibre. The phase difference is measured each time and from the results the delay is calculated. The measurement unit consists of standard components used in telecommunications as well as measurement technology. Essential reasons for the high measurement accuracy are:

a) The low attenuation due to the use of *dense wavelength division multiplex* (DWDM).
b) The principle of permanent calibration.
c) The use of sinusoidal measurement signals, whereby the measurement bandwidth can be reduced to 10 Hz, and the resulting large signal-to-noise ratios of SNR ≥ 90.6 dB.

By means of an optical switch, one single measurement unit is capable of measuring a multitude of transmission fibres. This reduces the overall costs significantly.

OUTLOOK

The accuracy can be improved further by the use of a higher maximum measurement frequency according to Eq. (12). Furthermore, the use of a network analyser prospectively enables the measurement of the transmission attenuation to detect damages on the fibres without additional expenditure.

REFERENCES

[1] M. Bousonville and J. Rausch „Universal Picosecond Timing System for the Facility for Antiproton and Ion Research", Physical Review Special Topics - Accelerators and Beams, Volume 12, Issue 4, 2009.

[2] M. Bousonville, Doctoral thesis, Technische Universität Darmstadt, Germany, 2009. http://tuprints.ulb.tu-darmstadt.de/1382

[3] M. Bousonville and P. Meissner „RF Reference Signal Distribution System for FAIR", Proceedings of the European Particle Accelerator Conference, Genua, 2008.

[4] M. Bousonville and J. Rausch „Reference Signal Generation with Direct Digital Synthesis for FAIR", 11th International Conference on Heavy Ion Accelerator Technology, Venedig, 2009.

[5] P. Moritz „BuTiS – Development of a Bunchphase Timing System", GSI Scientific Report, 2006.

[6] K. Czuba et al. „First Generation of Optical Fiber Phase Reference Distribution System for TESLA", CARE-Report-2006-037-SRF, Technische Universität Warschau and DESY, 2006.

[7] K. Czuba and H.C. Weddig „Design considerations for the RF phase reference distribution system for X-ray FEL and TESLA", Proceedings SPIE 5484, 2004.

[8] J. Frisch et al. „The RF Reference Distribution and Timing System for the NLC", XX International LINAC Conference, Monterey, California, 2000.

[9] J. Frisch et al. „A high stability, low noise RF distribution system", Proceedings of the Particle Accelerator Conference, Chicago, 2001.

[10] F.R. Lenkszus and R.J. Laird „A Bunch Clock for the Advanced Photon Source", Proceedings of the Particle Accelerator Conference, 1997.

[11] E. Peschardt and J.P.H. Sladen „Phase Compensated Fiber-optic Links for the LEP RF Refernce Distribution", Proceedings of the Particle Accelerator Conference, Chicago, 1989.

[12] E. Peschardt et al. „Transmission of a stabilized RF phase reference over a monomode fibre optic link", Electronics Letters, Vol. 22, Issue 16, 1986.

[13] M. Bousonville und J. Rausch „Velocity of Signal Delay Changes in Fibre Optic Cables", Proceedings of the 9th European Workshop on Beam Diagnostics and Instrumentation for Particle Accelerators, Basel, 2009.

RELIABILITY TESTS OF THE LHC BEAM LOSS MONITORING FPGA FIRMWARE

C. F. Hajdu, B. Dehning, S. Jackson, C. Zamantzas, CERN, Geneva, Switzerland

Abstract

The LHC Beam Loss Monitoring (BLM) system is one of the most complex instrumentation systems deployed in the LHC. In addition to protecting the collider, the system also needs to provide a means of diagnosing machine faults and deliver a feedback of losses to the control room as well as to several systems for their setup and analysis. It has to transmit and process signals from almost 4'000 monitors, and has nearly 3 million configurable parameters.

In a system of such complexity, firmware reliability is a critical issue. The integrity of the signal chain of the LHC BLM system and its ability to correctly detect unwanted scenarios and thus provide the required protection level must be ensured. In order to analyze the reliability and functionality, an advanced verification environment has been developed to evaluate the performance and response of the FPGA-based data analysis firmware. This paper will report on the numerous tests that have been performed and on how the results are used to quantify the reliability of the system.

INTRODUCTION

The Beam Loss Monitoring system [1] is one of the most critical among the numerous systems installed for the protection of the LHC. It has to prevent quenches in the superconducting magnets and protect the machine components against damage. The system comprises nearly 4'000 detectors, ionisation chambers and secondary emission-based monitors, mounted onto the elements under supervision. The analogue output signal of the sensors is digitised by data acquisition cards [2], generally referred to as Current to Frequency Converter (CFC), installed in the tunnel. The data is then transmitted to the Threshold Comparators (TC) [3] via redundant broadband optical links. The TCs, installed in VME crates distributed in surface buildings around the LHC, collect and analyse the data. Their FPGA-based processing algorithm calculates integrals of the signals over different time windows, compares them to their respective abort thresholds and can trigger a beam abort as appropriate through the Combiner and Survey (CS) card installed in the same VME crate.

The integrity of the whole signal chain needs to be verified in order to ensure that the system provides the required level of protection. Firmware reliability in particular is a key issue. Due to the great complexity and sequential nature of the design, exhaustive testing – that is, verification by applying every possible sequence of input combinations to the design and checking its outputs – of the TC firmware is impractical [4]. Therefore, an effort has been made to lay the foundations of a comprehensive verification environment instead, implementing different approaches of verification, each of them focusing on different aspects of the system under test (see Fig. 1).

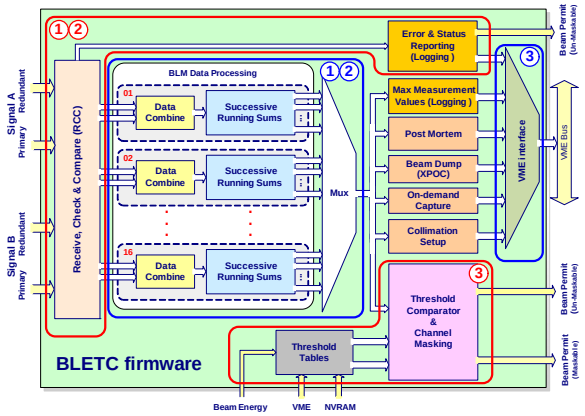

Figure 1: Block diagram showing the scope of the verification. Legend of the types of verification used: (1) Black box simulation, (2) Hardware-based approach, (3) Software-based approach.

Consequently, simulation testbenches, custom hardware and software suites have been designed and developed for the verification of critical blocks as well as to verify certain aspects of the behaviour of the installed system. The aim of this paper is to detail the implementation of these methods and the results obtained therewith.

SIMULATION

Functional simulation involves simulating the design description – in this case, in VHDL – to verify that the system meets the functional requirements stated in its

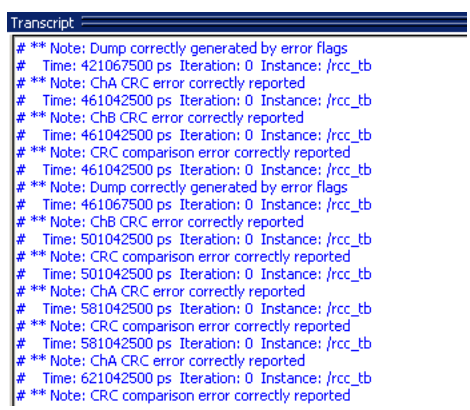

Figure 2: Excerpt of the output of the automatic checker for a test performed on the receiver part using ModelSim.

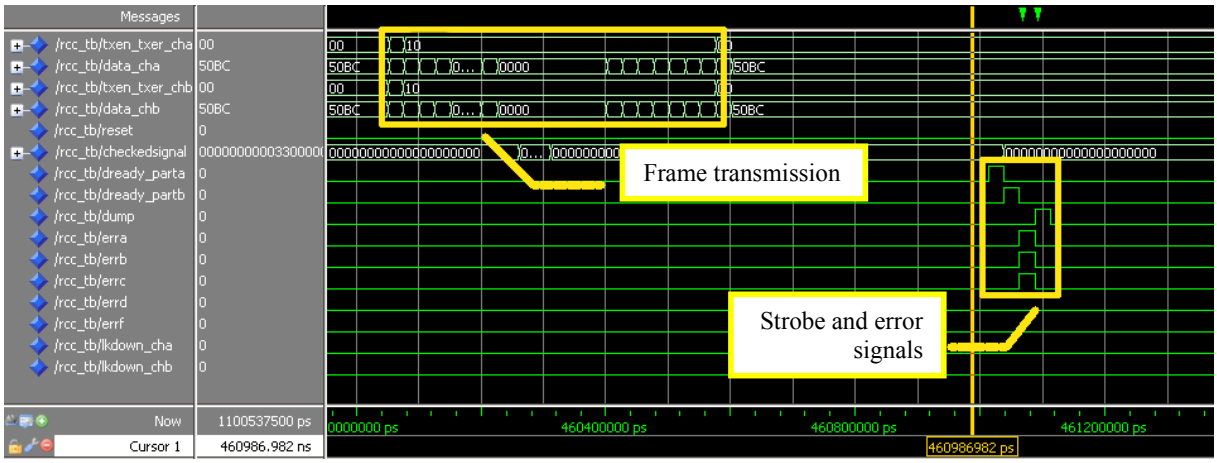

Figure 3: Example of the output waveform of the functional simulation performed on the receiver part using ModelSim.

specification. In order to carry out the functional simulation of the critical blocks of the Threshold Comparator firmware, several testbenches have been developed.

The development has been done following the rules of the "black box" methodology, that is, entirely based on the specification without any knowledge about the internal structure of the block. The testbench reads the stimulus to be passed to the Unit Under Test (UUT) from a text file and checks the outputs of the UUT versus the stimulus automatically. This facilitates regression testing: the testcases used for finding an error can very easily be re-executed for newer versions of the design, thus allowing to find out if it has regressed, that is, a previously fixed bug has reappeared. It also allows the comparison of the behaviour of different versions of the code by applying the same stimulus and comparing the outputs, thereby making it easier to detect new bugs.

The execution of the testbench was done in ModelSim. Sample outputs of the automatic checker and an output waveform can be seen in Fig. 2 and 3, respectively.

HARDWARE-BASED CHECK

In order to verify the quality of the deployed firmware and the behaviour of the Threshold Comparator card under real conditions, installed in the VME crate, a way to emulate the optical output signal of the CFC cards has been developed.

The hardware implementation of the Threshold Comparator consists of a standard VME-compatible FPGA carrier board [5], used throughout the Beam Instrumentation group at CERN, fitted with a mezzanine card [6] for the reception of the output signals of the CFC cards. Since every TC card receives signal from two CFC cards and the optical links are redundant, every TC mezzanine hosts four optical receivers.

For the purposes of this type of verification, a new mezzanine card and the corresponding custom FPGA firmware have been developed for the same FPGA carrier board (see Fig. 4). This mezzanine card hosts two Gigabit Optical Hybrid (GOH) transmitters [7], thus the setup allows the direct emulation of one CFC card. With the use of optical signal splitters, it is possible to increase the number of connections and drive several TC modules.

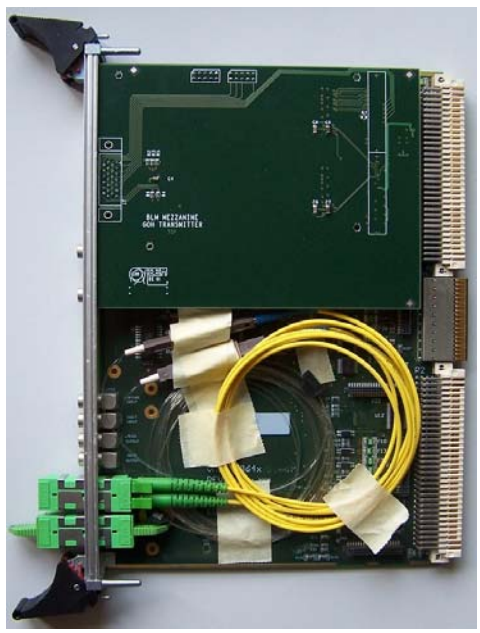

Figure 4: The VME64x carrier board with custom FPGA firmware and dual gigabit optical transmitter mezzanine developed to emulate the acquisition electronics.

This scheme makes it possible to emulate errors in the transmission or in the physical layer as well as to imitate wrong configurations. It allows the evaluation of the way the system handles the redundant data transmission and its response when any of the many self-checking mechanisms embedded in the transmission indicate a failure.

For example, single or multiple errors can be injected into the checksums, CFC card identity numbers, or frame sequence numbers being employed.

This setup also allows the transmission of arbitrary data to target the processing parts of the TC. The data can be either the direct output of the TC read back from a logging database, the contents of a TC internal circular buffer frozen after an event, or any imaginary loss scenario described in a text file and loaded into the VS internal memory. In that way, the verification environment can be used to compare the change of response between different versions of the firmware, or for quantifying the linearity of the internal data processing algorithms.

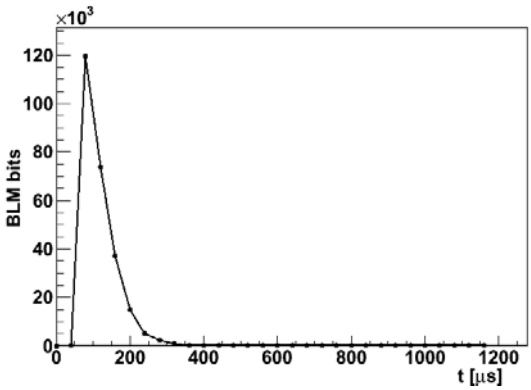

Figure 5: Recording of a single bunch loss in the LHC using the TC on-demand capture buffer. Each sample provides the integrated losses of the last 40 μs.

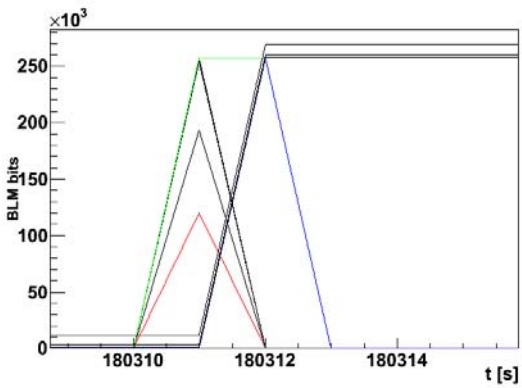

Figure 6: Time diagram of the response of the 12 integration histories as calculated by the TC following the VS transmission of the input stimulus shown in Fig. 5.

In addition, the playback of actual captured loss data from the LHC can provide valuable information to the physicists for the fine-tuning of the threshold values. For an example of data transmitted and the response of the system, see Fig. 5 and 6, respectively.

SOFTWARE-BASED CHECK

To make sure that the Threshold Comparator cards correctly decode the signals they receive and every one of them has the ability to request a beam abort whenever necessary, an exhaustive test of the block of the firmware comparing the measurements to predefined beam abort thresholds is required. This implies making all thresholds trigger a beam dump one by one. The 12 integrals of different lengths being calculated for each of the 16 detectors connected to one TC card at 32 beam energy levels correspond to 6'144 testcases per TC card, or 98'304 testcases for a VME crate of 16 TC cards.

In the VME crates hosting the TC cards and the CS card, a PowerPC-based CPU card, generally referred to as Front End Computer (FEC), is also part of the standard installation. Software processes running on its Linux-based LynxOS operating system have been developed to successively load purpose-made threshold maps into the memory of the TC card, thereby making one selected threshold trigger a beam abort, and check the results on both the TC and the CS cards. The flowchart of this process, called "Exhaustive Threshold Triggering", can be seen in Fig. 7.

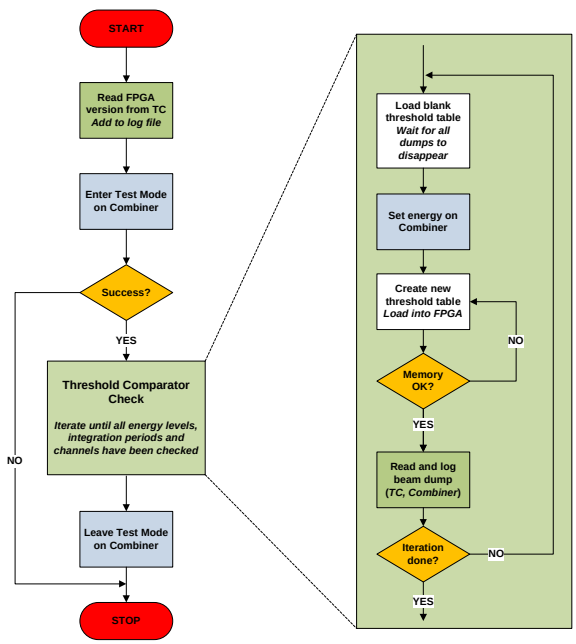

Figure 7: Simplified flowchart of the "Exhaustive Threshold Triggering" check executed on each TC module.

An iteration of the "Exhaustive Threshold Triggering" check on a single TC card requires about 12 hours to run and creates a log file with all executed testcases getting a "PASS" or "FAIL" grade.

During execution, the beam abort check also provides a robustness check of the highly critical non-volatile memory storing the threshold values and all other operational parameters by checking the contents of the memory against what was flashed. In case of mismatch, the flashing is repeated and the number of iterations required is saved into the log file.

During the development of the verification procedure, some doubts arose about the reliability of data transmissions over the VME interface. This led to the elaboration of a special test procedure which involved the

execution of the same read-write operation 500'000 times in succession. The results obtained were consistent for all iterations, which led to a greater confidence in the robustness of the implemented VME interface.

In addition to these tests, a script has been developed to read out the unique card identifiers stored on a chip on each TC and CFC card. These identifiers can be checked very easily versus any previous known state, thus replaced cards or changes in connectivity can be detected. The whole process requires a few minutes to execute and provides a quick check after a technical stop or an intervention to the system before the more elaborate Management of Critical Settings (MCS) procedure [8] can be executed.

CONCLUSIONS

Testing by the black box methodology has revealed some violations of specification, which resulted in an in-depth review of the block under test. A considerable part of the block has been rewritten, either to follow the specifications more closely or to enhance testability.

The verification tools have been developed in a modular structure that allows the implementation and inclusion of additional checks if further doubts arise for any part of the system.

It has been shown that the versatility achieved by using different methods to test the system accelerates the development of such a verification environment and also allows covering more cases by selective targeting.

As an additional advantage, many of the tools implemented have been re-used, with only small modifications, in the tedious commissioning phase of the complete system, in this case, tracking down non-conformities in the construction and electronic parts.

Finally, the verification suite provides the required additional safeguards and lays the foundations of a release protocol to be followed for future modifications of the reprogrammable parts of the mission critical BLM system.

REFERENCES

[1] B. Dehning, et al. "*The Beam Loss Monitoring System*", Chamonix 2004

[2] E. Effinger et al., "*The LHC Beam Loss Monitoring System's Data Acquisition Card*", 12th Workshop on Electronics for LHC and future Experiments (LECC 06), Valencia, Spain.

[3] C. Zamantzas et al., "*The LHC Beam Loss Monitoring System's Surface Building Installation*", 12th Workshop on Electronics for LHC and future Experiments (LECC 06), Valencia, Spain.

[4] Kenneth L. Short, "*VHDL for Engineers*", Prentice Hall, 2008, p. 254.

[5] Engineering Specification, "*VME64x Digital Acquisition Board for the LHC Trajectory and Closed Orbit System*", LHC Project Document No. LHC-BP-ES-0002, Version 1.1, 09-03-2004.

[6] Schematic files of the BLM Mezzanine Card (Rev. 3), *https://edms.cern.ch/document/493588/3*

[7] GOL Reference Manual (Preliminary), http://ab-div-bdi-bl-blm.web.cern.ch/ab-div-bdi-bl-blm/Electronics/GOH/gol_manual_v1.9.pdf

[8] C. Zamantzas et al., *"Configuration and Validation of the LHC Beam Loss Monitoring System"*, 9th European Workshop on Beam Diagnostics and Instrumentation for Particle Accelerators (DIPAC09), Basel, Switzerland.

RESULTS OF BACKGROUND SUBTRACTION TECHNIQUES ON THE SPALLATION NEUTRON SOURCE BEAM LOSS MONITORS*

J. Pogge, S. Zhukov, SNS ORNL, Oak Ridge, TN 37831, U.S.A.

Abstract

Recent improvements to the Spallation Neutron Source (SNS) beam loss monitor (BLM) designs have been made with the goal of significantly reducing background noise. This paper outlines this effort and analyzes the results. The significance of this noise reduction is the ability to use the BLM sensors [1], [2] distributed throughout the SNS accelerator as a method to monitor activation of components as well as monitor beam losses.

OVERVIEW

Any study of the effects and causes of system noise must contain some identification of the nature of the system noise and its sources. We will identify the sources of noise in the BLM circuits and show the results of reduction techniques used to mitigate these noise sources.

Identifying Noise Sources

The SNS BLM sensors are primarily high-gain transimpedence amplifiers that collect the change in charge when particles or energy are incident on the sensor. The effects of noise associated directly with components used in high-gain transimpedence amplifiers are actually surprisingly low. The largest source of noise is induced currents and Electro Motive Interference (EMI) [3] on the long cables from the sensors located in the LINAC tunnel and the data acquisition system located in the instrument galleries. The distance between the sensors and the front end amplifier is large typically on the order of 100 meters. External influences such as electrical and electromagnetic sources make up the majority of the background noise seen at the front end amplifier (Fig. 1).

Design Approach

Having sufficiently determined the noise associated with the measurements, the BLM amplifier was designed to mitigate the bulk of the system noise in the design:

- Ultra low noise input bias current Op Amps were used in the transimpedence amplifier stage. A classic large-series resistor is used to ensure the voltage gain was low while the current gain was sufficiently large for the signal range.
- A second amplifier stage identical to the signal stage is attached to a second cable terminated in the LINAC tunnel and routed in juxtaposition to the signal cable.
- The signal and background input transimpedence amplifiers and the subsequent background subtraction stage have a bandwidth at least 4x the desired system bandwidth to decrease any phase error or effects in the signal subtraction.
- Post background subtraction low-pass filter is available, selected through software, to further smooth any noise effects present on the subtracted signal.

The resulting signal can be adjusted to not only remove a significant amount of EMI noise present on the signal wire, but also allows removal of the induced radio frequency (RF) pulse present on the signal and the subtraction cable. The resulting signal is a closer representation to actual loss of beam present during LINAC operations. This data is fed directly to the integrators used for the SNS Machine Protection System (MPS) [4] with no error caused by excess induction of non-loss noise sources. Additionally, the loss signal is available for digitization and analysis. Loss spectrum has been an interesting study to determine if the source of the losses can be identified, as has a study of methods to determine actual activation levels by monitoring the growth of non noise-related signals during periods of no beam or RF.

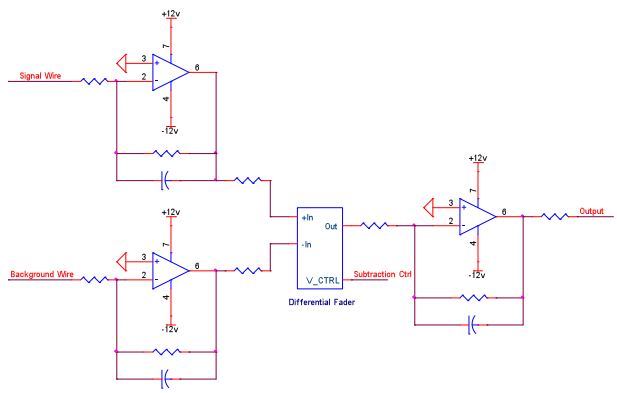

Figure 1: Front End Block diagram.

The new BLM amplifier module is a consolidation of four separate systems used on the current BLM design. This new circuit is a single-channel solution, including MPS, digital control and high-Voltage (HV) bias power supply. This new design helps to further reduce the noise associated with the Photo Multiplier Tube (PMT) and Ion Chamber BLM sensors by eliminating multiple sensors and allowing the digital, HV supply and amplifier to work

* ORNL/SNS is managed by UT-Battelle, LLC, for the U.S. Department of Energy under contract DE-AC05-00OR22725

in unison with small identifiable power sources and signal paths (Fig. 2).

INSITU RESULTS

A test was conducted using two BLM modules connected to a new Dual BLM sensor. This sensor has two separate PMT chambers, one sensitive to gamma/x-ray and neutrons, and the second sensitive to only gamma/x-ray losses. The purpose of this experiment is to use the new circuitry to subtract the neutron signals leaving only the neutron loss representing actual activation and loss. The RF pulses and resulting x-rays are removed from the analyzed signals. The results are checked using a much more expensive multi-channel analyzer (MCA) spectrum analyser, which would be cost prohibitive as a system solution. Data was taken with background subtraction enabled and disabled. Both sensors were placed downstream from the superconducting LINAC module 15, designated SCL:15c., in the SNS accelerator.

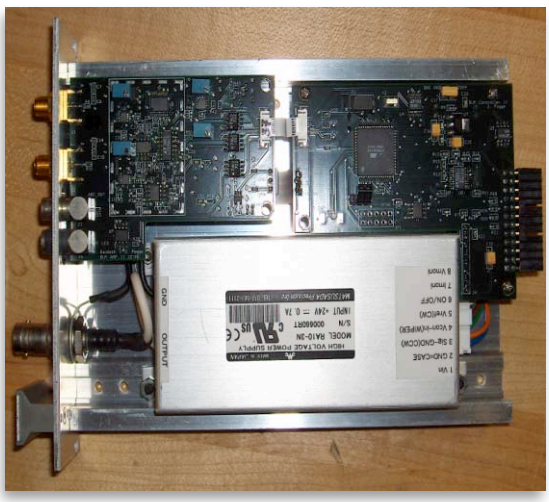

Figure 2: BLM module layout.

No Background Subtraction

Initially, data was taken with background subtraction disabled showing a signal similar to the original BLM amplifier. The pulse shown includes the RF signal represented by both x-rays incident on the PMT and a slight offset due to the induced RF currents on the BLM cable itself.

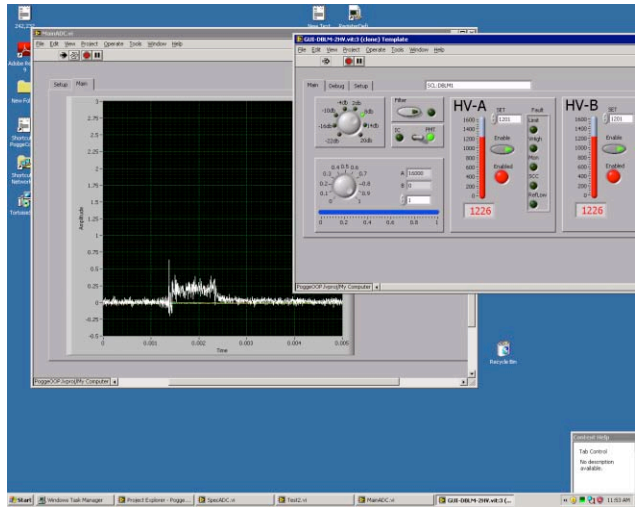

Figure 3: Background Subtraction disabled.

With Background Subtraction

Once background subtraction is enabled and adjusted the results are immediately visible. The resulting signal passed to both the data acquisition system and the MPS integrator sub-circuit. Figure 4 is a screen capture of background signals removed from the same BLM signal of interest.

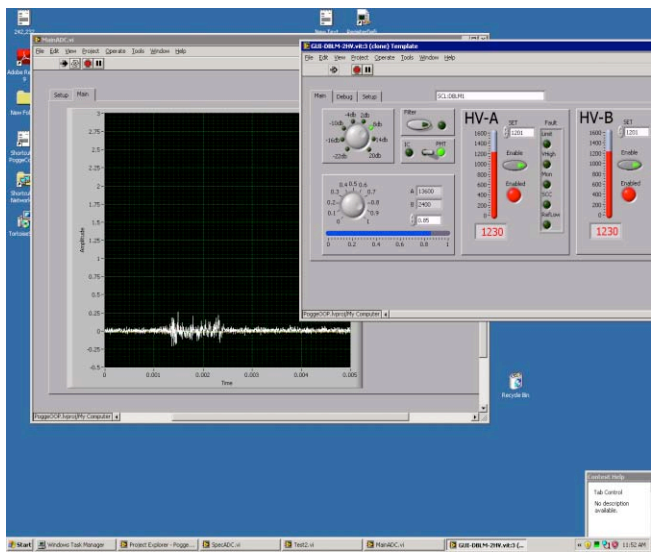

Figure 4: With background subtraction.

SPECTRUM ANALYSIS

The subtracted signal was then sent to an MCA spectrum analyzer in an attempt to identify the energy spectrum of the loss and, thus, the probable sources of the losses at the sensor location. Initially, the spectrum is as expected and the signals seen are promising for further processing and identification.

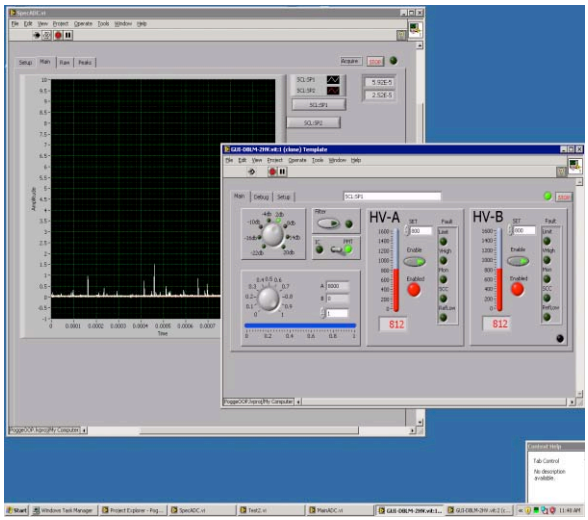

Figure 5: Background spectra.

It is clear that any residual noise in the system is negligible and the result of random signals on individual cables. The remaining noise is largely Gaussian white noise and is easily reduced by incorporating the internal low pass filters. Figure 5 was taken with the internal filters disabled.

As further proof that background subtraction is removing x-ray and noise signals that have little to do with actual losses, the HV power supplies servicing both PMT sensors present in the dual BLM are switched off. This leaves only signals not present on the PMTs themselves (Fig. 6). The resulting waveform is any induced RF or other EMI sources present on the four cables each > 100m from the LINAC tunnel to the system test rack located in the High-Energy Beta Transfer service building. Clearly the MCA has lost nearly all spurious peaks associated with random noise.

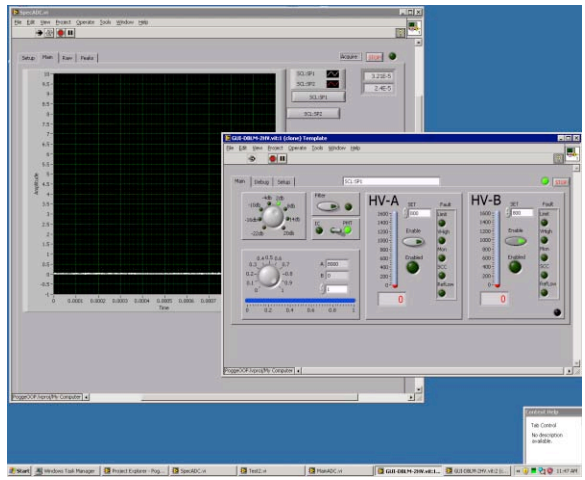

Figure 6: Background without HV.

CONCLUSIONS

The results of this test were dramatic; it has become clear that these systems will have the ability to monitor activation during accelerator downtime. Improved control and sensitivity allow the end user to easily adjust the MPS threshold levels to represent true loss levels. Additional new BLM systems will be deployed in areas where activation is probable and further studies are required. The new systems are also being deployed in areas that historically had been noisy and BLM data was used for only MPS.

REFERENCES

[1] Witkover, R. L. and Gassner, D., Design of an Improved Ion Chamber for the SNS, BIW2002, AIP Conf Proc 648 (2002) p. 337.

[2] Witkover, R. L. and Gassner, D., Preliminary Design of the SNS Beam Loss Monitoring System, BIW2002, AIP Conf Proc 648 (2002) .

[3] C. Sibley and D. Anderson, “SNS Noise Studies,” internal SNS document.

[4] C. Sibley, “Machine Protection Strategies for High Power Accelerators,” PAC03.

MODELING THE OPTICAL COUPLING EFFICIENCY OF THE LINAC COHERENT LIGHT SOURCE BEAM LOSS MONITOR RADIATOR*

J. C. Dooling, W. Berg, and B.X. Yang, ANL, Argonne, IL 60439, USA
M. Santana Leitner, A. S. Fisher, and H.-D. Nuhn, SLAC NAL, Menlo Park, CA 94025, USA

Abstract

A large-solid-angle, Cherenkov detector beam loss monitor has been built and tested as part of the Linac Coherent Light Source machine protection system (MPS). The MPS is used to protect the undulator magnets by detecting high-energy electron beam loss. These electrons produce other forms of radiation that can lead to demagnetization of the undulator magnets. Cherenkov light is generated when primary electrons, lost from the beam, create a shower of secondary electrons that transit through the Cherenkov radiator medium. The radiator consists of an Al-coated plate of high-purity, fused-silica 12.77 cm wide, 6.29 cm high, and 0.64 cm thick, which is formed into a tuning fork geometry that envelopes the beam pipe preceding each undulator. The radiator transports Cherenkov photons via internal reflection through a tapered region and stem into the photocathode of a compact photomultiplier tube (PMT).

We calculate the optical efficiency of the radiator η_c, that is, the probability that a photon generated within the fused silica will reach the exit aperture adjacent to the PMT. A simple model based on line sources summed across image planes is compared for the case of normally incident electrons with a more detailed Monte Carlo random-walk simulation called RIBO[1]. Both analytical and numerical models show the efficiency to be relatively uniform over the full range of transverse locations in the radiator. This is encouraging for the MPS detection scheme, which seeks to protect the undulator magnets over their entire cross section. As we expect, both analyses show η_c to be a strong function of the surface reflectivity R_f; η_c ~0.0084 for R_f=0.95, but drops to 0.0033 for R_f=0.90.

INTRODUCTION

High-energy electrons lost from third- or fourth-generation light source beams can lead to the generation of star events, which are strongly correlated with the demagnetization of undulator magnets[2]. Cherenkov radiation provides a natural method to observe beam loss from these machines[3]. Cherenkov radiators fabricated from high-purity, fused-silica have several desirable characteristics for detection of high-energy electrons. First, they can withstand high levels of radiation without darkening or suffering degraded transmission[4]; second, they offer immunity to scintillation noise from lower-energy x-ray photons; third, Cherenkov radiation is produced at optical wavelengths that can be detected with high-gain photomultiplier tubes (PMTs) providing low electrical noise signals.

The Linac Coherent Light Source (LCLS) beam loss monitor (BLM) diagnostic for the free-electron laser (FEL) undulators is composed of a fused-silica radiator encased in an anodized aluminum housing. The BLM is part of the LCLS machine protection system; as such, the radiator seeks to cover a broad area of transverse space or large solid angle to fully monitor beam loss into the FEL magnets. The radiator is roughly in the shape of a “tuning fork” or “Y” where the re-entrant cutout of the fork is occupied by the electron beam vacuum vessel. The BLM is integrated with the beam finder wire diagnostic located just upstream of each undulator magnet. A cross section of the BLM is presented in Figure 1. The large parallel surfaces (z-planes) of the radiator are polished to optical grade flatness; whereas, the x- and y-planes edge surfaces are flame polished. The entire radiator is coated with a reflective layer of aluminum; the exceptions being the exit aperture facing the PMT detector and two small circular areas in the stem, one of which is used to introduce a ``heartbeat'' optical pulse.

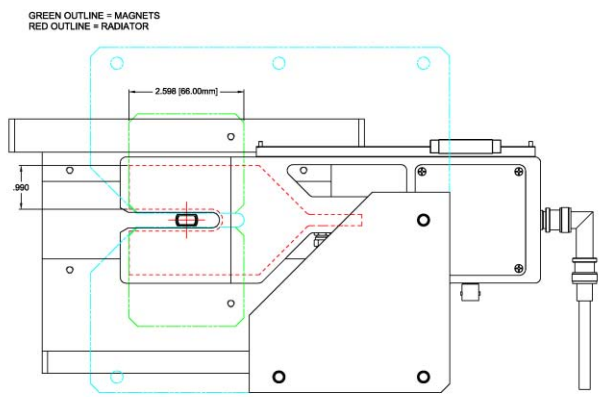

Figure 1: Cross sectional view of the beam loss monitor; view is looking upstream.

MODELING

The generation of photons from a super-luminal electron traversing a transparent medium of index of refraction n_r has been discussed in detail by a number of authors, for example[5,6].

*Work supported by the U.S. D.O.E. Office of Science, Office of Basic Energy Sciences, under contract numbers DE-AC02-06CH11357 and DE-AC02-76SF00515.

#dooling@aps.anl.gov

Analytic Image Line Source Approximation

A simple model based on normally incidence electrons is presented. We assume all electrons are energetic enough to completely traverse the radiator and remain above the minimum energy for Cherenkov light production; therefore, the path-length must exceed 0.64 cm, and the minimum energy may be determined from the Frank-Tamm formula[7],

$$dE=\frac{\mu(\omega)}{4\pi}e^2\omega\left[1-\frac{1}{n_r^2(\omega)\beta^2}\right]dx\,d\omega, \quad (1)$$

where ω is the angular frequency and μ(ω) and $n_r(\omega)$ are frequency-dependent permeability and index of refraction of the medium. The number of photons generated per electron over an incremental path length dx and frequency dω may be expressed as,

$$dN_p=\frac{dE}{\hbar\omega}=\frac{\alpha}{c}\mu_r(\omega)\left[1-\frac{1}{n_r^2(\omega)\beta^2}\right]dx\,d\omega, \quad (2)$$

where the fine structure constant $\alpha=e^2c\mu_o/2h$. We assume the material is non-magnetic at optical frequencies, therefore $\mu(\omega)=\mu_o$. Integrating over frequency, we obtain,

$$\frac{dN_p}{dx}=N_o(\omega_2,\omega_1)\left[1-\frac{1}{n_r^2\beta^2}\right], \quad (3)$$

where n_r represents the average refractive index over the frequency range and

$$N_o(\omega_2,\omega_1)=\frac{\alpha}{c}(\omega_2-\omega_1). \quad (4)$$

For ω in the optical range of frequencies defined by λ_1=600 nm and λ_2=150 nm,

$$N_o=2.35\text{x}10^3\,\frac{photons}{cm}. \quad (5)$$

The minimum energy for generation of Cherenkov radiation in the fused-silica radiator occurs when $v/c=\beta \geq n_r^{-1}$. At 400 nm, for example, n_r=1.47 and β_{min}=0.680, corresponding to a kinetic energy of 0.186 MeV. At this energy, the range of an electron in the radiator is short. The range may be expressed as,

$$t_r^{-1}=-\left[\frac{1}{\rho}\frac{dE}{dx}\right]\frac{\rho_{SiO_2}}{E}. \quad (6)$$

According to CSDA data for SiO_2[8], the mass stopping power in fused silica for a 0.2-MeV electron is 2.323 MeV-cm^2-g^{-1}; therefore, t_r=0.037 cm (ρ_{SiO2} =2.32 g/cm^3). The number of Cherenkov photons depends on the total path length and on electron kinetic energy as ln(kγ), where k is a constant. Thus, the number of photons initially grows rapidly with energy then effectively saturates as the path length exceeds the thickness of the radiator, d_r. The electron range exceeds the radiator thickness at kinetic energies of 2.4 MeV and above. For high-energy electrons (>4 MeV, β≈1), the index defines the opening angle of the Cherenkov cone, $\theta_c=\cos^{-1}(n_r^{-1})$ =47.1°.

The number of photons reaching the exit aperture from an incident electron located at a distance r_i may be expressed as,

$$N_{ap}=\sum_i^N S(r_i)\,T_{r_i}\,\delta A, \quad (7)$$

where δA is the area of the radiator exit aperture ($\delta A=d_r^2$) and $r_i=(x_i^2+y_i^2)^{1/2}$. The line source intensity is given by,

$$S(r_i)=\frac{N_o}{2\pi r_i}, \quad (8)$$

and the transmission function incorporating multiple reflections from the coated surface can be written as,

$$T_{r_i}=R_f^{n_{bi}}, \quad (9)$$

where R_f is the reflection coefficient of the aluminum coating, and n_{bi} is the number of bounces from the ith source or image. All image locations are determined in terms of the source position. The distance travelled by the photons from the electron source to the exit aperture will be lengthened by $\sec(\theta_c)=\beta n_r$. The actual distance travelled by the photons from one radiator face to another is the length of the hypotenuse, $l_h=d_r\sec(\theta_c)$ as shown in Figure 2. The horizontal distance covered in one bounce is $l_b=l_h\sin(\theta_c)=d_r\tan(\theta_c)$; if the line-of-sight distance from the source (or image) to the exit face is R_s, then the number of bounces can be calculated as $n_b=R_s/l_b$. The total distance a photon must travel from source to exit face is then $R_T=n_bl_h$. We then define the coupling efficiency as $\eta_c=N_{ap}/(N_od_r)$.

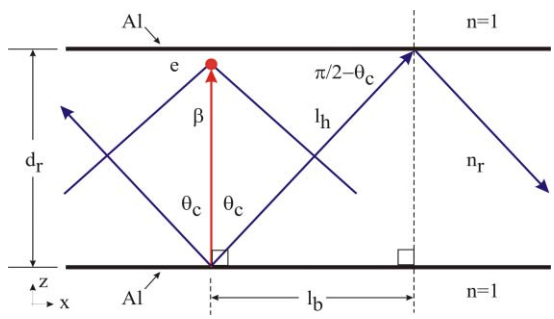

Figure 2: Radiator geometry with normally incident electron.

Looking at just the fork volume closest to the beam, the y-averaged coupling efficiency profile, η_{cx} is determined from the incident electron position and three additional image locations as indicated in Figure 3. Horizontal distance is measured from the radiator exit aperture. The y-averaged coupling efficiency η_{cx} is calculated for possible coating reflectivities of 0.85, 0.90, and 0.95 and plotted versus distance to the radiator aperture in Figure 4. Ideally, we want the response of the radiator to be as uniform as possible over the x-y region shared by the undulator magnets. Figure 5 presents the y-averaged η_{cx} assuming a 3-image model normalized by the average coupling efficiency over the range of x, $\langle\eta_{cx}\rangle$; that is, $\rho=\eta_{cx}/\langle\eta_{cx}\rangle$. Uniformity is seen to improve with higher coating reflectivities. The mean coupling efficiency values in the tuning fork regions seen in Figs. 4 and 5 are presented in Table 1. The distribution of coupling

efficiency predicted by the image model is presented in Figure 6.

Table 1: Mean Radiator η_c in the Tuning Fork

R_f	η_c
0.95	8.4×10^{-3}
0.9	3.3×10^{-3}
0.85	1.4×10^{-3}

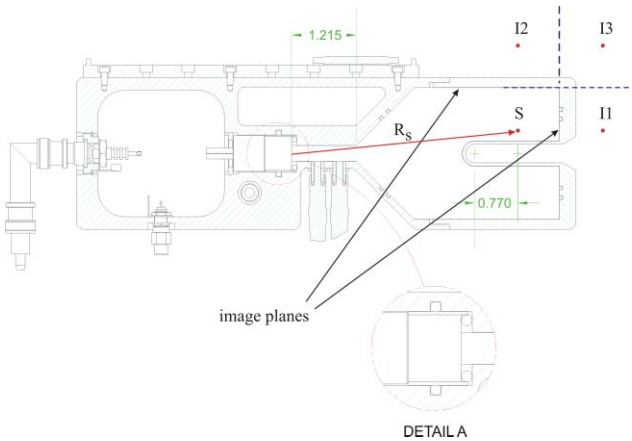

Figure 3: Incident electron position (S) and 3 image locations (I1-I3) in the BLM radiator. View is looking downstream.

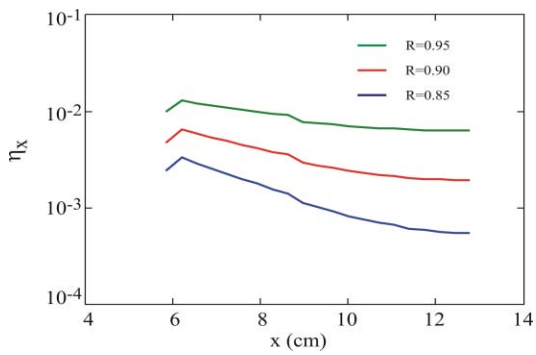

Figure 4: Y-averaged η vs. horizontal distance from the radiator exit aperture for R_f=0.85, 0.90, and 0.95.

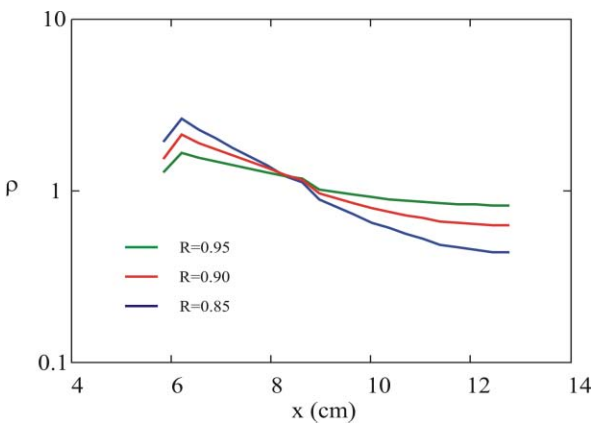

Figure 5: Ratio of y-averaged η normalized to its own mean value vs. horizontal distance from the radiator exit aperture for R_f=0.85, 0.90, and 0.95.

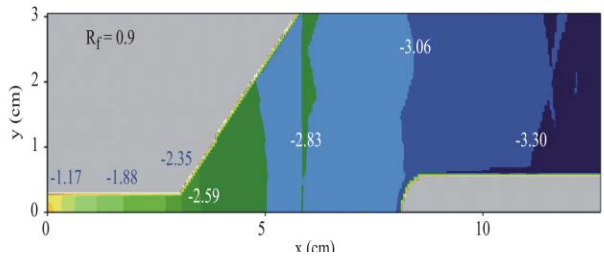

Figure 6: Coupling efficiency distribution in the radiator predicted by the image model for R_f=0.9 ($\log_{10}$ scale).

Monte Carlo Simulation of the Optical Coupling using the RIBO Code

Not only did the previous analytic model advance which coupling efficiencies can be expected from these BLMs, but also it will be instrumental to validate the applicability of the random-walk RIBO[1] simulation code, typically used for low-energy ion-transport problems but also capable to track photons. In future studies, this 3D Monte Carlo program will be used in conjunction with intranuclear cascade codes (i.e., FLUKA, MARS15[9]) to estimate the signals in the LCLS BLMs from showers generated and propagated along the radiation-sensitive undulator.

For this first-order study of the optical coupling of LCLS BLMs, electrons were assumed to hit perpendicularly against the front face of the quartz. This scenario represents the higher energy electrons, which are those with greater Cherenkov yield (N_p), as shown in Eq. 2. Photons were generated with uniform azimuthal angle at θ_c=47° from the normal. The birth coordinates of the photons were sampled within the full BLM so as to study the optical coupling as a function of the electron impact position at any point.

In this model, photons moved in straight paths between any two consecutive (elastic) collisions with the aluminum coating. The RIBO printing function was customized to dump, for every photon, its initial coordinates, the number of collisions with the coating walls from birth till collection in the photocathode, and the corresponding flight path through the quartz. With these data, for a given reflection coefficient, the "intensity" of any out-coming photon can be computed by using Eq. 9. Moreover, for detailed calculations with real showers, the individual flight path could be used to compute the attenuation of photons through the radiator material, although this factor is mostly negligible in quartz for Cherenkov light.

Computations were parallelized in the SLAC UNIX farm, where they ran as fast as 100 histories/s-CPU. Individual events were post-processed to sort them into 3.2 x 2.0 mm^2 pixels. The resulting efficiency maps were formatted like FLUKA[10, 11] USRBIN files, so that the FLAIR[12] GNUPLOT interface could be used to plot the data. Those are shown in Figure 7a-c for three reflection coefficients, R_f=0.95, 0.90 and 0.85, respectively. Fig. 7d

shows the R_f=0.90 case when the Cherenkov angle is 9% larger.

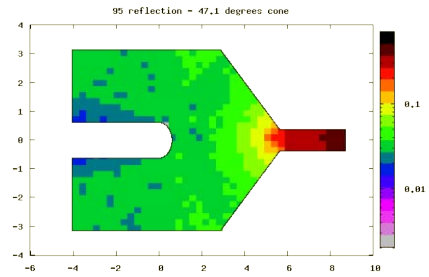

Figure 7a: θ_c=47.1°, R_f=0.95.

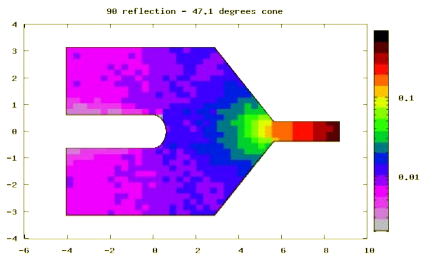

Figure 7b: θ_c=47.1°, R_f=0.90.

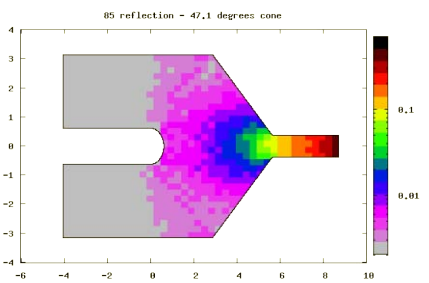

Figure 7c: θ_c=47.1°, R_f=0.85.

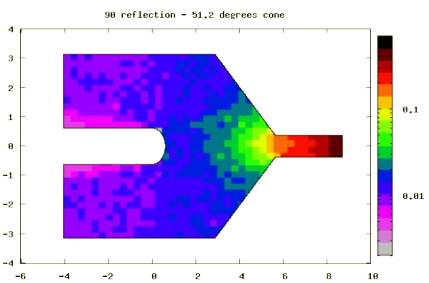

Figure 7d: θ_c=51.2°, R_f=0.90.

We observe consistency between the Monte Carlo results of Fig. 7 and the analytical curves of Fig. 4. This will allow performing more complex studies (i.e., BLM geometry optimization, realistic beam loss transport) with confidence in RIBO simulation results.

BEAM LOSS MEASUREMENT AND SIMULATION

Initially, five BLMs have been installed in the LCLS, on girders 1, 9, 17, 25, and 33; the full complement of 33 BLMs, one for each girder, will be installed this summer. During restart of the facility in April, a set of loss measurements were conducted with the beam finder wire (BFW) system. The BFW tests are used to verify BLM operation and obtain indications of beam position offsets and size in both horizontal (x) and vertical (y) planes. The LCLS undulator region has been modeled with the Monte-Carlo particle tracking codes MARS[13] and FLUKA to facilitate calibration of the BLMs. Beam loss electron fluence in the radiators is examined simultaneously with radiation deposition in the undulator magnets. For computational efficiency, we run the LCLS MARS model assuming a single loss point (for example, BFW01) and score electron fluences in all 33 radiators along the 132-m length of the undulator section. The BFW survey on the other hand, will use multiple loss points and then monitor the signal at a fixed BLM location, such as girder 33. Aside from the undulators, beam optics in the FEL section is that of a simple FODO lattice, which, with proper matching upstream, provides beam envelopes with modest betatron oscillations in both planes. Quadrupole focusing in the FEL is included in the Monte Carlo models. Because of the regularity in the beam in the FEL, we can compare the single point loss, multiple detector simulations with the multiple position loss, single detector profile by flipping the direction of the z-axis in the simulation case and then overlaying the result on the BFW/BLM measurements. This allows us a rough idea of how well the measurement and simulation agree. A comparison of measurement and simulation results using this method is presented in Figure 8. In the simulation, an average coupling efficiency of 1.4×10^{-3} is employed representing a reflectivity of 85%. We note that BFW data is not present from girders 9, 10, 11, 32, and 33 in x and girders 1, 8, 23, and 33 in y. Missing data in the simulation represents radiators that scored no events. The main burst of electron fluence occurs within the first 14 girders of the loss point; this is seen in both measurement and simulation.

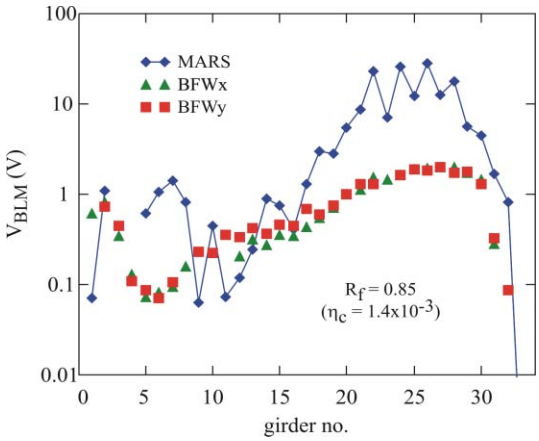

Figure 8: Comparison of BFW BLM loss measurements (single detector, multiple loss points) with MARS (multiple detectors, single loss point at BFW01).

DISCUSSION AND CONCLUSION

The curved surface of the cut-out acts as a defocusing cylindrical mirror; this and the wedge make the geometry difficult to model realistically with line sources. Note that the radiator region in the fork, closest to the vacuum chamber, is blocked from direct view of the exit aperture by the cut-out. This effect is seen in both models. In the line image model, conditions on the images are applied depending on the source position in x. In the simplified line-image model, effects such as diffraction around edges have been ignored.

The rapid reduction in coupling efficiency with distance from the exit aperture has been qualitatively verified by measurements carried out on a BLM prototype at the ANL Advanced Photon Source (APS)[14]. In reality, not all electrons will be entering the radiator at normal incidence; therefore, the single-angle bounce model is insufficient, and numerical approximations must be used. Finally, the Cherenkov cone angle of photon propagation is the same as the condition for total internal reflection; therefore steps must be taken to prevent large reflection at the exit face aperture. These steps can include using optical grease or introducing a wedge at the output aperture.

Regarding comparison of measurement and simulation, we see a relatively poor agreement in the prediction of signal intensity; in order to match the peak predicted signals with measurements, $\eta \leq 2.4x10^{-4}$ is required, corresponding to a reflectivity of 75%. We believe this is too low and must look elsewhere for the discrepancy. For example, maximum output voltages from the BLM electronics might be exceeded in the high-radiation regions leading to saturation.

Though the simple, line-image model presented here is insufficient to accurately predict the coupling coefficient, it does provide a method to address important radiator characteristics, such as coupling uniformity. More precise Monte Carlo methods, such as RIBO, are necessary to examine the effect of arbitrary electron incidence angles and energies.

REFERENCES

1. M. Santana Leitner, *A Monte Carlo code to optimize the production of radioactive ion beams by the ISOL Technique*, Ph.D. Thesis, UPC-ETSEIB (2005), CERN-THESIS-2006-031, 311 p.
2. Y. Asano, T. Bizen, and X. Marechal, J. Synchrotron Rad. **16** (2009), 317-324.
3. G.F. Knoll, *Radiation Detection and Measurement*, Wiley, New York, 1989, p. 682.
4. J. Cohen-Tanugi, et al., Nuc. Instrum. Meth. A **515** (2003), 680-700.
5. J.V. Jelley, British Journal of Applied Physics, **6** (1955), 227-232.
6. J.D. Jackson, *Classical Electrodynamics*, Wiley, New York, 1975, p. 638.
7. I.E. Tamm and I.M. Frank, Dokl. Akad. Nauk USSR **14** (1937) 109.
8. International Commission on Radiation Units and Measurements. ICRU Report 37, *Stopping Powers for Electrons and Positrons*.
9. N. Mokhov and S. Striganov, "MARS 15 overview," Tech. Report Fermilab-Conf-07/008-AD, 2007.
10. G. Battistoni, S. Muraro, P.R. Sala, F. Cerutti, A. Ferrari, S. Roesler, A. Fasso, *The FLUKA code: Description and benchmarking*, Proceedings of the Hadronic Shower Simulation Workshop 2006, Fermilab 6-8 September 2006, M. Albrow, R. Raja, eds., AIP Conference Proceeding 896, 31-49, (2007).
11. A. Fasso, A. Ferrari, J. Ranft and P.R. Sala, CERN-2005-10 (2005), INFN/TC_05/11, SLAC-R-773.
12. V. Vlachoudis, *FLAIR: A Powerful But User Friendly Graphical Interface For FLUKA*, Proc. Int. Conf. on Mathematics, Computational Methods & Reactor Physics, (M and C 2009), Saratoga Springs, New York, 2009.
13. W. Berg et al., Proceedings of LINAC08, Victoria, BC, Canada, (2008) 493-494.
14. B.X. Yang, et al., these proceedings.

NEW ELECTRON BEAM DIAGNOSTICS IN THE FLASH DUMP LINE

N. Baboi*, D. Lipka, O. Hensler, R. Neumann, M. Schmitz, P. Smirnov, H. Tiessen, K. Wittenburg, DESY, Hamburg, Germany
A. Ignatenko#, DESY, Zeuthen, Germany

Abstract

Additional beam diagnostics has been installed in the dump line at FLASH in 2009. Its purpose is to prevent damage by long high current electron beam pulses, as happened in autumn 2008, when a vacuum leak occurred near the dump vacuum window. Beam position monitors (BPM), scintillator-based loss monitors and temperature sensors were installed so-far. Additional BPMs and loss monitors have meanwhile been installed. These include a magnetic coupled BPM placed after the vacuum window. Magnetic loops are used in order to prevent the influence of the ions on the pick-up signals. 4 ionization chambers, consisting of air-filled tubes, and 4 glass fibers have been installed parallel to the vacuum pipe, along the last 2 m of the beam pipe. Beam halo monitors were installed next to the magnetic BPM. These consist of 4 diamond and 4 sapphire sensors operating as solid state ionization chambers. The halo monitors are very sensitive to charged particles crossing the detectors. These additional diagnostic monitors have been commissioned in autumn 2009, when they have contributed to the successful run of long pulses with 3 to 9 mA current and up to 800 μs length. Their performance is summarized in this paper.

INTRODUCTION

FLASH (Free electron LASer in Hamburg) [1] is at the same time a user and a test facility. A laser light tuneable in the range 40 – 6.5 nm is produced for several user beam lines. During special studies periods, various experiments are scheduled, in order to make tests for various accelerator projects, in particular for the European XFEL (X-ray Free Electron Laser) [2] and the ILC [3] (International Linear Collider) study. These have similarities with FLASH, in particular the superconducting technology used for beam acceleration. Also, they all plan to use long bunch trains.

The long bunch trains at FLASH have to be safely sent into the dump at the end of the linac. Beam loss monitors (BLM) and charge monitors are primarily used for the machine protection. This paper shows the limitations of the dump diagnostics used so far, describes the modifications made and summarizes the results of the initial commissioning of the new devices.

The FLASH Facility

A schematic view of the FLASH linac is shown in Figure 1 as of September 2009. A photo-electric gun generates pulses of electron bunches with an energy of about 5 MeV. These are accelerated to up to 1 GeV by 6 accelerating cryo-modules, each containing 8 TESLA superconducting cavities. Two magnetic bunch compressors reduce the bunch length to less than 100 fs. A collimator section lowers the radiation losses in the undulators, by reducing the parasitic transported dark current. The beam properties are measured in two matching sections. While passing through the 30 m long undulators, the electron bunches produce FEL (Free Electron Laser) light through the SASE (Self-Amplified Spontaneous Emission) effect. The electrons are then sent to the beam dump, designed for about 100 kW power of a 2 GeV beam [4]. The FEL light goes to one of the user beam lines. A bypass line is used during test and commissioning periods in order to protect the undulators.

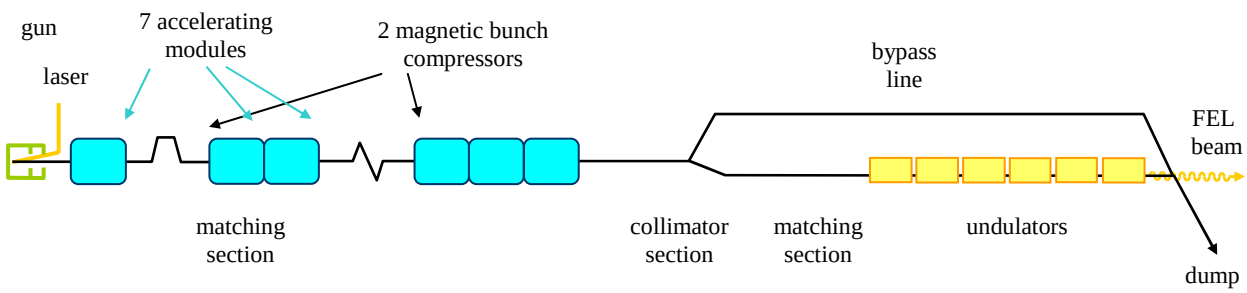

Figure 1 Schematic overview of FLASH (status 2009).

* nicoleta.baboi@desy.de
# On leave from NC PHEP BSU, Bogdanovich Str. 153, Minsk, Belarus

Requirements of the Beam Dump for FLASH

Long pulses with up to 800 bunches with a frequency of 100 kHz – 1 MHz and a charge of 1 nC per bunch are often required during user runs. Also some tests for the XFEL or the ILC require long pulses. Particularly demanding is the so-called 9 mA experiment, whose aim is to accelerate stably 800 µs pulses with 3 nC bunches and a repetition frequency of 3 MHz [5].

Typical FLASH parameters relevant for operation with long bunch trains are summarized in Table tab-flash.

Table tab-flash Typical FLASH parameters for user operation and for the 9 mA experiment (status 2009)

Parameter	Typical Values	9 mA run (goal)
Bunch charge	1 nC	3 nC
Bunch repetition frequency	0.1 – 1 MHz	3 MHz
Pulse repetition frequency	5 Hz	5 Hz
Max. pulse length	800 µs	800 µs
Energy	450 MeV – 1 GeV	max

Both the charge and the bunch repetition frequency are increased for 9 mA experiment with respect to the normal user operation, in order to approach the high beam current planned for the ILC.

FLASH Dump Line

The FLASH dump line – status Summer 2009 - is schematically shown in Figure 2. The electrons coming from the bypass and from the SASE undulators are directed towards the dump by one of two dipole magnets. Several corrector magnets and quadrupoles control the beam trajectory and size. An electrically modified sextupole magnet (rotator) distributes the beam in a circular manner on the dump and thus lowers the average power density impact. Several BPMs (beam position monitors) measure the beam position. A toroid reads the beam charge. An OTR (optical transition radiation) screen can be driven into the beam to check the beam size. BLMs (beam loss monitors) are distributed along the section. They are made of a scintillator material protected from light coming from the tunnel area. Their light is then transformed into a current by photomultipliers.

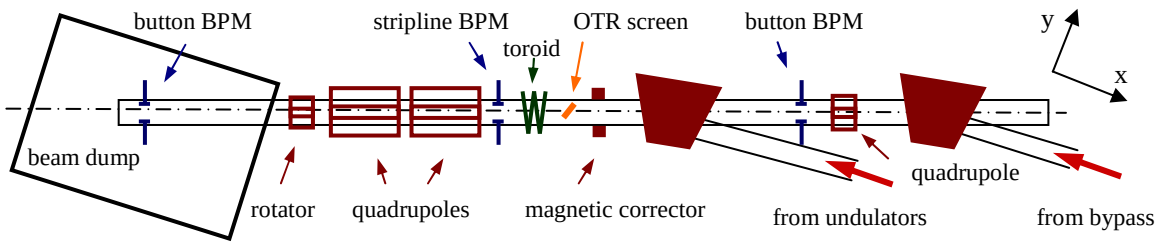

Figure 2 Schematic view of the dump beam-line at FLASH (status Summer 2009). The line has an angle to the horizontal of 19 deg. The beam comes from main beam-line or the bypass (right in this figure). Several BLM distributed along the line are not shown.

For runs with long pulses this existing diagnostics seemed to be sufficient. However in Autumn 2008, during a 9 mA experiment, a vacuum leak occurred near the window at the end of the beam pipe caused by a pulse with 550 bunches with a charge per bunch of 2.5 nC, a repetition frequency of 1 MHz and an energy of 890 MeV. Also the last BPM situated just in front of the vacuum window seemed to be damaged by radiation. This showed that the dump diagnostics system in the dump beam line has to be re-designed.

DUMP LINE MODIFICATIONS

Several new systems have been built and installed in FLASH in Summer 2009. Apart from a new button-type BPM installed between the quadrupoles, the modifications regard the last 2 m of beam line. This sections is shown in Figure 3. The button BPM previously placed just before the dump vacuum window (compare to Figure 2), has been moved upstream. Several pipes can be seen around the beam pipe: 4 of them host glass fibres together with Cerenkov fibres* and 4 larger ones are used to accommodate ionization chambers. After the vacuum window, a magnetic coupled BPM and a BHM (beam halo monitor) have been installed. The new systems were commissioned in September 2009, during the 2nd 9 mA run. They are described in this section.

* Not yet commissioned, therefore not described in this paper

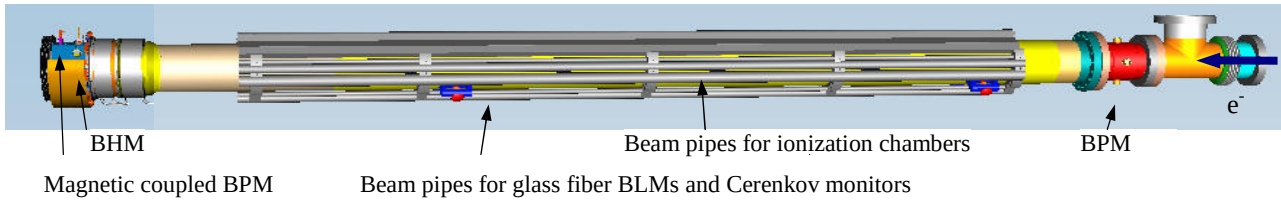

Figure 3 Drawing of the modified vacuum chamber after last magnet in Figure 2. The beam comes from the right.

Magnetic coupled BPM

A BPM has been added after the vacuum window, in an area filled with dry Nitrogen N_2. Since the signal of button-type pickups would be affected by ions produced by electrons in the gas, it was decided to use the magnetic field of the bunches for generating a position signal. For this, 4 wire loops have been designed, which are placed parallel to the beam for optimal coupling to the magnetic field of the charged particles only, as shown in Figure 4 [6].

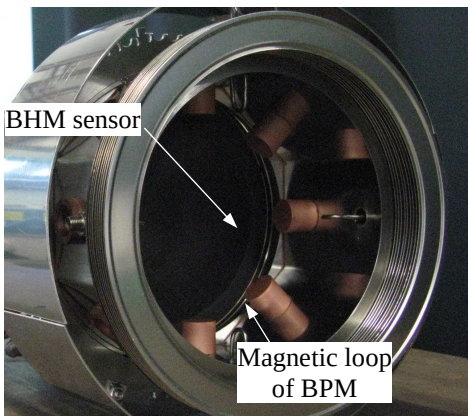

Figure 4 Beam pipe section after vacuum window, including magnetic coupled BPM and BHM.

The signal from each loop is low-pass filtered below 200 MHz to cut high frequency components of the compressed beam, as it is done for button BPMs in the other parts of FLASH. The processing electronics is based on the AM/PM principle [7].

The BPM signals have been analytically estimated and simulated with the CST code [8]. The signals from all pickups have been measured during the 9 mA run in September 2009. The comparison of one such signal to the simulation is shown in Figure 5. The agreement is good in the positive part of the signal. The differences in the negative part need more investigation.

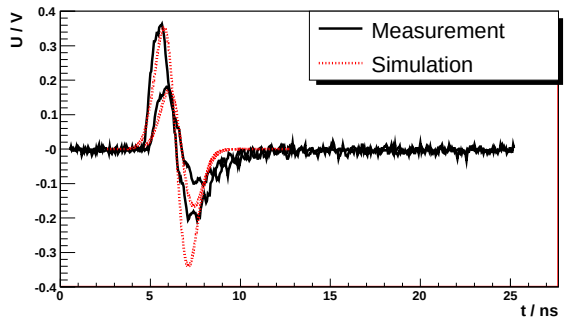

Figure 5 The signal voltage as a function of time from the vertical wires of the BPM. The amplitudes are corrected for the attenuation of the cables and low-pass filter.

Glass fibres

Along the last 2 m before the dump (see Figure 3), four BLMs consisting of glass fibres read out with photomultipliers have been installed around the pipe. These collect thus the beam losses which occur at each side of the beam pipe.

Ionization chambers

4 ionization chambers have also been placed along the last 2 m of beam pipe. These are air filled 3/8" Heliax HF cables. The ions created by the ionization radiation produced by beam losses are measured. The electronics has a large dynamic range, from 10^{-4} to 10^{4} µA.

Beam halo monitors (BHM)

The BHM consists of four 500 µm thick artificial mono-crystalline sapphire sensors and four 300 µm thick pCVD diamond sensors with an area of 12×12 mm^2 placed inside caps alternatively around the beam pipe, and next to the magnetic coupled BPM, as seen in Figure 4 [9]. These sensors operate like solid state ionization chambers. The sensors have to withstand high radiation doses.

In beam tests, the signals from the sensors have been seen to increase while the beam approached each sensor. The diamond sensors are more sensitive than the sapphires.

BEAM MEASUREMENTS

The new diagnostics systems described in the previous section have been commissioned during the 9 mA experiment in Autumn 2009. Figures 6-9 show 10 successive beam pulses as seen on various devices. The beam repetition frequency was 3 MHz, however only every 3rd was sampled by the ADCs for each device.

Figure 6 shows the bunch charge along each pulse, about 2.7 nC per bunch. There is a stronger charge variation at the beginning of the pulses which disappears towards the tail of the train. There are 200 bunches per pulse except for one pulse where the machine protection system has reduced the train.

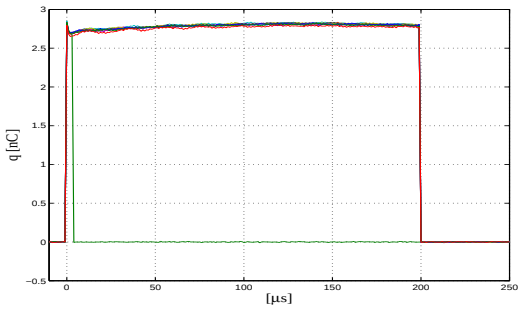

Figure 6 Bunch charge of 10 subsequent pulses.

Figure 7 shows that each of the 10 pulses had an offset from the beam-pipe axis of 2 to 5 mm in the horizontal direction and 4-5 mm in the vertical plane at the dump. Note that at the time of measuring, a slope calibration error may have been present.

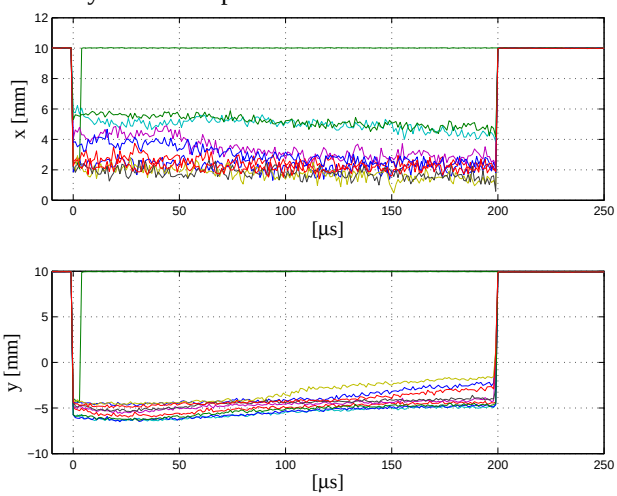

Figure 7 Bunch offset of 10 pulses, corresponding to Figure 6, as measured at the magnetic coupled BPM.

The ionizations chambers showed the signals from Figure 8. They measure integrated losses along the pulse, including losses from dark current which is transported along the linac. The signals are delayed with respect to the bunch arrival time due to the slow speed of the ions. The ionization chambers have a large dynamic range.

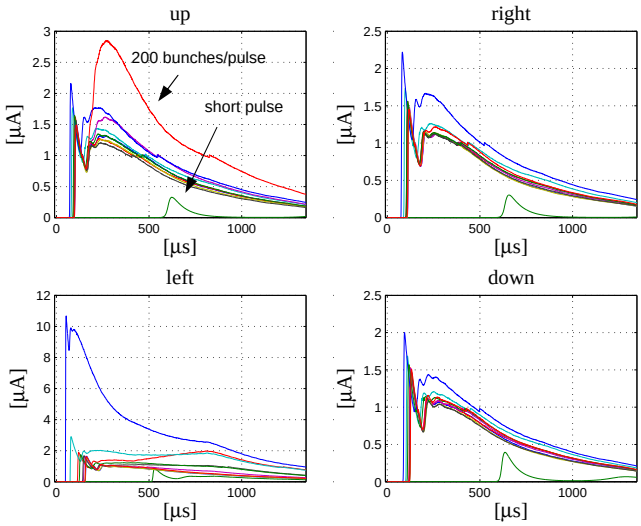

Figure 8 Signals from ionizations chambers corresponding to previous 2 figures. (Please note the different horizontal scale than for toroid, BHM and BPM plots.)

The signals from the beam halo monitors are shown in Figure 9. The up, right, down and left signals (in the beam direction) are from the sapphire sensors, while the remaining ones are from diamond sensors. One can see that the diamond sensors are more sensitive than the sapphire ones. In this case the losses were very small. The glass fibers BLMs placed along the 2 m just before the BHMs did not show any signal. In other cases with large losses (largely off-centered beam), the diamond sensors saturated while the sapphire ones showed a good signal. Therefore using the two types of sensor increases the dynamic range of the monitor.

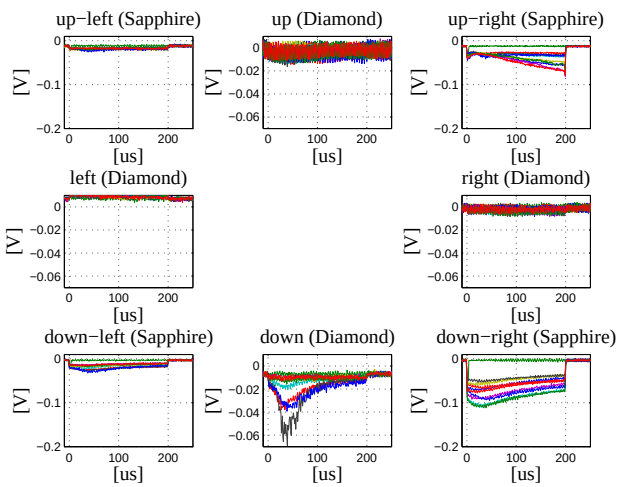

Figure 9 Signals from BHM sensors for 10 pulses corresponding to previous 3 figures. The up-right, down-right, up-left and down-left (in beam direction) sensors are diamonds, while the up, down, left and right signals are from sapphire sensors. Please note the different vertical scale.

CONCLUSION AND OUTLOOK

The additional diagnostics installed in the FLASH dump line has contributed to the successful 9 mA run in Autumn 2009. The various monitor types are complementary to each other and except for the transverse beam profile give a rather complete picture of the way the beam is dumped.

During the 9mA experimental run, pulses with 3 MHz bunch repetition frequency, 2 nC charge per bunch, a pulse length of 800 µs and an energy of 800 MeV have been achieved. A pulse length of 600 µs has been reached with 3 nC bunches, a record up to now.

After the 2 week long 9 mA run, the linac has been upgraded. The main changes are the installation of a new cryo-module, enabling a maximum energy of 1.2 GeV, the installation of a 3rd harmonic cryo-module in order to linearize the energy along the bunch, important for a more homogenous bunch distribution in the compression process and of a undulator section for a so-called seeding experiment. The pulses have now a frequency of 10 Hz, instead of 5 Hz before the upgrade. The commissioning of the linac is on-going.

Further investigations of the diagnostics installed in the FLASH dump line are going to be made during the current commissioning period as well as during further beam studies periods. Particularly the magnetic BPM and the BHMs will be studied in order to answer questions such as BPM constant and linear region, life time of BHM sensor etc.

Similar diagnostics is considered for installation in FLASH II, an extension of the current facility, and in the XFEL.

ACQKNOWLEDGEMENTS

We would like to thank our colleagues who took part in the planning, design, construction, and installation of the diagnostics described in this paper. Among them we particularly mention Annette Brenger, J. Kruse, J. Liebing, J. Lund-Nielsen, B. Michalek, Z. Pisarov, S. Vilcins-Czvitkovics, Thorsten Wohlenberg, and the whole FLASH crew.

REFERENCES

[1] S. Schreiber et al., “Operation of FLASH at 6.5nm Wavelength”, EPAC’08, Genoa, Italy, Jun. 23-27, 2008, p. 133 (2008); http://flash.desy.de.

[2] M. Altarelli et al. (eds), “XFEL: The European X-Ray Free-Electron Laser. Technical design report”, DESY-06-097 (2006); http://www.xfel.eu/.

[3] Phinney, N. Toge, N. Walker (eds), “ILC Reference Design Report”, ILC-REPORT-2007-001, DESY 07-046 (2007); http://www.linearcollider.org/.

[4] M. Maslov et al., “Design of a Beam Dump for the TTF-FEL Phase II (TTF2) Project”, TESLA-FEL 1999-06 (1999).

[5] N. Walker et al., “Operation of the FLASH Linac with Long Bunch Trains and High Average Current”, PAC09, Vancouver, BC, Canada, May 4-8, 2009 (2009).

[6] D. Lipka et al, “Magnetic Coupled Beam Position Monitor for the FLASH Dump Line”, these proceedings, TUPSM039 (2010).

[7] J. Lund-Nielsen et al., „Button Beam Position Monitors for FLASH”, DIPAC07, Venice, Italy, May 20-23, 2009, p. 201 (2007).

[8] Computer Simulation Technology (CST), http://www.cst.com.

[9] A. Ignatenko et al., to be published.

MULTI-CHANNEL MAGNET POWER-SUPPLY RAMP CONTROLLER FOR THE IUCEEM ALPHA SYNCHROTRON/STORAGE RING WITH CHANNEL ACCESS

Stanley Cohen, BiRa, Albuquerque, New Mexico, U.S.A.
Gary William East, Robert Ellis, IUCEEM, Bloomington, Indiana, U.S.A*

Abstract

A four-channel magnet-power-supply ramp controller has been designed and deployed at the new ALPHA (Advanced Electron Photon Facility) at the Indiana University Center for Exploration of Energy and Matter (IUCEEM). The first application is a power-supply controller. For all practical purposes, the system is a versatile arbitrary voltage-waveform-generator with full DAQ (data acquisition) capabilities that can be used in a variety of beam instrumentation settings. The real-time controller can generate four arbitrary independently-triggerable ramp profiles. A normalized wave-form vector is encoded as a Process Variable array and is uploaded and stored by the real-time controller as required. Each ramp array element is clocked out to a 16-bit DAC (Digital to Analog Converter) via a DMA FIFO and built-in FPGA. The duration of the waveform is programmable with a minimum time resolution of 20 μsec between profile values. Four bipolar DACs have an output range of +/- 10V. Eight digital I/O control bits are allocated for each control channel. Typically, these bits are used to monitor and control the power-supply operational state. The control-system interface uses the EPICS Channel-Access server accessible on Labview RT 2009.

ALPHA STORAGE RING

The Advanced eLectron PHoton fAcility (ALPHA) consists of an electron LINAC coupled to a storage ring which will provide the beam to a device test area[1]. Ultimately, it will provide a 20 MeV 68 mA electron beam. ALPHA is under construction at this time, commissioning is planned for the second quarter of 2010. There are a number of operating modes. In one mode of operation, the storage ring would modify the pulse structure to eliminate bunching of electrons emerging from the LINAC[2]. In another mode, the storage ring will capture bunches of electrons and compress their time width to provide high-intensity electron pulses. ALPHA will be capable of providing X-rays using high-efficiency Bremsstrahlung targets or by Inverse Compton Scattering.

This multi-mode operation requires beam management via sophisticated programmable power-supply control electronics.

The controller described below is an example of a system whose software and hardware architecture can be used as a versatile arbitrary voltage-waveform-generator with full DAQ (data acquisition) capabilities that can be deployed for a variety of beam instrumentation applications.

POWER SUPPLY RAMPING AND CONTROL REQUIREMENTS

The ALPHA storage ring requires a number of magnets to ramp their magnetic fields in response to a timing pulse. Four main dipoles are wired in series and are excited by a single 20 kW power supply. Other magnets, such as correctors and quadrupoles have individual supplies controlled and monitored by the system that will be described.

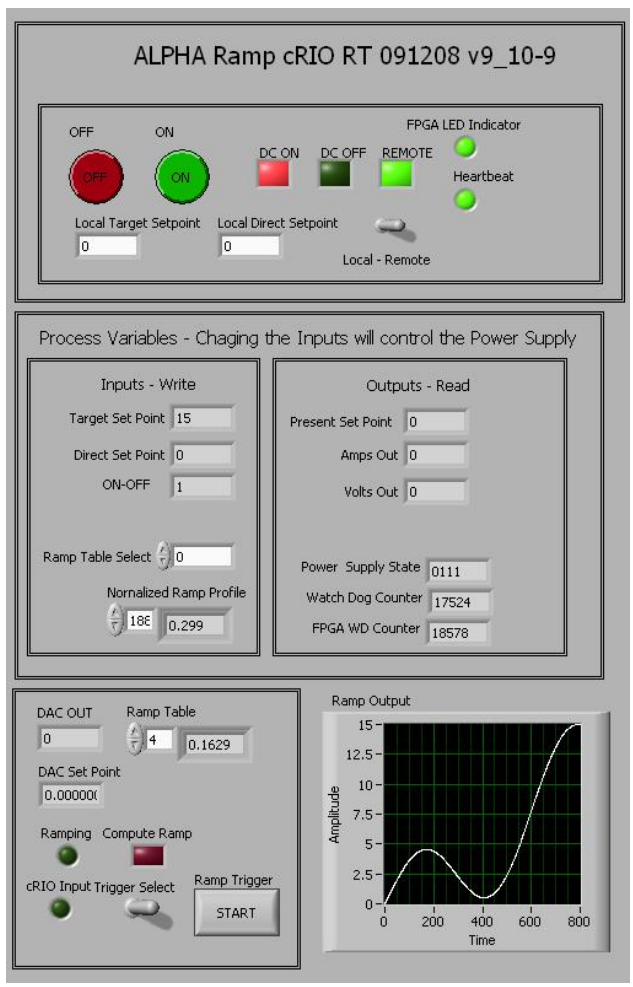

Figure 1: ALPHA ramping control panel.

* Work supported by the Naval Surface Warfare Center-Crane division (NSWC-Crane) Contract No. N00164-08-C-GM03

Each magnet is required to ramp from an initial to final magnetic field value following a specific ramp profile in one second. This ramp period may be longer during certain operations. Ramp initiation latency, the time between the trigger and ramp start must be less than 300 μsec. All of the power supplies in the system run in the constant-current mode and require an analog programming voltage of 0-10 V. In addition to the ramping waveform, the power-supply controller must monitor output voltage and current, and act as the state-machine [3] for each power-supply channel. This allows remote control and monitoring of power supply states, and interlock faults.

All controllers communicate with the accelerator control system using EPICS Channel-Access protocol [4].

CONTROL AND DATA-ACQUISITION TOPOLOGY

National Instruments cRIO and FPGA

The controller uses National Instruments (NI) hardware chassis (See Figure 1) based upon NI's Compact RIO (reconfigurable I/O), cRIO, and architecture. Physical connections are achieved through a series of BiRIO interface wiring cards[5] housed in a 19"-4U chassis.

The system architecture consists of four major parts. Real-time controller

1. Chassis-mounted signal conditioning modules
2. A Virtex II FPGA (field programmable gate array) that is the intermediate processor between the RT and the I/O modules.
3. Ethernet interface.
4. Channel-Access Server

The power of this configuration is contained in the FPGA which can run multiple, simultaneous processes. This is a true parallel process environment at a minimum of 40 MHz. See Figure 2.

The advantage of this arrangement is that the FPGA is programmed in Labview, not VHDL. Two pieces of software must be written, but all use the common graphical programming paradigm of Labview, the virtual instrument (VI). Labview FPGA contains all of the components to load and run the FPGA code.

The DAC ramping, hence power-supply ramping, is triggered and executed in the FPGA. he ramp profile data vector is calculated by the Real-Time processor and is sent to the FPGA via DMA transfer. The data rate is limited only by the PCI parallel bus speed, which is 33 MHz.

Ramp Vector Generation

The required capability of the controller is to deliver an arbitrary ramp waveform to the power supply. The power supply – magnet pair will create a time-dependent magnetic field. The beginning and end point values of the field are also arbitrary and can change with each time the ramp is executed. The shape of the ramp needs to remain the same. We have chosen to model the ramp as a normalized ramp vector, whose values can vary from 0 to 1. A utility program was written to convert a waveform to the normalized form. This allows the modelling without being constrained by the limits of the hardware. See Figure 3.

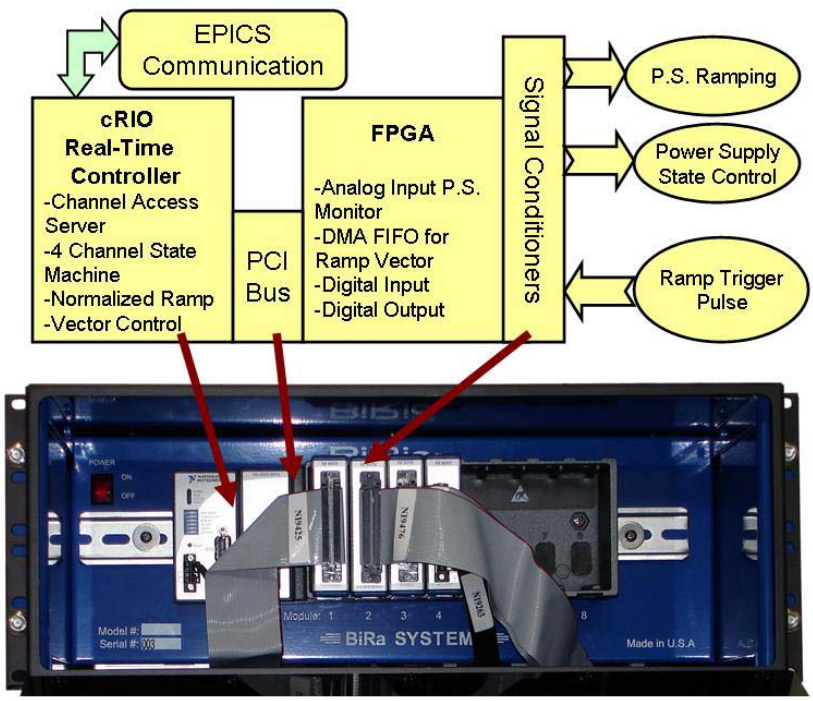

Figure 2: Real Time Architecture and cRIO hardware.

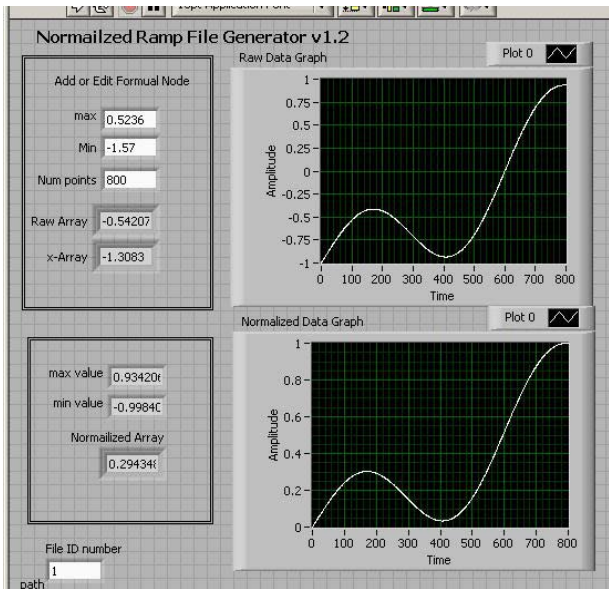

Figure 3: Normalized ramp vector generator. Compare the ordinate (y-axis) between the upper and lower graph. This shows the function: y =sin(x) +0.5sin(4x);

CHANNEL ACCESS INTERFACE

The most current version of Labview contains a Channel-Access server module that allows one to bind Labview shared variables to EPICS process variables (PV). This means that, shared variables are immediately accessible to the EPICS control system. A large number of process variable data types are allowed including floating point arrays. Arbitrary ramp vectors do not need to be stored on the cRIO real time processor, since they can be uploaded in a millisecond when required. The original design of the system was to store multiple ramp vectors on each controller for each power supply channel. The capability of the on-demand ramp profile change reduces configuration management tasks, since all of the profiles are stored at one central location.

Figure 4 shows the mapping of Labview shared variables to Channel-Access variables. Once the Real Tim application and the EPICS server are running on the cRIO processor, the PV's are immediately accessible via "caget" and "caput" [6] commands.

For development we wrote a control program that runs on a MS Windows XP computer using both LV shared variables and channel access variables. Both approaches worked provided reliable communications and control.

PV	Access Type	Variable Path	Data Type
10.1.1.227:EPICS_Ramp_PV_2:NRampData	Read/Write	IUCMB-ALPHA-3\EPICS Ramp PV 2.lvlib	Array of Double
10.1.1.227:EPICS_Ramp_PV_2:alvled	Read/Write	IUCMB-ALPHA-3\EPICS Ramp PV 2.lvlib	Boolean
10.1.1.227:EPICS_Ramp_PV_2:FPGALED	Read/Write	IUCMB-ALPHA-3\EPICS Ramp PV 2.lvlib	Boolean
10.1.1.227:EPICS_Ramp_PV_2:RampDataSz	Read/Write	IUCMB-ALPHA-3\EPICS Ramp PV 2.lvlib	Int32
10.1.1.227:EPICS_Ramp_PV_2:WDCntr	Read/Write	IUCMB-ALPHA-3\EPICS Ramp PV 2.lvlib	UInt32
10.1.1.227:EPICS_Ramp_PV_2:RemDirectStpt	Read/Write	IUCMB-ALPHA-3\EPICS Ramp PV 2.lvlib	Double
10.1.1.227:EPICS_Ramp_PV_2:RemTartetStpt	Read/Write	IUCMB-ALPHA-3\EPICS Ramp PV 2.lvlib	Double
10.1.1.227:EPICS_Ramp_PV_2:remonoff	Read/Write	IUCMB-ALPHA-3\EPICS Ramp PV 2.lvlib	UInt16
10.1.1.227:EPICS_Ramp_PV_2:RemRampTrig	Read/Write	IUCMB-ALPHA-3\EPICS Ramp PV 2.lvlib	Boolean

Figure 4: EPICS process-variable mapping.

CRIO CONTROLLER COMPONENTS

cRIO platform

We chose a integrated cRIO controller with four I/O modules for this application. National Instruments make a number of controllers with increasing levels of computing power and FPGA with increasing numbers of gates. The more powerful units have a separate controller with a PCI bus, to which one can attach a back plane that contains the FPGA. This allows one to match the controller and gate array to a specific application. We chose the NI model 9073 which has the real-time controller and FPGA on a single printed circuit board. The unit has a modest 266 MHz Freescale processor, Ethernet 10BaseT port, and a single RS-232 port. Labview Real-Time is built on top of Wind River Systems, VxWorks operating system. The serial port can be allocated as a console port to monitor the controller and have some limited access to the VxWorks operating system. Be aware that not all functions of VxWorks are accessible. The system includes four I/O modules, one each of 32-channel digital input unit, 32-channel digital output unit, 32-channel multiplexed 16-bit analog to digital converter (ADC) and four-channel 16-bit digital to analog converter (DAC).

The modules should be thought of as signal conditioners. The main job of the modules is to create a digital signal that can manipulated by the FPGA. This gives the user tremendous flexibility, while trading off the option of having the I/O modules working "right out of the box."

REAL-TIME OUTPUTS

The real-time controller can generate four arbitrary independently-triggerable ramp profiles. Each profile element is clocked out to a 16-bit DAC via a DMA FIFO and built-in FPGA. The duration of the waveform is programmable with a minimum time resolution of 20 µsec between profile values. Four bipolar DACs have an output range of +/- 10V. Eight digital I/O control bits are allocated for each control channel. Typically, these bits are used to monitor and control the power-supply operational state.

For practical purposes, the system is a versatile arbitrary voltage-waveform-generator with full DAQ (data acquisition) capabilities that can be used in a variety of beam instrumentation settings. The real-time controller can generate four arbitrary independently-triggerable ramp profiles. See Figure 5.

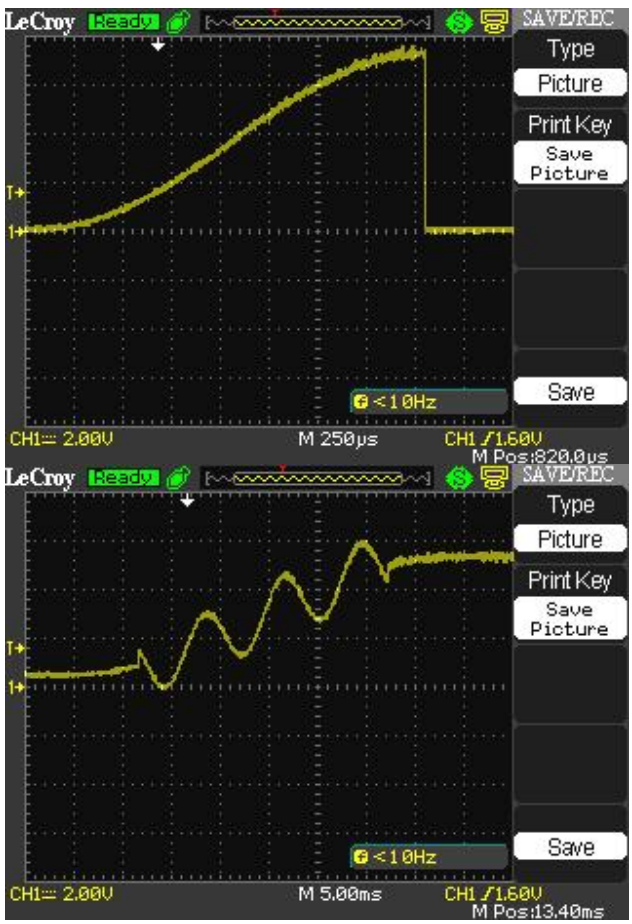

Figure 5: Actual DAC (analog-voltage output) ramp profiles.

REFERENCES

[1] ALPHA Home page: http://cme.physics.indiana.edu/alpha

[2] Lee SY, Kolski J, Liu Z, Pang X, Park C, Tam W, Wang F., Low energy electron storage ring with tunable compaction factor. Rev Sci Instrum. 2007 Jul;78(7):075107

[3] Wagner, F, et.al., Modeling Software with Finite State Machines, Auerbach Publications, (2006)

[4] "Experimental Physics and Industrial Control System" http://www.aps.anl.gov/epics/about.php

[5] Manufactured by BiRa Systems, Inc., Albuquerque, NM, 87107, www.bira.com

[6] "CA Commands," http://www.aps.anl.gov/epics/base/R3-14/8-docs/CAref.html#caget

FINAL FOCUS ION BEAM INTENSITY FROM TUNGSTEN FOIL CALORIMETER AND SCINTILLATOR IN NDCX-I*

S.M. Lidia#, F. Bieniosek, E. Henestroza, P. Ni, P. Seidl, LBNL, Berkeley, CA 94720, U.S.A.

Abstract

Laboratory high energy density experiments using ion beam drivers rely upon the delivery of high-current, high-brightness ion beams with high peak intensity onto targets. Solid-state scintillators are typically used to measure the ion beam spatial profile but they display dose-dependent degradation and aging effects. These effects produce uncertainties and limit the accuracy of measuring peak beam intensities delivered to the target. For beam tuning and characterizing the incident beam intensity, we have developed a cross-calibrating diagnostic suite that extends the upper limit of measurable peak intensity dynamic range. Absolute intensity calibration is obtained with a 3μm thick tungsten foil calorimeter and streak spectrometer. We present experimental evidence for peak intensity measures in excess of 400 kW/cm^2 using a 0.3 MV, 25 mA, 5-20 μsec K^{+1} beam. Radiative models and thermal diffusion effects are discussed because they affect temporal and spatial resolution of beam intensity profiles.

INTRODUCTION

The US Heavy Ion Fusion Science program is developing techniques for heating ion-beam-driven warm dense matter (WDM) targets [1-3]. Ion beams have several attractive features as drivers for generating WDM conditions:

- Precise control of local beam energy deposition *dE/dx*, nearly uniform throughout a volume, and not strongly affected by target temperature,
- Ability to use large sample sizes (~1 μm thick by 1 mm diameter),
- The ability to heat any target material: foams, powders, conductors, insulators, solids, gases, etc.

WDM conditions are obtained by combined longitudinal and transverse space-charge neutralized drift compression [3] of the ion beam to provide a hot spot on target with a beam spot size of ~1 mm, and pulse length from microseconds to nanoseconds. Local temperatures approaching 0.5 eV (~6000 K) have been observed in thin (50-150nm) foil targets of Au, Si, Pt, and C [4].

Beam profile measurements at the target plane are used to tune the beam transport system to optimize the beam intensity onto target foils. Alumina (Al_2O_3) scintillators are employed since they have a linear response over a large dynamic range and are relatively resistant to dose-related damage, at least at lower intensities. At higher intensities, greater than ~200kW/cm^2, saturation or other nonlinear effects may limit the upper range of measurable beam intensity. To address these issues, we have adapted our target diagnostic suite to examine the uses of thick foils for beam calorimetry measurements.

Tungsten has the highest melting temperature (3420°C) of the refractory metals from atmospheric pressure to ultra-high vacuum conditions. It is commonly used in high temperature applications (wire filaments, etc.) where high tensile strength is required.

The specific heat capacity, c_p, of tungsten (~24.4 J/mol/K) measures the temperature change expected from beam irradiation. Temperature-dependent values of the specific heat capacity can be found in standard references [5-6].

For beam calorimetry we use a 3μm thick solid tungsten foil, in which 300kV potassium ions deposit their energy within the first 100nm. The resolution of the optical system is ~11.4pixel/mm, or a pixel size of 88μm. On this length scale, the foil is thin compared to the resolution limit. The thermal diffusion length over a time *t* is given by

$$\delta_{th} = 2\sqrt{\kappa t}\,, \qquad (1)$$

*This work was supported by the Director, Office of Science, Office of Fusion Energy Sciences, of the U.S. Department of Energy under Contract No. DE-AC02-05CH11231.
#SMLidia@lbl.gov

where κ is the diffusivity (~68 μm ^{2}/μsec). Hence, the diffusion time over the pixel size is ~30μsec. This sets the upper time scale duration for resolvable processes. The diffusion time over the foil thickness is ~33ns. This sets the lower limit on temporal resolution. Within these limits, an instantaneous bulk heating or one-dimensional heat transport model provides an accurate approximation to the thermal dynamics.

PHYSICS OF THERMAL EMISSION

Blackbody radiation with emissivity

The Stefan-Boltzmann law [7] provides the basis for estimating the temperature of an object from its thermal radiation intensity:

$$P_{rad} = A\varepsilon\sigma_{SB}T^4, \qquad (2)$$

where P_{rad} is the total object irradiated power, A is the area of the radiating object held at a uniform temperature T, ε is the emissivity of the material, and σ_{SB} is the Stefan-Boltzmann constant. Direct observation of the 4th power law requires perfect detectors integrating across the entire spectrum. Real detectors will collect only a fraction of the spectrum, drastically altering the power law behavior to larger effective exponents.

Optical pyrometers are calibrated absolutely against NIST traceable radiation sources, eg. tungsten ribbon lamps, and measure intensity within a narrow wavelength band. Reconstructed temperature, T, can be obtained from a non-linear least-squares fit of measured spectra, $I(\lambda,T)$, to a radiation model. Using a Planck's Law model [7] with spectral emissivity ε(λ), the two-parameter fitting function is [8]

$$I(\lambda,T) = \varepsilon(\lambda)\frac{C_1}{\lambda^5}\left[e^{C_2/\lambda T} - 1\right]^{-1}. \qquad (4)$$

Tabulated emissivity data at 650nm is available [9].

Local temperature evolution

The local temperature in a material is governed by the interplay of heat fluxes and heat transport described by the one-dimensional heat equation:

$$\rho c_p \partial_t T = \partial_x\left(K\partial_x T\right) + S(x,t), \qquad (5)$$

where ρ is the material density and K is the conductivity. Here x defines the distance into the foil from the upstream side. The source term, S, describes the influx of beam ions impinging on the foil and depositing their kinetic energy within ~100nm. The boundary conditions can be written as

$$\left(K\partial_x T\right)_{U,D} = F_{U,D}(T), \qquad (6)$$

where the subscripts U,D refer to Upstream or Downstream, respectively, and F describes the various contributions to fluxes removing energy from the foil surfaces from evaporation, radiation, and thermionic emission. On the time and temperature scales of interest for the diagnostic, the cooling fluxes are neglected in the calculation of foil temperature.

Beam heating model

The one-dimensional heat transport equation has been modeled and solved numerically. Figure 1 shows the time evolution of the 3μm foil temperature under irradiation from a ~300-kV K^{+1} beam. A shelf in the temperature response is indicative of a material phase change.

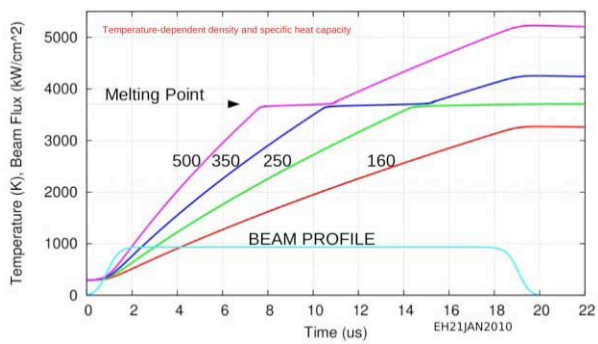

Figure 1: Temperature of the 3μm tungsten under prescribed ion beam irradiation.

EXPERIMENTAL RESULTS

The NDCX-I [10] facility generates a K^{+1} ion beam with kinetic energy 250kV-350kV, beam current 20-30mA, pulse duration ~3-20μsec, and repetition frequency ~0.05-0.1 Hz. Solenoid magnets are used for beam transport and envelope matching into a plasma-neutralized drift section. An 8 T final focus solenoid images the beam onto the target foil. Measured beam intensities >200kW/cm^2 are routinely produced.

Capacitive and resistive voltage dividers monitor the beam voltage, while Faraday cups provide beam current measurements. One hundred micron thick Al_2O_3 scintillators are used with gated, image-intensified 16-bit MCP cameras (Princeton Instruments PI-MAX) to image the beam profile. A fine metal mesh (biased to -300 V) prevents charge buildup on the scintillator. The ion beam deposits all its energy in the scintillator within 1μm. Horizontal and vertical slits are used with the scintillator or with a slit-Faraday cup to measure beam phase space. The target plane is instrumented with a scintillator and a camera (88μm resolution), and the Fast Faraday Cup with ~1ns temporal resolution.

Target diagnostics include a fiber-coupled relay lens light collection system (200μm probing spot) coupled to an absolutely calibrated, time-resolved streak-camera-based spectrometer (Hamamatsu C7700) or a four-band fast optical pyrometer [11]. A downstream fast current transformer (Bergoz FCT-016-20:1-VAC) captures the transmitted beam current at the target plane after the foil target spot melts and material is removed.

Beam profile tuning and energy variation

The ion beam transverse profile at the target plane was obtained using the gated camera (80mm, f/1.4, 2x teleconverter) with the scintillator and tungsten foils. Figure 2 shows the variation in beam profile as the beam energy was varied. The beam duration and camera gate was 5μsec. The final focus solenoid was held fixed at 8 T, while the upstream optics are adjusted to maintain energy-independent transverse beam envelopes and beta-functions. In the scintillator cases, the camera gain was 250 and the peak pixel value was ~23000, while in the foil cases the camera gain was 50 and the peak pixel value was ~15000. Under the same irradiation for 5μsec, the foil presents a much brighter radiation source.

The foil emission displays much greater sensitivity to the peak of the beam distribution than does the scintillator, but radiates much of its total power outside of the camera detector's spectral sensitivity range. The central core of the beam is peaked and generates a peaked irradiation profile. While scintillators exhibit nearly linear fluorescence intensity to energy deposition, the thermal emission intensity of the foil is highly nonlinear and follows a Planck intensity distribution, as shown in Eqn 4.

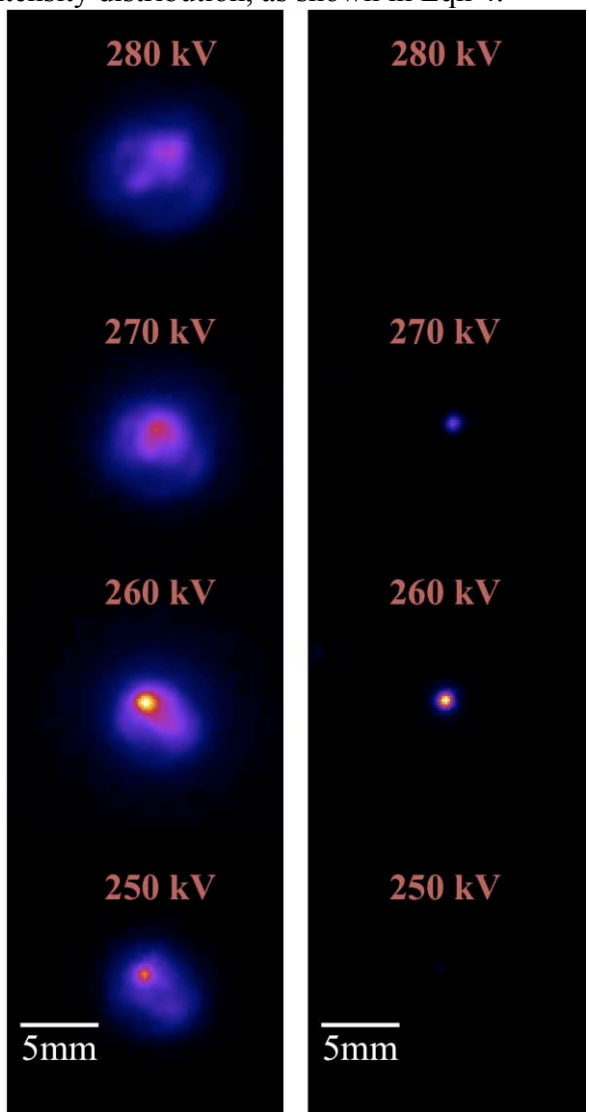

Figure 2: Scintillator (left) and tungsten foil (right) false color images of 5μsec beam irradiation. Peak intensity is white.

Normalized horizontal cross-sections of the 260kV beam energy scintillator and foil image profiles are shown in Figure 3. The raw foil intensity distribution is corrected via

$$I_{corr} = I_{raw}^{1/n}, \quad (7)$$

where the exponent n is chosen so that the foil intensity profile width matches that of the

scintillator. A best-fit match reveals $n = 9 \pm 1$, for a 1.05mm FWHM.

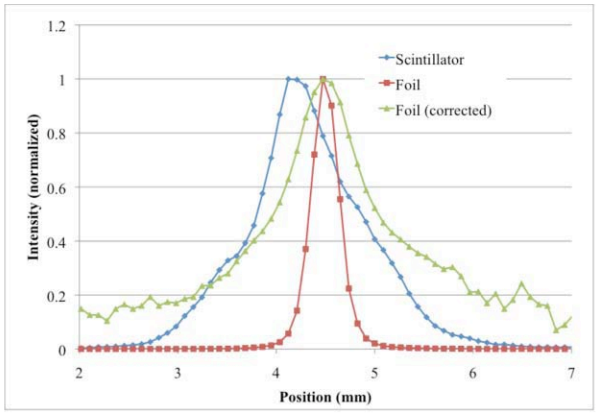

Figure 3: Horizontal cross-sections of scintillator and foil images of the 260kV beam.

Using this correction scaling, the variation of the peak intensity with beam energy is analyzed. Figure 4 shows the measured and the corrected intensities. Factors of ~100 in measured intensity indicate only a factor of ~2 in true intensity variation over the range of beam energies scanned.

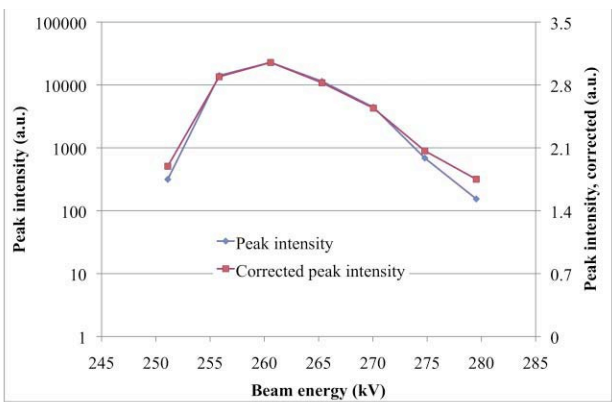

Figure 4: Measured and corrected peak intensity versus irradiating beam energy.

Beam Intensity from Scintillator Profile

The beam intensity profile is obtained from cross-calibration of the scintillator image with the beam power, obtained from beam voltage measurements and beam current in the target chamber Fast Faraday Cup. These are average values obtained over multiple shots. The calibrated beam intensity is shown in Figure 5 for a 260 kV beam energy, and 5.6 kW beam power over the 5µsec pulse duration. The peak beam intensity is estimated at ~248 kW/cm^2, based on scaling the total beam power to the entire acquired image distribution. Any hypothesized intensity-dependent saturation effects will only affect the peak valued pixel(s).

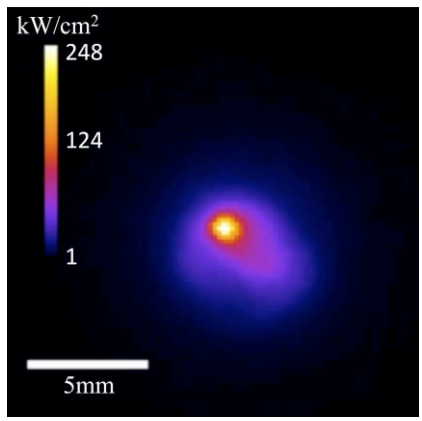

Figure 5: Calibrated beam intensity for 260kV beam energy, measured with the scintillator.

Foil Temperature from Optical Pyrometry

The calibrated streak-spectrometer was used to analyze the thermal emission at 650nm from the foil during and after beam irradiation (beam power 5.6kW, pulse duration ~10µsec). The foil spot temperature is calculated from Eqn. 4 assuming a spectral emissivity ε_{650nm} ~0.43. Signal to noise limits the detector's lower temperature threshold to ~1700K. Temperature error bars (+300K -150K) are estimated based on the relative uncertainty of the emissivity. The reconstructed temperature response is shown in Figure 6, averaged over 20 shots.

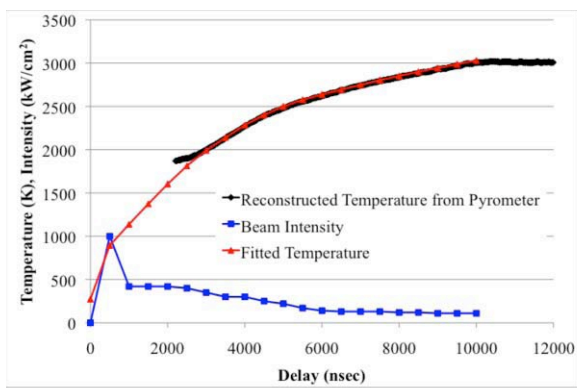

Figure 6: Measured foil temperature, estimated beam intensity and calculated foil temperature from pyrometer data.

Beam Intensity from Optical Pyrometry

Beam intensities were estimated by assuming a uniform irradiance over the 200µm analyzing fiber aperture, and then matching the calculated foil temperature rise to the reconstructed pyrometer temperature. The heat equation, Eqn. 5, was solved numerically, and the results are presented in Figure 6. The average beam intensity is estimated to be 430 kW/cm^2 between 0 and 4 µ sec, 133 kW/cm^2 between 4 and 10 µsec, and 260 kW/cm^2 between 0 and 10 µsec. This matches the predictions from the 1D thermal model (Figure 1) over the initial 4-5µsec beam heating period.

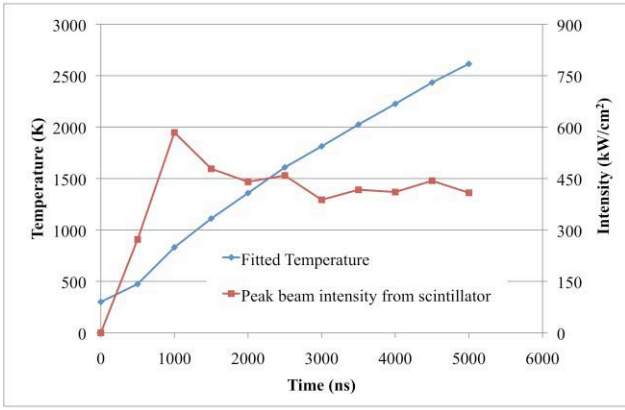

Figure 7: Renormalized peak beam intensity and calculated foil temperature.

Cross-calibration of Scintillator Beam Intensity

The scintillator intensity response is known to degrade and to possibly saturate under high beam irradiance. The peak beam intensities from time-resolved scintillator measurements are corrected to generate the measured temperature rise in the tungsten foil. A cross-calibration factor of 2.2 applied to the measured scintillator peak beam intensity generates the same foil temperature rise (to ~2400 K) by direct integration of Eqn. 5 over the ~5µsec beam pulse duration, shown in Figure 7. This results in a cross-calibrated peak beam intensity ~430kW/cm^2, averaged over the 5µsec beam pulse duration. This is to be compared with the measured peak intensity 248 kW/cm^2 obtained using only the scintillator and Faraday cup (Figure 5). In this case, the correction factor would be ~1.7. Hence, we see that there exists an empirical correction factor ~2 to be applied to the peak beam intensity derived solely from scintillator and Faraday cup measurements, and that this factor is an estimate to the degree of saturation of these beams in thin alumina scintillator wafers.

CONCLUSIONS

We have described a novel diagnostic capability that extends the dynamic range of scintillator-based beam profile measurements for intense ion beam characterization. We have described an empirical procedure to estimate the degree of saturation and deviation from linearity in scintillator materials. Calorimetric measurements support peak ion beam intensities of 430kW/cm^2 over a 200µm spot. This matches well with 1-D dynamic heating models.

REFERENCES

[1] J.J. Barnard, *et al*., Proc. 2005 Particle Accelerator Conference, p.2568.

[2] P.K. Roy, *et al*., *Nucl. Instrum. Methods Phys. Res.* **A** 577 (2007) 223-230.

[3] P.A. Seidl, et al., *Nucl. Instrum. Methods Phys. Res.* **A** 577 (2007) 215-222.

[4] F. Bieniosek, *et al*., Proc. Sixth Intl. Conf. on Inertial Fusion Sciences and Applications (IFSA2009), IOP Press.

[5] R.C. Weast (ed.), CRC Handbook of Chemistry and Physics, CRC Press, Inc., 1984.

[6] G.K.White and S.J. Collocott, *J. Phys. Chem. Ref. Data* **13** (1984) 1251-1257.

[7] See, for example, C. Kittel and H. Kroemer, Thermal Physics, W.H. Freeman and Company, 1980.

[8] P.A. Ni, *et al*., *Laser and Particle Beams*, December 2008.

[9] R.D. Larrabee, *J. Opt. Soc. Am.* **49** (1959) 619-625.

[10] S.M. Lidia, *et al*., Proc. 2009 Particle Accelerator Conference, TU6PFP092.

[11] P.A. Ni, *et al*., *Nucl. Instrum. Methods Phys. Res.* **A** 606 (2009) 169-171.

ADC CONSIDERATIONS AND ANALYSIS FOR BAND PASS SAMPLING SYSTEMS

Alfred J. DellaPenna Jr., Brookhaven National Laboratory, Upton, NY 11973, U.S.A.

Abstract

With increasing demand of acquiring data at high speed with high resolution, more digitizers have become available for this purpose. With digitizers becoming faster and faster at higher data rates with higher resolutions, the factors in choosing the proper digitizer for a design is not just the number of bits. Deciding factors include jitter, maximization of the effective number of bits (ENOB) and linearity over the band of interest, and most importantly phase noise. Does the part you are evaluating match with the data sheet? If not, what is different in your test setup? (Your evaluation can only be as good as the equipment you are using to test the device.) With the availability of evaluation boards from almost any of the ADC vendors, a more in-depth evaluation can be performed fairly easily. Even the GUI interface is usually included with the evaluation board. So for a small investment on several choices, one can make a side by side comparison and see actual results.

INSTRUMENT SETUP

Our initial setup is illustrated in Figure 1. We used a single tone (500 Mhz) from a HP signal generator as the analog input. The digitizer clock, which requires the more stable (lower jitter) signal, was supplied by the Rohde & Schwarz SMA100A signal generator. Along with the evaluation boards a mating digital interface was purchased for each so we could utilize the graphical user interface that the vendor had created. The interface to the computer was through a USB cable. The software was downloaded from the vendor's website.

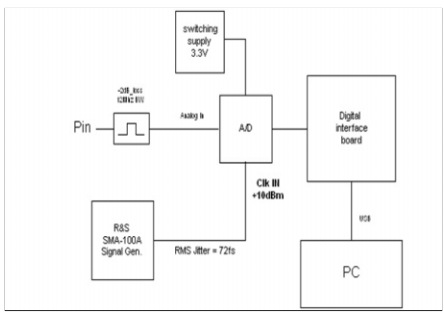

Figure 1: Digitizer setup. The analog input was from an Agilent N5181A. Software was downloaded from the digitizer vendor.

The onboard jumpers were usually set up at the factory; however, we did find that the evaluation boards allowed many different setup configurations. Choosing a setup that worked best for us took some time. Finally it was time to take some data.

We wanted to be sure it was a fair side by side evaluation of each digitizer. All of the evaluation boards had their analog input "protected" by limiting resistors; because of this, the same input signal did not use the same scale from one digitizer to another. This required us to either adjust the input to compare similar levels at the input to the digitizer, or modify the evaluation board itself (removing the limiting resistors). These modifications made the setup of all evaluation boards as close as possible, all running off the same supply and signal generators. Power sweeps were taken from -90 to +10 dBm and the associated plots were compared to each other. Figures 2-5 show the resultant Fast Fourier Transforms from each digitizer we were evaluating.

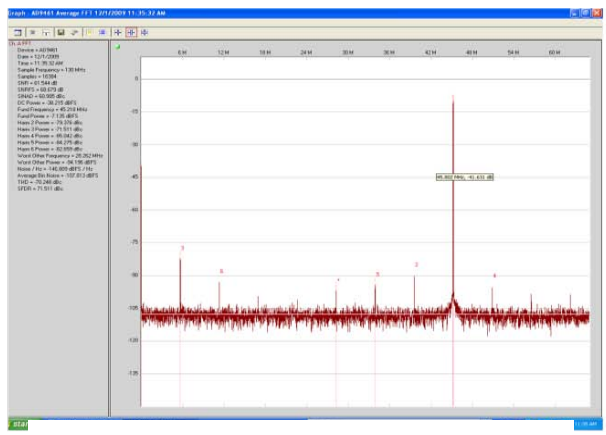

Figure 2: Analog Devices AF9461 FFT, power in +10 dBm.

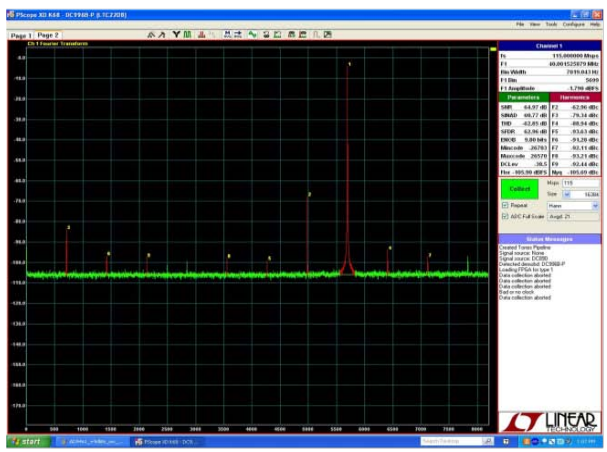

Figure 3: Linear Technology LTC2208 FFT, power in +10 dBm.

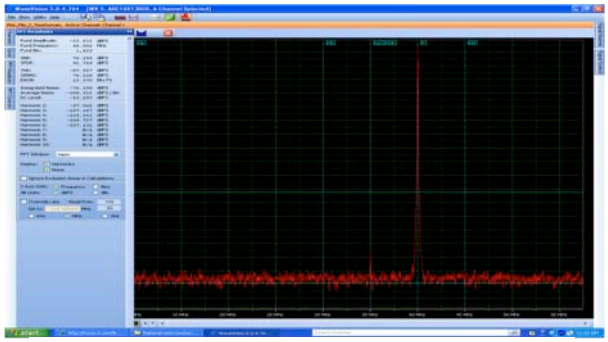

Figure 4: National Semiconductor ADC16V130 FFT, power in +10 dBm.

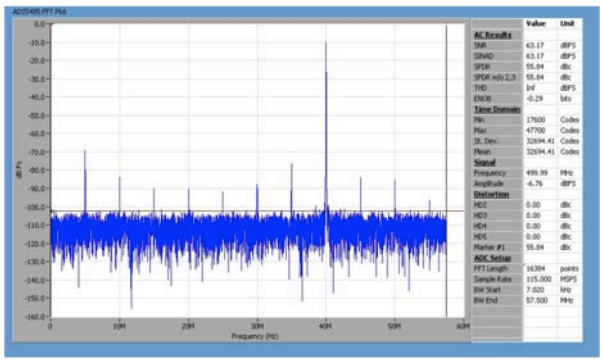

Figure 5: Texas Instruments ADS5485 FFT, power in +10 dBm.

MEASUREMENT OPTIONS

Almost all the digitizer software has different options, e.g., single tone, multi-tone. and time domain. Even masking of portions of the spectrum was available. In our application we worked in the frequency domain to look at the harmonic distortion in the spectrum. The signal level of the clock for the digitizer was also very critical; a low signal level on the clock would directly affect the SNR/SINAD results. We found that a signal level of +10dbm worked very well. For the analog input signal level, the input was brought up until the level exceeded the compression point of the digitizer (P1db). Then it was backed off by 1 or 2 dB. This ensured us of using the full range of the digitizer.

RESULTS

We did a side by side jitter measurement of the two signal generators. The associated phase noise plots along with jitter numbers are in Figures 6 and 7.

The data from all four plots, along with simulated data from the analog device part, were put into an Excel spreadsheet so that we could see the entire picture. Parameters other than SINAD and SNR were put into this spreadsheet as well. Figure 8 shows the results.

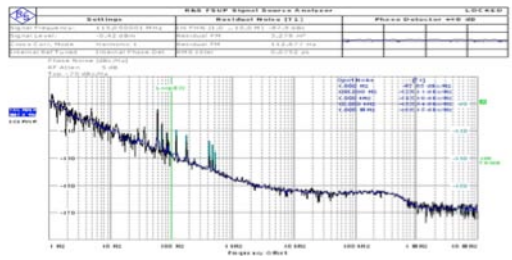

Figure 6: Phase noise of Rohde & Schwarz SMA100A.

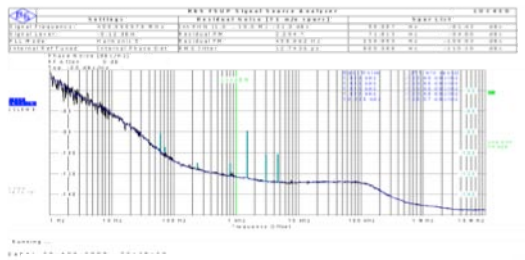

Figure 7: Phase noise of Agilent N5181A.

CONCLUSION

The data conversion market has made very user friendly advances in the way one can evaluate a product. Even the digital interface to the PC world has been handled. The GUI interface, and the available options to perform any number of tests on the product, are already built in. One thing to be aware of is the different front end protection before the digitizer; this will change the level that one digitizer sees compared to the other. You can either compensate for it or modify the board to ensure all tests are one to one. Another thing to watch for is that all the evaluation boards used here are connected to the PC through a USB connector. Using a slow USB 1.1 port may not work—we have seen it on two of the evaluation boards we tested. From our results, in our particular situation, we found that the Linear Devices LT2208 worked best for our application.

ACKNOWLEDGEMENTS

Kurt Vetter for his extremely helpful insight in so many matters. Belkacem Bacha , Marshall Maggipinto for their exceptional work in setting up evaluations and taking data.

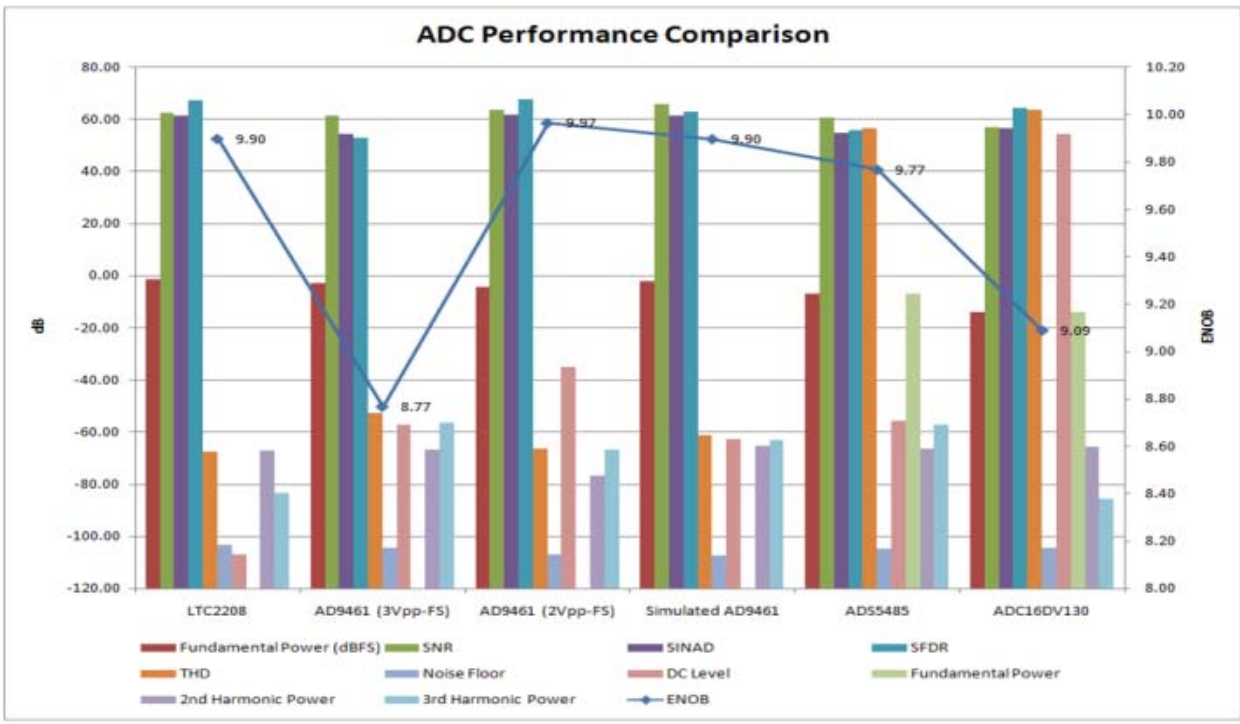

Figure 8: Integrated results of our tests.

NSLS-II INJECTOR SYSTEM DIAGNOSTICS

D. Padrazo, O. Singh, I. Pinayev, R. Fliller, T. Shaftan, B. Kosciuk, R. Meier, Y. Hu
Brookhaven National Laboratory, Upton, NY 11973, USA

Abstract

The NSLS-II Injector System Diagnostics will provide instrumentation in the linac, Booster, Transfer Lines and Beam Dumps for measuring key beam parameters. These instruments will be adequate for staged commissioning of NSLS-II injectors, and will allow sufficient beam diagnostics for tune-up and top-up operations. This paper summarizes the status of the NSLS-II injector system diagnostics, focusing on those intended for the transfer lines, including the Linac to Booster (LTB) and Booster to Storage Ring (BSR).

INTRODUCTION

The NSLS-II is a state-of-the-art 3-GeV synchrotron light source being developed at Brookhaven National Laboratory. The injection system will consist of a 200 MeV linac, a 3 GeV booster synchrotron, and associated transfer lines. The instrumentation in the linac will provide sufficient beam diagnostics to determine bunch charge, length, transverse size, position, and beam losses. The LTB and BSR will include key instruments to be used for beam commissioning and tune-up, particularly the beam dumps and those diagnostics elements within the booster vault. Measurements of beam charge, bunch train, bunch charge, energy jitter, emittance, and energy spread can be achieved. Booster diagnostics will provide measurements for orbit correction, injection matching and transverse profile. In addition, elements are provided to measure beam current, bunch train pattern, tune and chromaticity. This paper will detail the implementation of these diagnostics components for the NSLS-II Injector System.

LINAC DIAGNOSTICS

A turn-key procurement, the NSLS-II linac is specified to have an output energy of 200 MeV, energy spread of 0.5%, bunch length of 20 ps, and normalized emittance of 55 mm-mmrad. The linac will be capable of operating in single bunch mode with a charge of up to 0.5 nC, or in multibunch mode with a bunch train of 80 to 150 bunches, separated by 2 ns with a charge per train of 22 nC. The linac will have a 100 kV electron gun with thermionic cathode, sub-harmonic pre-buncher, 3 GHz pre-buncher, 3 GHz buncher, and a 3 GHz acceleration section. Linac diagnostics will consist of a Wall Current Monitor (WCM) after the gun, and another before the buncher. There will be a WCM, FLAG, and Beam Position Monitor (BPM) before each LINAC tank. This will provide sufficient diagnostics to determine bunch charge, length, transverse size, and position. The WCMs will also provide a measure of the beam losses in the linac. Refer to the Diagnostics Table of Elements and the Plan View of Injector as shown in Table 1 and Figure 1 respectively.

Table 1: Gun and Linac Diagnostic Elements

System	Qty	Type	Abbrv.	Parameter Measured
Electron Source (Gun)	2	Wall Current Monitor	WCM	Intensity; longitudinal beam characteristics
Linac	3	Fluorescent Screens	FLAGS	Position; transverse profile
Linac	3	Wall Current Monitor	WCM	Bunch charge; intensity; beam loss
Linac	3	Beam position monitor	BPM	Beam position

BOOSTER DIAGNOSTICS

A turn-key procurement, the NSLS-II Booster is a 158 m combined-function-magnet synchrotron with an extraction energy of 3 GeV for top-up injection. The beam emittance will be damped below 50 nm-rad, with trains of up to 150 bunches. The bunch length will be 15 ps, and the energy spread will be 0.08% when fully damped. The expected total charge out of the booster is estimated at 10 nC when the linac is in multi-bunch mode. Booster diagnostics are chosen for commissioning and robust operation.

The booster will have 36 BPMs placed at strategic points in the ring to allow for robust orbit correction. Six flags will be located in the booster for commissioning, injection matching and transverse profile measurements. Beam current will be measured with a DCCT. An FCT will monitor the bunch train pattern. A pair of stripline kickers will be available for tune and chromaticity measurements, also serving in a beam cleaner system. Synchrotron light will also be used in conjunction with a streak camera to measure the bunch length. The diagnostic elements of the Booster are listed in Table 2.

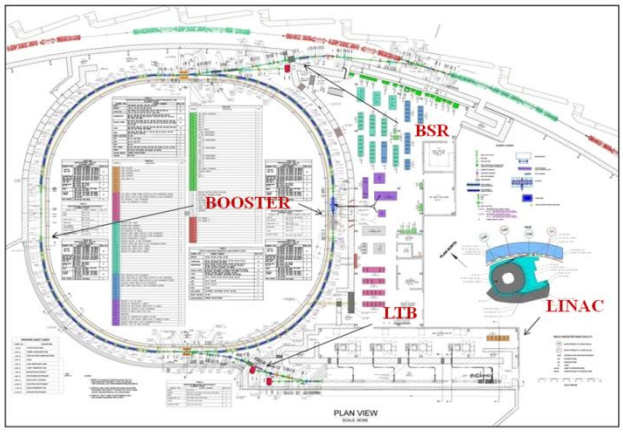

Figure 1: Injector system.

Table 2: Booster Diagnostic Elements

Qty	Type	Abbrv	Parameter or Role
1	DC Current Xfmr	DCCT	Beam current
1	Fast Current Xfmr	FCT	Bunch charge
1	Strip Line Detector	SLD	Tune meas.
1	Strip Line Detector	SLD	Bunch cleaning
6	Fluorescent Screens	FLAGS	Beam intensity, shape, position
1	Streak Camera	OBSC	Bunch length
1	FireWire Camera	FWC	Beam position, profile
36	Beam position monitor	BPM	Beam position; orbit

A Bergoz Fast Current Transformer (Figure 2) will be used for fill pattern monitoring. The FCT will be directly mounted on the beam chamber with a ceramic break and RF shielding, and will provide an

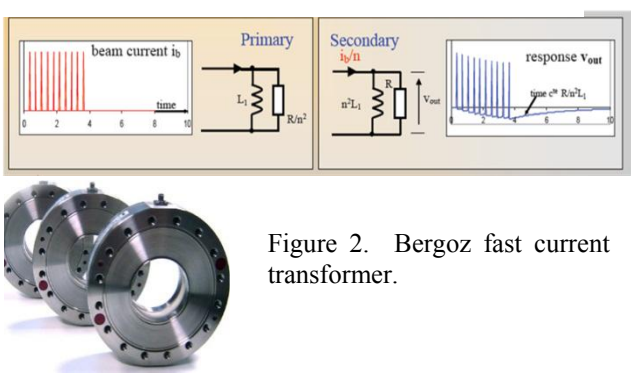

Figure 2. Bergoz fast current transformer.

electrical signal proportional to the charge of individual bunches. It has 1.75 GHz bandwidth with a 200 ps rise time. Fast ADC sampling (>1GS/s) of the FCT output voltage will make charge distribution available to the control system. The information obtained will be used in the top-off algorithm.

The ICT/BCM (Figure 3) will provide a multiply time integral output, which is proportional to the beam pulse charge irrespective of the bunch width or bunch frequency spectrum. For NSLS-II Linac injection, with the maximum 150 bunches (500 MHz RF), the bunch train to be integrated and measured is 298 ns long. It will pass through the ICT and the ICT output will be a 368ns long signal with a rise time of about 20 ns, a fall time of about 30 ns, and a flat top (if the 150 bunches are evenly charged). The Bergoz BCM is comprised of a chassis and module. It has a bipolar voltage output that is directly proportional to the total beam charge. BCM electronics are made in various versions. The BCM-IHR-E (Integrate-Hold-Reset) module has been selected to measure a single pulse or bunch trains up to 5 us long.

LINAC TO BOOSTER (LTB) TRANSPORT LINE DIAGNOSTICS

The layout of the LTB transport line was shown in Figure 1. It consists of 3 sections: a linac to achromatic section, an achromatic, and a matching section into the booster. In addition, there are two beam dumps located in the linac vault that will be used for commissioning, tune-up and diagnostics. Table 3 shows the available diagnostics in the LTB.

Table 3: Diagnostics—Transport Lines

Type	Qty (LTB)	Qty (BSR)	Resolution	Beam Parameter Measured
Screens (OTR + YAG)	9	10	10/30 μm	Energy spread; electron beam size, position
Fast current xfmr	2	2	~0.6 pC per bunch	Fill pattern; bunch charge
Energy slit	1	1	n/a	Beam energy spread
Integrating current xfmr	2	2	~10 pC per train	Injected bunch charge; injection efficiency
BPM (40× 90 mm elliptical)	1		30 μm	Beam position
BPM (40 mm round)	5	8	30 μm	Beam position
Faraday cup	2	1		Bunch charge

There are FLAGS at the start of the LTB, after the Energy Slit, and prior to booster injection that will be used for commissioning. An Integrating Current Transformer (ICT) and a Fast Current Transformer (FCT) measure the beam charge and bunch train at

each end of the LTB (Figure 3). An Energy Slit will be placed at the maximum dispersion location in the achromat, to remove any low energy particles.

Six BPMs are placed throughout the LTB. The first is at the end of the linac. One exists after the Energy Slit for online energy jitter measurement. Four BPMs are in the matching section for matching into the booster. There is also a Safety Shutter placed before the exit of the linac vault that will allow safe operation of the linac independent of the status of the booster. The beam dumps are equipped with FLAGs, including three FLAGs in the "straight ahead" beam dump for emittance measurement. The second beam dump will have sufficient dispersion to perform energy spread and energy jitter measurement. In each beam dump will be a Faraday cup, which will also act as a beam stop and will measure gross charge per train, capturing the entire charge of the electron beam and its shower for all dumps.

BOOSTER TO STORAGE RING (BSR) TRANSPORT LINE DIAGNOSTICS

Extraction from the booster is performed with a four bump scheme. A kicker imparts a 5 mrad angle, which is then followed by thin pulsed septum, and a large DC septum into the BSR line. The BSR line consists of 3 main sections, the booster extraction, an achromatic transport, and the matching section. There is also a beam dump in the booster vault for commissioning and tune up.

Extraction from the booster is performed with a four bump scheme. A kicker imparts a 5 mrad angle, which is followed by a thin pulsed septum, then a large DC septum leading into the BSR line. The BSR line consists of 3 main sections, the booster extraction, an achromatic transport, and the matching section. There is also a beam dump located in the booster vault for commissioning and tune up.

The BSR line has nine FLAGs. Two are placed before the first dipole to commission booster extraction. Three are in the achromat section for emittance measurements. Three are in the matching section for injection matching. The last FLAG is prior to the beam dump to allow for energy spread measurements. There is an FCT in the booster extraction section and near the injection point to measure the bunch train distribution.

There is an ICT (Figure 3) near the injection point to measure the bunch charge. Eight BPMs are placed in the transport line. Two BPMs are in the booster extraction section, three are in the achromat, and remainder are in the matching section. An Energy Slit near the maximum dispersion region limits the energy spread entering the storage ring. A Safety Shutter near the exit of the booster vault allows operation of the booster independent of the storage ring. The booster beam dump is equipped with a FLAG for energy spread measurements. It also has an ICT for bunch charge measurements. The beam dump will be used for booster commissioning and tune-up, allowing for characterization of the booster independent of the storage ring status. Incorporated into the beam dump will be a Faraday cup that will also act as a beam stop and will measure gross charge per train, capturing the entire charge of the electron beam and its shower.

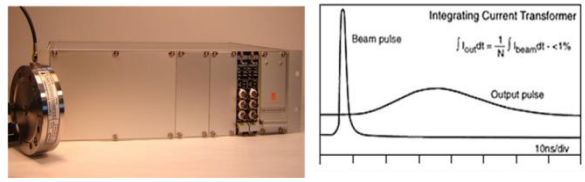

Figure 3. Integrating current transformer (ICT).

CONTROLS INTERFACE FOR DIAGNOSTICS

Diagnostics control subsystem will conform to NSLS-II control system standards. It will be EPICS-based and the preferred operating systems for IOCs (Input / Output Controller) are RTEMS (Real-Time Executive for Multiprocessor Systems) and Linux. For VME-based controls, the CPU board will be standardized as Motorola MVME3100. Whenever possible, diagnostics controls will use commercial off-the-shelf hardware to reduce cost as well to achieve better reliability. Although the NSLS-II Linac and Booster are turn-key solutions provided by vendors, the intention is to standardize the diagnostics controls for the whole machine. Each type of beam monitor requires controllers to process its output signal. The proposed electronics for the above groups and associated EPICS IOC platform are listed in Table 4.

BPM CHAMBER ASSEMBLY

The BPM system tracks the position of the beam by measuring the levels of the signals induced on the BPM pick-up electrodes. The signals are delivered to the receivers inside the temperature controlled rack outside the tunnel. The processed beam position is available to the control system for the orbit readback. Transport line parameters affecting the design of BPM receivers include; RF frequency of 499.68 MHz, 1-150 bunches, maximum multi-bunch charge of 39 nC in 80 bunches, and maximum single bunch charge of 1.0 nC. The BPM pick-up electrodes will be placed on two types of vacuum chamber. The first type (Figure 5) has a round vacuum chamber with inner diameter of 40 mm; the second type (Figure 7) has an elliptical cross-section with vertical aperture of 40 mm and horizontal aperture of 90 mm.

Table 4: Controls Electronics and IOC Platform

Type	Controls Electronics	EPICS IOC Platform
WCM and FCT	Acquiris Digitizer DC252 (10 bit, 4-8 GB/sec)	CompactPCT/ RTEMS
DCCT and ICT	• Hytec 8002 carrier board • Hytec IP-ADC-8401 (8 channel, 16 bit, 100 kHz) • Agilent 3458 DVM (8.5 digit, 18 bit, 2 kS/s) • GPIB-to-Ethernet converter	VME/RTEMS
BPM	• I-Tech Libera Brilliance (baseline) • Custom electronics developed in house	Embedded Linux IOC
Gigabit Ethernet cameras	Motorola MVME 3100 (CPU)	VME/RTEMS
Stepper motor based	• PRO-DEX OMS MAXV-8000 • HYTEC MDS-8	VME/RTEMS
Instrument controls	Windows-based network/spectrum analyzer	X86/Windows
Digital I/O and DAC	• Hytec 8001 carrier board digital TTL I/O • Allen-Bradley compactLogix for 24V digital output • Hytec IP-DAC-8402 (16 channel, 16 bit)	VME/RTEMS

The pick-up electrodes can be mounted on the DelSeal CF flange with an SMA coaxial feedthrough (Fig. 4). A button mounted on the pin will have 15 mm diameter. For the elliptical vacuum chamber (40×90 mm) the distance between button centers will be at least 28 mm (defined by the CF flange size), while for the round vacuum chamber due to the 45° tilt of an assembly distance between centers will be about 28.3 mm.

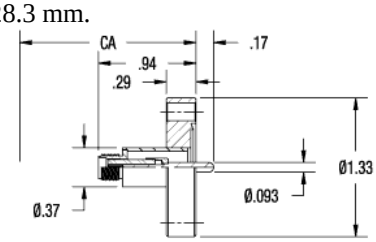

Fig. 4: Conflat flange with SMA coaxial feedthrough. Shown here is a possible model by MDC Vacuum Products. Dimensions in inches.

Round Chamber

Figure 5 shows the 40 mm round chamber assembly.

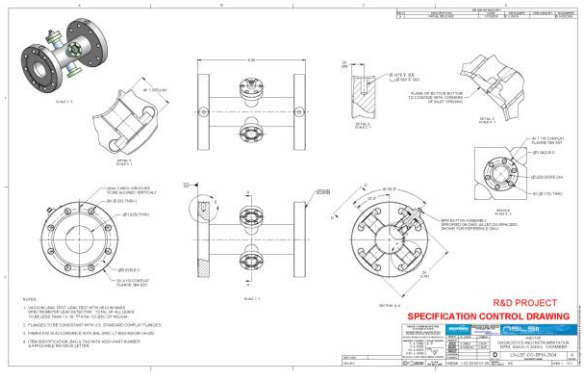

Figure 5: 40 mm round chamber assembly.

Sensitivity to the beam motion was found using a Matlab script for solving 2D electrostatic problems. The probe charge was placed in the different position inside a vacuum chamber and the induced charges on the buttons were found. For the round vacuum chamber, the ratio of difference over sum is shown in Fig. 6 for the horizontal and vertical planes.

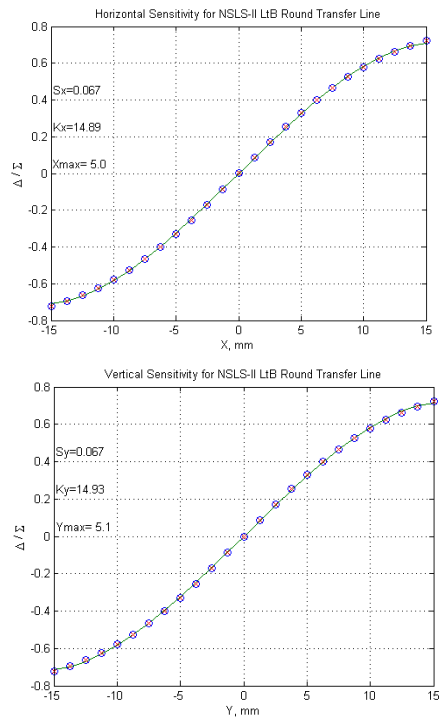

Fig. 6: Horizontal (top) and vertical (bottom) beam motion sensitivity for the round chamber. These figures have sensitivity numbers (Sxy), coefficients for calculating position from the measured BPM button voltages (Kxy), and limits were linearity drops by 10% from the central region. With centered beam, each button intercepts 12.4% of a passing charge.

Elliptical Chamber

Figure 7 shows the elliptical (40 x 90 mm) chamber assembly.

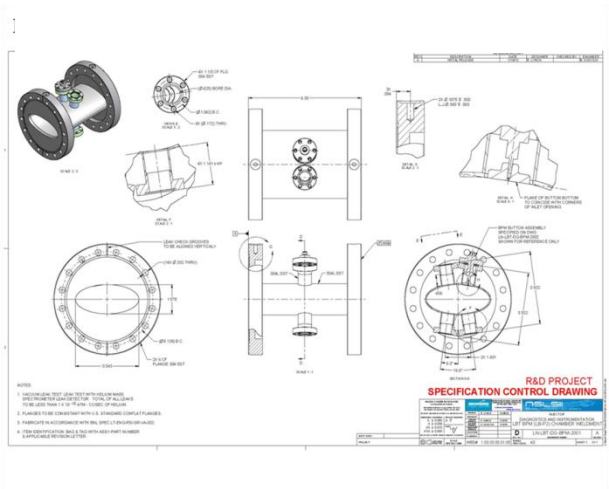

Figure 7: Elliptical (40 x 90 mm) chamber assembly.

For the elliptical vacuum chamber, the ratio of difference over sum is shown in Fig. 8. The sensitivity for beam motion in the horizontal plane is better but in the vertical plane is half as great. The latter fact can affect accuracy of vertical beam position measurements in the wide vacuum chamber.

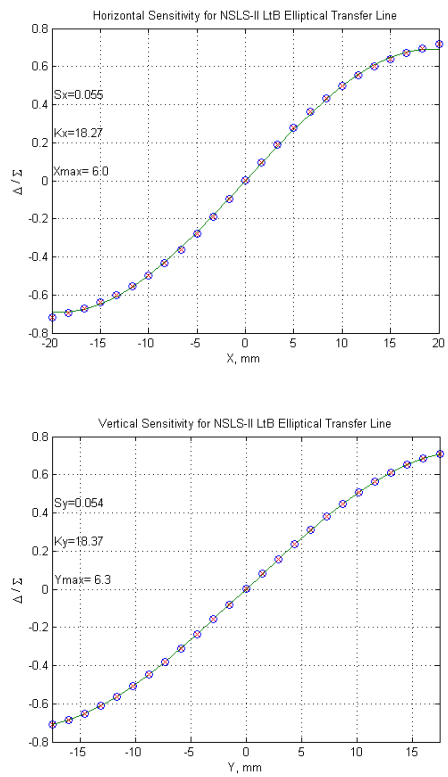

Fig. 8: Horizontal (top) and vertical (bottom) beam motion sensitivity for the elliptical chamber.

With the centered beam, each button intercepts 11.6% of a passing charge. Using the value for the fraction of induced charge, the signal on the button was evaluated for the button with 2.5 pF capacitance and 1 nC single bunch (Fig. 9). The power level of 6.4 dBm at 500 MHz frequency is for CW beam with 1 nC in each bunch. For a single pass the duration of the signal will be extended by a RF front end filter. For Libera Brilliance it is approximately 300 nanoseconds (therefore it will not be able to distinguish between single bunch and long pulse modes). Previous tests showed that for a 1 nC single bunch, Libera Brilliance provides resolution of 10 microns with k=10 mm. In our case, due to the larger vacuum chamber size, sensitivity is lower. Nevertheless, we should be able to reach the specified parameters of 10 × 1.5 / 0.5 = 30 microns.

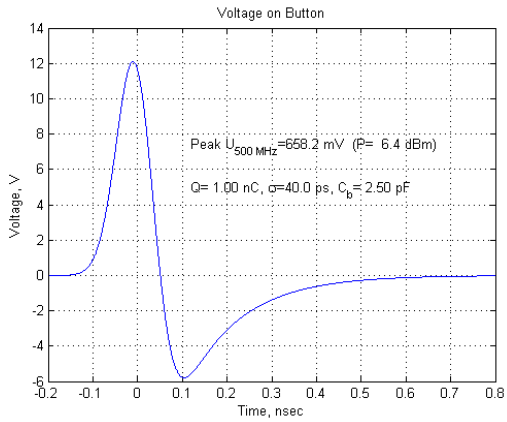

Fig. 9: Signal induced by a centered single bunch with 40 ps (rms) length and 1 nc charge on a button in the elliptical chamber.

REFERENCES

1. BNL-82306-2009-CP, “Beam Transport and Diagnostics for the NSLS-II Injection System” PAC09 Conference (Vancouver, Canada).
2. ”Preliminary Design of Beam diagnostics Control Systems” NSLS-II Controls Group (BNL).
3. “Injector Diagnostics and Instrumentation” BPM Button Assembly. BNL DWG # LN-LBT-DG-BPM-2002revA (BNL).
4. “Injector Diagnostics and Instrumentation” LBT BPM (LB-P1) Weldment BNL DWG # LN-LBT-DG-BPM-2001revA (BNL).
5. “Injector Diagnostics and Instrumentation” BPM Button Assembly (40mm x 40mm) BNL DWG # LN-LBT-DG-BPM-2004revA (BNL).
6. “Injector Diagnostics and Instrumentation” BPM Button Assembly (40mm x 40mm) BNL DWG # LN-LBT-DG-BPM-2004revA (BNL).
7. “Injector Diagnostics and Instrumentation” BPM Button Assembly Requirements Doc BNL DWG # LT-EL-IS-BD-LTB-0005-01 (BNL).
8. “Injector Diagnostics and Instrumentation” Integration LB-P1-BPMB BNL DWG # LT-EL-IS-BD-LTB-0005-08 (BNL).
9. “Beamline and Injection Systems Design” NSLS-II DOE Status Review Feb. 2010 (BNL).

BEAM INSTRUMENTATION REQUIREMENTS FOR THE HINS PROGRAM AT FERMILAB*

J. Steimel#, V. Scarpine, R. Webber, M. Wendt, FNAL, Batavia, IL 60510, U.S.A.

Abstract

A linear accelerator test facility called the High Intensity Neutrino Source (HINS) has begun operating at Fermilab. The goal of this program is to test new technology for the front end of an intensity frontier linac. Some of the new technologies that will be tested include: operation of multiple cavities from a single RF source using high-power vector modulators, round beam transport using superconducting, solenoidal focusing, accelerating beam with spoke cavities, and a transition to superconducting RF cavities at 10 MeV. The testing has been split into four different stages: 2.5 MeV beam from the RFQ alone, acceleration through six room temperature cavities with quadrupole focusing, acceleration through 18 room temperature cavities with solenoidal focusing, and acceleration through the room temperature section plus one cryomodule of superconducting spoke cavities. Each stage focuses on testing the beam quality with a particular new technology. This paper describes the instrumentation necessary to quantify the beam quality for each stage of the program.

INTRODUCTION

The Fermilab HINS program is building a low energy, linear, hadron, test accelerator for intensity frontier applications. Figure 1 shows one of the original proposed designs for HINS as the front end for an intense neutrino source [1]. The program has since been descoped to provide an accelerator that will be used as test bed to study novel, linear accelerator components and techniques. Successful designs and techniques will be utilized in the front-end design of ProjectX [2], a long-term plan to increase proton flux to MW levels for long baseline neutrino experiments at Fermilab.

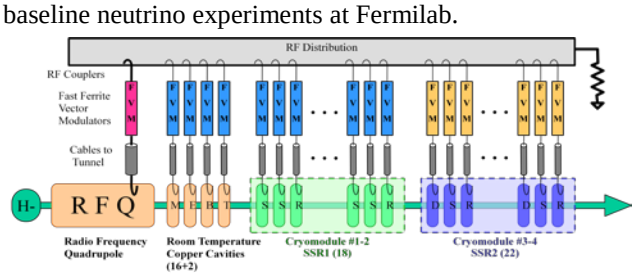

Figure 1: Original HINS proposal from 2006 showing a 90MeV beam line and four cryomodules.

There are four main concepts that the HINS program is currently prepared to test. First, it will test operation of multiple cavities from a single RF power source. One large RF power source is less expensive to procure and operate than many smaller sources. High power, ferrite vector modulators [3] (FVM) provide the fine amplitude and phase adjustments required for individual cavities. Second, it will test a lattice utilizing solenoidal focusing to propagate round beam. This lattice has been simulated to produce smaller beam halo at low energy than standard quad focusing [4]. However, the strength of the magnets needed for a practical solenoidal lattice require too much current for a normal conducting coil. These solenoid coils are superconducting. Third, the transition from normal conducting cavities to superconducting cavities will occur at 10 MeV. This is the lowest superconducting transition energy for any existing high-intensity hadron linac and is made possible by a spoke resonator cavity design [5]. This accelerator will also be the first to test any superconducting spoke resonator with beam. Fourth, the accelerator will be used to test advanced hadron linac instrumentation.

Testing of the different concepts will occur in four different stages based on resource availability. In the first stage, beam directly from the radio frequency quadrupole (RFQ) will be analyzed at 2.5 MeV. In the second stage, beam will be accelerated using six room temperature cavities with normal conducting quadrupole focusing. This will test beam operation with the FVMs. Once the cryogenic infrastructure is in place, the beam will be accelerated to 10 MeV using 18 room temperature cavities and superconducting solenoid focusing. This will test the beam halo and stability of the FVMs with many cavities. Once a spoke resonator cryostat is constructed, beam will be accelerated by the superconducting spoke cavities to test viability and stability of spoke cavity acceleration.

2.5 MEV RFQ

The 2.5 MeV beam line consists of a 50 keV proton source, a 2.5 MeV RFQ, a diagnostic line, and a beam dump. Figure 2 shows the layout of the 2.5 MeV diagnostic line. Beam studies on the RFQ were already performed with a simpler diagnostic line [6]. These studies verified the round beam profile from the RFQ. However, beam efficiency and beam energy were not precisely measured.

Ion Source

The HINS ion source is a duo-plasmatron, 50 keV, proton source [7]. The proton extractor is immediately followed by a low energy beam transport section (LEBT) consisting of two room temperature focusing solenoids, two dual plane dipole correctors, a beam stop, and a beam current toroid. Beam steering and emittance of the ion source are well characterized. The percentage of ions produced by the source that are protons is not as well

*Operated by Fermi Research Alliance, LLC under Contract No. DE-AC02-07CH11359 with the United States Department of Energy.
#steimel@fnal.gov

characterized. This parameter is important for determining the accelerating efficiency of the RFQ. The LEBT toroid measures the current due to all of the ion source ions, but the RFQ will accelerate only protons. A dedicated ion source experiment is planned to characterize the ion species before the RFQ beam studies continue.

Beam Energy Measurement

The initial plan for measuring the beam energy of the 2.5 MeV beam was to use beam time-of-flight measurements with the beam position monitors (BPM). However, there are no hard edges to the beam current pulse. The RF decay time of the RFQ is about 5 us, making correlating individual 3 ns buckets across the drift space nearly impossible. The only clean energy measurement came when the RFQ was intentionally sparked to provide a sharp, beam current profile.

To help verify the beam energy measurement, a spectrometer magnet will be installed in the diagnostic line. This will provide a sufficiently accurate bend to verify the absolute beam energy to within half a wavelength of the time of flight measurement. Once the absolute beam energy is confirmed, the time of flight measurement can be used to verify the average beam energy more accurately than the magnet. Using this beam energy information in conjunction with beam centroid information from the wire scanners, the dispersion of the magnet can be measured. The dispersion and difference in beam width between the straight ahead beam and bent beam reveal momentum spread.

Table 1: Instrument Acronyms for Figures

Acronym	Description
BPM	Beam Position Monitor
BSM	Bunch Shape Monitor (Longitudinal)
FD	Faraday Cup/ Dump
FFC	Fast Faraday Cup
HM	Halo Monitor
LW	Laser Wire
Q	Quadrupole Magnet
S	Horizontal and Vertical Slits
SEM	Secondary Emission Monitor
SM	Spectrometer Magnet
T	Toroid
WS	Wire Scanner

Emittance Measurement

The 2.5 MeV diagnostic line will include a quad triplet immediately after the RFQ. This will allow the beam to travel further down the beam line before space charge forces cause beam to fill the aperture, allowing for more instrumentation options. The non-linearities of the quad triplet should not have a significant effect on beam emittance.

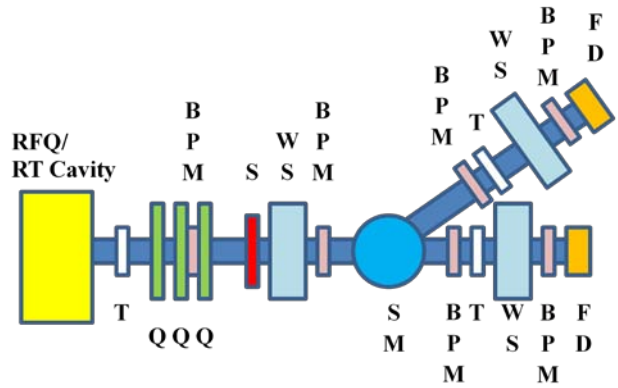

Figure 2: Proposed layout of diagnostic line for 2.5 MeV and six cavity test with protons.

Three wire scanners will be utilized for beam emittance measurements. Two other wire scanners are used downstream of the spectrometer magnet. One measures the profile of beam steered by the magnet, and the other measures the straight-ahead beam profile. This allows for possible momentum spread measurements and quantization of lower q/m particles that escape the RFQ. The upstream wire scanner also has slit scanners in front of it to allow measurement of beam emittance immediately after the quad triplet.

SIX CAVITY TEST

The next phase of the HINS program involves accelerating beam with room temperature cavities after the RFQ. The new lattice will utilize room temperature quadrupole focusing and six cavities (Fig .4). Most of the RF voltage in the cavities will go toward beam focusing. The final energy of the beam line will be approximately 3 MeV. The cavities will consist of two room temperature

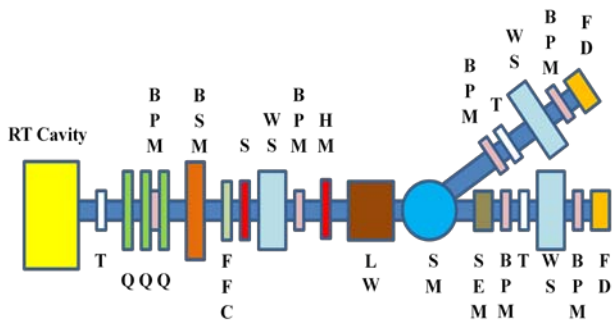

Figure 3: Proposed layout of diagnostic line for six cavity test with H^-.

buncher cavities and four room temperature triple spoke resonantors. A single klystron will power the RFQ and the six cavities, with individual phase and amplitude controlled by FVMs. The purpose of this configuration is

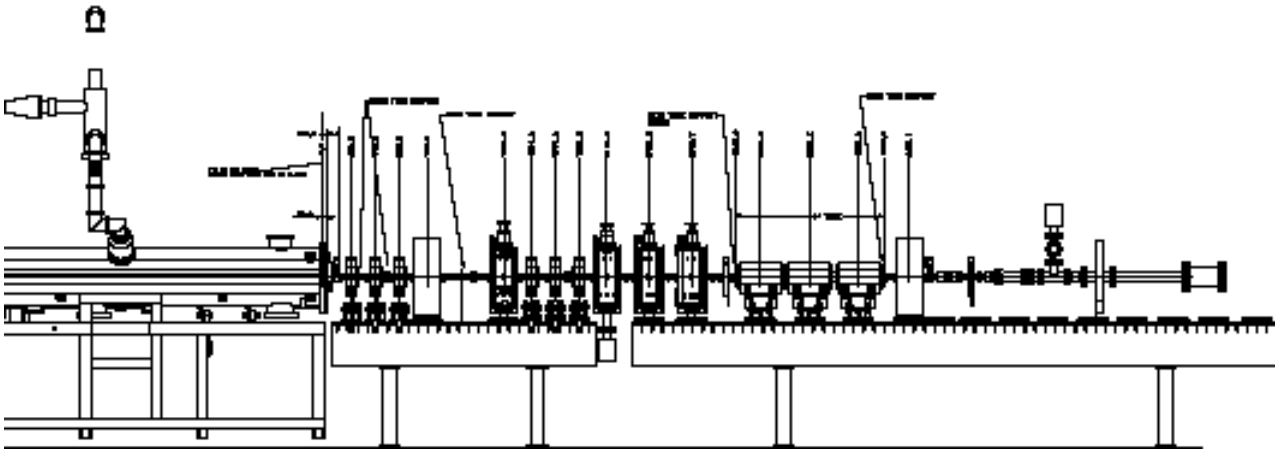

Figure 4: Proposed beam line layout for the six cavity test. The first large component is the RFQ, followed by three quadrupole magnets. The next item is a buncher cavities which is followed by the first of four room temperature triple-spoke resonators. This is followed another quadrupole triplet, three more spoke resonantors, and another quadrupole triplet. A second buncher cavity, diagnostic line, and dump finish out the beam line.

to verify beam operation through spoke resonators and to verify beam energy stability with FVM operation.

Initial Phase Instrumentation

The diagnostic line for the 2.5 MeV test will be repositioned to the output of the six cavity beam line. All of the measurements performed with the 2.5 MeV test will be repeated for the six cavity test. There will be special emphasis on the time of flight measurements because of between the BPMs will be operational for the six cavity test.

H^- Operation

The second phase of the six cavity test involves commissioning an H^- source. All of the present manifestations of ProjectX involve injecting multiple turns of beam into a synchrotron. This will require H^- acceleration and stripping at injection. There are few components of the six cavity test that operate differently with H^- or protons. However, the H^- operation offers a richer test bed for advanced accelerator instrumentation. For example, the spectrometer magnet may be used in conjunction with the straight ahead wire chamber to quantify ion neutralization. With H^-, there are plans to install and test a laser wire [8], longitudinal bunch shape monitor [9], secondary emission monitor, and halo monitor [10] (Fig. 3).

SUPERCONDUCTING LINAC TEST

As the specifications for ProjectX settle, the HINS program will need to align itself with the project's accelerator R&D. The next phases defined for the HINS program involve superconducting components and will require significant infrastructure investment. It will be important that these investments provide the tools to move Project-X forward. The following items are likely to be tested in some mode.

Superconducting Solenoids

The next phase of the HINS program, as heretofore

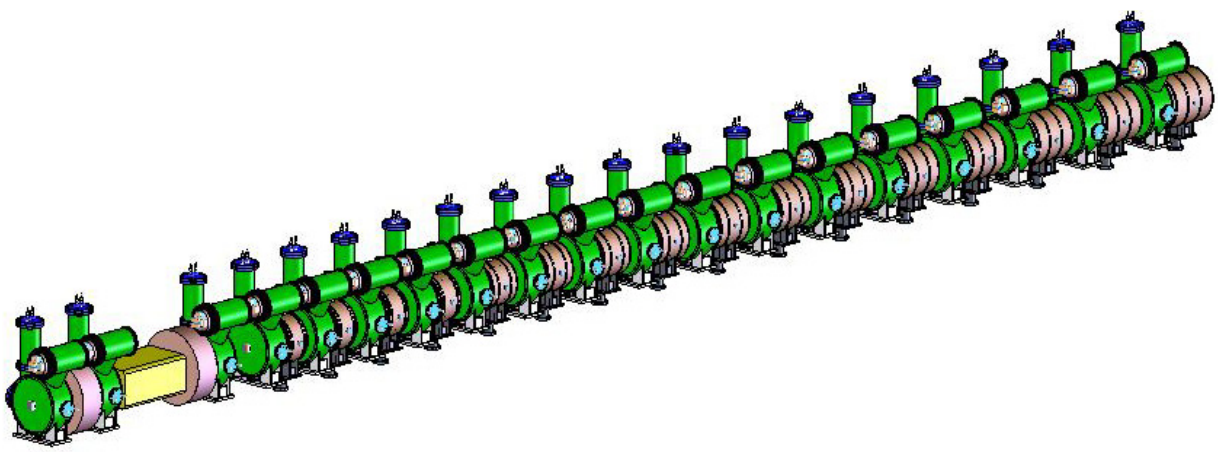

Figure 5: Proposed solid model of HINS 10 MeV room temperature cavity section. Green components are the superconducting solenoids.

planned, involved constructing a 10 MeV beam line with 18 room temperature cavities and superconducting solenoids as the focusing elements (Fig. 5). The solenoidal focusing keeps the beams round and minimizes the beam halo generation at low energies. Maintaining low emittance growth in the presence of space charge requires fast acceleration and strong focusing. The solenoid magnets required to maintain such a lattice have strengths on the order of 6T. Small errors in these magnets can have a substantial effect on the steering of such low energy beam. The main focus of this phase is to verify that the magnets can be aligned and/or corrected well enough to maintain stable beam position.

It is highly likely that some form of solenoid testing will occur within the scope of the HINS program. There are three possible versions that may be tested: a solo solenoid, a solenoid with dipole correctors, and a solenoid with a BPM. Regardless of the type(s) of solenoid(s) tested, correctors and BPMs will be a necessary part of the experiment. The BPMs will be used to verify the beam path through the center of the solenoid(s) and may also be used to help align multiple solenoids.

Figure 6: Picture of completed superconducting spoke resonator.

Superconducting Spoke Resonator Cryomodule

The final phase of the HINS program involves accelerating beam through a superconducting spoke resonator cryomodule. These cavity designs have never been tested with beam and could be very useful for high intensity, low energy acceleration. The HINS linac design called for pulsed cavity operation (1 ms at 10 Hz), however ProjectX has diverged from this and is likely to run continuous wave (CW). At present, any spoke resonator cryomodule test performed in the HINS facility will occur with a pulsed beam injector and the superconducting cavities running CW RF.

This phase is the culmination of the project. The cryomodule will include superconducting solenoid magnets that are similar to the magnets used in the room temperature section. The BPMs inside the cryomodule will be critical devices for determining proper beam steering and magnet alignment within the cryomodule. Measuring real time beam energy, halo formation, and beam neutralization (for H^-) are also critical measurements for extrapolating the efficiency and utility of a higher energy accelerating chain. All of the instruments used in the six cavity test will be used for the cryomodule test.

REFERENCES

[1] R. C. Webber et al., "Overview of the High Intensity Neutrino Source Linac R&D Program at Fermilab", LINAC08, Victoria, BC, Canada, September 2008, pp 36-40.

[2] S. Holmes, "Project X at Fermilab: Prospects and Plans", PAC09, Vancouver, BC, Canada, May 2009.

[3] R. Madrak & D. Wildman, "High Power 325 MHz Vector Modulators for the Femilab High Intensity Neutrino Source (HINS)", LINAC08, Victoria, BC, Canada, September 2008.

[4] P.N Ostroumov et al., "Beam Dynamics Studies of the 8 GeV Linac at FNAL", LINAC08, Victoria, BC, Canada, September 2008, pp 760-764.

[5] I. Gonin et al., "High Gradient Tests Results of 325 MHz Single Spoke Cavity at Fermilab", LINAC08, Victoria, BC, Canada, September 2008.

[6] V. Scarpine et al., "First Beam Measurements of the FNAL HINS RFQ", these proceedings.

[7] W.M. Tam et al., "Fermilab HINS Proton Ion Source Beam Measurements", PAC09, Vancouver, BC, Canada, May 2009.

[8] R. Connolly et al, "Laser Profile Measurements of an H- Beam", DIPAC01, Grenoble, France, May 2001.

[9] E. McCrory et al., "Longitudinal Emittance from the Fermilab 400 MeV Linac," LINAC96, Geneva, Switzerland, August 1996.

[10] S.G. Arutunian, "Vibrating Wire Sensors for Beam Instrumentation", BIW08, Lake Tahoe, CA, May 2008.

PHIL ACCELERATOR AT LAL – DIAGNOSTICS STATUS

J. Brossard#, F. Blot, S. Cavalier, A. Gonnin, M. Joré, P. Lepercq,
S. Letourneur, B. Mercier, H. Monard, C. Prevost, R. Roux, A. Variola,
LAL-CNRS-IN2P3/ Université Paris-Sud XI, bâtiment 200, 91898 Orsay, France.

Abstract

The "Photo-Injector at LAL" (PHIL : http://phil.lal.in2p3.fr/) is a new electron beam accelerator at LAL. This accelerator is dedicated to test and characterise electrons photo-guns and high-frequency structures for futur accelerator projects (like the next generation lepton colliders, CLIC, ILC). This machine has been designed to produce low energy (E<10 MeV), small emittance (ε # 10 π.mm.mrad), high current (charge # 2 nC/bunch) electrons bunch at low repetition frequency (ν_{rep}<10Hz) [1]. The first beam has been obtained on the 4th of november 2009. This paper will describe the current status and the futurs developpements of the diagnotics devices on this machine.

DESCRIPTION OF THE PHIL ACCELERATOR

PHIL is currently a 6 meters long accelerator with 2 diagnostics beam lines (see Figure 3). The direct beam line is mainly devoted to 2D transverse emittance and bunch length measurement. The deviate beam line is devoted to the mean and dispersion energy beam measurement. The injection in the deviated line is performed by a Tesla Test Facility (TTF) injector dipole.

The direct beam line is equipped with :

– 2 Beam Position Monitor (BPM).
– 1 phosphorescent transverse beam profile monitor.
– 1 Faraday Cup (FC).

One of the BPM is of the "button electrode" type, the other is of "re-entrant cavity" type. The beam profile monitor is a phosphorescent screen oriented at 45° from the beam axis. The screen is a cerium-doped yttrium:aluminium:garnet (YAG:Ce) crystal scintillator (300 µm thickness, 40 mm of diameter). Images have already been acquired on this first screen (located at 1925 mm from the photo-cathode). These preliminary measurements have shown that a millimeters size beam in both horizontal and vertical planes is already reachable (see Figure 2). The vertical and horizontal beam sizes are estimated using N differents images, after drak current substration (see Figure 1).

The FC is located at the end of the direct beam line.

The machine is also equipped with a false photo-cathode test pattern used to check the laser spot size and the position on the real photo-cathode.

Currently, the deviate beam line is only equipped with one Faraday Cup.

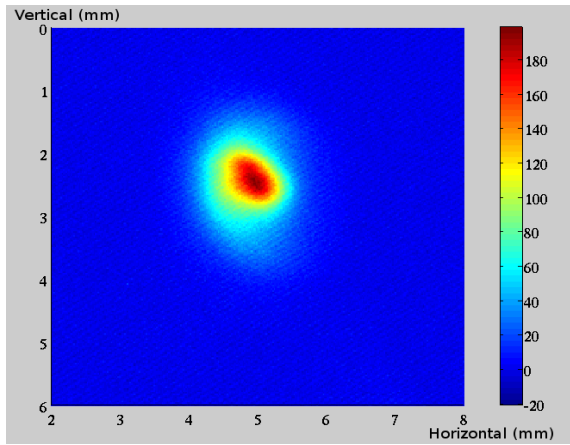

Figure 2: example of average transverse beam profile obtained at the first YAG:Ce screen station (1925 mm from the photocathode) using 10 images. For each images, the dark current has been substracted but not the jitter position.

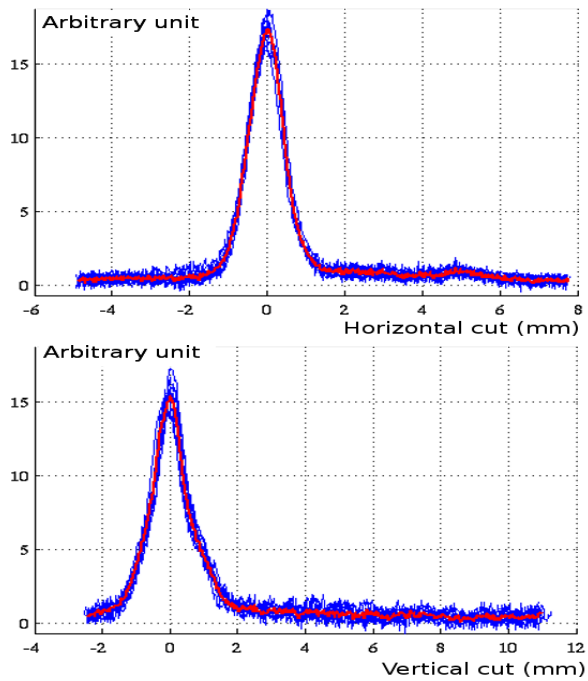

Figure 1: CCD intensity signal projected on horizontal and vertical axis (for 10 images) used for beam size estimation. The red curve is the average cut. On theses blues curves, the dark current and the jitter position have been substracted.

#brossard@lal.in2p3.fr

TRANSVERSE BEAM EMITTANCE, SIZE AND POSITION MEASUREMENTS

In 2010, three others phosphorescent YAG:Ce screen monitors will be installed on PHIL. The first one will be mounted at the entrance of the dipole. It will give important informations on the beam behaviour just before the dipole, which will be used to correctly prepare the beam for mean and energy spread measurement on the deviate line. It will also be used for 2D transverse emittance measurement using Kapchinskij-Vladimirskij equations and/or slit and/or pepper pot technique. The two others screens will be placed at the end of each beam lines, just before the Faraday cups. The one located on the direct beam line will be used to precisely define and control the transverse beam size and position for futurs users. The one located on the deviated beam line will be place just after the variable slit and will be used for cross-checked the mean and dispersion energy measurements done with the Faraday cup.

Each phosphorescent screen is associated with a versatile optical system (made of one or more achromatic lens) and a Giga-ethernet CCD camera (2 with 1/3" sensor format with 7.4 µm pixel size and 2 with 1/2" sensor format with 4.65 µm pixel size). The CCD dynamic is coded on 8 bit. In front of each camera a remote control optical density wheel is mounted in order to avoid pixel saturation during measurement.

CHARGE MEASUREMENT

For the charge measurement and the losses estimation, 2 Integrating Current Transformer (ICT) along the accelerator will be installed. One will be place at the exit of the photo-injector in order to characterise the beam charge at the beginning of the line, and one at the end of the direct beam line just before the BPM and the YAG:Ce screen. This will enable us to performed a beam charge, beam size and beam position measurement at the same time and location for the same bunch.

ENERGY SPREAD MEASUREMENT

The injector TTF dipole is a 60°[1] sector dipole with face angle of 18.24° [2]. The focal length L_D computed with the following formula

$$L_D = \frac{\rho * (c\,\alpha + \tan(u_1) * s\,\alpha)}{s\,\alpha - (\tan(u_1) + \tan(u_2)) * c\,\alpha - \tan(u_1) * \tan(u_2) * s\,\alpha}$$

where

$$s\,\alpha = \sin(\alpha) \quad \text{and} \quad c\,\alpha = \cos(\alpha)$$

with ρ=700 mm, α=60° and $u_1=u_2=18.24°$ is L_D=1242.70 mm. This distance is calculated from the center of the exit face dipole. A precise energy spread measurement require to inject - in the dipole - a beam without angular divergence and to monitor the horizontal beam size at a distance L_D after the dipole. In the current status, the girder supporting the elements of the deviate beam line is too short to performe such measurement. Thus, in the first commissioning part, the slit and the YAG:Ce screen monitor will be placed at a shorter distance, and energy spread estimation will be evaluated by comparison between measurement and the PARMELA software simulations [3]. The accuracy level of the energy spread measurement is – in this configuration - not yet established, and more numerical analysis are required.

[1] The deviation is performed in the horizontal plan.

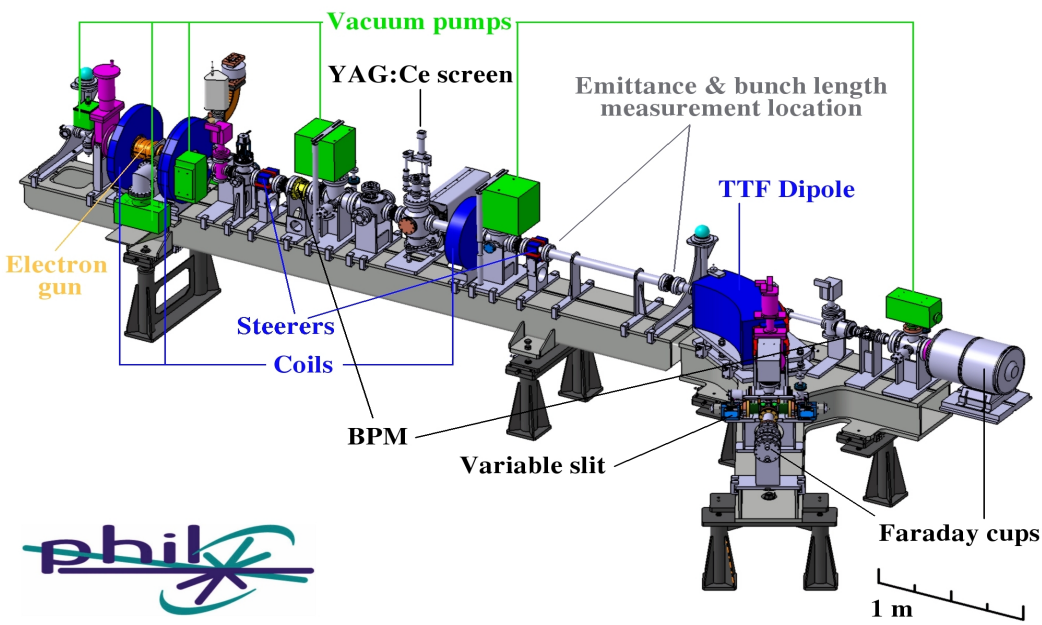

Figure 3: current and some futurs diagnostics on PHIL.

BUNCH LENGTH MEASUREMENT

A Cerenkov detector will be installed for bunch length measurement using a streak camera. The used streak camera is currently located in the laser room, wich is 17 meters away from the machine. This quite long distance associated with the streak camera type used migth be a limitation for the minimum signal level that can be detected. This device and the optical transport system have to be accurately studyed in order to determine the faisability and the accuracy of such measurement.

CONCLUSION

The “PHoto-Injector at LAL” (PHIL : http://phil.lal.in2p3.fr/) is a new electrons beam accelerator at LAL. The first electron beam generated with this machine is very recent (4th november 2009) and first beam measurements are currently used to test, calibrate and cross-checked existing diagnostics elements (beam position monitor, transverse beam profile monitor, charge monitor). Futurs diagnostics elements (energy spread, ICT, 2D transverse emittance, bunch length) are under study and we hope a complete installation of the news diagnotics for the end of 2010.

REFERENCES

[1] R. Roux & al., “PHIL : a test beamline at LAL”, Proceedings of EPAC 2008, Genoa, Italy.
[2] R. Chehab, “Progress in the Study and Construction of the TESLA Test Facility Injector”, Particle Acceleratopr Conference, Dallas, 1995.
[3] PARMELA software, from Los Alamos National Laboratory.

DESIGN STATUS OF THE DIAGNOSTIC SYSTEM FOR THE TAIWAN PHOTON SOURCE PROJECT

K.T. Hsu, C.H. Kuo, K.H. Hu, Jenny Chen, P.C. Chiu, C.Y. Wu, S.Y. Hsu

NSRRC, Hsinchu 30076, Taiwan

Abstract

The Taiwan Photon Source (TPS) is a 3 GeV synchrotron light source being built at the campus of NSRRC. Designs of various diagnostics are under way, and will be deployed in the future, to satisfy stringent requirements of TPS for commissioning, top-up injection, and operation. These designs, including beam intensity observation, trajectory and beam positions measurement, destructive profile measurement, synchrotron radiation monitors, beam loss monitors, orbit and bunch-by-bunch feedbacks, filling pattern, etc., are in the final design phase. Details of current status and implementation of the planned beam instrumentation system for the TPS will be summarized in this report.

INTRODUCTION

The TPS is a state-of-the-art synchrotron radiation facility featuring ultra-high photon brightness with extremely low emittance [1]. Civil construction was started from February 2010. The building will be finished in 2012. The campus of the NSRRC, which host the TPS and the existing 1.5 GeV Taiwan Light Source (TLS), is shown as Fig. 1. Machine commissioning is scheduled in late 2013. User service will start from 2014.

The TPS accelerator complex consists of a 150 MeV S-band linac, linac to booster transfer line (LTB), 0.15–3 GeV booster synchrotron, booster to storage ring transfer line (BTS), and 3 GeV storage ring. The latest generation diagnostic systems will help TPS to achieve its design goals. The storage ring has 24 double-bend achromat lattice cells with 6-fold symmetry. The main beam diagnostics related parameters for the booster synchrotron and the storage ring are summarized in Table 1.

Figure 1: Aerial view of the NSRRC campus. The upper left building is the existed TLS facility. The semi-underground building at upper right is the TPS facility.

Table 1: Major Parameters of the Booster Synchrotron and the Storage Ring

	Booster Synchrotron	Storage Ring
Circumference (m)	496.8	518.4
Energy (GeV)	150 MeV – 3 GeV	3.0
Natural emittance (nm-rad)	10.32 @ 3 GeV	1.6
Revolution period (ns)	1656	1729.2
Revolution frequency (kHz)	603.865	578.30
Radiofrequency (MHz)	499.654	499.654
Harmonic number	828	864
SR loss/turn, dipole (MeV)	0.586 @ 3 GeV	0.85269
Betatron tune ν_x/ν_y	14.369/9.405	26.18 /13.28
Synchrotron tune νs	-	0.00611
Momentum compaction (α_1, α_2)	-	2.4×10^{-4}, 2.1×10^{-3}
Natural energy spread	9.553×10^{-4}	8.86×10^{-4}
Damping partition $J_x/J_y/J_s$	1.82/1.00/1.18	0.9977/1.0/ 2.0023
Damping time $\tau_x/\tau_y/\tau_s$ (ms)	9.34/ 16.96 / 14.32	12.20/ 12.17 / 6.08
Natural chromaticity ξ_x/ξ_y	-16.86/-13.29	-75 / -26
Dipole bending radius ρ(m)	17.1887	8.40338
Repetition rate (Hz)	3	-

To get the benefits of the high brightness and small sizes of TPS sources, photon beams must be exceedingly stable, in position and in angle, to better than 10% of beam sizes and divergence. Table 2 gives the electron beam sizes and angular divergences for the selected TPS sources. The most stringent beam measurement and stability requirement will be for the vertical position at the 7 m straight for an insertion-device source (σ_y = 5.11 μm); this will require special consideration for measuring both electron and photon beams.

Table 2: The Electron Beam Sizes and Divergence

Source point	σ_x (μm)	$\sigma_{x'}$ (μrad)	σ_y (μm)	$\sigma_{y'}$ (μrad)
12 m straight center	165.10	12.49	9.85	1.63
7 m straight center	120.81	17.26	5.11	3.14
Dipole (1^o source point)	39.73	76.11	15.81	1.11

LINAC DIAGNOSTICS

The TPS 150 MeV linac system was contracted to the RI Research Instruments GmbH (formerly ACCEL Instruments GmbH) [2]. The schedule for delivery and commissioning is early 2011 at test site. The linac will move to the TPS building in late 2012 after TPS building available. Beam instrumentation comprises five YAG:Ce screen monitors for beam position and profile observation,

two fast current transformers (FCTs) [3] to monitor the distribution of charge and one integrating current transformer (ICT) for monitoring total bunch train charge. Wall current monitors (WCMs), which are formed by equally spaced broadband ceramic resistors, mounted on a flexible circuit board and wrapped around a short ceramic break, will give information on beam charge as well as longitudinal profiles of electron bunches. Linac diagnostics are summarized in Table 3. All of these diagnostics will be provided by the vendor. Acceptance test of the linac system will be performed at a temporary site near the TPS main building before its completion and moved to the TPS building later. It is also planned that beam position monitors (BPM) might be added between accelerator sections. These BPMs will be useful for RF phasing monitoring, feedback control and on-line beam position jitter observation.

Table 3: Linac Diagnostics

Monitor	Quantity	Beam parameters
YAG:Ce screen	5	Position, profile
WCM	1	Intensity distribution
FCT	2	Intensity distribution
ICT	1	Charge at exit of the linac

TRANSFER LINE DIAGNOSTICS

Planned diagnostics for the LTB and the BTS [1] are summarized in Tables 4 and 5 respectively. The YAG:Ce fluorescence screens will provide information on beam position and profile. The OTR screens are also to be used for high precision beam emittance and energy spread measurement at the diagnostic branch of the LTB and at a selected position in the BTS to avoid saturation of YAG:Ce screens. Integrating current transformer will provide information of beam charge pass LTB and BTS and hence on the beam losses during the injection cycle. The beam trajectory will be monitored with beam position monitors equipped with Libera Brilliance Single-Pass [4]; its functionality is similar to that of the BPM electronics for the booster and the storage ring, but it is equipped with aq high gain analogue board to improve its performance for single pass measurement.

Table 4: LTB Diagnostics

Monitor	Quantity	Beam parameters
YAG:Ce/OTR screen	6	Position, profile (1 at diagnostic branch). OTR screen will be adopted for the site of high precision profile measurement to avoid saturation of YAG:Ce screen.
FCT	2	Beam intensity
ICT	1	Beam charge
BPM and single pass electronics	7	Beam position
Energy define slit	1	1 pair of horizontal jar

Table 5: BTS Diagnostics

Monitor	Quantity	Beam parameters
YAG:Ce/OTR screen	3	Position, profile, booster extraction beam emittance
FCT	1	Beam intensity
ICT	2	Beam charge, installed at upstream and downstream of the BTS
BPM and single pass electronics	6	Beam position, relative intensity

BOOSTER DIAGNOSTICS

Booster diagnostics [1] will provide beam parameters including orbit, working tunes, circulating current and filling pattern, emittances for both planes, and bunch length. Planned diagnostics are summarized in Table 6. Fluorescent screens will be installed at the injection and extraction sections and at the other lattice cells to facilitate booster commissioning, troubleshooting and psychology needs—to see is to believe. The screen material will be YAG:Ce, which has excellent resolution of the beam image and exhibits high sensitivity and high radiation hardness. Booster orbit will be monitored with 60 BPMs with turn-by-turn capability. The BPM electronics will be the same as those in the storage ring to simplify maintenance. The sum signal from the receivers can be used to monitor fast history of the beam current.

Circulating current will be measured with Bergoz's NPCT, while bunch pattern will be monitored with a fast current transformer. For tune measurement, the electron beam will be excited with white noise using striplines. The beam response will be observed with a real-time spectrum analyzer connected to the dedicated BPM buttons with the front end. There will be an extra set of striplines for a bunch cleaning system and for users who need a specific filling pattern in the storage ring. Synchrotron radiation from a dipole will be used to observe the beam profile during energy ramping and emittance measurements. The capability to monitor bunch length with a streak-camera will be also provided.

Table 6: Booster Synchrotron Diagnostics

Monitor	Quantity	Beam parameters
NPCT	1	Averaged beam current
FCT	1	Filling pattern
BPM (4 button pick-ups)	60 (30)	Beam position
Set of striplines and amplifiers	2	Betatron tune, bunch cleaning system
YAG:Ce screen (Fluorescent screen)	6	Beam profile and position at injection, extraction, and at every lattice cells
Synchrotron light monitor, profile and streak camera (visible light)	2	Beam size (emittance), bunch length
Bunch cleaning system	1	-

STORAGE RING DIAGNOSTICS

The beam diagnostics system is designed to provide a complete characterization of the beam and the TPS storage ring, including averaged beam current, fill pattern, beam lifetime, closed orbit, working tunes, chromaticity, beam size, beam loss pattern, beam density distribution, emittance, bunch length, etc. A large number of beam monitors and devices will be installed in the storage ring. The types and quantities of these devices are listed in Table 7.

Table 7: Planned Storage Ring Diagnostics

Monitor	Quantity	Beam parameters
NPCT	1	Averaged beam current, beam lifetime
Sum signal of BPM buttons	1	Fill pattern, bunch current
BPM (4 button pick-ups)	168	7 BPM/cell
BPM (4 button pick-ups)	1	For bunch-by-bunch feedback pickups
Striplines	1	Betatron tune measurement
Transverse kickers and amplifiers	2	Horizontal and vertical kicker for transverse feedback and bunch cleaning usage.
YAG:Ce screen (Fluorescent screen)	1	Beam profile and position just after injection septum
PIN diode type beam loss monitors	4~6 per cell	Beam loss pattern
Scintillation loss monitor	24	High counting rate type beam loss monitor
Scrapers	2 sets per plane	1 set = 2 blades

Intensity monitor

A high precision averaged current measurement will be performed by Bergoz's NPCT [3]. The NPCT device provides a resolution of better than 1 $\mu A/Hz^{1/2}$ and has large dynamic range and bandwidth to make itself a versatile device for measuring lifetime and injection efficiency. Fill pattern of the storage ring observed from the sum signal of BPM buttons by wide bandwidth fast digitizer sampling at RF or a multiple of RF frequency will enable measurement of the bunch current to better than 0.5% accuracy. This information is sufficient for filling pattern control in top-up operation and various studies.

Electron Beam Position Monitor

Each cell will have five standard RF BPMs mounted on elliptical chambers, and two primary RF BPMs located in the ID straight section mounted on racetrack chambers. To achieve the highest level of orbit measurement resolution, the optimization of the button geometry to obtain a high resolution for both standard and primary BPMs is in progress. Prototype BPM equipped with 7 mm button diameter and 17.7 mm separations on the 60 × 30 mm elliptical chamber has been implemented. The BPM constant is around 13 mm in both planes were achieved with adequate linearity. The primary BPM is planned to install in 20 mm height racetrack chamber with monitor constants around 9 mm. The current generation standard BPM electronics—Libera Brilliance [4]—were chosen as the baseline design at the conceptual design phase. Updated BPM electronics platform equipped with more advanced parts and enhanced functionality are in serious consideration and being discussed with the possible vendor. Despite the performance of current generation BPM electronics can meet the stringent requirement of TPS, a new BPM platform is better to avoid obsolescence of parts and improve small defects in the existing products.

X-ray Beam Position Monitor

Up to two X-ray photon BPMs (XBPM) will be installed at each beamline. The electronics consists functionalities such as current to voltage conversion, range selection, bias, ADC, local signal processing, embedded EPICS, and delivery of slow data (~ 10 Hz rate) for control system access and fast data (~ 10 kHz rate) for feedback purposes. The fast data should be compatible with orbit feedback infrastructure. It can seamlessly be integrated with the orbit acquisition system and feedbacks. The BPM electronics will be embedded with EPICS for slow access form the machine control system side and beamline control system side. A commercial product like Libera Photon [4] might be a candidate with required functionalities. A prototype of Libera Photon has been tested intensively at the 1.5 GeV Taiwan Light Source [5].

Infrastructure for Orbit Measurement, Control and Feedback

Slow orbit acquisition will perform by channel access to the BPM platform embedded EPICS IOC up to 10 Hz rate. Fast orbit beam position will circulate around all BPM platform at a 10 kHz rate by using FPGA grouping scheme (e.g., Diamond Communication Controller or Gigabit Ethernet Grouping) or a new design. The orbit of the whole ring can be accessed from any BPM platform. Fast data from the XBPM will be integrated with the BPM systems in a seamless way.

The TPS will adopt a specially design high performance corrector power supply. The power supply will use analog regulator, adopt biased analogue PWM scheme to improve zero current crossover problem. The current sensing element is the LEM Danfysik Ultrastab 868-20I DCCT. Combining all of these schemes improves integrated noise level from DC to 1 kHz down to a few parts per million of the output full scale, corresponding to a nano-radian level kick for s slow corrector with maximum ± 600 μrad kick. Control of each cell's corrector will be through a specially designed 20 bits (or 18 bits) DAC module [6] as shown in Fig. 2. This module

will provide an EPICS CA interface via cPCI backplane of a standard EPICS IOC, for configuration and for setting and monitoring status. Up to four fast setting ports will be provided for a 10 kHz data stream. The four fast setting ports might configure as Rocket I/O and Gigabit Ethernet for different applications. The Rocket I/O is suitable for orbit feedback application with less overhead. The gigabit Ethernet interface to receive unidirectional UDP package via private Gigabit Ethernet can be used as global feed-forward applications.

The feedback calculation will be performed by the FPGA module in the BPM platform. This FPGA module will perform two functions: grouping the whole ring BPM data by using two counter-rotating redundant links around the ring; and serving as a feedback engine. BPM data grouping provides a way to distributed all BPM and XBPM data around the TPS storage ring at all BPM platforms at a 10 kHz rate. Orbit feedback computation will distribute to the FPGA modules and will be installed at the BPM platform in each cell. One or two sniffer (eavesdropping) nodes will be setup to capture orbit information with 10 kHz rate for more than 10 s of record time, and decimated data at lower rate with much longer record time will be supported for various applications and analysis. The functional block diagram of the orbit feedback infrastructure is shown in Fig. 3.

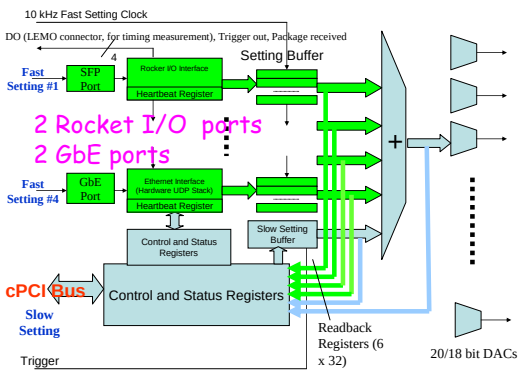

Figure 2: Functional block diagram of the corrector power supply control cPCI DAC module. The EPICS channel access is via backplane. The fast setting from feedback engines or feed-forward engines will sum with the EPICS CA slow setting.

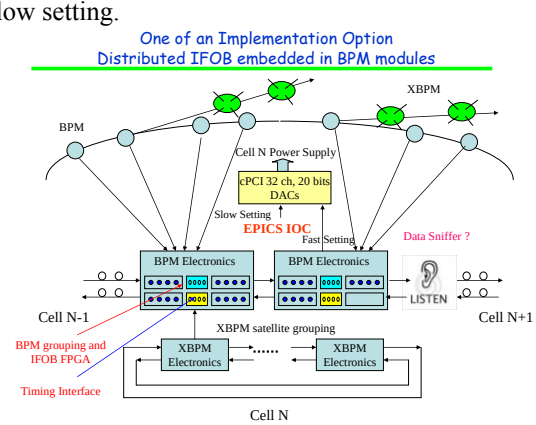

Figure 3: Functional block diagram of the orbit feedback infrastructure.

The DAC modules design will support feed-forward applications as well, such as global feed-forward orbit control and global skew quadrupoles feed-forward coupling control for elliptical polarized insertion devices operation. These feed-forward settings can be issued from EPICS IOCs or dedicated computers; more than 200 Hz rates are feasible. Beam excitation by noise can be performed by a similar scheme.

Bunch-by-Bunch Feedback and Diagnostics

Transverse coupled-bunch instability, mainly caused by the resistive wall impedance and other sources, will deteriorate beam quality. Bunch-by-bunch feedback is planned to suppressed instabilities to ensure TPS will achieve its design goals. The system will be implemented in vertical plane and horizontal plane. Planned transverse feedback kickers will adopt the SLS/ELETRA design and be compatible with the TPS vacuum vessel. A transverse signal pick-up will be used as an extra BPM and installed at a location of high beta function. Beside feedback functionality, the feedback electronics and software also support bunch oscillation data capture for analysis to deduce rich beam information, tune measurement, bunch clearing, beam excitation, etc.

Features of the planned system include the latest high dynamic range ADC/DAC (12/16 bits), high performance FPGA, flexible signal processing chains, flexible filter design, bunch feedback, tune measurement, bunch cleaning, various beam excitation scheme, flexible connectivity, and seamless integration with the control system. An on-line control interface to operate feedback system and off-line analysis tools should be included.

A functional block diagram of the planned bunch-by-bunch feedback system is shown as Fig. 4. Commercial feedback processor like Libera Bunch-by-Bunch from I-Tech [4] and iGp12 from Dimtel [7] are the candidates. Both have similar functionalities. Testing of the Libera Bunch-by-Bunch and the iGp are ongoing in the 1.5 GeV Taiwan Light Source.

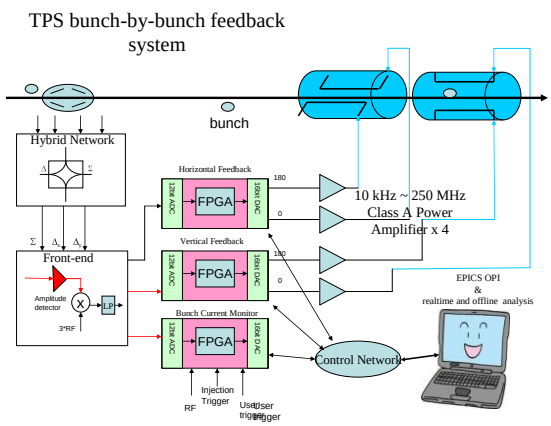

Figure 4: Functional block diagram of the bunch-by-bunch feedback system.

Beam Loss Monitor (BLM)

The storage ring plans to use coincidence PIN diode BLMs for loss pattern measurement. Scintillation detectors will also be used for high counting rate applications, such as loss mechanism selective experiments. Both PIN and scintillation type BLMs will work in counting mode. The data acquisition will be performed by the nearby EPICS IOC and can be performed synchronously. Distributed dosage measured on-line by using RADFET [8] is also under study. Fiber based Cerenkov radiation type BLMs are being considered.

Scraper

Two pairs of two-plane adjustable-position scrapers will be installed on the ring to be used both as protective devices and as diagnostic instruments for accelerator studies. One set of scrapers (H/V) will be installed in the dispersive section to measure the energy distribution of the electron beam. Another set will be installed in a straight section with zero dispersion in order to have information on the transverse size of the electron beam.

Synchrotron Radiation Diagnostics

The photon diagnostics for the TPS storage ring will utilize visible light and X-ray of the synchrotron radiation generated in a bending magnet. Planned photon diagnostics devices are summarized in Table 8. A cisible light beamline will be built to measure various beam parameters with a streak camera [9], CCD camera and interferometer. The streak camera operates at 250 MHz; synchroscan mode is preferred to observe beam behavior of consecutive bunches. Integrating the streak camera system with EPICS is preferred.

Two X-ray pinhole cameras, imaging the electron beam from bending magnets, is the baseline design for the TPS emittance measurement. They offer the required resolution and the dynamic range to measure the electron beam size accurately at all currents from below 1 mA to 500 mA stored beam current range. Optimization of the X-ray pinhole system will make it possible to measure very small beam sizes—a few microns typically. Its main function will include measurement of the electron beam energy spread and vertical beam size. Measuring the fill pattern by using time correlated single photon counting (TCSPC) is also being considered. An avalanche photodiode detector (APD) will be used to detect scattered X-ray photon as input of the TCSPC system. More than six orders of magnitude of dynamic range (10^6) can be achieved easily.

Table 8: Synchrotron Diagnostics

Monitor	Quantity	Beam parameters
X-ray pinhole camera	2	Emittance vertical and horizontal planes. Averaged profile as well as single turn profile
Time correlated single photon counting system (Visible light or X-ray)	1	Fill pattern, isolated bunch purity X-Ray APD
XBPM	1 or 2 per beamline	Position and angle of ID radiations
Visible light synchrotron light diagnostic station, Imaging and streak camera	1	Alternative beam size measurement (emittance), either imaging the vertical polarized synchrotron light or interferometer, bunch length
Streak camera	1	Visible beamline, Bunch length

SUMMARY

Beam diagnostics designs and implementation for the TPS are proceeding, as summarized in this report. The critical diagnostic systems, addressing beam stability and low emittance monitoring, are being investigated in the design phase. Major procurement are scheduled in 2011~2012. Optimizing the design, prototyping, and working out = specifications are current efforts. System integration is planned in 2013. Delivering a best diagnostic system to satisfy the stringent requirements of TPS is the goal.

ACKNOWLEDGEMENT

The author K.T. Hsu appreciates help from many experts, especially Robert Hettel, Michael Böge, Guenther Rehm, Greg Portman, Julien Bergoz, Dmitry Teytelman, Peter Milne, and the I-Tech team for brainstorming and discussion.

REFERENCES

[1] TPS Design Handbook, version 16, June 2009.
[2] Document 2008–BP-8067, “TPS Linac Technical Design Report”, ACCEL Instruments GmbH.
[3] Bergoz Instrumentation: http://www.bergoz.com.
[4] Instrumentation Technologies: http://www.i-tech.si.
[5] C.H. Kuo et al., “Diagnostics Update of the Taiwan Light Source”, these Proceedings.
[6] D-TACQ: http://www.d-tacq.com.
[7] Dimtel, Inc.: http://dimtel.com.
[8] RADFET: http://www.radfet.com/id4.html.
[9] http://www.optronis.com/streak-kameras.html.

DIAGNOSTICS UPDATE OF THE TAIWAN LIGHT SOURCE

C. H. Kuo, P. C. Chiu, Y. S. Cheng, Y. K. Chen, K. H. Hu, C. Y. Wu, Demi Lee, S. Y. Hsu, Jenny Chen, Y. T. Chang, C. J. Wang, Y.R. Pan, K.T. Hsu, NSRRC, Hsinchu 30076, Taiwan

Abstract

Diagnostics of the 1.5 GeV Taiwan Light Source (TLS) have been continuously upgraded since its operation started in 1993. The BPM electronics of the Taiwan Light Source (TLS) have been upgraded to Libera Brilliance in August 2008 to improve performance and functionality. Orbit feedback has also been migrated to a fast orbit feedback system to enhance orbit stability. Commercial photon BPM electronics were tested recently. A new-generation bunch-by-bunch feedback processor to improve beam stability was tested. Post-mortem diagnostic tools were gradually added to clarify reasons for beam trip. These upgrades contributed to improving beam quality and machine availability greatly.

INTRODUCTION

TLS was dedicated to the user in 1993. There have been several major upgrades recently, including a 2005 superconducting-RF upgrade and a 2008 BPM upgrade. The SRF system upgrade is improving beam quality and providing sufficient RF gap voltage for high current operation. Currently, the machine is operated at 1.5 GeV, 360 mA top-up injection. The BPM system upgrade also provides good diagnostics, which are essential to good quality machine operation. In the meanwhile, along with BPM upgrade, the orbit feedback system has also migrated to a fast orbit feedback system to enhance orbit stability, which is extremely important for a modern synchrotron light source.

To further improve beam availability, a beam trip event diagnostic has been deployed in the TLS. These diagnostic tools can clearly reveal and track causes of the beam trips and provide enough information to aid maintenance.

Libera Photon provides a good integration environment to correlate electron and photon beam motion. An earthquake detector has been installed lately as well, to record trip events caused by quakes. A new generation bunch-by-bunch feedback processor is also tested. All of these efforts above will be addressed respectively in the following sections.

CONTROL ENVIRONMENT ADAPTATION

The EPICS toolkits were chosen as the control system frameworks for the new 3 GeV synchrotron light source (Taiwan Photon Source, TPS). It has been decided that the control system for TLS should support both its existing control environment and EPICS as an upgrade-maintenance strategy to save resources and minimize development of the existing control system. New devices and/or replacement of the obsolete system are being considered to employ the EPICS directly. Gateways are implemented to exchange data between both environments and let them operate side by side. Modification for the control system has continuously proceeded during the last several years. New technology and improved maintenance are consequent advantages, along with manpower savings.

NEW BPM SYSTEM

Libera Brilliance [1] is employed to replace the existing BPM electronics for the TLS. Its integration started from 2007 until finished in August 2008 [2,3]. It was gradually deployed and performed without interfering with routine operation. There are 59 Libera Brilliances online, operating for more than one and half year. Adequate long-term reliability has been achieved.

Slow and Fast Data

New BPM system delivers high precision data at a 10 Hz rate for control system access with 0.1 μm resolution. The new BPM also delivers 10 kHz position data for fast orbit feedback applications and analysis applications with 0.2 μm resolution.

Turn-by-Turn Data and Post-mortem Data

Turn-by-turn data is also provided by Libera Brilliance. It is useful for accelerator physics study and helps to reveal fast beam motion such as beam excitation caused by the kicker and septum [2]. Post-mortem buffers as long as 256 kilosamples give turn-by-turn data before beam trip; this has proved to be a powerful diagnostic tool [2].

Some Observations by the New BPM System

The new BPM system unveils some effects that were not easily discovered systematically in the old BPM system. Several examples are summarized below.

A power supply with defects in its regulator might cause some 60 or 120 Hz strong perturbation. Fig. 1 is an example, showing a beam orbit motion that has 120 Hz power line noise. With the aid of the new BPM system, this perturbation was shown to come from a compensated corrector power supply of the insertion Device U9.

The leakage field of septum and kicker will also cause an orbit excursion and will have effects on the optical-radiation strength and precision. The experimental station should exclude the sampled data during injection by means of the provided gating signal. During the long shutdown of Spring 2010, mu metal was adopted to wrap the chamber and shield it from the field leakage. Figs. 2 and 3 show the orbit distortion caused by septum leakage before and after chamber shielding. The excursion is about half what it was before chamber shielding.

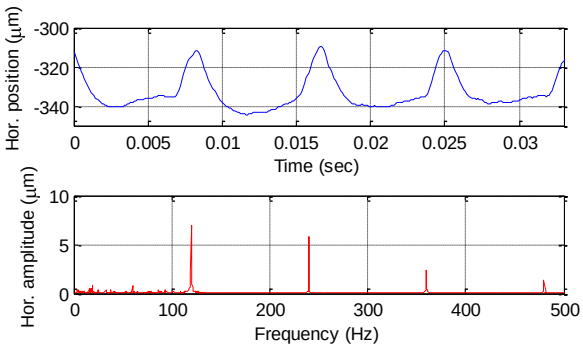

Figure 1: Orbit motion due to the ill power supply for undulator U9 end corrector.

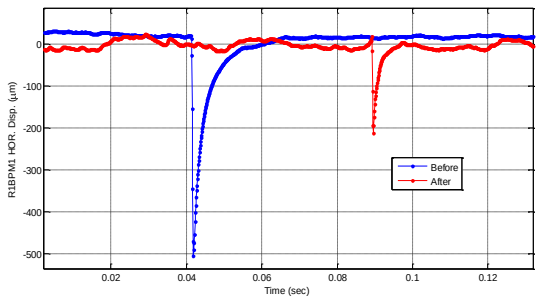

Figure 2: Orbit excursion at R1BPM1 caused by septum leakage before and after mu-metal was added.

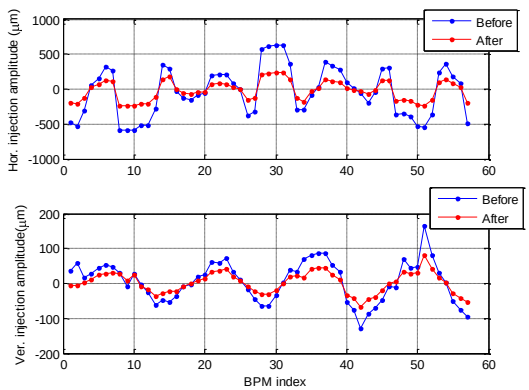

Figure 3: Amplitude of orbit distortion caused by septum leakage before and after septum shielding.

NEW ORBIT FEEDBACK SYSTEM

The infrastructure of the new orbit feedback system is shown in Fig. 4. The orbit controls for the horizontal and vertical plane are separated, which is different from the old version and increases flexibility and computation power. The reflective memory is employed to share fast orbit data without consuming extra CPU resources, and supports data acquisition for other subsystems. Libera Brilliance units are grouped together by a redundant multi-gigabit links via the LC optical links and copper "Molex" cables. This link supports data collecting among all Libera Brilliance units, assembling large packets via FPGA and sending the gathered data as unidirectional User Datagram Protocol (UDP) packages via Gigabit Ethernet. It reduce packet numbers in the network drastically, and eliminates jitter and package loss [3].

There are several kinds of corrector magnets installed in the TLS due to historical reasons. They have different system responses. To understand the compound response of the power supplies, correctors, vacuum chamber and the stored beam, pseudo-random binary sequence (PRBS) excitation is employed to measure system response and latency [3]. The responses of these correctors differ from each other. The bandwidth of some correctors can achieve to 80 Hz, but others may be below 30 Hz. Choosing the proper correctors for FOFB through measurements around the whole storage ring is thus necessary.

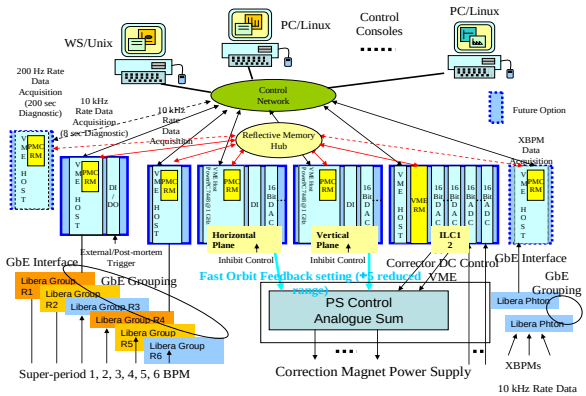

Figure 4: Infrastructure of the new orbit feedback system and the related subsystems.

The latency, which affects system performance, has been estimated. The I/O latency time is around 500 μs. Processing latency of the data acquisition and computation is the sum of several parts. Transfer BPM data, rearrangement and scaling takes around 40 μs; $S^{-1}U^T$ matrix (response matrix $R=USV^T$) and PID computation around 60 μs; V matrix computation and DAC settings 20 μs. The whole feedback loop takes about 120 μs. It implies that we can push feedback sampling frequency from the current 1.25 kHz to a higher frequency, under constrains of the current orbit feedback infrastructure, which is implemented in an economic way. The overall latency is about 620 μs; that includes calculation, chamber eddy current effect, BPM reading and corrector setting delay, etc.

Singular value decomposition (SVD) is used to invert the mapping of corrector excitation and orbit response in the feedback correction algorithm. To obtain a stable solution, Tikhonov regularization is also adopted.

The bandwidth and performance of FOFB were measured and estimated by PRBS excitation. The new FOFB should suppress noise to around 50 Hz (compared to the old 6 Hz) after all components are upgraded. The new BPM performance in wideband is better than before. As a result, vertical orbit stability can be reasonably expected to be submicron from dc to 50 Hz.

The feedback system improves beam stability, as shown in Figs. 5 and 6. The standard deviation of the 10 Hz rate data of all BPM vertical plane readings can be

reduced to 0.2 μm with feedback on (from 0.8 μm with it off) in the normal user mode. Horizontal and vertical orbit displacement can be less than 1 μm in SA readings.

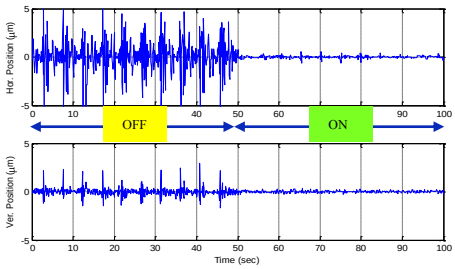

Figure 5: R6BPM7 10 Hz rate data for FOFB ON/OFF.

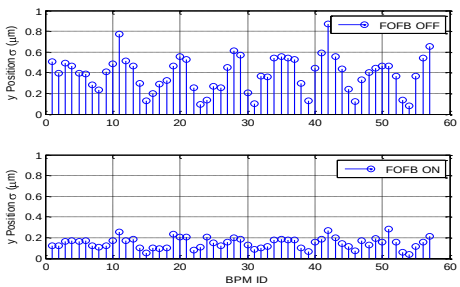

Figure 6: The standard deviation of vertical orbit displacement 10 Hz rate data between FOFB on/off.

Fig. 7 shows the R6BPM7 FA data spectrum with FOFB on and off. Orbit stability can be improved to sub-μm at this location with higher β function; thus overall RMS orbit stability should be sub-μm from dc to 50 Hz.

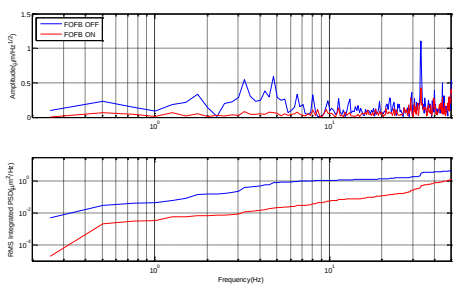

Figure 7: The spectrum and integrated PSD of R6BPM7 for FOFB on/off.

Fast insertion-device and phase changes are highly desirable. However, the old orbit feedback loop cannot effectively suppress the orbit excursion when they are faster than the limits of components and bandwidth. The wider bandwidth of the new orbit feedback loop allows increasing the motion speed. Fig. 8 (top) shows the 1 mm/s phase move of the EPU5.6. The orbit displacement is shown in Fig. 8 (bottom). It is clearly observed that the feedback loop can eliminate the orbit excursion.

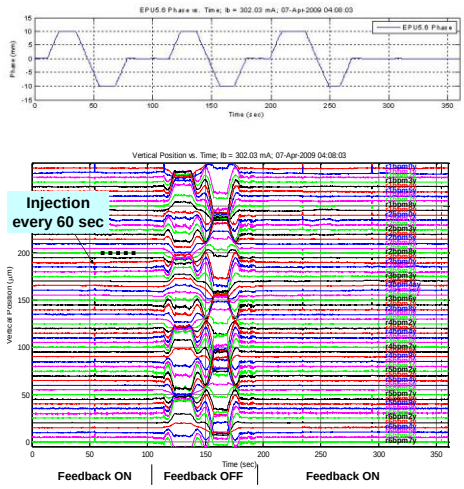

Figure 8: Effect of the new FOFB to suppress orbit excursion of 1 mm/sec phase change of EPU5.6. Top: History of the EPU5.6 phase motion at speed of 1 mm/s. Bottom: Beam position reading of all BPMs.

NEW PHOTON BPM ELECTRONICS-LIBERA PHOTON TEST

There are several kinds of photon BPMs with different designs at the beamline front ends of TLS. The electronics and data acquisition system cannot be integrated into the machine control system with the beamline or frond-end data acquisition in seamless ways due to historical reasons. Currently, one signal might split into several ways into different data acquisition systems in the current scheme. To provide better integration and efficient usage of the photon BPM, a single integrated system is under construction. The goal is to integrate with the machine control system to allow access from the beamline control system or the other clients, embedded current-to-voltage converter, embedded high performance ADCs, local computation capability, and integrated control system interface. Commercially available Libera Photon [1] satisfies all of these requirements and could integrate photon BPMs into control system seamlessly. Libera Photon combines several important components into one box.

Fig. 9 shows the observation at beamline 10. One of the vertical correctors (RCVCSPS21) was driven by a square wave. The relationship between photon BPM and Libera Brilliance reading are shown in Figs. 9 and 10. It can be observed that with FOFB off, the corrector changes will displace orbit position over 10 μm, while with FOFB on, the displacement is almost suppressed for the same corrector change. An injection transient is also clearly observed in Fig 10. The behaviour is quite similar to that of the electrical BPM in Fig. 2, where the field leakage disturbed both the electrical and the photon BPMs. Fig. 11 shows the photon displacement when the EPU5.6 phase was changed with/without FOFB. It can also be observed clearly that FOFB could almost suppress the

displacement to a sub-micron level from several hundreds of microns.

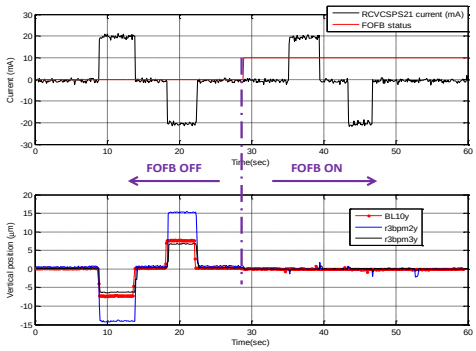

Figure 9: Beamline 10 photon BPM 10Hz reading signal related to the ring BPM.

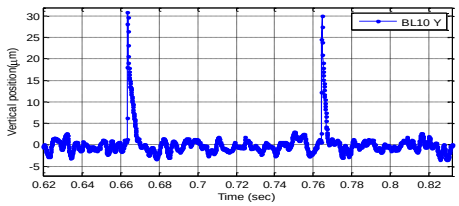

Figure 10: Beamline 10 photon BPM 10 kHz rate reading during injection.

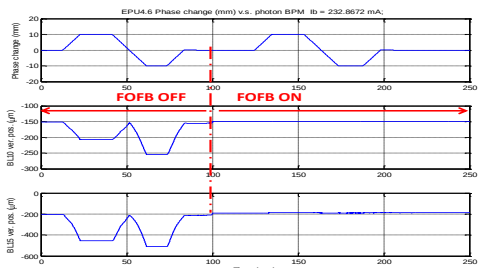

Figure 11: Beamline #10 & #11 photon BPM vertical position change vs. EPU 4.6 phase change with/without FOFB.

COMMISSIONING OF THE iGp BUNCH-BY-BUNCH SIGNAL PROCESSOR

Bunch-by-bunch feedback was deployed in 2005 in transverse and longitudinal planes [4]. To explore functionality of the new generation bunch-by-bunch feedback solutions and provide a better diagnostics, two kind of commercial products, iGp [5] and Libera Bunch-by-Bunch, are considered. Their tests are ongoing. Both systems provide good control system integration. It is planned to upgrade the bunch-by-bunch feedback system to enhance functionalities and get better performance.

Commissioning of the iGp for the longitudinal plane had taken only 20 min to enable the feedback back into operation based upon existing bunch-by-bunch feedback infrastructure. Noise floors were half those of the existing feedback system. The transverse feedback used opposite striplines in skew position as feedback kicker. A two-peak, 16-tap filter was designed as shown in Fig. 12. Instabilities of both transverse planes were suppressed successfully after 3 hours' effort. The iGP waveform interface is shown in Fig. 13. The lower right corner of Fig. 13 shows two notches in averaged spectrum corresponding to vertical and horizontal rejected betatron sideband. It can be a high resolution betatron tune monitor without exciting beam.

To explore bunch cleaning, the multibunch stored beam was killed, leaving one bunch as shown in Fig. 14. Due to low kick efficiency of the transverse excitation system, a vertical orbit bump was intentionally produced, exciting betatron motion of the unwanted bunches so they can be scraped by the ID cambers.

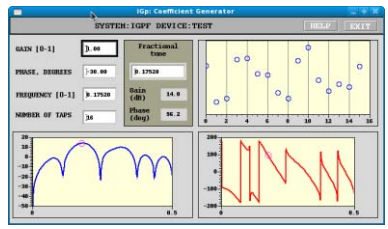

Figure 12: Two-peak, 16-taps filter for suppressing instabilities in vertical and horizontal planes using striplines installed at skew positions.

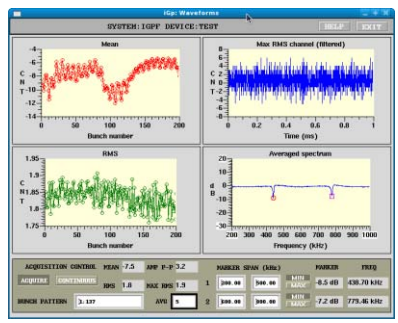

Figure 13: iGP for transverse feedback.

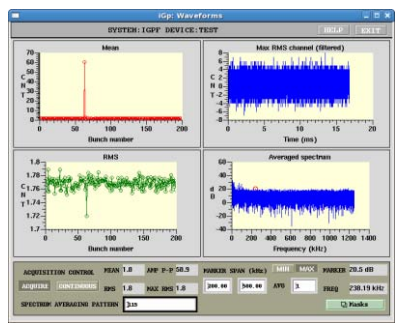

Figure 14: Bunch cleaning test; all bunches were killed except the selected bunch.

REMOTE WAVEFORM ACCESS

The TLS will share the same control room with the TPS in the future. To accommodate to this situation, remote access waveform data in the control room is

necessary. Waveform data includes microwave pulses, pulse magnet current waveform, beam signals, beam spectrum, etc. EPICS support was prepared for existing Ethernet-based equipment, such as oscilloscopes, spectrum analyzers, etc., to save limited resources. A dedicated EPICS soft-IOC was set up to support these. Specific displays were developed with EDM and Matlab toolkits. Commercial EPICS scopes from ZTEC [6] were tested also. Dedicated cables to send signals to control room won't have to be built in the future. Fig. 15 (a) shows the injection pulse magnet current waveform display at the control console. The oscilloscope is installed near the pulse magnet power supplies. Fig. 15 (b) shows the beam spectrum displayed at the control console.

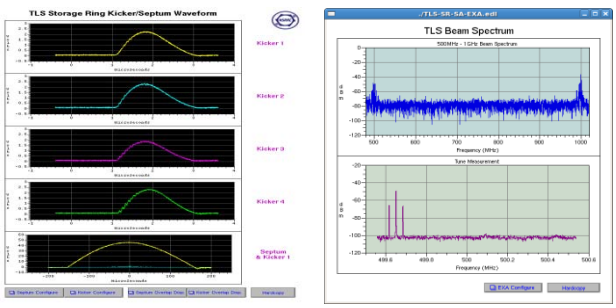

(a) (b)

Figure 15: (a) Storage ring injection kickers and septum waveforms. (b) Beam spectrum remote access.

POST-MORTEM DIAGNOSTICS

Besides beam stability, high availability of user service is another important issue. Analyzing the causes of trip events can help to improve reliability of subsystems and reduce troubleshooting efforts to minimize machine downtime to achieve high availability. Various diagnostics tools can capture beam trips, interlock signals of superconducting RF system, waveforms of the injection kickers, quench and interlock signals of the superconducting insertion device, and instability signals of the stored beam for post-mortem analysis, which is routine, especially for nontrivial events. Trip event analysis can point to subsystem improvements to avoid dangerous operation conditions, and consequently improve system reliability [7]. An earthquake detector has been installed to reveal the consequences of trips caused by the earthquake. The existing fault diagnostic system still cannot reveal all fault events, but the reliability of the TLS was improved by the new tools.

Fig. 16 shows what happened when an earthquake occurred at sea on the Pacific Ocean side of Taiwan. The P wave arrived at NSRRC 42 seconds later. The arrival time of the S wave lag about 30 seconds from the P wave. It means that the source is about 230 km far away form the TLS site. The SRF system trip happened 20 seconds after the S wave arrived. The trip was caused by the vibration of the Nb cavity, which resulted in deformation of the cavity and provoked a resonance frequency shift, which induced reflective power beyond the trip level.

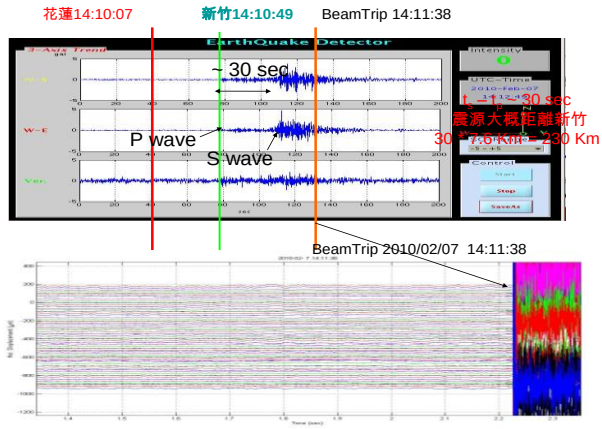

Figure 16: Earthquake signals record by the earthquake switch (top). Post-mortem data from BPM (bottom).

SUMMARY

Diagnostics of the TLS have been continuously upgraded using available resources to improve performance and avoid obsolescence. Strategies for upgrade-maintenance and minimum prepared spare parts led us to an opportunity to adopt updated technology and improve performance. Current efforts include integration of the photon BPM system, remote waveform access, new bunch-by-bunch feedback with much better functionality, and better integration with the control system.

ACKNOWLEDGEMENT

The author K.T. Hsu thanks help from many experts, especially Dmitry Teytelman, Boyd Shaw, and I-Tech team for brainstorming and discussion.

REFERENCES

[1] I-Tech website: http://www.i-tech.si/.
[2] C.H. Kuo et al., "Commissioning of New BPM System and its Related Diagnostic System for TLS", and "Fast Orbit Feedback System Commissioning of the TLS", Proc. of PAC 2009.
[3] C.H. Kuo et al., "BPM System and Fast Orbit Feedback System for TLS", Proc. of DIPAC 2009, Basel, Switzerland, May 25-27.
[4] K.H. Hu et al., "Commissioning of FPGA-based Transverse and Longitudinal Bunch–by-Bunch Feedback System for the TLS", AIP Conference Proceedings 868, Beam Instrumentation Workshop 2006, Batavia, Illinois, USA, 1-4 May 2006.
[5] Dimtel website: http://dimtel.com/.
[6] ZTEC website: http://www.ztecinstruments.com/.
[7] K.H. Hu et al., "Post-mortem Diagnostics for the Taiwan Light Source", Proc. of the Accelerator Reliability Workshop 2009 (ARW 2009), TRIUMF, Vancouver, B.C., Canada, January 26-30, 2009.

RECENT UPGRADE OF THE PITZ FACILITY*

J. W. Bähr[1], H. Al-Juboori, A. Donat, U. Gensch, H.-J. Grabosch, L. Hakobyan, M. Hänel, R. Heller, Y. Ivanisenko, L. Jachmann, M. A. Khojoyan, G. Klemz, W. Köhler, G. Koss, M. Krasilnikov, A. Kretzschmann, H. Leich, M. Mahgoub, J. Meißner, D. Melkumyan, M. Otevrel, M. Penno, B. Petrosyan, M. Pohl, S. Rimjaem, C. Rüger, M. Sachwitz, B. Schöneich, J. Schultze, A. Shapovalov, F. Stephan, M. Tanha, G. Trowitzsch, G. Vashchenko, L. V. Vu, T. Walther,† A. Brinkmann, K. Flöttmann, W.Gerdau, S. Lederer, L.Lilje, F. Obier, D. Reschke, S. Schreiber, DESY, Hamburg, Germany

J. Saisut, C. Thongbai, Chiang Mai University and Thailand Center of Excellence in Physics, Thailand

J. Knobloch, D. Richter, Helmholtz-Zentrum Berlin für Materialien und Energie GmbH, Berlin, Germany

P. Michelato, L. Monaco, C. Pagani, D. Sertore, INFN / LASA, Segrate MI, Italy

G. Asova, I. Bonev, L.Staykov, I. Tsakov, INRNE Sofia, Bulgaria

W. Sandner, I. Will, MBI Berlin, Germany

A.Naboka, V. Paramonov, RAS / INR Moscow, Russia

B. L. Militsyn, B. Muratori, STFC / DL / ASTeC, Daresbury, United Kingdom

M.Korostelev, The Cockroft Institute, Daresbury Laboratory, Warrington, United Kingdom

T. Vilaithong, Thailand Center of Excellence in Physics, Thailand

W. Ackermann, W.F.O. Müller, S. Schnepp, T. Weiland, TEMF, TU Darmstadt, Darmstadt, Germany

I. Ullmann,Universitaet Erlangen, Erlangen, Germany

J. Rönsch-Schulenburg, J. Rossbach, Universität Hamburg, Hamburg, Germany

Abstract

The Photo Injector Test facility at DESY, Zeuthen site (PITZ), is dedicated to develop and optimize high brightness electron sources for short wavelength Free-Electron Lasers (FELs) like FLASH and the European XFEL, both in Hamburg (Germany). Since October 2009 a major upgrade is ongoing with the goal to improve the accelerating components, the photocathode drive laser system and the beam diagnostics as well. The essential new feature in the running will be an in-vacuum 10 MW RF directional coupler to be used for the RF monitoring and control. In this context a significant improvement of the RF stability is expected. RF pulses of 800 microseconds with 10 Hz repetition rate will be used. The most important upgrade of the diagnostics system will be the implementation of a phase space tomography module (PST) consisting of three FODO cells each surrounded by two screen stations. The goal is an improved measurement of the transverse phase space at different charge levels. The upgraded facility will be described.

INTRODUCTION

High brightness electron sources for short wavelength Free Electron Lasers (FEL) are being developed and optimized at the Photo Injector Test facility at DESY, Zeuthen site [1]. In the recent running break major

* Supported by : EU contract: IASFS RII-CT-2004-506008

[1] Corresponding author:J.Baehr: juergen.baehr@desy.de

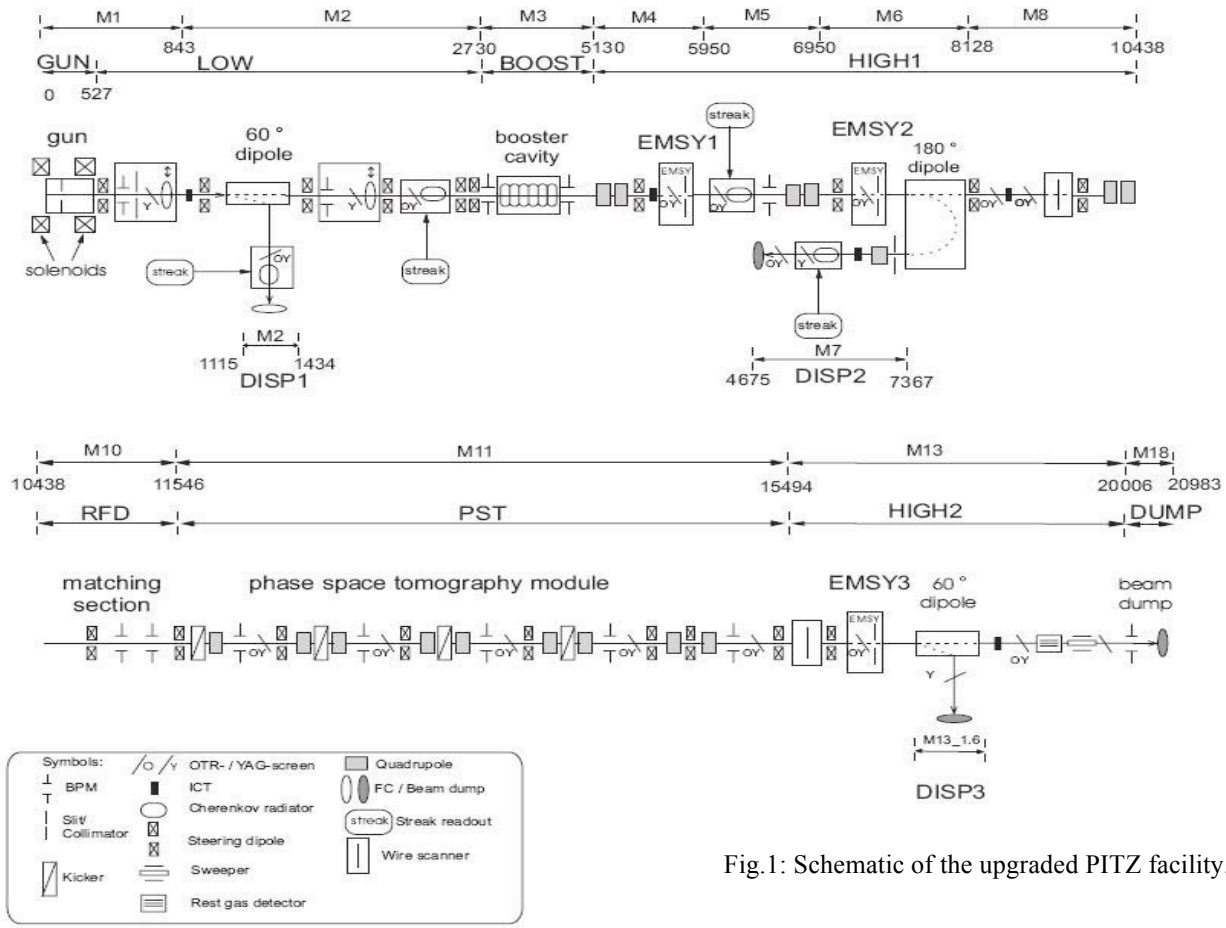

Fig.1: Schematic of the upgraded PITZ facility.

components are being replaced or newly installed. The major items of this upgrade are the exchange of the electron gun, the exchange of the booster cavity and the installation of a phase space tomography module. The schematic of the upgraded facility is shown in Fig.1. A gun of the same type as the previous one is installed now in PITZ. The conditioning has started and the gun will be characterized in 2010. Currently, a peak RF power of 2.7 MW was reached during gun conditioning.

NEW 10 MW IN-VACUUM RF COUPLER

In the previous PITZ setup [2] signals from 2 directional couplers (5 MW each) have been used to control the RF power in the gun cavity. This setup implies ceramic vacuum windows after each coupler and a T-combiner to mix both waves and feed them into the gun cavity. A possible cross-talk of both directional couplers and uncertainty in the gun cavity response complicated significantly the operation of the LLRF system. The feed-back loop became extremely complex, non-reliable and could not be used for the beam measurements. This resulted in large gun phase fluctuations since only the RF feed-forward has been applied [3].

To improve the control on the RF in the new PITZ gun (gun prototype 4.1) a newly developed 10-MW in-vacuum directional coupler has been installed [4] after the T-combiner. The main advantage of its usage compared to the previous RF feeding scheme is a direct control on the combined forward wave and on the wave reflected from the gun cavity. First signals from antennas of the 10-MW in-vacuum directional coupler are shown in Fig.2, where the amplitude (power) and the phase of gun forward and reflected pulses are presented. After the upgrade of the RF system, the optimization of the phase shifter position located in one of two arms of the 10-MW klystron became more straightforward. It is reduced to the maximization of the gun forward power amplitude while the gun is being kept close to the resonance temperature. Preliminary studies on the possibility of feedback loop implementation have been done at a power level of ~0.3 MW and different gun resonance temperatures. The feed-back applied at these conditions resulted in an improvement of the gun phase stability by a factor of about 3. Preliminary measurements of the RF phase jitter of the vector sum with a closed feed back loop yielded the RMS value of ~0.2 deg. More detailed studies on LLRF regulation are foreseen when the nominal RF power in the gun cavity (~7 MW) will be achieved.

THE NEW BOOSTER CAVITY

A new booster cavity based on a Cut Disk Structure (CDS) was developed and will be mounted at PITZ in spring 2010 [5]. The booster cavity will have an improved cooling system. It will be able to accelerate electrons above 20 MeV/c and will be suitable for long bunch trains. The booster cavity is under preparation to be inserted in the beam line of PITZ.

The photo injector arrangement is a full metal system and operates in the ultra high vacuum range. The residual gas should be free of hydrocarbons and the contribution to the total pressure of oxygen or oxygen containing gases should be negligible. Otherwise, one would get an oxidation or poisoning of the photo cathode and consequently reducing its life time. Presently, a vacuum conditioning of the booster is running to reduce the out-gassing rate. It is done by baking at a separated test arrangement. After that, the booster will be installed at PITZ whereby the pumping will start using turbo molecular pumps. Later an ion getter pump arrangement supplemented by titanium sublimation pumps will allow stable RF conditions.

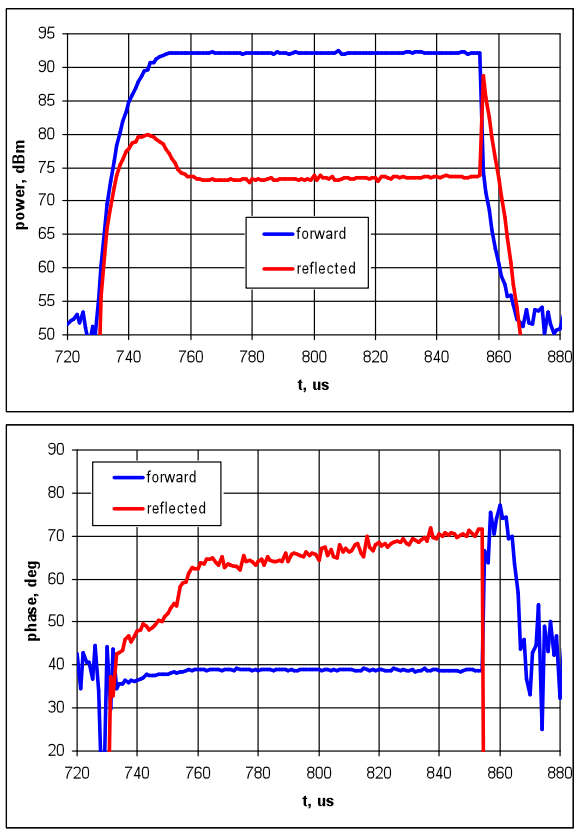

Fig. 2: Signals from 10-MW in-vacuum coupler - forward and reflected RF pulses. RF power in dBm (upper Fig.) and the phase along the RF pulse (below) have been measured at the power level of ~1.6 MW for the pulse length of 100 µs. No feed-back has been used for this measurement.

THE PHASE SPACE TOMOGRAPHY MODULE

The module consists of three FODO cells, whereby pairs are separated by a screen station. The number of screens, namely four, has been chosen in order to obey the requirement for as much as possible projections used for the reconstruction. The tomography theory proposes equidistant angular steps between each two projections, wherefrom the phase advance between two adjacent screens is 45 degrees. It has been shown in [5] that such a phase advance delivers the smallest emittance measurement discrepancy using a multi-screen method with four screens. An upstream cell with identical geometry can be used as well to increase the number of projections.

The desired systematic uncertainty of the measured emittance is below 10%. This corresponds to a relative deviation of the measured spot size on a screen of 10 %. As the geometry of the module is rather compact with short but strong focusing quadrupole magnets, the 10 % deviation of the spot size sets tight requirements on the mechanical alignment of the components. Those are given in the table 1 below:

Table 1: Components mounting tolerances in rms values.

Misalignment	Value	Units
Longitudinal quadrupole off-set	0.1	µm
Quadrupole roll angle	10	mrad
Quadrupole pitch angle	20	mrad
Quadrupole yaw angle	20	mrad
Longitudinal screen off-set	0.1	µm
Screen rotation around x- and y- axes	10	mrad

The positioning of the screen stations and quadrupoles is done by means of a laser tracker and a hexapod,; see Fig. 3. Five of those screen stations and eleven quadrupoles have to be installed in the module.

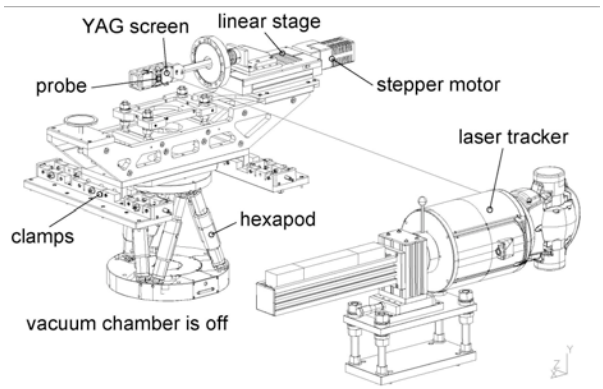

Fig. 3: The alignment of a screen station of the tomography section by a laser tracker and a hexapod.

IONIZATION PROFILE MONITOR

An Ionization Profile Monitor (IPM) [7] will be inserted in the rear part of the beam line, in the first step only for one projection of the beam profile. One of the advantages

of such a device is the possibility to work at high bunch charge and long bunch trains.

The IPM consists of an electrode, called the "Repeller plate", and a high spatial resolution detector (MCP). Both components have a definite potential. Additional electrodes are installed to provide an uniform electrical field between the Repeller plate and the MCP; see Fig 4. The residual gas inside the beam tube is ionized by the electron beam. The produced ions are accelerated in a homogeneous electrical field toward the MCP. After amplification inside the MCP, electrons hit a phosphor screen. A CCD camera records the phosphorescence to a computer for further evaluation.

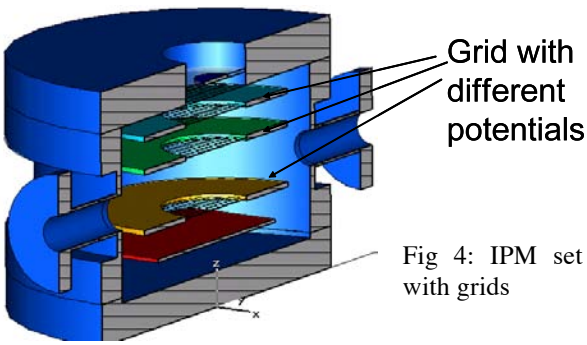

Fig 4: IPM set up with grids

LASER SYSTEM

For generation of flat-top pulses an Yb:YAG laser system is used. This laser generates long pulse trains that contain up to 800 individual "micropulses" in the train. A flat-top shape of the individual pulses of the train is accomplished by means of a multicrystal birefringent filter [8]. In this filter, the flat-top pulse shape is obtained by stacking several replicas of the input pulse, where the number of replicas is by one larger than the number of crystals used. The temperature of the individual crystals is precisely controlled in such a manner that the light field of the neighbouring replicas of the input pulse interfere constructively. High-quality flat-top pulses with rising and falling edges of approx. 2 ps duration are generated this way. In contrast to other arrangements [9,10], the produced pulses exhibit a precisely linear polarisation, which allows to further amplify them in a diode-pumped Yb:YAG amplifier chain and convert them to the fourth harmonics ($\lambda = 257.5$ nm) while maintaining the flat-top shape.

The duration of the pulses emerging from the bi-refringent filter depends on the effective number of crystals in it. Changing the pulse shape is accomplished by appropriately rotating the birefringent crystals in the shaper. Figure 5 shows the flat-top pulses of approximately 23.4 ps duration (FWHM) generated by using thirteen 2.7 mm thick YVO_4 crystals in the shaper following further amplification in Yb:YAG amplifier stages and after conversion to the fourth harmonics. An innovation of the laser beam line is the integration of a gated intensified CCD camera. A fraction of the UV laser beam propagating from the laser to the photo injector is split off and directed onto a fast intensified CCD camera.

The shape of the UV pulse was measured by cross-correlating it with a second femtosecond infrared pulse.

Like the photocathode, this camera is at an image position of the aperture that is used for generating the spatial flat-top profile. By selecting an exposure time of approximately 500 ns as well as an appropriate trigger, it is possible to measure the spatial intensity distribution for each laser bunch within the pulse train. These images will be used to extract position, size and intensity of the UV laser beam as well as their variations within the pulse train. Fig. 6 shows a first example of such a measurement.

The air conditioning in the laser room was improved with the goal to minimize oscillations of the temperature. The maximum temperature oscillation is now +/- 0.1 degree as specified.

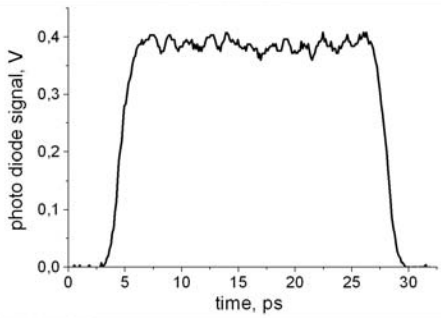

Fig. 5: Flat-top UV pulse of 23 ps duration produced by the photo injector drive laser at PITZ.

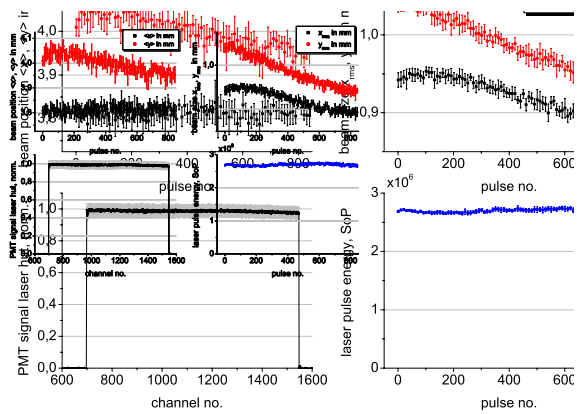

Fig. 6: Variation of beam position (upper left), beam size (upper right) and laser pulse energy (lower right) during a train of 850 laser bunches derived from the signal of the gated, intensified CCD camera. For comparison, the UV pulse energy as observed using a photomultiplier (PMT) on the laser table is also depicted (lower left).

THE BEAM INHIBIT SYSTEM (BIS)

The BIS is an independent hardware, which protects parts of the system from destruction due to false operation. The logic is processed by a Siemens SPS S7-300 [10].

Communication with the control system is via Ethernet UDP protocol. The BIS detects the state of magnets, vacuum valves, screens, cathode, shutters, Emittance Measurement Systems (EMSYs) and Faraday cups to define maximum pulse length for the klystron, charge and numbers of laser pulse. The operating modes can be predefined or self-detected from the state of the facility.

TV SYSTEM – CAMERA TESTS

The following cameras were tested in the lab:

- JAI (CCD): TM-2040, BM-141 [12].
- Prosilica (CCD): GC-13050, GC-1380, GE-1380 [13]
- PhotonFocus (CMOS): D1312-80, D1312-40 [14]

All cameras have a GigE interface. The Prosilica GC-1350 was measured each time as a reference camera. The main criteria in the comparison are sensitivity of the camera, shutter speed, signal to noise ratio and radiation hardness.

The camera measurement procedure is in two parts:

- Taking frames for different gain levels with closed cap, called dark frame, which gives a noise distribution in the camera itself.
- Taking frames for different gain levels from the object, which was illuminated by a lamp.

Also some other important features like gain range, possibility to adjust the black level, shutter control were studied. All cameras except PhotonFocus series have a possibility to control the gain at range approximately up to 24 dB. All cameras except PhotonFocus series and JAI TM-2040 have good noise distribution, mean and rms values. Unfortunately all Prosilica series have automatic black level control and look up tables made in such a way that they cut in a part of the signal. All the cameras have a good controllable shutter speed with a minimum shutter time of about 10 us. A radiation hardness test is foreseen in the near future. The summary plots are shown in Figures 7 and 8. To summarize we can say that the JAI BM-141 is the best choice for our measurements.

CONCLUSION

A major upgrade of the PITZ facility is ongoing. The electron gun is exchanged and under commissioning. A new accelerating booster cavity is under preparation to Be installed in the beam line. The upgrade of the beam diagnostics is ongoing mainly by installation of the phase space tomography module. The complete restart is assumed in summer 2010.

REFERENCES

[1] F. Stephan et al., Photo Injector Test Facility and Construction at DESY, FEL 2000, Durham.

[2] F. Stephan et al., Detailed characterization of electron sources at PITZ, yielding first demonstration of European X-ray Free-Electron Laser beam quality, Phys.Rev. Special Topics-Acc. And beams, 13, 020704, (2010)

[3] F.Stephan, M.Krasilnikov, "High Brightness Beam Measurements at PITZ", talk at Workshop on the physics and applications of high brightness electron beams, Maui, Hawaii,16-19.11.2009, http: //pbpl.physics.ucla.edu /HBEB/.

[4] MEGA Industries, H28 Sanford Drive, Gorham, ME 04038.

[5] V.V. Paramonov et al., Design Parameters of the Normal Conducting Booster Cavity for the PITZ-2 Test Stand.

[6] G. Asova et al., Phase space tomography diagnostics at the PITZ facility, Proceedings ICAP 2006, Chamonix, France.

[7] A. Hofmann et. al., EPAC2008, Genoa

[8] I. Will, G. lemz, Generation of flat-top picosecond pulses by coherent pulse stacking in a multicrystal birefringent filter, Opt. Express 16, 14922 (2008).

[9] S. Zhou, et al., Efficient temporal shaping of ultrashort pulses with birefringent crystals, Appl. Opt. 46, 8488-8492 (2007).

[10] I. Bazarov et al., Efficient temporal shaping of electron distributions for high-brightness photoemission electron guns, Physical Review ST – Accel. Beams 11, 040702 (2008).

[10] http://www.automation.sicmens.com

[12] http://www.jai.com/

[13] http://www.prosilica.com/

[14] http://www.photonfocus.com/

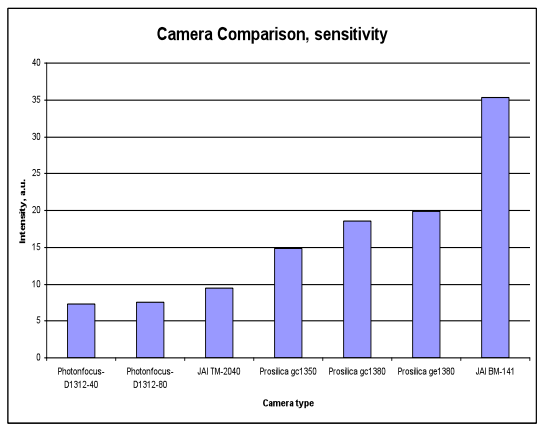

Fig. 7: CCD camera sensitivity comparison (arb. units).

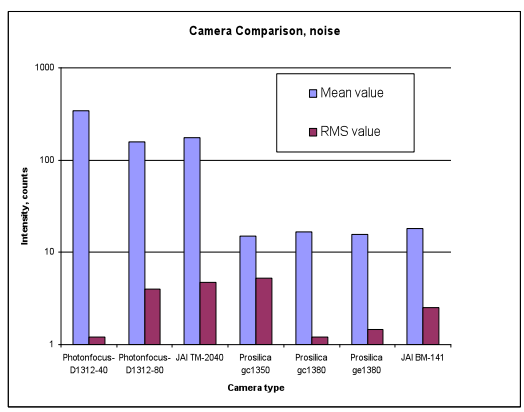

Fig. 8: CCD camera noise in counts.

BEAM BASED MONITORING OF THE RF PHOTO GUN STABILITY AT PITZ

M. Krasilnikov*, F. Stephan, DESY, Zeuthen, Germany

Abstract

The stability of the photo injector is a key issue for the successful operation of linac based free electron lasers. Several types of jitter can impact the stability of a laser driven RF gun. Fluctuations of the RF launch phase and the cathode laser energy have significant influence on the performance of a high brightness electron source. Bunch charge measurements are used to monitor the stability of the RF gun phase and the cathode laser energy. A basic measurement is the so called phase scan: the accelerated charge downstream of the gun is measured as a function of the launch phase, the relative phase of the laser pulses with respect to the RF. We describe a method which provides simultaneous information on RMS jitters from phase scans at different cathode laser energies. Fluctuations of the RF gun phase together with cathode laser energy jitter have been measured at the Photo Injector test facility at DESY in Zeuthen (PITZ). Obtained results will be presented in comparison with direct independent measurements of corresponding instability factors. Dedicated beam dynamics simulations have been done in order to optimize the method performance.

INTRODUCTION

The stability of the phase in the RF photo gun is one of the most important specifications for the linac based FELs. The requirements on the RF phase stability are derived from the desired electron beam parameters such as bunch-to-bunch and pulse-to-pulse energy spread, the bunch compression in the injector, and the arrival-time of the beam at the undulators.

The RF systems in the injector of the XFEL require tight control of the RF field in the gun. The RF launch phase stability is expected to be in the order of 0.1 deg for the phase [1]. The shot-to-shot stability in energy of the cathode laser pulses is expected to be 2% (RMS) for single pulses and 1% (RMS) averaged over a pulse train [1]. This determines the stability of the bunch charge, which could be slightly better than the cathode laser one due to space charge related effects.

The photo injector test facility at DESY in Zeuthen (PITZ) develops electron sources for FELs like FLASH and the European XFEL at DESY in Hamburg. The stability of the electron source is one of the central issues of the research program at PITZ. This paper presents a method for precise monitoring of the gun stability, including RF phase and the cathode laser energy.

*mikhail.krasilnikov@desy.de

PHOTO INJECTOR IN ZEUTHEN

The PITZ photo injector consists of an L-band RF gun supplied with a cathode load-lock system and solenoids for space charge compensation. The cathode laser system is able to generate trains of electron pulses including temporal and transverse laser beam shaping. Further on the electron beam line contains a booster cavity and a big variety of beam diagnostics systems for the characterization of the electron beam at different energies.

The RF gun cavity is a 1½-cell normal conducting copper cavity, operated at a resonance frequency of 1.3 GHz with a peak power of up to ~7 MW. The RF power to the gun is supplied by a 10 MW multibeam klystron through two equal output ports. In front of the gun the RF pulses from both waveguides are combined using a custom T-shape combiner. No field pickups are available for the current gun cavity design. Before 2010 the control of the RF feed to the gun was realized via two directional couplers installed before the T-combiner. Cross-talking of both directional couplers under not well-known resonance conditions of the gun cavity made the control of the RF field in the gun practically impossible. So, no routine feed back was available and only the feed forward had been used. After the facility upgrade in spring 2010 a 10 MW in-vacuum directional coupler has been installed after the T-combiner. Measurements of the combined RF pulses should provide a possibility for better control on the field in the gun closing a feedback loop for the amplitude and phase stabilization.

The PITZ photo cathode laser system is developed by the Max-Born Institute (MBI, Berlin) and is capable to generate trains of flat-top pulses with up to 800 micropulses with 1 MHz frequency at 10 Hz repetition rate. An individual micropulse with a typical duration of ~20 ps (FWHM) and very short rise and fall time (~2 ps) has a wavelength of 257 nm, the pulse energy provides the possibility to emit high charge electron bunches (up to several nC) from Cs_2Te cathodes.

The master oscillator (MO) is one of the major components of the timing system at PITZ. Its fundamental frequency of 9.027775 MHz is used for timing and diagnostics and to generate harmonics for the synchronization of the low-level RF (144^{th} harmonics – 1.3 GHz) and the photo cathode laser system (3^{rd} , 6^{th} and 144^{th} harmonics – 27, 54 MHz and 1.3 GHz correspondingly).

A detailed description of the diagnostics available at PITZ can be found in [2, 3]. Most related to the subject of this work are bunch charge measurements, monitoring of the RF phase and amplitude in the gun and the laser pulse energy diagnostics. The bunch charge at PITZ can be measured using Faraday Cups (FCs) and Integrating

Current Transformers (ICTs) [4]. Whereas the FC being a ground-insulated copper absorber intercepts the whole electron beam, an ICT monitors the bunch charge without interception. The 70-ns output signals from ICTs give the charge with a precision of ~30 pC [2] and are more suitable to measure the bunch charge in the range from 100 pC to several nC. Faraday cups can measure much lower charges down to several pC with a precision of ~ 2 pC [2].

Recently more reliable RF measurements became available at PITZ. They are based on signals of forward and reflected waves obtained from antennas of the 10 MW in-vacuum directional coupler. The vector sum phase can be used to estimate the phase jitter in the RF gun.

To monitor the cathode laser pulse energy an industrial energy meter is integrated in the cathode laser diagnostics system before the laser beam enters the vacuum beam line. The laser pulse energy fluctuations within the pulse train and shot-to-shot jitter is monitored by a photomultiplier tube (PMT).

PHASE SCAN

The RF gun phase scan for a given laser energy – measurement of the accelerated charge downstream of the gun as a function of the cathode laser launch phase – is one of the basic measurements to characterize emission properties of an RF photo gun. A phase scan measured at PITZ is shown in Fig.1. This measurement has been performed using the first FC (~0.8 m from the cathode). RF peak power in the gun is plotted at the right axis in Fig.1a, its mean value is ~1.09 MW. The main solenoid current of 210 A has been applied to focus beams with high energy at the FC location.

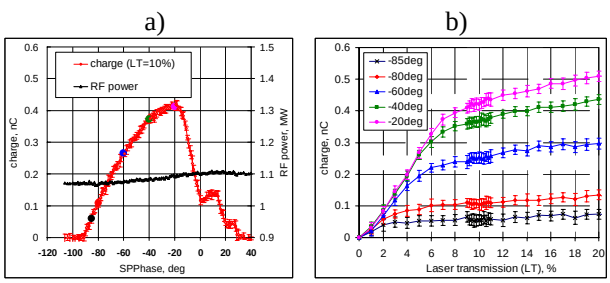

Figure 1: a) Measured phase scan for a bunch charge. The set point RF phase (SPPhase) is used for the horizontal axis. It has an arbitrary (but fixed) offset to the mathematical phase of the gun cavity resonator. b) Bunch charge measured for selected RF phases as a function of the cathode laser pulse energy (laser transmission - LT).

The shape of the phase scan is impacted from many parameters of the gun. The space charge density at the cathode due to the laser temporal and transverse profiles at the given laser pulse energy determines the charge dependence in the phase range from the field zero-crossing to the phase of the maximum beam energy gain from the gun (-90 deg to -40 deg in Fig.1a) [2]. A Schottky-like effect – a charge production enhancement due to the presence of a high electric field at the cathode – contributes in an additional slope in the phase scan for the phases corresponding higher RF field during the photo emission (-40 deg to -20 deg in Fig.1a) [5].

The control of the cathode laser pulse energy is realized at PITZ by means of a polarizer based attenuator. By its rotation the laser transmission (LT) can be tuned in order to adjust the energy of the laser pulse hitting the photo cathode. The laser transmission scans for selected RF phases are shown in Fig.1b. Initial (linear) parts of these curves are typically used for the quantum efficiency (QE) determination, their further (nonlinear) behaviour is strongly influenced by the space charge effects during emission.

PHASE SCAN FOR GUN STABILITY MEASUREMENTS

Fig.2a shows a simulated phase scan. Standard PITZ gun conditions have been applied: electric field of 60 MV/m at the cathode, a flat-top cathode laser temporal profile with 20 ps FWHM and 2 ps rise and fall time, ~0.4 mm RMS laser spot size. These and all other fixed parameters were taken from a simulation setup optimized to minimize the beam emittance in the PITZ photo injector. Additionally a Schottky constant of 0.005 nC/(MV/m) has been used in these ASTRA simulations [6]. A 2D phase scan – simulated accelerated charge as a function of the RF phase and the laser pulse energy – is shown in Fig.2b. The value $qe \cdot E$ used for one of horizontal axis can be treated as a charge which could be extracted from the cathode if no space charge or Schottky-like effects would be applied. Zero RF phase on these plots refers to the gun phase with maximum mean energy gain (the beam energy is plotted at the right axis in Fig.2a).

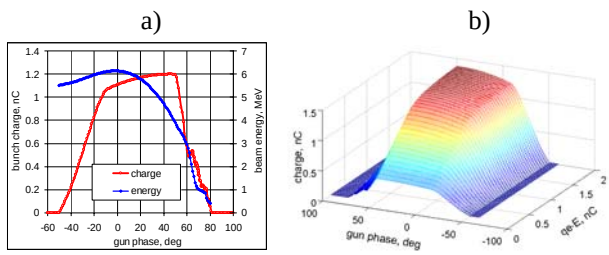

Figure 2: a) Simulated phase scan: bunch charge (left axis) and mean beam kinetic energy (right axis). b) 2D scan – bunch charge vs. the RF gun phase and the cathode laser pulse energy E, factor qe is related to the QE of the cathode.

The dependence of the bunch charge on the gun phase and the laser energy can be used to determine gun phase and laser energy jitters. The main assumption of the method is an independence of the jitters of the RF launch phase and the cathode laser pulse energy, so the distribution function of the RF launch phase ϕ and the

laser energy E can be presented by a 2D Gaussian distribution:

$$\mathrm{P}_2(\phi,E)=\frac{1}{2\pi\sigma_\phi\sigma_E}\exp\left(-\frac{\Delta\phi^2}{2\sigma_\phi^2}-\frac{\Delta E^2}{2\sigma_E^2}\right), \quad (1)$$

where $\Delta\phi=\phi-\phi_0$ and $\Delta E=E-E_0$ are RF phase and laser energy centred around the point of interest, σ_ϕ and σ_E are the RMS jitters of the phase and laser energy respectively. In order to find the probability distribution $P_1(Q)$ of the bunch charge one can integrate (1) along the curve of equal charge:

$$G(\phi,E)=\mathrm{Q}, \quad (2)$$

where $G(\phi,E)$ is a 2D charge phase scan (e.g. Fig.2b). Equation (2) determines for a given (fixed) charge Q a flat curve. Assuming a parameterization of this curve:

$$\begin{aligned}\phi&=F_\phi(Q,\xi)\\ E&=F_E(Q,\xi)\end{aligned}, \quad (3)$$

where ξ is a scalar parameter, the charge probability distribution can be found from:

$$\mathrm{P}_1(Q)=\int \mathrm{P}_2\left(F_\phi(Q,\xi),F_E(Q,\xi)\right)\cdot\sqrt{\left(\frac{\partial F_\phi}{\partial\xi}\right)^2+\left(\frac{\partial F_E}{\partial\xi}\right)^2}\,d\xi \quad (4)$$

A rough estimation of the dependence (2) is the Taylor expansion up to linear terms:

$$Q=\left.\frac{\partial Q(\phi,E)}{\partial\phi}\right|_{(0)}\Delta\phi+\left.\frac{\partial Q(\phi,E)}{\partial E}\right|_{(0)}\Delta E, \quad (5)$$

where partial derivatives are taken in the point of interest $(0)\equiv(\phi_0,E_0)$. Using equation (5) in the integration of (4) yields Gaussian distribution function for the charge fluctuations with RMS width:

$$\sigma_Q=\sqrt{\left(\left.\frac{\partial Q(\phi,E)}{\partial\phi}\right|_{(0)}\right)^2\sigma_\phi^2+\left(\left.\frac{\partial Q(\phi,E)}{\partial E}\right|_{(0)}\right)^2\sigma_E^2}. \quad (6)$$

The formula (6) can be used to estimate the jitters of the RF phase and the laser energy by measuring the charge jitter for various RF phases and different levels of the cathode laser pulse energy. In principle, two measured points (ϕ_{01},E_{01}) and (ϕ_{02},E_{02}) are sufficient to resolve the linear system:

$$\begin{pmatrix}\left(\left.\frac{\partial Q}{\partial\phi}\right|_{01}\right)^2 & \left(\left.\frac{\partial Q}{\partial E}\right|_{01}\right)^2\\ \left(\left.\frac{\partial Q}{\partial\phi}\right|_{02}\right)^2 & \left(\left.\frac{\partial Q}{\partial E}\right|_{02}\right)^2\end{pmatrix}\times\begin{pmatrix}\sigma_\phi^2\\ \sigma_E^2\end{pmatrix}=\begin{pmatrix}\sigma_{Q1}^2\\ \sigma_{Q2}^2\end{pmatrix} \quad (7)$$

in order to obtain (σ_ϕ,σ_E). Practically the matrix in (7) can be ill-conditioned or/and determined with a rather large discrepancy. More reliability can be achieved by taking into consideration also nonlinear behaviour of the function $G(\phi,E)$. This could be realized by producing a charge histogram (Fig. 3b) using a folding of the 2D Gaussian probability distribution (1) with the mapping function $G(\phi,E)$ (Fig.3a). A fitting of the obtained charge histogram to the measured one should result in the RMS jitter values (σ_ϕ,σ_E).

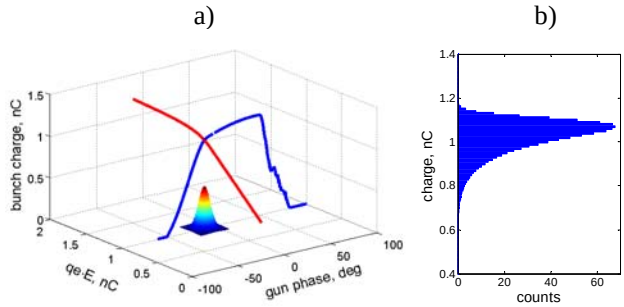

Figure 3: Simulated procedure of the gun phase monitoring: a) folding of the 2D Gaussian distribution with charge dependence on RF phase and laser pulse energy; b) charge histogram obtained from the folding.

Fig. 3 shows the simulations of the gun jitters for the gun phase -10 deg. To illustrate the method to measure the phase and the laser energy jitter 5 deg RMS phase jitter and 5% RMS laser pulse energy jitter were applied. The envelope of the charge histogram for these conditions, obtained by mapping the Gaussian probability function with a nonlinear surface $Q=G(\phi,E)$ is shown in Fig.4 with a blue curve.

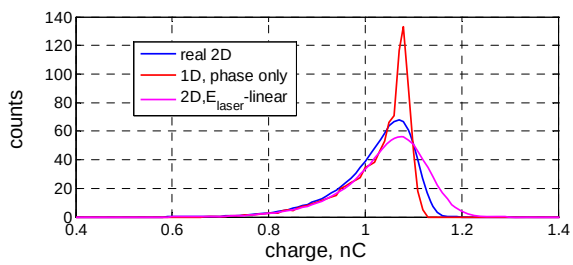

Figure 4: Simulated charge histogram, reconstructed using different approaches.

The red curve in Fig.4 depicts the charge histogram reconstruction if only phase jitter is applied (a similar approach has been described e.g. in [7]). It's clearly seen that the exclusion of the laser energy jitter from the reconstruction procedure results in significant underestimation of the charge jitter and therefore overestimation of the phase jitter if compared to measurements. The magenta curve corresponds to the 2D linear approach (see Eq. (5)). This approach overestimates the charge jitter and therefore underestimates the phase and the laser energy jitter if compared to measurements.

Indeed, the nonlinearity of the charge dependency (especially on the laser pulse energy) leads to the damping of the charge fluctuations.

The general approach is simultaneous simulations of the measured charge histograms at various gun phases by minimizing the functional:

$$\Phi(\sigma_\phi, \sigma_E) = \sum_n w_n \cdot \int \left| QH_n^{meas} - QH_n^{sim} \right| dq \qquad (7)$$

Here $QH_n^{meas}(q)$ and $QH_n^{sim}(q)$ are measured and simulated histograms for a set of chosen phases $\{\phi_n\}$. This approach is illustrated by Fig. 5, where five representative simulated charge histograms are shown.

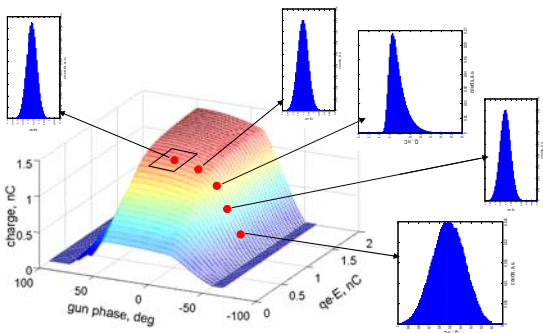

Figure 5: Charge histograms obtained for marked points in the 2D phase scan. Assumed phase and laser pulse energy jitters are 5 deg and 5% respectively.

To optimize the choice of the phases $\{\phi_n\}$ the linear approach (5) can be used. Simulated contributions to the charge fluctuations from the phase and laser energy jitters are shown in Fig.6. Whereas the gun phase of -10 deg corresponds to equal contributions from the phase and laser energy jitter to charge fluctuations, the charge fluctuations at the phase of -30 deg are fully dominated by the RF phase jitter.

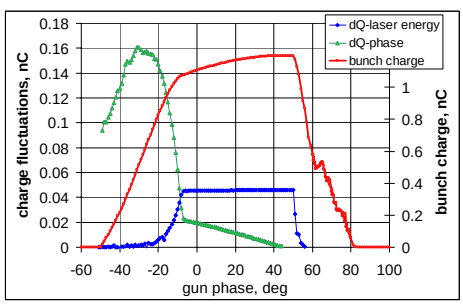

Figure 6: Simulated linear contributions to charge fluctuations from phase and laser pulse energy jitters $(\sigma_\phi = 5\,\text{deg}, \sigma_E = 5\%)$. The total charge is plotted at the right axis.

EXPERIMENTAL TESTS

A new gun cavity is under conditioning now at PITZ. The full expected RF power (of ~7 MW) is not yet achieved, therefore some preliminary stability monitoring tests have been performed at reduced peak power in the gun (~0.85 MW). The gun temperature has been tuned in order to keep the gun cavity strictly at resonance. The basic phase scan is shown in the centre plot at Fig.7. Estimated contributions from RF phase and laser pulse energy jitter are shown in the centre plot as well.

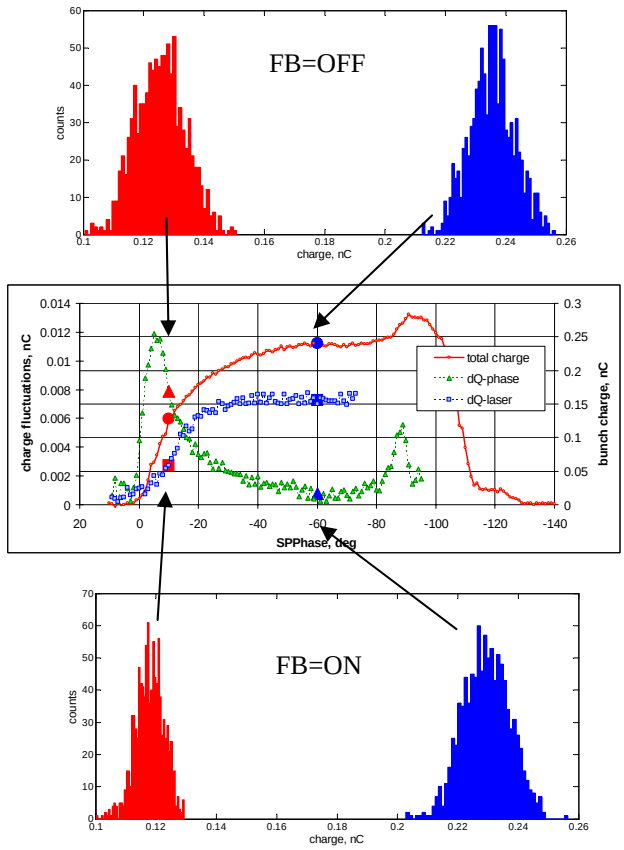

Figure 7. Experimental tests of the method for the opened (FB=OFF) and for the closed feed back loop (FB=ON) of the LLRF system applied to the gun.

An upper plot of charge histograms for various phases at Fig.7 have been measured with opened loop of the LLRF feed back, corresponding histograms with closed feed back loop are shown in the bottom plot.

The above mentioned procedure applied to these sets of measured data resulted in the laser energy jitter of ~11%. Closing the LLRF feed back loop reduced the RF phase RMS jitter from 0.82 deg to 0.32 deg. It should be noticed that all these preliminary measurements have been done at a reduced RF power in the gun, so the klystron was rather far from the saturation. Cross check measurements of the phase fluctuations have been done using a vector sum of signals from the 10 MW in-vacuum directional coupler and resulted in 0.43 deg and 0.16 deg phase jitter for the cases with and without feed back respectively.

The phase scan shown in Fig.1 has been used to test the general approach (7). Charge histograms have been fitted at four phases (SPPhase=-80; -60; -40; -20 deg). Corresponding histograms with fit curves are shown in

upper plot of Fig.8. The phase scan and contributions to the charge fluctuations from the phase and laser pulse jitter are shown in bottom plot in Fig.8. The applied method yielded an RMS jitter of 1.77 deg for the RF phase and 12.5 % for the laser pulse energy. No feed back has been applied for these measurements. It should be also mentioned that these measurements have been done using short Gaussian laser pulses with ~2ps FWHM, which is significantly shorter the nominal value (20 ps). This can partially explain rather high laser energy jitter, PMT measurements of the laser pulse energy on the laser table are in good agreement with the RMS value obtained from electron beam charge measurements.

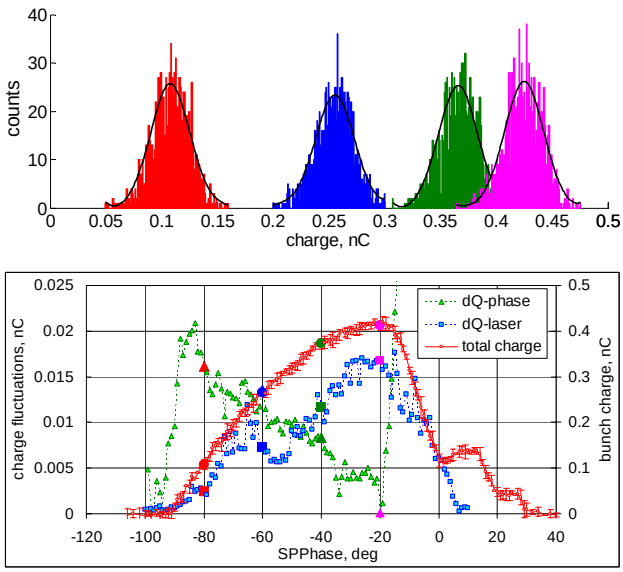

Figure 8. Results of the general approach to the gun phase and laser pulse energy jitter monitoring. The measurements have been performed at ~ 1.09 MW in the gun cavity with opened feed back loop.

SYSTEMATIC LIMITATIONS ON RESOLUTION OF THE METHOD

There are several sources of systematic limitations of the proposed method. The bunch charge measurements using FC or ICT with a scope readout is usually disturbed by the noise of the scope base line and by the jitter of the background due to the dark current fluctuations. A method to reduce the signal dependence on the dark current intensity can be based on a dark current envelope fitting corresponding to the actual peak power in the gun. This has to be tested in future when the nominal power level in the gun (7MW) will be achieved. A dependence of the extracted charge on the RF gradient in the gun is not included in the above described method. However for some conditions when the electric field at the cathode plays a significant role in the emission process the RF field jitter (e.g. due to the resonance temperature fluctuations) could contribute in the bunch charge jitter as well. This can also include the klystron nonlinearity – namely the dependency of the output RF power on the set point RF phase, which can be a substantial effect by the operation of the klystron close to saturation. If RF gradient in the gun is well controlled by the LLRF system these effects are assumed to be rather small.

Another factor limiting the method performance is the laser timing synchronization to the MO, which are intrinsically included in the measured phase jitter. Using measurements from the directional coupler it should be possible to estimate this jitter as well.

SUMMARY AND OUTLOOK

The presented technique to monitor the RF gun launch phase and the cathode laser pulse energy has been tested at the Photo injector test facility at DESY in Zeuthen (PITZ). It is rather robust and based on the electron beam charge measurements for various gun launch phases and different levels of cathode laser pulse energy. The preliminary results obtained for various machine conditions have been compared to the direct measurements. The systematic limitations and source of discrepancies of the method have been discussed.

In the nearest future extensive gun stability studies are foreseen at PITZ. More detailed phase jitter measurements have to be performed for different resonance conditions of the gun cavity at significantly higher levels of the peak RF power. Cross check of the laser pulse energy jitter obtained using presented method with direct measurements of energy meter and PMT in the PITZ tunnel should be available soon.

REFERENCES

[1] The Technical Design Report of the European XFEL, http://xfel.desy.de/tdr/tdr/

[2] F. Stephan et al., Detailed characterization of electron sources at PITZ yielding first demonstration of European X-ray Free-Electron Laser beam quality, Phys. Rev. ST Accel. Beams, 13, 020704 (2010).

[3] J. Baehr et al., “Recent upgrade of the PITZ facility”, these proceedings.

[4] Integrating current transformer model ICT-122-070-20:1, Bergoz Instrumentation, ww.bergoz.com

[5] J.-H. Han, PhD thesis, University of Hamburg, Germany, 2005.

[6] K. Floettmann, ASTRA particle tracking code, http://www.desy.de/~mpyflo/

[7] H. Schlarb et al., “Precision RF gun phase monitor system for FLASH”, Proc. EPAC’06 conf., Edinburg, UK, (2006).

SLOW ORBIT FEEDBACK AT RHIC*

V. Ptitsyn, A. Marusic, R. Michnoff, M. Minty, G. Robert-Demolaize, T. Satogata, BNL, Upton, New York, U.S.A.

Abstract

Slow variations of the RHIC closed orbit have been strongly influenced by diurnal variations. These variations affect the reproducibility of RHIC operation and might have contributed to proton beam polarization degradation during past polarized proton runs. We have developed and commissioned a slow orbit feedback system in RHIC Run-10 to diminish these variations and improve energy ramp commissioning and tuning efficiency. This orbit feedback uses multiple dipole correctors and orbit data from an existing beam position monitor system. The precision of the orbit feedback system has resulted directly from application of an improved algorithm for measurement of the average orbit, from improved survey offsets and numerous measures taken to ensure deterministic delivery of the BPM data. Closed orbit corrections are calculated with an online model-based SVD algorithm, and applied by a control loop operating at up to 1 Hz rate. We report on the feedback design and implementation, and commissioning and operational experience in RHIC Run-10.

INTRODUCTION

The accelerator RHIC [1] at Brookhaven National Laboratory has been operating for eleven years providing collisions of heavy ion as well as polarized proton beams for experiments exploring quark-gluon matter and other specific features of Quantum Chromodynamics. The control of closed orbit of the circulating beam is especially important for the operation with polarized protons. The vertical orbit should be maintained with high precision, below 300 μm of the orbit rms value, in order to ensure the preservation of the proton beam polarization during the acceleration ramps to 250 GeV [2].

The development of the slow orbit feedback was motivated by several reasons. First, the feedback was expected to simplify and speed-up the process of acceleration ramp setup and development. Because of magnet realignments done quite regularly between the RHIC runs as well as because of different machine lattices used from year to year, and even in the course of the same RHIC run, the tuning of RHIC acceleration ramps has been a popular kind of control room work, which often could take more than one day. The orbit feedback, together with other developed feedbacks (tune, coupling, chromaticity) intended to shrink the time scale of the ramp development to less than one control room shifts.

The second reason for the feedback development was to make the closed orbit reproducible from one acceleration ramp to another. And the third reason was related with holding the closed orbit at required precision level during the course of the beam stores. The main problem for the reproducibility of the orbit on the ramps as well as for maintaining a constant orbit at the store was seen to be caused by diurnal slow orbit variations. Although these orbit variations were noted long ago until recently there has been no attempt to develop the feedback in order to tackle the problem. In 2009 RHIC has the first run for physics experiments with the proton beams accelerated to 250 GeV. A considerable polarization loss observed during the acceleration to 250 GeV stimulated the work towards better control of possible depolarization factors, including the control of the beam closed orbit both during the energy ramp and at store.

The additional appeal to address the problem of diurnal orbit variations came from a consideration to move the RHIC working point (betatron tunes) close to an integer value. The move of the working point can be advantageous for the polarization preservation as well as for improving the beam lifetime at the store energy. The closed orbit variation, however, would increase accordingly to the $1/\sin(\pi*Q)$ law as the betatron tune Q is pushed towards an integer value.

SLOW ORBIT VARIATIONS IN RHIC

Diurnal variations of the beam closed orbit in RHIC have been noted several years ago. An example of the variations observed during the stores of proton beams in 2005 is shown in Figure 1. Since this region (as well as the IR6 region) contains an experimental detector, the low-beta* optics is applied there, which effectively leads to enhancement orbit excursions in the quadrupole triplets surrounding the interaction point.

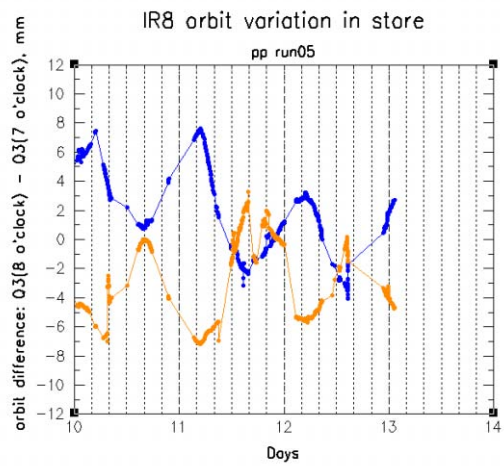

Figure 1: An example of the diurnal orbit variation is shown from RHIC Run-5. The difference of vertical orbit measured on left and right side of IP8 in Blue and Yellow RHIC rings is plotted.

* Work supported by Brookhaven Science Associates, LLC under Contract No. DE-AC02-98CH10886 with the U.S. Department of Energy.

The observed orbit variations are more pronounced in vertical plane. The analysis of waveforms of the orbit variations indicated that sources of the orbit excitation would be located in interaction regions, with the dominating source in IR4 area. As the interaction region magnets are enclosed inside a cryostat, a technique to measure possible movement of the IR quadrupoles inside the cryostat using gamma rays had been suggested [3]. The measurement of quadrupole movement has been never realized though since the decision to develop the slow orbit feedback system was made. Having the orbit feedback we would be able not only to address already identified sources of the closed orbit errors but also to compensate for any other, may be less pronounced, sources. In addition, the orbit feedback was expected to help with development of new acceleration ramps (for instance, ramps to a different store energy or ramps with a different optical lattice).

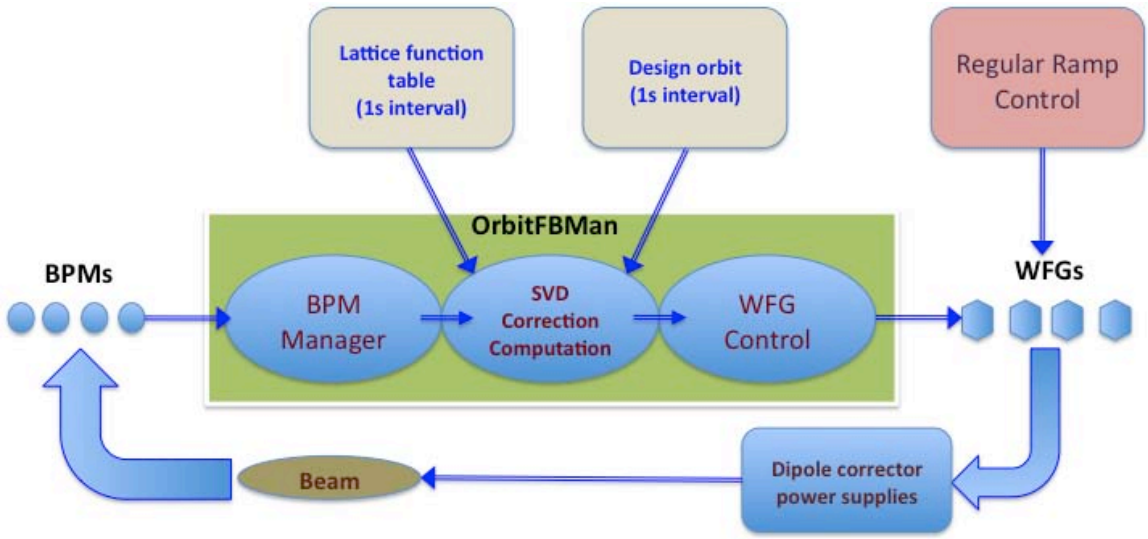

Figure 2: The general scheme of the slow orbit feedback at RHIC.

FEEDBACK IMPLEMENTATION

The slow orbit feedback was implemented using the hardware already present in RHIC. There are 117 dipole corrector magnets and about 150 Beam Position Monitors (BPMs) in each (horizontal and vertical) plane in each of two RHIC rings. These correctors and BPMs have been used during RHIC runs for routine orbit corrections as well as for local orbit control in specific locations. Several orbit correction methods were implemented in the RHIC orbit correction system, including SVD, Sliding Bumps and MICADO algorithms. The correction of the orbit on an acceleration ramp was done by feed-forwarding corrector strength calculated on the basis of orbit measurements from a previous ramp. As the orbit varied with the time such feed-forward correction could not be perfect.

The feedback made use of all existing dipole correctors and BPMs and did not require installing any additional magnets or orbit measuring devices. Yet, the implementation of the feedback during the ramp and for continuous use at the store demanded considerable modifications in corresponding systems in order to accommodate the feedback requirements.

The general scheme of the slow orbit feedback implementation is shown in Figure 2. In the core of the feedback system is the control code OrbitFBMan which encompassed all major parts of the system: the BPM data collection for the orbit input, the orbit correction computation and the application of calculated corrector strength adjustments, with selected gain, to the actual dipole corrector magnets.

The slow orbit feedback is based on steering the measured orbit either to a design orbit or a golden orbit. The design orbit is a combination of several specific local orbit bumps (like bumps in the interaction regions in order to prevent the beam-beam collisions during the acceleration ramp) while the golden orbit is the orbit based on BPM measurements all around the ring, taken at a specific moment. The correction computation is done on the basis of SVD algorithm. During the feedback operation a proper selection of the cut-off parameter for SVD eigenvalues presents an important tool to balance between the quality of the correction and its robustness against possible BPM misbehavior. The correction has to avoid affecting the orbit radial offset (average horizontal shift of the orbit). The control of the radial offset is done by varying RF frequency and by adjusting the bending field of main dipole magnets, and the feedback orbit correction should not interfere with those actions. Therefore, the dispersive component of measured orbit has to be excluded. In order to determine the orbit dispersive component the corresponding momentum offsets is calculated using the orbit data at the arc BPMs and the online model calculation of the horizontal dispersion function. The dispersive component of measured orbit corresponding to the calculated

momentum offset is subtracted from the orbit data before the correction computation.

The online model (OptiCalc) is used to calculate the optical functions (beta-functions, betatron phase advances and the dispersion function) required for the correction computation. The OptiCalc model is interwoven with the RHIC magnet control system and provides closest approximation to the machine lattice. During the acceleration ramp the RHIC lattice is continuously changing, since required values of beta-function in the interaction regions are very different at the injection and at the store lattices. In order to accommodate those changes for the orbit feedback a table of optical parameters is created beforehand, using the OptiCalc. The table contains all lattice functions required for the input for the feedback correction with 1s interval.

Like the lattice functions, the design orbit for the correction is also changing along the acceleration ramp. The local orbit bumps presented in the interaction regions as well at several other locations are changed in its amplitude or removed completely during the ramp. Thus, when the feedback is applied on the acceleration ramp the design orbit used as the goal orbit for the correction computation should be constantly updated. At the store the golden orbit taken at the beginning of the store, after the collisions in experimental locations have been perfectly optimized, serves as the goal orbit to be maintained by the feedback.

Several modifications were done in the BPM system to suit the feedback requirements. The algorithm of evaluating the average orbit from collected multi-turn data was refined in order to improve the quality of the measured closed orbit data [4]. Also, the code on BPM front-end computers was reworked to be able to provide deterministic delivery of the BPM data with up to 1 Hz rate. The collection of BPM data from front-end computers, their synchronization as well as exception handling of faulty BPMs was incorporated directly into the OrbitFBMan code. That provided the fastest way of getting the orbit input for the feedback correction. It was found also that the BPM offsets, relative to the center of a nearby quadrupole, had not been correctly accounted inside the system for most of the BPMs. The problem was corrected so that the orbit could be corrected to the center of the quadrupoles with much better accuracy than before.

The OrbitFBMan also incorporated the control of distribution of the computed correction to the actual dipole corrector magnets. The original system of the magnet power supply control in RHIC is based on the use of Wave Form Generators (WFGs). The WFGs are computing modules which calculate and output required magnet power supply currents as a function of time. In order to integrate the orbit feedback into the existing magnet control system, the code controlling WFGs was modified to accept the feedback correction and deliver it to power supplies at 720Hz rate. The computed feedback correction is added up on top of the dipole corrector strength changes provided from the regular ramp control system. The OrbitFBMan checks that computed corrections are within specifications for a maximum requested current I and for a maximum rate of change dI/dt. These specifications are determined on the basis of exception handling by estimates of maximum anticipated, physically realistic change and are significantly tighter than those given by the power supply limits. For instance, the maximum ramping rate of the corrector magnets differs because of different magnet inductances of different magnets.

The integration between the orbit feedback system and regular magnet control system is enhanced by the possibility to feed-forward a feedback correction used on a recent ramp to the magnet settings contained in the regular ramp control system. Another possibility is provided by so-called “replay” of the correction. In this mode the feedback correction used on a previous ramp can be applied again on any of next ramps on top of the magnet settings controlled by the regular ramp system. Both the feed-forward and “replay” techniques provide the way to use the feedback correction on following ramps even if the feedback is kept off. The techniques became essential tool during the work on the acceleration ramp development.

The OrbitFBMan also manages logging of all essential feedback parameters and allow for engaging and disengaging of orbit feedback smoothly. It provides an ability to ramp down the feedback correction so that the current of the dipole correctors become defined only by the regular magnet control system.

The slow orbit feedback is realized on the basis of a simple control loop. The efficiency of the feedback correction efficiency is governed by adjusting the loop gain (the fraction of the calculated corrector strength applied on each step) and the value of SVD eigen-value cut-off parameter.

With all modifications done to BPM and the magnet control system the orbit feedback was expected to operate at 1 Hz rate.

FEEDBACK COMMISSIONING

Commissioning of the slow feedback system was done during this year (2010) RHIC run.

Initial tests were done at the injection energy (10 GeV/n) of Au ions and attempted the correction towards zero goal orbit (without any orbit bumps). The tests explored an optimal operation mode of the feedback, a proper choice of the loop gain and the SVD cut-off parameter. Some initial problems were created by incorrect database information, concerning BPM locations, which led to large local orbit excursions. Also, some of misbehaving BPMs had to be fixed or excluded from the correction.

After that the slow orbit feedback was successfully attempted on RHIC acceleration ramp. The orbit feedback has proved itself as an effective tool of the ramp development. It was used routinely for several energy and lattice changing setups during the machine operation as well as at specific beam experiments. The Figure 3 shows an example of the orbit feedback application on the

acceleration ramp. The slow orbit feedback worked successfully trough the transition region of the ramp and interacted well with other control loops and feedbacks used on the ramp (for instance, with the rf radial loop or with the dipole field feedback which regulates main bending field in Yellow ring). Especially we would like to point out to a remarkable achievement when several feedbacks, controlling the orbits, betatron tunes, transverse coupling and chromaticities, were applied simultaneously with great success during a development of the acceleration ramp to 19.5 GeV/n Au ion energy.

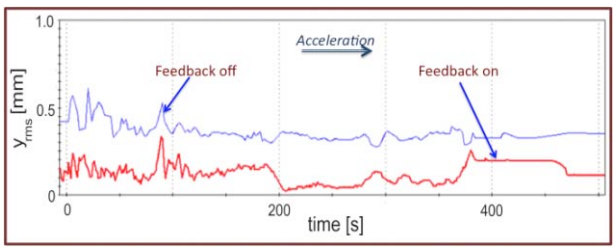

Figure 3: Comparison of vertical orbit rms, measured in Blue ring on two consecutive ramps. The orbit rms on the ramp without feedback affected by the diurnal orbit variations. The ramp with the feedback on produces considerably improved orbit.

Several tests were done with the slow orbit feedback activated at the store. In this case the feedback correction was using a golden orbit, measured at some short time before the feedback activation, as the goal orbit. Encouraging results were obtained demonstrating that the feedback can effectively counteract the slow orbit changes at the store (Figure 4) without deterioration of the experimental backgrounds or beam lifetimes. However the level of the orbit variation from one feedback correction application to another was larger than desired. Possible causes of this problem, like limited resolution of the corrector magnets power supplies, and discrepancies between the optics provided by the online model and the actual machine lattice, are under consideration.

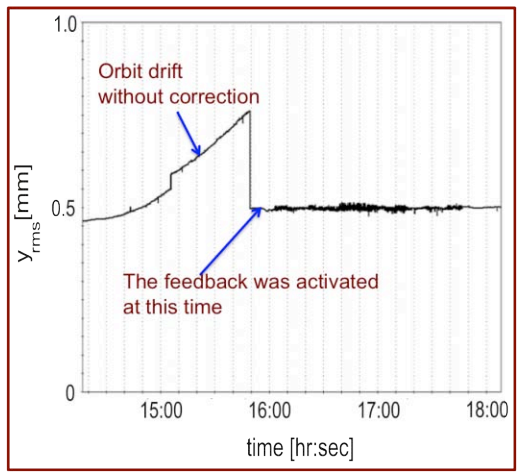

Figure 4: The orbit feedback activated at the store corrects for slow orbit deterioration.

CONCLUSIONS

The closed orbit feedback has been developed and successfully commissioned during RHIC Run-10. In the next RHIC run the slow orbit feedback will be used from the very beginning of the run as a tool of acceleration ramp development and setup. The ultimate goal would be to apply the feedback on every acceleration ramp to counteract diurnal orbit variations.

Also, we will continue to pursue the application of the feedback to maintain a golden orbit during the stores. Related with this development, the concurrent application of the slow orbit feedback together with a fast orbit feedback will be attempted in order to look into possible interactions between the feedbacks. The fast feedback has been under recent development [5] in order to compensate the observed orbit oscillations at frequencies around 10 Hz. Ideally, both slow and fast orbit feedbacks should be run concurrently during the course of RHIC stores.

REFERENCES

[1] T. Roser, “RHIC and its upgrade programs”, EPAC’08, Genoa, FRXAGM01, p. 3723, (2008).
[2] I. Alekseev, et al., “Polarized Proton Collider at RHIC”, Design Manual, (1998).
[3] P. Thieberger, W.W. MacKay, V. Ptitsyn, D. Trbojevic, C-A/AP/225, (2005).
[4] R. Michnoff, et al., “RHIC BPM system average orbit calculations”, PAC’09, Vancouver, TH5RFP013, (2009).
[5] R. Michnoff et al, "10 Hz global orbit feedback," currently under development.

NSLS2 TRANSVERSE FEEDBACK SYSTEM DESIGN

Weixing Cheng
NSLS-II, Brookhaven National Laboratory, Upton, NY 11973

Abstract

A diffraction-limited storage ring like NSLS2 requires stringent beam stability. Even with careful design of vacuum component to limit the geometric impedance, due to resistive wall impedance and fast-ion effect, transverse instabilities will happen at low current (~15mA). An active transverse feedback system has been designed to cure the coupled bunch instability. The system will have less than 200 micron seconds damping time at 500mA to suppress the fast-ion instabilities, which is severe in vertical plane due to small beam size.

INTRODUCTION

Bunch-by-bunch feedback systems have been proved effective to cure the coupled bunch instabilities. Third generation light sources and particle colliders need to run at high beam current to get the desired brightness and luminosity. Even with careful design of the vacuum chamber and other methods to cure the instabilities, there may be residual betatron oscillation or synchrotron oscillation. An active feedback system is straight forward to achieve the design current and required stability. Those methods to increase the tune spread by introduce non-linear field (like Chromaticity or Octupole magnets) may limit the dynamic aperture, which is not suitable especially at top-off operation. Active feedback has no side effect on the dynamic aperture and typically helps to suppress the injection transient.

Feedback systems are generally composed of three parts: RF front end to detect the transverse position error signal or longitudinal phase information; digitizer to sample and filter the error signals, as well as feedback gain control, phase adjustment etc; corrector module including high power amplifier and kickers. Shunt impedance of the kicker should be sufficient to kick the beam effectively with reasonable power. With the recent development of digital technology, especially the FPGAs (Field Programmable Gate Array), there is no reason to select digital feedback processors other than FPGA based. In a digital feedback loop, one can easily get rid of the DC offset as well as revolution harmonics by using digital filters. The digital delay adjustment avoids the use of long cables to do one-turn delay. The feedback digitizer itself is a powerful diagnostic tool with large memory to store the bunch-by-bunch position/phase information. Bunch oscillation and unstable modes can be revealed by transient measurements. The digitizer can be used to measure the tune of each individual bunch, or to clean unwanted bunches.

Treating the bunch as a rigid particle, the central motion of beam position/phase can be written as damped harmonic oscillation with external force. Eq (1) gives the oscillations in longitudinal plane, transverse plane is similar.

$$\ddot{\tau} + 2d_r\dot{\tau} + \omega_s^2\tau = f(t) = f^{wk} + f^{fb} \qquad (1)$$

Where

$$f^{fb} = -\frac{\alpha e}{E_0 T_0} V^{fb}(t)$$

with,

$$V^{fb}(t) = -jG^{fb}\tau \approx -\frac{G^{fb}}{\omega_s}\dot{\tau}$$

f^{wk} – wake force from the past bunches,
f^{fb} – kick force from the feedback system.

Beam stabilization requires the damping rate (radiation damping + feedback damping) be larger than the wake field excitation rate. Be aware that the wake field caused coupled bunch instability growth rate is proportional to the beam current. More feedback gain is needed for higher beam current. However, active feedback gain is not infinite, it's limited by the high power amplifier. Besides, with too much gain, the noise in loop might be amplified too much to excite the beam.

Instability growth rate has been estimated for the NSLS-II storage ring, see next section for more information. It shows that for transverse (especially vertical plane), feedback system is mandatory to achieve the designed goal of 500mA and preserve the low emittance < 1 nm.rad. Longitudinal instability in not expected to be a problem because of the use of superconducting RF cavity. The baseline design of NSLS-II will have feedbacks for horizontal and vertical planes. Some major parameters related to the transverse feedback are listed in Table 1.

Table 1, main parameters for NSLS-II feedback system

Parameter	Value	Unit
E	3	GeV
f_{rf}	499.68	MHz
h	1320	
f_{rev}	378.55	kHz
T_{rev}	2.64	μs
Q_X/Q_Y	33.36/16.28	
f_X/f_Y	136/106	kHz
$\varepsilon_x/\varepsilon_Y$	0.9/0.008	nm.rad
τ_x/τ_Y	54/54 (w/o DW)	ms
	23/23 (3 DW)	ms
Resolution	3	μm

τ_{FB}	200	μs
Dynamic range	+/- 0.5 (V)	mm
	+/- 1.5 (H)	mm
R_{Shunt}	>10	kOhm
Power	2*500	W
Stripline length	30	cm

INSTABILITY SOURCES

Transverse coupled bunch oscillations are driven by high-Q wake fields. Bunches generate these wake fields by interacting with the surroundings. Main contributions to the transverse coupled bunch instability include:

- Cavity like structures and discontinuities in the chamber;
- Resistive wall of the surrounding chamber;
- Ion and fast-ion instabilities.

For the modern collider machine and 3rd generation light source, beam emittance and size are getting smaller. With smaller vertical gap of vacuum chamber (in-vacuum undulator, small gap IDs), resistive wall and ion instabilities are the main issues affecting running at high current. Discontinuity in the vacuum chambers can cause wake field while beam passing through. The wake field will act back on the beam itself and cause instabilities. Impedance and wake fields for various components in NSLS2 storage ring have been calculated using GdFidl[1].

Resistive Wall

Resistive wall impedance in the ring can be written as:

$$Z_{//}(\omega) = (1-i)\frac{C}{2\pi b}\sqrt{\frac{\mu\omega}{2\sigma}}$$
$$Z_{\perp} = \frac{2c}{\omega b^2}\cdot Z_{//} \qquad (2)$$

Where C is the ring circumference; b is the chamber radius (height if the chamber is not round); μ is magnetic permeability of pipe material; σ is conductivity of pipe material and ω is the angular frequency.

Eq. (2) assumes the same chamber pipe shape all around the ring, which is not true for the real machine. One should replace the ring circumference C with chamber length L. Since the resistive wall impedance depends strongly on chamber height (for transverse resistive wall ~$1/b^3$). Third generation light sources will have many small gap insertion devices, vertical resistive wall impedance and corresponding instability growth rate are expected to be large.

Knowing the impedance, transverse coupled bunch instability growth rate can be calculated from:

$$\tau_g^{-1} = \frac{eI_0\omega_0\beta}{4\pi E}\left\{\sum_{n=1}^{\infty}\mathrm{Re}\left[Z_T(\omega_{\mu,n}^{-})\right] - \sum_{n=0}^{\infty}\mathrm{Re}\left[Z_T(\omega_{\mu,n}^{+})\right]\right\} \qquad (3)$$

Where

$$\omega_{\mu,n}^{+} = n\omega_{RF} + \left(\mu\omega_{rev} + \omega_{x,y}\right)$$
$$\omega_{\mu,n}^{-} = n\omega_{RF} - \left(\mu\omega_{rev} + \omega_{x,y}\right)$$

n = 0, 1, 2,... and μ = 0, 1, 2, ..., Harmonic Number -1; μ is called the mode number.

As a simple estimation for NSLS2, assume there are 100 meter 7mm gap ID chambers with Aluminum material, the vertical growth rate can be calculated from Eq. (2) and (3) for different modes. The strongest unstable mode (mode -1) has the growth rate about 1300 1/sec (with growth time 0.77ms). It's impossible to damp this by synchrotron radiation damping only (damping time ~23ms with three damping wigglers).

Its worth to note that Eq. (2) stands for single material chamber. For those chambers with coating of different material can refer to [2]. Longitudinal growth rate contributed from resistive wall has been calculated as well. The fastest growth rate is less than 2.5 1/sec (with growth time > 400ms). There expected to be no problem from the longitudinal resistive wall.

Fast-ion

Residual gas in the vacuum chamber maybe ionized and trapped by the beam space-charge potential. Ion trapping is important to electron storage rings. Once happened, it may result in lifetime decrease, emittance growth and coherent beam oscillation etc.

Leaving some buckets empty (ion gap) in the filling pattern is effective and widely used to cure the conventional ions. Ions cannot survive for more than one turn. However, even with the ion gap in NSLS2, ions can still accumulate during one pass of the bunch train, which is called fast-ion instability. Fast-ion can result in tune shift and emittance blow up along the bunch train.

Ions with atomic mass larger than critical mass will be trapped, the critical mass was defined by:

$$A_{crit} = \frac{N_b r_p c T_b}{2\sigma_{x,y}\left(\sigma_x + \sigma_y\right)} = \frac{N_b r_p L_{sep}}{2\sigma_{x,y}\left(\sigma_x + \sigma_y\right)} \qquad (4)$$

Where N_b is number of particles per bunch;

$$r_p = \frac{1}{4\pi\varepsilon_0}\frac{e^2}{m_p c^2}$$

is proton classical radius ~ 1.5×10^{-18} m; A is atomic mass of ion; T_b (or L_{sep}) is bunch separation and σ_x σ_y the RMS beam size.

Critical mass depends on the beam size, which varies along the ring. Figure 1 shows the critical mass in one super cell of NSLS2 storage ring. For the calculation, we use horizontal and vertical emittance of 0.9/0.008 nm.rad respectively and relative energy spread 0.09%.

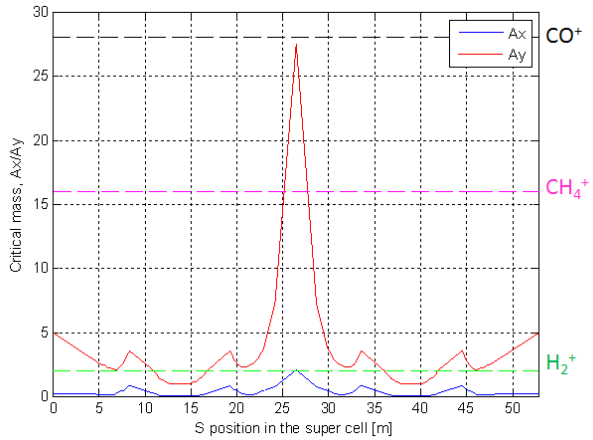

Figure 1, Ion trap critical mass in NSLS2 supercell (start from center of long ID).

We can see from the plot, at short ID, vertical beam size is small, the strong beam force can over focus ions and cause the ions motion to become unstable. That's why the critical mass is highest in vertical at the short ID. Horizontally almost all the ions are trapped, even H_2^+ captured in most of ring. Vertically $CH4^+$ and CO^+ will be captured in most part of the ring, while H_2^+ will be trapped at dispersion region.

Ion oscillating frequency can be written as:

$$\omega_{ion} = 2\pi f_{ion} = \left[\frac{2N_b r_p c}{A\sigma_{x,y}(\sigma_x+\sigma_y)T_b}\right]^{1/2} \qquad (5)$$

CO^+ (A=28) is considered to be the dominant ion in the NSLS2 ring. At 500mA, evenly filled in 1040 bunches, the ion frequency is around 20MHz in horizontal plane and ~50MHz vertically. Ion frequency will shift as the bunch current is varied.

Ion oscillation frequency will be different from Eq (5) due to: non-linearity of electron potential; beam density variation at different transverse position; beam size variation along the ring and bunch-to-bunch current variation etc. Considering the ion oscillation spread, fast ion instability growth rate can be analytically expressed as:

$$\frac{1}{\tau} \approx \frac{r_e c \beta_y \lambda_{ion}}{3\gamma\sigma_y(\sigma_x+\sigma_y)} \frac{1}{\Delta\omega_i/\omega_i} \qquad (6)$$

Where $\Delta\omega_i$ is the ion oscillation frequency spread along the ring. Select $\Delta\omega_i/\omega_i$ =30% matches the simulation result well; β_y is average beta function and λ_{ion} is ion density

$$\lambda_{ion} = \frac{n_b N_b}{K_B T}\sigma_{ion} p$$

Assume single bunch train of 1040 bunches, CO+ ion density of 1nTorr at the end of train is $5.3\text{x}10^4$ m^{-1}, ion oscillation frequency spread ~30%, beam size 100μm/10 μm, average vertical beta function ~10m, the calculated rise time is ~13us. (If use 0.3nTorr CO, and 250 bunches per train, the growth time ~200μs, which is close to the simulation [3]).

The bunch-by-bunch feedback system is designed to have the damping time less than 200 μs, which is about 75 turns of NSLS2 storage rings.

BPM AND STRIPLINE KICKER

Normal multi-chamber RF BPM design [4] will be adopted as the transverse feedback pickup. Sensitivity and signal strength of the BPM has been analyzed. The detection will be at three times RF frequency, where the BPM button has peak signal. However, the antechamber structure will decrease the cutoff frequency to less than 1GHz even with RF shielding. To avoid the possible trapped TE mode, dedicated BPM housed in non antechamber structure will be used.

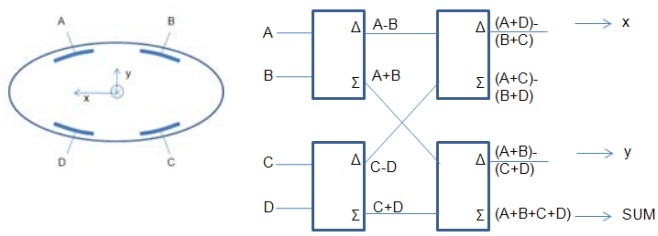

Figure 2, hybrid network to get the position error signal in RF front end.

Assume BPM buttons with sensitivity Kx = Ky =10mm, the hybrid output from the RF front end with small position offset ΔX is (Figure 2)

$$(V_A+V_D) - (V_B+V_C) = 4*\Delta V$$

while,

$$\Delta X = K_x \frac{(V_A+V_D)-(V_B+V_C)}{(V_A+V_B+V_C+V_D)} = K_x \frac{\Delta V}{V_0}$$

$$\Delta V = \frac{1}{K_x}\cdot\Delta X\cdot V_0$$

Where V_0 is the signal strength with the beam passing through the center, and ΔV is signal strength change with position offset ΔX.

The NSLS2 button BPM has about -7dBm at 500MHz with 500mA full current, which corresponding to 0.1Vrms. With 1μm offset and Kx=10mm, the output signal from the hybrid network is:

$$4\cdot\Delta V = 4\cdot\frac{1}{K_x}\cdot\Delta X\cdot V_0 = 0.04mV$$

This corresponds to -75 dBm.

In the real machine, transverse feedback doesn't need to have the sensitivity to detect 1μm beam oscillation. Depending on the location of BPM, the vertical beam size

is typically around 10 μm (horizontal beam size is 10 times larger, no detection sensitivity problem), feedback control needs to have 30% beam size resolution which is ~3 μm. (Don't like the orbit feedback which has small bandwith, the users will see these kind of slow beam movement; but for the betatron oscillation, user's experiments typically cannot seen it, effect of betatron oscillation is 'effective' emittance/beamsize increase. If the oscillation can be controlled <30%, the effective beamsize change is less than (1^2+30%^2)-1 = 9%, which is negligible.) With 3 μm beam position offset, the output from the hybrid has -65dBm signal.

Noise of the BPM button signal and hybrid outputs can be estimated from thermal noise. With 250MHz bandwidth and temperature ~20 degC, the noise floor is about -90 dBm. Considering detection resolution of 3 μm, which has -65dBm output at the hybrid, there is 25dB noise figure budget in the feedback loop.

BPM signal output has maximum amplitude around ~1.5GHz. NSLS2 normal RF BPM gives -7dBm at 500MHz with 500mA. If the bunch feedback detection frequency is selected to be 3*f_{rf}, ~6dB more signal can be gained. Figure 3 shows the BPM button signal power at 500mA. The cable loss value was based on 100 feet LDF2-50 3/8'' Heliax cable.

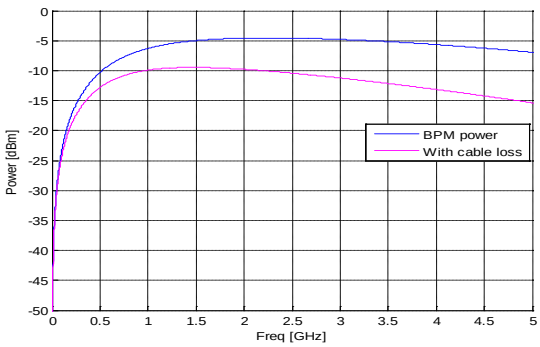

Figure 3, BPM button output signal power (with and without cable loss)

The high power amplifiers and stripline kickers are the feedback actuators. They are the most expensive parts of the system. Design of the kicker should provide sufficient shunt impedance while minimizing the beam impedance. Stripline has been proved effective as transverse kicker. It has higher shunt impedance at lower frequency, which is suitable if the main instability contribution is from resistive wall and ions. Required power can be calculated if the stripline shunt impedance, damping time and initial oscillation amplitude are known.

$$\Delta\theta = -\frac{2\alpha}{f_{rev}}\cdot\frac{\Delta x}{\sqrt{\beta_m\cdot\beta_k}} = -2\cdot\frac{1}{\tau}\cdot T_{rev}\cdot\frac{\Delta x}{\sqrt{\beta_m\cdot\beta_k}}$$

$$V_\perp = \Delta\theta\cdot\frac{E}{e} = -2\cdot\frac{1}{\tau}\cdot T_{rev}\cdot\frac{E}{e}\cdot\frac{\Delta x}{\sqrt{\beta_m\cdot\beta_k}} \qquad (7)$$

in which, $\Delta\theta$ is deflecting angle while beam passing through; $V_\perp$ is transverse deflecting voltage; E is the beam energy; α/τ are feedback damping rate/time; Δx is initial beam oscillation amplitude; β_m/β_k – beta function at BPM and kicker.

From Panofsky-Wenzel theorem, electric field and magnetic field have the same kick effect when the power is fed to the stripline kicker from the downstream port:

$$\Delta\theta \approx \frac{\Delta p_\perp}{p_{//}} = \frac{V_\perp}{E/e} = \frac{2\int_{stripline} E_\perp dt}{Energy/e}$$

Kicker shunt impedance is defined as:

$$R_{shunt} = \frac{V_\perp^2}{2P} \qquad (8)$$

Taking shunt impedance 10 kOhm, which is not hard to get with 30-cm stripline, the required damping time of 200μs, β_m=12/10m and β_k = 7/21 m (vertical/horizontal). Figure 4 plots required power at different initial oscillation amplitude.

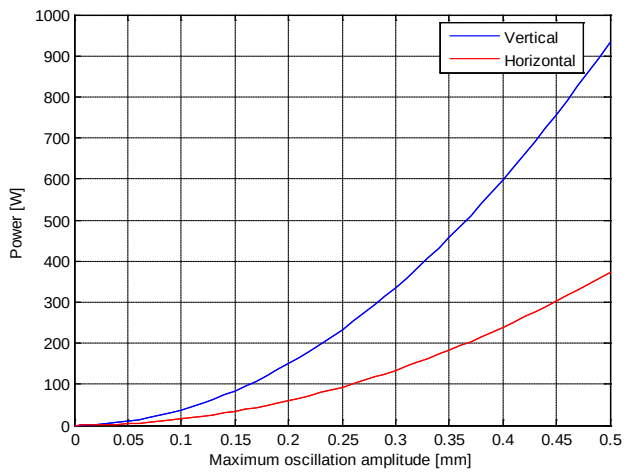

Figure 4, required power vs. initial oscillation amplitude for NSLS2 feedback.

To damp an oscillation of up to +/- 0.5mm in the vertical plane, we need 1000W power (2*500W) which is commercially available.

Its worth to mention that bunch might never have chance to get large oscillation if the feedback is always on. In this case the needed power is really small. Full power may be needed only for machine study purpose, if the feedback loop is switched off and the instability is allowed to grow.

Transverse shunt impedance of stripline with opposite electrode distance d and length l can be written as:

$$R_\perp = 2Z_c\left(\frac{2g_\perp l}{d}\right)^2\left(\frac{\sin kl}{kl}\right)^2 \qquad (9)$$

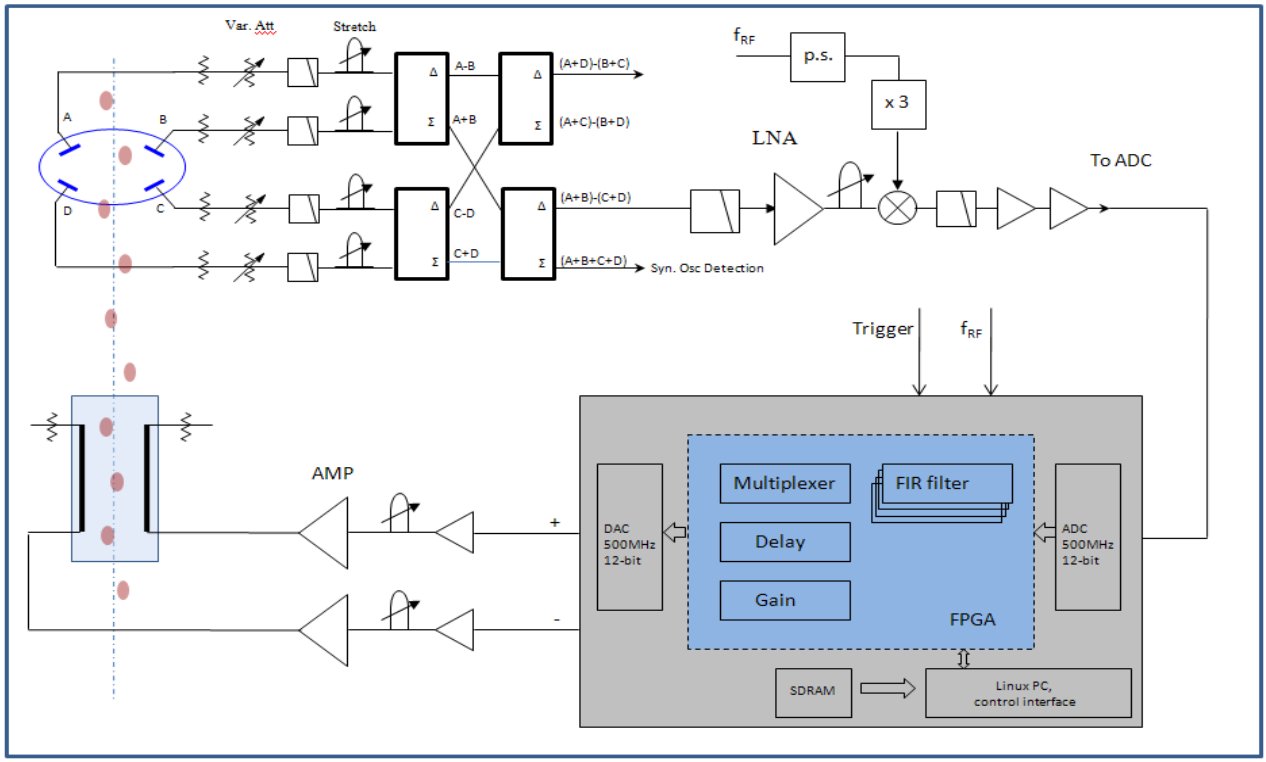

Figure 5, Layout of NSLS2 transverse feedback system for vertical plane

With longer stripline kicker, the shunt impedance is bigger at low frequency but the bandwidth decreases. To separate between bunches in case the instability mode around 250MHz happens; stripline electrodes typically select less than half of the bunch space, which is 30cm with 500MHz RF frequency.

A two plate 30cm stripline in round chamber has been designed with shunt impedance > 10kOhm till 200MHz [5]. Field uniformity is within 5% in 10mm range.

SUMMARY

NSLS2 transverse feedback system has been designed to cure the instabilities with growth rate as fast as 200μs. BPM detector signal strength and sensitivity has been analyzed. Normal RF BPM proves sufficient to be used as feedback pickup. RF front end will generate the low-noise bunch-by-bunch position information to be fed to digitizer. The detection frequency was selected to 3*Frf due to higher signals at that frequency. Commercial 500MHz FPGA based digitizer will be used. See Figure 5 for the layout. Stripline kicker design shows >10kOhm shunt impedance with 30cm electrode, beam impedance of the kicker is under investigation. Future work will deal with feedback system during the top-off injection, single high-current bunch in hybrid fill mode, bunch clearing and tune measurement using the feedback digitizer. NSLS2 storage ring might need positive chromaticity. The feedback behavior at positive chromaticity needs to be investigated.

The author thanks NSLS2 staff for helpful discussion, as well as the support and comments of Sam Krinsky and Om Singh.

REFERENCES

[1] A. Blednykh, 'Impedance Calculations for the NSLS2 Storage Ring', PAC09
[2] W. Cheng, 'Design of Transverse Instability Feedback System', internal technical note
[3] G. Stupakov and L. Wang"Fast Ion Instability in the NSLS-II", NSLS2 technical note
[4] P. Cameron, 'BPM Button Optimization to Minimize Distortion Due to Trapped Mode Heating', PAC09
[5] W. Cheng, 'Preliminary Design of NSLS2 Stripline Kicker', internal technical note

SYNCHROTRON LIGHT MONITOR SYSTEM FOR NSLS-II

Weixing Cheng
NSLS-II, Brookhaven National Laboratory, Upton, NY 11973

Abstract

A visible synchrotron light diagnostic beam line has been designed at the NSLS2 storage ring, using the dipole radiation. The 'cold-finger' configuration has been selected to block the central x-rays. Beam power on the first mirror is less than 1W, no water cooling is required for the in-vacuum mirror. The beam line layout and major applications will be discussed in this paper. Two vacuum ports are reserved in the NSLS2 booster ring to monitor the transverse profile as well as bunch length measurement during ramping. There will be a synchrotron light port in the BTS transport line to observe the injection beam behavior during top-up operation.

INTRODUCTION

The ultra high brightness NSLS-II storage ring is under construction at Brookhaven National Laboratory. It will have 3GeV, 500mA electron beam circulating in the 792m ring, with very low emittance (0.9nm.rad horizontal and 8pm.rad vertical). The ring is composed of 30 DBA cells with 15 fold symmetric. Three damping wigglers will be installed in long straight sections 8, 18 and 28 to lower the emittance [1]. While electrons pass through the bending magnet, synchrotron radiation will be generated covering a wide spectrum. There are other insertion devices in the storage ring which will generate shorter wavelength radiation as well. Since the NSLS-II visible diagnostic beam line will use the radiations from bending magnet, we will discuss the dipole radiation only in this paper.

Synchrotron radiation has been widely used as diagnostic tool to measure the transverse and longitudinal profile. Three synchrotron light beam lines dedicated for diagnostics are under design and construction for the NSLS-II storage ring: two x-ray pin-hole camera beam lines with the source points from Cell 24 BM_A (first bending in the DBA cell) and Cell25 three-pole wiggler; the third beam line is using visible part of radiation from Cell 30 BM_B (second bending magnet from the cell). Pinhole beam lines designs can be found in the paper. [2] Our paper focuses on the design of the visible beam line. Synchrotron light monitors along the injector chain will be discussed as well.

Table 1 lists major parameters related to the NSLS2 storage ring

Parameter	Value	Unit	Comment
General machine parameters			
E	3	GeV	Energy
f_{rf}	499.68	MHz	RF freq.
h	1320		har. #
f_{rev}	378.55	kHz	
T_{rev}	2.64	μs	
C	791.96	m	
I	500	mA	
ε_x	0.9	nm.rad	with 3 DW
ε_y	0.008	nm.rad	
σ_E/E	0.09%		with 3 DW
Bending magnet parameters			
ρ	25.02	m	bending radius
B	0.4	Tesla	
E_c	2.4	keV	
λ_c	0.52	nm	
Bunch length related			
Vc	3.1	MV	
U0	287	keV	bend loss
	674	keV	total loss with 3DW
α	3.63E-4		
fs	3.32	kHz	
σ_t	15.66	ps	RMS bunch length
Beam size related			
β_x	2.7763	m	
β_y	19.5252	m	
η_x	0.1370	m	
σ_x	133.05	μm	
σ_y	12.50	μm	

SOURCE POINT

NSLS-II ring has 30 DBA cells, each cell has two bending magnets which bend the electron beam 6-deg each. Synchrotron radiation extracted from the beginning of bending magnets, with horizontal opening angle 0 to 4.25mrad. The nominal source point for user's beam line is 2.125mrad +/- 1.5mrad. To use the same extraction configuration is highly desired for the visible diagnostic beam line. Synchrotron radiation from the dipole has natural open angle depending on the radiation wavelength. With longer wavelength, the synchrotron radiation from dipole will have larger natural open angle. See Equation (1). For the 500nm green light, which will be used on the optic table for various measurements, the natural opening angle is ~1.2mrad. To avoid the bending magnet edge radiation, the diagnostic beam line horizontal aperture was selected from 1.25mrad to 4.25mrad. Edge radiation has been investigated and 1.25mrad is large enough to avoid the edge radiations at visible light range. On the other hand, edge radiations can be a useful diagnostic tool. We keep the option to move the aperture to intercept these kinds of radiations.

$$\theta_{SR_\sigma_rms} \approx 0.4097\left(\frac{\lambda}{R}\right)^{1/3}$$
$$\theta_{SR_\pi_rms} \approx 0.5497\left(\frac{\lambda}{R}\right)^{1/3} \quad (1)$$
$$\theta_{SR_rms} \approx 0.4488\left(\frac{\lambda}{R}\right)^{1/3}$$

Equation (1) listed the natural open angle of σ and π modes as well as total effect of bending magnet radiations. R is the bending radius, λ is radiation wavelength. Longer wavelength radiation will have larger natural open angle.

Several possible source points have been evaluated. The horizontal beam size will be around 100 microns or larger if the source point location has some dispersion. The visible beam line will be able to measure the horizontal beam size of 100 microns. From the measured beam size at dispersion location, it's easy to extract the beam energy spread. This gives a supplementary method to measure the energy spread to pinhole camera. Vertical beam size in the NSLS2 will be ~10 microns, which will be dominated by diffraction resolution of visible light. We can rely on the pinhole for vertical beam size measurement. At the visible beam line we plan to test the double-slit interferometer [3] and pi-mode beam size measurement [4].

Cell 30 straight section will be occupied by the injection system. There is no user's beam line from that straight. Thus Cell 30 BM_B is selected to be the source of visible synchrotron radiation light beam line. Since the source point is located just after the injection, it gives the advantage to measure the injected beam during commissioning and machine studies. Cell 30 is heavily shielding area where there is much higher radiation compared to rest of the ring. The beam line can be moved to RF cavity sections if radiation safety is a concern.

Figure 1 shows the schematic layout of visible diagnostic beam line with racks shown on the mezzanine floor. The synchrotron light monitor (SLM) lab will be outside the tunnel to conduct the measurements/studies, with optical table of 3m *1.5m. It's hard to fit the lab on the mezzanine floor as preferred. The current design is to locate the SLM lab on the experiment floor, using the beam line port from Cell 30 ID, where no user's beam line exists.

Total power within 3mrad horizontal fan will be ~70W. After the cold finger, the power on to the first mirror is about 0.5W, since most of the power near the central plane is blocked by cold finger. Vacuum window and mirrors will further filter the UV radiations, typical power into the SLM lab is around several mW level.

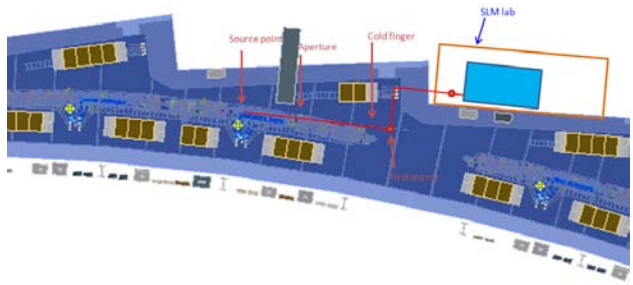

Figure 1, layout of visible synchrotron diagnostic beam line of NSLS2 storage ring.

Crotch absorber and fixed mask will define the SLM aperture to +/-1.5mrad horizontally and +/-3.5mrad vertically. Size of the open aperture is determined by the measurement resolution and light intensity. There are more discussion about the system resolution in the following sections. The first mirror will be about 7-meters away from the source point. Beam height inside the tunnel is 1.2m and 1.4m on the experiment floor, proper vertical elevation is necessary to bring the light on to the optical table.

FIRST MIRROR

The first mirror in the visible diagnostic beam line is essential to reflect the light outside the vacuum. The surface of the mirror must have minimum deformation with high head load. The flatness should be less than 1/10 of measurement wavelength. Basically there are three approaches for the first mirror design, as shown in Figure 2.

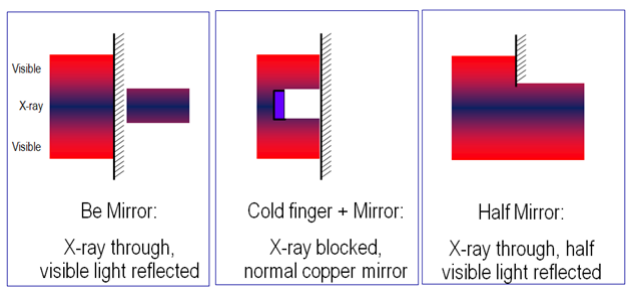

Figure 2, first mirror configurations in the visible diagnostic beam line.

The first option will adopt mirror made from low atomic mass material (like Beryllium). X-ray will pass through the mirror while visible part of the radiation will be reflected from the polished surface. Although the mirror material has small atomic mass, the mirror will suffer from heating problem and deformation at high current. Besides, toxic Beryllium is not easy to handle. The second type of mirror configuration combines a stick absorber and mirror. The thin absorber was called 'cold' finger which blocks the central part of the radiation, most of the central part has shorter wavelength radiation. By selecting appropriate open angle of the cold finger, the power onto the mirror could be very small (several Watt

or even less than 1W). The mirror could be made from SiC or copper. No water cooling is needed due to low power shining on the mirror. We plan to have retractable cold finger which could be moved out the beam while beam current is low. The cold finger could track the electron beam vertical position as well. For the NSLS2 SLM beam line, we will adopt this configuration. Temperature sensors will be attached to the mirror, monitoring any potential heating issues.

The third type of configuration uses half mirror to intercept only top (or bottom) half of long wavelength radiation. Central x-ray will not illuminate the mirror. The advantage of this configuration is central x-ray cone can still be used by users' experiment or other diagnostic purpose (like bunch purity monitor using x-ray APD). Compared to the cold finger configuration, half mirror loses half of the intensity. In some measurements like monitoring injected beam profile, more photons are needed. Besides these three widely-used configurations, other approaches might exist but with difficulties. For example: one can use two half mirrors to intercept the top and bottom radiation. The difficulty is hard to align two half mirrors in the same plane. Or we can cut a slit in the mirror to let the x-ray pass through the slit, the difficulty is there is always a round corner near the slit edge. Some may add a fork shape to block the slit edge before the mirror, which increases the complicity.

A finite element analysis simulation has been done to estimate the thermal load effect on the first mirror. With 500mA stored beam and all the 3mrad horizontal open aperture radiation fan incident on the mirror (Glidcop material, 100mm*100mm*25mm size), with radiation cooling only, the highest temperature of the mirror will be 274 °C [5]. In other words, the mirror is still safe without water cooling even the cold finger was moved out the beam by accident.

MEASUREMENT ERRORS

The visible diagnostic beam line spatial resolution is contributed from several factors, including the depth-of-field error, curvature error and diffraction error etc. Chromatic error can be minimized by using band pass filter before the camera. For some applications, we may need polarizer.

Depth-of-field error

As illustrated in Figure 3, slit with horizontal open angle +/- θ_x will accept the radiation from a curvature with length of $2R\theta_x$, where R is bending radius. Besides the open angle of the slit, synchrotron radiation itself has natural opening angle. With lower frequency (longer wavelength) radiation, the natural open angle is bigger, see Eq (1). In another words, even if the slit open angle is 0, there still is synchrotron light coming through due to the natural open angle of synchrotron radiation. With visible light, which is typically much longer than critical wavelength, the open angle is ~ 1mrad.

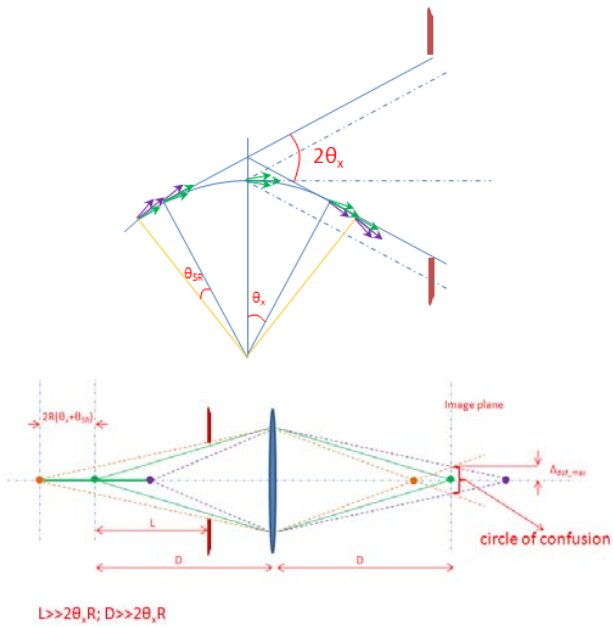

Figure 3, depth-of-field error

In Figure 3, including the synchrotron radiation natural open angle, light within +/- (θ_x + θ_{SR}) will pass through the slit and reach to the CCD camera. With 1:1 image onto the CCD, even if the transverse beam size were 0, some finite size area on the image plane will be illuminated. This area is called "circle of confusion", radius of this circle is defined as depth-of-field error. With simple math, one can get the radius:

$$\Delta_{dof_\max} \approx R\theta_x\left(\theta_x + \theta_{SR}\right) \qquad (2)$$

Assume the light in the circle-of-confusion is uniformly distributed, then RMS value of depth-of-field error can be written as:

$$\Delta_{dof_rms} = \frac{\Delta_{dof_\max}}{\sqrt{6}} \qquad (3)$$

For the NSLS-II storage ring SLM beamline: bending magnet radius R = 25m; detecting wavelength λ = 500nm; slit horizontal open angle (half) θ_x = 1.5mrad; synchrotron radiation natural open angle $\theta_{SR} \sim 0.45(\lambda/R)^{1/3}$ = 1.2 mrad (for 500nm light). We calculate the depth-of-field error: Δ_{dof_max} ~ 101 um and Δ_{dof_rms} ~ 41 um. This value may be still over estimated. The distribution in circle-of-confusion could be Gaussian like instead of uniform. Depth-of-field error applies to both planes (horizontal and vertical).

Curvature error

Since the SLM source is coming from the bending magnet, the curvature of the electron beam contributes an error term that limits the horizontal resolution. Curvature error can be calculated as:

$$\Delta_{cur_\max} = \frac{R}{\cos\theta_x} - R \approx \frac{R\theta_x^2}{2} \qquad (5)$$

$$\Delta_{cur_rms} = \sqrt{\frac{1}{2\theta_x}\int_{-\theta_x}^{\theta_x}\left(\frac{Rx^2}{2}\right)^2 dx} = \frac{R}{2}\sqrt{\frac{2\theta_x^5}{5}\frac{1}{2\theta_x}}$$

$$= \frac{R\theta_x^2}{2}\frac{1}{\sqrt{5}} = \frac{\Delta_{cur_\max}}{\sqrt{5}} \qquad (6)$$

Again for the NSLS-II diagnostic beam line, with bending radius 25m and 1.5mrad horizontal open angle, we get Δ_{cur_max} ~ 28um, Δ_{cur_rms} ~ 13um. Curvature error applies to horizontal plane only.

Diffraction error

Any image system with aperture will have a diffraction error. Contrary to the depth-of-field and curvature error, diffraction error increases while the aperture decreases. With horizontal slit opening angle θ_x and synchrotron radiaiton natural open angle θ_{SR} , a rough estimate of diffraction error:

$$\Delta_{diff} = \begin{cases} 0.5\dfrac{\lambda}{\theta_x} & if \quad \theta_x < \theta_{SR} \\ 0.5\dfrac{\lambda}{\theta_{SR}} & if \quad \theta_x \geq \theta_{SR} \end{cases} \qquad (7)$$

The diffraction error from Eq (7) is far too big, for the NSLS2 SLM beamline. With bending radius R = 25m, measuring wavelength λ = 500nm and horizontal open angle θ_x = 1.5mrad, one gets Δ_{diff_rms} ~ 167 um.

It's worth to note that Eq (7) only stands for uniform illuminated slit (or circular iris, which has diffraction error 0.61λ/θ). However, this is not the case for synchrotron radiation. Hoffmann has quantitative treated the issue using Fraunhofer diffraction. RMS of diffraction error can be expressed as (for σ-mode only) [6]:

$$\Delta_{diff} = 0.21\left(\lambda^2 R\right)^{1/3} \qquad (8)$$

Diffraction resolution improves with shorter wavelength and with smaller bending radius. Larger machines typically have larger bending magnet radius. For NSLS2 the bending radius R=25m, which is much bigger compared to other median energy light sources. Special magnet with strong bending (smaller R) could help to improve the resolution. One could use UV light instead of visible, which could improve the diffraction resolution by 20-30%. The problem using UV is safety concerns, and not so many optic components available in the market. It seems not worth to do that way.

Notice that Eq (8) is correct for $\theta_x > \theta_{SR}$. Besides, if there is cold finger or slit in the beam line to let the x-ray through, that changes the E-field. Diffraction error should be calculated again. CLS has done detailed analysis for their diagnostic beam line using half mirror [7]. Anyway, Eq (8) gives very close estimate of diffraction error.

For the NSLS-II beamline, with bending radius R = 25m, measuring wavelength λ = 500nm, the RMS diffraction error from Eq. (8) is Δ_{diff_rms} ~ 39 um. Diffraction error applies to both planes (horizontal and vertical).

From above analysis, total measurement errors from the NSLS2 beam line can be estimated. With horizontal 1.5mrad and vertical 3mrad opening and wavelength of 500nm, measurement errors for both planes are close to 58um. With this resolution, it's possible to measure the horizontal beam size (σ_x ~100um). Vertical beam size is buried in the measurement errors.

APPLICATIONS

After the first mirror and vacuum window, synchrotron light will be steered to the end station where experiments will be carried on. We will have a 3m*1.5m optic table in the SLM shed. Major measurements using the visible light include: streak camera to measure the bunch length and longitudinal profile; fast gated camera to measure the transverse profile of single bunch in single turn; other applications like FleaCCD to monitor the profile, interferometer to measure the vertical beam size, synchrotron radiation fluctuation to measure the bunch length, bunch purity measurement using MCP-PMT etc.

Layout of the possible setups on the optic table are shown in Figure 4,

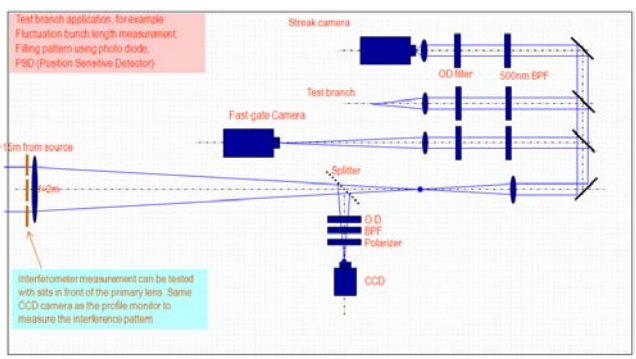

Figure 4, optic table setups in the SLM end station

Streak camera will measure the bunch length, synchronous phase and longitudinal profile at various

machine conditions to get machine parameters such as: broadband impedance, microwave instability threshold, beam loading, injection transient etc. Intensified CCD camera with 2ns minimum gate will be used to measure the transverse profile of every individual bunch. This is especially important for the injection beam tuning and characterization. Beam size blowup along the bunch train due to wake field could be measured from the gated camera as well. Other tests/measurements applicable at the end station include the double slit interferometer to measure the vertical beam size, photon counting using multichannel plate photon multiplier (MCP-PMT) to measure the bunch purity, position sensitive detector to measure the beam central position, pockels cell to measure the bunch-to-bunch motion etc.

INJECTOR SLM

NSLS-II injector consists of 200MeV LINAC, the LINAC to booster transport line (LTB), 200MeV to 3GeV booster and booster to storage ring transport line (BTS). The LINAC will be a turn-key machine from vendors, while the booster will be semi turn-key system. Synchrotron light from the booster ring and BTS are useful diagnostic tools as non-interceptive method. Two synchrotron light ports are required in the booster ring and one port in the BTS is under consideration.

It's highly desired to measure the booster transverse profile and bunch length during the energy ramping. There are two light ports in the booster. One of them will be used for transverse profile monitoring. This monitor will be located inside the booster tunnel with minimum optic lens. Light from the other port will be guided outside the tunnel and onto the optic table, where streak camera bunch length measurements and other monitoring system can be setup. It's very interesting to have a synchrotron light profile monitor in the BTS during top-up operation. With that one can monitor the real-time injection bunches. It will be very helpful during the top-up injection.

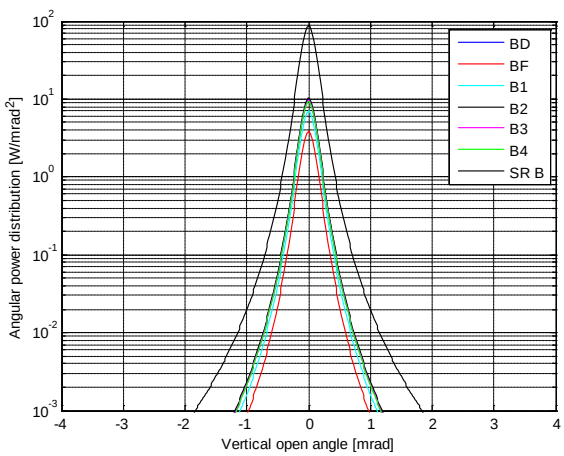

Figure 5, synchrotron radiation power angular distribution.

There are two types of combined function dipole magnets in the booster ring – defocusing dipole (BD) and focusing dipole (BF). There are 8 BD and 7 BF in one quarter of the booster lattice, with 32 and 28 for the whole booster ring. In the BTS transport line, there are two types of dipoles as well. One type of them is close to the booster extraction and storage ring injection point. These are not suitable for diagnostics due to very limited space. The other type has 4 dipoles with 1.3m length each, named B1, B2, B3 and B4 in the BTS. B2 will switch the beam to storage ring or beam dumper. We calculated the dipole radiation power based on the magnet specifications. Figure 5 shows the power angular distribution in these magnets. Peak power in the booster dipole is less than 10W/mrad^2 with 20mA circulating beam. Compared to 500mA storage ring, where the peak power is 88W/mrad^2.

SUMMARY

Visible diagnostic beam line has been designed at the NSLS-II storage ring. Various applications have been defined to characterize the 1nm.rad machine. Measurement resolution has been estimated. Synchrotron light ports in the booster ring and BTS have been proposed.

The author would like to thank Vishy Ravindranath for the first mirror thermal analysis, Om Singh and Sam Krinsky for their encouragement and supervision.

REFERENCES

[1] NSLS-II preliminary design report, http://www.bnl.gov/nsls2/project/PDR/

[2] I. Pinayev, *et al*, 'Preliminary Design of Pinhole Camera for NSLS-II Project', PAC09, Vancouver, Canada (2009).

[3] T. Mitsuhashi, 'Beam Profile and Size Measurement by SR Interferometer' in *Beam Measurements*, Ed. by S. Kurokawa, et al, p. 399-427, World Scientific (1999).

[4] A. Anderson, 'Recent Results from the Electron Beam Profile Monitor at the Swiss Light Source', DIPAC07, Venice, Italy, 2007

[5] Vishy Ravindranath, private communication

[6] A. Hofmann, 'Diagnostic with Synchrotron Radiation', CERN 98-04

[7] J. Bergstrom and J. Vogt, 'The Optical Diagnostic Beam Line at the CLS', NIM A, Vol 562, p 495.

CONTINUOUS BUNCH-BY-BUNCH 16-BIT DATA ACQUISITION USING DDR2 SDRAM CONNECTED TO AN FPGA*

J. Weber, M. Chin, LBNL, Berkeley, CA, U.S.A.

Abstract

A hardware system that acquires and stores a large buffer of bunch-by-bunch 16-bit data has been realized. A high resolution (up to 16-bit) analog-to-digital converter (ADC), or bank of ADCs, samples the analog signal at the bunch frequency. The digitized data is fed into a Field Programmable Gate Array (FPGA), which contains an interface to a bank of Double Data Rate SDRAM (DDR) type memory. With appropriate data bus widths, the FPGA bursts the ADC data into the DDR fast enough to keep up with the bunch-by-bunch ADC data continuously. The realized system demonstrates continuous data transfer at a rate of 1GByte/sec, or 16-bit data at 500MHz, into a 64MByte DDR. This paper discusses the implementation of this system and the future of this architecture for bunch-by-bunch diagnostics.

INTRODUCTION

For many years, beam motion in particle accelerators has been understood well enough to design bunch-by-bunch feedback systems capable of stabilizing the beam. Until recently, these systems lacked the diagnostic capability to monitor the RMS motion of each bunch and store it continuously for an extended period. This information can be used to compute the various coupled bunch modes of oscillation. Monitoring the strength of each mode over time can provide valuable insight that could ultimately be used to better stabilize the beam. High bit resolution is desirable to increase the accuracy of the modal analysis.

One method of capturing long records of high resolution bunch-by-bunch data is digitizing the beam signal with one or several high resolution ADCs, sending the data to a high performance FPGA to pack into a buffer in a large DDR or bank of DDRs (see Figure 1). Only recently has the combination of ADC/FPGA/DDR technologies achieved the performance required to make such a measurement on an accelerator beam with a bunch rate of 500MHz or greater, such as at the Advanced Light Source (ALS).

A new transverse feedback system (TFB) is under development at the ALS that includes hardware capable of performing large bunch-by-bunch captures [1]. We have developed firmware for the FPGA that demonstrates the ability to capture up to 16-bit data at 500MHz and store it in a 64MB DDR, giving us the ability to capture over 15ms of continuous bunch-by-bunch data. This paper describes the hardware requirements and firmware options to achieve the measurement, as well as an example targeted for the ALS TFB and the NSLS-II RF BPM, and the future of this technology for bunch-by-bunch measurements.

* This work was supported by the Director, Office of Science, Office of Basic Energy Sciences, of the U.S. Department of Energy under Contract No. DE-AC02-05CH11231.

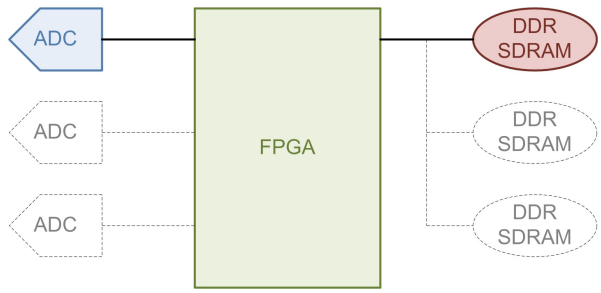

Figure 1: ADC-FPGA-DDR model for bunch-by-bunch data acquisition.

HARDWARE REQUIREMENTS

To capture bunch-by-bunch data, the effective sampling rate of the ADC circuit must match the maximum bunch rate of the accelerator. This can be accomplished by using a single ADC if the sampling rate and bit resolution are sufficient, or by time-interleaving samples from multiple ADCs. Ideally, a single ADC is used to eliminate sources of error caused by multi-ADC sampling, such as phase and amplitude mismatch and thermal drift. The ALS TFB system requires 12-bit resolution and 500Msps sampling, but at the time no single ADC was available that met those requirements. Instead, two 12-bit ADCs are used, each sampling at 250Msps and clocked 180 degrees out of phase to achieve an effective sampling rate of 500Msps.

The FPGA must be able to clock the related logic fast enough to process all the ADC data continuously. In a single ADC system, the FPGA must be clocked at the full bunch rate, unless the ADC has multiple parallel output data buses. In a multi-output ADC or multi-ADC system, the FPGA clock rate can be reduced since the data can be processed in parallel, although this uses additional logic resources. In practice, it is recommended to clock the FPGA well below its specified maximum clock rate since the amount of logic used in the FPGA is large enough that routing at such high frequencies becomes problematic or impossible. The ALS TFB uses a Xilinx Virtex-5 LX50 speed grade -1 FPGA clocked at 250MHz to match the ADC sampling rate, well below the FPGA maximum output clock frequency of 450MHz [2].

The FPGA provides the clock and control interface to the DDR chips, which all must be clocked synchronously and fast enough to transfer the ADC data continuously. At the basic level, the DDR theoretical bandwidth can be calculated by multiplying the maximum allowable DDR clock rate by 2, then by the data bus width. For the ALS TFB, which uses a DDR2 with maximum clock rate of 200MHz [3], the theoretical bandwidth is 200MHz × 2 ×

4 Bytes = 1.6 GByte/s. The ADC data is 12-bits wide, but since it is simpler to transfer data to the DDR without crossing byte boundaries, the ADC values are packaged as 2 Bytes, so the required DDR transfer rate is 250Msps × 2 × 2 Bytes = 1.0 GByte/s. Although the theoretical bandwidth appears to be sufficient to meet the requirement, the firmware implementation impacts the maximum achievable continuous transfer rate. This will be explored in greater detail in the following sections.

FIRMWARE

There are many ways to implement firmware that transfers data from the ADC to DDR. On one extreme, an entirely custom logic solution can be developed, which provides the most flexibility to optimize the design for the specific application. On the other extreme, it is also possible to use design examples and configurable cores from the FPGA manufacturer with minimal customizations to field a less flexible solution more quickly.

For the ALS TFB system, the Xilinx Multi-Port Memory Controller core (MPMC) was selected as the DDR interface. For the Avnet Xilinx Virtex-5 LX50 evaluation board used in the ALS TFB system, the default design includes the MPMC. The MPMC can be configured to use up to 8 separate ports, which is important if the DDR is connected to multiple interfaces. All ports are arbitrated internally in the MPMC using one of the standard arbitration schemes, or a user-defined scheme.

The MPMC supports several types of interface ports. The most basic and high performance of these is the Native Port Interface (NPI), which was chosen to stream the ADC data to the DDR in the ALS TFB design. In addition, the MPMC has a PLB port that the Microblaze embedded processor uses to access OS and program code stored in the DDR. Figure 2 shows the MPMC connections in the ALS TFB system.

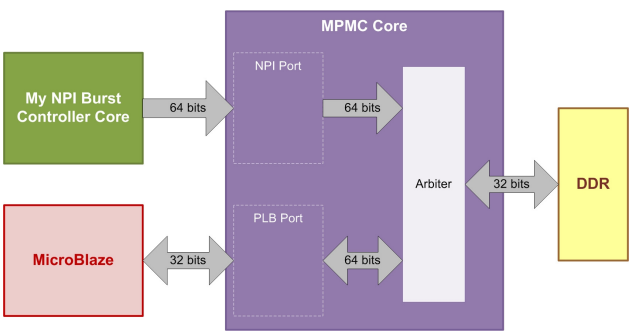

Figure 2: Multi-Port Memory Controller connections in the ALS TFB system.

Native Port Interface (NPI)

My NPI Burst Controller Core (My NPI core) is a custom logic core that transfers the ADC data to the MPMC (Figure 3). One 12-bit value from each ADC is packed into a 32-bit word and clocked into the burst FIFO in My NPI core continuously at 250MHz. Once the burst FIFO contains enough data for a 64-word burst, the control logic in My NPI core enables a 64-word transfer to the write FIFO in the MPMC NPI port at the DDR clock rate of 200 MHz. When the transfer is complete, My NPI core control logic requests a burst write from the NPI port to DDR.

The burst FIFO provides a mechanism for the ADC data to cross clock domains from the ALS RF clock domain (fRF/2 = 250MHz) to the DDR clock domain (LO 100MHz × 2 = 200MHz) as well as some amount of buffering to allow continuous ADC data acquisition in case the NPI burst request is held off by the MPMC arbiter. The burst FIFO can be as deep as the resources available in the FPGA allow. The NPI port write FIFO is required for NPI burst transfers to DDR.

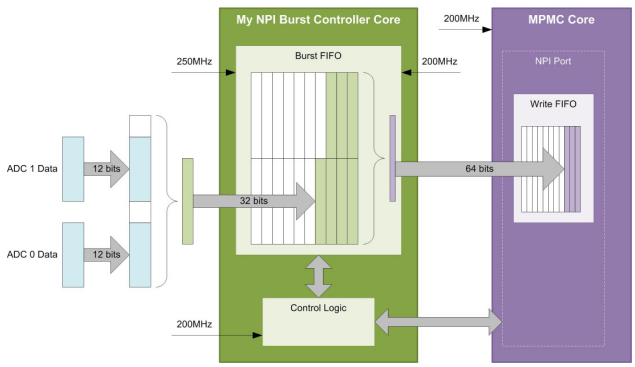

Figure 3: My NPI Burst Controller core architecture.

The maximum continuous transfer rate via an NPI port in burst mode depends on the DDR clock rate, the DDR data width, and the NPI port data width. For the ALS TFB using the maximum DDR clock rate (200MHz), DDR data width fixed in hardware (32 bits), maximum NPI data width (64 bits), and maximum NPI burst size (64 words), the maximum continuous transfer rate is 1.138 GByte/s [4] or 225ns per burst.

MPMC Arbitration

For a single port MPMC system, the maximum NPI burst transfer rate would be sufficient to meet the 1 GByte/s rate required to transfer the ADC data. However, in a multi-port system, the MPMC arbitration scheme must balance the performance needs of all ports to avoid starving any one port and potentially losing critical data. There are several standard arbitration schemes and a configurable custom scheme available in the MPMC. For the ALS TFB system, we base-lined the performance of two schemes: round-robin and custom with the NPI port configured to always have top priority. For each case, the Microblaze ran a simple standalone program out of FPGA Block RAM. The code requests single reads of DDR data in a tight loop to approximate a program executing out of DDR. The code for this program is shown below:

```
#include "xio.h"

int main (void)
```

```
{
    Xuint32 data;
    Xuint32 addr;

    addr = 0x8F000000;
    while (1) {
        data = XIo_In32(addr);
    }
}
```

The default MPMC arbitration scheme is round-robin. In this scheme, each port is sequentially given top priority (i.e. port 1, 2, 3, 1, 2, 3, etc.). For the ALS TFB with a 2 port MPMC, this results in the top priority alternating between the 2 ports (port 1, 2, 1, 2, etc.). Simulations using this scheme indicate that the NPI burst interface does not get enough service to sustain continuous transfer of the ADC data because alternating transactions limited the continuous NPI burst throughput to 256 Bytes per 285 ns (Figure 4A), or 0.90 GByte/s.

Next, the MPMC arbitration scheme was modified so that the NPI port always has priority. This means that the NPI port is serviced as soon as possible after a transaction request, and the PLB port is only serviced if there is no request pending from the NPI port. This scenario was also simulated, and a typical pattern of transactions for this case is shown in Figure 4B. PLB port transactions only occur about every 2 NPI bursts so that the NPI interface can transfer 256 * 2 = 512 Bytes every 510 ns, or just over 1 GByte/s.

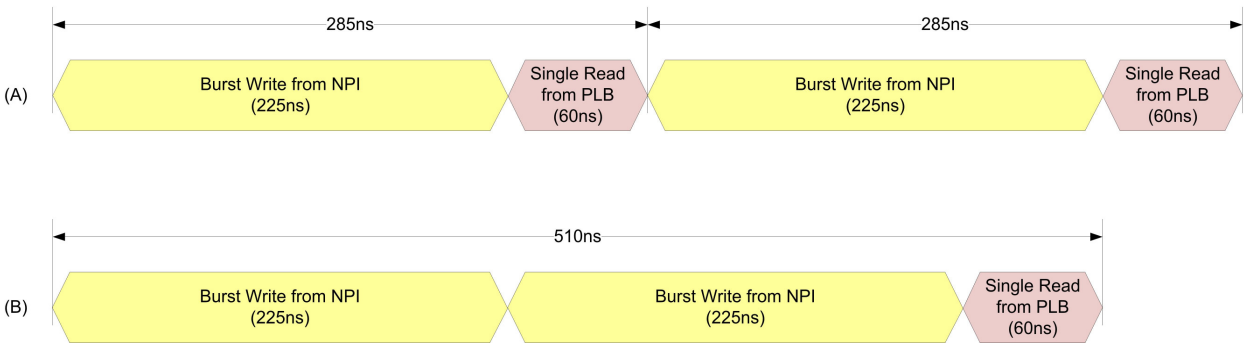

Figure 4: Typical DDR transaction timing diagrams for different MPMC arbitration schemes. (A) Round-robin arbitration. (B) Custom arbitration with the NPI port always the highest priority.

The design was built and tested on the ALS TFB hardware and ran continuously for several hours without corrupting the ADC data capture buffer. This was verified both by monitoring a latched version of the burst FIFO full signal and by reading out the data in the buffer after a stop capture trigger. A slightly modified version of My NPI core (64-bit input port) was built and successfully tested on the Xilinx ML507 evaluation board for potential use in the NSLS-II RF BPM system [5].

This project is now ready to be integrated with Ethernet software that provides remote access to the system. On a shared network, the Ethernet software must handle variable rates of traffic coming from the network, the software load is usually nondeterministic, and the behavior can be difficult to simulate or even test in hardware.

For a complex system with nondeterministic Ethernet software, the software must, at a minimum, handle the expected payload required for system operation. In most systems, this payload is well known and worst-case scenarios can be simulated and tested on an isolated network. To make the system more robust against traffic on a shared network, the software can be optimized to ignore irrelevant traffic and minimize the burden on the DDR. This challenge is not unique to Ethernet interfaces; any nondeterministic external interface that requires software access to the DDR will cause the same behavior.

FUTURE CONSIDERATIONS

The MPMC core is a flexible and capable solution for FPGA embedded processor systems demanding multi-tasking capability from their DDR SDRAM banks. The ALS TFB design is an example of how the MPMC can be configured to efficiently support two interfaces with very different requirements. The MPMC arbitration scheme used is one of simplest; in the custom scheme, time slot prioritization can be used to precisely tune the arbitration to the specific needs of the application and maximize the DDR bandwidth efficiency. Also, the depth of the burst FIFO can be adjusted to compensate for longer periods of port starvation due to the configuration of the arbitration scheme. For more complex designs requiring many MPMC ports, the arbitration scheme is critical to meet the demands of all your port interfaces.

Many of the Xilinx FPGA evaluation boards now use a DIMM interface to DDR SDRAM to support much larger depths of memory, allowing easy memory upgrade by replacing only the DIMM module, not the FPGA board. FPGA and DDR clock rates continue to climb and DDR transfer bandwidths increase proportionally, limited only by the maximum burst size and the data bus bandwidth. For example, the Xilinx ML605 Combines a Virtex-6 FPGA with a 512MB DDR3 SO-DIMM 64 bits wide that can be clocked at 533MHz, which could support a theoretical transfer rate of 8.5 GByte/s, more than 5 times greater than the ALS TFB system.

CONCLUSION

Continuous 16-bit bunch-by-bunch data acquisition at 500 MHz has been realized on the ALS TFB system. The MPMC core provides a fairly flexible interface to the DDR that includes multi-port arbitration. The NPI port provides the highest performance burst transaction of the port types supported by the MPMC. The performance requirements for each port must be carefully considered and addressed by the arbitration scheme. The future of the technologies in use will support ever increasing demands on resolution, bandwidth, and buffer length for bunch-by-bunch data capture.

ACKNOWLEDGEMENTS

The authors would like to thank David Robin, Greg Portmann, and the rest of the ALS Physics Group for supporting and motivating this project. Also, thanks to Kurt Vetter and Kiman Ha for informal discussions and emails contributing to this effort and for testing the firmware on the ML507 evaluation platform.

REFERENCES

[1] J. Weber, M. Chin, “ALS FPGA-Based Transverse Feedback Electronics”, BIW08, Tahoe City, CA, May, 2008. <http://accelconf.web.cern.ch/AccelConf/BIW2008/papers/tuptpf017.pdf>.

[2] Xilinx. “Virtex-5 FPGA Data Sheet: DC and Switching Characteristics”, DS202 (v5.2), June 25, 2009, <http://www.xilinx.com/support/documentation/data_sheets/ds202.pdf>.

[3] Micron. “256Mb: x4, x8, x16 DDR2 SDRAM Features”, 256MbDDR2.pdf – Rev. M 7/09 EN, July, 2009. <http://download.micron.com/pdf/datasheets/dram/ddr2/256MbDDR2.pdf>.

[4] Xilinx. “Multi-Port Memory Controller (MPMC) (v5.04.a)”, DS643, December 2, 2009, <http://www.xilinx.com/support/documentation/ip_documentation/mpmc.pdf>.

[5] K. Vetter, et al, “NSLS-II RF Beam Position Monitor”, these proceedings.

ACHIEVING HIGH-SPEED DATA ACQUISITION FOR REAL-TIME BEAM CONTROL AND MEASUREMENT

R. Soden, Y. Maumary, P-F. Maistre, Agilent Technologies SA, Plan-les-Ouates, Switzerland
S. Narciso, G. Hill, Agilent Technologies, Inc. Loveland, CO, U.S.A.

Abstract

Digital data acquisition in real-time applications falls into two categories: digitizing a stream of data without missing a single sample point, and capturing a stream of triggered events without missing a single trigger.

Maintaining these data streams over long periods requires an optimized combination of analog signal conditioning, precise digitization, digital data reduction and high-speed data transfer. This paper describes suggested methods to reduce the amount of measurement data required, reduce the amount of that data that is to be transferred to a measurement where possible, and then transferring this reduced data in the most rapid fashion. Our approach uses a combination of hardware, firmware and software elements that are designed to work together, optimizing performance and managing the data bottlenecks.

New hardware standards and architectures are discussed that improve the capabilities of today's technologies, providing access to higher data and measurement flux. Applications presented in this paper include high trigger rate capture for beam steering and fill pattern monitoring in charged particle accelerators.

THE KEY ASPECTS OF REAL-TIME MEASUREMENT

Measurement in real time requires a constant flow of accurate data. Maintaining the flow and the accuracy of the data transferred requires specific considerations to the techniques used.

Accurate measurement

Measuring once takes half the time of measuring twice! But to have confidence in a measurement means using equipment that is properly specified and meets those specifications.

These specifications need to go beyond the banner specifications of Bandwidth, Sampling rate, Resolution, and into the secondary specifications that talk of distortion and noise, which deteriorate signals and measurement.

Figure 1 shows the how noise and distortion are typically specified for high-speed digitizers. There are a number of surprising interactions between performance aspects that contribute to diminish the accuracy of the final acquisition. The effective number of bits (ENOB) antonymous to signal to noise and distortion (SINAD), provides a good measure of how all other performance aspects add up to the quality of the measurement of the final system.

Previous work has discussed noise and distortion in detail[1]. Unfortunately there is no simple answer to the question "Which digitizer should I use in my system?" Instead, each application and device must be reviewed on a case-by-case basis, with a view to optimizing the required measurement.

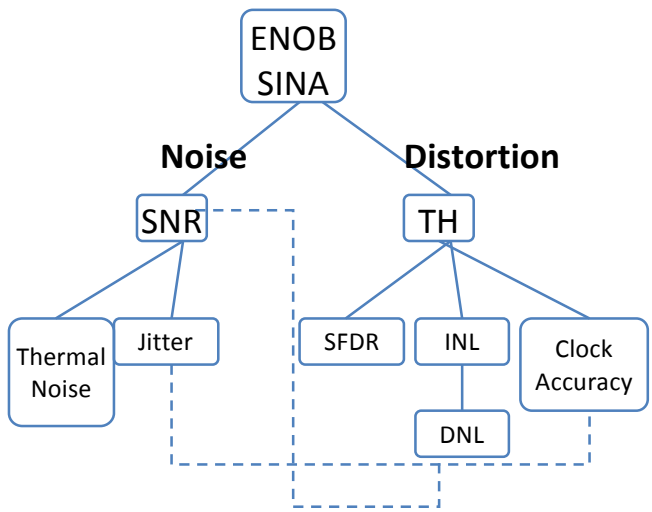

Figure 1: Noise and distortion specifications.

Data reduction

Smart handling of the acquired data on the card can reduce the amount of data that needs to be transferred to the system.

Segmented acquisition of only required data is the first step (trigger, delay, acquisition of pre-determined length vs, trigger, acquire), thus acquiring only the required data, not the preamble and post-acquisition data.

Data processing within on-board field programmable gate arrays (FPGAs) can be used on the module to reduce data down to a measurement.

Peak detection identifies peaks and troughs in data, outputting only peak heights and peak times, rather than the entire data waveform.

Waveform averaging captures repetitive signals and averages them to remove random noise.

Real time FFT processing reduces a temporal signal into its frequency power spectrum.

Data transfer

Optimized data transfer is achieved through the mix of how the data is transferred, and the bus over which the data is passed.

Today, high-speed solutions use a number of different bus systems:

- PCI –up to 532 MB/s - low latency 64-bit/66 MHz
- PCIe – up to 8 GB/s - 16 lane 2.0 (16x)
- VME/VXS - 3.125 Gbps with aggregate up to 2.5 GBytes/s
- Optical data ports - up to 4.25 Gbps

Burst transfer rate is the key parameter to maximize the measurement throughput.

- Burst transfer rate depends on the size of the transfer.
- Burst transfer rate depends on the chip set payload size.

Figure 2 shows the maximum trigger rate TR_{max} for a segmented acquisition process as a function of the segment size *Seg*.

This example assumes we have a single channel acquisition with 8-bit ADC resolution. Data transfer is accomplished over a PCI Express (PCIe) bus interface with a maximum data rate of 1100 MB/s (PCIe 8x standard). As most high-speed digitizers combine a smaller amount of fast memory a larger amount of slower, but less expensive, acquisition memory, we assume an internal fast memory of 600 kS and an external DDR2 memory of 512 MS. The latency in these memories limits the inter-segment dead time. That is the dead-time between two segments when an acquisition cannot be made. For the purposes of this calculation we assume a dead time of 800 ns for the internal memory (*DTi*) and 1800 ns for the external memory (*DTe*).

Two factors limit the maximum trigger rate in this calculation. The first is this dead-time:

$$if\ Seg < 600kS, \quad TR_{\max} = \frac{1}{DTi + \left(Seg / SR \right)},$$

$$if\ 600kS < Seg < 512MS, \quad TR_{\max} = \frac{1}{DTe + \left(Seg / SR \right)}$$

where SR is the sampling rate of the acquisition. Maximum trigger rate is the inverse of the period needed to acquire the defined segment length at the defined sampling rate, plus the fixed dead-time between segments, as defined by the requirements of the segment length.

The second factor in the trigger rate is the data rate of the PCIe interface. As we are limited to 1100 MB/s through the 8x PCIe, $Data_{8x}$, our accumulation rate of data cannot exceed this limit without halting the acquisition. This accumulation rate, is simply the product of the segment size Seg and the Trigger rate,

$$Seg \times TR_{\max} < Data_{8x}.$$

With shorter segment lengths, trigger rates are limited by the inter-segment dead-time. As segment lengths increase, the impact of this fixed-length dead-time decreases, most notably for the higher sampling rates.

The backplane bottleneck presented by the PCIe interface limits our acquisition only as we approach these higher sampling rates. From Figure 2 we can see that for all sampling rates over 1 GS/s, the maximum trigger rates are identical for segment lengths over 110 kS.

This is even more apparent in Figure 3, where we use the PCIe x4 standard backplane for our model. Here the data rates are limited to around 500 MB/s, and we see that sample rates over 500 MS/s are limited by this bottle neck for segment lengths in excess of 800 samples.

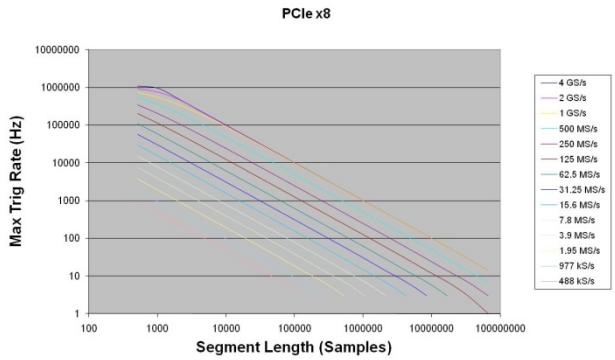

Figure 2: Maximum trigger rate as a function of segment size in a segmented acquisition process, using a PCIe x8 interface.

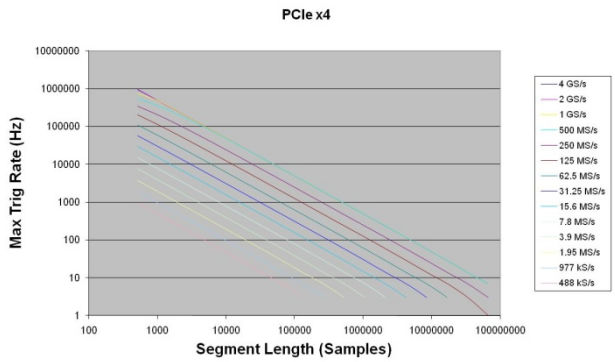

Figure 3: Maximum trigger rate as a function of segment size in a segmented acquisition process, using a PCIe x4 interface.

Operational Software

The final aspect to be discussed is the software environment within which the real-time processes are controlled and monitored.

The software code must be optimized for the available system resources. Our low-level kernel takes advantage of hardware configuration and bus to maximise throughput. It uses Scatter-Gather DMA with multibuffer single stream for high speed data transfer. A high level API gives access to the kernel; this is easy to program to, with an entry point at the level of SCPI commands.

REAL-TIME MEASUREMENT EXAMPLES

The use of these measurement principles in high-speed real-time beam instrumentation is proven. Examples include the OASIS system at the Large Hadron Collider at CERN and fill pattern monitoring at the Australian Synchrotron.

Beam control at the LHC, CERN

The performance of the LHC depends on the performance of the injector chain. Along that chain, the Open Analogue Signal Information System (OASIS) acquires and displays analog signals in the acceleration domain.

The signals come from every CERN accelerator and are sampled using various types of digitizers. The digitizers are co-located with front-end computers (FECs) that perform first-level processing. This preserves bandwidth when the acquired data is sent through an Ethernet network for display on a workstation running a dedicated virtual oscilloscope (Vscope) application.

Vscope is a software oscilloscope that takes data from various types of digitizers and displays all waveforms as if they came from the same type of hardware module. Through this scheme, CCC personnel can perform side-by-side comparisons of multiple signals from throughout the injector chain. The OASIS architecture aligns the signals to ensure meaningful comparisons by synchronizing acquisition settings across all of the hardware digitizers.

Figure 4 shows an OASIS Vscope example bunch rotation, similar to that seen in the LHC beam. More than 2,000 individual signals are available to the operators and physicists who use OASIS. They are looking for a variety of indicators from the LHC and its injector chain: instabilities in the proton bunches; quality of the beams; current in the fast-pulsing magnets (“kickers”); phase relationships between the kickers; and the state of the RF signals in the accelerating cavities. All of these characteristics help determine if conditions are optimum for whichever experiments are scheduled for a given shift.

High-performance digitizers are used to perform wideband beam monitoring and monitor forward and reverse RF signals in the accelerator cavities. In a literal sense, the beam monitoring measurements are made possible by Agilent U1064A digitizers, which provide sufficient speed and bandwidth to capture the signals of interest. In the RF measurements, Agilent digitizers measure direct and reflected energy and thereby help determine the final energy provided to the beam during each revolution around the accelerator.

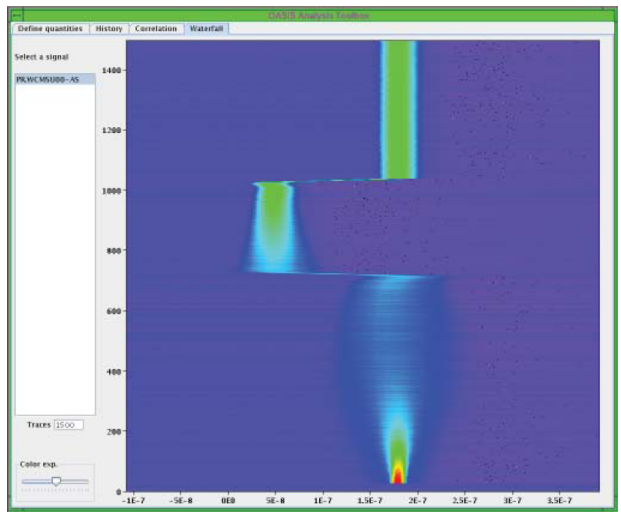

Image courtesy of CERN. © Copyright CERN Geneva.

Figure 4: An OASIS Vscope screen showing an example bunch rotation similar to that seen in the LHC beam.

Real-time measurement of the fill pattern at the Australian Synchrotron

The Australian Synchrotron is a third generation light source, operating at 3.0 GeV with an expected electron bunch width of 20 ps. The storage ring’s harmonic number is 360 and its period of revolution is 720.5 ns.

To ensure a high-quality beam, the synchrotron uses fill-pattern monitoring (FPM) to measure real-time intensity distribution of electron bunches in the storage ring[2]. Knowledge of the electron fill-pattern profile is important for experiments that require precise spatial and temporal control. For experiments that are spatially and temporally sensitive, a source with a known temporal-intensity profile makes it possible to analyze the effects of the radiation source on the results.

The combination of an ultra-fast photo diode, suitable electronics and the Agilent Acqiris digitizer enables real-time measurements of fill patterns with a resolution of one RF bucket. This use of the FPM is now an integral part of the control system software at the Australian Synchrotron.

NEXT GENERATION HARDWARE ARCHITECTURES FOR REAL-TIME CONTROL AND MEASUREMENT

New advances in hardware interfaces allow high-speed serial buses with data transfer rates beyond that of older parallel bus architectures. These new bus architectures are implemented in a number of different form factors that lend themselves to different applications.

PCI Express, or PCIe, is a high-speed serial replacement for the PCI and PCI-X bus.

Data rates of PCIe currently reach up to 8 GB/s for 16 lane PCIe v2.0, this will increase to 16 GB/s with v3.0. However the latency of PCIe is actually higher than some of the older architectures.

The transfer of short bursts of data can be dominated by bus "handshaking." It is often wiser, when possible, to collect bursts of data together in bank and read the entire bank out in one go. We have found that for data packets of less than around 30kB, such as pulse data, standard parallel PCI (64-bit/66 MHz) can outperform the serial 4 lane PCIe bus. To truly take advantage of these improved data rates, we need to combine them with on-board FPGA data processing that can make the measurement on the card.

AXIe is an open standard based on AdvancedTCA, designed to create a robust ecosystem of components, products and systems for general purpose instrumentation and semiconductor test.

The hardware standard provides a larger footprint than both cPCI and VME, and as such can provide greater performance density per inch of 19" rack space than those standards. Board footprints provide space for high performance signal conditioning and sensing, with high power/cooling capacity for high-performance analog and digital subsystems. Multi-module synchronization is possible using the AXIe trigger buses, star trigger, sync, and clock resources. AXIe also has a local bus between adjacent modules, using LVDS pairs, for high speed module-to-module communications.

CONCLUSIONS

This article describes a number of considerations and techniques needed to optimize high speed data acquisition in real-time applications.. Application of these to beam instrumentation enables continuous streams of accurate data in raw data flow or high trigger rate applications. Finding the right combination that meets the requirements of the system in question will always require specific knowledge—not only of the application, but also of the digitizing capabilities of the hardware.

REFERENCES

[1] R. Soden, "Interpreting Quoted Specifications when Selecting Digitizers", Agilent Measurement Journal 2004, No. 4,

[2] D. J. Peake; M. J. Boland, R. Dowd, G. S. LeBlanc, M. J. Spencer, Y.-R. E. Tan, R. P. Rassool, "Measurement of the Real Time Fill-Pattern at The Australian Synchrotron", Nuclear Instruments and Methods in Physics Research Section A: Accelerators, Spectrometers, Detectors and Associated Equipment, Volume 589, Issue 2, 1 May 2008, pages 143-149.

TUNING THE BEAM: A PHYSICS PERSPECTIVE ON BEAM DIAGNOSTIC INSTRUMENTATION *

M.S. Gulley#, Los Alamos National Laboratory, Los Alamos, NM 87545, U.S.A.

ABSTRACT

In a nutshell, the role of a beam diagnostic measurement is to provide information needed to get a particle beam from Point A (injection point) to Point B (a target) in a useable condition, with 'useable' meaning the right energy and size and with acceptable losses. Specifications and performance requirements of diagnostics are based on the physics of the particle beam to be measured, with typical customers of beam parameter measurements being the accelerator operators and accelerator physicists. This tutorial will be a physics-oriented discussion of the interplay between tuning evolutions and the beam diagnostics systems that support the machine tune. This will include the differences between developing a tune and maintaining a tune, among other things. Practical longitudinal and transverse tuning issues and techniques from a variety of proton and electron machines will also be discussed.

MOTIVATION

This is intended to be an 'end-user perspective', with the view that the accelerator operator and accelerator physicist are the primary users of beam diagnostic instrumentation. This is also intended to be a comparison of machines, not just a "LANSCE" talk. If this works, it will trace my experiences in going from an experimenter to an accelerator physicist to supervising operators to supervising beam diagnostic instrumentation personnel.

WHO IS THE TUNER?

To begin a discussion of this nature, one first must ask what is meant by a 'physics perspective'. As I struggled with this question, the first thing that I realized was that to understand such a perspective, one must begin by understanding the user.

Is there such a thing as a typical accelerator physicist? Of course not. However, there are certain commonalities. Let us start out with education. The education of most accelerator physicists comes from a couple of different areas. The first area is, of course, formal education and/or training in accelerator physics. This, actually, is not a common thing to find, at least in my experience. I performed an informal poll of my colleagues at and beyond the Los Alamos Neutron Science Center (LANSCE), which is where I work, and found a decided lopsidedness to the origins of many of the physicists there. Jeff Kolski is a graduate student from Indiana University working on his thesis performing studies of our Proton Storage Ring (PSR). So, he is developing the background one might expect from an 'accelerator physicist'; accelerator physics. Yuri Batygin, new to our Operations Physics Team, is also formally trained in accelerator physicst in the former USSR.

Now let's look at the other end of the scale, starting with me. I came from a background of accelerator-based atomic physics. Several of my colleagues, such as Larry Rybarcyk, Rod McCrady, Chandra Pillai, Glen Johns, and Thomas Spickermann all were experimental nuclear and/or particle physicists. Many of us landed at some point in our careers here at the accelerator to do experimental physics and eventually ended up moving over into the operation, design and modeling of accelerators. I have had numerous conversations where one of us would point to an area and make a comment about the first experiment we were involved in here.

The next question is "what, if anything, does this mean?" One thing that it means is that the odds are against the average physics graduate student walking into a physics program that has accelerator physics as a subject area. That is not surprising. I did an informal search for physics programs that included accelerator physics and found fewer than ten institutions in the US that offered programs of various types in fields of accelerator physics or beam physics. This is compared to institutions that number in the rough range of three hundred or so that offer graduate studies in physics.

The next question that can be asked is about the other major brand of accelerator tuner, the accelerator operator. Operators come from a different mold than the physicist does, typically. So, where does the typical operator come from? This question is as least as machine dependent as the first one. At LANSCE, many of the operators have a background of having served in the Navy's Nuclear Power School. This is the school that trains sailors and civilians for shipboard nuclear power plant operation and maintenance of naval nuclear ships and submarines. These 'navy Nukes' have several of the qualities needed for accelerator operation. They have experience with large, complex systems. They, in fact, have experience with large, complex systems that will kill you if you do not pay attention to what you're doing. They have experience with radiological environments. They have strong technical backgrounds.

LANSCE has also had some success with hiring operators with backgrounds in nuclear power plant operation. Another area that LANL has explored has been 'local talent'. What has been done is to go out and find qualified candidates who are in a local electrical/mechanical technician program and have them do an apprenticeship at the accelerator.

*Work supported by the Department of Energy (DOE) under Contract No. DC-AC52-06NA25396. (LA-UR-10-02861)
#gulley@lanl.gov

Not surprisingly, another common area that operators come from is physics. Many accelerators, such as Fermilab and Jefferson Lab, look to physics BA/BS recipients as potential operators. These operators also have a strong technical background and a basic understanding of the physics behind the machine.

REQUIREMENTS

The next question one might ask to get a better understanding of a physics perspective is "what does the typical tuner want?" This question is asked from the perspective of what one wants in beam diagnostic instrumentation. The first thing that the tuner wants is to get what could be referred to as reliable measurements. This means that the equipment works, the results are trustworthy, and the measurements are timely. The term 'timely' is pretty open to interpretation, but if one is spending most of the time waiting for the diagnostics system to go through an evolution of obtaining and displaying data, then that is where there is usually a problem.

There is a relationship between the person who knows what the equipment does and how it works and the person who understands the information it generates. Do the tuners care about the details of the equipment functionality? Generally, yes. Keep in mind the typical tuner has a technical background and is the sort of person who dismantled the first VCR player the family owned to see how it worked. So, part of the process of developing confidence in the results the equipment is providing is to understand what is going on to get the data. This history that the typical tuner has can be used to the advantage of everyone.

WHAT DO WE NEED TO KNOW?

Physically, we need the beam to get from point A (which is usually a source or injector system) to point B (which is typically a target) in the right condition. What is meant by the right condition? There are a number of things to consider. First, where is the beam within the beam pipe? This is the zeroth order part of the transverse tune. Next is the beam focusing the way that it should and at the points in the transport that it should? This gets us into looking at the phase distribution of the beam with this aspect being the transverse distribution. Next, what is the beam energy and how well is it being bunched? This gets us into the other aspects of the distribution of the beam, which is the longitudinal distribution. Other parameters that we need to know about are things like beam intensity and how well the beam is being transmitted along the accelerator or transport. The other parameter that has to be kept in mind is basically how all of these aspects of the beam are related to each other.

TRANSVERSE TUNING

This can be generally referred to as the "keep it between the ditches" part of the tune. The beam needs to be bent by the right amount at the right locations. Even with benders, corrector or steering magnets need to be strategically placed. In addition, other elements, such as quadrupole magnets, will have an impact on the steering of the beam. The other part to this is proper focusing of the beam.

One may ask one's self, "what can possibly go wrong?" as far as transverse tuning goes. Mis-steered beam will create havoc in a number of ways, including creating spill and transmission problems all the way to damaging equipment. Looking at Figure 1, one can see a dark spot in the center of the picture which is a hole in the beam pipe. In this case, an issue with the accelerating structure and run permit system upstream of this area allowed beam that was roughly 89 MeV into a bender magnet set for 100-MeV beam.

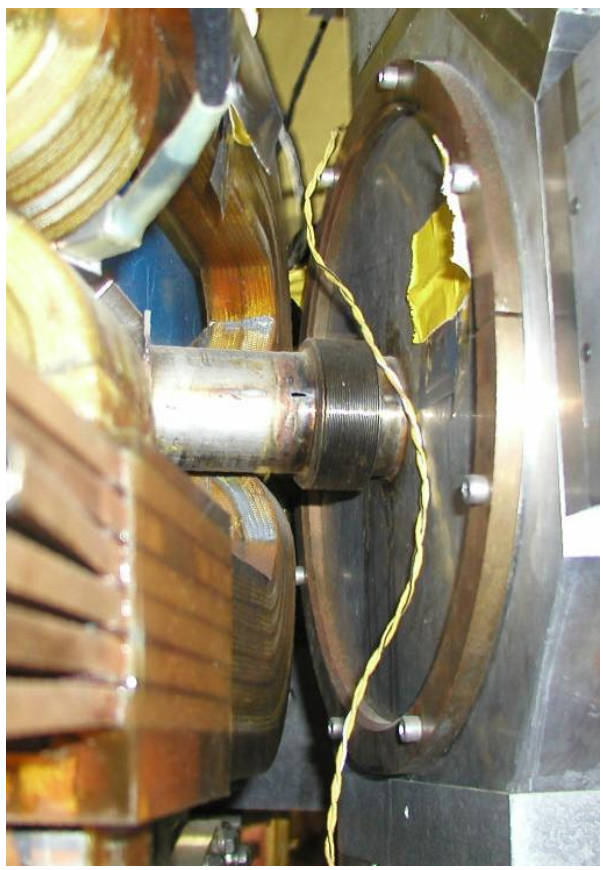

Figure 1. The dark spot in the center is a hole created by an 89-MeV proton beam in a beam pipe in the Transition Region of the LANSCE accelerator.

TRANSVERSE DEVICES

There are a number of transverse devices that are commonly used for diagnosing the beam. Examples include wire scanners and harps. These provide interesting information to the tuner in the form of showing what a cross section of the beam looks like. One can

quickly and easily see how Gaussian the beam looks. Another device commonly used is a phosphorescent screen. These screens are straightforward but they usually cannot handle full beam currents. Also, unless one is digitizing the image and analyzing it, one can only get qualitative information from it. There is also a plethora of different devices intended for directly producing the emittance of the beam. Another type of transverse device is any one of a variety of beam position monitor. These have the characteristic of primarily measuring the position of the centroid of the beam, without necessarily showing information about the cross-sectional profile of the beam the way a diagnostic like a wire scanner can.

So what are we doing with this information? We are interested in the emmitance because it needs to be within certain values or the beam will expand too much for reasonable transmission. We also need to confirm that it is going to focus properly at the locations that we want it to focus at. The sort of locations we are interested in are areas like the center of a beam buncher or chopper, and so on. Also, the beam needs to have the proper characteristics at injection points of accelerating structures.

PARTICLE PARAMETERS

The primary thing that a tuner is concerned with is the particles that make up the beam. Table 1 shows some typical numbers of particles in each bunch or macropulse for a variety of different machines. The thing to notice here is that the number of particles in a bunch is huge. Numbers are typically between 10^9 and 10^14.

Facility	# of Particles per bunch/macropulse
LANSCE	5.9e13 H+ 3.3e13 H-
SNS	1.6e14
ISIS	2.5e13
APS	2.3e12
ALS	4.16e9
LHC	1.1e11

Table 1. Typical numbers of particles per bunch or macropulse at a sampling of facilities.

Why does this matter? Because, given the ability to do so, the tuner would try to understand the machine better by knowing what each and every particle is doing in each of six coordinates in its phase space. The six coordinates that make up this vector quantity are the horizontal and vertical positions of the particle, the angle of the particle's trajectory with respect to the horizontal and vertical axes, the particle's momentum, and phase.

Not surprisingly, this cannot be done easily. There are simulation codes in use that make use of macroparticles to simulate groups of individual particles and these codes can handle number such as 10^5 macroparticles. Figure 2 shows what a simulation of the LANSCE low-energy beam transport using the Beampath code looks like.

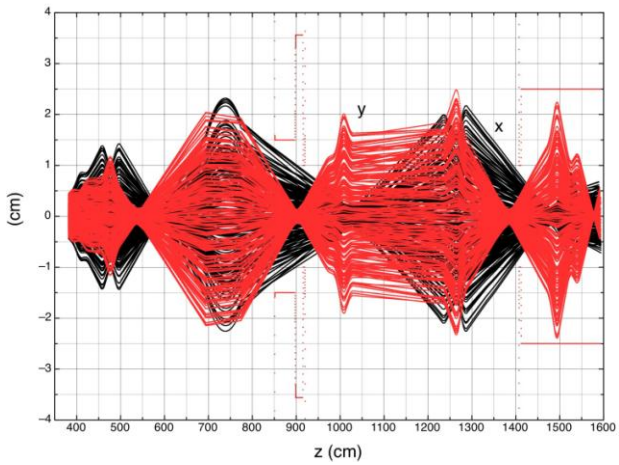

Figure 2. Beampath simulation of the LANSCE low-energy beam transport. The red paths are the vertical plane and the black paths are the horizontal plane. Courtesy of Yuri Batygin.

One thing that needs to be pointed out with this type of simulation is that it is time-intensive. It is not conducive to tuning a beam line in real time, despite that fact that it creates a simulation that might come closer to the real thing than a standard envelope calculation.

As a result, many beam simulation tools use beam envelope calculations for real-time tuning. These tools can take information from actual emittance measurements and do a reasonable job of predicting the transport of the beam, assuming the details of the transport are known reasonably well. Thus the emittance ellipse becomes an important tool in the process of tuning a beam line. Instead of looking at individual particles or macroparticles, we look at the integral of different parts of the phase distribution of the group of particles. This is where the beam envelope concept comes in. Transversely, we look at what the envelope of the position and angle of the beam looks like. The area of this envelope is what is referred to as the emittance of that part of the distribution. Figure 3 shows an example of such an emittance ellipse. From it, one can see relevant parameters for one axis, namely the x-axis in this case, with x representing the position of the particles and x' representing the angle the particles are traveling with respect to the x-axis. Various parameters of the ellipse are also called out such as the maximum extent in the x and x' axes, the x and x' intercepts. These values are described in terms of the emittance (ε) as well as the so-called Twiss parameters

(α, β, and γ). These will be discussed more later and are the characteristics of the envelope emittance ellipse that can be determined from the measurements and used to predict the action of the beam.

Emittance is the area of the beam ellipse and as such has

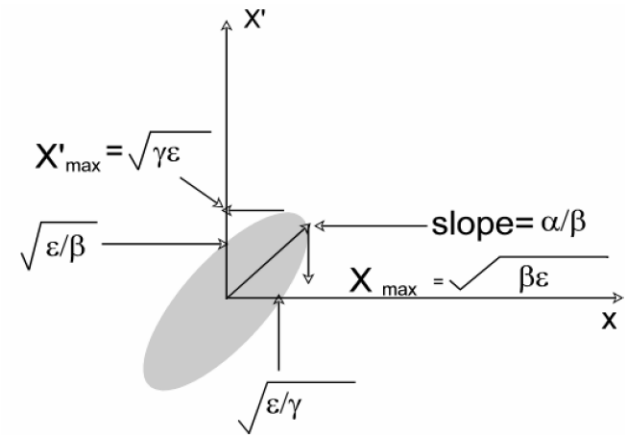

Figure 3. An example of an emittance ellipse.

units of distance times angle. Typical units used are mm times mrad. But there are numerous ways to express this quantity. Since the rad is a dimensionless quantity, it can be left off and simply implies. As a result, one can see emittance expressed as μm. Table 2 shows some emittance values from a sampling of different machines.

Facility	Emittance	Normalized Emittance
APS	2.5 nm-rad	
ISIS Source		.2 π mm mrad
ALS	6.8E-9 m*rad	10/0.7 μm
SRC Aladdin	40 π nm rad	
SLC		50/8 μm
SPS-LHC		3 μm/3.5 μm
LANSCE (750 keV)	5 π mm mrad	.2 π mm mrad
LANSCE (800 MeV)	.2 πmm mrad	.3 π mm mrad

Table 2. Emittance measurements from a sampling of machines. Notice the variety of ways of reporting the emittance units.

One can see that there are various ways of reporting emittance, starting with natural emittance vs. normalized emittance and going into different units (μm rad, mm mrad, etc.), which can lend itself to confusion on what the relative sizes of emittance at different machines are. It is also worth pointing out that there is a wide spread in the size of the particle beams at different facilities, which covers several orders of magnitude. Storage ring colliders such as PEO-II, KEKB and LEP often have rms spot sizes between 100 to 200 μm horizontally and just a few μm vertically. Sizes in some of the linear colliders such as NLC or TESLA get down into the range of a few hundred nm horizontally and a few nm vertically. High intensity proton machines such as SNS or LANSCE can have rms spot sizes up to a couple of mm.

TWISS PARAMETERS

It has been mentioned that the beam envelope can be described by an ellipse. The details of how this is derived are available in any one of a number of accelerator physics texts. The equation is that of an ellipse in phase space for either of the transverse planes:

$$\gamma x^2 + \alpha x x' + \beta x'^2 = \varepsilon \qquad \text{Eq. 1}$$

The important thing to note is the information one can extract from the different Twiss parameters. The beam size is the square root of β times the emittance. Similarly, the beam spread is the square root of γ times the emittance. α gives insight into whether the beam is converging, diverging, or columnar. It is worth quoting Minty and Zimmermann [1] at this point; "Thus, the actual values of β, α and γ can be deduced from the measured beam distribution. It is a challenge to the accelerator physicist to make them coincide with their design values."

Having an understanding of what the elements of the equation means is one thing, but another useful thing to know is what the size and shape of the emittance ellipse implies qualitatively. For our first example, in Figure 4 one sees two ellipses, one of which is vertical and one horizontal. The vertical orientation means there is not much spread in the x position, but quite a bit in the x' position. This is a beam at a focal point. Inversely, a horizontal spread indicates a wide beam that is columnar.

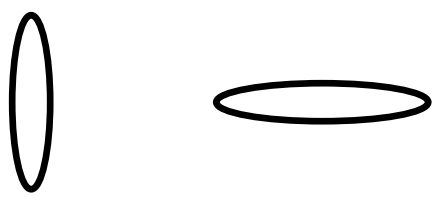

Figure 4. Emittance ellipses for a focused beam and a columnar beam.

Most emittance measurements show an ellipse at an angle (see Figure 5). In such a case, the beam is neither focused or columnar, but somewhere in between. It is important

for the tuner to get an intuitive feel for what is going on in such a case, because one can quickly determine what is going on. Another point to note is that often the emittance ellipse will not be a nice, geometrically simple ellipse. This is the case when non-linear forces have had an effect on the particle beam. An example of such a distribution is shown in Figure 6.

Figure 5. Emittance ellipses for a beam that is focusing and one that is diverging.

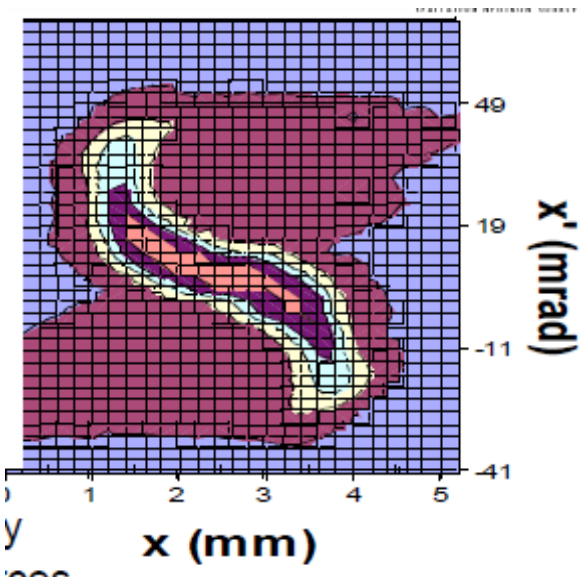

Figure 6. Measured emittance at SNS [2].

The color-coded emittance graph as seen in Figure 6 is one way to graphically represent the emittance ellipse. Another way is shown in Figure 7.

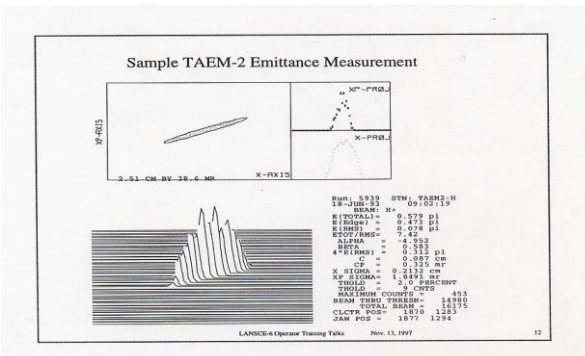

Figure 7. Sample output of the Emittance Replay program from LANSCE.

The reason that some amount of effort has been expended in going over a general description of the emittance is because the quantities associated with it are at the heart of what the person tuning the beam is trying to understand. Basically, we try to understand what the distribution of the particles in phase space is doing. Further, and very importantly, this is a dynamic process. As one looks through texts and presentations, the emittance is presented as a graph and it lends itself towards being interpreted as a static measurement when, in fact, it is a snapshot of what the beam is doing at a very particular moment and place.

LONGITUDINAL TUNING

The next important concept related to the particle distribution is the longitudinal component. Most of what we have discussed until now is about understanding how the bunch of particles is distributed within the beam pipe. The other important aspect is how to measure the acceleration of the beam and know that it is reaching the right energy and is staying together longitudinally while doing it. Accelerators are radio-frequency (RF) devices and as such, we need to understand how the bunch of particles needs to interact with the RF. In general, the particles need to see the RF field when the field will stably accelerate the particles. Not all particles will be at this point for synchronous acceleration. Some will be a bit too fast and some too slow. By picking the synchronous phase to be less than zero, the slower and faster particles will naturally tend towards being bunched. Figures 8 and 9 show this requirement to get the particle bunch properly phased with the RF.

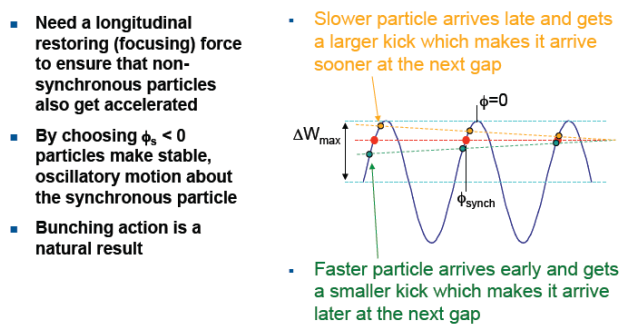

Figure 8. Choosing ϕs such that the motion about the synchronous particle is stable. Courtesy of Larry Rybarcyk.

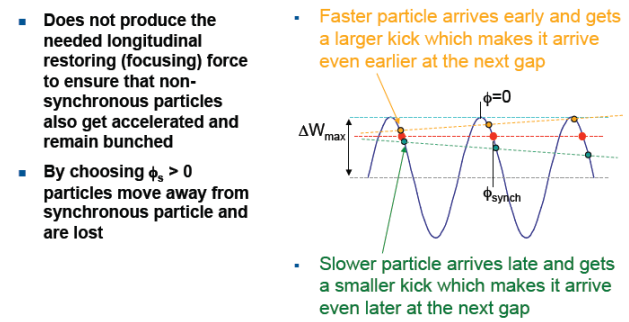

Figure 8. Choosing ϕs such that the motion about the synchronous particle is not stable. Courtesy of Larry Rybarcyk.

To maintain the stable motion of the beam, longitudinally it needs to be within a phase space region bounded by what is generally referred to as the separatrix, or more colloquially, the "fish". The separatrix is a nice graphical way to show where the areas are in which the particles will exhibit stable motion (meaning they will continue to accelerate) and which particles will "get lost". This means they don't get accelerated properly and eventually become spill of some sort. This relationship is shown graphically in Figure 9.

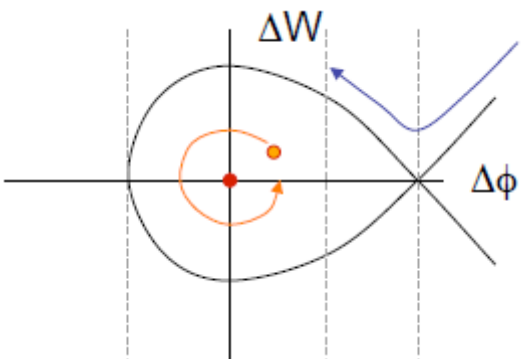

Figure 9. Examples of stable and unstable motion within phase space. Courtesy of Larry Rybarcyk.

MEASURING THE LONGITUDINAL TUNE

How this tune gets measured is dependent on the machine and energy level. A common method used at a number of machines is the absorber and collector technique. Here, a device, usually a slab of metal whose thickness is designed to completely absorb particles below a certain energy, is placed in the beam. A collector, such as a Faraday cup, is placed behind the absorber and measures the amount of beam current getting through the collector. By scanning though the RF phase of the accelerating structure, one can plot out the results and see the optimal RF phase setting. Figure 10 shows an example from LANSCE, but the technique is comparable at other machines.

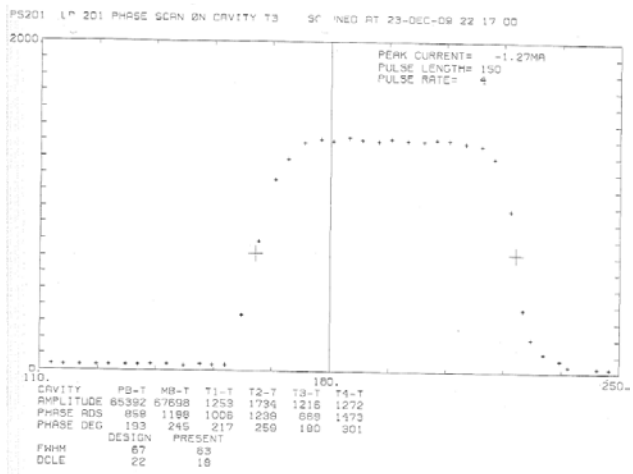

Figure 10. Example of a phase scan of Module 2 at LANSCE.

Another common procedure for longitudinal tuning as the particles get up to higher energies is the Delta-T scan. In this procedure, beam position monitors between accelerating cavities measure the difference of the phase of the beam between the RF accelerating field being on and off. The measurements from the two devices are then compared to the design and appropriate adjustments to the phase and amplitude can then be made to optimize the settings [3].

INDIRECT TUNING - SPILL

Up to this point we have looked at issues around getting the beam to do what we want it to. Now we will mention what happens when it is doing what we do not want it to do. Most machines have some method of detecting the particles that have "gotten lost". Either they have fallen out of the longitudinal bucket, scraped on something, etc. These particles eventually hit something and the result will send out secondary radiation such as gamma rays that can be detected. This is called spill. Spill detectors are often either scintillation material or ionization chambers. I mention this because minimizing spill is a part of the tuning process and a discussion of it gets us into the realm of what is the relation between setting up a tune and maintaining a tune. After an acceptable tune is established using instrumentation for determining the emittance and acceleration of the beam, the tune typically needs to be optimized. At LANSCE, this usually involves a lot of "tweaking" of accelerator elements to improve certain beam parameters. These parameters are most often the beam transmission and the spill levels. The optimization of the beam parameters is where the tune maintenance skills of the accelerator operators often come into play. Figure 11 shows the spill monitoring of the LANSCE linac for a well-established tune.

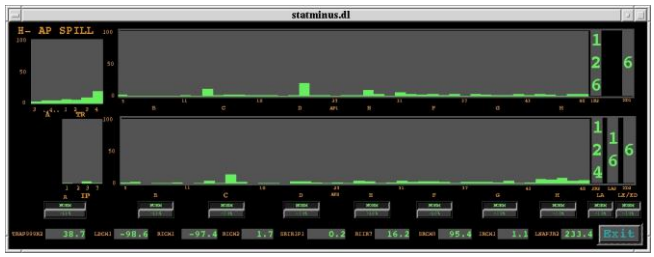

Figure 11. Linac spill monitors for the LANSCE accelerator.

THE CONTROL ROOM

The control room is worth mentioning because in many ways it is the human-machine interface for a tuner. Furthermore, the control room has evolved over the decades in some interesting ways. Figure 12 shows a series of control rooms over the decades.

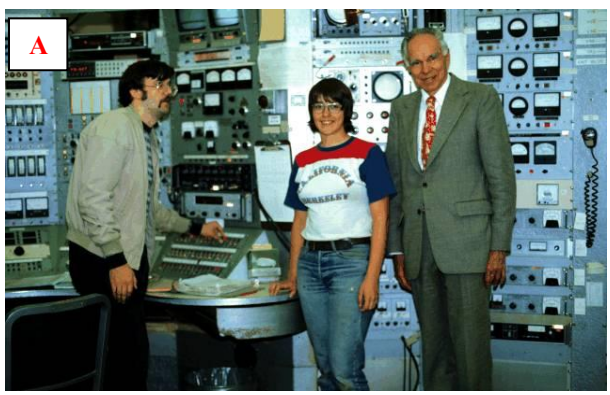

Figure 12. Controls rooms from A) the 88-inch cyclotron, B) the Advanced Light Source, C) the Advanced Photon Source, and D) the Large Hadron Collider.

CONCLUDING REMARKS

Physicists care about the phase distribution of the particles in the accelerator beam, both transversely and longitudinally. This is what we want the instrumentation to tell us.

REFERENCES

[1] Measurement and Control of Charged Particle Beams, M.G. Minty and F. Zimmermann, Springer 2003.

[2] M. Stockli, "Emittances, Straight and Simple: their Usefulness and their Limitations", LANL Seminar, February 28, 2008.

[3] K. Crandall and D. Swenson, "Side Coupled Linac Turn-on Problem", MP-3-98, February 9, 1970.

ION BEAM PROPERTIES AND THEIR DIAGNOSTICS FOR ECR ION SOURCE INJECTOR SYSTEMS

D. Leitner, LBNL, Berkeley, CA 94720, U.S.A

Abstract

Electron Cyclotron Resonance (ECR) ion sources are essential components of heavy-ion accelerators due to their ability to produce the wide range of ions required by these facilities. The ever-increasing intensity demands have led to remarkable performance improvements of ECR injector systems mainly due to advances in magnet technology as well as an improved understanding of the ECR ion source plasma physics. At the same time, enhanced diagnostics and simulation capabilities have improved the understanding of the injector beam transport properties. However, the initial ion beam distribution at the extraction aperture is still a subject of research. Due to the magnetic confinement necessary to sustain the ECR plasma, the ion density distribution across the extraction aperture is inhomogeneous and charge state dependent. In addition, the ion beam is extracted from a region of high axial magnetic field, which adds a rotational component to the beam, which leads to emittance growth. This paper will focus on the beam properties of ions extracted from ECR ion sources and diagnostics efforts at LBNL to develop a consistent modeling tool for the design of an optimized beam transport system for ECR ion sources.

INTRODUCTION

Because of their versatility, reliability, and their ability to produce ions throughout the periodic system ECR ion sources have become the injector of choice for many heavy ion facilities. Furthermore, the development and refinement of ECR ion sources over the last three decades has provided remarkable improvements in their performances. For example in 1974, the first ECR ion source Supermafios produced 15 eμA of O^{6+}, 30 years later in 2003 the VENUS (Versatile ECR ion source for Nuclear science) ECR ion source produced 2.8 emA of O^{6+}. These remarkable improvements were made possible by advances in permanent magnet strengths, and ECR design technology. The main driving components for improving the performance of ECR ion sources were formulated in Geller's famous ECR scaling laws, stating that higher magnetic fields and higher frequencies will increase the performance of ECR ion sources. Following these scaling laws a series of ECR ion sources were developed using normal conducting magnet technology and permanent magnets. In the last decade with advances in superconducting magnet technology, the next generation of high field superconducting sources has been developed utilizing frequencies of 24 to 28 GHz and magnetic confinement fields of several Tesla. These third generation superconducting ECR sources are now the injector of choice for next generation heavy ion facilities such as the Radioactive Ion Beams Factory (RIBF) at RIKEN, and the Facility for Rare Isotopes (FRIB) proposed to be built at Michigan State.

The magnetic fields in an ECR ion source serve both to confine the plasma and to provide a closed surface where the microwave can heat the electrons through electron cyclotron resonance. In most ECR ion sources the magnetic confinement fields are produced by combining a radial sextupole field with an axial mirror field, which provides a magnetic field increasing in both radial and axial directions. This "minimum-B" field configuration produces stable and dense plasmas. The magnetic field strength must be optimized for the selected ECR heating frequency to ensure efficient electron heating in addition to strong confinement. Ideally, the radial field strength should be twice the resonant field. The axial solenoid-mirror field-strength on the injection side of the ion source can be three to four times the ECR resonant field, while it is typically 2 times the resonant field at the extraction end. In case of the VENUS ECR ion source, which has been developed as prototype injector for Facility for Rare Isotopes FRIB and was designed for optimum operation at 28 GHz, the corresponding electron cyclotron resonance field strength is 1 T, but in order to achieve sufficient plasma confinement, the magnetic field at in injection are in the between of 3.5 to 4 T, at extraction 2 to 2.5 T and 2T radially at the plasma wall.

HEAVY ION INJECTOR BEAMS

In the last 10 years, the intensity and charge state requirements for the next generation nuclear science facilities have increased dramatically. For example for FRIB and RIBF, the intensities required for the heaviest ion beams are more than an order of magnitude higher than routinely used at currently operated heavy ion facilities. In particular, uranium beams are one of the most important and challenging beams for these facilities and will be used as an example to describe the characteristics of ion beams produced by ECR ion sources. For both facilities, about 0.5 mA uranium ion current is required from the front end of the driver LINAC (in the case of RIBF as a single charge beam of U^{35+} and in case of FRIB as combined current of U^{33+} and U^{34+}).

Of all currently operating ECR ion sources the fully superconducting ECR ion source VENUS at LBNL has produced the highest uranium intensities to date:

namely about 0.2 mA of uranium in the charge states 33+ to 35+, which is close to the requirements of FRIB, but about a factor 2 lower than required by RIBF in RIKEN. As illustration, figure 1 shows a charge state distribution (CSD) of such a high intensity uranium spectrum from the VENUS source. The following general characteristics for ion beams extracted from ECR ion sources can be noticed in figure 1. Besides the charge state required by the accelerator many more charge states are present in the extracted beam (in case of uranium 20 or more). In addition, the beam also contains high intensity oxygen ion beams, since oxygen gas is routinely used in ECR ion source plasmas to enhance the heavy ion charge state performance. Consequently, several milliamps of total heavy-ion-beam current have to be extracted and transported. Space charge in the extraction region and the beam line become important challenges for the design of the analyzing system and beam line. In addition, the beams have to be extracted from a high magnetic field region at the peak of the source solenoid field at the extraction, which influences the beam depending on the magnetic rigidity of the ions.

As the uranium example shows, even today's highest performance ECR ion sources cannot or can only barely match the intensity requirements of the next generation heavy ion accelerators for the heaviest beams. Therefore, a better understanding and careful optimization of the ion beam transport system has become a necessity and a focus of the ECR ion source community. Ion beam diagnostic systems have been developed to measure the properties of the extracted and transported ion beams.

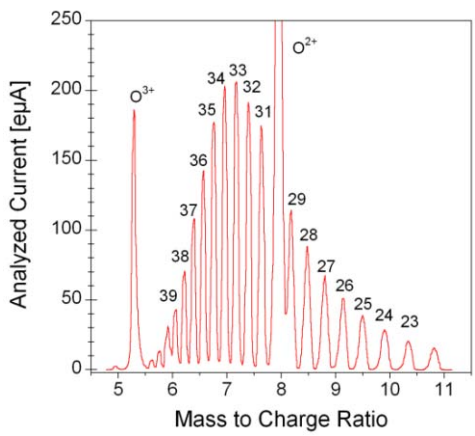

Figure 1: Uranium charge state distribution for a high intensity tune optimized for 33+ to 34+.

The multispecies ion beams make ECR ion source injectors and front ends inherently more complicated than single species injectors. In addition, the user programs at heavy ion facilities typically require a wide variety of ion species, e.g. in cases of FRIB more than 40 ion species (many of which are rare and expensive isotopes). For the different driver beams the ion beam intensities required by the driver LINAC vary widely in order to maximize the available beam power on target. Therefore the front end cannot be optimized on a single ion beam or intensity.

In the following sections, ion beam diagnostic methods for ion beams extracted from ECR ion sources are discussed. Data are presented for the VENUS ECR ion source which was characterized for a wide range of ion beams to obtain data for the FRIB LINAC driver design.

ION BEAM EMITTANCE DIAGNOSTICS

As in most other injector ion beam lines, emittance scanners are an important part of the ion beam diagnostics. All the typical methods such as electrostatic scanners (Allison-type), slit scanners, wire scanners, as well as pepperpot scanners are in use [1]. Since these diagnostic methods are well established and described in detail elsewhere, the principles are summarized only briefly below.

For the Allison-type emittance scanner [2], the beam enters through an entrance slit, gets deflected by parallel plates through the exit slits where the signal is detected in a Faraday Cup. The Faraday Cup signal is measured in dependence of the deflection voltage. The divergence of the beam is calculated from the applied voltage on the deflection plate and the length of the applied electric field (see Figure 2)

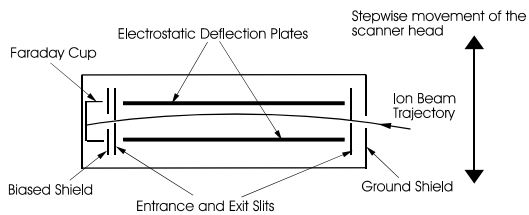

Figure 2: Measurement principle of the electrostatic emittance scanner.

The beam divergence is determined for each location as the scanner is moved stepwise through the beam. By scanning the beam with a second unit (rotated by 90 degree), the ion beam emittance in both transverse directions (x and y) can be measured. The resolution of this method is only limited by the width of the entrance and exit slits and the lengths of the deflection plates and can provide high resolution emittance data. However, the disadvantages of this type of emittance measurement method are that the scans are rather slow and that the ion beam intensity is integrated over the slit opening of the scanner (the same is true for wire and slit scanners).A pepperpot emittance scanner on the other hand can give fast, time-resolved 4D emittances. In this case a hole mask is inserted into the beam and the beam is imaged on a scintillator downstream. Figure 3 shows an example of a pepperpot diagnostics instrument developed at the KVI in Groningen [3].

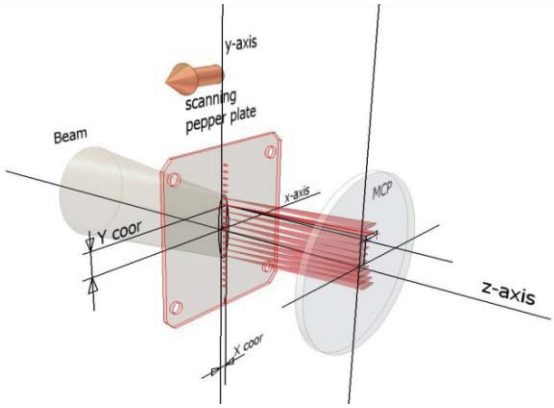

Figure 3: Pepperpot emittance scanner developed at KVI, Groningen. Image taken from [3].

As the scanner collects both transverse angles and locations simultaneously, two dimensional data can be extracted. This opens the possibility to extract coupled phase space information and to diagnose fast transient effects in the plasma. For this reason, scintillator based as well as multichannel plate pepperpot scanners are being developed in many ECR ion source groups [3-5].

ION BEAM EMITTANCES FOR BEAMS EXTRACTED FROM ECR ION SOURCES

As described in the previous section, the ion beam properties of ions extracted from ECR ion sources are complex. Therefore, their characteristics are discussed in detail in the next section and put into context with experimental measurements performed on the VENUS ECR ion source.

For an ECR extraction system two main contributions to the ion beam emittance have to be considered [6] the ion beam temperature and the induced beam rotation due to the decreasing axial magnetic field present at the extraction aperture.

The emittance due to the ion temperature can be estimated by assuming a Maxwellian temperature distribution inside the plasma:

$$\varepsilon_{TEMP}^{xx'-rms-norm} = 0.016\, r \sqrt{\frac{kT_i}{M/Q}} \qquad (1)$$

where ε is the normalized x-x' rms emittance in π mm mrad, r is the plasma outlet hole radius in mm, kT_i is the ion temperature in eV, and M/Q is the ratio of ion mass in amu to ion charge state and is dimensionless.

Assuming an uniform plasma density distribution across the plasma outlet hole, the emittance due to beam rotation induced by the decreasing magnetic field in the vicinity of the extractor can be described by Busch's theorem (assuming $\varepsilon^{100\%} = 5 \cdot \varepsilon^{rms}$, a waterbag distribution):

$$\varepsilon_{MAG}^{xx'-rms-norm} = 0.032 \cdot r^2 \cdot B_0 \cdot \frac{1}{M/Q} \qquad (2)$$

where ε is the normalized x-x' rms emittance in π mm mrad; r the plasma outlet hole radius in mm; B_0 the axial magnetic field [T]; M/Q is the ratio of ion mass in amu to ion charge state and is dimensionless.

The beam rotation due to the decreasing magnetic ECR ion source field becomes the dominating contribution to the ion beam emittance when following condition, as derived by combining equation (1) and (2), is satisfied:

$$B_0 \cdot r \geq 0.5 \cdot \sqrt{kT_i} \cdot \sqrt{M/Q} \qquad (3)$$

Following the estimate by M. Leitner et. al [6], Table 1 summarizes the minimum magnetic field values where the emittance value starts to be dominated by the ion beam rotation. In the table, the VENUS plasma outlet aperture radius of 4 mm and an assumed ion temperature of 2 eV is used to compute the maximum field values. Keeping in mind that the extraction field of third generation superconducting ECR ion sources is in the order of 2 T, it is evident that the magnetic field is the main contributor to the ion beam emittance for these high field sources. However, the same is true for most ECR ion source operating above 6 GHz.

Table 1: Magnetic field values where the emittance starts to be dominated by the ion beam rotation for light to heavy ions

Ion	M/Q	Magnetic field at extraction
H^+	1.00	>0.18 T
O^{6+}	2.67	>0.29 T
Ar^{8+}	5.00	>0.40 T
Xe^{18+}	6.89	>0.46 T
U^{33+}	7.21	>0.47 T

An important consequence of this dependence is that the emittance values of the ions extracted from ECR ion sources are dependent on the magnetic rigidity. Therefore, once the magnetic field at the extraction region is defined for the ECR injector, a rough estimate of the emittance can be made using equation (2).

As an illustration, Figure 4 shows the calculated magnetic emittance for FRIB ions over the operation region for 1 T and 2 T fields (heating frequency range from 14 GHz – 28 GHz) and 8 mm diameter extraction aperture. Because the ion beam emittances are strongly dependent on the beam rigidity the acceptance of the accelerator (which is constant for all ions) has to be

chosen carefully to match the ion beam over the required range or emittance defining collimators must be used to define the beam emittance in the low energy beam transport (LEBT).

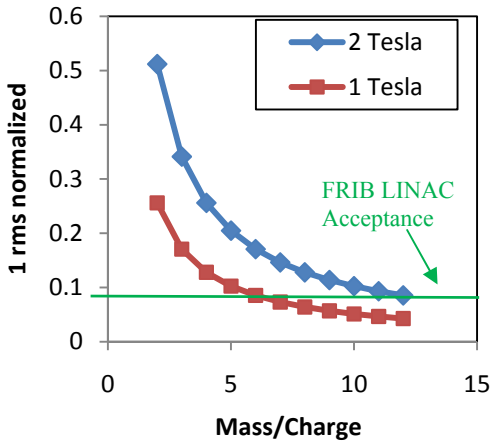

Figure 4: Calculated 1 rms normalized magnetic emittance for FRIB driver linac ions for 1T and 2 T fields at extraction. The FRIB driver linac acceptance of .1 π mm mrad is also indicated.

From figure 4, one might expect that it would be best to choose low frequencies, low magnetic field ECR ion sources as injector to minimize the emittance. This is true for low and single charge state ions, but for high charge state ions the increase in density in higher performance sources exceeds the emittance increase due to the increase in magnetic field. In addition, experiments [7] have shown that the simple model described in the previous section is not sufficient to explain the measured emittance values and that the ion confinement in the plasma plays an important role for the extracted ion beam emittance.

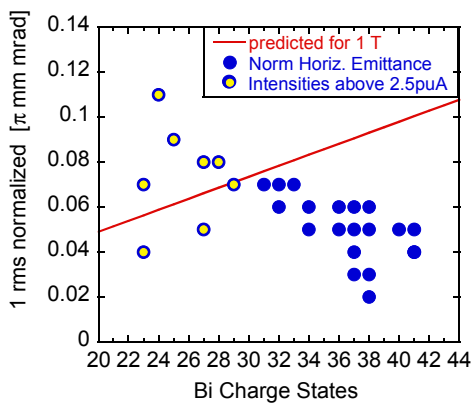

Figure 5: Emittance value versus ion charge state for bismuth extracted from a 1T axial field. As comparison, the predicted emittance dependence from the magnetic field is also shown.

Measurements indicate that within an ion charge state distribution, higher charge state ions have lower emittances than lower charge state ions, a trend which contradicts the theoretical prediction. As an example, figure 5 shows an emittance measurement for medium to high charge state ions of Bi extracted from the VENUS ECR ion source with a 1 T magnetic field present at the extraction region [8]. The trend towards lower emittances for higher charge states can be clearly seen.

One possible interpretation for this dependence is that higher charge state ions are confined closer to the axis and are extracted from a smaller (virtual) extraction hole. These results are consistent with the model that highly charged ions are created closer to the center of the ECR plasma, where hot electrons are confined. The low charge state ions on the other hand can be produced at the outer shell of the ECR plasma and therefore can have higher emittance values [7].

In addition, it is experimentally observed, that the emittance values for ions with the same magnetic rigidity but different masses decreases for heavier masses. Figure 6 shows an emittance measurement performed on the AECR-U ion source at LBNL for various charge states of oxygen, bismuth, krypton, and single charged ions of hydrogen and helium [7]. For the same mass to charge ratio, heavier ions have lower emittances than lighter ions. Similar results were found in the VENUS source (see figure 6) and other sources [4,9].

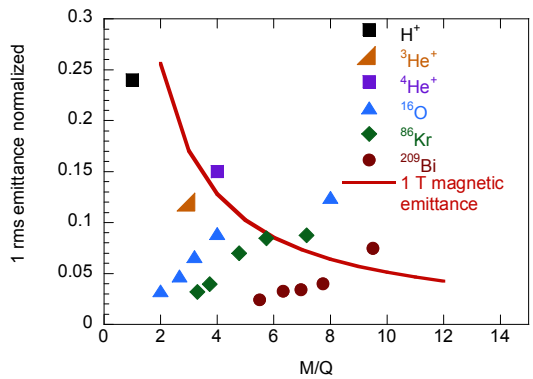

Figure 6: Emittance measurements on the AECR-U for various masses in comparison with predicted emittances for an extraction magnetic field of 1 T.

Another important contribution to emittances measured from ECR ion sources is the plasma stability. The ion beam emittance can easily change a factor of 2 or 3 at comparable ion beam intensities for unstable plasma conditions. Therefore, the emittance should always be determined for a range of plasma conditions to quantify the possible range of emittance values (see figure 7).

One of the causes of this wide spread in emittance values can be the plasma chamber wall condition, which strongly influences the plasma confinement and stability. If the ECR source had been opened to ambient

atmosphere or the ion beam had been changed from one metal to another, it can take 2 to 3 days before the lowest emittance and peak performance values can be achieved. Consequently, during rapid beam changes involving high intensity metal ion beams, the source and beam transport tunes have to be balanced between maximum intensity and beam quality. The emittance measurement is then used as an online ion source tuning aid.

DEPENDENCE OF THE MEASURED EMITTANCE ON THE AXIAL MAGNETIC EXTRACTION FIELD

Since 2000 the LBNL ECR ion source VENUS has been developed as a prototype injector source for the FRIB facility. Therefore, extensive ion beam emittance studies have been performed to characterize the ion source. Since the VENUS ECR ion source is fully superconducting the confinement field can be adjusted and optimized for different ECR heating frequencies and the influence of the magnetic field on the emittance can be studied with the same beam line and experimental set-up. In case of the VENUS ECR ion source the source is equipped with an 18 GHz as well as a 28 GHz microwave system. The extraction fields used when operated using 18 GHz are tuned to field strengths between 1.2 and 1.6 T and for 28 GHz field between 2 and 2.4 T. Figure 7 shows a summary of a series of emittance measurements for xenon ion beams produced using 18 GHz and 28 GHz confinement fields and heating. It can be clearly seen that the emittance values for 28 GHz operation are in general higher than for 18 GHz operation. Within the data set a wide spread of the emittance data can be seen, which is due to the varying plasma conditions.

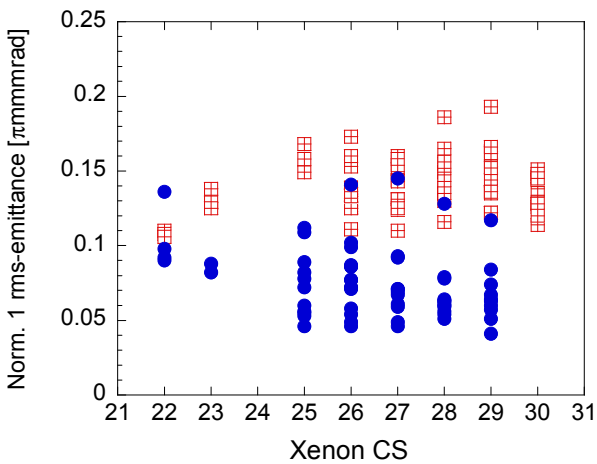

Figure 7: Measured emittance of medium charge state xenon ion beams extracted from VENUS for 18 and 28 GHz operation.

Figure 8 and 9 show measured ion beam emittances for light and heavy ion beams extracted from the VENUS ECR ion source. As expected, 18 GHz emittances (figure 8) are smaller than 28 GHz emittances (figure 9). The values scale roughly linear with the change in magnetic field, but in both cases the emittance values are below the predicted emittances (solid lines) for a beam that would fill the full plasma extraction electrode. This observation also supports the argument of a smaller 'virtual' extraction hole.

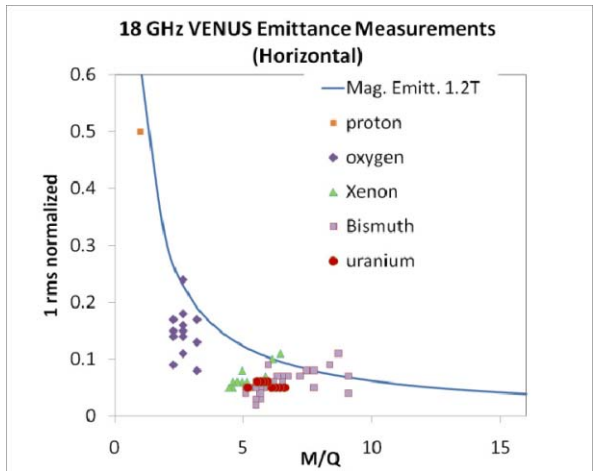

Figure 8: Measured ion beam emittances for ion beams extracted from the VENUS ECR ion source using 18 GHz plasma heating and confinement fields.

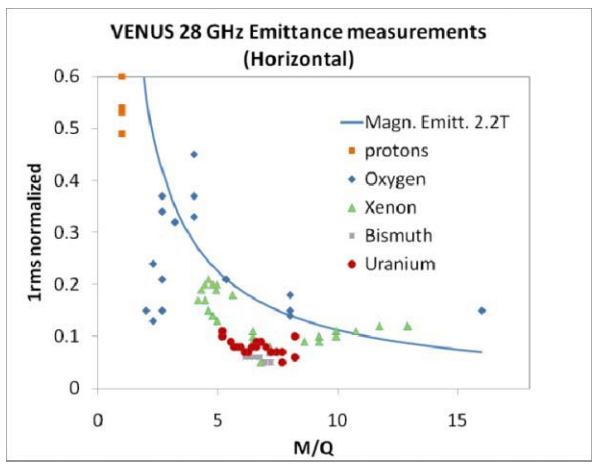

Figure 9: Measured ion beam emittances for ion beams extracted from the VENUS ECR ion source using 18 GHz plasma heating and confinement fields.

INFLUENCE OF THE ION BEAM INTENSITY ON THE EMITTANCE

The influence of the ion beam intensity on the emittance was also investigated. The measurements show that the emittance values of a single charge state remain nearly constant over a wide range of intensities as long as the total extracted ion beam current (the sum over all species present in the extracted beam) remains similar.

In figure 10 data for low to high ion beam intensities for Bi^{31+} and Bi^{29+} are shown together with total transported ion beam from the ion source. The

emittance varies ±10% over this intensity range if the total extracted beam is nearly constant. Contrary, the emittance seems to grow linearly with the intensity if the total extracted ion beam intensity increases (figure 11). One possible explanation could be space charge effects in the extraction region.

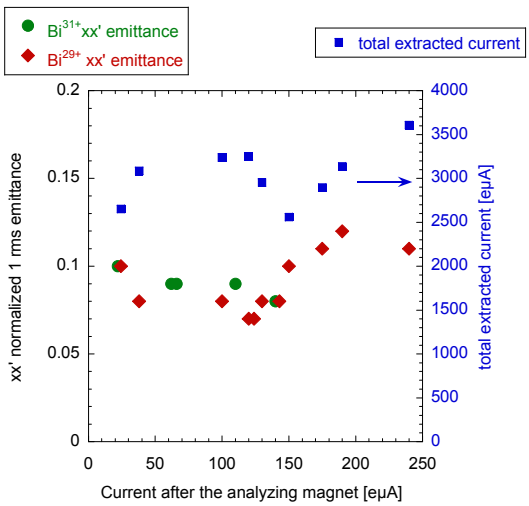

Figure 10: Emittance measurements for low and high intensity beams of Bi^{29+} and Bi^{31+}. The total extracted and transported beam is also plotted.

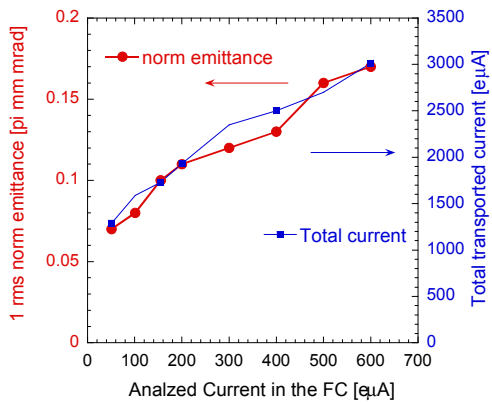

Figure 11: O^{6+} ion beam emittance in dependence of the extracted ion beam intensity. On the left axis the beam emittance is plotted, on the right axis the total ion beam current is plotted.

DEFINING AND MEASURING INITIAL CONDITIONS OF THE IONS BEAMS AT THE EXTARCTION APERATURE

One of the simplifications of equation 2 is the assumption that the ion density across the plasma outlet aperture is homogenous. However, measurements using optical ion beam diagnostics and beam emittance scanners have clearly shown that this assumption is incorrect. As an example, figure 12 shows a picture of a multispecies beam extracted from the AECR-U containing argon and oxygen ions about 1.5 m downstream of the extraction hole close to the object point of the mass analyzing magnet. A solenoid lens upstream was optimized to focus Ar^{11+}. The other charge states are either over-focused or under-focused by the magnetic lens and some can be seen as rings around the core of the beam. The complex structure of the beam can be easily seen.

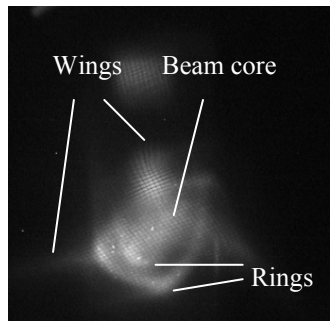

Figure 12: Picture of a non mass analyzed beam on a quartz plate containing charge state distributions of argon and oxygen. Different charge states and ions are visible as rings in the picture, since the solenoid lens is optimized to focus only one of the charge states.

OPTICAL BEAM DIAGNOSTICS USED FOR THE LOW ENERGY BEAM LINES

As the kinetic energy of the ions in low energy beam lines are small, only a few materials are suitable as scintillators. Three scintillator crystals, KBr, quartz, and BaF_2 have been tested at LBNL and compared with each other. In addition, CsI(TI) crystals are successfully used in ANL as scintillator for a pepperpot emittance scanner [5]. Typically to avoid charging of the insulator surfaces, highly transparent meshes are placed before the scintillator material. Of the scintillator materials tested at LBNL, KBr has the highest light yield (about 4 times higher than quartz and BaF_2, see figure 13) [4].

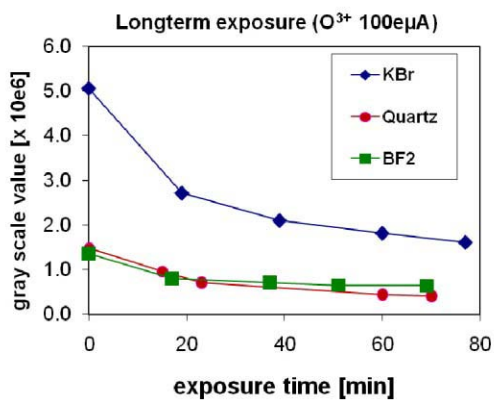

Figure 11: Longterm exposure of KBr, Quartz, and BF_2 with 100eμA of O^{3+}

All of the scintillators showed about the same degradation in light yield for prolonged exposure to high intensity beams (figure 11). Because of this degradation of light yield the exposure time to the beam should be

minimized and the crystal cleaned from time to time or exchanged. This is in particular critical for optical pepperpot emittance scanners to avoid measurement errors due to the light yield changes in the most intensive regions of the beam.

For the high intensity beams quartz crystals are used as they are inexpensive and can be easily changed. For the optical pepperpot KBr crystals are used to maximize the light yield and sensitivity of the diagnostic [10].

MODELING OF THE INITIAL ION BEAM DISTRIBUTION AT THE EXTRACTION APERTURE

In order to correctly simulate the ion beam transport, the initial conditions at the plasma extraction aperture must be known. Since there is currently no generally accepted model of how to derive the correct initial conditions, assumptions must be made [12]. Optical diagnostics are important tools to validate and develop these models.

LBNL has developed a semi-empirical model to describe the ion beam distribution at the extraction aperture. In this model, ion sputter marks found inside the plasma chamber are used as initial distribution of the ions inside the plasma chamber and tracked to the extraction aperture [11]. While this model is overly simple and cannot describe the complex processes in the plasma, it results in several observed features such as the triangular structure of the beam and the reduced spatial distribution at the extraction aperture (see figure 14) [12].

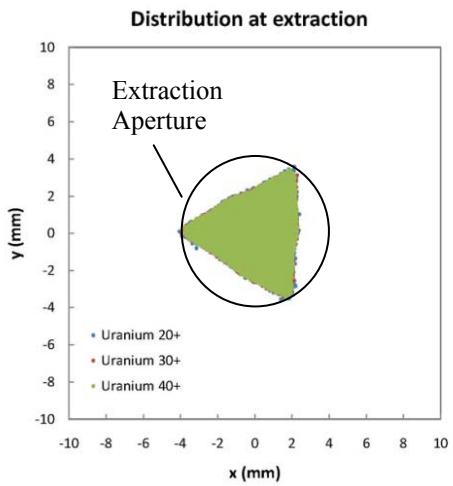

Figure 14: Spatial distributions for uranium ions at the extraction aperture [12]

In addition, the beam models can also experimentally reproduce observed hollow structures of some ion beam species due to space charge forces in focal points of the beam line. Figure 15 shows a comparison of a simulated multispecies ion beam profile (oxygen and carbon CSD) and its image on the quartz scintillator plate. Qualitatively the agreement is good.

However, one of the limitations of the model is that it assumes the same initial spatial distribution of the ions at the bias disk for all charge states and therefore cannot describe the emittance reduction for the highest charge states as observed in the experiments (see figures 5 and 6) nor can it describe the emittance reduction for heavy masses for beams that have the same rigidity. Further refinements will be needed in an iterative process between experiment and simulations to derive to initial conditions with charge state and mass dependent ion beam distributions.

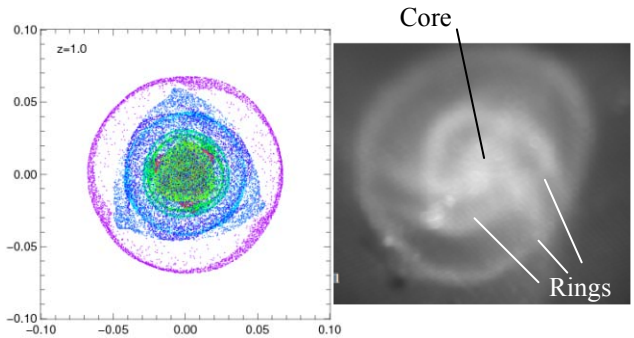

Figure 15: Comparison of a simulated multispecies beam containing oxygen and carbon ions and the image of the beam on a quartz scintillator. The beam line solenoid lens has been optimized on O^{7+} and so the lower charge states are underfocused (rings on the outer parts of the image) [13].

NEUTRALIZATION LEVEL OF THE BEAM

Ionization of background gas by the passing ion beam produces both low energy electrons and ions inside of the beam envelope. These electrons can be confined by the beam and effectively reduce the beam's positive space-charge potential, while the newly created positive background gas ions are ejected from the beam center. Since ECR ion source injectors are mostly used in CW mode, it has been generally assumed that ECR ion beams in magnetic transport systems are fully neutralized. However, on VENUS it was experimentally observed that the ion beam transmission decreased with increasing ion beam current, which would be consistent with space charge effects in the beam. To measure the level of neutralization an electrostatic energy analyzer was constructed at LBNL that measures the energy of background gas ions expelled by the space charge potential of the ion beam.

It could be demonstrated that at low beam line pressures (10^{-8} mbar) used for high charge state ion beam injectors, the neutralization times are too long to fully neutralize the ion beam. At this low pressure, the loss rate of confined electrons seems to exceed the rate of their trapping. Only when the pressure was raised to the low 10^{-6} mbar, close to fully neutralized beams could be observed [13]. This is consistent with measurements at the cyclotron institute in Jyvaskyla where it was

observed that the ion beam emittance values decreased with increasing pressure in the beam line [9]. However, increasing the pressure in the beam line also increases the charge exchange rate of highly charged ions, and is therefore not an option for high charge state ion injectors. Simulations show that using a 70 to 80% neutralization level agrees well with experimental emittance and beam profile measurements [12], but further measurements will be necessary to determine the degree of neutralization along the beam line and in various beam line components (in particular inside the analyzing magnet).

SUMMARY

Properties of the ion beams extracted from ECR ion source plasmas and transported through a low energy beam transport line are complex. Multispecies ion beams with triangular density distributions are extracted from a high magnetic field region that adds a rotational component to the beam, which leads to transverse emittance growth in dependence of the magnetic rigidity. In addition, the confinement of the ions in the plasma and the plasma stability influence the emittance values. Ideally the ion beam distribution inside the center of the ECR ion source plasma should be measured. But since this is challenging there is a need for highly spatial-resolved ion beam diagnostics that can provide 2D beam profile and 4D emittance measurements along the beam line to iteratively develop a consistent model for the initial ion distribution at the extraction aperture. In addition, in order to further refine the simulation models diagnostics should be developed to determine the degree of beam neutralization along the beam transport line.

ACKNOWLEDGEMENTS

This work was supported by the Director, Office for Energy Research, Office of High Energy and Nuclear Physics, Nuclear Physics Division of the U.S. Department of Energy under Contract DE AC03-76SF00098.

REFERENCES

[1] P. Strehl, *Beam Instrumentation and Diagnostics* (Springer, Berlin-Heidelberg, 2006).

[2] J. D. S. P. W. Allison, D. B. Holtkamp, IEEE Trans. Nuc. Sci. **NS-30**, 2204 (1983).

[3] H. R. Kremers, J. P. M Beijers, S. Brandenburg, S. Saminathan, V. Mironov, and T. Thuillier, in *ECRIS08,* (R. Pardo, R. Vondrasek, Chicago, IL USA, 2008).

[4] M. Strohmeier, J. Y. Benitez, D. Leitner, C. M. Lyneis, D. S. Todd, and M. Bantel, Rev. Sci. Instrum **81**, 02B710 (2010).

[5] S. A. Kondrashev, A. Barcikowski, B. Mustapha, P. N. Ostroumov, and N. Vinogradov, Nucl. Instrum. Methods Phys. Res. A **606**, 296 (2009).

[6] M.A. Leitner, D.C. Wutte, and C. M. Lyneis, in *2001 Particle Accelerator Conference*, Chicago, 2001).

[7] D. Wutte, M. Leitner, and C. M. Lyneis, Physica Scripta **T92**, 247 (2001).

[8] D. Leitner, C.M. Lyneis, S.R. Abbott, D. Collins, R.D. Dwinell, M. L. Galloway, M. Leitner, and D. S. Todd, NIMB **235**, 486 (2005).

[9] O. Tarvainen, (2010), p. personal communication.

[10] M. Strohmeier, in *Fakultät Elektro- und Informationstechnik* (Hochschule Karlsruhe – Technik und Wirtschaft, Karlsruhe, 2009).

[11] D.S. Todd, D. Leitner, C. Lyneis, and D. P. Grote, Rev. Sci. Instrum. **79**, 02A316 (2008).

[12] D. Winklehner, D. Todd, D. Grote, D. Leitner, J. Benitez, M. Strohmeier, and F. Aumayr, in *Beam Instrumentation Workshop 2010*, Santa Fe, 2010).

[13] D. S. Todd, D. Leitner, and M. Strohmeier, in *Beam Instrumentation Workshop*, Tahoe City, CA, 2008).

AN INSTRUMENTATION WISH LIST FOR HIGH POWER/HIGH BRIGHTNESS ERLS *

D. Douglas#, Jefferson Lab, 12000 Jefferson Avenue, Newport News, VA 23606, U.S.A.

Abstract

The advent of the energy recovering linac (ERL) brings with it the promise of linac-quality beams generated with near storage ring efficiency. This potential will not, however, be fulfilled without overcoming a number of technical and operational challenges. We will review the basics of ERL dynamics and operation, and give examples of idiosyncratic ERL behavior and requirements posing particular challenges from the perspective of diagnostics and instrumentation. Beam performance parameters anticipated in next-generation ERLs will be discussed, and a "wish list" for the instrumentation of these machines presented.

"TRADITIONAL" ACCELERATORS

Energy Recovering Linacs [1] comprise a class of electron accelerators using novel architecture to generate outstanding beam quality with high wall plug efficiency. Initially conceived almost half a century ago [2] and first realized a decade later in a reflectively symmetric geometry [3], contemporary ERLs are most easily understood as an evolution of the recirculating linac [4].

"Traditional" accelerators typically fall into one of two classes: synchrotrons (including storage rings and cyclotrons for the purposes of this discussion), or linear accelerators. In synchrotrons, the accelerated beam passes many times through a modest radiofrequency (RF) accelerating system, gaining a small amount of energy on each pass. Most of the accelerator consists of the transport system, which draws little additional power. Storage rings can therefore generate extremely high beam powers using modest wall plug power. In such systems, a few megawatts of RF drive and similar levels of DC power (for the transport system) can be used to generate gigawatts of beam power (e.g. 0.5 A at 2 GeV). As the beam is circulated many times, it is however susceptible to degradation from error sources and beam dynamical effects such as synchrotron radiation. Storage rings, though efficient, thus provide only limited beam quality.

In contrast, linear accelerators (linacs) accelerate the beam rapidly through multiple RF structures using only limited beam transport. Most of the required power is therefore devoted to RF drive; moreover, in conventional (normal conducting) linacs, the final beam power is typically limited by wall losses in the accelerating structures. For example, a linac with a megawatt of RF drive (with very modest DC power for additional beam transport use) will produce at most a megawatt of beam power (e.g. 50 μA at 20 GeV). Linacs are thus electrically inefficient - but as the beam is only in the machine for a single pass though the accelerator (and there is little or no bending) the beam quality does not degrade: performance is source limited. It is thus possible to generate very high quality beams – an advantage that outweighs the power inefficiency in many applications. The high beam quality (brightness) provided by linacs has motivated efforts to make them more cost effective. As a consequence, numerous methods are available to control cost, improve efficiency, and enhance the performance of these systems.

RECIRCULATION, SUPERCONDUCTING RF, AND ENERGY RECOVERY

Recirculation provides a simple means of controlling linac cost while maintaining final energy: simply "reuse" the linac accelerating structure multiple times, thereby reducing the required length. In a "recirculating" linac, the beam is transported from the end of the linac back to the front, and reinjected in phase with the RF fields for further acceleration. This approach leverages the low cost of beam transport relative to RF, so that the cost/performance optimum for a system lies somewhere between "straight" and "circular". The result [5] (Figure 1) is a system of lower cost than a conventional linac, but which provides better beam quality than a storage ring.

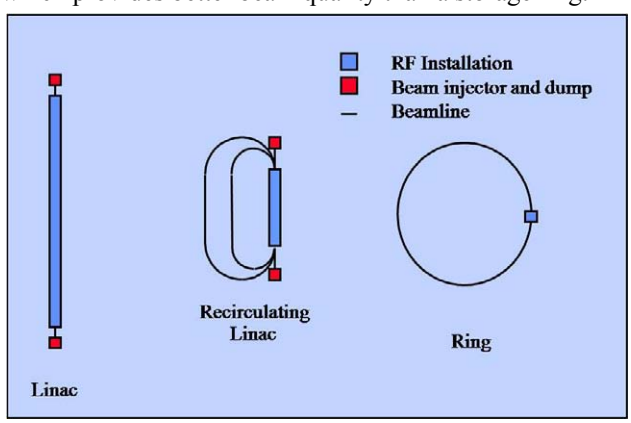

Figure 1: Evolution of conventional accelerator topology into that of the recirculating linac [6].

Superconducting RF (SRF) acceleration [7] provides a second means of linear accelerator cost/performance optimization. SRF cavities have essentially no wall losses and allow high gradient continuous-wave (CW) operation. This reduces the RF power required to reach a specific energy, increases average current, and significantly improves beam quality by avoiding the transients inherent in pulsed RF systems. The resulting reduction in RF power demand is sufficient to offset the cost of the

*Work supported by the Commonwealth of Virginia, the Air Force Research Lab, the Joint Technology Office, the Office of Naval Research, and by DOE Contract DE-AC05-060R23177.
#douglas@jlab.org

required cryogenic plant and to compensate for any additional RF system complexity.

Use of recirculation and SRF introduces additional beam handling and sensitivity to error sources, and thereby engenders susceptibility to instability and performance degradation. Application of these technologies in large-scale systems such as CEBAF [8] demonstrates, however, that it is possible manage such effects. Even so, RF power remains an obstacle to the use of recirculating linacs, as a simple example illustrates. A nuclear-science system such as CEBAF generates a 4 GeV, 200 μA beam, consequently requiring of order 800 kW of RF power – a manageable (affordable) level. A recirculating linac x-ray light source would, however, require 100 mA at 5 GeV (or ½ GW of RF power) to generate the necessary photon fluxes. Not only would a dedicated electrical plant would be needed to serve the accelerator, the disposal of a gigawatt of "waste" electrons presents an intractable design issue.

Such RF power-draw and waste-beam disposal issues can be addressed by use of energy recovery: after acceleration to – and use at – full energy, the electron beam is returned to the linac and reinjected – *180° out of phase with the linac accelerating RF fields*. As the beam is "antisynchronous", is then *decelerated* as it traverses the accelerator structure. Beam power is deposited back into the RF cavities and is available to accelerate later bunches; after traversing the linac, the beam is returned to essentially injection energy – and power – levels, and thus disposal presents only a modest radiation issue. The use of SRF technology avoids wall losses and ensures the recovery process can proceed with excellent efficiency.

Energy recovery has been tested in high power [9] and large scale [10] systems, reliably reducing RF power demands while preserving beam quality and maintaining overall accelerator performance. Figure 2 characterizes RF power utilization in CEBAF-ER, a 1 GeV ERL operational mode of the CEBAF accelerator [11]. The red trace shows a low-level RF signal quantifying the required RF power without energy recovery over a 400 μsec interval. During a 250 μsec beam macropulse (followed by a short diagnostic pulse) RF power is required and the measured signal rises; turn-on and turn-off transients are manifested as exponential rise and fall of the signal value. The blue trace presents the same

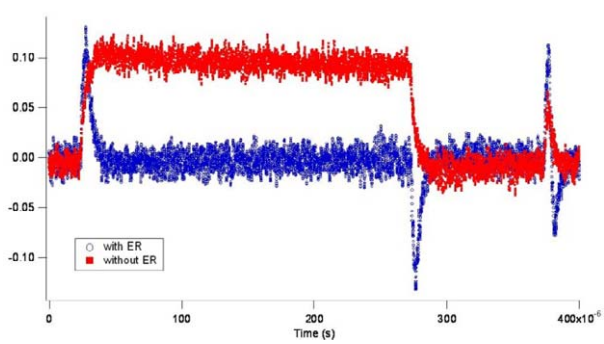

Figure 2: RF power draw during beam macropulse in CEBAF-ER without (red) and with (blue) energy recovery

signal with the use of energy recovery. Save for the turn-on and turn-off transients, *no* RF power (other than that needed to establish the fields in the SRF cavities) is needed: the recovered beam supplies all the power required for acceleration. Transient behavior during beam turn-on and turn-off is due to cavity beam loading and detuning, and constitutes a topic of considerable interest in the process of optimizing the RF drive system [12].

ERLs thus have both good acceleration efficiency and high beam quality. The use of SRF insures that there are no cavity wall losses; energy recovery returns essentially all beam power to the linac, so there is "no" beam loading: only the injected beam power must be provided. If a machine injects 0.1 A at 10 MeV (1 MW), accelerates it to 100 MeV, and energy recovers, the system requires 1 MW of power. If the system, in contrast, injects 0.1 A at 10 MeV (1 MW), accelerates to 10 GeV, and recovers, it *still requires only 1 MW*. As energy recovery recycles the "waste" (post-use) beam to drive the RF, it saves on RF costs and avoids high power radiation from the beam dump. Not only is it a natural "two-beam accelerator", the "recovered" beam is at low energy – and thus low *power* – making the design and fabrication of the beam dump much easier.

Energy recovery thus provides near-linac-quality beam at near-storage-ring efficiency. It is therefore an effective means of design cost optimization and – as the resulting systems are of novel architecture and operate in a non-traditional region of parameter space – allows the study of numerous physical phenomena in combinations that are typically inaccessible in traditional accelerator designs.

ERL PERFORMANCE

Existing ERLs have generated relatively high power (MW-class [13]) and high energy (GeV [14]) beams; the technology holds promise for orders-of-magnitude extension in both parameters so as to provide GW beam powers at GeV energy scales. Figure 3 presents an ERL "landscape" showing potential routes to both high energy and high power. To date, systems have been operated along the energy axis of this parameter space; the impending initial operation of the BNL ERL test-bed will explore increasingly high current behavior [15].

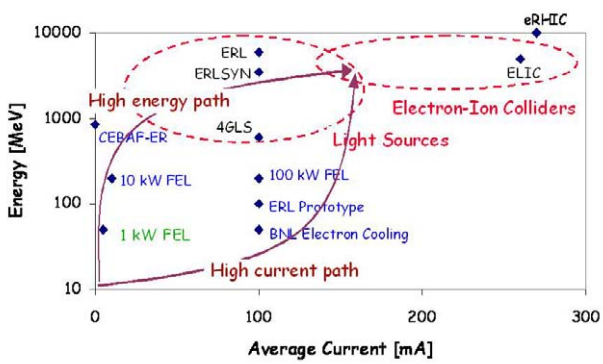

Figure 3: ERL Current/Energy landscape illustrating parameter set for existing (1 kW FEL, 10 kW FEL, CEBAF-ER) and proposed ERLs [16].

ERL applications tend to fall into two classes: use as FEL drivers, and as sources of synchrotron radiation or beams for investigating fundamental interactions.

FEL Driver ERLs

FEL drivers are defined by the electron beam required at the laser, which needs a high peak current and a beam transverse geometric emittance meeting the $\lambda_{FEL}/4\pi$ limit. The former is met at single bunch charges of 0.1 –1 nC by use of appropriate bunch length compression (see below). The latter is met by source normalized emittances of 1-10 mm-mrad and acceleration to high energy so as to adiabatically damp to the geometric emittance envelope of the FEL. For photons from THz to soft x-ray this motivates use of energies of tens of MeV to a few GeV. The FEL interaction is a coherent collective phenomenon; very high photon powers/fluxes can thus be obtained using modest CW repetition rates (100s of kHz – few MHz), beam currents of mA to tens of mA, and attendant beam powers at megawatt levels.

Light Sources

ERL-based light sources try to leverage the brightness advantage possessed by linacs over storage rings. Though linacs generally provide superior longitudinal emittances, modern ultra-low emittance rings provide smaller transverse emittances at energies below a few GeV (above which radiation excitation dominates). As a consequence, ERLs of this class are x-ray sources having electron beam energies lying in the 5-10 GeV range, and (to provide appropriate brightness) run 100s of mA currents in high repetition rate beams (GHz) with bunches of tens to 100s of pC. The lower charge allows for exceptional source performance (0.1 - 1 mm-mrad normalized emittance) and provides operational modes giving at least partial transverse coherence. Beam powers in such systems are extremely high, being near or at GW levels.

ERLS of either class hold advantages over traditional machines. They allow flexible time structure, spanning the range of single bunches to CW bunch trains. Moreover, they allow independent manipulation of various portions of the beam phase space essentially independently of other sub-spaces – they are fully six-dimensional systems, allowing transverse matching to desired spot sizes at specified locations, longitudinal matching to specific bunch length/energy spread combinations (via use of transverse-longitudinal coupling), and partial or full transverse phase space exchanges through the use of horizontal-vertical coupling. They can therefore generate beams of controlled peak current, specified momentum spread, and transverse emittances ranging from flat to round.

UNIQUE PROPERTIES/CHALLENGES

The operational flexibility and the beam power and brightness available from ERLs create potential for unique behavior. As beam powers are extremely high, the beam is continually renewed from the source, and the system never goes to equilibrium, halo is a monumental issue. This is best understood by contrast to storage rings: ERLs are quite unlike storage rings with respect to beam loss; they are instead equivalent to the *injection chain* of storage rings. Given the high CW beam power, losses must remain in the 10^{-5} – 10^{-6} range, equivalent to an injection efficiency of 99.999% or better: only one to ten of every million electrons provided by the source can be lost during acceleration, handling, recovery, and transport to the dump without potential machine damage.

Numerous other features distinguish ERLs from traditional classes of machine. ERLs do not have a closed orbit, nor are they even necessarily betatron stable. They might not, therefore, have uniquely defined Twiss parameters, but rather admit an infinite number of lattice function solutions. Physically, this is because the beam and the lattice are not the same; one cannot simply equate Twiss parameterizations, betatron functions, and lattice functions in an ERL, in stark contrast to their equivalence in an electron storage ring at equilibrium. ERLs do not, of course, go to quantum equilibrium (as the beam is in the machine much less than a damping or excitation time)

Unique as well is the fact that ERLs will have multiple beams (at least 2, but perhaps 4, 6, 8,...) in different focusing/accelerating structures – even while they are physically in the same devices. This is because different passes through linac are phased and or focused differently depending on energy. Depending on the machine configuration, multiple beams can also share common transport systems – though this will be nominally at a common energy and separated by (modulo) a half-RF period in phase. These features have significant impact on the process of multipass orbit correction (see example below) and the design of beam position monitors (BPMs) capable of distinguishing amongst the various passes and phases/timings of beam. The most obvious challenge is the dynamic range in current: from single bunch to high frequency CW. Less evident, though no less daunting, is the observation that RF-based diagnostics can be faced with the problem of discriminating between two CW bunch trains separated by only half an RF period. This task is often rendered more difficult by behavior similar to that in the accelerating cavities: the response of the diagnostic to the presence of one pass cancels out the response to the other (as they are out of phase with one another) and the device output is null.

ERLs utilize a variety of (nonlinear) longitudinal manipulations to compress the bunch in duration and/or energy. An example of this – bunch compression in an FEL driver – will be discussed below, and serves to highlight the type of beam and lattice longitudinal diagnostic of practical use in these systems. From the perspective of active beam stabilization, it is worthwhile to observe that ERL topology is similar to that of storage rings, and thereby allows feedback and feed-forward system implementation more easily than is typically possible in a conventional linac.

Given the novel machine architecture and the power advantages provided by energy recovery, it is unsurprising that ERLs face beam dynamics challenges common to all traditional classes of accelerator. One might cynically argue that they are a hybrid of storage rings and linacs and thus are susceptible to the problems of both. More realistically, because ERLs generate high power, high brightness beams, virtually all fundamental phenomena become relevant. These have been exhaustively discussed in the proceedings of recent workshops [17]; here we simply cite examples of major concern.

Beam Self-Interactions

This class of phenomena includes effects based on electrons interacting with one another via their charge or equivalently the bunch wake-field. Examples include space charge effects – both transverse and longitudinal (SC, LSC), coherent synchrotron radiation (CSR), and microbunching instabilities (MBI) mediated by either of the former (or other, external) effects.

Beam/Environment Interaction

Included here are beam interactions with modes in superconducting cavities and vacuum system components. Examples: beam break up (BBU), resistive wall, and the impact of environmental wakes and impedances of all kinds. Of particular interest for high-brightness ERL applications is the interaction of the beam with interceptive diagnostics such as view foils, for which coherent transition radiation (COTR) effects [18] can render high-precision measurements difficult.

Quantum Excitation

As in all electron transport systems, quantum excitation can lead to beam quality degradation. This is of particular concern in ERLs because they engender use of more bending than traditional linac configurations but unlike storage rings effectively have no compensatory damping mechanism and do not settle into an equilibrium.

Stray Power Deposition

As noted above, high power ERL beams preclude tolerance of beam loss at all but the lowest levels; halo is therefore a critical concern. In addition, ERL beams can generate unacceptably large power deposition when the beam current couples to the environment. Common concerns include RF heating and loss of power into propagating higher order modes (HOMs), resistive wall effects (as mentioned above), and CSR/THz power deposition. Existing systems have observed losses of tens to hundreds of Watts into such phenomena; proposed systems could – without proper design – experience tens of kW to MW losses.

Effects of Field Errors

ERLs invoke, by their very nature, transverse-longitudinal coupling to generate and manage the energy recovery process. This in turn creates a unique opportunity for DC magnetic field errors to lead to energy errors; field inhomogeneities thereby lead to energy spread after energy recovery and can impede the recovery process. This effect will be discussed in some detail in the next section.

EXAMPLES OF ERL IDIOSYNCRACIES

The challenges confronting ERLs are most easily contextualized by specific examples. At some point (typically, full energy) the beam will engage in a useful activity – interact with a target, generate light, drive an FEL – which will remove energy and degrade beam quality. Managing this degraded beam through energy recovery (in light of adiabatic antidamping) renders ERL operation a rather more complex matter than simply arranging for the beam to ride the RF crest up to full energy and resting in the trough of the waveform back down. We therefore offer five examples of the issues encountered in ERL design and operation.

Nonlinear Longitudinal Matching: FEL Drivers

FEL driver ERLs must satisfy two fundamental requirements: they have to deliver a bunch with high peak current and adequate beam quality *to* the FEL (to generate the required FEL gain), and they must recover the exhaust beam *from* the FEL (to provide the RF power needed for the acceleration of high average currents). The first of these involves performing a bunch compression with a high-brightness beam; the second is typically made difficult by the FEL-induced growth in beam energy spread, which can readily exceed 10% of the full beam energy after lasing. As a consequence, the system must not only recover the bunch energy centroid – in order to re-use the beam RF power – it must perform an energy compression during recovery so as to avoid beam loss in the linac back-end and at the beam dump. Figure 4 presents a schematic of the longitudinal matching scenario employed in such systems. The individual phase-energy plots indicate the orientation of the longitudinal phase space at key locations around the machine.

To avoid space-charge or LSC driven degradation of beam quality, the injector provides a long bunch with small momentum spread. This is accelerated off-crest in the linac, creating a phase-energy correlation (chirp). The momentum compaction of linac-to-wiggler recirculation transport rotates the “chirped” bunch upright, generating a short bunch at the wiggler. This bunching process is equivalent to producing a “parallel to point” image of the injected longitudinal phase space at the wiggler. Present transport systems (e.g. the Jefferson Lab (JLab) IR Upgrade FEL) typically produce bunch lengths of order 150 fsec rms at 100 MeV and peak currents of order 400 A [19]; recent design work motivated by the need to mitigate CSR effects, suggests shorter bunches and higher peak currents are accessible [20].

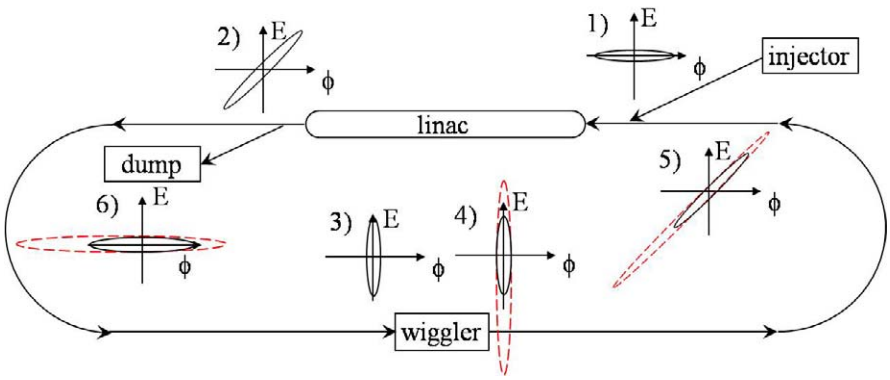

Figure 4: Longitudinal matching scheme for FEL driver ERL, showing phase/energy plots at critical locations: 1) injection; 2) end of linac (1st pass); 3) wiggler entrance; 4) wiggler exit (black: no lasing, dashed red, lasing); 5) reinjection, 6) beam dump. Centroid energy/phase and bunch length/energy spread change when laser turns off /on.

Unlike conventional linac FEL drivers, ERLs do not in general utilize harmonic RF to linearize bunch compression; reasons for this will be discussed below. Instead, the nonlinear longitudinal aberrations of the linac-to-wiggler transport are adjusted with sextupoles (or higher-order multipoles) to compensate for the curvature of the RF waveform, transport lattice aberrations, and phase space distortions due to CSR. Control of T_{566} is a standard practice in existing machines; higher order effects can be managed similarly [21].

When delivered to the wiggler the short bunch drives the FEL interaction, which does not affect the bunch length or transverse beam properties, but which shifts the central energy downward (as the FEL extracts power from the beam) and generates a very large momentum spread. This is depicted in the phase space diagrams adjacent to the wiggler in Figure 4; the growth in momentum spread is evident in Figure 5, which shows the beam in the JLab 115 MeV FEL driver at a dispersed point (η=0.7 m) in the recovery transport system downstream of the wiggler, without lasing (left image: full momentum spread ~2-3%, or 3 MeV) and with lasing (right image: full momentum spread ~10%, or ~12 MeV). This is, as well, indicative of the rather large momentum acceptance required of the recirculator.

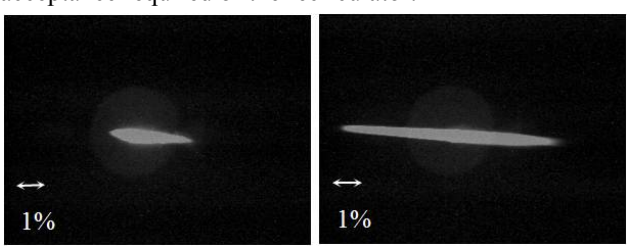

Figure 5: Synchrotron radiation image in recovery arc (dispersion of 0.7 m); left: no lasing, right: lasing

Recirculator path length is adjusted to control the phase of the reinjected beam and to select a recovery phase operating point providing sufficient RF gradient to allow for compression of the highest-energy components of the exhaust beam (Figure 6). We note that this phase is typically *not* 180° away from the acceleration phase and as a consequence power balance in the linac is not exact; the energy recovery is "incomplete" [22].

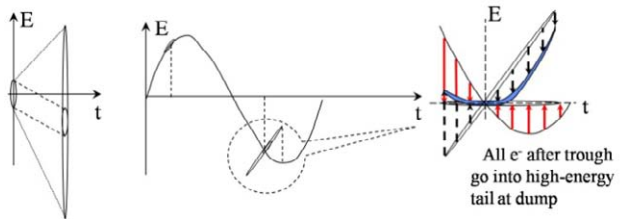

Figure 6: Choice of recovery phase. Left: lasing removes energy/increases energy spread; center, right: beam recovery phase must be far enough from trough to provide RF gradient needed for full energy compression.

Recirculator momentum compactions (M_{56}, T_{566}, W_{5666}) are used to rotate, curve, and torque the bunch so that an appropriate phase/energy correlation occurs at reinjection. This shaping is done using quadrupoles, sextupoles, and octupoles and fits the beam to the nonlinear variation of the RF waveform, insuring that a full energy compression occurs as the beam reaches the dump. In analogy to the bunching process described above, this is a "point to parallel" image of the longitudinal phase space from the wiggler to the dump. We thus note that as the laser turns off and on, the variation in the central energy of the exhaust beam will – as a consequence of this imaging process – be rotated into a phase variation through the linac; at the dump the energy does not change. The resulting phase transients in the high power beam as it is decelerated introduce fascinating beam loading effects and impose potentially severe constraints on the design of RF drive systems for high power ERLS [23].

As noted above, ERL drivers avoid use of harmonic RF for linearization. This is because the recovered beam can exceed 30° in length at the RF fundamental (90° at the harmonic) – so the linearization expansion converges poorly. Even harmonics cannot be used in energy recovered systems [24], so extending the technique to higher order requires fifth-harmonic RF, introduces

prohibitively small apertures (intercepting halo) and high impedances (wake fields), effects that prove problematic in high power systems even at the third harmonic.

Practical implications of this process are shown in Figure 7, which presents "before and after" images of the JLab IR Demo high power beam dump. Limited initial understanding of the longitudinal matching process led to incomplete energy compression during recovery, resulting in scraping of halo and mechanical damage.

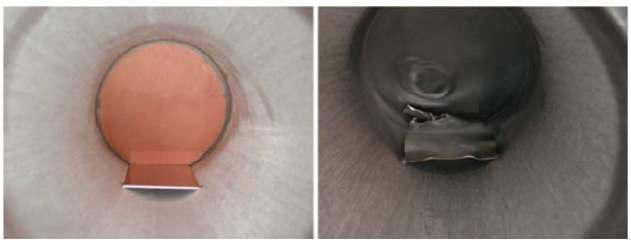

Figure 7: Pre- (left) and post-operations (right) images of JLab IR Demo dump showing damage from improperly-performed longitudinal match [25].

Multipass Orbit Correction

Recirculating linacs face special problems when correcting orbits because of the use of common elements for the transport of multiple beams at different energies [26]. ERLs share this issue; the energy of each pass differs from that of the (all) other(s) at any point along the linac(s), as a consequence the response to steering differs. The JLab IR Upgrade FEL [27] (shown in Figure 8) illustrates the problem. If the first pass beam is subjected to a closed orbit bump in the second two accelerating cryomodules, the recovered beam – at much lower energy at that location – is strongly deflected (Figure 9).

Because both common error sources and common transport elements – such as orbit steering correctors and focusing trims - act on different energies differently, such systems benefit from localized observation and correction of errors. This dictates a need for multipass BPMs capable of resolving the positions of multiple high-frequency CW bunch trains separated by as little as half an RF period. The same hardware could well be called upon for observation of single-shot pulse trains – or even individual bunch trajectories – in some applications.

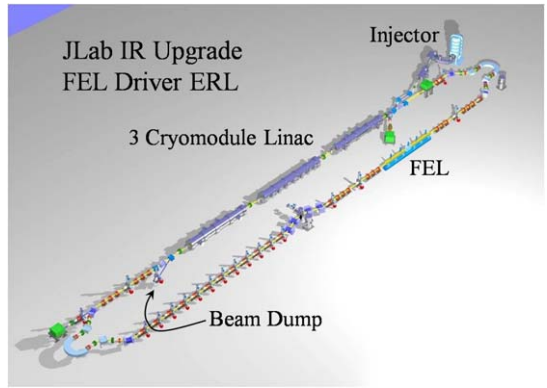

Figure 8: JLab IR Upgrade FEL; injector outside ring, at upper right; three-cryomodule linac on upper axis; FEL in lower axis. Beam dump to interior of ring at lower left.

Collective Effects

ERLs live to generate high brightness, high power beams; collective effects are a "logical consequence" of this lifestyle. The JLab ERL systems have been challenged by several effects [28], including

- LSC (degrading compressed bunch length [29])
- BBU (leading to current limitations [30])
- CSR (limiting deliverable beam quality [31])

ERL instrumentation and control systems must be able to observe, characterize, and quantify collective effects of these – and other – types. Figure 10 illustrates the use of streak camera data to assess the impact of LSC in the JLab IR Upgrade FEL. Measurements of the longitudinal phase space as a function of acceleration phase indicate that beam momentum spread increases while accelerating on the falling part of the waveform [32], this helps confirm simulations that provided guidance for mitigating the impact of the phenomenon [33]. Similarly, BBU control requires instrumentation to measure (and potentially feed back on) higher-order mode (HOM) power. CSR presents signatures such at beam steering as a function of compression [34] that can potentially be (and occasionally have been, at JLab!) misinterpreted as lattice dispersion errors due to magnetic field errors or transport lattice nonlinear aberrations.

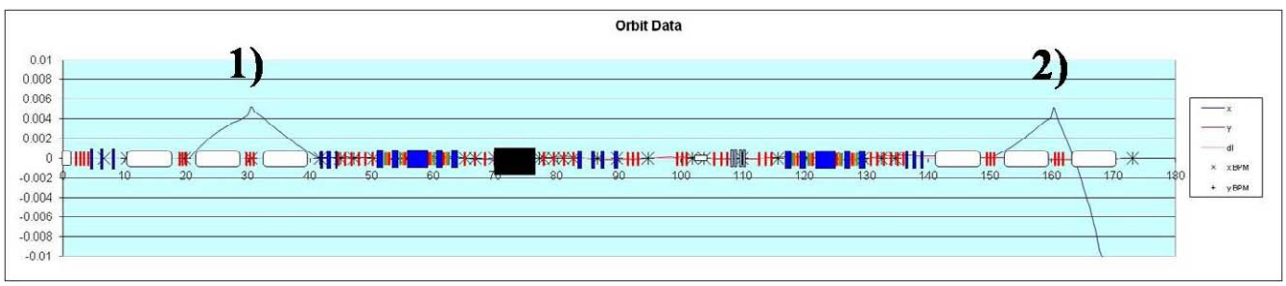

Figure 9: Simulation of orbit bump in common transport region of JLab IR Upgrade FEL. A closed orbit bump imposed on the first (acceleration) pass across the second two accelerating cryomodules (closed upon entry to the recirculation arc, left side of graphic, 1)) results in a severe deflection of the second (energy recovered) pass as it traverses the final cryomodule and approaches the beam dump (right side of graphic, 2)).

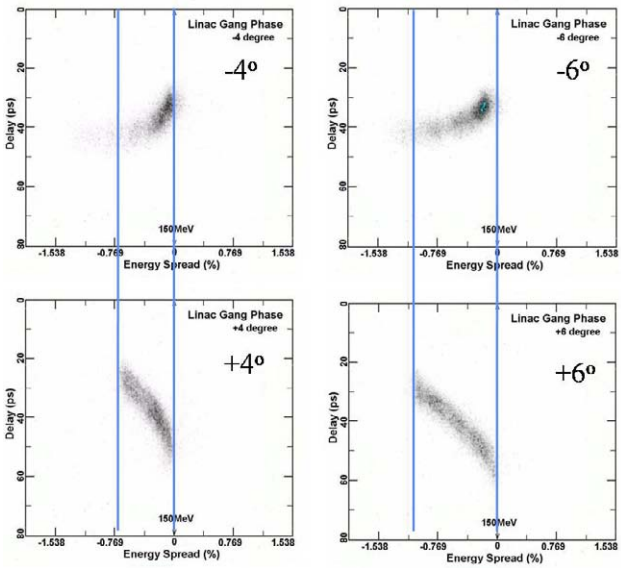

Figure 10: Streak camera data showing LSC effects. Top: acceleration on falling portion of RF waveform. Bottom: acceleration on rising portion. Top case has enlarged momentum spread and irregularity in density distribution.

Transverse-Longitudinal Coupling: The Impact of Magnetic Field Inhomogeneities

Imperfections in magnet field quality have long been recognized as a source of performance limitations in accelerators. In transport lines and linacs, field inhomogeneities lead to beam envelope mismatch, orbit-dependant optics, phase space distortion, and emittance degradation. The mechanism for such effects is simple – field deviations lead to position-dependent bending of some portions of the beam in a manner deviating from design and/or that experienced by other portions. The resulting unanticipated spread in beam angular distribution manifests itself as a focusing error (if linear) or a phase space distortion (if nonlinear).

In conventional accelerators, these errors are of primary significance in transverse phase space. In ERLs they can be longitudinally deleterious as well, by virtue of the six-dimensional nature of the beam dynamics ("synchro-betatron coupling" in synchrotron parlance). As ERLs rely – as described above – upon momentum compaction control to provide longitudinal phase space matching, the presence of angular errors can lead to unexpected changes in bunch length and RF phasing. These in turn alter the energy spread, limiting performance – either at full energy (*e.g.*, by generating excessive energy spread at user experiments) or after energy recovery (by yielding an unmanageably large energy spread at the beam dump).

We can assess the performance impact of field inhomogeneities by evaluating the energy spread after energy recovery caused by such errors. The application over a length l of an error field ΔB to a portion (hereafter, referred to as a "filament") of a beam leads to unintended bending of the filament through an angle $\delta\theta = \Delta Bl/B\rho$. If this occurs at a location from which the transfer matrix to reinjection has a nonzero dependence of path length on angle, or M_{52} (as is often the case, if the error is in a recirculation magnet), a path length error $\delta l = M_{52}\,\delta\theta$ will evolve. When reinjected, the beam filament will thus no longer be synchronous with the nominal RF phase; instead, it will experience a phase offset $\delta\phi = 2\pi\,\delta l/\lambda_{RF}$.

The energy recovered by deceleration through a linac with energy gain E_{linac} at phase ϕ is $E = E_{linac}\cos\phi$; the energy shift resulting from a phase offset $\delta\phi$ from a nominal phase set point ϕ_0 is therefore as follows.

$$\Delta E = E_{linac}\,[\cos(\phi_0+\delta\phi) - \cos(\phi_0)] \cong -E_{linac}\sin\phi_0\,\delta\phi$$

It is assumed that energy compression is desired during energy recovery, and that deceleration (and acceleration) therefore occurs off-trough (crest). (If the acceleration (energy recovery) are on crest (trough, $\phi_0 = 0$), the sine goes away and the energy offset is quadratic in $\delta\phi$.) Folding the preceding expressions together yields an expression relating the imposed field error to the energy offset generated after energy recovery.

$$\Delta E = -\left(\frac{2\pi M_{52}}{\lambda_{\mathrm{RF}}}\right) E_{linac}\sin\phi_0\left(\frac{\Delta Bl}{B\rho}\right)$$

The filament thus ends up at the "wrong" final energy, with error depending on the RF wavelength, the field quality (ΔBl), the details of the transport (M_{52}), and the linac energy gain (E_{linac}). Given that there will be variations in field error across the full beam, different filaments will be transported to different final energy offsets – thereby increasing the energy spread of the beam after energy recovery. By viewing ΔB as a bounding value or tolerance on the field variation and M_{52} as an average value for the path length term, we can then interpret ΔE as an estimate of the final energy spread.

This result can be rewritten to emphasize the effect of each term. M_{52} is constrained by the symplectic condition to be a combination of dispersive and betatron components of the matrix: $M_{52} = M_{22}M_{16} - M_{12}M_{26}$. Control of final momentum spread is therefore promoted by the use of small dispersion and betatron function values. Use of lower linac energy gain also reduces sensitivity. The impact of dipole field quality is made clear by noting $(\Delta Bl/B\rho) = (\Delta B/B)(l/\rho) = (\Delta B/B)\,\theta$, where θ is the bend angle. The induced energy offset is thus

$$\Delta E = -\,[(2\pi M_{52}/\lambda_{RF})\,E_{linac}\sin\phi_0\,](\Delta B/B)\theta\,,$$

which is directly proportional to the relative field error $\Delta B/B$. The total angle will typically be π (such as in the energy recovery transport of an FEL driver) or 2π (as in a generic ERL recirculator); to maintain a fixed energy spread after energy recovery, the relative field error must therefore *decrease* as the linac energy *increases*.

This latter observation implies yet another viewpoint. Note that the energy spread at the dump depends on $E_{linac}/B\rho$. For injection energies small relative to the linac

energy the rigidity will however be approximately 33.3564 kg-m/GeV × E_{linac}. The energy error after energy recovery is thus *independent* of the full energy, and is influenced by only the lattice parameters, RF wavelength (M_{52}/λ_{RF}) and the absolute error integral ΔBl.

$$\Delta E = -\left(\frac{2\pi M_{52}}{\lambda_{\mathrm{RF}}}\right)\sin\phi_0\left(\frac{\Delta Bl}{33.3564\ \mathrm{kg\text{-}m/GeV}}\right)$$

The error field integral producing a specific energy error (energy spread) at the dump is thus *independent* of the linac energy. As the machine full energy increases (implying increased total field integral required to transport the higher energy beam), the tolerable relative error integral will *decrease*, as noted above.

The coupling of transverse steering errors into the longitudinal motion can potentially seriously constrain the performance of recirculating linacs and ERLs. This is not limited to the generation of unanticipated energy spread after energy recovery that is discussed above. Field errors in recirculation transport during acceleration can lead to bunch lengthening and result in growth of momentum spread in any recirculating linac. Synchrotron radiation excitation, with an associated shift in energy at dispersed or compactional locations of the beam transport, will drive the evolution of bunch length errors (longitudinal emittance) in a fashion similar to the degradation of transverse emittance, again leading to growth of momentum spread at full, as well as recovered, energy.

These effects all encourage the use of "better" magnets, lower linac energy gains (between transport system modules with compaction management [35]), and smaller M_{52} values (dispersions, beam envelopes). We note that the effect of poor magnet field quality is not "undoable" – the steering induced by field errors can be corrected or compensated; it does however require provision for this compensation. Diagnostics (for example, phase transfer function measurement systems [36]) and correction knobs (multipole correctors) should be made available if it is not possible to achieve the desired performance with the magnet field quality available within the constraints imposed by the system budget.

The preceding treatment mentioned only in passing the case of on-crest acceleration and energy recovery. In such cases, the resultant energy spread is linear in the linac energy gain and quadratic in the phase (or field integral) error, suggesting that the product (which goes as linac energy divided by the square of the beam rigidity) will *decrease* with increasing linac energy. This would imply that on-crest/in trough acceleration/energy recovery is quite desirable. This is in fact often the case in recirculating, non-energy recovering linacs such as CEBAF, which accelerates a short, small momentum spread bunch on crest so as to take maximum advantage of the available gradients and to limit growth in bunch length and momentum spread. However, for higher charge-state machines (such as FEL drivers and light sources) it may be preferable to accelerate and recover off crest or out of trough. Off-crest acceleration allows transport of longer bunches without undue excitation of wakefields and CSR; the bunch is compressed only where the time structure is needed. Extraction of large amounts of power from the beam (either in an FEL, as a CSR source, or as a source of incoherent synchrotron radiation) will typically lead to generation of energy spread, which, when decelerated, will adiabatically antidamp to large relative energy spreads after energy recovery.

Key to this discussion is the observation that between the limit of on-crest operation (with no energy compression and large final energy spread from adiabatic antidamping) and off-crest operation (with energy compression and potential for large final energy spread due to field-error induced bunch lengthening) there is an optimum at which the two sources of energy spread cross over, minimizing the total final spread. At this point, appropriate longitudinal diagnostics (for both lattice and beam) and accelerator tuning range can compensate for errors that could render the system otherwise inoperable.

Halo

As indicated in the discussion of "unique properties and challenges", halo is a serious concern. In that discussion, we did not, however, characterize what halo actually is. "Halo" includes all beam elements outside the beam core. Sources include stray/scattered drive laser light – and so called "ghost pulses" from incomplete suppression by electro-optical drive laser gating – in photocathode guns [37], cathode relaxation leading to temporal tails at bunch formation, beam dynamical effects (such as space charge) acting during the beam formation and capture process [38], and nonlinear collective effects (space charge, microbunching instabilities, CSR, environmental wake fields,...) during acceleration and beam handling.

Halo management is critical in ERL operation so as to avoid beam loss. Because of exceptionally high (GW) beam powers, losses must be – as noted – at 10^{-5} or 10^{-6} levels to avoid activating or damaging beamline components. This engenders some difficulty inasmuch as halo is characterized by emittances that can be significantly larger than those of the core beam and – recalling our observation that the lattice and the beam are not characterized by the same Twiss parameters – is not described by core betatron functions. Consequently, apertures cannot be specified by "rms beam sizes" – these are completely irrelevant to the halo, which is defined by different emittance and by envelopes that can be completely mismatched to the transport lattice focusing structure, which is typically optimized for the core. ERL beams are decidedly non-Gaussian (Figure 11).

Systems thus need a large "working aperture" allowance so as to accommodate these largely unknown and machine-dependent effects. Instrumentation with exceptional dynamic range – as much as six orders of magnitude [39] – must be developed to characterize halo properties, and controls devised that will allow management of halo without introduction of untoward effects on the beam core.

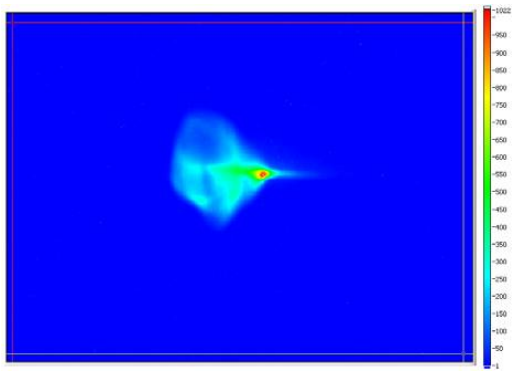

Figure 11: Non-gaussian "hummingbird" in JLab IR Upgrade FEL driver ERL (courtesy P. Evtushenko).

IMPLICATIONS FOR DIAGNOSTICS

These examples give guidance on ERL instrumentation requirements. There is a clear need for a full suite of longitudinal diagnostics, including means of measuring time of flight (for phasing and synchronism purposes), bunch length, and lattice properties such as linear and nonlinear path-length and energy correlations (e.g., in TRANSPORT notation, M_{55}, M_{56}, T_{566},...). Transverse diagnostics must measure positions (and potentially spot sizes) of multiple beams in common transport, in an operationally non-invasive manner. This is all the more challenging because beam time structure can be nearly infinitely variable (from single bunches to CW beam) and include virtually all timing patterns of bunch trains. In addition, accelerated and recovered beams will be separated by modulo one-half RF period – and may, in high power ERLs, be separated by *only* half an RF period during CW operation. The beam fields may then cancel in the resonant structures used for some types of diagnostic, suppressing available signal levels.

These basic requirements and concerns are aggravated by the need to separately characterize the accelerator transport lattice and the beam. As noted, the lattice need not be betatron stable, nor is there a closed orbit. As a result, lattice diagnostics cannot rely on traditional methods such as "pinging" the beam and looking for sidebands on the beam spectrum; there is no "tune" to serve as a reference. Similarly, "tune shifts as a function of focusing strength" do not provide "the" beta function: there *is* no unique betatron function. Instead, the system is characterized by separate (and potentially non-unique) lattice functions and beam envelopes.

ERL "lattices" are analyzed using difference-orbit measurements: the beam is treated as a macroparticle and steered in angle, time, or energy, and transfer matrix values determined from the response. As there is no closed orbit or requirement of betatron stability, phase advances are measured by counting oscillations. ERLs are thus at a disadvantage relative to storage rings, wherein each BPM can take numerous readings (beam positions at each of many turns) and thereby improve measurement resolution. In ERLs, precision is limited by the number and resolution of BPMs and the tolerable orbit excursion, as well as by magnet field quality, lattice nonlinearities, and potentially even collective effects like CSR, which – as mentioned above – may generate lattice-error-like effects during some operations. Instrumentation systems must provide a means of capturing the signatures of such phenomenon and extracting the required information.

The "beam" that is accelerated and recovered in the separately characterized lattice must be subjected to its own management (such as matching to the lattice) and tuning (to achieve optimum system performance), and thus requires additional appropriate diagnostics. First amongst these will be phase space tomography tools providing emittance and beam envelope (and coupling) data, to give insight into various lattice and beam dynamically induced phase space distortions.

A DIAGNOSTICS WISH LIST

A comprehensive diagnostics list was compiled during the 2009 ERL Workshop [40]. Experience suggests that the resolution of phase advance and matrix elements is a basic issue for lattice control, with limits set by the number of available diagnostics (particularly BPMs). The ability to resolve of beam properties is also limited by the number of available diagnostics (in multi-monitor measurements) and the dynamic operating range of the system, as it is in general not possible to run full power beam into an intercepting diagnostic, nor change focusing for a quad scan or tomographic measurement at high power. Finally, the diagnostic suite for an ERL must support excellent beam stability and synchronization.

The operation of existing machines gives specific guidance as to diagnostics that have (or would have) proven useful. These include high resolution multi-pass BPMs working over broad dynamic range (μA to 100s mA) and with flexible beam timing (single shot to CW), beam time of flight and phase transfer function measurement systems [41], and tomographic systems for the entire six-dimensional beam phase space. This requires high resolution/ large dynamic range profile monitors and bunch length measurement systems such as Martin-Puplett interferometers and THz (FTIR) spectrometers. As discussed above, halo is a serious concern in high power systems, so some type of "halo monitor" [42] is needed. Longitudinal manipulations are aided by an available streak camera. Finally, means of monitoring beam noise and stability [43] will be needed to meet the synchronism requirements in FEL drivers and beam stability demands in ERL-based light sources.

Energy recovering linacs are systems of novel architecture presenting great potential to serve as sources of uniquely bright, high power beams. This potential will however be realized only at the cost of meeting numerous beam dynamic and operational challenges. Extensive instrumentation and sophisticated controls are, therefore, absolutely necessary for successful operation of the next generation of ERLs – the diagnostic systems of which must be designed and implemented with full awareness of the idiosyncracies of these devices.

ACKNOWLEDGMENTS

We have presented results from work by many colleagues at Jefferson Lab to understand and operate both CEBAF and the IR/UV FEL. Financial support was provided by the Commonwealth of Virginia, Air Force Research Lab, Joint Technology Office, Office of Naval Research, and DOE Contract DE-AC05-060R23177.

REFERENCES

[1] L. Merminga *et al.*, "High-Current Energy-Recovering Electron Linacs," Annual Review of Nuclear and Particle Science 53 (2003) 387.
[2] M. Tigner, Nuovo Cimento 37 (1965) 1228.
[3] S.O. Schriber *et al.*, IEEE Trans. Nuc. Sci. NS-24 (1977) 1061.
[4] R.E. Rand, "Recirculating Electron Accelerators," Accelerators and Storage Rings, Vol. 3, Harwood Academic, New York (1984); JB Flanz and CP Sargent, IEEE Trans. Nuc. Sci. NS-32 (1985) 3213.
[5] *ibid*.
[6] L. Merminga *et al., op cit.*
[7] C.W. Leemann *et al.*, "The Continuous Electron Beam Accelerator Facility: CEBAF at the Jefferson Laboratory," Annual Review of Nuclear and Particle Science 51 (2001), 413.
[8] *ibid.*
[9] C. Tennant, "Progress at the Jefferson Laboratory FEL," to appear in PAC'09, Vancouver, May 2009, TH3PBI03, (2009); S. Benson *et al.,* "High Power Operation of the JLab IR FEL Driver Accelerator," PAC'07, Albuquerque, June 2007, p. 79 (2007).
[10] A. Bogacz *et al.,* "CEBAF Energy Recovery Experiment," PAC'03, Portland, May 2003, p.195 (2003).
[11] *ibid.*
[12] T. Powers and C. Tennant, "Implications of Incomplete Energy Recovery in SRF-Based Energy Recovery Linacs," ERL'07, Daresbury, May 2007, p.75 (2007).
[13] C. Tennant, *op. cit.,* S. Benson *et al., op. cit.*
[14] A. Bogacz, *op. cit.*
[15] D. Kayran *et al.,* "Status of High Current R&D Energy Recovery Linac at Brookhaven National Laboratory", LINAC'08, Victoria, October 2008, p. 453 (2007).
[16] L. Merminga *et al., op. cit.*
[17] See Proc. ERL'05, Newport News, March 2005, Nuc. Inst. Meth.-A 557 (2006) pp. 1-382; Proc. ERL'07, Daresbury, May 2007; Proc. ERL'09, Ithaca, June 2009; www.lepp.cornell.edu/Events/ERL09/; Proc. DoE BES Workshop "Accelerator Physics of Future Light Sources", Gaithersburg, September 2009, to appear in Nuc. Inst. and Meth.
[18] H. Loos *et al.,* "Observation of Coherent Optical Transition Radiation in the LCLS Linac," FEL'08, Gyeongju, August 2008, p. 485 (2008).
[19] S. Benson *et al., op. cit.,* C. Tennant, *op. cit.*
[20] D. Douglas, "Possibility of Recirculation Systems for High Brightness Beams," ERL'09, Ithaca, June 2009; www.lepp.cornell.edu/Events/ERL09/.
[21] D. Douglas, "The Jefferson Lab 1 kW IR FEL," LINAC'00, Monterey, August 2000, p. 716 (2000).
[22] S.V. Benson and D.R. Douglas, "Use of Incomplete Energy Recovery for the Energy Compression of Large Energy Spread Charged Particle Beams," US Patent #7166973, 23 January 2007.
[23] T. Powers and C. Tennant, *op. cit.*
[24] A half-period phase separation at the fundamental becomes a full period at an even harmonic, so the harmonic RF accelerates (or decelerates) *both* passes.
[25] K. Jordan, private communication.
[26] R.M. Bodenstein, M.G. Tiefenback, "Multipass Steering Protocols at Jefferson Lab," PAC'07 Albuquerque, June 2007, p. 3648 (2007).
[27] C. Tennant, *op. cit.*
[28] *ibid.*
[29] C. Hernandez-Garcia *et al.,* "Longitudinal Space Charge Effects in the JLab IR FEL SRF Linac", FEL'04, Trieste, August 2004, p. 363 (2004); S. Zhang *et al.,* "Temporal Characterization of Electron Beam Bunches With a Fast Streak Camera at JLab FEL Facility", FEL'05, Stanford, August 2005, p. 641 (2005).
[30] C. Tennant *et al.,* Phys. Rev. ST Accel. Beams **8**, 074403 (2005); C. Tennant *et al.*, Phys. Rev. ST Accel. Beams **9**, 064403 (2006).
[31] CSR effects are described in detail in K.L.F. Bane *et al.*, Phys. Rev. ST Accel. Beams 12, 030704 (2009).
[32] S. Zhang, *op. cit.*
[33] C. Henandez-Garcia, *op. cit.*
[34] K.L.F. Bane *et al., op. cit.*
[35] Use shorter linacs and multiple compaction managed recirculation arcs, in analogy with generating phase advance by using numerous, closely spaced, weaker quadrupoles rather than a few very strong ones.
[36] D. Hardy *et al.*, "Automated Path Length and M_{56} Measurements at Jefferson Lab", PAC'97, Vancouver, May 1997, p. 2265 (1997).
[37] When a drive laser beam passes through a window, it scatters, leading to halo production from a photocathode. This scattering can be at the 10^{-4} level (S. Benson, private communication).
[38] P. Evtushenko, unpublished simulation and machine study of JLab IR Upgrade injector.
[39] A.P. Freyberger, "Large Dynamic Range Beam Profile Measurements", PAC'03, Portland, May 2003, p. 2565 (2003).
[40] P. Evtushenko, "Instrumentation Needs from All Working Groups," ERL'09, Ithaca, June 2009; www.lepp.cornell.edu/Events/ERL09/
[41] D. Hardy *et al., op. cit.*
[42] A.P. Freyberger, *op. cit.*
[43] P. Evtushenko and D. Sexton, "Electron Beam Timing Jitter and Energy Modulation Measurements at the JLab ERL", BIW'08, Lake Tahoe, May 2008, p. 247 (2008).

LANSCE BEAM INSTRUMENTATION AND THE LANSCE REFURBISHMENT PROJECT

R. C. McCrady, B. Blind, J. D. Gilpatrick, C. Pillai, J. F. Power, L. J. Rybarcyk, J. Sedillo, M. Gruchalla, Los Alamos National Laboratory, Los Alamos, NM 87544, U.S.A.

Abstract

The heart of the LANSCE accelerator complex consists of Cockroft-Walton-type injectors, a drift-tube linac (DTL) and a coupled-cavity linac (CCL). These systems are approaching 40 years of age and a project to re-establish high-power capability and to extend the lifetime is underway. Many of the present beam diagnostic systems are difficult to maintain, and the original beam position monitors don't provide any data at all. These deficiencies hamper beam tuning and trouble-shooting efforts. One thrust of the refurbishment project is to restore reliable operation of the diagnostic systems. This paper describes the present diagnostic systems and their limitations and the envisaged next-generation systems. The emphasis will be on the uses and requirements for the systems rather than the solutions and engineering aspects of the refurbishment.

INTRODUCTION

Figure 1 is a diagram of the accelerator complex at the Los Alamos Neutron Science Center (LANSCE). Presently protons and H^- ions are delivered to five experimental areas. The facility was originally designed for performing nuclear physics experiments with pions, muons and protons as probes with a primary beam power of 1MW. We currently produce about 125kW of beam power at one-half of the original duty factor due to a change of mission and aging of the system. The LANSCE-R (refurbishment) project aims to restore the higher-power operation and to ensure the on-going reliable operation of this accelerator facility.

One thrust of the LANSCE-R project is to extend the lifetime and restore reliable operation of the beam diagnostic systems in the linac. Some of the present systems are difficult to maintain, and the original beam position monitors (BPMs) do provide any data at all.

The large beam power and the various beam time-structures required at the experimental areas provide challenges in making diagnostic systems that can be used for production operations. The following sections describe the various beam conditions that drive the requirements for performance of the diagnostic equipment.

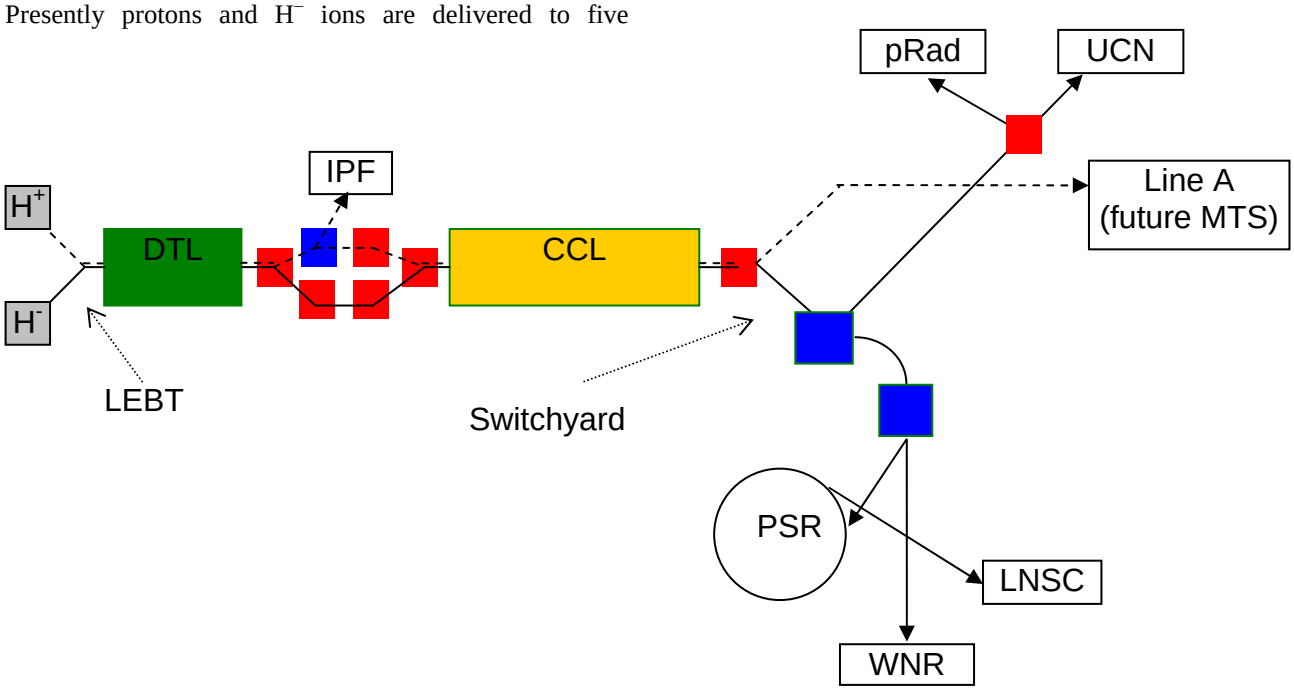

Figure 1: Schematic depiction of the LANSCE accelerator and experimental areas. Proton (H^+) beam lines are shown as dashed lines and H^- beam lines are shown as solid lines. The Low-Energy Beam Transport (LEBT) merges the two beam species and directs them into the linac. The beam switchyard, just downstream of the linac, directs beam to the various experimental areas. Blue squares denote pulsed magnets for switching beam delivery on a per macropulse basis. The experimental areas are: IPF: Isotope Production Facility; pRad: Proton Radiography; UCN: Ultra-Cold Neutrons; MTS: Materials Test Station (under development); LNSC: Lujan Neutron Scattering Center; WNR: Weapons Neutron Research. The beam to the LNSC is compressed in the Proton Storage Ring (PSR).

LANSCE REFURBISHMENT

The LANSCE-R project aims to restore the capability for high-power (1MW) beam operation and to ensure the continued reliable operation of the LANSCE accelerator. The scope of the refurbishment is limited to the core accelerator driver common to all experimental facilities, i.e. the injectors, linac and beam switchyard. Included are: linac radio-frequency (RF) systems, control and timing systems, DC magnet power supplies, water systems, vacuum systems, beam deflectors, spare drift tubes for the DTL, and some beam diagnostics. Because the control systems interact with nearly every other system, changes will be required for even those components not explicitly within the scope of the refurbishment.

The diagnostic systems to be refurbished are: beam position monitors, beam phase monitors and wire-scanner beam profile monitors. Those not included, but requiring new interfaces to the control system are: beam current monitors, beam loss monitors, collimator current monitors, multi-wire beam profile monitors, slit-and-collector phase-space measurement systems, and energy-discriminating beam absorber/collector systems.

Drivers for Requirements on Diagnostics

The requirements on performance of diagnostic systems are driven by two rather different sets of beam conditions: 1) Initial tune-up after long outages, and 2) Production operations. The major differences between these two sets of conditions lie in the time-structures of the beams; these will be described in the following sections.

The beam diagnostics also serve two distinct purposes: 1) Determining the setpoints of the accelerator equipment that result in optimum beam transport, and 2) Diagnosing problems with accelerator equipment. The second purpose will drive requirements on the bandwidths and data rates from the diagnostic systems.

BEAM TIME-STRUCTURES

After a long maintenance outage of several months we perform an initial tune-up with 150μs-long beam pulses whose peak currents are 1mA to 10mA. For these tune-ups fairly modest performance is required of the diagnostic systems. One of the most important requirements is long-term stability of the measurements; for example the beam position and angle at the injection to the CCL should be repeatable year-to-year.

For production operations, additional time-structure is imposed on the beams; these complicate the measurements and also invoke requirements on synchronization of measurements with the beam time-structure. In this section the time structures of the beams are described.

Three time-structures are germane to the diagnostic systems and will be described here: macropulses, minipulses and micropulses.

Macropulses

Presently, for production operations, macropulses occur at a rate of 60Hz and last typically 625μs, though one goal of LANSCE-R is to restore the original macropulse rate of 120Hz. During a macropulse the RF accelerating fields in the linac are present and stable, pulsed magnets are in their necessary states, and the ion sources are producing beams; in short, the accelerator is "on". Both protons and H^- ions can be accelerated simultaneously but each beam species is delivered to a single experimental area during a given macropulse.

Of the 60 macropulses that occur in one second, 20 are for H^- beam to the Lujan Neutron Science Center (LNSC), and 40 are for protons to the Isotope Production Facility (IPF) and H^- to the Weapons Neutron Research facility (WNR). Individual macropulses are sent on demand to the Proton Radiography facility (pRad) or to the Ultra-Cold Neutron experiment (UCN); these macropulses are substituted for IPF/WNR macropulses.

These combinations of beam species and destinations are known as beam "flavors." An important capability of the diagnostic systems is to associate measurements with beam flavors. Presently we set up the timing system to trigger data collection on particular beam flavors' macropulses; the upgraded systems will need to have a similar capability, and may offer greater flexibility in this regard.

Another aspect of macropulses that impacts diagnostic performance is the macropulse length. In particular the L/R time constants for transformer-type beam current monitors must be much longer than the macropulses to allow accurate measurements.

Micropulses

In radio-frequency accelerators beam particles are accelerated during a particular part of the RF cycle; the resulting beam consists of a train of bunches (micropulses) at the frequency of the accelerating field. The initial stage of acceleration at LANSCE is in a DTL operating at 201.25MHz. Each micropulse contains a few $\times 10^8$ ions and is 50-100ps long.

This micropulse structure provides a strong narrow-band signal that is useful in some beam diagnostics, particularly beam position monitors.

Minipulses

In the low-energy beam transport (LEBT) for the H^- beam, where the beam energy is 750keV, a travelling-wave beam chopper can impose on the beam time-structures on the scale of tens of nanoseconds.

For long-bunch (LB) beam to the Proton Storage Ring (PSR), whose ultimate destination is the LNSC, the minipulses are about 300ns long and have a frequency of 2.8MHz. This provides a gap in the accumulated beam that allows time for a pulsed kicker to turn on to extract the beam from the PSR. For WNR, ~20ns-long minipulses are pre-bunched and each is accelerated in a

single DTL RF cycle to yield intense single-micropulse pulses. For beam to pRad a variety of minipulse patterns are used, but usually a 100ns-long precursor pulse is followed a few hundred microseconds later by several 60ns-long minipulses.

The frequencies and lengths of all of the minipulses can be modified to suit users' needs or to modify the average beam current to allow operators to cope with varying conditions of the accelerator. These adjustments are frequently made, and beam diagnostics need to provide useful data under these conditions.

BEAM POSITION AND PHASE MONITORS

There are presently two separate systems for measuring the phase and the transverse position of the beam. The beam phase measurement is used solely in the Δt tuneup procedure [1]. This procedure is carried out with unchopped beams and the system has no provision for synchronizing the phase measurement with the minipulse structure; thus the system is not useful for H^- beams during production operations. A transducer for the present system is shown in Figure 2. It is a metal cylinder about 1cm long with a diameter of about 5cm, which is the diameter of the beam pipe in this area. This cylinder couples capacitively to the beam; the 201.25MHz signal induced by the micropulse structure of the beam travels via a TNC connector and a solid-shield cable to the phase measurement instrumentation. The phase measurement is an I and Q measurement relative to a sample of the 201.25MHz reference oscillator for the DTL [2]. The response of these transducers is sensitive to the transverse position of the beam; reducing this sensitivity is desirable in the new system.

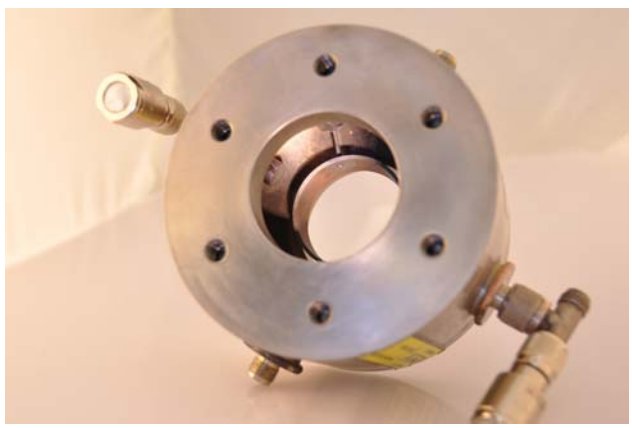

Figure 2: Photograph of a present transducer module for beam phase measurements.

The present transducer module for the beam position measurements is shown in Figure 3. Each transducer is a rigid wire with one end soldered to the beam pipe and the other end connected to the center conductor of a cable via a TNC vacuum feed-through connector. This is a so-called "B-dot" transducer, as the time rate of change of the beam-induced magnetic field through the loop induces the signal. ($\dot{B} \equiv \partial B / \partial t$.) There is presently no functioning instrumentation to provide data from this system.

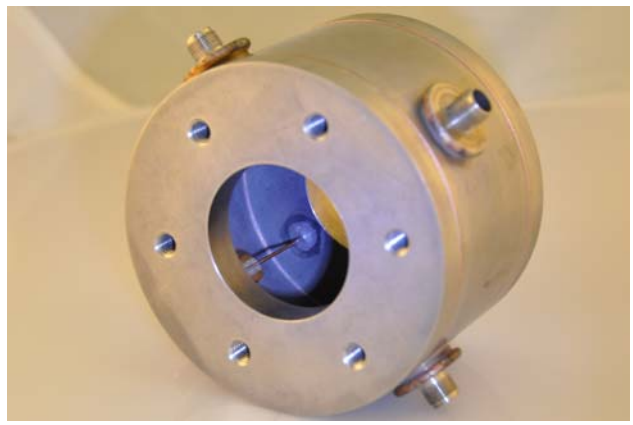

Figure 3: Photograph of a present transducer for beam position measurements.

In the new system under development for LANSCE-R a single set of transducers will provide signals for the phase and position measurements. A prototype transducer is shown in Figure 4. It is a stripline-type electrode with one end grounded to the beampipe. Signal formation can be understood in terms of image currents [3].

These new transducers are designed to fit into the locations of the existing transducers for the Δt and BPM systems.

Figure 4: Photograph of a prototype transducer for the new beam position and phase measurement system.

BPPM Requirements

Table 1 shows requirements for the BPPM system. The resolutions shown in this table will be achievable only with unchopped beam (no minipulse structure) and after 100μs of steady beam conditions. This corresponds to tune-up conditions, where precision is most valuable.

Phase and position measurements are required for beams with minipulse structures but with relaxed requirements on accuracy and precision. Synchronization with the minipulses is necessary so that measurements are made at a specific time during the minipulses; this will require distribution of the minipulse reference oscillator

signal to the BPPM systems or it may be possible to use events from the timing system, or triggering from the beam signal itself with an adjustable delay. Synchronization among the BBPMs, to provide a measurement from many devices of the same time-slice of beam, is also of great value.

The system will be able to report data on a per-minipulse basis for H^- beam to the proton storage ring, i.e. at 2.8MHz; this allows correlation of data with existing downstream diagnostic systems.

For the H^- beam to WNR, which normally has single-micropulses spaced at 1.8μs, measurements are difficult. An existing downstream system has this capability, so the inclination is to require it for the new system in the linac, but cost/performance trade-offs must be considered. A requirement for measurements of this type of beam is still under consideration.

Table 1: Requirements for the BPPM system.

Parameter	Value
Frequency of Measurement	201.25 MHz
System Response Time	50 ns
Averaging Window for System Resolution Specifications	100 μs
Position Resolution (% of radius, RMS)	0.46% (0.1mm)
Position Accuracy (% of radius)	±4.6
Position Range (% of inner electrode radius)	±60
Phase Resolution (RMS)	0.25°
Phase Linearity	±2°
Beam Current Resolution (RMS)	0.05 mA
Beam Current Accuracy	N/A
Beam Current Range	0.9 to 21 mA
Timing Uncertainty	±50 ns

For unchopped beams, such as the proton beam to IPF, the system should be able to measure at a rate of about 1MHz.

Of great importance, both for tune-ups and for equipment trouble-shooting, is the long-term stability of measurements. For example, measuring the beam position and angle at the injection to the CCL then using those same parameters for the tune-up the following year is very valuable. The requirements on accuracy should address this issue. The plans for this system provide for easy in-situ calibration with no manipulation of the hardware by sending signals to each electrode and picking them up on the others.

Another mode of data reporting that will be required is a single measurement, at a fixed time during each of many macropulses for a given beam flavor. This allows one to observe variations in conditions on timescales of several seconds. This capability in other diagnostic systems has proven to be very valuable.

BPPM Locations

BPPMs will be installed after DTL modules 2, 3 and 4, and one will be installed in the beam transport between the DTL and CCL. BPPMs will also replace the 28 existing Δt transducers in the CCL, and an additional two BPPMs will be located in the CCL to allow characterization of the injection parameters of the beam.

BEAM PROFILE MONITORS

Scanning-wire-type beam profile monitors [4] are currently used throughout LANSCE for tune-up and trouble-shooting. Replacement of many in the linac and some of those in the beam switchyard is included in the scope of LANSCE-R. Several in the linac will be removed.

A photograph of the type of transducers used in the present systems is shown in Figure 5. The wires are crossed and the actuator is mounted 45° from vertical; both horizontal and vertical profiles are measured with a single actuator. The crossed wires can complicate the measurement, especially for H^- ions, as secondary electrons from one wire can induce signal on the other.

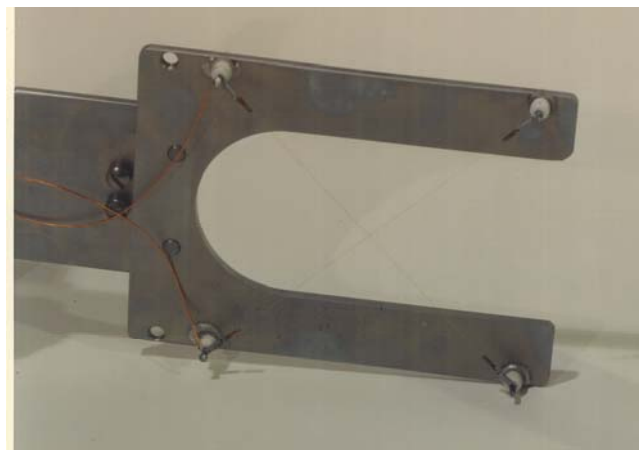

Figure 5 Photograph of a present wire-scanner fork. Note that the wires cross near the center of the aperture.

Most of the wire-scanners in the linac use 125μm-thick tungsten wires. When scanning, this material produces a great deal of localized beam spill; so much that these devices cannot be used under production conditions, greatly limiting their value in trouble-shooting. These tungsten wires rarely break, however. The wire-scanners in the beam switchyard use more fragile 100μm-thick SiC fibers; most can be run during production operations.

In addition to the wire thickness and material, the time the wire stays in the beam contributes to the beam spill produced during a scan. The present system is controlled by a centralized computer through an antiquated control system, with data and commands issued on a per-step basis. The speed of data and commands, as well as the nature of the motor controllers, results in scans that are

slower than ideal. The upgraded system will be controlled by a dedicated local computer interacting directly with the devices and data will be reported on a per-scan basis. The motor control will be optimized for rapid scanning and accurate wire positioning.

Table 2: Requirements for the wire-scanner system.

Parameter	Value
Sensing Wire or Fiber Materials	SiC, W, or C
Sensing Wire or Fiber Diameters (mm)	<0.15
Minimum Distribution Horizontal or Vertical Width, rms (mm)	1.0
Minimum Projected Distribution Bin Width (mm)	0.1
Typical Minimum Beam Macropulse Length (μs)	150
Typical Repetition Rate (Hz)	4
Minimum/Maximum Peak Secondary Electron Emission Current (μA)	-1/-2000 & +0.01/+500
Distribution Minimum Peak-to-Edge Ratio	100:1
Amplifier Response Time Constant (μs)	~10
Maximum Sampling Rates within a Single Macropulse (MS/s)	0.1
Linear Peak Actuator Velocity, under Closed Loop Control (mm/s)	>8
Wire Location Repeatability or Precision (% rms distribution width)	<10
Absolute Wire Location Accuracy (mm)	1
Peak Beam Current Range (mA)	21 to 0.9
Timing System Resolution (ns)	~ 100

Requirements on the wire-scanner parameters are shown in Table 2. These parameters are driven by the need to use the wire-scanners in tune-up and production conditions and to provide performance at least as good as that from the present systems. The upgraded systems should provide measurements during both tune-up and production if possible. RMS beam-spot sizes to be measured are a few millimeters. Step sizes of 0.1mm will provide a good sampling density for these profiles.

With 100kSamples/second, the system will be able to provide average beam profiles as a function of time along macropulses. This kind of measurement is not possible with the present system except by running many scans with different timing specifications, a very labor-intensive effort.

The upgraded system should have the wires oriented in a way that prevents cross-talk between the wires. Figure 6 shows the proposed scheme; this is already used in some H^--specific beamlines and is found to be effective. This arrangement requires a longer stroke than that shown in Figure 5.

We don't anticipate a need for synchronization with minipulses and among devices for this system, as changes in beam profiles at LANSCE typically occur on the scale many microseconds.

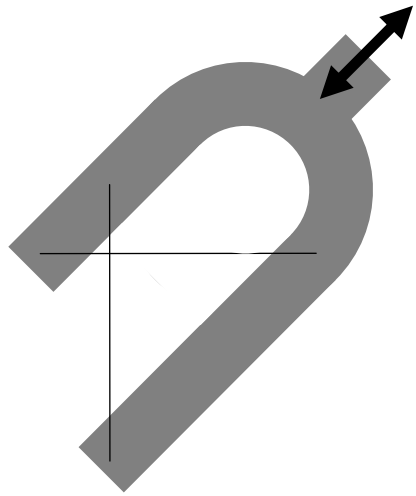

Figure 6 Wire locations on the actuator fork to eliminate cross-talk between the wires. The crossing point of the wires needs to be outside the beam-pipe aperture.

OTHER DIAGNOSTIC SYSTEMS

The BPPMs and wire-scanners are the only two diagnostic systems to be replaced on a system-wide basis under LANSCE-R, but because the control system is to be replaced the interfaces to the control system will need to be replaced for the remaining diagnostic systems. The diagnostics presently interface with the control systems via RICE (Remote Instrumentation and Control Equipment). The interface includes analog-to-digital converters, binary indications and pulse commands to control and read the measurements. Programs run on centralized computers and synchronization is effected through a multi-layer scheme of networks and computer buses. The new control system will be based on EPICS (Experimental Physics and Industrial Control System) with device-level computers controlled by and serving data via a network to applications requesting those services.

The individual systems are described in the following sections; a summary and comparison of these systems follow the descriptions.

Slit-and-Collector Beam Phase Space Measurement System (EM)

There are ten slit-and-collector [5] systems for measurements of transverse beam phase-space distributions; each can measure in the vertical and horizontal planes. The slit and the 76-wire collector step together across the beam, so in the present system coordination of motor and data collection results in a

great deal of communication between the user's computer and the device-level systems. The present system is multiplexed, with a small number of motor controllers, amplifiers and analog-to-digital converters. Some of the multiplexing is effected electronically, but the signals from the wires to the amplifiers are swapped manually by moving cable connectors.

The plan for the refurbishment is to field a device-level computer that will perform coordination of device motion and data collection and will pass to the user scan-level data sets. The system may be multiplexed, but the preference is to move toward a single electronics chain per channel.

Harps (HP)

There are 17 multi-wire beam profile measurement systems [6] in the injector/linac area; each measures horizontal and vertical profiles with 76 thin wires. The devices can be inserted and retracted, but no coordination between motion and data collection is required, as the device is in a fixed location for an entire data-collection cycle. The electronics chains are those also used for the EM system described above; in total there are 74 motors and about 4100 signal wires included in these systems.

The plan for these devices is to implement a new interface to the control system along with the EM systems as described above.

Absorber/Collector (AB)

This system is used for the initial tune-up of some of the RF systems' setpoints. There are four sets of these devices; each absorber, when inserted into the beam-pipe, allows protons of some minimum energy to pass to the collector (Faraday cup), while protons below that energy are stopped. A relatively small number of data channels for motion control and data collection are required and the volume of data is small.

Beam-Current Monitors (CM)

Transformer-type beam current monitors [7] are present along the injector/linac area. These are used to monitor beam transmission and some provide inputs to the machine protection system. Beam current measuements need to be associated with their respective beam flavors. Some of the amplifiers for these devices have selectable gains.

Beam-Loss Monitors (AP, LM)

Cans of liquid scintillator viewed by photomultiplier tubes detect ionizing radiation produced by beam particles that escape the beam vacuum envelope. Two instrumentation systems provide signals to the control system, one (AP) providing low-bandwidth signals for machine protection and refinement of machine parameters, the other (LM) providing high-bandwidth signals more useful for trouble-shooting.

Collimator Current Monitors (BA)

Collimators, both stationary and movable, are present in the low-energy beam transport area. The beam currents on these devices are measured and are available in the data system.

The motor controllers for the movable collimators are identical to those used in the EM system.

Summary of Other Diagnostics

Table 3: Characteristics that drive requirements for the interfaces to the new control system for diagnostic systems not within the scope of LANSCE-R.

	EM	HP	AB	CM	AP	LM	BA
Motor control	x	x	x				x
Signals per device	160	160	6	1	5	1	1 to 5
Timed data	x	x	x	x		x	x
Used in prod.				x	x	x	x
Inter-device Synch.				x		x	
Per-scan data	x						

Table 3 shows several characteristics that underlie the requirements for the interfaces to the new control system for diagnostic systems that aren't to be refurbished under LANSCE-R.

Motor controllers, along with their position encoders and limit switches are required for beam-intercepting diagnostics and for the movable collimators.

The EM and HP systems have many analog signals to be conditioned and digitized.

All of the systems except for APs need to deliver "timed" data, that is data collected at specific times during macropulses, or better yet, vectors of data collected along the macropulses.

Several of the systems are non-intercepting, and can be used during production operations. More flexible timing and correlation of data may be required for these systems.

Data from the CM and LM systems need to be synchronized so that data from all of the devices of each type can be taken for a particular time-slice of beam.

Only the EM systems will be required to provide data on a per-scan basis, i.e. coordinating device motion and data collection, then reporting one package of data from the scan.

SUMMARY

The refurbishment of the core of LANSCE, including some diagnostic systems and the control system, has necessitated a close look at the requirements of the diagnostic systems and the data they provide. The

diagnostics should be useful for initial tune-ups as well as during production operations and should aid in setting equipment parameters, general trouble-shooting, optimization and beam studies. Flexibility in the ways that data are collected and reported is valuable, too.

While some questions remain, we have identified the major requirements for these systems and work on designing solutions is underway.

ACKNOWLEDGEMENTS

LANSCE-R is a large complex project involving many managers, administrators, scientists, engineers and technicians. Included in the list of authors of this paper are those people who have contributed to developing the requirements for the beam diagnostic systems. We gratefully acknowledge the efforts of all the people who have contributed to the progress of LANSCE-R.

This work was supported by the U. S. Department of Energy under contract DE-AC52-06NA25396.

REFERENCES

[1] K. Crandall, “The Δt Tune-Up Procedure,” Proceedings of the 1972 Proton Linac Conference, Los Alamos, October 1972, p. 122, University of California Publication UC-28.

[2] I. Campbell, “LAMPF Delta-t Hardware Review,” Unpublished, Los Alamos National Laboratory, 1992.

[3] R. Shafer, “Beam Position Monitoring,” BIW89, Upton, NY, October, 1989, AIP Conference Proceedings No. 212, p. 127 (1990)

[4] J. Galayda, “Beam Profile Measurements,” BIW89, Upton, NY, October, 1989, AIP Conference Proceedings No. 212, p. 127 (1990)

[5] O. R. Sander, “Transverse Emittance: Its Definition, Applications, and Measurement,” BIW89, Upton, NY, October, 1989, AIP Conference Proceedings No. 212, p. 127 (1990)

[6] R. Chehab, J. Bonnard, G. Humbert, B. LeBlond, J. L. Saury, “A Multiwire Secondary Emission Monitor for Small Emittance Beams,” (PAC 1985) IEEE Tran. Nuc. Sci. NS-32, pp 1953-1955 (1985).

[7] R. Talman, “Beam Current Monitors,” BIW89, Upton, NY, October, 1989, AIP Conference Proceedings No. 212, p. 1 (1990)

DEVELOPMENT OF BEAM CURRENT MONITOR WITH HIGH-Tc SQUID AT RIBF

T. Watanabe*, N. Fukunishi, Y. Sasaki, M. Kase, A. Goto and O. Kamigaito
RIKEN Nishina Center for Accelerator-Based Science, Wako-shi, Saitama 351-0198, Japan

Abstract

A highly sensitive beam current monitor with a high-critical-temperature (high-Tc) superconducting quantum interference device (SQUID) and a high-Tc current sensor, that is, a high-Tc SQUID monitor, has been developed for use in the radioisotope beam factory (RIBF) at RIKEN. As reported in the present work, the high-Tc SQUID monitor allows us to measure the DC of high-energy heavy-ion beams nondestructively in such a way that the beams are diagnosed in real time and the beam current extracted from the cyclotron can be recorded without interrupting beam user experiments. Both the high-Tc magnetic shield and the high-Tc current sensor were fabricated by dip-coating a thin layer of Bi_2-Sr_2-Ca_2-Cu_3-O_x (2223-phase, Tc=106 K) on a 99.9% MgO ceramic substrate. Unlike other existing facilities, all the high-Tc devices are cooled by a low-vibration pulse-tube refrigerator, enabling us to downsize the system. Last year, aiming at its practical use, the high-Tc SQUID monitor was installed in the RIBF. Using the monitor, a 1 μA Xe beam intensity (50 MeV/u) was successfully measured with 100 nA resolution. Here we report the present status of the facility, details of the high-Tc SQUID monitoring system and the results of the beam measurement.

INTRODUCTION

Accelerator complex of RIBF

The RIBF project to accelerate all elements from hydrogen to uranium up to an energy of 440 MeV/u for light ions and 350 MeV/u for heavy ions started in April 1997 [1]. Figure 1 shows a schematic layout of the RIBF facility. The research activities in the RIBF project make extensive use of the heavy-ion accelerator complex, which consists of one linac and four ring cyclotrons, i.e., a variable-frequency linac (RILAC), the RIKEN ring cyclotron (RRC), a fixed-frequency ring cyclotron (fRC), an intermediate-stage ring cyclotron (IRC) and a superconducting ring cyclotron (SRC). Energetic heavy-ion beams are converted into intense RI beams via the projectile fragmentation of stable ions or the in-flight fission of uranium ions using a superconducting isotope separator, BigRIPS [2]. The combination of these accelerators and BigRIPS is expected to greatly expand our knowledge of the nuclear world into the presently inaccessible region on the nuclear chart. We succeeded in accelerating a uranium beam to 345 MeV/u in March 2007, by which new RIs, the neutron-rich palladium isotopes of $_{125}$Pd and $_{126}$Pd, were discovered [3, 4].

In 2008, the RIBF succeeded in providing heavy-ion beams of $_{48}$Ca and $_{238}$U with particle currents of 170 pnA and 0.4 pnA, respectively, at an energy of 345 MeV/u. The search for new isotopes using in-flight fission of the 345 MeV/u uranium beam has continued. Consequently, fission fragments have been analyzed and identified using BigRIPS and we have observed 45 new neutron-rich isotopes. From the operational point of view, however, the intensity of the uranium beam should be greatly increased. Furthermore, RIBF research conflicts with ongoing research on the synthesis of super-heavy elements using a gas-filled recoil separator (GARIS), because both of them use the RILAC. To reconcile this conflict, a new additional injector linac for the RIBF (RILAC2) has been proposed and is now under construction. We have therefore constructed a superconducting electron cyclotron resonance (ECR) ion source that is capable of providing a microwave power of 28 GHz, a radio frequency quadrupole (RFQ) linac and three drift tube linacs (DTLs). The new injector, which will be ready in FY2010, will hopefully enable the independent operation of the RIBF experiments and research on super-heavy element synthesis [5].

Technical issues related to Faraday cups

It is essential to keep the beam transmission efficiency as high as possible, because the production of the RI beam requires an intense primary beam during beam user experiments. Furthermore, activation produced by beam loss should be particularly avoided. In this facility, to evaluate the beam transmission efficiency, about 50 Faraday cups are used. A Faraday cup is used in the conventional method of measuring the beam current. However, the beam cannot be used while it is being measured, and there is a danger of melting and activating the cup. Furthermore, it is difficult to completely suppress the high-energy secondary electrons that are produced by heavy-ion beams. When an accelerated particle collides with the surface of a Faraday cup, secondary electrons are always generated. If these electrons escape from the insulated cup area, the reading of the beam current is incorrect by the number of lost electrons. Thus, the suppression of secondary electrons is very important for measuring the beam current precisely. Normally, this can be achieved by applying a high negative voltage close to the entrance of the cup. However, since the electrical field on the beam axis is lower

* wtamaki@riken.jp

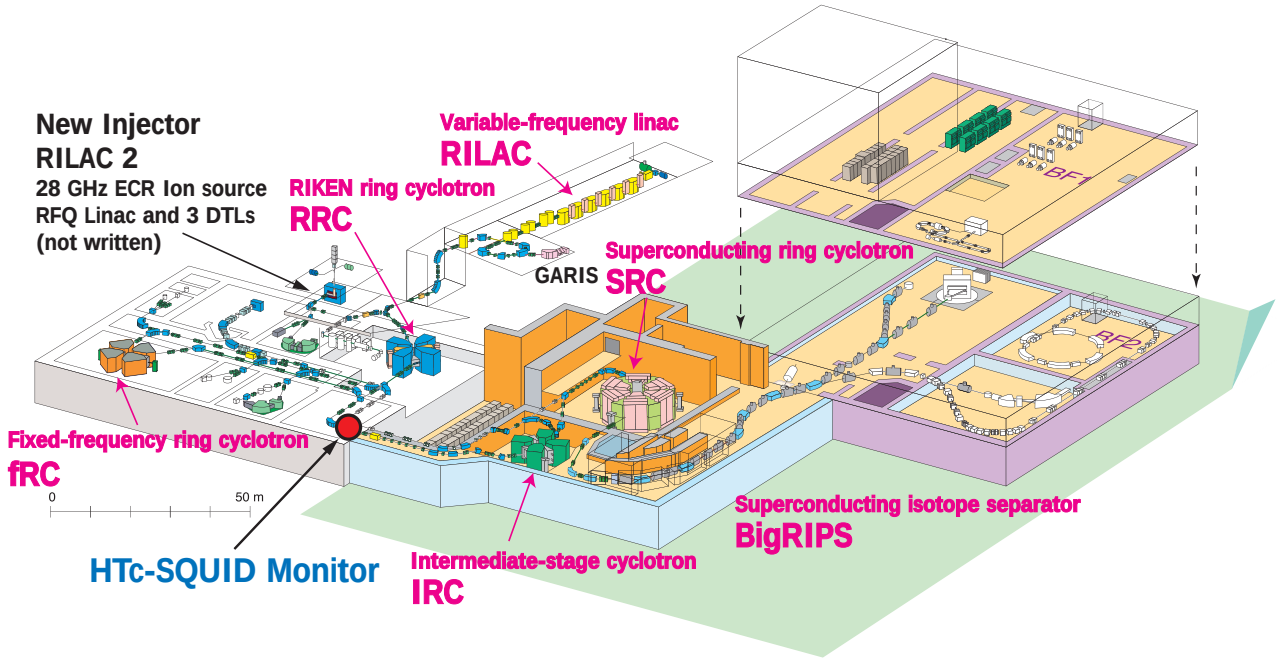

Figure 1: Schematic bird's-eye view of the RIBF facility.

than that on the edge, it is difficult to completely suppress the high-energy secondary electrons that are produced by high-energy heavy-ion beams. To evaluate the number of secondary electrons generated by a beam, a high positive voltage is used for suppression. A measurement result obtained by applying the suppression voltage for a 10.7 MeV/u $^{238}_{92}U^{72+}$ beam is shown in Fig. 2. From this result, the current generated by the secondary electrons was found to be eight times stronger than that of the uranium beam. To resolve this technical issue, a study of the high-Tc SQUID monitor has been started at RIKEN [6, 7, 8]. The high-Tc SQUID monitor has been installed in the beam transport line between the fRC and the IRC aiming at its practical use in the RIBF.

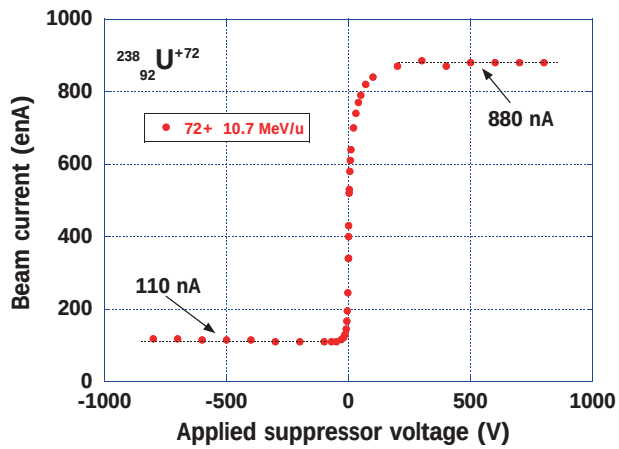

Figure 2: Measurement result obtained by applying suppression voltage for 10.7 MeV/u $^{238}_{92}U^{72+}$ beam. To evaluate the number of secondary electrons generated by the beam, a high positive voltage was used for suppression.

Cryogenic current comparator

The application of superconducting technology to the precise measurement of current has been extensively developed for the liquid helium regime [9]. The first cryogenic current comparator, the so-called CCC, based on SQUIDs for measuring beam currents was built at PTB in Berlin in 1977 [10]. This group was the first to use a CCC based on SQUIDs for measuring beam current, and a 108 nA electron beam generated by a Van de Graaff accelerator was observed. Because the accelerator at the PTB was shut down and it became difficult to fabricate the SQUID, the development of this device was stopped. However, modern technologies that apply superconductivity have led to a new era of accelerators. A new type of CCC has been built at GSI, and a 300 MeV/u neon beam extracted from SIS, the heavy-ion synchrotron at GSI, was measured [11]. In 2001, the group of Dr. L. Hao began investigating high-Tc CCC designs incorporating a flux concentrator and a high-Tc SQUID. They outlined a proposal for the precise determination of the Faraday fundamental constant using a purely physical system and employing a high-Tc CCC to measure the current of charged particle beams [12].

Motivation

In the present work, the reason for using the SQUID as a beam current monitor is that it has a very high magnetic

Table 1: Comparison of cooling costs.

	1 day	1 year
Liquid He for low-Tc	\$430 (20L / day)	\$157,000
Refrigerator for high-Tc	\$10 (1.9kW / day)	\$3,650

sensitivity. The Earth's magnetic field is on the order of 10^{-5} T and that of environmental noise is on the order of 10^{-6} T. On the other hand, the range of the magnetic field induced by the heart and brain and measured by SQUIDs is from 10^{-10} to 10^{-13} T. Furthermore, the magnetic field produced by a 1 nA beam at a distance of 10 cm is 2×10^{-15} T, ten orders of magnitude smaller than the Earth's magnetic field. From this comparison, it becomes apparent how difficult it is to measure the current of a faint beam. The sensitivity of a DC current transformer (DCCT) is about 1 μA. The function of a DCCT is based on the modulation of a magnetic material, and the limiting factor is the Barkhausen noise produced by the wall-jumping of a magnetic region. In the present work, by using high-Tc devices including the SQUID, we aim to downsize the system and reduce the running costs. This is illustrated by comparing the costs of a low-Tc SQUID monitor and a high-Tc SQUID monitor, which have operational temperatures of the superconductor and the SQUID of 4.2 K and 77.3 K, respectively. If the low-Tc SQUID monitor consumes 20 L of liquid helium per day [13], it costs a total of \$157,000 per year. On the other hand, the high-Tc SQUID monitor only requires electricity, costing about \$3,650 per year. Table 1 shows a comparison of the cooling costs, which were estimated using Japanese prices. Its low cost is the major advantage of using the high-Tc SQUID monitor.

HIGH-T_C SQUID MONITORING SYSTEM

Fundamental principles of high-Tc SQUID monitor

A schematic drawing of the high-Tc SQUID monitoring system is shown in Fig. 3(a). Both the high-Tc magnetic shield and the high-Tc current sensor were fabricated by dip-coating a thin Bi_2-Sr_2-Ca_2-Cu_3-O_x (Bi-2223) layer on a 99.9% MgO ceramic substrate. When a charged particle (ion or electron) beam passes along the axis of the high-Tc tube, a shielding current produced by the Meissner effect flows in the opposite direction along the wall of the high-Tc tube so as to screen the magnetic field generated by the beam. Since the outer surface is designed to have a bridge circuit (Fig. 3(b)), the current generated by the charged particle beam is concentrated in the bridge circuit and forms an azimuthal magnetic field Φ around the bridge circuit. The high-Tc SQUID is set close to the bridge circuit and can detect the azimuthal magnetic field with a high S/N ratio. In particular, we adopt a SQUID gradiometer to increase the S/N ratio (Fig. 6). Since the SQUID gradiometer has two pickup coils that are wound in opposite directions and

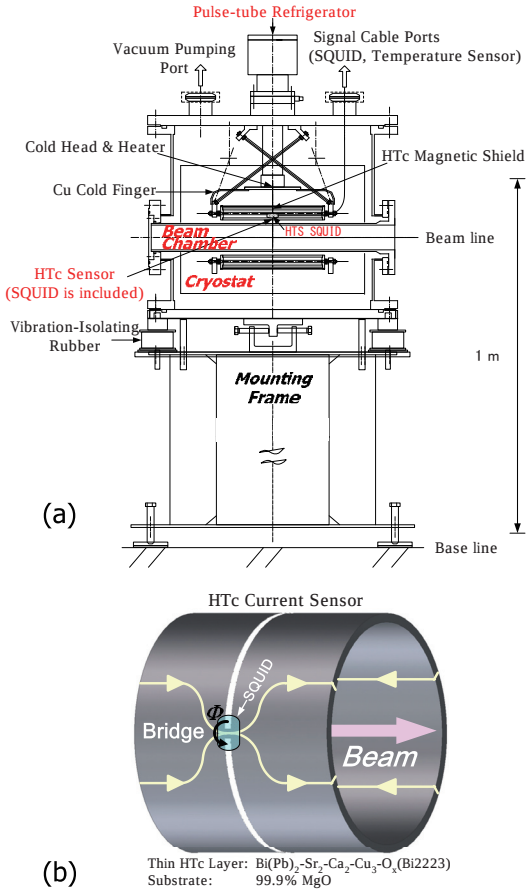

Figure 3: Schematic drawing of the high-Tc SQUID monitoring system (a) and the current sensor (b).

connected in series, the signal level is expected to be improved by a factor of 2, while the background noise can be significantly reduced by more than 40 dB.

The high-Tc SQUID monitoring system consists of two vacuum chambers completely separate from each other:

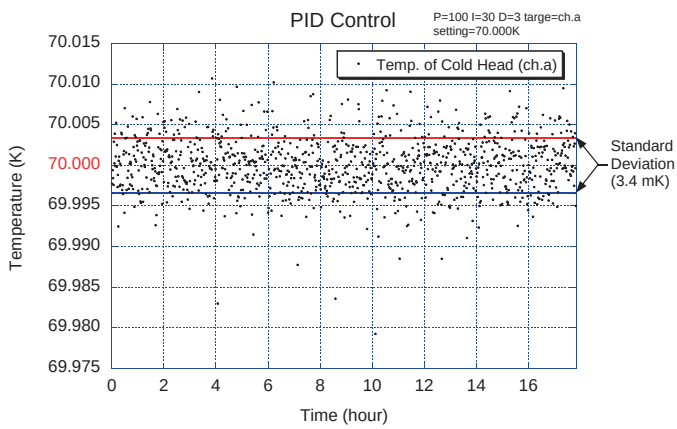

Figure 4: Plots of the temperature of the cold head as a function of time. The standard deviation of the temperature over a period of 18 h was 3.4 mK.

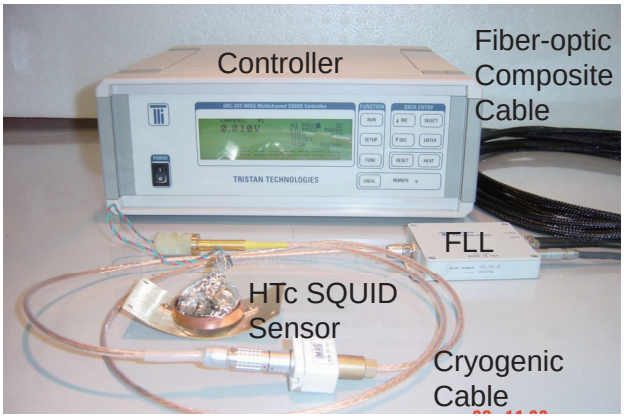

Figure 5: High-Tc SQUID system (Model BMS-G, manufactured by Tristan Technologies) [14].

one chamber contains a cryostat in which the high-Tc SQUID, a high-Tc magnetic shield and a high-Tc current sensor are cooled, and the beam passes through the other chamber. In the present work, all the fabricated high-Tc devices are cooled by a low-vibration pulse-tube refrigerator with a refrigeration power of 11 W at a temperature of 77 K. The operation temperature can be adjusted in the range of 64 K to 90 K (the critical temperature of the high-Tc SQUID) using a heater, since the pulse-tube refrigerator is capable of cooling the system to temperatures lower than liquid-nitrogen temperature. Furthermore, it is possible to stabilize the temperature of the high-Tc SQUID with an accuracy of 5 mK using a PID feedback controller, which includes four thermometers and a heater. PID stands for proportional, integral and derivative and the PID feedback controller calculates these three separate parameters. The temperature of the cold head was measured as a function of time. Figure 4 shows plots of the temperature of the cold head as a function of time. The deviation of the temperature over a period of 18 h was controlled within 3.4 mK (1σ) . The high-Tc SQUID system (Model BMS-G, manufactured by Tristan Technologies [14]) contains an HTG-10R low-noise high-Tc SQUID gradiometer (Y-Ba_2-$Cu_3O_{7-\delta}$) [15, 16, 17], a controller, a flux-locked loop (FLL), a cryogenic cable and a fiber-optic composite cable. Figure 5 shows the high-Tc SQUID system, and the specifications

Table 2: Specifications of the high-Tc DC SQUID system.

Noise level	34 fT/cm/$\sqrt{Hz}$ @ 5 kHz
Operation temperature	77 K
Feedback gain	1, 2 ,5, 10, 20, 50, 100, 200, 500
High-pass filter	DC, 0.3 Hz
Low-pass filter	5 Hz, 500 Hz, 5 kHz, 25 kHz
Data accuracy (AD)	16 bit
Data acquisition rate	20,000 words/s
Remote control	IEEE-488, RS-232

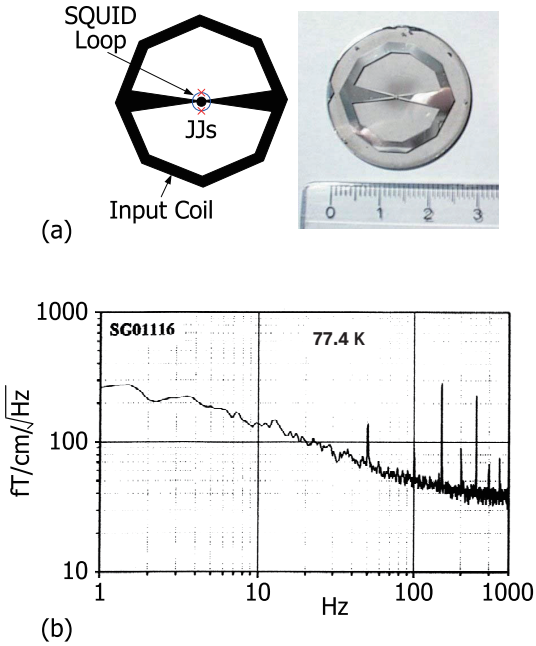

Figure 6: (a) Schematic drawing and photograph of the high-Tc SQUID gradiometer (HTG-10R [15, 16, 17]). (b) Measured noise spectrum in frequency domain, indicating a 1/f noise structure. White noise is reasonably low compared with the case of using a conventional high-Tc SQUID, in which white noise is over 1 pT/cm/$\sqrt{Hz}$.

of the system are given in Table 2. The high-Tc SQUID gradiometer is composed of an input coil and a SQUID loop with two Josephson junctions (Fig. 6(a)). Figure 6(b) shows the measured noise spectrum in the frequency domain, which indicates a 1/f noise structure. White noise is reasonably low compared with the case of using a conventional high-Tc SQUID, in which white noise is over 1 pT/cm/$\sqrt{Hz}$. The coefficient of the magnetic field relative to the output voltage of the SQUID gradiometer is 2.43 nT/V when the maximum gain of 500 is selected.

Principle of SQUID operation

A DC SQUID consists of two superconductors separated by thin insulating layers to form two parallel Josephson junctions (Fig. 7). A constant bias current I_b is maintained at the critical current, which is the maximum current that a superconductor can carry with zero resistance. The critical current changes periodically in response to a magnetic flux quantum phi zero of 2.07×10^{-15} weber. Therefore, this results in the voltage also changing similarly to the absolute value of the cosine function in response to the magnetic flux quantum.

The SQUID sensor is typically operated in a null detection mode where the FLL provides a negative feedback to maintain a linear operation as shown in Fig. 8. The modulated SQUID signal is amplified, filtered, demodulated and integrated in the FLL. Thus, the FLL output signal is pro-

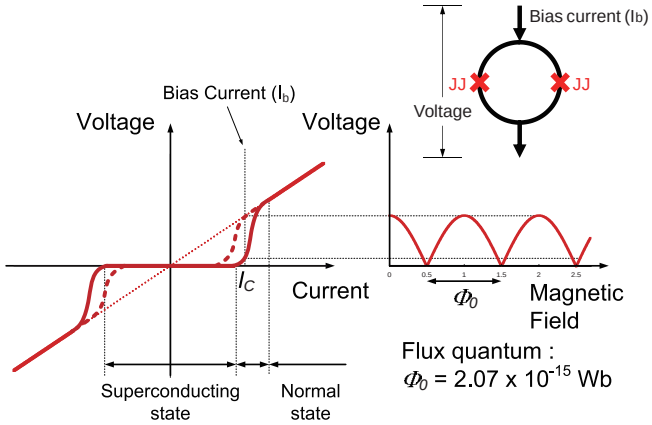

Figure 7: Principle of SQUID operation.

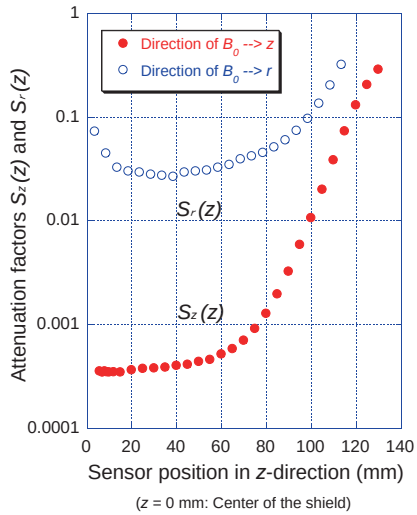

Figure 9: Measurement results for attenuation factors $S_z(z)$ and $S_r(z)$, where the directions of the external magnetic field B_0 (3.5 μT, 1 Hz) are the z-direction (•) and x-direction (○), respectively.

portional to the change in magnetic flux density B at the SQUID pickup coil. A modulation oscillator and a synchronous detector are used to create an FLL circuit similar to a negative feedback phase-locked circuit. The sensor package (shaded region) in Fig. 8 is kept below the critical temperature T_c.

High-Tc and permalloy shields

A cylindrical Bi-2223 high-Tc magnetic shield (148 mm diameter and 250 mm length) was fabricated by dip-coating a thin (300 μm) Bi-2223 layer on a 99.9% MgO ceramic substrate. A high-Tc magnetic shield has an advantage that the magnetic shielding effect is independent of the frequency of environmental magnetic noise, even in the low-frequency band [20]. The critical current (I_c) of 4500 A/cm^2 and the critical temperature (T_c) of 106 K of the Bi-2223 cylindrical high-Tc shield were obtained by a DC four-probe method using a small sample of Bi-2223. To measure the field distribution inside the high-Tc shield and to obtain the attenuation factors, we constructed a measurement system [19]. The system is composed of an X-Y-Z stage driven by stepping motors, a G10 rod which is fixed on the X-Y-Z stage and attached to two high-Tc SQUID probes, a liquid N_2 Dewar vessel and a Helmholtz coil that supplies an external field. Hereafter, we define the direction of the cylindrical axis as the z-direction and the direction perpendicular to the axis as the r-direction. If the external fields B_{z0} and B_{r0} exist, the attenuation factors

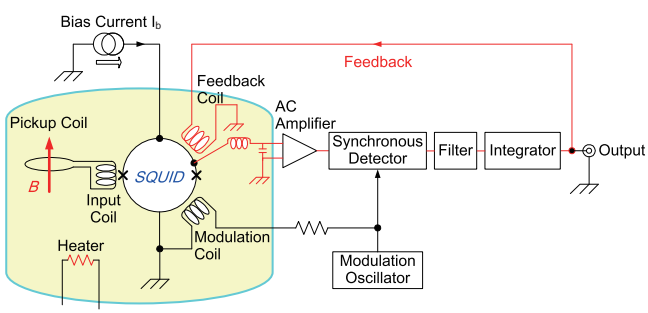

Figure 8: The SQUID sensor is typically operated in a null detection mode where the FLL provides a negative feedback to maintain a linear operation. The modulated SQUID signal is amplified, filtered, demodulated and integrated in the FLL. Thus, the FLL output signal is proportional to the change in magnetic flux density B at the SQUID pickup coil. The sensor package (shaded region) is kept below the critical temperature T_c.

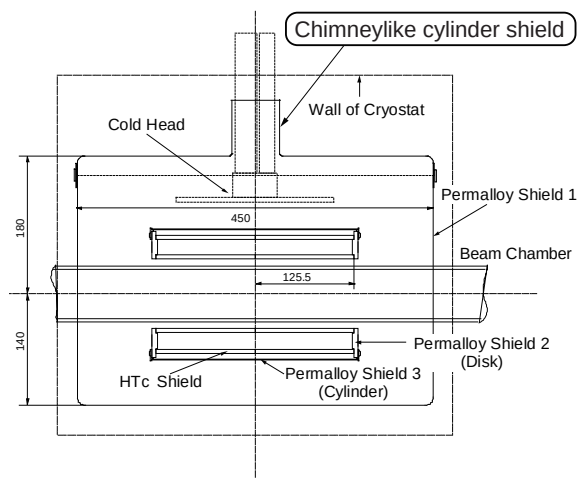

Figure 10: Magnetic shields composed of high-Tc shield, permalloy shield 1, permalloy shield 2 (disk) and permalloy shield 3 (cylinder).

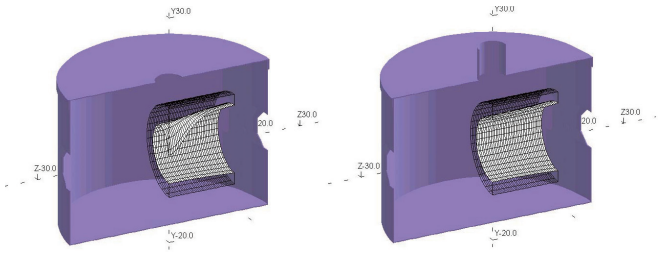

Figure 11: Calculated results showing that the shielding effect is improved when a chimney-like cylinder shield is added.

$S_z(z)$ and $S_r(z)$ are defined as

$$S_z(z) = B_z(z)/B_{z0},$$
$$S_r(z) = B_r(z)/B_{r0},$$

where $B_z(z)$ and $B_r(z)$ are the z and r components of the magnetic field at position z, respectively. Figure 9 shows the measurement results for attenuation factors $S_z(z)$ and $S_r(z)$, where the directions of the external magnetic field B_0 (3.5 μT, 1 Hz) are the z-direction (•) and x-direction (○), respectively. From these measurement results, the attenuation factors of $S_z(0) = 5 \times 10^{-4}$ and $S_r(0) = 8 \times 10^{-2}$ were obtained.

Because the attenuation factor of $S_r(0)$ of the high-Tc magnetic shield is too large, we attempt to reinforce the high-Tc magnetic shield. On the basis of various calculations using the finite element method program OPERA-3d [20], three permalloy shields, permalloy shield 1, permalloy shield 2 (disk) and permalloy shield 3 (cylinder), were constructed around the high-Tc shield, as shown in Fig. 10. A calculation showed that the shielding effect with a chimneylike cylinder shield is three times higher than that without the shield (see Fig. 11). To confirm the shielding effect of the reinforced system, a measurement was carried out. A field of 10^{-5} T produced by a Helmholtz coil was attenuated to 10^{-11} T, which was measured by the SQUID. A strong magnetic shielding system having an attenuation factor of 10^{-6} was thus obtained.

Beam position

We investigated whether the principle of a conventional beam position monitor could be applied to the SQUID monitor. The beam position pickup has a pair of isolated electrodes (or two pairs if two beam position coordinates are being measured). The deviation of the beam center with respect to the vacuum chamber can be monitored by measuring the difference in the voltage of each electrode induced by the beam.

We then fabricated a smaller version of the position sensor, as shown in Fig. 12(a). The high-Tc current sensor is divided into two parts by a slit, and a high-Tc SQUID is set on each bridge. To measure the position dependence

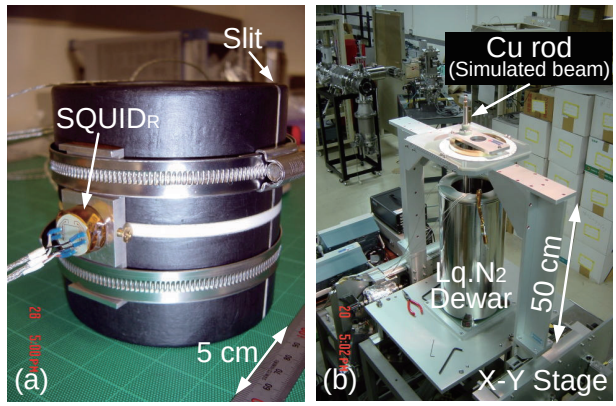

Figure 12: (a) Smaller version of position sensor, which is divided into two parts by a slit; a SQUID is set on each bridge. (b) Position measurement system, which is composed of an X-Y stage driven by stepping motors and a Cu rod, which is fixed on the X-Y stage and plays the role of a simulated beam.

of the output voltage of each SQUID, we converted a measurement system that had been used to measure the field distribution inside a high-Tc magnetic shield into a position measurement system. This system is composed of an X-Y stage driven by stepping motors and a Cu rod, which is fixed on the X-Y stage and simulates a beam. Figure 13 shows a schematic drawing of the position sensor, where D is the width of the sensor, Δx is the beam position from the center, and V_R and V_L represent the output voltage of each SQUID. If the beam is positioned at the center, the output of each SQUID should be equal. However, if the beam is shifted to the right side, it is expected that the output voltage V_R will be larger than V_L. Usually, the beam position

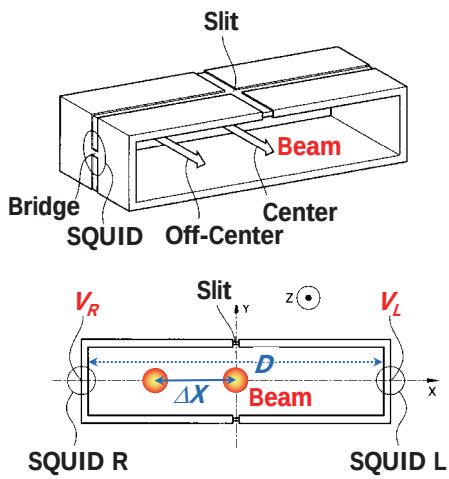

Figure 13: Schematic drawing of the current sensor of the high-Tc SQUID monitor.

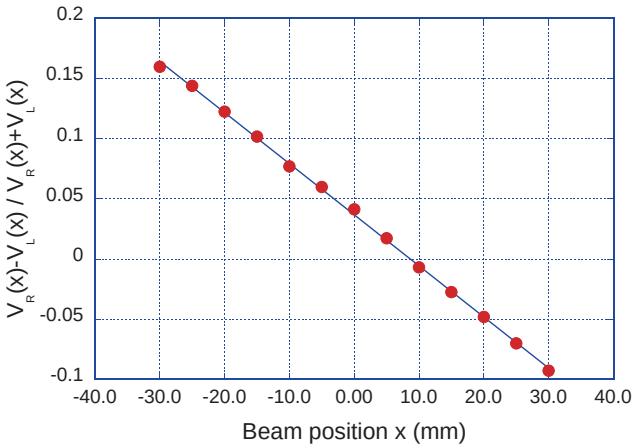

Figure 14: Measured values of Δ/Σ plotted versus the Cu rod position when a sinusoidal simulated current (1 mA, 5 Hz) was used.

Δx is obtained by the following relationship:

$$\Delta x = \frac{1}{\varepsilon}\frac{D}{2}\frac{\Delta}{\Sigma} = \frac{1}{\varepsilon}\frac{D}{2}\frac{V_R - V_L}{V_R + V_L},$$

where ε is the position sensitivity of the monitor. The measured values of Δ/Σ are plotted versus the Cu rod position in Fig. 14, for which a sinusoidal simulated current (1 mA, 5 Hz) was used, and thus we discovered that the beam position and beam current can be measured simultaneously in real time by dividing the current sensor into two parts and setting a SQUID on each bridge. The output voltage of the right SQUID, V_R, is not equal to that of the left SQUID, V_L, when the simulated beam is positioned at the center according to Fig. 14 because the output voltage of the SQUID is very sensitive to the setting accuracy. However, it was difficult to install the SQUIDs on the bridge accurately because each SQUID was bound by two stainless-steel bands (Fig. 12).

EXPERIMENTAL RESULTS

Prior to the beam measurements in the RRC hall, preliminary measurements were successfully carried out as follows: (1) a first beam test of the high-Tc SQUID monitoring system in the beam transport line of the ECR ion source in the CNS experimental hall and (2) a second beam measurement at the E1 experimental hall in RIKEN to measure the current of the high-energy heavy-ion beam. Aiming at its practical use for accelerator operations, the authors installed the high-Tc SQUID monitoring system in the beam transport line in the RRC hall (Fig. 1).

However, the SQUID electric circuit, which has a dynamic range of 100 dB (from 1 μA to 0.1 A) and a frequency range from DC to 25 kHz, did not function normally owing to the following reasons: (1) an RF background was caused by the high-power RF cavities of the RRC, which can produce a total power of 0.6 MW; (2) a large stray magnetic field was induced by the main magnetic field of the RRC (max. 1.67 T); (3) there was a neutron radiation dose of 25.5 Sv/year and a gamma radiation dose of 3.0 Sv/year. The radiation doses of neutrons and gamma rays were measured using an ionization chamber and a ^{3}He proportional counter, respectively. The actual radiation doses where the high-Tc SQUID monitor is in-

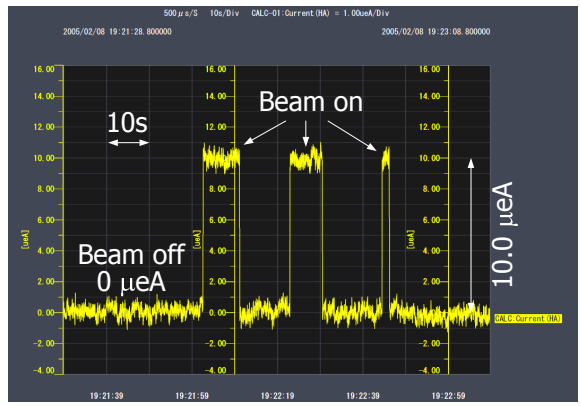

Figure 15: A 10 μA $^{40}Ar^{15+}$ beam intensity (63 MeV/u) was succesfully measured in real time with 500 nA resolution when a 1 μA beam produced a magnetic flux of $6.5\times10^{-3}\Phi_0$ at the input coil of the high-Tc SQUID.

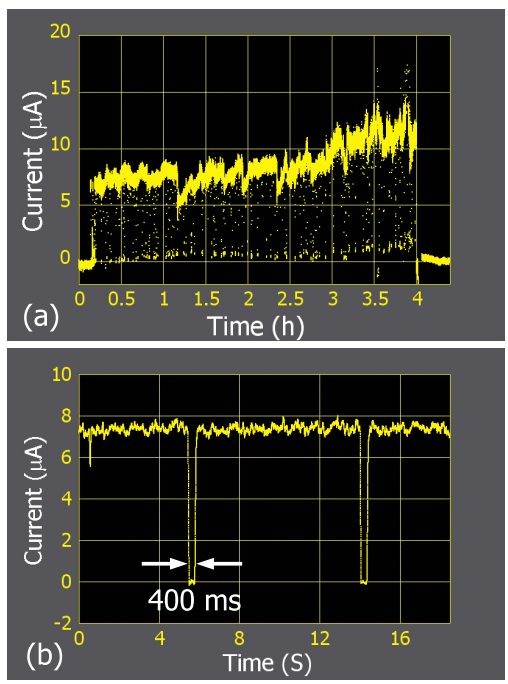

Figure 16: (a) Measurement of 63 MeV/u Ar beam extracted from RRC, which was successfully recorded for approximately 4 h without interrupting beam user experiments. (b) Magnified image of (a) showing dips in current caused by ECR ion source discharge, which recovered within 400 ms.

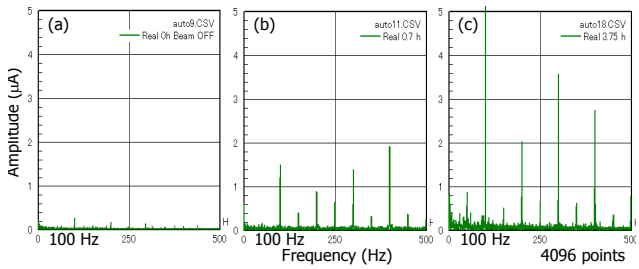

Figure 17: Results analyzed by performing fast Fourier transform (FFT) of measurements shown in Fig. 16(a) at 0 h (beam off) (a), 0.7 h (b) and 3.75 h (c).

stalled are expected to be higher than the above values, because both dosimeters were located 4 m above the high-Tc SQUID monitor. These data gave tentative criteria for judging the risk of radiation damage. After overcoming these difficulties by reinforcing the RF shield and surrounding the FLL circuit with lead and concrete blocks, there were no more problems with the beam current measurement. As a result, a 10 μA $^{40}Ar^{15+}$ beam intensity (63 MeV/u) was successfully measured with 500 nA resolution, as shown in Fig. 15, where a 1 μA beam produced a magnetic flux of $6.5\times10^{-3}\Phi_0$ at the input coil of the high-Tc SQUID.

Furthermore, a prolonged 4 h recording of the Ar beam current extracted from the RRC without interrupting beam user experiments was achieved, as shown in Fig. 16(a). In this recording, several dips in beam intensity due to ECR ion source discharge can be observed at irregular intervals of 10 s to 60 min. Figure 16(b) shows a magnified image of Fig. 16(a), which indicates that the dips in current caused by ECR ion source discharge recovered within 400 ms. The current signals were analyzed by performing a fast Fourier transform (FFT) in the frequency domain, the results of which are shown in Fig. 17. The amplitude of ripples in the modulated beam current increased with the beam current.

All recording and control systems were connected to a PC-based data acquisition system. Through the Ethernet, these systems were linked to a laptop in the main control room located 200 m from the RRC hall. The sampling time for data acquisition was 500 μs, and 100 data points were averaged to improve the S/N ratio.

PRACTICAL USE OF HIGH-T_C SQUID MONITOR FOR RIBF

Upgrade and measurement results

Aiming at its practical use in accelerator operations at the RIBF, we developed a new high-Tc SQUID with a high-permeability core that was installed in the two input coils of the high-Tc SQUID to improve sensitivity [7]. Figure 18 shows a photograph of the new high-Tc SQUID with two holes containing a high-permeability core. The core is composed of 80% Ni and Mo, Re and Fe. The output voltage of the high-Tc SQUID controller as a function of the simulated beam current is plotted in Fig. 19. From these measurement results, the calibration equation is obtained as

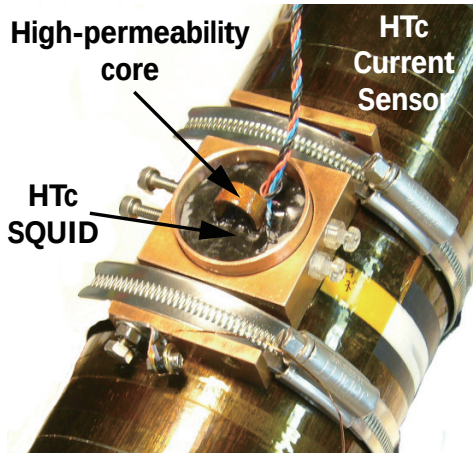

Figure 18: Photograph of new high-Tc SQUID with two holes containing high-permeability core.

$$\begin{aligned} V_s &= S_{co} \times I_b \times G/500 \\ &= 46.60 \times I_b \times G/500, \end{aligned}$$

where S_{co}, I_b, V_s and G are the coupling efficiency (mV/μA), the beam current (μA), the output voltage of the SQUID controller (mV) and the gain, respectively. A test using a simulated beam current indicated a 2-fold improvement in gain, because the coupling efficiency S_{co} of the high-Tc SQUID monitor when it was not equipped with the magnetic core was 22.8 mV/μA. The transfer of the magnetic field produced by the simulated beam current to the SQUID was thus improved. The high-Tc SQUID monitor was upgraded with the new high-Tc SQUID and the mag-

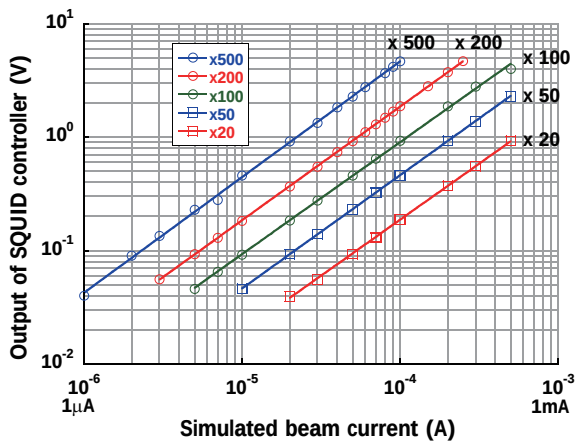

Figure 19: Plot of output voltage of the high-Tc SQUID controller as a function of simulated beam current.

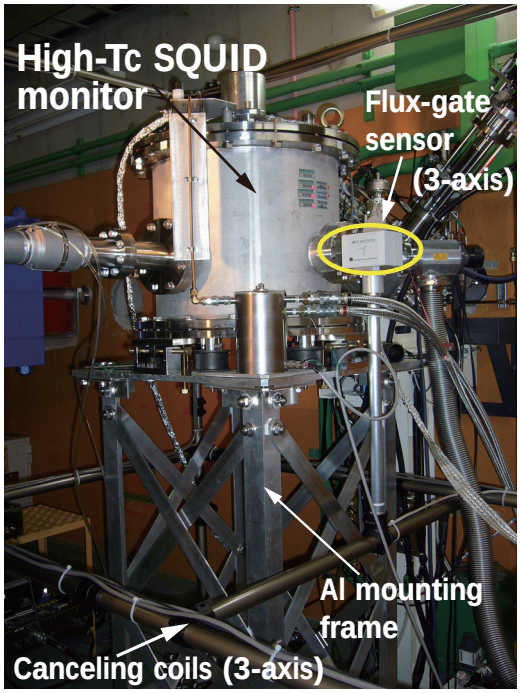

Figure 20: High-Tc SQUID monitor equipped with the Al mounting frame and the noise cancellation system, which was installed in the transport line between the fRC and the IRC (Fig. 1).

netic core, following which the high-Tc SQUID monitor was reassembled. For the purpose of canceling environmental magnetic noise, the previous mounting frame made of iron was replaced with one made of aluminum with a relative permeability of 1. Figure 20 shows the high-Tc

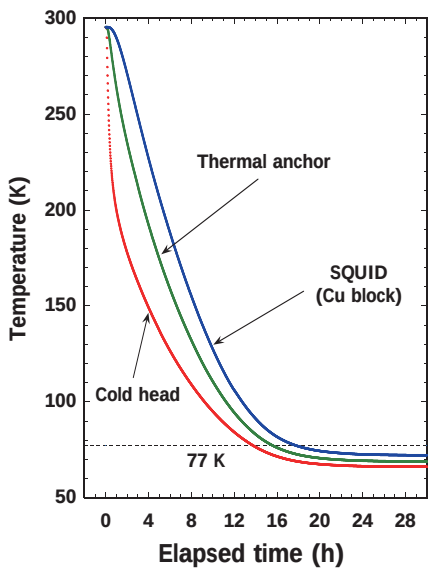

Figure 21: Cooling processes recorded for over 30 h using silicon diode thermometers.

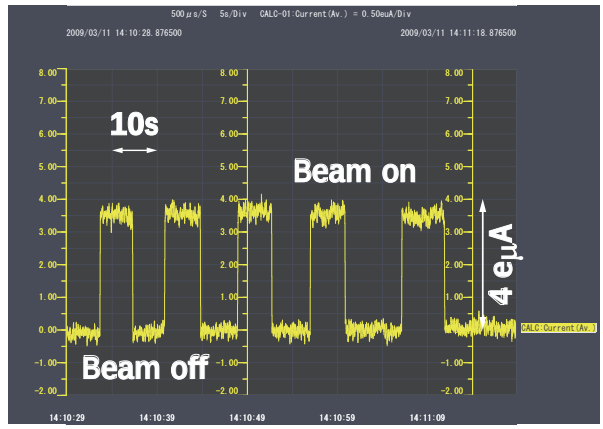

Figure 22: Measurement result for a 3.6 μA $^{132}Xe^{20+}$ (10.8 MeV/u) beam.

SQUID monitor equipped with the Al mounting frame and the noise cancellation system, which was installed in the transport line between the fRC and the IRC (Fig. 1). Figure 21 shows the results of the cooling processes; the temperatures of the cold head, the thermal anchor and the Cu block holding the SQUID were recorded for over 30 h using silicon diode thermometers. The temperature of the high-Tc SQUID was found to reach that of liquid nitrogen (77 K) after 16.5 h. As a result, this year we were able to measure a 3.6 μA $^{132}Xe^{20+}$ (10.8 MeV/u) beam (Fig. 22) and a 1 μA $^{132}Xe^{41+}$ (50.1 MeV/u) beam for use in the accelerator operations at RIBF.

Noise reduction

To obtain a higher measurement resolution, we paid close attention to the reduction of noise. A noise-cut transformer, which is completely isolated from the power circuit and not affected by AC source noise, was introduced to remove normal-mode and common-mode noise, where the noise that flows along one line of the leading wires in one direction and along the other line in the return journey is called normal-mode noise, and the noise that flows along both lines in the outward journey and to earth in the return jouney is called common-mode noise. Furthermore,

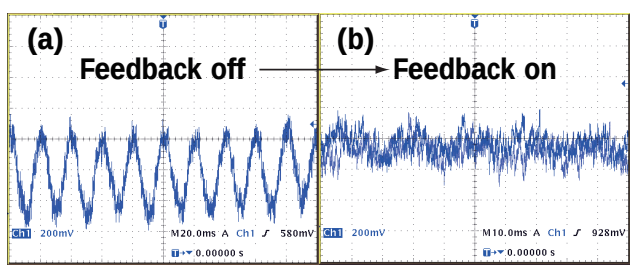

Figure 23: Effect of removing environmental noise by introducing the noise cancellation system.

all instruments were fixed on a large aluminum plate and the grounds of the instruments were connected to the plate. The signal cables were carefully wired to reduce unnecessary loops as much as possible and all AC lines were covered with braided wires.

The design of the noise cancellation system is based on a three-axis Helmholtz cage and feedback control engineering. Three-axis flux-gate sensors are placed near the equipment. A signal is fed through the proprietary controller to a compensation coil, producing precisely calibrated electromagnetic fields. The preliminary result in Figs. 23(a) and (b) shows the effect of the removal of environmental noise by introducing the noise cancellation system.

The data acquisition and control program, currently being written using LabVIEW [21] is almost complete, but some modification is necessary.

The authors are grateful to M. I. Faley of Forschungszentrum Juelich GmbH for valuable discussions on the high-Tc SQUID, A. Ichinose of Central Reserch Institute of Electric Power Industry for fabricating the high-Tc devices and E. Nemoto of JEOL DATUM, Ltd., for cooperation regarding the noise cancellation system.

REFERENCES

[1] Y. Yano, Nucl. Instrum. Methods B **261** (2007) p. 1009.

[2] T. Kubo et al., IEEE Trans. Appl. Supercond. **17** (2003) p. 97.

[3] Y. Yano, Proc. Int. Nuclear Physics Conf. (INPC2007), Tokyo, Japan, June 2007; Proc. 22nd Particle Accelerator Conf. 07 (PAC07), Albuquerque, New Mexico, U.S.A., June 2007.

[4] T. Ohnishi et al., J. Phys. Soc. Jpn. **77** No.8 (2008) p. 083201.

[5] O. Kamigaito et al., Proc. 11th Int. Conf. on Heavy Ion Accelerator Technology (HIAT09), Venice, Italy, June 2009.

[6] T. Watanabe et al., Supercond. Sci. Technol. **17** (2004) p. S450.

[7] T. Watanabe et al., J. Phys. **43** (2006) p. 1215.

[8] T. Watanabe et al., J. Phys. **97** (2008) p. 012248.

[9] I. K. Harvey, Rev. Sci. Instrum., **43** (1972) p. 1626.

[10] K. Grohman, et al., Superconducting quantum interference devices and their applications, Walter de Gruyter & Co. (1977) p. 311.

[11] A. Peters et al., AIP Conf. Proc. **451** (1998) p. 163.

[12] L. Hao et al., IEEE Trans. Appl. Supercond. **11** No.1 (2001) p. 635.

[13] T. Tanabe et al., Nucl. Instrum. Methods Phys. A **427** (1999) p. 455.

[14] Tristan Technologies, http://www.tristantech.com/.

[15] M. I. Faley et al., IEEE Trans. Appl. Supercond. **11** No.1 (2001) p. 1383.

[16] M. I. Faley et al., Supercond. Sci. Technol. **19** (2006) p. S195.

[17] M. I. Faley et al., J. Phys. **43** (2006) p. 1199.

[18] Y. Ishikawa et al., Proc. 4th Int. Symp. on Superconductivity (ISS-4) (1992) p. 1073.

[19] S. Watanabe et al., Proc. 8th European Particle Accelerator Conference (2002) p. 1992.

[20] Vector Fields, http://www.vectorfields.com/.

[21] National Instruments, http://www.ni.com/.

OVERVIEW ON E-XFEL STANDARD ELECTRON BEAM DIAGNOSTICS

D. Nölle, DESY, D-22607 Hamburg, Germany, for the XFEL Team

Abstract

The European XFEL is a 4th generation synchrotron radiation source, under construction in Hamburg [1,2]. Based on different Free-Electron Laser and spontaneous sources, driven by a 17.5 GeV superconducting accelerator, it will be able to provide several user stations with photons simultaneously. Due to the superconducting technology high average as well as peak brilliance can be produced. Flexible bunch pattern will allow for optimum tuning to the experiments demands. This paper will present the current planning of the electron beam diagnostics. An overview of the entire system will be given, as well as detailed insight into the main diagnostic systems, like BPM, charge and transmission diagnostics, beam size and beam loss monitor systems.

INTRODUCTION

The European XFEL (E-XFEL) is an international X-ray Free-Electron Laser user facility currently under construction close to DESY in Hamburg. The facility is constructed and will be operated by a limited liability company with shareholders from currently 12 counties.

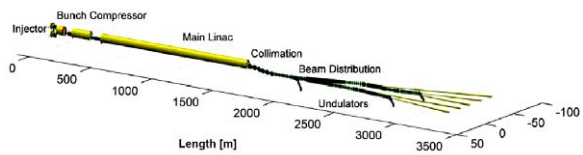

Fig. 1: Sketch of the layout of the E-XFEL.

DESY acts as the host laboratory and leads the accelerator consortium, that is in charge for the construction of the accelerator. Like FLASH [3] E-XFEL will be based on superconducting TESLA RF technology. Therefore, it can provide high duty cycles. Electron beams with pulse lengths up to 600 µs and a bunch repetition rates up to 4.5 MHz will be accelerated up to 17.5 GeV at a RF repetition rate of 10 Hz*. The shortest FEL wavelength will be 0.1 nm corresponding to photon energies of about 10 keV. To make optimum use of the high duty cycle, the long bunch trains can be distributed into 2 SASE undulator lines, which will be ramified into additional lines for "secondary undulators" that make use of the spent beam producing either FEL or spontaneous radiation. In a first phase up to 5 beam lines can be served simultaneously. The time structure of the beam can be adjusted independently for both main SASE undulators (SASE I and SASE II) by means of a kicker/septum scheme in the beam distribution system.

* At lower gradient even higher rep rates are possible.

Table 1: Design Beam Parameters of E-XFEL

Parameter	**Value**	**Unit**
Maximum energy	17.5	GeV
normalized emittance	1-2	mm mrad
typical beam sizes (RMS)	20-200	µm
bunch charge	0.1-1	nC
min. bunch spacing	222	ns
max. macro-pulse length	600	µs
bunches within macro-pulse	1 - 2700	
bunch pattern	arbitrary	
RF repetition rate	< 30	Hz

The facility starts at the DESY site. Close to the HERA cryo-plant that is going to be refurbished, the injector building and the entry shaft is under construction. From this building a tunnel, 6-20 m below surface, will head towards North West to the directions of Schleswig-Holstein. After about 2 km a shaft building is located, where the main tunnel splits up into the tunnels of the two main undulators, that further down split up into the 5 undulator and photon tunnels heading towards the experimental hall, located about 3.4 km after the gun.

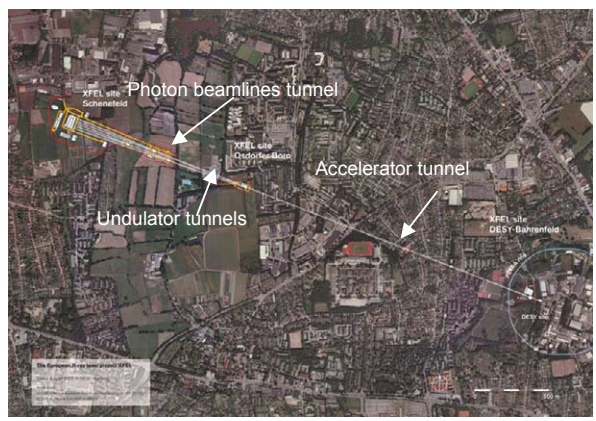

Fig. 2: Birds view of the E-XFEL site. DESY is marked by the PETRA III ring.

The current status of the facility can be described as follows: Groundbreaking for the civil construction took

place in winter 2008/2009. Tunnel boring starts in summer 2010. Tendering processes for long leading items, like the cavities, have already started. The E-XFEL company was founded in fall 2009. Currently the negotiations with all contributing labs on contracting the in-kind contributions are in their final phase.

The construction is scheduled to take about 5.5 years. According to this planning commissioning should start in 2014. SASE is expected to follow about 1 year later.

STANDARD BEAM DIAGNOSTICS

This paper focuses on standard beam diagnostics like beam position, charge, beam size and beam loss. These systems are currently in the design phase. First prototypes are available or will be constructed soon. A description of special diagnostic systems can be found in Ref. [4].

Beam Position Monitor System

The E-XFEL BPM system will be provided by a collaboration of PSI, CEA and DESY. DESY will produce the mechanics for all BPMs, except the re-entrant cavity BPMs. The BPM electronics except the front-end of the re-entrant cavity BPM, the firmware and embedded software for all BPMs will be provided by PSI. For the re-entrant cavity BPMs the monitors and the front-ends are supplied by CEA.

E-XFEL will distinguish between standard BPMs with moderate resolution and precision BPMs, where higher performance is required. For the standard BPMs the button type will be used. Precision monitors will be different cavity BPM types. About one third of the BPMs in the accelerator modules will be re-entrant cavity BPMs. About every third RF-Section of the LINAC, consisting of 4 accelerator modules, will be equipped with monitors of this type. High precision cavity BPMs with a 10 mm beam pipe will be integrated in so called undulator intersections. These are standard components, consisting of a phase-shifter, a quadrupole assembled on a xy-stage, the cavity BPM, an absorber, vacuum pump and bellows. Everything is assembled with high precision on a granite block. On this block the BPM is considered to be the element to be aligned, first by the survey and then more precisely by beam based alignment.

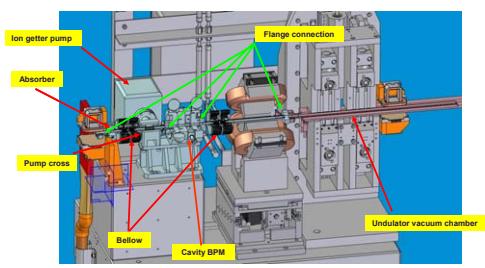

Fig. 3: E-XFEL standard undulator intersection.

In addition before and behind the undulator sections there will be some of these cavity BPMs to allow for precise beam based alignment. Further high precision (cavity) monitors with a 40.5 mm beam pipe diameter will be used for critical sections in the machine, like the vicinity of the bunch compression chicanes, the collimation and distribution section, as well as after the undulators. This type will also be used for the Intra Bunchtrain Feedback System (IBFB) currently developed by PSI [5].

Table 2: BPM Resolution Requirements of E-XFEL

BPM Type	#	Diameter	Single Bunch Res.
Standard Button	228	40.5 mm	50 µm
"cold" BPMs	101	78 mm	≤ 50 µm
Cavity BPM	117	10 mm	1 µm
Cavity BPM	12	40.5 mm	1 µm

Button BPM

Button BPMs will be the standard BPMs for all beamlines, also in the XFEL cryo-modules. Here they are rigidly connected to the quadrupoles at the end of the accelerator module string [6].

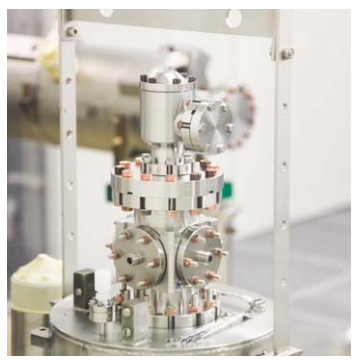

Fig. 4: Button BPM for the cryo-modules, already assembled to the superconducting quadrupole package. This monitor is part of the PXFEL3 prototype accelerator module.

The development of this BPM is almost finished. The custom made feedthroughs have passed the cryogenic tests successfully. The series production is planned to start this year.

The button BPM electronics will be based on an analogue front-end that transforms the pickups signal into a low-frequency bandwidth-limited signal of some 10ns length that are processed by a fast ADC followed by an FPGA. First prototypes are under test at FLASH and PSI.

Reentrant Cavity BPM

The re-entrant cavity BPM has the potential of better resolution compared to the standard button type [7]. From the mechanical point of view, the interfaces to the outside world of the cryo-module are identical. Also for this BPM the development is advanced. The feedthroughs are

qualified for the operation in the cold. A prototype is currently mounted in the PXFEL2 E-XFEL cryo-module prototype. The RF front-end based on a down conversion scheme with IQ detection is under development at CEA. The electronics will be integrated into the modular BPM framework developed and supplied by PSI. Beam tests are scheduled with a prototype installed at FLASH.

Cavity BPM

Two types of cavity BPMs based on the development of T. Shintake for SCSS will be used [8]. Both types with a beam pipe diameter of 10 mm and 40.5 mm, respectively, consist of a reference and dipole resonator and have very similar RF parameters. Especially the frequency of 3.3 GHz and the loaded Q of about 70 allow using the same electronics for both types. Special care is taken to minimize the orthogonal coupling of the dipole modes to the coupling slots of the dipole cavity [9]. The use of stainless steel results in rather low internal Q, preventing cross talk between consecutive bunches for all cavity modes even at the short bunch spacing of 220 ns. The design relies on precise fabrication, no tuning foreseen. Up to now all BPM prototypes have been in the tolerance of ±20 MHz. First beam measurements are in good agreement with the simulations. The RF front-end, currently developed at PSI, will be based on down conversion and IQ detection. It will ensure high resolution and low drift.

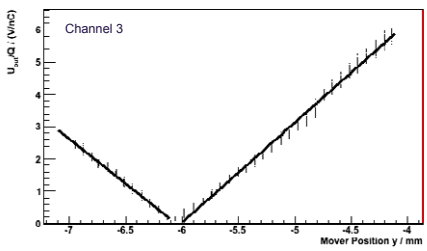

Fig. 5: Beam measurement of the sensitivity of the dipole resonator versus y-position for the 10 mm type. The sensitivity of 2.71 ± 0.3 V/nCmm agrees well with the simulation result (2.84 V/nCmm).

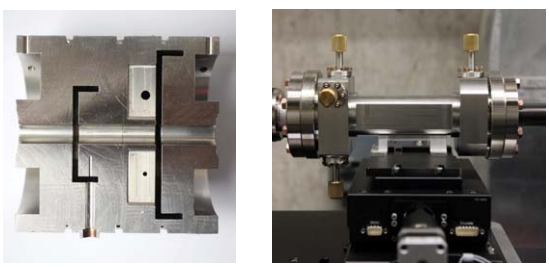

Fig. 6: Both types of E-XFEL cavity BPMs; on the left a cut through the type for the undulator sections. The right picture shows the 40.5 mm type of the cavity BPM on a precision translation stage installed in FLASH. The distance of reference (right) to dipole cavity (left) reduces crosstalk through the big beam pipe.

For extended beam tests, a BPM test section was integrated in FLASH directly after the SASE undulator. 3 cavity BPMs of the 10 mm, and one of 40.5 mm type are mounted on high precision translation stages, to allow for precise calibration and resolution measurements. In addition there is also an array of 3 button BPMs similar to the E-XFEL standard beam pipe BPMs. All signals are available over short cables outside the FLASH tunnel.

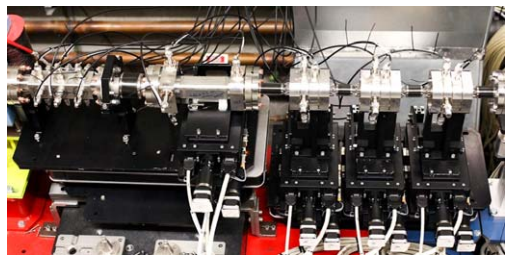

Fig. 7: E-XFEL BPM test section in FLASH.

BPM Electronics

The overall BPM electronics system follows a modular design approach maximizing the amount of commonly used hard- and software for all BPM types. The BPM electronics consists of analogue RF front-ends (RFFE) specific for each pickup type, and a generic FPGA-based digital back-end carrier board with two ADC mezzanine modules. The RFFEs and the digital back-end board with its ADC mezzanine modules are plugged into a common customized crate that contains one generic digital back-end as well as either four button BPM RFFEs or two cavity or re-entrant BPM RFFEs.

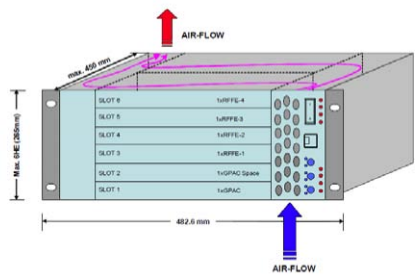

Fig. 8: Picture of a BPM electronics unit for E-XFEL.

This generic modular hardware approach is also employed for the IBFB-specific low-latency BPM and signal processing hardware[10] allows minimizing the overall development and maintenance effort and provids a unified control and timing system interface for all BPMs in the machine.

XFEL CRATESYSTEM

E-XFEL will use xTCA systems as the crate standard. A special group was created to extend the xTCA standards for physics purpose [11]. According to these extensions XFEL will use double size AMC boards. Two standard boards for XFEL are currently under development, a commercial 16 bit 125 MHz ADC with 10

channels, and an in house developed versatile interface board with 4 fast serial links (DAMC02) [12]. Both boards supply a high amount of processing power due to a VIRTEX 5 FPGA on board.

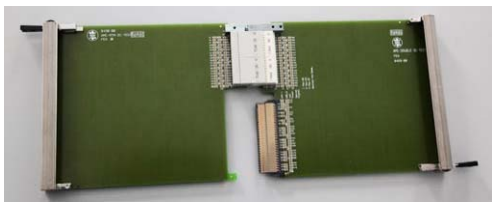

Fig. 9: Double sized AMC "dummy" board with a rear transition module (RTM).

For extended IO purpose the boards can be extended by so called rear transition modules (RTM), again doubling the space for the electronics. Different applications will be adapted to these boards by means of special RTMs. The diagnostics will make use of these boards with special RTMs for toroids, wire-scanners and beam loss monitors.

BEAM SIZE MEASUREMENTS

For all SASE machines the optimisation of the emittance transport is essential for the FEL performance. E-XFEL will have special diagnostic sections after the injector, the two bunch compressors and in the collimation section to measure the projected and the slice emittance. These stations will combine 4 beam size measurements to determine the local twiss parameters as well as the emittance. This allows controlling the optics and matching to the next sections.

Up to the second bunch compressor the beam size measurements will be done by means of OTR screens. These screens will include on axis and off axis OTR targets. The off axis targets will be used in combination with kicker magnets deflecting a single bunch out of the 650 µs long bunchtrain onto the screen. In addition this bunch can be streaked by a transverse mode structure to get access to slice parameters [4]. Resolution of the OTR stations has to be between 30 and 10 µm depending on their location. Since LCLS has reported problems with coherent effects with their OTR systems due to the strongly compressed beam [13], the E-XFEL OTR chambers provide ports to install additional wire scanners.

On-axis and off-axis operation requires different focal spots. In addition the imaging of a streaked beam requires large field of view. Both aspects are tackled by the use of Scheimpflug's principle, known from large format cameras. It allows extending the depth of field by choosing appropriate angles between the object, the image and the lens plane. If these planes have a common intersection line, the entire screen plane is imaged well focused onto the image plane. An angle of 67.5° between beam axis and screen surface was chosen. A magnification close to 1:1 has to be used to achieve the required resolution. With large view fields large CCD chip cameras will be required.

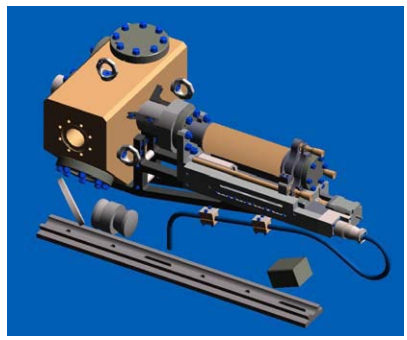

Fig. 10: 3D view of an E-XFEL OTR station. Due to the angle with the beam the OTR is emitted under 45° in backward direction. Scheimpflugs´s principle is drafted by the tilted camera box. The blind flanges are the ports for the wire-scanners.

Due to the small beam size in the high energy sections wire scanners will be used for measurements. They have to provide fast scans, i.e. the wire is driven through the beam during one RF-pulse with a speed of 1 m/s. The technical progress allows using linear motors. The trigger of a scan has to be precisely synchronized to arrival of the beam. A prototype has shown a trigger jitter of less than 10 µs, corresponding to a position or bunch number jitter of less than 10 µm or 10 bunches.

CHARGE MEASUREMENT

To ensure proper beam transport the transmission has to be close to 100%. Therefore the bunch charge has to be measured at various places along the LINAC. Furthermore, charge has to be well controlled for stable SASE operation. The current transformers (toroid) will be of the same type already in use at FLASH. The electronics will be based on the DAMC02 µTCA/RTM boards with fast sampling ADC and FPGA post-processing. Single toroids will be linked to their neighbours by fast optical links to release alarms to the machine protection system with few µs latency in case of imperfect transmission. A fast link to the LLRF will provide charge information for beam loading compensation.

DARK CURRENT

With the long RF pulse trains of the superconducting LINACs dark current suppression is essential. The biggest source of dark current is the normal conducting RF gun with a gradient up to 60 MV/m. Electrons emitted there might be transported through the entire facility. At FLASH dark current is one main source for activation of machine components. Monitoring dark current is substantial for optimizing the suppression systems.

Therefore, a dark current monitor based on a 1.3 GHz stainless steel cavity similar to the reference cavity of the cavity BPMs was developed [14]. Prototypes are installed at FLASH and PITZ. First measurements are expected

this spring. These sensitive monitors are also suited for charge measurements in case of very low charge operation of FLASH or E-XFEL.

Fig. 11: 1.3 GHz cavity dark current monitor with one coupling antenna in front.

BEAM LOSS AND MACHINE PROTECTION

The superconducting E-XFEL LINAC is able to transport about 600 kW CW beam power at 17.5 GeV. Thus a machine protection system (MPS) is essential to prevent the machine from mechanical damage, but also to minimize activation and radiation damage.

The MPS will be an upgraded version of the FLASH system [15]. Slow signals from magnets, RF, vacuum and screens will be used to check for the correct machine state and will block beam operation or allow for only single or few bunches depending on the status of the machine. Fast signals from beam loss monitors or transmission measurements will interrupt the bunch train. The logic units collecting, communicating and evaluating the input channels and creating the alarms will be implemented in the FPGA of the DAMC02 µTCA board [16].

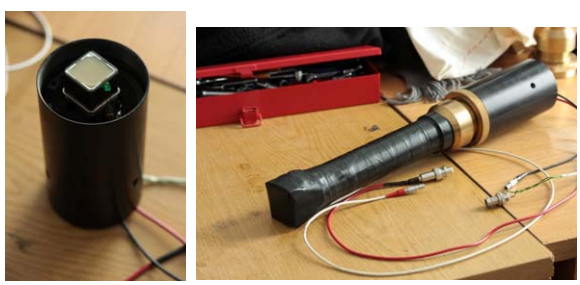

Fig. 12: First prototype of an XFEL BLM. On the left a view to the photomultiplier with the test LED, on the right a test setup to be installed in FLASH. The goal is a compact design.

The beam loss monitors will be based on photomultipliers. The monitors itself will be produced by IHEP, Protvino, the electronics will be developed and produced at DESY. The BLM readout will also base on the DAMC02 hardware. The signals from 8 monitors will be processed by one readout unit. The shaped data from the BLM is digitized by 14 bit 50 MHz ADCs located on a RTM, integration of losses and alarm generation is done in the FPGA of the DAMC02 board. The latency of the system is about 300 ns plus cable delay. A second µTCA board produces the test signals to drive the LED implemented in the BLM.

SUMMARY

The developments for the standard beam diagnostics for E-XFEL are in an advanced state. The design of the main systems is clear, and partners within E-XFEL collaboration are fixed. First prototypes are already under test at FLASH.

REFERENCES

[1] "XFEL Technical Design Report", DESY 2006-097, http://xfel.desy.de.

[2] R. Brinkmann, "The European XFEL Project", FEL´06, Berlin, MOBAU03, p. 24, (2006), http://www.JACoW.org.

[3] V. Ayvazyan, et al., Eur. Phys. J. D, 37, 297, (2006)

[4] C. Gerth, "Electron Beam Diagnostics for the European X-Ray Free-Electron Laser" DIPAC´07, Venice, MOO2A02, p. 17, (2007) http://www.JACoW.org.

[5] B. Keil et al., "Design of an Intra-Bunch-Train Feedback System for the European X-Ray FEL", DIPAC'07, Venice, p.232 (2007), http://www.JACoW.org.

[6] D. Nölle et al., "BPMs for the XFEL Cryo-Module", DOPAC´07, Venice, TUPB12, p.84 (2007), http://www.JACoW.org.

[7] C. Simon et al., "Beam Position Monitors using a Reentrant Cavity", DIPAC´07, Venice, TUPB15, p.93, (2007), http://www.JACoW.org.

[8] H. Maesaka et al., "Development of the RF Cavity BPM of XFEL/SPRING-8", DIPAC'09, Basel, MOPD07, p. 56, (2007), http://www.JACoW.org.

[9] D. Lipka et al., "Orthogonal coupling in Cavity BPM with Slots", DIPAC'09, Basel, MOPD02, p. 44, (2009), http://www.JACoW.org.

[10] B. Keil et al., "The PSI DSP Carrier (PDC) Board – a Digital Back-end For Bunch-to-bunch and Global Feedbacks In Linear Accelerators and Storage Rings", EPAC 2008, Genoa, p.3272 (2008).

[11]PICMG formed a Technical Committee Focused on Large-Scale Physics Applications, http://www.picmg.org.

[12] P. Vetrov, private communication, 2010.

[13] H. Loos et al., "Commissioning of the LCLS LINAC", LINAC08, Victoria, p. 1095 (2008).

[14] D. Lipka et al., "Dark Current Monitors for X-FEL at 1.3 GHz", DESY, Technical Note, 2008/1.

[15] L. Fröhlich et al., "First operation of the FLASH machine protection system with long bunch trains", LINAC'06, Knoxville, USA, pp. 262–264, 2006.

[16] Igor Cheviakov et al., "Machine Protection System for the XFEL", DESY internal document, 2010.

ELECTRO OPTICAL SAMPLING OF COHERENT SYNCHROTRON RADIATION FOR PICOSECOND ELECTRON BUNCHES WITH FEW pC CHARGE

F. Müller, B. Steffen#, V. Schlott (PSI, Villigen, Switzerland)
Pavel Chevtsov (JLAB, Newport News, Virginia)

Abstract

Electro Optical (EO) sampling is a promising nondestructive method for measuring ultra short (sub-ps) electron bunches. The FEMTO slicing experiment at the Swiss Light Source modulates about 3 pC of the 5 nC electron bunch longitudinally. The coherent synchrotron radiation (CSR) emitted by this substructure was sampled by 100 fs long pulses from an Yb fiber laser in EO crystals of gallium phosphide. The broadening of this ps long structure over four turns of the synchrotron could be measured with sub-ps resolution.

INTRODUCTION

Femto slicing [1] is a technique to manipulate the temporal profile of a long (some 10 ps) electron bunch in a storage ring with a short pulse laser (100 fs). The very high electric field of the laser pulse (up to 10^9 V/m) modulates the energy of the electrons in a slice of the length of the laser pulse. After the first dispersive section this pure energy modulation is transferred into a longitudinally one. The resulting electron distribution consists of two humps containing the low and the high energy sliced electrons and a central dip, from where the sliced electrons have been removed (see Fig. 1). The dip will lead to an enhancement of synchrotron radiation in the millimeter wavelength range (THz) emitted at following dipole magnets of the storage ring.

To measure the time structure of synchrotron radiation pulses electro optical measurement techniques, developed for electron bunch length measurements, can be used. These techniques employ birefringence an electric field induces in an electro-optically active crystal like gallium phosphide (GaP) to transfer the time structure of the electric field onto a laser pulse which can be measured with fs accuracy. It has been shown that sub-ps electron bunches of some 100 pC charge can be measured with about 200 fs resolution applying the spectral decoding technique [2, 3] by using the Coulomb field of the relativistic electron bunch directly. By imaging and focusing the coherent radiation emitted from the electron bunch onto the crystal, the resulting field strength can be enhanced leading to larger EO signals [4].

In this paper we present results of the first direct measurements of coherent synchrotron radiation pulses from the sliced electron bunches at the Swiss Light Source (SLS) in time domain. We applied the technique of electro optical spectral decoding using a ytterbium fiber laser [5] which has been synchronized to the SLS rf master clock.

#present address: DESY, Germany, email: bernd.steffen@desy.de

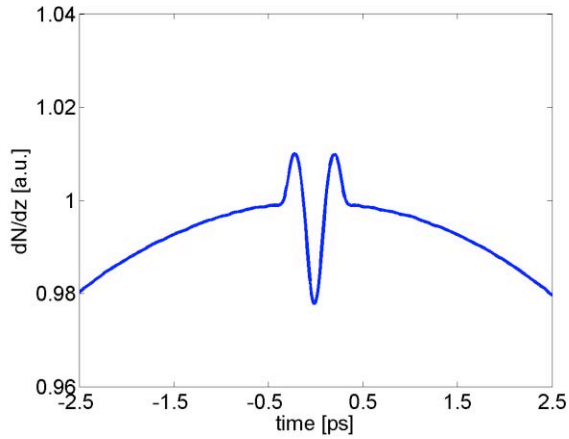

Figure 1: Charge distribution of the sliced electron bunch at the SLS right after the slicing.

FEMTO-SLICING AT THE SLS

The FEMTO slicing setup at the SLS is used to generate sub-ps hard x-ray pulses for pump-probe experiments at the μ XAS beam line. The slicing setup consists of a modulator (wiggler) for energy modulation, chicane dipoles for pulse separation, and a radiator (in-vacuum undulator).

A laser pulse from a regenerative Ti:Sa amplifier (30 fs rms, 2 kHz, 2.5 mJ, 800 nm) overlaps with the co propagating electron bunch in the modulator and induces an energy exchange between the laser pulse and the electron bunch. Depending on the relative phase between the two pulses, the electrons can either gain or loose energy. Since the electron bunch in the SLS storage ring is about 35 ps (rms) long, only a small number of electrons is energy modulated. According to simulations, a laser pulse energy of 2 mJ provides a maximum energy modulation of 1% (24 MeV) within this slice. The core bunch contains 5 nC and the slicing efficiency is about $6 \cdot 10^{-4}$ which leads to a charge of the modulated particles of approximatly 3 pC.

The chicane between modulator and radiator induces a spatial (±2 mm) and angular (±0.5 mrad) horizontal offset of the sliced beam at the radiator center which is used to separate the fs x-ray pulse for the ps background in the μ XAS beam line. Additionally the chicane is a dispersive element which transfers the pure energy modulation in to a longitudinally one which is slightly broader than the initial modulation. X-ray diffraction measurements on high-amplitude phonon dynamics of photoexcited

bismuth are consistent with an effective x-ray pulse length of 140±30 fs FWHM [6].

After passing the FEMTO slicing experiment the modulation has the typical bipolar shape as shown in figure 1. One hump contains the electrons which gained energy and the other one the electrons which lost energy. Both are separated by a dip from which the modulated electrons have been removed. Due to the linear momentum compaction factor of the SLS storage ring, this modulation smears out from turn to turn and finally vanishes (see Fig. 5 for particle tracking simulations). For a comprehensive description of the FEMTO slicing experiment at the SLS see [6, 7].

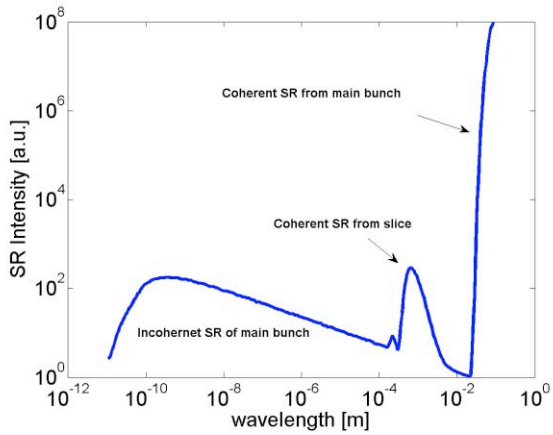

Figure 2: Spectrum of the synchrotron radiation emitted by the sliced electron bunch.

The spectrum of the synchrotron radiation (SR) emitted by the sliced bunch is depicted in figure 2. The core bunch generates incoherent SR, while the FEMTO-sliced particles radiate coherently at wavelength in the order of the slicing length. Therefore the SR spectrum is coherently enhanced in the THz range, where the radiation intensity is proportional to the square of the number of emitting electrons.

ELECTRO OPTICAL DETECTION

Electro optically active crystals like GaP become birefringent in the presence of an electric field. Electro optic detection techniques use this effect to measure fast changing electric fields by sampling the change in birefringence with short laser pulses. This techniques can be used to measure the temporal profile of electron bunches by sampling their Coulomb field or the emitted coherent synchrotron or transition radiation.

For small electric fields (up to MV/m), the EO effect is dominated by the Pockels effect and linear with the electric field strength. For a properly oriented GaP crystal and electric field direction, the two orthogonal polarized components of a laser oriented along the principal axes of the EO crystal receive a relative phase retardation of

$$\Gamma = \frac{\omega d}{c(n_1 - n_2)} = \frac{\omega d}{c} n_0^3 r_{41} E_{THz}, \qquad (1)$$

where ω is the angular frequency of the laser, d the thickness of the EO crystal, and n_1 and n_2 are the refractive indices along the principal axes. n_0 is the refractive index of the (isotropic) crystal at vanishing electric field, r_{41} its electro optic coefficient, and E_{THz} the applied electric field.

With suitable optical elements this relative phase shift or polarisation rotation can be transferred into an amplitude modulation of the transmitted laser light. For all measurements reported in this paper the setup and the electric field strength were such that the change in transmitted laser light is linear in the applied electric field strength.

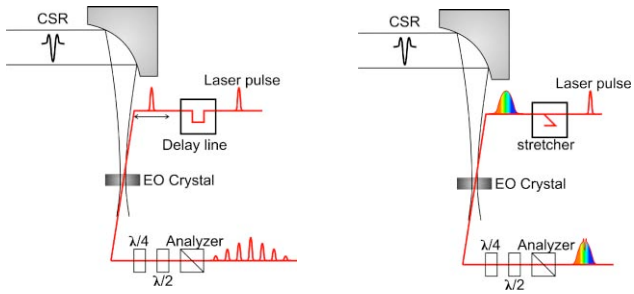

Figure 3: Scheme of the setup for EO sampling (left) and spectrally decoded detection (right).

Results from two different electro optical techniques are reported in this paper: electro optical sampling using a variable delay (Fig. 3, left) and single shot measurements using electro optical spectral decoding (Fig. 3, right).

For the electro optical sampling (EOS) a short (≈100 fs) laser pulse is sent through the crystal in parallel with the electric field pulse of the CSR and the relative delay for consecutive laser pulses is changed to sample the longitudinal profile of the THz field pulse. Since the profile is not measured in a single shot, this technique is sensitive to fluctuations of charge and profile as well as arrival time jitter between CSR and the laser pulse.

Spectrally resolved electro optical decoding (EOSD) is a single shot technique, where the broadband laser pulse is stretched in a dispersive material or grating stretcher, resulting in a known frequency vs. time relation. The laser pulse is now longer than the THz field pulse and only a part of the chirped laser pulse is modulated in the EO crystal. This intensity modulation can be retrieved measuring the spectrum of the laser pulse using a spectrometer. Due to frequency mixing between the laser and the THz field pulse, signal distortions become a problem for short pulses and strongly stretched laser pulses. For the Yb doped fiber laser used here significant distortions are expected for field pulses shorter than ≈300 fs (rms).

For a more comprehensive description of electro optical detection techniques and theory see [3, 8].

EO-SETUP AT THE INFRARED BEAMLINE

The measurements presented here were done at the infrared beamline [9] of the Swiss Light Source (SLS). The 2.4 GeV electron beam emits synchrotron radiation in a 1.4 T dipole magnet. The SR is collected by a slotted mirror over an angle of 61 mrad (corresponding to a source length of 350 mm) and transported over 9 m by three times 1 to 1 imaging optics to the experimental area outside the accelerator bunker. At the experiment the SR is focused by a 250 mm off-axis paraboloid mirror onto a

5 mm thick GaP crystal (Moltech, Berlin), leading to a focal spot of 5-10 mm.

The EO probe laser is a self built amplified ytterbium fiber laser system [5] synchronized to the SLS rf master clock, delivering 10 nJ pulses at 1 MHz with a useful bandwidth of about 120 nm centered at 1050 nm. Since FEMTO slicing of the electron bunch is done with a independently synchronized Ti:Sa laser, the laser to laser stability and the relative jitter plays a decisive role for pulse length measurements. This jitter determines how long the chirped laser pulse has to be in order to ensure a temporal overlap. It can be deduced from a cross correlation between the two lasers. The relative jitter between the two lasers was measured to about 50 fs (rms).

The Yb fiber laser pulses were chirped to about 100 fs (rms) in a grating compressor for the sampling and 3 ps (rms) for the SD measurements, respectively. They were sent via a polarizer under a slight angle through the GaP crystal. After passing the crystal the laser was directed through a quarter waveplate, a half waveplate, and an analyzing polarizer to an optical fiber. All measurements were done with the half waveplate 2-4° away from crossed polarizer settings to ensure good linearity in the measured signals. For the EO sampling the pulses were detected by an InGaAs photodiode (ET-3010, EOT) and the readout and averaging was done by an oscilloscope. For EOSD a spectrometer (Andor Shamrock 303i) equipped with an InGaAs camera (Andor iDus490-1.7) was used.

RESULTS

Figure 4 shows EO sampling measurements for several round trips. The EO setup is sensitive enough to detect up to turn 3, which according to beam tracking simulations is already a few ps long, providing a much weaker THz signal than turn 0. For EO sampling measurements the laser is delayed by a delay stage in steps of 100 fs and each data point is averaged over 100 shots. The CSR is extracted at the infrared beamline, which is located about three quarters of a round trip in the SLS storage ring after the FEMTO slicing experiment. Due to the SLS momentum compaction factor, the modulation is already several times longer than directly after the laser interaction and it gets further broadened for every additional turn, as seen in the simulated longitudinal charge distribution of the sliced electron bunch shown in figure 5 [10].

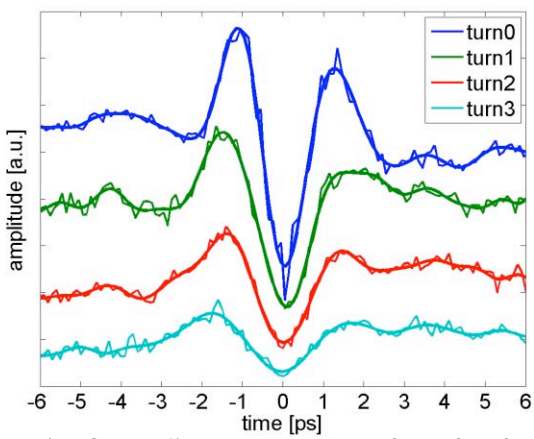

Figure 4: EO sampling measurements of turn 0 to 3.

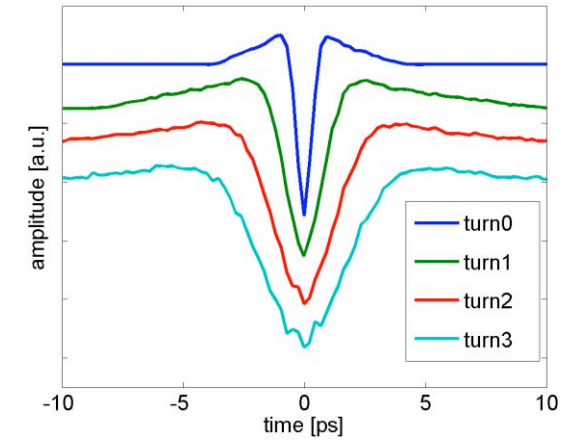

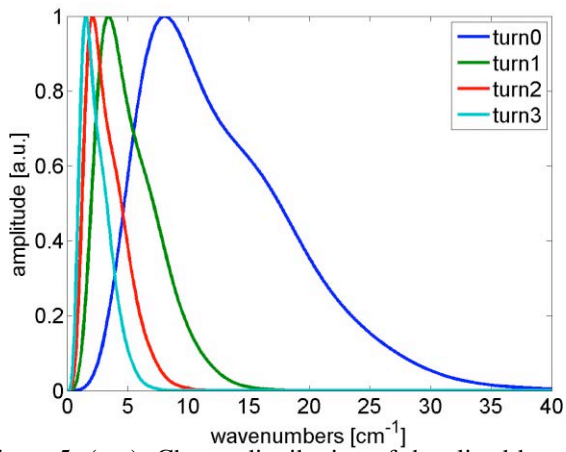

Figure 5: (top): Charge distribution of the sliced bunches from turn 0 to turn 3; and (bottom) the corresponding spectra.

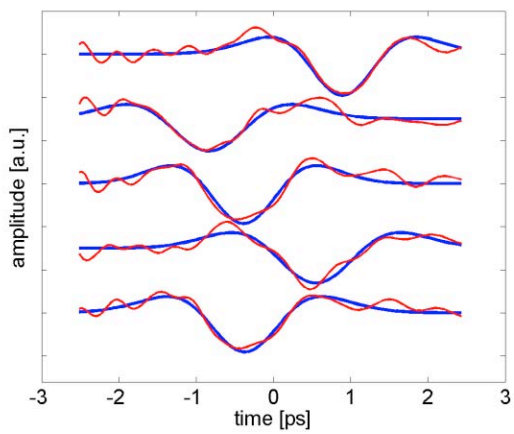

Figure 6: Five consecutive EOSD measurements of turn 0 (red); the blue line shows a fitted double Gaussian distribution.

The signal from the dip in turn 0 has been measured to 510 fs (rms) and increases to about 800 fs (rms) at turn 3. However, large fluctuations of consecutive shots at a single EO sampling point in the central region of the bunch indicate a significant timing jitter between the sampling laser and the sliced electron bunch. In order to reduce these effects, single shot measurements were performed for turn 0 using EO spectral decoding.

A set of single shot EOSD measurements is shown in figure 6. The red line indicates the measurement and the blue one a double Gaussian fit. The pulse length is 365±50 fs (rms), which is clearly shorter than it has been determined to 510 fs (rms) from EO sampling measurements for turn 0. Large fluctuations in the arrival time of the sliced electron bunch could be measured with EOST resulting in a jitter of 630 fs (rms) for 500 shots, which leads to a significant distortion and a corresponding broadening of the sampling results. Although a clear source for this comparatively large arrival time jitter at the IR beamline could not be identified so far, the slicing laser to EO laser jitter, which has been measured to 50 fs rms is definitely not the dominating source. Amplitude and phase jitter of the storage ring rf, timing distribution as well as mechanical vibrations in the IR beamline are major suspects.

The arrival time can be determined and corrected for each single shot EOSD measurement before averaging leading to an improved signal to noise ratio without introducing additional pulse broadening as shown in figure 7. From the modulation a maximum field strength of 20 kV/m at the crystal can be derived.

The spectrum of the sliced bunch of turn 0 at the IR beamline measured with an IR spectrometer (Bruker IFS 66 V) shows a strong suppression of wavelengths longer than 10 mm as compared to the spectrum derived from the simulated particle distribution (blue curve of Fig. 8, top). Taking this into account by an assumed transfer function of the IR beamline, the measured longitudinal profile for turn 0 is in excellent agreement with the simulated distribution (Fig. 8, bottom).

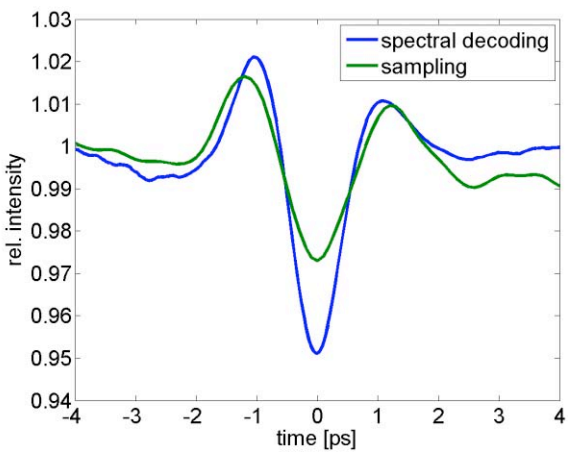

Figure 7: Arrival time jitter corrected average of 500 EOSD measurements of turn 0 and the corresponding sampling measurement.

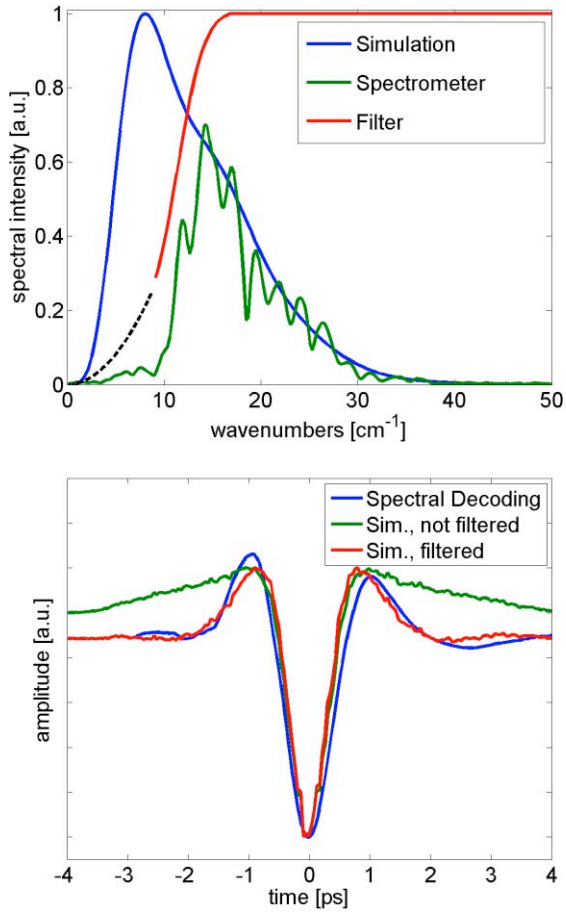

Figure 8: top: measured spectrum of the sliced bunch at turn 0 highpass filter (green), the spectrum derived from particle tracking simulations (blue), and the assumed transfer function of the IR beamline, bottom: EOSD measurement (blue) compared to the simulation directly (green) and the simulation filtered with the assumed transfer function of the IR beamline (red).

CONCLUSION

The longitudinal time structure of coherent synchrotron radiation pulses from a sub-ps modulation containing a charge of approximately 3 pC was determined in a single shot EO spectral decoding measurement at the IR beamline of the SLS. The measured longitudinal profile of the field pulse is in good agreement with particle tracking simulations. Further experiments to find the source of the relatively large arrival time jitter are in preparation.

ACKNOWLEDGMENTS

Many thanks to A. Streun for the particle tracking simulations, to P. Lerch, L. Quaroni, and H. Sigg, for the help at the IR beamline and the spectral measurements of the sliced Femto bunches and G. Ingold, S. Johnson ,and P. Beaud from the FEMTO team for the slicing.

REFERENCES

[1] A. Zholents *et al.*, "Femtosecond X-Ray Pulses of Synchrotron Radiation", Phys. Rev. Lett., Vol 76, No 6, 1996.

[2] B. Steffen *et al.*, "Single-shot electron-beam bunch length measurements", Phys. Rev. ST Accel. Beams, 12:032802, 2009.

[3] B. Steffen, "Electro-optic methods for bunch length diagnostics at FLASH", PhD thesis, University of Hamburg, DESY-THESIS-2007-020, 2007.

[4] G. Berden *et al.* "Time resolved single-shot measurements of transition radiation at the THz beamline of FLASH using electro-optical spectral decoding", Proceedings of EPAC 2006, Edinburgh, Scotland, TUPCH027, 2006.

[5] F. Müller *et al.*, "Ytterbium fiber laser for electro-optical pulse length measurements at the Swiss FEL", Proceedings DIPAC 09, Basel, TUPD31, 2009.

[6] P. Beaud *et al.*, "Spatiotemporal Stability of a Femtosecond Hard X-Ray Undulator Source Studied by Control of Coherent Optical Phonons", Phys. Rev. Lett., 99, 174801, 2007.

[7] D. Kalantaryan *et al.*, "Laser beam interaction and calculation of the sliced bunch radiation spectra for the SLS FEMTO beam line", Proceedings of EPAC08, Genoa, Italy, 2009.

[8] S. Casalbuoni *et al.*, "Numerical studies on the electro-optic sampling of relativistic electron bunches", Phys. Rev. ST Accel. Beams, 11:072802, 2008.

[9] http://sls.web.psi.ch/view.php/beamlines/ir/

[10] A. Streun, private communication, 2010.

BEAM HALO IMAGING USING AN ADAPTIVE OPTICAL MASK*

H. D. Zhang, R. B. Fiorito#, A. G. Shkvarunets, S. Bernal, I. Haber, R. A. Kishek, P. G. O'Shea,
University of Maryland, College Park, MD, USA
S. Artikova, MPI- Heidelberg, Heidelberg, Germany
C. Welsch, Cockcroft Institute, University of Liverpool, Liverpool, UK

Abstract

We have developed a technique that employs a digital micro-mirror array to produce an image of the halo of an electron beam with an enhanced dynamic range. Light produced by the beam intercepting a phosphor screen is first imaged onto the array; an adaptive mask is created and applied to filter out the beam core; and the result is reimaged onto an intensified CCD camera. We describe the optics used, the masking operation and preliminary results of experiments we have performed to study beam halo at the University of Maryland Electron Ring.

INTRODUCTION

Beam halo in intense beams is a phenomenon typically caused by parametric resonances or nonlinear forces due to space charge. It can lead to a number of undesirable effects, such as nuclear activation, emission of secondary electrons, and increased noise in the detectors. For high average power machines, halos can be damaging even if the number of particles in the halo is orders of magnitude below that in the core of the beam [1].

Halo can be observed by imaging visible light emitted by beam particles interacting with various types of screens, e.g. phosphor, YAG, OTR; or with optical synchrotron or edge radiation. However, there is usually an extreme contrast between beam core and halo; the ratio of halo to core intensity can be 10^{-5} or less. Therefore, a high dynamic range imaging system is required to view the details of the halo distribution. Also in any real optical system diffraction and scattering in the lenses due to the high core intensity can contaminate the halo image observed.

To solve these problems, several approaches have been considered. One is to allow the core intensity to saturate the camera. However, with sensitive CCD's and especially intensified CCD's, blooming and possible damage problems exist. Other methods are: passive spatial filtering, e.g. coronagraphy [2]; use of a high dynamic range (28 bit) camera such as the Spectra-Cam CID [3]: and, recently [4], an mask technique based on a digital micro-mirror array (DMA).

The DMA method has the advantages that the mask is adaptive to any shape beam and that a high dynamic range (DR) is achievable with a low cost camera; a DR~10^5 has been previously measured with a laser and a standard 8 bit CCD camera [4]. However, it has also been observed that the DMA produces a cross like diffraction pattern when illuminated by the laser; i.e. the DMA acts like a 2D grating. Since this may have a negative effect in an actual optical system used to image the beam, it is important to test the DMA in such a system.

We have developed an imaging method using a DMA to measure the halo of the electron beam at the University of Maryland Electron Ring (UMER) [5]. UMER is suitable machine to do halo experiments and test the theory of halo formation in space charge dominated beams. The beam is low energy (10 keV) but high current (10's of mA) with a variable pulse length (20-100 ns) and repetition rate (20-60 Hz). Radiation exposure is of minimal concern so that experiments can be easily set up and run *in situ*. Moreover, the beam is quite reproducible and stable over long time periods (hrs).

In the following sections, we will describe the optics system we have developed to image the beam with a DMA, the algorithm to spatially filter the image of the beam, our measurements of the dynamic range and optical performance of the system and finally preliminary beam halo images obtained with an adaptive mask.

EXPERIMENT SETUP

Digital micro-mirror array

The DMA we use is the DMD Discovery 1100 manufactured by Texas Instruments Inc. [6]. This type of device which is widely used in projectors and digital TV's is made up of hundreds of thousands of microscopic mirrors. A segment of the array and a mechanical drawing of one element are shown in Fig. 1(a) and 1(b) [6]. Each mirror on the chip can be individually addressed and rotated to either $+12^{\circ}$ or -12° with respect to the normal, when a voltage is applied to electrodes situated underneath the corners of each micro-mirror. When the voltage to the DMA is zero, all the mirrors are in a nominally flat, floating state.

Light from an external source can be reflected from mirrors in one state, e.g. $+12^0$, along a desired optical path, while the light reflected by mirrors in the opposite (-12^0) state will be directed 48^0 away from this optical path. When incorporated into an imaging system the device can be used as a spatial light modulator. The parameters of the device are shown in Table 1 [6].

*Work supported by the US Office of Naval Research, the Joint Technology Office and the US Department of Energy.
#rfiorito@umd.edu

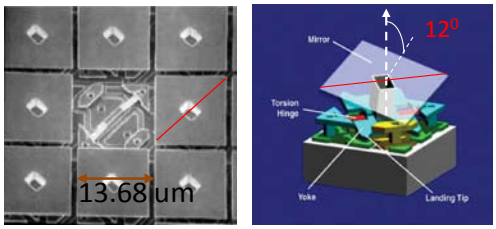

(a) (b)

Figure 1: (a) segment of the DMA; (b) mechanical drawing of individual micro-mirror and substructure .

Table 1: DMD Discovery 1100 Parameters

Parameter	Value
Mirror size	13.68 μm x 13.68 μm
switching rate	9,600 frames/s
PC interface	USB 2.0
Resolution	1024 x 768 pixels

Optical system

The basic layout of our optical imaging system is presented in Fig. 2 which shows a test bench setup. The optics implemented on UMER is essentially the same except the target screen in the real experiment is replaced by a phosphor screen.

Two lenses seen in the lower part of Fig. 2 are used to adjust the magnification and to focus the target onto the surface of the DMA, which is normal to the axis, when the device is in the floating state. When all mirrors switched to the $+12^0$ (or +) state, the image of the target is directed into a second optical channel (top part of Fig. 2) and refocused onto a 16 bit, gated, intensified, cooled CCD (PIMAX2). Since the rotation axis of the micro-mirrors is not parallel to the vertical or horizontal direction of the array, which corresponds to the sides of a micro-mirror, but rather along the diagonal of the later, the DMA must be rotated by 45^0, as shown in Fig. 3(a), to maintain the optical axis in the horizontal plane.

The two lenses used in the second channel control the magnification and focus of the image onto the CCD. Note that the camera is tilted horizontally by 24^0 with respect to the optical axis to compensate for the depth focusing problem produced by the $+12^0$ tilt angle of the micro mirrors. This angle produces differences in the path lengths of the rays which emanate from different horizontal source points on the DMA. This method is commonly used in photography and is known as Scheimflug compensation [7].

The position and tilt angle of the camera are adjusted to achieve a clear undistorted image of the target and the DMA itself as shown in Fig. 3(b). The target we use is a

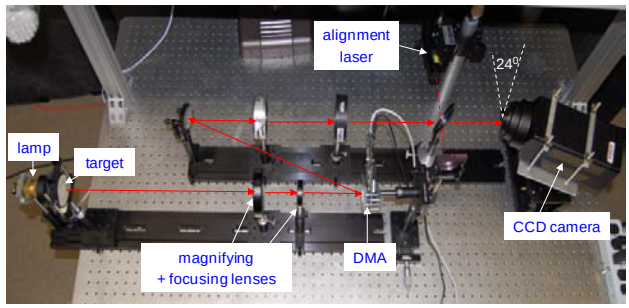

Figure 2: Optical imaging system incorporating the DMA.

semi-transparent rectangular grid overlaid with a circle with a diameter of 32 mm, the same size as the phosphor screens used to image the beam.

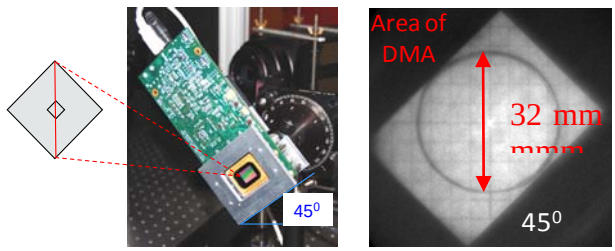

(a) (b)

Figure 3: (a) DMA device rotated by 45^0 and resulting orientation of a single micro-mirror; (b) image of the test target on the ICCD with Scheimflug compensation.

Algorithm for mask generation

Because of the 45^0 orientation of DMA and the differences in the number of pixels between the CCD and the DMA, we need to do a coordinate transformation and rescaling before we can generate an optical mask on the DMA. The algorithm shown schematically in Fig. 4 is described as follows.

First we take a calibration picture in order to observe the edges of the DMA on the camera and consequently to determine the size of DMA (Δx, Δy) in units of camera pixels. Any point of interest (x_0, y_0), can then be transformed to the DMA coordinates by calculating the distance between the point and the edges of the DMA. Next linearly magnify the image on the DMA originally given in units of camera pixels to its size in DMA pixels.

We then choose selected points on the beam image as a first step in generating a mask. For example, we can use points in the 'core' of the beam as the selected points, by (1) specifying a particular geometric area (e.g. a circular disk) overlaid on the 'core' visually, or (2) setting an intensity threshold to define the 'core'. Then we program the DMA, to blank out the 'core' pixels by setting them to -12^0 (see the red dot in Fig. 4). Finally, we reimage the beam with the mask set on the DMA.

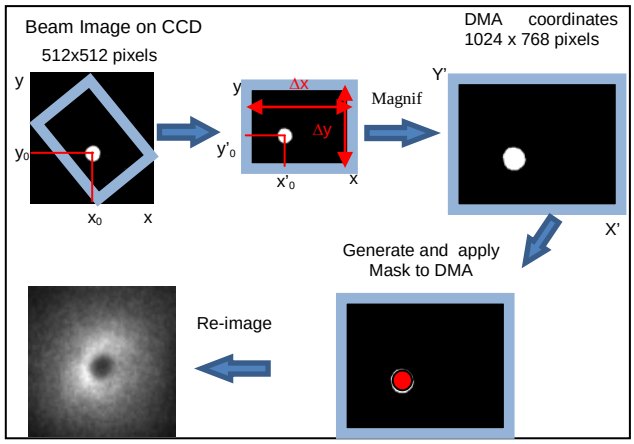

Figure 4: Schematic of mask generation algorithm.

RESULTS

Test of the Performance of the DMA

We first tested the effectiveness of the DMA to filter (reject) light from the phosphor screen by changing the DMA pixels from all ' + ' to all ' – '.When all the pixels of the DMA are '+', the light from the beam on the phosphor screen passes through the optics. We then integrate until the peak intensity approaches saturation on the CCD (64K counts); see Fig. 5(a). When all pixels are switched to '-', almost all of the light from the phosphor screen is reflected out of the optical path and only a very low level (~200 counts) from stray light scattered from the edges of the DMA is visible; see Fig. 5(b). Note the difference in the intensity scales between Fig. 5(a) and 5(b).

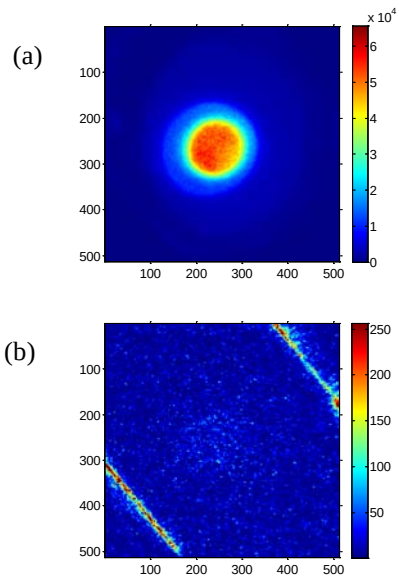

Figure 5: (a) Image with all DMA pixels set to $+12^0$; (b) image with all pixels set to -12^0; vertical and horizontal coordinates are given in terms of CCD pixels.

Next we did an experiment to test if the DMA affects the quality of the image. We compared images for three different cases using: 1) the DMA with all pixels set to '+' and Scheimflug compensation; 2) the DMA with all pixels in the floating state and no compensation; and 3) a simple mirror, which replaces the DMA and no compensation.

Fig. 6 shows the resulting beam images taken for each of these cases. Note that the optics must be slightly adjusted between configurations. This causes slight differences in the magnification and number of peak counts for each case. So we have normalized the intensities by the peak values in each image in order to concentrate on differences in the beam profile. No major differences are observed. We conclude that diffraction and scattering by the DMA mirrors has little if any effect on the quality of the beam images.

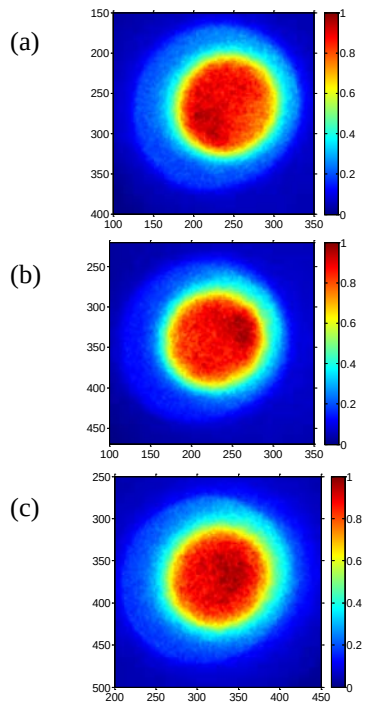

Figure 6: Comparison of beam images (close ups) with: (a) all DMA pixels set to '+' and Scheimflug compensation; (b) all DMA pixels floating and no compensation; (c) simple mirror and no compensation.

Dynamic Range Measurement

In order to determine the dynamic range of our optical system we observed an intense beam (I=23mA) focused to a 2.85 mm diameter on the phosphor screen, the minimum achievable size with our solenoid focusing magnet. We then generated a number of circular masks with different radii but a common origin, i.e. the position of the peak intensity of the beam observed without a mask.

For each mask we selected the appropriate number of gates on our ICCD camera necessary to bring the peak intensity in the image to near the saturation level of the camera. Note the small highlights visible in the upper left hand part of pictures in the second row. These are due to scattering of the phosphor light from a metal edge on the screen. We added a second small mask to block out these highlights which is seen as black dots on the lower images of Fig. 7.

To obtain a background image, we turned the beam off and integrated for the same number of gates used to obtain the beam image. Background subtracted images are shown in Fig. 7; the number below each picture is the number of gates used to obtain that particular image. By taking the horizontal line scans of all beam profiles (note for reference the horizontal red line in Fig. 7) and normalizing by the number of gates taken for each image, we can present the results as a series of plots as shown in Fig. 8. Each of the scans in the Fig. 8 corresponds to one of the pictures in Fig. 7. Note that the intensity fluctuations in tails of the beam profiles get smaller as more integration is applied. Moreover, the noise level outside the screen decreases to ~10^{-5}. Using the data presented in Fig. 7, and Fig. 8, we can reconstruct the 2D beam profile as shown in Fig. 9.

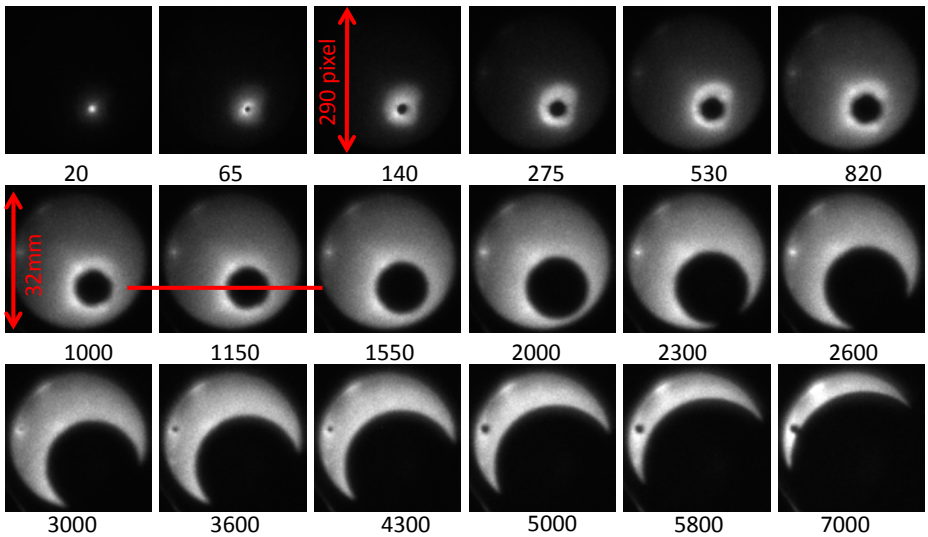

Figure 7: Images of the same beam with the DMA set to concentric circular mask of successively larger radii; number below image denotes the number of frame integrations on the ICCD camera.

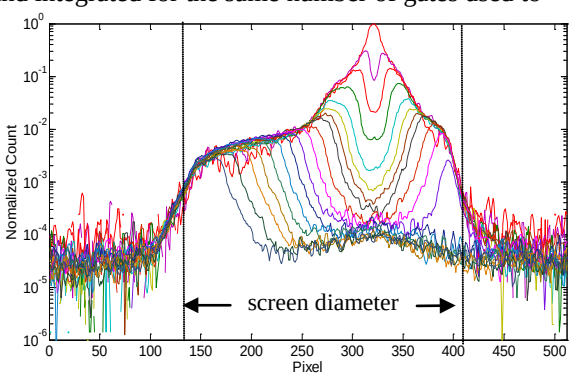

Figure 8: normalized horizontal scans of beam profiles presented in Fig. 7.

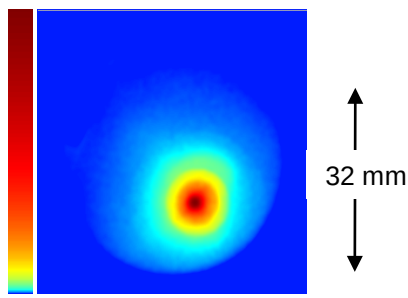

Figure 9: Reconstructed beam profile using color logarithmic intensity scale.

Halo imaging with an adaptive mask

Fig. 10 (a) shows a black and white image of the beam with halo that was previously presented above in Fig. 5. Note that neither the core nor the halo distributions are axisymmetric. However, by setting a threshold condition (e.g. 10^4 counts), we use the DMA to can create an adaptive optical mask to block out the 'core', i.e. all pixels in the beam image with intensity levels greater than a given value. As described above, we can then increase the number of gates to better view the halo distribution by

bringing the peak intensity of the halo close to saturation. The ratio of the number of frames integrated with the DMA mask (180) to those taken without the mask (900) is 5, which effectively increases the dynamic range of the measurement.

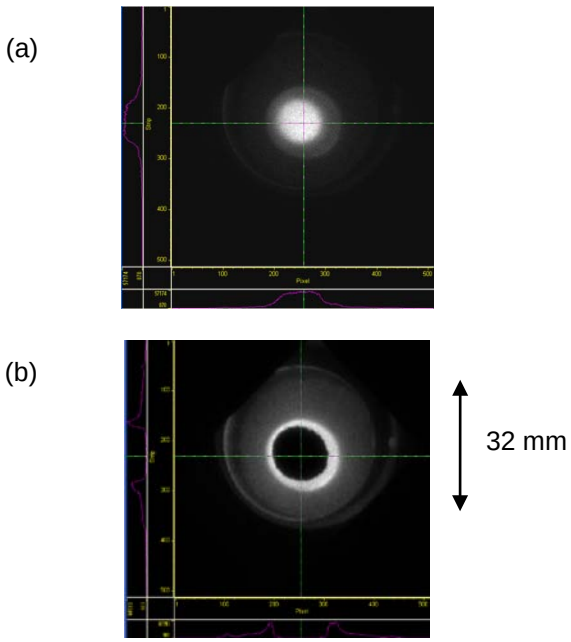

Figure 10: (a) Beam profile with core and halo; (b) profile of the halo after applying adaptive threshold mask with intensity level of 10^4 counts.

By lowering the threshold level and increasing the integration time, similar to what was done with the circular masks (see Fig. 7), we can view the tail of the halo distribution, up to the limit of the screen size, with a further increase in dynamic range.

CONCLUSIONS AND FUTURE WORK

We have developed a flexible optical system employing a DMA to adaptively mask the beam central core and image the halo with an improved dynamic range. We show that a dynamic range of close to 10^5 is achievable using the DMA to image and mask the UMER electron beam with a simple phosphor screen. This performance matches earlier measurements which used the DMA and a laser only. Furthermore, we have performed tests to show that the DMA has excellent extinction (~10^5) and that effects of diffraction and scattering due to the DMA on beam images are minimal.

Some features of UMER and the imaging screen used in our measurements, such as the highest beam intensity achievable, the efficiency of the phosphor, the ratio of the beam to the screen size, scattered light and background, limited our measured dynamic range. This limit may be exceeded at other machines which have a higher intensity beam and/or with improved optics.

We plan to study the halo evolution around the UMER ring using the DMA as well as apply our technique to a higher energy accelerator using other beam based emissions, e.g. OTR or optical edge radiation.

REFERENCES

[1] J. Wei, W. Fischer, P. Manning (eds.), Beam Halo Dynamics, Diagnostics and Collimation, Proc. of 29th ICFA Advanced Beam Dynamic Workshop, AIP Conf. Proc. 693, Melville, NY (2003).

[2] T. Mitsuhashi, "Design and construction of coronagraph for observation of beam halo", Proceedings of EPAC 2004, Lucerne, Switzerland (2004).

[3] C. P. Welsch, E. Bravin and T. Lefevre, "A beam halo monitor based on adaptive optics", Proc. SPIE 6616,9 (2007).

[4] J. Egberts, S. Artikova, C. P. Welsch, "Flexible core masking technique for beam halo measurements with high dynamic range", Proceedings of DIPAC09, Basel, Switzerland (2009).

[5] R. A. Kishek, et. al. 'The University of Maryland ele ctron ring (UMER) enters a new regime of high tune shift rings', Proc. of PAC 07, p. 820 (2007).

[6] Texas Instruments Inc., "DMD Discovery 1100 Controller Board and Starter Kit", 2005.

[7] T. Scheimflug, "Improved Method and Apparatus for the Systematic Alteration or Distortion of Plane Pictures and Images by Means of Lenses and Mirrors for Photography and for other purposes", GB Patent No. 1196. issued 12 May 1904; see also http://www.trenholm.org/hmmerk/#SR

DITANET CONTRIBUTING TO STATE-OF-THE-ART DIAGNOSTICS DEVELOPMENTS

C.P. Welsch

University of Liverpool and the Cockcroft Institute, UK

on behalf of the DITANET consortium

Abstract

DITANET is the largest-ever EU funded training network in beam diagnostics. The network members - universities, research centers and industry partners - are developing diagnostics methods for a wide range of existing or future particle accelerators, both for electron and ion beams. This is achieved through a cohesive approach that allows for the exploitation of synergies, whilst promoting knowledge exchange between partners. In addition to its broad research program, the network organizes schools and topical workshops for the beam instrumentation community.

This contribution gives an overview of the Network's research portfolio, summarizes the main research results from the first two years of DITANET and presents past and future training activities.

INTRODUCTION

The DITANET project officially started on 1.6.2008 and consists of ten network beneficiary partners and presently 17 associated and adjunct partners. The training network brings together Universities, research centres, and the industry sector with the aim to jointly train the next generation of young scientists in beam instrumentation.

A core idea of DITANET is that all network members interact and collaborate closely, promote the exchange of trainees and staff within the network, and jointly organize training events, workshops and conferences open also to external participants.

The participation of industry is an integral part of the training within DITANET and all partners from industry are included as members of the supervisory board to ensure that industry-relevant aspects are covered in the different projects carried out within the network and to enhance knowledge transfer. In addition, they offer internships to the students from the network to complement the scientific training and thus actively contribute to building the bridge between the academic and the industrial sector.

RESEARCH

DITANET covers the development of diagnostic methods for a wide range of existing and future accelerators. The developments target beam profile, current, and position measurement. This section presents some of the research outcomes to date.

The Ultra-low Energy Storage Ring

The international Facility for Antiproton and Ion Research (FAIR), to be located at the site of the GSI Helmholtz Centre for Heavy Ion Research in Darmstadt, Germany comprises a series of rings to provide intense beams of antiprotons, unstable exotic nuclei and highly charged ions.

The Facility for Low-energy Antiproton and Ion Research (FLAIR) is based on the need for high-brightness high-intensity low-energy antiproton beams. Antiprotons from the new experimental storage ring (NESR) will be injected into the Low energy Storage Ring (LSR) at an energy of 30 MeV. They will then be cooled and further decelerated to 300 keV energy. The Ultra-Low energy Storage Ring (USR) [1], presently being developed by the QUASAR Group, will provide electron-cooled beams of antiprotons in the energy range between 300 and 20 keV.

These boundary conditions put challenging demands on the USR beam instrumentation. Some important beam parameters are summarized in Table 1.

Table 1: USR beam parameters

Energy	300 keV → 20 keV
Relativistic β	0.025 → 0.006
Revolution frequency	178 kHz → 46 kHz
Revolution time	5.6 μs → 21.8 μs
Intensity	1 μA → tens of fA
RF frequency (h = 10)	1.78 MHz → 459 kHz
Bunch repetition time (h = 10)	560 ns → 2.2 μs
RF bucket length (h = 10)	4.4 m
Charge per bunch (h = 10)	0.3 pC ($2 \cdot 10^6$ pbars)

Depending on whether slow or fast extraction will be applied, the beam intensity and the time structure of the extracted beam will vary in a wide range.

*Work supported by the EU under contract PITN-GA-2008-215080.
#carsten.welsch@quasar-group.org

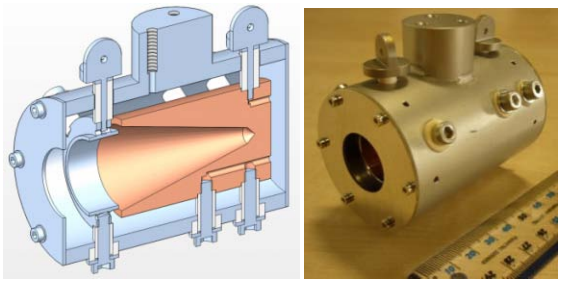

Figure 1: Faraday Cup for the USR

A Faraday cup was designed, based on an existing layout at the MPI-K, Heidelberg. It was optimized for the energy region of interest and allows for the measurement of beams with a maximum diameter of 20 mm, Fig 1.

The shape of the beam stopper was chosen in order to optimise the secondary electrons collection efficiency. The shape of the stopper as well as of the suppressing electrode that shall contain the emitted charges inside the cup was optimized with CST Studio and more detailed results are presented elsewhere in this workshop [2]. The cup will be used for first tests with beam at the Clatterbridge Centre for Oncology this summer.

Additional parts of this ESR project cover the design and optimization of a capacitive beam position monitor [3] and investigations into different screen materials for beam profile monitoring of low energy, low intensity beams [4]. For the latter, measurements were already realized in close collaboration with INFN, Italy.

Emittance Measurement at HIT

The transverse emittance of the ion beam at the Heidelberg Ion Therapy Center (HIT) will be measured within the Low Energy Beam Transport (LEBT) using a pepper-pot measurement system. At HIT, two ECR sources produce ions (H, He, C and O) at an energy of 8keV/u with different beam currents from about 80 µA to 2mA.

The mechanical design of the pepper–pot system is the result from collaboration between DITANET partners GSI and HIT and is shown in figure 2.

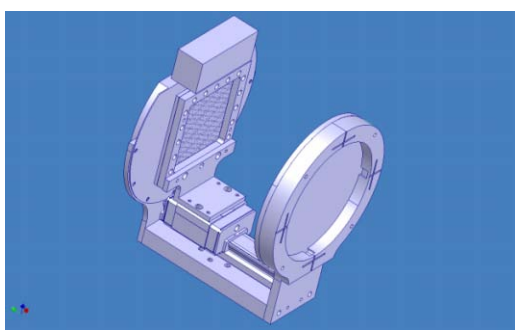

Figure 2: Illustration of the pepper-pot scintillator bench.

Critical to the performance of the emittance measurement is the performance of the scintillating screen. To enable high spatial resolution, the screen material should interact with the impinging particle beam in a similar way across the entire screen surface. For most materials that also satisfy the necessary vacuum and light yield conditions, this is not the case.

Detailed studies into different materials, aiming at identifying the optimum solution for the energy and intensities in question, were carried out at the MPI-K in Heidelberg. In these tests, the following materials were studied: (1) Inorganic Doped Crystal (YAG:Ce, YAP:Ce, Caf2:Eu), (2) Inorganic Undoped Crystal (Sapphire, YAG), Quartz and Borosilicate glass (Herasil 3 & 102, Infrasil 301 & 302, Suprasil 1 & 300), and Borosilicate Glass D 263 T.

During these runs, the scintillator was placed in the beam path at a 45 degree angle. The images were recorded with a conventional CCD camera. It was possible to place three scintillators on a common support and to test them under the same operating conditions. The detailed results of this study are presented in [5].

Longitudinal Beam Profile Measurements at the Large Hardron Collider

The Large Hadron Collider at CERN will accelerate protons up to an energy of 7 TeV. An optical arrangement has been made which focuses synchrotron light from two LHC magnets to image the cross-section of the beam. It is also planned to use this setup to produce a longitudinal profile of the beam by use of fast Single Photon Counting. This is complicated by the bunched nature of the beam which needs to be measured with a very large dynamic range.

The primary source of the synchrotron light is a 9 m long superconducting bending magnet with a uniform vertical magnetic field. In order to keep the beam trajectory constant, the magnetic field strength is increased in proportion to the beam energy. The field strength in this magnet is varied from 0.25 T to a maximum of 3.9 T. The nature of the synchrotron light emitted in the bending magnet can be calculated analytically [6] or computed using a simulation code such as Synchrotron Radiation Workshop (SRW) [7]. Not only the power emitted by each proton but also the spectrum and angular distribution of the light depend on the γ of the protons i.e. on their energy. The light will therefore change during the LHC's accelerating cycle. The total light emitted is simply the sum of the light from individual protons. Thus the light intensity can be used as a proxy for proton density at different points along the beam.

In order to allow the monitor to be used at lower beam energies, an additional undulator magnet has been installed just upstream of the bending magnet. It increases the emission of synchrotron light drastically without negative impact on the motion of the stored beam. In this case the emitted spectrum is dominated not by the critical frequency but by interference effects arising from the periodic structure of the undulator. This particular undulator has been designed to emit visible synchrotron

light at proton energies below those at which the radiation from the bending magnet can be used.

In order to monitor not only the transverse beam profile, but also the longitudinal density profile of the LHC beam, the detector should allow for a detection of time structures with a resolution of 50ps. In addition, two functionalities are requested. Firstly, there should be a fast integration mode which can measure the bunch parameters (bunch length, density distribution) with an integration time of 1 ms. Secondly, there should be a high-sensitivity mode which can produce a full longitudinal profile showing all the bunches with a sensitivity of $5x10^5$ protons per 50ps bin. This implies a dynamic range of more than 30,000 compared to the maximum density at the centre of the bunch. Of particular importance is to measure the tails of the bunches and the nominally empty spaces between bunches. Given the small amount of light available and the fast time resolution required, time-correlated single photon counting will be used to construct the profile. An avalanche photo diode (APD) operated in the Geiger mode is suitable for detecting single photons with such high time resolution. Different detectors were already characterized in an optical lab at CERN [8] and will be used for tests with beam in the near future.

Intensity Modulated Radiation Therapy

Within a collaboration between the national accelerators center (CNA), the department of atomic, molecular and nuclear physics of the University of Seville, Virgen Macarena Hospital of Seville, the engineering school of the University of Seville and the private company INABENSA (ABENGOA), an active research is ongoing on a project dedicated to radiotherapy with high-energy photon beams.

This collaboration exploits the knowledge and expertise of these groups on nuclear instrumentation, electronic and mechanical design, theoretical calculations, Monte Carlo simulations and analysis of nuclear reactions, and transfers it to the medical field and in particular to radiotherapy treatments.

The aim of the project is to validate a novel method to obtain a map of doses in the pre-treatment of patients with Intensity Modulated Radiation Therapy (IMRT). The method uses a mathematical algorithm and Geant4 Monte Carlo simulations. Measurements are performed at Virgen Macarena Hospital using the 6-MV photon beam produced by a Siemens Primus accelerator.

The detector used for dose measurements is a commercial single-sided silicon strip detector of 500 μm thickness, Fig. 3. Its active area of 50x50 mm^2 is divided into 16 narrow strips (3 mm width each) and a separation of 0.1 mm between strips. This type of detector is widely used in nuclear physics experiments for time of flight measurement and particle or fragments identification.

Figure 3: Picture of the silicon strip detector inside the phantom for the characterization of its dosimetric response.

Preliminary tests with the detector and with a dedicated electronics have been carried out irradiating the device with 6 MV photon beams in order to study the response of the device and of the electronics with different radiation fields at different doses. The device showed a good linearity with respect to the dose accumulated, a good uniformity in the response of the strips and a good percent depth dose profile. These preliminary tests with this detector are very encouraging and it is planned to use it in further measurements for obtaining a dose map during a dedicated treatment.

Finally, in order to improve the actual spatial resolution, it is planned to investigate into the possible use of 2D silicon detectors.

Beam Halo Measurements at UMER

A thorough understanding of halo formation and its possible control is highly desirable for essentially all particle accelerators. Particles outside the beam core are not only lost for further experiments, they are also likely to hit the beam pipe, and activate this, as well as accelerator and experimental components in close proximity, which makes work on the accelerator costly and time consuming. Well established techniques for transverse beam profile measurements of electron or high energy hadron beams are the observation of synchrotron radiation, optical transition radiation or the like. A particular challenge, however, is the detection of particles in the tail regions of the beam distribution in close proximity of the very intense beam core. A flexible core masking technique based on a DMD micro mirror array which allows for a fast mask generation to blank out the central core and to focus the measurement on the tails of the distribution was developed in close collaboration between the University of Liverpool, the MPIK, CERN, ViALUX and the University of Maryland [9,10]. An example of a measurement with the adaptive mask is shown in the following Fig. 4.

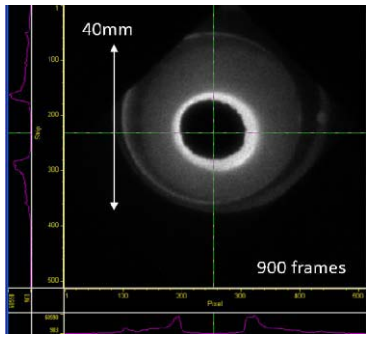

Figure 4: Beam profile measurement with core deflected by DMD at UMER.

This research project was not part of the original DITANET research program, but illustrates nicely how the structures and links created by the network can help paving the way for new developments.

TRAINING

Although training within DITANET is mainly by training through research, all network partners also provide an extensive local training to their Marie Curie Fellows. This is mostly realized in the frame of a structured PhD program and in collaboration with partners from different sectors. In addition, DITANET organizes network-wide events, such as Schools, Topical Workshops, and conferences that have to be attended by the network trainees, but are also open to the wider diagnostics community. This section provides a short summary of past events.

DITANET School on Beam Diagnostics

From March, 30th - April, 3rd 2009 the first DITANET School on Beam Diagnostics took place at Royal Holloway, University of London. The School was combined with the first DITANET annual meeting and brought together more than 70 researchers from major Research Centers, Universities and private industry from all over the world.

The School started with an introduction to accelerator physics and the definition of particle beams, before basic beam instrumentation, for example beam energy, beam current and transverse beam profile measurement were covered. Later in the week more advanced topics, e.g. the monitoring of the machine tune and electron cloud diagnostics were presented. An excursion to Rutherford Appleton Laboratory including visits to ISIS and DIAMOND on Wednesday, April 1st as well as two tutorials and one poster session complemented the broad program.

A particular highlight was a dedicated industry session on the last day where lecturers from Thermo Fisher Scientific, TMD, Thales, ViALUX, and Instrumentation Technologies gave an insight into cutting edge R&D activities in the industry sector with a focus on differences as compared to research in academia.

School on Complementary Skills

DITANET organized a Complementary Skills School at the University of Liverpool from 15th-19th March 2010. This course aimed at providing the network's early stage and experienced researchers with the necessary skills base for a future career in both, the academic and industry sectors.

After an introduction session, the participants focused on different presentation techniques and discussed best practice as well as common mistakes. Day two started with an introduction to project management, before putting a focus on individual presentations. All participants had to give a 5 minute presentation on their research projects that was recorded and then assessed individually. On Wednesday, the school triggered discussions about the benefits from and challenges in international networking. Representatives from Tech-X UK and Inventya reported on their personal experiences, before a session on time management concluded the morning. On Thursday, time and self management, a session on work/life balance as well as two hours on intellectual property rights and patent law confronted the trainees with a number of important skills and triggered many discussions. Finally, an extended session on scientific writing completed the week.

Topical Workshop Series

The first DITANET topical workshop took place on November, 24th and 25th in Hirschberg-Großsachsen, near Heidelberg, in Germany. It focused on the diagnostics of low energy and low intensity ion beams and brought together around 40 scientists and engineers from all over the world. Its particular aim was to join early stage researchers both from within the network and from the wider community with renowned experts to allow for establishing important contacts for their careers and for reviewing the status of the different R&D activities.

The first day started with an introduction to the future Facility of Antiproton and Ion Research, where many of the monitors presently under development in different groups will be used to monitor all beam characteristics with a high precession. It then stretched to the beam instrumentation used at different storage ring and cyclotron facilities around the world.

The second day concentrated on electrostatic storage rings which are the ideal tool for lowest beam energies down to a few tens of keV and intensities as low as 10^4 pps. Presentations were given on the ELISA (ISA, Arhus), DESIREE (MSL, Stockholm), CSR (MPI-K, Heidelberg), and USR (FAIR, Darmstadt) facilities and triggered interesting discussions on these challenging developments.

This workshop marked the beginning of a workshop series that will be organized by the network. A workshop on "longitudinal beam profile measurements in high accelerators and light sources" will be organized on July 12th and 13th at the Cockcroft Institute, UK.

Detailed information on all past and future events is accessible via the network's homepage [11].

NETWORK STRUCTURE

DITANET initially consisted of the following network beneficiaries: University of Liverpool (coordinator, UK), CEA (France), CERN (Switzerland), DESY (Germany), GSI (Germany), HIT GmbH (Germany), IFIN-HH (Romania), Stockholm University (Sweden), Royal Holloway University of London (UK), and the University of Seville/Centro Nacional de Aceleradores (Spain).

It is complemented by twelve associated partners from all over the world: ESRF (France), idQuantique (Switzerland), INFN (Italy), Instrumentation Technologies (Slovenia), MPI for Nuclear Physics (Germany), PSI (Switzerland), THALES (France), Thermo Fisher Scientific (USA), TMD Technologies Limited (UK), TU Prague (Czech Republic), ViALUX (Germany), and WZW Optics (Switzerland).

In addition, the network introduced *adjunct partnerships* for institutions that are active in R&D fields closely related to the network and that share the network's training visions. These partners agreed to contribute to the training and joined the consortium after the official project start. They are an important part of DITANET's long term strategy in establishing lasting bonds and partnerships across institutes and disciplines in Europe. So far Diamond Detectors Ltd. (UK), the University of Dundee (UK), the University of Uppsala (SE), the University of Maryland (USA) and Lawrence Berkeley National Lab (USA) joined DITANET as adjunct partners.

DISSEMINATION

The DITANET web site is hosted by the University of Liverpool and can be found at www.liv.ac.uk/ditanet. It is a central point for all information regarding the network and includes information about each of our partners, their trainees and the projects in which they are involved.

In addition, it provides information on events and is a collection point for all presentations and papers within the Network by providing external links in addition to uploaded documents.

The network issues a newsletter quarterly by e-mail to partners and colleagues in beam diagnostics and accelerator science across the world. Its aim is to inform and disseminate, providing information on members of the DITANET project, its partners, trainees and its scientific work.

Copies of the newsletter are freely accessible via the DITANET website which also provides a facility for on-line subscription.

An annual prize is part of the network's wider dissemination strategy. It is awarded for an outstanding contribution to the field of beam instrumentation for particle accelerators and presented to a researcher in the first five years of his/her professional career.

The 2010 prize was awarded to Frank Becker (GSI) for his research on beam induced fluorescence (BIF). The prize was awarded in March 2010 in Brussels as part of the annual meeting. On this occasion, the award winner gave a presentation of his prize winning work.

CONCLUSION

Two years after the start of DITANET, first results from its broad research program become visible and were summarized in this contribution. In close collaboration between the network beneficiaries and the partners from across the world, with a very prominent role of industry, accelerator instrumentation is pushed beyond existing limits. In addition, the network offers a wide training program to its trainees as well as to the wider community and past events were briefly described.

The newly introduced adjunct partnership status allows additional institutions that share the network's ideas and visions to join the DITANET frame and participate to its research and training program.

REFERENCES

[1] C.P. Welsch, et al., "An ultra-low-energy storage ring at FLAIR", NIM A 546 (2005) 405–417
[2] J. Harasimowicz, C.P. Welsch, "Faraday Cup for Low-energy, Low-intensity Beam Measurements at the USR", Proc. BIW, Santa Fe, USA (2010)
[3] J. Harasimowicz, C.P. Welsch, "Beam Position Monitor Development for the USR", Proc. BIW, Santa Fe, USA (2010)
[4] L. Cosentino et al., "Scintillating Screen Studies for Low Energy, Low Intensity Beams", Proc. IPAC, Kyoto, Japan (2010)
[5] M. Ripert et al, "A Pepper-pot emittance device for 8 keV/u light ion beams – general layout and investigations on the screen material", Proc. BIW, Santa Fe, USA (2010)
[6] A. Hofmann, "The Physics of Synchrotron Radiation", Cambridge University Press, 2004
[7] O. Chubar, P. Elleaume, "Accurate and efficient computation of synchrotron radiation in the near field region", Proc. Europ. Part. Acc. Conf., Stockholm, Sweden (1998)
[8] A. Jeff et al., "Spatial and Temporal Beam Profiles for the LHC using Synchrotron Light", Proc. SPIE Photonics, Brussels, Belgium (2010)
[9] J. Egberts et al., "Flexible core masking technique for beam halo measurements with high dynamic range", JINST 5 P04010 (2010)
[10] R. Fiorito et al., "Beam Halo Imaging with an Adaptive Optical Mask", Proc. BIW, Santa Fe, USA (2010)
[11] http://www.liv.ac.uk/ditanet

BEAM LOSS MONITORS (BLMS): PHYSICS, SIMULATIONS AND APPLICATIONS IN ACCELERATORS

A. Zhukov, ORNL, Oak Ridge, TN, U.S.A.

Abstract

Beam loss monitors are common devices used in hadron and lepton accelerators. Depending on accelerator specifics, BLMs could be just diagnostics or could play an essential role in the machine protection system (MPS). This tutorial discusses different types of BLMs and their applicability to different accelerators. It covers traditional BLMs like ionization chambers and scintillator-based devices, and also less common techniques like those based on fiber optics and avalanche diodes. The tutorial gives an overview of the underlying physics involved in beam loss detection, and recent advances in computer simulation of particle interaction with matter helpful for BLM modeling. Options for signal processing electronics are described, as well as interfaces to both the control system and the MPS.

INTRODUCTION

Definition

First we want to define a beam loss and a beam loss monitor. Charged particles are accelerated in accelerators and supposed to follow design trajectory along the beam line. Some of the particles deviate from the prescribed path and hit the beam pipe. They then interact with media and create radiation. So the beam loss is *unintentional* interaction of beam particles with media causing radiation. A beam loss monitor is intended to detect this radiation. Sometimes the particles interact with materials by design; good examples of that are Faraday cups, wire scanners, collimators, scrapers and other insertable devices. The presence of such devices complicates analysis of BLM signals since they add significantly to radiation field around them. In addition, there are other sources of radiation that do not involve direct interaction of primary particles with materials. These sources include synchrotron radiation and cavity X-rays. An ideal BLM should be sensitive to radiation caused by loss and insensitive to other sources of radiation. While one can imagine a beam loss detector that is not a radiation detector we won't discuss such devices in this paper.

BLM Purpose

The ultimate goal of a BLM system is to identify the loss level and if possible, the loss's location and time structure. This could result in a beam abort if the loss level endangers equipment (for example, by burning a hole in a drift tube or quenching a superconducting magnet). It also can provide feedback for better beam tuning. Residual activation is a big problem for high power hadron machines; the BLMs can help to limit that.

General BLM-specific considerations

While beam loss monitors are commonly used as beam diagnostics devices, beam loss is a somewhat standalone topic of beam instrumentation. This is probably due to the nature of the physics processes the BLMs rely on. Other diagnostics devices usually are directly coupled with Accelerator physics and electrodynamics principles. BLMs involve many different parts of physical science, such as: electrodynamics, high-energy particle detectors, nuclear physics, radiation protection, neutron physics, etc. Due to this fact, beam diagnostics overview papers typically mention the physics processes inside BLMs briefly and interpret a BLM as a black box with known parameters and detector response function. We will try to give an overview of radiation detector physics here and refer to corresponding literature for more in-depth information [1,2,3].

The other important fact to consider is the sensitivity of loss monitors to real world geometry. Usually, a BLM is a radiation detector which is placed in an accelerator tunnel in the vicinity of the beam pipe; almost everything that is located nearby could potentially influence the BLM by attenuating (or in some cases increasing) the radiation field measured by the detector. This fact makes detailed analytic calculations of losses almost impossible in any non-ideal case. Fortunately many computer codes exist to address this problem. These codes account for both the vast distribution of involved physics and the complex physical layout of modern accelerators.

BLM PHYSICS ASPECTS

Electromagnetic interaction of charged particles with a medium

As we will see later the interaction of charged particles with materials is the most important thing to consider while designing a BLM. When a charged particle passes through matter, it loses its energy by ionization and atomic excitation. These processes are dictated by the EM interaction between atomic electron and incident charged particle.

The Bethe-Bloch equation is the main formula governing this process:

$$-\frac{dE}{dx} = 0.31\,\frac{MeV}{g/cm^3} z^2 \frac{Z}{A}\frac{1}{\beta^2}\left(\ln\frac{2 m_e c^2 \gamma^2 \beta^2}{I} - \beta^2 - \frac{\delta}{2}\right), \quad (1)$$

where Z/A is the ratio of atomic charge and the atomic mass number, z is the charge of the incident particle (in units of electron charge), m_e is the electron's rest mass and I is the ionization potential – a property of the atom; all other variables denote standard relativistic quantities.

This formula gives the average energy loss (*stopping power*) of a heavy particle (not an electron or positron) per unit of length (expressed in g/cm^3 to account for the fact that the probability of interaction is proportional to atom concentration; to obtain energy loss per cm one should multiply (1) by the material density in g/cm^3). Simple relativistic kinematics [4] shows that the numerator of the logarithmic term is a maximum of energy transferrable to the released electron. The energy loss of a proton in nitrogen is shown in Fig. 1.

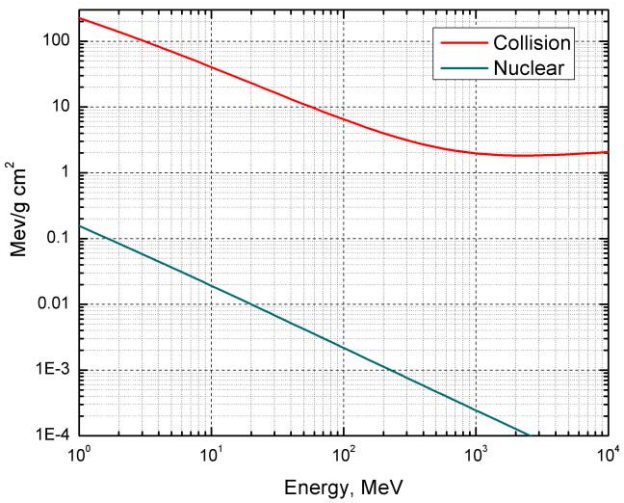

Figure 1: Stopping power for proton in nitrogen. NIST data [5].

In order to obtain the formula for electrons one has to consider the mass equality of the incident particle and the released electron; also, there is no way to distinguish between incident electrons and shell electrons after a collision. This gives a different maximum energy transfer for a relativistic electron [4].

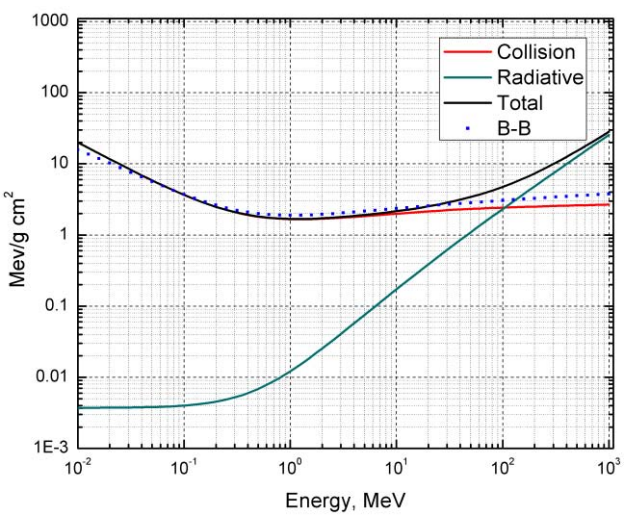

Figure 2: Stopping power for electrons in nitrogen, NIST data [5] and Bethe-Bloch (B-B) evaluation.

For this and other reasons (discussed later), the stopping power curve looks different for electrons, as shown in Fig. 2. This curve is given by a modified Bethe-Bloch equation:

$$-\frac{dE}{dx} = 0.31\,\frac{MeV}{g/cm^3}\,\frac{Z}{A}\,\frac{1}{\beta^2}\left(\ln\frac{m_e c^2\gamma}{2I} - \beta^2 - \frac{\delta}{2}\right). \qquad (2)$$

Since Eqns. (1) and (2) define average loss, it is important to understand the size of the fluctuations of this value. It is parameterized by a Landau distribution [4], but the actual distribution could be even wider. Also, the particles are subject to *range straggling*, caused by fluctuations in path lengths of particles having the same initial energy. For heavy particles it range varies within several percents. This explains different shapes for the curves of stopping power vs. penetration depth (the Bragg peak for heavy particles and lack of it for electrons).

Electrons also experience bremsstrahlung due to Coulomb interaction with the atomic nucleus and at some energy the collisional loss is equal to the radiative loss. Classical electrodynamics theory gives

$$-\left.\frac{dE}{dx}\right|_{rad} \approx \frac{Z^2}{A}\,\frac{1}{m^2c^4}\,E\ln\frac{183}{Z^{1/3}}, \qquad (3)$$

where the square of particle mass in the denominator reflects the fact that radiative loss is negligible for heavy particles.

The ratio of collisional and radiative loss is given by (energy in MeV):

$$-\frac{dE/dx|_{rad}}{dE/dx|_{col}} \cong \frac{EZ}{700}. \qquad (4)$$

Since the radiative loss is proportional to energy, it is useful to introduce the parameter X_0 – radiation length. We can then write (3) in common exponential attenuation form:

$$-\left.\frac{dE}{dx}\right|_{rad} = \frac{E}{X_0} \qquad (5)$$

Equations 1-5 allow estimating the scale of energy loss by charged particles inside a BLM detector volume.

Gamma and X-ray interactions

While gamma particles could not be primary particles for an accelerator, they are always present as secondaries. They participate in three interactions:

- Photoelectric absorption (dominant for low energies: ~30 keV).
- Compton scattering (100 keV~2 MeV).
- Pair production.

During photoelectric absorption, a photon interacts with the whole atom and kicks out an electron. Usually (with about 80% probability) the absorption happens in a K shell. The photoelectric cross section is proportional to Z^5. The Born approximation [6] of Eqn. (4) gives a good

description for K-shell absorption in the non-relativistic case:

$$\sigma_{photo}^{K} = \left(\frac{32}{\varepsilon^{7}}\right)^{1/2} Z^{5} \alpha^{4} \sigma_{Th}^{e} \quad , \qquad (4)$$

where

$\varepsilon = E \frac{E^{\gamma}}{m_e c^2}$ is the reduced photon energy,

and $\sigma_{Th}^{e} = 6.65 \cdot 10^{-25} cm^{2}$ is the Thompson cross section for elastic scattering of photons on electrons. In addition to the kicked out electron, a characteristic X-ray or Auger electron can also appear. The Auger electrons usually have much lower energy than the primary photoelectron and are of no interest.

The Compton effect describes the interaction of photons and quasi-free atomic electrons. Eq. 5 gives the energy dependence of the scattered photon.

$$h\nu' = \frac{h\nu}{1 + \frac{h\nu}{m_e c^2}(1 - \cos\theta)} \qquad (5)$$

The angular distribution is given by the Klein-Nishina formula [7,10] and is shown in Fig. 3. The higher energy of the incident photon corresponds to forward scattering, while at low energies, backscattering is also highly probable.

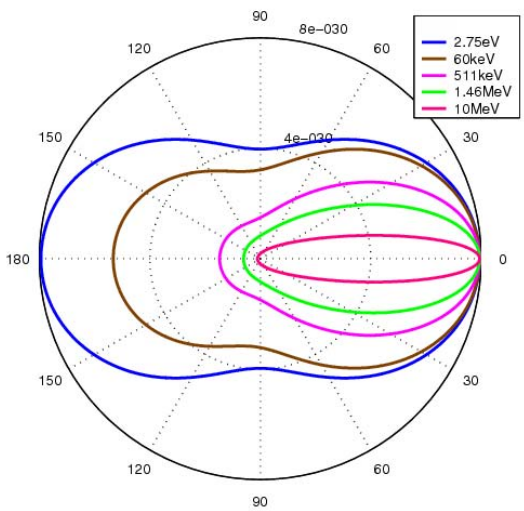

Figure 3: Angular distribution of scattered photons [11].

Pair production takes place in the Coulomb field of a nucleus. It becomes possible when photon's energy is higher than $2m_ec^2$ [8].

Considering that the incident photon disappears in one of three processes, the number of photons penetrating a thickness *z* of material is described by exponential decay.

$$I(z) = I_0 e^{-\mu z} \quad , \qquad (6)$$

where μ is the total attenuation coefficient of all three processes [9]. It is common practice to measure the thickness in g/cm^2, which is simply the linear thickness multiplied by material density. Fig. 4 shows a typical cross section's dependence on the photon's energy.

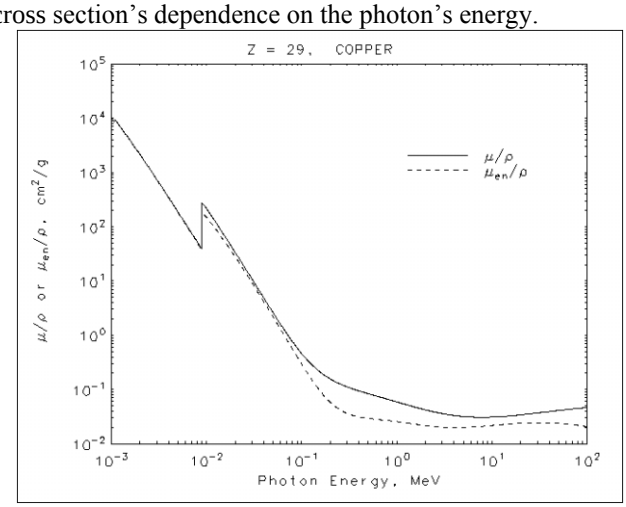

Figure 4: Energy dependence of attenuation coefficient [41].

Nuclear interactions

High energy hadrons interact with the nucleus. Different models could be used to describe such interactions. Just to name a few:

- Evaporation [12,13].
- Multifragmenation [14].
- Fermi breakup [15].
- Low energy neutron interactions [16].
- Cascading [17].

For hadron accelerators, the processes of great interest are evaporation and low energy neutron transport. The first process is the main source of neutrons in hadron machines, and the second one describes neutron propagation in accelerator materials and detectors.

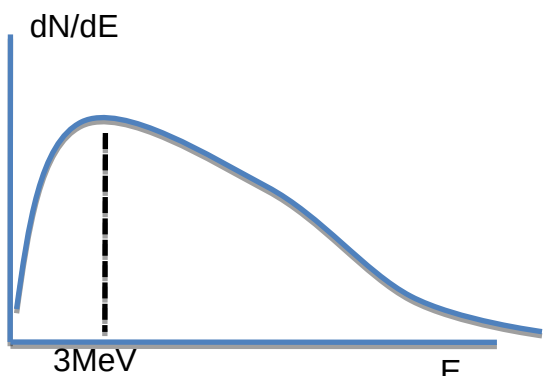

Figure 5: Energy spectrum of evaporation neutrons.

The evaporated neutrons have an average energy of 3 MeV but the spectrum extends up to 20 MeV; a sketch is shown in Fig. 5. A typical scenario of neutron generation includes cascade development, evaporation of neutrons (and other hadrons), and their further propagation.

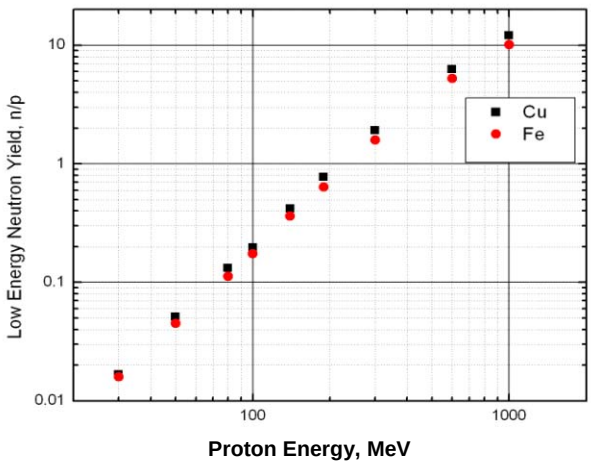

Figure 6: Evaporation neutron yield from a copper target as a function of incident proton energy [18].

The cross sections for low energy neutron interactions are contained in well-known tabulated data. Figures 7-9 contain cross-sections of different interaction types in different materials [19].

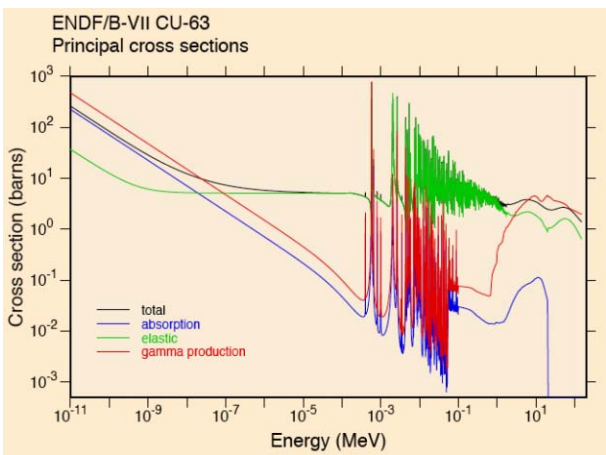

Figure 7: Neutron scattering on copper.

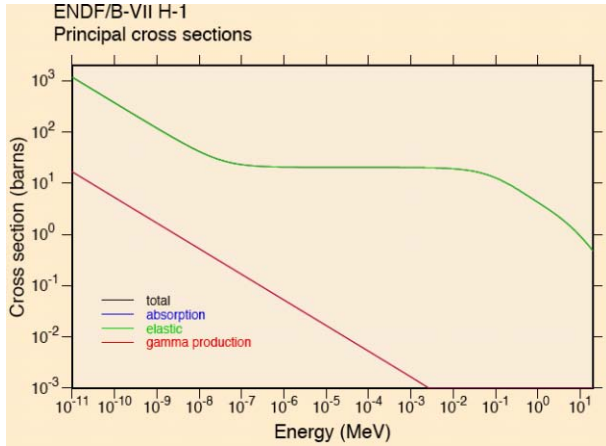

Figure 8: Neutron scattering on hydrogen. The high elastic cross section makes hydrogen the most efficient neutron moderator.

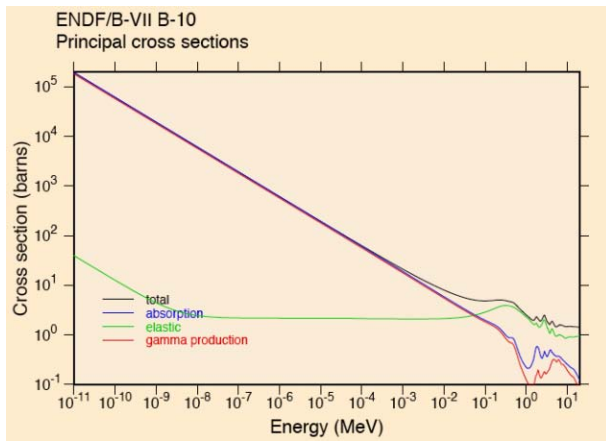

Figure 9: Neutron scattering on boron. High absorption cross section allows boron's use for neutron detection.

Radioactivity

Radioactivity is not directly related to beam loss, but is considered in order to limit residual activation of accelerator elements and surroundings. Also, the residual activation itself is a valuable source of information about beam loss. If the gamma spectrum is measured, one can try to find out what isotopes are producing it, then further estimate this particular isotope production, and finally, estimate beam loss that could cause such production.

Radioactivity is the random process of nucleus disintegration. The number of isotopes decreases exponentially with time (Eq. 7):

$$N(t) = N_0 e^{-\lambda \cdot t} \quad . \tag{7}$$

Historically the isotopes are characterized by the half-life (period after which half the radioactive isotope has undergone decay).

Radiation units [20]

Many radiation units exist, and such a multiplicity often leads to confusion. A loss monitor's signal is usually proportional to energy deposited by radiation in the sensitive volume of the detector or to particle flux inside it. Thus the main unit of interest is the gray (Gy), which is 1 joule of deposited energy per kilogram. Rad is also used; 1 rad = 0.01 Gy.

If a signal is proportional to particle flux, then flux units are used, for example, $1/cm^2/s$ (number of particles per unit area per second).

The other units, less important for BLMs, are:

- Sievert (Sv), a Gy multiplied by a quality factor for biological impact.
- REM or Röntgen Equivalent in Man; 1 REM=0.001 Sv (obsolete unit).
- Curie (Ci); 1 Ci=3.7×10^{10} disintegrations per second.

LOSS MONITOR TYPES

A great variety of loss monitor types exists. We will talk about ionization chambers, scintillators, PIN diodes, secondary emission monitors, and, briefly, Cherenkov light detectors. We will follow an excellent overview given in [21].

Ionization Chamber

An ionization chamber is filled with gas and has a high voltage bias applied to electrodes. The chambers can have different shapes but usually are coaxial cylinders.

Figure 9: SNS ionization chamber. Contents = 113 cm^3 of argon; HV= –1000V; sensitivity 70 nC/rad.

The radiation ionizes gas inside the chamber and the resulting charge is collected by electrodes. The shape of the electrode defines the time characteristics, while the sensitivity depends on the total volume of the chamber. Depending on high voltage (HV), the ion chamber can operate in different modes as shown in Fig. 10. When HV is low, a recombination process takes place before the ions and electrons are actually collected by the electrodes. Increasing the HV brings the chamber into ionization mode when all charge is completely collected. Further increase of the HV leads to the proportional mode, when the ions create secondary ionization and an avalanche.

The most typical mode is ionization because the chamber sensitivity stays the same for fluctuating HV.

The common gases used for ion chambers are argon and nitrogen, but air will work as well. The HV ranges from several hundred V to several kV.

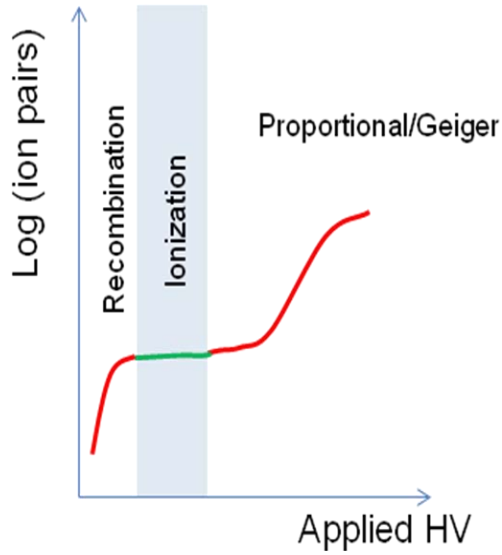

Figure 10: Different modes of ionization chambers.

If time resolution is important, the geometry should be optimized to improve the response time of the ion chamber. The response time of the SNS ion chamber is around 1-2 μs [21]. From the signal side, the ion chamber is a current source, so a transimpedance amplifier is used for analog front end electronics.

The main advantages of ionization chambers include:

- Calibration determined by geometry (no HV dependence).
- No maintenance (even a leaking nitrogen chamber continues to work in air).
- Radiation hard (10^8 rad).

Currently, ion chambers are the main type of loss monitor type used in hadron machines (SNS, LHC, RHIC, Tevatron).

There is also a variation of ion chamber in which the detector is very long (3 m or even longer). An example is shown in Figure 11.

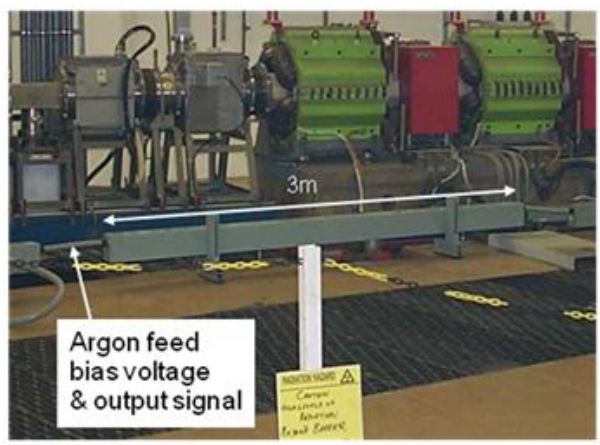

Figure 11: Long ion chamber at ISIS [22].

Solid state Ion Chamber – PIN photodiode

The same principle of charge creation is used in semiconductors. The radiation creates electron-hole pairs and the charge is collected by biased plates as in Fig. 12.

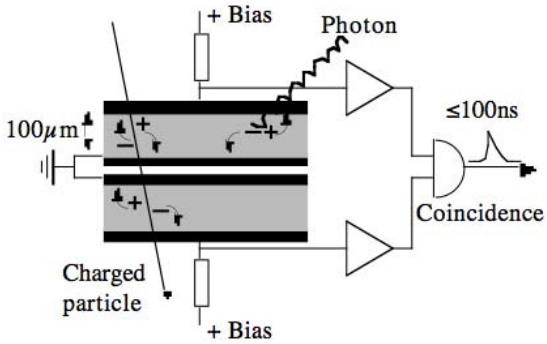

Figure 12: PIN diode schematics in coincidence mode [21,23].

The PIN diode is much faster than the ion chamber, with a response time of about 5 ns. While it can be used in waveform mode, counter mode is more common. The combination of two PIN diodes makes a loss monitor insensitive to gamma radiation (because gammas produce signal in one detector diode only).

Scintillator based detectors

The scintillator based detectors are probably the second most popular for beam loss monitoring, after ion chambers. The scintillation itself is a molecular effect. The fluorescent material emits UV light in response to energy deposited by a particle. This light is in turn absorbed by a material that emits visible light. The visible light is detected by a photocathode. One has to match the wavelengths of these two materials and also match the photocathode sensitivity. A vast review of scintillators is given in [24].

Usually scintillating materials are dissolved in plastics or liquid so it is possible to obtain almost arbitrary shapes. Figs. 12 and 13 show different scintillator based detectors.

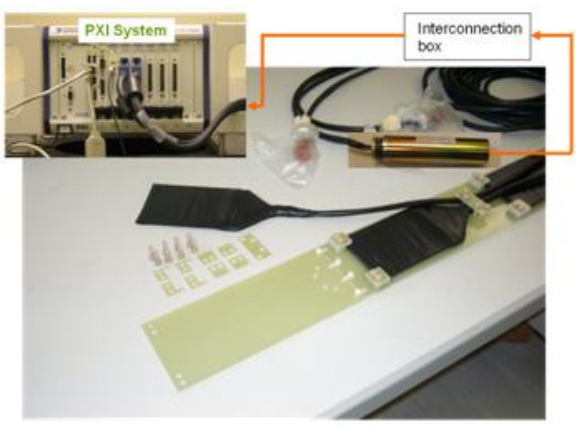

Figure 12: Scintillator detector at ISIS [22].

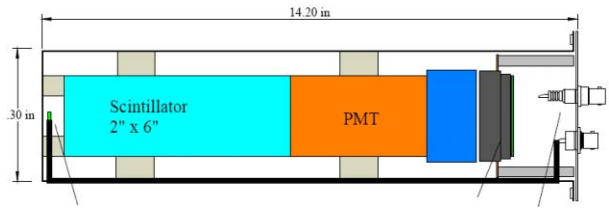

Figure 13: Fast loss monitor at SNS.

The scintillators are usually used with photo-multiplier tubes. This gives a typical signal gain of 10^5–10^8 which can be regulated by the applied HV. This gain is achieved in the accelerator tunnel, which simplifies further signal conditioning (in the case of the ion chamber there is no pre-amplification). See Fig 13.

Modification of the scintillator material can effectively change its sensitivity to different types of radiation. SNS neutron detectors use a scintillator doped with LiFxZnS(Ag) and slow neutrons are detected by means of the ^{6}Li(n,alpha) reaction. In this case, the scintillator detects secondary alphas from this reaction)[18].

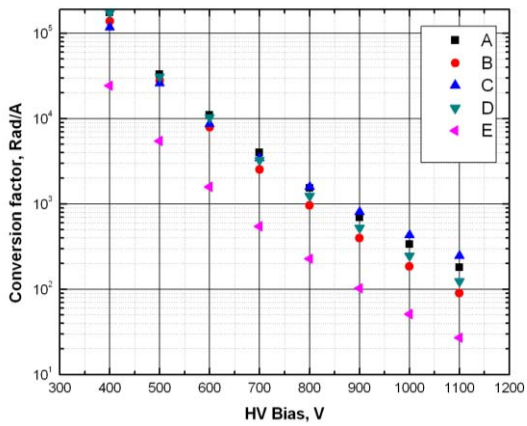

Figure 13: Sensitivity dependence of SNS scintillator-based neutron detectors on HV[18]

Scintillator-based detectors are easy to test with a built-in LED. They have fast response (20-100 ns), and more important, the response time spread is around 1–5 ns.

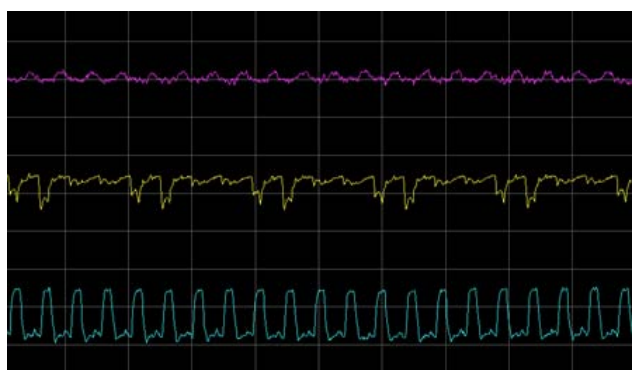

Figure 15: Scope screenshot (2 μs/div) of fast loss monitor at SNS. Detector resolves the ~700 ns mini-pulse structure of the SNS linac.

If a PMT-based detector is used in waveform mode, it effectively represents a current source similarly to an ion chamber. Both detectors require HV of the same scale, so it is often quite easy to use the same set of cables/electronics for both types of detectors.

Scintillators have the big disadvantage of being not being extremely radiation tolerant (~100 kGy decreases sensitivity by factor of 2, but numbers vary greatly depending on scintillator type). The transparency degrades with exposure, making calibration difficult.

Secondary Emission Monitor

The secondary emission monitor (SEM) is somewhat different than detectors discussed earlier. It exploits secondary emission from the surface caused by particles crossing this surface (the detectors discussed above use volume rather than surface as the main sensitive part). Understanding the principles of operation requires solid state physics knowledge. A good introduction to the theory of secondary emission regarding loss monitoring is given in [26].

The secondary yield depends on incident energy according to the Sternglass formula; [25] see Fig. 16.

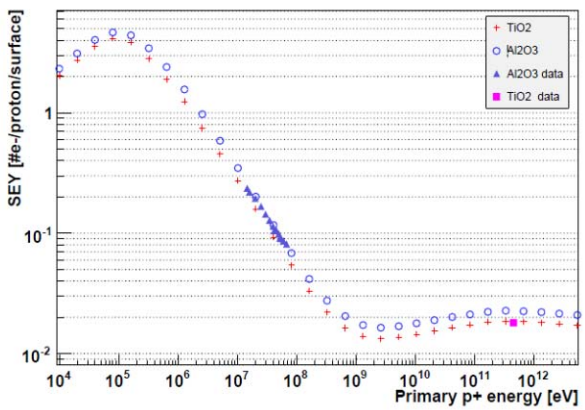

Figure 16: Secondary electron yield per incident proton [26].

The SEMs are very radiation hard and have low sensitivity (see Table 1). It makes sense to put them into high radiation areas where other detectors would be saturated or damaged by radiation. The LHC uses a combination of ionization chambers and SEMs [26].

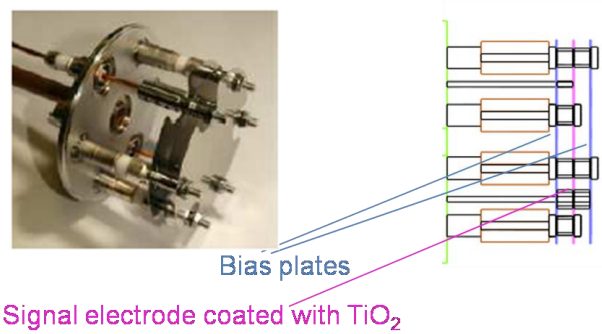

Figure 17: Large Hadron Collider SEM [26].

Cherenkov light detector

When an electron travels in a medium faster than the speed of light in that medium, the medium itself radiates photons. Photon yield is described by

$$\frac{dN}{dx} = 2\pi\alpha \sin^2\Theta \cdot \left(\frac{1}{\lambda_1} - \frac{1}{\lambda_2}\right) \quad , \qquad (8)$$

where $\cos(\Theta) = \frac{1}{\beta n}$, $\alpha = \frac{1}{137}$, and $\lambda_{1,2}$ is the wavelength interval.

Considering photocathode sensitivity, we are interested in a 350-500 nm interval, which gives [21]

$$\frac{dN}{dx} = 390 \sin^2\Theta \cdot \frac{photons}{cm} \quad . \qquad (9)$$

Cherenkov detectors are widely use in light sources. The configuration of the detector is very specific to the accelerator, accounting for electron energy and geometrical factors.

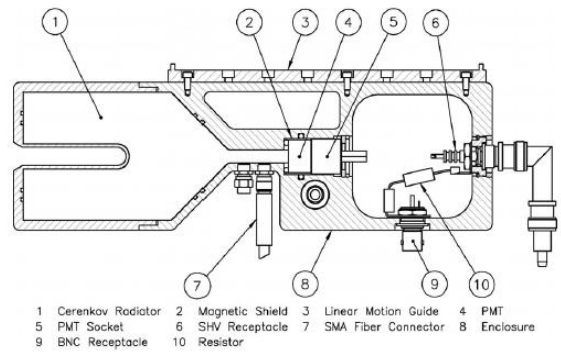

Figure 18: Cherenkov detector at the Linac Coherent Light Source (LCLS) [27].

Other types of detectors

We don't include a detailed discussion of diamonds and fibers in this paper. Diamond detectors are relatively new and not widely used in accelerators, but are quite promising, with high dynamic range, high sensitivity, and radiation hardness [28]. Fiber detectors could be effectively used to determine loss location using the optical transition radiation (OTR) technique [21].

Avalanche diodes [29] can substitute for PMTs in some situations. They are compact and insensitive to magnetic field, but they require very stable temperature and voltage control, and they respond to direct radiation much more strongly than to the light emitted by scintillator. There was an attempt at using avalanche diodes coupled to scintillating fiber at SNS. No significant advantage over PMTs was achieved.

Loss monitor selection

It is hard to come up with a common recipe for loss monitor selection, since the choice will strongly depend on accelerator specifics. Here are generic things to consider:

- Sensitivity and dynamic range.
- Analog output or counter. This choice can significantly affect the system design, so it has to be done very carefully.
- Radiation hardness. The type of radiation is also very important for scintillators and PIN diodes. The "light" radiation (electrons and gammas) usually causes less damage.
- Calibration importance. If absolute values are required, then calibration should be simple or unnecessary (ion chambers).
- Test procedure complexity (an LED could be used for scintillators, but not for ion chambers).
- Time resolution. If beam pulse structure should be resolved, ion chambers are ruled out.
- Reliability.
- Complexity of electronics. An ion chamber will require electronics of large dynamic range; the gain of PMT-based detectors can be adjusted with HV.
- Size and cost. Depending on the goals, the required size could be from several millimeters up to several meters and sometime higher.

Some loss monitor parameters are summarized in Table 1 [21].

Table 1: Sensitivity for different loss monitors.

Detector	Energy to create one e^- [e^-/eV]	Sensitivity [nC/rad]
Plastic scintillator (1 ltr)	250-2500	10^4 $Gain_{PMT}$
Inorganic scintillator (1 ltr)	50-250	10^5 $Gain_{PMT}$
Ion chamber (1 ltr)	22-95	500
PIN diode 1cm^2	3.6	50
SEM (8 cm^2)	2-5% (dE/dx)	10^{-3} $Gain_{PMT}$
Cherenkov light (1 ltr)	10^5-10^6	270 $Gain_{PMT}$

As rough guidance for high intensity hadron accelerators, we would suggest: ion chambers for machine protection; scintillators for good time resolution and changing gain with HV; and SEMs for high radiation areas. For electron machines, the list would be: PIN diodes as a low cost solution and no sensitivity to gammas; Cherenkov detectors; and scintillators.

BEAM LOSS SIMULATION

Ideal BLM system

While no ideal system exists, it is useful to formulate the main features of such a hypothetical system:

- Radiation detector with high dynamic range to be used for both regular (low) loss and irregular (high and fast) loss.
- Sensitive only to radiation caused by beam loss.
- Allows one to find out the amount of beam lost (conversion from radiation intensity to actual number of primary particles).
- Resolves time structure of loss.
- Resolves spatial distribution of beam loss.

Consider the simplified system that accounts for only one type of secondary particle as sketched in Fig. 19.

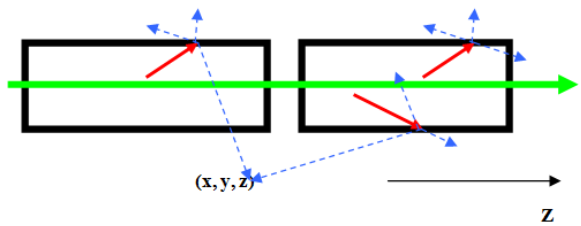

Figure 19: Sketch of beam loss process.

$$N_0 = \iiint N(X,Y,Z)\,dXdYdZ \tag{10}$$

$$L(x,y,z) = \iiint N(X,Y,Z)P(x,y,z,X,Y,Z)\,dXdYdZ \tag{11}$$

$$Ld = \int L(e,x,y,z)S_d(e)\,de \tag{12}$$

where N_0 is the total number of lost particles, $N(X,Y,Z)$ is the spatial density of lost particles, $P(e,x,y,z,X,Y,Z)$ is the probability of secondary particles having energy e reaching position (x,y,z), L is the number of secondary particles in (x,y,z), L_d is the BLM signal, and S_d is the detector response function. To effectively determine $L(x,y,z)$, a computer simulation is used.

The ultimate goal of a BLM system is to solve Eq. (11) and find $N(X,Y,Z)$. Even in the case of an infinite number of ideal BLMs, the solution of (11) could be non-unique. Of course we don't have an infinite number of detectors, so even the measurement of $L(x,y,z)$ presents a challenge.

Figs. 20 and 21 demonstrate that the choice of BLM can significantly change the measured loss pattern. The same losses in the SNS [18] warm linac are measured by different types of detectors: ionization chambers and neutron detectors. The losses are caused by insertion of different Faraday cups. The Faraday cups are installed between Drift Tube Linac (DTL) tanks where beam energy is 7.5 MeV (FC1) to 72.5 MeV (FC5). BLMs are numbered from 1 (installed at ~3 MeV) to 20 (~90 MeV). The ionization chambers respond to nearby loss and thus are able to resolve loss location, but they will be insensitive to loss occurring between two detectors. Conversely, the neutron detectors respond to any loss, close or remote, and are effectively covering a wider region, but are incapable of spatial resolution.

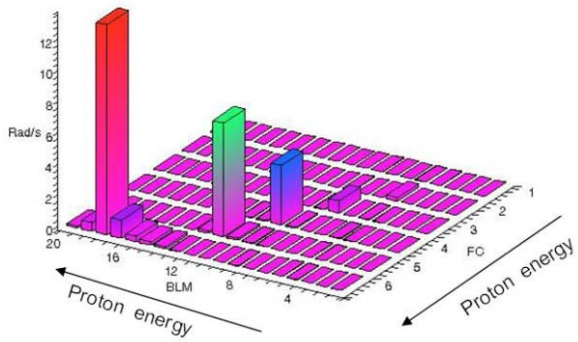

Figure 20: Losses measured by ionization chambers [18].

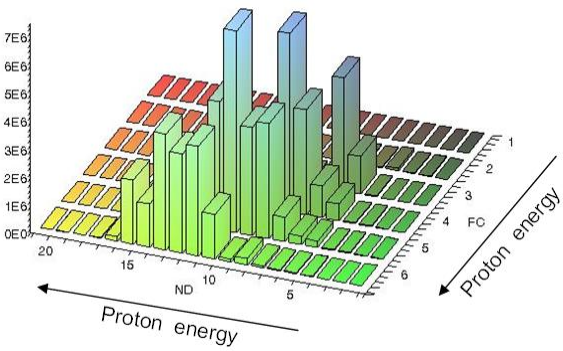

Figure 21: Losses measured by neutron detectors [18].

This is explained by a neutron's ability to penetrate beam pipes (the main materials are copper and steel, which don't attenuate neutrons effectively), whereas ionization chambers detect mainly gammas, which are effectively attenuated by these materials.

Monte Carlo codes

The standard way of simulating radiation propagation in a medium is to employ Monte Carlo codes. Modern codes include vast physics models and capabilities to simulate realistic beam line geometries.

Among most widely used codes are:

- MCNPX (LANL/ORNL) [30].
- MARS (FNAL) [31].
- GEANT4 (CERN/SLAC and others) [32].
- FLUKA (CERN/INFN) [33].
- SHIELD (INR), for hadrons only [34].

A typical simulation would contain stages (each stage using the code that is good for that particular stage) as shown in Fig. 22. It includes loss simulation of primaries by some beam dynamics code (e.g., PARMILA [35]), and then generation of secondaries and their transport in a medium.

While all these codes have some advantages and disadvantages, we will describe GEANT4 as the code that is most flexible for modification and applicable in most situations.

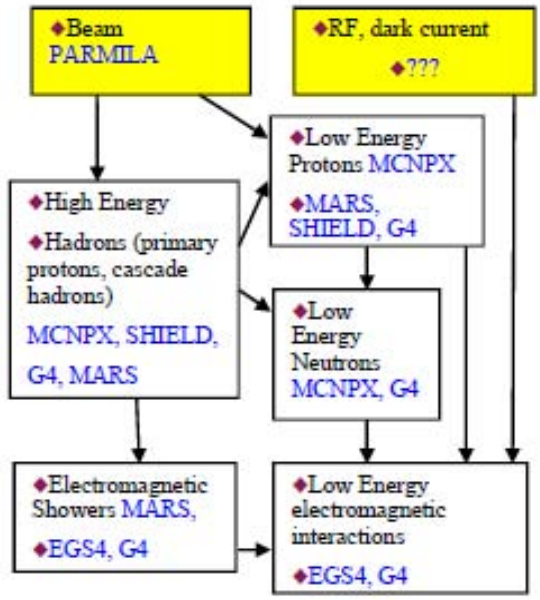

Figure 22: Applicability of different Monte Carlo codes to loss simulation.

GEANT4

The very important difference between GEANT4 (G4) and other simulation codes is that it is not a final, user-ready program but a toolkit. It is written in C++ while almost all others are FORTRAN. The use of Object Oriented Design allows effective decoupling of different physics models and other modules. To understand or modify an existing physics model, one need only examine the piece of code responsible for this particular type of interaction. This allows user to apply expertise in a narrow specific field without danger of influencing the other parts of the code, where default models could be used. Different statistical techniques (such as event biasing or Russian roulette) can be easily added as needed. Deep granularity of physics processes makes possible to apply different models to the particles at different energies and in different geometrical locations.

Usually the process of geometry definition is difficult and tedious, since different codes use different input formats that are not always compatible. G4 allows importation of CAD system files, so one can concentrate on physics processes rather than on geometrical assumptions and configuration. It has powerful visualization tools and its quality is comparable to CAD visualization.

Like all other Monte Carlo codes, G4 is easily parallelizable, and performance per CPU stays almost constant with an increasing number of CPUs.

G4 contains different physics models, and the user can define which one to use. The electromagnetic interactions include:

Photon processes

- γ conversion into e^+ e^- pair
- Compton scattering
- Photoelectric effect
- Rayleigh scattering
- Gamma-nuclear interaction in hadronic sub-package

Electron and positron processes

- Ionization
- Coulomb scattering
- Bremsstrahlung
- Nuclear interaction in hadronic sub-package
- Positron annihilation

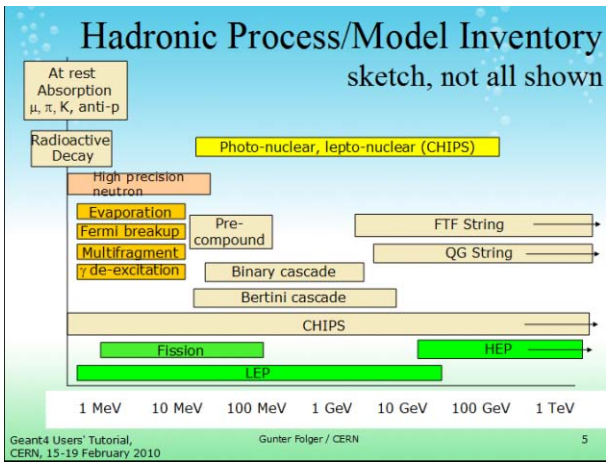

Figure 23: Hadronic models in G4 [36].

One of the possible extensions of G4 physics is described in [26] where a model of secondary electron emission is added to standard G4 to simulate SEM loss monitors at LHC.

Common use cases

The simulations are frequently used for calculations of thresholds for machine protection [37]. This is a straightforward simulation when the loss rate is limited by equipment specifics and the BLM response signal is simulated for the maximum allowable loss rate.

The other quite common application is obtaining knowledge about the loss monitor detector itself, i.e., calculating the detector response function L_d. A rigorous investigation was done by the LHC team to build detector response functions for their BLMs[37].

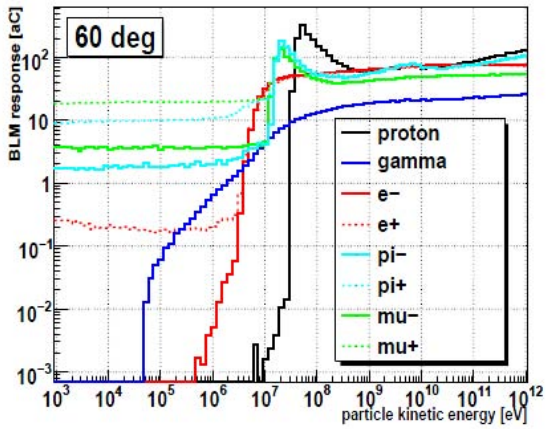

Figure 24: LHC BLM response function [37].

A good way to benchmark simulations is to create intentional loss and measure the BLM's response. The response of neutron detectors to insertion of Faraday cups (Fig. 25) was simulated with the code SHIELD.

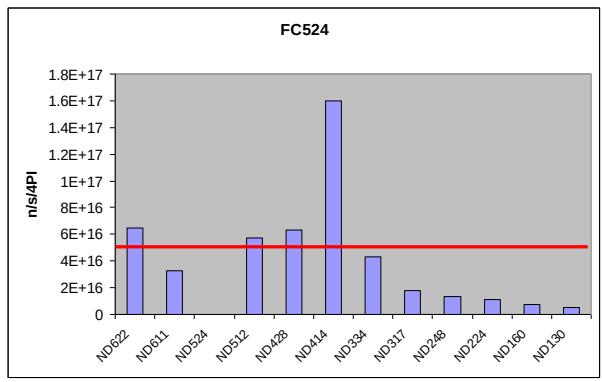

Figure. 25: Neutron detector measurements (blue bars) vs. simulation (red line) [18].

Fig. 25 demonstrates that ND414 was not calibrated correctly and that either the angular distribution is incorrect in the model or the geometrical assumptions are poor (remote detectors in a backward direction show lower signal than the measurement).

Proposed loss simulation for new machine

As previously mentioned, it is now possible to import CAD geometry into the simulation program. Therefore, it would be beneficial to have the whole machine designed in one CAD package. The process of loss simulation could be briefly described with the following steps.

The machine setup (geometry/materials/fields) should be imported into G4. Machine specific loss physics has to be researched:

- Perform benchmarking of G4 with other codes (MCNPX, FLUKA, MARS) for physics models of interest for several primitive geometry test cases.
- Compare simulation data with experiment.
- Rule out discrepancies.
- Modify G4 physics.

The most probable loss locations can be obtained from accelerator physics specialists, and corresponding loss scenarios should be simulated to obtain a feeling for the loss pattern and scale. This will allow determination of a detector candidate.

The list of loss sensitive equipment should be collected as soon as possible and the maximum admissible losses simulated. This will give the prediction of threshold levels and offer detector candidates dedicated to machine protection.

Considering the BLMs as tuning devices will probably result in a completely different list of requirements and will lead to different detector candidates.

Additional tasks: Try to build a model of an ideal detector that will satisfy all requirements. Perform simulation of the ideal detector's response to insertable devices. Perform "scan" simulations (for different point losses along the machine) of the whole accelerator and build the function P(x,y,z,X,Y,Z) from (11).

While it seems to be very hard to implement, it is quite possible with current computing power, and will be easier in the future. This procedure reverses the common process in which existing designs are simulated—it actually allows simulations to drive the design.

MACHINE PROTECTION SYSTEM (MPS)

Almost all high power/high energy machines use BLMs in a protection mechanism that inhibits the beam if loss exceeds some threshold. It is extremely important in hadron machines. We will compare the MPS systems of SNS [38] and LHC [39,40] to demonstrate the evolution during the last two decades.

The SNS BLM protection system is an "old school" analog-based design where the loss signals from ~350 BLMs are integrated by analog integrators and afterwards compared with a DAC level representing the maximum permissible loss level. The detector signals (current from ionization chambers or PMTs) are brought from the accelerator tunnel, then amplified in the Analog Front End (AFE), and then split into three signals to be fed into the digitizer and integrator. The leaky integrator discharges itself before the next pulse comes (in 16 ms).

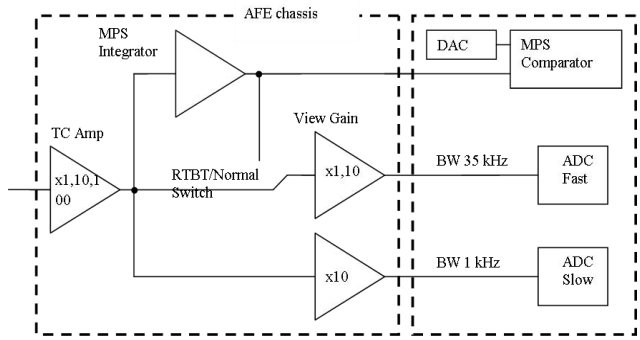

Figure 26: SNS AFE schematics.

The comparator interlocks the beam within 15 microseconds after the integrated signal exceeds the threshold. In addition to this fast hardware-based limit, a slow 1 second limit is calculated in software. In this way, SNS has two limits per BLM. One is purely hardware-based and the second one is software-based.

The LHC MPS system [39] consists of more than 3500 BLMs and uses an FPGA-based design. The analog current signal is converted into a frequency signal and 40 microsecond sum, which is pushed into an FPGA. Several running sums are calculated (with time windows from 40 microseconds to several seconds).

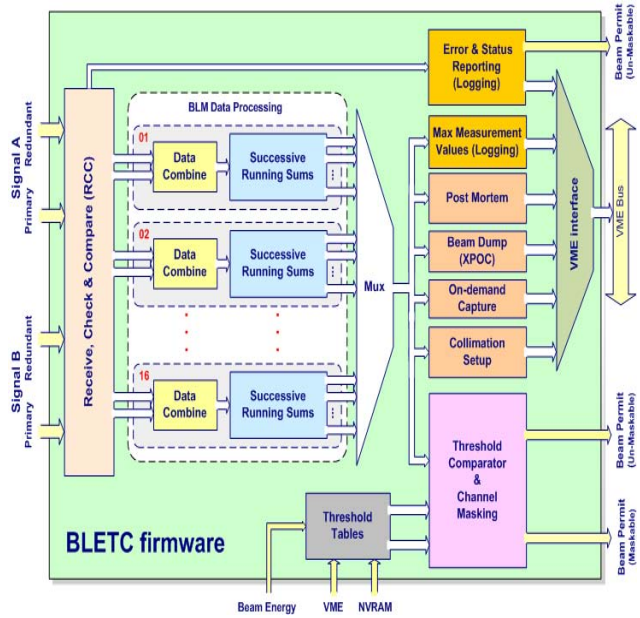

Figure 27: The schematic of LHC MPS [40].

The limits depend on beam energy so every BLM effectively has a two-dimensional array of limits. All limits are calculated by the FPGA.

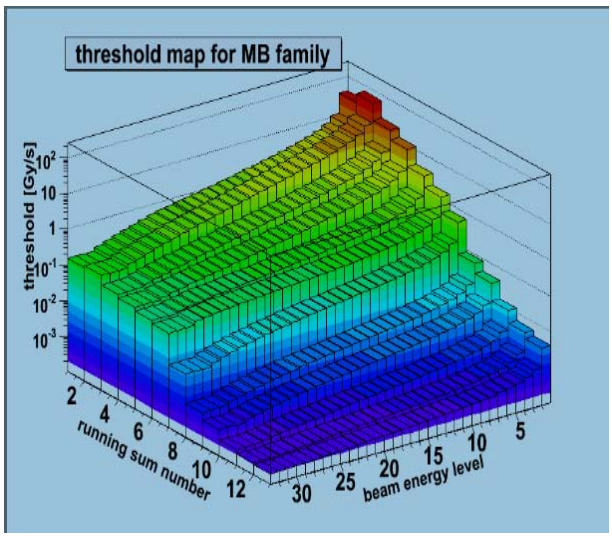

Figure 28: Two-dimensional array of limits for LHC BLM [39].

The functionality of hardware-based and software-based interlocking is merged into an FPGA, introducing much higher degree of flexibility. Table 2 summarizes these two approaches.

Table 2: Analog vs FPGA based MPS design

	Analog (SNS)	**FPGA (LHC)**
Analog FE	Outside of the tunnel (current signal over long cables)	In the tunnel, digital link to controlling FPGA
Integration	Hardware integration one window (16mS leaky integrator)	FPGA digital integration many windows
Additional Integration	Software integral over 1 second	N/A
Limits	Set by software, reinitialized every IOC reboot	Limits set in software and loaded into non-volatile memory in FPGA
Timing System	Independent	Independent
Preamplifier Gain	Jumper settings	N/A
Reliability	Analog component	Complex FPGA code verification procedure
HV distribution	Daisy chained 1-4 BLMs with HV current/HV voltage monitoring in software. Next generation system will have a dedicated PS per BLM.	Daisy chained over 400-600 BLMs with 2 redundant HVPS, FPGA monitoring of HV health

CONCLUSIONS

There are many ways to detect beam losses, but no single best way because every machine is different. Ion chambers remain the most widely used detectors, especially among hadron machines. The new advances in materials improve loss monitor characteristics, but the underlying physics principles are the same—usually it is ionization loss Eq. (1-2).

Computer simulations are widely used in BLM design, and it will probably step up to the next level in the nearest future.

The electronics used to interface BLMs to the machine protection system changed significantly with availability of FPGAs.

ACKNOWLEDGEMENT

ORNL/SNS is managed by UT-Battelle, LLC, under contract DE-AC05-00OR22725 for the U.S. Department of Energy.

REFERENCES

Three books are extensively cited in this paper. *Particle Detectors* [3] and *Radiation Detection and Measurement* [2] give brilliant overviews of detectors and detector principles. *An Introduction to the Passage of Energetic Particles through Matter* [1] thoroughly discusses different physics processes and contains compilation of many data sources regarding cross-section and other experimental data.

[1] N.J. Carron , *An Introduction to the Passage of Energetic Particles through Matter*, Taylor & Francis, 2007.
[2] G. Knoll, *Radiation Detection and Measurement*, third edition, John Wiley & Sons, 2000.
[3] G. Grupen, B.A. Shwartz, *Particle Detectors*, second edition, Cambridge University Press, 2008.
[4] Ibid, pp. 2-11.
[5] M.J. Berger et al "Stopping-Power and Range Tables for Electrons, Protons, and Helium Ions", NIST, http://www.nist.gov/physlab/data/star/index.cfm.
[6] G. Grupen, B.A. Shwartz, *Particle Detectors*, 2nd ed., Cambridge University Press, 2008, pp. 32-33.
[7] Ibid, pp. 34-35.
[8] Ibid, pp. 36-37.
[9] Ibid, pp. 38-41.
[10] Klein, O; Nishina, Y (1929). Z. f. Phys. **52**: 853 and 869.
[11] http://en.wikipedia.org/wiki/Klein%E2%80%93Nishina_formula.
[12] V. E. Weisskopf and D. H. Ewing. Phys. Rev. **57**, 472 (1940).
[13] I. Frenkel, Sov. Phys. **9**, 533 (1936).
[14] J.P. Bondorf, A. S. Botvina, A.S. Iljinov, I.N. Mishustin , K. Sneppen., Physics. Reports. **257**, 133 (1995).
[15] E. Fermi, Prog. Theor. Phys. **5**, 1570 (1950).
[16] ENDF/B-VI: Cross Section Evaluation Working Group, ENDF/B-VI Summary Document, Report BNL-NCS-17541 (ENDF-201) (1991), edited by P.F. Rose, National Nuclear Data Center, Brookhaven National Laboratory, Upton, NY, USA.
[17] M. P. Guthrie, R. G. Alsmiller and H. W. Bertini, Nucl. Instr. Meth. **66** (1968), 29.
[18] A. Zhukov, S.Assadi "Beam Loss Simulation of SNS LINAC", FRPMN060, in Proceedings of the Particle Accelerator Conference (PAC 07), Albuquerque, New Mexico, 25-29 Jun 2007, p. 4138.
[19] ENDF/B-VII Incident-Neutron Data, http://t2.lanl.gov/data/neutron7.html.
[20] G. Grupen, B.A. Shwartz, *Particle Detectors*, 2nd ed., Cambridge University Press, 2008, pp. 71-76.
[21] K. Wittenburg, "Beam Loss Monitors", CERN Accelerator School 2008, http://cas.web.cern.ch/cas/France-2008/Lectures/Wittenburg-BLM.pdf.
[22] D.J. Payne et al, "Beam Diagnostics at ISIS", Workshop on High Intensity, High-Brightness Hadron Beams, August 25-29, 2008 http://ics-web4.sns.ornl.gov/hb08/WGF10.PDF.
[23] J. Bergoz, personal communication.
[24] G. Knoll, *Radiation Detection and Measurement*, third edition, John Wiley & Sons, 2000, pp. 219-265.
[25] E.J. Sternglass, Theory of Secondary Electron Emission by High-Speed Ions, Phys.Rev. 108(1957)1.
[26] D. Kramer, "Design and Implementation of a Detector for High Flux Mixed Radiation Fields", PhD thesis, http://ab-div-bdi-bl-blm.web.cern.ch/ab-div-bdi-bl-blm/Talks_and_papers/Kramer/thesis_DKramer.pdf.
[27] W. Berg et al., "Development of a Beam Loss Monitor System for the LCLS Undulator Beamline", TUP043, in Proceedings of LINAC08, Victoria, BC, Canada,http://epaper.kek.jp/LINAC08/papers/tup043.pdf.
[28] E. Griesmayer, "Diamond Detectors as Beam Monitors", these Proceedings.
[29] G. Knoll, *Radiation Detection and Measurement*, third edition, John Wiley & Sons, 2000, pp. 287-292.
[30] MCNPX, Version 26E, LA-UR-07-6632 2007, https://mcnpx.lanl.gov/opendocs/versions/v26e/v26e.pdf.
[31] N.V. Mokhov, S.I. Striganov, "MARS15 Overview", Fermilab-Conf-07/008-AD (2007), in Proc. of Hadronic Shower Simulation Workshop, Fermilab, September 2006, AIP Conf. Proc. 896 (2007) 50-60.
[32] J.Apostolakis et al., "Geometry and physics of the Geant4 toolkit for high and medium energy applications", Radiation Physics and Chemistry **78** (2009), 859-873.
[33] F. Ballarini et al., "Nuclear models in FLUKA: present capabilities, open problems and future improvements" ND2004, Santa Fe, 26 Sep - 1 Oct 2004, SLAC-PUB-10813.
[34] N.M.Sobolevsky, "The SHIELD Transport Code: a Tool for Computer Study of Interaction of Particles and Nuclei with Complex Media," in Proceedings of the 3rd Yugoslav Nuclear Society International Conference (YUNSC 2000), Belgrade, October 2-5, 2000. The VINCA Institute, Belgrade, 2001, p. 539.
[35] Phase and Radial Motion in Ion Linear Accelerators (PARMILA), http://laacg.lanl.gov/laacg/services/download_PMI.phtml.
[36] Geant4 Users' Tutorial, CERN, Feb. 15-19, 2010 http://indico.cern.ch/conferenceDisplay.py?confId=58317.
[37] M. Stockner, "Beam Loss Calibration Studies for High Energy Proton Accelerators", thesis http://cdsweb.cern.ch/record/1144077/files/CERN-THESIS-2008-099.pdf.
[38] Witkover, R. L. and Gassner, D., "Preliminary Design of the SNS Beam Loss Monitoring System", BIW2002, AIP Conf Proc 648 (2002).
[39] B. Dehning et al., "First Experience with the LHC Beam Loss Monitoring System", CERN-ATS-2009-025, pesented at the Particle Accelerator Conference (PAC09) May 4-8 2009, Vancouver, Canada.
[40] C. Zamantzas, "Reliability Tests of the LHC Beam Loss Monitoring FPGA Firmware", TUPSM089, these proceedings.
[41] C.T. Chantler et al "Detailed Tabulation of Atomic Form Factors, Photoelectric Absorption and Scattering Cross Section, and Mass Attenuation Coefficients for Z = 1-92 from E = 1-10 eV to E = 0.4-1.0 MeV", NIST, http://www.nist.gov/physlab/data/ffast/index.cfm

HIGHLIGHTS FROM DIPAC 2009

V. Schlott, PSI, Villigen, Switzerland

Abstract

The 9th European Workshop on Beam Diagnostics and Instrumentation for Particle Accelerators (DIPAC 2009) was hosted by Paul Scherrer Institute (PSI) and took place at the Hotel Mercure Conference Center in Basel, Switzerland from May 25th – 27th 2009. A record number of 210 registered participants contributed to an exciting scientific program with ten invited talks, fourteen contributed orals and 118 poster contributions. In this talk, I will provide an overview of the various fields of beam instrumentation, which have been discussed during the workshop. A number of highlights from the scientific program have been selected, illustrating some of the outstanding achievements in accelerator diagnostics, which have been presented at DIPAC 2009.

INTRODUCTION

The DIPAC workshop series represents the European pendant to the biannual Beam Instrumentation Workshop in the US. The 9th DIPAC edition [1] was held by Paul Scherrer Institut (PSI) at the Hotel Mercure Conference Center in Basel, Switzerland from May 25th – 27th 2009. As a strong increase in the number of participants could already been observed at DIPAC 2007 in Venice (189 participants), DIPAC 2009 reached a record number of 206 registered participants presenting 142 contributions (10 invited, 14 contributed talks and 118 poster presentations). Since the workshop duration of 2½ days needed to be kept due to organizational reasons, the program committee decided to omit the parallel discussion sessions in favour of an additional (third) poster session, while providing sufficient time for discussions during the 7 plenary oral sessions. An industrial exhibition, a workshop dinner in Schloss Bottmingen and an optional visit of the accelerator-based large research facilities at PSI completed the workshop program. The scientific program of DIPAC 2009 could be divided into the following categories:

- diagnostics overviews and commissioning experience
- BPM systems and position stability / stabilization
- transverse profile and emittance measurements
- beam charge and loss monitors
- longitudinal diagnostics, timing & synchronization

The vast majority of the presentations were of excellent quality and almost all of the presenters submitted their papers by the end of the workshop, so that the proceedings could be made available over JACoW [2] and in a printed hard copy within 4 months after the event.

For this paper, I have selected highlights from each of the above categories, trying to spread the choices over the different accelerator types and particle species at the same time. Still, the list of the quoted contributions is of course not complete and my personal interest and present field of work has certainly influenced the selection.

COMMISSIONING EXPERIENCE

Almost 20 contributions presented an overview of diagnostics systems for specific accelerators and reported about the first commissioning experiences with their beam instrumentation.

First Experiences with LHC Beam Diagnostics

Rhodri Jones reported on the first results from LHC beam diagnostics, which could be obtained during injection tests and the subsequent days of circulating beam in LHC [3]. Thanks to years of planning, testing, hardware commissioning and excellent collaborations with internal and external groups, all LHC diagnostics devices were available and operational from the very beginning. Injection and the first turn in LHC could be observed on a 1 mm thick alumina screen by the LHC beam observation (BTV) system on 10/9/2008.

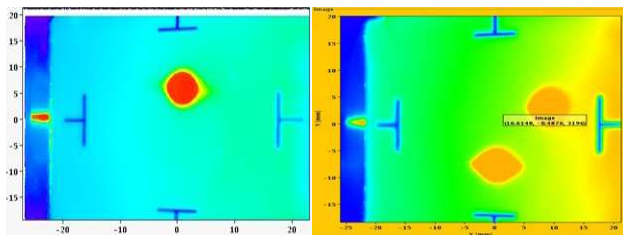

Figure 1: First injection into LHC (left side) and first full turn in LHC (right side) as recorded by the BTV system. Courtesy of Rhodri Jones.

The signal to noise level of the beam loss monitor (BLM) system, consisting of over 4000 N_2 filled ionisation chambers and secondary emission monitors, is 2 orders of magnitude lower than the signal from the pilot bunch ($2x10^9$ protons). This should be sufficient to allow safe and quenchless injection with a total intensity up to $5x10^{11}$. Likewise, the high sensitivity of the beam charge monitors (~ $7x10^8$ protons or 1.3 μA and a dynamic range from $2x10^9$ to $5x10^{14}$) allowed the observation of the first circulating beam in ring 2.

The 1054 BPMs in combination with the powerful on-line optics software provided in the beam threading mode first turn position data to allow for checks of BPM polarity and machine optics errors. The BPM system resolution of ~ 5 μm in orbit mode with a single pilot bunch confirmed the lab sensitivity measurements. Still, electronics drifts induced by air temperature variations could be observed in some locations.

The availability of the tune, chromaticity and coupling measurements at an early stage, being capable of measuring tunes with only a few turns allowed to adjust

injection tunes in order to circulate the beam long enough to attempt the first RF beam capture.

LCLS Commissioning and Cavity BPMs

Clearly, one of the highlights at DIPAC 2009 was the report from Steve Smith on the LCLS commissioning presenting the first exciting results, which have been obtained with lasing at 1.5 Å in the nominal "250 pC mode" and the short-pulse "20 pC operation mode" of the LCLS accelerator.

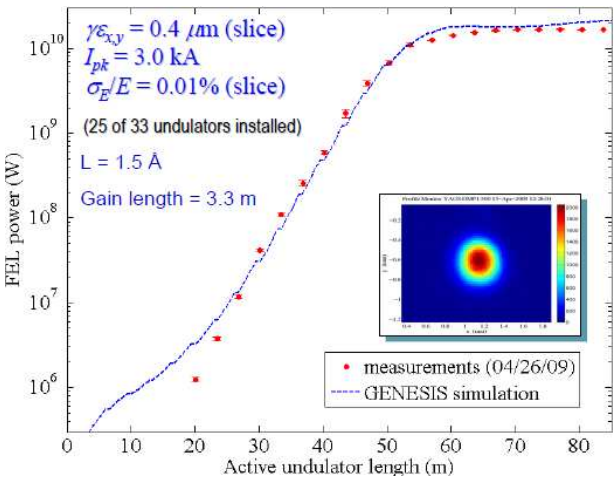

Figure 2: FEL power gain length measurement at 1.5 Å made by kicking the beam after each undulator sequentially (red points), a prediction (blue line) and the laser spot on a YAG screen [4]. Courtesy of Steve Smith.

A short overview of the LCLS diagnostics system was provided, highlighting the important contribution of the X-band cavity beam position monitor system (SLAC and Argonne National Laboratory collaboration) to the successful and very efficient LCLS commissioning. A more detailed description of this system will be given in the following paragraph.

Beam Diagnostics for XFEL / SRing8

Hirokazu Maesaka reported on the experience and results from the XFEL / Spring8 diagnostics systems, which have been achieved at the SCSS test facility [5]. Compact, low Q cavity BPM pick-ups resonating at 4760 MHz and made from stainless steel have been designed as precision BPMs for the undulator sections. Their position resolution including a IQ demodulation electronics and a 12 bit VME ADC has been determined with a dedicated test set-up to ~ 200 nm (rms) at 0.3 nC beam charge. By using the monopole cavity signals from two adjacent BPMs and comparing their phase differences, the arrival time jitter of the SCSS electron beam could be measured to ~ 50 fs (rms) with a resolution of 27 fs.

In addition, the design and test of a high resolution imaging system for beam profile measurements has been presented. The customized lens system is mounted on a motorized translation stage to provide a 1x to 4x magnification. The optical resolution was determined to 2.5 μm (HWHM) using a grid distortion target. Figure 3 shows a comparison of profile measurements with the horizontally focused 250 MeV SCSS beam. The images were taken with a 100 μm thick stainless steel OTR screen and a YAG:Ce screen.

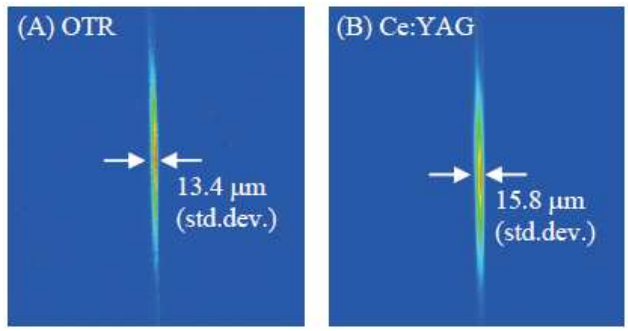

Figure 3: Beam images taken by an OTR screen (A) and a YAG:Ce screen (B). The magnification of the lens system was set to 4. Courtesy of Hirokazu Maesaka.

Finally, the design of a 1.7 m long C-band travelling wave RF deflecting structure, named RAIDEN, was presented. It is a periodically disk-loaded waveguide with race track shaped irises to separate horizontal and vertical modes. Two of these RAIDEN structures will be used in the XFEL / Spring8 allowing bunch length and sliced beam parameter measurements with a few fs time resolution.

Further Commissioning Reports

The new hard x-ray synchrotron radiation source PETRA III has been commissioned at DESY, Hamburg. Klaus Balewski reported on the first beam physics and commissioning results and summarized the performance of the diagnostics systems [6]. He highlighted a fast current monitor for control of top-up operation, a wire system, which monitors mechanical movements of BPM blocks and the X-ray diagnostics beam line using a compound refractive lens and a pinhole camera for measurement of the ultra-low (1 nmrad) emittance beam.

Yongbin Leng gave an overview of the SSRF (Shanghai Synchrotron Radiation Facility) beam instrumentation and reported on the commissioning results of their diagnostics systems [7]. The LIBERA BPM system allowed them to obtain high precision beam position information in the LINAC (33 μm single-shot) as well as turn-by-turn (3 μm @ 694 kHz) and closed orbit data (200 nm @ 10 Hz) in the storage ring. Their diagnostics beam line is equipped with two visible light synchrotron radiation interferometers for determination of beam sizes (< 10 μm spatial resolution), a fast, gated (3 ns gate width) camera for injection studies and a 2-D streak camera (Hamamatsu C5680) for bunch length and multi-bunch instability studies. For damping of these instabilities, a digital transverse multi-bunch feedback system has already been commissioned.

BPM SYSTEMS AND BEAM STABILITY

Almost 40 contributions reported on the design of BPM pick-ups and electronics and dealt with all aspects of beam position stability in different accelerator types. In this respect, BPM systems and beam stability turned out to be an "evergreen" topic during DIPAC 2009.

Beam Position and Orbit Stability

Boris Keil reviewed the beam stability and BPM system requirements for linear and circular accelerators [8]. He compared different pick-up types and electronics circuits for sub-micron beam position measurements in view of their applicability in different accelerator types. For storage ring based light sources with low emittance and low coupling, he stated that the fulfilment of the $\sigma/10$ stability criterion not only demands sub-micron beam position measurements at kHz bandwidth to allow for global and local orbit feedbacks, but that it also requires an overall stability concept, which includes features like top-up operation, filling pattern feedbacks, temperature control and the inclusion of photon monitors. In LINAC-based light sources beam-based alignment (BBA) of the undulator segments represents the driving factor for sub-μm BPM resolution and extremely low drift performance. Thus, BBA methods like dispersion free steering permit the alignment of undulator segments on a micron level.

Nicolas Hubert presented the latest achievements in beam orbit stability at 3rd generation light sources [9]. He presented an overview of orbit feedback implementations in storage rings world-wide (see table 1).

Table 1: overview of orbit feedbacks in SR light sources

SR Facility	FB type (user mode)	# of sets of correctors	Bandwidth
ALBA*	fast	1	DC – 130 Hz
ALS	slow & fast	1 (fast corr. are subset of slow ones)	DC – 60 Hz
APS	slow & fast	1 (fast corr. are subset of slow ones)	DC – 100 Hz
DIAMOND	fast	1	DC – 130 Hz
ELETTRA	fast	1	DC – 150 Hz
ESRF	slow & fast	2	DC – 150 Hz
ESRF-U*	fast	1	DC – 150 Hz
NSLS II*	slow & fast	2	DC – 500 Hz
PETRA III*	slow & fast or only fast	2	dead band or DC – 500 Hz
SLS	fast	1	DC – 100 Hz
SOLEOL	slow & fast	2	DC – 250 Hz
SPEAR3	fast	1	DC – 100 Hz
SSRF*	slow & fast	2	DC – 100 Hz

* feedback systems that are not yet commissioned

He explained the concepts of global and local orbit feedbacks and reviewed the performance requirements of sub-system components to allow for sub-micron stability from DC to a few hundred Hz. As the most efficient orbit correction strategy, he identified the interaction between fast and slow orbit feedback systems. In this scheme, the slow system corrects for the difference between the actual and the "golden" orbit and removes the orbit created by the DC component of the fast correctors, while fast orbit feedback corrects any transient disturbance in the storage ring. Applying this approach, SOLEIL could improve long term stability at the bending magnet source points in the vertical to about 2 μm.

BPM Pick-Up Design and Cavity BPMs

Piotr Kowina presented the successful application of FEM-based (finite element methods) simulations to design characteristic features of BPM pick-ups leading to optimized BPM realizations in hadron accelerators [10]. As examples from the FAIR project [11], he presented the optimization steps in the design of a linear cut BPM for proton and ion synchrotrons and a button-type BPM for low energies ($0.1 \leq \beta \leq 0.37$) in proton LINACs. For the linear cut BPM, the insertion of separating rings between the electrodes increased the position sensitivity by a factor of two. In case of the button-type BPM, the frequency dependent position sensitivity of low β beams was compared for the first three harmonics of the accelerator frequency at 325 MHz, 650 MHz and 925 MHz. The resulting two dimensional position maps are presented in figure 4 for $\beta = 0.1$ and $\beta = 0.3$.

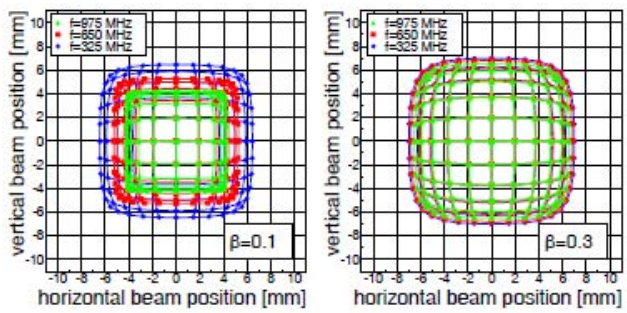

Figure 4: Response of button-type BPM on variation of transv. beam position for $\beta = 0.1$ (left) and $\beta = 0.3$ (right). Courtesy of Piotr Kowina.

The operating principle of high resolution cavity BPMs, which are typically used in high energy electron accelerators, was explained by Dirk Lipka and examples of recent developments and measurement results from LCLS, Spring8 / XFEL, European XFEL and ILC were presented [12]. As an impressive example from a successfully commissioned XFEL facility, Steve Smith presented the design and performance of the LCLS X-band cavity BPMs [13]. The 10 mm diameter TM_{010} monopole mode and the position sensitive TM_{110} dipole mode copper cavities are 36 mm apart, providing 130 dB isolation. The cavities are installed between the undulator segments and connected via rigid waveguides to the 3-channel heterodyne receiver electronics, which is placed below the undulator stands. The x, y and reference signals

are down-converted to an intermediate frequency of 25 - 50 MHz, digitized at a sampling rate of 119 MS/s by a 4-channel, 16 bit VME digitizer in the technical gallery. Undulator BPMs are typically calibrated by mechanically moving the cavity pick-ups, while transfer line BPMs, which are not mounted on movers, are calibrated by moving the beam. BPM resolution has been determined with stable beam (< 10 μm jitter) via correlation between BPMs, using least-square fits of the predicted BPM position as a linear combination of the position measured in adjacent BPMs. Typical (median) resolutions of $\sigma_x \sim 440$ nm with few above 1 μm and $\sigma_y \sim 230$ nm with none above 1 μm have been achieved.

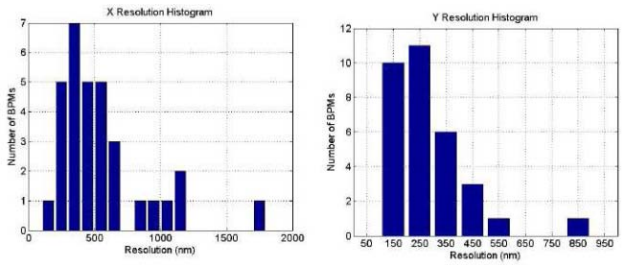

Figure 5: Histogram of measured LCLS X-band cavity BPM resolutions. Courtesy of Steve Smith.

TRANSVERSE PROFILE MONITORS

Almost 40 contributions dealt with the measurement of transverse profiles and emittances in various types of accelerators. A large variety of physical properties and techniques such as transition, diffraction and synchrotron radiation, wire and laser scanners as well as fluorescence and ionization of residual gases have been applied to visualize the particle beams.

SNS Electron Scanner

For the non-invasive measurement of the transverse beam profile in the Spallation Neutron Source (SNS) accumulator ring, an electron scanner has been designed by the Budker Institute of Nuclear Physics and Willem Blokland presented the first experimental results with this device [13].

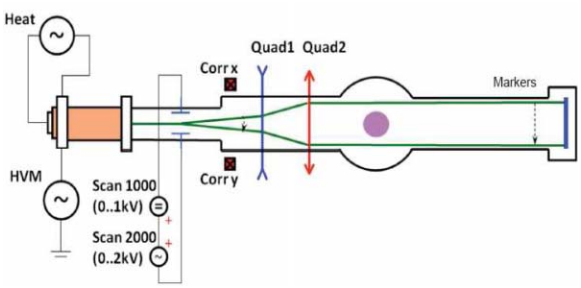

Figure 6: Schematic Diagram of SNS electron scanner. Courtesy of Willem Blokland.

A 75 keV electron beam is projected on a diagonal line by a pair of deflector plates and sent through the proton beam. This titled sheet of electrons is deflected from a straight line when passing through the proton beam and the projection can be visualized on a phosphor screen at the end of the electron scanner. The derivative of the projection results in the transverse proton beam profile. The deflector plate ramp time of 20 ns allows viewing of 3-dimensional bunch profiles or the visualization of profiles from any turn during the accumulation cycle.

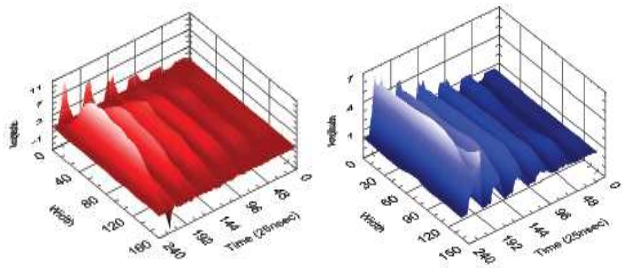

Figure 7: Bunch profiles from multiple accumulation turns. Horizontal (red) and vertical (blue) scales are given in pixels of 0.3 mm, time scale is in 25 ns per count. Courtesy of Willem Blokland.

Studies of Light Yield from Gases and Screens

For online transverse profile measurements of high intensity ion beams, Frank Becker studied the beam induced fluorescence (BIF) of different residual gases (Xe, Kr, Ar, He, N_2) by using an imaging spectrograph in the visible spectral range [14]. After irradiation with 5 ms long beam pulses of $3 \cdot 10^{11}$ S_{6+} ions at 5.16 MeV/u, nitrogen gas could be identified as the most suitable choice for a BIF profile monitor, providing the highest light yield and undistorted profile widths.

Gero Kube investigated the light yield of luminescent screens of different materials, having been illuminated by high energy (855 MeV) and high brilliant electron beams at the X1 beam line of the Mainz Microtron MAMI [15]. He compared YAG:Ce with diamond, Al_2O_3, Al_2O_3:Cr (Cromox), ZrO_2 (Z700-20A) and ZrO_2:Mg (Z507). Although the beam profiles measured with YAG:Ce screens were slightly distorted, it seems to be the most suitable material, providing the highest light yield (one order of magnitude more than Cromox) without showing any material degradation as in case of ZrO_2.

LONGITUDINAL DIAGNOSTICS

More than 20 contributions dealt with the measurement of longitudinal particle beam properties, such as bunch pattern and bunch lengths, beam arrival time and the implementation of highly stable reference systems for synchronization of particle beams with accelerator sub-systems on a femto-second scale.

Sliced Beam Parameter Measurements

The application of standing wave or travelling wave transverse RF deflecting structures (TDS) for time resolved (sliced) beam parameter measurements has been presented by David Alesini as one of the key diagnostics for the full characterization of beam properties in LINAC-based Free Electron Lasers [16]. A TDS induces a linear correlation between the longitudinal and the transverse coordinates of short particle (electron) bunches, when

passing at the zero crossing of the RF deflecting voltage. The deflected beam can be imaged on a screen monitor downstream of the TDS, providing a measurement of the longitudinal bunch profile with femto-second time resolution. The characterization of the "sliced" energy distribution (longitudinal phase space) can be achieved by inserting a spectrometer (dipole) magnet in the beam path between TDS and screen monitor. The transverse "sliced" emittances can either be determined by a quadrupole scan performed with a triplet in front of the TDS or by a suitable (FODO) beam lattice downstream of the TDS providing sufficient phase advance in the transverse (non-deflected) plane. Image processing software allows the determination of "sliced" beam parameters by dividing the deflected beam profiles in time slices, which are equal to the width of the un-deflected beam size. Examples of "sliced" emittance measurements and the visualization of the longitudinal trace space using the SPARC TDS are shown in figure 8.

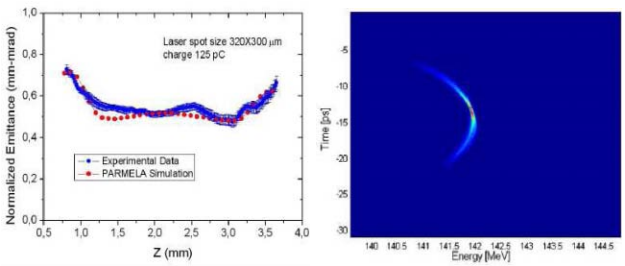

Figure 8 (left): Comparison between "sliced" emittance measurements and PARMELA simulations. Right side: longitudinal trace space of the 140 MeV beam at SPARC. Courtesy of David Alesini.

BLM WITH OPTICAL FIBERS

Friedrich Wulf presented a comprehensive and very instructive overview of beam loss monitoring with optical fibers [17]. He divided optical fiber based loss monitor systems into two categories: the integrating optical power meter as local and global dosimeter systems and the optical time domain reflectometer for time or spatially resolved loss measurements.

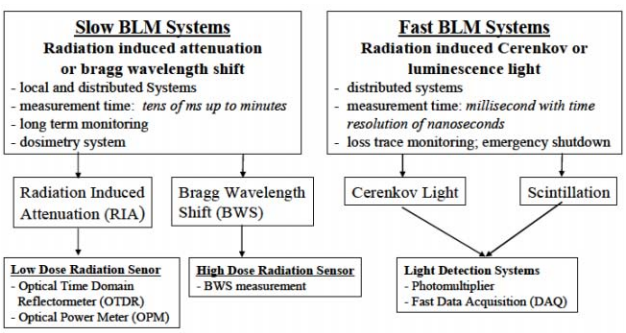

Figure 9: Classification flow chart of beam loss monitor systems using optical fiber sensors. Courtesy of Friedrich Wulf.

For total dose measurements the radiation induced attenuation (RIA) in optical fibers can be used up to a few thousand Gray, while Bragg wavelength shifts are useful for high dose applications. The detection of radiation induced Cerenkov light or luminescence in an optical fiber allows for fast or localized detection of radiation sources. For both applications, the individual characterization of each fiber lot turns out to be indispensible and a key for the actual use of optical fibers as radiation sensors (loss monitors).

As an example for a fiber based monitoring of the total ionization dose (TID) along an accelerator facility, the accumulated dose rate at FLASH has been presented [18].

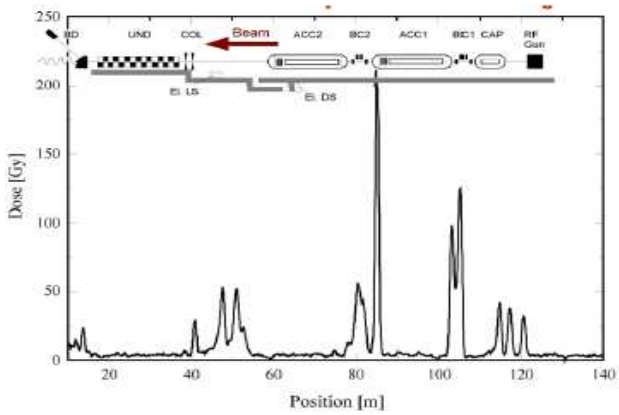

Figure 10: Measured TID at the entire FLASH beam line. Courtesy of Friedrich Wulf.

A fast loss monitor system based on Cerenkov light, which is synchronized to the bunch clock, can provide high position resolution (up to 25 cm) along a beam line, when calibrated with beam line components (e.g.: OTR screens, slits etc.) at known locations. By putting four fibers around the beam pipe (see inlet of figure 11), it is even possible to define the direction of the centroid of the Bremsstrahlung shower.

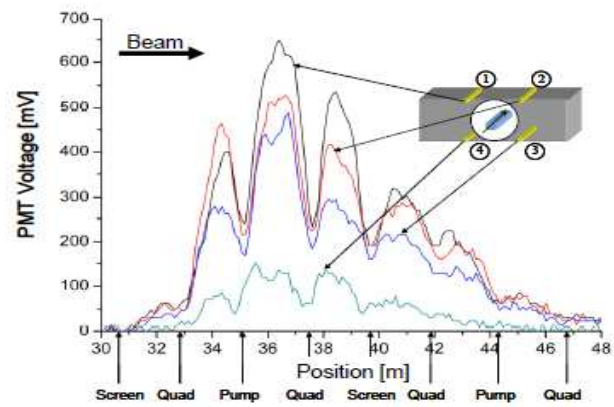

Figure 11: Example of a beam loss position monitor measurement at an interesting part of the accelerator. Courtesy of Friedrich Wulf.

FUTURE REQUIREMENTS

The instrumentation requirements for future accelerator based facilities were reviewed by some contributions, providing perspectives for new trends and tightened performance specifications of diagnostics systems.

The beam diagnostics for the FAIR project at GSI [11, 19] needs to cover for example not only a wide range of intensities for different ion species (10^{11} U_{28+} / pulse to 10^{13} protons / pulse) but should also provide non-invasive turn-by-turn beam profile measurements for monitoring fast profile changes in the SIS 100 heavy ion synchrotron.

Low charge (10 pC) and ultra short pulse (< 10 fs) operation of compact X-ray Free Electron Laser projects such as the SwissFEL at PSI [20, 21] demand not only sub-micron beam trajectory control along the SASE radiation sources (undulators) but also highest RF (< 0.05° S-, C- and X-band phase control) and beam arrival time (< 10 fs) stability on the order of the electron / photon bunch lengths. Optical master oscillators and actively stabilized optical and RF link distributions of the reference signals provide potential solutions for such tight specifications [22]. Electro-optical beam arrival time monitors [23] are newly developed instrumentation to measure the longitudinal stability of the electron bunches on a sub-10 fs scale and to control the amplitude and phase stability of RF systems to the desired level.

The achievement of highest luminosities at future linear colliders (like e.g. the Compact Linear Collider (CLIC) project) require not only beam trajectory measurement and control along the accelerator and in the interaction points to a nanometer scale but may also include the active stabilization of large scale objects like quadrupole magnets on the same level [24]. While first feasibility studies for new measurement systems are already on the way [25], it became clear that only the gradual improvement of diagnostic and feedback systems as well as the high standard of beam instrumentation as presented during DIPAC 2009 will allow a successful realization of these very ambitious future projects.

REFERENCES

[1] For more detailed information about DIPAC 2009 and a full overview of the workshop contributions, please visit the DIPAC 2009 web-page under http://dipac09.web.psi.ch/

[2] http://www.jacow.org/

[3] R. Jones, "Performance and First Experience with the LHC Beam Diagnostics", Proc. DIPAC'09, Basel, Switzerland, 2009

[4] S. Smith et al., "LCLS Cavity Beam Position Monitors", Proc. DIPAC'09, Basel, Switzerland, 2009

[5] H. Maesaka et al., "Beam Diagnostic System of XFEL/Spring8", Proc. DIPAC'09, Basel, Switzerland, 2009

[6] K. Balewski et al., "Commissioning Results of Beam Diagnostics for the PETRA III Light Source", Proc. DIPAC'09, Basel, Switzerland, 2009

[7] Y. Leng et al., "SSRF Beam Diagnostics System Commissioning", Proc. DIPAC'09, Basel, Switzerland, 2009

[8] B. Keil, "Beam Position measurement with Sub-Mircon Resolution", Proc. DIPAC'09, Basel, Switzerland, 2009

[9] N. Hubert et al, "Global orbit Feedback Systems Down to DC using Fast and Slow Correctors", Proc. DIPAC'09, Basel, Switzerland, 2009

[10] P. Kowina et al, "FEM Simulations – a Powerful Tool for BPM Design", Proc. DIPAC'09, Basel, Switzerland, 2009

[11] For more information on the FAIR project, please see: http://www.gsi.de/fair/

[12] D. Lipka, "Cavity BPM Designs, Related Electronics and Measured Performances", Proc. DIPAC'09, Basel, Switzerland, 2009

[13] W. Blokland et al, "Electron Scanner for SNS Ring Profile Measurements", Proc. DIPAC'09, Basel, Switzerland, 2009

[14] F. Becker et al, "Beam Induced Fluorescence Monitor & Imaging Spectrography of Different Working Gases", Proc. DIPAC'09, Basel, Switzerland, 2009

[15] G. Kube et al, "Investigation of the Light Yield of Luminescent Screensfor High Energy and High Intensity Electron Beams", Proc. DIPAC'09, Basel, Switzerland, 2009

[16] D. Alesini et al, "Sliced Beam Parameter Measurements" Proc. DIPAC'09, Basel, Switzerland, 2009

[17] F. Wulf et al, "Beam Loss and Beam Profile Monitoring with Optical Fibers", Proc. DIPAC'09, Basel, Switzerland, 2009

[18] H. Henschel et al, "Fibre Optic Sensor Solutions for Particle Accelerators", Proc. 17th Int. Conf. on Optical Fibre Sensors, Bruges, Belgium, pp 515-518.

[19] M. Schwickert et al, "Beam Diagnostic Developments for FAIR" Proc. DIPAC'09, Basel, Switzerland, 2009

[20] Y. Kim et al, "Beam Diagnostics and RF System Requirements for the SwissFEL Test Facility", Proc. DIPAC'09, Basel, Switzerland, 2009

[21] For more information on the SwissFEL project, please see: http://fel.web.psi.ch/

[22] S. Hunziker et al, "Towards an Ultra Stable Reference Distribution for the New PSI 250 MeV Injector" Proc. DIPAC'09, Basel, Switzerland, 2009

[23] F. Löhl et al, "High Precision Beam Arrival Monitor" Proc. DIPAC'07, Venice, Italy, 2007

[24] J. Carwadine, "Physics Requirements for LINAC Stabilization and Technical Solutions", Proc. DIPAC'09, Basel, Switzerland, 2009

[25] For more information on CLIC beam stability, please see: http://clic-stability.web.cern.ch/clic-stability/

List of Authors

Italic papercodes indicate primary authors

— A —

Abbott, M.G. MOCNB01
Ackermann, W. TUPSM103
Aleksandrov, A.V. *MOIMNB02*
Al-Juboori, H.M. TUPSM103
Allison, S. TUPSM083
Alvarez, M. TUPSM074, TUPSM075
Arthur, J. MOCNB04
Artikova, S.T. WECNB03
Asova, G. TUPSM103

— B —

Baboi, N. TUPSM039, *TUPSM093*
Bacha, B. TUPSM033
Baehr, J.W. *TUPSM103*
Bai, M. TUPSM070
Bantel, M. TUPSM061
Barnes, P.G. TUPSM007
Becker, F. *TUPSM020*
Belohrad, D. B. *TUPSM051*
Benitez, J.Y. TUPSM058, TUPSM061
Berg, W. TUPSM042, TUPSM091
Bernal, S. WECNB03
Bieniosek, F.M. TUPSM020, TUPSM096
Billing, M.G. TUCNB01
Blair, G.A. TUPSM006
Blaskiewicz, M. TUPSM085
Blednykh, A. *TUPSM033*, TUPSM034
Blokland, W. *TUPSM003*
Blot, F. TUPSM100
Boccardi, A. TUPSM066
Böge, M. TUCNB01
Boehme, C. *TUPSM005*
Bonev, A. TUPSM103
Boogert, S.T. TUPSM026
Boorman, G.E. TUPSM006
Borga, A.O. *TUPSM025*, TUPSM086
Borrelli, A. TUPSM033
Bosco, A. TUPSM006
Bousonville, M. *TUPSM088*
Brenger, A. TUPSM039
Brennan, J.M. TUPSM085
Brill, A.R. TUPSM042
Brinkmann, A. TUPSM103
Briscoe, B. TUPSM011
Brossard, J. *TUPSM100*
Browne, J. TUPSM083, TUPSM084
Bucconi, A. TUPSM087
Buechel, A. TUPSM060
Bui, H. TUCNB02
Byrd, J.M. *MOCNB04*, TUPSM081, TUPSM082

— C —

Cameron, P. TUPSM035
Cavalier, S. TUPSM100
Chacon, P. TUPSM014, TUPSM016
Chae, Y.-C. TUPSM064
Chaurize, S. TUPSM076
Chen, J. TUPSM101, TUPSM102
Cheng, W.X. TUPSM065, *TUPSM109*, *TUPSM110*
Chevtsov, P. WECNB02
Chin, M.J. TUPSM112
Chiu, P.C. TUPSM101
Chritin, N.C. TUPSM032
Cohen, S. *TUPSM095*
Collins, J.T. TUPSM050
Connolly, R. *TUPSM010*, *TUPSM011*
Conradie, J.L. TUPSM005
Corbett, W.J. *TUPSM065*
Cross, G.M. TUPSM007

— D —

Dawson, W.C. TUPSM068, TUPSM070
De Monte, R. TUPSM025
De Santis, S. *TUPSM072*
Decker, G. *TUCNB02*, TUPSM043, TUPSM049, TUPSM050
Degen, C. TUPSM011, TUPSM068
Dehler, M.M. TUCNB01
Dehning, B. MOCNB02, TUPSM089
Della Penna, A.J. TUPSM037, *TUPSM097*
DeLong, J.H. TUPSM037
Den Hartog, P.K. TUPSM043
Denard, J.-C. TUPSM023
Dietrich, J. TUPSM005
Dobos, D. MOCNB02
Donat, A. TUPSM103
Dooling, J.C. TUPSM042, *TUPSM091*
Doolittle, L.R. MOCNB04, TUPSM081, TUPSM082
Dorn, C. TUPSM060
Douglas, D. *WEIMNB02*
Dusatko, J.E. *TUPSM083*, *TUPSM084*

— E —

East, G.W. TUPSM095
Eddy, N. TUPSM031
Effinger, E. MOCNB02
Ekdahl, C. TUPSM012
Ellis, R.W. TUPSM095
Ensinger, W. TUPSM019

Erwin, L. TUPSM042, TUPSM050

— F —

Fellenz, B.J. TUPSM031
Ferianis, M. TUPSM025, TUPSM086, *TUPSM087*
Ferreira, M.J. TUPSM033
Fiorito, R.B. *WECNB03*
Fisher, A.S. TUPSM065, TUPSM084, TUPSM091
Fite, J.M. TUPSM010
Fitzgerald, J. TUPSM031
Fliller, R.P. TUPSM098
Floettmann, K. TUPSM103
Forck, P. TUPSM019, TUPSM020, TUPSM071
Fox, J.D. TUPSM080
Frayer, D. *TUPSM012*
Frisch, J.C. MOCNB04
Fukuma, H. TUPSM041
Fukunishi, N. WEIANB02

— G —

Gabor, C. *TUPSM006*
Gaio, G. TUPSM087
Gasior, M. TUCNB01, TUPSM066, *TUPSM067*
Gensch, U. TUPSM103
Giacomini, T. TUPSM020
Gibbs, W.S. *MOKNB01*
Gilbert, B. *TUTNB01*
Gilpatrick, J.D. MOKNB01, MOKNB02, *TUPSM014*, TUPSM016
Gonnin, A. TUPSM100
Goto, A. WEIANB02
Goto, M. TUPSM062
Grabosch, H.-J. TUPSM103
Griesmayer, E. *MOCNB02*
Grote, D.P. TUPSM058
Gruchalla, M.E. TUPSM014, *TUPSM016*
Guetlich, E. TUPSM019
Guinchard, M. TUCNB01
Gulley, M.S. *WETNB01*

— H —

Ha, K.M. TUPSM037
Haber, I. WECNB03
Hacker, K.E. *MOFNB02*
Hänel, M. TUPSM103
Hagmann, M.J. *TUPSM053*, *TUPSM054*
Hajdu, C.F. TUPSM089
Hakobyan, L. TUPSM103
Hama, H. *TUCNB03*
Hanna, B.M. TUPSM076
Harasimowicz, J. *TUPSM047*, *TUPSM048*, *TUPSM047*, *TUPSM048*
Haseitl, R. TUPSM019, TUPSM020
Heller, R. TUPSM103
Henestroza, E. TUPSM096
Hensler, O. TUPSM093
Hill, G. TUPSM113
Hinode, F. TUCNB03
Hiramatsu, S. TUPSM041
Hoffmann, D.H.H. TUPSM020
Holder, D.J. TUPSM103
Hoyt, J.E. TUPSM049
Hseuh, H.-C. TUPSM033
Hsu, K.T. *TUPSM101*, *TUPSM102*
Hsu, S.Y. TUPSM101
Hu, K.H. TUPSM101, TUPSM102
Hu, Y. TUPSM098
Huang, G. MOCNB04, *TUPSM081*, *TUPSM082*
Hubert, N. TUPSM023
Hülsmann, P. TUPSM071

— I —

Ignatenko, A. TUPSM093
Ilinski, P. *MOCNB03*
Intermite, A. *TUPSM046*, *TUPSM046*
Iriso, U. *TUPSM073*, *TUPSM074*
Ishii, H. TUPSM041
Ivanisenko, Ye. TUPSM103

— J —

Jachmann, L. TUPSM103
Jackson, S. TUPSM066, TUPSM089
Jansson, A. TUPSM009
Jao, S. TUPSM010
Jensen, L.K. TUPSM051
Johnson, A.S. TUPSM001
Johnson, B.R. TUPSM085
Johnson, D. TUPSM012
Johnson, R.G. TUPSM027, TUPSM028
Jones, K.W. *MOKNB02*
Jones, O.R. *MOIMNB01*, TUPSM051, TUPSM066
Jore, M. TUPSM100
Joshi, N.Y. TUPSM026

— K —

Kamerdzhiev, V. TUPSM005
Kamigaito, O. WEIANB02
Kase, M. WEIANB02
Kawai, M. TUCNB03
Khojoyan, M.A. TUPSM103
Kishek, R.A. WECNB03
Klemz, G. TUPSM103
Koehler, W. TUPSM103
Kolski, J.S. *TUPSM018*

Kosciuk, B.N. TUPSM033, TUPSM034, TUPSM037, TUPSM098
Kosicek, A. *TUPSM063*
Koss, G. TUPSM103
Kotturi, K.D. TUPSM084
Kowina, P. TUPSM071
Krasilnikov, M. *TUPSM104*, TUPSM103
Krejcik, P. TUPSM083
Kretzschmann, A. TUPSM103
Krinsky, S. TUPSM033
Kuo, C.H. TUPSM101, TUPSM102
Kuzmin, A.M. TUCNB01

— L —

Leban, P. *TUPSM023*, TUPSM063
Lederer, S. TUPSM103
Lee, D. TUPSM101
Lee, S.-H. TUPSM043
Leich, H. TUPSM103
Leitner, D. TUPSM058, TUPSM061, *WEIMNB01*
Lensch, T. *TUPSM040*
Lepercq, P. TUPSM100
Letchford, A.P. TUPSM006
Letourneur, S.B. TUPSM100
Li, Y. TUPSM072
Lidia, S.M. *TUPSM096*
Lill, R.M. TUCNB02, TUPSM028, *TUPSM049*, *TUPSM050*
Lipka, D. *TUPSM039*, TUPSM093
Loehl, F. *MOFNB01*
Loos, H. *MOIANB01*
Ludwig, M. TUPSM051
Lumpkin, A.H. *TUPSM001*
Lund-Nielsen, J. TUPSM039
Lunin, A. TUPSM032
Lyapin, A. TUPSM026
Lyneis, C.M. TUPSM061

— M —

Macek, R.J. TUPSM018
Maesaka, H. TUPSM062
Mahgoub, M. TUPSM103
Maistre, P.-F. TUPSM113
Martin, D.J. TUPSM029
Martinez, D. TUPSM014, TUPSM016
Marusic, A. TUPSM068, TUPSM108
Matsubara, S. TUPSM062
Maumary, Y.A. TUPSM113
McCrady, R.C. TUPSM018, *WEIANB01*
McManamy, T.J. TUPSM003
Mead, J. TUPSM037
Medvedko, E. A. *TUPSM027*
Meier, R. TUPSM098
Meissner, J. TUPSM103
Melkumyan, D. TUPSM103
Meng, W. TUPSM011, TUPSM070
Mercier, B.M. TUPSM100
Mernick, K. TUPSM068, TUPSM070, *TUPSM085*
Meusel, O. TUPSM059
Meyer, T. TUPSM009
Mian, G. TUPSM087
Michelato, P.M. TUPSM103
Michnoff, R.J. TUPSM011, TUPSM108
Militsyn, B.L. TUPSM103
Minty, M.G. TUPSM011, TUPSM068, TUPSM108
Miyahara, F. TUCNB03
Mok, W.Y. TUPSM065
Molloy, S. TUPSM026
Monaco, L. TUPSM103
Monard, H. TUPSM100
Morgan, A.F.D. MOCNB01, *TUPSM026*
Mori, K. TUPSM041
Moritz, P. TUPSM071
Morris, D.K. TUPSM009
Mueller, F. WECNB02
Müller, W.F.O. TUPSM103
Muñoz, R. TUPSM074
Munson, D.V. TUPSM072
Muratori, B.D. TUPSM103
Muto, T. TUCNB03

— N —

Nanbu, K. TUCNB03
Napoly, O. TUPSM038
Narciso, S.J. TUPSM113
Nayak, S. TUPSM011
Neumann, Re. TUPSM093
Ni, P.N. TUPSM020, TUPSM096
Noelle, D. *WECNB01*
Norum, S.R. TUPSM084
Norum, W.E. TUPSM044, TUPSM064
Nuhn, H.-D. TUPSM091

— O —

Obier, F. TUPSM103
Obina, T. TUPSM041
Oddo, P. *TUPSM070*
Olmos, A. TUPSM074, *TUPSM075*
Olsen, J.J. TUPSM084
Oohara, H. TUCNB03
O'Shea, P.G. WECNB03
Otake, Y. *TUPSM062*
Otevrel, M. TUPSM103

— P —

Padrazo, D. *TUPSM098*
Pagani, C. TUPSM103
Pai, C. TUPSM070

Palmer, M.A. TUPSM072
Paramonov, V.V. TUPSM103
Pavlovic, L. TUPSM025, *TUPSM086*
Payne, S.J. TUPSM007
Penno, M. TUPSM103
Perez, F. TUPSM073, TUPSM074, TUPSM075
Pernegger, H. MOCNB02
Pertica, A. TUPSM007
Peters, A. TUPSM060
Petrosyan, B. TUPSM103
Pfingstner, J. TUCNB01
Pietryla, A.F. TUPSM042
Pinayev, I. *TUPSM034*, *TUPSM035*, TUPSM037, TUPSM098
Pogge, J. *TUPSM090*
Pohl, M. TUPSM103
Power, J.F. TUPSM014, TUPSM016
Predonzani, M. TUPSM025, TUPSM086, TUPSM087
Prestel, J.-P. TUPSM038
Prevost, C. TUPSM100
Prieto, P.S. TUPSM031
Ptitsyn, V. *TUPSM108*
Putignano, M. *TUPSM045*, *TUPSM045*, TUPSM046

— R —

Raparia, D. TUPSM011
Ratzinger, U. TUPSM059
Rausch, J. TUPSM088
Ravindran, M.M. *TUVNB01*
Rehm, G. *MOCNB01*, TUPSM026
Reichau, H. *TUPSM059*
Reschke, D. TUPSM103
Richter, D. TUPSM103
Rimjaem, S. TUPSM103
Ripert, M.B. *TUPSM060*
Robert-Demolaize, G. TUPSM108
Rodriguez Esparza, S. *TUPSM013*
Rönsch-Schulenburg, J. TUPSM103
Roser, T. TUPSM070
Rossbach, J. TUPSM103
Rossi, F. TUPSM086, TUPSM087
Rouvière, N. TUPSM038
Roux, R. TUPSM100
Rowland, J. MOCNB01
Ruan, J. TUPSM001
Rueger, C. TUPSM103
Russo, T. TUPSM011, TUPSM068, TUPSM070

— S —

Sachwitz, M. TUPSM103
Saewert, A. TUPSM031
Saisut, J. TUPSM103
Salom, A. TUPSM073
Sandner, W. TUPSM103
Santana-Leitner, M. TUPSM091
Santucci, J.K. TUPSM001
Sasaki, Y. WEIANB02
Satogata, T. TUPSM108
Savioz, J.-J. TUPSM051
Scarpine, V.E. *TUPSM076*, TUPSM099
Scheidt, K.B. TUPSM063
Schlott, V. WECNB02, *THIMNB01*
Schmickler, H. *TUCNB01*, TUPSM032
Schmitz, M. TUPSM093
Schnepp, S. TUPSM103
Schoeneich, B. TUPSM103
Schreiber, S. TUPSM103
Schreiner, J. TUPSM060
Schultze, J. TUPSM103
Sebek, J.J. *TUPSM029*
Sedillo, J.D. *TUPSM015*
Seidl, P.A. TUPSM096
Semenov, A. TUPSM031, TUPSM077
Sertore, D. TUPSM103
Severino, F. TUPSM085
Shaftan, T.V. TUPSM098
Shapovalov, A. TUPSM103, *TUPSM057*
Shaw, L. *MOVNB01*
Shea, T.J. TUPSM003
Shibata, K. TUPSM041
Shkvarunets, A.G. WECNB03
Shoaf, S.E. TUPSM044
Sikora, J.P. TUPSM072
Simon, C.S. *TUPSM038*
Singh, O. TUPSM033, TUPSM034, TUPSM037, TUPSM098
Slimmer, D. TUPSM009
Smirnov, P.A. TUPSM093
Smith, B.G. TUPSM014, TUPSM016
Smith, S.R. TUPSM028, TUPSM027
Soby, L. TUPSM032
Soden, R.A.J. *TUPSM113*
Solyak, N. TUPSM032
Springer, U. *TUPSM071*
Stancari, G. *TUPSM077*
Staples, J.W. MOCNB04, TUPSM081, TUPSM082
Staykov, L. TUPSM057
Steffen, B. *WECNB02*
Steimel, J. TUPSM076, *TUPSM099*
Steinhagen, R.J. *TUPSM066*, TUPSM067
Stephan, F. TUPSM104, TUPSM103
Stevens, J.B. TUPSM044
Straumann, T. TUPSM029
Strohmeier, M.M. TUPSM058, *TUPSM061*
Sun, X. TUPSM049
Susen, R. TUPSM040
Sylte, M.V. TUCNB01

— T —

Tamasaku, K. TUPSM062
Tanaka, H. TUPSM062
Tanaka, Y. TUCNB03
Tanha, M. TUPSM103
Taylor, M.A. TUPSM014
Tejima, M. TUPSM041
Tepikian, S. TUPSM010
Thurman-Keup, R. TUPSM001
Tian, Y. TUPSM037
Tiessen, H. TUPSM093
Tinta, D.T. TUPSM023
Tobiyama, M. *TUPSM041*
Todd, D.S. TUPSM058, TUPSM061
Todd, T. TUPSM009
Togashi, T. TUPSM062
Togawa, K. TUPSM062
Trabocchi, C. TUPSM010
Trowitzsch, G. TUPSM103
Truchard, J.T. TUVNB01
Tsakov, I.I. TUPSM103

— U —

Uzun, I. MOCNB01

— V —

Valishev, A. TUPSM077
Van Winkle, D. *TUPSM080*
Variola, A. TUPSM100
Vashchenko, G. TUPSM103
Vetter, K. TUPSM033, *TUPSM037*
Voy, D.C. TUPSM031
Vu, L.V. TUPSM103

— W —

Wachter, J.V. TUPSM029
Wagner, C. TUPSM059
Walasek-Hoehne, B. *TUPSM019*, TUPSM020
Walther, T. TUPSM103
Wang, X.H. TUPSM103
Watanabe, T. *WEIANB02*
Webber, R.C. TUPSM076, TUPSM099
Weber, J.M. *TUPSM112*
Weiland, T. TUPSM103
Weis, T. TUPSM005
Weisse, S. TUPSM103
Welsch, C.P. TUPSM045, TUPSM046, TUPSM047, TUPSM048, WECNB03, *WEDNB01*, *WEDNB01*
Wendt, M. TUPSM031, *TUPSM032*, TUPSM099
Wenndorff, R.W. TUPSM103
Werner, M. TUPSM040
White, G.R. TUPSM027
White, W.E. MOCNB04
Whitehead, S.A. *TUPSM007*
Wilcox, R.B. MOCNB04, TUPSM081, TUPSM082
Wildman, D. TUPSM076
Wilinski, M. *MOFNB03*, *TUPSM068*
Will, I. TUPSM103
Winde, M. TUPSM103
Winkelmann, T.W. TUPSM060
Winklehner, D. *TUPSM058*, TUPSM061
Wittenburg, K. TUPSM039, TUPSM093

— X —

Xu, J.Z. TUPSM050

— Y —

Yakovlev, V.P. TUPSM032
Yang, B.X. TUCNB02, *TUPSM042*, *TUPSM043*, *TUPSM044*, TUPSM050, TUPSM091
Yang, M.-J. TUPSM009
Yao, C. *TUPSM064*
Young, A. *TUPSM028*, TUPSM080

— Z —

Zagel, J.R. *TUPSM009*
Zamantzas, C. *TUPSM089*
Zhang, D.H. *TUPSM031*, TUPSM076
Zhang, H.D. WECNB03
Zhukov, A.P. TUPSM090, *THTNB01*
Ziomek, C.D. MOVNB01

Institutes List

ADI
Beaverton, Oregon
- Gilbert, B.

ANL
Argonne
- Berg, W.
- Brill, A.R.
- Bui, H.
- Chae, Y.-C.
- Collins, J.T.
- Decker, G.
- Den Hartog, P.K.
- Dooling, J.C.
- Erwin, L.
- Hoyt, J.E.
- Lee, S.-H.
- Lill, R.M.
- Pietryla, A.F.
- Shoaf, S.E.
- Stevens, J.B.
- Sun, X.
- Xu, J.Z.
- Yang, B.X.
- Yao, C.

Agilent Technologies Inc.
Loveland
- Hill, G.
- Narciso, S.J.

Agilent Technologies SA
Plan-les-Ouates
- Maistre, P.-F.
- Maumary, Y.A.
- Soden, R.A.J.

BNL
Upton, Long Island, New York
- Bacha, B.
- Bai, M.
- Blaskiewicz, M.
- Blednykh, A.
- Borrelli, A.
- Brennan, J.M.
- Briscoe, B.
- Cameron, P.
- Cheng, W.X.
- Connolly, R.
- Dawson, W.C.
- DeLong, J.H.
- Degen, C.
- Della Penna, A.J.
- Ferreira, M.J.
- Fite, J.M.
- Fliller, R.P.
- Hseuh, H.-C.
- Hu, Y.
- Ilinski, P.
- Jao, S.
- Johnson, B.R.
- Kosciuk, B.N.
- Krinsky, S.
- Marusic, A.
- Mead, J.
- Meier, R.
- Meng, W.
- Mernick, K.
- Michnoff, R.J.
- Minty, M.G.
- Nayak, S.
- Oddo, P.
- Padrazo, D.
- Pai, C.
- Pinayev, I.
- Ptitsyn, V.
- Raparia, D.
- Robert-Demolaize, G.
- Roser, T.
- Russo, T.
- Satogata, T.
- Severino, F.
- Shaftan, T.V.
- Singh, O.
- Tepikian, S.
- Tian, Y.
- Trabocchi, C.
- Vetter, K.
- Wilinski, M.
- Ha, K.M.

Bira
Albuquerque, New Mexico
- Cohen, S.

CEA
Gif-sur-Yvette
- Napoly, O.
- Simon, C.S.

CELLS-ALBA Synchrotron
Cerdanyola del Vallès
- Alvarez, M.
- Iriso, U.
- Muñoz, R.
- Olmos, A.
- Perez, F.
- Salom, A.

CERN
Geneva
- Belohrad, D. B.
- Boccardi, A.

- Chritin, N.C.
- Dehning, B.
- Dobos, D.
- Effinger, E.
- Gasior, M.
- Griesmayer, E.
- Guinchard, M.
- Hajdu, C.F.
- Jackson, S.
- Jensen, L.K.
- Jones, O.R.
- Kuzmin, A.M.
- Ludwig, M.
- Pernegger, H.
- Pfingstner, J.
- Savioz, J.-J.
- Schmickler, H.
- Smith, S.R.
- Soby, L.
- Steinhagen, R.J.
- Sylte, M.V.
- Zamantzas, C.

CLASSE
Ithaca, New York
- Billing, M.G.
- Li, Y.
- Loehl, F.
- Palmer, M.A.
- Sikora, J.P.

Cockcroft Institute
Warrington, Cheshire
- Harasimowicz, J.
- Intermite, A.
- Putignano, M.
- Welsch, C.P.

DELTA
Dortmund
- Weis, T.

DESY Zeuthen
Zeuthen
- Al-Juboori, H.M.
- Donat, A.
- Gensch, U.
- Grabosch, H.-J.
- Hakobyan, L.
- Heller, R.
- Hänel, M.
- Ignatenko, A.
- Ivanisenko, Ye.
- Jachmann, L.
- Khojoyan, M.A.
- Klemz, G.
- Koehler, W.
- Koss, G.
- Krasilnikov, M.
- Kretzschmann, A.
- Leich, H.
- Mahgoub, M.
- Meissner, J.
- Melkumyan, D.
- Otevrel, M.
- Penno, M.
- Petrosyan, B.
- Pohl, M.
- Rimjaem, S.
- Rueger, C.
- Sachwitz, M.
- Schoeneich, B.
- Schultze, J.
- Shapovalov, A.
- Staykov, L.
- Stephan, F.
- Tanha, M.
- Trowitzsch, G.
- Vashchenko, G.
- Vu, L.V.
- Walther, T.
- Wang, X.H.
- Weisse, S.
- Wenndorff, R.W.
- Winde, M.

DESY
Hamburg
- Baboi, N.
- Baehr, J.W.
- Brenger, A.
- Brinkmann, A.
- Floettmann, K.
- Hacker, K.E.
- Hensler, O.
- Krasilnikov, M.
- Lederer, S.
- Lensch, T.
- Lipka, D.
- Lund-Nielsen, J.
- Neumann, Re.
- Noelle, D.
- Obier, F.
- Reschke, D.
- Schmitz, M.
- Schreiber, S.
- Smirnov, P.A.
- Susen, R.
- Tiessen, H.
- Werner, M.
- Wittenburg, K.

Diamond
Oxfordshire
- Abbott, M.G.
- Morgan, A.F.D.
- Rehm, G.
- Rowland, J.

- Uzun, I.

ELETTRA
Basovizza
- Borga, A.O.
- Bucconi, A.
- De Monte, R.
- Ferianis, M.
- Gaio, G.
- Mian, G.
- Pavlovic, L.
- Predonzani, M.
- Rossi, F.

ESRF
Grenoble
- Scheidt, K.B.

FNRF
Chiang Mai
- Saisut, J.

FZJ
Jülich
- Dietrich, J.
- Kamerdzhiev, V.

Fermilab
Batavia
- Chaurize, S.
- Eddy, N.
- Fellenz, B.J.
- Fitzgerald, J.
- Hanna, B.M.
- Jansson, A.
- Johnson, A.S.
- Lumpkin, A.H.
- Lunin, A.
- Meyer, T.
- Morris, D.K.
- Prieto, P.S.
- Ruan, J.
- Saewert, A.
- Santucci, J.K.
- Scarpine, V.E.
- Semenov, A.
- Slimmer, D.
- Solyak, N.
- Stancari, G.
- Steimel, J.
- Thurman-Keup, R.
- Todd, T.
- Valishev, A.
- Voy, D.C.
- Webber, R.C.
- Wendt, M.
- Wildman, D.
- Yakovlev, V.P.
- Yang, M.-J.
- Zagel, J.R.
- Zhang, D.H.

GSI
Darmstadt
- Becker, F.
- Bousonville, M.
- Dorn, C.
- Forck, P.
- Giacomini, T.
- Haseitl, R.
- Hülsmann, P.
- Kowina, P.
- Moritz, P.
- Springer, U.
- Walasek-Hoehne, B.

HIT
Heidelberg
- Buechel, A.
- Peters, A.
- Ripert, M.B.
- Schreiner, J.
- Winkelmann, T.W.

Hamamatsu Photonics K.K.
Hamamatsu-city
- Goto, M.

Helmholtz-Zentrum Berlin für Materialien und Energie GmbH
Berlin
- Richter, D.

I-Tech
Solkan
- Kosicek, A.
- Leban, P.
- Tinta, D.T.

IAP
Frankfurt am Main
- Meusel, O.
- Ratzinger, U.
- Reichau, H.
- Wagner, C.

INFN/LASA
Segrate (MI)
- Michelato, P.M.
- Monaco, L.
- Pagani, C.
- Sertore, D.

INRNE
Sofia
- Asova, G.
- Bonev, A.
- Tsakov, I.I.

IPN
Orsay
- Prestel, J.-P.
- Rouvière, N.

IUCMB
Bloomington, Indiana
- East, G.W.
- Ellis, R.W.

JAI
Egham, Surrey
- Boogert, S.T.
- Joshi, N.Y.

JASRI/SPring-8
Hyogo-ken
- Matsubara, S.
- Togashi, T.

JLAB
Newport News, Virginia
- Chevtsov, P.
- Douglas, D.

KEK
Ibaraki
- Fukuma, H.
- Hiramatsu, S.
- Ishii, H.
- Mori, K.
- Obina, T.
- Shibata, K.
- Tejima, M.
- Tobiyama, M.

LAL
Orsay
- Blot, F.
- Brossard, J.
- Cavalier, S.
- Gonnin, A.
- Jore, M.
- Lepercq, P.
- Letourneur, S.B.
- Mercier, B.M.
- Monard, H.
- Prevost, C.
- Roux, R.
- Variola, A.

LANL
Los Alamos, New Mexico
- Chacon, P.
- Ekdahl, C.
- Gibbs, W.S.
- Gilpatrick, J.D.
- Gruchalla, M.E.
- Gulley, M.S.
- Jones, K.W.
- Kolski, J.S.
- Macek, R.J.
- Martinez, D.
- McCrady, R.C.
- Power, J.F.
- Rodriguez Esparza, S.
- Sedillo, J.D.
- Smith, B.G.
- Taylor, M.A.

LBNL
Berkeley, California
- Benitez, J.Y.
- Bieniosek, F.M.
- Byrd, J.M.
- Chin, M.J.
- De Santis, S.
- Doolittle, L.R.
- Henestroza, E.
- Huang, G.
- Leitner, D.
- Lidia, S.M.
- Lyneis, C.M.
- Munson, D.V.
- Ni, P.N.
- Norum, W.E.
- Seidl, P.A.
- Staples, J.W.
- Strohmeier, M.M.
- Todd, D.S.
- Weber, J.M.
- Wilcox, R.B.
- Winklehner, D.

LLNL
Livermore, California
- Grote, D.P.

Life Imaging Technology
Palo Alto, California
- Mok, W.Y.

MBI
Berlin
- Sandner, W.
- Will, I.

MEPhI
Moscow
- Shapovalov, A.

MPI-K
Heidelberg
- Artikova, S.T.

NSRRC
Hsinchu
- Chen, J.
- Chiu, P.C.
- Hsu, K.T.
- Hsu, S.Y.
- Hu, K.H.
- Kuo, C.H.
- Lee, D.

NSTec
Los Alamos, New Mexico
- Frayer, D.
- Johnson, D.

National Instruments
Austin
- Ravindran, M.M.
- Truchard, J.T.

NewPath
Salt Lake City, Utah
- Hagmann, M.J.

ORNL
Oak Ridge, Tennessee
- Aleksandrov, A.V.
- Blokland, W.
- McManamy, T.J.
- Pogge, J.
- Shea, T.J.
- Zhukov, A.P.

PSI
Villigen
- Böge, M.
- Dehler, M.M.
- Mueller, F.
- Schlott, V.
- Steffen, B.

RAS/INR
Moscow
- Paramonov, V.V.

RIKEN Nishina Center
Wako
- Fukunishi, N.
- Goto, A.
- Kamigaito, O.
- Kase, M.
- Sasaki, Y.
- Watanabe, T.

RIKEN/SPring-8
Hyogo
- Maesaka, H.
- Otake, Y.
- Tamasaku, K.
- Tanaka, H.
- Togawa, K.

Royal Holloway, University of London
Surrey
- Blair, G.A.
- Boorman, G.E.
- Bosco, A.
- Molloy, S.

SLAC
Menlo Park, California
- Allison, S.
- Arthur, J.
- Browne, J.
- Corbett, W.J.
- Dusatko, J.E.
- Fisher, A.S.
- Fox, J.D.
- Frisch, J.C.
- Johnson, R.G.
- Kotturi, K.D.
- Krejcik, P.
- Loos, H.
- Martin, D.J.
- Medvedko, E. A.
- Norum, S.R.
- Nuhn, H.-D.
- Olsen, J.J.
- Santana-Leitner, M.
- Sebek, J.J.
- Smith, S.R.
- Straumann, T.
- Van Winkle, D.
- Wachter, J.V.
- White, G.R.
- White, W.E.
- Young, A.

SOLEIL
Gif-sur-Yvette
- Denard, J.-C.
- Hubert, N.

STFC/DL/ASTeC
Daresbury, Warrington, Cheshire
- Holder, D.J.
- Militsyn, B.L.
- Muratori, B.D.

STFC/RAL/ASTeC
Chilton, Didcot, Oxon
- Gabor, C.

STFC/RAL/ISIS
Chilton, Didcot, Oxon
- Barnes, P.G.
- Cross, G.M.
- Letchford, A.P.
- Payne, S.J.
- Pertica, A.
- Whitehead, S.A.

TEMF, TU Darmstadt
Darmstadt
- Ackermann, W.
- Müller, W.F.O.
- Schnepp, S.
- Weiland, T.

TU Darmstadt
Darmstadt
- Guetlich, E.
- Hoffmann, D.H.H.

TUD
Darmstadt
- Rausch, J.

Technical University Darmstadt
Darmstadt
- Ensinger, W.

The University of Liverpool
Liverpool
- Harasimowicz, J.
- Intermite, A.
- Putignano, M.
- Welsch, C.P.

Tohoku University, School of Scinece
Sendai
- Hama, H.
- Hinode, F.
- Kawai, M.
- Miyahara, F.
- Muto, T.
- Nanbu, K.
- Oohara, H.
- Tanaka, Y.

UCL
London
- Lyapin, A.

UMD
College Park, Maryland
- Bernal, S.
- Fiorito, R.B.
- Haber, I.
- Kishek, R.A.
- O'Shea, P.G.
- Shkvarunets, A.G.
- Zhang, H.D.

Uni HH
Hamburg
- Rossbach, J.
- Rönsch-Schulenburg, J.

UniDo/IBS
Dortmund
- Boehme, C.

University of Applied Sciences Karlsruhe
Karlsruhe
- Bantel, M.

ZTEC Instruments
Albuquerque
- Shaw, L.
- Ziomek, C.D.

iThemba LABS
Somerset West
- Conradie, J.L.

BIW10 REGISTERED PARTICIPANTS (177)

Aleksandrov, Alexander
Oak Ridge National Laboratory

Artinian, Sebastien
GMW/Bergoz Instrumentation

Baboi, Nicoleta
DESY

Bachimanchi, Ramakrishna
Jefferson Lab

Barnes, Peter
STFC/RAL/ISIS

Baros, Dolores
Los Alamos National Laboratory

Barry, Walter
Lawrence Berkeley National Laboratory

Batygin, Yuri
Los Alamos National Laboratory

Becker, Frank
GSI Helmholtzzentrum für Schwerionenforschung GmbH

Belohrad, David
CERN

Bergoz, Julien
GMW/Bergoz Instrumentation

Boehme, Christian
University of Dortmund, Germany

Bonal, David
National Instruments

Borga, Andrea
Sincrotrone Trieste

Bousonville, Michael
GSI Helmholtzzentrum für Schwerionenforschung GmbH

Brossard, Julien
LAL-IN2P3-CNRS

Brown, Alex
Diamond Detectors Ltd.

Byrd, John
Lawrence Berkeley National Laboratory

Canfield, Brad
TDK-Lambda Americas

Cheng, Weixing
Brookhaven National Laboratory

Chin, John
Magnetic Metals Corp

Chin, Michael
Lawrence Berkeley National Laboratory

Cohen, Stanley
BiRa Systems, Inc.

Combettes, Bruno
Photonis

Connolly, Roger
Brookhaven National Laboratory

Corbett, Jeff
SLAC National Accelerator Laboratory

Debelle, Thierry
National Instruments

Decker, Glenn
Argonne National Laboratory

Della Penna, Al J.
Brookhaven National Laboratory

Dietrich, Juergen
Forschungszentrum Juelich

Dooling, Jeffrey
Argonne National Laboratory

Douglas, David R.
Jefferson Lab

Dusatko, John
SLAC National Laboratory

East, Gary
Indiana University

Erickson, John
Los Alamos National Laboratory

Evtushenko, **Pavel**
Jefferson Lab

Ferianis, Mario
Sincrotrone Trieste

Fiorito, Ralph
University of Maryland

Ford, Dan
Ophir-Spiricon

Frayer, Daniel
National Security Technologies, LLC

Gabor, Christoph
STFC/RAV (ASTEC)

Garcia, Fernanda
Fermilab

Gasior, Marek
CERN

Gilbert, Barrie
Analog Devices, Inc.

Gillespie, William
University of Dundee

Gilpatrick, Doug
Los Alamos National Laboratory

Gratz, Jeff
Matsusada Precision, Inc.

Griesmayer, Clara
Cividec Instrumentation

Griesmayer, Erich
Cividec Instrumentation

Gruchalla, Michael
Los Alamos National Laboratory

Gulley, Mark
Los Alamos National Laboratory

Hacker, Kirsten
DESY/University of Hamburg

Hagmann, Mark
Newpath Research L.L.C.

Hama, Hiroyuki
Tohoku University

Hamill, Alan
Photonis

Hansli, Matthias
Technische Universitat Darmstadt

Harasimowicz, Janusz
University of Liverpool

Hassell, Robin
Agilent Technologies

Hsu, Kuo-Tung
NSRRC

Huang, Gang
Lawrence Berkeley National Laboratory

Ilinski, Petr
Brookhaven National Laboratory

Iriso, Ubaldo
CELLS

Jacobs, Ken
University of Wisconsin, SRC

Jansson, Andreas
Fermilab

Johns, Glen
Los Alamos National Laboratory

Johnson, Kenneth
Los Alamos National Laboratory

Jones, Kevin
Los Alamos National Laboratory

Jones. Rhodri
CERN

Jordan, Kevin
Jefferson Lab

Kawall, David
University of Massachusetts

Kibilko, Mark
CAEN Technologies, Inc.

Kirsch, Matthias
Struck Innovative Systeme GmbH

Kolski, Jeffrey
Los Alamos National Laboratory

Kosciuk, Bernie
Brookhaven National Laboratory

Kosicek, Andre J.
Instrumentation Technologies

Kowalski, Powel
BiRa Systems, Inc.

Kowina, Piotr
GSI Darmstadt

Krasilnikov, Mikhail
DESY

Kutac, Vincent
Los Alamos National Laboratory

Laprade, Bruce
Photonis

Latam, Chris
Oerlikon Leybold Vacuum

Leban, Peter
Instrumentation Technologies

Leitner, Daniela
Lawrence Berkeley National Laboratory

Lensch, Timmy
DESY

Lidia, Steven
Lawrence Berkeley National Laboratory

Lill, Robert
Argonne National Laboratory

Lipka, Dirk
DESY

Loehl, Florian
Cornell University

Loos, Henrik
SLAC

Lumpkin, Alex
Fermilab

Madison, Terry
Los Alamos National Laboratory

Marawar, Ravi
National Instruments

Marques, Sergio
Brazilian Synchrotron Light Source

Marroquin, Pilar
Los Alamos National Laboratory

Marshall, Patrick
Matsusada Precision, Inc.

McCrady, Rodney
Los Alamos National Laboratory

McDonnell, Ed
National Instruments

Mernick, Kevin
Brookhaven National Laboratory

Militello, Sal
Oerlikon Leybold Vacuum

Morgan, Alun F. D.
Diamond Light Source

Murray, Dave
Times Microwave Systems

Nölle, Dirk
DESY

Oddo, Peter
Brookhaven National Laboratory

Otake, Yuji
RIKEN

Padrazo, Danny
Brookhaven National Laboratory

Papadopoulos, Christos
Lawrence Berkeley National Laboratory

Pasquinelli, Ralph J.
Fermilab

Parber, Jonathan
Times Microwave Systems

Payne, Steve
STFC, Rutherford Appleton Laboratory

Pieck, Martin
Los Alamos National Laboratory

Pillai, Chandra
Los Alamos National Laboratory

Pinayev, Igor
Brookhaven National Laboratory

Pogge, James
SNS Oak Ridge

Portmann, Gregory
Lawrence Berkeley National Laboratory

Ptitsyn, Vadim
Brookhaven National Laboratory

Ravindran, Murali
National Instruments

Reed, Jeff
Pearson Electronics, Inc.

Rehm, Guenther
Diamond Light Source

Reichau, Hermine
J.W.G. University Frankfurt

Repic, Borut|
Instrumentation Technologies

Richter, Brian
GMW Associates

Ripert, Marion
Heidelberg Ion Beam Therapy Center

Rodriguez Esparza, Sergio
Los Alamos National Laboratory

Rossi, Fabio
Sincrotrone Trieste S.C.p.A.

Russo, Thomas
Brookhaven National Laboratory

Sanchez, Manuel
Times Microwave Systems

Sanfelici, Lucas
Brazilian Synchrotron Light Source

Scarpine, Victor
Fermilab

Schlott, Volker
Paul Scherrer Institut

Schmickler, Hermann
CERN

Schwellenbach, David
National Security Technologies, LLC

Sebek, James
SSRL/SLAC

Sedillo, James
Los Alamos National Laboratory

Serio, Mario
INFN-LNF

Shapovalov, Andrey
DESY

Shaw, Boyd
ZTEC

Shea, Thomas
Oak Ridge National Laboratory

Shelley, Fred
Los Alamos National Laboratory

Simon, Claire
CEA/Saclay

Singh, Om
Brookhaven National Laboratory

Smith, Brian
Los Alamos National Laboratory

Smith, Stephen
SLAC/CERN

Soden, Richard
Agilent Technologies

Spruit, Dan
TDK-Lambda Americas

Stancari, Giulio
Fermilab

Steimel, Jim
Fermilab

Sun. Xiang
Argonne National Laboratory

Tanaka, Hitoshi
RIKEN

Teytelman, Dmitry
Dimtel, Inc.

Tobiyama, Makoto
KEK, Accelerator Laboratory

Toshiyuki, Mitsuhashi
SLAC National Accelerator Laboratory

Truchard, James
National Instruments

Van Winkle, Daniel
KEK, Accelerator Laboratory

Vetter, Kurt
Brookhaven National Laboratory

Walasek-Hoehne, Beata
GSI

Wang, Jingsong
CST of America

Watanabe, Tamaki
RIKEN Nishine Center

Waters, Chris
Pearson Electronics, Inc.

Webber, Robert
Fermilab

Weber, Jonah
Lawrence Berkeley Nation
al Laboratory
Welsch, Carsten P.
University of Liverpool

Wendt, Manfred
Fermilab

Whitehead, Sarah
STFC/RAL/ISIS

Wilcox, Nicholas
National Security Technologies, LLC

Wilinski, Michelle
Brookhaven National Laboratory

Winkler, Marty
Times Microwave Systems

Wissman, Mark
Jefferson Lab

Wittenburg, Kay
DESY

Yang, Bingxin
Argonne National Laboratory

Yao, Chihyuan
Argonne National Laboratory

Yin, Yan
YY Labs, Inc.

Young, Andrew
SLAC

Zagel, James
Fermilab

Zamatzas, Christos
CERN

Zhang, Dehong
Fermilab

Zhang, Hao
IREAP, University of Maryland, College
Park Energy Research Facility

Zhukov, Alexander
Oak Ridge National Laboratory